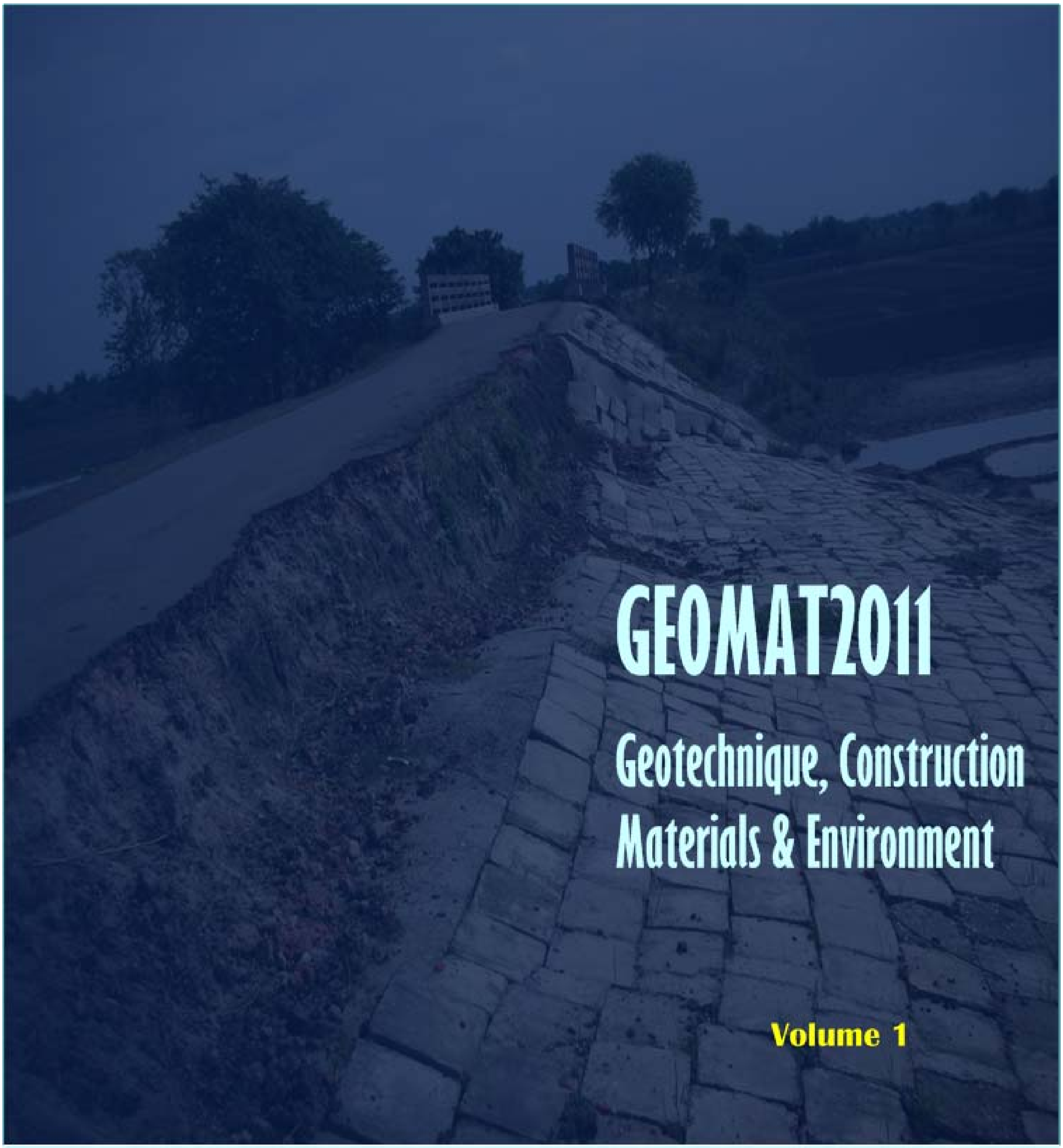

GEOMAT2011

Geotechnique, Construction Materials & Environment

Volume 1

Md. Zakaria Hossain and Toshinori Sakai — Editors

GEOMAT2011 MIE
GEOTECHNIQUE, CONSTRUCTION MATERIALS AND ENVIRONMENT

PROCEEDINGS OF FIRST INTERNATIONAL CONFERENCE - GEOMAT2011
GEOTECHNIQUE, CONSTRUCTION MATERIALS AND ENVIRONMENT MIE JAPAN, 21-23 NOVEMBER, 2011

Geotechnique, Construction Materials and Environment

Volume 1

Edited by

Md. Zakaria Hossain
Department of Environmental Science and Technology
Mie University

Toshinori Sakai
Department of Environmental Science and Technology
Mie University

THE GEOMATE INTERNATIONAL SOCIETY, MIE 2011

Published by:
The GEOMATE International Society
Tsu city, Mie, Japan
E-mail: geomate@gi-j.com
www.gi-j.com

ISBN Number: 978-4-9905958-0-7 C3051

Printed in Japan

First International Conference on Geotechnique, Construction Materials and Environment, Mie, Japan, Nov.21-23, 2011, ISBN: 978-4-9905958-0-7 C3051

Table of Contents

Construction materials

Environment

First International Conference on Geotechnique, Construction Materials and Environment, Mie, Japan, Nov.21-23, 2011, ISBN: 978-4-9905958-0-7 C3051

Preface

The First International Conference on Geotechnique, Construction Materials and Environment GEOMAT2011 is organized in Center Palace Miyako Hotel, Tsu city, Mie Japan in conjunction with Japanese Geotechnical Society (JGS), Japanese Society of Irrigation Drainage and Rural Engineering (JSIDRE), Mie University, JCK Comp. Ltd and Glorious International. It aims to provide with great opportunities to share common interests on geo-engineering, construction materials, environmental issues, water resources, and earthquake and tsunami disasters. The key objective of this conference is to promote interdisciplinary research from various regions of the globe. On Friday 11 March at 14:46 Japan Standard Time, the north east of Japan was severely damaged by the tragic earthquake and tsunami. The conference is dedicated to the tragic Tohoku-Kanto earthquake and tsunami disasters.
The conference has 3 major themes with 17 specific themes including

- Advances in Composite Materials
- Computational Mechanics
- Foundation and Retaining Walls
- Slope Stability
- Soil Dynamics
- Soil-Structure Interaction
- Pavement Technology
- Tunnels and Anchors
- Site Investigation and Rehabilitation
- Ecology and Land Development
- Water Resources Planning
- Environmental Management
- Public Health and Rehabilitation
- Earthquake and Tsunami Issues
- Safety and Reliability
- Geo-Hazard Mitigation
- Case History and Practical Experience

The proceedings contain 7 keynote papers along with 115 technical papers from 22 countries. The technical papers are selected from the vast number of contributions submitted, after review of the abstracts. The final papers included in the proceedings have been peer reviewed rigorously and revised as necessary by the authors. We are grateful to the authors of the contributed papers for their resourceful papers and their help in maintaining the high assessment of the papers and the co-operation in complying with the requirements of the editor and the reviewers. We wish to express our sincere thanks to the Organizing Committee Members, National Advisory Committee Members and International Advisory Committee Members for their valuable supports. We acknowledge the support of Japanese Geotechnical Society (JGS), Japanese Society of Irrigation Drainage and Rural Engineering (JSIDRE), Mie University, JCK Comp. Ltd and Glorious International.

Prof. Dr. Toshinori Sakai
Conference Chairman

Dr. Md. Zakaria Hossain
Conference Secretary

Organization

Scientific Committees:

Conference Chairman: Prof. Dr. Toshinori Sakai, Mie University, Japan
Conference Honorary Chairman: E/Prof. Dr. Sohji Inoue, Mie University, Japan

Conference Organizing Committee:

Prof. Dr. Takamitsu Kajisa, Mie University, Japan
Prof. Dr. Ishiguro Satoru, Mie University, Japan
Prof. Dr. Sigeko Haruyama, Mie University, Japan
A/Prof. Dr. Atsushi Ishii, Mie University, Japan
A/Prof. Dr. Maasaki Kondo, Mie University, Japan
A/Prof. Dr. Kenji Okajima, Mie University, Japan
A/Prof. Dr. Ryoei Ito, Mie University, Japan

National Advisory Committee:

Prof. Dr. Fumio Tatsuoka, Tokyo University of Science, Japan
Prof. Dr. Kazunori Uchida, Kobe University, Japan
Prof. Dr. Fusao Oka, Kyoto University, Japan
Prof. Dr. Jing-Cai Jiang, University of Tokushima, Japan
Prof. Dr. Akira Murakami, Kyoto University, Japan
E/Prof. Dr. Tadatsugu Tanaka, University of Tokyo, Japan
A/Prof. Dr. Kingshuk Roy, Nihon University, Japan
A/Prof. Dr. Md. Shahin Hossain, Nagoya Institute of Technology, Japan
A/Prof. Dr. Sayuri Kimoto, Kyoto University, Japan
Engr. Hirondo Inagali, President, JCK Com. Ltd. Japan
A/Prof. Dr. Inui Toru, Kyoto University, Japan
A/Prof. Dr. Fujisawa Kazunori, Okayama University, Japan
A/Prof. Dr. Inoue Kazuya, Kobe University, Japan

International Advisory Committee:

Prof Sai Vanapalli, University of Ottawa, Canada
Prof. Dr. Mounir Bouassida, National School of Engineering of Tunis
Prof. Dr. Lilia Robles Austriaco, Angles University Foundation, Philippines
Prof. Dr. A.S.M. Abdul Awal, University Technology Malaysia, Malaysia
Prof. Dr. Muhammad Ibn Ibrahimy, International Islamic University, Malaysia
Prof. Dr. Zahurul Islam, Bangladesh University of Engineering and Technology, Bangladesh
Prof. Dr. Bujang B.K. Huat, University Putra Malaysia, Malaysia
Prof. Dr. Nemy Banthia, University of British Columbia, Canada
Prof. Dr. Ian Jefferson, University of Birmingham, UK
Prof. Dr. John Bolander, Univesity of California, USA
Prof. Dr. Shamshul Chowdhury, Roosevelt University, USA
Prof. Dr. Isabel Pinto, University of Coimbra, Portugal
A/Prof. Mark Jaksa, University of Adelaide, Australia
A/Prof. Dr. William Sebudde Kaggwa, University of Adelaide, Australia
Dr. John N. Mukabi, President of Kenya Geotechncal Society, Kenya

Conference Secretariat:

Dr. Zakaria Hossain, Associate Professor
Division of Environmental Science and Technology
Graduate School of Bioresources
Mie University, 1577 Kurima Machiya-cho
Tsu-city, Mie 514-8507, Japan
E-mail: zakaria@bio.mie-u.ac.jp
Tel: +81-59-231-9578、Fax: +81-59-231-9591

Editorial Committee:

Md. Zakaria Hossain
Md. Bellal Hossain
Toshinori Sakai
Md. Toriqul Islam

Executive Committee:

Toshinori Sakai
Md. Zakaria Hossain
Md. Bellal Hossain
Kazuki Ito
Md. Toriqul Islam
Muhammad Ibn Ibrahimy
Ms. Emi Ueno
Ms. Mayumi Matsumoto

GEOMAT2011 MIE
GEOTECHNIQUE, CONSTRUCTION MATERIALS AND ENVIRONMENT

PROCEEDINGS OF FIRST INTERNATIONAL CONFERENCE - GEOMAT2011
GEOTECHNIQUE, CONSTRUCTION MATERIALS AND ENVIRONMENT MIE JAPAN, 21-23 NOVEMBER, 2011

Geotechnique, Construction Materials and Environment

Volume 2

Edited by

Md. Zakaria Hossain
Department of Environmental Science and Technology
Mie University

Toshinori Sakai
Department of Environmental Science and Technology
Mie University

THE GEOMATE INTERNATIONAL SOCIETY, MIE 2011

Published by:
The GEOMATE International Society
Tsu city, Mie, Japan
E-mail: geomate@gi-j.com
www.gi-j.com

ISBN Number: 978-4-9905958-0-7 C3051

Printed in Japan

Table of Contents

First International Conference on Geotechnique, Construction Materials and Environment, Mie, Japan, Nov.21-23, 2011, ISBN: 978-4-9905958-0-7 C3051

Preface

The First International Conference on Geotechnique, Construction Materials and Environment GEOMAT2011 is organized in Center Palace Miyako Hotel, Tsu city, Mie Japan in conjunction with Japanese Geotechnical Society (JGS), Japanese Society of Irrigation Drainage and Rural Engineering (JSIDRE), Mie University, JCK Comp. Ltd and Glorious International. It aims to provide with great opportunities to share common interests on geo-engineering, construction materials, environmental issues, water resources, and earthquake and tsunami disasters. The key objective of this conference is to promote interdisciplinary research from various regions of the globe. On Friday 11 March at 14:46 Japan Standard Time, the north east of Japan was severely damaged by the tragic earthquake and tsunami. The conference is dedicated to the tragic Tohoku-Kanto earthquake and tsunami disasters.

The conference has 3 major themes with 17 specific themes including

- Advances in Composite Materials
- Computational Mechanics
- Foundation and Retaining Walls
- Slope Stability
- Soil Dynamics
- Soil-Structure Interaction
- Pavement Technology
- Tunnels and Anchors
- Site Investigation and Rehabilitation
- Ecology and Land Development
- Water Resources Planning
- Environmental Management
- Public Health and Rehabilitation
- Earthquake and Tsunami Issues
- Safety and Reliability
- Geo-Hazard Mitigation
- Case History and Practical Experience

The proceedings contain 7 keynote papers along with 115 technical papers from 22 countries. The technical papers are selected from the vast number of contributions submitted, after review of the abstracts. The final papers included in the proceedings have been peer reviewed rigorously and revised as necessary by the authors. We are grateful to the authors of the contributed papers for their resourceful papers and their help in maintaining the high assessment of the papers and the co-operation in complying with the requirements of the editor and the reviewers. We wish to express our sincere thanks to the Organizing Committee Members, National Advisory Committee Members and International Advisory Committee Members for their valuable supports. We acknowledge the support of Japanese Geotechnical Society (JGS), Japanese Society of Irrigation Drainage and Rural Engineering (JSIDRE), Mie University, JCK Comp. Ltd and Glorious International.

Prof. Dr. Toshinori Sakai
Conference Chairman

Dr. Md. Zakaria Hossain
Conference Secretary

Organization

Scientific Committees:

Conference Chairman: Prof. Dr. Toshinori Sakai, Mie University, Japan
Conference Honorary Chairman: E/Prof. Dr. Sohji Inoue, Mie University, Japan

Conference Organizing Committee:

Prof. Dr. Takamitsu Kajisa, Mie University, Japan
Prof. Dr. Ishiguro Satoru, Mie University, Japan
Prof. Dr. Sigeko Haruyama, Mie University, Japan
A/Prof. Dr. Atsushi Ishii, Mie University, Japan
A/Prof. Dr. Maasaki Kondo, Mie University, Japan
A/Prof. Dr. Kenji Okajima, Mie University, Japan
A/Prof. Dr. Ryoei Ito, Mie University, Japan

National Advisory Committee:

Prof. Dr. Fumio Tatsuoka, Tokyo University of Science, Japan
Prof. Dr. Kazunori Uchida, Kobe University, Japan
Prof. Dr. Fusao Oka, Kyoto University, Japan
Prof. Dr. Jing-Cai Jiang, University of Tokushima, Japan
Prof. Dr. Akira Murakami, Kyoto University, Japan
E/Prof. Dr. Tadatsugu Tanaka, University of Tokyo, Japan
A/Prof. Dr. Kingshuk Roy, Nihon University, Japan
A/Prof. Dr. Md. Shahin Hossain, Nagoya Institute of Technology, Japan
A/Prof. Dr. Sayuri Kimoto, Kyoto University, Japan
Engr. Hirondo Inagali, President, JCK Com. Ltd. Japan
A/Prof. Dr. Inui Toru, Kyoto University, Japan
A/Prof. Dr. Fujisawa Kazunori, Okayama University, Japan
A/Prof. Dr. Inoue Kazuya, Kobe University, Japan

International Advisory Committee:

Prof Sai Vanapalli, University of Ottawa, Canada
Prof. Dr. Mounir Bouassida, National School of Engineering of Tunis
Prof. Dr. Lilia Robles Austriaco, Angles University Foundation, Philippines
Prof. Dr. A.S.M. Abdul Awal, University Technology Malaysia, Malaysia
Prof. Dr. Muhammad Ibn Ibrahimy, International Islamic University, Malaysia
Prof. Dr. Zahurul Islam, Bangladesh University of Engineering and Technology, Bangladesh
Prof. Dr. Bujang B.K. Huat, University Putra Malaysia, Malaysia
Prof. Dr. Nemy Banthia, University of British Columbia, Canada
Prof. Dr. Ian Jefferson, University of Birmingham, UK
Prof. Dr. John Bolander, Univesity of California, USA
Prof. Dr. Shamshul Chowdhury, Roosevelt University, USA
Prof. Dr. Isabel Pinto, University of Coimbra, Portugal
A/Prof. Mark Jaksa, University of Adelaide, Australia
A/Prof. Dr. William Sebudde Kaggwa, University of Adelaide, Australia
Dr. John N. Mukabi, President of Kenya Geotechncal Society, Kenya

Conference Secretariat:

Dr. Zakaria Hossain, Associate Professor
Division of Environmental Science and Technology
Graduate School of Bioresources
Mie University, 1577 Kurima Machiya-cho
Tsu-city, Mie 514-8507, Japan
E-mail: zakaria@bio.mie-u.ac.jp
Tel: +81-59-231-9578、Fax: +81-59-231-9591

Editorial Committee:

Md. Zakaria Hossain
Md. Bellal Hossain
Toshinori Sakai
Md. Toriqul Islam

Executive Committee:

Toshinori Sakai
Md. Zakaria Hossain
Md. Bellal Hossain
Kazuki Ito
Md. Toriqul Islam
Muhammad Ibn Ibrahimy
Ms. Emi Ueno
Ms. Mayumi Matsumoto

GEOMAT2011 MIE
GEOTECHNIQUE, CONSTRUCTION MATERIALS AND ENVIRONMENT

PROCEEDINGS OF FIRST INTERNATIONAL CONFERENCE - GEOMAT2011
GEOTECHNIQUE, CONSTRUCTION MATERIALS AND ENVIRONMENT MIE JAPAN, 21-23 NOVEMBER, 2011

Geotechnique, Construction Materials and Environment

Volume 1

Edited by

Md. Zakaria Hossain
Department of Environmental Science and Technology
Mie University

Toshinori Sakai
Department of Environmental Science and Technology
Mie University

THE GEOMATE INTERNATIONAL SOCIETY, MIE 2011

Published by:
The GEOMATE International Society
Tsu city, Mie, Japan
E-mail: geomate@gi-j.com
www.gi-j.com

ISBN Number: 978-4-9905958-0-7 C3051

Printed in Japan

Table of Contents

Construction materials

Environment

First International Conference on Geotechnique, Construction Materials and Environment, Mie, Japan, Nov.21-23, 2011, ISBN: 978-4-9905958-0-7 C3051

Preface

The First International Conference on Geotechnique, Construction Materials and Environment GEOMAT2011 is organized in Center Palace Miyako Hotel, Tsu city, Mie Japan in conjunction with Japanese Geotechnical Society (JGS), Japanese Society of Irrigation Drainage and Rural Engineering (JSIDRE), Mie University, JCK Comp. Ltd and Glorious International. It aims to provide with great opportunities to share common interests on geo-engineering, construction materials, environmental issues, water resources, and earthquake and tsunami disasters. The key objective of this conference is to promote interdisciplinary research from various regions of the globe. On Friday 11 March at 14:46 Japan Standard Time, the north east of Japan was severely damaged by the tragic earthquake and tsunami. The conference is dedicated to the tragic Tohoku-Kanto earthquake and tsunami disasters.

The conference has 3 major themes with 17 specific themes including

- Advances in Composite Materials
- Computational Mechanics
- Foundation and Retaining Walls
- Slope Stability
- Soil Dynamics
- Soil-Structure Interaction
- Pavement Technology
- Tunnels and Anchors
- Site Investigation and Rehabilitation
- Ecology and Land Development
- Water Resources Planning
- Environmental Management
- Public Health and Rehabilitation
- Earthquake and Tsunami Issues
- Safety and Reliability
- Geo-Hazard Mitigation
- Case History and Practical Experience

The proceedings contain 7 keynote papers along with 115 technical papers from 22 countries. The technical papers are selected from the vast number of contributions submitted, after review of the abstracts. The final papers included in the proceedings have been peer reviewed rigorously and revised as necessary by the authors. We are grateful to the authors of the contributed papers for their resourceful papers and their help in maintaining the high assessment of the papers and the co-operation in complying with the requirements of the editor and the reviewers. We wish to express our sincere thanks to the Organizing Committee Members, National Advisory Committee Members and International Advisory Committee Members for their valuable supports. We acknowledge the support of Japanese Geotechnical Society (JGS), Japanese Society of Irrigation Drainage and Rural Engineering (JSIDRE), Mie University, JCK Comp. Ltd and Glorious International.

Prof. Dr. Toshinori Sakai
Conference Chairman

Dr. Md. Zakaria Hossain
Conference Secretary

Organization

Scientific Committees:

Conference Chairman: Prof. Dr. Toshinori Sakai, Mie University, Japan
Conference Honorary Chairman: E/Prof. Dr. Sohji Inoue, Mie University, Japan

Conference Organizing Committee:

Prof. Dr. Takamitsu Kajisa, Mie University, Japan
Prof. Dr. Ishiguro Satoru, Mie University, Japan
Prof. Dr. Sigeko Haruyama, Mie University, Japan
A/Prof. Dr. Atsushi Ishii, Mie University, Japan
A/Prof. Dr. Maasaki Kondo, Mie University, Japan
A/Prof. Dr. Kenji Okajima, Mie University, Japan
A/Prof. Dr. Ryoei Ito, Mie University, Japan

National Advisory Committee:

Prof. Dr. Fumio Tatsuoka, Tokyo University of Science, Japan
Prof. Dr. Kazunori Uchida, Kobe University, Japan
Prof. Dr. Fusao Oka, Kyoto University, Japan
Prof. Dr. Jing-Cai Jiang, University of Tokushima, Japan
Prof. Dr. Akira Murakami, Kyoto University, Japan
E/Prof. Dr. Tadatsugu Tanaka, University of Tokyo, Japan
A/Prof. Dr. Kingshuk Roy, Nihon University, Japan
A/Prof. Dr. Md. Shahin Hossain, Nagoya Institute of Technology, Japan
A/Prof. Dr. Sayuri Kimoto, Kyoto University, Japan
Engr. Hirondo Inagali, President, JCK Com. Ltd. Japan
A/Prof. Dr. Inui Toru, Kyoto University, Japan
A/Prof. Dr. Fujisawa Kazunori, Okayama University, Japan
A/Prof. Dr. Inoue Kazuya, Kobe University, Japan

International Advisory Committee:

Prof Sai Vanapalli, University of Ottawa, Canada
Prof. Dr. Mounir Bouassida, National School of Engineering of Tunis
Prof. Dr. Lilia Robles Austriaco, Angles University Foundation, Philippines
Prof. Dr. A.S.M. Abdul Awal, University Technology Malaysia, Malaysia
Prof. Dr. Muhammad Ibn Ibrahimy, International Islamic University, Malaysia
Prof. Dr. Zahurul Islam, Bangladesh University of Engineering and Technology, Bangladesh
Prof. Dr. Bujang B.K. Huat, University Putra Malaysia, Malaysia
Prof. Dr. Nemy Banthia, University of British Columbia, Canada
Prof. Dr. Ian Jefferson, University of Birmingham, UK
Prof. Dr. John Bolander, Univesity of California, USA
Prof. Dr. Shamshul Chowdhury, Roosevelt University, USA
Prof. Dr. Isabel Pinto, University of Coimbra, Portugal
A/Prof. Mark Jaksa, University of Adelaide, Australia
A/Prof. Dr. William Sebudde Kaggwa, University of Adelaide, Australia
Dr. John N. Mukabi, President of Kenya Geotechncal Society, Kenya

Conference Secretariat:

Dr. Zakaria Hossain, Associate Professor
Division of Environmental Science and Technology
Graduate School of Bioresources
Mie University, 1577 Kurima Machiya-cho
Tsu-city, Mie 514-8507, Japan
E-mail: zakaria@bio.mie-u.ac.jp
Tel: +81-59-231-9578、Fax: +81-59-231-9591

Editorial Committee:

Executive Committee:

Geotechnique

First International Conference on Geotechnique, Construction Materials and Environment, Mie, Japan, Nov.21-23, 2011, ISBN: 978-4-9905958-0-7 C3051

Developments of Geosynthetic-Reinforced Soil Technology in Japan: Retaining Walls and Bridge Abutments

Tatsuoka, F., Department of Civil Engineering, Tokyo University of Science

ABSTRACT: The construction of permanent geosynthetic-reinforced soil (GRS) retaining walls (RWs) with a full-height rigid facing for railways, including high-speed train lines, started about twenty years ago in Japan. The total length of this type of GRS RW is now more than 125 km, replacing traditional gravity-type RWs or cantilever reinforced concrete RWs and steel-reinforced soil RWs. Many were also constructed replacing traditional type RWs and embankments that collapsed during recent earthquakes, heavy rainfalls and storms. By taking advantages of this technology, a number of bridge abutments with geosynthetic-reinforced backfill were constructed. The latest version, called the GRS integral bridge, comprises a continuous girder integrated to a pair of RC facing with the backfill reinforced with geosynthetic reinforcement layers firmly connected to the back of the facing. The advantages of the GRS integral bridge are presented. It is proposed to apply these new technologies to the recovery of embankments, RWs and bridges that were damaged by earthquakes, floodings, storms and tsunami.

Keywords: Bridge abutment, Full-height rigid facing, Geosynthetic-reinforced soil, Retaining walls, Staged construction

1. INTRODUCTION

Construction of geosynthetic-reinforced soil retaining walls (GRS RWs) and geosynthetic-reinforced steep-sloped embankments has become popular these two decades in Japan. A couple of unique technologies of GRS structure were developed in Japan, including several new type bridge abutments comprising geosynthetic-reinforced backfill.

1.1 GRS RWs having a staged-constructed FHR facing

GRS RWs having a stage-constructed full-height rigid (FHR) facing is now the standard RW construction technology for railways including bullet train lines in Japan, replacing traditional type RWs (Tatsuoka et al., 1997, 2007). Fig. 1 shows a typical wall. This new type GRS RW has been constructed at more than 850 sites in Japan, and the total wall length is more than 123 km as of March 2011 (Fig. 2).

This new type GRS RW has the following features (Fig. 3):

a) The use of a FHR facing that is cast-in-place using staged construction procedures. The geosynthetic reinforcement layers are firmly connected to the back of the facing, which is essential for high static and dynamic wall stability, as illustrated in Fig. 4.

b) The use of a polymer geogrid for cohesionless soil to ensure good interlocking and a composite of non-woven and woven geotextiles for high-water content cohesive soils to facilitate both drainage and tensile reinforcing of the backfill. The latter makes possible the use of low-quality on-site soil as the backfill if necessary.

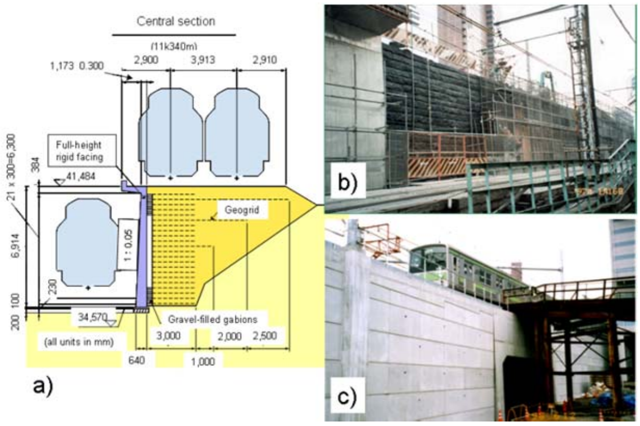

Fig 1. GRS RW having a FHR facing for Yamanote Line (one of the busiest urban railways in Japan) flying over Chuo Line (another busiest urban railway) in Tokyo (constructed during 1995–2000): a) typical cross-section; b) wall under construction; and c) completed wall.

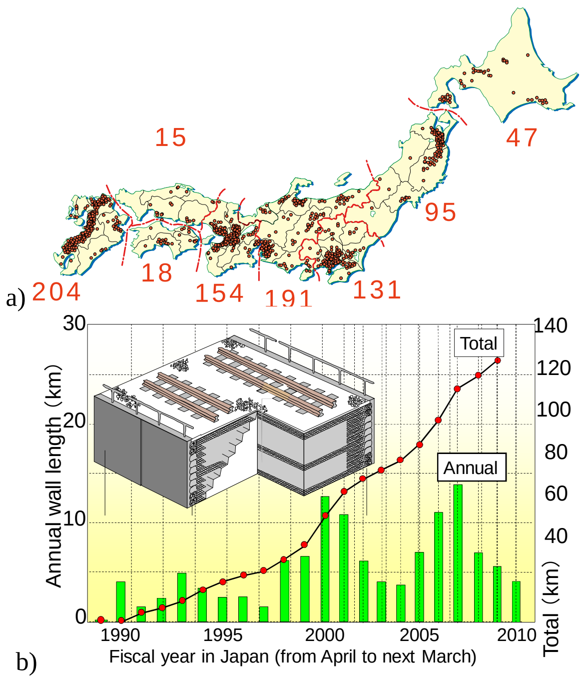

Fig. 2. a) Locations; and b) length of GRS RWs with a staged-constructed FHR facing (as of March 2011).

\

c) The use of relatively short reinforcement, made possible by using planar geosynthetic reinforcement, which has a relatively short anchorage length necessary to activate the tensile rupture strength.

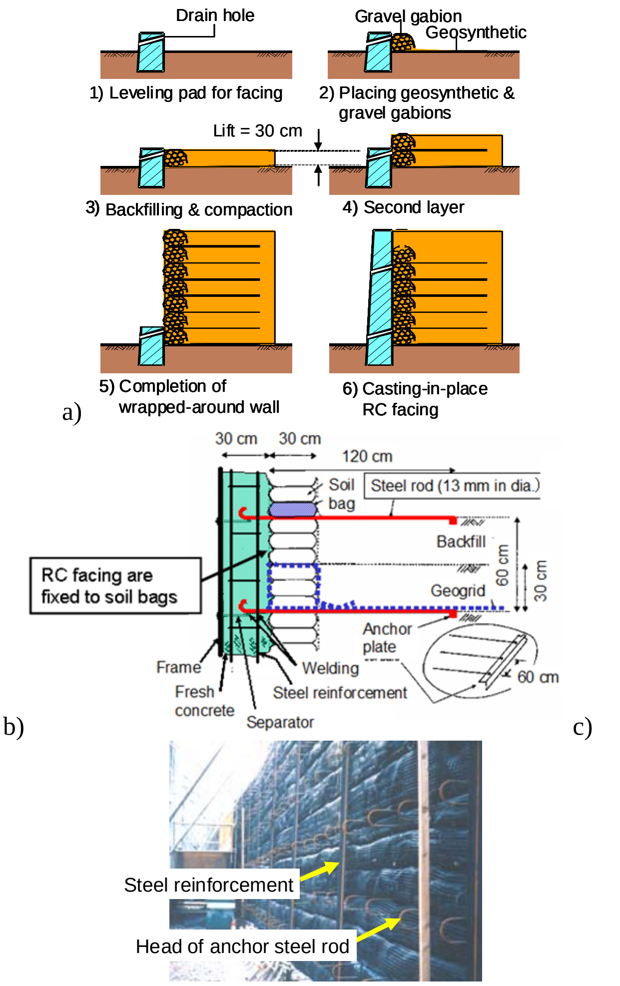

Fig 3. Staged construction of a GRS RW: a) respective construction steps; b) details of connection between the facing and the reinforced backfill; and c) typical view of the wall face before casting-in-place FHR facing.

The staged construction consists of the following steps (Fig. 3a): 1) a small foundation element for the facing is constructed; 2) a full-height GRS wall with wrapped-around wall face is constructed by placing gravel-filled bags at the shoulder of each soil layer; and 3) after the major part of ultimate deformation of the backfill and the subsoil layer beneath the wall has taken place, a thin (i.e., 30 cm or more) and lightly steel-reinforced concrete facing is constructed by casting-in-place fresh concrete directly on the wall face, which makes the FHR facing firmly connected to the main body of the backfill. Fig. 3b shows the details of the connection of the FHR facing to the main body of the reinforced backfill and Fig. 3c shows typical view of the wall face before casting-in-place FHR facing at the site presented in Fig. 1. A good connection can be made between the RC facing and the main body of the geosynthetic-reinforced backfill the following two mechanisms. Firstly, the fresh concrete can be easily penetrated into the inside of gravel-filed gabions through openings of the geogrid. Secondly, extra water from fresh concrete is absorbed by gravel inside the gabions, which prevents negative effects of bleeding phenomenon of concrete. It is to be noted that the gabions wrapped-around with geosynthetic reinforcement and filled with gravel function that are placed at the shoulders of soil layers functions as; not only a) a temporary facing structure during construction that makes backfill-compaction more easily and resists against earth pressure generated by compaction and further backfilling at higher levels of the wall; but also b) a drainage layer after construction; and c) a buffer that protects the connection between the FHR facing and the reinforcement layers against relative displacement that takes place after construction. Moreover, concrete form on both sides of the facing and its propping, which becomes more expensive at a high rate as the wall becomes higher, is necessary to construct a conventional RC cantilever RW. On the other hand, only external concrete form without any external propping while not using internal concrete form is necessary with this new GRS RW system (Fig. 3b).

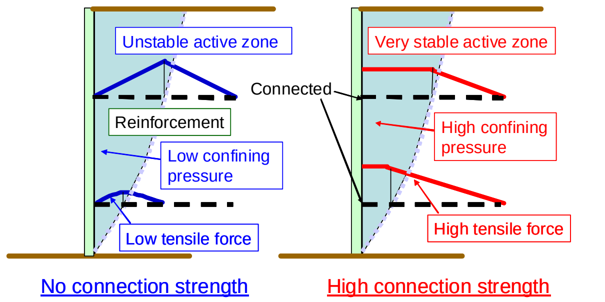

Fig. 4. Effects of firm connection between the reinforcement and the facing (Tatsuoka, 1992).

The importance of connecting reinforcement layers to the rigid facing is illustrated in Fig. 4. If the wall face is loosely wrapped-around with geosynthetic reinforcement without gabions placed at the shoulder of respective soil layers or the reinforcement layers are not connected to a rigid facing, no tensile force is activated at the wall face in the reinforcement while no significant earth pressure is activated at the wall face. No earth pressure at the wall face means no lateral confining pressure activated to the active zone of the backfill, which results in low stiffness and low strength of the active zone and therefore intolerably large deformation and displacement of the active zone (Fig. 4a). On the other hand, with this new GRS RW system, as the gabions function as a temporary facing structure, high earth pressure can be activated at the wall face before placing a FHR facing. As wrapping-around geosynthetic reinforcement at the wall face is buried in the fresh concrete layer, eventually the reinforcement layers are firmly connected to the FHR facing and the earth pressure that has been activated to the temporary facing structure comprising gabions wrapped-around with a geogrid is resisted by a FHR facing consisting of a lightly steel-concrete layer and a pile of gabions. The importance of this firm connection for a high wall stability is illustrated in Fig. 4b. That is, relatively large earth pressure, similar to the active earth pressure develops in the unreinforced backfill retained by a conventional RW, can be activated on the back of the FHR facing because of a high connection strength between the reinforcement and the facing and a high facing rigidity. This high earth pressure results in high confining pressure in the backfill, therefore high stiffness and high strength of the backfill, which results in high performance of the wall.

The geosynthetic reinforcement that is required to maintain the stability of GRS RW having a staged constructed FHR facing becomes relatively short when compared to metal strip reinforcement. This is because: 1) the anchorage length of planar geosynthetic reinforcement to resist against the tensile load equal to the tensile rupture strength of reinforcement becomes much shorter; and 2) a FHR facing prevents the occurrence of local failure in the reinforced zone of the backfill by not allowing failure planes to pass through the wall face at an intermediate height. Factor 2) becomes more important when the backfill is subjected to concentrated load on the top of the facing or immediately behind the wall face on the crest of the backfill.

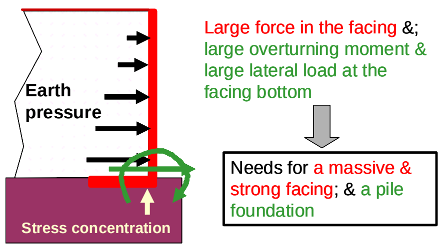

Fig. 5. Traditional type RW as a cantilever structure.

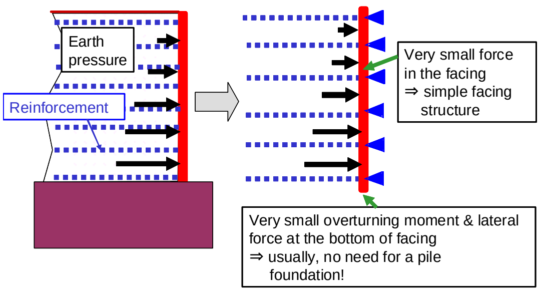

Fig. 6. GRS RW with a FHR facing as a continuous beam supported at many points with a small span (Tatsuoka, 1992; Tatsuoka et al., 1997).

1.2 GRS-RWs as non-cantilever strutures

A conventional type RW is basically a cantilever structure that resists against the active earth pressure from the unreinforced backfill by the moment and lateral thrust force at its base (Fig. 5). Therefore, large internal moment and shear force is mobilized in the facing structure while large overturning moment and lateral thrust force develops at the base of the facing. A large stress concentration may develop at and immediately behind the toe on the base of the facing, which makes necessary the use of a pile foundation in usual cases. These disadvantages become more serious at a high rate with an increase in the wall height.

Relatively large earth pressure, similar to the one activated on the traditional type RW, may be activated on the back of the FHR facing of this new type GRS RW because of firm connection between the reinforcement and the FHR facing. Despite the above, as the FHR facing behaves as a continuous beam supported at many levels with a small span, typically 30 cm, only small force is activated in the facing structure (Fig. 6). Because of the above, the facing structure becomes rather simple while the overturning moment and lateral thrust force activated at the facing base becomes small, which makes unnecessary a pile foundation in usual cases. The case histories until today have validated that the GRS RW having a stage-constructed FHR facing is much more cost-effective (i.e., much lower construction cost, much speedy construction using much lighter construction machines), therefore a much less total emission of CO_2 than the traditional type RW. Despite the above, the performance of the new type GRS RW is equivalent to, or even better than, that of traditional type RW.

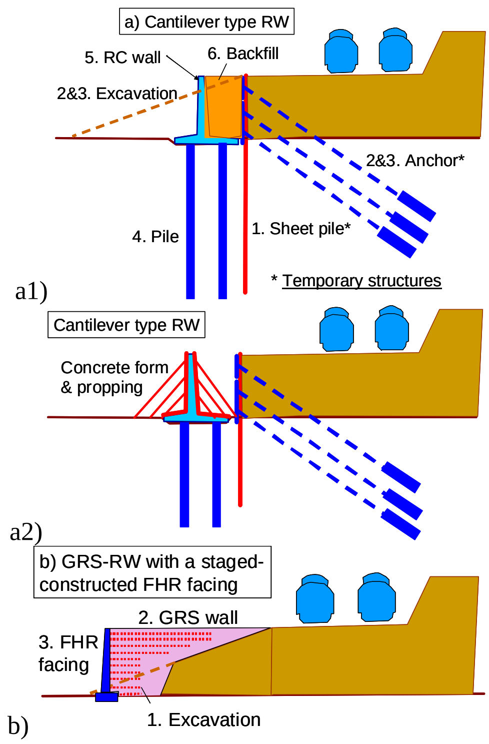

Fig. 7. Reconstruction of a gentle slope of embankment to a vertical wall: a1) & a2) the traditional method; and b) the new method (the numbers indicate construction sequence).

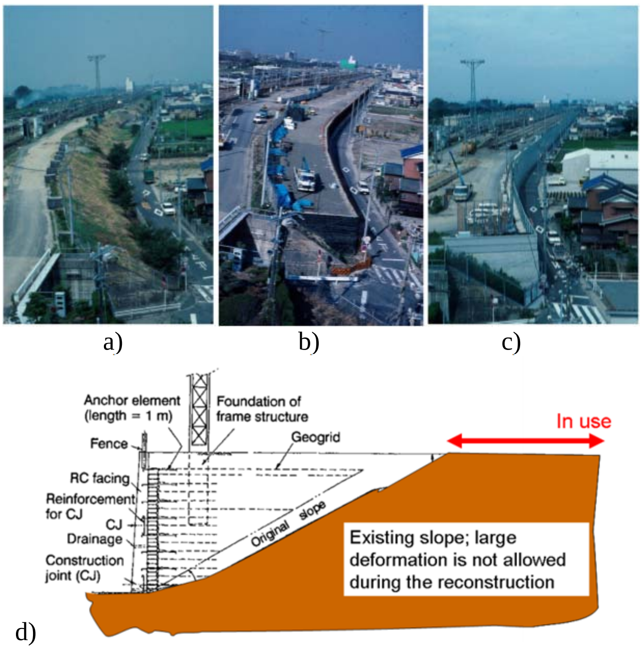

Fig. 8. a) Before; b) during; and c) after reconstruction of embankment slope to a GRS RW having a FHR facing; and d) typical cross-section, a yard for bullet trains (Shinkan-Sen) in Nagoya; average wall height= 5 m; total length= 930 m; & construction period= 1990 -1991 (Tatsuoka et al., 1997).

1.3 Reconstruction of slopes of existing embankments

One of the reasons for a popularity of this new type GRS RW is a high cost-effectiveness when reconstructing gentle slopes of existing embankment to vertical RWs, compared with the traditional method (Fig. 7a). In particular, when the stiff bearing soil layer is deep, expensive temporary structures (i.e., ground anchor, sheet piles and concrete form with its propping) becomes necessary with the traditional method. On the other hand, with the new method (Fig. 7b), such temporary structures as listed above are not used while the number of construction steps is much smaller, the occupied space is much smaller and the construction period is much shorter. Fig. 8 shows a typical case history. Moreover, by the new method, taking advantage of a FHR facing supported by reinforcement layers for a full wall height, super-structures that may exert large lateral load, such as electric poles and high noise barrier walls, can be constructed either immediately behind the wall face without a deep pile foundation (Fig. 8d), or directly on the FHR facing. In this respect, three-dimensional effects of FHR facing (Fig. 9, make a GRS RW very strong against concentrated load applied to the top of the facing. That is, the FHR rigid facing of this new GRS RW system is continuous not only in the vertical direction but also in the lateral direction. One unit of FHR facing, separated from horizontally adjacent units by vertical construction joins in the facing concrete, has some length, about 10 m. Therefore, the whole FHR facing unit can resist against concentrated vertical or lateral load applied to the facing top with a help of all the reinforcement layers that are connected to the facing unit. Moreover, a foundation that is embedded inside the reinforced backfill can exhibit large lateral resistance against the lateral load acting in the direction normal to the wall face (Fig. 9a). The features of FHR rigid facing described above become most advantageous when a FHR facing functions as a foundation for a super-structure. The most typical application is bridge abutments made of GRS RWs having a staged constructed FHR facing, as described in Chapter 4.

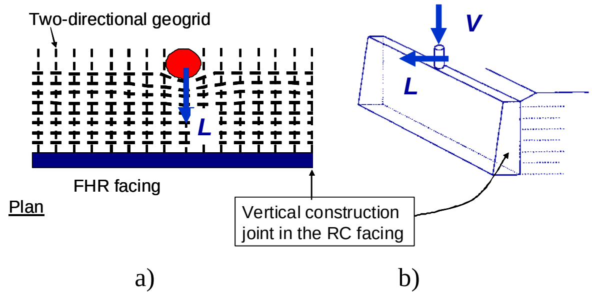

Fig. 9. 3-D resistance of FHR facing/geogrid system against lateral load acting to; a) a vertically long structure located inside the reinforced zone; and b) the top of the facing (Tatsuoka et al., 1997).

1.4 Summary

No case of collapse and excessive deformation has been reported among many case histories of this new type GRS RW (Fig. 2). This may be attributed mainly to the following factors: a) a good compaction of the backfill is ensured due to a relative small vertical spacing of geogrid layers (i.e., 30 cm) and no rigid facing existing during backfill compaction; b) all potential problems due to deformation and displacements of wall and ground can be recognised and dealt with before the construction of a FHR facing; c) gabion bags stacked immediately behind the FHR facing ensure good drainage and act as a buffer when relative displacement tends to take place between the facing and the reinforced backfill after having been opened to service; d) the use of planar geogrid, rather than metal strips (which are much easier to pull out); and f) the GRS RWs are designed against high seismic loads; it was confirmed that duly designed and constructed GRS RWs can survive such severe earthquakes as the 1995 Kobe Earthquake (Tatsuoka et al., 1998), as described in Chapter 3. The design rupture strength of geogrid is usually determined by the a-seismic design, and, therefore, the design rupture strength is not reduced to account for creep rupture by long-term static loads. Yet, no case history in which the wall has exhibited noticeable creep deformation has been reported.

2. RECONSTRUCTION OF EMBNAKMENTS AND RETAINNG WALLS COLLAPSED BY NATURAL DISASTERS

2.1 Collapse by earthquakes

Numerous embankments and traditional type RWs collapsed by floodings, earthquakes and storms in the past in Japan (e.g.,

Fig. 10). Previously, most of the collapsed soil structures were reconstructed to respective original traditional types despite that they are not cost-effective and their resistance against natural disasters is insufficient. From the beginning of the 1990's, reconstruction of railway embankments that collapsed by heavy rainfalls and floodings to embankments having geosynthetic-reinforced steep slopes or GRS RWs having a stage-constructed FHR facing or their combination started based on the successful experiences described above.

Fig. 10. Gravity type RW without a pile foundation at Ishiyagawa that collapsed during the 1995 Kobe Earthquake (Tatsuoka et al., 1997, 1998).

Fig. 11. GRS RW having a FHR facing at Tanata; a) immediately after construction & a typical cross-section; and b) one week after the 1995 Kobe Earthquake (Tatsuoka et al., 1997, 1998).

High performance during the 1995 Kobe Earthquake of a GRS RW of this type that had been constructed at Tanata validated its high-seismic stability (Fig. 11). Many gentle slopes of embankment and traditional type RWs that collapsed by the 1995 Kobe Earthquake and subsequent earthquakes were reconstructed to GRS RWs having a stage-constructed FHR facing (Tatsuoka et al., 1977, 1998). Fig. 12 shows reconstruction of one of the three railway embankments supported by gravity type RWs at the slope toe that totally collapsed during the 2004 Niigata-ken Chuetsu Earthquake. GRS RWs having a FHR facing were constructed at these three sites because of not only much lower construction cost and much higher stability (in particular for soil structures on a steep slope), but also much faster construction and a significant reduction of earthwork when compared to reconstruction to the original embankments. The new type GRS RWs are also much more cost-effective and the construction is faster than bridge type structures. During this earthquake, road embankments collapsed at numerous places in mountain areas and many of them were reconstructed to GRS RWs or embankments having geosynthetic-reinforced steep slopes.

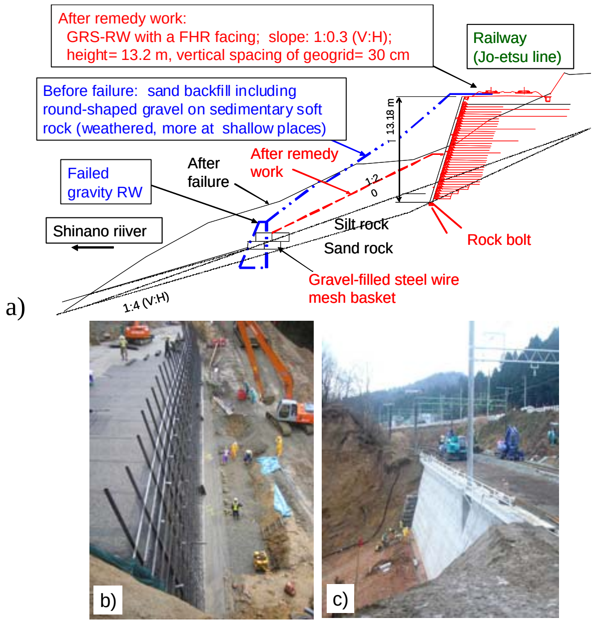

Fig. 12. a) Railway embankment that collapsed during the 2004 Niigata-ken Chuetsu Earthquake and its reconstruction to a GRW RW having a FHR facing; b) the wall during reconstruction; and c) the completed wall (Morishima et al., 2005).

The March 25th 2007 Noto-hanto Earthquake caused severe damage to embankments of Noto Toll Road (opened in 1978). The north part of this road runs through a mountainous area for a length of 27 km. The damage concentrated into this part, where eleven high embankments filling valleys were extensively collapsed (Koseki et al., 2008). The collapsed embankments were basically reconstructed to GRS RWs while ensuring the drainage of ground and surface water.

The 2011 Great East Japan Earthquake was the most disastrous earthquake in Japan after the World War II. The damage was a combination of that from seismic motions and the accompanying tsunami, and was of much greater scale than that caused by the previous inland fault earthquakes in Japan. A great number of embankments and retaining walls that had not be designed and constructed following the current seismic design standard collapsed. In comparison, a number of GRS RWs having staged constructed FHR facing described in Chapter 2 that had been constructed in affected areas of this earthquakes performed very well. Several embankments that collapsed were reconstructed to this type of GRS-RWs (Fig. 13). The details of these case histories will be reported in the near feature.

Fig. 13. a) Embankment collapsed in the Nagano-Niigata Border Earthquake induced on the day after this disaster; and b) reconstruction to embankment retained by a GRS-RW having a FHR facing, between Yokokura and Morinomiya, JR East Iiyama Line (by the courtesy of the East Japan Railway Co.)

2.2 Floodings and storms

The GRS-RW technology described in Chapter 2 has also been used to restore soil structures that collapsed by floodings and storms. Fig. 14 shows a typical case. Railway embankments that had been constructed in several narrow valleys collapsed by over-flow of flood water of heavy rainfall. These embankments were reconstructed by using the GRS-RW technology. A large diameter drainage pipe was arranged crossing the respective embankments. The interaction between the drainage pipe and the FHR facing was very small, because the FHR facing was constructed after major deformation of the embankment and supporting ground had taken place. This restoration method was employed also in many other similar cases (Tatsuoka et al., 1997).

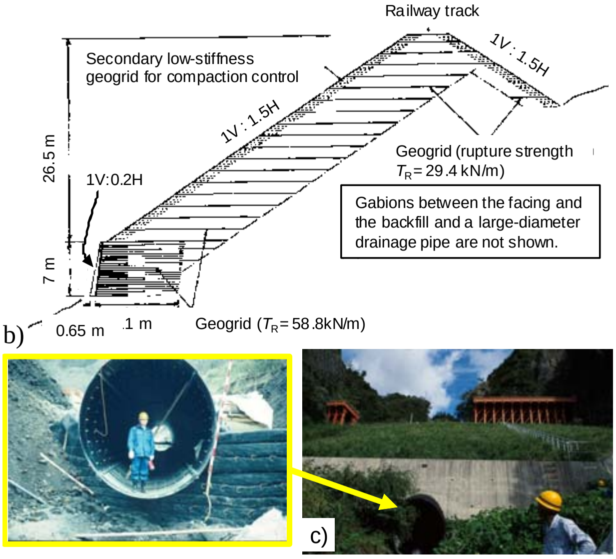

Fig. 14. a) Railway embankment damaged by rainfall in 1989; b) reconstructed cross-section; and c) after reconstruction in 1991 (Tatsuoka et al., 1997; 2007).

A great number of embankments for roads and railways retained by gravity-type or leaning type RWs along rivers and seashores often collapsed during floodings and storms. This is due usually to over-turning failure of the RWs caused by scouring in the supporting ground (Fig. 15a). This type of failure results from the fact that the conventional type RW is a cantilever structure of which the stability is controlled by the bearing capacity at the bottom of the RW (Fig. 5). On the other hand, GRS-RWs with a FHR facing is not such a cantilever structure as above (Fig. 6), therefore, much more stable and cost-effective (Fig. 15b). Fig. 16a this type of failure of a gravity-type RW for a length of 1.5 m along a sea shore facing the Pacific Ocean, west-south of Tokyo. The failure was triggered by scouring in the supporting ground by strong wave actions during a typhoon September 2007. The wall was restored by the GRS-RW technology. The FHR facing has a strong resistance against storm waves and stable against scouring in the supporting ground. Reinforced soil RWs with a discrete panel facing is not relevant in such cases, as the lost of stability of a single panel by, such as erosion of the backfill from connections between adjacent panels, may easily result into a failure of the whole wall.

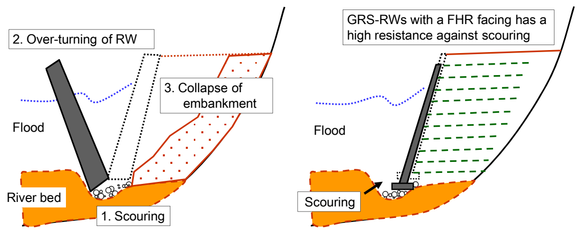

Fig. 15. Schematic diagrams showing: a) collapse of conventional type RW by flooding (the numbers show the sequence of events); and b) high performance of GRS-RW with a FHR facing

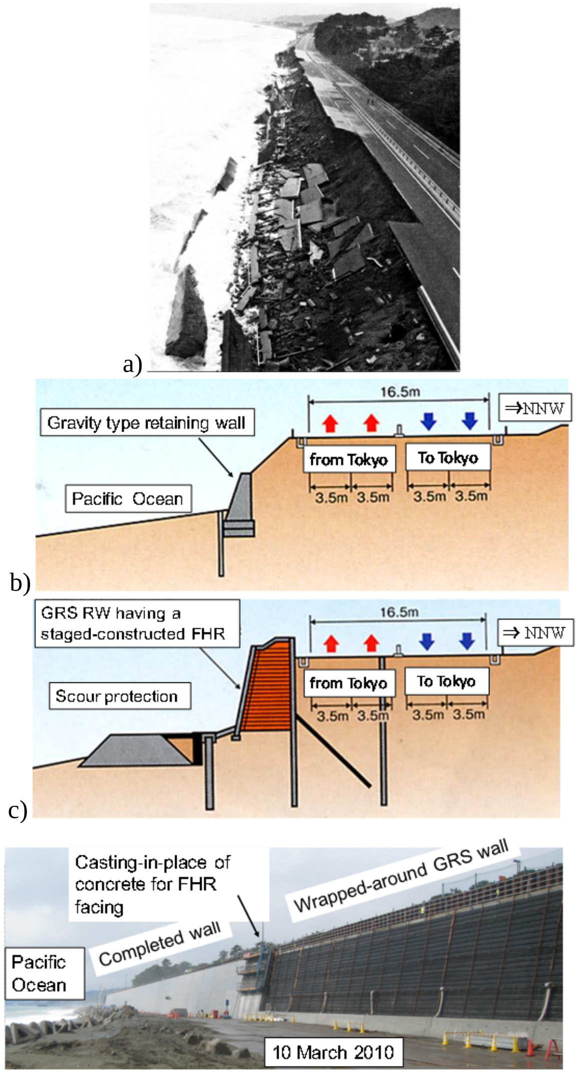

Fig. 16. Seawall of Seisho by-pass for National Road No. 1 in Kanagawa Prefecture, southwest of Tokyo: a) collapse for a length of about 1 km by Typhoon No. 9, 29th Aug. 2007; b) original structure; c) reconstructed seawall; and d) the wall during construction (a, b & c: by the courtesy of the Ministry of Land, Infrastructure, Transport and Tourism)

Every year, a number of old small scale irrigation dams collapsed by earthquakes and floodings in Japan. Fig. 17 shows the restoration of such a dam as above that collapsed by the 2007 Noto-Hanto Earthquake. The spillway section was reconstructed by reinforcing the fill by using soil bags having a tail and a wing to be integrated with the adjacent soil bags when stacked to have a high resistance against over-flow and seismic load.

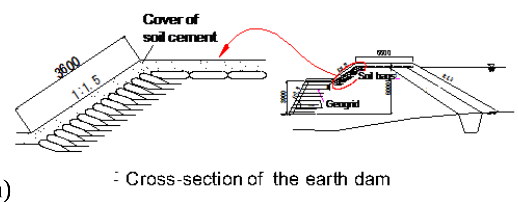

a)

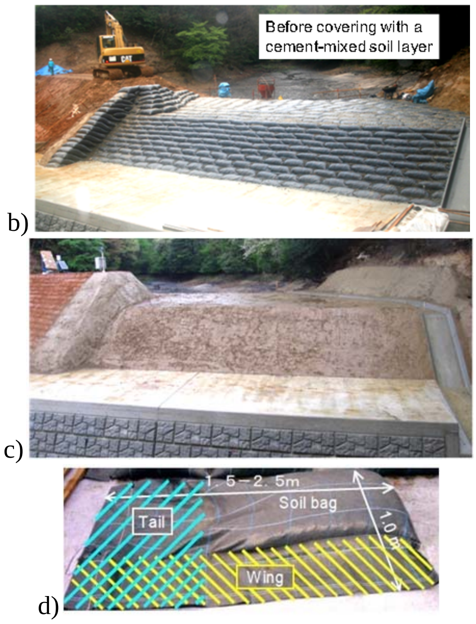

Fig. 17. Restoration of the earth-fill dam of Hirata Ike, Ishikawa Prefecture, that collapsed by the 2007 Noto-Hanto Earthquake (Mohri et al., 2009).

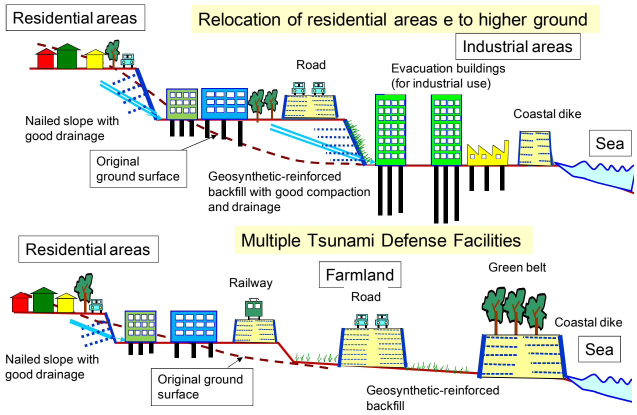

Fig. 18. Multiple tsunami defense facilities and relocating residential areas to higher ground using soil-reinforcement technology

3.3 Possible applications to restoration from the damage by the 2011 Great East Japan Earthquake

To counter the danger of tsunami, multiple tsunami defense systems could be considered as well as relocating residential areas to higher ground. In this earthquake, a great number of coastal dikes covered with concrete slabs and panels were washed away because of overflow of deep tsunami. To prevent such overflow, embankments that are high enough might be constructed with a gentle slope using conventional technology. Then the width of the embankments and the quantity of earthworks would be extremely large. Where road and railway embankments are expected to function as secondary tsunami barrier and evacuation location, a specific height will be required. Again, if normal embankments with gentle slopes are constructed, they will be wide and involve large quantities of earthworks. Another proposal is to relocate residential areas to higher ground. However, in this earthquake, a great number of embankments and retaining walls in residential areas that had been constructed using old technology collapsed in and around Sendai City.

To make the projects of multiple tsunami defense facilities and relocating residential areas to higher ground successful, it is proposed to use the technology of GRS-RW with a FHR facing explained in Chapter 2, in addition to the execution of appropriate compaction control and provision of suitable drainage. Figs. 18a and b schematically show this proposal.

4 DEVELOPMENT OF GRS INTEGRAL BRIDGE

4.1 Problems with conventional type bridges

A traditional type bridge comprises a single simple-supported girder supported by a pair of abutments via fixed (or hinged) and moveable bearings (or bearings), or multiple simple-supported girders supported by a pair of abutments and a single or multiple pier(s) via bearings. The traditional type abutment, which may be a gravity structure (unreinforced concrete or masonry) or a RC structure, has the following many drawbacks (Fig. 19).

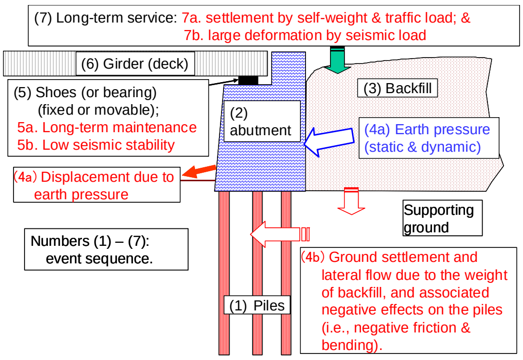

Fig. 19. Several major problems with conventional type bridge abutments.

Firstly, as the abutment is a cantilever structure that retains unreinforced backfill (Fig. 5), earth pressure activated on its back induces large internal force as well as large thrust force and overturning moment at the bottom of the abutment. Therefore, usually, the abutment becomes massive, while a pile foundation becomes necessary unless the supporting ground is strong enough. This drawback becomes more serious at an increasing rate with an increase in the wall height. Secondly, although only small movement is allowed once constructed, the backfill are constructed after the abutments are constructed. Hence, when constructed on soft ground, many piles may become necessary to prevent movements of the abutments due to earth pressure as well as settlement and lateral flow in the subsoil caused by the backfill weight. Large negative friction may develop along the piles. The piles may become much longer than the wall height when the soft ground is thick. Thirdly, the construction and long-term maintenance of girder bearings (i.e., girder bearings) and connections between simple-supported girders are generally costly. Moreover, the bearings and connections are weak points when subjected to seismic loads. Fourthly, a bump may be formed behind the abutment by long-term settlement of the backfill due to its self weight and traffic loads. Lastly, the seismic stability of the backfill is relatively low; the backfill may deform largely by seismic loads. Furthermore, the abutment supporting the girder via a fixed shoe is also relatively low, while the girder may dislodge at a movable shoe.

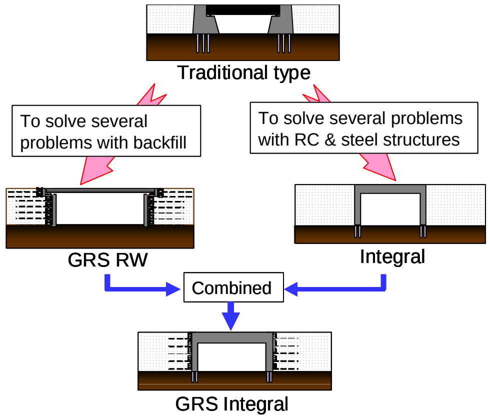

Fig. 20. Development of new type bridges.

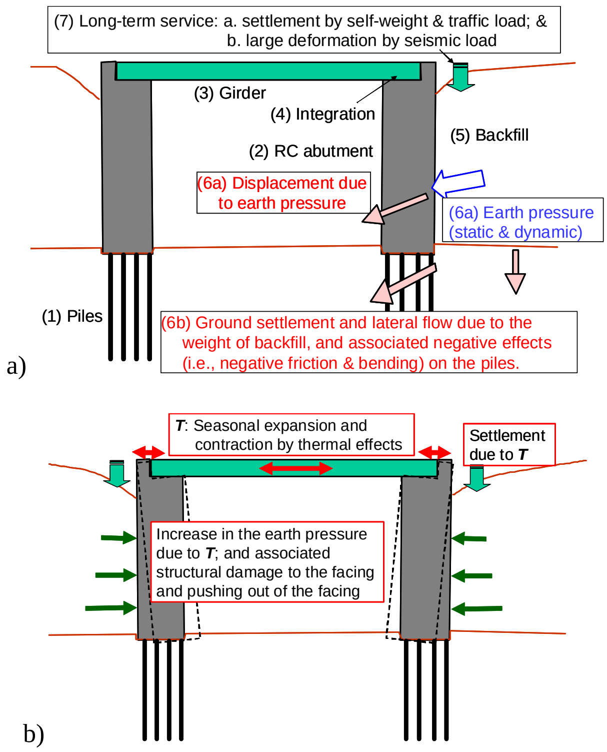

Fig. 21. Integral bridge: a) construction sequence and associated problems; and b) a new problem.

4.2 Integral bridge and GRS-RW bridge

To alleviate these problems with the conventional bridge type, three new bridge types have been proposed (Fig. 20). The integral bridge has been proposed to alleviate problems with the structural part (usually reinforced concrete) of the traditional type bridge. This type is now widely used in the UK, the USA and Canada, mainly due to low construction and maintenance cost resulting from no use of bearings and the use of a continuous girder. Furthermore, the seismic stability of integrated bridge is higher than the traditional type (as shown later). However, as the backfill is not reinforced, thus not unified to the structural part, the backfill and the structural part do not help each other. Therefore, this new bridge type cannot alleviate some old problems with the traditional type bridges (Fig. 21a) and their static and seismic stability is not very high. Moreover, as the girder is integrated to the abutments, seasonal thermal expansion and contraction of the girder results into cyclic lateral displacements of the abutments (Fig. 21b). This results in; 1) development of high earth pressure on the back of the abutment (i.e., facing); and 2) large settlements in the backfill (England et al., 2000). The effects of daily thermal effects are negligible.

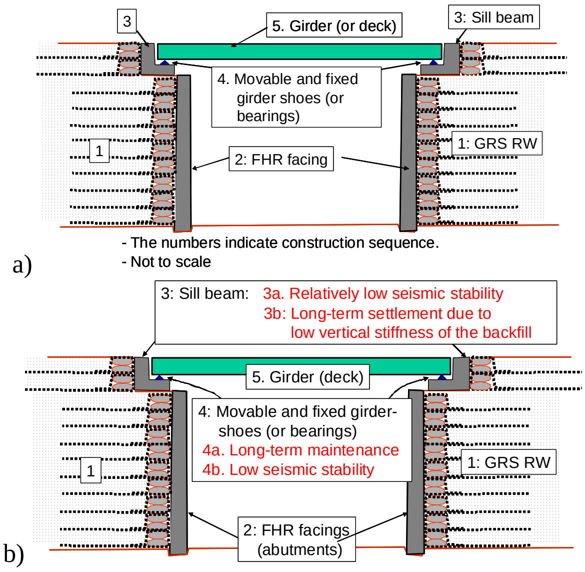

Fig. 22. GRS-RW bridge: a) construction sequence; and b) unsolved old problems.

Taking advantages of the stage-construction procedure (Fig. 3), many bridges comprising a pair of GRS RWs with a FHR facing that support a simple-supported girder were constructed (Tatsuoka et al., 1997). Although this bridge type, called the GRS-RW bridge (Fig. 22), is more cost-effective than the traditional type (Fig. 19), it has the following problems: 1) The length of the girder is limited due to low stiffness of the backfill supporting the sill beam. 2) The construction and long-term maintenance of bearings is costly. Moreover, the bearings are weak against seismic loads. 3) Although the seismic stability of GRS RWs with a FHR facing is very high (e.g., Tatsuoka et al., 1998; Koseki et al., 2006), it is not the case with the sill beam supporting the girder via a fixed shoe, because the mass of the sill beam is much smaller than the girder while the anchorage capacity of the reinforcement layers connected to its back is small due to their shallow depths.

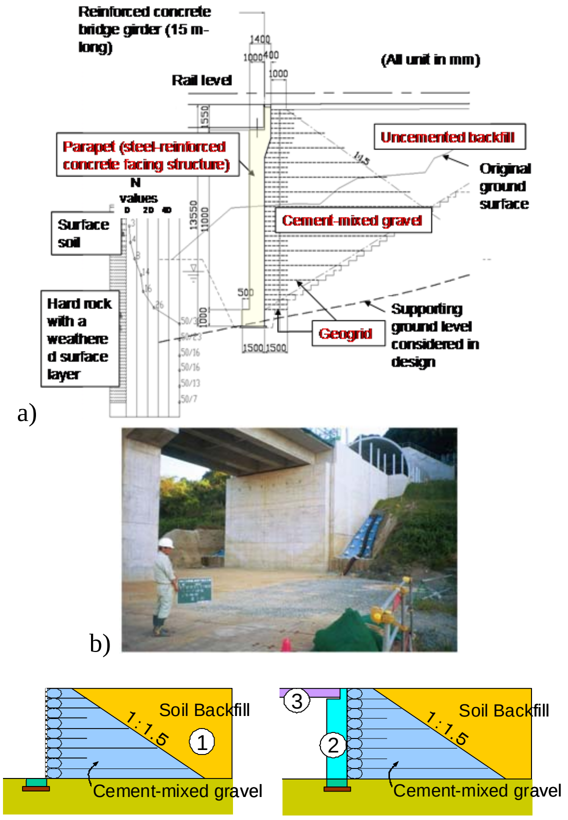

Fig. 23. A bridge abutment at Takada, Kyushu, for a new bullet train line (Tatsuoka et al., 2005); a) structural details; b) lateral and vertical loading tests of the facing; and c) staged construction .

It was then proposed and adopted to place a girder on the top of the FHR facing via a shoe (Watanabe et al., 2002; Tatsuoka et al., 2005). This proposal was adopted by Japanese railway engineers and the first prototype was constructed for a new bullet train line in Kyushu (Fig. 23). The abutment was constructed by the staged construction procedure placing a girder on the top of the RC facing via a fixed shoe. The conventional type RC abutment (Fig. 19) laterally supports the unreinforced backfill, which may activate large static and dynamic earth pressure on the back of the facing. In contrast, with this new type abutment, the reinforced backfill laterally supports a thin RC facing that supports the girder, without the backfill activating static and dynamic earth pressure on the facing. Following this project, a number of similar bridge abutments (nearly 60) were constructed recently and are being planned. Despite the above, this type of abutment is not free from several problems due to the use of girder bearings.

4.3 GRS integral bridge

To alleviate these many problems with the traditional type bridge (Fig. 19) as well as those with the integral bridge (Fig. 21) and the GRS-RW bridge, Fig. 23) and its improved version (Fig. 23), Tatsuoka et al. (2008a & b, 2009) proposed another new type bridge, called the GRS integral bridge (Fig. 24). This new type bridge combines the integral bridge and the GRS-RW bridge taking advantages of their superior features while alleviating their drawbacks.

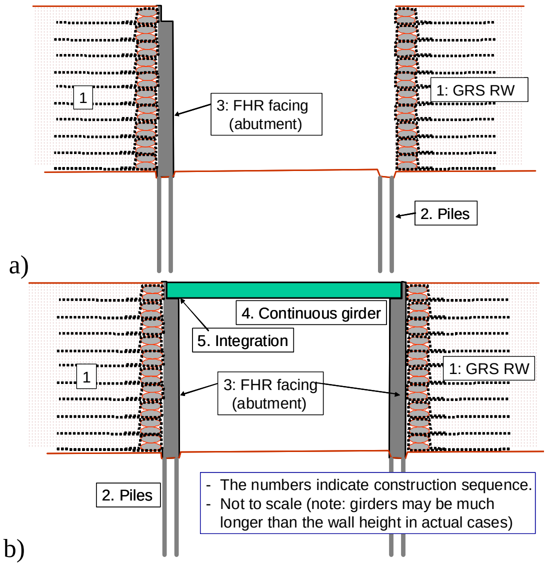

Fig. 24. GRS integral bridge.

The GRS integral bridge has the following features:

1) The backfill is reinforced with geosynthetic reinforcement layers that are firmly connected to the back of the FHR facings (i.e., the abutments). If it is necessary to ensure very high performance of the bridge, particularly during severe earthquakes, the backfill may be cement-mixed.
2) The abutments are constructed by the following staged construction procedure:
   a) A pair of GRS walls (without a FHR facing, the wall face being wrapped-around with geogrid reinforcement) are first constructed.
   b) Pile foundations to support the FHR facings are constructed, if necessary. If the deformation of the supporting ground by the construction of the backfill is not significant, pile foundations may be constructed before the GRS walls for better constructability.
   c) FHR facings are constructed by casting-in-place fresh concrete on the wall face.
   d) A continuous girder is placed on and integrated to the crest of the facings.

This staged construction procedure is a modification of the one described in Fig. 3 and, therefore, it has the same advantages. That is, firstly the connection between the reinforcement and the facing is not damaged by differential settlement between the facing and the backfill during wall construction. Then, construction of abutments on relatively compressible subsoil without using heavy piles becomes possible. Secondly, by compacting well the backfill allowing sufficient outward movements at the wall face, sufficient tensile force can be mobilized in the reinforcement during the construction of GRS walls (w/o a FHR facing).

Bridge type	Cost & period of construction	Maintenance cost	Seismic stability	Total
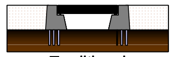 Traditional	1 *A, B*	1 *C, D*	1 *F, G* 252 gal*	3
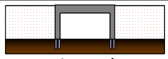 Integral	2 *B*	1 *D, E*	2 *F* 641 gal*	5
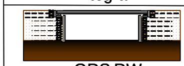 GRS RW	3	1 *C, D'*	2 *G'* 589 gal*	6
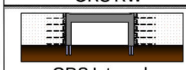 GRS Integral	3	3	3 1,048 gal*	9

(* Failure acceleration in model shaking table tests)

A= needs for massive abutments because of cantilever structure.
B= needs for piles because of; 1) cantilever-structure abutments; and 2) limited allowable post-construction displacements despite the construction of backfill after piles & abutments.
C= high cost for construction and long-term maintenance of girder bearings (i.e., bearings) and their low seismic stability.
D= long-term backfill settlement by self-weight and traffic loads.
D' = long-term settlement of sill beam.
E= lateral cyclic displacements of the abutment caused by thermal expansion and contraction of the girder, resulting in high earth pressure and large backfill settlement by the dual ratchet mechanism.
F= large backfill settlement and large dynamic earth pressure
G= low seismic stability due to independent performance of two abutments
G' = low seismic stability of the sill beam.

Fig. 25. Rating of four different bridge types based on cost & performance (the higher points, the higher rating).

With conventional type bridges (Fig. 19) and GRS-RW bridges (Fig. 22), the length of a single simple-supported girder is restricted to avoid excessive lateral seismic load to be activated to the abutment on which a fixed bearingsupports the girder. With integral bridges (Fig. 21), the girder length is limited to avoid excessive large cyclic lateral displacements at the top of the abutments by seasonal thermal expansion and contraction of the girder. The girder length is restricted also to limit the lateral seismic load activated to the abutments. With the GRS integral bridge, such restrictions as above are much looser, therefore, the actual length of the girder relative to the abutment height could be generally much longer than the one depicted in Fig. 24. The girder length limit for GRS integral bridges would be larger than the value for conventional type integral bridges, which is presently specified to be 50 - 60 m in the USA to restrict the maximum thermal deformation of the girder to four inches (about 10 cm). More research will be necessary in this respect.

Many series of model tests (cyclic static loading tests and shaking table tests) were performed to validate the advantageous feature of the GRS integral bridge over other types of bridges, as reported in details by Tatsuoka et al. (2009). Fig. 25 compares the characteristic features of the four different bridge types described in the precedent sections. The rating presented in this figure is only an approximation. That is, the full point allocated to each item is three, which is reduced one by one when any of the listed negative factors *A* - *G* is relevant. The horizontal accelerations at which the respective bridge models collapsed in the shaking table tests explained below are listed. A total full point equal to nine is given only to the GRS integral bridge.

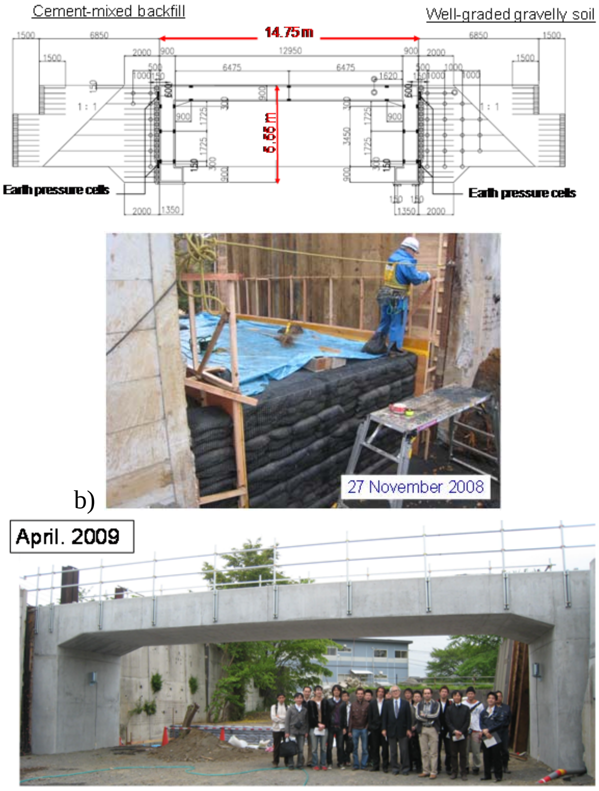

Fig. 26 A full-scale model of GRS integral bridge under construction (Nov. 2008) at Railway Technical Research Institute, Japan: a) dimensions; b) abutment under construction; and c) completed model.

A full-scale model of GRS integral bridge was constructed at Railway Technical Research Institute in 2008 (Fig. 26). The model was constructed taking advantage of a pair of full-scale models of GRS-RW with a FHR facing constructed 1998. A high constructivity of GRS integral bridge was confirmed. The long-term behaviour is now being observed. In 2011, the first prototype GRS integral bridge is now under construction for a new bullet train line at Kikonai between Shin-Aomori and Shin-Hakodate stations, at the south end of Hokkaido (Fig. 27). The bridge is heavily instrumented to observe the long-term behaviour. The details of the construction and behaviour during and after construction will be repored in the near future. Although the span is not long, it is considered that this case history is the historical first step for a number of GRS integral bridges to be constructed in the coming years.

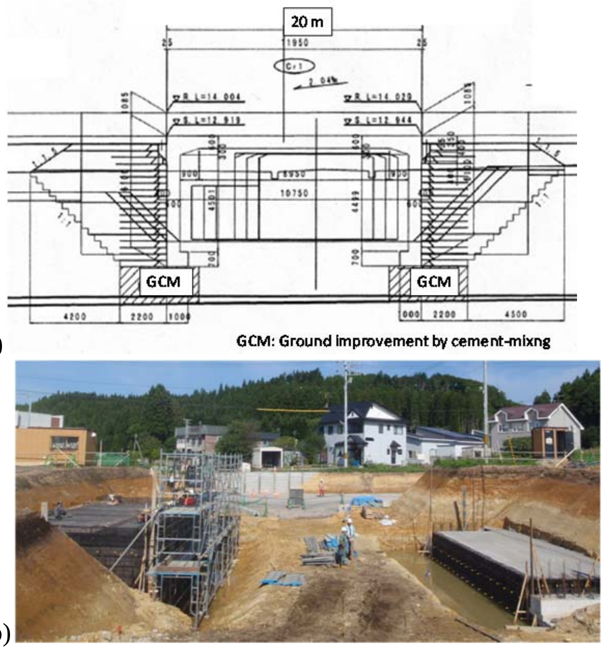

Fig. 27 The first GRS integral bridge for the new bullet train line at Kikonai between Shin-Aomori and Shin-Hakodate stations: a) overall dimensions; and b) a picture at the end of August 2011 (by the courtesy of Mr. Yamada, Y.).

Fig. 28 A view from the upstream of Tsuyagawa Bridge, between Motoyoshi and Rikuzenkoizumi stations, Kesenuma line, East Japan Raiway (taken by the author)

Fig. 29 A view from the seaside of Namiitagawa bridge, between Namitagawa and Kirikiri stations, Otsuchicho, Yamada Line, East Japan Raiway (taken by the author).

A great number of bridges lost their girders by strong tsunami forces during the 2011 East Japan great earthquake (Figs. 28 & 29). These girders, for which measures had been taken to prevent dislodging from the abutments but not to resist against the tsunami forces, were washed away. On the other hand, most of the short-span single-girders for local roads located near the modern bridges that lost girders survived tsunami forces (Fig,. 29). This is likely because these short-span bridges are plugged into the RC RWs on both sides of a river without using bearings: i.e., these bridges are actually integral bridges. This fact indicates that GRS integral bridges may have a sufficient resistance against tsunami forces. Moreover, as seen from Fig. 29, the unreinforced backfill of many bridges was washed out by tsunami forces. On the other hand, the backfill of GRS integral bridges also has a high resistance against tsunami forces by being reinforced with geogrid layers connected to the facings. It is strongly recommended to reconstruct these bridges damaged by tsunami to GRS integral bridges. Furthermore, GRS integral bridges are particularly relevant for newly constructed bridges if tsunami forces are to be taken into account.

5 CONCLUSIONS

Geosynthetic-reinforced soil retaining walls (GRS RWs) having a stage-constructed full-height rigid (FHR) facing have been constructed as important permanent RWs for a total length of more than 125 km in Japan since 1999 until today (March 2011). Although these GRS RWs are mainly for railways, many others were also constructed for highways and other types of infrastructure. Its current popular use is due to not only high cost-effectiveness, but also high performance that is equivalent to, or even better than, other modern RWs. This success can be attributed to;

1) the use of a proper type of reinforcement (i.e., a geogrid for cohesionless soil and a nonwoven/woven geotextile composite for high-water content cohesive soil);
2) casting-in-place of a FHR facing by staged construction procedures in such that reinforcement layers are firmly connected to the facing; and
3) taking advantages of the rigidity of the facing in design.

Many embankments and traditional type RWs that collapsed during recent severe earthquakes, heavy rainfalls and associated floodings and storms, in Japan were reconstructed to embankments with steep geosynthetic-reinforced slopes or GRS RWs with a stage-constructed FHR facing or their combination. It was validated that this technology is highly cost-effective in restoring collapsed old soil structures.

A new bridge type, called the GRS integral bridge, is proposed, which comprises an integral bridge and geosynthetic-reinforced backfill. GRS integral bridges exhibit essentially zero settlement in the backfill and no structural damage to the facing when subjected to lateral cyclic displacements of the facing caused by seasonal thermal expansion and contraction of the girder, while their seismic stability is very high. These features and high cost-effectiveness of the GSR integral bridge are due to that: 1) bearings are not used; 2) the girder is continuous without any connections; 3) the backfill is reinforced with geogrid layers firmly connected to the facing; and 4) FHR facings are stage-constructed after the construction of full-height geosynthetic-reinforced soil walls and then pile foundations (if necessary).

6 ACKNOWLEDGEMENTS

This paper is based on a long-term research for about 30 years performed by the author and his colleagues. The author sincerely appreciates all helps and efforts of his previous and current colleagues at University of Tokyo and Tokyo University of Science in performing this long-term research. The support of Dr Tateyama, M. and his colleagues at the Railway Technical Research Institute, Japan, is highly appreciated.

7 REFERENCES

[1] England, G, L., Neil, C, M. and Bush, D, I., Integral Bridges, A fundamental approach to the time-temperature loading problem, Thomas Telford, 2000.

[2] Koseki, J., Bathurst, R.J., Guler, E., Kuwano, J. and Maugeri, M., Seismic Stability of Reinforced Soil Walls, *Proc. 8th International Conference on Geosynthetics, Yokohama*, 2006, Vol.1, pp. 51-77.

[3] Koseki, J., Tateyama, M., Watanabe, K. and Nakajima, S. 2008. Stability of earth structures against high seismic loads, *Keynote Lecture, Proc. 13th ARC on SMGE*, Kolkata, Vol. II.

[4] Morishima, H., Saruya, K. and Aizawa, F., Damage to soils structures of railway and their reconstruction, *Special Issue on Lessons from the 2004 Niigata-ken Chu-Etsu Earthquake and Reconstruction, Foundation Engineering and Equipment (Kiso-ko)*, October, 2005, pp.78-83 (in Japanese).

[5] Mohri, Y., Matsushima, K., Yamazaki, S., Lohani, T. N., Tatsuoka, F. and Tanaka, T., "New direction of earth reinforcement - Disaster prevention for earth fill dam –", *Gesynthtetics International,* IS Kyushu 2007 Special Issue, 16(4), 2009, pp. 246-273.

[6] Tatsuoka, F., Roles of facing rigidity in soil reinforcing, *Keynote Lecture, Proc. Earth Reinforcement Practice, IS-Kyushu '92* (Ochiai et al. eds.), 1992, Vol.2, pp.831-870.

[7] Tatsuoka, F., Tateyama, M, Uchimura, T. and Koseki, J., Geosynthetic-reinforced soil retaining walls as important permanent Structures," *Geosynthetic International,* 1997, Vol.4, No.2, pp.81-136.

[8] Tatsuoka, F., Koseki, J., Tateyama, M., Munaf, Y. and Horii, N., Seismic stability against high seismic loads of geosynthetic-reinforced soil retaining structures, *Keynote Lecture, Proc. 6th Int. Conf. on Geosynthetics,* Atlanta, 1998, Vo.1, pp.103-142.

[9] Tatsuoka, F., Tateyama, M., Aoki, H. and Watanabe, K., Bridge abutment made of cement-mixed gravel backfill, *Ground Improvement, Case Histories, Elsevier Geo-Engineering Book Series, Vol. 3* (Indradratna & Chu eds.), 2005, pp.829-873.

[10] Tatsuoka, F., Tateyama, M., Mohri, Y. and Matsushima, K., Remedial treatment of soil structures using geosynthetic-reinforcing technology, *Geotextiles and Geomembranes*, 2007, Vol.25, Nos. 4 & 5, pp.204-220.

[11] Tatsuoka, F., Hirakawa, D., Nojiri, M., Aizawa, H., Tateyama, M. and Watanabe, K., Integral bridge with geosynthetic-reinforced backfill, *Proc. First Pan American Geosynthetics Conference & Exhibition,* Cancun, Mexico, 2008a, pp.1199-1208.

[12] Tatsuoka, F., Hirakawa, D., Aizawa, H. Nishikiori, H. Soma, R and Sonoda, Y., Importance of strong connection between geosynthetic reinforcement and facing for GRS integral bridge, *Proc. 4th GeoSyntheticsAsia*, Shanghai, 2008b.

[13] Tatsuoka, F., Hirakawa, D., Nojiri, M., Aizawa, H., Nishikiori, H., Soma, R., Tateyama, M. and Watanabe, K., A new type integral bridge comprising geosynthetic-reinforced soil walls, *Gesynthtetics International*, IS Kyushu 2007 Special Issue, 2009, Vol.16, No.4, pp.301-326.

[14] Watanabe, K., Tateyama, M., Yonezawa, T., Aoki, H., Tatsuoka, F. and Koseki, J., Shaking table tests on a new type bridge abutment with geogrid-reinforced cement treated backfill," *Proc.* 7th *Int. Conf. on Geosynthetics*, Nice, 2002, Vol.1, pp.119-122.

First International Conference on Geotechnique, Construction Materials and Environment, Mie, Japan, Nov.21-23, 2011, ISBN: 978-4-9905958-0-7 C3051

Seepage-deformation Coupled Numerical Analysis of Unsaturated River Embankment Using an Elasto-plastic Model

F.Oka, and S.Kimoto, Department of Civil and Earth Resources Engineering, Kyoto University
R.Kato, Nikken Sekkei Civil Engineering Ltd.

ABSTRACT: In the present paper, a water-soil coupled elasto-plastic finite element analysis method is proposed for unsaturated river embankments by incorporating unsaturated soil-water characteristics. The simplified three-phase method have been developed based on the multi-phase porous theory by assuming that the compressibility of pore air is very high. For the constitutive model for soils, we have used an elasto-plastic model considering both the strain-induced degradation and the change of suction. Using the proposed method, we have analyzed a model test of the seepage flow through the unsaturated embankment and compared with the experimental results. And we have found the proposed method is applicable for the numerical modeling of unsaturated embankment with seepage flow. In addition, we have studied the effect of material parameters on the behavior of unsaturated embankment during the seepage flow by the parametric study. From the parametric study, the effects of the strain-induced degradation and of the change of saturation are clarified.

Keywords: unsaturation, embankment, seepage-deformation coupled analysis, elasto-plastic model

1. INTRODUCTION

In recent years, river embankments have been failed due to heavy rains in the world. It is well known that the one of the reason for the failure of the river embankment is seepage flow due to a rise of the river-water table.

In the present paper, we have numerically analyzed the deformation behavior of river embankment as well as the seepage flow during a rise of the water level using a soil-water coupled analysis method. We have analyzed a model test of the seepage flow through the unsaturated embankment and compared with the experimental results. In addition, we have studied the effect of material parameters on the behavior of unsaturated embankment during the seepage flow through the parametric study.

2. SEEPAGE-DEFORMATION COUPLED ANALYSIS OF UNSATURATED SOIL

2.1 Stress variables for the mixture

The total stress tensor is assumed to be composed of three partial stress values for each phase.

$$\sigma_{ij} = \sigma_{ij}^s + \sigma_{ij}^f + \sigma_{ij}^a \tag{1}$$

where σ_{ij} is the total stress tensor, and σ_{ij}^s, σ_{ij}^f, and σ_{ij}^a are the partial stress tensors for solid, liquid, and gas, respectively. The partial stress tensors for unsaturated soil can be given as follows:

$$\sigma_{ij}^f = -nS_r p^f \delta_{ij} \tag{2}$$

$$\sigma_{ij}^a = -n(1-S_r) p^a \delta_{ij} \tag{3}$$

$$\sigma_{ij}^s = \sigma'_{ij} - (1-n) S_r p^f \delta_{ij} - (1-n)(1-S_r) p^a \delta_{ij} \tag{4}$$

where σ'_{ij} is the skeleton stress [1], p^f and p^a are the pore water pressure and the pore gas pressure, respectively, n is the porosity, and S_r is the degree of saturation.

The skeleton stress is used as the basic stress variable in the model for unsaturated soil. Summing up Eqs.(2)-(4) we have the total stress tensor as

$$\sigma'_{ij} = \sigma_{ij} + P^F \delta_{ij}, \qquad P^F = S_r p^f + (1-S_r) p^a \tag{5}$$

where P^F is the average pore pressure.

Adopting the skeleton stress provides a natural application of the mixture theory to unsaturated soil. Equation (5) is similar to Bishop's definition for the effective stress of unsaturated soil. In addition to Equation (5), the effect of suction on the constitutive model should always be taken into account. This assumption leads to a reasonable consideration of the collapse behavior of unsaturated soil, which has been known as a behavior that cannot be described by Bishop's definition for the effective stress of unsaturated soil. Introducing suction ($p^c = -(p^a - p^f)$) into the model, however, makes it possible to formulate a model for unsaturated soil, starting from a model for saturated soil, by using the skeleton stress instead of the effective stress. An elasto-plastic model [2] has been be extended to unsaturated soil using the skeleton stress as well as the effect of suction.

2.2 Mass conservation

The mass conservation law for the three phases is given by

$$\frac{\partial \bar{\rho}^J}{\partial t} + \frac{\partial (\bar{\rho}^J \dot{u}_i^J)}{\partial x_i} = 0 \tag{6}$$

where $\bar{\rho}^J$ is the average density for the J phase and $\dot{u}_i^J$ is the velocity vector for the J phase.

$$\bar{\rho}^s = (1-n)\rho^s \tag{7}$$

$$\bar{\rho}^f = nS_r \rho^f \tag{8}$$

$$\bar{\rho}^a = n(1-S_r)\rho^a \tag{9}$$

where J =s, f, and g in which super indices s, f, and g indicate the solid, the liquid, and the gas phases, respectively. ρ^J is the mass bulk density of the solid, the liquid, and the gas.

2.3 Conservation of linear momentum for the three phases

The conservation law of linear momentum for the three phases is given by

$$\bar{\rho}^s \ddot{u}_i^s - Q_i - R_i = \frac{\partial \sigma_{ij}^s}{\partial x_j} + \bar{\rho}^s b_i \tag{10}$$

$$\bar{\rho}^f \ddot{u}_i^f + R_i - S_i = \frac{\partial \sigma_{ij}^f}{\partial x_j} + \bar{\rho}^f b_i \tag{11}$$

$$\bar{\rho}^a \ddot{u}_i^a + S_i + Q_i = \frac{\partial \sigma_{ij}^a}{\partial x_j} + \bar{\rho}^a b_i \tag{12}$$

where b_i is a body force, Q_i denotes the interaction between solid and gas phases, R_i denotes the interaction between solid and liquid phases, and S_i denotes the interaction between liquid and gas phases.

These interaction terms Q_i and R_i can be described as

$$R_i = nS_r \frac{\gamma_w}{k^f} \dot{w}_i^f \tag{13}$$

$$Q_i = n(1-S_r)\frac{\rho^a g}{k^a} \dot{w}_i^a \tag{14}$$

When we assume that the interaction between liquid and gas phases is small and ca be neglected, S_i can be described as

$$S_i \cong 0 \tag{15}$$

where k^f is the water permeability coefficient, k^a is the air permeability, $\dot{w}_i^f$ is the average relative velocity vector of water with respect to the solid skeleton, and $\dot{w}_i^a$ is the average relative velocity vector of air to the solid skeleton. The relative velocity vectors are defined by

$$\dot{w}_i^f = nS_r\left(\dot{u}_i^f - \dot{u}_i^s\right) \tag{16}$$

$$\dot{w}_i^a = n(1-S_r)\left(\dot{u}_i^a - \dot{u}_i^s\right) \tag{17}$$

Using Equation (16), Equation (11) becomes

$$\bar{\rho}^f(\ddot{u}_i^s + \frac{1}{nS_r}\ddot{w}_i^f) + R_i = \frac{\partial \sigma_{ij}^f}{\partial x_j} + \bar{\rho}^f b_i \tag{18}$$

When we assume that $\ddot{w}_i^f \cong 0$ and use Equations (3), (6), and (16), Equation (18) becomes

$$nS_r\rho^f \ddot{u}_i^s + nS_r \frac{\gamma_w}{k^f}\dot{w}_i^f = -nS_r\frac{\partial p}{\partial x_i} + nS_r\rho^f b_i \tag{19}$$

After manipulation, the average relative velocity vector of water to the solid skeleton and the average relative velocity vector of air to the solid skeleton are shown as

$$\dot{w}_i^f = -\frac{k^f}{\gamma_w}(\frac{\partial p}{\partial x_i} + \rho^f \ddot{u}_i^s - \rho^f b_i) \tag{20}$$

$$\dot{w}_i^a = -\frac{k^a}{\rho^a g}(\frac{\partial p}{\partial x_i} + \rho^a \ddot{u}_i^s - \rho^a b_i) \tag{21}$$

2.4 Equation of motion for the whole mixture

Based on the above fundamental conservation laws, we can derive equations of motion for the whole mixture. By adding Equations (10)-(12) and using Equations (7), (8), and (9)we have

$$\rho\ddot{u}_i^s + nS_r\rho^f(\ddot{u}_i^f - \ddot{u}_i^s) + n(1-S_r)\rho^a(\ddot{u}_i^a - \ddot{u}_i^s) = \frac{\partial \sigma_{ij}}{\partial x_j} + \rho b_i \tag{22}$$

where ρ is the mass density of the mixture as $\rho = \bar{\rho}^s + \bar{\rho}^f + \bar{\rho}^a$, and $\ddot{u}_i^s$ is the acceleration vector of the solid phase.

From the following assumptions,

$$\ddot{u}_i^s \gg (\ddot{u}_i^f - \ddot{u}_i^s), \quad \ddot{u}_i^s \gg (\ddot{u}_i^a - \ddot{u}_i^s), \tag{23}$$

the equations of motion for the whole mixture are defined as

$$\bar{\rho}\ddot{u}_i^s = \frac{\partial \sigma_{ij}}{\partial x_j} + \bar{\rho} b_i \tag{24}$$

2.5 Continuity equations for the fluid phase

Using the mass conservation law for the solid and the liquid phases, given in Equation (6), and assuming the incompressibility of soil particles, we obtain

$$\frac{\partial\left\{nS_r(\dot{u}_i^f - \dot{u}_i^s)\right\}}{\partial x_i} + S_r\dot{\varepsilon}_{ii}^s + nS_r\frac{\dot{\rho}^f}{\rho^f} + n\dot{S}_r = 0 \tag{25}$$

Incorporating Equation (20) and $p^f = -K^f\varepsilon_{ii}^f$ (K^f : volumetric elastic coefficient of liquid, ε_{ii}^f : volumetric strain of liquid) into the above equation leads to the following continuity equation for the liquid phases:

$$-\frac{\partial}{\partial x_i}\left[\frac{k^f}{\gamma_w}\left(\rho^f\ddot{u}_i^s + \frac{\partial p^f}{\partial x_i} - \rho^f b_i\right)\right] + S_r\dot{\varepsilon}_{ii}^s + n\dot{S}_r + nS_r\frac{\dot{p}^f}{K^f} = 0 \tag{26}$$

Similarly, we can derive the continuity equation as:

$$-\frac{\partial}{\partial x_i}\left[\frac{k^a}{\rho^a g}\left(\rho^a\ddot{u}_i^s + \frac{\partial p^a}{\partial x_i} - \rho^a b_i\right)\right] + (1-S_r)\dot{\varepsilon}_{ii}^s - n\dot{S}_r + n(1-S_r)\frac{\dot{p}^a}{K^a} = 0 \tag{27}$$

2.6 Air pressure

When we assume that the air is elastic and that its constitutive equation is given by $p^a = -K^a\varepsilon_{ii}^a$ (K^a : volumetric elastic coefficient of air, ε_{ii}^a : volumetric strain of air), Equation (27) becomes

$$K^a\left\{-\frac{\partial}{\partial x_i}\left[\frac{k^a}{\gamma_w}\left(\rho^a\ddot{u}_{ii}^s + \frac{\partial p^a}{\partial x_i} - \rho^a b_i\right)\right] + (1-S_r)\dot{\varepsilon}_{ii}^s - n\dot{S}r\right\} + n(1-Sr)\dot{p}^a = 0 \tag{28}$$

When the air compressibility is very large, compared with the other phases, we can set $K^a \cong 0$. In other words, from Equation (28), we obtain $\dot{P}^a \cong 0$. The above discussion means that we can assume that $P^a = 0$ if initial air pressure $P_{ini}^a = 0$. This shows that the continuity in Equation (28) is always satisfied.

Since saturation is a function of the pressure head, the time rate for saturation is given by

$$n\dot{S}_r = n\frac{dS_r}{d\theta}\frac{d\theta}{d\psi}\frac{d\psi}{dp}\dot{p}^c = n\frac{1}{n}C\frac{1}{\gamma_w}\dot{p}^c = \frac{C}{\gamma_w}\dot{p}^c \tag{29}$$

where $\theta = \dfrac{V_w}{V}$ is the volumetric water content, $\psi = \dfrac{p^c}{\gamma_w}$ is the pressure head, and $C = \dfrac{d\theta}{d\psi}$ is the specific water content.

Using Equation (29), Equation (26) becomes

$$-\frac{\partial}{\partial x_i}\left[\frac{k^f}{\gamma_w}\left(\rho^f \ddot{u}_i^s + \frac{\partial p^f}{\partial x_i} - \rho^f b_i\right)\right] + S_r \dot{\varepsilon}_{ii}^s + \left(\frac{nS_r}{K^f} + \frac{C}{\gamma_w}\right) = 0 \quad (30)$$

The apparent volumetric elastic coefficient of pore water, $\bar{K}^f$, is defined as

$$\frac{1}{\bar{K}^f} = \frac{S_r}{K^f} + \frac{C}{n\gamma_w} \quad (31)$$

Then, the continuity equation can be written as

$$-\frac{\partial}{\partial x_i}\left[\frac{k^f}{\gamma_w}\left(\rho^f \ddot{u}_i^s + \frac{\partial p^f}{\partial x_i} - \rho^f b_i\right)\right] + S_r \dot{\varepsilon}_{ii}^s + \frac{n}{\bar{K}^f}\dot{p}^f = 0 \quad (32)$$

3 UNSATURATED SEEPAGE CHARACTERISTICS

The soil-water characteristic model proposed [3] is used to describe the unsaturated seepage characteristics for which effective saturation S_e is adopted as

$$S_e = \frac{\theta - \theta_r}{\theta_s - \theta_r} = \frac{nS_r - \theta_r}{\theta_s - \theta_r} \quad (33)$$

where θ_s is the volumetric water content at the saturated state, which is equal to porosity n, and θ_r is the residual volumetric water content retained by the soil at the large value of suction head which is a disconnected pendular water meniscus.

In order to determine the soil-water characteristics, effective saturation S_e can be related to negative pressure head ψ through the following relation:

$$S_e = \left(1 + (\alpha\psi)^{n'}\right)^{-m} \quad (34)$$

where α is a scaling parameter which has the dimensions of the inverse of ψ, and n' and m determine the shape of the soil-water characteristic curve. The relation between n' and m leads to an S-shaped type of soil-water characteristic curve, namely,

$$m = 1 - \frac{1}{n'} \quad (35)$$

Specific water content C, used in Equation (29), can be calculated as

$$C = \alpha(n'-1)(\theta_s - \theta_r)S_e^{1/m}(1 - S_e^{1/m})^m \quad (36)$$

Specific permeability coefficient k_r, which is a ratio of the permeability of unsaturated soil to that of saturated soil, is defined [4] by

$$k_r = S_e^b\left\{1 - (1 - S_e^{1/m})^{n'}\right\} \quad (37)$$

Applying the above-mentioned relations, we can describe the unsaturated seepage characteristics.

In the analysis, the unsaturated region is treated in the following manner:

In the embankment, the initial suction, i.e., the initial negative pore water pressure, is assumed to be constant. Below the water level, the pore water pressure is given by the hydrostatic pressure. In the transition region between the water level and the constant suction region, we assume that the pore water pressure is linearly interpolated (Figure 1).

When the pressure head is negative, the increase in soil modulus due to suction is considered.

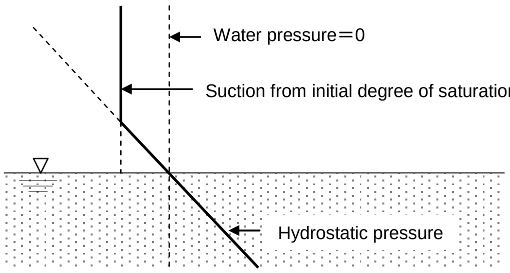

Fig 1. Initial pressure

4 ELASTO-PLASTIC MODEL CONSIDERING BOTH STRAIN-INDUCED DEGRADATION AND CHANGE OF SUCTION

For the constitutive model, we use elasto-plastic model extended to unsaturated soil [2][5]. In this study, we consider both the strain-induced degradation and the change of suction.

4.1 Effect of strain-induced degradation

For considering the strain-induced degradation, we change overconsolidation boundary surface to Equation (38).

$$\sigma'_{mb} = \left\{\sigma'_{mbf} + \left(\sigma'_{mbi} - \sigma'_{mbf}\right)\exp(-\beta z)\right\}\exp\left(\frac{1+e_0}{\lambda - \kappa}v^P\right) \quad (38)$$

$$z = \int dz = \int \left(d\varepsilon_{ij}^P d\varepsilon_{ij}^P\right)^{1/2} \quad (39)$$

where σ'_{mbf} is the convergence value of σ'_{mbi} ($\sigma'_{mbf} = n^*\sigma'_{mbi}$, n^* is the reduction rate of σ'_{mbi}), β is material parameter for adjust the speed of convergence of σ'_{mbi}.

4.2 Effect of change of suction

For considering the change of suction, we change overconsolidation boundary surface to Equation (40).

$$\sigma'_{mb} = \sigma'_{mbi}\exp\left(\frac{1+e_0}{\lambda - \kappa}v^P\right)\left[S_{IE} + S_I\exp\left\{-s_d\left(\frac{P_i^C}{P^C} - 1\right)\right\}\right] \quad (40)$$

where S_{IE} is the strength reduction rate of after releasing the suction, S_I is the strength increase rate in initial suction ($S_{IE} + S_I = 1.0$), s_d is the parameter of adjusting the speed of change of strength, P_i^C is initial suction, P^C is the current suction. Finally, Overconsolidation boundary surface is defined as

$$\sigma'_{mb} = \left\{\sigma'_{mbf} + \left(\sigma'_{mbi} - \sigma'_{mbf}\right)\exp(-\beta z)\right\} \exp\left(\frac{1+e_0}{\lambda - \kappa}v^P\right)\left[S_{IE} + S_I\exp\left\{-s_d\left(\frac{P_i^C}{P^C} - 1\right)\right\}\right] \quad (41)$$

Next, for considering the change of suction, we change the plastic shear coefficient to function of suction. Then, we define the parameter B^* which adjust the speed of kinematic hardening as

$$B_{suc}^* = B_0^* \left[S_{IBE} + S_{IB} \exp\left\{ -s_{db} \left(\frac{P_i^C}{P^C} - 1 \right) \right\} \right] \tag{42}$$

where S_{IBE} is the strength reduction rate of after releasing the suction, S_{IB} is the strength increase rate in initial suction ($S_{IBE} + S_{IB} = 1.0$), s_{db} is the parameter of adjusting the speed of change of strength.

5 NUMERICAL ANALYSIS OF A RIVER EMBANKMENT

In the numerical analysis we have used a finite element method to solve governing equations. The computer program LIQCA2D-SF11 [5] has been developed and used.

5.1 Finite element mesh and boundary conditions

Figure 2 shows the model of the river embankment and the finite element mesh used in the analysis and the position of gauges at experiment. The soil parameters for Yodogawa sand are listed in Table 1, which is a soil used for the reconstruction of levee of Yodo river [6]. For the simplified model, the effect of suction and the strain-induced degradation is not considered. Initial saturation of embankment is 60% and the coefficient of permeability for saturated soil is shown in Table 2. The air permeability is not specified because the analysis is simplified such that the air pressure is always zero, as indicated in Equation (28). Taking account of the previous analysis [7], we set the water characteristic curve and specific permeability as Figure 3. The water level-time profile is shown in Figure 4.

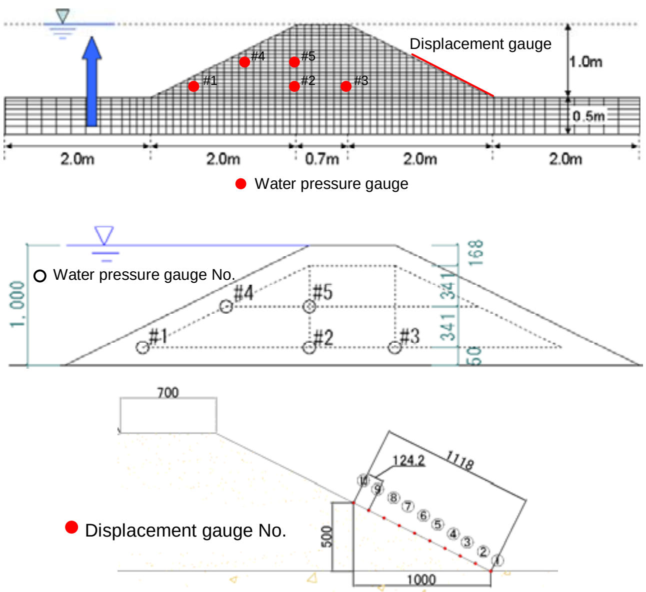

Fig 2. Model of embankment and the finite element mesh.

Table 1. Material parameters

Soil	yodo
Method※	2
Initial void ratio e_0	0.535
Compression index λ	0.0804
Swelling index κ	0.009
Normalized Ini. shear modulus G_0/σ'_{m0}	250.0
Gravitational acceleration g (m/s^2)	9.8
Density ρ (t/m^3)	1.9
Stress ratio at phase transformation M_m^*	1.270
Stress ratio at failure M_f^*	1.270
Hardening parameter B_0^*	800
Hardening parameter B_1^*	20
Hardening parameter C_f	600
Quasi-OCR OCR^*	1.3
Anisotoropy parameter C_d	2000
Dilatancy parameters D_0^*,n	2.0, 2.0
Plastic ref. strain γ_{ref}^{P*}	0.008
Elastic ref. strain γ_{ref}^{E*}	0.08

Table 2.Coefficient of permeability for saturated soil(m/s)

Embankment		Surface element on river side	
Horizontal	Vertical	Horizontal	Vertical
4.79×10^{-5}	4.79×10^{-6}	8.79×10^{-7}	8.79×10^{-7}

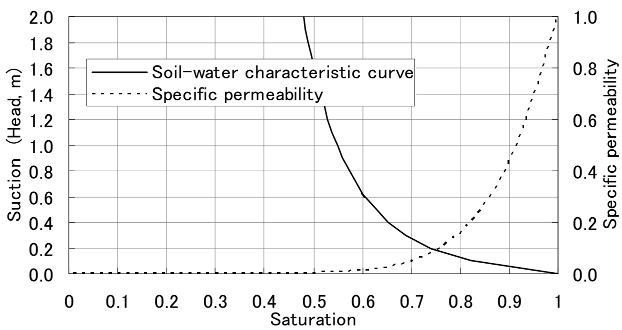

Fig 3. Water characteristic curve and specific permeability.

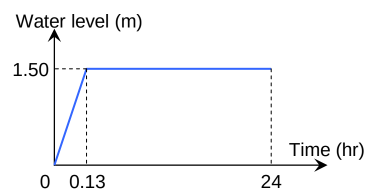

Fig 4. Water level.

5.2 Results

The distribution of saturation is illustrated in Figures 5. After the water level of the river reached the crest of the embankment, the seepage flow infiltrated from the river side to the back side. The distribution of the horizontal local hydraulic gradient after 24 hours is illustrated in Figure 6. The horizontal local hydraulic gradient at the toe of the embankment on the back side was not over 0.5. In the Guide for Structural Investigations of River Embankments, the allowable gradient for Piping is 0.5 [8]. And then, the accumulated plastic deviatoric strain ($\gamma^p = \int d\gamma^p$, $d\gamma^p = (de_{ij}^p de_{ij}^p)^{1/2}$) was 2.45% at the toe of the embankment (Figure 7).

The time histories of water pressure both experiment and analysis at a water pressure gauge point are illustrated in Figure 8. The level of the pressure rise of the analysis is the same as that of experiment. After 24 hours, the value of water pressure of analysis agrees with that of experimental result.

The time histories of displacement of normal to the surface on the back side of the embankment are illustrated in Figure 9. Both analysis and experiment, displacement has occurred rapidly after 5 hours. After 24 hours, the maximum value of displacement of analysis was about 2.4mm and that of experiment was 2.8mm. Hence, we have found the proposed method is applicable for the numerical modeling of unsaturated embankment with seepage flow.

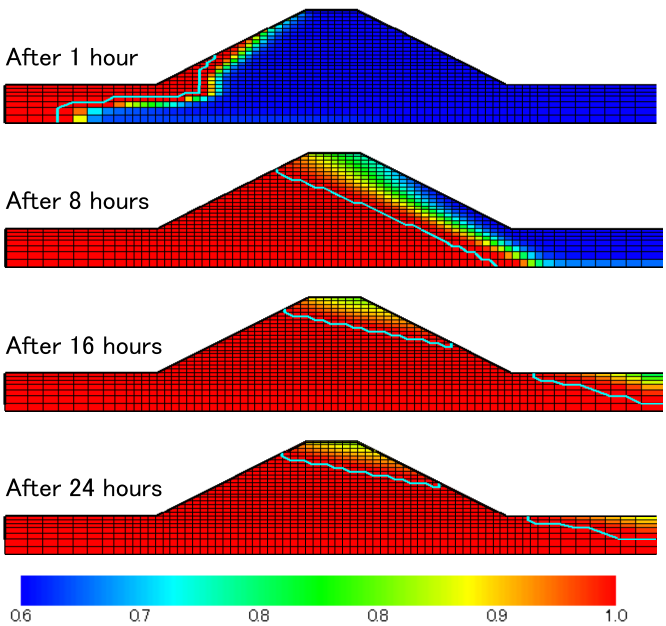

Fig 5. Distribution of saturation and infiltration line.

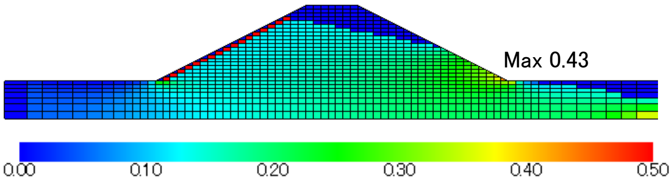

Fig 6. Distribution of horizontal local hydraulic gradient (After 24 hours).

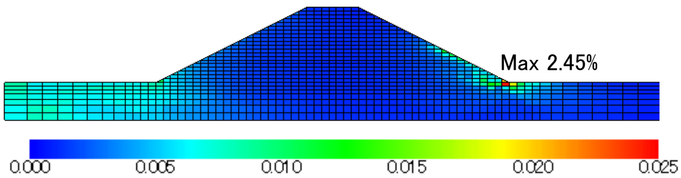

Fig 7. Distribution of γ^p (After 24 hours).

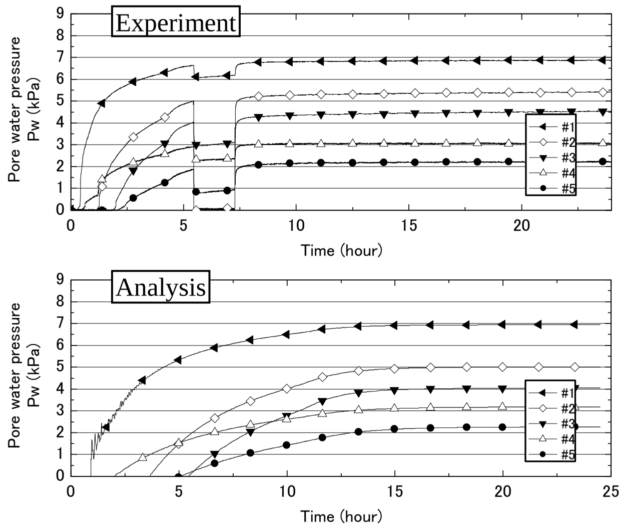

Fig 8. Time histories of water pressure.

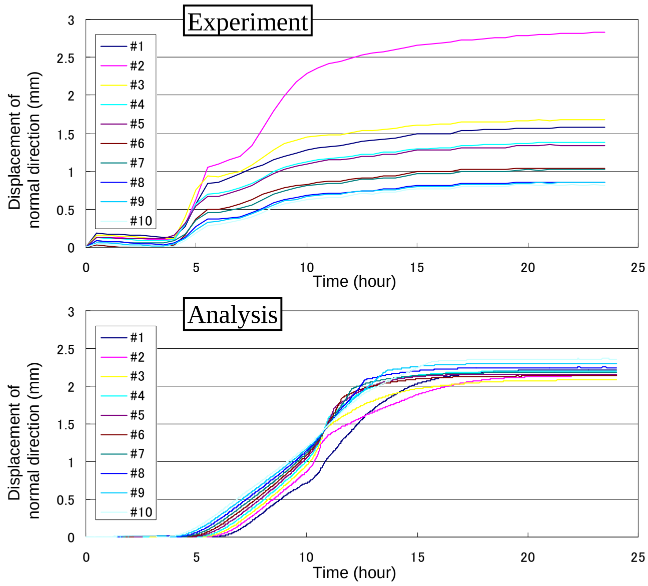

Fig 9. Time histories of displacement of normal direction.

6 PARAMETRIC STUDY OF THE EFFECT OF THE STRAIN-INDUCED DEGRADATION AND OF THE CHANGE OF SUCTION

6.1 Finite element mesh and boundary conditions

Figure 10 shows the prototype model of river embankment and the finite element mesh used in the analysis. The soil parameters for Yodogawa sand are same as Chapter 4. But, we set coefficient of permeability for saturated soil as 4.79×10^{-5} (m/s) in all elements. The rising rate of the water level is 1/3 (m/hour) until the water level reaches the crest of the embankment (18 hours), and then it remains constant for 24 hours. And then, we change strain-induced degradation parameters and/or suction parameters (Equation (41), Equation (42)) in Case1 ~ Case7. The analysis cases and the results from this study are listed in Table 3. In this table, γ^p is the accumulated plastic deviatoric strain at the toe of the embankment on the river side.

6.2 Numerical results

The distribution of saturation is illustrated in Figure 11. The water level of the river reached the crest of the embankment after 18 hours. Then, the seepage flow infiltrated from the river side to the land side. The distribution of the horizontal local hydraulic gradient after 24 hours is illustrated in Figure 12. The horizontal local hydraulic gradient at the toe of the embankment on the land side was more than 0.5.

The distributions of saturation are presented in Figure 13 (Case 4, 7). Compared with the result of Case 0, we have found that strain-induced degradation parameters and the suction parameters do not affect infiltration. The reason is because continuity equations are not changed if we consider both the strain-induced degradation and the change of suction.

The distributions of the accumulated plastic deviatoric strain is illustrated in Figure 14. In the cases, i.e. Cases 2, 4, 6, 7, in which we take account of the decrease in B^* due to the decrease of suction associated with the water infiltration, larger strain occurs over the wide area of embankment. The results listed in Table 3 show that considering the strain-induced degradation and/or the decrease in suction leads to the larger value of the accumulated plastic deviatoric strain at the toe of the embankment on the front side.

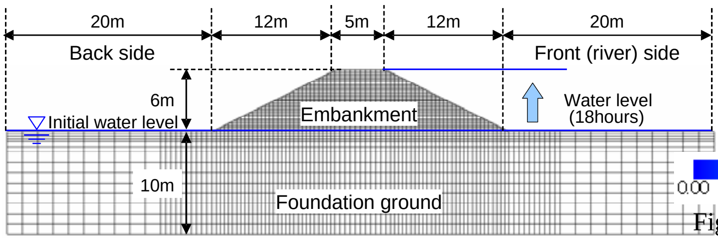

Fig 10. Model of embankment and the finite element mesh.

Table 3. Analysis cases and the results

Case	Suction parameter						Strain-induced degradation parameter		After 24hours γ^p (%)
	S_{IE}	S_I	s_d	S_{IBE}	S_{IB}	s_{dB}	n^*	β	
0	—	—	—	—	—	—	—	—	9.34
1	0.5	0.5	0.25	—	—	—	—	—	11.88
2	—	—	—	0.5	0.5	0.25	—	—	19.03
3	—	—	—	—	—	—	0.5	50	12.72
4	0.5	0.5	0.25	0.5	0.5	0.25	—	—	20.33
5	0.5	0.5	0.25	—	—	—	0.5	50	12.30
6	—	—	—	0.5	0.5	0.25	0.5	50	15.85
7	0.5	0.5	0.25	0.5	0.5	0.25	0.5	50	15.72

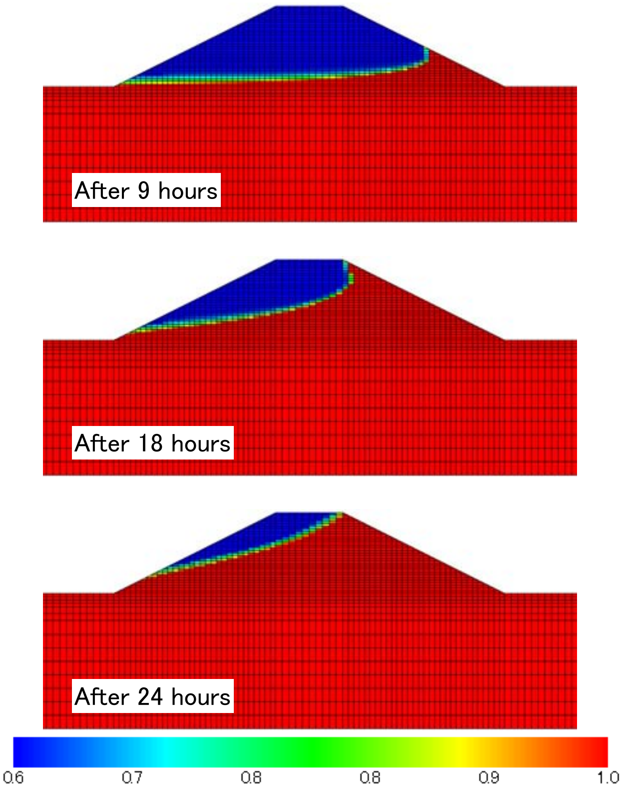

Fig 11. Distribution of saturation (Case 0).

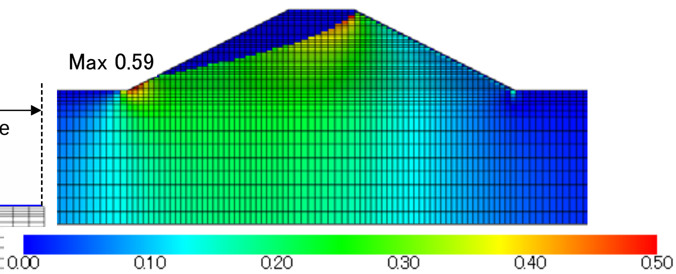

Fig 12. Distribution of horizontal local hydraulic gradient (Case 0, after 24 hours).

Considering the suction dependency of the parameter B^* (Case 2, 4, 6, 7), we can observe comparatively larger strain compared with other cases for the decrease in suction.

7 CONCLUSIONS

We have analyzed a model test of the seepage flow through the unsaturated embankment and compared with the experimental results. From the comparison between numerical and experimental results, we have found the proposed method is applicable for the numerical modeling of unsaturated embankment with seepage flow.

By the parametric study, it has been found that considering the strain-induced degradation and/or the change of suction leads to the larger accumulated plastic deviatoric strain at the toe of the embankment on the front side. In particular, in the case with the decrease in the parameter B^* due to the change of suction, large strain occurred over the wide area of embankment. However, strain and/or suction-induced degradation does not affect infiltration pattern.

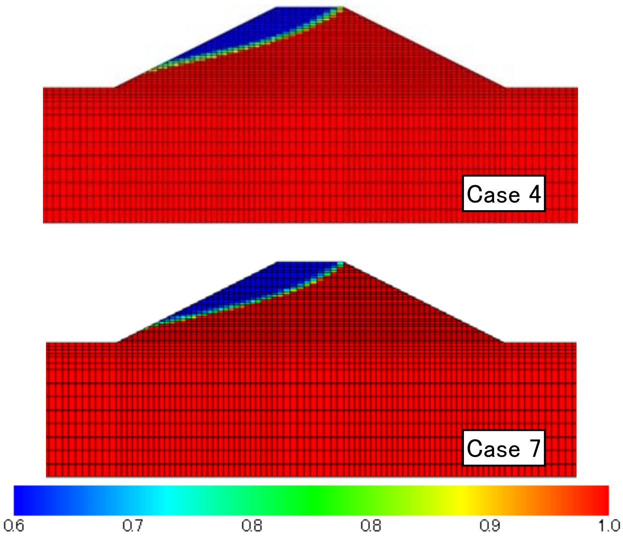

Fig 13. Distribution of saturation (After 24 hours).

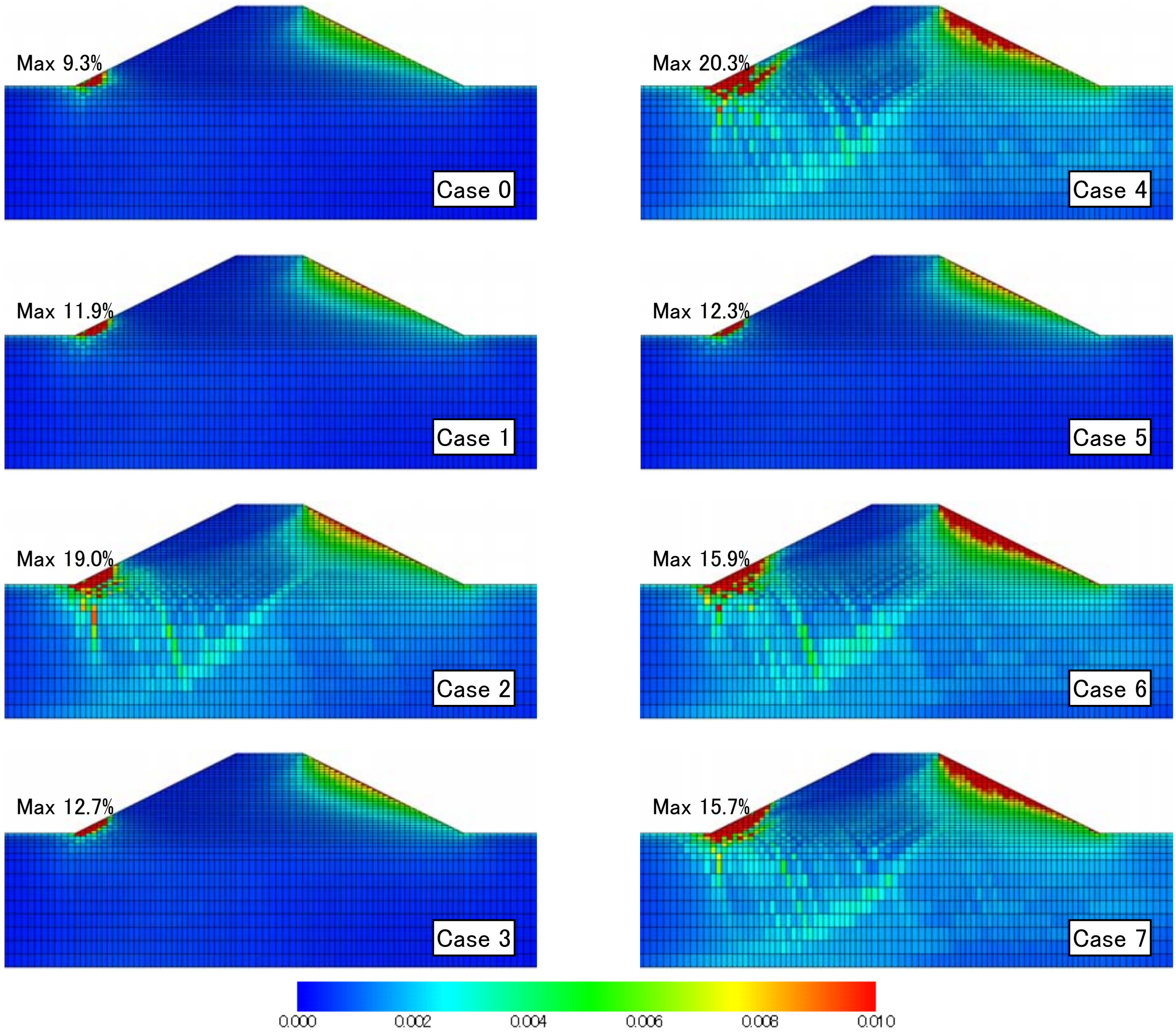

Fig 14. Distribution of γ^p (After 24 hours).

8 REFERENCES

[1] Jommi, C., “Remarks on the constitutive modelling of unsaturated soils”, Experimental Evidence and Theoretical Approaches in Unsaturated Soils, Tarantino, A. and Mancuso, C. eds., Balkema, 2000, pp.139-153.

[2] Oka,F, A.Yashima,A.Tateishi,Y.Taguchi and S.Yamashita, “A cyclic elasto-plastic constitutive model for sand considering a plastic-strain dependence of the shear modulus”, Geotechnique, 49, 5,1999, pp.661-680.

[3] van Genuchten,M.T.,”A closed-form equation for predicting the hydraulic conductivity of unsaturated soils”, Soil Sci. Soc. Of Am. J.,44,1980, pp.892-898.

[4] Brooks, R.H. and Corey, A.T., “Hydraulic properties of porous media, Hydrology Papers”, Colorado State University, 1964, pp.24.

[5] Kato,R. “Development of unsaturated seeage-deformation coupled simulation method and its application to river embankment”, PhD Thesis, Kyoto University, 2011

[6] Kinki Regional Development Bureau, Ydogawa River Office, “ Research report on reinforcement of river embankment against seepage and overflow”, 2010

[7] Morinaka,Y., “ Multi-phase seepage-deformation coupled analysis of river embankment using FEM and MPM ” ,Master Thesis, Graduate school of Engineering, Kyoto University, 2010.

[8] Japan Institute of Construction Engineering, Guide for Structural Investigations of River Embankments, 2002.

[9] F. Oka, S. Kimoto, N. Takada, H. Gotoh and Y. Higo, “A seepage-deformation coupled analysis of an unsaturated river embankment using a multiphase elasto-viscoplastic theory”, Soils and Foundations, Vol.50, No.4, 2010, pp.483-494.

First International Conference on Geotechnique, Construction Materials and Environment, Mie, Japan, Nov.21-23, 2011, ISBN: 978-4-9905958-0-7 C3051

Progressive Failure of Shallow Anchor in Dense Sand Evaluated by 2D and 3D Finite Element Analysis and Model Tests

Toshinori SAKAI, Dept. of Environmental Science and Technology, Graduate school of Bioresources, Mie University, Japan
Md. ROKONUZZAMAN, Dept. of Civil Engineering, Khulna University of Engineering & Technology, Bangladesh

ABSTRACT: The progressive failure of a shallow anchor embedded in granular materials was evaluated in terms of scale, embedment, and shape effect by conventional 1 g tests and extensive elastoplastic finite element (FE) analysis. The model tests were performed using a trap door and isolated anchors in Toyoura and Soma sands. The FE analysis employed a constitutive model for a non-associated strain hardening/softening elastoplastic material. This model incorporated the effect of shear band thickness. Progressive failure depended on the density of the testing bed, h/D, and the anchor shape. The shape effect of an isolated anchor was considered to be due to progressive failure.

Keywords: anchor, progressive failure, scale effect, shape effect, shear band

1. INTRODUCTION

Anchors are widely utilized for stabilizing towers, bridges, slopes, and various other structures. Several studies have investigated the uplift resistance of anchors [1–3]. Theoretical studies have focused on stability analysis based on rigid plastic and elastoplastic FE analysis [4–6]. Rigid plastic analysis is widely employed for designing structures due to its convenience. However, it requires making arbitrary assumptions regarding the shape of the failure surface observed during model tests. If all tests are conducted in the same granular materials with a constant density, the values of Nq (= $T/A\gamma h$, where T is the uplift capacity, γ is the effective unit weight of sand, h is the embedment depth, and A is the anchor area) obtained by rigid plastic analysis will remain relatively constant for constant h/D (where D is the diameter or the smallest dimension of the anchor). De Beer [7] discussed the scale effect of the footing problem and showed that the bearing capacity factor generally decreases with increasing footing width. The scale effect is caused by the progressive failure and crushing of sand particles subjected to a high confining pressure. Since anchor uplifting is generally performed at low confining pressures in conventional 1 g tests, crushing of sand particles is expected to be negligible during such tests. The failure of sand mass is usually progressive and it is linked to the development of a narrow shear band of localized deformation. The appearance of a shear band is frequently accompanied by a softening phenomenon. Few studies have employed numerical models that fully consider progressive failure with shear banding [8,9]. Anchor problems typically consider three kinds of anchors: strip, circular, and rectangular anchors, which respectively correspond to plane strain, axisymmetric, and three-dimensional problems. Most studies adopt a two-dimensional design approach for calculating the anchor uplift resistance [10–12]. Ovesen [13] found that an isolated anchor did not correspond to a two-dimensional problem. Meyerhof and Adams introduced an empirical shape factor to calculate the peak uplift load based on plane strain assumptions for circular and rectangular anchors. Dickin [14] proposed embedment and shape factors. Isolated anchors are currently designed based on empirical methods. Few researchers have proposed rigorous numerical models that consider the shape effect. The present study seeks to explain the progressive failure of a shallow anchor in granular materials at the 1 g level and it compares the failure mechanisms in isolated and strip anchors to determine the shape effect on the uplift resistance.

2. TESTING APPARATUS

Tests were performed using an anchor pullout machine for isolated anchors and a trap-door testing apparatus for strip anchors. The cylindrical container used in these tests was 59

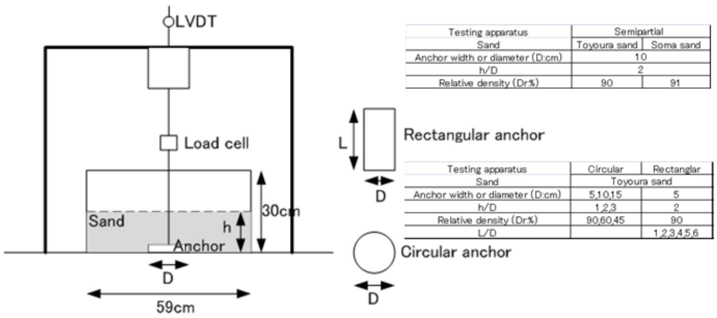

Testing apparatus	Semipartial	
Sand	Toyoura sand	Soma sand
Anchor width or diameter (D:cm)	10	
h/D	2	
Relative density (Dr:%)	90	91

Testing apparatus	Circular	Rectanglar
Sand	Toyoura sand	
Anchor width or diameter (D:cm)	5,10,15	5
h/D	1,2,3	2
Relative density (Dr:%)	90,60,45	90
L/D		1,2,3,4,5,6

Fig.1 Anchor testing apparatus

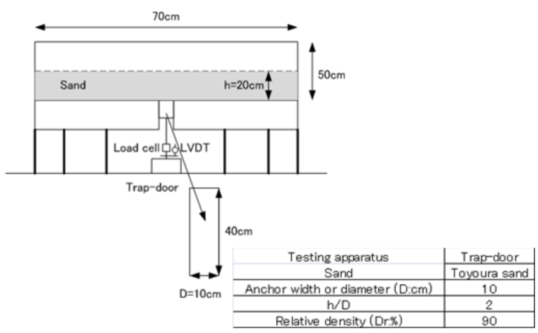

Testing apparatus	Trap-door
Sand	Toyoura sand
Anchor width or diameter (D:cm)	10
h/D	2
Relative density (Dr:%)	90

Fig.2 Trap-door testing apparatus

cm in diameter and 30 cm in height (Fig. 1). Flat circular and square anchors made of 0.5-cm-thick steel plate with widths (B) or diameters (D) of 5, 10, and 15 cm were used. The rectangular anchors had aspect ratios (L/B, where L is the length of the anchor) of 1, 2, 3, 4, 5 and 6. The trap-door testing apparatus consisted of a glass-walled box and a trap door. The testing apparatus was 70 cm long, 50 cm high, and 40 cm wide (Fig. 2) and the trap door width (D) was 10 cm. These dimensions were selected so that boundary effects could be neglected. Granular masses were prepared by pluviating air-dried Toyoura and Soma sands, which had mean particle diameters of 0.16 and 0.45 mm and relative densities of Dr = 90, 60, and 45% and Dr = 91%, respectively. The tests were performed for embedment ratios (h/D; h: granular mass depth) of 1, 2, and 3. All tests were conducted under normal gravity conditions. To study the propagation of the shear band, colored granular layers were placed against the front glass wall of the apparatus.

3. NUMERICAL MODELS

In the FE analysis, the shear band effect was introduced in the constitutive equation. An elastoplastic model with a non-associated flow rule and strain hardening/softening material properties was used in the constitutive model. A Mohr–Coulomb yield function and a Drucker–Prager plastic potential function were employed. Four-node Lagrangian elements were used with reduced integration. A dynamic relaxation method with a return mapping algorithm was applied to the integration algorithm.

To include the mesh-size effect induced by softening of the material, a characteristic length scale was introduced. It is a function of the shear band thickness and the ratio of the shear band area to the FE area:

$$S = \frac{F_b}{F_e} \qquad (1)$$

where Fb is the shear band area in each FE and Fe is the FE area. The shear band thickness was used based on the results of shear band thickness studies.

The yield function（f）and plastic potential function（Ψ）are given by the following expressions,

$$f = 3\alpha(\kappa)\sigma_m + \frac{\sqrt{J_2}}{g(\theta)} - \gamma(\kappa) = 0 \qquad (2)$$

$$\Psi = 3\alpha'(\kappa)\sigma_m + \sqrt{J_2} - \gamma(\kappa) = 0 \qquad (3)$$

$$\kappa = \int d\varepsilon^p \qquad (4)$$

where, σ_m is the mean stress, J_2 is the second invariant of deviatoric stress and θ is the Lode angle.

In 2D FE analysis, the frictional hardening/softening function $\alpha(\kappa)$ is expressed as

$$\alpha(\kappa) = \left\{ \frac{2\sqrt{\kappa\varepsilon_f}}{\kappa + \varepsilon_f} \right\}^m \alpha_p \quad \text{(hardening-regime; } \kappa \le \varepsilon_f) \qquad (5)$$

$$\alpha(\kappa) = \alpha_r + (\alpha_p - \alpha_r)\exp\left\{ -\left(\frac{\kappa - \varepsilon_f}{\varepsilon_r} \right)^2 \right\}$$

(softening-regime; $\kappa > \varepsilon_f$) (6)

where, m , ε_f and ε_r are the hardening/softening material parameters.

The parameters of α_p and α_r are estimated using the following equations,

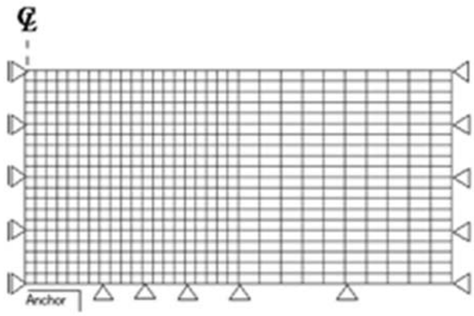

Fig.3 2D FE mesh

Table 1 Summarize the parameters used in the FE analysis

	2D FE analysis		3D FE analysis
Density (ρ_d:g/cm^3)	1.63	Density (ρ_d:g/cm^3)	1.63
Void ratio (e)	0.62	Void ratio (e)	0.62
Relative density (D_r)	0.95	Relative density (D_r)	0.95
Coefficient of shear modulus (G_0)	500	Coefficient of shear modulus (G_0)	150
Residual friction angle (ϕ_r:degrees)	33	Residual friction angle (ϕ_r:degrees)	35
	–	Peak friction angle (ϕ_p:degrees)	45
Poisson's ratio (ν)	0.3	Poisson's ratio (ν)	0.3
Sear band thickness (SB:cm)	0.3	Sear band thickness (SB:cm)	0.3
ε_f	0.1	B	0.5
ε_r	0.1	C	0.5
ε_d	0.3		
m	0.1		
β	0.1		

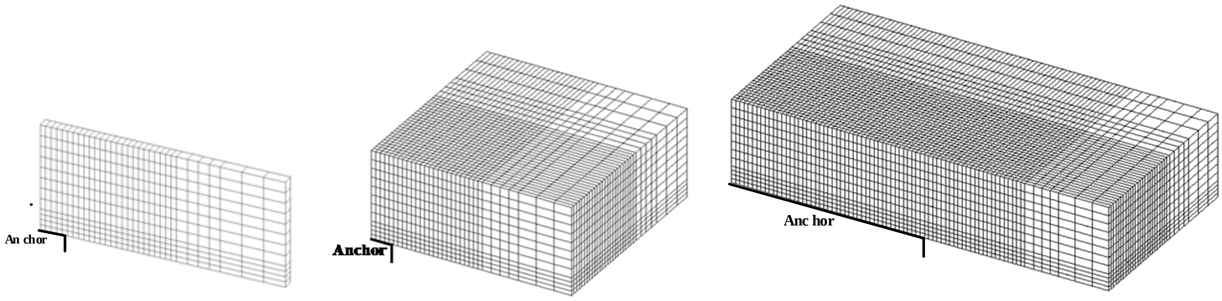

Fig.4 3D FE meshes

$$\alpha_p = \frac{2\sin\phi_p}{\sqrt{3}(3-\sin\phi_p)} \tag{7}$$

$$\alpha_r = \frac{2\sin\phi_r}{\sqrt{3}(3-\sin\phi_r)} \tag{8}$$

where, ϕ_p and ϕ_r are the peak and residual friction angle, respectively.

The peak friction angle of ϕ_p is estimated from the empirical relations proposed by Bolton (1986).

$$I_r = D_r\left\{5-\ln\left(\frac{\sigma_m}{150}\right)\right\}-1 \quad (\sigma_m \geq 147\,\mathrm{kN/m^2}) \tag{9}$$

$$I_r = 5D_r - 1 \quad (\sigma_m < 147\,\mathrm{kN/m^2}) \tag{10}$$

$$\phi_p = 3I_r + \phi_r \tag{11}$$

where, D_r is relative density.

The plastic potential function $\alpha'(\kappa)$ is defined as,

$$\alpha'(\kappa) = \frac{2\sin\psi}{\sqrt{3}(3-\sin\psi)} \tag{12}$$

The dilatancy angle of ψ is estimated from modified Rowe's stress-dilatancy relationship,

$$\sin\psi = \frac{\sin\phi_{mob} - \sin\phi'_r}{1-\sin\phi_{mob}\sin\phi'_r} \tag{13}$$

$$\phi'_r = \phi_r\left[1-\beta\exp\left\{-\left(\frac{\kappa}{\varepsilon_d}\right)^2\right\}\right] \tag{14}$$

where, β and ε_d are the stress-dilatancy material parameters.

The function $\gamma(\kappa)$ can be neglected in the case of cohesionless soil.

The elastic moduli are estimated from modified the equation proposed by Hardin(1968) and are given the following equations in case of clean sand:

$$G = G_0\frac{(2.17-e)^2}{1+e}\sigma_m^{0.5} \tag{15}$$

$$K = \frac{1(1+\nu)}{3(1-2\nu)}G \tag{16}$$

where, ν is Poisson's ratio, e is the void ratio and G_0 is the constant of initial shear modulus.

In 3D FE analysis, simple hardening/softening functions were used for 3D problems to save computational time. The frictional hardening/softening function $\alpha(\kappa)$ and $\alpha'(\kappa)$ are expressed as

$$\alpha(\kappa) = \alpha_p + \frac{\alpha_1\kappa}{B+\kappa} \tag{17}$$

$$\alpha_1 = -(\alpha_p - \alpha_r) \tag{18}$$

$$\alpha_p = \frac{2\,sin\,\phi_p}{\sqrt{3}(3-sin\,\phi_p)} \tag{19}$$

$$\alpha_r = \frac{2\,sin\,\phi_r}{\sqrt{3}(3-sin\,\phi_r)} \tag{20}$$

$$\alpha'(\kappa) = \alpha'_p\left(1-\frac{\kappa}{C+\kappa}\right) \tag{21}$$

$$\alpha'_p = \frac{2\,sin\,\psi_0}{\sqrt{3}(3-sin\,\psi_0)} \tag{22}$$

The values of ε_f, ε_r, ε_d, m , B and C were evaluated on the back-prediction of a triaxial compression test by comparing results of finite element analysis with experiment. Table 1 summarizes the parameters used in the finite element analysis. The details of the numerical method were shown in reference of Sakai and Tanaka [8,9].

Fig. 3 shows the FE mesh used for the 2D analysis. The failure mechanism in the rectangular anchor foundation is compared with those in the square and strip anchors to determine how the shape effect affects the uplift resistance. In this regard, 3D models with H/D = 2, D = 50 mm, and L/D = 1, 2, 3, 4, 5, 6, 7, 8, 10, and 20, and a 3D plane strain model (L/D = ∞) were created to investigate how the shape effect affects the uplift resistance of the rectangular anchors. Some meshes are shown in Fig. 4.

4. PROGRESSIVE FAILURE

Fig. 5 shows shear band development in a sand mass. These tests were performed in dense Toyoura sand on a trap door with D = 10 cm and h/D = 2. Two almost identical shear bands developed from the edges of the trap door into the sand mass. As the trap door moved upward, outer primary shear bands became inactive and additional steeper inner shear bands developed. The shear bands propagated upward.

Fig. 6 shows the development of shear bands in Toyoura and Soma sands in a semipartial testing apparatus at a displacement of 5.0 mm. Since similar shear bands developed from the edges of the trap door, photographs were taken from the left-hand side. A secondary steeper shear band developed

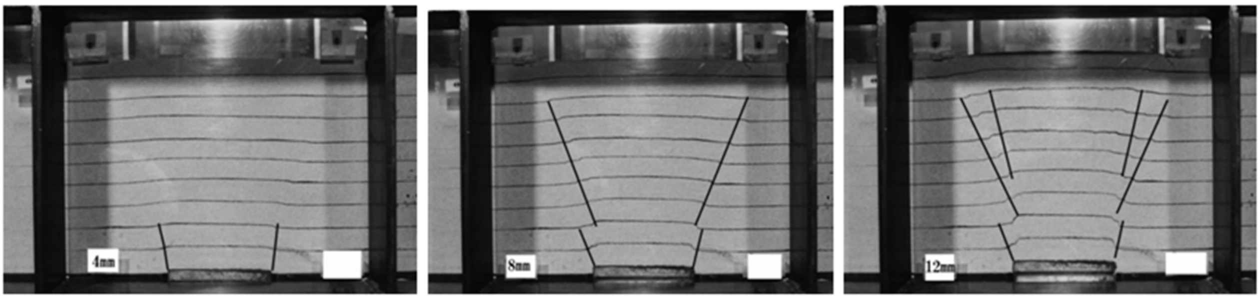

(a)Disp.=4mm (b) Disp.=8mm (c)Disp.=12mm

Fig.5 Shear band development in trap-door test (D=10cm, h/D=2, dense) in Toyoura sand after the outer primary shear band became inactive. Shear band propagation was greater for smaller grain diameters. Toyoura and Soma sands had shear band thicknesses of about 3 and 9 mm, respectively. The observed shear band thicknesses were about 20 times greater than the mean grain diameter. Fig. 7 compares the uplift resistance against displacement curves obtained using Toyoura sand with different densities and a circular anchor with D = 5 cm. For high-density sand, the uplift resistance clearly decreases after the maximum uplift resistance is attained and obvious softening occurs. For loose conditions, the uplift resistance remains almost constant after the maximum uplift resistance is realized and softening is not obvious. The residual uplift resistances were similar for all densities. Fig. 8 shows shear band propagation at a displacement of 10 mm for dense and medium conditions. Shear band propagation progressed more in dense conditions. Fig. 9 compares the Nq and displacement curves (D = 5 and 10 cm; h/D = 1 and 3) obtained using a circular anchor. For the embedment ratio, h/D = 3, a remarkably large displacement difference is required to attain peak Nq between D = 5 and 10 cm. Remarkable progressive failure occurs for h/D = 3.

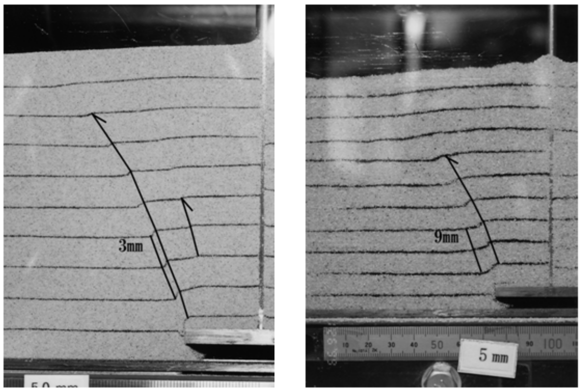

(a)Toyoura Sand (b) Soma Sand

Fig.6 Shear band development in sand mass (D=5cm, Disp.=5mm)

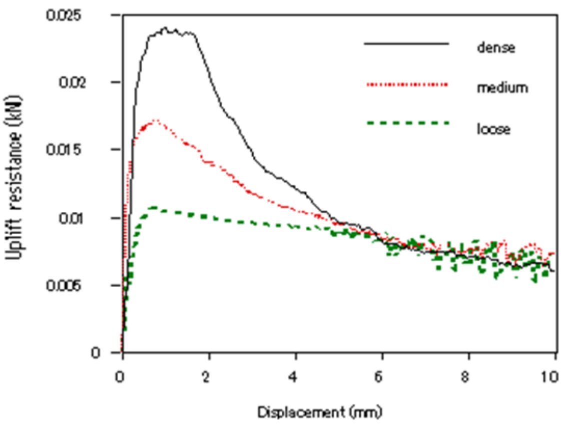

Fig.7 Uplift resistance-displacement curves on circular anchor obtained by experiments (Toyoura sand, D=5cm)

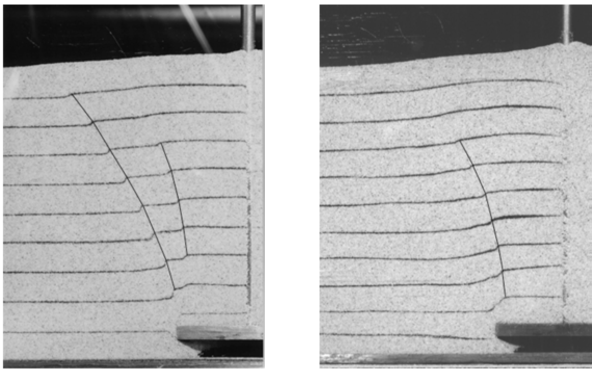

(a) Dense (b) Loose

Fig.8 Shear band development in dense and loose condition (Toyoura sand, D=5cm, Disp=10mm)

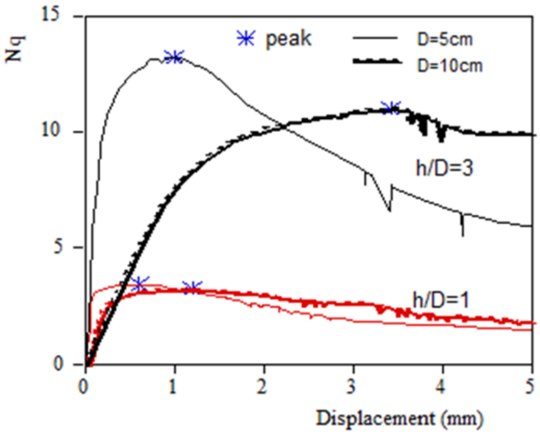

Fig. 9 Nq-displacement curves obtained by experiments (Dense)

5. SCALE EFFECT

Fig. 10 compares the numerically and experimentally obtained uplift resistance–displacement curves in loose, medium, and dense beds for a circular anchor. These curves were obtained for a circular anchor with Toyoura sand for D = 10 cm and h/D = 2. These results reveal that the numerically calculated maximum uplift resistance, displacement corresponding to the maximum uplift resistance, and residual uplift resistance coincide with those obtained from experimental results. Figs. 11 and 12 show that the shear band propagates upward from the edge of the anchor plate and that the directions of the narrow localized zones obtained from the distributions of the maximum shear strain in FE analysis almost coincide with the directions of the outermost shear bands observed experimentally for loose, medium and dense sands. Fig. 13 shows the relationship between the peak Nq and D obtained by experiment and numerical analysis for dense, medium, and loose beds. Both experimental and numerical results show that the peak Nq generally decreases with increasing D in the dense bed and that peak Nq does not decrease in the loose bed. The scale effect was clearly observed in the dense bed. Fig. 14 shows the relationship

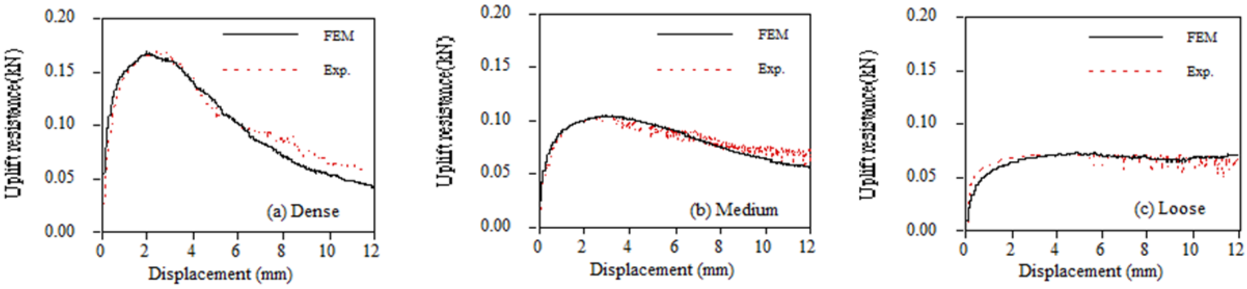

Fig.10 Uplift resistance-displacement curves on circular anchor obtained by experiment and numerical (D=10cm)

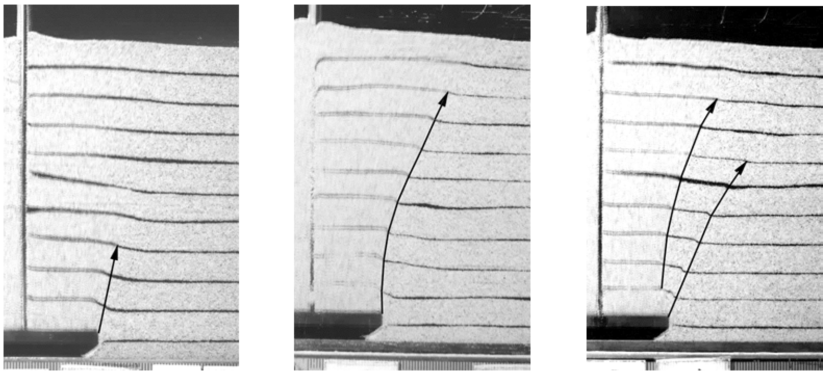

(a) loose (b)medium (c)dense

Fig.11 Experimental shear band development on circular anchor (Toyoura sand, D=5cm, Disp.=from 4mm to 5mm)

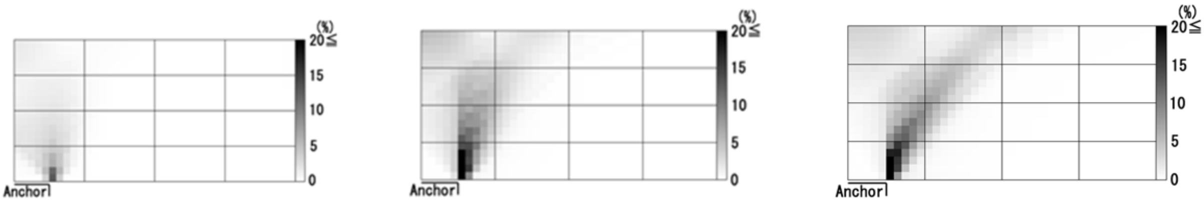

(a) loose (b) medium (c) dense

Fig.12 Maximum shear strain distribution on circular anchor (D=5cm, Disp=2.5mm)

between the peak Nq and D obtained by experiment and numerical analysis for h/D = 1, 2, and 3. Both the experimental and numerical results show that the peak Nq generally decreases with increasing D. The reduction in the peak Nq with increasing D becomes remarkable with increasing h/D. The scale effect was remarkable for h/D = 3. Fig. 15 shows the relationship between the peak Nq and D obtained experimentally and by numerical analysis for strip and circular anchors. The results for both anchors exhibit a scale effect, but it is particularly remarkable for the circular anchor.

6. SHAPE EFFECT

The curves in Fig. 16 depict the experimental and numerical relationships between the pullout resistance and the displacement factor for the square and rectangular anchors with L/D = 1, 2, 3, 4, 5, and 6 (D = 50 mm and h/D = 2). The experimental and numerical results agree closely with each other. Fig. 17 shows the relationship between the mobilized peak resistance factor (Nq) and L/B. It decreases rapidly with increasing L/B when L/B < 6 and it decreases gradually as L/B increases above 6 to the strip anchor condition (L/B = ∞). Fig. 18 shows that the outermost shear band in the numerical analysis outcropped on the ground surface for L/B = 1 and L/B=6. Fig. 19 shows a characteristic photograph of the ground surface for L/B = 1. The failure mechanism of the shallow anchor is associated with the progressive formation of a shear band. To clarify the failure mechanism of the rectangular anchors, Fig. 20 shows a plot of the numerical maximum shear strain distribution in rectangular (L/B = 6), strip (L/B = ∞), and square (L/B = 1) anchors at displacements of δ/D = 0.016 (at the peak) and 0.04 (after the peak uplift load). The shear strain distribution is not uniform in the propagating upward shear bands in the anchor. It is slower or less progressive at the corners of the square anchor

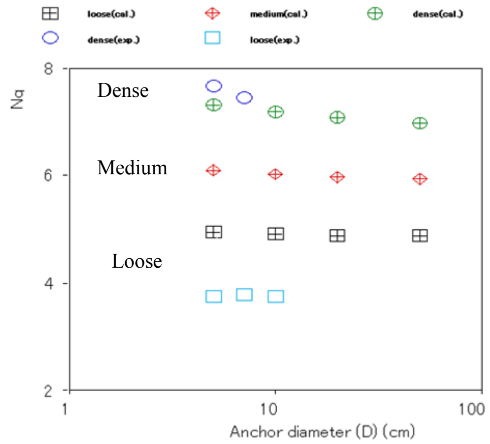

Fig.13 Peak Nq –D-density relationship

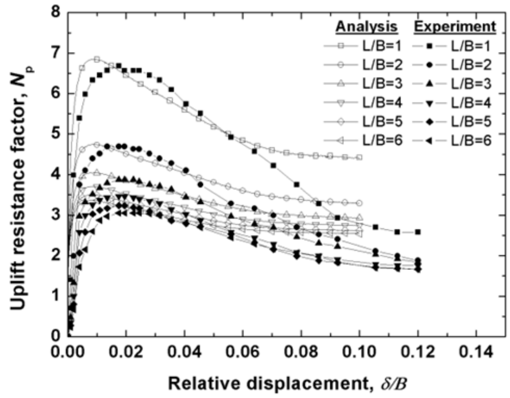

Fig.16 Relative displacement-uplift resistance curves of rectangular anchor in dense sands

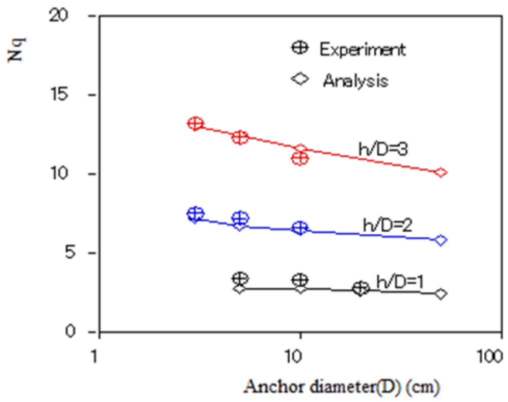

Fig.14 Peak Nq –D-h/D relationship in dense sands

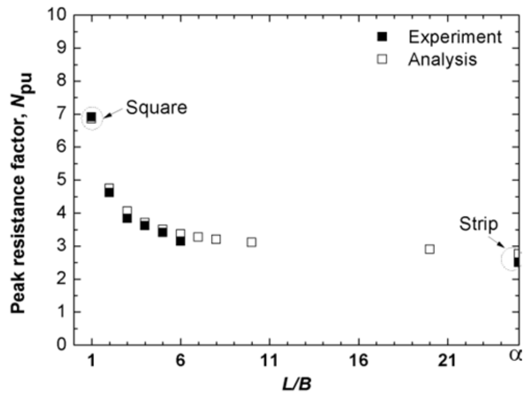

Fig. 17 Peak Nq –L/B relationship in dense sands

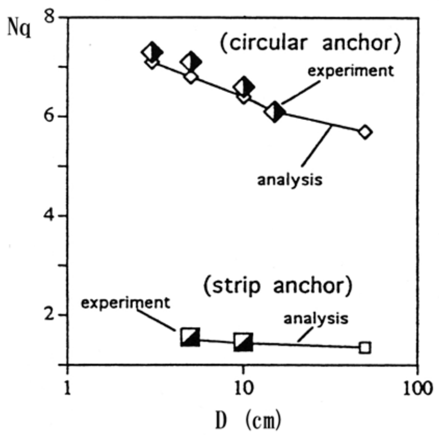

Fig.15 Peak Nq -D relationship
(strip and circular anchor, Dense)

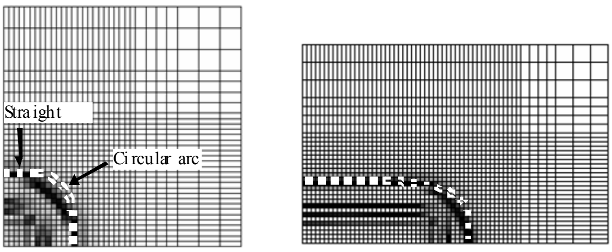

(a) L/B=1 (square) (b)L/B=6

Fig.18 Outermost shear strain distribution in dense sands

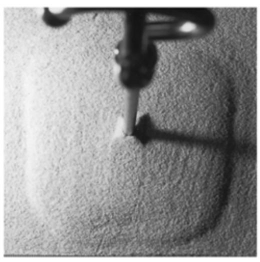

Fig.19 Deformed ground obtained by experiment

than in the strip anchor region of the rectangular anchor. Thus, as L/B increases, the strip-type mechanism starts to dominate over the square-type mechanism. Consequently, the softening rate decreases after the peak uplift resistance factor is obtained and the mobilized peak resistance factor decreases with increasing L/B.

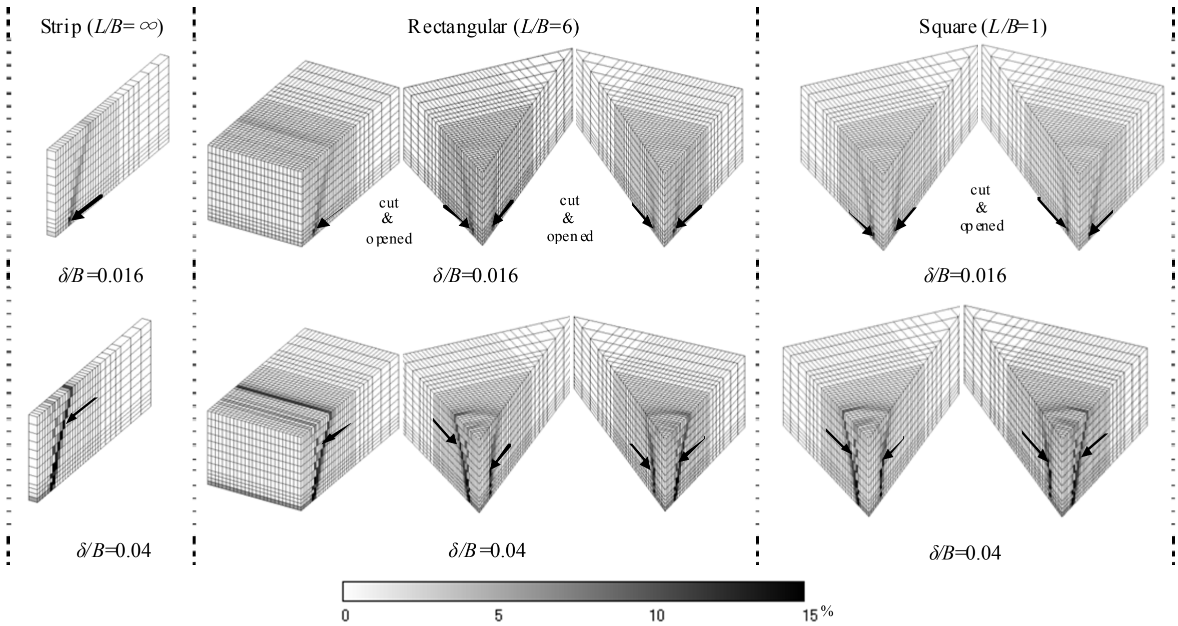

Fig.20 Maximum shear strain distribution obtained by 3D FE analysis (Dense)

7. CONCLUSION

This study sought to explain the progressive failure of shallow anchors in granular materials by performing conventional 1 g tests and extensive numerical studies. The conclusions can be summarized as follows:

1) Shear band propagation was investigated for various anchor problems. Progressive failure was found to depend on the testing bed density, h/D, and the anchor shape. The scale effect of the anchor in dense sands is considered to be due to progressive failure. It was not clearly observed in loose beds, for small h/D, or for strip anchors.

2) The failure mechanisms of rectangular and strip anchors were compared to determine the effect of the shape effect on the uplift resistance. The shape effect is considered to be due to progressive failure. The softening rate decreases after the peak uplift resistance factor is obtained and the mobilized peak resistance factor decreases with increasing L/B. It is thus necessary to use 3D models to model the effects of geometrical factors.

8. REFERENCES

[1] Balla, W. "The resistance to breaking out of mushroom foundations for pylons," Proc. 5th Int. Conf. on Soil Mechanics and Foundation Engineering, pp.569-576, 1961

[2] Meyerhof, G. G. and Adams, J. I. "The ultimate uplift capacity of foundations," Can. Geotech. J. 5, pp.225-244, 1968

[3] Matsuo, M. "Study on the uplift resistance of footing (1)," Soils anf Foundations, 7, pp.1-37, 1968

[4] Davie, J. R. and Sutherland, H. B. "Uplift resistance of cohesive soils," J. Geotec. Engrg. Div. 103(9), pp.935-952, 1977

[5] Walters, J. V. and Thomas, J. N. "Shear zone development in granular materials," Proc. 4th Int. Conf. on Numerical Method in Geomech, pp.263-274, 1982

[6] Rowe, R. K. and Davies, E. H. "The behavior of anchor plates in sand," Geotechnique, 32, pp.25-41, 1982

[7] de Beer, E. E. "Bearing capacity and settlement of shallow foundations on sand," Proc. of a Symp. held at Duke University, 1965

[8] Sakai, T. and Tanaka, T. "Scale effect of a shallow circular anchor in dense sand," Soils and Foundations, 38(2), pp93-99, 1998

[9] Sakai, T. and Tanaka, T. "Experimental and numerical study of uplift behavior of shallow circular anchor in two-layered sand," J. of Geotechnical and Geoenvironmental Engineering, 133(4), pp.469-477, 2007

[10] Vermeer, P. A. and Sutjiadi, W. "The uplift resistance of shallow embedded anchors," Proc. 11th Int. conf. on Soil Mechanics and Foundation Engineering, 4, pp.1635-1638, 1985

[11] Murray, E. J. and Geddes, J. D. "Uplift of anchor plates in sand," J. of Geotechnical Engineering, 113, 202-215, 1987

[12] Merifield, R. S. and Sloan, R. S. "The uplift pullout capacity of anchors in frictional soils," Can. Geotech. J. 43, pp.852-868, 2006

[13] Ovesen, N. K. "Centrifuge tests of the uplift capacity of anchors," Proc. 7th European Conf. Soil Mech. And Found. Eng., 4, pp.318-323, 1981

[14] Dickin, E. D. "uplift behavior of horizontal anchor plates in sand," J. of Geotechnical Engineering, 114, pp,1300-1317, 1988

[15] Vardulakis, I., Graf, B. and Gudehus, G. "Trap-door problem with dry sand; a statistical approach based upon model test kinematics," Int. J. Numer. Anal. Meth. Geomech., 5, pp.57-78, 1981

[16] Yoshida, T., Tatsuoka, F., Siddiquww, M. S. A., Kamegai, Y. and Pak, C. "Some observation of zone of localization in model tests on dry sand," Proc. 3rd Int. Workshop on Localisation and Bifurcation Theory for Soils and Rocks, pp.165-180, 1993

[17] Sakai, T. and Tanaka, T. "Uplift behavior of circular and square anchor foundations in dense sand," Doboku Gakkai Ronbunsuu C, 65(1), pp131-137, 2009

First International Conference on Geotechnique, Construction Materials and Environment, Mie, Japan, Nov.21-23, 2011, ISBN: 978-4-9905958-0-7 C3051

Design of Single Pile Foundations Using the Mechanics of Unsaturated Soils

Vanapalli S.K., Civil Engineering, University of Ottawa, Ottawa, Canada
Taylan Z.N, Civil Engineering, Istanbul Technical University, Istanbul, Turkey

ABSTRACT: The load carrying capacity of single piles are commonly estimated using the well known α [1], β [2-3] and λ [4] methods. These methods are also used in engineering practice for unsaturated soils even though the α, β and λ methods are based on conventional saturated soil mechanics. In this study, a series of single model pile tests were conducted in a laboratory environment to study the influence of matric suction on the pile shaft capacity in a statically compacted fine-grained soil. The results of the study show that the shaft capacity of single piles is significantly influenced by the contribution of matric suction. Based on the experimental results, the conventional α, β and λ methods were modified to estimate the total shaft resistance of piles in unsaturated soils by including the influence of matric suction. The modified methods can also be used for estimating the variation of shaft capacity of single piles with respect to matric suction using the Soil-Water Characteristic Curve (*SWCC*) and the saturated shear strength parameters. The modified α, β and λ methods are promising for use in engineering practice to estimate the ultimate shaft bearing capacity of single piles placed in unsaturated soils.

Keywords: Unsaturated soils, pile design, modified α, β and λ methods, *SWCC*, matric suction

1 INTRODUCTION

In geotechnical engineering practice, conventional soil mechanics principles are used for the design of pile foundations assuming the soil is in a state of saturated condition [5], [6]. However, in many situations, the ground water table is at a great depth and natural soils are typically found in a state of unsaturated condition. This is particularly true for soils in arid and semi-arid regions. Several geotechnical structures such as highways, embankments, dams are constructed on or with compacted unsaturated soils in which pile foundations may be placed. The stresses associated with these foundations are distributed within the unsaturated soil zone above the ground water table.

Several recent studies on shallow foundations [7]-[10] have shown that the bearing capacities of both coarse and fine-grained soils are significantly influenced due to the contribution of matric suction. However, limited numbers of studies are reported in the literature [11]-[14] that consider the influence of matric suction or capillary stresses on the load carrying capacity of pile foundations. Typically, pile foundations are designed assuming saturated, dry or submerged soil conditions.

In this paper, the α method by Skempton [1], β method by Chandler and Burland [2], [3] and λ method by Vijayvergiya and Fotch [4] are modified such that they can be used for estimating the ultimate shaft resistance of piles in unsaturated soils. The modified α, β and λ methods are similar to the conventional techniques used in the design of piles in geotechnical engineering practice. These methods are presented in a functional form such that they can be used for estimating the variation of the shaft capacity of the single piles with respect to matric suction using the saturated soil properties and the Soil-Water Characteristic Curve *(SWCC).* The proposed modified equations take the conventional form of the α, β and λ methods used for saturated soils when the matric suction value is set to zero.

A series of single model pile tests placed in statically compacted unsaturated glacial till with various degrees of saturation were performed in a laboratory environment to study the influence of matric suction on the shaft resistance. The results of these experimental studies were interpreted using the modified α, β and λ methods. There was a reasonably good comparison between the measured ultimate shaft capacity of the single model piles and those estimated using the proposed methods (i.e., modified α, β and λ methods).

2 BACKGROUND

The reliable determination of soil-structure interaction parameters requires cumbersome laboratory or field tests. Alleviating the need of such cumbersome tests; empirical methods are proposed to estimate the skin friction, f_s based on the conventional shear strength parameters and the information related to the variation of effective stresses along the length of the piles.

$$f_s = f\left(\sigma'_v, \phi', c_u\right) \tag{1}$$

where, σ'_v = vertical effective stress, ϕ'= effective friction angle, and c_u = undrained shear strength.

The functional form of (1) suggests that the skin friction, f_s can be analyzed in terms of either total or effective stress approach considering the loading and drainage conditions (i.e., *TSA* or *ESA*), respectively.

Experimental programs were planned to determine the contribution of matric suction on the shaft resistance and not the bearing resistance. In other words, the contribution of end bearing capacity is not measured in the present study.

2.1 The β Method (ESA)

In both coarse and fine-grained soils, the skin friction, f_s mobilized along the length of the pile is a key parameter that is required in the estimation of the load bearing capacity of pile foundations. If a pile is loaded at a relatively slow rate (i.e., to achieve drained conditions) the skin friction resistance can be estimated using (2) [2].

$$f_s = c' + K_0 \sigma'_v \tan\phi' \quad (2)$$

where, K_0 = mean lateral earth coefficient at rest, c' and ϕ' = effective cohesion and internal friction angle of soil, respectively, and σ'_v = vertical effective stress along the pile length.

The shear strength of soils associated with cohesion decreases significantly due to the remolding and softening effects during pile installation. This leads to an assumption that effective cohesion can be neglected along the pile shaft, particularly in coarse-grained soils and other soils with low percentage of fines such as silty sands and normally consolidated clays. Hence, (2) can be incorporated in (3) with the introduction of a coefficient, β [2], [3].

$$Q_f = f_s A_s = \beta \sigma'_v \pi d L \quad (3)$$

where, β is a coefficient which is equal to $K_o \tan \delta'$, δ'= effective angle of friction along the soil/pile interface, A_s = surface area of the pile, σ'_v = vertical effective stress at the mid of the pile shaft, L = length of pile, and d = diameter of pile.

The coefficient, β values typically vary from 0.30 to 0.60 for fine and coarse-grained soils [2], [3].

2.2 The α Method - (TSA)

Undrained lading conditions can be assumed when a pile is loaded at a relatively fast rate in saturated fine-grained soils. The ultimate shaft resistance can be estimated for such loading conditions extending the *TSA*. In other words, the ultimate shaft capacity of a pile, Q_f is dependent on the undrained shear strength, c_u of the soil. Hence, the unit skin resistance, f_s can be expressed as (4) using undrained shear strength, c_u and the adhesion factor, α.

$$f_s = \alpha c_u \quad (4)$$

where, α = adhesion factor between soil and pile.

There is a large data base of in-situ pile load tests including bored and driven piles supporting this method dating back to 1950s. This method is commonly referred in the literature as the α method. The studies show that adhesion factor, α is not constant but decreases with increasing undrained shear strength, c_u of the soil and varies from close to unity for low strength soft clays and reach almost to a value of 0.4 for stiff clays for c_u values greater than150 kPa [16], [1]. The ultimate shaft capacity, Q_f for cylindrical piles using the α method can be estimated as (5).

$$Q_f = f_s \times A_s = \alpha c_u \pi d L \quad (5)$$

where, d = pile diameter, and L = length of pile.

The adhesion factor, α can be computed from American Petroleum Institute charts which are given as a relationship between the adhesion factor and the undrained shear strength. Alternatively, (6) can also be used for estimating the α value.

$$\alpha = 0.5\psi^{-0.5} \quad \text{if } \psi \le 1$$
$$\alpha = 0.5\psi^{-0.25} \quad \text{if } \psi > 1 \quad (6)$$

where $\psi = c_u/\sigma'_v$ and σ'_v = vertical effective stress [17].

2.3 The λ Method

The conventional λ method combines the total (i.e., undrained) and effective (i.e., drained) stress approaches for calculating the shaft capacity of piles driven into fine-grained soils [4]. This technique is useful in reducing the sensitivity of the shear strength parameters measured using the *TSA* and *ESA*. The total shaft capacity is calculated using the relationship shown in (7).

$$Q_f = \lambda \left(\sigma'_{v(avg)} + 2c_u \right) \pi d L \quad (7)$$

where, $\sigma'_{v(avg)}$ = the mean effective stress, c_u = undrained shear strength along the pile length, λ = frictional capacity coefficient which is a function of entire embedded depth of pile. The coefficient λ varies from 0.12 to 0.5 for pile penetration of 0 to 70 m based on the 42 piles load test data gathered and presented by [4].

3 ESTIMATION OF THE ULTIMATE SHAFT CAPACITY (*USC*) OF PILES IN UNSATURATED SOILS

3.1 Modified β method

Researchers ([18], [19]) proposed a model (8) to predict the variation of shear strength with respect to matric suction using the *SWCC* and the effective shear strength parameters (i.e., c' and ϕ') as given below.

$$\tau = \left[c' + (\sigma_n - u_a) \tan\phi' \right] + \left[\left(u_a - u_w \right) (S^\kappa)(\tan\phi') \right] \quad (8)$$

where, c' = effective cohesion, $(\sigma_n - u_a)$ = net normal stress, ϕ' = effective internal friction angle, $(u_a - u_w)$ = matric suction S = degree of saturation, κ = fitting parameter used for shear strength.

The contribution of matric suction towards the shear strength, τ_{us} can be expressed as (9) which is the second part of (8).

$$\tau_{us} = \left[\left(u_a - u_w \right) (S^\kappa)(\tan\phi') \right] \quad (9)$$

The contribution of matric suction, towards the ultimate shaft capacity of a single pile, $Q_{(ua-uw)}$ can be estimated using (10) as given below.

$$Q_{(u_a-u_w)} = \tau_{us}\, A_s = \left[\left(u_a - u_w\right)(S^{\kappa})(\tan\delta')\right]\pi d\, L \qquad (10)$$

Equation (10) suggests that the variation of ultimate shaft capacity with respect to matric suction can be estimated using the *SWCC* and effective interface friction angle, δ'.

A general expression for estimating the ultimate shaft capacity of piles in unsaturated soils, $Q_{f(us)}$ can be obtained by combining (3) and (10) as given below

$$\begin{aligned} Q_{f(us)} &= Q_{f(sat)} + Q_{f(u_a-u_w)} \\ &= \left[\beta\sigma_v' + \left\{\left(u_a - u_w\right)(S^{\kappa})(\tan\delta')\right\}\right]\pi d\, L \end{aligned} \qquad (11a)$$

The relationship between the fitting parameter, κ and plasticity index, I_p provided for predicting the shear strength of unsaturated soils [20] can be used for estimating the ultimate shaft capacity of a single pile. More details of this method are available in [14]. Equation (11a) shows that there is a smooth transition between the ultimate shaft capacity of a single pile from an unsaturated to saturated condition. This relationship will be the same as (3) when matric suction is equal to zero (i.e., for saturated soils).

The contribution of cohesion component associated with the adhesion, c_a' under drained loading condition may not be negligible for evaluating the pile capacity of fine-grained soils for the β method (see (11b). In other words, there will be some contribution of adhesion, c_a' towards the ultimate shaft capacity which will be mobilized with time after the installation of the pile. Therefore, the ultimate shaft capacity of piles in unsaturated fine-grained soils under drained loading conditions can be estimated by modifying (11a) as given below.

$$Q_{f(us)} = \left[c_a' + \beta\left(\sigma_z'\right) + \left(u_a - u_w\right)(S^{\kappa})(\tan\delta')\right]\pi d\, L \qquad (11b)$$

where, c_a' = adhesion component of cohesion for saturated condition, δ'= effective angle of interface along the soil/pile.

3.2 Modified α method

Several investigators related the load bearing capacity of a single pile to the undrained shear strength, c_u of the fine-grained soils ([16], [21]-[28]). In the present study, the conventional α method is modified such that it can be extended for interpreting the results of model piles tested under unsaturated soil condition. In addition, a model is proposed for estimating the variation of ultimate shaft capacity of model piles with respect to matric suction.

The equation (12) [9] can be used to estimate the variation of undrained shear strength with respect to matric suction using the *SWCC* and undrained shear strength for saturated condition, $c_{u(sat)}$.

$$c_{u(unsat)} = c_{u(sat)}\left[1 + \frac{\left(u_a - u_w\right)}{\left(P_a / 101.3\right)}\left(S^{\upsilon}\right) / \mu\right] \qquad (12)$$

where, $c_{u(sat)}$, and $c_{u(unsat)}$ = undrained shear strength under saturated and unsaturated conditions, respectively, P_a = atmospheric pressure (i.e. 101.3 kPa), and ν, and μ = fitting parameters.

The fitting parameter ν is dependent on the soil type (i.e., coarse or fine-grained soils) and is equal to 1 for coarse-grained soils and 2 for fine-grained soils. The fitting parameter μ however is a function of plasticity index, I_p.

$$\begin{aligned} &\mu = 9 && (8.0 \le I_p(\%) \le 15.5) \\ &\mu = 2.1088\, e^{0.0903(I_p)} && (15.5 \le I_p(\%) \le 60) \end{aligned} \qquad (13)$$

Following the procedure described in section 3.1, the ultimate shaft capacity of piles in unsaturated soils under undrained loading conditions can be estimated by combining (4) and (12) as given below.

$$Q_{f(us)} = \alpha c_{u(sat)}\left[1 + \frac{(u_a - u_w)}{(P_a / 101.3)} S^{\upsilon} / \mu\right]\pi dL \qquad (14)$$

The undrained shear strength under saturated condition, $c_{u(sat)}$ and the *SWCC* are required to estimate the variation of ultimate shaft capacity of pile, $Q_{f(us)}$ with respect to matric suction. Equation (14) will be the same as (4) when the matric suction value is set equal to zero.

3.3 Modified λ method

The λ method was modified to propose (15) to include the influence of matric suction in the estimation of shaft resistance of piles in unsaturated soils.

$$Q_{f(us)} = \lambda\left[\sigma'_{v(avg)} + 2c_{u(sat)}\left(1 + \frac{(u_a - u_w)}{(P_a / 101.3)} S^{\upsilon} / \mu\right)\right]\pi d L \qquad (15)$$

The form of (15) will be as same as the conventional λ method once the matric suction is set to zero. Equation (15) can also be used to estimate the variation of total shaft resistance of pile, $Q_{f(us)}$ with respect to matric suction. The required information for (15) are the undrained shear strength under saturated condition, $c_{u(sat)}$ and the *SWCC*. More details of this method are discussed while analyzing the results.

4 TESTING PROGRAM

A series of model pile load tests were performed in saturated and unsaturated compacted fine-grained soil under drained and undrained loading conditions. The soil chosen for this study is a glacial till obtained from Indian Head, Saskatchewan, Canada. The key objective of the test program is to determine the influence of matric suction on the ultimate shaft capacity of model piles.

4.1 Soil Properties

The properties of the tested soil are summarized in Table I. Procedures followed for determining some of the test results summarized in Table I are not detailed in this paper due to space limitations. The shaft bearing capacity of model piles were proposed to be determined at three different water contents; 13% (dry of optimum), 16% (dry of optimum) and 18% (close of optimum). These water contents were chosen from the compaction curve data. The dry densities of the compacted soil at these water contents were respectively equal to 14.5 kN/m^3, 16.1 kN/m^3 and 16.7 kN/m^3. The matric suction values of the tested compacted soils were measured using the axis-translation technique [29] with a modified null pressure plate [30]. The measured matric suction values were 205 kPa, 110 kPa and 55 kPa for water contents of 13%, 16%, 18% respectively. The experiments were not conducted for the water contents on the wet of optimum side since the degree of saturation values were greater than 90%, which resulted in significantly low matric suction values.

The measured *SWCC*s of the specimens prepared with initial water contents of 13%, 16% and 18% are presented in Fig. 1. These *SWCCs* were measured following the drying path using the pressure plate apparatus. More details of the matric suction measurements using both the modified null pressure plate and the *SWCC* using pressure plate are discussed in [31], [32].

Table I. Properties of the tested soil

Soil Properties	Indian Head till
Optimum water content, w_{opt} (%)	18.6
Maximum dry unit weight, γ_{dmax} (kN/m^3)	16.7
Saturated unit weight, γ_{sat} (kN/m^3)	18.5
Sand *(%)*	28
Silt *(%)*	42
Clay *(%)*	30
Liquid limit, *LL* (%)	32.5
Plastic limit, *PL* (%)	17
Plasticity index, I_p (%)	15.5
Interface friction angle (soil/pile) δ' (deg.) (Sat/Unsat)	25/27
Apparent cohesion, c'_a (kPa) (Sat/Unsat)	20/100
Effective cohesion, c' (kPa) (Sat)	15
Effective friction angle, ϕ' (deg.) (Sat)	23
Undrained shear strength, c_u (kPa)	11.5

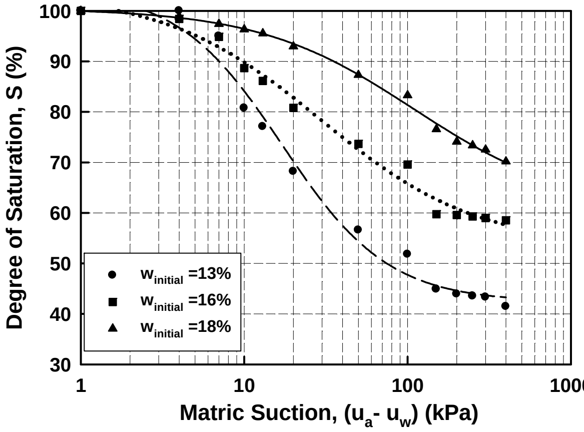

Figure 1. *SWCCs* for the Indian Head till prepared at three different initial water contents.

The soil-water mixture (hereafter referred to as soil) was placed in a tank (300 mm in diameter and 300 mm in height). The soil was compacted statically with 350 kPa stress into the test tank using a specially designed compaction base plate. The compaction and model pile load tests were conducted using a conventional triaxial test loading frame (Fig. 2).

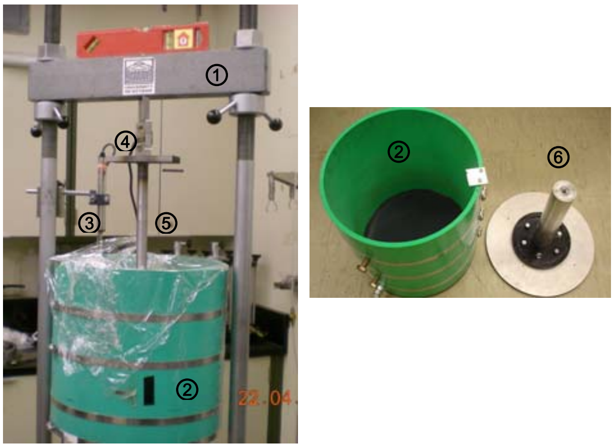

Figure 2. Test setup for model pile loading test: ① Adjustable height loading frame ② Test tank ③ LVDT ④ Load cell ⑤ Model pile, ⑥ Compaction base plate.

4.2 Testing Methodology and Equipment Details

Special testing procedures were followed to determine the ultimate shaft capacity of the model pile placed in the statically compacted soil. The model piles were loaded in saturated/unsaturated compacted soils for both drained and undrained loading conditions. The soil sample collected from the field was air-dried for several days, subjected to gentle pulverization, passed through a sieve with an opening size of 2 mm (i.e., #10 sieve), and oven-dried.

The oven dried soil, after reaching the room temperature in the laboratory, was mixed with distilled water at predetermined initial water contents. The prepared soil-water mixture was placed in sealed double plastic bags and then stored in a humidity controlled box for at least 3 days to ensure uniform water content conditions throughout the sample.

After the soil was compacted under static loading conditions in five layers in the test tank, a thin wall sampling tube of 18.7 mm diameter with 1 mm of wall thickness was used to create a hole down to a depth of 220 mm. The sampling tube along with the soil column embedded into it was removed out of the compacted soil. The model pile used in the study was made out of stainless solid steel cylindrical rod with 20 mm diameter. The model pile (hereafter referred to as D-20 pile) was slightly larger in diameter in comparison to the diameter of sampling tube in order to obtain a good contact between the walls of the drilled shaft and the model pile. After the borehole drilling was completed, model pile was jacked down to a depth of 200 mm. A gap with 20 mm of length at the tip of the pile was intentionally left to eliminate the end bearing resistance while loading the model pile. In other words, the void was created to facilitate in the measurement of shaft resistance without any contribution from the end bearing resistance. The tests described were conducted under unsaturated (UNSAT) conditions.

However, when the pile was loaded under saturated (SAT) condition, the compacted unsaturated soil was gradually saturated by allowing downward flow of water from the top of the soil through the compaction base plate which had apertures. The compactor plate was placed on top of the compacted soil sample and fixed to the loading frame in order to avoid possible volume change due to swelling. After the saturation process was completed, the model pile was installed using same procedure described for the pile testing under unsaturated condition.

A piezometer attached to the side of the tank was used to check the saturation condition. The soil was assumed to be saturated as the level of water in the piezometer reached the same water level within the test tank. The degree of saturation was also verified by measuring matric suction with a tensiometer that was placed in the compacted soil. The tensiometer reading of $(u_a - u_w) = 0$ kPa provided another indication that the compacted soil is saturated. In addition to these checks, small chunks of soil specimens were collected from the tank for water content measurements after the loading tests were completed. The average water content from these tests was 31% which corresponds to a degree of saturation equal to 96% calculated from mass-volume relationships. This value can be considered to be close to saturation conditions for the present study because there is other evidence to support the soil is saturated.

A strain rate of 0.0120 mm/min was chosen for loading the pile to achieve drained loading conditions [18][33]. A relatively fast loading rate of 1 mm/min was used to simulate undrained loading conditions [34].

The soil samples prepared with an initial water content of 13% were tested under both unsaturated and saturated conditions considering both the drained and undrained loadings (i.e., SAT-Drained, SAT-Undrained, UNSAT-Drained, UNSAT-Undrained). Only the tests under unsaturated conditions were conducted (i.e., UNSAT-Drained, UNSAT-Undrained) for other soil samples with initial water contents of 16% and 18%. The details of the experimental program of the present study are summarized in Fig. 3 as a flow chart.

5 MODEL PILE TEST RESULTS AND ANALYSES

5.1 Test Results

The model pile test results obtained for both saturated and unsaturated soil samples are presented in Fig. 4 through Fig. 7. The shaft carrying capacity of the model piles loaded in the soils compacted with different compaction water contents (i.e., 13%, 16%, and 18%) is significantly different depending on the soil (saturated or unsaturated) and drainage (drained or undrained) conditions. The trends of the load versus displacement behavior of model piles from the present study are similar to the results published on results on other fine-grained clays in the literature [1],[3].

Figure 3. Flow chart of the testing program.

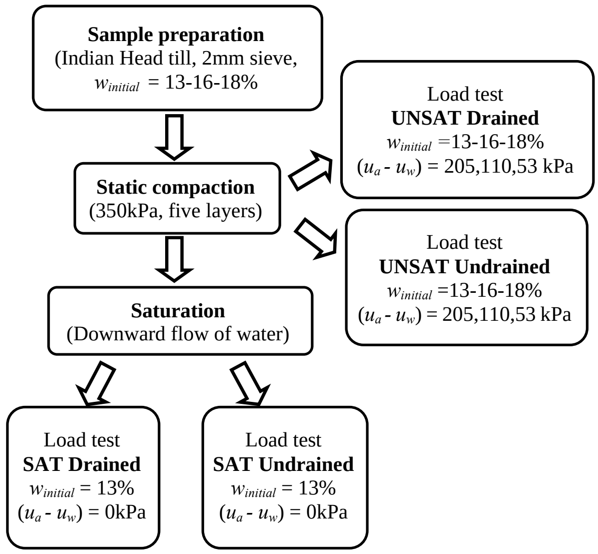

5.2 Interpretation of the Test Results

The measured shaft bearing capacity values for the D-20 pile were interpreted using the modified α, β and λ methods proposed in this paper. In addition, comparisons are provided between the measured and estimated shaft bearing capacity values.

The ultimate shaft bearing capacities for the model piles was estimated using the modified α method assuming undrained loading conditions. The undrained shear strength values for the compacted soils required for the modified α method were determined by conducting unconfined compression tests on the samples collected from the testing tank after model pile tests. The undrained shear strength values were also estimated using the equation (12). The test results are summarized in Table II.

Table II. Comparison between the measured and estimated ultimate shaft capacities using the modified α method for undrained loading.

$w_{initial}$	$(u_a - u_w)$	c_u[1]	c_u[2]	α[3]	Back Cal. α value	Est.[4] $Q_{f(us)}$	Meas. $Q_{f(us)}$
(%)	kPa	kPa		-	-	kN	kN
13	0	11.5	-	0.90	0.70	0.13	0.10
18	53	58	52	0.82	0.68	0.59	0.50
13	205	68	57	0.75	0.79	0.64	0.68
16	110	80	65	0.67	0.55	0.67	0.55

$(u_a - u_w)$ = matric suction
[1] Undrained shear strength from unconfined compression tests.
[2] Undrained shear strength calculated by using (12)
[3] α value obtained using the correlation charts [24]
[4] Calculated shaft bearing capacity by using (14).

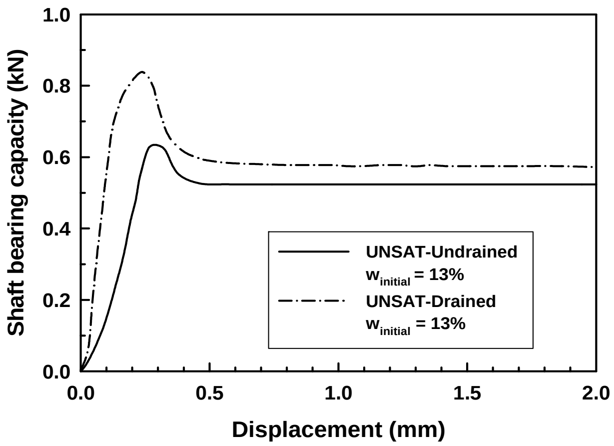

Figure 4. Model pile test results in an unsaturated soil compacted at an initial water content of 13% under drained and undrained loading conditions.

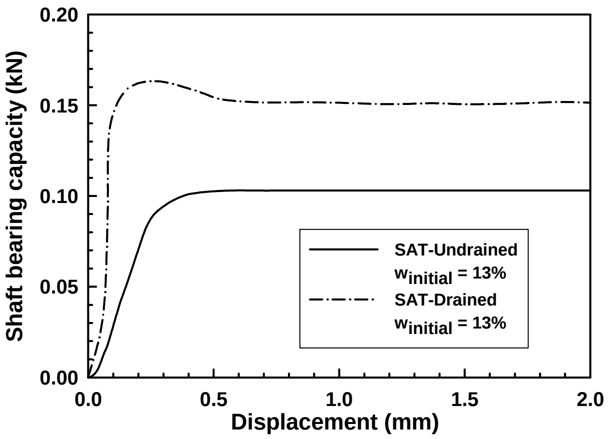

Figure 5. Model pile test results in a saturated soil compacted at an initial water content of 13% under drained and undrained loading conditions.

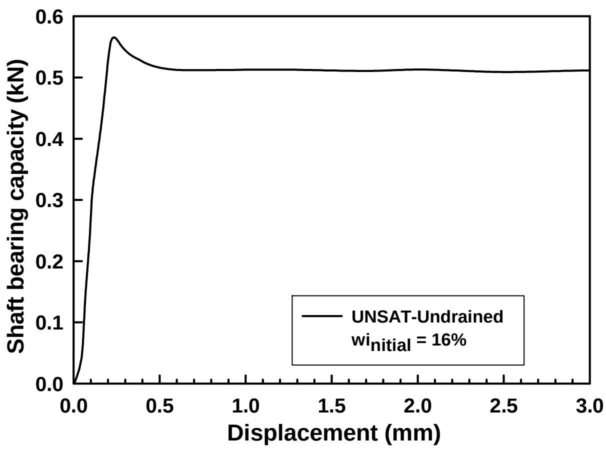

Figure 6. Model pile test results in an unsaturated soil compacted at an initial water content of 16% under undrained loading conditions.

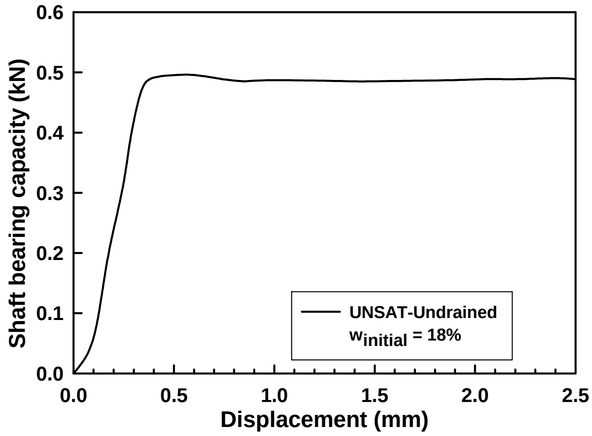

Figure 7. Model pile test results in an unsaturated soil compacted at an initial water content of 18% under undrained loading conditions.

The measured ultimate shaft capacity and those estimated using the conventional (i.e. (2)) modified (i.e., (11b)) β method for the saturated and unsaturated soils, respectively under undrained conditions are summarized in Table III. The fitting parameter κ in (10) was determined using the relation given in [20]. The coefficient, β = 0.3 was used for both the saturated and unsaturated soils based on the soil-pile interface friction angle, δ' (see Table III) since the influence of matric suction on δ' is relatively less.

Table III. Comparison between the measured and estimated ultimate shaft capacities using the modified β method for drained loading.

$w_{initial}$	$(u_a - u_w)$	β	δ'	c'_a	Est. $Q_{f(us)}$	Meas. $Q_{f(us)}$
%	kPa	-	°	kPa	kN	kN
13	0	0.3	25	20	0.25	0.16
13	205	0.3	27	100	0.60	0.80

The measured ultimate shaft capacity values and those estimated using the modified λ method (i.e. (15)). Vanapalli and Taylan [35] analyzed the data available in the literature [4] and suggested the relationship between λ and the ratio of pile diameter to pile penetration depth, d/L are summarized in Table IV. A value of λ = 0.32 was used in the present study. More details with respect to using this value are detailed in [35].

Table IV. Comparison between the measured and estimated ultimate shaft capacities by using the modified λ method

$w_{initial}$	$(u_a - u_w)$	Meas. c_u	λ	Est. $Q_{f(s),(us)}$	Meas. $Q_{f(s),(us)}$
(%)	kPa	kPa	-	kN	kN
13	0	11.5	0.32	0.09	0.10
18	53	58	0.32	0.47	0.50
13	205	68	0.32	0.55	0.68
16	110	80	0.32	0.64	0.55

The measured and estimated results are summarized and presented in Fig. 8. Each circle shown in Fig. 8 represents the results of the three different methods with different matric suction and initial water contents. The difference between the measured and estimated shaft bearing capacities in terms of percentage varies between 6 to 36%. The difference is more significant for the results obtained using the modified β method (11b). Such a behavior can be attributed to the effect of loading rate and also due to the difficulties associated with the opening a hole using the thin wall tube during which some disturbance may have occurred.

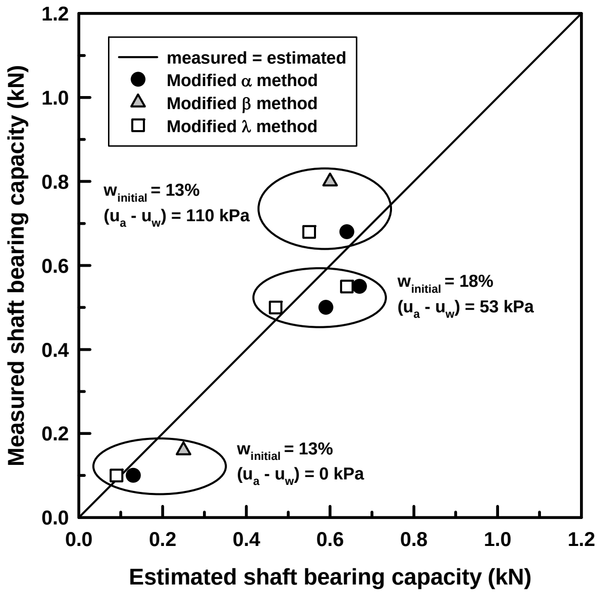

Figure 8. Measured and estimated ultimate shaft bearing capacities calculated by using the modified α, β and λ methods for compacted Indian Head till samples

6 SUMMARY AND CONCLUSIONS

The conventional α, β and λ methods are commonly used in engineering practice for estimating the ultimate shaft bearing capacity of single piles in saturated soils. In the present study, these methods are modified such that they can be used to estimate the variation of ultimate shaft capacity of single piles with respect to matric suction using the *SWCC* and the conventional shear strength parameters. There is a smooth transition between the modified and conventional methods and are convenient to estimate the shaft capacity of piles in unsaturated and saturated soil conditions.

A series of model pile load tests were conducted on statically compacted fine-grained soil (i.e., compacted Indian Head till) in a laboratory environment to study the validity of the modified α, β and λ methods. The test results of the study presented in this paper show significant increase in shaft capacity due to the contribution of matric suction. The modified α, β and λ methods provided reasonably good comparison with the model pile load test results conducted in a laboratory environment.

The authors based on the experience of the present study suggest different techniques of testing to alleviate some experimental problems. Instead of drilling a hole into the initially compacted soil, it is suggested to compact the soil around the pile using a specially designed compactor. Such a technique would reduce disturbance during pile installation for tests and likely provide better correlation results as it eliminates the problems associated with the soil disturbance. In addition, this technique also provides better contact between the pile and the soil.

The results summarized in this paper are based on the studies undertaken using one compacted fine-grained soil. More experimental and numerical studies are in progress to check the validity of the modified α, β and λ methods for different coarse and fine-grained soils. These studies will be useful to better understand the influence of matric suction on the load carrying capacity of the piles. The results of the studies conducted to date are promising for using the modified α, β and λ methods in engineering practice to estimate the ultimate shaft bearing capacity of single piles placed in unsaturated fine-grained soils.

7 ACKNOWLEDGMENTS

The first author thanks NSERC, Canada for providing funding support in the form of Discovery Research Grant. The second author thanks The Scientific and Technological Research Council of Turkey (TUBITAK) for providing the financial support during this research. The authors would like to thank Jean Claude Celestin (Technical Officer, Geotechnical Lab, University of Ottawa), Won Taek Oh, Ph.D. candidate, University of Ottawa and Mudasser Mohamed Anis Noor and Nicholas Tang, undergraduate students of University of Ottawa for their time, help and assistance in the testing program. Thanks also go to Hana Adem and Won Taek Oh, Ph.D candidates, University of Ottawa for thier assistance in proof reading and editing this paper.

8 REFERENCES

[1] Skempton AW, "Cast-in-situ bored piles in London clay," Géotechnique, vol. 9, Dec. 1959, pp. 153-173.

[2] Chandler RJ, "The shaft friction of piles in cohesive soils in terms of effective stress," Civil Engineering and Public Works Review, vol. 63, 1968, pp. 48-51.

[3] Burland JB, "Shaft friction of piles in clay-a simple fundamental approach," Ground Engineering, vol. 6-3, 1973, pp. 30-42.

[4] Vijayvergiya VN, Focht JA, "A new way to predict capacity of piles in clay," in Proc. Offshore technology Conf., 1972, pp. 865-871.

[5] Poulos HG, "Pile behaviour-theory and application," Géotechnique, vol. 39, Sept. 1989, pp. 365-413.

[6] Douglas DJ, "Prediction study-driven piles," in Proc. 5th Australian-New Zealand Conf. on Soil Mechanics, Special edition, 1989, pp. 84-88.

[7] Georgiadis K, Potts DM, Zdravkovic L, "Behavior of a footing on a partially saturated soil," Numerical models in geomechanics, NUMOG VIII, 2002, pp. 451-456.

[8] Vanapalli SK, Mohamed FMO, "Bearing capacity of model footings in unsaturated soils," in Proc. on Physics, Experimental Unsaturated Soils Mechanics, 2007, pp. 483-494.

[9] Oh WT, Vanapalli SK, "A simple method to estimate the bearing capacity of unsaturated fine-grained soils," in Proc. 62nd Canadian

Geotechnical Conf & 10th Joint CGS/IAH-CNC Groundwater Conf., 2009, pp. 234-241.
[10] Vanapalli SK, Oh WT, "Interpretation of the bearing capacity of an unsaturated soils extending the effective and total stress approaches," in Proc. 5th Int. Conf. on UNSAT, 2010, pp. 1223-1229.
[11] Douthitt B, Houston W, Houston S, Walsh K, "Effect of wetting on pile friction," in Proc. of 2nd Int. Conf. on UNSAT, 1998, pp. 219-224.
[12] Costa YD, Cintra JC, Zornberg JG, "Influence of matric suction on the results of plate load tests performed on a lateritic soil deposit," Geotechnical Testing J., vol. 26, June 2003, pp. 219-227.
[13] Georgiadis K, Potts DM, Zdravkovic L., "The influence of partial soil saturation pile behaviour," Géotechnique, vol. 53, Feb. 2003, pp. 11-25.
[14] Vanapalli SK, Eigenbrod KD, Taylan ZN, Catana C, Oh WT, Garven E, "A technique for estimating the shaft resistance of test piles in unsaturated soils," in Proc. 5th Int. Conf. on UNSAT, 2010, pp. 1209-1216.
[15] McClelland B, "Design of deep penetration piles for ocean structures," J. of the Geotechnical Engineering Division, ASCE, vol. 100, July 1974, pp. 705-747.
[16] Tomlinson MJ, "The adhesion of piles driven in clay soils," in Proc. 4th Int. Conf. on Soil Mech. and Foundation Eng., vol. 2, 1957, pp. 66-71.
[17] API Recommended Practice for Planning, Designing and Constructing Fixed Offshore Platforms-Working Stress Design. 2A-WSD, 2000.
[18] Vanapalli SK, Fredlund DG, Pufahl DE, Clifton AW, "Model for the prediction of shear strength with respect to soil suction," Canadian Geotechnical J., vol. 33, July 1996, pp. 379-392.
[19] Fredlund DG, Xing A, Fredlund MD, Barbour SL, "The relationship of the unsaturated soil shear strength to the soil-water characteristic curve," Canadian Geotechnical J., vol.33, July 1996, pp. 440-448.
[20] Vanapalli SK, Fredlund DG, "Comparison of different procedures to predict unsaturated soil shear strength," in Proc. the Conf. on Advances in Unsaturated Geotechnics Geo-Denver, 2000, 195-209.
[21] Peck RB, A study of the comparative behaviour of friction piles, Highway Research Board, no. 36, 1958.
[22] Woodward R, Boitano J, "Pile loading tests in stiff clays," in Proc. 5th Int. Conf. on Soil Mechanics and Foundation Engineering, 1961, pp. 177-184.
[23] Kerisel J, "Vertical and horizontal bearing capacity of deep foundation in clay," in Proc. Symp. on Bearing Capacity of Settlement of Foundations, 1965, pp. 45-52.
[24] Sowers GB, Sowers GG, Introductory soil mechanics and foundations. New York: The Macmillan Company, 1970.
[25] API Recommended practice for planning, designing and constructing fixed offshore platforms, API RP2A, 1974.
[26] McCarthy DR, Essentials of soil mechanics and foundations. Reston Publishing Company, 1977.
[27] Weltman AJ, Healy PR, Piling in boulder clay and other glacial tills. Construction Industry Research and Information Association, Report PG5, 1978.
[28] Dennis ND, Olsen RE, "Axial capacity of steel pipe piles in clay," in Proc. Geotechnical Practice in Offshore Engineering. ASCE, 1983, pp. 370-388.
[29] Hilf JW, An investigation of pore water pressure in compacted cohesive soils. Ph.D. dissertation. 1956.
[30] Power, K. and Vanapalli, S.K. 2010. Modified null pressure apparatus for measurement of matric suction. *ASTM Geotechnical Testing Journal*, American Society of Testing Materials, 33(4): 335-341.
[31] Vanapalli SK, Taylan ZN, "Modeling the load carrying capacity of single piles in unsaturated soils using the modified α and the β methods," in Proc. 13th Int. Conf. on IACMAG, 2011, pp. 599-607.
[32] Vanapalli SK, Taylan ZN, "Model piles behavior in a compacted fine-grained unsaturated soil," in Proc. 15th European Conf. on ESMGE, 2011, pp. 683-689.
[33] Gan, JKM, Fredlund DG, Rahardjo H, "Determination of the shear strength parameters of an unsaturated soil using the direct shear test," Canadian Geotechnical J., vol. 25, Aug .1988, pp. 500-510.
[34] Vanapalli SK, Oh WT, Puppala AJ, "Determination of the bearing capacity of unsaturated soils under undrained loading conditions," in Proc. 60th Canadian Geotechnical Conf., 2007, pp. 1002-1009
[35] Vanapalli SK, Taylan ZN, "Estimation of the shaft capacity of model piles in a compacted fine-grained unsaturated soil," in Proc. 14th Pan-Am Conf. on Soil Mechanics and Geotechnical Engineering & 64th Canadian Geotechnical Conf., 2011 (In CD).

First International Conference on Geotechnique, Construction Materials and Environment, Mie, Japan, Nov.21-23, 2011, ISBN: 978-4-9905958-0-7 C3051

Problematic Soil: In Search for Solution

Bujang B.K. Huat

Department of Civil Engineering, Universiti Putra Malaysia, Serdang, Selangor, Malaysia

ABSTRACT: Soils are considered to include all naturally occurring loose or soft deposit overlying the solid bedrock. They are formed of the disintegration and decomposition of rocks and also by decomposition of organic materials. Compared with rocks, soils are softer in term of strength and more compressible, thus giving more problems to engineering compared with rocks. But is soil really a problem, or the theory is? Perhaps the later is more valid.

In Malaysia, soils found can generally be termed as tropical soils. They range from residual soils which normally are soils formed by in-situ weathering of parent rocks to soft clays and organic soils including peat. Soft soils generally have low shear strength and high compressibility. As such, problems like large settlements, flooding and damage to infrastructure due to soil subsidence, foundation failure due to lateral movement of soil, etc, are common. Residuals soil on the other hand are generally considered to be better in term of engineering properties compared with the soft soils, but by virtue of their existence in sloping ground, landslides are a major concern. Some 400 landslides have been reported (more than 30 were major landslides), involving both cut and natural slopes with a total loss of more than 200 lives and billion of Ringgit in damage to properties have been reported in the country over the last two decades or so.

In meeting the above mentioned challenges, some research works have been done at Universiti Putra Malaysia. These include proper analysis and design of piles against lateral loading; fundamental understanding on the properties and behavior of soft soils, both soft clays and peat; methods to improve/stabilize the soils; slope assessment system for landslide prediction, bio-engineering technique to stabilize slope; and use of waste materials as an economical solution to repair slopes.

In this paper, some recent works in particular those related to peat, will be described.

Keywords: Bio-engineering, Landslide, Soft Soil, Malaysia, Soil Stabilization

1. INTRODUCTION

Malaysia lies in areas with tropical climates (the A category climate in the Köppen Classification System). This climate is extensive, occupying almost all of the continents between latitudes 20°N to 20°S of the equator.

The key criterion for an A category climate is for the coolest month to have a temperature of more than 18 ºC making it the only true winterless climate category of the world. Another characteristic is the prevalence of moisture. Warm, moist and unstable air masses frequent the oceans at these latitudes. As a consequence, this climate zone has abundant sources of moisture giving rise to high humidity.

Due to this climatic condition, weathering of parent rocks (igneous, sedimentary or metamorphic), mainly chemical weathering, is the main agent for soil formations in the tropical country like Malaysia. The soils formed by the weathering are largely left in place, thereby literally called residual soil, and whose character depends on the parent rock it develops from. In addition to the residual soils, transported soils are also found in Malaysia. Another type of soils that can be found in Malaysia is the organic soils. Peat actually represents an accumulation of disintegrated plant remains, which have been preserved under condition of incomplete aeration and high water content [1-6].

2. PROBLEMS ASSOCIATED WITH SOFT AND SLOPING GROUND

Many towns and cities are actually located close to river mouths, deltas, lakes or alluvial flats. These are usually the areas of soft compressible soils. The soils usually have low undrained shear strength with high void ratio (high compressibility). Other areas that bring many problems to engineering are the swampy and peaty area where the soils have high organic content.

Landslides, problems usually associated with slopes (sloping ground), are serious geologic hazard common most countries of the world. Since 1975, some 400 landslides has been reported in Malaysia (more than 30 were major landslides), involving both cut and natural slopes with a total loss of more than 200 lives and billion of Ringgit in damage to properties[1-6].

3. SOME RECENT RESEARCH WORKS DONE AT UNIVERSITI PUTRA MALAYSIA

3.1.1 Laboratory Simulation of Pile In An Excavation

For this study a model test tank of 300 mm (W) x 800 mm (L) x 600 mm was used. The model test pile was instrumented with strain gauges. The soil was well graded medium fine sand with friction angle of 31^{o} and the max sand density was 13.8 kN/m^3.

Figure 1a shows the initial laboratory setup. Figure 1b shows the FEM model in PLAXIS 3D. Figure 1c and 1d shows the results of the FEM model by PLAXIS 3D Foundation. Both the experimental and FE results were apparently in good agreement [7-9].

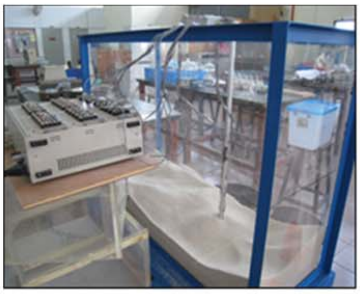

(a) Initial laboratory setup

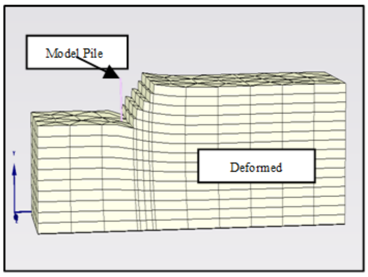

(b) FEM model in PLAXIS 3D

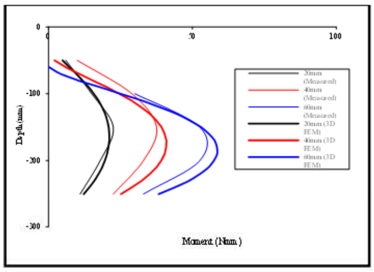

(c) Pile bending moment

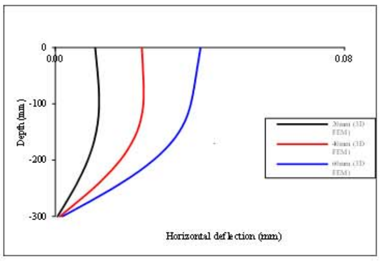

(d) Pile deflection

Figure 1 Laboratory setup, FE model, bending moment and horizontal deflection of pile

3.1.2 Case study: passive piles failure in open excavation

The Majestic Hotel is located in Malacca, the capital of a state of the same name - one of the fourteen Malaysian states.

The top 300mm layer of soil showed SPT 'N' value of 4-6 blows, followed with a SPT 'N' value average of zero with thickness of 5.0m to 7.0m. Undrained samples collected at depths of 3.0m to 4.5m were subjected to undrained unconsolidated test in the laboratory gave the undrained shear strength of 16kN/m^2 to 20kN/m^2. The unit weight of the very soft marine clay was about 16 kN/m^3 to17.5kN/m^3. The liquid limit of the soil was high which was mostly at about 55% to 75%. Plasticity index ranged from 20% to 45%. The soil consisted of a very high percentage of silt and clay; in the range of 70% to 90%.

The subsequent layer of soil was made up of a layer of stiff to very stiff silt. Generally, this layer had a thickness of 4m to 12m. After this layer, a layer of hard silt was encountered with intermittent layer of 3m to 4m medium to very dense gravel. The superstructure was designed to be supported by end-bearing piles comprising of group of 300mm diameter spun pile with nominal thickness of 60 mm. The piles were terminated at the hard layer on the very stiff silt or medium to very dense gravel layer. Figure 2 (a) shows a group of broken piles on site and (b) illustrates the 3D FEM of the broken piles using Plaxis 3D Foundation.

(a) A group of broken piles on site

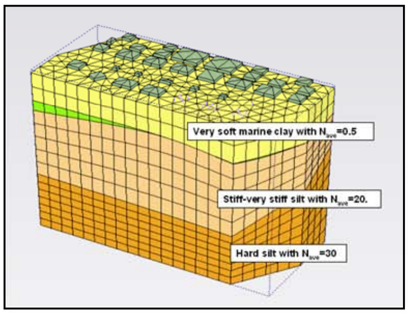

(b) FEM model in PLAXIS 3D

Figure 2 Broken piles and 3D FEM model of the pile and foundation

Hardening Soil model was applied as the soil constitutive model. The results at the end of the excavation phase showed that 70% of the modeled piles had either reached the critical cracking moment or exceeded the pile's cracking moment, and therefore confirmed as broken piles. Further excavation on site showed that cracked was found near to the transition layer of the very soft clay and the very stiff silt, confirming the location of the crack occurred at the location of maximum moment from the 3D FE analysis [7-9].

3.1.3 Predicting Passive Pile Response in Open Excavation

By using the similar Hardening Soil model, a single pile subjected to an open excavation in soft clay underlain by stiff clay was modeled using 3D FEM modeling in undrained condition. The width of the model was three times of pile diameter. Few of the parameters were based on the pile properties, soil properties and excavation configuration. Figure 3 shows the model in 3D FE stimulation.

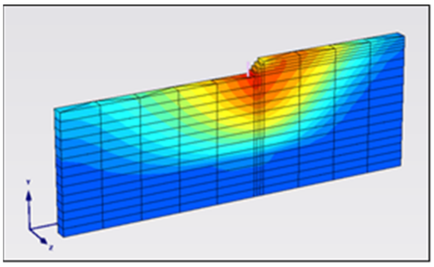

Figure 3. Total horizontal soil displacement in FE model

The soil stiffness ranges from very soft to medium stiff clay underlain by a hard layer. The effects of few parameters are clearly shown in design charts namely the soil stiffness, spun pile diameter and depth function. These few parameters showed significant effect when applied to cases with different soil stiffness (c_u=10 kPa, 20 kPa and 30 kPa), pile diameter (300 mm, 450 mm and 600 mm) and depth function ranging from 2 to 7. Figure 4 shows the design charts for a particular configuration [7-9].

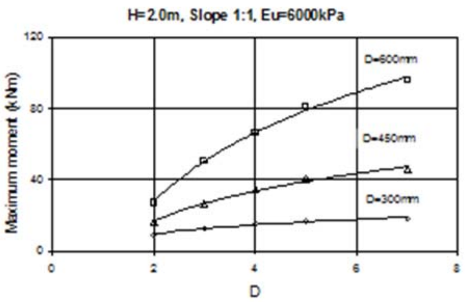

Figure 4 Maximum moment for pile in excavation

3.2 Stabilization of Peat

3.2.1 Shallow Stabilization

The effects of adding various percentages of chemical binders (OPC) from 5 to 50% in terms of wet weight of peat and other additives - polypropylene fibers, steel fibers, silica fume (micro silica), ground granulated blast furnace slag and fly ash on the strength of fibrous peat were investigated.

The results were shown in Figure 5. In general adding the chemical additives proved to have increased the soil strength substantially. Additions of additives are also beneficial, except for blast furnace slag, and fly ash where there appear to be no additional gain. Air curing was found to be generally better than moist curing. The best additive was apparently the polypropylene fibers (about 0.15% or 1.5 kg polypropylene fiber per cubic meter of peat at its natural water content) [10-11].

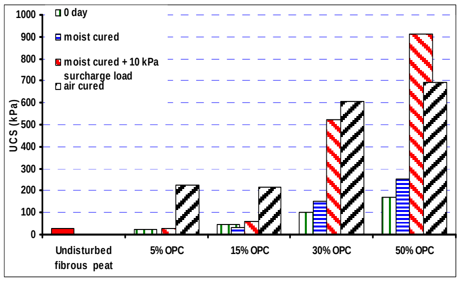

(a) Unconfined Compressive Strength of untreated fibrous peat and peat treated with OPC after 90 days curing

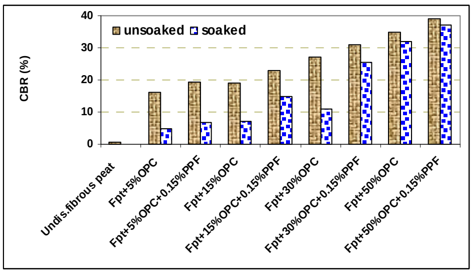

(b) CBR of untreated fibrous peat and peat treated with OPC and polypropylene fibers after 90 days curing

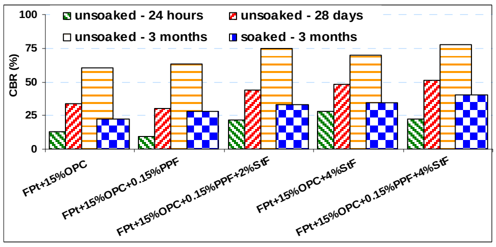

(c) CBR of untreated fibrous peat and peat treated with OPC, polypropylene and steel fibers after 3 months curing

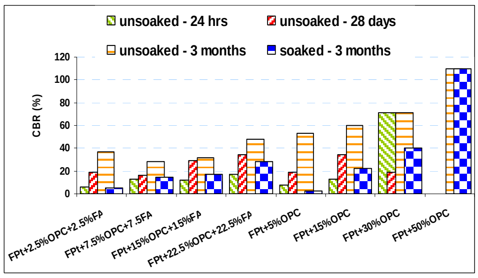

(d) CBR of untreated fibrous peat and peat treated with OPC and fuel ash after 3 months curing

Figure 5. Effects of OPC and additives on peat.

3.2.2 Deep Stabilization

Deep stabilization involved installing 'columns' of peat added with OPC and other additives into pre-bored hole set in peat sample. This stabilization technique is akin to those of cement or sand column as applied to soft clays. Peat with cement column was then tested in triaxial for strength and Rowe cell for compressibility.

The cement column technique involved casting in place a 20 mm diameter column (which gave an area ratio of 0.16) inside a 50 mm sample. The cement column was formed by adding peat with varying percentage of cement (OPC), the proportions of cement to peat ratio chosen are (100:0), (75:25) and (25:75) compacted to inside a PVC tube. The column was cured for 45 days in a soaking basin, before being inserted inside a pre-bored hole.

Figure 6 illustrates the effect of the cement column on the shear strength and compressibility of peat, measured with triaxial and Rowe cell test respectively. It was found that the cement column significantly improved both the shear strength (100% increase) and compressibility of peat, in particular column with higher dosage of cement. The peat gained strength with the addition of cement and probably the presence of cations initiated the flocculation because of the cementation phenomena among the soil particles and cement.

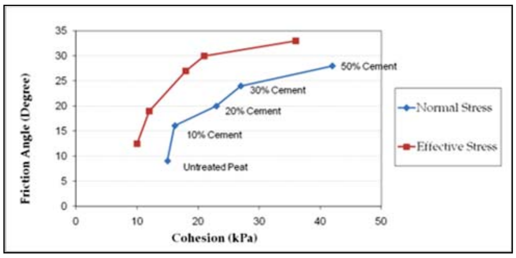

(a) Shear strength parameters of peat

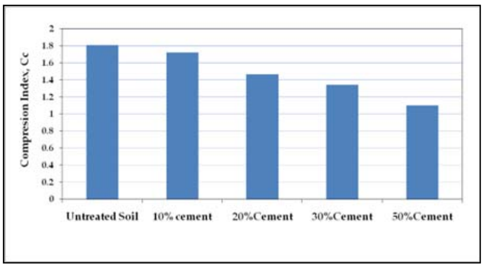

(b) Compression index of peat

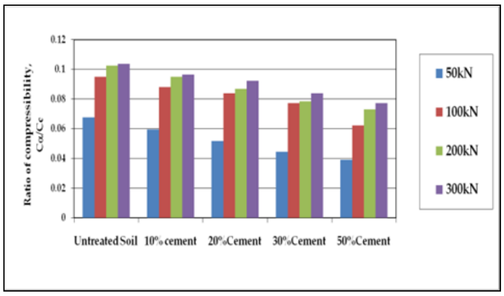

(c) Secondary compression (re-compression) index

Figure 6 Effects of precast cement columns on peat

To simulate a field condition, test at larger scale was carried out (Figure 7). Instrumentation included pore pressure gauge, LVDT, horizontal strain gauge and pressure cell.

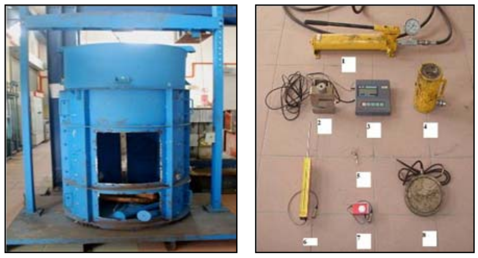
Figure 7 Test tank

Precast cement column, 1.0m long and 200 mm and 300 mm diameter were made of peat mixed with OPC and additives (polypropylene fiber, silica fume, polypropylene and steel fibers). The cement column was again shown to be beneficial in improving the load carrying capacity of peat (Figure 8)[10-11].

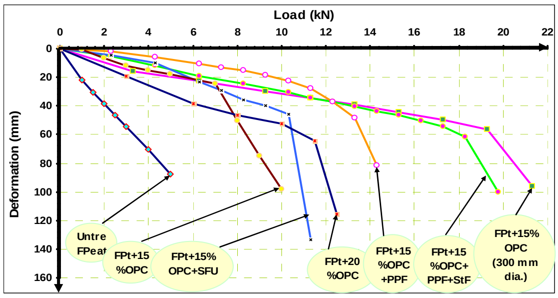

(a) Load-deformation of untreated peat and peat treated with precast cement column

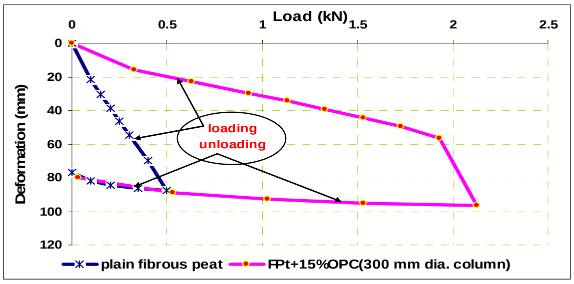

(b) loading-unloading

Figure 8 Load carrying capacity of fibrous peat with and without precast cement column

3.2.3 Stabilization by Injection and Vacuum

The Deep Mixing Method (DMM) is today accepted world-wide as a soil improvement method and is based on mixing binders, such as cement, lime, fly ash and other additives, with the soil to form columns of a hardening material. DMM coupled with vacuum technique appears to be the solution for deep stabilization of peat. To do this, a laboratory scale of new DMM technique (injection-vacuum apparatus) was specially designed and developed as shown in Figure 9. In this study, the effects of cement, sodium silicate, calcium chloride, and kaolinite grouts on peat properties in new DMM technique were investigated [12-14].

The results showed that the application of vacuum would help speed up the stabilization process. The low strength and loose matrix of peat meant that usage high power injection pump for stabilizing is not possible. In this method low power injection pump is applied by aiding of vacuum pump to increase the stabilized area. In comparison with conventional vacuum and preloading method as well as new injection methods, this method is believed to be more cost-effective.[12-14].

Figure 9 Small scale of new DMM technique

3.2.4 Electro-osmotic properties of peat

We began a study in 2007 to look at the role of organic matter on electro-osmotic properties of peat; and to investigate the behavior of electro-osmotic flow in peat. The ζ was measured with a zeta-meter as a function of pH values ranging from 1.91 to 11.5. All measurements were made in 0.0001 M NaCl solutions and pH adjustments were made using dilute HCl or NaOH solutions.

Figure 10 shows the relationship between peat zeta potential (ζ) of peaty soils with soil pH. The variations in ζ with pH were probably related to the nature of electrical energy field in peaty soils. [15-17]

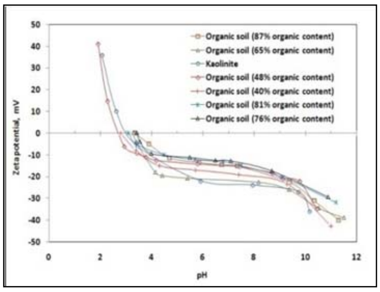

Figure 10 Zeta potential – pH relationship

3.2.5 Electro-osmotic Phenomena in Peat

The test apparatus consisted of an acrylic unit with a central cylinder of 150 mm in length and 169 mm in internal diameter, as shown in Figure 11. The volume of both the cathode and the anode compartments were 2243 mL. Titanium disks were used as the electrodes.

Peat samples were treated for 3-days period. The effluent was collected to calculate the coefficient of electro-osmotic conductivity.

Figure 11 Electro-migration test system

The results showed that the coefficient of electro-osmotic conductivity and the 3-day energy expenditure was found to increase with increase in the degree of peat humification (Figure 12). The H8 peat had the highest electro-osmotic conductivity and energy expenditure. Peat had a net negative charge and the direction of electro-osmotic flow was from anode to cathode. The study showed all charges on the soils' surfaces were strongly pH-dependent. The very highly decomposed (H8) peat had the significant differences in electro-osmotic properties in comparison with H5 and H3 peat [15-17].

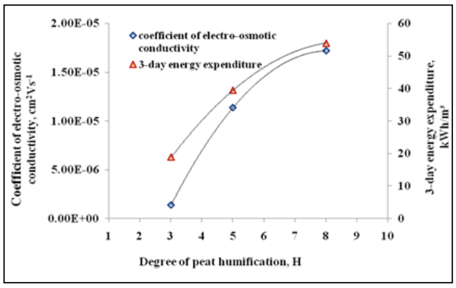

(a) Coefficient of electro-osmotic conductivity-degree of humification-energy expenditure

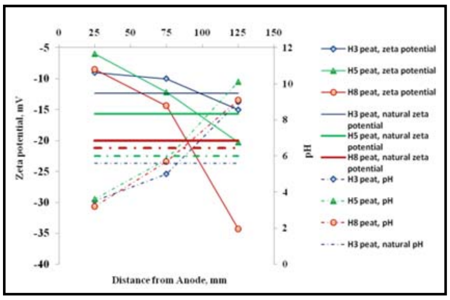

(a) Zeta potential – pH

Figure 12 Electro-osmotic phenomena in peat

3.3 Slope Assessment System for predicting landslide

In our work, we developed a slope assessment system (SAS) for cut slopes underlain by granitic formation using discriminant analysis. From the available data, the following physical parameters were selected, namely: slope feature, location, height of slope, angle of slope, feature aspect in degrees, plan profile, cross profile, distance to ridge, batter, slope shape, and main cover type. These data in form of continuous variables/parameters were transformed into various classes and were used in the statistical analysis and regression equation for the computation of instability score (individual discriminant scores). The database was compiled between 1994 and 2003 on a total of 36 slopes, 21 slopes from the Tapah – Cameron Highland road, and 15 slopes from Kuala Lumpur – Bentung old road [18-21].

From the results, it was seen that the higher the significant value of F to add new and to delete variables, higher the Eigen-values and χ^2 produced. The Wilk's λ however became smaller. Generally the number of significant parameters would increase with increase of the significant value of F to add and to delete. Discriminant function of the 86 failed and 53 not failed slopes was computed. The boundary of discriminant function separating these two groups (failed and not failed slope) was calculated using the average of the two group's mean. Groups mean for not failed and failed slopes were -0.91 and 0.58 respectively. The value of discriminant function separating these two groups (noted as g) could be calculated. $g = (Y_f + Y_s) / 2$, where, Y_f = Mean of failed group; Y_s = Mean of not failed group.Value of g for the model is -0.165.Using this g value, the boundary condition separating failed and not failed slopes is as follow; Not failed if $Y < -0.165$, otherwise failed. The hazard rating was designed using the maximum and minimum value of discriminant function. The maximum value of discriminant function was 5.906 and minimum value was -7.083. Table 1 below shows the hazard rating designed for the SAS [18-21].

Table 1 Hazard rating designed for the new SAS

Range	Rating
2.871 to 5.906	Very high
-0.165 to 2.871	High
-3.459 to -0.165	Low
-7.083 to -3.459	Very low

The results of the comparative study are as shown in Table 2.

Table 2 Evaluation SAS in predicting landslides

(1) Number of assessed slopes	36
(2) Numbers of actual landslide or failed slope	25
(3) Numbers of Slope classified as high hazard	28
(4) Number of slopes classified as high hazard that actually failed	24
(5) % of correctly classified failed slopes	96%

This SAS appears to be satisfactory.

3.4 Use of Bio-engineering for Stabilizing Slope

Bio-engineering in our context refers to the use of plants to enhance the stability of hill slopes primarily against shallow-seated. This is the basic principle of what is termed as the live pole technique.

Our first challenge was to identify suitable plant species for such an application. Our study led us to 10 potential tropical plant species. Based on screening trial and observations of distribution/location and shape of growing roots three species were initially identified as the best candidate for the live pole, namely: Hibiscus tiliaceus (*Ht*), Dillenia indica (*Di*) and Dillenia suffruticosa (*Ds*). The shade house experiment was replicated but with mineral soils (aerisols, ferralsols, histosols, luvisols, regosols, gleysols, fluvisols) that commonly formed the Malaysian slopes. From this experiment, only 2 species, *Ht* and *Ds* were found later to be the most suitable (Figure 13)[22-25].

Hibiscus tiliaceus   Dillenia indica   Dillenia suffruticosa

Figure 13 Rooting trial (root growth along stem)

We carried out shear test to measure the effect of root on soil strength. Unfortunately the conventional shear box was not good enough to represent the effect of root in a soil mass. For this, we have to design and fabricate our own large shear box. This box had a sample size of 300mm x 300mm x 200mm, compared with conventional equipment whose sample size is only 50x50mm.

The results showed that the presence of roots had significantly improved the shear strength of the soil and it also showed that the effect was mainly on the cohesion. Root of *Ht* has enhanced the cohesion component of shear strength by 593% (at 30 cm depth) and 722% (at 50 cm depth) as compared to the unplanted soil.

To assess the suitability of the plant species and live pole in real situation, a field trial was carried out. A meta-stable slope in the vicinity of the university (UPM) campus was selected. The planting operation was done in two days. All fresh cuttings of *Ht* and *Ds* had initial lengths of 2.10 to 2.30, diameters between 50 to 70 mm at upper end and 50 to 80 mm at butt end; and almost straight, smoothly tapered and with no bends or branch points forming large bifurcations. At the end of the 12 months monitoring period, 2 *Ht* and 2 *Ds* live poles were exhumed in order to study the root growth and properties of the live poles in a field condition as shown in Figure 14.

A visual comparative study of *Ds* and *Ht* live poles showed that about 25% of the embedded length of *Ht* was rooted, for *Ds* it was about 31% Figure 15). However, the roots of *Ht* seemed longer (230 to 1230 mm long) and thicker (0.5 to 5.7 mm diameter) compared with roots of *Ds* (length: 350 to 1060 mm; diameter: 0.5 to 2.5 mm).

Figure 14 Exhumed live poles from the site

(a) *Ds* pole

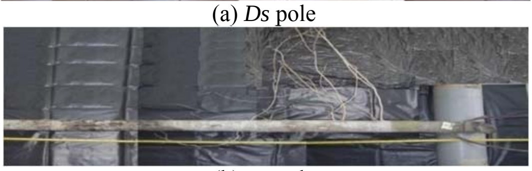

(b) *Ht* pole

Figure 15 Roots of exhumed *Ht* and *Ds* pole

A finite element analysis was carried out to illustrate the benefit of live pole in stabilizing slope against shallow failures using 2D Plaxis. As expected, the factor of safety of the slope increased markedly. The live pole reinforcement was apparently more effective if poles were installed in closer array and soil had higher original cohesion [22-25].

3.5 Low Cost Repair for Failed Slopes

In order to apply scrap car tires as slope repair, we began by designing suitable tests and then tested the locally produced (scrap) car tires. We carried out tensile tests on commonly available sizes, i.e. R12 to R15. Mean tensile strength of 55.81 kN, with standard deviation 15.19 kN was obtained from the pull-out test, with statistic probability of tensile strength greater than 20 kN was 99%. Two attachment systems were considered and tested in laboratory for tension, the wire rope and U-clip, and polymer rope of different numbers of wrap and knots. For the wire rope and U-clip system, a 12 mm diameter wire rope with its compatible size U-clip was selected for testing purpose. Whilst for polymer rope, 12 mm diameter polypropylene was chosen for ease of handling and economy. The rope was tightened on the cross beam of tensile machine and pull until the rope rupture. The polypropylene rope had a working load of 25kN was a suitable attachment for scrap tire wall.

Next we needed to design and study the performance of the propose tire system. A full scale field trial was carried. A total of 2100 numbers of scrap car tires in 25 layers was used. It only took 5 unskilled workers 20 workings days to complete the structure. Instrumentation like settlement plates and pressure cells were installed to monitor the performance of the trial wall (Figure 16).

Figure 16 Constructing the trial scrap tire wall

The following software (GawaWin, Prokon and MacStars) were used for the preliminary design. Some basic design assumptions were (1) maximum bearing capacity of base was 100 kPa, (2) effective internal friction was 28^o, (3) no water level, (4) surcharge was 10 kPa, (5) factors of safety against sliding, overturning, bearing failure and overall slope stability were 1.5, 1.5, 3.0 & 1.5 respectively. As shown in Figure 17, the propose scrap tire system was apparently the most cost effective for wall of 2m to 6m. The significant advantage of the propose scrap tire system was the reduced cost of wall materials and construction. Most of the wall components (scrap tires and back fill soils) were recycled material [26].

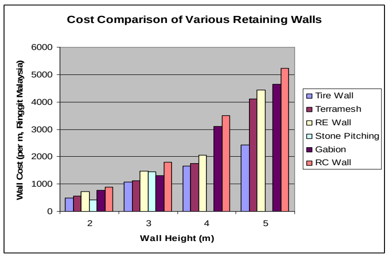

Figure 17 Cost per linear meter of various retaining wall systems versus height

4 CURRENT RESEARCH

We are currently working on some research projects including:

4.1 Electro-Biogrouting of Soft Soils

Biogrouting is a new method to stabilize sandy soils through precipitation of $CaCO_3$ between grains. This process decreases the permeability about 98% and increases the soil strength up to 12Mpa. It is created by bacterium Bacillus Pasteurii and enzyme urease that hydrolyze urea to carbonic dioxide and ammonia. A major problem in biogrouting is the distribution of bacteria injected into the soils. We are going to use electrokinetics in order to transport bacteria towards the cathodes to get a uniform distribution of bacteria and enzyme in the soft soil mass.

4.2 Acid Rain Intrusion Effects on Slope Failure Phenomena and Mechanisms

Acidic deposit that fall to Earth from the atmosphere is named acid rain. It is caused by sulfur dioxide (SO2) and nitrous oxide (N2O). Acidic rainfall as an environmental factor has a potential to affect slope stability. However, the slope failure phenomena and mechanism cannot be explained with a simple mechanical-physical concept. A new approach is needed to explain the underlying mechanism of water attack on soil using physicochemical concept including ion exchange effects.

This fundamental research will integrate and blend traditional theory with physicochemical concepts in order to provide a framework for the analysis of soil behavior under acid rain intrusion effects. The obtained results will be discussed in the light of chemico-mechanical model. The outcome will explain the "why" and "how" the mechanical soil behavior under acid rain intrusion effects in an environmental context.

5 CONCLUSIONS

In this paper, we presented some research works which have been carried out at Universiti Putra Malaysia. These include proper analysis and design of piles against lateral loading; fundamental understanding on the properties and behavior of soft soils, both soft clays and peat; methods to improve/stabilize the soils; slope assessment system for landslide prediction, bio-engineering technique to stabilize slope; and use of waste materials as an economical solution to repair slopes.

6 ACKNOWLEDGMENT

The financial assistance from the Ministry of Science, Technology and Innovation Malaysia, as well as the Universiti Putra Malaysia for the researches mentioned in this paper is gratefully acknowledged. So are the input of my research students, past and present.

7 REFERENCES

[1] Huat BBK., Ali FH, Barker D, Singh H. & Omar H., Landslides in Malaysia: Occurrences, Assessment, Analysis and remediation/Preventive Solutions. Universiti Putra Malaysia Press. 2008, 468p.

[2] Huat BBK & Ali F, Essential Soil Mechanics for Engineers. Universiti Putra Malaysia Press,2007, 518p.

[3] Huat, BBK & Ali F, Ground Improvement Techniques. Universiti Putra Malaysia Press, 2007, 383p.

[4] Huat BBK, Ali F, Omar H & Singh H, Foundation Engineering: Design and Construction in Tropical Soil. Taylor and Francis, United Kingdom, 2006, 243p.

[5] Huat, BBK, Han KK, Loh, WC & Aziz A, Retaining Structures: Design and Construction in Tropical Soils. Universiti Putra Malaysia Press, 2006.

[6] Huat BBK, Organic and Peat Soils Engineering, Serdang: University Putra Malaysia Press, 146 p.

[7] Kok ST & Huat BBK, Numerical Modeling of Laterally Loaded Piles. American Journal of Applied Sciences. Vol. 5(10), 2008,pp. 1403-1408

[8] Kok ST, Bujang BKH, Jamaloddin N, Mohd Saleh J, Gue SS, A Review of Basic Soil Constitutive Models for Geotechnical Application, EJGE Vol 14, 2009, pp 1-18.

[9] Kok ST, Bujang BKH, Jamaloddin N, Mohd. SJ, Gue SS, A Case Study of Passive Piles Failure in Open Excavation. Journal of Deep Foundation Institute, Vol. 3, No. 2, 2009, pp. 50-57.

[10] Kalantari B, Prasad A. & Huat BBK, Stabilising Peat Soil with Cement and Silica Fume. Proceedings of the Institution of Civil Engineers: Geotechnical Engineering. 163 GE1, 2011, pp. 33-40.

[11] Kalantari B & Huat BBK, Improving Unconfined Compressive Strength of Peat with Cement, Polypropylene Fibers, and Air Curing Technique. Global Journal of Researches in Engineering. Vol. 10(1) 2010, pp 9-15.

[12] Huat, BBK, Kazemian,S & Barghchi M, A State of Art Review of Peat: General Perspective. International Journal of the Physical Sciences 6(8), 2011, pp. 1988-1996.

[13] Kazemian, S, Huat BBK, Prasad A & Barghci M, A State of Art Review of Peat: Geotechnical Engineering Perspective. International Journal of the Physical Sciences, Vol. 6(8), 2011, pp. 1974-1981.

[14] Kazemian S, Huat BBK, Effects of Aggressive pH Media on Peat Treated by Cement and Sodium Silicate Grout. J. Cent South Univ Technol. Vol. 18, 2011, pp 840-847

[15] Asadi A, Huat BBK, Hanafi MM, Mohamed, TA & Shariatmadari N, Chemico-geomechanical Sensitivities of Tropical Peat to Pore Fluid pH Related to Controlling Electrokinetic Environment. Journal of the Chinese Institute of Engineers. Vol.34(4), 2011, pp. 481-487

[16] Asadi A, Huat BBK, Hanafi MM, Mohamed TA, and Shariatmadari N, Role of Organic matter on Electroosmotic Properties and Ionic Modification of Organic Soils. Geosciences Journal, Vol 13(2) 2009, p p 175-181.

[17] Asadi A, Huat BBK, Hanafi MM, Mohamed TA, Shariatmadari N, Physicochemical Sensitivities of Tropical Peat to Electrokinetic Environment. Geosciences Journal, Vol 14(1), 2010, pp. 65-75.

[18] Singh H, Huat, BBK & Jamaludin S, Slope Assessment Systems: A Review and Evaluation of Current Techniques Used for Cut Slopes in the Mountainous Terrain of West Malaysia. Electronic Journal of Geotechnical Engineering, Vol.13, 2008, pp. 1-24.

[19] Jamaludin S, Huat BBK & Omar H. Evaluation and Development of Cut-Slope Assessment Systems for Peninsular Malaysia in Predicting Landslides in Granitic Formations. Journal Technology B. Universiti Technology Malaysia. Vol. 44B, 2006, pp 31-46.

[20] Jamaludin S, Huat BBK and Omar H. Evaluation of Systems for Predicting Landslides of Cut Slopes in Granitic and Meta-sediment Formations. American Journal of Environmental Sciences. Special Issues on Recent Advances in Landslide Engineering and Technology. NY, USA. 2(4), 2006, pp. 135-141

[21] Huat BBK & Jamaludin S, Evaluation of Slope Assessment System in Predicting Landslides along Roads Underlain by Granitic Formation. American Journal of Environmental Sciences. Vol. 1(2), 2005, pp. 90-96

[22] Huat BBK & Kazemian S. Study of Root Theories in Green Tropical Slope Stability. Electronic Journal of Geotechnical Engineering. Vol.15Q, 2010, pp. 1815-1824.

[23] Mafian S, Huat BBK, A Rahman N, Singh H. Potential Plant Species for Live Pole Application in Tropical Environment. American Journal of Environmental Sciences, Vol. 5(6), 2009, pp. 759-764.

[24] Mafian S, Huat BBK.& Ghiasi V. Evaluation of Root Theories and Root Strength Properties in Slope Stability. European Journal of Scientific Research. Vol.30(4), 2009, pp. 594-607.

[25] Mafian S, Huat BBK, Barker DH, Rahman NA & Singh H, Live Poles for Slope Stabilization in the Tropical Environment. Electronic Journal of Geotechnical Engineering. Vol.14G, 2009, pp. 1-25.

[26] Huat BBK, Aziz AA & Loh WC, Application of Scrap Tires as Earth Reinforcement for Repair of Tropical Residual Soil Slope. Electronic Journal of Geotechnical Engineering. Vol. 13 B, 2008, pp. 1-9.

First International Conference on Geotechnique, Construction Materials and Environment, Mie, Japan, Nov.21-23, 2011, ISBN: 978-4-9905958-0-7 C3051

Characterization and Modeling of Various Aspects of Pre-failure Deformation of Clayey Geomaterials – Fundamental Theories and Analyses

John N. MUKABI., EngineerIntel – Research & Development Department, Kensetsu Kaihatsu Consultants, Nairobi, Kenya

ABSTRACT: The recently preferred Performance–Based Design (PBD) fundamentally entails that, deformation in ground and foundation soils, along with the reciprocal and/or retrospective structural deformation and stress states, are comprehensively analyzed by adopting sophisticated methods, particularly for structures within high exposure seismic action regions. The soil mechanics concept of deformation resistance, which principally constitutes the fundamental postulates on kinematic hardening, is considered as one of the most vital conceptual approach in this regard.
In this part of the paper therefore, fundamental theories related to the recently proven Modified Critical State Theory (MCST), "Consolidation and Shear Stress Ratio" (CSSR) functions as well as the) mathematical concepts on Yield Strain Limit (YSL proposed in this Study, that may enable the effective use of retrospective analysis in simulating, predicting and characterizing the variation in the behavior of clayey composite ground and geomaterials under various loading conditions, are analytically introduced and subsequently applied.

Keywords: deformation, yield sub-surfaces, consolidation stress-strain history, loading rate, reconstitution

1. INTRODUCTION

1.1 Imposed Geo-changes in Ground and Geomaterial

When subjected to various modes of loading and environmental conditions, most ground and geomaterials undergo geotechnical changes that are, as far as the geotechnical engineer is concerned, of great exigency in terms of project costs, particularly in developing countries which suffer, more predominantly, in lack of adequate project funding. On the other hand, although conventional approaches such as the limit equilibrium-based methods provide information to resist a design seismic force for example, they are not able to predict structural performance under critical loading conditions. Furthermore, notwithstanding the simplicity and popularity of the Equivalent Linear procedure, its main limitation is characterized by the lack of providing any prediction of earthquake induced permanent displacements. Due to these factors, and the increased frequency, intensity and changes in trend of seismic action in recent times, and in consideration of the degree of devastation caused within short time periods on civil engineering structures that have been subjected to earthquake and tsunami loading, it is virtually a definitive prerequisite that multi-stage advanced and sophisticated methods of analyses with the effective ability to probe and/or predict the transformed ground and material geo-characteristics, be employed.
It is therefore imperative that, for structures which require higher performance, the geotechnical engineer, through the use of sophisticated methods, determines relatively precise and reliable Value Engineering (VE) based cost-effective design parameters taking into serious account prevalent loading factors, environmental conditions and structural sustainability.

1.2 Methods of Testing and Geotechnical Investigation

Laboratory tests were comprehensively performed in Japan by using sophisticated automated triaxial testing systems equipped with a local strain measurement device; the Local Deformation Transducer (LDT), whilst various geophysical methods of survey were employed in undertaking the in-situ geotechnical investigations. The seismic survey was mainly adopted in determining the in-situ initial elastic and/or shear moduli. On the other hand, the Transient Electromagnetic Method (TEM) utilizing sounding technology was used in deriving in-situ bearing capacity, strength and elastic stiffness by correlating the measured resistivity to the geotechnical parameters through a newly proposed quasi-empirical method [1]. The main mechanical methods adopted were the Standard Penetration Test (SPT) and the Dynamic Cone Penetration Test (DCPT). Standard and modified laboratory tests were also carried out extensively in the East and Central African Region using conventional triaxial and unconfined compression testing equipment.
Details of the methods of testing and testing equipment can be referenced from [2], [3].

1.3 Geomaterials Adopted for Laboratory Testing

The well cemented and highly structured Pleistocene clays adopted for this study were sourced and tested in Japan. The clays were mainly sourced from: Osaka Bay, (the construction site of the Kansai International Airport); Tokyo Bay Clay (the construction site of the Trans Tokyo Bay Highway connecting Kawasaki City and Kisarazu City in Chiba Prefecture); OAP Clay (the construction site of skyscraper buildings in Osaka City), and Suginami Clay (the construction site of the Kandagawa Flood Control Project in Tokyo). Other clays that were investigated include the Ariake Holocene Clay, which is a very soft, sensitive and highly structured clay underlying the Ariake area in Kyushu, Japan [2].
Lateritic gravel and black cotton soil, which are in predominant existence in most parts of Africa, were sourced from various construction sites in East and Central Africa, and tested in the laboratory under varying modes of loading and geotechnical conditions. Black cotton soils, formed in the Quaternary period from in-situ weathering of basic igneous, metamorphic and pyroclastic rocks, are highly expansive, problematic and extremely susceptible to moisture ~ suction variations.

2. FUNDAMENTAL THEORETICAL AND CONCEPTUAL CONSIDERATIONS

2.1 Brief Background of the MCS Theory

The fundamental postulates of the MCST (Modified Critical State Theory) were first proposed by [4] while investigating the effects of consolidation stress ratio and strain rate on the peak stress ratio of clay. In that study, they concluded that, possibly due to different structure formation, the stress rate at q_{max} and the maximum stress ratio $[q/p']_{max}$ increased as the consolidation stress ratio $K_c = \sigma'_r/\sigma'_a$ decreased. Following further research, and by demonstrating the inadequacies of the conventional Critical State Theory (CST), [5], [6] proposed the need for modification of the CST and most of the theories based thereon, which characterize the strength and deformation behavior of clays assuming that failure for normally consolidated clays occurs at the Critical State Line (CSL) irrespective of the drain condition, strain rate and stress path traversed. The mathematical derivatives of the MCST and its applications are reported in detail by [7]. Typical examples demonstrating that the CSL is not unique but rather dependent on varying geo-changes and transformed states are depicted in Figs. 2.1 and 2.2.

For clay subjected to cyclic loading at frequencies between 0.02Hz and 01.Hz, [8] defined a Cyclic Failure Line (CFL) which is clearly strain rate dependent as shown in Fig. 2.1. From this figure it can be noted that the gradient of the normalized stresses reduces as the frequency increases.

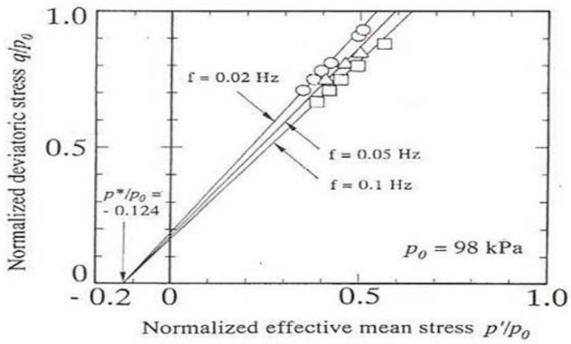

Figure 2.1 Stress states at failure of clay under undrained cyclic loading and Cyclic Loading's Failure line (CFL) [8].

In their study on cemented sand subjected to undrained cyclic loading, [9] also suggested that there exists a Phase Transformation Line (PTL) which plots well above the conventional CSL. Their results also showed that the CFL overshoots the CSL [$(\mu_f)_{CFL}$ = 2.25, while $(\mu_f)_{CSL}$ = 1.61].

On the other hand, Fig. 2.2 distinctly shows that the CSL is not unique and varies with drainage conditions and consolidation stress-strain history.

Consequently, the MCST takes into account three important features: 1) the clay structure in relation to the consolidation stress-strain-time history; 2) the initial pre-shear state of stress in relation to the modified CSL; and, 3) the fact that under a constant rate of strain during undrained shear, stress paths for higher consolidation stress ratio values traverse for longer periods and distances to peak resulting in larger straining that contributes to larger structural changes that culminates in the "overshooting" phenomenon of the conventional CSL [4].

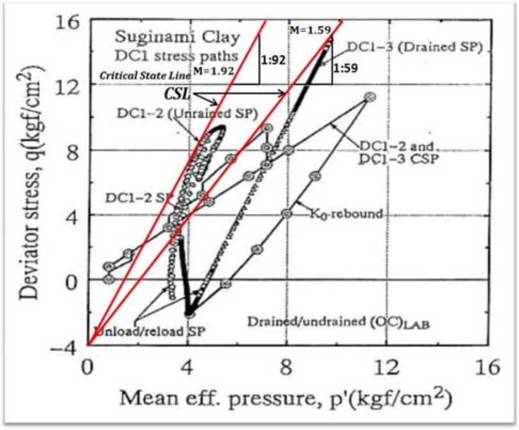

Figure 2.2 Effective reconsolidation and shear stress paths for undrained and drained Suginami clay specimens [2].

Consequently, under the MCST framework, the expression $q = Mp'$ that locates the conventional CSL is therefore modified to retrofit the modified CSL_M as:

$$q = \psi' p'. \tag{1}$$

where,

$$\psi' = \frac{(\eta_{max})_I}{\{\kappa_I - [{}^{\Delta\phi'}/_{\delta_{CSR}}] \times f_{CSR}\}} \tag{2}$$

In this case, q is the deviator stress, ψ' is the stress path locating modifier, p' is the mean effective stress, κ_I is the transformation function of $\Delta\phi'$, which is defined as the differential normalizing parameter of the angle of internal friction, δ_{CSR} is the cubic exponent of the Consolidation Stress Ratio (CSR) function, which is expressed as, f_{CSR}. On the other hand, the modified λ_M constant, which would project the CSL_M onto the υ–$\lambda\ell n$p' space when analyzing changes in volume (voids) is expressed in the relation;

$$\lambda_M = \lambda_I \times [A_{\lambda_M} f_{CSR} + B_{\lambda_M}] \tag{3}$$

hence,

$$v_1 = N - \lambda_M lnp' \tag{4}$$

and,

$$v_2 = \Gamma - \lambda_M lnp' \tag{5}$$

The deviator and mean effective stresses, q_f and p'_f at failure are then derived as:

$$q_f = \psi' exp[(\Gamma - v_2/\lambda_M] \tag{6}$$

and,

$$p'_f = exp[(\Gamma - v_1/\lambda_M] \tag{7}$$

where, A_{λ_M} and B_{λ_M} are material constants, while N, Γ and λ_M are mapping constants.

2.2 Brief Introduction of CSSR Functions

The geo-mathematical derivations of the CSSR Functions developed within the MCST framework and their applications in correcting for the effects of SHANSEP (Stress History and Normalized Engineering Properties) consolidation, ageing and reconstitution, are reported in detail by [10].

On the other hand, details of the pragmatic applications of the versatile CSSR functions including correction for, and simulation of, field conditions, retrospective characterization and retracing of consolidation and shear stress histories, multi-stage construction control of foundations and embankments on soft and problematic soils and, in modification of constitutive models based on the conventional CST, are discussed in detail by [7], [10].

2.3 Theoretical Considerations for Determination of Sub-yield Boundary Surfaces

Within the framework of classical visco-elasto-plastic theory, the strength and yielding characteristics of geomaterials at relatively large strains are described by defining a yield locus whereby the behavior within this locus is considered either rigid, linear elastic or non-linear elastic. Nevertheless, recent research has shown that such simplifications are inadequate in characterizing the overall stress-strain behavior of geomaterials over a wide range of stress-strain. As a consequence, most researchers have proposed multiple kinematic yield surfaces to better describe the elasto-visco-plastic behavior observed within the larger scale yield envelope.

Consequently, most of the recent constitutive models describing the plastic behavior of geomaterials including clays, sands and soft rocks subjected to cyclic loading are derived from the elasto-visco-plasticity theory along with the concept of the non-linear kinematic hardening rule. However, despite the various numerical and modeling research that has been reported, a quantitative method of determining the limiting boundaries of the sub-yield surfaces based on experimental testing is not yet proposed. In the method proposed in this Study, three kinematic sub-yield surfaces, namely; Y_I: representing the Initial Yield Surface within which the quasi-elastic properties are defined, Y_S: representing the Secondary Yield Surface which characterizes the intermediate non-linear and irreversible deformation behavior, and Y_T: the Tertiary bounding limit where large scale straining and yielding occurs, are considered as schematically shown in Fig. 2.3.

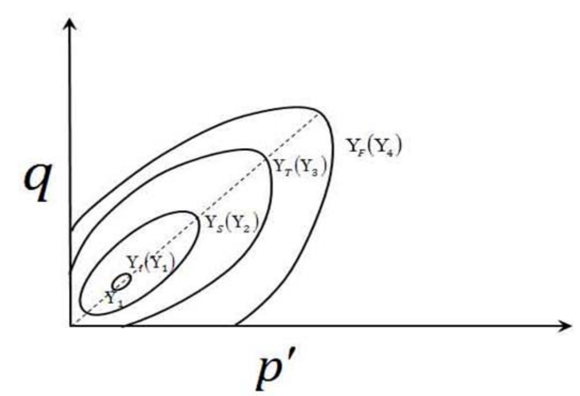

Figure 2.3 A schematic representation of multiple kinematic yield surfaces.

For stiff geomaterials having relatively large initial and secondary yield surfaces, the quasi-elastic properties are important as bench marks for both geotechnical engineering analyses and the construction of a general framework of pre-failure characterization.

Theoretically, as proposed by [11] and partly by [12], in quantitatively determining the yield strains for the respective yield loci , the following considerations, most of which are scientifically and quantitatively confirmed in this Study for the first time, are made: 1) when the stress transcends the Y_I and Y_S sub-yield boundary surfaces, the preceding surface is kinematically engaged and dragged with the stress point; 2) when Y_I boundary is engaged with some associated energy loss, it is considered that particle contacts start to experience local yielding due to normal stress concentrations developing small plastic strains; 3) significant plastic straining is delayed until the stress point engages the Y_S sub-yield surface at which stage a significant number of contact points probably start to fail in shear, leading to inter-particle slippage resulting in a marked shift in the direction of the strain increment vector; 4) as demonstrated in this Study, a further feature of the Y_S envelope is that it defines the threshold at which drained and undrained cyclic loading starts to affect the soil significantly whereby sharp increases are observed in the ratio of plastic to elastic strains, creep rates at constant stresses, energy dissipation in local cycles, hysteretic damping ratio and rate of pore pressure development; 5) the strains developed by a stress path which progresses towards the Y_F locus (failure envelope) become increasingly plastic and time-dependent in their nature (refer to Fig. 2.5); 6) a sharp change in stress path direction leads to re-entry into the preceding yield surface and, 7) destructuration leads to the disappearance of the existing initial yield surface transferring the stress point to the subsequent locus hence the prevalence of pseudo-elastic characteristics depicting lower stiffness and/or apparently longer pseudo-elastic range.

Furthermore, this Study also sets out to confirm, on the basis of experimental data and analysis that, the size and shape of the yield surfaces, particularly Y_I and Y_S, are mostly influenced by: 1) recent stress and time history as the stress point transcends to the current stress-state; 2) structuration due to ageing (Long Term Consolidation) and cementation occurring at the current stress-state as particles agglomerate; 3) loading rate and path of perturbing stresses or strains; 4) drainage conditions and, 5) mode of loading static (monotonic, cyclic) or dynamic.

Based on the foregoing theoretical and practical considerations, mathematical derivations which provide a sufficiently applicable method of determining pre-failure sub-yield strain limits and the respective elastic stiffness and deformation modulus, are developed.

As shown in Fig. 2.4, an apparent (estimated) initial Young's modulus $E^{a}_{\max}$ is first determined. An arbitrary modulus ratio, α is introduced within the region of small strains whereby $1.0 < \alpha \leqq 0.95$. Considering the intersection properties of the parameters in Fig. 2.4, a square relation expressed in (8) is developed.

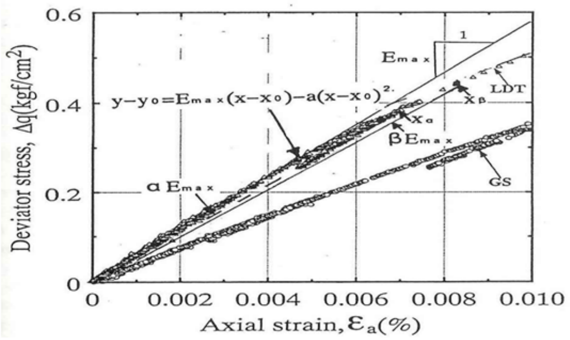

Figure 2.4 Graphical representation of stress-strain parameters applied for mathematical determination of Yield Strain Limits (YSL) [2].

$$\Delta q_i - \Delta q_o = E^a_{\max}\left[(\varepsilon_a)_i - (\varepsilon_a)_o\right] - a\left[(\varepsilon_a)_i - (\varepsilon_a)_o\right]^2 \tag{8}$$

The tangent moduli E_α at point α and E_β at point β are thence expressed as;

$$E_\alpha = (dq/d\varepsilon_a)\varepsilon_\alpha = E^a_{\max} - 2a\left[(\varepsilon_a)_\alpha - (\varepsilon_a)_o\right] \tag{9}$$

and,

$$E_\beta = (dq/d\varepsilon_a)\varepsilon_\beta = E^a_{\max} - 2a\left[(\varepsilon_a)_\beta - (\varepsilon_a)_o\right] \tag{10}$$

where, q_i, q_0 are arbitrarily designated deviator stresses at the corresponding ε_α, ε_β strain levels.

Solving (9) and (10) simultaneously and substituting for a in to (8), we obtain (11), which defines the initial Yield Strain $(\varepsilon_a)_{Y_I}$ that locates the boundary of the quasi-linear elastic range, i.e.; the Initial Yield Surface upon transformational mapping into the $q \sim p'$ space. Hypothetically, the magnitude is defined as the length of the major radial axis of the Y_I elliptical surface depicted in Fig. 2.3.

(1) $(\varepsilon_a)_{Y_I}$ ***: Initial Yield Strain (ELS)***

$$(\varepsilon_a)_{Y_I} = (\varepsilon_a)_\beta - \left[\frac{E^a_{\max} - E_\alpha}{2(E_\alpha - E_\beta)}\right] \times \left[(\varepsilon_a)_\beta - (\varepsilon_a)_\alpha\right] \tag{11}$$

and,

$$E_{\max} = \frac{\left((\Delta q_i - \Delta q_o) + \left[\dfrac{E_\alpha - E_\beta}{2\{(\varepsilon_a)_\beta - (\varepsilon_a)_\alpha\}}\right] \times \left[(\varepsilon_a)_i - (\varepsilon_a)_o\right]^2\right)}{2\left[(\varepsilon_a)_i - (\varepsilon_a)_o\right]} \times 100 \tag{12}$$

where,

$$(\varepsilon_a)_\alpha = \frac{E_\beta}{E_\alpha} \times (\varepsilon_a)_\Delta, \; E_\beta = \beta E_{\varepsilon_a = 0.01\%}, \; E_\alpha = \alpha E^a_{\max}.$$

(2) $(\varepsilon_a)_{Y_S}$ ***: Secondary Yield Strain (Intermediate Strain Limit)***

The secondary yield strain which quantitatively defines the intermediate strain boundary is computed from (13).

$$(\varepsilon_a)_{Y_S} = (\varepsilon_a)_\gamma - \left[\frac{E_\alpha - E_\beta}{2(E_\beta - E_\alpha)}\right] \times \left[(\varepsilon_a)_\gamma - (\varepsilon_a)^{Y_S}_\beta\right] + (\varepsilon_a)_\beta - \left[\frac{E^a_{\max} - E_\alpha}{2(E_\alpha - E_\beta)}\right] \times \left[(\varepsilon_a)_\beta - (\varepsilon_a)_\alpha\right] \tag{13}$$

where, $(\varepsilon_a)^{Y_S}_\beta = \dfrac{E_\gamma}{E_\beta} \times (\varepsilon_a)_\beta$, $E_\gamma = \beta E_{\varepsilon_a = 0.1\%}$, $(\varepsilon_a)_\gamma = 0.1\%$.

(3) $(\varepsilon_a)_{Y_T}$ ***: Tertiary Yield Strain (Pre-failure Large Scale Plastic Strain Limit)***

This is the zone where large scale yielding occurs and may be quantified from the proposed (14).

$$(\varepsilon_a)_{Y_T} = (\varepsilon_a)_f - \left[\frac{E_\beta - E_\gamma}{2(E_\gamma - E_\delta)}\right] \times \left[(\varepsilon_a)_f - (\varepsilon_a)^{Y_T}_\gamma\right] + (\varepsilon_a)_\beta - \left[\frac{E^a_{\max} - E_\alpha}{2(E_\alpha - E_\beta)}\right] \times \left[(\varepsilon_a)_\beta - (\varepsilon_a)_\alpha\right]. \tag{14}$$

where, E_δ = modulus at $(\varepsilon_a)_f$ (strain at failure) and, $(\varepsilon_a)_{Y_T} = \dfrac{E_\delta}{E_\gamma} \times (\varepsilon_a)_\gamma$.

An example of the application of the proposed mathematical relations for determining the sub-yield strain limits is demonstrated in Figs. 2.5 and 2.6.

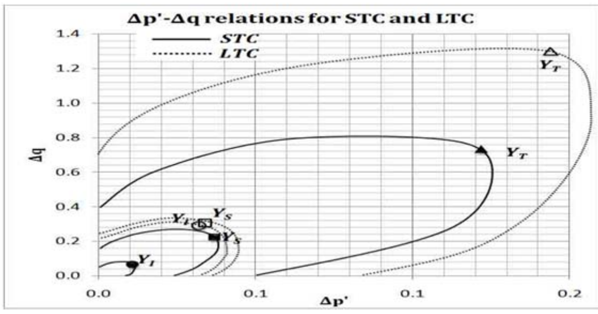

Figure 2.5 Yield surfaces traced from computed YS.

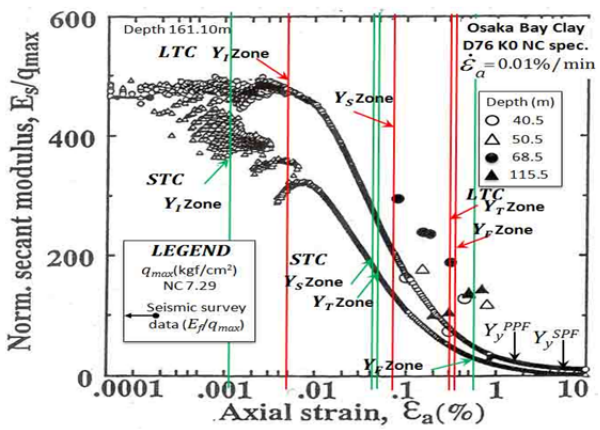

Figure 2.6 Zoned sub-yield surfaces $\{(\varepsilon_a)_{ELS}(Y_I)\} \sim \{(\varepsilon_a)_{FYS}(Y_F)\}$ based on computed LTC/STC Yield Strains.

The results of Long Term Consolidation (LTC) and Short Term Consolidation (STC) Osaka Bay clay specimens shown in Figs. 2.5 and 2.6 clearly demonstrate that: 1) multiple kinematic yield surfaces exist and, 2) the multiple pre-failure sub-yield surfaces expand in size with prolonged ageing (LTC).

3 CHARACTERIZATION OF VARIOUS ASPECTS OF PRE-FAILURE DEFORMATION

3.1 Preamble

Adequate assessment, evaluation and analyses of soil parameters to be adopted for design are crucial in enhancing the levels of precision of analyzing and characterizing the behavior of geotechnical structures.
Essentially, this implies that the choice and design of the experimental technique to be adopted for soil characterization is most vital since its effectiveness entails a compromise between technical and financial factors. The shortcomings however, of stress-strain models developed on the basis of laboratory test results of reconstituted specimens are significantly demonstrated in this Study. For example, [11] emphasized that realistic prediction of ground deformations and structural displacements are only possible when relatively sophisticated laboratory stress-strain tests using highly undisturbed samples and/or careful field tests are performed. This essential factor is also elaborated in this Study.
Adopting a sophisticated automated triaxial testing system with the capability of measuring axial strains of $\varepsilon_a < 10^{-5}$ and performing single tests on single specimens subjected to varying geotechnical conditions over a very wide range of strains $\{\varepsilon_a < 10^{-5}\%$ to $\varepsilon_a < 20\ \%\}$, the pre-failure deformation characteristics of relatively stiff structured clays are evaluated for purposes of determining and analyzing parameters for design, construction and prediction. Experimental simulation is comprehensively undertaken regarding the possible changes that may be impacted by varying modes and levels of loading on such geotechnical features as multiple kinematic yielding, effects of recent stress-strain-time history, anisotropy, structuration, destructuration, non-linearity in respect to the time-dependency of stress-strain behavior of clayey geomaterials and cyclic loading in both compression and extension for purposes of enhancing the sophistication of the retrospective analysis for modeling, simulation and prediction.

3.2 Influence of Consolidation Stress-strain Histories

Moderate to strong vibrations and ground motions may cause abrupt changes in the recent consolidation stress-strain-time history transforming it to a "new current state". It is therefore important to evaluate such changes in order to capture a more realistic picture of the field behavior for purposes of determining the relevant and most appropriate design parameters. Simulation of the impact of such changes is made in Figs. 3.1 ~ 3.3.
It can be noted from these figures that, although the initial deformation resistance defined in terms of Elastic Yield Strain $\{(\varepsilon_a)_{ELS}(Y_I)\}$ varies considerably with the consolidation stress ratio and secondary consolidation time history, the initial modulus is only dependant on the consolidation stress ratio, whilst secondary consolidation time history has virtually insignificant effects on this parameter. From Fig. 3.1, however, it can further be noted that, prior to the end of primary consolidation, the initial modulus varies considerably with consolidation time.

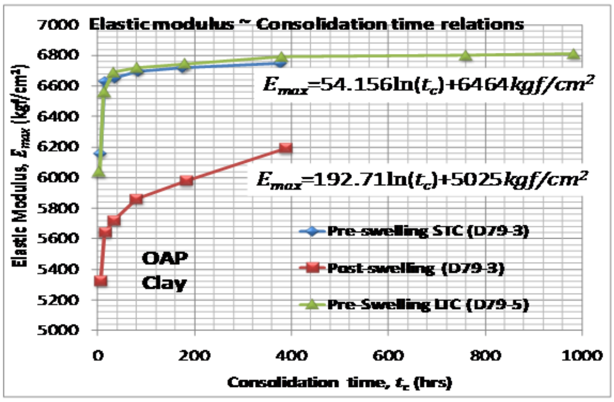

Figure 3.1 Effect of Long Term Consolidation on Initial modulus, E_{max} within the Elastic Limit Strain $\{(\varepsilon_a)_{ELS}(Y_I)\}$.

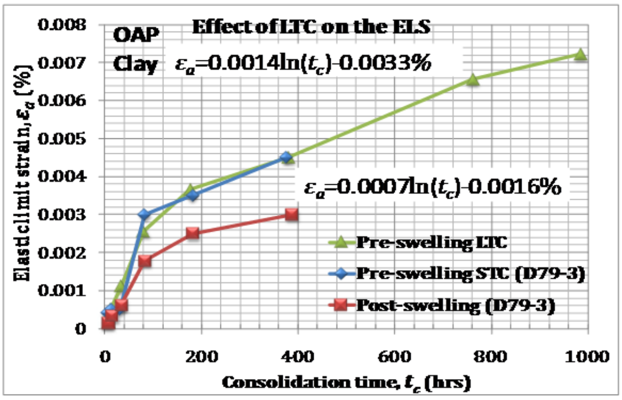

Figure 3.2 Effect of Long Term Consolidation on the Elastic Limit Strain $\{(\varepsilon_a)_{ELS}(Y_I)\}$.

Fig. 3.3, which simulates cyclic loading→ unloading→ reloading in short term and long term consolidation shows that: 1) the initial modulus decreases exponentially with increasing Over-Consolidation Ratio (OCR) and is practically insensitive to the hysteritic load ↔ unload ↔ reload cycles; 2) the initial modulus is virtually the same at constant OCR notwithstanding creep effects (secondary consolidation time); 3) long term secondary consolidation has practically no effect on the initial modulus. However, it was found to significantly increase the size of the initial yield surface $\{(\varepsilon_a)_{ELS}(Y_I)\}$ and; 4) loading ↔ unloading ↔ reloading cycles in consolidation have minimum impact on Y_I when compared at a constant OCR.
Equation (15), generated from this investigation, defines the generalized relation between the initial shear modulus, G_0 and the Over-consolidation Ratio (OCR) for relatively stiff to hard clays.

$$G_0 = \{(G_0)_{\sigma ss} / G_R \times OCR^{-0.39}\} \times (G_0)_{\sigma ss} \,. \tag{15}$$

where, $(G_0)_{\sigma ss}$ is the initial modulus at the designated stress point and $G_R = 290\ MPa$ is the reference initial shear modulus as determined in this Study.

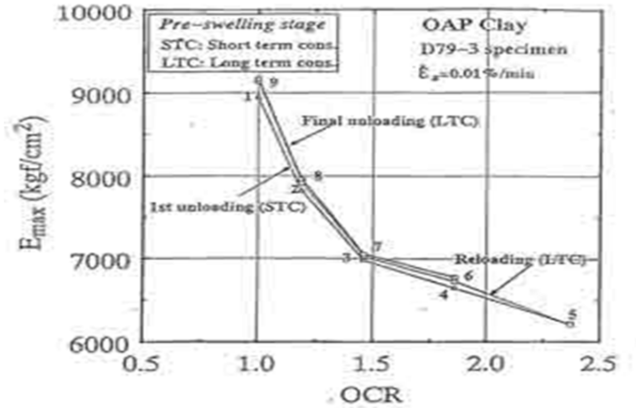

Figure 3.3 Effect of OCR and LTC on initial modulus.

3.3 Impact of Loading Rate on Small Strain Parameters

The effect of viscosity on small strain characteristics of various geomaterials has been a topic of study for a number of researchers. Although most results have shown that viscous effects may be minimal in the region of very small strains, whether or not they can be ignored has still been debatable.

In order to investigate the effects of strain rate on the small strain behavior of relatively stiff to very stiff undisturbed Pleistocene clay, CUTC tests were undertaken on Osaka Bay and OAP clays under quasi-static-monotonic loading with small load ↔ unload ↔ reload cycles within the range of $0 \leq \varepsilon_a \leq 0.005\%$ at different strain rates ($\dot{\varepsilon}_a$), part of the results of which are summarized in Fig. 3.4. CUTC/E and CDTC/E cyclic loading through seven varying strain rates $6.8 \times 10^{-5} \leq \dot{\varepsilon}_a \leq 0.34\%/\mathrm{min}$ for single amplitudes of $(\varepsilon_a)_{SA} = 5 \times 10^{-5}\%$ and $(\varepsilon_a)_{SA} = 5 \times 10^{-3}\%$ were also performed.

At every stress state and small strain shear stage, the creep rates were monitored during the secondary consolidation stage until they attained a minimal value of $\dot{\varepsilon}_a$ =0.0058%/day basically with the objective of ensuring that no interaction occurs between the creep rates and the slowest strain rate which was designated after preliminary investigations were carried out at a creep strain rate of $\dot{\varepsilon}_a$ =0.098%/day ($\dot{\varepsilon}_a$ =6.8×10^{-5}%/min).

It can be derived from the results in this figure that: 1) the characteristics per loading cycle are practically similar and independent of Strain Rate (SR) even when the slowest SR, $\dot{\varepsilon}_a = 6.8 \times 10^{-5}$ %/min and the fastest SR, $\dot{\varepsilon}_a = 3.4 \times 10^{-1}$ %/min (5,000 times faster) are compared; 2) dependency of the initial stiffness, E_{eq} becomes slightly more significant as the strain rate becomes much slower, whereas it is practically insensitive once the loading rate is in the range of $\dot{\varepsilon}_a$ >0.002%/min and, 3) through the comparison of drained and undrained initial stiffness, it can be noted that the difference becomes more significant $\{(E_{eq})_u$ - $(E_{eq})_\alpha\}$ as the strain rate becomes exceedingly slower, confirming the effects of time-dependent viscosity even in the region of very small strains and the existence of an Elastic Limiting Line (*ELL*) for slower rates of axial strain; 4) the effect of strain rate is clearly significant in the Y_S region $(\varepsilon_a)_{SA} = 5 \times 10^{-3}\%$, whereby the Y_S locus expands with increasing strain rate; 5) for $(\varepsilon_a)_{SA} = 5 \times 10^{-3}\%$, when the strain rate $\dot{\varepsilon}_a$ <0.03%/min, the damping ratio is seen to increase as the strain rate decreases, a characteristic which may be attributable to the creep effects associated with smaller equivalent Young's modulus at slower loading rates. Essentially therefore, it can be considered that even at very small strain rates, viscosity cannot be ignored and that, as suggested by [11], [12], an upper bound limit may exist for E_o or G_o values for extremely large strain rates, acting as an envelope for an *ELL* for the initial stress~strain relations in Y_I zone.

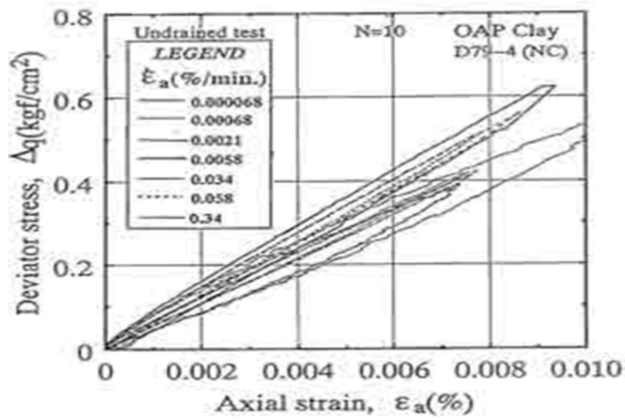

Figure 3.4 Summary of small strain cyclic behavior for a single amplitude $(\varepsilon_a)_{SA} \leq 5 \times 10^{-3}\%$ $\{(\varepsilon_a)_{SYS}(Y_S)\}$ for varying strain rates, 0.000068%/min ≤ $\dot{\varepsilon}_a$ ≤ 0.34%/min).

3.4 Geo-changes Due to Varying Stress States in Reconsolidation and Destructuration

In this section, the impact due to varying "current stress states" and that of destructuration on some of the natural well cemented and highly structured Pleistocene and Holocene clays found in Japan, is analyzed in consideration of the change in the geotechnical state and behavior in retrospect to, and as a result of, moderate to strong vibrational and/or seismic ground motion. In so doing, four causes of structural destruction namely; swelling, light densification through cyclic prestraining, heavy densification through SHANSEP reconsolidation and remolding through reconstitution, are considered. It is important to note that in Japan, undisturbed saturated Pleistocene clays usually exist deep in the ground, where the confining pressure is relatively large, making them highly sensitive to destructuration.

(1) Stress states for varying reconsolidation regimes

In order to investigate the influence of reconsolidation stress path and regime on the "current" stress states, specimens of OAP clay were reconsolidated to various stress states and axial stresses equivalent to the field overburden pressure (σ'_{a0}) tracing different stress paths.
Fig. 3.5 shows varying stress states at which the small strain deformation characteristics were investigated by performing small cyclic TC probing tests. Fig. 3.6 depicts the influence of current stress state-induced anisotropy on the normalized Elastic Limit Strain $\{(\varepsilon_a)_{ELS}(Y_I)\}$ for both normally and over- consolidated specimens.
The results in this Study showed that the initial shear and Young's modulus as well as the Y_I zone are stress state dependent notwithstanding the consolidation stress ratio, when compared at the same stress state and magnitude. Furthermore, the size of the initial yield surface Y_I exhibits interesting characteristics, whereby upon virgin loading at constant p' (stress points 1→2 →3), Y_I expands in size. However, once it is unloaded and offset (stress points 6→7→8) and reloaded at constant p' (stress points 8→9), Y_I is compressed, contracting in size. When compared to other results from the same Study which are not reported herein, consistent expansion of Y_I with K_c loading and K_o rebounding was observed. It is considered that, this tendency, perhaps as a result of the memory of the most recent history, seems to persist in K_o compression (stress points 9→11), only to recover through K_o rebound indicating that the initial yield surface is significantly influenced by the current stress state-induced anisotropy.

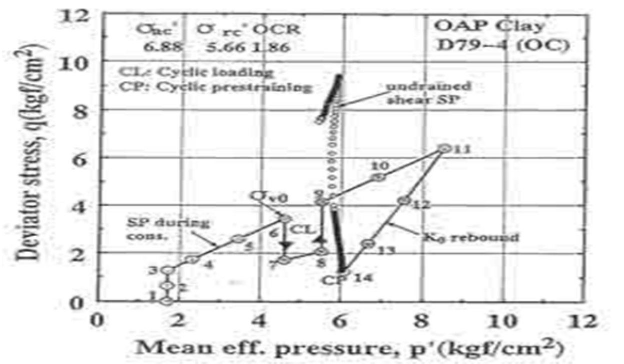

Figure 3.5 Stress paths during reconsolidation and, stress states at which small strain Cyclic Loading (CL) and Cyclic Prestraining (CP) were performed during drained and undrained shear.

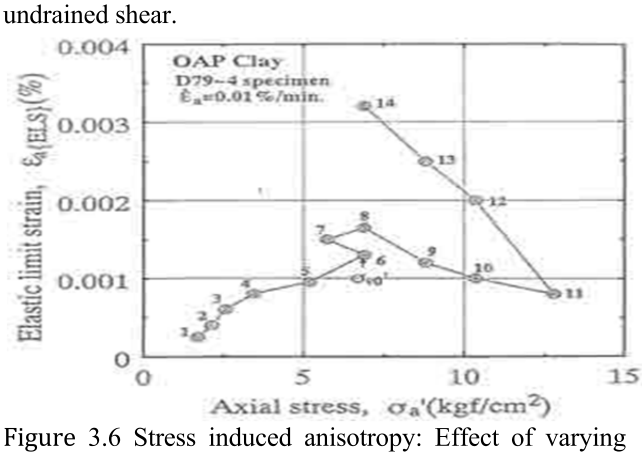

Figure 3.6 Stress induced anisotropy: Effect of varying "current stress" states on Elastic Limit Strain $\{(\varepsilon_a)_{ELS}(Y_I)\}$.

(2) Influence of destructuration due to swelling
Fig. 3.7(a) compares the reconsolidation and undrained shear stress paths for intact LTC, intact STC and LTC subjected to swell for OAP clay specimens. The three specimens were all reconsolidated through a similar stress path to the in-situ state of stress ($\sigma'_{a0} = 690$kPa) and equivalent OCR conditions (OCR=1.86). On the other hand, Fig. 3.7(b) shows the pre- and post- failure large strain characteristics of the same.
It can be noted from these figures that destruction through swelling affects the shear stress characteristics in the p'–q plane, impacts on the overall stress~strain behavior and causes significant reduction in the maximum shear strength notwithstanding the effects of relative ageing (secondary consolidated effected for 376Hrs.), as discussed in the preceding sections.

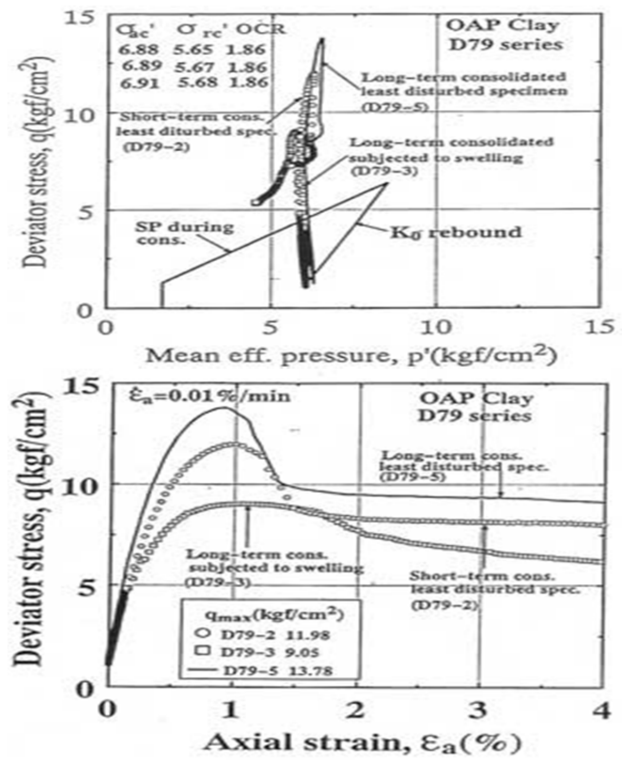

Figure 3.7 (a) Reconsolidation stress paths and, (b) Deviator stress-axial strain relations for $\varepsilon_a \leq 4\%$

On the other hand, the stress - strain characteristics in the Y_S zone for pre-swelling and post-swelling behavior are shown in Figs. 3.8 (a) and (b) respectively. It can be derived that swelling contracts the Y_T, Y_S and Y_I sub-yield surfaces and causes reduction in the initial modulus and deformation resistance. It can therefore be concluded, by inference that, swelling causes damage to the inherent structural components such as bonding, particle matrix, water cation, thixotropic and creep related cementation, particle agglomeration and orientation, among other intrinsic geo-properties. Comparison of Figs. 3.8 (a) and (b) indicates that restructuration was not achievable through ageing for a period of 376Hrs. of secondary consolidation.
Nevertheless, it can be observed that there is a tendency of structural recovery with ageing. Such recovery, as determined from the GECPRO model, would require a

secondary consolidation period of at least 9,897hrs (412days) to achieve maximum stiffness and 32,859hrs (1369days) to recover the original size of the initial yield surface aged at constant consolidation stress state conditions of $(\sigma'_{a0} = 690\text{kPa})$ and *OCR*=1.86. Whether the structural components can be fully recoverable is a matter that certainly requires further comprehensive research.

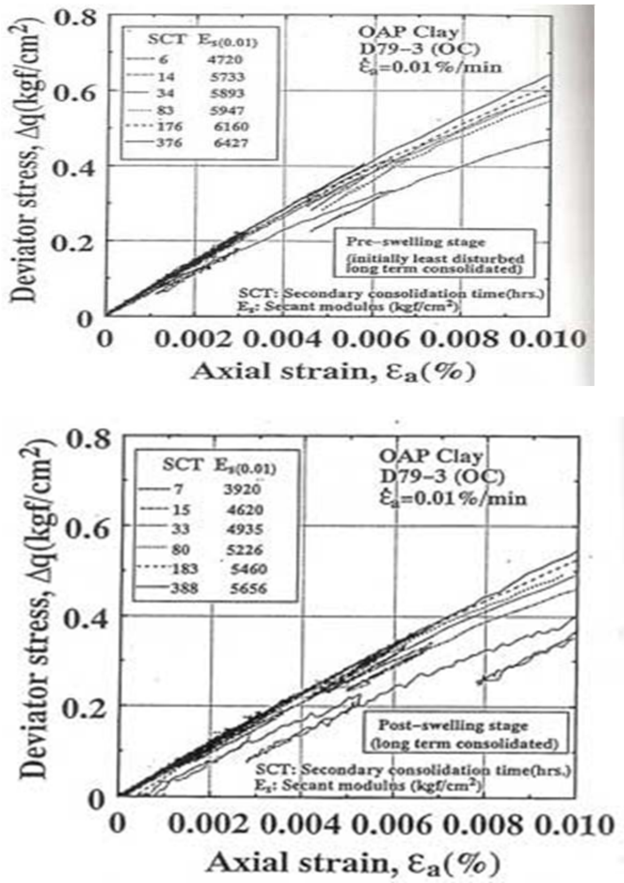

Figure 3.8 Effect of LTC on the small strain $\{(\varepsilon_a)_{SYS}(Y_S)\}$ behavior $(\varepsilon_a \leq 0.01\%)$ for: (a) pre-swelling and, (b) post-swelling conditions.

(3) Structural damage caused by over-densification

The SHANSEP reconsolidation procedure was applied on two specimens, TS3-2 and TS3-3; whose characteristics were compared with those of a Normally Consolidated Intact (NCI) Specimen T-9-3 of the Ariake clay as shown in Fig. 3.9 (a).

The small stress-strain results are shown in Fig. 3.9 (b). It can be noted that, as a result of structural destruction: 1) the SHANSEP specimen exhibits excessive deformation; 2) the peak shear stress ratio of the SHANSEP specimens is much lower, i.e., $[(q/p'_e)_{OCR=4} = 0.328] < [(q/p'_e)_{OCR=2} = 0.456 < [(q/p'_e)_{OCR=1} = 0.689]$.

As a result of different structure formation and/or degree of destruction, the following derivations can be made from these figures; 1) all three specimens exhibit very different stress-strain characteristics at all levels of strain and multiple kinematic sub-yield surfaces; 2) the influence of the different stress-strain-time histories experienced during reconsolidation can be clearly observed; 3) the magnitude of deformation resistance decreases significantly with increasing degree of SHANSEP.

It can therefore be concluded that reconsolidation to a higher stress level exceeding the yield stress level $(\sigma'_a)_y$ destroyed the inherent structure of the natural, sensitive and highly structured Holocene Ariake clay.

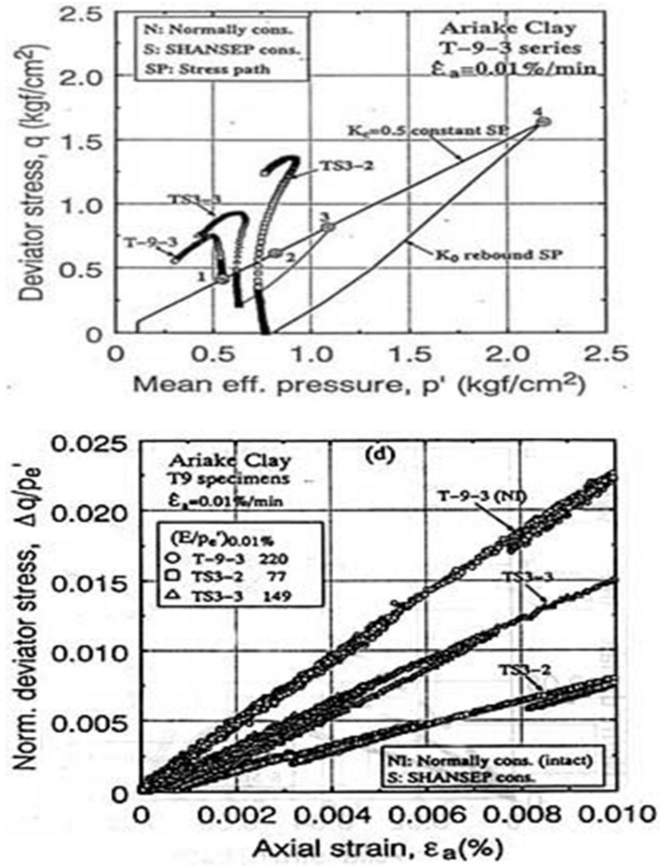

Figure 3.9 (a) SHANSEP reconsolidation effective stress paths, and (b) Normalized small stress-strain $\{(\varepsilon_a)_{SYS}(Y_S)\}$ behavior $(\varepsilon_a \leq 0.01\%)$.

(4) Destruction caused by reconstitution

An experimental regime was designed to study the behavior of reconstituted Pleistocene clay that was, in its' initial state, naturally well cemented and highly structured stiff overconsolidated OAP clay. The results comparing stress – strain behavior and the strain level dependency of the stiffness of the intact and reconstituted specimens are shown in Figs.3.10 and 3.11 respectively.

A number of derivations can be made from the results in this Study including: 1) it was observed that the specimens trace different shear stress paths right from the small strain region throughout to failure and post-failure; 2) the yielding characteristics are quite different between the two specimens; 3) the stress path of the reconstituted specimen transcends to a critical state at a stress ratio $\{\{\mu_R = 1.319, \text{where } \mu = (q/p')_{CS}\}$, which is well below that located by the intact specimen $(\mu_R = 1.636)$ and, 4) reconstitution caused a large drop in the inherent suction stresses, shear strength and stiffness. These observations imply that factors other than the decrease in void ratio such as the breakage of the bonds between particles are the attributes; $\{e_I = 1.49$, while $e_R = 1.371\}$.

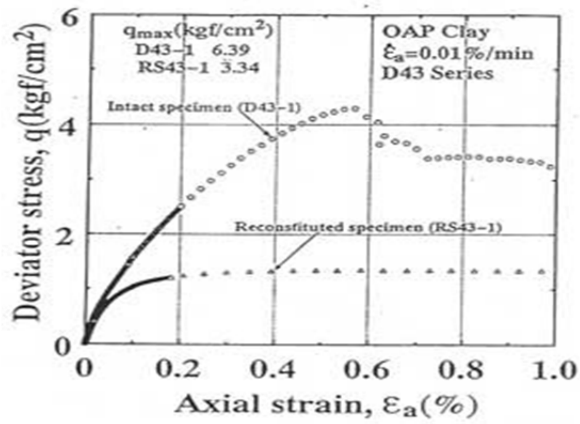

Figure 3.10 Overall stress-strain relations for intact and reconstituted specimens $\{(\varepsilon_a)_{T,FYS}(Y_{T,F})\ (\varepsilon_a \leq 1\%)\}$

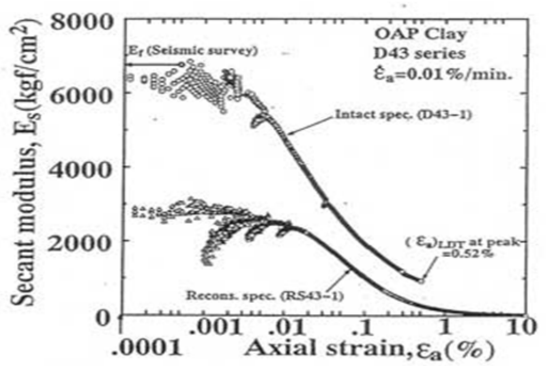

Figure 3.11 Strain level dependant decay curves for intact and reconstituted specimens, $\{(\varepsilon_a)_{ELS}(Y_I)\} \sim \{(\varepsilon_a)_{FYS}(Y_F)\}$.

A comparison of the undrained shear characteristics between the intact and reconstituted specimens shows that the destructuration during reconstitution caused: 1) a drastic drop in the peak strength $\{(q_{max})_I = 639$kPa and $(q_{max})_R = 334$kPa, while normalization accounting for voids ratio effects results in $[(q/p'_e)_{max}]_I = 0.319$ and $[(q/p'_e)_{max}]_R = 0.107]$; 2) conspicuous strain softening (post-failure brittle behavior) for the intact specimen compared to the ductile behavior of the reconstituted one; 3) the stress-strain behavior in the intermediate strain levels is significantly different; 4) the intact specimen exhibits less non-linear response; 5) the maximum stiffness of the reconstituted specimen, $[E_{max}]_R$ = 287MPa is much lower than that of the intact one, $[E_{max}]_I$ = 634MPa; 6) the intact specimen exhibits better recoverable behavior in the region of very small strains and, 7) the intact specimen exhibits a much higher level of deformation resistance.

In general, these results confirm that, whilst the intact specimens sustained most of their structural components from the region of very small strains throughout the pre-failure zone up to the post-failure plastic yielding zone, the reconstituted ones seem to have attained a totally different "structure" having completely lost the inherent and intrinsic structures.

4. CHARACTERIZATION OF BLACK COTTON SOIL SUBJECTED TO TRAFFIC TYPE VIBRATORY LOADING

Traffic induced subsurface stress can be characterized by dynamic cyclic loading impacting numerous cycles and continuous rotation of stress axes that cause subsidence and progressive distortion as well as deformation once the stresses and strains overshoot the initial yield subsurface. While investigating the contraction of soil subjected to traffic-type stress application by applying strip loading idealization of a moving train, [15] concluded that cyclic stress induced by travelling strip loading generates a ground subsidence that is twice as large as that observed from cyclic triaxial compression tests i.e. $(\Delta\varepsilon)_{TL}=2(\Delta\varepsilon)_{CT}$. They attributed the anomaly to stress axis rotation.

In this Study, twelve full-scale field experimental testing sections were designed and constructed with six varying pavement layers and structural configurations founded on Black Cotton Soil (BCS), and subjected to different modes and cycles of static and dynamic loading [16]. The sub-base and base course layers, constituent of lateritic soils, were stabilized by applying the OBRM (Optimum Batching Ratio Method) and the OPMCS (Optimum Mechanical and Chemical Stabilization) technologies respectively [17]. In analyzing their effect on the BCS subgrade and upper layers, the equipment was considered to be essentially symmetrical about a longitudinal axis and the wheel loads were summed up to give axle loads which were adopted as nominal values in the computation and analysis of their static impact on the layers of construction. The dynamic component however, was simulated as moving constant wheel loads whose transfer mechanisms occur very slowly relative to the frequencies involved in the vertical dynamics of the equipment. In carrying out these analyses, the mid elements of each layer are adopted in relation to the applied stresses. Fig. 3.12 depicts deformation characteristics simulating deterioration in deformation resistance due to the effect of dynamic vibratory loading on stabilized and non-stabilized BCS subgrades.

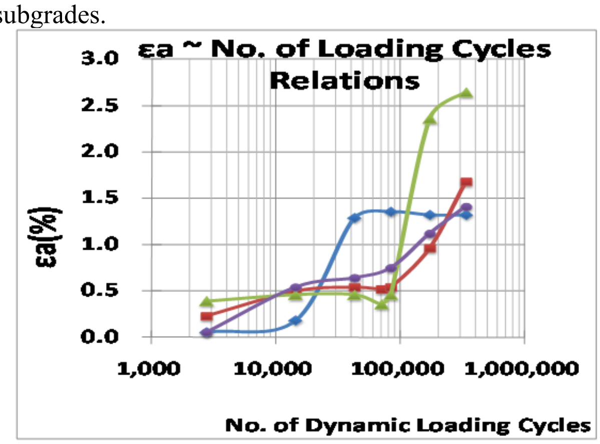

Figure 3.12 Deformation resistance depicted in terms of strain vs. dynamic loading cycles (converted axles) tested on specimens after 7 days cure of Western Kenya Black Cotton Soil

From Fig. 3.12, it can be derived that: 1) after 100,000 converted axles, the deformation of the non-stabilized BCS specimens increases drastically (it collapsed after 336,000 cycles); 2) prolonged curing increases deformation resistance of stabilized BCS immensely, 3) the magnitude of plastic straining is largely reduced by stabilizing BCS, and by subjecting it to controlled dynamic loading within the initial yield surface $\{(\varepsilon_a)_{ELS}(Y_I)\}$ whilst applying very small amplitude pre-straining [16].

Comparison of the stress - strain characteristics of BCS and the Japanese Kanto Loam is made in Fig. 3.13. The specimens were initially subjected to dynamic loading and subsequently loaded under static conditions up to failure. It can be observed that, notwithstanding the magnitude, both BCS and Japanese Kanto Loam exhibit a significant increase in strength with increased initial dynamic pre-straining at very small strain amplitudes.

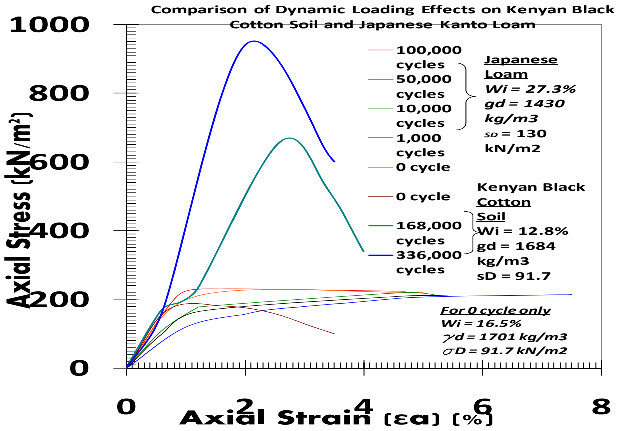

Figure 3.13 Deformation behavior in the post-linear elastic zone $\{(\varepsilon_a)_{ELS}(Y_I)\}$ and depiction of cyclic pre-straining effects on the characteristics of Western Kenya Black Cotton Soil and Japanese Kanto loam.

5. CONCLUSIONS

Overall, the following conclusions are derived from the study reported in this paper.

1) The conventional Critical State Theory is inadequate in effectively modeling the behavior of well cemented and highly structured natural clays.
2) The MCST introduced in this Study may be useful as a basis for further research, retrospective analysis, simulation, prediction and performance based design.
3) Practically all the results in this study show that, although the properties in the region of linear elasticity are virtually insensitive to the effects of consolidation stress-strain-time histories, and loading rate, they are highly susceptible in the subsequent sub-yield surfaces in the region of small to moderate strains.
4) The magnitude of the initial modulus and size of sub-yield surfaces are "current" stress state dependent.
5) Remolding (reconstitution) completely destroys the intrinsic structure of structured clays. Theories and concepts based on tests performed on reconstituted clay specimens cannot therefore model the behavior of natural clays.

6. ACKNOWLEDGMENT

The author is highly indebted to Prof. Fumio Tatsuoka formerly of the University of Tokyo under whose guidance this research was initiated. Special appreciation is extended to the Japan International Cooperation Agency (JICA), Taisei Corporation, Japan, and Kajima Corporation, Japan, for sponsoring most of this research as well as the Materials Testing & Research Department of the Ministry of Roads, Kenya and members of the Kenya Geotechnical Society Research Team for their support.

7. REFERENCES

[1] Mukabi JN, "Derived empirical relations and models of vital geotechnical engineering parameters based on geophysical and mechanical methods of testing", in Proc. 15th African Regional Conf. on SMGE, Maputo, 2011, pp. 320-329.

[2] Mukabi JN, "Deformation characteristics at small strains of clays in triaxial tests", PhD Thesis, Institute of Industrial Science, University of Tokyo, 1995.

[3] Mukabi JN, "Innovative laboratory and in-situ methods of testing in geotechnical engineering, to be published in the Proc. of the Int. Conf. of the Inst. of Engineers Kenya , Nairobi, 2013.

[4] Mukabi JN, Tatsuoka F, "Effects of consolidation stress ratio and strain rate on the peak stress ratio of Kaolin," the 27th Annual meeting of the JSSMFE, Kochi, 1992, pp. 655-656.

[5] Mukabi JN, Tatsuoka F, "Influence of reconsolidation stress history and strain rate on the behaviour of kaolin over a wide range of strain," Proc. 12th ARC on ISSMGE: Geotechnics for Developing Africa, Durban, 1999, pp. 365-377.

[6] Mukabi JN, Tatsuoka F, "Effects of stress path and ageing in reconsolidation on deformation characteristics of stiff natural clays", Proc. 2nd I.S Pre-failure characteristics of geomaterials, Torino, 1999, vol. 1, pp. 131-140.

[7] Mukabi JN, Kotheki S, Mathematical derivative of the modified Critical State Theory and its application in Soil Mechanics. Procs. 2nd International Conf. on Applied Physics & Mathematics, 2010 IACSIT, Kuala Lumpur, pp. 484-492.

[8] Murakami S, Hayashi S, Ochiai H, Umezaki T, "A stress parameter for the behavior of clay under cyclic loading", Proc. 1st Int. Symp. on Pre-failure Deformation of Geomaterials, Sapporo, 1994, pp. 477-482.

[9] Yeoh CK, Airey D, "Undrained cyclic loading of a cemented sand", Proc. 1st Int. Symp. on Pre-failure Deformation of Geomaterials, Sapporo, 1994, pp. 95-100.

[10] Mukabi JN, "Application of Consolidation and Shear Stress Ratio (CSSR) concepts in foundation design and construction" Proc. 14th ARC on SMGE Vol. II, Yaoundé, 2007, pp.172-193.

[11] Tatsuoka F, Jardine RJ, Presti DL, Benedetto HD, Kodaka T, "Characterizing the pre-failure deformation of geomaterials". XIV IC on SMFE, Theme Lecture, Hamburg, 1999, pp. 2129-2164.

[12] Mukabi JN, "Behavior of clays for a wide range of strain in triaxial compression". Msc. Thesis, IIS, Uni. of Tokyo, 1991.

[13] Sica S., de Magistris F.S., Vinale F, "Seismic behaviour of geotechnical structures", Annals of Geophysics, 2002, Vol. 45, N. 6, pp. 799-815.

[14] Tatsuoka F, Shibuya S, "Deformation characteristics of soils and rocks from field and laboratory test", Keynote Lecture, 9th Asian Regional Conference on SMFE, 1992, Vol. II, pp.101-170.

[15] Towhata I, Kawasaki, Y, "Contraction of soil subjected to traffic-type stress application", Proc. 1st Int. Symp. on Pre-failure Deformation of Geomaterials, Sapporo, 1994, pp. 305-310.

[16] Mukabi JN, Kotheki S, Ngigi A, Gono K, Njoroge BN, Murunga PA, Sidai V, "Characterization of black cotton soil under static and dynamic loading", Proc. Int. Conf. on GE, 2010, Tunis, pp. 67-81.

[17] Kogi SK, Mukabi JN, Ndeda M, Wekesa S, "Analysis of enhanced strength and deformation resistance of some tropical geomaterials through application of in-situ based Stabilization techniques", to be published, Proc. 1st Int. Conf. on GEOMAT, Mie, 2011.

First International Conference on Geotechnique, Construction Materials and Environment, Mie, Japan, Nov.21-23, 2011, ISBN: 978-4-9905958-0-7 C3051

The Maintenance of Ground Anchors in Nippon Expressway

Yuu FUJIWARA,Nippon Expressway Research Institute Company Limited
Toshinori SAKAI, Mie University

ABSTRACT: On expressway in Japan since around 1970, the ground anchor (the anchor) has been adopted. Since then, construction has been increasing in the mountainous road, which increases the slope of the cut earth stabilization measures for Industry and Labour landslide measures. This has increased the amount of construction of anchor every year. And that number is now more than 120,000 books. Anchor performs maintenance on a regular basis, you need to make sure it is functioning properly. In particular, make sure to keep tension force is introduced to the anchor is important. How to determine the tension force is twofold. One is how to measure and install a load meter anchor. Second, there is a Lift-off test tensile load is applied directly to the anchor. During shared lift often tested. But, however, Lift-off test, no uniform standards have been done differently at each site. There is also a problem that takes time to conduct the test. Therefore, efforts to improve the efficiency of test methods and testing concrete.

Keywords: groundanchor,Lift-off test,expressway,soil

Fig.1 Groundanchor

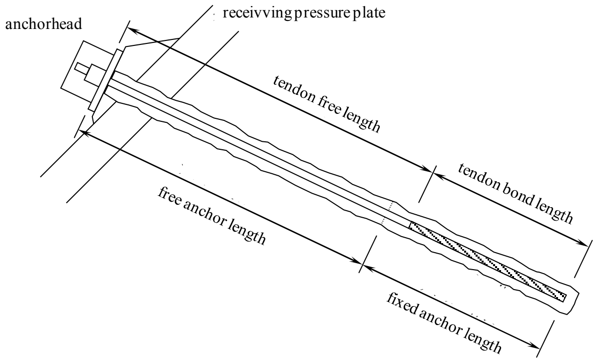

Fig.2 Groundanchor's structure

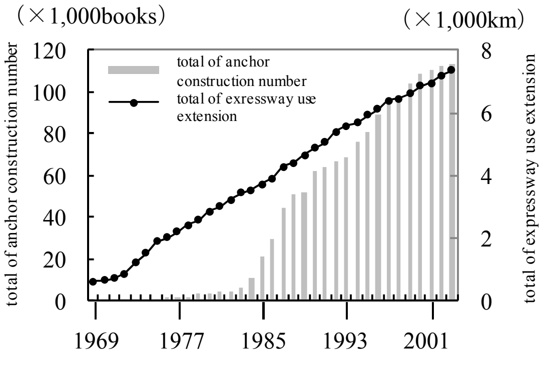

Fig.3 Anchor'construction situation in expressway

1. INTRODUCTION

Ground anchors (hereinafter referred to as anchors) are a countermeasure of stabilizing against the landslide and cut slope(Fig.1).

Anchors are composed of anchorhead and piston plate exposed on the surface, and tension member and anchorbody built in the ground(Fig.2). Construction of the anchor, the anchor reclamation to ground the body is done in a way that fixing the head was anchored in a state of tension force to the tension, this tension is exerted on the pull. In the mid-1960s the highway was first adopted by ground anchors. Thereafter, the annual increase with an increase in the amount of construction of road construction in mountainous regions, which now number more than 120,000 books(Fig.3).

The construction of the initial anchor, the water and air infiltration due to insufficient corrosion features on the perimeter of the body pulling the anchor and the anchor head or anchor, and a structure susceptible to progressive degradation of the material tensile other. In late 1975, now seen as symptoms of lifting the anchor and jump out, JH Old for This (NEXCO present), the regular aspects of construction law has been anchored since around 1985 have been working on making the inspection and maintenance.

Society in 1988, the old soil (JGS current) standards have been revised, the anchor started to be adopted and improved corrosion protection capabilities. Has been applied to the local design guidelines based on the criteria established in 1992 in this former JH. Thereafter, the implementation of emergency measures and the anchor steel bar, in order to improve assessment accuracy and efficient execution of survey work and health inspections anchor, hammering due to periodic inspection and detailed visual inspection due to daily inspections and and to confirm that status. In this paper, we describe the contents of the initiatives on the anchor in the maintenance of highways.

2. MAINTEANCE OF THE ANCHOR

Inspection of the anchor in the highway, depending on its purpose inspection items, inspection methods, inspection frequencies have been established(Table 1).

Daily inspection, for example, corrosion of materials Status

Table 1 Anchor's check type

check type	content
Initial check	Check that is evaluated and judged by measuring adjacent watching, slapping sound, and load to see how matters stand in the early after structure is completed, and to understand progress condition of the following damage adequately before it begins to use it.
Daily checkup	It checks by adjacent watching or.hope. watching getting off if necessary to find damage of the anchor placing region of the management district whole etc. at the early stage based on watching on the car. The fourth/two weeks. It does at the frequency of the seventh/two weeks.
Regular service	Check done to understand situation of chiefly individual anchor of anchor installation slope based on adjacent watching on foot. It does at the frequency once/year.
Detailed check	Check done to execute adjacent watching, slapping sound, and other concrete checks 〈 measurement and load measurement 〉 of anchor installation slope on foot, and to understand situation of chiefly individual anchor. Frequency.do.
Temporary check	Check done if necessary in supplementation and abnormal weather etc. of daily checkup.
Soundness investigation	Investigation that observes, checks head established body in detail in the one done when damage of strangeness etc. are confirmed in anchor installation slope, and full investigation is needed, and measures load in addition.

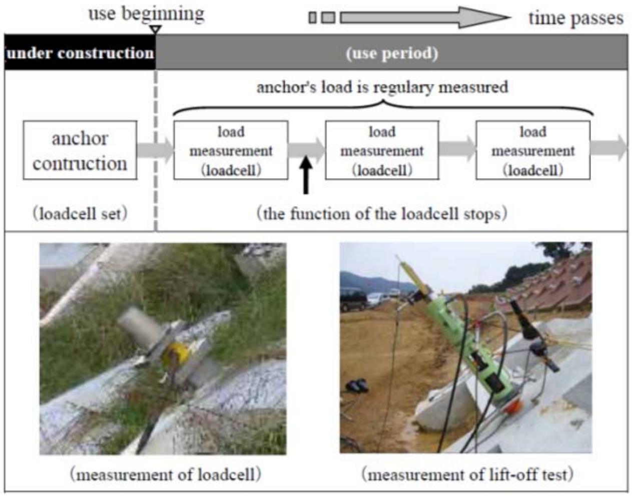

Fig.4 Anchor load management

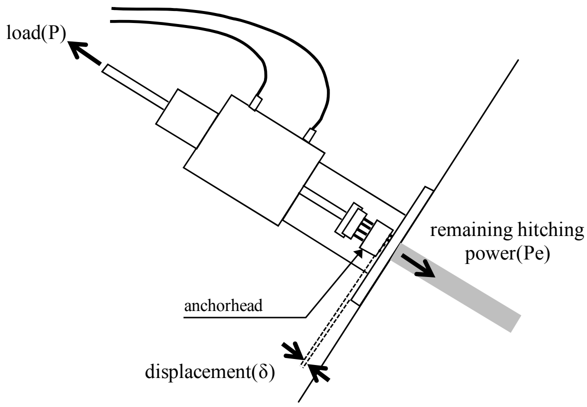

Fig.5 Lift-off test

tension anchor fixing and visual equipment, lifting and peeling to confirm the availability of protective concrete by hammering. If you notice unusual changes in the shape of the various inspection results, a survey to examine the health of the anchor. The study is detailed observation of the body fixing Verification head to remove the protection work of the anchor head, measure the residual tensile force necessary to evaluate the soundness of the anchor.

2.1 Residual tensile strength of anchor Management

Upon maintaining the anchor, the tension continued to investigate the residual, that is important to continue to take appropriate action. The anchor introduced the ability to settle when the initial tension, tensions may weakened slightly cut into the material loss due to set tension on the anchor head. Each method considered in this loss of the anchor set, the introduction of the initial tension force so that force is slightly lower than allowable tension force when fixing anchors. When fixing the anchor, the residual tensile strength of the anchor tends to decrease due to soil creep and relaxation of tension wood, and will gradually converge to a constant value.

Anchor for the highway, Figure 4 shows the flow of the general management of the residual tensile strength. In the construction phase, the ground Instability is a concern because of the slope by excavating to install a load meter for some of the anchor, we will proceed to construction, making sure to close the residual tensile strength. In-service for the anchor, the load management is done on a regular basis in a way to measure the residual tension load cell was installed at construction. And the total comes to be degraded over time due to load, however, usually is very difficult load meter replacement, etc., will anchor the remaining tension in the Lift-off test conducted to measure.

2.2 Lift-off test

Lift-off test, a hydraulic jack installed on the head portion of the extra length of the anchor tension member is performed by loading a tensile load. Figure 5 shows the status of the Lift-off test in fixing wedge type anchors. Fixing wedge Lift-off test of the type anchor, the anchor head portion of the extra length, pooling the head provisional established to secure the tension bar and the extra length portion is performed by loading a tensile load to the tension bar. In the process of loading, the residual tension when the anchor isconfirmed, the unloading of the load carried into the wild. Figure 6 shows the state of the anchor head in the process of loading unloading Lift-off test. In addition, a general load is drawn at the time - the shape of the curve in Figure 7 shows the displacement. In the process of loading the Lift-off testThe stage, before starting off the head anchor plate,

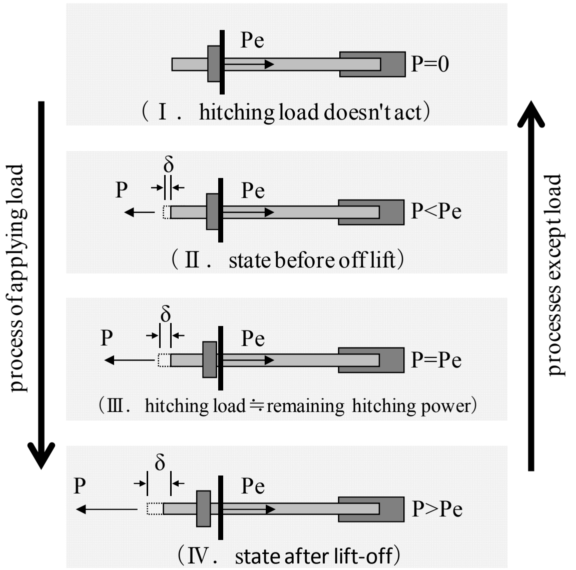

（P ： load of hydraulic lifter, Pe ： remaining hitching power）
Fig.6 When the tension load is put and when it excludes it

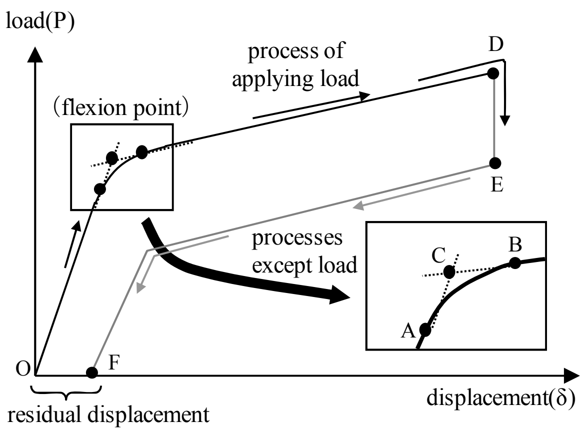

Fig.7 by Lift-off test load - displacement curve

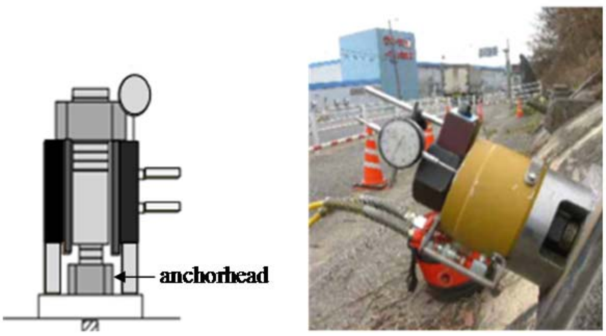

Fig.8 SAAM jack

anchor head displacement is small, the load - displacement curve shows a linear gradient of steep slope (Fig. 5; Ⅱ, -6 figure; O → A). Increase the tensile load of hydraulic jacks even begin to anchor the head away from the plate immediately after the load was equal to the residual tension

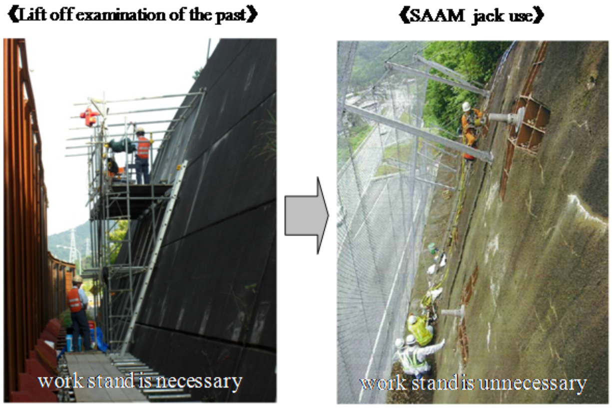

Fig.9 Comparison with examination in the past

Table 2 Result of lift off examination using SAAM jack

slope No	test day	slope Inclination	Number of examinati	Remarks
No.10	2008/12/2	1:0.5	6	
	2008/12/3	1:0.5	9	
	2008/12/4	1:0.5	12	
	2008/12/5	1:0.5	1	
No.11	2008/12/5	—	1	
No.12	2008/10/27	1:1.2	1	※Most of the preparation
	2008/10/28	1:1.2	8	
	2008/10/29	1:1.2	15	
No.13	2008/10/30	1:0.5	5	
	2008/10/31	1:0.5	5	
	2008/11/4	1:0.5	6	
	2008/11/5	1:0.5	5	
	2008/11/6	1:0.5	7	
No.14	2008/7/30	1:0.8	5	
	2008/7/31	1:0.8	6	
	2008/8/1	1:0.8	4	
No.15	2008/8/20	1:1.0	17	
	2008/8/21	1:1.0	**24**	**※maximum number**
		total	137	
slope Inclination (1 : 0.5～1 : 0.8)		total	71	
		average	5.9	
slope Inclination (1 : 1.0～1 : 1.2)		total	65	※2008/10/27 is excluded
		average	16.3	

loading (Fig. 5; Ⅲ, -6 Figure; point A). This phenomenon is generally called "lift" is called a load - a measurement of the load-displacement curve at the time the lift-off "the lift" and it is. And further increase the tensile load was lifted off and then begin to gradually change in the slope of the linear gradient between OA (-5 figure; Ⅳ, -6 figure; A → B). Once that change is constant, the tensile load transmitted to the anchor free length portion, the load - displacement curve shows a gradual linear slope depends on the tensile modulus of the material (Fig. 5; Ⅳ, -6 Figure; B → D). Residual tensile strength of the anchor, JGS criterion 5), according to the head started away from the anchor plate (0.1 ~ 1.0mm) has been measured at the load. After the loading of the tensile force necessary to evaluate the residual tensile strength of anchor loading to unloading the load (Figure 6; D → E → F). In addition, after completing one cycle of loading unloading, the residual displacement is the difference between before and after loading displacement (Figure 6; OF) may occur. Residual tensile strength, if reduced to less than 90% of time fixing force or tension increased over 120% of the anchor design strength, may not be anchors healthy functioning.

3. Efforts to improve the maintenance of anchor

Lift-off test, set a foothold in the cut earth surface For the implementation method Only in some cases you need to do a test using a large crane. Because of the limited test volume and number of test cases will require significant cost and time. SAAM has been developed in the laboratory jack Mie Sakai (Fig. 8), may be to generate a large tensile strength lightweight and compact construction. Therefore, since it eliminates the need for such a temporary scaffolding was required that the conventional test, it is possible to quickly investigate a number of anchors (Figure 9). The condition can be performed more than 20 per day, it is possible to dramatically extend the enforcement decree of the day. SAAM test is carried out by the jack lift anchor and head for the slope of the study six of No.1 ~ No.6, examined the distribution of residual tension strength of the anchor (Table 2).

About 137 tests were carried out this anchor lift / day on average for six of the slope gradient is 1:0.5 to 1:0.8, were able to present an average of 16 in 1:1.0 to 1:1.2. For the implementation of good work at the point where the slope gradient is testing many loose number of tests per day, could be carried out up to 24. Construction is considered a significant capacity Given that this was about 2-3 per day of conventional test methods.

Currently, NEXCO, they can be applied in the field trials utilizing the SAAM lift jack, which repeated studies.

4.CONCLUSION

Anchor conducted after the construction and maintenance, it is important that you make sure it is functioning properly. However, the situation has not been adequate maintenance of effort it takes to be a huge amount of maintenance and construction.

Future, by further analysis of the data accumulated in NEXCO, efforts shall be made to establish the technique more efficient and effective maintenance.

5. REFERENCES

[1] JGS, ground anchor design and construction standards, the same commentary, 2000

First International Conference on Geotechnique, Construction Materials and Environment, Mie, Japan, Nov.21-23, 2011, ISBN: 978-4-9905958-0-7 C3051

Stress Distribution in Khon Kaen Loess under Spread Footing

Pairoj Yodsa-nga and Watcharin Gasaluck Department of Civil Engineering, Faculty of Engineering, Khon Kaen University, Thailand.

ABSTRACT: Loess is the non-plastic fine grain soils distributed in Northeast Thailand. The stress distribution in loess due to surcharge load was studied. Plate bearing test was carried out at 3-m depth in loess. Five small total pressure cells were installed for getting the stress increment in soils during the test. The test results were compared to the results calculated by 3 mathematical models. Boussinesq's method and finite element method gave the outputs those were not agreed with the test because linear stress-strain behavior was utilized. Walter's method provided the better output. This method does not accept the solid mechanic assumption but non-linear stress-strain behavior was employed. Both the test and Walter's method show the change of influence factor along with the change of load. Finite element method may give the reasonable output if the appropriate model condition is specified. The contact pressure pattern should be considered as well. All mathematical models used the uniform pressure pattern that some researchers did not agree with. The actual pattern should be studied and used in the mathematical models. The better result might be obtained.

Keywords: Loess, Stress Distribution, Boussinesq's method, Walter's method, finite element method

1. INTRODUCTION

Stress distribution in soils is very important in foundation works. Not only the design but also the analysis of foundation settlement needs this information, especially the stress distributions of spread footing group that the overlap of pressure bulb may cause the failure.

The classical Boussinesq's method invented in 1883 is usually used for estimating stress distribution in soils mass due to surcharge load[1]. It is the mathematical model that the soil is assumed to be semi-infinite solid and its strength parameters are not taken in to account. In other words the model assumption is doubted that soil type has no effect on stress distribution behavior. Contact pressure between rigid footing and soils was assumed to be constant. Hansbo [2] made the conclusion of the contact pressure in clay, silt and sand studied by some researchers, only the rigid footing on ground surface gave the contact pressure that agreed with Boussinesq's method.

Walter [3] developed the mathematical model for estimating stress distribution in soil mass. Compression and shear modulus of elasticity were the important parameters in the model. Furthermore, the relationship between compression and shear modulus of elasticity was different from solid mechanic theory. The output reasonably shows the effect of soil characteristics on stress distribution behavior.

Finite element method is becoming popular along with the fast development of computer. It is the powerful device that could be used for any complicated soil model. The problem of finite element method is its difficulty, and then commercial program is necessary. Difficulty and price of the program obstruct engineers to use it.

The research presented in this paper was done to compare the stress distribution in Khon Kaen loess due to the load acted on 0.3x0.3 m steel plate with the outputs obtained from classical mathematical models and PLAXIS 3-D, the computer program based on finite element method.

2. SITE CHARACTERISTIC

Northeast Thailand comprises an area of about 168,800 square kilometers or about one-third of the total area of the country. Some soils in Northeast Thailand are silty sand, clayey sand, sandy silt, clayey silt, sandy clay and silty clay of the Quaternary age, with an overlying bedrock of sandstone and shale of Mesozoic age [4].

Khon Kaen Province is located in Northeast Thailand. The loess deposits exist above the water table in abundance in Khon Kaen. The thickness normally ranges from a few to more than six meters. Fig. 1 is the distribution of loess in Northeast Thailand. The loess characteristic is non-plastic red sandy silt or silty sand (ML or SM). Most of the soil particles are 0.005 to 0.042 millimeter in size. Soil grains have a smooth and sub-rounded surface. The microstructure is unconsolidated and loose to medium dense. The pore sizes are usually 200-500 micrometers although some can be as large as 1 millimeter. Small clay content is presented in the form of clay bridge bonds [5]. Undisturbed Khon Kaen loess's photograph taken by Scanning Electron Microscope is shown in Fig.2. Under the 90 percent standard Proctor test condition, it is classified as slightly to moderately dispersive, ND3 [6].

Fig. 1 Distribution of loess in Northeast Thailand.

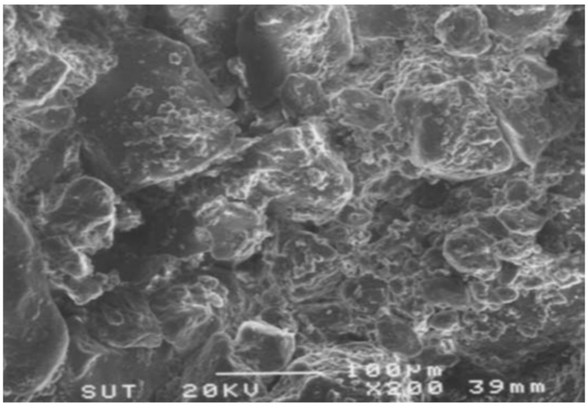

Fig. 2 Undisturbed loess.

3. METHODOLOGY

3.1 Field and Laboratory Tests

Plate bearing test was done at the 3 m depth in Khon Kaen loess. The plate size was 0.3x0.3 m, the thickness was 2.5 cm. Load was applied to the plate by the hydraulic jack acting against dead load. Five 3-cm holes were bored, earth pressure cells were placed at the bottom. The holes were filled with loess in many layers; each layer was about 10-cm thick. The density of the filled loess was about the natural density of loess around the holes, it was controlled by the loess weight of each layer. Fig. 3 shows the position of installation. Soil sample was collected and tested for getting its parameters in laboratory. Triaxial tests were done on the undisturbed samples with natural water content to get the strength parameters.

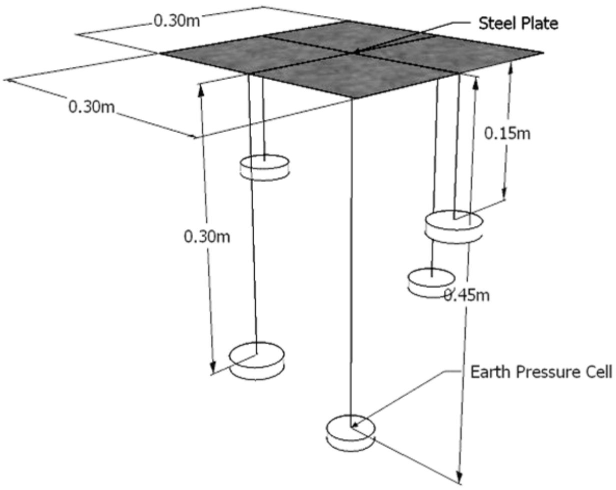

Fig. 3 The installation of earth pressure cells.

3.2 Mathematical Models

According to Boussinesq's method, (1) to (4) provides the vertical stress (σ_z) at any point P in the soils under a uniform distributed load acted on the ground surface. Fig. 4 shows the meaning of the parameters used in those equations. I_σ is called influence factor.

$$\sigma_z = qI_\sigma \tag{1}$$

$$I_\sigma = \frac{1}{4\pi}\left[\begin{array}{l}\dfrac{2mn\left(m^2+n^2+1\right)^{1/2}}{m^2+n^2+m^2n^2+1}\;\dfrac{m^2+n^2+2}{m^2+n^2+1} \\ +\tan^{-1}\dfrac{2mn\left(m^2+n^2+1\right)^{1/2}}{m^2+n^2-m^2n^2+1}\end{array}\right] \tag{2}$$

$$m = \frac{B}{z} \tag{3}$$

$$n = \frac{L}{z} \tag{4}$$

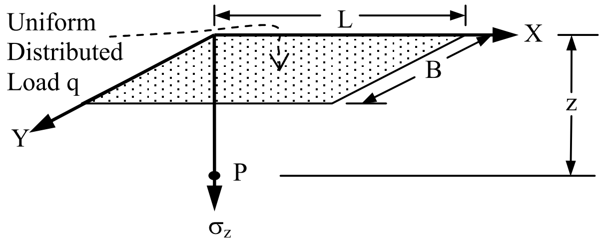

Fig. 4 The parameters used in Boussinesq's equation.

Walter's method is quite complicated. Equation (5) is the vertical stress at any point P shown in Fig. 5. The values of c^2 and λ can be found by (6) and (7). E, G and ν are compression modulus of elasticity, shear modulus of elasticity and Poisson's ratio respectively. In (5) θ_{z1} is the solid angle subtended at the point (x, y, z/c) by the loaded area. The solid angle is defined as the area on a sphere of unit radius intersected by the elements extending from the point (x, y, z/c) to the bearing area. Also, θ_{z2} is the solid angle subtended at the point (x, y, cz) by the loaded area. There are double values for c^2; the upper and lower signs are used for c^2 and $1/c^2$ respectively.

$$\sigma_z = \frac{q}{2\pi\left(c^2-1\right)}\left(c^2\theta_{z1}-\theta_{z2}\right) \tag{5}$$

$$c^2 = \frac{1-\nu}{\nu}\,\frac{\dfrac{E}{G}\pm\sqrt{\dfrac{E^2}{G^2}-4\nu\left(1+\nu\right)\left(\dfrac{E}{\lambda}+\dfrac{E}{G}\right)}}{\dfrac{2E}{\lambda}+\dfrac{E}{G}\mp\sqrt{\dfrac{E^2}{G^2}-4\nu\left(1+\nu\right)\left(\dfrac{E}{\lambda}+\dfrac{E}{G}\right)}} \tag{6}$$

$$\lambda = \frac{E\nu}{\left(1+\nu\right)\left(1-2\nu\right)} \tag{7}$$

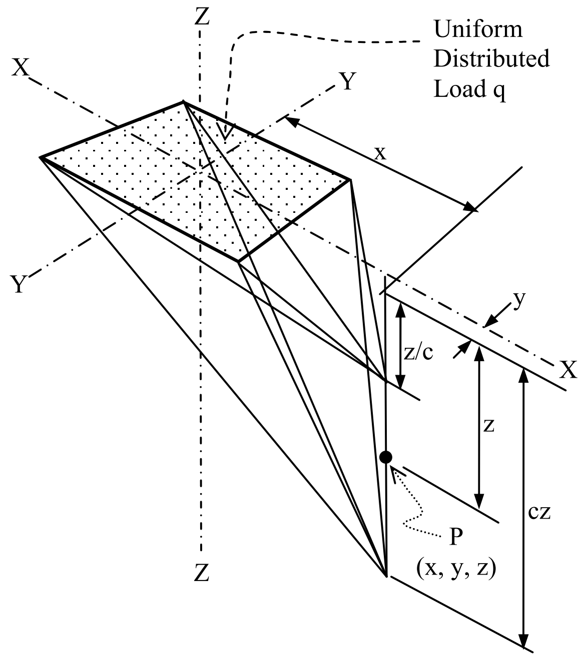

Fig. 5 The parameters used in Walter's equation.

Note that the solid equation, E = 2G(1 + ν) is not employed in this method. The assumption is that the shear modulus of soil is smaller than the value obtained from the solid equation. This assumption has been supported by many researchers such as [7] and [8].

The soils parameters used in the mathematical models were from laboratory tests. Compression modulus of elasticity (E) was 52580 kPa. Poisson's ratio (ν) was 0.25. In case of Walter's equation, two values of shear modulus of elasticity (G) were used. The first value was 20000 kPa which was near to the 21032 kPa obtained from solid equation. The second one was the 15000 kPa which was assumed due to the behavior of soils at medium strain level [7]. Modulus parameters were not used for Boussinesq's equation. The PLAXIS 3-D used solid mechanic theory in the analysis.

4. RESULTS AND DISCUSSIONS

Table. 1 shows the comparison of the influence factor (I_σ) obtained from the 3 methods of calculation and plate bearing test. The test results show that the stress distribution in soils was not constant for all plate pressure. The increase of plate pressure caused the decrease of influence factor at the point under consideration. In other words, the higher pressure made the high strain of soils, then, shear modulus of elasticity reduced. The smaller shear modulus of elasticity made the smaller influence factor at the point under consideration. Walter's method gave the result that agreed with the test's result, the reduction of shear modulus of elasticity caused the reduction of influence factor. This could be considered that after the pressure acted on the soils, the void ratio was decreased and then the soils became harder. Therefore, the settlement induced the better distribution behavior. It means that the pressure distributes broader in soils.

Table. 1 The influence factor (I_σ) obtained from the calculations and test.

Position	Depth	Walter		Boussinesq	PLAXIS 3-D	Test's results	
		G, kPa				Pressure on plate, kPa	
		20000	15000			654	2725
	0.5B	0.200	0.136	0.400	0.500	0.271	0.150
	B	0.141	0.098	0.240	0.290	0.181	0.150
	1.5B	0.157	0.099	0.179	0.190	0.129	0.100

The double consolidation tests of Khon Kaen loess showed the large decrease of void ratio due to the high pressure [9& 10]. The undisturbed loess in Fig. 1 had the void ratio of about 0.8. At the pressure of about 2000 kPa, the ratio became about 0.4 as shown in Fig. 6. It could be concluded that Walter's method provided the reasonable result which was affected by soils strain level.

PLAXIS 3-D is usually used under the condition of Mohr-Coulomb Model which solid mechanic theory is employed. This model gave the result that was quite different from the test's result. The example of its output is shown in Fig. 7. Hardening Soil Model should be more suitable but it needs complicated parameters. Boussinesq's method also gave the constant influence factor. The comparison between the calculated influence factors and the tested ones are shown in Table. 2.

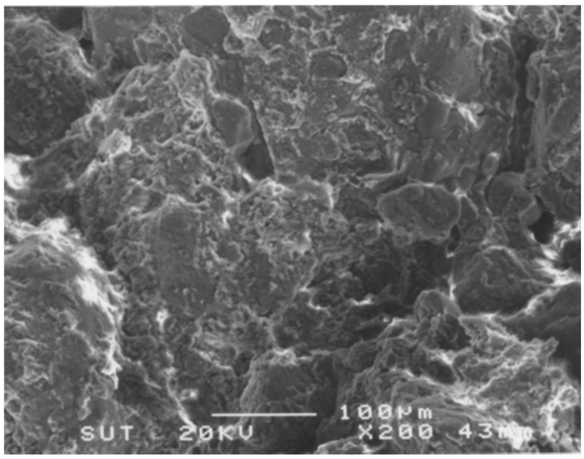

Fig. 6 The loess under about 2000 kPa pressure.

The pattern of contact pressure between plate and soils would account for the difference between the factors obtained from calculations and test. This study had the assumption that the contact pressure was uniform but some researchers reported that the contact pressure varied in pattern depending upon soils type as shown in Fig.8. The Khon Kaen loess having characteristic between SM and ML should have the pattern as between (a) and (b) of Fig. 8.

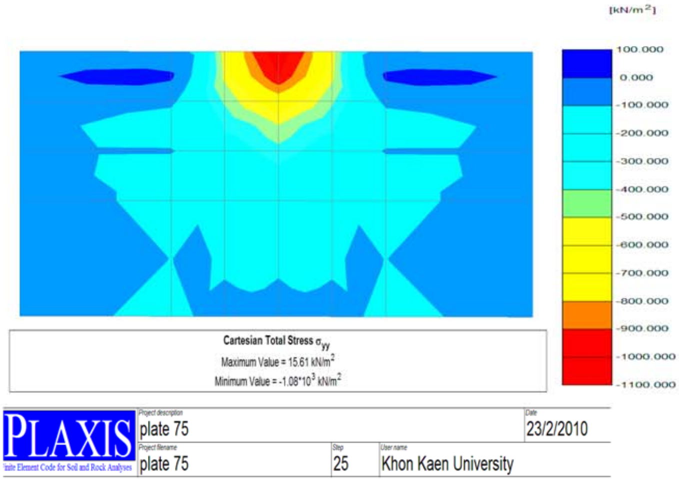

Fig.7 Stress distribution along the section at the center of plate calculated by PLAXIS 3-D.

Table. 2 The percentage difference between calculated influences factors (I_σ) and the test results.

Position	Depth	Pressure = 654 kPa			Pressure = 2725 kPa		
		Walter	Boussinesq	PLAXIS	Walter	Boussinesq	PLAXIS
	0.5B	-26.0	47.6	84.5	-9.1	167	233
	B	-22.0	32.8	60.2	-34.9	60.2	93.3
	1.5B	22.0	38.7	47.3	-1.0	78.9	90.0

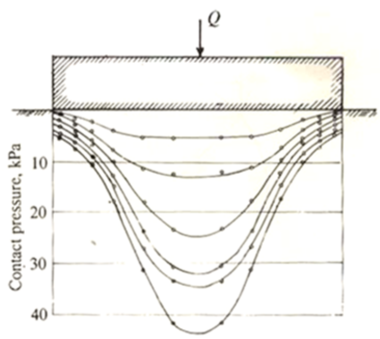

(a) Sand (Faber, 1993)

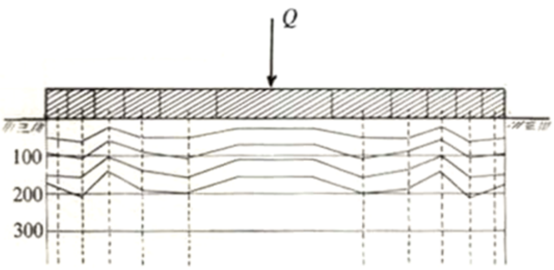

(b) Silt (Helenelund, 1965)

Fig. 8 Contact pressure under uniform distributed load [2].

5. CONCLUSION

The stress distribution in soil mass due to distributed load is presented as the load multiplied by the number called influence factor (I_σ). The classical Boussinesq's method gives the constant value of the factor even if the surcharge load changes and soils type has no effect on factor. The field test results show that the factor could change along with the change of surcharge load magnitude. This conclusion is supported by the study about the non-constant shear modulus of elasticity at the medium strain level. Walter's method provides the output reasonably because solid mechanic theory is not adopted in this method. Finite element method gives the output that is similar to Boussinesq's method because Mohr-Coulomb Model is usually employed. Hardening Soil Model should be tried. It is the more complicated model that non-linear stress-strain behavior is applied,

Contact pressure pattern should be considered as well. It is usually assumed to be uniform in any method but some researchers reported that the actual pattern is not uniform.

6. ACKNOWLEDGMENT

The authors wish to acknowledge financial assistant from Department of Civil Engineering, Faculty of Engineering, Khon Kaen University for the research presented in this paper.

7. REFERENCES

[1] Boussinesq J, "Application des Potentials a L'Etude de L'Equilibri et due Mouvement des Solides Elastiques," Gauthier- Villars, Paris, 1883.

[2] Hansbo S. "Foundation Engineering," The Netherland, Elsevier, 1994, pp. 107-110.

[3] Walter HW, "Stresses in Soils under a Foundation," J. of The Franklin Institute, vol. 239, issue 6, June 1945, pp. 445-465.

[4] Udomchoke V, "Origin and Engineering Characteristics of the Problem Soils in the Khorat Basin, Northeastern Thailand," Doctoral degree dissertation, Asian Institute of Technology, Bangkok, Thailand, 1991.

[5] Phien-wej, N, Pientong, T, & Balasubramaniam, AS, "Collapse and Strength Characteristics of Loess in Thailand," Eng. Geology 32, 1992, pp. 59-72.

[6] Gasaluck W, Luthisungnoen P, Angsuwotai P, Muktabhant C & Mobkhuntod S, "On the Design of Foundation in Collapsible Khon Kaen Loess," Proc. an Int. Conf. on Geotechnical & Geological Eng.(CD), Melbourne, Australia.2000.

[7] Santos JA & Correia AG, "Shear Modulus of Soils under Cyclic Loading at Small and Medium Strain level," Proc. 12WCEE 2000, 2000, paper no.0530.

[8] Cabalar AF, "Dynamic Properties of Various plasticity Clay," EJGE, 2009, pp. 1-11.

[9] Gasaluck W & Houngjing S, "Problematic Soils in Northeast Thailand," 40th Anniversary Commemorative Volume of the SEAGC, 2007, pp. 269-282.

[10] GasakuckW & Veerasiri T,"The Collapse of Foundaton in Khon Kaen Soil and the Rehabilitation by Means of Composite Piles" Geotechnical Special Publication No.116, Deep Foundation 2002, Vol.1 ASCE, 2002, pp. 474-485.

First International Conference on Geotechnique, Construction Materials and Environment, Mie, Japan, Nov.21-23, 2011, ISBN: 978-4-9905958-0-7 C3051

The Effect of Sheet Pile Length on the Capacity of Improved Pile Foundation on Sand under Vertical and Moment Loading

Tuan Van Nguyen, Pongsakorn Punrattanasin
Department of Civil Engineering, Faculty of Engineering, Khon Kaen University,
Email: ngtuanhue@gmail.com, ppunrattanasin@gmail.com,

ABSTRACT: This paper is to investigate how the sheet pile length affects the capacity of improved pile foundation. The improved pile foundation, in this study, can be defined as a pile foundation skirted by sheet piles around the periphery of pile cap. A series of 1g physical modeling tests were conducted on sand under vertical and moment loading by the way that the vertical load was applied at different positions from the pile cap centerline. Besides the center of pile cap, four other points with increasing eccentricities were considered. Two types of model pile foundation were used in the experiments and their loads and settlements were measured by using a load cell and linearly variable differential transducers (LVDTs). The effect of sheet pile length on the capacity of existing pile foundation can be evaluated by the results of load-settlement relationship. The results show that the sheet piles significantly enhances the foundation capacity under vertical and moment loading. In addition, the results reveal that the capacities go up with the increasing sheet pile lengths.

Key words: sheet pile length, pile foundation, capacity, sand

1. INTRODUCTION

Enhancing the foundation bearing capacity has been drawing a lot of researchers' interest because it is one of the key issues in foundation structure design. Due to the high application to various soil conditions, various types and sizes of superstructures, pile foundation is usually priority choice to satisfy both safety and economy in case of weak soil and great bearing loading requirement. In order to improve the pile foundation capacity, Nguyen and Punrattanasin [1] adopted the design concept of sheet pile foundation which was defined as a shallow foundation with sheet piles skirted by sheet piles around the periphery of the footing [2],[3]. Installing sheet piles around the pile foundation which is called improved pile foundation is one of the ways to significantly improve the pile foundation capacities in terms of vertical, horizontal and moment [1], [4], [5]. In this paper, a series of 1g physical modeling tests was continuously conducted on sand under combined vertical and moment loadings with variety of sheet pile length to study how the length of sheet pile affects the foundation bearing capacities. All tests were completed with the same initial condition so that the experimental results can then be properly compared and discussed. From the results of this study, an appropriate sheet pile length was also revealed.

2. EXPERIMENTAL WORKS

This paper reports the results of a series of 1g loading tests of pile foundation model with variety of sheet pile length on sand under the combined vertical-horizontal loading. The purpose of these tests is to investigate sheet pile length's effect on the moment capacity of pile foundations. In order to properly compare and discuses the experimental results, all the tests were done with the same initial condition.

2.1 Model Foundation

The model foundations include four identical steel piles (200mm in length and 14mm in diameter), a steel pile cap (70mm x 70mm x 30mm) and four 1mm-thick steel sheet piles with variety of lengths. The distance from the center to center of piles in the group is 3d or 42mm (d is the pile diameter). The four piles are screwed into the pile cap whose top surface has not only a central groove for pure vertical load but also many grooves in order that the load can be applied with different eccentricities. The pile cap with many grooves is shown in Figure 1. The sheet piles of which length is measured from the bottom of pile cap are also connected to the pile cap by screws. A succession of sheet pile lengths (Ls) of 10mm, 20mm, 30mm and 40mm or Ls/ L ratios of 0.05, 0.1, 0.15 and 0.2 were used in this study (L: length of pile). The variety of sheet piles is shown in Figure 2. In addition, both sides of sheet pile surface are not glued with sand or any material, so the roughness of the sheet pile is assumed to be smooth.

Figure 1. Pile cap with grooves

Figure 2. Variety of sheet pile lengths

Beside the models of pile foundation with sheet piles at the four sides of pile cap (PFFS), the pile foundation model was used in this research with the aim of comparison. Both of them (shown in Figure 3) under combined vertical and moment loads were embedded in the same sand and initial condition.

Figure 3. Two types of model foundations: PF and PFFS

2.2 Loading System

The test program in this study was performed at Department of Civil Engineering, Khon Kean University, Thailand, by using a new combined loading apparatus designed and constructed by Nguyen and Punrattanasin [6]. The outstanding point of this apparatus is that it can be highly applicable for any combination of vertical, horizontal and moment loadings and displacement paths can be generated and applied to model foundations with precise force, position and direction. There are four main parts in the loading apparatus: loading system, measuring system, control system and data acquisition system. Besides, the loading apparatus includes a soil container which is linearly and smoothly movable out of the loading system by means of its four wheels moving on two rails in order to easily prepare the soil before testing.

Two air cylinders were respectively used for apply vertical and horizontal loads on the foundation. They were mounted on a gantry system which is clearly shown in Figure 4. The gantry system includes a fixed part and unfixed part moving along four rails on four I section beams by means of its eight wheels. The horizontal and vertical air cylinders were mounted respectively on the fixed and unfixed parts. Hence, in terms of eccentric loading cases, the vertical loading system was horizontally moved to a position in order that it can apply the desired eccentric point on the footing. In other words, moment loading could be generated by this way. The loads and the displacements of the model of foundation were measured via load cells and linearly variable differential transducers (LVDTs). Portable data logger was used to record the data from load cells and LVDTs through a computer. Due to the small size of the pile cap, two arms attached to the surface of the pile cap via screws were used to measure the vertical settlement of the foundation. The arms are rigid enough to ignore their own bending. Figure 4 respectively shows the 3D schematic drawing and general view of the combined loading system.

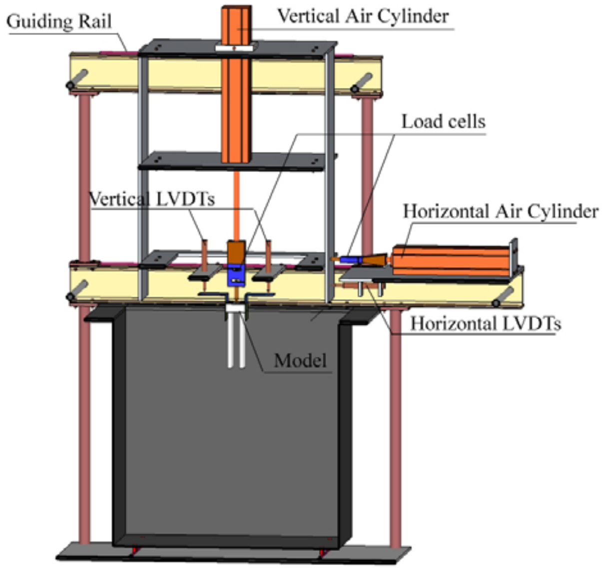

(a) 3D cross section schematic drawing

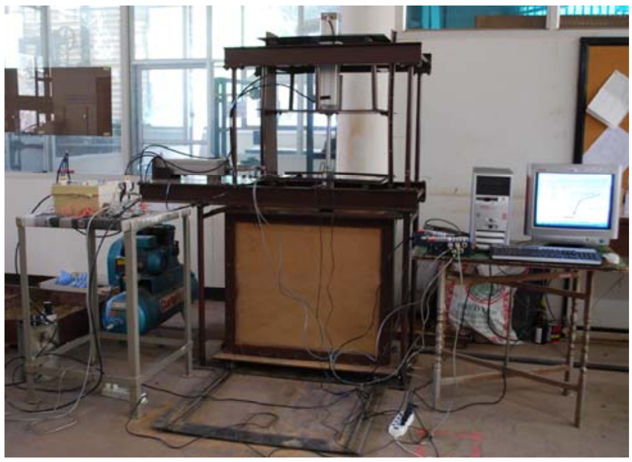

(b) General view

Figure 4. The combined loading apparatus

2.3 Soil Sample Preparation

Dry sand, the Puttaisong sand which is easily found in the Northeast of Thailand, used in this research is uniformly graded sand, sorted by particle sizes. The sand was poured from a hopper into the soil container, a steel box with inner dimensions of 80cmx40cmx80cm in length, width and depth, respectively. Its size is large enough with no apparent influences of boundary effects [7]. In order to create the same initial condition for all the tests, the height between the bottom of the hopper and deposited sand surface was chosen to be 50 mm and periodically adjusted to the rise of the sand surface to maintain the constant height until the sand was fully poured into the container. In other words, the uniform sand, of which relative density is constant, could be achieved through this way. In addition, pouring the sand until the container became full means that there was no apparent influence from effects caused by the bottom of the container [7]. Table 1 summarizes the properties of the sand. After pouring sand, the loading system applied the vertical load at the center of the pile cap to drive the pile foundation into the sand until touchdown. In case of pure vertical loading, the load kept applying until failure. In cases of eccentric loadings, the vertical loading system was horizontally moved to a position in order that it can apply the desired eccentric point on the footing.

Table 1. Physical properties of experimental sand

Type	Sand
Unit weight (kN/m3)	14.39
D60 (mm)	0.395
D30 (mm)	0.360
D10 (mm)	0.240
Uniformity coefficient, Cu	1.646
Coefficient of graduation, Cc	1.367

2.4 Detail of The Tests

A series of 25 loading tests were conducted and reported in this paper. Two kinds of foundations were used in this research. They are pile foundation (PF) and pile foundation with four sheet pile (PFFS). In terms of PFFS, a succession of sheet pile lengths (Ls) of 1cm, 2cm, 3cm and 4cm or Ls/ L ratios of 0.05, 0.1, 0.15 and 0.2 were used in turn (L: length of pile). Besides the centre of pile cap, four other points with E= e/B = 0.1, 0.167, 0.25 and 0.333 were made for eccentric vertical loading cases (e: eccentricity, B: width of pile cap). Each foundation took turns to be applied by a centric loading and four eccentric loadings.

3. EXPERIMENTAL RESULTS

A foundation under an eccentric vertical load V may be considered as subjected to a vertical load V and a moment M, which is equal to the load V times its distance from the centre. In other words, to generate the moment, the model foundations are applied a vertical force at different distances from the pile cap centerline. It should be noted that the horizontal displacements of model foundations were neglected in all experiments until the failure conditions were approached. The results of the series are graphically shown in Figures 5 at Ls/L ratio of 0, 0.05, 0.1, 0.15 and 0.2, respectively. In this paper, the load at a settlement of 0.1B (7mm) was chosen as the ultimate bearing capacity of the foundation [8]. All the values of bearing capacities were summarized in Table 2

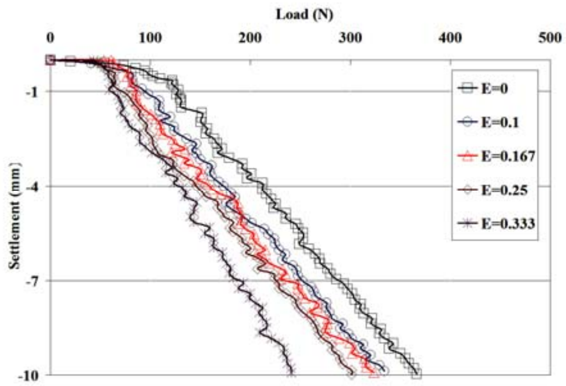

(a) Ls/L= 0cm

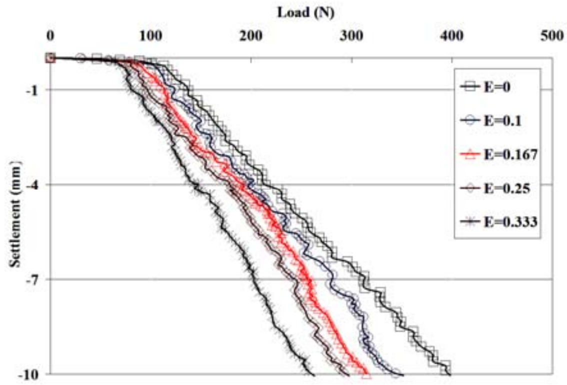

(b) Ls/L= 4cm

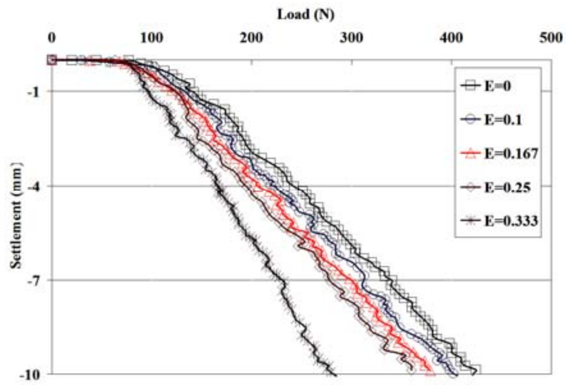

(c) Ls/L= 5cm

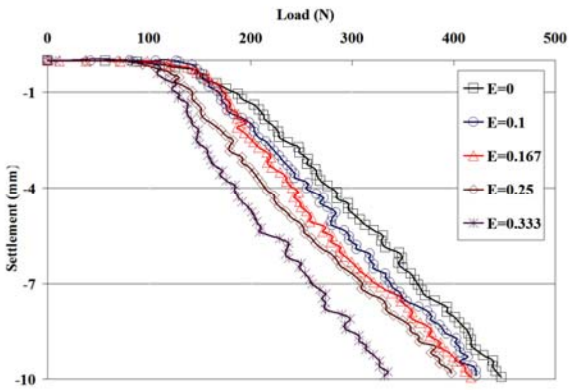

(d) Ls/L= 6cm

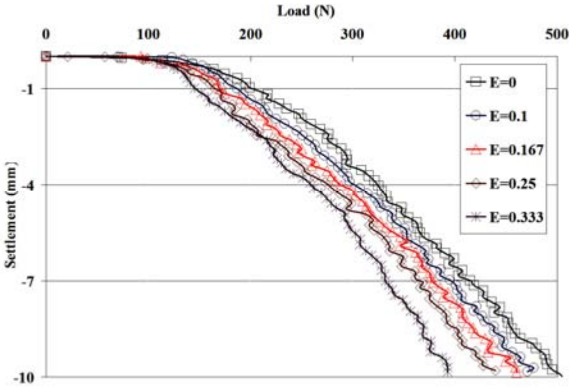

(e) Ls/L= 7cm

Figure 5. Vertical load- settlement relationship of model foundations with different Ls/L ratio

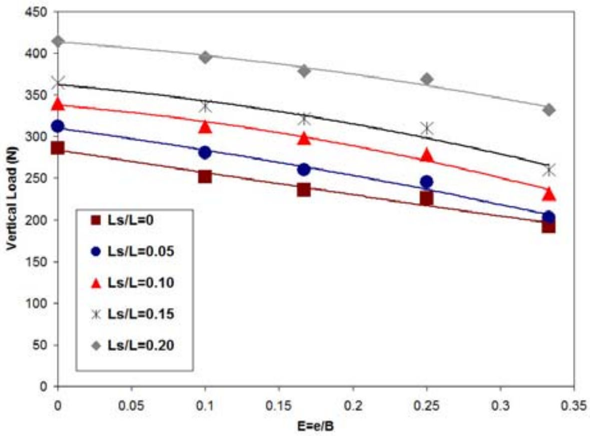

Figure 7. Bearing capacity of various type of pile foundation model under eccentric loads

Table 2. The bearing capacity of all kinds of foundations

Improved Pile Foundation with Ls/L =	Bearing Capacity (N)				
	E=0	E=0.1	E=0.167	E=0.250	E=0.333
0	286	252	236	226	193
0.05	312	280	260	245	203
0.10	340	312	298	279	232
0.15	365	337	321	310	260
0.20	415	395	379	369	332

Table 3. The moment capacities' value and greater percentage compared with PF of all kinds of foundations

Moment Capacity	Foundations with Ls/L =				
	0	0.05	0.10	0.15	0.20
Value (Ncm)	527	553	681	807	1281
Greater percentage compared with PF (%)	0	4.9	29.3	53.2	143.3

Table 2 obviously presents that the bearing capacities of the foundations rise moderately with increasing length of sheet piles regardless of eccentricities. This shows more clearly in Figure 6. The increasing capacities could be explained by contribution of (1) the skin friction along the sides of the sheet piles, (2) the end bearing of the sheet piles and (3) the confinement effect of soil inside sheet piles and pile cap.

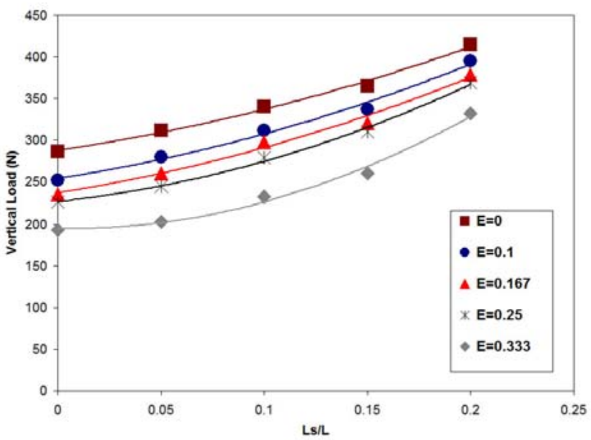

Figure 6. Eccentric vertical capacity of foundations with different sheet pile lengths

As expected, no matter how long the sheet piles are, certain decreases of the capacities with increasing eccentricity are expressed in Figure 7, where the bearing capacity V is plotted against the ratio of the eccentricity (e) over the width of pile cap (B).

Figure 7 also reveals that the capacities enhance gradually when the sheet pile lengths raise and they quickly go up at the ratio Ls/L of 0.2.

In order to determine moment capacities, the effect of the moment acting on the foundations is plotted in Figure 8 at different Ls/L ratios in terms of a normalized diagram on M-V plan with respect to Vmax (centric bearing capacity of pile foundation) [2].

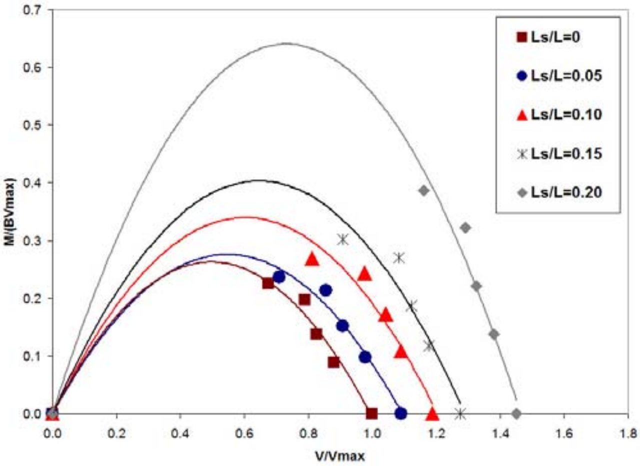

Figure 8. Normalized load-moment relationships

Figure 8 indicates that the maximum moment of foundations (M_{max}) can be approximated by M_{max}/BV_{max} ratio. It should be noted that V_{max} is maximum centric vertical of the pile foundation (PF). From Figure 8, the M_{max}/BV_{max} ratio are 0.263, 0.276, 0.340, 0.403 and 0.64 in cases of Ls/L equals 0, 0.05, 0.1, 0.15 and 0.2, respectively. In terms of the foundation moment capacity, the values and the greater percentage compared with PF are shown in Table 3 which illustrates that the longer sheet piles are, the greater moment capacity gets. It is interesting to note that the moment capacity also soar up at the ratio Ls/L equals 0.2.

4. CONCLUSION

The series of twenty five physical modeling tests were conducted on sand under a series of eccentric loadings to evaluate the influence of sheet pile length on the pile foundation capacities. The moment capacity of foundations could be determined from a series of eccentric capacities. The results clearly demonstrate that attaching four sheet piles around the pile foundations provides significant improvements in capacities both vertical and moment. The capacities dramatically increase when the ratio Ls/L reaches 0.2. In deed, the greater percentages of capacities compared with pile foundation are 45.1% and 143.3% in terms of vertical and moment respectively.

5. ACKNOWLEDGMENT

This research was financially supported by the research fund from Faculty of Engineering and Graduate School, Khon Kaen University and Khon Kaen University Scholarship for Human Resource Development to Neighboring Countries.

6. REFERENCES

[1] Nguyen, T.V. and Punrattanasin, P., “The Capacity of Improved Pile Foundation on Sand under Vertical and Moment Loading”, Proceedings, 3rd Technology and Innovation for Sustainable Development International Conference, Nong Khai, Thailand, 2010, pp 126-130.

[2] Punrattanasin, P., Kusakabe, O., Murat, O., Koda, M., Nishioka, H. 2002. Sheet Pile Foundation on Sand under Combined Loading – A Literature Review and Preliminary Investigation, Technical Report of Tokyo Institution of Technology (65): 57-85.

[3] Nishioka, H., Koda, M., Hirao, J., Higuchi, S. 2008. Development of sheet pile foundation that combines footing with sheet pile. QR of RTRI 49(2): 73-78.

[4] Takemura, J., Izawa, J., Hiroaki. and Yamana., “Centrifuge Model Tests of Pile-Sheet Pile Combined Foundation Subjected to Lateral and Moment Loading”, Proceedings, 6th Regional Symposium on Infrastructure Development, Bangkok, Thailand, 2009.

[5] Nguyen, T.V. and Punrattanasin, P., “The Capacity of Improved Pile Foundation on Sand under Vertical and Horizontal Loading”, International Conference Advances in Geotechnical Engineering - ICAGE, Perth, Australia, 2011 (full paper accepted).

[6] Nguyen, T.V. and Punrattanasin, P., “Development of Combined Loading Apparatus for Physical Modelling”, Research and Development Journal of the Engineering Institute of Thailand, 2011, (accepted and will be published).

[7] Al-Mhaidib, A.I. 2006. Experimental Investigation of the Behavior of Pile Groups in Sand under Different Loading Rates. Geotechnical and Geological Engineering 24:889-902.

[8] Punrattanasin, P., Gasaluck, W., Muktabhant, C., Angsuwotai, P. and Patjanasuntorn, A., “The Effect of Sheet Pile Length on the Capacity of Sheet Pile Foundation”, Proceedings, 17th International Conference on Soil Mechanics and Geotechnical Engineering, Alexandria, Egypt, 2009, pp 598-601.

First International Conference on Geotechnique, Construction Materials and Environment, Mie, Japan, Nov.21-23, 2011, ISBN: 978-4-9905958-0-7 C3051

Investigation of a Reliable Reinforcing Method for Embankment Ground

H. M. Shahin, T. Nakai, M. Kikumoto, R. Sakai, Y. Yoshida, I. Saito, N. Nagao & K. Toda

ABSTRACT: In this research, effectiveness of reinforcing in embankment ground has been investigated and reinforcing mechanism has been clarified by laboratory model tests and the corresponding numerical simulations. Three reinforcing methods are employed, namely, sheet pile alone, sheet pile with tie-rod, and a composite method of sheet pile with nailing. The numerical analyses are carried out with a finite element program called FEMtij-2D, using the elastoplastic subloading t_{ij} model. In the case of the reinforcing with the sheet pile alone, no reasonable increase of the bearing capacity of the reinforced ground is observed. In contrast, in the case of the composite reinforcing method of sheet pile with nailing, a significant increase of the bearing capacity is seen as the lateral displacement of upper part of the sheet pile is impeded due to the inclusion of the nailing. The finite element program FEMtij-2D properly predicts the results of the model tests on the reinforced embankment.

Keywords: Embankment, reinforced ground, bearing capacity, finite element analysis

1. INTRODUCTION

Many railways and highway embankments are built on soft soils because of the limitation of firm ground and the requirements for a straighter alignment. In these cases, it is necessary to strengthen the soft ground to avoid any failure which may occur due to dynamic load, such as earthquake load. Three classes of failure can be identified: internal instability of the embankment, instability of the foundation soil and overall instability involving both the embankment and the foundation [2], [3]. Sometimes, beside the deformation and failure of the embankment, lateral displacement of the ground affects the surrounding structures which are located in a close proximity to the construction site. To prevent any damage to the surrounding structures or failure of the embankment it is inevitably required reinforcing the subsoil beneath the embankment. In recent years, many designers around the world are specifying base reinforcement as one of the solutions for the short-term instability to make use of the tensile strength of the reinforcement to limit the spreading of the embankment and lateral displacement of the foundation [6], [8]. In this research, effectiveness of reinforcing in embankment ground has been investigated and reinforcing mechanism has been clarified by laboratory model tests and the corresponding numerical simulations. To analyze the behavior of reinforced earth structure on soft ground, it is necessary to consider – (i) the elastoplastic behavior of soil, (ii) soil/reinforcement interaction, and (iii) soft ground consolidation systematically and simultaneously [1]. The numerical analyses are carried out with a finite element program called FEMtij-2D, using the elastoplastic subloading t_{ij} model [5]. This model can describe the typical stress, deformation and strength characteristics of soils, such as the influence of the intermediate principal stress, the influence of stress-path dependency of the plastic flow and the influence of the density and/or the confining pressure.

2. OUTLINE OF MODEL TESTS AND ANALYSES

2.1 Model Tests

Fig. 1 shows an apparatus for laboratory model test. The model test is conducted with the aspect ratio of 1:100 between the model tests and prototype scale. The width of the ground is 100cm having the height of 50cm. A stack of aluminum rods, in which two kinds of round rods having diameters of 1.6mm and 3.0mm are mixed in the weight ratio of 3:2, was used as the model ground. The unit weight of the mass of aluminum rods is 20.8kN/m^3 at model stress level. The width of the loading plate is 12cm with the thickness of 3cm which corresponds to the width of the embankment in real field. The sheet piles are emulated with aluminum boards. The thickness of the aluminum board is obtained considering the similarity ratio between the model tests and prototype scales. Here, two types of rigidities – flexible and stiff with the thickness of 0.3mm and 0.5mm, respectively, are employed. The distance

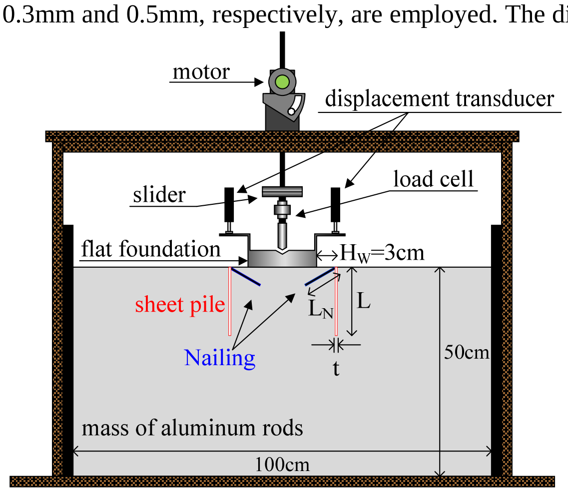

Fig. 1 Apparatus for laboratory model

Table I: Patterns of experiments

		L (cm)	t (mm)
no sheet pile	Case 1	0	0
sheet pile	Case 2	24	0.3
	Case 3	24	0.5
sheet pile+Nailing (L_N=9cm)	Case 4	24	0.3
	Case 5	24	0.5
	Case 6	12	0.5

of the sheet pile from the edge of the loading plate, H_w, is 3cm. In the nailing method, a tracing paper is being spread into the ground with an angle of 30° from the horizontal direction. In the tracing paper, aluminum rods were glued with an interval of 1cm to provide frictional behavior in the nailing. The load is applied on the loading plate with a motor which is attached in the loading device, and the magnitude of the load is measured with a load cell installed in the tip of the device. A slider is attached in the loading device to permit the lateral displacement of the base loading plate. Photographs are taken during the experiments and they are used later as input data for the determination of ground movements with a program based on the technique of Particle Image Velocimetry (PIV). Several model tests have been conducted varying the length of the sheet pile L=12cm, 24cm, thickness of the sheet pile t=0.3mm, 0.5mm, and the length of the nailing L_N=0cm, 6cm, 9cm, to investigate the effects the stiffness of the sheet pile, and the lengths of the sheet piles and nailing into the ground deformation. Among them six cases of experiments will be discussed in this paper, the patterns are listed in Table I.

2.2 Numerical Simulations

An elastoplastic constitutive model for soils, called the subloading t_{ij}-model [5], was used in finite element analyses. This model requires only a few unified material parameters, but can describe properly the following typical characteristics of soils: (1) influence of intermediate principal stress on the deformation and strength of soil; (2) influence of stress path on the direction of plastic flow is considered by splitting the plastic strain increment into two components; (3) influence of density and/or confining pressure. Model parameters for the aluminum rod mass are shown in Table II. The parameters are fundamentally the same as those of the Cam clay model [7] except for the parameter *a*, which is responsible for the

Table II. Material parameters for aluminum rods

λ	0.008	Same parameters as Cam- clay model
κ	0.004	
N (e_{NC} at p=98kPa & q=0kPa)	0.3	
$R_{CS}=(\sigma_1/\sigma_3)_{CS(comp.)}$	1.80	
ν_e	0.20	
β	1.20	Shape of yield surface (same as original Cam-clay at β=1)
a	1300	Influence of density and confining pressure

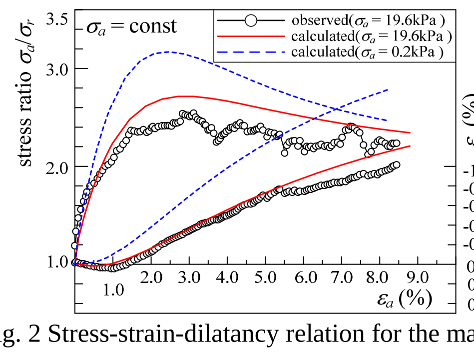

Fig. 2 Stress-strain-dilatancy relation for the mass of aluminum rods

influence of density and confining pressure. Where, λ and κ are the slope of loading and unloading curve of *e-lnp* graphs at the loosest state. *N* is the void ratio at mean principal stresses (p) 98kPa in the above mentioned loading curve and ν_e is the Poisson's ratio. The parameter β controls the shape of yield surface. These parameters can easily be obtained from traditional laboratory tests. The parameters can be determined through conventional triaxial tests and consolidation test. Fig. 2 shows the results of biaxial tests for the mass of aluminum rods used in the model tests. The figure shows the positive and negative dilatancy of aluminum rod mass; and it is clear that the strength and deformation behavior are very similar to those of dense sand.

Fig. 3 shows the mesh used in the finite element analyses for the analyses of the model tests. Isoparametric 4-noded elements are used to represent the soil. The mesh is well refined with elements of finer mesh in most regions. The sheet piles and soil nailing are modelled using elastic beam elements. The frictional behavior (friction angle δ=18°) between the reinforcements and the ground is simulated using elastoplastic joint elements [4]. The frictional angle, δ=18°, was obtained from a laboratory model test. Both vertical sides of the mesh are free in the vertical direction, and the bottom face is kept fixed. The analyses were carried out under plane strain conditions, since the aluminium rods do not deform in the out of plane direction. The analyses are carried out with the same conditions of the model tests. The initial stresses of the ground are calculated by applying the body forces due to self-weight (γ=20.4kN/m^3), starting from a negligible confining pressure (p_0=9.8×10^{-6}kPa) and an initial void ratio e=0.35. After self-weight consolidation the void ratio of the ground was 0.28 at the bottom and 0.30 at the top.

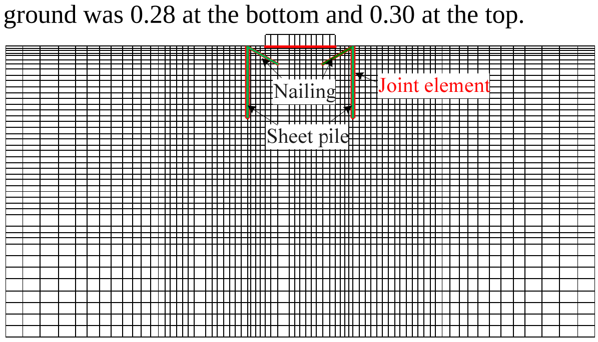

Fig.3 Mesh for Finite Element Analyses

3. RESULTS AND DISCUSSIONS

Fig. 4 shows the observed and computed results of load-displacement curves. Figure (a) represents the results of the model tests, and figure (b) illustrates the results of the numerical simulations corresponding to the model tests. The vertical axis indicates the vertical load q_v normalized with γB (γ: unit weight of soil, B: width of the foundation) that corresponds to the coefficient of bearing capacity, and the horizontal axis is the vertical displacement normalized with foundation width *B*. The observed load- displacement relations do not start form the origin, because of having the self-weight of the foundation. Comparing the results of case 2 (sheet pile with L=24 and t=0.3mm) and case 3 (sheet pile with L=24 and t=0.5mm) in the model tests, it is found that the stiffer and longer sheet pile produces a much stronger reinforcing effect as generally expected. However, both case 1 and case 2 do not have a big difference with the result of case 1 (no sheet pile i.e. no reinforcement) when comparing it in the point of the ultimate bearing capacity. Hence, it can be understood that reinforcing with sheet pile alone does not have much effect of reinforcement to increase the ultimate bearing capacity of the ground if the ground is medium dense soil. On the other hand, three cases of experiments where nailing is combined with the sheet pile demonstrate a high bearing capacity including the ultimate bearing capacity in the same ground. Comparing the results of case 4 (sheet pile with nailing, L=24cm and t=0.3mm) and case 5 (stiffer sheet pile with nailing, L=24cm and t=0.5mm), it is revealed that the bearing capacity is higher in case 5 until it reaches the failure state. However, case 6, the same dimensions as case 5 except the length of the sheet pile (L=12cm), produces almost equal amount of bearing capacity as case 6. It means that even a shorter sheet pile increases bearing capacity of the ground significantly if the sheet pile possesses a sufficient stiffness and combined with a nailing. The computed results not only qualitatively but also quantitatively predict well the observed load-displacement curves of various kinds of tests patterns.

Fig. 5 illustrates the distribution of shear strain of the model tests and finite element analyses during ultimate bearing capacity. In the model test it is taken at v/B=0.06, and for the simulation it is from v/B=0.10. The distributions of shear strain of the model tests are obtained using Particle Image Velocimetry (PIV) technique. In this paper, two images are divided into a finite area; the average movement rate of the mass of aluminum rods of each area is extracted as nodal displacements. The strain for one grid is calculated from these displacements by using the shape functions and the B matrix (strain- displacement matrix) that is usually used in finite element method to relate displacements and strains. It is seen in the figures that for case 2 and case 3, where sheet pile alone is employed for reinforcing, though it seems that the sheet piles slightly restrict strain compare to the case of no sheet pile (case 1) but larger shear strains concentrate locally at a narrow zone in the shallow ground. Therefore, a significant effect of reinforcement can no longer be achieved when sheet pile alone is used as reinforcement of the ground. Moreover, the reinforcing effect is not reflected in the bearing capacity

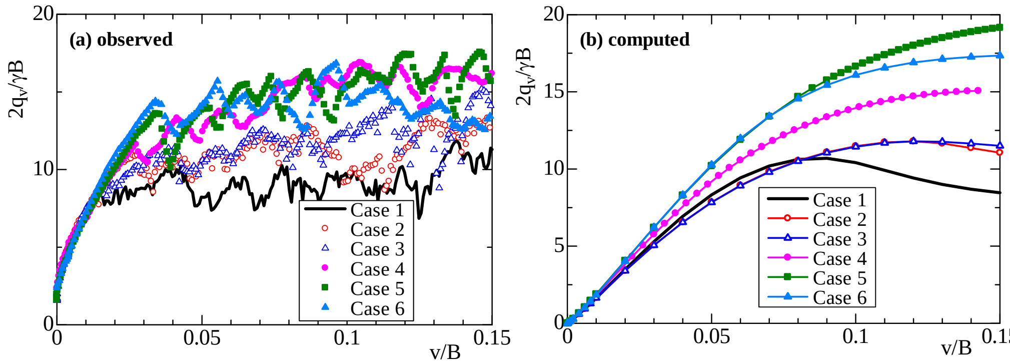

Fig. 4 Vertical load vs. vertical displacement under concentric loadings

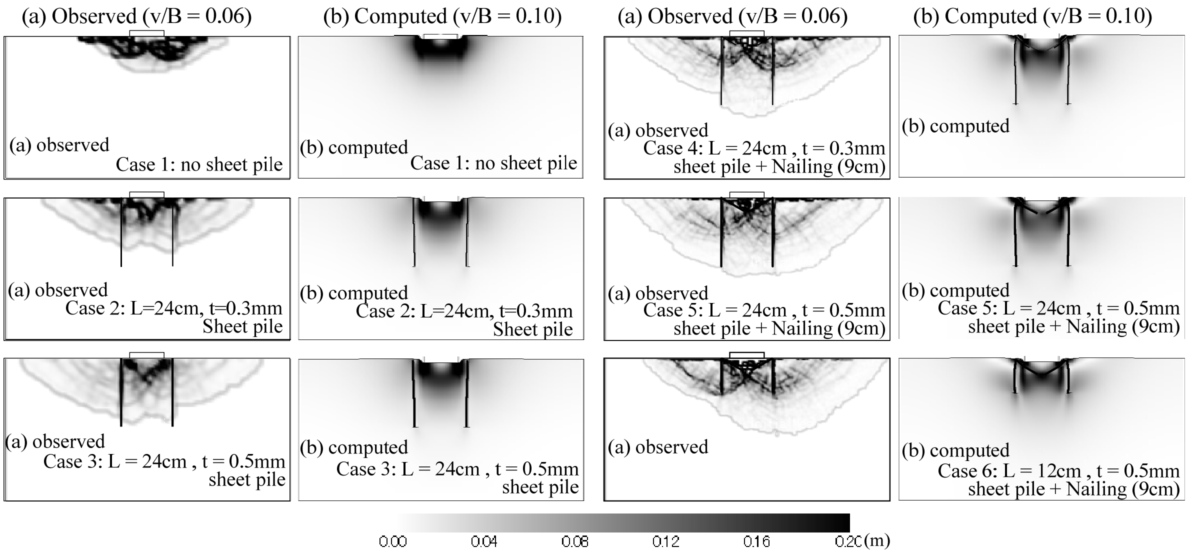

Fig. 5 Shear strain distributions

though the sheet pile is arranged in this way so that it can intercept the shear surface. It can be speculated that this is because of the upper part of the sheet pile which is displaced to the opposite side of the loading plate. For case 4, case 5 and case 6 where sheet piles are combined with nailing, it is revealed that a wider region of shear strain with greater intensity is developed even in the surrounding soil compared with case 1 (no reinforcement). Therefore, it can be said that the sheet pile where the nailing is combined can decrease the influence on the surrounding soil even if the sheet pile is shorter with higher stiffness. The shear strain of the numerical analyses shows very good agreement with the results of the model tests.

Fig.6 shows the lateral displacement of the left sheet pile at the ultimate bearing capacity. It is seen that the lateral displacement of the upper part of the sheet pile is restricted in the case when nailing is combined with the sheet pile. On the other hand, there is almost no difference of the lateral displacement at the upper part of the ground between the no reinforcing and the reinforcing with the sheet pile alone. The reinforcing with the sheet pile alone does not produce a significant effect of reinforcement which is confirmed in this figure. It is thought that the resistance force controls the lateral displacement because the tensile force acted on the nailing with the subsidence of the loading plate. Therefore, it can be said that it is important to control the upper part of the sheet pile to achieve a significant reinforcing effect.

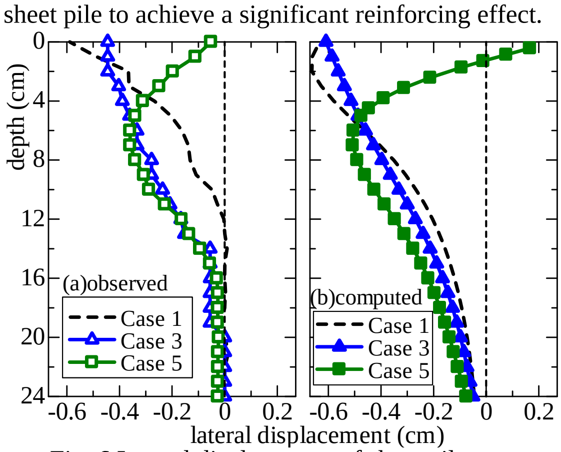

Fig. 6 Lateral displacement of sheet pile

4. SOIL-WATER COUPLING ANALYSIS OF REAL EMBANKMENT

In the previous section it was seen that the numerical analysis can well reproduce the results of the model tests in the all cases of test patterns. In this section, soil-water coupling analysis considering the construction process of real ground embankment will be discussed. In the introduction, it was mentioned that embankments that are built on soft soils are subjected to huge deformation or sometimes to failure of the whole structure, which emphasizes the necessity of strengthening the soft ground to avoid any failure. Fig. 7 illustrates the ground types with the dimensions of the embankment to be analyzed in this section. The levee crown width is 5m, the bottom width is 25m, and the height is 5m of the embankment with an inclination of 1:2. Fig. 8 shows the mesh for the finite element analyses. Considering the symmetric ground half section was taken for the analyses. The width of the ground is 62.5m having 60m in depth. The bottom face is assumed as fixed boundary condition. The vertical faces are kept free in lateral directions. The analyses are carried out considering soil-water coupled and plane strain conditions. The top surface of the ground is allowed to drain, and all other faces are assumed as impermeable boundaries. Therefore, water can not flow across the boundaries of the ground except the top surface. The water table is assumed at the top of the ground. To consider the soft soil, parameters of Fujinomori clay (bulk unit weight, γ_t=18.52kN/m³) is used as the base ground, and Toyoura sand (bulk unit weight, γ_t=15.48kN/m³) is used as the material of soil fill. The material parameters are shown in Table III. The coefficient of permeability for the ground is assumed as 10^{-7}m/min. Two types of grounds, normally consolidated clay (OCR=1.0) and over consolidated clay (OCR=2.0), are used to investigate the dependency of ground stiffness. Fig. 9 shows the stress-strain-dilatancy relation at triaxial condition for (a) Fujinomori clay with normally consolidated condition and (b) Toyoura sand with relative density Dr=75% under constant cell pressure. The stress level chosen for the curve is equal to 294kPa which is the same vertical stress level at the middle of the base ground considered in the finite element analyses. The figures confirm that clay shows negative dilatancy, while sand exhibits positive dilatancy. The construction of the soil fill was achieved by gradually raising the unit weight of the soil, and the construction is done in three layers from the bottom to the top. After completion of the construction, the analyses keep running until the complete

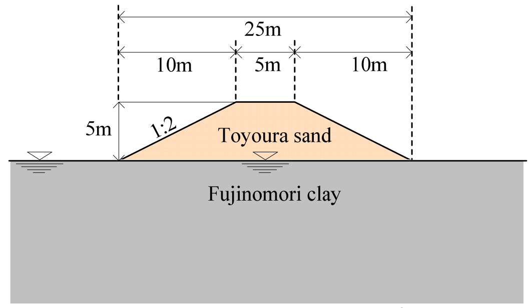

Fig. 7 Dimensions and ground types of embankment

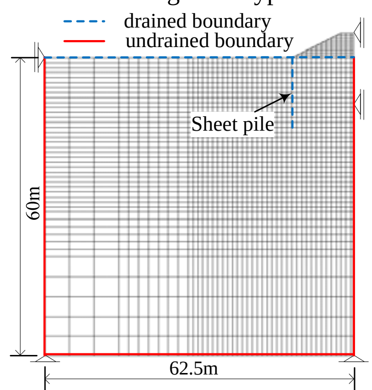

Fig. 8 Mesh for FEA – real ground

Table III. Parameters for Fujinomori Clay and Toyoura Sand

Parameters	Fujinomori Clay	Toyoura Sand
λ	0.10390	0.070
κ	0.00990	0.0045
N (e_{NC} at p=98kPa & q=0kPa)	0.9220	1.10
$R_{CS}=(\sigma_1/\sigma_3)_{CS(comp.)}$	3.20	3.20
ν_e	0.20	0.20
β	1.50	2.00
a	500	$a_{(AF)}$=30 $a_{(IC)}$=500

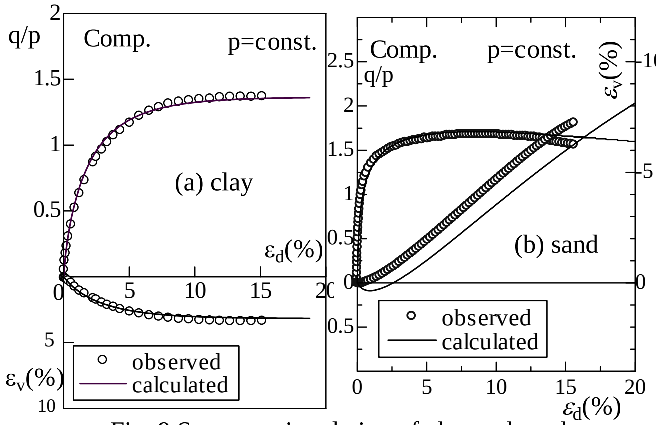

Fig. 9 Stress-strain relation of clay and sand

dissipation of excess pore water pressure which is generated during the construction of the embankment. Similar to the model test sheet piles with 2 types of stiffness having the lengths of 15m and 30m are used for reinforcing the ground. In the case of composite reinforcing, nailing is added with the sheet pile the same way as the model tests. The analysis without reinforcing the ground has also been carried out to grasp the reinforcing effect in soft ground.

Fig. 10 represents displacement vectors of ground with OCR=1.0 and OCR=2.0. The figures shows that the shape of the embankment is not maintained due to the excessive deformation of the base ground having OCR=1.0 when reinforcement was not installed (no reinforcement). In this case, the base ground flows outwardly during soil fill. It can be seen that for the same type of the ground the upheaval of the ground level is curbed in the reinforced ground with sheet piles and composite reinforcement. It is because the reinforcement restricts the lateral flow of the base ground. Comparing the results between the flexible and stiff sheet piles, it is seen that larger displacement occurs in the sheet piles with less stiffness for the ground of OCR=1.0. On the other hand, for the over consolidation ratio equals to 2.0, the shape of the embankment is maintained even in the case where the reinforcement is not installed. Therefore, in stiffer soil reinforcement is not required in stiffer soil which confirms the results of the other researchers.

Figs. 11 shows surface settlement profiles immediately after construction and after complete consolidation. Here, the complete consolidation means that stage when the excess pore water pressure completely dissipates. For over consolidation ratio OCR=1.0, the ground upheaves by about 2m immediately after completion of the soil fill in the case of no reinforced ground, and it becomes about 1.5m after complete consolidation at the toe of the embankment. For the same ground, the subsidence of the embankment in the central portion of the base ground is about 2m immediately after completion of the soil fill, and it is around 3m after complete consolidation. In the reinforced ground with sheet pile, the amount of the subsidence is controlled due to the reinforcement, for the stiff sheet pile the subsidence is about 0.6m immediately after construction and it is about 1.6m after total consolidation in the central portion, for the flexible sheet pile the embankment settles at around 0.8m after the construction and about 1.8m after complete consolidation. For over consolidation ratio OCR=2.0, the maximum subsidence of the embankment is considerably less compare to the normally consolidated soil (OCR=1.0). At the toe of the embankment, the ground upheaves immediately up to 0.35m after the completion of the soil fill in the case of no reinforced ground, and it becomes about 0.15m after complete consolidation. For the same ground, the subsidence of the embankment in the central portion is about 0.4m

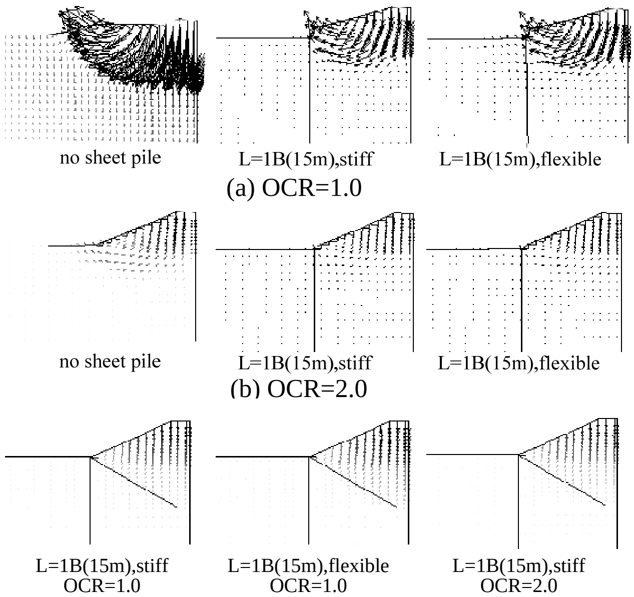

Fig. 10 Displacement vector in the ground

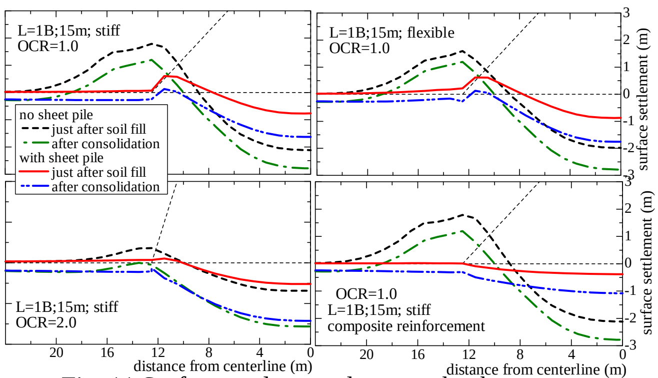

Fig. 11 Surface settlement due to embankment

immediately after completion of the soil fill, and it is around 0.9m after complete consolidation. For the same ground regardless of the rigidity of sheet piles, the subsidence of the embankment in the central portion of the base ground is about 0.24m immediately after completion of the soil fill, and it is around 0.76m after complete consolidation. However, it is much smaller in the case of the composite reinforcement than the other cases for both stiff and flexible reinforcing.

Fig. 12 shows the lateral displacement along the depths which are located at the toe and 3m away from the toe of the embankment. Along the vertical direction from the toe of the embankment, the maximum lateral displacement occurs at the point of 2m in depth from the ground level in the no reinforcement ground in the normally consolidation (OCR=1.0) ground, and the magnitude of the lateral displacement is 2.5m. Along the vertical line of 3m away from the toe of the embankment, the maximum lateral displacement, about 2m, occurs at the surface and it decreases with the increase of depth. Though the lateral displacements along the line of 3m away from the toe of the embankment are smaller than that of the line at the toe of the embankment, but at the surface almost same displacement occurs. In the reinforcing ground with sheet pile alone, the maximum lateral displacement occurs at the surface for both locations. In this ground, the lateral displacement is about 0.12m in the case of stiffer sheet pile, and it is about 0.35m for the flexible sheet pile after complete consolidation. For the composite reinforcement, the lateral displacement is smaller than the other cases. The lateral displacement along the line of 3m away form the toe decreases with the progress of consolidation. As the excess pore water pressure dissipates after the construction, the phenomenon of reducing lateral displacement can be speculated.

In the overconsolidated ground (OCR=2.0), along the vertical direction from the toe of the embankment, the maximum lateral displacement occurs at the point of 1m in depth from the ground level in the no reinforcing ground. Along the vertical line of 3m away from the toe of the embankment, the

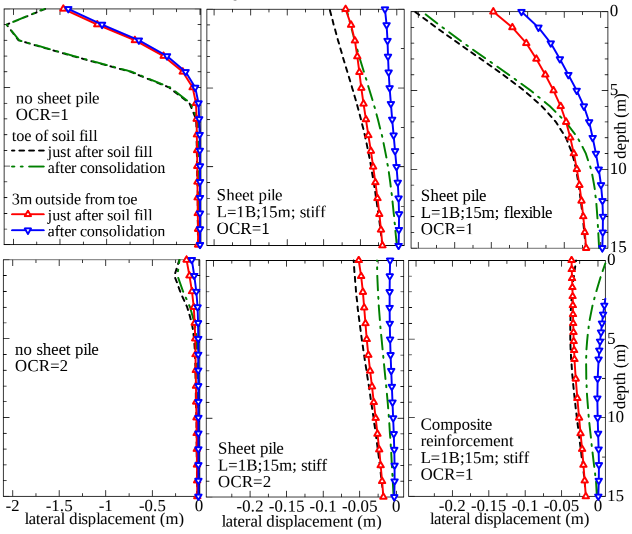

Fig. 12 Lateral displacement at two sections along depth

maximum lateral displacement (0.2m) occurs at the surface. The lateral displacement decreases with the advancement of the consolidation at both faces. In general, the magnitude of lateral displacement is smaller in the case of the stiffer sheet pile than that of the flexible sheet pile the same as the normally consolidated ground. As a whole, the reinforcing with the sheet piles and soil nailing restrict the lateral displacement and the maximum displacement occurs at the surface the same as the normally consolidated ground.

5. CONCLUSION

In this research effectiveness of reinforcing in embankment ground has been investigated with laboratory model tests and numerical simulations. It is found that in the case of the reinforcing with the sheet pile alone, no reasonable increase of the bearing capacity of the reinforced ground is observed as the upper part of the sheet pile is displaced outwardly with the loading even when it is set up in the position where the widening of the shear surface is restricted well. In contrast, in the case of the composite reinforcing method (sheet pile with nailing), a significant increase of the bearing capacity is seen as the lateral displacement of upper part of the sheet pile is impeded due to the inclusion of the nailing. Even the shorter length of the sheet pile produces almost the same effects as those of the longer sheet pile when nailing is appended in the reinforcing method. The finite element program FEMtij-2D properly predicts the results of the model tests on the reinforced embankment. The subsidence of the embankment and the lateral displacement of the ground can be reduced introducing reinforcement in a real ground. The stiffer sheet pile and the composite reinforcement where soil nailing is combined with the sheet pile cause a significant reinforcing effect in a soft ground. The finite element analyses can give a guideline for the prediction of deformation pattern and for the optimum dimensions of the reinforcement in the soft ground.

REFERENCES

[1] Bergado D. T, Chai, J. C. & Miura N., “FE analysis of grid reinforced embankment system on soft Bangkok clay”, Computers and Geotechnics, Vol. 17, No. 4, 1995, pp. 447-471.

[2] Hird C. C. & Jewell R. A., “Theory of reinforced embankments”, Reinforced Embankments: Theory and Practice in the British Isles, London: Thomas Telford, 1990, pp. 115-139.

[3] Hird C. C., Pyrah I. C., & Russell D., “Finite element analysis of the collapse of reinforced embankments on soft ground”, Geotechnique, Vol. 40, No. 4, 1990, pp. 633-640.

[4] Nakai T., “Finite element computations for active and passive earth pressure problems of retaining problems”, Soils and Foundations, Vol. 25, No.3, 1985, pp. 98-112.

[5] Naka T. & Hinokio T., “A simple elastoplastic model for normally and over consolidated soils with unified material parameters”, Soils and Foundations, Vol. 44, No.2, 2004, pp. 53-70.

[6] Monnet J., Galera I. & Mommessin M., “Some theoretical approaches about reinforced embankments on weak soil”, Computers and Geotechnics, Vol. 7, No. 1, 1989, pp. 37-52.

[7] Roscoe K. H. & Burland J. B., “On the generalized stress-strain behaviour of ‘wet’ clay” J. Heyman & F. A. Leckie (eds.), Engineering plasticity (Cambridge: Cambridge University Press), 1968, pp.535-609

[8] Sharma J. S. & Bolton M. D., “Finite Element Analysis of Centrifuge Tests on Reinforced Embankments on Soft Clay”, Computers and Geotechnics, Vol. 19, No. 1, 1996, pp. 1-22.

First International Conference on Geotechnique, Construction Materials and Environment, Mie, Japan, Nov.21-23, 2011, ISBN: 978-4-9905958-0-7 C3051

Evaluation of Stamps and Latex Shell Influence on Stabilometer Testing Results, Modeled with Simulia Abaqus

Dr. Dmitriy Volik, Kuban State Agricultural University, Russian Federation

ABSTRACT: Triaxial tests is often used, along with other research methods, in order to define parameters of geotechnical data. The main topic being conferred in work is analysis of influence, exerted by stamp and latex shell, upon the results of triaxial machine soil testings. The stabilometer modeling and verification was produced. Calibration of soil model parameters, derived from triaxial tests, is brought in work. The necessity of three dimensional simulation of soil testing process is pointed out in order to take into account stamp and shell influence.

Keywords: Triaxial machine test, soil model, Simulia Abaqus modeling, stamp and shell influence, modified Drucker-Prager/cap plasticity model.

1. INTRODUCTION

Nonlinear models are frequently used in geotechnical computational mechanics, which allow various implementation features of soil behavior to be taken into account. In order to define parameters of nonlinear soil models, data of triaxial tests is often used, along with other research methods.

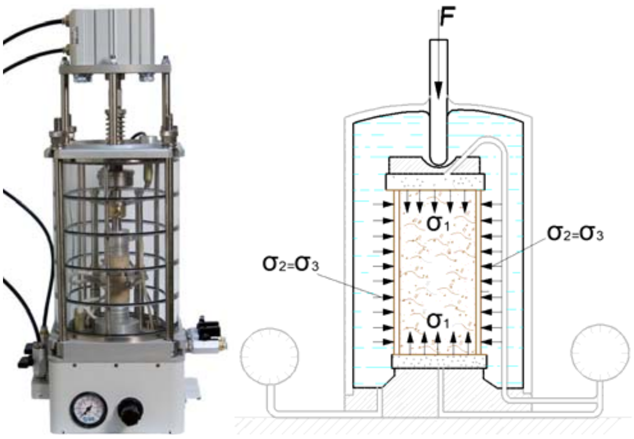

Fig. 1. Triaxial machine (NPO «Geotek»), and its principal scheme

As generally known, uniform hydrostatic pressure $\sigma_2=\sigma_3$ is maintained in the triaxial machine camera. In order to divide mediums of stabilometer camera and soil pores the sample is contained inside a flexible latex shell, while the vertical component of deviatoric load σ_1 is imposed on the soil sample via firm stamps at the bottom and at the top (Fig. 1.). As a result, during the experiments the soil sample interacts with the stamps and the latex shell via their contact surfaces. Therefore, based on the triaxial tests we obtain parameters of a model that describes the system behavior: stamp – soil sample – latex shell. If necessary, parameters are calibrated; graphs, obtained on their basis, are compared with laboratory data. Therefore, it appears possible to obtain a similar behavior of a mathematic model and a triaxial machine. However, the above mentioned parameters simulate the behavior of the "stamps – soil sample – latex shell" a system, whereas parameters, which simulate the behavior of the soil sample only, are required in case of geotechnical tasks. The main goal is to obtain parameters of the soil sample only, considering that an "ideal" triaxial machine, which would test the soil sample without stamps and latex shell influence, does not exist.

This work set outs an analysis of stamps and latex shell influence on the results of soil tests in a triaxial machine. In order to evaluate the influence (to allow for an inaccuracy) of stamps and latex shell in the triaxial machine, a modeling of a three-dimensional "stamps – soil sample – latex shell" system is carried out through the program complex of Simulia Abaqus, following a 4-stage methodology:

The first stage involves creation of a three-dimensional system model (stamps – soil sample – latex shell) in the Simulia Abaqus program complex. It will be referred to as a stabilometer model further on.

The second stage includes verification of stabilometer model parameters to conform with the behavior of the triaxial machine. Verification has to be carried out for each soil sample separately. In the given example it is middle-size grain sand and loamy clay.

The third stage requires exclusion of the stamp and latex shell from the stabilometer model, thereby obtaining an "ideal" stabilometer model.

The final stage involves a comparative analysis of the behavior of the stabilometer model and the"ideal" stabilometer model, in order to evaluate the influence of the stamp and latex shell.

2. STABILOMETER MODELING WITH SIMULIA ABAQUS

1/8 part of stabilimeter (stamp – soil sample – latex shell) was simulated in Simulia Abaqus. As a visualization of the results, 1/8 part was reflected/ copied in order to receive a visual effect of the model second part presence (Fig. 4.)

2.2 Soil model

In order to describe a soil behavior, modified Drucker-Prager/Cap model is used in the analysis.

The cap model is appropriate to soil behavior because it is capable of considering the effect of stress history, stress path, dilatancy, and the effect of the intermediate principal stress. The yield surface of the modified Drucker‑Prager/cap plasticity model consists of three parts: a Drucker‑Prager shear failure surface, an elliptical Cap, and a smooth transition region between the shear failure surface and the Cap (Fig. 3.).

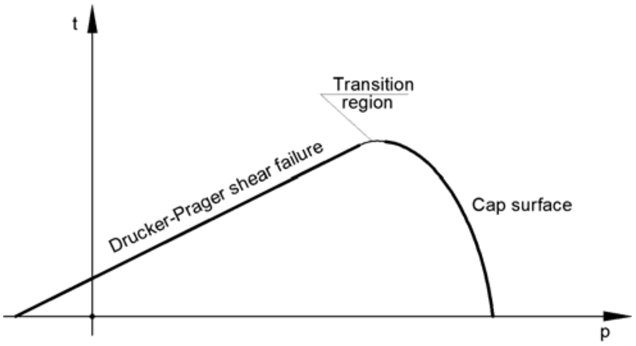

Fig. 3. Drucker‑Prager/cap plasticity model yield surface

The Drucker‑Prager shear surface is a perfectly plastic yield without hardening. Plastic flow on this surface produces inelastic volume increase - dilation.

The Cap surface bounds the yield surface in hydrostatic compression. On the Cap surface plastic flow causes the material to compact correspond to hardening mechanism. Besides, the Cap surface helps control volume dilatancy when the material yields in shear by providing softening as a function of the inelastic volume increase created as the material yields on the Drucker–Prager shear failure and transition yield surfaces. The model uses associated flow in the Cap region and nonassociated flow in the Drucker‑Prager shear failure and transition region.

The hardening/softening law is a user –defined piecewise linear function relating the hydrostatic compression yield stress, and the corresponding volumetric plastic strain.

The nonlinear elastic behavior modeled by using the porous elasticity model including tensile strength. During compression, the void ratio decreases. This behavior is expressed by the logarithmic bulk modulus.

2.3 Stabilometer modeling

Stamps and shell are modeled within the limits of linear elasticity. Steel and rubber has been accepted as materials for stamp and latex shell respectively. Non-linear contact between a stamp, soil sample and latex shell is simulated. Model was meshed by C3D8 solid elements.

For soil initial conditions production the Geostatic Abaqus procedure was applied.

Load is imposed to a model in two stages, repeating laboratory experiments in stabilometer, according to the CD scheme [1]:

The first stage involves sample recompression via a uniform hydrostatic pressure σ_2 (σ_3) to the natural level of a proper soil weight σ_v. This stage is a very important because this will determine the initial stresses in all soil elements.

On the second stage, vertical pressure σ_1 is increased with a maintained compression σ_2 (σ_3) till a relative vertical strain achieves ε_1=12% [1].

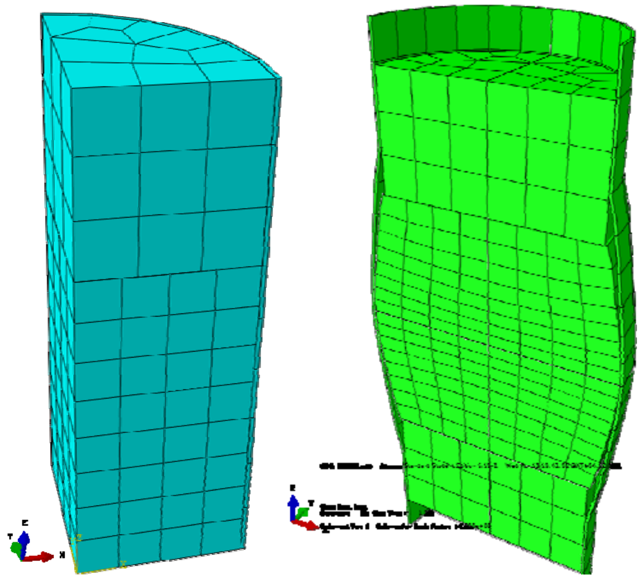

Fig. 4. Finite elements mesh – 1/8 parts, more than 900 nodes. Deformed model - second part (reflection/ copy of 1/8 parts relative to XY and YZ)

During the triaxial tests, soil samples, which are used, are those of moist middle-size grain sand and loamy clay, of 38 mm in diameter and 76 mm in height.

The latex shell thickness is 0,1mm.

3. STABILOMETER MODEL VERIFICATION

First of all, it should be mentioned, that characteristics of ground model are standardized for a full compliance of a its model behavior with the results of laboratory tests according to the relation $\varepsilon 1(\sigma 1)$. Calibration is carried out for several curves with a different value of the uniform compression $\sigma 2$ ($\sigma 3$). Example of the compliance of stabilometer model behavior with the results of triaxial tests of one of the curves is illustrated on the (Fig.5).

For a verification, deflected mode of stabilometer model is examined and compared to the features of behavior of laboratory ground samples in the same conditions.

Analysis of a deflected mode of the stabilometer model is given below.

Following features, relevant for a given process, are shown in the Fig. 5:

1. Maximum magnitudes of stress intensity in soil are located in the shape of a “cross”, which is registered on computed tomography using of full-scale specimen [3].
2. Relative sliding and local break away of a latex shell from a stamp and soil.
3. Latex shell, consequently, acquires a barrel-type shape [2].
4. Soil flowing under the latex shell [2].
5. Stress intensity has a similar distribution to both

models made in Abaqus and LS-DYNA [2] programs.

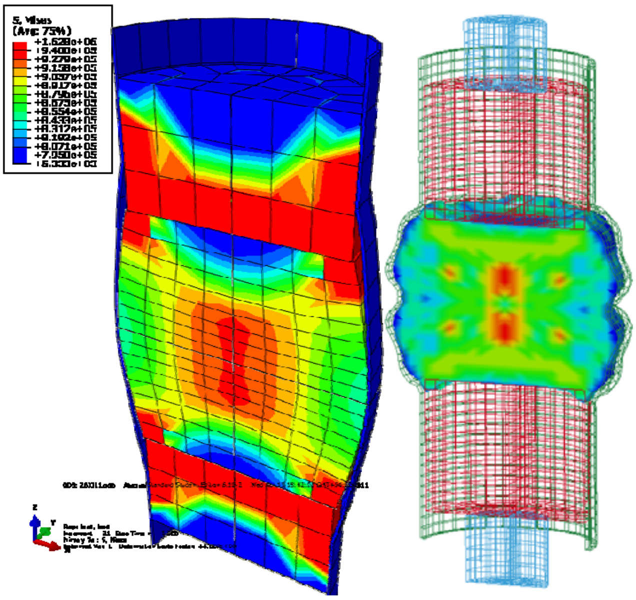

Fig. 5. Stress intensity according to Mises criterion, Pa. Left fig. – Simulia Abaqus; Right fig. – LS-DYNA [2]

A fact of presence of listed features in tests as well is an basis for a deduction about the qualitative similarity in a behavior of stabilometer model.

4. THE STAMP AND LATEX SHELL INFLUENCE EVALUATING

Specific differences in a behavior of stabilometer model and a model of an "ideal" stabilometer are represented on the graphs below Fig. 6.

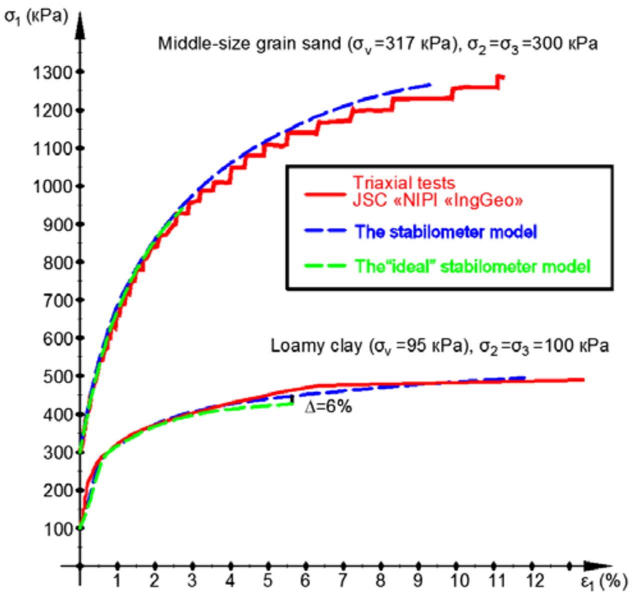

Fig. 6. Relation graph ε1(σ1)

As is obvious from the graphs, the sample destruction occurs significantly earlier without a stabilizing influence of a latex shell and a stamp.

Behavioral curves of a sandy soil register an insignificant influence of stamps and shell in the stabilometer model. This type of a soil is often used as a base for pile foundations in the city of Krasnodar.

Stamps and shell influence in the system with a clay soil may comprises up to 6%. Therewith, a loamy clay is used as a base for building foundation slabs in the constructions in Krasnodar, reaching 16-17 floors.

It is necessary to compare plastic strain in the stabilometer model and the"ideal" stabilometer model, in order to evaluate the influence of the stamp and latex shell.

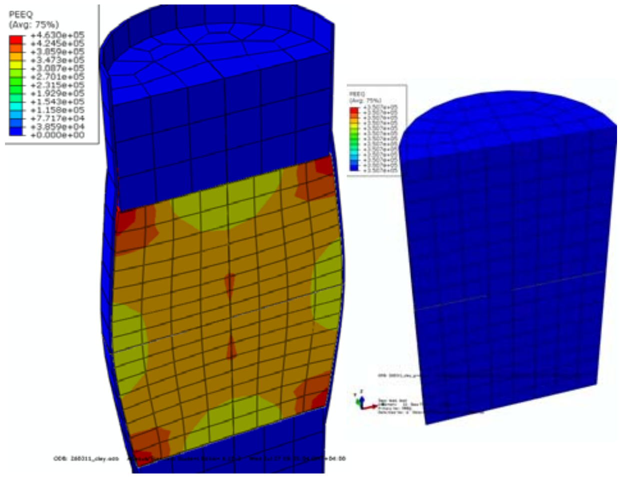

Fig. 7. Equivalent plastic strain at integration points. Left fig. – the stabilometer model; Right fig. – the "ideal" stabilometer model

Apparently from the Fig. 7, ground samples undergo various deformed states. Ground in a stabilometer model has a barrel-shaped strained shape (presumably, due to a shell influence), whereas ground sample in the "ideal" stabilometer has a regular cylindric shape.

Moreover, intensity of plastic strains in stabilometer model are placed in a shape of a cross.

In a model of the "ideal" stabilometer, intensity of plastic strains in distributed equally in the whole sample. To summarize, it can be resumed that the stamps and shells influence not only in quantity, but also in quality.

Difficulties occur in evaluating the influence of stamps and shells, relying only on the difference of 6% between curves on a graph point, which is close to the critical state of a sample. It may be assumed that, in some spots under the foundation, conditions are far from the limit equilibrium of a ground.

However, a practical task is suggested to be solved, in order to evaluate an influence of stamps and shell.

Thereto, calculation of a tank settlements on a loamy clay was carried out. Calculation was carried subject to a ground consolidation during hydrotests of a tank and next several cycles of a filling-drawdown.

A tank with a diameter of 11 meters, product lever 22meters. Ground base with a calculated zone 20 meters deep. Permeability coefficient of a loamy clay k=0,000001 m/c.

Calculations are performed with parameters of foundation grounds, defined including stamp and shell influence, and without it.

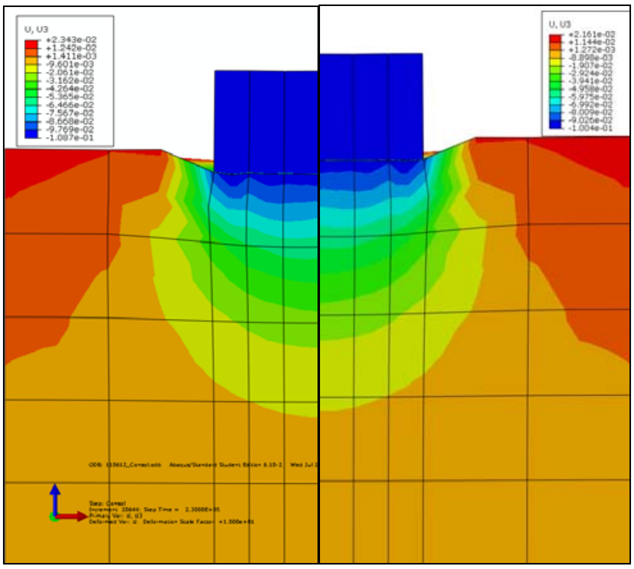

Fig. 8. Vertical displacements in models, m. Left side – adjusted soil model data; Right side – non adjusted

As shown at the Fig. 8., tank foundation settlements are significantly underestimated with unadjusted soil model parameters, that have 0,10m. Maximum base settlement under reservoir foundation with adjusted soil model data is 0,11m. The underestimated settlement is 9% even with the coarse elements mesh model.

5. CONCLUSION

Via Simulia Abaqus program complex, a system model "stamps – soil sample – latex shell", has been simulated, which makes it possible to predict laboratory tests in the triaxial machine.

Stabilizing influence of shell and stamps enables a soil sample to describe a curve ε_1 (σ_1) of a twice greater length till the moment of destruction.

A shell and stamp contribution considerably increases a system stiffness "stamps – soil sample – latex shell", in case of soft soil tests (clay soil of plastic consistency, loose fine sand etc.).

Ground in a stabilometer model has a barrel-shaped strained shape (presumably, due to a shell influence), whereas ground sample in the "ideal" stabilometer has a regular cylindric shape. Intensity of plastic strains in stabilometer model are placed in a shape of a cross. In a model of the "ideal" stabilometer, intensity of plastic strains in distributed equally in the whole sample. To summarize, it can be resumed that the stamps and shells influence not only in quantity, but also in quality.

The underestimated maximum settlement of the tank foundation on a loamy clay base is 9% with unadjusted soil model parameters.

Stabilometric experimental curves represent a combined behavior of a sample, shell and a stamp. Consequently, model parameters, based on these curves, which are used for predictions of a soft soil behavior, should be applied with adjustments.

In order to detect parameters of a soil model, it is necessary to take into account stamp and shell influence by means of three-dimensional simulation of a sample testing process.

6. REFERENCES

[1] GOST 12248-96. Soils. Methodology of laboratory assessment of strength and deformability properties. Russian Federation standard. Moscow. – 1997.

[2] Muiseimnik A. Y. Identification of soil model parameters / A. Y. Muiseimnik, G. G. Boldyrev, D. V. Arefyev // Engineering Geology. – 2010. - №3. – p. 38-43.

[3] Batiste, S. N. Shear Band Characterization of Triaxial Sand Specimens Using Computed Tomography / S. N. Batiste, K. A. Alshibli, S. Sture, M. Lankton // Geotechnical Testing Journal/ -Vol. 27. - -№6. – 2004.

First International Conference on Geotechnique, Construction Materials and Environment, Mie, Japan, Nov.21-23, 2011, ISBN: 978-4-9905958-0-7 C3051

Characterizing the Interaction of Geomat with Fine Grained Black Cotton Soils

Wekesa S., Mukabi J. & Okado J., Research &Development Department, Kensetsu Kaihatsu Ltd, Nairobi, Kenya
Kogi S. & Ndeda M., Materials Testing & Research Department, Ministry of Roads, Nairobi, Kenya
Ogallo J., Department of Civil Engineering, University of Nairobi, Nairobi, Kenya

ABSTRACT: Black Cotton Soils (BCS), which are highly problematic in nature when it comes to their use as construction materials for geo-structures, are normally in extensive existence in most parts of Africa. As a consequence, it is extremely important to advance Research & Development (R & D) related to BCS in order to develop cost-effective geotechnical engineering methods of its utilization. On the other hand, over the past 20years, tremendous advances have been made in the research and development of geosynthetics technologies and their appropriate geotechnical engineering applications.

Results based on laboratory tests are reported and the role of the increased interaction between the geomat and BCS in the functional aspects is quantitatively analyzed through the application of advanced analytical tools. It is derived and concluded that the degree and extent of the geomat-BCS particle interaction is dependent on several factors mainly including particle size, texture, shape, moisture-suction variation and location of embedded geomat relative to the layer thickness.

Keywords: BCS, Soil particle-geomat interaction, Characteristics, Geosynthetics.

1. INTRODUCTION

Black Cotton Soils (BCS) are usually tropical clays which are essentially products of physical and chemical in-situ weathering of igneous, sedimentary and metamorphic rocks under varying environmental conditions. The formation of these soils is highly influenced by a complex interaction of various variables such as weathering, erosion and climatic changes as well as type of original parent rock, local topography, drainage and cycle factors which strongly influence their geotechnical engineering behavior. As a consequence, their characterization for use as suitable engineering materials is exceedingly complex since they are highly susceptible to various environmental changes.

Given the recent advances that have been, and are being made in the research of geosynthentics materials based on monitoring of the instrumented structures throughout the years, new design methods have been realized and the versatility of their applications for soil reinforcement, environmental protection and performance during major earthquakes, have increasingly become appreciated [1]-[4]. Nevertheless, hardly any research has been devoted to an in-depth study of the quantitative characterization of the fine grained soil particle-geomat interaction in terms of enhancement of strength and deformation resistance [5], [6]. This study therefore, considers the importance of undertaking comprehensive geo-scientific and geotechnical engineering investigations into the fundamental aspects of the interactive properties thereof.

Based on some of the typical results from this study, it is derived and concluded that the degree and extent of the geomat-BCS particle interaction is, besides the intrinsic properties of the BCS and also dependent on the layer thickness defining the active zone and confining pressures and tensile forces.

2. INTRODUCING SOME TYPICAL BCS PHYSICAL, CHEMICAL AND MECHANICAL CHARACTERISTICS

2.1 Typical Intrinsic Physical Properties and Basic Classification

Table 1 is a summary of the typical intrinsic physical properties of the BCS encountered in most parts of the East and Central African Region [7]. The global classification of BCS, on the other hand, is presented in Table 2 [8].

Table 1 Summary of typical physical properties of BCS

Property	Value
Liquid Limit LL (%)	37~83
Plasticity Index PI (%)	16~45
Moisture Content w (%)	16~40
Shrinkage Limit SL (%)	8~20
Percent Passing 75 μ m	75~95
Free Swell (%)	70~165
Swelling Pressure kN/m^2	0~80
Linear Shrinkage (%)	18~35
Specific Gravity G_s	2.47~2.56
Dry Density γ_d kg/m^3	1920~2050

Table 2 Global classification of BCS

Soil Parameter	Classification		
	Moderate Swellability	High Swellability	Very high Swellability
Dry Density γ_d	<15kN/m^3	$15\leq \gamma_d \leq 16$	>16
Clay content C<0.002	<40%	$40\leq c \leq 55$	>55
Liquid Limit (LL)	<48%	$40\leq LL \leq 55$	>65
Plasticity Index (PI)	<30%	$30\leq PL \leq 40$	>40
Shrinkage Index (IS)	<30%	30~60	>60
Swell Pressure	<120kN/m^2	120~600	>600

It can basically be derived from these tables that these soils are extremely fine grained and highly susceptible to pore-grain moisture-suction matrices characterized mainly by swelling due to wetting and shrinkage due to drying (also refer to Fig. 2.1 [8]-[11].

2.2 Response to Physical-chemical Variations and Environmental Changes

A study was carried out by [9]-[11] to determine the response of BCS as influenced by varying physical-chemical and environmental conditions. Fig. 2.1 depicts part of the typical results from these reference citations.

To simulate the effects of rapid drying on the PI characteristics of CON-AID treated material, a comparison of air and oven (110°C) dried untreated (neat) and treated material was carried out. Figure 2.1(b) is a plot of these results. It can be noted that CON-AID treated material is neither influenced by rapid drying effects nor curing period and maintain the same magnitude of PI (28) as in previous cases.

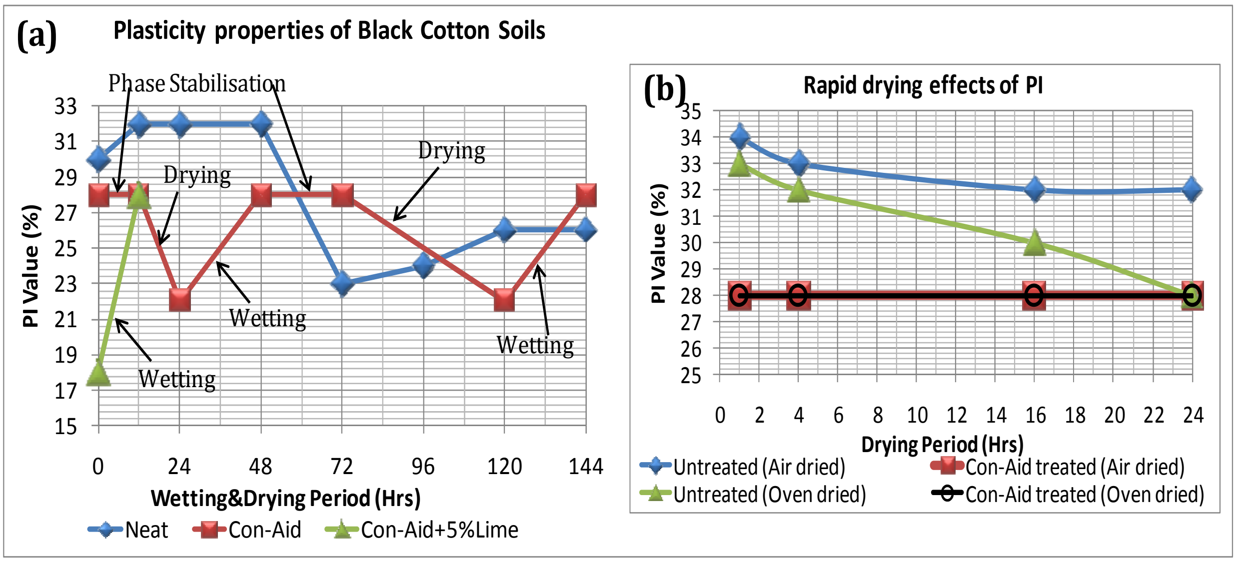

Figure 2.1 Simulation of impact of drastic environmental changes on black cotton soil subjected to varying physical-chemical conditions

Furthermore, the characterization of BCS subjected to varying drying/wetting (environmental changes) with different chemical additives can be observed from Fig. 2.1. These results basically show that BCS are highly influenced by changes in environmental conditions and that the degree of these changes depends on their current physical-chemical state. It can further be noted from Fig. 2.1 (b) that the intensity and period of the drying is significantly influenced by the chemical additive. Detailed analyses of the interactive characterization of this behavior are reported in [9].

2.3 Typical Shear Strength Characteristics when Subjected to Moisture-Suction Variation

As stated in the introduction, the behavior of BCS is highly influenced by the changes in moisture-suction conditions.

Fig. 2.2 shows that: 1) a slight increase in moisture content can significantly impact on the strength magnitude and overall characteristics of the BCS; and, 2) at higher moisture contents, the effects on characteristics of dynamically loaded and statically loaded BCS specimens are significantly different in the initial and subsequent yield surfaces. However, at failure, the maximum strengths and residual behavior are virtually the same. This may imply that, similar to most of the other geomaterials, BCS are sensitive to various intrinsic and extrinsic influences within the initial, secondary and tertiary yield surfaces [12]. This fact can also be confirmed from Figs. 2.4 and 2.5 in sub-section 2.4, which depict the effect of Cyclic Prestraining (CP) under controlled loading conditions whereby the bearing capacity, strength and deformation resistance tend to be enhanced [13], [14].

From the foregoing perspectives, it was considered that the study of the influence of geomat reinforcement on the geotechnical engineering behavior of BCS may make an interesting research subject.

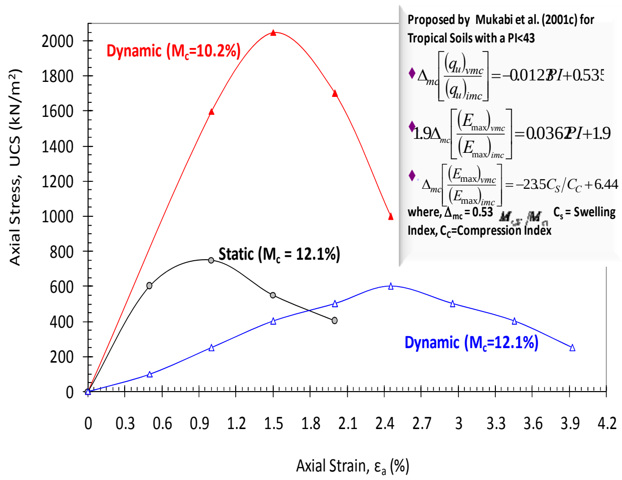

Figure 2.2 Effect of moisture-suction variation on statically

and dynamically loaded tropical black cotton soil.

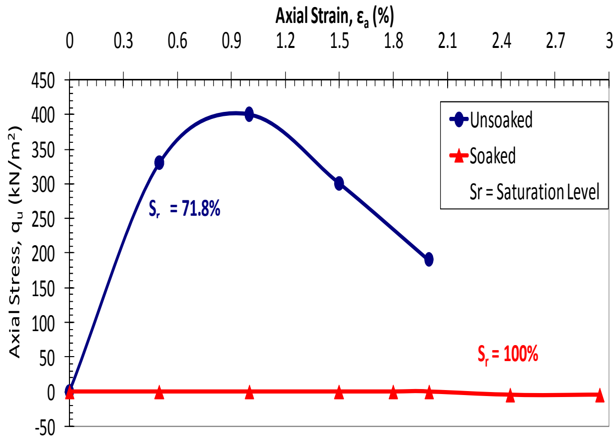

Figure 2.3 Effect of saturation level on the shear strength of black cotton soil.

The results in Figs. 2.2 and 2.3 are a clear indication of the fact that BCS is extremely sensitive to the slightest of moisture-suction variation and that the degree of this influence can be quite detrimental.

2.4 Typical Shear Strength and Deformation Resistance Characteristics as a Result of Controlled Stage Loading

Figs. 2.4 and 2.5 show the characteristics of BCS subjected to controlled stage loading within the initial yield surface, constituent also of CP effects [12].

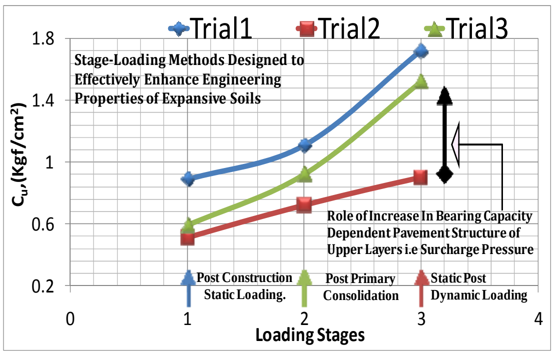

Figure 2.4 Effect of long-term static and dynamic stage loading on the shear strength properties of black cotton soils [10].

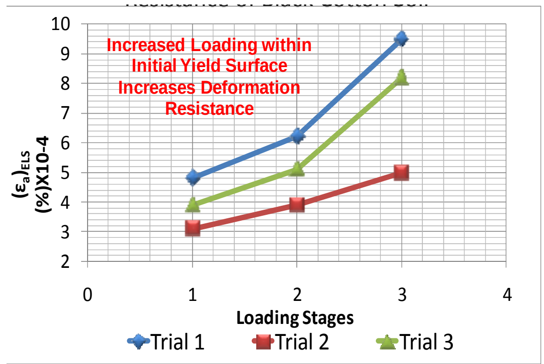

Figure 2.5 Effect of long-term static and dynamic stage loading on the deformation resistance of black cotton soils [10].

The results depicted in Figs. 2.4 and 2.5 are a clear indication that the shear strength and deformation resistance of BCS can be enhanced significantly when subjected to controlled stage loading within the Initial Yied Surface $\{(\varepsilon_a)_{ELS}(Y_I)\}$ [12], [14].

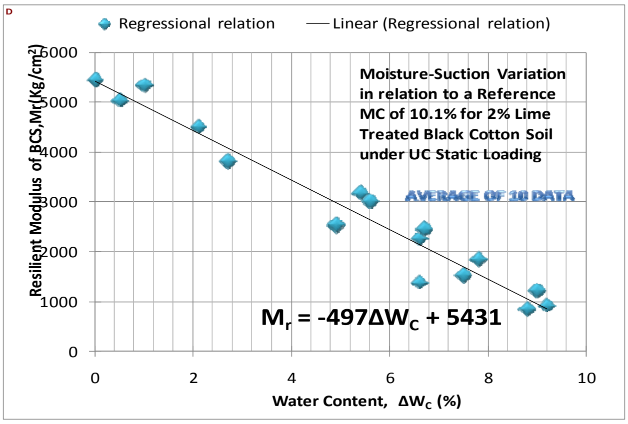

Figure 2.6 Influence of moisture-suction variation on the resilient modulus of slightly lime treated black cotton soil at equilibrium moisture content.

On the other hand, Fig. 2.6 shows the susceptibility of BCS to moisture~suction variation. The following derivations can be made from these figures: 1) the effects of moisture-suction variation are quite steady once the BCS is treated with a 2% hydrated lime (chemical) content; 2) a virtually linear relation seems to exist between the resilient modulus with the increase in moisture content in this case. This may be implicit of the fact that the chemical treatment (the addition of hydrated lime) somehow contained and streamlined the aggregation and agglomeration of the BCS particles. This particular interaction of physical-chemical containment is one of the features of correlative interest of this study in regard to whether or not the geomat reinforcement would exhibit analogous and/or virtually similar effects in reference to the improvement of the vital geotechnical engineering properties, as do the chemical additives; and, 3) slight increases in moisture content lead to a drastic reduction in the resilient modulus of the BCS notwithstanding the control chemical treatment.

3 METHODS OF TESTING

Conventional and modified laboratory and field methods of testing were adopted in this Study. The main mechanical methods of laboratory testing included the conventional and modified Unconfined Compressive Strength (UCS) adopting larger size specimens ($\phi \geq$ 20cm), conventional Consolidated Undrained Triaxial Compression (CUTC), Consolidated Drained Triaxial Compression (CDTC), modified simple shear and modified UCS dynamic loading under varying moisture – suction conditions and modes of reinforcement.

In order to correct for the specimen size, a full scale plate loading test was carried out in the field. Details of the methods of testing are reported in [15].

4 DISCUSSIONS OF TEST RESULTS

4.1 Stress-strain Relations

Fig. 3.1 shows the stress-strain characteristics of the interaction between BCS particles and geosynthetics. Of particular interest is the behavior of geomat reinforced BCS. The specimens were tested under varying environmental conditions as well as modes and types of geosynthetic reinforcement. All imbedding locations are measured from the bottom of the specimens.

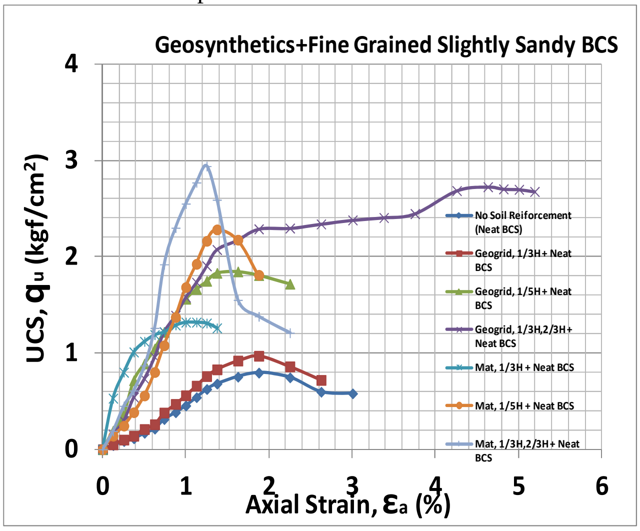

Figure 3.1 Stress-strain characteristics of reinforced and neat black cotton soil.

The following derivations can be made from Fig. 3.1: 1) the contribution of both geomat and geogrid reinforcement to the enhancement of the Unconfined Compressive Strength (UCS) of BCS is highly influenced by the location where it is imbedded; 2) geomat reinforced BCS exhibits better and superior stress-strain characteristics when compared with the geogrid reinforced BCS. This can mainly be attributed to the fact that, due to the mesh size of the geogrid relative to the grain size of the BCS, the interlocking mechanism is significantly limited curtailing the role of the geogrid as a reinforcing element; 3) the double mat reinforcement, which resulted in the highest strength and deformation resistance seems to have a casing effect whereby stress mobilization and distribution are simultaneously activated; and, 4) the stress-strain and failure characteristics are influenced by the mode and type of reinforcement in all cases.

In order to study the impact of varying modes and types of reinforcement on the behavior of agglomerated BCS particles, OPMCS (Optimum Mechanical and Chemical Stabilization) [16], was introduced into the testing regime. Fig. 3.2 is a summary of some of the typical UCS results that were obtained from this study. Reference can also be made to Figs. 3.3 and 3.4. It can be noted in all cases that the optimum location for single reinforcement for both geomat and geogrid is 1/5 from the bottom of the specimen for non-stabilized geomaterials. It can further be observed that due to the effect of OPMC stabilization, the contribution of geosynthetic reinforcement is hardly noticeable in the compression zone. In this case, it can therefore be concluded that whereas geosynthetics contribute largely to mobilization and distribution of tensile stresses and containment of tensile straining OPMC contributes immensely to the enhancement of compressive stresses and control of compressive straining [5].

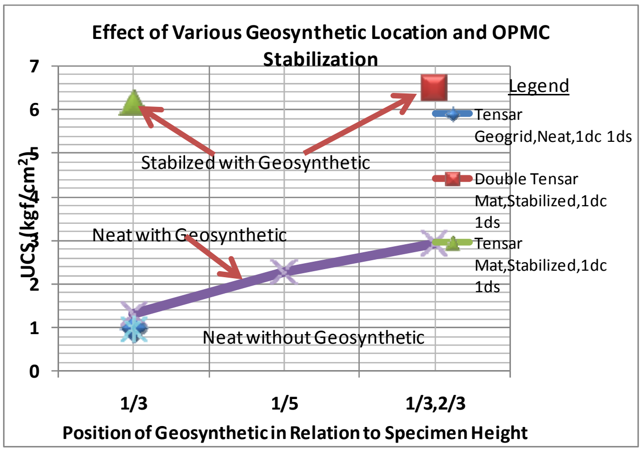

Figure 3.2 Effects of location and stabilization on the geosynthetics-BCS particle interaction as a measure of UCS.

4.2 Angle of Internal Friction

The objective of measuring the angle of internal friction was mainly to correlate the parameter to the interlocking mechanism of the geosynthetic and geomaterial particles. Some typical results are presented in Fig. 3.3.

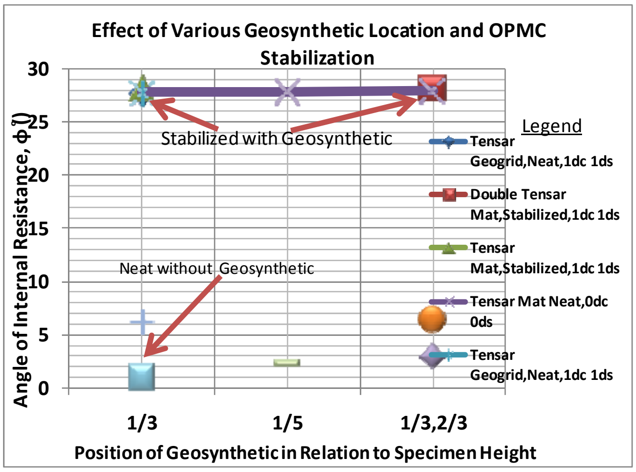

Figure 3.3 Effects of location and stabilization on the geosynthetics-BCS particle interaction as a measure of angle of internal resistance to simulate interlocking mechanisms.

The results in this figure confirm the findings reported in section 3.1. However, it can be noted that: 1) at high moisture contents, BCS exhibits very low internal resistance notwithstanding geosynthetic reinforcement. Consequently, moisture control in BCS is quite essential in all cases; 2) OPMC stabilization contributes significantly to the enhancement of the magnitude of angle of internal friction due mainly to particle agglomeration; and, 3) presumably due to the monolithic state that it assumes after aggregation and agglomeration, the location, mode and type of reinforcement have practically no influence on the OPMC stabilized geomaterials in this case.

4.3 Elastic Stiffness

The elastic stiffness was derived in terms of Young's modulus as depicted in Fig. 3.4. Similar to the cases reported in the preceding sections, the influence of location, mode and type of geosynthetic reinforcement on the magnitude of the elastic stiffness was investigated.

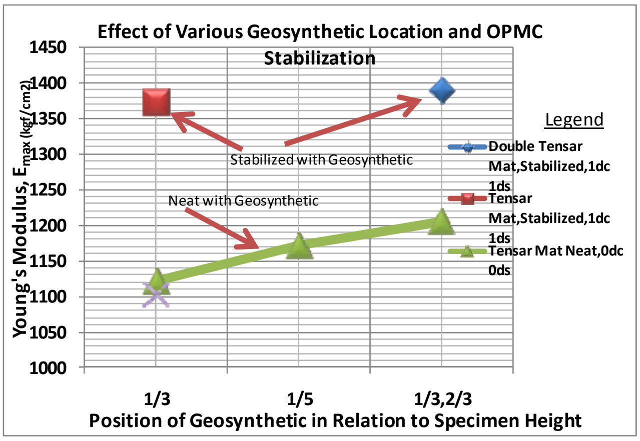

Figure 3.4 Effects of location and stabilization on the geosynthetics-BCS particle interaction as a measure of elastic stiffness.

It can be noted that magnitude of the elastic stiffness is influenced by all the three factors.

4.4 Typical Failure Characteristics

All specimens tested in this Study were loaded to post-failure conditions and the progressive deformation and failure characteristics were carefully monitored, observed and investigated.

Cored specimens were also adopted for purposes of analyzing the progressive deformation and failure modes in comparative terms.

Figure 3.5 Example of typical shear banding and failure characteristics.

Fig. 3.5 shows some typical shear banding and post-failure state of OPMCS plus geomat reinforced specimens.

It can be inferred from this figure that: 1) significant shear banding occurs within the interface of the geomat and the stabilized geomaterial; 2) the section that is sandwiched by the geomats hardly exhibits any shear banding; 3) the specimens exhibit fairly uniform failure characteristics; 4) due to scale effect, failure seems to have been constrained in the compression zone thus the occurrence of failure at the interfaces; 5) due to 4) above, it is imperative to further investigate these characteristics on larger specimens and full-scale experimental sections.

5 CONCLUSIONS

Laboratory investigation was undertaken to study the characteristics of the interaction of geomat and fine grained black cotton soils. In general it was observed that the degree and extent of the geomat-BCS particle interaction is dependent on several factors mainly including particle size, texture, shape, moisture-suction variation and location of embedded geomat relative to the layer thickness defining the active zone, confining pressures and tensile forces.

The following specific conclusions can be made from the results reported in this study.

1. The geotechnical engineering properties of black cotton soils are highly susceptible to moisture-suction variations.
2. The interaction between geomat and black cotton soil is significantly influenced by the location of imbedding, mode and type of geosynthetic reinforcement.
3. Whereas geomats were found to be effective in enhancing the strength and deformation properties of fine grained black cotton soils, the influence of geogrids was minimal in this case.
4. Geosynthetic reinforcement contributes largely to mobilization and distribution of tensile stresses and containment of tensile straining, whilst OPMC stabilization contributes immensely to the enhancement of compressive stresses and control of compressive straining.
5. Where OPMC stabilization contributes significantly to the enhancement of the magnitude of angle of internal friction due mainly to particle agglomeration, the role of geosynthetic reinforcement may appear minimal in the short-term. However, due to scale and short-term loading effects, it is important that full scale experimental testing be undertaken under long-term dynamic loading simulating various environmental changes and conditions.

6 ACKNOWLEDGMENT

The authors wish to acknowledge the Japan International Cooperation Agency (JICA), White Nile Oil Exploration

Company, England, and Kajima Corporation, Japan, for sponsoring most of this research as well as the University of Nairobi, Materials Testing and Research Department, Ministry of Roads, Kenya and Tensar International, England for their technical support. The authors are also indebted to Brian Reddings and Sylvester Kotheki for their efforts in compiling the data, as well as members of the Kenya Geotechnical Society Research Team for their contributions during the entire study. The acknowledgement would be incomplete without recognizing the input of Prof. Bernard Njoroge of the University of Nairobi.

7 REFERENCES

[1] Enni MP, Tatsuoka F, Bathurst RJ, Stevenson PE, Zornberg JG, "Advances in geosynthetics materials and applications for soil reinforcement and environmental protection works", EJGE, Bouquet, 2008.

[2] Tatsuoka F, Koseki J, Tateyama M, "Performance of earth reinforcement structures during the Great Hanshin Earthquake", Special Lecture, Procs. Int. Symp. On Earth Reinforcement, IS Kyushu '96, Balkema, vol. 2, pp 973-1008.

[3] Tatsuoka F, Koseki J, Tateyama M, Munaf Y, Horri N, " Seismic stability against high seismic loads of geosynthetic-reinforced soil retaining structures", Keynote Lecture, 6th Int. Conf. on Geosynthetics, 1998, Atlanta, vol. 1, pp. 103-142.

[4] Zornberg JG, "Discrete framework for limit equilibrium analysis of fibre reinforced soil", geotechnique, 2002, vol. 52, No. 8, pp. 593-604.

[5] Mukabi JN, "The role of enhanced research in geotechnical engineering for pragmatic infrastructure development within Vision 2030", Keynote Lecture, Procs. Int. Conf., IEK, 2007, pp. 11-62.

[6] Mukabi JN, "Case Study Analysis of OPMC improved foundation ground, pavements and geo-structures employing the GECPRO model", to be published in Procs. Of ISSMGE International Symposium on Ground Improvement (IS-GI), Brussels, 2012.

[7] Gichaga FJ, Visweswaranya TG, Sahu BK, "Prediction of swell of black cotton soils in Nairobi", Procs. Int. Symp. On prediction and performance in geotechnical engineering, 1987, Alberta, pp.259-266.

[8] Gono, K., Mukabi, J.N., Koishikawa, K., Hatekayama, R., Feleke G., Demoze W., Zelalem A., "Characterization of some engineering aspects of Black Cotton Soils as pavement foundation materials", Procs of the Int. Civil Engineering Conference on Sustainable development in the 21st Century, Nairobi, 2003.

[9] Mukabi JN, Kotheki S, Ngigi A, Gono K, Njoroge BN, Murunga PA, Sidai V, "Characterization of black cotton soil under static and dynamic loading- Testing and Analyses", Proc. Int. Conf. on GE, 2010, Tunis, pp. 67-77.

[10] Mukabi JN, Kotheki S, Ngigi A, Gono K, Njoroge BN, Murunga PA, Sidai V, "Characterization of black cotton soil under static and dynamic loading- Discussions and Applications", Proc. Int. Conf. on GE, 2010, Tunis, pp. 78-89.

[11] Mukabi, J.N., Murunga P.A, Wambura J.H. & Maina J.N., " Behaviour of con-Aid treated fine grained Kenyan soils". Geotechnics for Developing Africa, Wardle, Blight & Fourie (eds) Balkema, Rotterdam, 1999, ISBN 90 809 082 5.pp.583~519.

[12] Mukabi JN, "Characterization and modeling of various aspects of pre-failure deformation of clayey Geomaterials – Fundamental theories and analyses", Proc. 1st Int. Conf. on GEOMAT, Mie, 2011.

[13] Wekesa S, Mukabi JN, Sidai V, Kotheki S, Okado J, Ogallo J, Amoyo G, Ngigi L, "Quantitative analysis to verify the theory of soil particle agglomeration and its' influence on strength and deformation resistance of geomaterials", Procs. 15th ARC on SMGE, Maputo, 2011, pp. 330-335.

[14] Mukabi JN, "Characterization and modeling of various aspects of pre-failure deformation of clayey Geomaterials – Applications in modeling", Proc. 1st Int. Conf. on GEOMAT, Mie, 2011.

[15] Mukabi JN, "Innovative laboratory and in-situ methods of testing in geotechnical engineering, to be published in the Proc. of the Int. Conf. of the Inst. of Engineers Kenya , Nairobi, 2013.

[16] Kogi SK, Mukabi JN, Ndeda M, Wekesa S, "Analysis of enhanced strength and deformation resistance of some tropical geomaterials through application of in-situ based Stabilization techniques", to be published, Proc. 1st Int. Conf. on GEOMAT, Mie, 2011.

First International Conference on Geotechnique, Construction Materials and Environment, Mie, Japan, Nov.21-23, 2011, ISBN: 978-4-9905958-0-7 C3051

Soil Liquefaction Susceptibility Zoning due to Earthquake Using GIS and Geotechnical Data

Bhuyan Md. Habibullah. Rama Mohan Pokhrel. Jiro Kuwano.
Shinya Tachibana , Department of civil and environmental engineering, Saitama University, Japan.

ABSTRACT: Liquefaction is an earthquake ground failure mechanism that occurs in loose, saturated granular sediments (particularly sand and silty sand) and has caused extensive damage to the ground. Liquefaction potential zoning is the process of estimating the response of soil layers under earthquake excitations and the variation of earthquake characteristics on the ground surface. Ground conditions play important roles in the prediction of hazards caused by earthquake. Thus to evaluate seismic hazards for a wide area, ground formation history along with soil properties must be known. This paper describes the ground conditions and behavior of Satte city as a result of Earthquake. In this paper, Geographical Information System (GIS) is used to obtain soil liquefaction hazard map. Spatial variations of soil properties are estimated from the available borehole locations where SPT N-values, water table depth and grain size distribution are known. Geomorphological land classification components such as mountain and hill, terrace, valley plain, alluvial fan, natural levee, delta, sand dune, reclaimed land, drained land, former river channel etc. are investigated to attain soil liquefaction hazard map. Methodologies of hazard assessment and the resulting maps will be presented. These maps can be useful for assessing the approximate areas affected by hazards and for disaster prevention planning.

Keywords: Liquefaction potential, PGA, GIS, Satte city.

1. INTRODUCTION

Soil liquefaction is one of the most devastating types of geological effects induced by earthquake. It is well recognized that numerous engineering structures have been severely damaged due to liquefaction of the supporting soils during earthquake.
Japan is situated in a seismically very active zone because of its location in marginal areas of the Pacific, Philippine Sea, North American, and Eurasian plates. This is why it is struck by frequent earthquakes. Past Earthquake history in Japan resembles it.
These frequent earthquake ultimately affect not only human being but also social, cultural and mostly financial status of the region. The 1964 Niigata earthquake and 1995 Kobe earthquake were the most destructive liquefaction effects observed in Japan [1]. However, at most recent March 11'2011 Gigantic Tohoku Pacific Earthquake was the strongest to hit Japan and one of the top five largest earthquakes in the world since seismological record-keeping began. It was followed by a tsunami with waves of up to 10 m. The disaster left thousands dead and inflicted extensive material damage to buildings and infrastructure that led to significant accidents at four major nuclear power stations and 4,460 people missing.
The Satte city of Saitama Prefecture is targeted as a case study in this paper. Saitama Prefecture has been affected by several destroying earthquakes of magnitudes greater than eight in the past times. The great Kanto Earthquake of magnitude 8.3 in 1923 hit this area which was the latest great one before March 11'2011 Gigantic Tohoku Pacific Earthquake. The great Kanto Earthquake devastated Tokyo, the port city of Yokohama, Surrounding prefectures of Saitama, Chiba, Kanagawa, and Shizuoka, and caused widespread damage throughout the Kanto region.
Among the various geomorphological units, the reclaimed land, drained land, river channel, lowland between sand dunes or bars, marginal part of sand dune, natural levee and banking area in swampy lowland are most susceptible to liquefaction [2]. From the Satte city geological map in Fig.1, it is observed that this city is built up in lowland area. Yellow color shows natural levee, an elongate embankment compounded of sand and silt and deposited along both banks of a river channel comprises some major area of the city. Moreover, river plain and old river plain consist of almost the rest of the city.
Around 50 borehole points of Satte city are considered for this research work. Borehole data analyses are done in Excel for different PGA and Liquefaction potential Index refer to (6) is found from Excel calculation at final stage. These values are given as input in GIS according to corresponding latitude and longitude of borehole points and liquefaction potential map are originated accordingly. Finally, the obtained liquefaction potential map are evaluated with recent March 11'2011 Gigantic Tohoku Pacific Earthquake liquefaction history.

1.1 Study area

According to April 1, 2011, the Satte city has an estimated population of 54,444, with household number is 21,449 and the density of 1,603.658 persons per km². The total area is 33.95 km². The city was founded on October 1, 1986. The city is located at 36°04′30″N and 139°43′45″E. Average altitude of the city is 9 meter. The city is almost downstream of Tone River. It is at Saitama prefecture in Kanto region and 43 km from Tokyo at N-W corner.
At March 11'2011 Gigantic Tohoku Pacific Earthquake, the highest PGA observed 3.0 g (USGS 2011) [3] in Japan. However, at Satte City of Saitama Prefecture, the observed PGA was 0.3 g [4]. In this paper, the liquefaction potential has been calculated by using 0.15 g and 0.3 g PGA for Satte city.

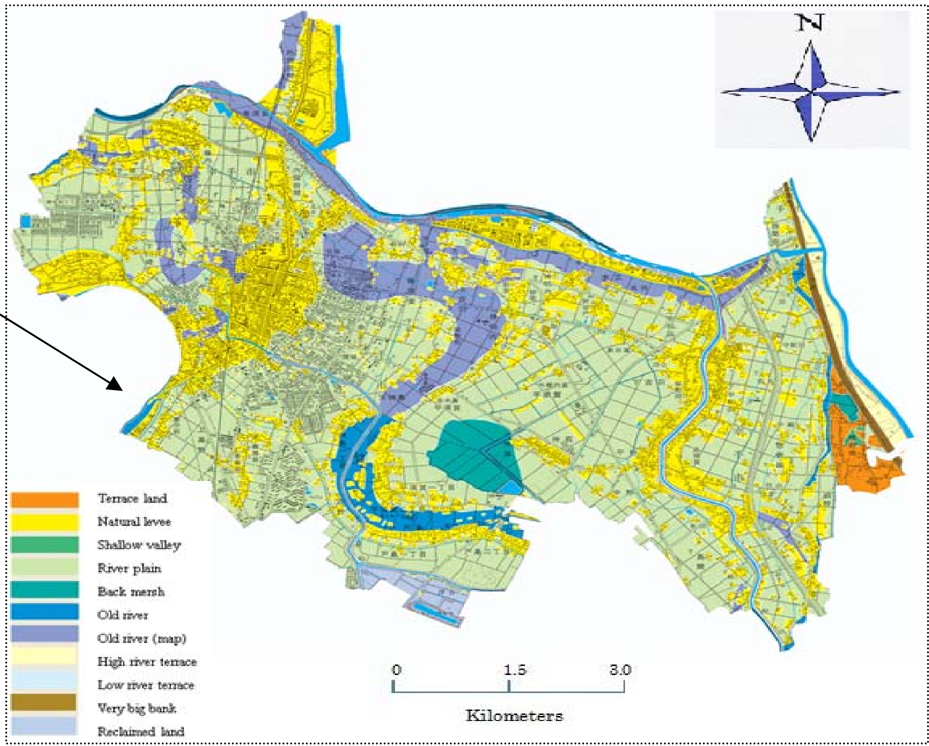

Fig.1 Satte city Geological Map

2 METHODOLOGY

Liquefaction potential for Satte city is evaluated by using the geotechnical data as type of soil, SPT N-value, depth of water table, mean grain size and unit weight of soil. These geotechnical data were collected from subsoil investigation reports (borehole log) as shown in Fig. 3. The borehole data in the study area were collected from different depths ranging from 10 m to 50 m below ground surface. However, in this study, borehole data parameters are considered up to 20m from ground surface. It is considered that no liquefaction affect on ground for soil properties below 20m depth.

According to [5], an ability to resist the liquefaction of a soil element at an arbitrary depth may be expressed by the liquefaction resistance factor (F_L) identified by the following equation

$$F_L = \frac{R}{L} \tag{1}$$

When the factor F_L at a certain soil is less than 1.0, we evaluated that the soil liquefies during earthquake.
In equation (1), R is the in situ resistance or undrained cyclic strength of a soil element to dynamic loads during earthquakes. The value of R is determined by the following equations based on mean particle diameter (D_{50}) as follows:

for 0.04mm $\leq D_{50} \leq$ 0.6mm

$$R = 0.0882\sqrt{\frac{N}{\sigma v`+0.7}} + 0.225\log_{10}\frac{0.35}{D_{50}} \tag{2}$$

for 0.6 mm $\leq D_{50} \leq$ 1.5 mm

$$R = 0.0882\sqrt{\frac{N}{\sigma v`+0.7}} - 0.05 \tag{3}$$

Where N is the number of blows of the standard penetration test, $\sigma v`$ is the effective overburden pressure (in kgf/cm^2) and D_{50} is the mean particle diameter (in mm) illustrated in Table 1.

Due to seismic motion, the dynamic load induced in the soil element can be estimated by the following equation:

$$L = \frac{\Gamma_{\max}}{\sigma v`} = \frac{\alpha_{s\max}}{g}\frac{\sigma v}{\sigma v`} r_d \tag{4}$$

Where $\Gamma_{\max}$ is the maximum shear stress (in kgf/cm^2), $\alpha_{s\max}$ is the maximum acceleration at the ground surface (in gals), g is the acceleration due to gravity (=980 gals), σv is the total overburden pressure (in kgf/cm^2), and r_d is the reduction factor of dynamic shear stress to account for the deformation of the ground. Iwasaki et al. proposed the following equation of r_d from a number of seismic response analyses of the ground:

$$r_d = 1.0 - 0.015Z \tag{5}$$

Where Z is the depth in meters.

It is evident that the damage to foundations of structure due to soil liquefaction is considerably affected by the severity of liquefaction. An index of liquefaction potential, P_L, can be introduced to express the severity of liquefaction as follows:

$$P_L = \int_0^{20} F \cdot W(Z)dZ \qquad (6)$$

Where F = 1.0 $-$ F_L for $F_L \leq 1.0$, F= 0 for $F_L > 1.0$ and W (z) =10 $-$ 0.5Z (Z in meters) demonstrated in Fig. (2). For the case of F_L = 0.0 for the entire range from Z= 0 to 20meters, P_L becomes 100, and for the case of $F_L \geq 1.0$ for the entire range from Z= 0 to 20meters, P_L becomes 0.

Liquefaction potential calculation Excel sheet sample is attached herewith in Table 2. Stress at every 1m is calculated based upon soil type and average density and the following overburden stress is calculated. Based upon the depth of water level from ground, pore water pressure is calculated and effective stress is found subtracting pore water pressure from overburden pressure. Subsequent that, reduction factor for dynamic shear stress r_d is considered based on depth according to (5). Afterward the in situ resistance of soil R is considered conferring (2) or (3) based on mean particle diameter attached in Table 1. In next step, dynamic load induced in the soil element by seismic motion, L is intended according to (4). Finally an ability to resist liquefaction F_L and Liquefaction potential index P_L is calculated according to (1) and (6) respectively.

Liquefaction potential Index, P_L values of borehole data are plotted in GIS for 150 gal and Fig. 4 is the representation of that. This zoning map shows that most of the area has low risk for liquefaction according to guideline proposed by [5]. The rest 30% of the borehole points show high risk of liquefaction.

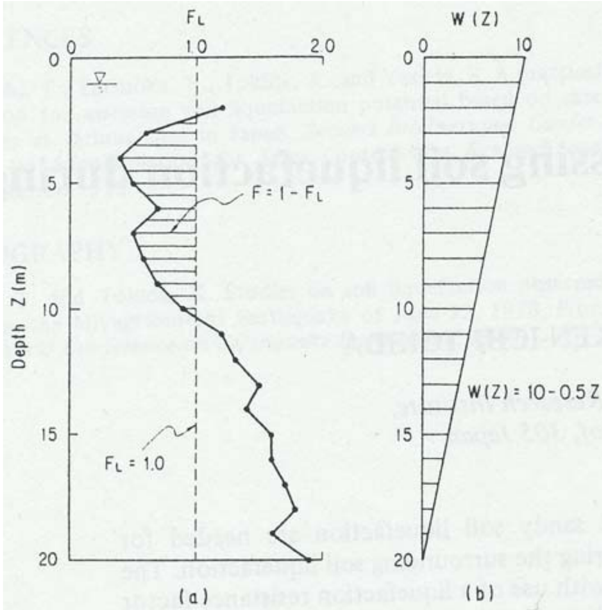

Fig. 2 Definition of P_L

Table 1 Average values of the Unit Weights and Mean particle Diameters of Different Type of Soil.(This table was used only when these values were not tested) [5]

Soil Type	Unit Weight (t/m3)	Mean Particle Diameter, D_{50} (mm)
Surface soil	1.7	0.02
Silt	1.75	0.025
Sandy Silt	1.8	0.04
Silty Sand	1.8	0.07
Very fine Sand	1.85	0.1
Fine Sand	1.95	0.15
Medium Sand	2.0	0.35
Coarse Sand	2.0	0.6
Gravel	2.1	2.0

Table 2: Calculation of Liguefaction Potential Value for one borehole of PGA 300 gal

Depth(m)	Soil Type	Avg. Density	g	Stress,1m	Ovd. Pres.	D fr. WT	Pore Pres.	Eff. stress	kgf/cm^2	N	rd	R	PGA	L	FL	IL
1.3	surface soil	1.7	9.8	16.66	21.658	0	0	21.658	0.21879	4	0.981	0.4637	300	0.3002	1.5449	0
2.3	silt	1.7	9.8	16.66	38.318	0.15	1.47	36.848	0.37224	1.7	0.966	0.368	300	0.3074	1.1972	0
3.3	sand and silt	1.7	9.8	16.66	54.978	1.15	11.27	43.708	0.44154	5	0.951	0.4425	300	0.366	1.2089	0
4.3	silt	1.7	9.8	16.66	71.638	2.15	21.07	50.568	0.51084	0	0.936	0.2579	300	0.4057	0.6356	2.8603
5.3	silt	1.6	9.8	15.68	87.318	3.15	30.87	56.448	0.57024	0	0.921	0.2579	300	0.4359	0.5916	3.0016
6.3	clayey silt	1.7	9.8	16.66	103.978	4.15	40.67	63.308	0.63954	0	0.906	0.2579	300	0.4553	0.5664	2.9699
7.3	clayey silt	1.7	9.8	16.66	120.638	5.15	50.47	70.168	0.70884	0	0.891	0.2579	300	0.4687	0.5502	2.8561
8.3	clayey silt	1.7	9.8	16.66	137.298	6.15	60.27	77.028	0.77814	0	0.876	0.2579	300	0.4777	0.5398	2.6921
9.3	clayey silt	1.7	9.8	16.66	153.958	7.15	70.07	83.888	0.84744	0	0.861	0.2579	300	0.4834	0.5334	2.4962
10.3	sandy silt	1.7	9.8	16.66	170.618	8.15	79.87	90.748	0.91674	0	0.846	0.212	300	0.4866	0.4356	2.7376
11.3	sandy silt	1.7	9.8	16.66	187.278	9.15	89.67	97.608	0.98604	0	0.831	0.212	300	0.4878	0.4345	2.4599
12.3	sandy silt	1.7	9.8	16.66	203.938	10.15	99.47	104.468	1.05534	0	0.816	0.212	300	0.4873	0.4349	2.1756
13.3	sandy silt	1.7	9.8	16.66	220.598	11.15	109.27	111.328	1.12464	0	0.801	0.212	300	0.4856	0.4365	1.8877
14.3	sandy silt	1.7	9.8	16.66	237.258	12.15	119.07	118.188	1.19394	0	0.786	0.212	300	0.4827	0.4391	1.5986
15.3	sandy silt	1.7	9.8	16.66	253.918	13.15	128.87	125.048	1.26323	0	0.771	0.212	300	0.4789	0.4425	1.31
16.3	silt	1.7	9.8	16.66	270.578	14.15	138.67	131.908	1.33253	0	0.756	0.2579	300	0.4744	0.5436	0.8444
17.3	silt	1.7	9.8	16.66	287.238	15.15	148.47	138.768	1.40183	0	0.741	0.2579	300	0.4692	0.5496	0.608
18.3	silt	1.7	9.8	16.66	303.898	16.15	158.27	145.628	1.47113	0	0.726	0.2579	300	0.4635	0.5564	0.377
19.3	silt	1.7	9.8	16.66	320.558	17.15	168.07	152.488	1.54043	0	0.711	0.2579	300	0.4572	0.564	0.1526
20	silt	1.7	9.8	16.66	337.218	17.85	174.93	162.288	1.63943	0	0.7	0.2579	300	0.4453	0.5792	0
																31

The following guideline proposed by [5] is used to assess the liquefaction potential.

$P_L = 0$: Liquefaction risk is very low

$0 < P_L \le 5$: Liquefaction risk is low

$5 < P_L \le 15$: Liquefaction risk is high

$15 < P_L$: Liquefaction risk is very high

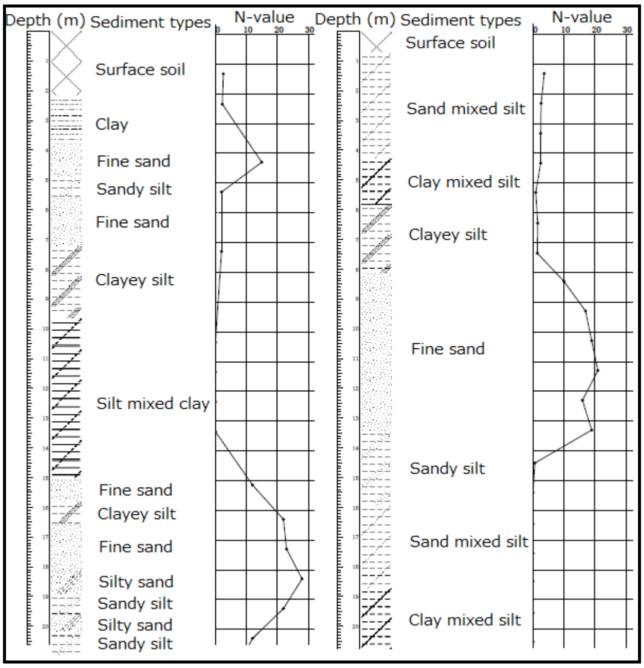

Fig. 3 Typical borehole log of Satte city

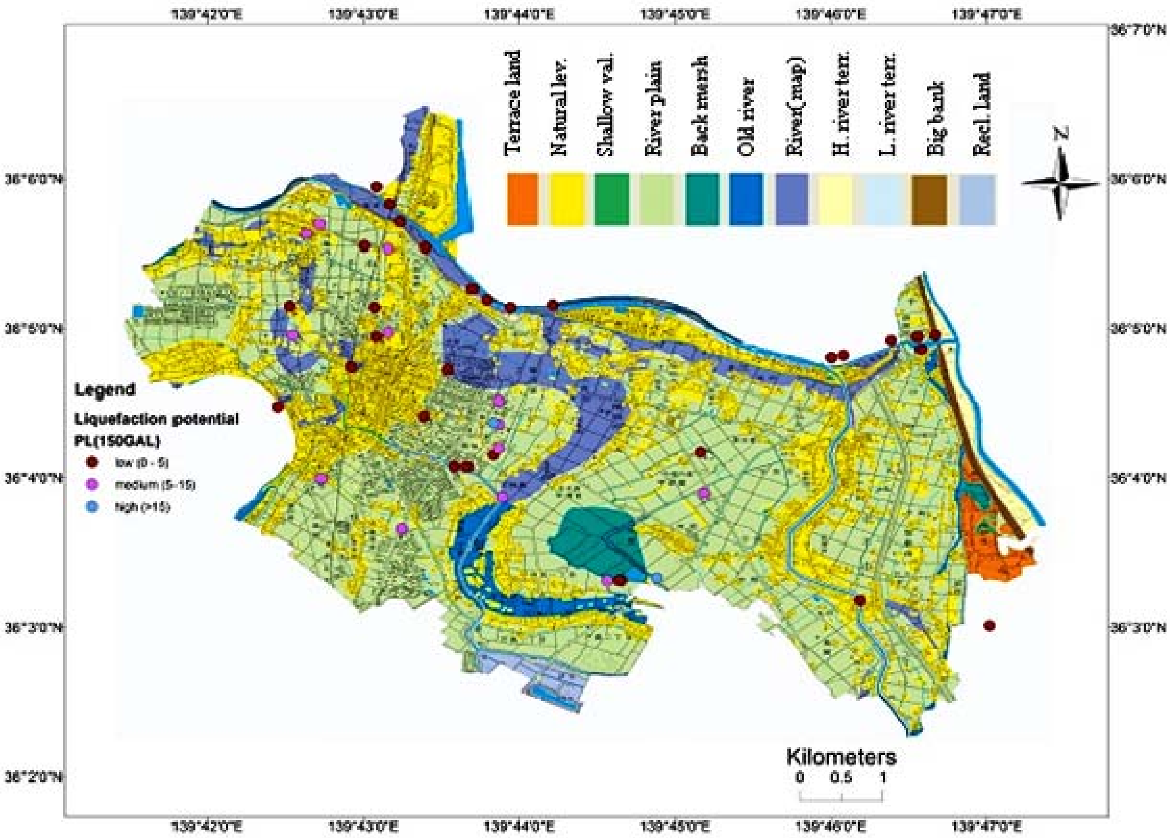

Fig. 4 Liquefaction Potential at borehole locations of Satte city at PGA 150 gal

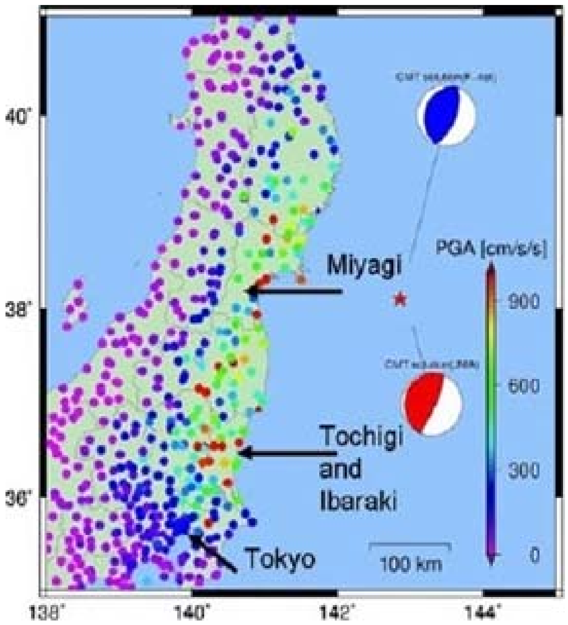

Fig. 5 Distribution of peak ground acceleration provided by NIED, ERI (The University of Tokyo), AIST, and PARI

The distribution of peak ground acceleration (PGA) in Fig. 5 implies that the rupture process during the earthquake was not uniform, and contained several asperities radiating strong ground motions. Another point to note is that Tokyo and its surrounding area near the bottom of the Fig. 5 were subjected to strong shaking. Therefore, damage occurred at many places therein. Moreover, according to latitude and longitude of Satte city (36°04′30″N and 139°43′45″E), it is observed that Satte city of Saitama Prefecture faces 300 gal of PGA (Fig. 5) during the recent March 11’2011 Gigantic Tohoku Pacific Earthquake.

According to Fig. 5, the observed PGA (300 gal) for Satte city is applied in GIS to observe liquefaction and it is observed that all the borehole points show high to very liquefaction values ranges from 7 to 51 as shown in Fig. 6. Satte and Kuki city sites are visited just after the March 11’2011 Gigantic Tohoku Pacific Earthquake. Sand boiling through the ground and paved road, house and electric post tilting, manholes coming up the ground are the consequences of liquefaction which match with the analysis attached in Fig. 6. Moreover, Seismic Damage and Liquefaction history Map at March 11’2011 Tohoku Pacific Earthquake attached in Fig. 7 evaluates high to very high risk of liquefaction.

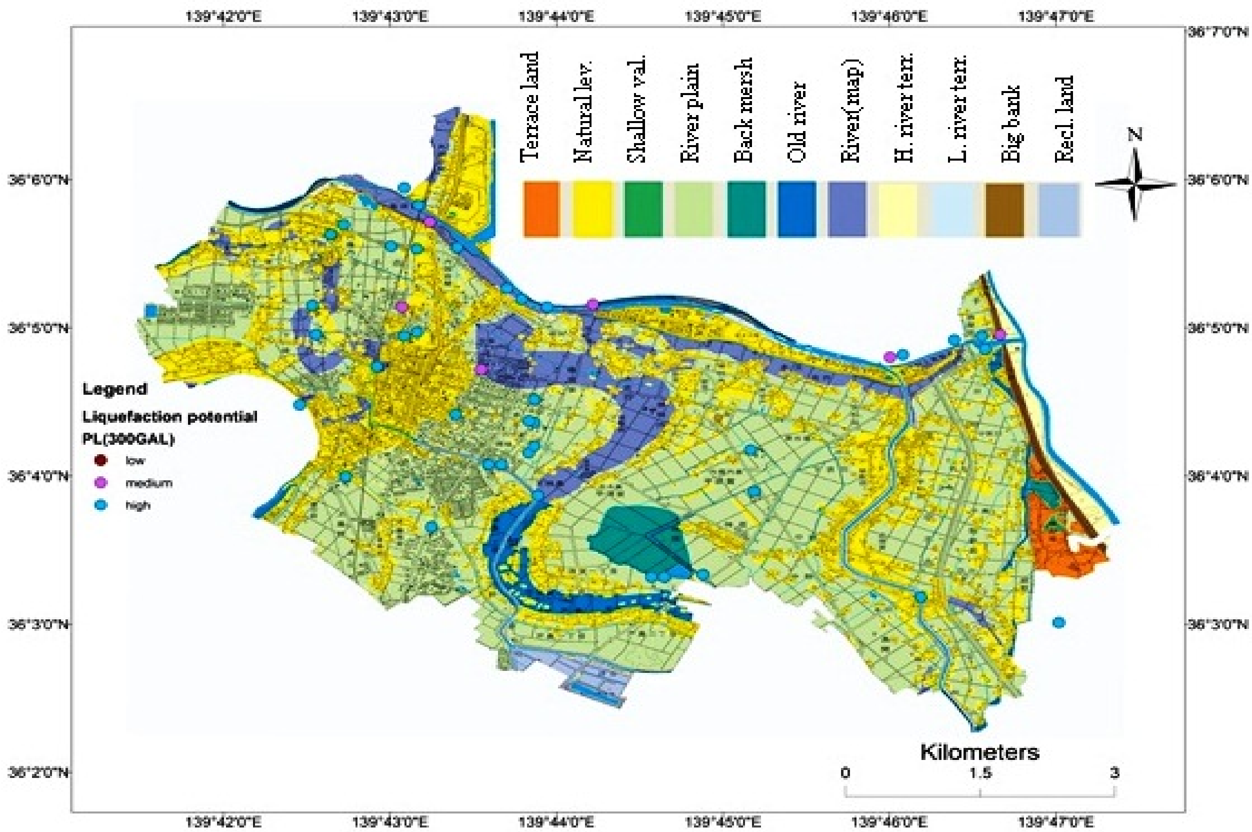

Fig. 6 Liquefaction Potential at borehole locations of Satte city at PGA 300 gal

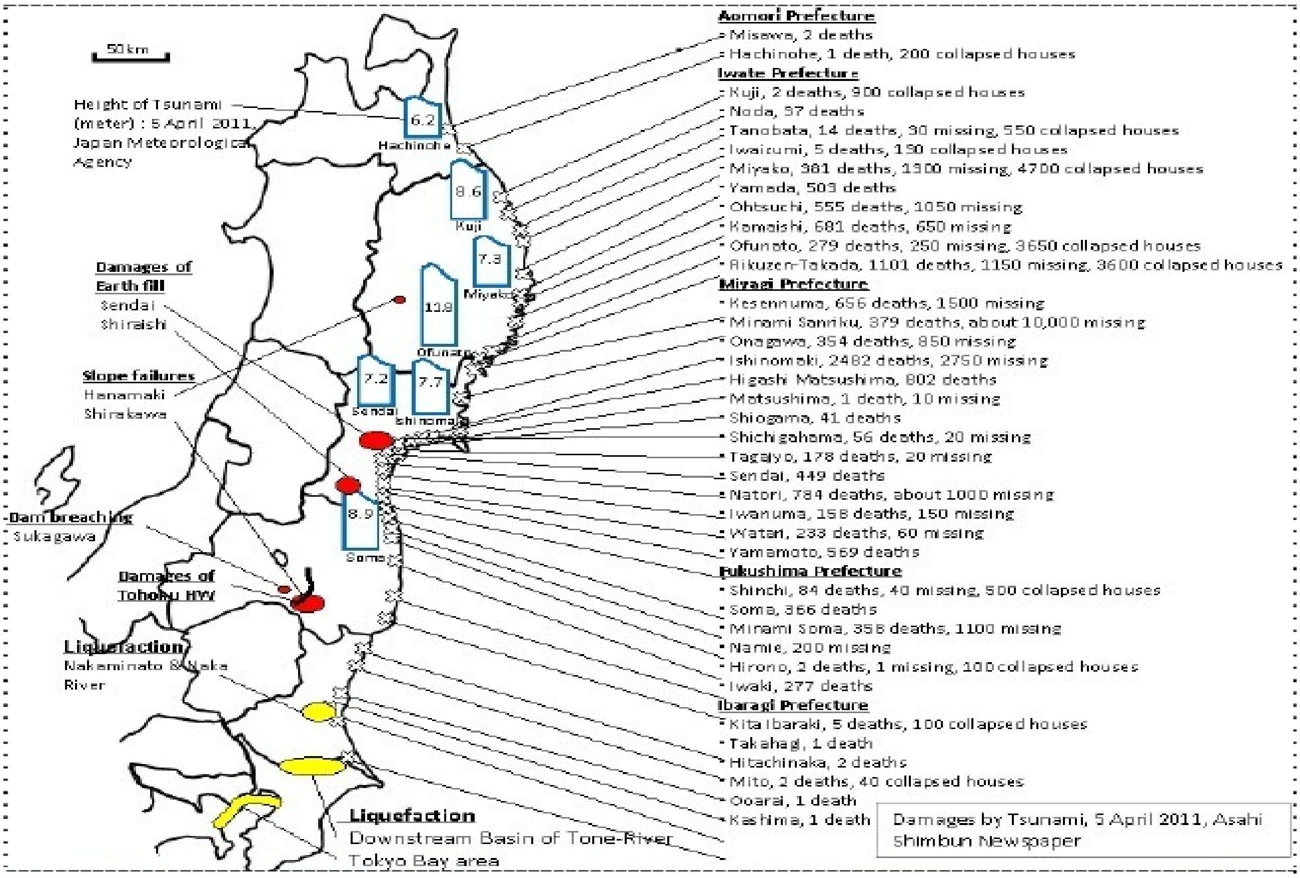

Fig. 7 Seismic Damage and Liquefaction history map at March 11'2011 Tohoku Pacific Earthquake [3]

3 CONCLUSION

Geotechnical problems are made up of liquefaction in foundations and associated ground deformations. Due to damage effect, the post-earthquake response and restoration works have been made difficult and delayed. In this paper, around 50 borehole data are analyzed to draw liquefaction potential map for Satte city. In case of 150 Gal PGA, the borehole points display low to medium risk for liquefaction whereas for 300 Gal PGA, the borehole points display high to very high risk for liquefaction which is a representation of recent 2011 Tohoku Pacific Earthquake. These features have not been considered in the conventional design philosophy and should be discussed from now on. Geotechnical Damage due to the 2011 Christchurch, New Zealand Earthquake and 2011 Tohoku Pacific Earthquake in Japan prompts us considering this true fact. People are now aware of ground surface and this is why geotechnical engineers need to work hard now a days. These maps can be useful for assessing the approximate areas affected by hazards and for disaster prevention planning.

4 ACKNOWLEDGMENT

The first author acknowledges to the Asian Development Bank (ADB)-JSP for its support by providing scholarship for this research work.

5 REFERENCES

[1] Pokhrel, R.M., Kuwano, J., Tachibana,S., "Liquefaction hazard zonation mapping of the Saitama City, Japan," Journal of Nepal Geotechnical Society, vol. 40, 2010, pp. 69-76

[2] Kotoda, K., Wakamatsu, K., and Oya, M., "Mapping Liquefaction Potential based on Geomorphological land classification," in Proceedings of Ninth World Conference on Earthquake Engineering, August 2-9,1988, Tokyo-Kyoto, JAPAN(Vol. III).

[3] http://earthquake.usgs.gov/earthquakes/eqinthenews/2011/usc0001xgp

[4] Towhata et al., "Earthquake News on Gigantic Tohoku Pacific Earthquake in Japan,"April'2011, ISSMGE Bulletin, Volume 5, 2011, Issue2, page 46-66.

[5] Iwasaki, T., Arakawa, T., Todika, K., "Simplified Procedure for assessing Soil Liquefaction during Earthquakes," in Proc. International Conference on Soil Dynamics and Earthquake Engineering, 1981

First International Conference on Geotechnique, Construction Materials and Environment, Mie, Japan, Nov.21-23, 2011, ISBN: 978-4-9905958-0-7 C3051

Evaluation on the Results of Multistage Shear Test

Hormdee D., Kaikeerati N., Department of Civil Engineering, Khon Kaen University, Thailand

ABSTRACT: Shear strength is a very important soil property to determine the stability of foundations, retaining walls, slopes and embankments. In order to solve those problems in geotechnical engineering, shear strengths are usually determined from laboratory tests performed on specimens prepared by compaction in the laboratory or undisturbed samples obtained from exploratory soil borings. In order to determine the shear strength parameters, the soil specimens are required at least 3 identical samples. To eliminate the effects of soil variability on the result, multistage testing is used to maximize the amount of shear strength information that can be obtained from only one specimen by using several confining pressures. Test results demonstrate that is possible and convenient to perform multistage shear test on compacted soil to measure shear strength. The direct shear tests were carried out using the multistage technique and the results are quite well comparable to those of traditional shear tests.

Keywords: Multistage Test, Shear Strength Parameters, Hyperbolic Stress-Strain Relationship, Direct Shear Test

1. INTRODUCTION

The most widely used laboratory equipments for investigating the strength and deformation behavior of soils is either the triaxial or direct shear apparatus. The apparatus is versatile and can be used for the measurement of many parameters, including shear strength characteristics, consolidation characteristics and the permeability of soil. Its key features include facilities for the control of the magnitude (but not direction) of the principal stresses, the control of drainage, and the measurement of pore pressures [1].

In traditional tests, each specimen undergoes a phase of consolidation and shearing and thus supplies a single stress versus strain trend and of course only one state of stress at failure. A series of three or more specimens, consolidated at various stress levels, supplies an ensemble of stress data allowing identification of a failure envelope and thus shear strength parameters. Sometimes it is impossible to have a set of homogeneous or identical re-compacted specimens, for economic reasons or because some soils formations may be difficult to sample. In such circumstances the multistage shear testing technique appears to be an attractive alternative. This technique has been successfully used to determine shear strength parameters by just one sample.

Kenney and Watson [2] conducted multistage undrained tests (MCU). They report reasonable consistent between c' and ϕ' obtained from MCU tests with the values obtained by using conventional undrained tests (CCU). MCU tests were conducted by consolidating and loading it until about failure strain, then repeating the process twice again with two higher cell pressure. The total strain that the sample was subjected to during MCU test amounted to about 25%.

To avoid subjecting the sample of high strain, Sridharan and Narasimha Rao [3] investigated a new approach to multistage testing, which made use of Kondner's [4] hyperbolic stress-strain relationship for predicting the state of stress at failure from the stress-strain and pore-water pressure-strain curves of soils can be approximated by rectangular hyperbola, for which the equation is shown in Eq.1.

$$\varepsilon_s/\tau = a + b\varepsilon_s \quad (1)$$

where:

ε_s = shear strain
τ = shear stress
a = y-interception of ε_s/τ and ε_s relationship
= $1/E_i$ (from asymptotic value)
b = slope of ε_s/τ and ε_s relationship
= $1/\tau_f$ (from asymptotic value)
E_i = initial tangent modulus and
τ_f = failure shear strength, with the normal stress, σ_n

Similarly for predicting pore-water pressure (u), Sridharan and Narasimha Rao [3] used Eq.2.

$$\varepsilon/u = a_u + b_u\,\varepsilon \quad (2)$$

where:

a_u = y-interception of ε/u and ε relationship
b_u = slope of ε/u and ε relationship
= $1/u_f$. and
u_f = pore-water pressure at failure

The multistage test suggested by Sridharan and Narasimha Rao [3] referred to as NMCU tests consisted of: (1) assessing whether the soil lends itself to extrapolation using Kondner's method, (2) consolidating the sample to a cell pressure and shearing it to 2 to 4% axial strain, (3) repeating the consolidation-shear sequence at two higher cell pressure, (4) using Kondner's method to predict failure stressed at each cell pressure, and (5) using the results for all three cell pressure together to determine shear strength parameters. Sridharan and Narasimha Rao [3] report success using this method, however using Kondner's method the value of τ_{ult} and u_f predicted were higher than actual. Sridharan and Narasimha Rao [5] had suggested that in extrapolating data using Kondner's method better prediction is possible if one extrapolates only to a finite value of strain using (1) and (2) rather than to the asymptotic value of infinite strain. They had tentatively suggested using a strain of 15%

Even though the multistage testing technique has been used with some success in the past to determine shear strength parameters, to define undrained shear strength [6],[7] or effective shear strength both in unsaturated [8],[9] and saturated soils [3],[10] in triaxial apparatus and in direct shear apparatus [11] but still lacking in concerning and carrying out on the drain condition of testing especially in direct shear apparatus.

In this paper, a series of single and multistage testing is performed using direct shear apparatus as drained condition to investigate on the shear strength parameters of the single stage-multistage comparative study. The preparation of the soil specimens is controlled as the field condition by using field dry density and optimum moisture content (OMC).

2. METHODOLOGY

2.1 Preparation of Specimens

The red Khon Kaen loess soil sample was collected as disturbed sample at a depth of 3-4 m. The index properties and compaction characteristics are shown in Table.1.

Table.1 Properties of soil

Property	Khon Kaen loess soil
Specific gravity (G_s)	2.64
Liquid limit (LL)	21.2%
Plastic limit (PL)	14.3%
Unified Soil Classification System (USCS)	SM-SC
OMC	9.25 %
$\gamma_{d\ max}$	2.02 g/cm^3
$\gamma_{d,field}$	1.81 g/cm^3

The experimental program was a parametrical study aiming at studying the effect of important reconstituted conditions of soil such as initial water content, initial dry density on shear strength parameters. As using disturbed samples, they were prepared in 'identical' fashion by controlling initial water content as OMC and initial dry density as the field dry density (that is about 89.6% of compaction) by using hydraulic jack slowly pressing to 60 mm in squared width and 20 mm in height.

2.2 Single Stage Procedure

To perform the shear strength testing, a two-stage loading procedure was used in each of these tests. In the first stage, a consolidation was applied. In the direct shear test, the consolidation was applied by applying a vertical load to the horizontal plane, becoming the eventual failure plane. In traditional tests, each specimen undergone a phase of consolidation and shearing and thus supplied a single stress versus strain trend and of course only one state of stress at failure [7]. A series of 3 or 4 specimens, consolidated at various confining stress levels, supplied an ensemble of stress data allowing identification of a failure envelope and thus shear strength parameters.

In this paper, the series results of single stage testing were carried out in direct shear apparatus to compare with the results of multistage series. Single stage tests were conducted till 8-15% strain on four samples at confining pressures of 100, 200, 300 and 400 kPa. And the loading rate was 0.002% strain per minute for direct shear test as drained condition required.

2.3 Multistage Procedure

A multistage test induces more than one consolidation and shearing on the same soil specimen loaded inside a direct shear box. Specimen preparation and initial test stages of saturation are identical to those of traditional direct shear. Especially the saturation stage in triaxial test, it is required more or less 5 days to gain the value of B (pore pressure) parameter more than 0.9 and to finish the settlement in this process. This method enables substantial homogeneity of the results and appreciable time consuming.

After saturated and consolidated specimen in stage I is finished, in the shearing stage the specimen is sustained to produce a significant amount of shear stress. Then the specimen is released from horizontal stress. To start the next stage, the specimen is subjected to a higher normal stress before the following shearing stage takes place.

In this paper, the strain for each compression stage has been carried up to only 3% in each test. In all cases, the peak value of shear strength are expected for strain values greater than 8%, as is the case of many clayey and silty-clayey soils of medium to low plasticity [7] and also as is the case of many not dense condition of compacted soil. The normal stress and loading rate in multistage test were used the same as a series in single stage test. In the results of direct shear test, the test was conducted to not failure but carried to 3% of strain in each stage, and the ultimate peak values are predicted by making use of Kondner's hypothesis [4].

3 RESULTS AND DISCUSSION

Direct shear tests were carried out in both single stage and multistage test saturated specimens with normal stresses of 100, 200 ,300 and 400 kPa. The single direct shear testing result on saturated condition is shown in Fig.1.

In consideration of the hyperbolic stress-strain relationship, the hyperbolic model represents the nonlinear stress-strain curve of soil using hyperbola. It can be seen that transforming the hyperbolic equation result in a linear relationship between ε_s/τ and ε_s , shown in (1). The validity of Kondner's hypothesis is shown in Fig. 2. The stress dependent stress-strain behavior of soil is represented by varying the initial tangent modulus, E_i, and the failure shear strength, τ_f with the normal stress, σ_n.

These plots do produce straight line relationships and as such indicate that the behavior of soils lends itself to prediction by Kondner's technique. The failure shear stress (τ_f) for single tests have been predicted from asymptotic values and using (1) for failure strains of 10, 15, and 20%.

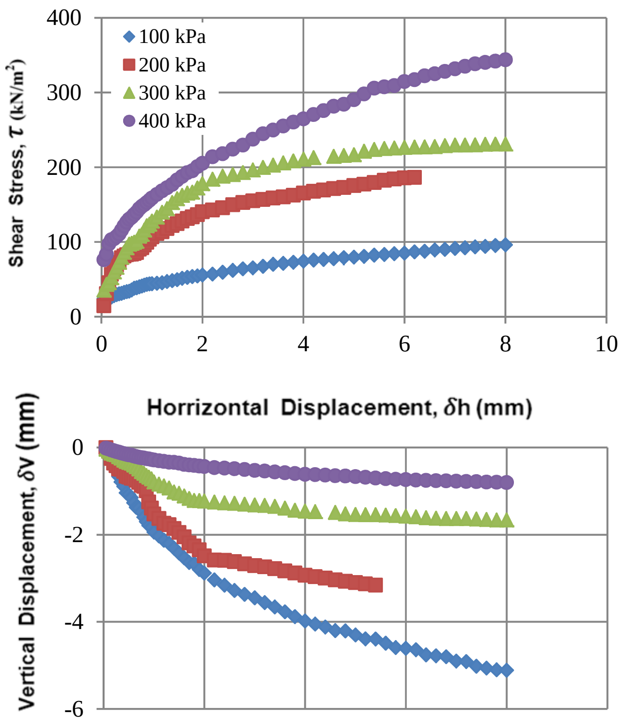

Fig.1 Testing results in single stage direct shear test

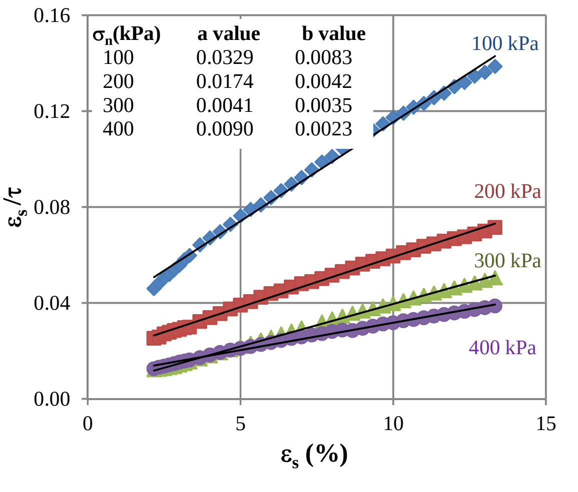

Fig.2 Hyperbolic representation of stress-strain curve in single stage direct shear test

The predicted and experimentally obtained values of τ_f are presented in Table. 2. Also presented in this table is value of percentage agreement, which is the ratio if predicted to experimentally obtained values. A study of Table. 2 shows that the value of τ_f predicted by using ε_s approaching infinity is always higher than experimental values. Agreement with experimental value is better when value of strain used is about 15%.

Since Kondner's technique was found to be valid for Khon Kaen Loess soil, it is possible to conduct the multistage direct shear test to predict failure stresses. Fig.3 presents the plot of ε_s/τ versus ε_s for multistage direct shear test carried up to 3% strain in each stage that are predictably linear Table.3 presents the values of τ_f predicted from asymptotic value. As can be seen from the Fig.4, the predicted results of strength parameters in multistage test are relatively validity by giving the quite lower value of internal friction angle (about 4% of error) with no cohesion. So the prediction of failure stresses using Kondner's relation is nearly perfect when results are extrapolated to a value of finite strain determined by analyzing data of single stage test.

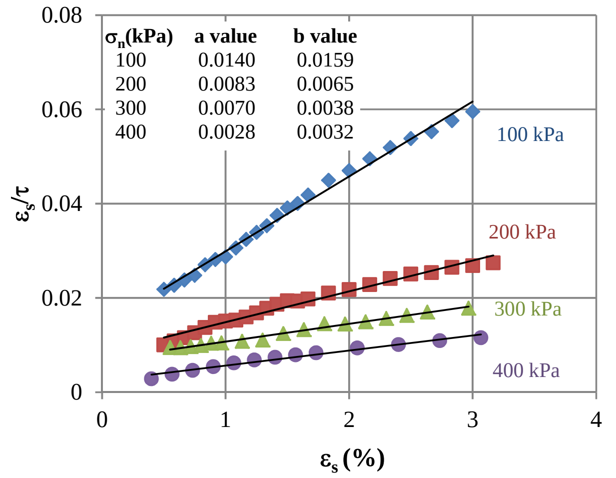

Fig.3 Hyperbolic representation of stress-strain curve in multistage direct shear test

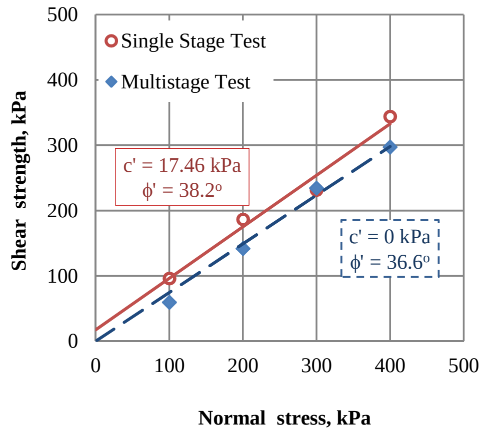

Fig.4 Failure Envelope in Direct Shear Test

4 DISCUSSION AND CONCLUSIONS

Testing results demonstrate that is possible and convenient to perform multistage shear test on compacted soil to measure shear strength. The drained direct shear test was carried out by using the multistage technique and, as shown, the results are quite well comparable to those of traditional shear tests. The proposed multistage shear testing procedure can be used to evaluate the shear strength parameters from a single test.

Table. 2: Predicted and Experimental values of τ_f in single stage direct shear tests.

σ_n, kPa	Experimental Value of τ_f, kPa	Asymptotic Value of 1/b	Percentage Agreement	Predicted Value of τ_f Using (1) for Shear Strain of 10%, kPa	Percentage Agreement	15%, kPa	Percentage Agreement	20%, kPa	Percentage Agreement
100	96.2	120.5	125.3	86.3	89.7	95.3	99.1	100.6	104.6
200	186.5	238.1	127.6	168.4	90.2	186.6	100.0	197.2	105.7
300	231.1	263.2	113.8	226.2	97.9	237.3	102.7	243.3	105.3
400	343.9	434.8	126.4	312.5	90.9	344.8	100.3	363.6	105.7
Average Percentage Agreement			123.3		92.2		100.5		105.3

Table.3: Predicted Values of τ_f for Khon Kaen Loess Soil

σ_n, kPa	Experimental Value of τ at 3% Strain, kPa	Value of τ_f Obtained from Asymptotic Value, kPa	Predicted Value of τ_f Using (1) for Shear Strain of 15%, kPa
100	50.4	62.9	59.4
200	115.3	153.8	141.8
300	166.1	263.2	234.4
400	265.2	312.5	297.0

5 ACKNOWLEDGEMENT

The authors would like to greatly acknowledge the Thailand Research Funding for their sponsorship. The help rendered by senior project's students and other staffs at Department of Civil Engineering, Khon Kaen University in preparing the soil samples is acknowledged.

6 REFERENCES

[1] Head, KM, Manual of Soil Laboratory Testing. Vol.3: Effective Stress Tests. London, UK Pentach Press, 1986.

[2] Kenny, TC and Watson, GH. "Multi-stage Triaxial Test for Determining c' and f' of Saturated Soils," in Proceedings of the 5th International Conference on Soil Mechanics and Foundation Engineering, Vol. 1, Praris, France, 1961, pp. 191-195.

[3] Sridharan, A and Narasimha Rao, S, "A New Approach to Multi-stage Triaxial Test," Journal of Soil Mechanics and Foundation Division, Proceedings of the American Society of Civil Engineer, Vol. 98, No. SM11, Nov. 1972, pp. 1279-1286.

[4] Kondner, RL, "Hyperbolic Stress-Strain Response, Cohesive Soils," Journal of Soil Mechanics and Foundation Division, Proceedings of the American Society of Civil Engineer, Vol. 89, No. SM11, Jan. 1963,pp. 115-143.

[5] Sridharan, A and Narasimha Rao, S, "Hyperbolic Representation of Strenght, Pore Pressure and Volume Changes with Axial Strain in Triaxial Tests," in Proceedings of the Symposium on Strength and Deformation Behavior of Soils, Vol. 1, Bangalore, India, 1972, pp. 33-42.

[6] Anderson, WF, "The Use of Multi-Stage Triaxial Tests to Find the undrained Strength Parameters of Stony Boulder Clay," in Proceedings, Institution of Civil Engineers, Pt. 2, Vol, 57, Thomas Telford Ltd., London, 1974, pp. 367-373.

[7] Soranzo, M, "Results and Interpretation of Multistage Triaxial Compression Test", Advanced Triaxial Testing of Soil and Rock, ASTM STP 977, ASTM, Philadelphia, 1988, pp. 353-362.

[8] De Beer, EE, "The Cell Test", Geotechnique, Vol.2, No. 2, 1950, pp. 162-172.

[9] Ho, DYF and D. G. Fredlund, DG, "A Multi-Stage Triaxial Test for Unsaturated Soils", Geotechnical Testing Journal, Vol. 5, No. 12, 1982, pp. 18-25.

[10] Kenny, TC and Watson, GH "Multiple-Stage Triaxial Tests for Determining c' and ϕ' of Saturated Soils", in Proceedings, Fifth International Conference on Soil Mechanics and Foundation Engineering, Paris, Vol. 1, 1961, pp. 191-195.

[11] Gan, KY and Fredlund, DG, "Multistage Direct Shear Testing of Unsaturated Soils", Geotechnical Testing Journal, Vol. 11, No. 2, 1988, pp. 132-138.

First International Conference on Geotechnique, Construction Materials and Environment, Mie, Japan, Nov.21-23, 2011, ISBN: 978-4-9905958-0-7 C3051

Verification of Effects of Countermeasures for Seepage of River Levees by On-site Monitoring of the Water Level of Levees

Hiroyuki MASUYAMA[1]. Yukiko SAITO[2]. Masanori ISHIHARA[3]. Tetsuya SASAKI[4]. Hirotoshi MORI[5]

1,2,3,4, Soil Mechanics and Dynamics Research Team, PWRI (Public Works Research Institute)

5, Policy Bureau, Ministry of Land, Infrastructure, Transport and Tourism

ABSTRACT: Japan is a country where many floods occur. Therefore, importance is attached to safety with respect to seepage in Japan. There are however, a few cases where the performance of countermeasures has been confirmed at rivers. To verify the effects of countermeasure methods with respect to seepages at rivers, on-site monitoring and three-dimensional seepage flow analyses were executed during this study. The monitoring of landside countermeasures targeted drains. Drains are typical measurements in landsides. The monitoring of waterside countermeasures targeted sheet piles and seepage control sheets.

As a result, the effects of countermeasures were confirmed by on-site monitoring.

Keywords: river levee, on-site monitoring, drain, sheet pile, three-dimensional seepage analysis

1. INTRODUCTION

Improvement of safety with respect to seepage is advanced in order of 1.checks for safety, 2. extraction of weak point portions, 3.selection of countermeasures, 4. construction, 5.monitoring, and 6.maintenance.

It is necessary to prove certainty with respect to the effects of countermeasures for river levees so as to advance their reinforcement. The effects of countermeasures in the cross section are shown in Fig-1.

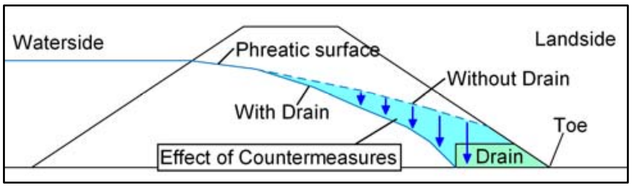

Fig-1 Effect of countermeasures in cross section

It is important to monitor the on-site water levels of river levees. The authors have compiled "The Water level of the levees observation manual" [1], and have observed the water level of river levees on-site. Additionally, Authors have clarified a three-dimensional complex seepage flow of river levees [2]–[5].

Some interesting results are introduced in this study.

2. COUNTERMEASURES TO TARGET

Tab-1 shows the list of targeted countermeasures. Monitoring of landside measures targeted three different drains. Monitoring of waterside measures targeted the seepage control sheets and sheet piles. Fig-2 shows the location map of the targeted site.

Tab-1 List of countermeasures to target

No.	1	2
Measures position	Landside (Drain A)	Landside (Drain B)
Measures Cross Section	Retaining Wall, Drain A, Toe	Toe, Drain B, Retaining Wall
No.	3	4
Measures position	Landside (Drain C)	Waterside (Sheet pile)
Measures Cross Section	Toe, Waterway, Drain C	Seepage Control sheet, Sheet pile

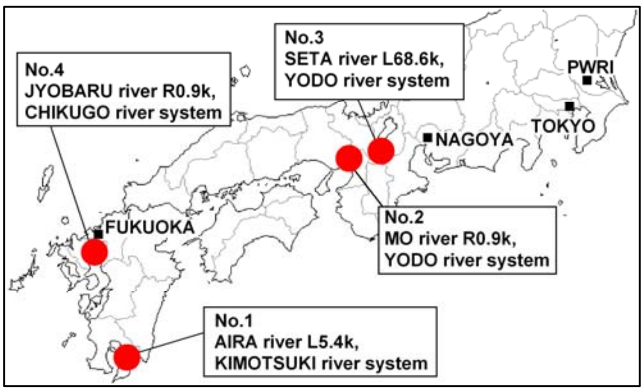

Fig-2 Location map of targeted site

3. OBSERVATION HOLE

An observation hole in the cross section is shown in Fig-3.

Observation holes use hole up dug by boring. A tube is set up in the hole up dug by boring.

The hydraulic pressure type water meter is made to hang in the tube and is set up. The strainer is installed in the vicinity of the water meter. Mud accumulation is installed under the hole.

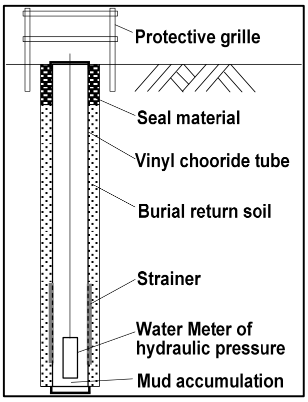

Fig-3 Observation hole in cross section

4. MONITORING OF EFFECT OF LANDSIDE MEASURES (Drain A)

Aira River levees are composed of sandy soil (coefficient of permeability ks=1.0E-5m/s), including Shirasu, which is a pyroclastic flow deposit that is peculiar to the region on the foundation subgrade in the layer of sand. PWRI executed the installation and data observation of the observation hole.

The plan, the geological features profile, and the cross section are shown in Fig-4, 5 and 6. In the monitor section, there is a section where the seepage control sheet is used together with the drain.

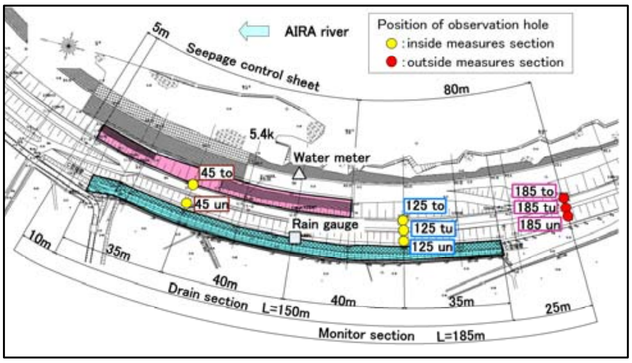

Fig-4 Monitor part in plan

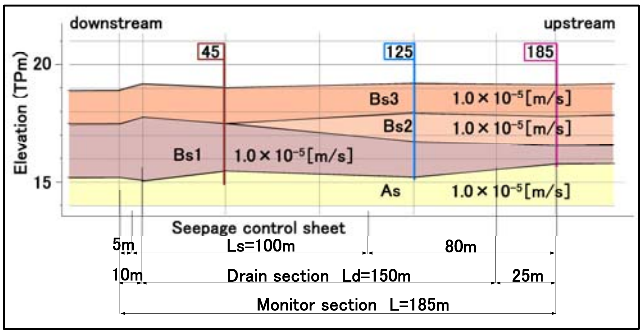

Fig-5 Monitor part in profile (position of levee crown land side shoulder)

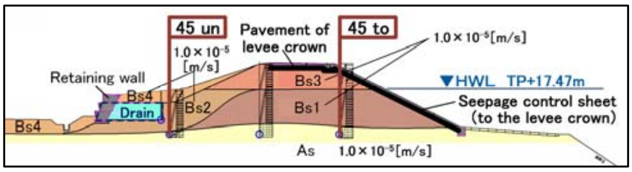

Fig-6 Monitor part in the cross section (section of 5.2k+180m)

Observations were carried out as of August, 2009, and are continuing into August, 2011. The observation frequency of the water level of the levee is made for other periods once every five minutes and once every two minutes during the flood season from June to October. Additionally, water meters of rivers and rain gauges were set up.

Floods with a large influence on the water level of the levee have not occurred at the AIRA River since observations at the beginning of August, 2009. Fig-7 shows the observational results of June 19th, 2010 where water levels rose most than in any other period. Water levels of levees rise as a result of rainfall. The water level of levees in sections with drains is lower than the water level of levees in the section without drains. As a result, the effects of the drain can be confirmed. Continuous monitoring is scheduled for the future. The effects of the drain are confirmed.

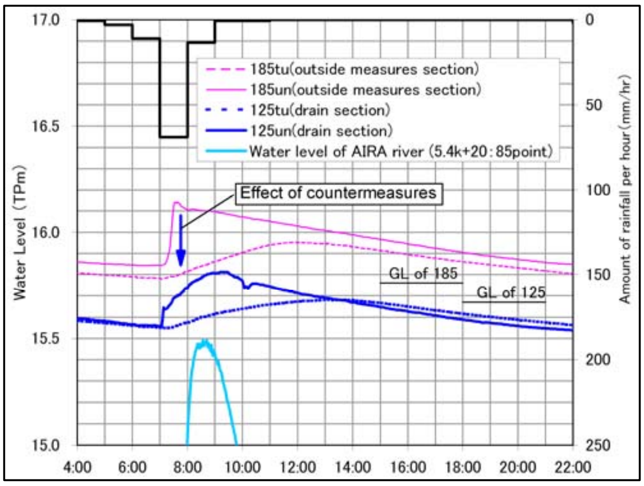

Fig-7 Observational results of water level of the levee on June 19th, 2010

5. THE MONITORING OF EFFECTS OF LANDSIDE MEASURES (Drain B)

The on-site monitoring of drain measures was done in the vicinity of the YODO River water system MO River 0.9k points. Fig-8 shows the plan of the observation hole.

The monitoring results, as shown in Fig-9 and 10, were obtained in the small flood that occurred on July 19th in 2006.

The flood that showed the effect of the drain for the observation period did not occur.

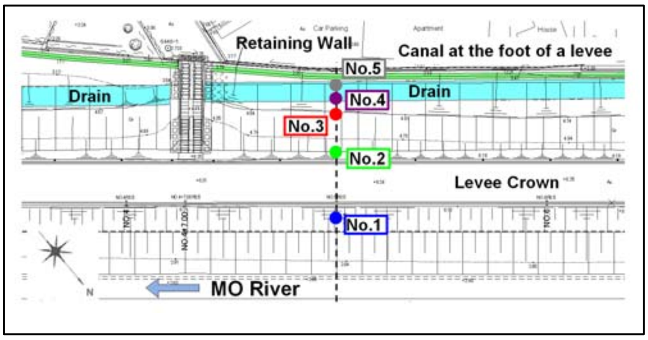

Fig-8 observation hole in plan

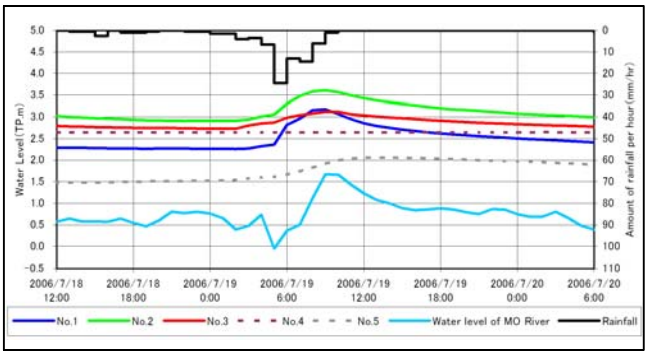

Fig-9 Observational results of water level of the levee and on July 19th, 2006

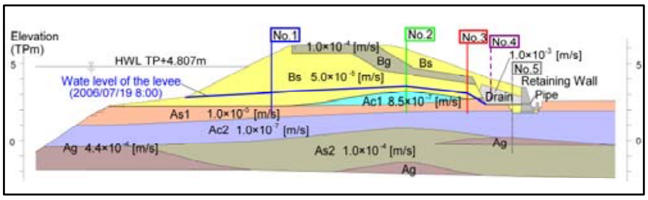

Fig-10 Water level of the levee in the cross section at the monitoring site at 8:00 on July 19th, 2006

The seepage flow analysis on two dimensions was done based on the observational results. Fig-11 shows the analytical model chart. It also analyzed no measures and the effects of measures were verified. Fig-12 shows the effects of measures of the drain that were obtained in the analysis.

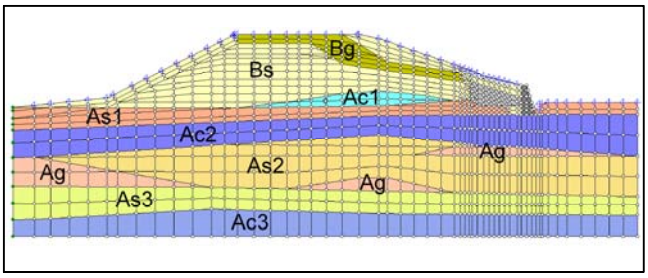

Fig-11 Analytical model chart

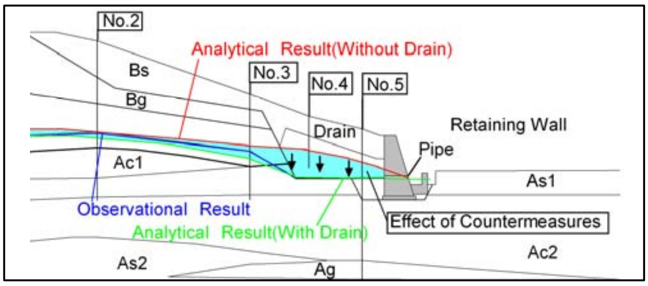

Fig-12 Water level of levee in cross section

6. THE MONITORING OF EFFECTS OF LANDSIDE MEASURES (Drain C)

The on-site monitoring of drain measures was carried out in the vicinity of the YODO River water system at SETA River 68.6k points. Fig-13 shows the plan of the observation hole. Fig-14 shows the levee in cross section.

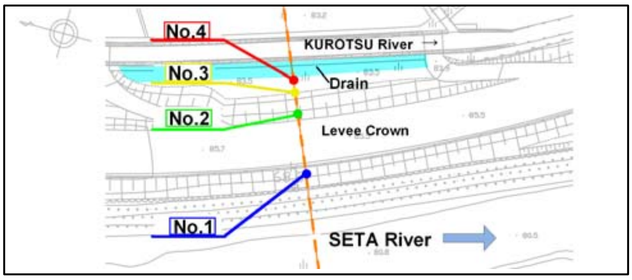

Fig-13 the plan of the observation hole

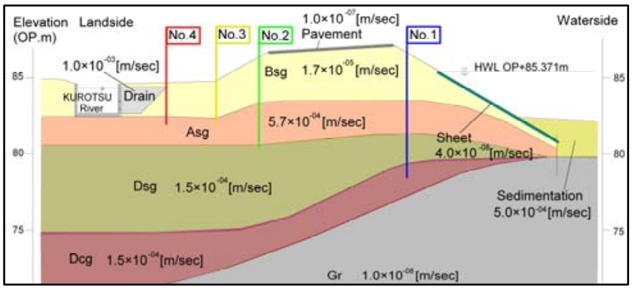

Fig-14 SETA river levee in cross section

When flooded by discharging the SETA River ARAI Weir, the rising of the water level of the levee was generated for the observation period(fig-15).

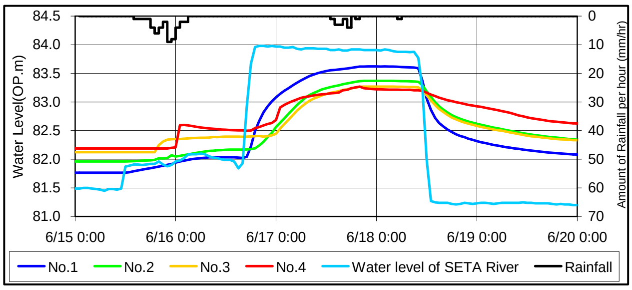

Fig-15 Observational results of the water level of the levee on June 15th - 20th, 2006

The seepage flow analysis on two dimensions was carried out based on observational results. Fig-16 shows the analytical model chart.

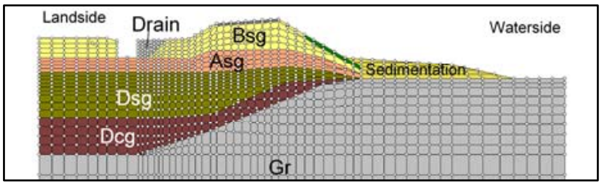

Fig-16 Analytical model chart

It also analyzed no measures. The effects of measures were verified. Fig-17 shows the effect of measures of the drain obtained by the analysis.

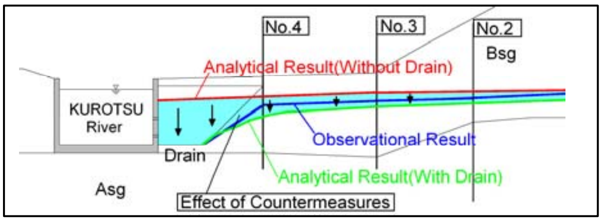

Fig-17 Water level of the levee in the cross section

7. THE MONITORING OF EFFECTS OF WATERSIDE MEASURES (SHEET PILE)

7.1 On-site monitoring

1) Monitoring procedures

The seepage control sheet and sheet pile were set up in the toe of the levees at the JYOBARU River. It was set it up in the 80m section. The plan, the geological features profile, and the representative crossing section are shown in Fig-18-20. The JYOBARU River levees are composed of decomposed granite soil (coefficient of permeability ks=7.0E-4m/s of Bs1 and coefficient of permeability ks=5.0E-5m/s of Bs2) that weathers the Mesozoic granite on the foundation subgrade of ARIAKE clay that piled up thickly.

Since October, 2009, observation data has been collected so far for one year or more. This is continued in August, 2009. The observation frequency of the water level of the levee is once an hour. Additionally, Public Works Research Institute set up a water meter for the river and a rain gauge in October, 2010, beginning observations.

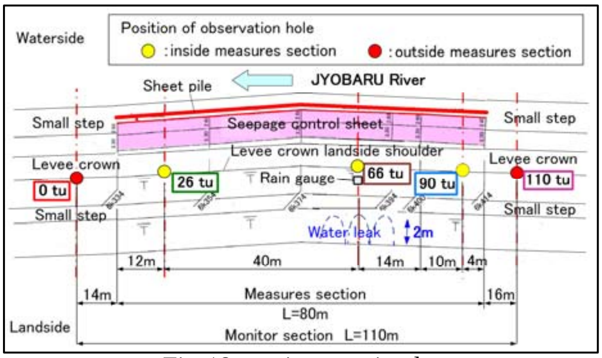

Fig-18 monitor part in plan

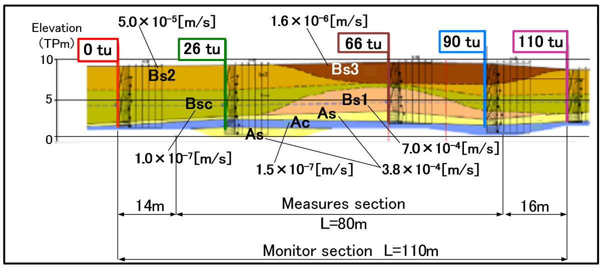

Fig-19 Monitor part in profile
(position of levee crown landside shoulder)

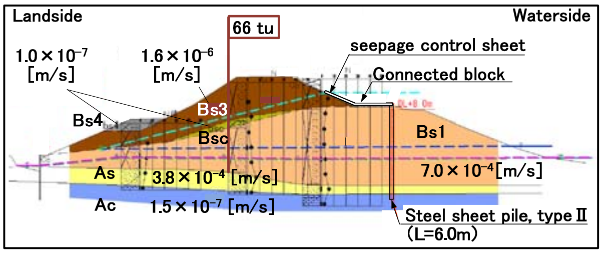

Fig-20 Monitor part in cross section (section of 6.4k-14m)

2) Monitoring results

Fig-21 shows the time history from 2010/7/11 to 2010/7/15. The water level exceeded the estimated high-water level at 8 and 9:00AM on the morning of July 14th. After beginning observations, the maximum water level that had been observed at the HIDEKI Bridge was high in second during the middle of this flood. The water level of the river levee was confirmed to follow roughly that in Fig-21, the water level of river. The water levels of levees of 0tu and 110tu in the outside measurement section are high. Additionally, the water levels of levees of 90tu have risen within the measurement section.

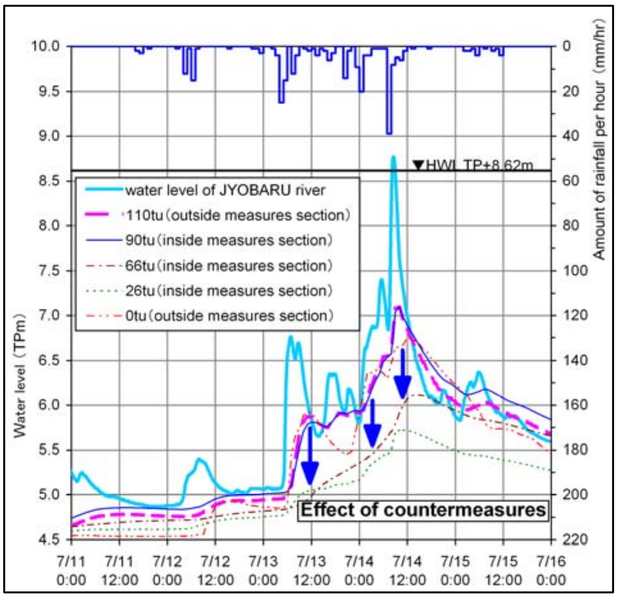

Fig-21 Observational results of water levels of the levee on July 11th - 16th, 2010

The water level of the levee at the levee crown landside paste shoulder position at the time of 9:00 when the water level of the river reached the peak water level on the 14th is shown in Fig-22. As for the water level of the levee in the section where the measures with sealing sheet piles and the seepage control sheet were executed, it was lower than the section without measures by more than 1m. The effects of measures were confirmed with Fig-22. Moreover, the water level has not decreased in the upstream edge in the measures section. Therefore, it has been understood that there is a section where the effect of measures decreases by a three-dimensional seepage flow.

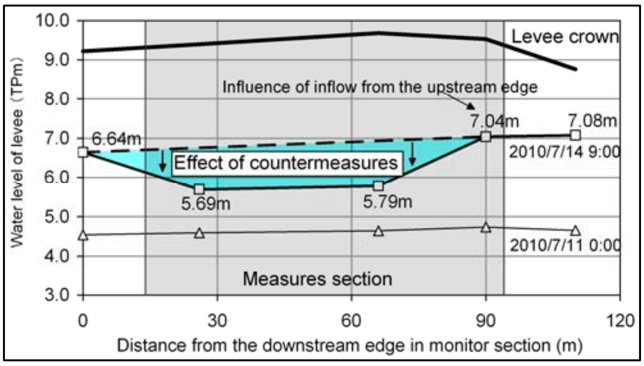

Fig-22 water level of levee at flood peak

7.2 The three-dimensional seepage analysis

The waterside measures followed sheet piles and the seepage control sheet in the vicinity of the CHIKUGO River water system and JYOBARU River 6.4k points.

1) Analytical model

The range where an analytical model has been built is shown in Fig-23. In the direction of the determination of the length and breadth of the levee, the range of an analytical model was made in the range of 600m×300m. This includes the range in which on-site monitoring is carried out. The curve of the river channel is not seen within the range of the analysis. Therefore, the shape of an analytical model was made into a rectangle.

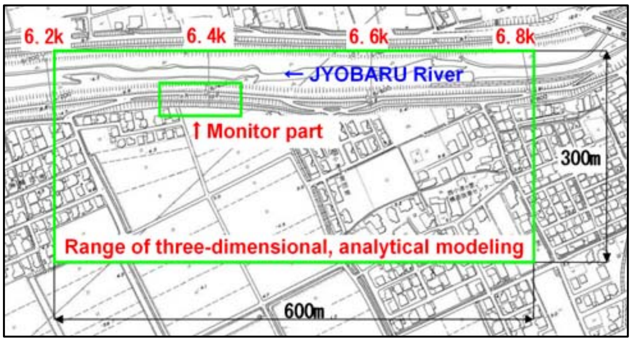

Fig-23 Range of modeling of analysis

The soil layer composition and coefficient of permeability of the levees and the foundation subgrade were set as shown in Fig-24. This is based on the results of the survey during the emergency of the 2009/07/26 disaster that were restored based on soil profiles (Fig-19 etc.) and soil test results. The measures reflect the shape of ground as of July, 2010. The modeled seepage control sheet and sealing sheet pile on the waterside with the levee crown pavement are shown in Fig-25. Penetration characteristics of measures were set respectively as 10cm in thickness based on technological standards [6]. The coefficient of permeability was converted into a value of 10cm in thickness.

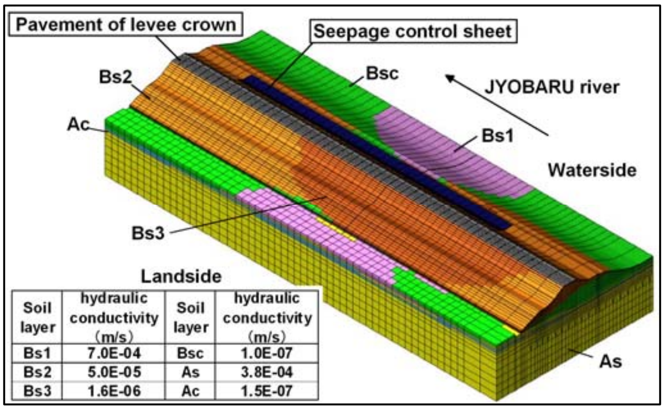

Soil layer	hydraulic conductivity (m/s)	Soil layer	hydraulic conductivity (m/s)
Bs1	7.0E-04	Bsc	1.0E-07
Bs2	5.0E-05	As	3.8E-04
Bs3	1.6E-06	Ac	1.5E-07

Fig-24 Analytical model in the vicinity of river levees

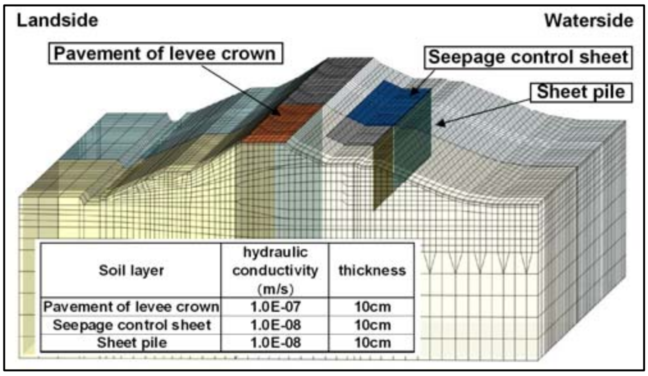

Soil layer	hydraulic conductivity (m/s)	thickness
Pavement of levee crown	1.0E-07	10cm
Seepage control sheet	1.0E-08	10cm
Sheet pile	1.0E-08	10cm

Fig-25 Analytical model in measures section

The rainfall and water level of the river in 2010/7/11 - 2010/7/15 were set based on observational results. However, the seepage flow reacted in hypersensitivity when the rainfall condition was given. The analysis was emanated. Therefore, the analysis was executed without giving the rainfall.

2) Analytical result

The comparison between analytical results and observational results is shown in Fig-26. This is with respect to the water level of the levee of the monitored part. Fig-26 is a time history of the water level of levees of 0tu, 90tu, and 110tu. Changes in the water levels of the levee for one week from 7/10 show roughly the same tendencies as this Fig with an analytical value and an observed value. Therefore, it is thought that this analytical model and technique roughly catch the seepage flow.

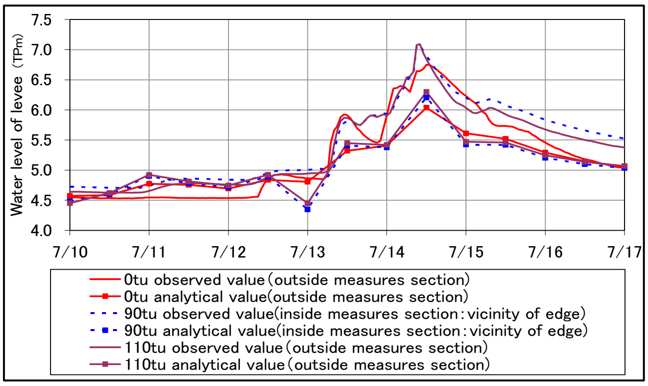

Fig-26 Time history of water level of the levee (outside measures section and edge)

The profiles of the water levels of the levees at the flood peak are shown in Fig-27. The water level of the levees in the measures section lowered relatively more than the water level of levees outside the measures section. Therefore, countermeasures for sealing sheet pile and the seepage control sheet can be confirmed.

Moreover, the flow of the direction of the running water in the river levee was seen from the flow velocity vector shown in Fig-28 at the edge in the sealing sheet pile section. The effect of infiltration measures were confirmed as well as the monitoring results. As a result, the influence of three-dimensional seepage flow at the edge of the measures section was reproduced during this analysis.

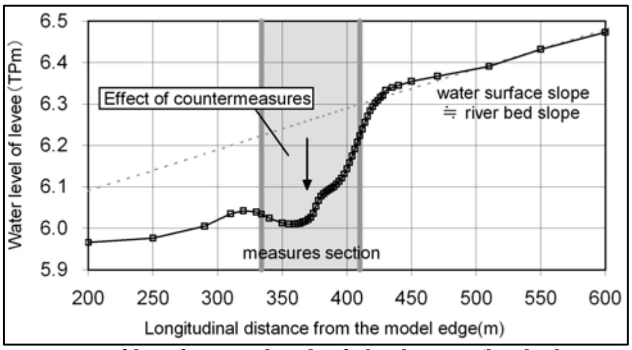

Fig-27 Profile of water level of the levees (landside paste shoulder)

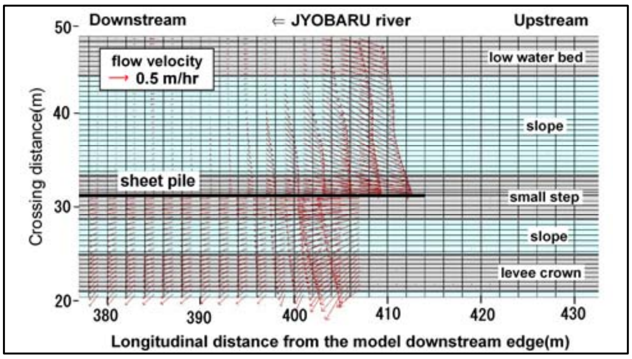

Fig-28 Flow velocity vector plane on sealing sheet pile upstream side in the vicinity of GL-1.5m

8. CONCLUSION

To verify the effect of infiltration measures of the river levee, on-site monitoring and three-dimensional seepage flow analyses were executed.

As a result, the effect was confirmed by the observation of the water level of levees and analytical results with respect to the drain section of landside measures.

Additionally, the effect of measures for the seepage control sheet for the water side measures and the sheet pile section were achieved by the observation of the water level of levees and the analysis.

Moreover, the situation in which three-dimensional seepage flow was caused, was confirmed at the edge in the measures section.

It is important to execute on-site monitoring continuously in the future so as to confirm the effect of long-term infiltration measures based on the results, and to make the best use of such for methods of managing design methods and for maintenance.

9. ADDRESS OF THANKS

For cooperation at the OSUMI River national road office, in the INAGAWA River Office, the BIWAKO River Office, and the CHIKUGO River Office in on-site monitoring.

Rainfall data was offered to the KANOYA City AIRA Synthesis Branch Office. Thank you very much.

10. REFERENCES

[1] The Cooperative research report of PWRI (Public Works Research Institute)., The Cooperative research report concerning development of method of observing water level of the levee management technology upgrade, ” The Water level of the levees observation manual” No.377, 2008.3.

[2] Yukiko Saito, Kazushi Furumoto, Hitoshi Taninaka, Hidetoshi Kohashi,” Influence of longitudinal seepage flow on stability of river Levee”, Proceedings of the 62th Annual Conference of JSCE (Japan Society of Civil Engineers) 3-284, 2007.9.

[3] Yukiko Saito, Hitoshi Taninaka, Hidetoshi Kohashi, Kazushi Furumoto, ”Influence of longitudinal soil profile on stability of river Levee” River technological thesis collection vol.14, pp.79-84, 2008.6. ,press release by JSCE

[4] Yukiko Saito, Hirotoshi Mori, Satoshi Arakane, Tetsuya Sasaki, ”The Influence of three-dimensional seepage flow to the performance of countermeasures for river levees”, River technological thesis collection vol.16, pp.329-334, 2010.6. ,press release by JSCE

[5] Hiroyuki Masuyama, Yukiko Saito, Hirotoshi Mori, Tetsuya Sasaki, ”On-site monitoring and three-dimensional seepage flow analysis on the effect of countermeasures for river levees”, River technological thesis collection vol.17, pp.275-280,2011.7. ,press release by JSCE

[6] Japan Institute of Construction Engineering (JICE) , ”Technological standard of structure investigation of river leveest” 2002.7

First International Conference on Geotechnique, Construction Materials and Environment, Mie, Japan, Nov.21-23, 2011, ISBN: 978-4-9905958-0-7 C3051

Influence of Decreasing of Soil Suction on Unconfined Compressive Strength for Bentonite

T. Nishimura., Department of Civil Engineering, Ashikaga Institute of Technology, Japan

ABSTRACT: This study focuses on shear strength of compacted bentonite at different suction values. The soil used in this test program is sodium bentonite mixed with silica sand. Soil-water characteristic curve was measured using vapor pressure technique which can provide a relationship between high soil suctions and volumetric water content. Measured soil-water characteristic curves were observed few effects of compaction effort. Unconfined compression testing on the compacted bentonite with soil suctions higher than 2.8 MPa were conducted out. Vapor pressure technique was useful to apply high soil suctions to all compacted bentonite. Stress and strain curves were measured for various soil suctions, and were indicated the changing of shear properties due to soil suctions. Relationship between soil suction and shear strength were evidence in a linear failure envelope. In addition, influence of rate of axial strain on unconfined compressive strength was observed in this study.

Keywords: Bentonite, Soil suction, Vapor pressure technique, Unconfined compressive strength, Relative humidity.

1. INTRODUCTION

It is knowledge that bentonite consist of artificial barrier for radioactive waste disposal system. Highly swelling behavior of compacted bentonite is useful to maintain safety for geo-environment. Geotechnical engineers and geo-environmental engineers require interpreting mechanical properties of compacted bentonite. Many experimental papers were published regard to some futures (i.e., thermo conductivity, chemical properties, hydro-conductivity, mineralogical composition and swelling behavior). On the other hands, yield surface and constitutive models for expansive soil as like to compacted bentonite were suggested in high soil suction ranges with experimental test results. Osmotic technique or vapor pressure technique was effectively for applying of high soil suction more than that of 1.5 MPa. Compacted bentonite with high soil suction induced the reduction of shear strength due to changing of relative humidity without water seepage. Therefore, it is important to predict to decrease both stiffness and shear strength after reduction of soil suction. There are lacks to study shear properties of compacted bentonite subjected to change of relative humidity.

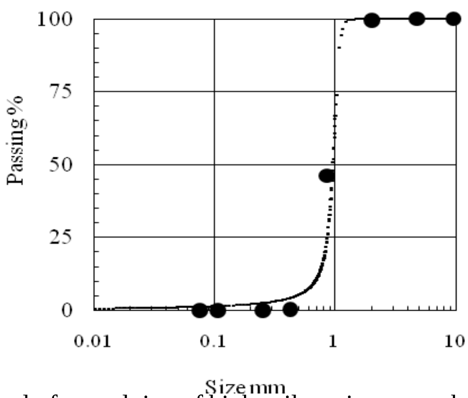

Fig. 1. Grain size distribution for silica sand.

This study focuses on the influence of decreasing of soil suction on shear strength of compacted bentonite. Before performing of unconfined compression test, all compacted bentonite specimens were placed in different relative humidity conditions using vapor pressure technique. As results, the different soil suctions were applied to specimens, and were measured the unconfined compressive strength. This study presents the relationship between unconfined compressive strength and soil suctions.

2. TESTING PROGRAM

2.1 Soil material

Sodium bentonite was used for this test program. Silica sand was mixed into the bentonite with a ratio of 30 % by dry weight. The silica sand had a grain size distribution as shown in Fig. 1. The specimen was statically compacted in the steel mold. The mold had a height of 30 cm and a diameter of 5 cm, respectively. Also, the inside of mold was treated in order to decreasing the friction. The soil specimen had a dry density of 1.6 g/cm^3 as target value.

2.2 Unconfined compression apparatus

This testing program used a modified triaxial compression apparatus. The basic construction of a modified triaxial compression apparatus is similar to the equipment suggested by Nishimura and Fredlund (2003). The modified triaxial compression apparatus consisted mainly of a triaxial chamber, a pedestal, a steel mould, a double glass burette, a differential pressure transducer, a difference displacement sensor, load cell sensor and relative humidity control circulation system. The relative humidity control circulation system was established using a conventional pump, along with a small chamber with salt solution. The air flow maintained a constant relative humidity surrounding the compacted bentonite.

2.3 Vapor pressure technique

Soil suction theoretically has a range from 0 kPa to 10^6 kPa

Table 1. Relationship between relative humidity (RH) and suction values for different salt solutions at 20 degrees (Delage et al., 1998).

Salt solutions (Chemical symbol)	Relative humidity (%)	Suction (kPa)
K_2SO_4	98	2,830
KNO_3	95	6,940
$NH_4H_2PO_4$	93.1	9,800
NaCl	75	39,000
$Mg(NO_3)_2 \cdot 6H_2O$	54	83,400
$MgCl_2 \cdot 6H_2O$	33	148,000
LiCl	11	296,000

which consists of matric suction and osmotic suction. Vanapalli et al., (1999) indicated that a suction value over than 1500 kPa can be considered as high suction. The low suction (< 1500 kPa) can be controlled in a pressure plate apparatus using a porous plate or a micro porous membrane. The conventional shear testing apparatus is modified through the use of the axis translation technique. The axis translation technique consists in increasing the ambient air pressure to values greater than atmospheric, so as to translate the pore-water pressure into the positive range. In particular axis translation technique may be not suitable for investigating unsaturated soils at high degree of saturation because of the discontinuity of the air phase. The high suction can be controlled using a vapor pressure technique. High suction values can be achieved by controlling relative humidity (RH) using several different salt solutions in a desiccator (Delage et al., 1998). The salt solution method was used in this study to achieve high suction values as summarized in Table 1. The glass desiccator was then placed in a temperature controlled chamber for at least one month to allow the specimens to achieve an equilibrium condition with respect to the controlled suction.

2.4 Measurement of soil-water characteristic curve for bentonite

The compacted bentonite specimen with initial water content from 4.4 % to 5.9 % was placed in glass desiccators with different salt solutions. The seven different salt solutions summarized in Table 1 were used in the test program. The gravimetric water content of each soil specimens was measured after achieving the equilibrium condition. As a result, the relationship between measured gravimetric water content and soil suction in high soil suction range can be obtained. The initial samples had a diameter of 2.0 mm and a height of 1.0 cm, respectively.

2.5 Unconfined compression test

The specimens were statically compacted at initial water content from 4.4 % to 5.9 %. The initial soil suction of the specimen was measured using the soil-water characteristic curve which gave a suction value of 110 MPa.

The two desired suction values were 148 MPa and 2.8 MPa corresponding to RH of 33 % and 98 %. Figure. 2 shows the bentonite specimens were remaining under constant relative

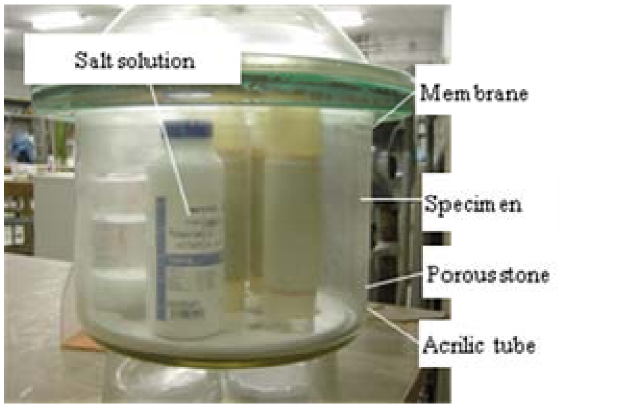

Fig. 2. Applied soil suction .in the glass desiccator.

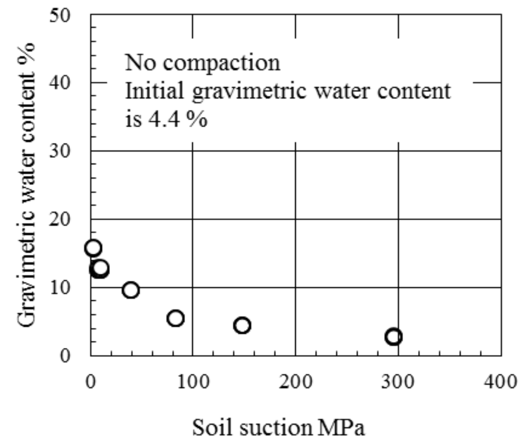

Fig. 3. Soil-water characteristic curve for bentonite.

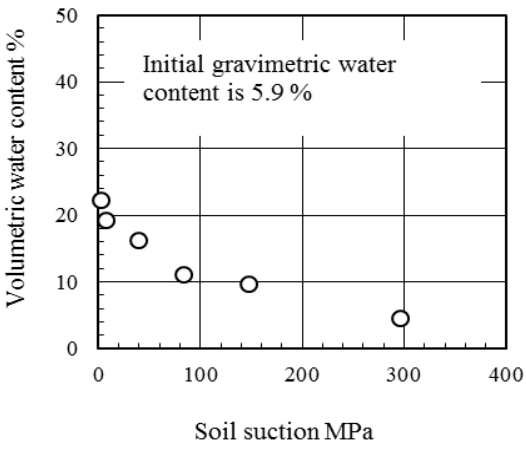

Fig. 4. Soil-water characteristic curve for compacted bentonite.

humidity in the glass desiccators. At least one month, the bentonite specimens were placed to equilibrium with required soil suction. The bentonite obviously occurred the swelling expansion when the soil suction decreased to 2.8 MPa from

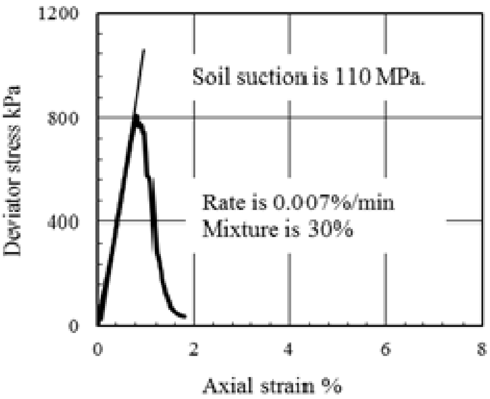

Fig. 5. Volume deformation of compacted bentonite by changing of soil suction.

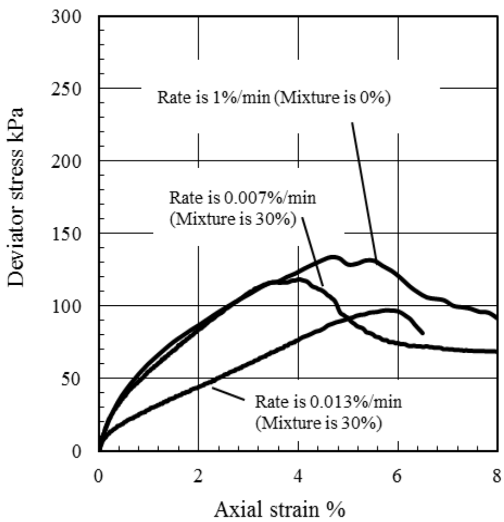

Fig. 6. Influence of rate of axial strain on stress and strain curves.

110 MPa (i.e. initial soil suction). On the contractor, the bentonite specimen was little shrinkage was observed due to increase of soil suction comparing initial soil suction (i.e. 110 MPa). After ensuring equilibrium conditions, the bentonite specimen having three differences soil suctions were set up in the modified triaxial compression apparatus. The specimen was sheared at a rate of 0.007 % per minute and compression process was remained to at least 8.0 % in axial strain or until a peak value of deviator stress was observed. For the bentonite specimen having soil suction of 2.8 MPa three difference rates were applied in the unconfined compression testing which were 1 % per minute, 0.013 % per minute and 0.007 % per minute.

3 TEST RESULTS

3.1 Soil-water characteristic curve

Relationship between gravimetric water content or volumetric water content and soil suction of the bentonite are shown in Figs. 3 and 4. These are difference between two soil-water characteristic curves in compaction or not. Changing of gravimetric water content is described against soil suction because all bentonite samples were no compacted condition. Other hand, the soil-water characteristic curve in Fig. 4 was possible to order a volumetric water content that the bentonite samples remained a round column in shape throughout the SWCC testing. Both gravimetric water content and volumetric water content decreased with increasing of soil suctions. The decreasing of moisture in bentonite was large when soil suction regard from 2.8 MPa to 83.4 MPa. Beyond soil suction was 83.4 MPa, the moisture smoothly decrease with soil suction. Two soil-water characteristic curves described similar tendency that is few influence of compaction effort on the soil-water characteristic curve for bentonite. Figure 5 show relationship between volume deformation of compacted bentonite and soil suction. Initial compacted bentonite had a diameter of 2 cm and a height of 1 cm, respectively. Also, it is predicted that initial soil suction was 110 MPa. Changing of soil suction induced the volume change due to vapor hydraulic seepage. The measured volume strain was over 30 % when soil suction approached to 2.8 MPa. On the contrary, little shrinkages were measured when soil suction was over 110 MPa. Eventually, changing of soil suction gave similar tendency either volumetric water content or volume strain.

3.2 Stress versus strain curve with various soil suctions

Unconfined compression testing with three difference rate of shearing was previously conducted using the bentonite having a soil suction of 2.8 MPa. Applied rates of shearing were 0.007 %/ per minute, 0.013 % per minute and 1.0 % per minute. Figure 6 shows stress and strain curves. It was not seem to be coincident in three curves. There were large differences among three test results even maximum deviator stress. For rate of 0.0 13 % per minute the low stiffness was observed comparison to other two stress and strain curves.

Stress and strain curves for compacted bentonite with three difference soil suctions were determined from unconfined compression testing as shown in Figs. 7 to 9. Figure 7 shows the curve of compacted bentonite having a mixture 30 % when soil suction is 110 MPa. At beginning of shear the deviator stress increased rapidly, and approached to peck value. Beyond the axial strain was 0.77 %, the bentonite failure that large reduction was described. For soil suction of 148 MPa obtained stress and strain curves were similar to that of soil suction of 110 MPa. Increasing of deviator stress was rapidly as shown in Fig. 7. Axial strains at failure had range from 0.84 % to 1.49 %. Few scatters were observed in three specimens.

On contractor, the bentonite with soil suction of 2.8 MPa described the stress and strain curves as shown in Fig. 9. The deviator stress increased smoothly in shear process. The bentonite remained the increasing of deviator stress that axial strain was till 2 %. The deviator stress approached maximum value when the axial strain was 3.8 % or 4.8 %. After the bentonite failure, shear resistance described smoothly

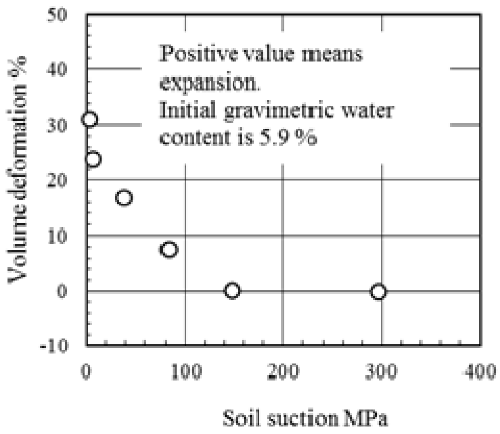

Fig. 7. Stress and strain curve with soil suction of 110 MPa.

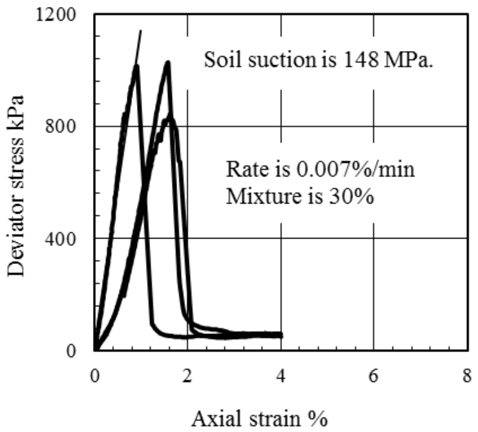

Fig. 8. Stress and strain curve with soil suction of 148 MPa.

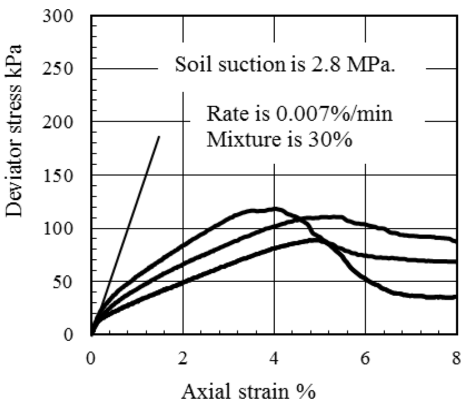

Fig.9. Stress and strain curve with soil suction of 2.8 MPa

reduction. It is clear that unconfined compressive strength for soil suction of 2.8 MPa was low in comparison with those of other soil suctions. Also, the stiffness was calculated from the stress and strain curves, and summarized in Table 2. It is evidenced that reduction of soil suction closely related to decreasing of the stiffness.

Table 2. Summary of stiffness with three difference soil suctions.

Soil suction (MPa)	Stiffness (MPa)
2.8	5.8
110	100.5
148	127.9

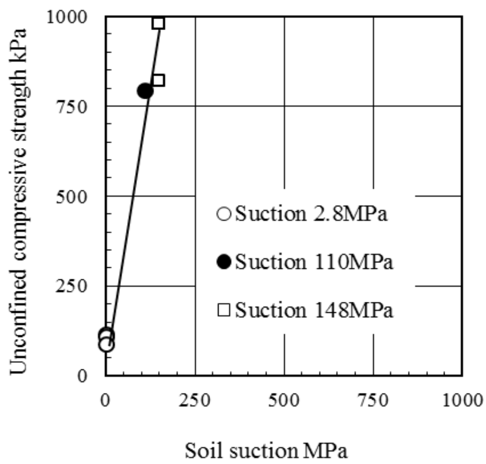

Fig.10. Relationship between unconfined compressive strength and soil suction.

3.3 Relationship between shear strength and suction

The relationship between unconfined compression strength and soil suction in the compacted bentonite are shown in Fig. 10. The failure envelope regard to soil suction was linear relations in range from 2.8 MPa to 148 MPa. The shear strength of compacted bentonite had effectively influence of soil suction, and the angle of friction regard to soil suction was evaluated as 79.9 degrees.

4 CONCLUSIONS

This study focuses on both soil-water characteristic curve and shear strength for compacted bentonite using vapor pressure technique. The decreasing of volumetric water content was obviously large in drying process when soil suction regard from 2.8 MPa to 83.4 MPa. Beyond soil suction was 83.4 MPa, it smoothly decreased with soil suction. Also, decreasing of soil suction closely related to reduce the shear strength for compacted bentonite.

5 REFERENCES

[1] Nishimura, T. and Fredlund, D.G., "A new triaxial apparatus for high total suction using relative humidity control", *12th Asian Regional Conference on Soil Mechanics and Geotechnical Engineering*, 4-8 August Singapore, 2003, pp.65-68

[2] Vanapalli, S.K., Fredlund, D.G. and Pufahl, D.E. ,"The influence of soil structure and stress history on the soil-water characteristics of a compacted till." *Geotechnique*. Vol.49, No.2, 1999, pp.143-159.

[3] Delage, P., Howat, M.D. and Cui, Y.J., "The relation-ship between suction and swelling properties in a heavily compacted unsaturated clay." *Engineering Geology*, 50, 1998, pp.31-48.

The Relationship between Soil Suction and the Maximum Unsaturated Undrained Shear Strengths of Compacted Khon Kaen Soil

R. Nuntasarn. Weerawat Wannakul., Department of Civil Engineering, Khon Kaen University

ABSTRACT: The objective of this study was to evaluate the maximum unsaturated undrianed shear strengths of compacted Khon Kaen soil, which were determined from unconsolidated undrained triaxial tests. The samples were compacted at 85% of maximum dry density by standard method. The samples were not measured soil suction during the test, but rather estimated soil suction from a soil water characteristic curve (SWCC) based on the volumetric water content of samples during the test. The drying soil water characteristics curve (SWCC) for the compacted Khon Kaen soils was determined from three methods, which were a hanging column method, a pressure plate method and an isopiestic humidity method. The maximum unsaturated undrained shear strength of compacted Khon Kaen soils was investigated in the transition zone. The relationship between soil suction and the maximum unsaturated undrained shear strength of compacted Khon Kaen soil was a good related in the form of exploration of the value of R^2 = 0.98.

Keywords: unconsolidation undrained triaxial test, soil water characteristic curve, soil suction, maximum unsaturated undrained shear strength

1. INTRODUCTION

The objective of this study was to evaluate the maximum unsaturated undrianed shear strengths of compacted Khon Kaen soil, which were determined from unconsolidated undrained triaxial tests.

The samples were not measured soil suction during unconsolidated undrained triaxial tests, but rather estimated soil suction from the soil water characteristic curve (SWCC) based on the volumetric water content of the sample during the test. The drying soil water characteristics curve (SWCC) for the compacted Khon Kaen soils was determined from three methods, which were hanging column method, pressure plate and isopiestic humidity method.

The volumetric water content during UU test was calculated from an initial moisture content of sample and volume change of soil during shear as presented in (1).

$$\theta_w = \frac{V_w}{V} = \frac{w.Ws}{V_i - \Delta V} \tag{1}$$

Where θ_w = volumetric water content; V_w = volume of water; V = total volume of soil; w = moisture content; V_i = initial volume of specimen; ΔV = volume change of specimen; and W_s = mass of dry soil.

Due to both of pore water and pore air pressures were not measured during unconsolidated undrained triaxial tests. Therefore the maximum unsaturated undrained shear strength of compacted Khon Kaen soils was related to the total stress.

2. BASIC PROPERTIES

The basic and engineering properties of Khon Kaen soils are presented in Table 1.

The USCS classifications of Khon Kaen soil based on the results of soil particle distribution curves and Atterberg limits.

The maximum dry density and optimum moisture content Khon Kaen soil was determined by standard compactive effort (ASTM D698 – 00a).

Table 1. The basic and engineering properties of Khon Kaen soils

Particle Size Distribution	
Clay (%)	13
Silt (%)	31
Sand (%)	56
Atterberg Limit	
LL (%)	20.3
PL (%)	14.5
PI (%)	5.8
USCS Classification	SM -SC
Gs	2.65
Standard Compaction	
OMC (%)	8.25
Maximum dry density (t/m^3)	2.00

3. SOIL WATER CHARACTERISTIC CURVE

The initial dry density, moisture content and void ratio of compacted Khon Kaen samples were 1.7 t/m^3 (or 85% of maximum dry density), 14 % and 0.47, respectively.

The drying soil water characteristics curve (SWCC) for the compacted Khon Kaen soils was determined from three methods, which were a hanging column method, a pressure plate and an isopiestic humidity method.

According to [1], the hanging column method was used to determine suctions in the range of 0 to 9.81 kPa.

The pressure plate method (refer to [2]) was used to determine SWCC for a suction values between 10 to 1,500 kPa.

Finally, SWCC at suctions above 1500 kPa were determined from the isopiestic humidity method. In this method three solutions, which were Copper Sulphate ($CuSO_4$), Ammonium Chloride (NH_4Cl) and Sodium Hydroxide ($NaOH.H_2O$) were used to determine SWCC at 3,900, 30,900 and 365,183 kPa for a suction value, respectively. Data points above 1500 kPa were total suction values [3].

The relationships between soil suction and volumetric moisture content are illustrated in Fig. 1.

Fig. 1 showed that the projected air entry value for compacted Khon Kaen soils was equal to 12 kPa and a very low residual volumetric moisture content of 1.0%. Therefore the suction range of transition regime was between 12 to 45,000 kPa.

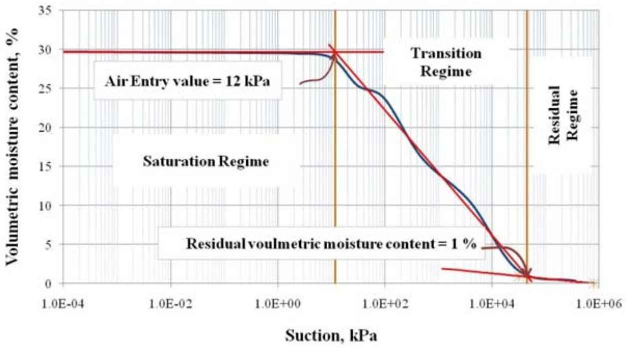

Fig. 1. The relationship between soil suction and volumetric moisture content of compacted Khon Kaen soil

4. UNSATURATED UNDRAINED SHEAR STRENGTH

Ten samples of Khon Kaen soils were compacted into a mold with a diameter of 50 mm and 100 mm high to obtain the initial dry density, moisture content and ratio of 1.7 t/m^3, 14%, and 0.47, respectively. All samples were determined an undrained shear strength by the unconsolidated undrained test (UU test) at a confining pressure of 100 or 200 kPa. Two samples were tested immediately after compaction. Another eight samples were air dried for 2, 12, 24 or 72 hours prior to undrained shear. The initial moisture content was measured after shear to determine the initial soil suction by assumed the moisture content during testing was not changed.

The volume changes of soil samples were monitored as the sample was loaded at an axial strain rate of 0.1 % via the volume of water flowing out of, or into, the triaxial chamber. The volumetric water content during UU test was calculated from an initial moisture content of sample and a volume change of soil during shear as presented in (1).

The summaries of initial test condition and result of UU test for unsaturated compacted Khon Kaen soils is provided in Table 2 and 3, respectively.

The relationship between stress and strain of unsaturated compacted Khon Kaen soils for UU test in Fig. 2 showed the strain hardening behavior, except that soil samples were air dried for 72 hours prior to shear. Therefore the failure was defined as 15% axial strain except that soil samples with 72 hours air dried. The failure of soil samples with 72 hours air dried was defined as the maximum deviator stress.

The relationship between axial and volumetric strain, as presented in Fig. 3, indicated that the sample, which was air dried for 72 hours and subjected to confining pressure of 200 kPa, exhibited dilation. The initial moisture content and volumetric moisture content of this sample was 3 % and 4 %, respectively, which was corresponded to soil suction of 15,230 kPa.

Table 2. The initial condition of unconsolidated undrained test for compacted Khon Kaen soils

Sample	Initial moisture content (%)	Initial volumetric moisture content (%)	Initial soil suction (kPa)
CP =100 kPa (0 hrs-air dry)	14.9	25	53
CP =200 kPa (0 hrs-air dry)	14.4	21	188.5
CP =100 kPa (2 hrs-air dry)	14.3	24	87
CP =200 kPa (2 hrs-air dry)	13.6	20	245
CP =100 kPa (12 hrs-air dry)	10.8	18	419
CP =200 kPa (12 hrs-air dry)	9.6	16	705
CP =100 kPa (24 hrs-air dry)	8.8	15	1000
CP =200 kPa (24 hrs-air dry)	7.2	12	2026
CP =100 kPa (72 hrs-air dry)	4.7	6	9263
CP =200 kPa (72 hrs-air dry)	3.1	4	15230

Table 3. The summaries of unconsolidated undrained test for compacted Khon Kaen soils

Sample	soil suction at failure (kPa)	σ_{3f} (kPa)	σ_{1f} (kPa)	τ_{max} (kPa)
CP = 100 kPa (0 hrs-air dry)	37	100	170	35
CP = 100 kPa (2 hrs-air dry)	52	101	183	41
CP = 100 kPa (12 hrs-air dry)	270	98	259	81
CP = 100 kPa (24 hrs-air dry)	716	98	344	123
CP = 100 kPa (72 hrs-air dry)	8779	101	1281	590
CP = 200 kPa (0 hrs-air dry)	118	201	304	52
CP = 200 kPa (2 hrs-air dry)	149	199	348	75
CP = 200 kPa (12 hrs-air dry)	460	199	487	145
CP = 200 kPa (24 hrs-air dry)	1576	198	647	225
CP = 200 kPa (72 hrs-air dry)	17467	198	1560	681

The plot between deviator stress and soil suction for samples with high soil suction as provided in Fig. 4 indicated that the soil suction dropped significantly after the peak deviator stress had been reached as presented in Fig. 2 due to the behavior of soils as a strain-softening. On the other hand, the stress-strain behavior of samples with low soil suctions

indicated the strain hardening (see Fig. 2). Therefore the soil suction remained constant thereafter the residual soil suction had been reached as presented at Fig. 5.
Fig. 6 and 7 presented that the soil suction of unsaturated compacted Khon Kaen soils with a high initial soil suction value was deceased continuously with axial strained. Meanwhile the soil suction of the other soil samples was quite constant with axial strain.

5 DISCUSSION

The soil suction range, which used in this experiment, was between 35 to 17,500 kPa. This range of soil suction was on the transition zone. This indicated that the samples were unsaturated. According to [4] the soil suction range between 100 to 10,000 kPa is on the adsorbed film regime. The bonding between water and the soil particle on this regime is short-range solid-liquid interaction mechanism. A soil suction value of the samples, almost all is in the adsorbed film regime. This explained that the bonding between water and soil particle of the compacted Khon Kaen soils was short-range solid-liquid interaction mechanism.
Fig. 8 showed the extended Mohr circles at failure as total confining pressure of 100 and 200 kPa. The typical Mohr circles at failure of compacted Khon Kaen soils as total confining pressure of 100 and 200 kPa was presented in Fig. 9 and 10, respectively. Fig. 9 and 10 was illustrated the total stress path of various soil suctions. Then the plot of maximum shear versus soil suction on a log scale as 100 and 200 kPa total confining pressure was illustrated in Fig. 11 and 12, respectively. Fig. 11 and 12 was provided the path of soil suction in term of total stress. These paths showed a good non-linearly correlation between the maximum undrained shear strength and soil suction. However, a soil suction value of this study was not measured but it was estimated from SWCC.

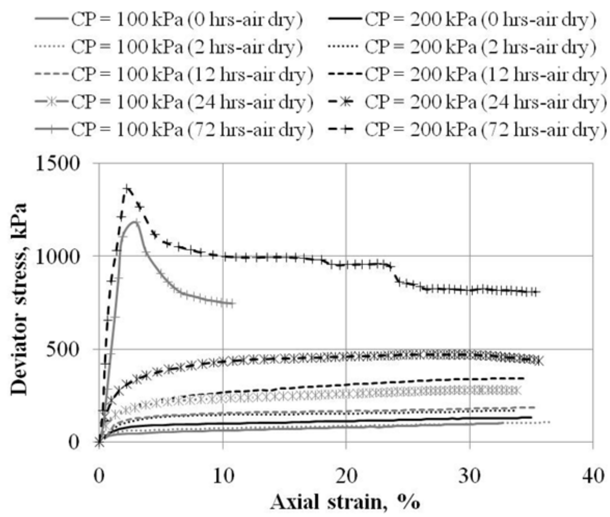

Fig. 2. The stress-strain curve of unsaturated compacted Khon Kaen soils from UU testing

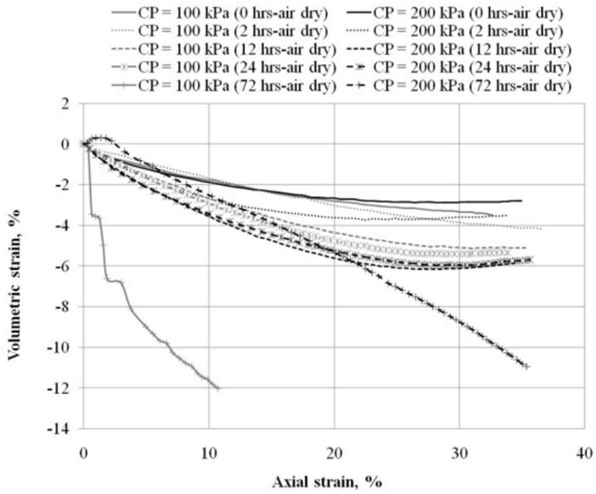

Fig. 3. The relationship between vertical and volumetric strain of unsaturated compacted Khon Kaen soils from UU testing

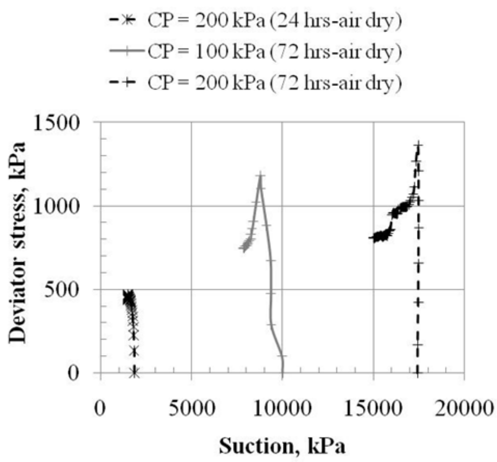

Fig. 4. The relationship between a high suction and deviator stress of unsaturated compacted Khon Kaen soils from UU testing

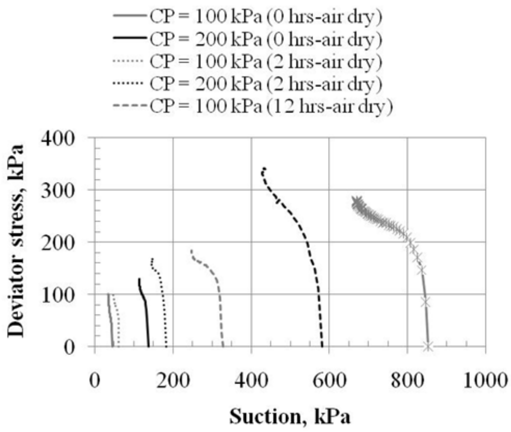

Fig. 5. The relationship between a low suction and deviator stress of unsaturated compacted Khon Kaen soil from UU testing

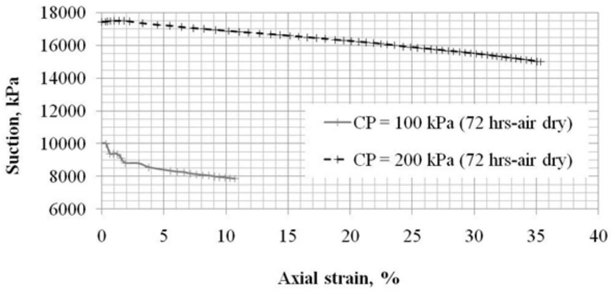

Fig. 6. The relationship between a high suction and axial strain of unsaturated compacted Khon Kaen soils from UU testing

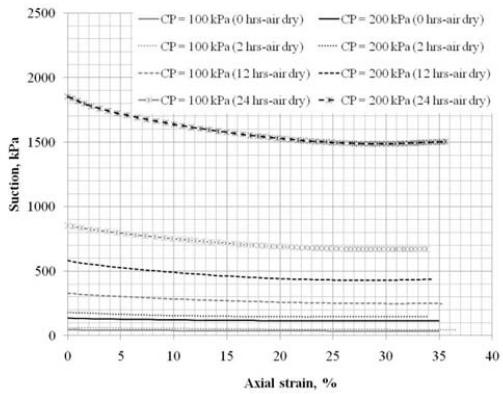

Fig. 7. The relationship between a low suction and axial strain of unsaturated compacted Khon Kaen soils from UU testing

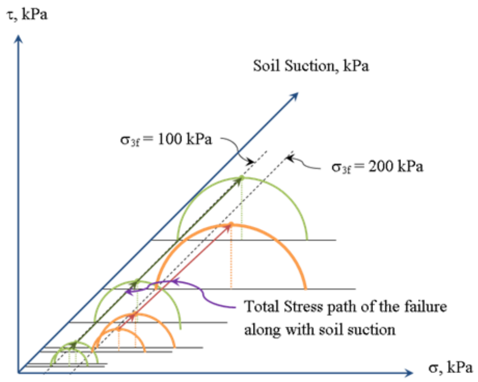

Fig. 8. The extended Mohr circles of compacted Khon Kaen loess

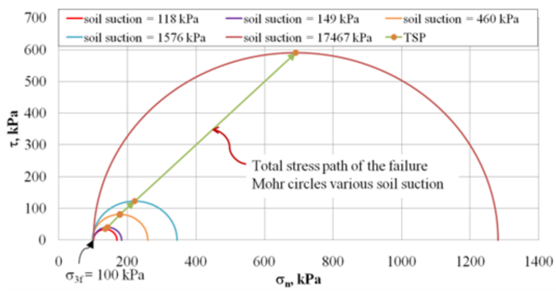

Fig. 9. Typical Mohr circles at failure with various soil suctions for compacted Khon Kaen soils as 100 total confining pressures

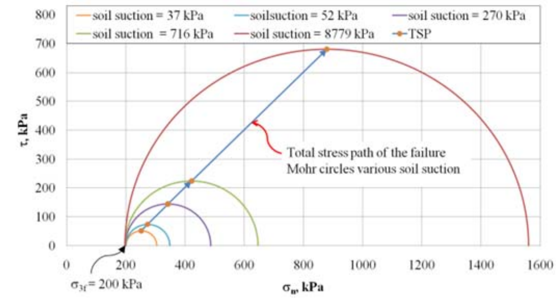

Fig. 10. Typical Mohr circles at failure with various soil suctions for compacted Khon Kaen soils as 200 total confining pressures

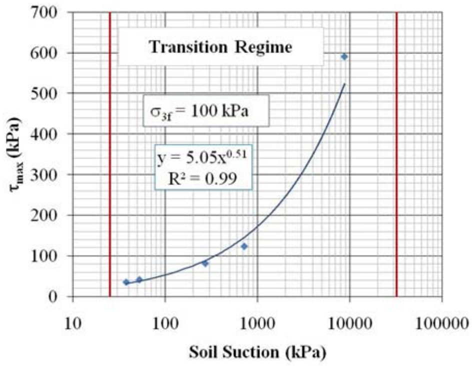

Fig. 11. The soil suction path of compacted Khon Kaen loess as 100 kPa total confining pressure

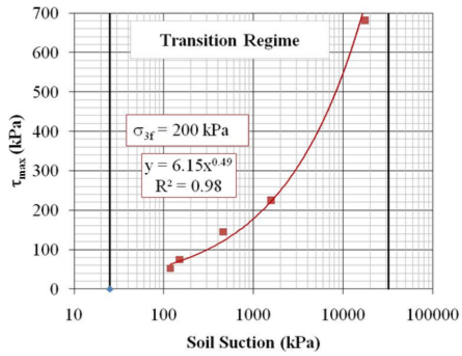

Fig. 12. The soil suction path of compacted Khon Kaen loess as 200 kPa total confining pressure

6 CONCLUSION

Khon Kaen loess was compacted at 85% of maximum dry density by standard compactive effort to determine the unsaturated undrained shear strength parameter from the unconsolidated undrained test. Due to the pore water and pore air pressure did not measure during test, since the soil suction was estimated from SWCC.

The SWCC of compacted Khon Kaen loess showed the residual volumetric moisture content of 1.0 % and the air entry value of 12 kPa.

Finally, the path of soil suction during undrained unconsolidation test in term of total stress showed a good non-linearly correlation between the maximum undrained shear strength and soil suction.

7 ACKNOWLEDGMENT

Acknowledgement is given to Faculty of Engineering, Khon Kaen University for the support of this re-search. Sincere thanks are extended to Dr. Ketsuda Dejbhimon and Mrs Pornpis Chuson, for the favor of using instruments in this study. Special thanks to Ms. Nichapat Banreangthong, Mr.Tanakorn Dua-ngkantai, Mr. Nanthiwa Soontararuk, Mr. Piyanat Jantosut, Mr. Veeraphon Tansa, Ms. Pemiga Thong-tan, and everyone who have been involved directly and indirectly in the preparation of this research.

8 REFERENCES

[1] ASTM - American Society for Testing Material, 'Standard Test Methods for Determination of the Soil Water Characteristic Curve for Desorption Using a Hanging Column, Pressure Extractor, Chilled Mirror Hygrometer, and/or Centrifuge1', (ASTM D6836 – 02), West Conshohocken, PA., 2002

[2] ASTM - American Society for Testing Material, 'Standard Test Method for Capillary-Moisture Relationships for Coarse- And Medium-Textured Soils by Porous-Plate Apparatus', (ASTM D2325-98), West Conshohocken, PA., 1998

[3] Lu, N. and Likos, W.J., Unsaturated Soil Mechanics, John Wiley & Sons, Inc., Hoboken, New Jersey., 2004, ch. 10

[4] McQueen, I.S. and Miller, R.F., 'Calibration and Evaluation of Wide-Range Gravimetric Method for Measuring Soil Moisture Stress', Soil Science, 10(3), 1968, pp 521-527.

First International Conference on Geotechnique, Construction Materials and Environment, Mie, Japan, Nov.21-23, 2011, ISBN: 978-4-9905958-0-7 C3051

Interpretation of Coaxial and Non-Coaxial Strain on Directional Variation of Undrained Strength of clay

J.Rajaraman[1] and K. Thiruvenkatasamy[2]

ABSTRACT: The term stresses on soils, soil samples are much discussed by soil researchers , but the strains are not. Stresses are invisible ,but the strains [deformations] are visible. Strain describes the distortion of a body in response to an applied force. Strain is homogeneous when any two portions of the body that were similar in form and orientation before are similar in form and orientation after strain. Homogeneous by definition means the strain is homogeneous. Conversely, heterogeneous strain implies heterogeneous deformation. Because heterogeneous strain is more complex to describe than homogeneous strain, even heterogeneously strained bodies or regions are analyzed by separating them into homogeneous portions. In other words, homogeneity of deformation is a matter of scale.

In this paper the directional variation of undrained strength of clay as identified by Casagrande and Corrillo [1]. [3]. is taken as illustration and interpreted in terms of Coaxial and Non coaxial strain as analytical tool.

1. INTRODUCTION

Isotropic stress acts equally in all directions, it results in a *volume change* of the body.Deviatoric stress, on the other hand, changes the *shape* of a body [2]

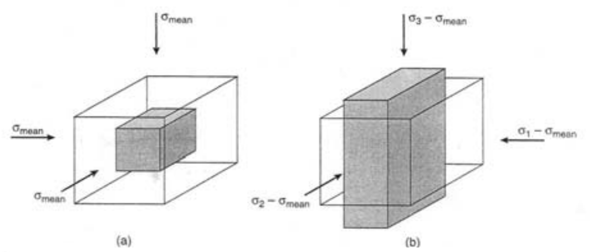

Figure 1 The mean (hydrostatic) and deviatoric components of the stress. (a)mean stresscauses volume change and (b) Deviatoric stress causes shape change

In a homogeneously strained, two-dimensional body there will be at least two material lines that do not rotate relative to each other, meaning that their angle remains the same before and after strain. A material line connects features , such as an array of grains, that are recognizable throughout a body's strain history. The circle deforms and changes into an ellipse. In homogeneous strain, two orientations of material lines remain perpendicular before and after strain. These two material lines form the axes of an ellipse that is called strain ellipse.The principal incremental strain axes rotate to the finite strain axes, a scenario that is called non- coaxial strain accumulation.The case in which the same material lines remain the principal strain axes at each increment is called coaxial strain accumulation.

2.0 Undrained Shear Strength of Clay

Let the undrained shear strength of a soil specimen with its axis vertical be referred to $S_{u[V]}$. Similarly let the undrained shear strength with its axis horizontal be referred to as $S_{u[H]}$, If $S_{u[V]} = S_{u[i]} = S_{u[H]}$ the soil is isotropic. Here $S_{u\{i\}}$ is the undrained shear strength when he major principal stress makes an angle i with the horizontal. If the soil is anisotropic, $S_{u[i]}$ will change with direction. Cassagrande and Corrillo proposed the following equation for the directional variation the undrained shear strength; $S_{u[i]} = S_{u[H]} + [S_{u[V]} - S_{u[H]}] \sin^2 i$. For this illustration the figures and calculations are transformed into Coaxial and Non-coaxial diagrams with minimum changes. The Circle and the strained ellipsoids help to identify the anisotropic behavior of clay. Since the sample is pure clay only pure shear is involved and and the simple shear is applicable only for sand .The following figure 2 explains simple shear and pure shear . [2]

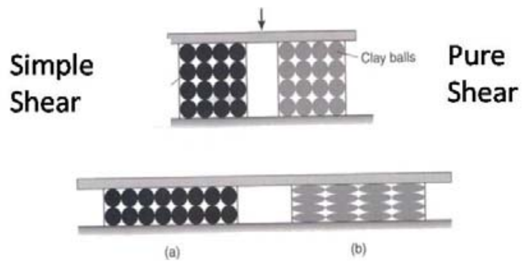

Figure 2 The rigid spheres slide past one another to Accommodate the shape change without distortion of the individual marbles . In figure 2b the shape change is achieved by changes in the shape of individual clay balls to ellipsoids, are quite different.

2. VARIATION OF UNDRAINED SHEAR STRENGTH

In this paper the directional variation of undrained strength of clay as identified by as Casagrande and Corrillo [1] .[3]. is taken as illustration and interpreted in terms of Coaxial and Non coaxial strain as analytical tool.

O Anisotropy in undrained shear strength:

Owing to the nature of the deposition of cohesive soils and

1,2 Professor, Department of Harbour Engineering and Off Shore Technology , AMET University, 135 East Coast road, Kanathur -603 112 , CHENNAI, INDIA
E-Mail rajaraman.usha44@gmail.com[1]
swamy2667@yahoo.co.in[2]

subsequent consolidation, clay particles tend to become oriented perpendicular to the direction of the major principal stress.

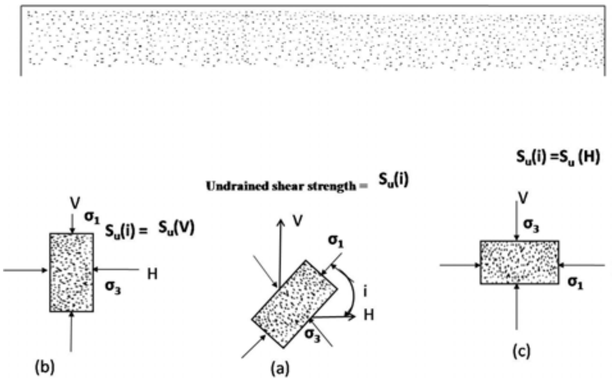

Figure 3 Strength anisotropy in clay.

Parallel orientation of clay particles could cause the strength of the clay to vary with direction, or in other words the clay could be anisotropy with respect to strength. This can be demonstrated with the aid of the above figure, in which V, H are vertical and horizontal directions that coincide with lines perpendicular and parallel to the bedding planes of a soil deposit.

If a soil specimen with its axis inclined at an angle i with the horizontal is collected and subjected to an undrained test, the undrained shear strength can be given by

$$S_u(i) = \frac{\sigma_1 - \sigma_3}{2} \qquad (1)$$

Where $S_u(i)$ is the undrained shear strength when the major principal stress makes an angle i with the horizontal.

Let the undrained shear strength of a soil specimen with its Axis vertical [i.e; $S_{u(i=90^o)}$] be referred to as $S_{u(V)}$ Figure 3(a). Similarly the undrained shear strength with its axis horizontal [i.e; $S_{u(i=0^o)}$] be referred to as $S_{u(H)}$ figure 3(c).

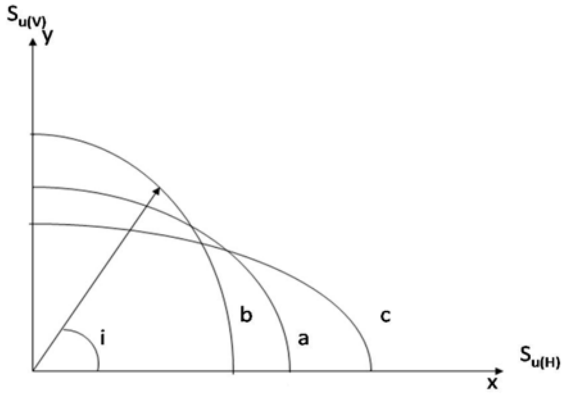

Figure 4 Directional Variation of undrained strength of clay.

If $S_{u(V)} = S_{u(i)} = S_{u(H)}$, the soil is isotropic with respect to strength, and the variation of undrained shear strength can be represented by a circle in a polar diagrams shown by curve a in figure 4.

If If the soil is anisotropic, $S_{u(i)}$ will change with direction. Casagrande and Carrillo (1944) proposed the following equation for the directional variation of the undrained shear strength ;

$$S_{u(i)} = S_{u(H)} + [S_{u(V)} - S_{u(H)}] \sin^2 i \qquad (2)$$

4. COAXIAL AND NON-COAXIAL STRAIN ANALYSIS

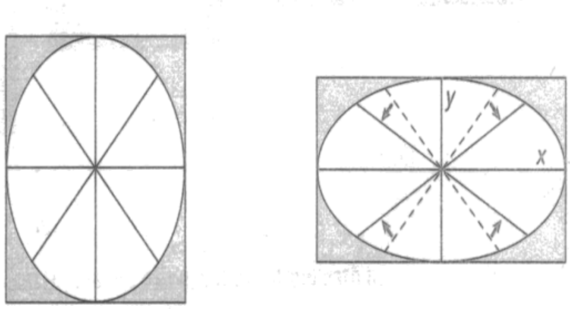

Figure 9 Homogeneous strain describes the transformation of a square to a rectangle or a circle to an ellipse. Two material lines that remain perpendicular before and after strain are the principal axes of the strain ellipse [solid lines]. The dashed lines are material lines that do not remain perpendicular after strain; they rotate toward the long axis of the strain ellipse.

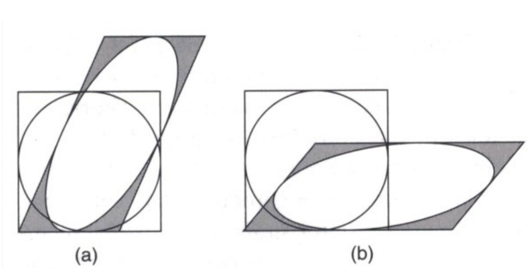

Figure10 A combination of simple shear [a special case of non-coaxial strain] and pure shear [coaxial strain]is called general shear or general non-coaxial strain. Two types of general shear are transtension [a] and transpression[b],reflecting extension and shortening components.

5. COAXIAL STRAIN INTERPRETATION

Now the discussion can be extended to co-axial strain analysis .The following figures will be useful for interpretations.

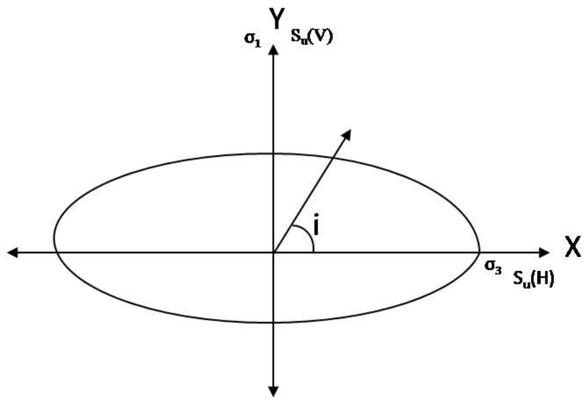

Figure 5.

When i =0 the major principal stress makes an angle 90^0 with the horizontal plane(bedding plane) as identified in figure 3b.Since σ_1 is compressive stress acting vertically down , the circle becomes ellipse elongated along x direction and compressed in y direction. This is similar to the curve c shown in figure 4

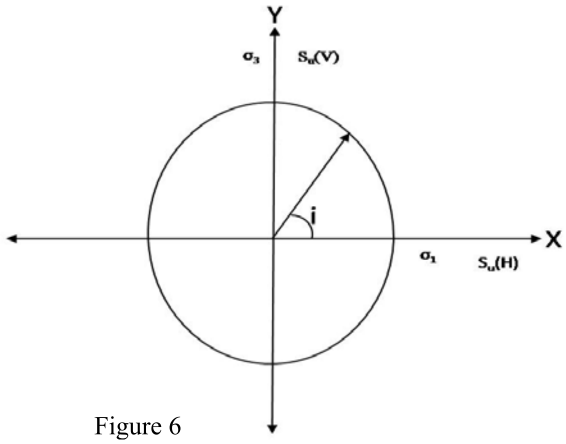

Figure 6

When σ_1 acts parallel to the bedding plane as compressive axial stress and i =90^o the major principal stress σ_1 makes an angle 90^o with the vertical. In this case the circle becomes ellipse elongated in y direction and compressed in x direction. This is similar to curve b in figure 4.

This circle representing the curve a in figure 4 and it takes a path in between the deformed ellipse representing the directional variation of the shear strength. The combined diagram of figures 5, 6 &7 is given below.

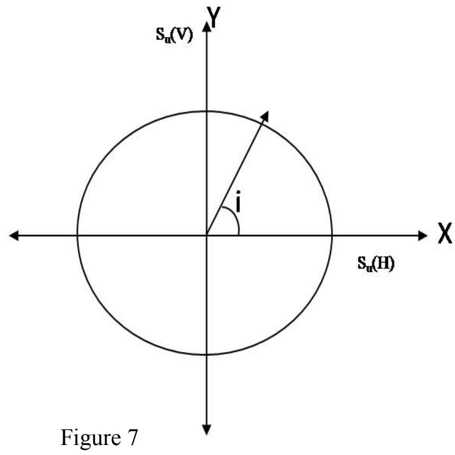

Figure 7

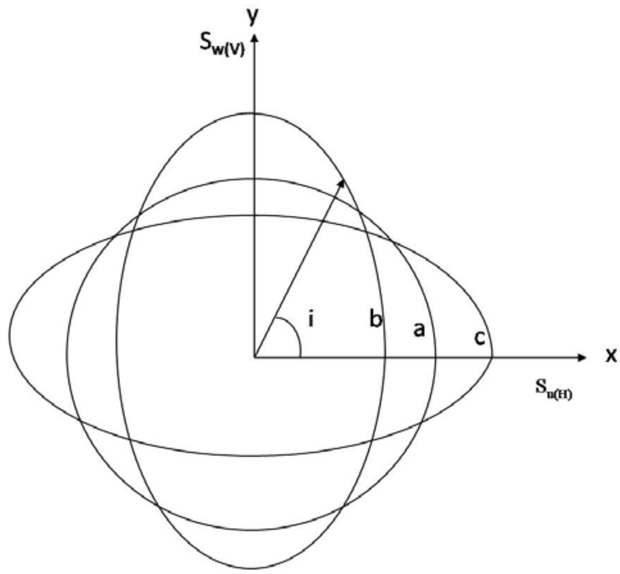

Figure 8 Co-Axial strain on clay (pure Shear)

5.1 Coaxial Strain and Anisotropy

When $S_{u(V)} > S_{u(H)}$, the nature of variation of $S_{u(i)}$ can be represented by curve b in figure 2. If $S_{u(V)} < S_{u(H)}$, the variation of $S_{u(i)}$ Is given by curve c .The coefficient of anisotropy can be defined as :

$$K = \frac{S_{u(V)}}{S_{u(H)}}$$

In the case of natural soil deposits , the value of K can vary from 0.75 to 2.0. K is generally less than 1 in overconsolidated clays.

2. Figure 4 is confined to quadrant 1only.Figure 8 covers all 4 quadrants. And includes figure 4 (curve b,a and c).
3. Strain ratios measured agree with the the familiar coefficient of anisotropy (K) which ranges from 0.75 to 2.0 (as shown in Table I)
4. X axis and Y axis form material lines perpendicular to each other. As a result the deformation X/Y or Y/X as strain ratio are calculated
5. i and strain ratios are related as shown in Table II

TABLE I Coaxial Strain And Anisotropy (K)

Serial No:	Curve	X	Y	X/Y	Y/X	Strained figure
1.	a	2.3	2.3	1.0	1.0	Near circle
2.	b	1.7	3.1	-	1.82	Ellipse
3.	c	3.1	1.7	1.82	-	Ellipse

TABLE II Shear Strength and Coaxial Strain Ellipses

i	MPS	MPS angle with Horizontal	Deformed figure	Elongated along	Compressed in
o	σ_1	90^0	Ellipse	X direction	Y direction
90^0	σ_1	MPS angle with vertical 90^0	ellipse	Y direction	X direction
45^0	$\sigma_1 = \sigma_3$ or $\sigma_1 - \sigma_3 = 0$ deviatoric stress is zero	MPS angle with vertical or horizontal 45^0	circle	Neither elongation	Nor compression

i = angle with the horizontal plane (bedding plane)
MPS – major principal stress
σ_1, σ_3 are major and minor principal stresses.

6. CONCLUSION :

1. Pure clay is associated with pure shear or coaxial strain .No simple shear.

7 . REFERENCES

1.Casagrande A. and N. Carrillo, Shear failure of anisotropic materials, in *contribution to soil mechanics* 1941-1953 , Boston society of Civil engineers , Boston , Mass ., 1944
2. Van der pluijm, ben a, *Earth Structure*-2003
W.W.Norton & company inc, New York 10110.
3.Das Braja M,2008*Advanced Soil Mechanic*, Taylor & Francis pp.433-435.

First International Conference on Geotechnique, Construction Materials and Environment, Mie, Japan, Nov.21-23, 2011, ISBN: 978-4-9905958-0-7 C3051

FEM Analysis of Innovative Shallow Foundation System for Reactive Soils

Mostafa A. Ismail, Advanced Geomechanics, Perth WA, Australia

Mohamed A. Shahin, Curtin University, Department of Civil Engineering, Perth WA, Australia

ABSTRACT: Granular pile anchor foundations (GPAF) are a promising foundation system that can be used to mitigate the serious consequences of volumetric changes of reactive soils, both during expansion and shrinkage. This paper presents results from 3D finite element analyses, using PLAXIS software, undertaken on a typical double-story building constructed over a system of GPAF in a reactive soil. The study investigates the ability of the GPAF system to resist the forces induced by soil movement due to moisture variation, and the impact of this resistance on the straining actions affecting the superstructure. The results confirm the efficiency of the GPAF system in arresting the movement of the reactive soil, which in turn improves the structural responses of the building in terms of induced deformations, angular distortions and internal forces.

1. INTRODUCTION

Reactive soils are clays that swell and shrink with changing moisture content, and are found in many arid and semiarid regions around the world. For example, it is estimated that 20% of the Australian surface soil can be classified as reactive [1]. There are several factors that influence the swelling and shrinking potential of clay soils, including the amount and type of clay minerals, cation exchange capacities, availability of moisture and the initial water content. The swell/shrink ground movements associated with reactive soils pose significant challenge to the geotechnical community as they cause distress to foundations of lightweight structures and cracking in retaining walls, pavements, canal beds and linings [2, 3].

Despite the numerous foundation systems that have been developed over the past decades to control the movements induced by reactive soils, substantial financial losses are still incurred every year in many places around the world. For example, the American Society of Civil Engineers estimated that about one quarter of all homes in the US have experienced some damage from reactive soils; the financial losses incurred by property owners exceed those caused by natural disasters such as earthquakes, floods, hurricanes and tornadoes combined [4]. In Australia, and despite the stringent regulatory requirements, most of the lightweight buildings constructed on reactive soils experience some distortional damage during their early lives [5].

The literature includes numerous solutions for construction on reactive soils, including replacement of the entire reactive material, pile foundations [6], soil stabilization using additives [7, 8], and implementation of special types of foundations such as drilled and friction piers [3]. One promising, special foundation solution that has been recently proposed is the granular pile anchor foundation (GPAF). The GPFA is an innovative technique that has shown great potential as a solution to founding structures safely into reactive soils. The GPAF system was first proposed by Phanikumar and Ramachandra Rao [9] for reactive soils under heave conditions and was later pursued by other investigators [e.g. 10, 11] via laboratory and field trials. In an attempt to determine the controlling parameters of the GPAF technique to resist the heave and shrinkage induced by reactive soils, the efficiency of the technique was further investigated numerically by Ismail and Shahin [12] using the finite element method (FEM). Despite the success of the GPAF reported by the above investigators, it is yet to be applied in practice, primarily due to the limited field trials.

In this paper, the performance of the GPAF system under heave and shrinkage is investigated by 3D numerical analysis for a typical double-story, four-bay structure founded in reactive soil. The investigation explored the efficiency of the system in arresting the ground movements induced by soil heave/shrinkage, and the implications of this on the internal forces experienced by the superstructure.

2. CONCEPT OF GPAF SYSETM

Fig. 1 shows the concept of the GPAF system, which is a hybrid solution in which a shallow foundation is supported on a granular pile that derives its resistance from the interface between the granular pile and surrounding reactive soil.

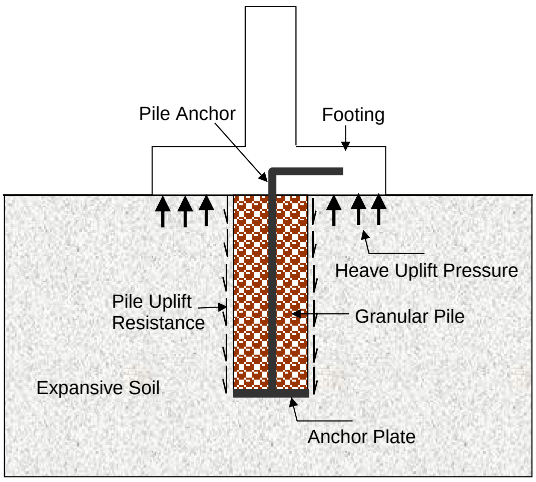

Fig. 1: Typical GPAF system

As can be seen in Fig. 1, a typical GPAF system consists of a pile of granular material installed into the reactive soil. A concrete footing is then constructed above the granular pile and connected to it via a steel anchor that is monolithically casted with the concrete footing to transfer the load between the footing and the pile. The uplift resistance is mobilized as skin friction along the periphery of the granular pile at its interface with the surrounding soil. The force in the pile anchor is transmitted to this interface via a base plate that is rigidly connected to the pile anchor. According to this arrangement of the anchorage system between the footing and granular pile, the latter cannot only reinforce the ground (as in the case of soft clay and loose sand) but can also effectively resist the uplift forces from an expansive soil. As can be inferred from Fig. 1, the uplift resistance of the GPAF system is a function of the self-weight of the pile-footing assembly, interface shear strength, surface area of the granular pile and normal stress developed during expansion of the soil surrounding the pile. In the experiment performed by Phanikumar et al. [13], the undrained shear strength of the expansive clay surrounding the granular pile was shown to have increased by about 20%, compared with the clay in the free field zone due to the expansion-induced normal stresses.

3. NUMERICAL ANALYSES OF TWO-STORY BUILDING RESTING ON GPAF SYSTEM

In order to investigate the efficiency of the GPAF system in practice, a two-story four-bay frame building resting on a system of GPAF is considered in the current study. The problem is analyzed by numerical modeling using the commercially available finite element software PLAXIS 3D Foundation [14].

3.1 Problem Identification

The two-story frame building considered in the current study is 6 m high (each story is 3 m in height), and is 20 m × 20 m in plan with each bay having dimensions of 5 m × 5 m. A ceiling slab of 160 mm thick is assumed for each story. The slabs are supported by beams, 300 mm wide and 400 mm deep, which in turn rest on square columns of dimensions 300 mm × 300 mm. The dead load of each structural component of the frame building is considered according to the material unit weight of that component, and an additional distributed live load of 5 kPa is also assumed to act on top of the slabs. All concrete materials (including footings) are made of concrete of an elastic modulus of 35 GPa, Poisson's ratio of 0.2 and unit weight of 24 kN/m^3.

The GPAF system consists of square pad footings of dimensions 2 m × 2 m, each supported on a group of three granular piles of 0.5 m in diameter and 3.0 m in length. A schematic diagram of the arrangement of the three granular piles within the pad footing is shown in Fig. 2. A group of piles is used rather than a single pile to enhance the rotational stiffness and stability of the system. The problem is analyzed using the 3D model presented in Fig. 3, which has a discretized mesh that consists of 17,880 wedge elements of 15 displacement nodes and 6 Gaussian stress points each.

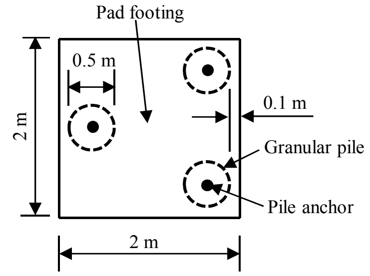

Fig. 2: Schematic diagram of the pad footing with three granular pile anchors

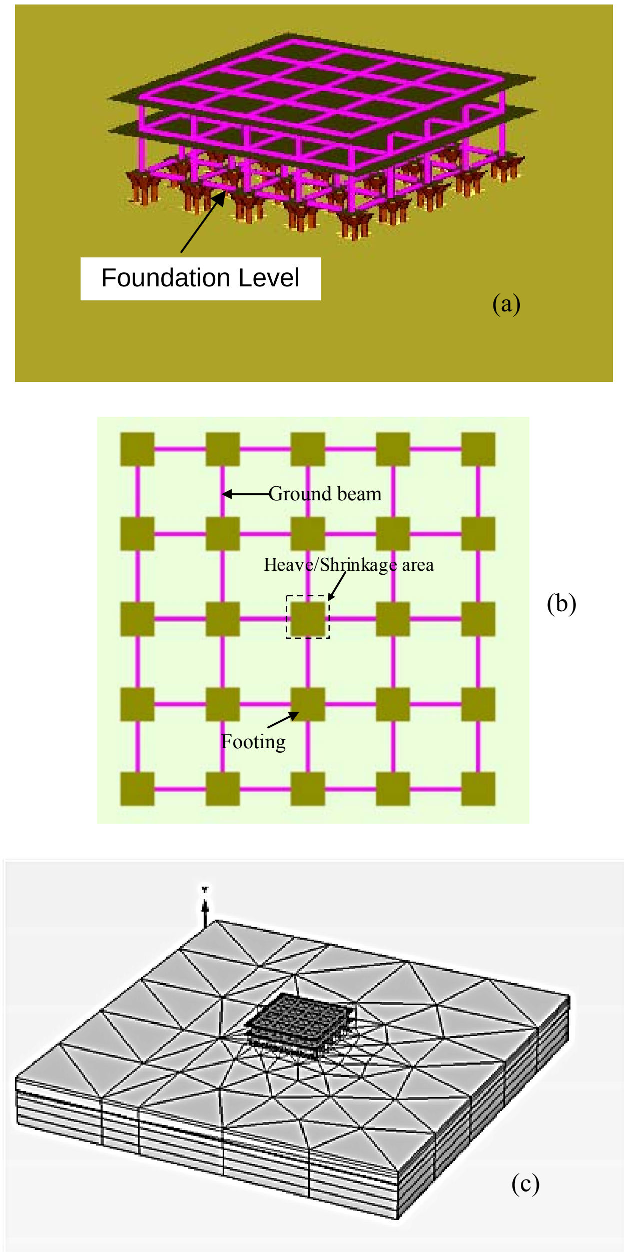

Fig. 3: FEM 3D model: (a) double-story building including GPAF system; (b) plan view of building foundation; (c) mesh discretization

The idealized ground profile consists of a gently sloping reactive clay layer of an average thickness of 3.5 m (across the footing foot print) overlying dense sand of an average thickness of 11.5 m. The model is strategically refined around the footing and granular piles to improve the accuracy of the analysis and the boundaries are located farther from the area of interest to minimize the boundary effect. The concrete footings are located 1.0 m below the ground surface and are modeled using a Mindlin's plate element of thickness of 0.6 m. The pile anchor is modeled as an elastic embedded pile [14] of 75 mm in diameter with an elastic modulus of 200 GP. The steel base plate is modeled as an infinitely rigid plate. All pad footings are connected by concrete tie beams (see Fig. 3b), 300 mm wide and 600 mm deep.

3.2 Soil Models and Parameters

The reactive clay is modeled using a Mohr-Coulomb (MC) model and is assumed to behave in a drained manner during expansion and shrinking. The underlying dense sand and granular pile material are best modeled using the hardening soil constitutive model (HS). The HS model [15] is a non-linear elastic plastic formulation which adopts multiple yield loci as a function of plastic shear strain and a cap to allow volumetric hardening. The non-linear stress strain relationship is represented by a hyperbolic formula, with primary loading governed by a secant deformation modulus (E_{50}) at 50% of the material strength. Loading and unloading within the current yield surface are assumed to be elastic (defined by a separate modulus, E_{ur}) with failure governed by the Mohr-Coulomb failure criterion. Both E_{50} and E_{ur} evolve with the minor effective stress, σ'_3, according to the following formula:

$$E_{50} = E_{50}^{ref}\left(\frac{c\cos\phi - \sigma'_3\sin\phi}{c\cos\phi + p_{ref}\sin\phi}\right)^m \quad (1)$$

where: c is the soil effective cohesion, ϕ is the effective peak friction angle, m is the exponent that controls the dependency of the stiffness on stress and p_{ref} is the reference stress corresponding to E_{50}^{ref}. A summary of the material parameters used for all soils are presented in Table 1. It should be noted that the properties of the reactive clay are those evolving after the wetting/drying event and during expansion/shrinking. In reality, the strength of a reactive soil degrades during expansion and increases during shrinking (due to suction), but this is not modeled in this study.

The rate of volume change at which reactive clays would normally encounter depends on the location from the source of moisture and magnitude of overburden pressure. In the current study, a leaking event of an underground water facility located underneath the central column is assumed to cause arbitrary values of heave and shrinkage of 20% and 10%, respectively, over the layer thickness of the affected area underneath the central footing, as shown in Fig. 3b. Both heave and shrinkage were modeled by applying equivalent volumetric strains to the affected area. The heave and shrinkage events are applied independent of each other, starting from the stage after application of the dead and live loads.

Table 1. Soil properties used in the finite element analyses

Parameter	Soil Type		
	Reactive Clay	Dense Sand	Granular Pile
γ(kN/m^3)$^{(1)}$	15	20	20
E_{50}^{ref} (MPa)	2	75	200
E_{oed}^{ref} (MPa)	–	75	200
E_{ur}^{ref} (MPa)	–	200	600
c (kPa)	2	0.1	0.1
ϕ (°)	24	36	40
$v_{ur}^{(2)}$	0.35	0.2	0.2
p_{ref}(kPa)	–	100	100
m	–	0.5	0.5
$K_0^{(3)}$	0.6	0.4	0.4

(1) Soil unit weight; (2) Unload-reload Poisson's ratio; (3) Coefficient of earth pressure at rest.

4. RESULTS AND DISCUSSION

In order to investigate the efficiency of the GPAF system in enhancing the behavior of the two-story building constructed over a reactive soil, an additional independent analysis is carried out for the building resting on pad footings without the GPAF and the results are compared with those obtained from the analysis of the building resting on the GPAF system. The comparison is made for the top beams of the central frame (i.e. beams B1 to B4 in Fig. 4). The comparison results in terms of induced deformations due to heave and shrinkage are shown in Fig. 5, and the angular distortions and bending moments due to heave are given in Table 2.

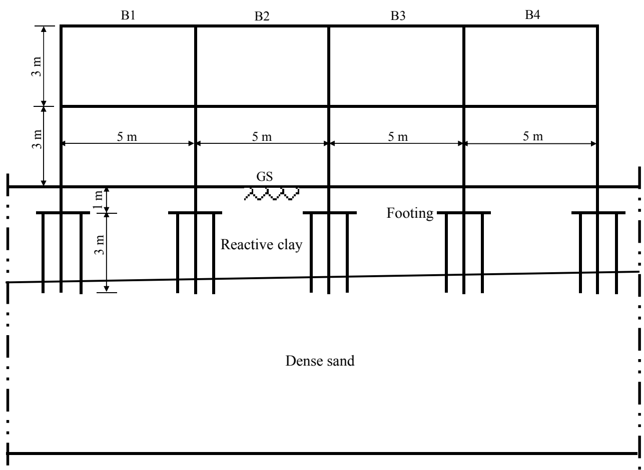

Fig. 4: Schematic diagram of the central frame

It can be seen from Fig. 5 that the ability of the pad footings to resist the vertical movements induced by soil heave is significantly improved when the GPAF system is used. The maximum vertical displacement induced by soil heave for beams B1–B4 without the GPAF system is found to be equal to 6.7 mm, whereas negligible vertical movement is developed when the GPFA system is used. More importantly, it can be seen from Table 2 that all beams undergo much less angular distortions when the GPFA system is used. For example, the angular distortion of beam B2 without the GPAF system is some 300 times greater than that experienced when the GPAF system is used.

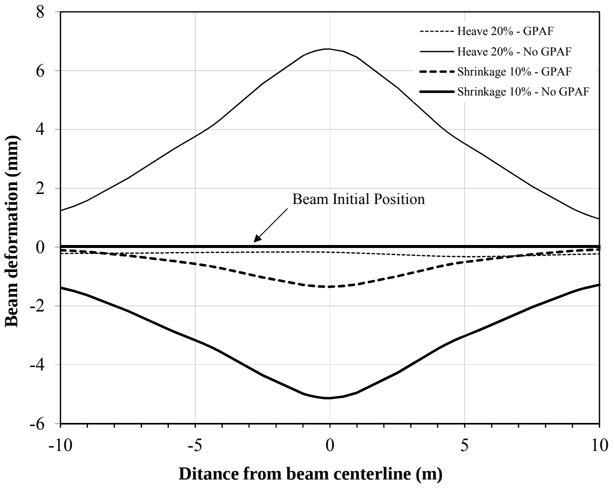

Fig. 5: Deformation of central beams B1 to B4 due to heave and shrinkage

Table 2. Angular distortions and internal forces of central beams B1 to B4 due to heave

Beam Number		Angular distortion ($\times 10^{-5}$)	Maximum negative moment (kN.m)	Maximum positive moment (kN.m)
B1	GPAF	0.6	44.6	23.0
	No GPAF	50	81.2	29.3
B2	GPAF	0.2	59.8	26.0
	No GPAF	59	130.2	25.3
B3	GPAF	2.8	58.0	28.0
	No GPAF	64	132.4	28.6
B4	GPAF	1.8	44.0	25.0
	No GPAF	51	79.7	29.6

Note: 20% Heave: Free field heave = 75 mm

Previous investigations found in the literature did not address the suitability of the GPAF system to resist shrinkage events when reactive soil loses moisture. However, it can be readily shown from Fig. 5 that under such event the GPAF system is capable of arresting the shrinkage and significantly reducing its induced settlement. It is found that the maximum beam settlement induced by soil shrinkage for the building with GPAF system is reduced by about 75% compared with the case of no GPAF system. It should be noted that the capacity of the GPAF system to resist shrinkage is a result of its ability to bear directly on the piles (while still in contact with the shrinking soil), which in turn could engage the bearing capacity of the sand layer that embrace the base plate (there are evidences that down drag forces are transferred to the shrinking soil). Given that the granular pile has no tension or bending capacity, it is therefore expected that the maximum capacity to resist shrinkage will be reached when the shrinking soil detaches itself completely from the granular pile. In such case the shrinkage resistance can be significantly improved by encasing the granular pile into a stiff, geogrid case to stop the pile from bulging.

As can be seen in Table 2, the use of the GPAF system significantly reduced the maximum negative bending moments of all beams, but slightly reduced the maximum positive bending moments. For example, the maximum negative and positive moments of beam B1 are 81.2 and 29.3 kN.m, respectively, for the case without the GPAF system, whereas these values are reduced to 44.6 and 23.0 kN.m, respectively, for the case with the GPAF system.

The practical implication of the above results is that the use of the GPAF system for light-weight structures can significantly reduce the superstructure damage induced by reactive soils, leading to immense savings on the cost of structural repairs and ongoing maintenance.

5. SUMMARY AND CONCUSIONS

This paper presented results from 3D FEM analyses of the granular pile-anchor foundation (GPAF) system as a plausible foundation solution for light-weight structures built on reactive soils. The paper investigated the superstructure response of two-story, four-bay frame building to the ground heave/shrinkage induced by reactive soils.

The results indicate that the effect of the GPAF system in reducing the vertical displacement and angular distortion induced by soil heave are quite significant. It was shown that the maximum vertical displacement of 6.7 mm that is developed at the top beams of the central frame in the case of no GPAF has been totally arrested by the GPAF system, and no heave induced vertical displacement is produced. It was also shown that the GPAF system reduced the maximum angular distortion of the top beams dramatically. In accordance with this, the GPAF system is found to reduce the maximum negative and positive bending moments of the top beams by 56% and 21%, respectively, compared with the maximum negative and positive bending moments produced in the case of no GPAF system. It was also observed that the resistance to shrinkage is improved immensely when the GPAF system is used. The maximum settlement induced by shrinkage for the top beams of the central frame is reduced by 75% compared with the case of no GPAF system.

The above results conclude that the GPAF system is a promising foundation technique that can be potentially used to reduce the detrimental impacts of reactive soils under both heave and shrinkage conditions.

6. REFERENCES

[1] Richards BG, Peter P, and Emerson WW, "The effects of vegetation on the swelling and shrinking of soils in Australia," Geotechnique, 33(2), 1983, pp. 127-139.

[2] Al-Rawas A, and Goosen MFA, Reactive soils, recent advances in characterization and treatment. London: Taylor & Francis, 2006.

[3] Chen FH, Foundations on reactive soils. New York: Elsevier, 1988.

[4] Wray WK, So your home is built on expansive soils: a discussion of how expansive soils affect buildings. New York: American Society of Civil Engineers, 1995.

[5] Barthur R, Jaksa MB, and Mitchell PW, "Design of residential footings built on expansive soil using probabilistic methods," in Proceedings of the 7th Australia New Zealand Conference on Geomechanics, 1996, Adelaide, pp. 369-374.

[6] Nusier OK, Alawneh AS, and Abdullatit BM, "Small-scale micropiles to control heave on reactive clays," Ground Improvement, 162(1), 2009, pp. 27-35.

[7] Ene E, and Okagbue C, "Some basic geotechnical properties of reactive soil modified using pyroclastic dust," Engineering Geology, 107(1-2), 2009, pp. 61-65.

[8] Khattab SAA, Al-Mukhtar M, and Fleureau JM, "Long-term stability characteristics of a lime-treated plastic soil," Journal of Materials in Civil Engineering, 19(4), 2007, pp. 358-366.

[9] Phanikumar BR, and Ramachandra Rao N, "Increasing pull-out capacity of granular pile anchors in reactive soils using base geosynthetics," Canadian Geotechnical Journal, 37(4), 2000, pp. 870-881.

[10] Phanikumar BR, Srirama Rao A, and Suresh K, "Field behaviour of granular pile-anchors in reactive soils," Ground Improvement, 161(G14), 2008, pp. 199-206.

[11] Sharma RS, Phanikumar BR, and Nagendra G, "Compressive load response of granular piles reinforced with geogrids," Canadian Geotechnical Journal, 41(1), 2004, pp. 187-192.

[12] Ismail AM, and Shahin MA, "Finite element analyses of granular pile anchors as a foundation option for reactive soils," in International Conference on Advances in Geotechnical Engineering, 2011, Perth, Western Australia, in press.

[13] Phanikumar BR, et al., "Granular pile anchor foundation (GPAF) system for improving the engineering behavior of expansive clay beds " Geotechnical Testing Journal, 27(3), 2004, pp. 1-9.

[14] Brinkgreve RB, and Broere W, PLAXIS 3D foundation manual, Version 2.2. The Netherland: Delft University of Technology and PLAXIS, 2008.

[15] Schanz T, Vermeer PA, and Bonnier PG, "The hardening-soil model: formulation and verification," Beyond 2000 in Computational Geotechnics, Brinkgreve RBJ, Editor. Rotterdam: Balkema, 1999, pp. 281-290.

First International Conference on Geotechnique, Construction Materials and Environment, Mie, Japan, Nov.21-23, 2011, ISBN: 978-4-9905958-0-7 C3051

Delay Times of Elastic Waves at Discontinuities in Laminated Specimens

Yota Togashi*, Kazuo Tani*, Tetsuji Okada** and Hiroaki Sato**., *Yokohama National University and **Central Research Institute of Electric Power Industry

ABSTRACT: In order to design rock structures, deformation properties for discontinuous rock mass should be understood. For the former method of elastic wave velocity measurement, some PS logging studies showed that S wave velocities of rock masses, V_s, were found to be dependent on the RQD values. However, the influence of the discontinuities of rock masses was not studied yet. Therefore, a series of elastic wave velocity measurements were conducted using the laminated specimens of metals and rock cores to investigate the influence of the discontinuities. Results demonstrated that as number of discontinuity n increase, elastic wave velocity (V_p, V_s) become smaller. It is seemed because delay of running time. As axial compression stress σ_a increase, delay time at discontinuity t_d become smaller. It is expected that as σ_a increase discontinuity become closed.

Keywords: Ultrasonic wave, Elastic wave velocity, Discontinuity, Rock, Shear modulus

1. INTRODUCTION

In order to design rock structures, deformation properties of discontinuous rock mass should be understood. For the former method of elastic wave velocity measurement, some PS logging studies showed that S wave velocities of rock masses, V_s, were found to be dependent on the RQD values [1]- [2]. However, the influence of the discontinuities of rock masses for elastic wave velocity was not studied yet.
Therefore, a series of elastic wave velocity measurements were conducted using the laminated specimens of metals and rock cores to investigate the influence of the discontinuities.

2. METHODOLOGY

2.1 Laminated specimens

Photo1 shows laminated specimens. Table1 shows physical properties of materials for laminated specimens. These data is measured in continuous specimens (n=0 in Photo1). Laminated specimens have boundaries which are discontinuous in horizontal direction to loading plane. As table1 show, laminated specimens are made from Aluminum, Nylon, Mudstone, Basalt. Height of specimens H = 93.0~100mm.

2.2 The model for delay times of elastic waves at discontinuities

Figure1 shows the model for delay times of elastic waves at discontinuity t_d. In this model, discontinuities are modeled by boundaries between element &element. There are two assumptions for this model. The first was that total time of wave propagation was continuous from top

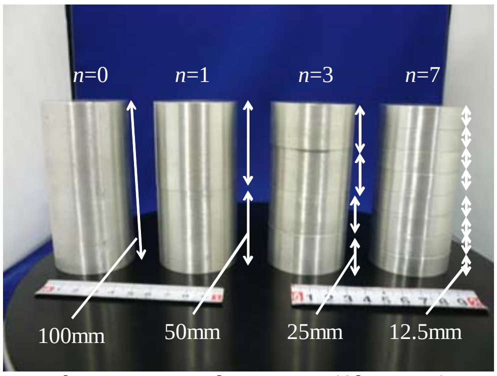

Photo1 Laminated specimens (Aluminum)

Table1 Physical properties of material for laminated specimens

Materials	V_p(m/s)	V_s(m/s)	ν_d	G_d(MPa)	E_d(MPa)
Aluminium	6452	3091	0.351	2.642E+04	7.139E+04
Nylon	2673	1057	0.41	1.282E+03	3.607E+03
Basalt	5271	2616	0.34	1.799E+04	4.810E+04
Mudstone	2165	677	0.45	8.652E+02	2.502E+03

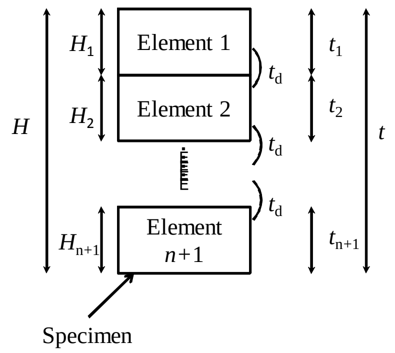

Figure1 Model for delay times of elastic wave

of specimens to that of bottom. The second was that t_d is constant values for any discontinuities in each specimen.
From the second assumption, elastic wave velocity in the element is described as

$$V_0 = \frac{H_1}{t_1} = \frac{H_2}{t_2} = \ldots = \frac{H_{n+1}}{t_{n+1}} \tag{1}$$

Continuous equation of running time t equation (2) and height of the specimen H equation (3) are described as

$$t = \sum_{i=1}^{n+1} \frac{H_i}{V_0} + nt_d \tag{2}$$

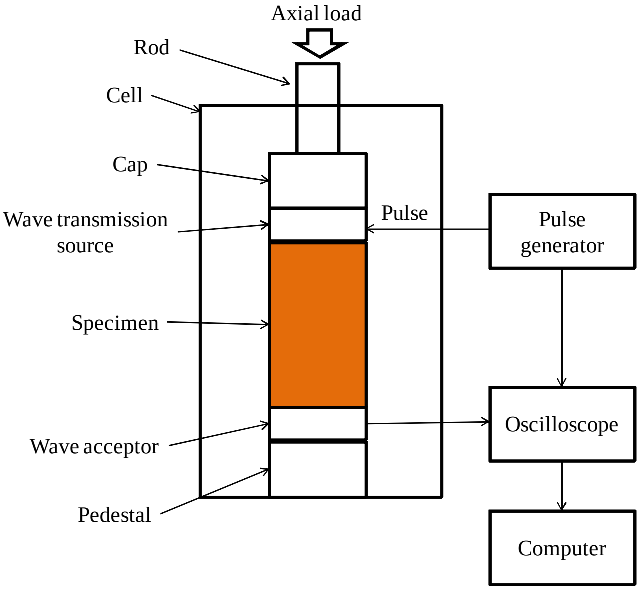

Figure2 Test apparatus

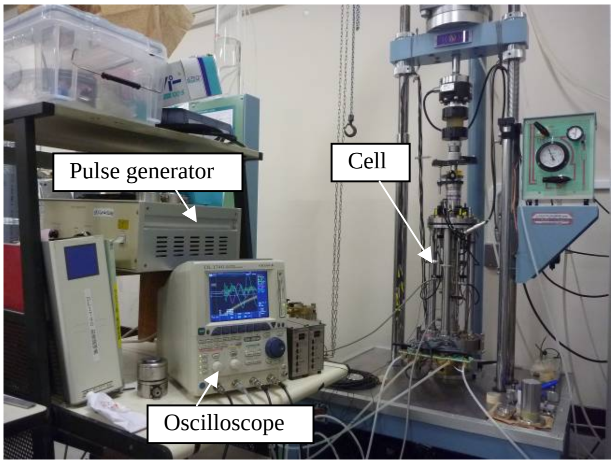

Photo2 Conditions for tests

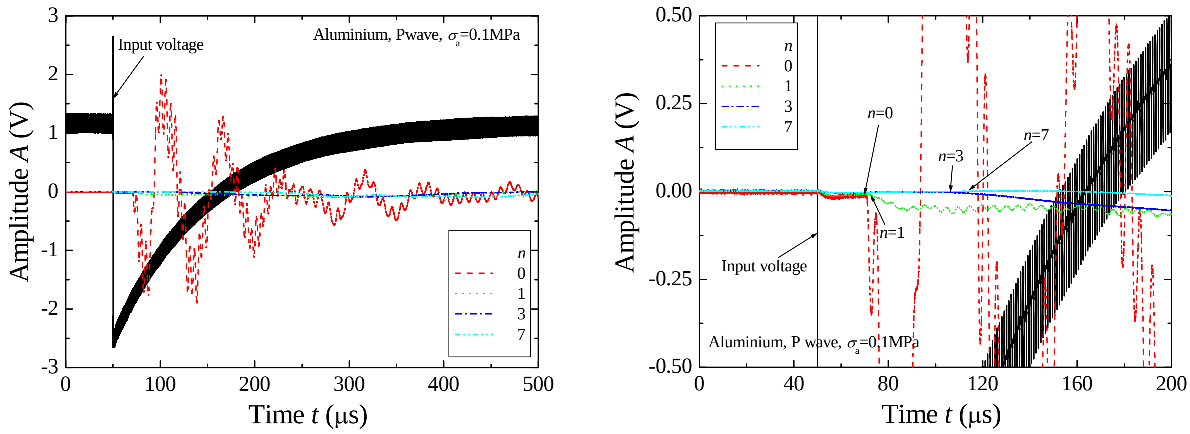

Figure3 P wave time-lines for aluminum (left: overall view, right: enlarged view)

The definition of velocity, equation (3) is described as

$$V=\frac{H}{t}=\frac{\sum_{i=1}^{n+1}H_i}{t}=\frac{1}{\dfrac{1}{V_0}+\dfrac{nt_d}{H}} \tag{3}$$

2.3 Ultrasonic wave velocity measurements under axial compression

Figure2 shows the test apparatus. Photo2 shows conditions of test. As Fig2 shows, ultrasonic wave velocity measurements under axial pressure ($\sigma_a \fallingdotseq$ 0.1&0.5MPa) are conducted. Frequencies of wave transmitter are 100kHz (S wave) and 200kHz (P wave). Bonding is done in boundary between wave transmitter and acceptor and specimens. Amount of bonding is 0.05~0.21g. The data by these tests are outputted in oscilloscope by 100MS/s sampling interval. The data used for analysis are average values by 128 times stacking.

3 TEST RESULTS

Figure3 shows time-lines taken from wave acceptor for aluminum laminated specimens. Allow lines show reading points of running times. As the values *n* increases, reading points become larger in direction of time axis. And also as the values *n* increases, wave amplitude *A* becomes smaller. It is shown that the wave energy was damped then running times are delayed at discontinuity because as the values n increases, the reading point become less-visible.

Figure4 shows the relationships between *n* and P wave velocity V_p. Figure5 shows the relationships between *n* and S

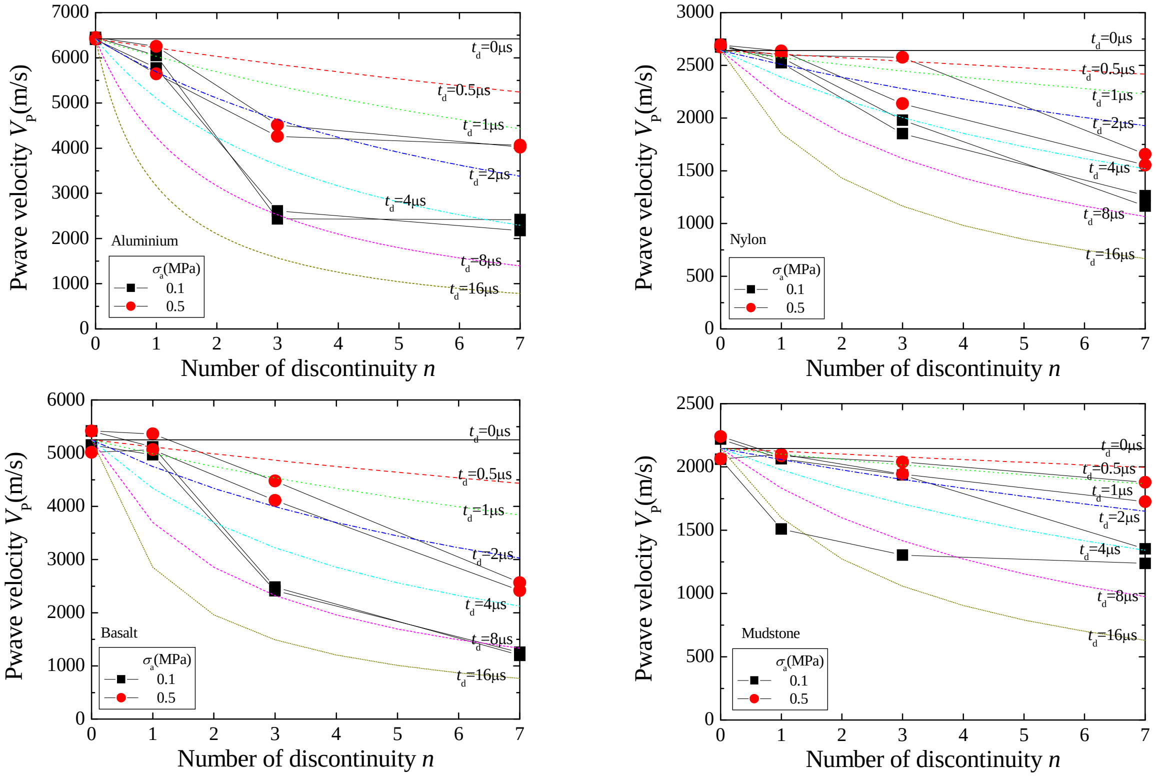

Figure.4 the relationships between P wave velocity V_p & n

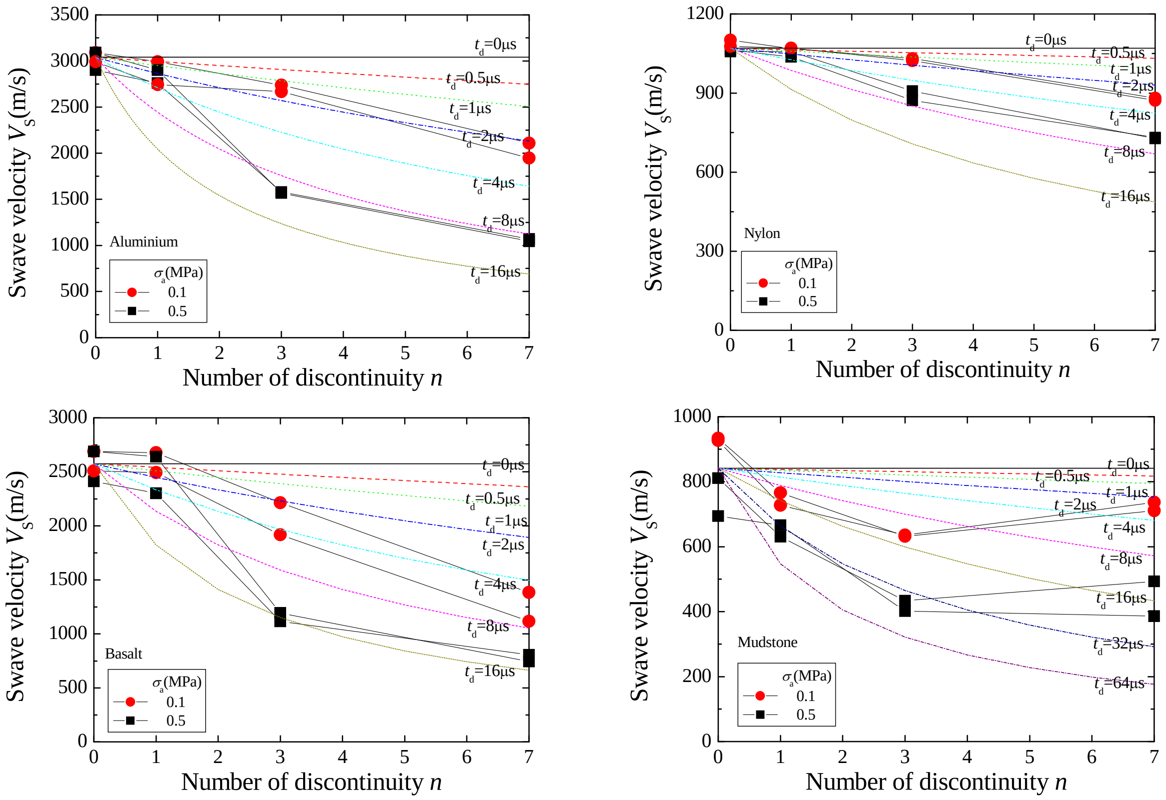

Figure5 the relationships between S wave velocity V_s & n

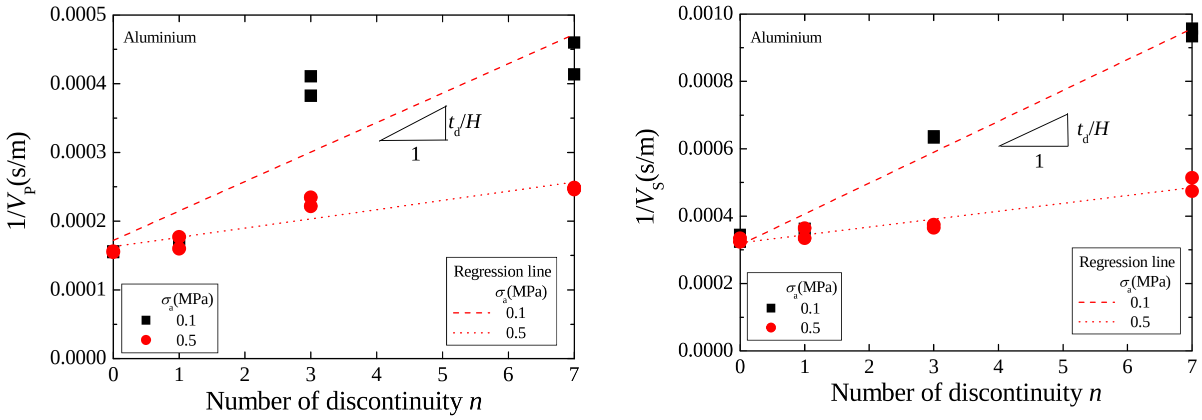

Figure6 Relationships between $1/V$ and n for aluminum

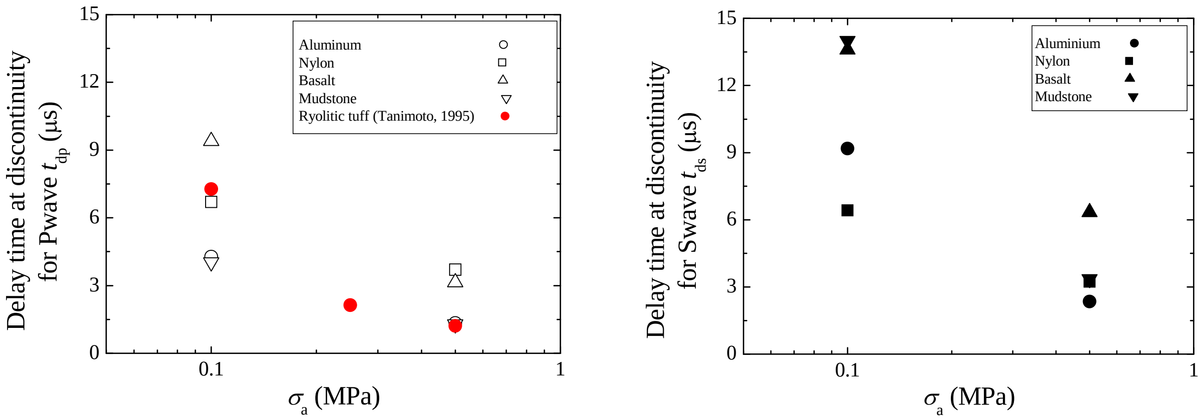

Figure7 Relationships between t_d and σ_a (left: P wave, right: S wave)

wave velocity V_s. In these figures, model curves are also shown for the t_d values of 0 to 64μs. As the values n increases, the elastic wave velocities (V_p, V_s) become smaller. It is because delay of running time. It would appear that the wave amplitude was damped by discontinuity then running time was delayed.

Figure6 shows the relationships between $1/V$ & n for aluminum. t_d are calculated from the shapes of different material's regression lines.

Figure7 shows relationships between t_d & σ_a. As σ_a increase, t_d becomes smaller values. It is expected that as σ_a increase discontinuity become closed.

In this figure, there are some data by Tanimoto et al (1995) [3]. Their test apparatus is almost same from ours, but their studies differ from ours about specimen's height and placing of discontinuities (in Tanimoto's studies, placing of discontinuities are by central.). Almost same tendency between our data & Tanimoto's is shown in figure7, so it is expected that placing of discontinuity is not dominant for this model.

4 CONCLUTIONS

In order to clarifying delay of elastic wave velocity at discontinuity, a series of elastic wave velocity measurements were conducted using the laminated specimens of metals and rock cores.

1) As number of discontinuity n increase, elastic wave velocities (V_p, V_s) become smaller. It is seemed because delay of running time at discontinuities.

2) As axial compression stress σ_a increase, delay time at discontinuity t_d become smaller. It is expected that as σ_a increase discontinuity become closed.

5 REFERENCES

[1] Sato, H., Higashi, S., Shiba, Y., Sato, K., Takahashi, K., Tsuruga, T,. "Attenuation characteristics of seismic motion based on earthquake observation records Part3." Civil Engineering Research Laboratory Rep.No.N07013, CREIPI, 2007.

[2] Ishii, K., Tani, K., Okada T. and Sato H. "Elastic wave velocity measurement of aluminum specimen modeling discontinuity in rock mass" Geo-Kanto, JGS, pp.258-259, 2009 (in Japanese).

[3] Tanimoto, C. and Kishida, K. "Fundamental study on seismic wave propagating property through several kinds of rock joint under uniaxial stress," , Journal of JSCE, No. 523/ III- 32, 49-58, 1995.9.

[4] Togashi, Y., Tani, K., Okada, T. & Sato H. "Ultra sonic velocity measurement for laminated specimens", Proc. 41st Japan Sym. on Rock Mechanics, JSCE, 2012 (subbmitted).

First International Conference on Geotechnique, Construction Materials and Environment, Mie, Japan, Nov.21-23, 2011, ISBN: 978-4-9905958-0-7 C3051

Geotechnical Investigation of Valleys using Lightweight Dynamic Cone Penetration Test for Landslide Risk Assessment

Takashi Hanaoka, Takashi Tsuchida, Shouichi Kawabata, Shouta Nakagawa, Hiroshima University

ABSTRACT: Counter-measures by using the regulations, information technology and the education to the residents are important because it take a tremendous time and cost for implementing physical disaster prevention measures to all potentially dangerous areas. The purpose of this study is to develop the site-investigation of natural valley using lightweight cone penetration test (LWDCPT), in order to implement the risk assessment of individual valleys with the slope stability analysis based on the models of valley obtained by the investigation. A series of investigation was carried out at four valleys in Higashi-Hiroshima city, which are put on the list of valleys potentially dangerous for mud and debris flows during heavy rain. LWDCPT was performed at both sides of valley with each descending to 20 meters with reference to head of valley until gradient of valleys become below 12.5 degrees, in which the necessary time for the site-investigation by two persons was about eight hours per one valley.

Keywords: Geotechnical investigation, Lightweight cone penetration test, Individual natural valley, Ground model

1. INTRODUCTION

In Hiroshima Prefecture, 31,987 valleys and slopes are listed as areas of dangerous for slope failure and debris flow, and this is the largest number in Japan. Counter-measures by using the regulations, information technology and the education to the residents are important because it take a tremendous time and cost for implementing physical disaster prevention measures to all potentially dangerous areas. In Hiroshima Prefecture, the prefectural land is divided into 350 unit areas of 5 kilometers square, and in each unit area, the criteria using the rainfall indexes, such as the soil water index and rainfall intensity, are determined on the basis of past records of landslide disasters due to heavy rain. In this system, a warning for an expected landslide or an evacuation order is made for each unit area, however, the risk of individual slopes in each area cannot be shown.

To assess the safety of an individual valley or slope, the geotechnical slope stability analysis is necessary. However, one major problem in natural slopes is that there has been little information on geotechnical conditions because of the extreme difficulty associated with ground investigation on the steep slopes covered with vegetation. The purpose of this study is to develop the site-investigation method of natural valley using lightweight cone penetration test (LWDCPT), in order to implement the risk assessment of individual valleys with the slope stability analysis based on the models of valley obtained by the investigation.

We focused on the large number of potentially dangerous valleys in Higashi-Hiroshima City, and selected four valleys in as same unit. The areas painted in yellow in Fig. 1 show the potentially dangerous valleys in Saijo Town of Higashi Hiroshima City. Fig. 2 shows the selected four valleys, which is in the red circle in Fig. 1, which are included in one 5km×5km regional mesh for the present risk assessment. Accordingly, the risks in these four valleys are same in the present method, and the purpose of this study is to evaluate the risks of the four valleys individually.

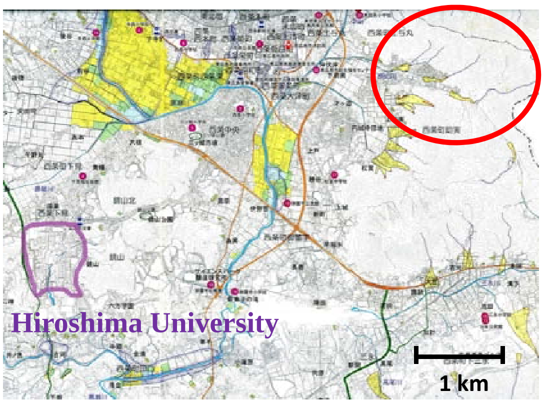

Fig. 1. Valleys at risk of landslide of in the town of Saijo.

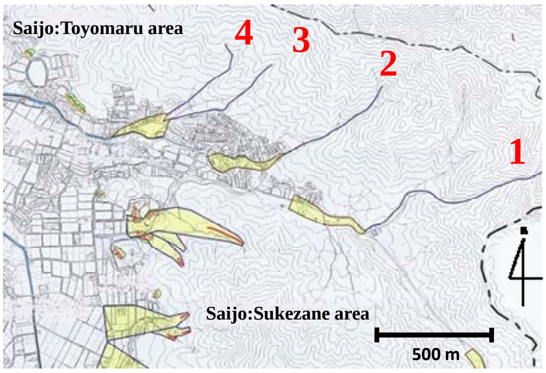

Fig. 2. Valleys where the survey were carried out.

2. GEOTECHNICAL INVESTIGATION

Geotechnical investigation was carried out in order to model the valleys for the seepage analysis and the slope stability analysis. The necessary items of modeling are slope gradient, thickness of surface soil and strength parameters. We explain how to determine of these items.

2.1 Light weight cone penetration test

LWDCPT has been designed and developed in France since 1991 (Langton, D.D., 1999). The schematic view of LWDCPT is shown in Figure 3. The mass is about 20 kg, and mainly consists of an anvil with a strain gauge bridge, central acquisition unit (CAU), and a dialogue terminal (DT). The below from the hammer to the anvil provides energy input, and a unique microprocessor records the speed of the hammer and the depth of penetration. The dynamic cone resistance (q_d) is calculated from the modified form of Dutch Formula as shown in Equation (1) (Cassan, M., 1988).

$$q_d = \frac{1}{A}\frac{\frac{1}{2}MV^2}{1+\frac{P}{M}}\frac{1}{x_{90^\circ}} \tag{1}$$

Where, x_{90° = penetration due to one below of hammer by 90° cone,
A = area of the cone,
M = the mass of striking hammer,
P = the mass of the struck materials, and
V = speed of the impact of the hammer.

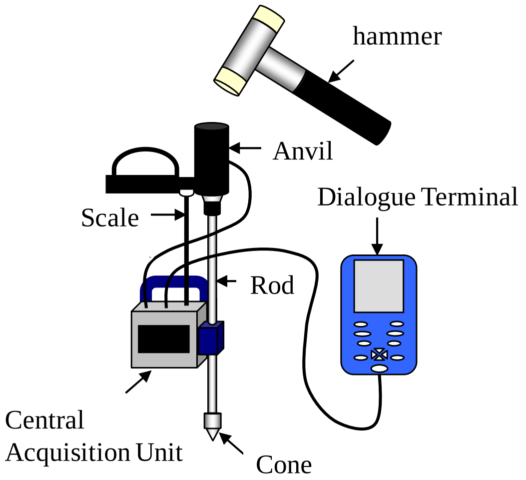

Figure 3. Outline of LWDCPT.

Photo 1. Appearance of LWDCPT (Valley 1).

Photo 1 shows appearance of LWDCPT. The advantages of LWDCPT are that the detail measurements are possible by getting a penetration resistance value with each hitting, and that in virtue of the lightweight and the simple, even for the non-specialist of geotechnical investigation, the operation is easy and safe.

2.2 Selection of the testing points in a valley

A geotechnical investigation of the valleys was carried out under the following policies.

(1)The headwater area was determined by using topographical data and a field trip. About six geotechnical investigation points were selected in the headwater area, and along the valley the geotechnical testing points were selected at intervals of 20 meters, downward.

(2) A test of the valley was carried out at both sides of the valley, which are 5 located meters away from the center of valley. The tests were carried out the headwater down to the valley, the gradient of which is larger than 12.5 degree.

(3) The sampling was carried out at both sides of four

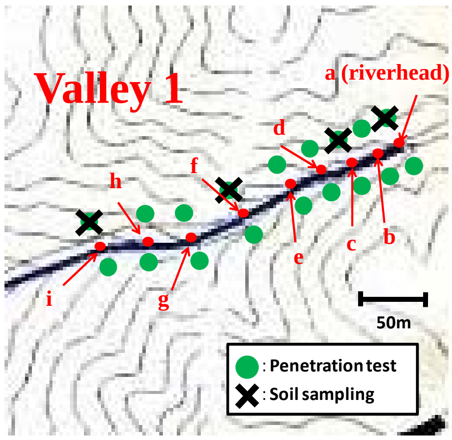

Fig.4. A example of selection of geotechnical investigation points (Valley 1).

Table 1. Number of geotechnical investigation points.

	Valley 1	Valley 2	Valley 3	Valley 4
Number of LWCPT	9	4	7	7
Number of soil sampling	4	4	4	4

Photo 2. Site of the geotechnical investigation. (Valley 4)

investigation points in each valley.
Fig. 4 shows a example of selected of testing points (Valley 1). Table 1 shows the number of geotechnical investigation points of the four valleys. Photo 2 shows the site of the geotechnical investigation in Valley 1. The testing points were nine and the soil sampling points were four in Valley 1.

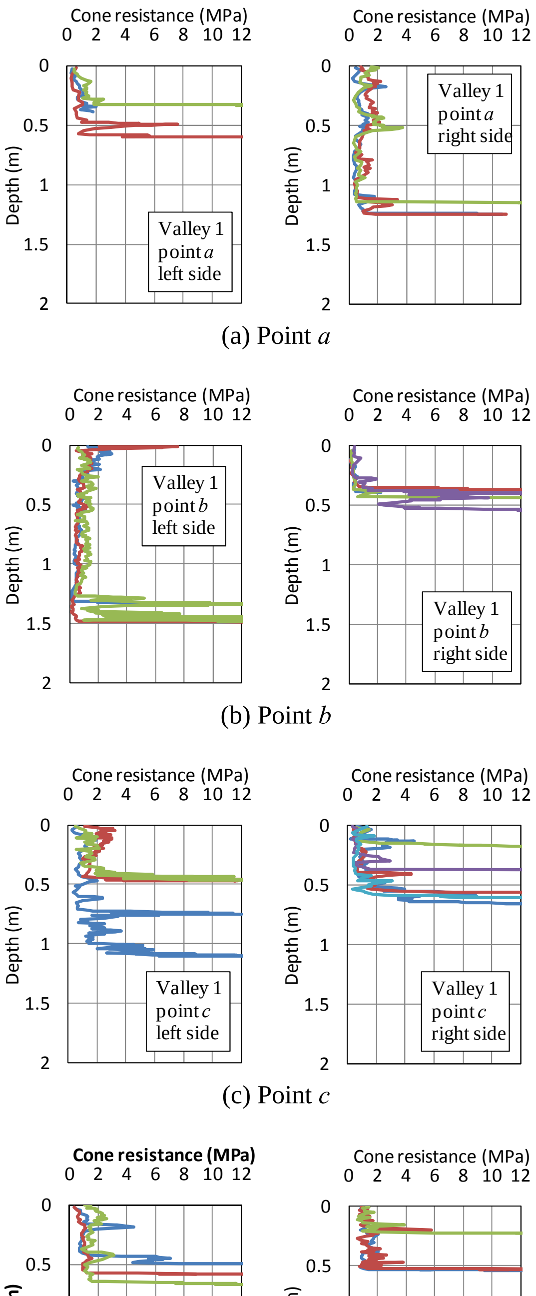

(a) Point *a*

(b) Point *b*

(c) Point *c*

(d) Point *d*

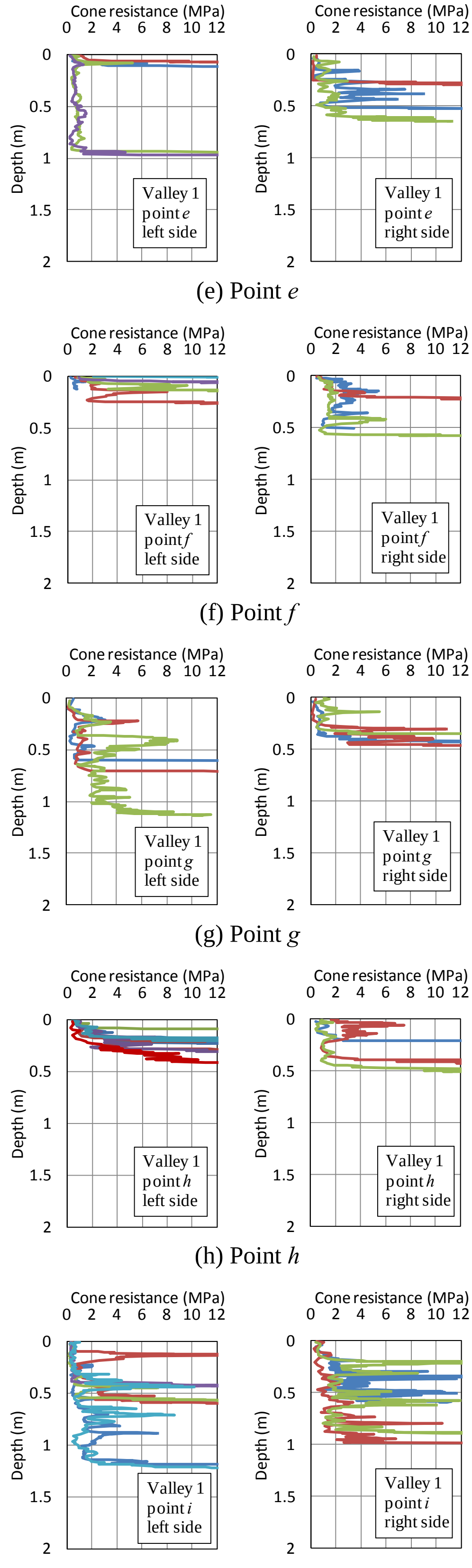

(e) Point *e*

(f) Point *f*

(g) Point *g*

(h) Point *h*

(i) Point *i*

Fig. 5. Penetration resistance q_d with depth

Table 2. Thicknesses of surface soil each point (Valley 1)

	left side	right side	average
a	0.60 m	1.24 m	0.92 m
b	1.48 m	0.53 m	1.01 m
c	1.10 m	0.65 m	0.88 m
d	0.66 m	0.53 m	0.60 m
e	0.97 m	0.65 m	0.81 m
f	0.26 m	0.58 m	0.42 m
g	1.13 m	0.46 m	0.80 m
h	0.42 m	0.48 m	0.45 m
i	1.22 m	0.99 m	1.11 m

2.3 Investigation of thickness of surface soil

LWDCPT was continued until over 10 MPa value through three hitting in a row. Because, the relationship between the penetration resistance q_d of LWDCPT and N_d value of the portable dynamic cone penetration test (PDCPT) was proposed by Tsuchida et al. (2011), as shown in Equation (2).

$$q_d = \frac{1}{4} N_d \qquad (2)$$

That is, over 10 MPa of q_d is considered to be equal to over 40 of N_d value, which can be estimated as the basement rock.Fig.5 shows penetration resistance q_d with depth in Valley 1. The thickness of surface soil of each point in Valley 1 was estimated as the average value both sides. Table 2 shows thicknesses of surface soil each point in Valley 1.

2.4 Estimation of strength parameters

Using these results, the cohesion and the internal friction angle of the ground were estimated using the equations suggested by Tsuchida et al. (2011). In these equations, the degree of saturation S_r and the penetration resistance of LWDCPT q_d are necessary. In order to obtain degree of saturation S_r, the tube sampling was carried out at the point in Fig. 4 (Valley 1). The appearance of tube sampling is shown in Photo 3. The corrected penetration q_{d5} was calculated by using Equation (3), where q_{d5} is the penetration resistance under 5kPa effective overburden stress and the correction from q_d to q_{d5} are made as follows:

$$q_{d5} = q_d - 0.01 \times (\gamma_t \cdot z - 5) \qquad (3)$$

Photo 3. Tube sampling

where, q_d = penetration resistance (MPa), γ_t = unit weight (kN/m^3), and z = depth(m).
The cohesion and internal friction angle of the ground were calculated by Equation (4) and (5), which were proposed by Tsuchida et al. (2011),

$$\phi_d = 29.9 + 1.61 \cdot \ln(q_{d5}) - 0.142 S_r \qquad (4)$$

$$c_d = 10.6 + 1.19 \cdot \ln(q_{d5}) - 0.041 S_r \qquad (5)$$

where, c_d = apparent cohesion of drained condition(kN/m^2), ϕ_d = apparent internal friction angle of drained condition (degree), and S_r = degree of saturation (%).
Table 3 shows the estimation of strength parameters in Valley 1.

3 MODELING OF VALLEYS BY INVESTIGATION

Fig. 6 shows modeling of four valleys by geotechnical investigation. The average values of the thickness of Valley 1, Valley 2, Valley 3 and Valley 4 were 0.79 m, 0.70 m, 0.57 m, and 1.31 m, respectively. The average values of the slope gradients of Valley 1, Valley 2, Valley 3, and Valley 4 were 14.4 degree, 16.3 degree, 16.1 degree, and 18.1 degree, respectively. In the present risk assessment method, these four valleys were included in a mesh for the assessment. By carrying out geotechnical investigation shown in this study, it is possible to model the valley and assess the risk by the

Table 3. Estimation of strength parameters (Valley 1).

	a	b	c	d	e	f	g	h	i
wet density ρ_t (g/cm^3)	1.35								
degree of saturation S_r (%)	33.61								
wet unit weight γ_t (kN/m^3)	13.21								
q_{d5} (MPa)	1.18	0.54	0.96	1.33	0.73	1.68	0.86	1.16	0.67
e	0.93	0.99	0.94	0.92	0.97	0.90	0.95	0.93	0.97
ϕ_d (degree)	34.9	33.7	34.6	35.1	34.2	35.5	34.4	34.9	34.0
c_d (kN/m^2)	9.4	8.5	9.2	9.6	8.8	9.8	9.0	9.4	8.7

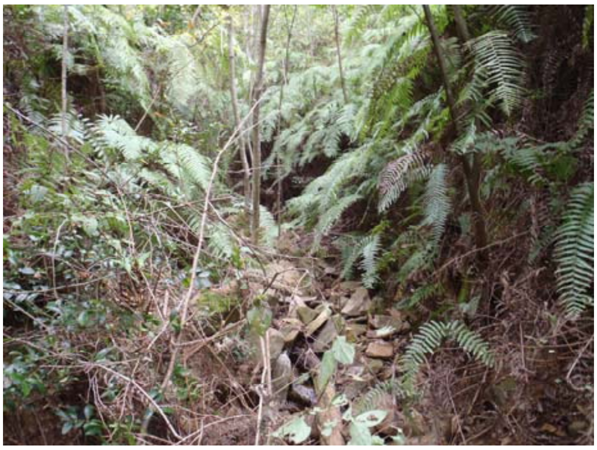

Photo 4. The steep slope.

Photo 5. The gravel under the ground.

stability analysis individually.

As already discussed, in Hiroshima Prefecture, 31,987 valleys and slopes are listed as areas of dangerous for slope failure and debris flow. Therefore, it is difficult to investigate all dangerous areas in a short period with the limited budget of local government. It is preferable in order to become a practical method that the investigation method is as simple and inexpensive as possible. As one way, it is considered that to request volunteers, who are not experts but members of autonomy disaster prevention organization in the area, to investigate the valleys. Thus, the investigation method which everyone can do and personal error not observed is preferable.

4 CONSIDERATION

The purpose of this study is to develop the procedure of site investigation of natural valley using lightweight cone penetration test (LWDCPT), in order to implement the risk assessment of individual valleys. From the investigations of four valleys, the following points were found;

1) The operation of investigation in this study is very easy, and it seems that even a non-experts can carry out the investigation based on a manual of this method. However, some investigation points, LWDCPT cannot work well, because of many tree roots or gravels under the ground and the much steepness of slope. In these cases, non-expert may not cope. And if the penetration resistance appears large value, sometimes, it is difficult to judge whether there is a gravel of a large diameter at this point, or it reaches bedrock as shown in Photo 5.
2) In this investigation, two LWDCPT were used by two persons (one person use one machine), and other two persons took undisturbed and disturbed samples at the site. It took eight hours to investigate all investigation points in Valley 1 which has largest investigation points (9 points) in the four valleys. Therefore, it is possible to investigate each valley in a day. However, in case of investigate points are over 10 points, it may be necessary to increase investigator or to take two days.

5 CONCLUSIONS

The geotechnical investigation using the LWDCPT was carried out in order to model natural valley or slope for the stability analysis. The advantages of LWDCPT are that the detail measurements are possible by getting a penetration resistance value with each hitting, and that in virtue of the lightweight and the simple, even for the non-specialist of geotechnical investigation, the operation is easy and safe. Thickness of surface soil and strength parameters were able to be estimated. Four valleys, which are same risk assessment in present method, were able to be modeled individually. It took eight hours to investigate all testing points in Valley 1 which has largest number testing points (9 points) in the four valleys. In case of investigate points under this, it is possible to investigate a valley in a day. However, in case that testing points over more than 10 points, it is necessary to increase investigator in order to improve efficiency or divide two days.

6 REFERENCES

[1] Higashi Hiroshima City: http://www.city.higashihiroshima.hiroshima.jp/site/bousai/hazard.html

[2] Hiroshima Prefecture, http://www.pref.hiroshima.lg.jp/page/1171592994610/index.html

[3] Langton, D.D., “The PANDA-lightweight penetrometer for soil investigation and monitoring material compaction,” Ground Engineering, September 1999, pp. 33-37.

[4] Cassan, M., “Les essays in situ en mechanique des sols, realization et interpretation,” Eyrolles, Paris, 2nd ed. Vol. 1, pp. 146-151.

[5] Tsuchida T, Athapaththu A.M.R.G., Kano S, Suga K, “Estimation of in-situ shear strength parameters of weathered granitic (Masado) slopes using lightweight dynamic cone penetrometer,” Soils and Foundations, vol. 51, No. 3. (to be published), 2011.

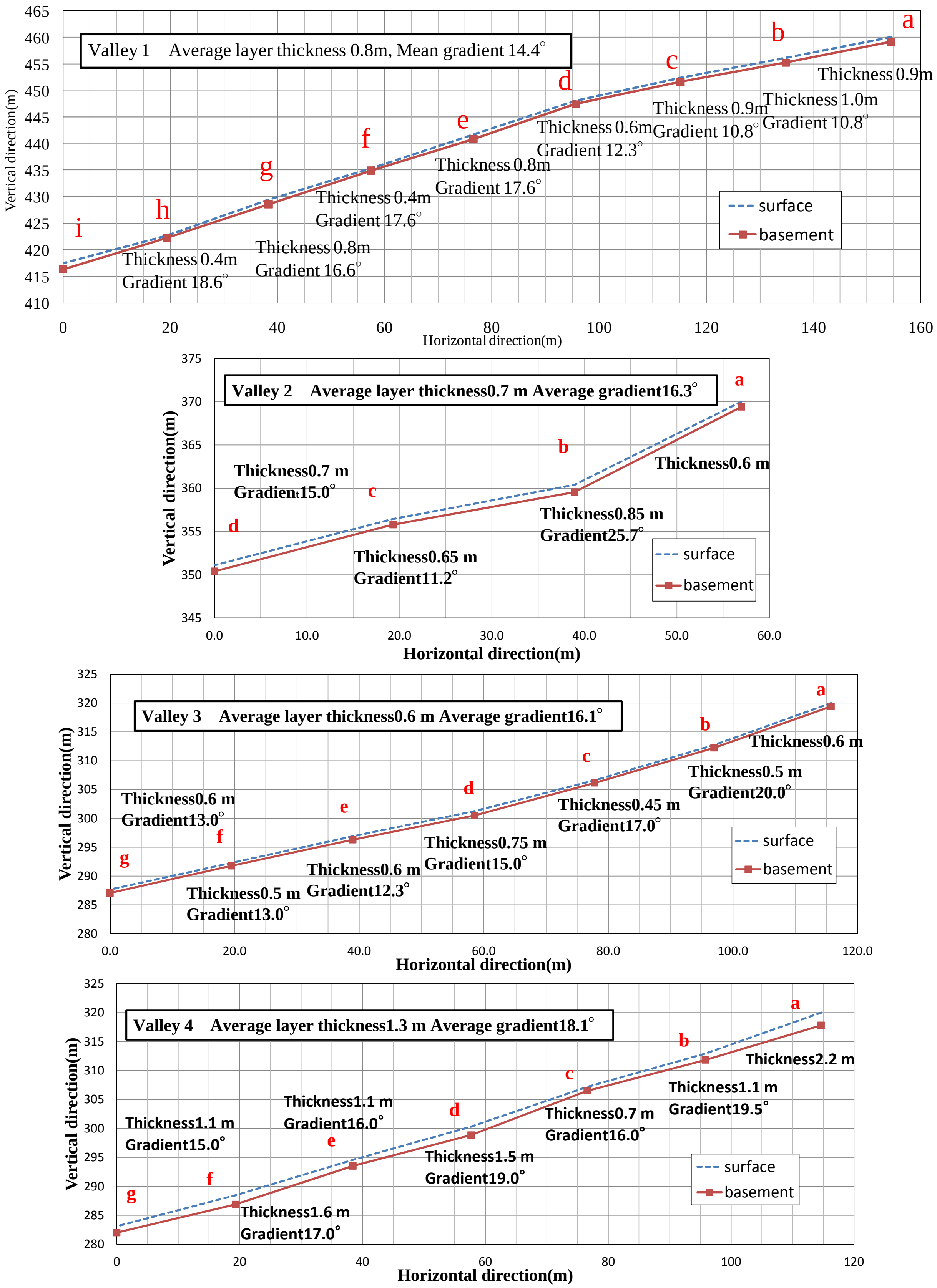

Fig. 6. Model cross-section of 4 valleys in Higashi-Hiroshima City.

Study on Individual Landslide Risk Assessment of Natural Valleys and Slopes during Heavy Rain Based on Geotechnical Investigation and Analysis

Shouichi Kawabata. Takashi Tsuchida. Takashi Hanaoka. Shouta Nakagawa., Hiroshima University

ABSTRACT: In Hiroshima Prefecture, the prefectural land is divided into 350 unit areas of 5 kilometers square, and in each unit area, the criteria using the rainfall indexes, such as the soil water index and rainfall intensity, are determined on the basis of past records of landslide disasters due to heavy rain. However, in this system, the risk of individual valleys or natural slopes in each area cannot be shown. In this study, a series of investigation was carried out at four valleys in Higashi-Hiroshima city, which are put on the list of valleys potentially dangerous for mud and debris flows during heavy rain. For the conditions continuous rain, the infiltration analysis during the rain, the ground water seepage analysis and the slope stability analysis were carried out based on the ground models obtained by the site investigation. The risk of slope failure for each of four valleys was given as the risk assessment point, and was compared and discussed.

Keywords: Risk Assessment, Landslide, Site Investigation, Ground Water

1. INTRODUCTION

Hiroshima Prefecture has 31,987 hazardous areas for landslide disasters, the largest number in Japan in [1]. In Hiroshima, a regional soil called Masado soil, a weathered granite, widely covers the surfaces of natural slopes. From a geotechnical point of view, the failures of natural slopes are mainly caused by rises in groundwater levels and the loss of inbound shear strength of Masado soil due to both continuous and intensive seasonal rains.

Fig. 1 shows present risk assessment method and purpose of this study. The present regional risk assessment method utilized by the Hiroshima Prefecture government is thoroughly based on the measured rainfall and the rainfall-failure relationship in each 5 km×5 km area obtained

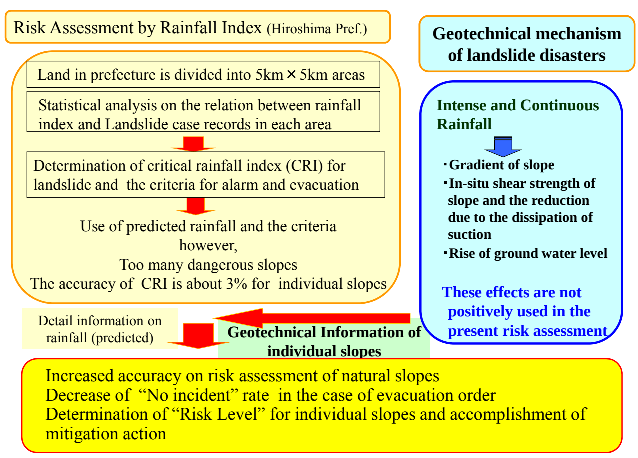

Fig. 1. Valleys at risk of landslide of in the town of Saijo.

from the past records of the disasters. In this system, the risks of slope failure and evacuation orders are given for an area 5 km×5 km, and the risks to individual slops cannot be shown. Accordingly, it can be said that the present risk assessment method is an empirical one, and is not a theoretical or geotechnical one. In this study, Geotechnical investigations of four natural valleys in Higashi Hiroshima City were carried out using a lightweight dynamic cone penetration test and a soil sampling. In order to improve the present risk assessment method, landslide risk assessments of these valleys for some predicted rain conditions were made by using a seepage analysis, a ground water level analysis, and a slope stability analysis of each valley.

2. SELECTION OF VALLEYS

In the selection of valleys for the study, we focused on the large number of potentially dangerous valleys in Higashi-Hiroshima City. Fig.2 shows the selected four valleys, which are included in one 5 km×5 km regional mesh for the present risk assessment based on the rainfall index. Accordingly, the risks in these four valleys are the same as in the traditional method, but the purpose of this study is to evaluate the risks to the four valleys individually.

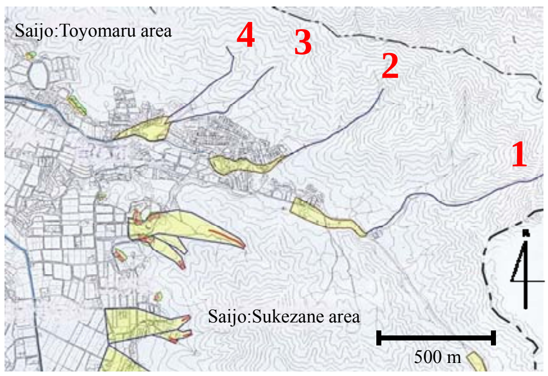

Fig. 2. Valleys where the survey were carried out in [2].

3. GEOTECHNICAL INVESTIGATION METHOD OF NATURAL VALLEYS

Table 1 shows geotechnical investigation points. A geotechnical investigation of the valleys was carried out under the following policies.

Table 1. Geotechnical investigation points.

	valley1	valley2	valley3	valley4
penetration test	9	4	7	7
soil sampling	4	4	4	4

(1) The headwater area was determined by using topographical data and a field trip. About six geotechnical investigation points were selected in the headwater area, and along the valley the geotechnical testing points were selected at intervals of 20 meters, downward.
(2) A test of the valley was carried out at both sides of the valley, which are 5 located meters away from the center of valley. The tests were carried out the headwater down to the valley, the gradient of which is larger than 12.5 degree.
(3) The sampling was carried out at both sides of four investigation points in each valley.

4. RESULTS OF THE GEOTECHNICAL INVESTIGATION

The thickness of the surface soil was estimated by analyzing the penetration resistance of each geotechnical investigation point. In Fig.3, the penetration resistance q_d of lightweight dynamic cone penetration test with depth, which was measured at point 9 in Valley 1, is shown in [3]. Slope models were made using the estimated thickness of the surface soil and the slope gradients. With these results, a model cross-section of each valley was made, as shown in Fig.4. The horizontal distance of the cross-section was determined by the geotechnical investigation point, and the thickness of the surface soil came out of the average from the estimated values of both sides, which were 5 meters away from the center of the valley. The average values of the thickness of Valley 1, Valley 2, Valley 3, and Valley 4 were 0.8 m, 0.7 m, 0.6 m, and 1.3 m, respectively. The average values of the slope gradients of Valley 1, Valley 2, Valley 3, and Valley 4 were 14.4 degree, 16.3 degree, 16.1 degree, and 18.1 degree, respectively. Furthermore, the void ratio, the density of soil particles, the degree of saturation, and the unit weight were obtained by the laboratory tests of soil samples taken in each valley.
Using these results, the cohesion and the internal friction angle of the ground were estimated using the equations suggested by Tsuchida *et al.* (2011).
With these results, cohesions were estimated to be between 8.2 kN/m^2 and 11.2 kN/m^2, and the internal friction angles were between 29.6 degree and 36.4 degree.

5. SEEPAGE ANALYSIS

Fig. 5 shows the model of the rainfall seepage in this study. When it rains continuously and the rainfall begins to infiltrate into the ground, the volumetric moisture content of the upper soil layer rises to a certain value θ_h from the surface layer. Afterwards, the unsaturated layer maintains the volumetric water content θ_h and descends toward the lower layer. This unsaturated layer is called the high moisture content belt (HMCB). The underground water level is formed in the soil layer when the HMCB reaches the impermeable layer, and the groundwater level starts to gradually rise from the impermeable layer upward, as shown in Fig. 5.
To figure out this process, a one-dimensional unsaturated seepage analysis was carried out at each point of the valleys. The primitive equation used for the unsaturated seepage analysis is that used in the expression of Richards in [6]. The expression of Richards is given by the following equation:

$$C(\psi)\frac{\partial \psi}{\partial t}+\frac{\partial}{\partial z}\left(-k(\psi)\frac{\partial(\psi+z)}{\partial z}\right)=0 \qquad (1)$$

where, ψ =pressure head(cmH$_2$O), $C(\psi)$= specific moisture capacity, $k(\psi)$= hydraulic conductivity (cm/s). The rainfall seepage boundary condition in the surface of the ground is

Photo 1. Site of the geotechnical investigation. (Valley 3)

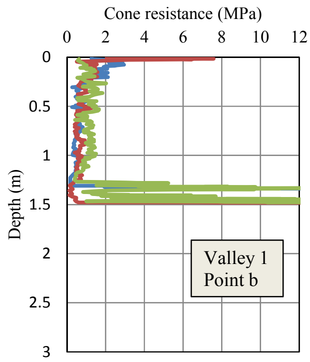

Fig. 3. Penetration resistance qd with depth (Valley 1).

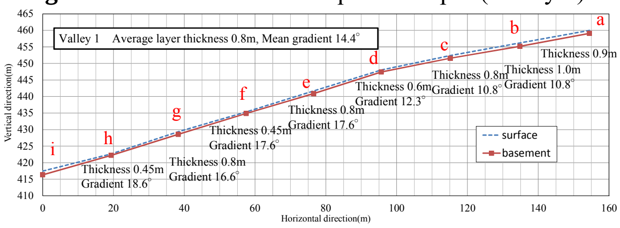

Fig. 4. Model cross-section of Valley 1 in Higashi-Hiroshima City.

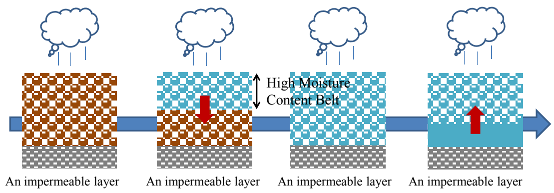

Fig. 5. Conceptual diagram of rainfall seepage.

given by the following equation:

$$R = q = K(\psi)\left(\frac{\partial \psi}{\partial z} + 1\right) \tag{2}$$

where, R= amount of rainfall, q= flow velocity in a surface. Suction was calculated by using the difference approximation expression of Richards' equations. The volumetric moisture content was calculated by applying the obtained suction value to the soil moisture characteristic curve, in which the initial pressure head and the total head are determined by the experiments on weathering granite (Masado) carried out by Yuri (2010); that is, the saturated volumetric moisture content was 0.433, the residual volumetric moisture content was 0.158, the saturated hydraulic conductivity was 0.006 cm/s and the initial volumetric moisture content was 0.300. Fig. 6 shows the soil moisture characteristic curve used in this study.

Fig. 7 shows an example of the one-dimensional seepage analysis at Point b in Valley 1 under a rain intensity of 5 mm/hour. As shown in Fig. 7, HMCB is formed from the surface, and goes downwards. After 14.1 hours, the HMCB reaches the bottom of the soil layer, and after the saturated layer is formed at the bottom after 21.15 hr, the groundwater level rises.

The volumetric moisture content in HMCB is closely related to the rainfall intensity, and the descending speed of HMCB is decided by the rainfall intensity regardless of the thickness of the surface. The seepage analysis also clarified the link between rainfall intensity in each thickness of the surface and the time necessary for the formation of groundwater levels in the soil layers.

6. GROUND WATER LEVEL ANALYSIS

A portion of rain water evaporates from the surface of ground, and some is also intercepted by objects such as trees and the grasses. The rain water that infiltrates into the ground forms a high moisture content belt (HMCB) and descends from the surface to the bottom. When the HMCB reaches the basement rock, it flows here as underground water, and it flows out to the surface of the ground when the water table reaches the surface. An equilibrium relation exists among the amount of rainfall supplied in a certain period, the amount saved on the surface, and the volume of water that flows out from the surface. Here, it is thought that the amounts of evapotranspiration and that intercepted by trees and grasses are very small compared with the amount of the rainfall, and those were neglected. If all the amounts of rainfall infiltrate in the ground, the following equation can be derived:

$$R_{input} = Gw + Gw_{out} \tag{3}$$

where, R_{input}= amount of rainfall, Gw= amount of rainfall saved in the layer, and Gw_{out}= net amount of water flowing out due to the groundwater flow.

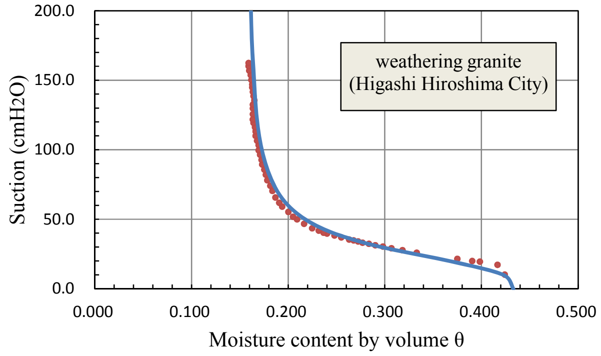

Fig. 6. Soil moisture characteristic curve used in this study (Yuri, 2010).

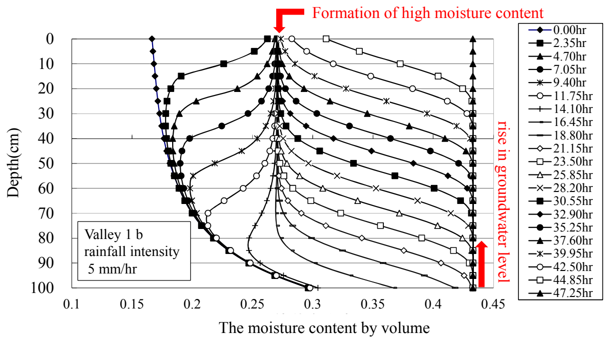

Rainfall intensity 5 mm/hr

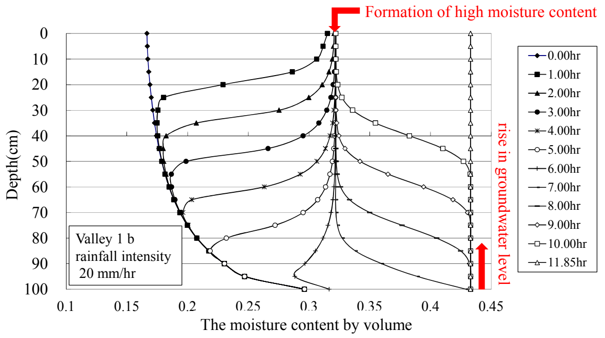

Rainfall intensity 20 mm/hr

Fig. 7. Change of volumetric moisture content.

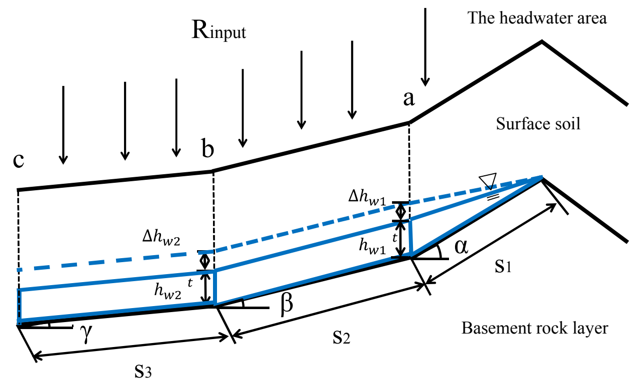

Fig. 8. High moisture content belt descent process, and groundwater level rise process.

Fig. 8 showed the computing model of the groundwater level rise.

Water change for each Δt (hr) at Point *a* of Fig. 8.The amount of rainfall between the ridge and Point *a* is:

$$R_{input} = r \times s_1 \cos\alpha \times \Delta t \tag{4}$$

where, r=rainfall intensity(mm/hr), s_1= slope length(m).

The amount saved as underground water in the ground of Section S_1 in Δt is:

$$Gw = \frac{1}{2} n_e \left(h_{w1}^{t} + \Delta h_{w1}\right) s_1 \cos\alpha - \frac{1}{2} n_e h_{w1}^{t} s_1 \cos\alpha \tag{5}$$

where, n_e=effective porosity, h_{w1}^{t} =groundwater level of Point *a* in *t* (m), and Δh_{w1} =groundwater level rise amount of Point *a* in Δt (m).

In addition, the amount where underground water flows of Section S_1 in Δt is:

$$Gw_{out} = k \sin\alpha \cdot h_{w1}^{t} \cos\alpha \cdot \Delta t \tag{6}$$

where, k= hydraulic conductivity.

By substituting Equations (4), (5), and (6) into Equation (7), we obtain the following:

$$h_{w1}^{t+\Delta t} = \frac{2\left(r \cdot s_1 - k \sin\alpha \cdot h_{w1}^{t}\right) \cdot \Delta t}{s_1\left(\theta_s - \theta_h\right)} + h_{w1}^{t} \tag{7}$$

where, $h_{w1}^{t+\Delta t}$ =groundwater level of Point *a* in Δt (m),

θ_s = saturated moisture content by volume.

Water change for each Δt (hr) in Point b of Fig. 8.As well as the Equation (7):

$$h_{w2}^{t+\Delta t} = \frac{2\left\{r \cdot s_2 - k \sin\beta \cdot \left(h_{w2}^{t} - h_{w1}^{t}\right)\right\} \cdot \Delta t}{s_2\left(\theta_s - \theta_h\right)} + h_{w2}^{t} + h_{w1}^{t} - h_{w1}^{t+\Delta t} \tag{8}$$

where, $h_{w2}^{t+\Delta t}$ =groundwater level of Point *b* in Δt (m), h_{w1}^{t} =groundwater level of Point *a* in *t* (m), s_2= slope length (m) .

Equation (7) is used in Point a of Fig.8. Equation (8) is used in the other Points of Fig.8.

Fig. 9 shows the changes with the lapse of groundwater level.

7. SLOPE STABILITY ANALYSIS AND RISK ASSESSMENT

Results of the one-dimensional unsaturated seepage analysis, the slope stability analysis in the high-moisture belt descent process, and the groundwater level rise process were accomplished based on the physical property values obtained in the in situ geotechnical investigation, and on the estimated strength parameters. Fig. 10 shows the high moisture belt descent process and the groundwater level rise process. The slope stability analysis was done as a slide surface with a

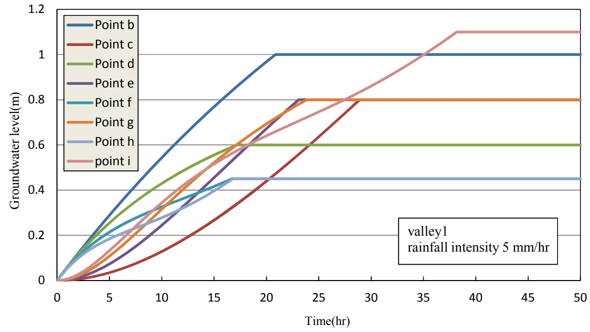

Fig. 9. Groundwater level with the lapse of time after HMCB reaches the bottom of lay (Valley 1).

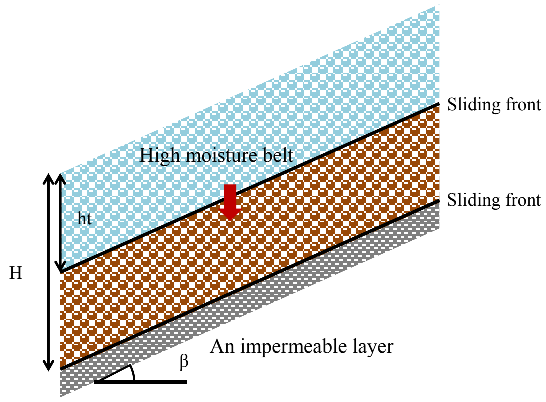

High moisture content belt descent process

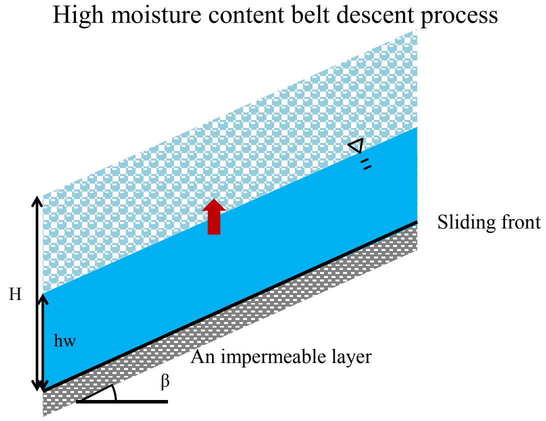

Groundwater level rise process

Fig. 10. High moisture content belt descent process, and groundwater level rise process.

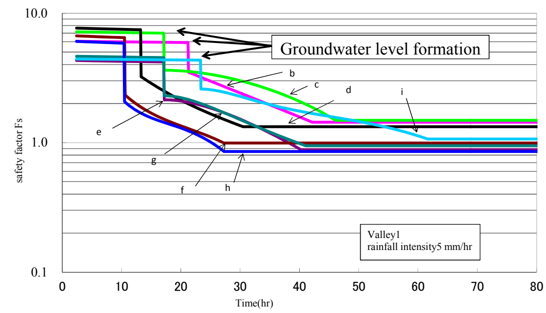

Fig. 11. Changes with the lapse of time of safety factors of a slope.

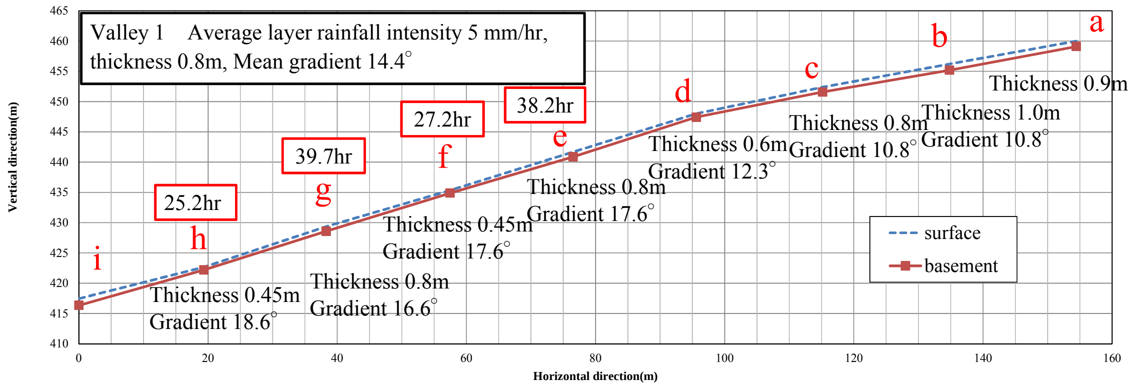

Valley 1

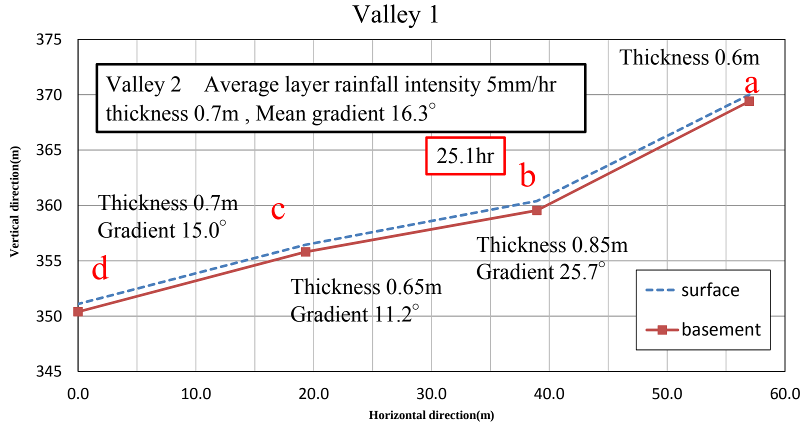

Valley 2

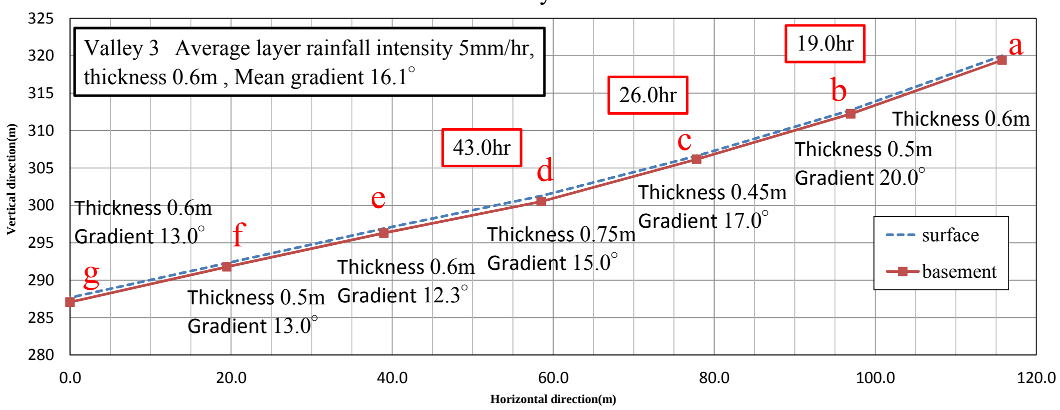

Valley 3

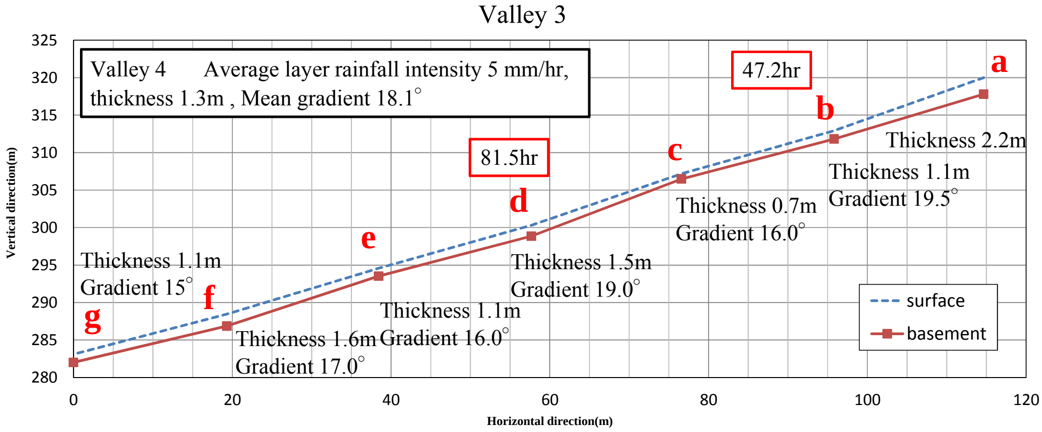

Valley 4

Fig. 12. Time in which the safety factor of a slope becomes less than one (Rainfall intensity 5 mm/hr).

basement rock and a lower side of the high moisture belt during the HMCB descent process, and as a slide surface with the basement rock during the groundwater level rise process.

Slope stability analyses were also carried out in different rainfall conditions: in the various points of the valleys. those being, rainfall intensities of 5 mm/hr, 20 mm/hr, and 50 mm/hr. Fig. 11 shows the results of the slope stability analysis with a rainfall intensity of 5 mm/hr in Valley 1. In addition, Fig. 12 shows the required time in which the safety factor of the slope becomes less than one, in the points in Valley 1 when the rainfall intensity is 5 mm/hr.

Table 2 shows the risk assessments of the four valleys relatively. In Table 2, the risk assessment points in each valley are given by:

・Time when a safety factor of a part of the valley becomes less than 1.0.

・Range of the valley where the safety factor becomes less than 1.0

And finally, the total risk assessment value was calculated as a sum of the three risk assessment points. It was shown that Valley 1 is the most dangerous. However, a social importance, the number of residences downstream is not thought this study. It will be necessary to investigate social importance in the future.

Table 2. Relative risk assessment of four valleys.

	Valley 1	Valley 2	Valley 3	Valley 4
Maximum slope gradient(°)	18.6	25.7	20.0	19.5
Average thickness of the surface soil(m)	0.8	0.7	0.6	1.3
Time that the safety factor of slope becomes less than one in rainfall intensity 5mm/hr(hr)	25.2	25.1	19.0	47.2
Time that the safety factor of slope becomes less than one in rainfall intensity 20mm/hr(hr)	5.2	7.7	5.2	12.2
Time that the safety factor of slope becomes less than one in rainfall intensity 50mm/hr(hr)	2.3	3.7	2.4	5.7
Risk assessment point 1 1) Time that it becomes less than safety factor 1（On a scale of 1 to 5）	4.1	3.8	5	1
Risk assessment point 2 2) Range that it becomes less than safety factor 1（On a scale of 1 to 5）	5	1	3	3
Total risk assessment overall risk assessment （On a scale of 1to10）	9.1	4.8	8	4

8. CONCLUSION

In Hiroshima Prefecture, the prefectural land is divided into 350 unit areas of 5 kilometers square, and in each unit area, the criteria using the rainfall indexes, such as the soil water index and rainfall intensity, are determined on the basis of past records of landslide disasters due to heavy rain. However, in this system, the risk of individual valleys or natural slopes in each area cannot be shown. In this study, a series of in-situ geotechnical investigation of four potentially dangerous valleys inn Higashi-Hiroshima City were carried out. Models of the valleys for the geotechnical analysis were constructed by the investigation results. The one-dimensional infiltration analysis during the rain, the ground water seepage analysis, and the slope stability analyses when the rainfall intensities were 5, 20, and 50 mm/hr were continuously carried out. Based on these analysis, the risk of the four valleys were shown quantitatively .The risk of slope failure for each of four valleys was given as the risk assessment point, and was compared and discussed. The methods developed in this study are a useful to assess the landslide risk of individual slopes in potentially dangerous areas.

REFERENCES

[1] Higashi Hiroshima City: http://www.city.higashihiroshima.hiroshima.jp/site/bousai/hazard.html

[2] Hiroshima Prefecture, http://www.pref.hiroshima.lg.jp/page/1171592994610/index.html

[3] Langton, D.D., “The PANDA-lightweight penetrometer for soil investigation and monitoring material compaction,” Ground Engineering, September 1999, pp. 33-37.

[4] Cassan, M., “Les essays in situ en mechanique des sols, realization et interpretation,” Eyrolles, Paris, 2nd ed. Vol. 1, pp. 146-151.

[5] Tsuchida T, Athapaththu A.M.R.G., Kano S, Suga K, “Estimation of in-situ shear strength parameters of weathered granitic (Masado) slopes using lightweight dynamic cone penetrometer,” Soils and Foundations, vol. 51, No. 3. (to be published), 2011.

[6] Richards,L.A. , “Capillary Conduction of Liquids in Porous Mediums,” Physics 1, 1931, pp. 318-333.

[7] Yuri H, “Influence of rainfall characteristics and soil properties on soil moisture change,” master's thesis of graduate school of Hiroshima university, 2010, pp. 61-89.

First International Conference on Geotechnique, Construction Materials and Environment, Mie, Japan, Nov.21-23, 2011, ISBN: 978-4-9905958-0-7 C3051

Analyses of Piping under Foundation of Weirs in Different Ground Density by FEM

OKAJIMA Kenji, Department of Environmental Science and Technology, Mie University

ABSTRACT: Creep flow theories that are Bligh's and Lane's equation have been used as the safety criteria against piping under foundation of weirs. These methods were not able to estimate the mechanism leading to piping under foundation of weirs. In this study the effectiveness of our FEM for piping analysis under foundation of weirs was verified by model experiments.
These model experiments were carried out in five patterns and had same creep length by changing the installation position and length of cut-off wall in high ground density. These critical water heads of model experiments were different from each pattern. It was clear that creep flow theories were not able to predict these differences in high ground density.
The finite element analysis employs the elasto-plastic constitutive equations with a non-associated flow rule and strain hardening-softening. The constitutive equations based on the yield function of Mohr-Coulomb and the plastic potential function of Drucker-Prager. The finite element is 4-noded iso-parametric element with one point integration. The explicit dynamic relaxation method combined with the generalized return-mapping algorithm is applied. The elasto-plastic constitutive relations including the effect of the shear band are employed. A simplified and generalized version of mesh size-dependent softening modulus method (Tanaka and Kawamoto, 1989) is used in this study.
Our FEM predicted these critical water heads of model experiments. Maximum shear strain contour line by our finite element analysis indicated that shear strain concentrated in similar soil mass as Terzaghi assumed in the seepage failure equation. The analyses of piping under foundation of weirs in different ground density indicated that the critical water head approach to constant with the position of cut-off wall in loose ground density and the domain for concentration of maximum shear strain in same weir shape changed by each ground density.

Keywords: Piping, Creep theory, FEM, Relative density

1. INTRODUCTION

Creep flow theories are applied to the design criteria against piping of foundation of a weir. Bligh's creep flow theory was developed as the empirical equation for the design of floating type weirs in permeable layer through many experiences in 1910 (Bligh)[1]. After suggestion of this theory it was indicated that vertical sections of the creep length contribute more to reduce the danger of piping than horizontal sections of the length. In the response to this, Lane (1935)[2] suggested the weighted creep flow theory. These creep flow theories were based on the assumption that the cause of piping was erosion along the contact surface between soils and weir.
The purpose of this study is the reexamination of these practical safety criteria against seepage failure. We conducted a series of model experiments that have same creep length, and then evaluated these practical safety criteria and the validity of the elasto-plastic FEM by applying to the experiments in high relative density sand.
The condition of the foundation of weir is different in each weir. So we estimated the impact of relative density in the foundation of the weir on the critical water head by the elasto-plastic FEM.

2. CREEP THEORIES

To prevent piping at the down-stream side of a weir, practical manuals indicate that a safe creep length have to be ensured under the surface of the weir and along the side of the weir. The creep length to be ensured must be larger than the values calculated by two methods.
The first method is Bligh's method.

$$L_B \geq C_B \Delta H \tag{1}$$

Where L_B is the creep length that is measured along the bottom face of the weir, C_B is Bligh's creep ratio which varies depending on the type of the foundation soil, and ΔH is the water head. For example the fine sand C_B is 15. The critical head is ΔH_{CB} when $L_B = C_B \Delta H_{CB}$.
The second method is Lane's method.

$$L_L \geq C_L \Delta H \tag{2}$$

Where L_L is the weighted creep length.

$$L_L = \sum l_v + k_v / k_h \sum l_h \tag{3}$$

Where, l_v is the creep length of vertical direction (inclination angle of more than 45 degrees), l_h is the creep length of horizontal direction (inclination angle of lower than 45 degrees). k_v is the vertical coefficient of permeability and k_v is the horizontal coefficient of permeability. However, k_v / k_h has been used 1/3 customarily. C_L is Lane's creep ratio which varies depending on the type of the foundation soils. For example the fine sand C_L is 7.0. ΔH is the water head. The critical head is ΔH_{CL}, when $L_L = C_L \Delta H_{CL}$.

3 MODEL EXPERIMENTS

The experimental apparatus was consisted of a glass-walled sand box. The size was 1000mm long, 500mm high and 200mm wide. The permeable layers in these model experiments were made by using clean sand. The sand was the Toyoura sand with a specific gravity of 2.64, a mean diameter (D_{50}) of 0.16 mm and a uniformity coefficient of 1.46. The weir was made of rigid acrylic plates. The weir was fixed to sand box and was sealed by silicon rubber and silicon adhesion bond to prevent water and sand from spilling out. The sandpaper was pasted on the bottom and side of the weir to prevent roofing. The cut-off wall was made of aluminum plate. The sand layers were prepared by pouring dry sand using hopper into stored water and deleting air during the soil particle falling. The high density of the sand layers was obtained: the relative density was about 85% (Figure1).

After setting up the water levels of both upstream and downstream side equal, the downstream water level was lowered incrementally (5mm after an hour). The deformation of the sand layer was measured. When piping or boiling occurred, the water head was defined to attain the critical water head.

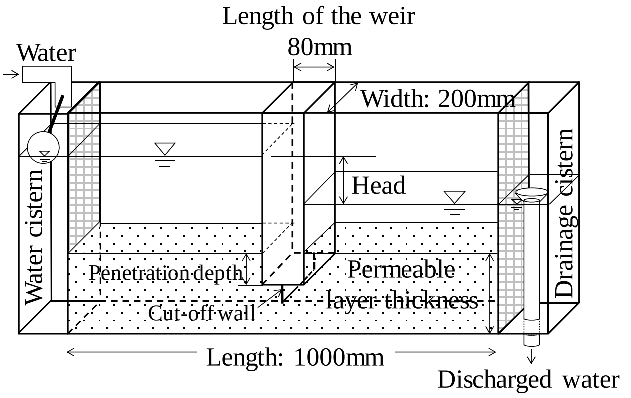

Figure 1 The layout of the test apparatus

The data of a series of model experiments are indicated in Figure2. All patterns had same creep length in which Bligh's creep length is 180mm and Lane's creep length is 123mm. These data were obtained by conducting 2 or 3 times in each experiment. These experiments are divided into 3 groups (Figure1). The first group was named "Depth group" to change penetration depth of the weir: 10-40-M, 20-30-M and 50-0 (penetration depth - depth of cut-off wall - the position of cut-off wall). From these experiments we can evaluate the influence of the depth of the weir for piping. The second group was named "Position group" to change the position of a cut-off wall: 10-40-L, 10-40-M and 10-40-R. From these experiments we can evaluate the influence of the position of the cut-off wall for piping.

Table1 shows results of model experiments that are relative density (%), critical water head, the kind of seepage failure (Piping or Boiling) and average of critical water head. Piping was observed in some patterns of model experiments. The heaving was observed because sand ground in down-stream side deformed. Relative densities were about 85% from 81.2% to 88.9%. Critical water heads in each pattern were similar water heads. In these model experiments the reproducibility was observed.

These model experiments had same creep length. Bligh's and Lane's creep flow theories predict a critical water head with patterns. However, each critical water head was different from the other pattern. The result indicated that creep flow theories were not able to predict the critical water head in the hard foundation.

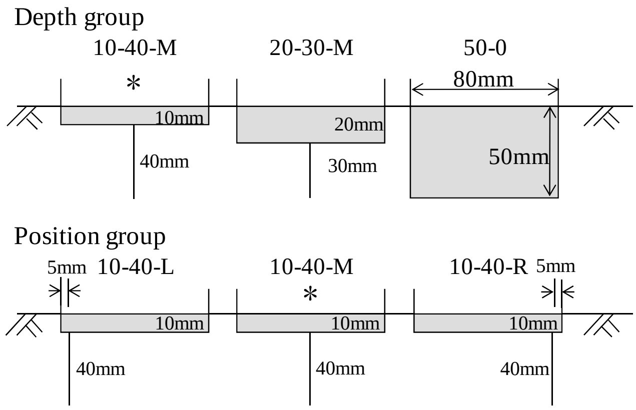

Figure 2 Patterns of model experiments

Table1 Results of model experiments

Pattern	Relative Density	Critical water head	Piping / Boiling	Average of critical water head
	%	mm		mm
10-40-M	82	80	Piping	87
	86.3	90	Piping	
	83.6	90	Piping	
20-30-M	84.7	140	Piping	137
	86.1	145	Boiling	
	84.5	125	Piping	
50-0	88.9	250	Boiling	258
	85.1	251	Boiling	
	81.4	271	Boiling	
10-40-L	87.4	70	Piping	73
	81.2	75	Piping	
	81.5	75	Piping	
10-40-R	82.6	155	Boiling	170
	83.1	175	Boiling	
	87.4	180	Boiling	

4 SEEPAGE FAILURE ANALYSES BY ELASTO-PLASTIC FEM

4.1 Finite element method and analysis conditions

In this study the finite element analysis consisted of two steps. The first step is the seepage flow analysis by FEM. The second is the seepage failure analysis by the elasto-plastic FEM to input effective stress regarding the seepage force as the external force.

The finite element analysis employs the elasto-plastic constitutive equations with a non-associated flow rule and strain hardening-softening. The constitutive equations based on the yield function of Mohr-Coulomb and the plastic potential function of Drucker-Prager. The finite element is 4-noded iso-parametric element with one point integration. The explicit dynamic relaxation method combined with the generalized return-mapping algorithm is applied. The elasto-plastic constitutive relations including the effect of the shear band are employed.

A simplified and generalized version of mesh size-dependent softening modulus method (Tanaka and Kawamoto, 1989)[3] is used in this study. A material model for a real granular material (i.e., Toyoura sand) with a high angle of internal friction is used with the features of nonlinear pre-peak, pressure-sensitivity of the deformation and strength characteristics of sand, non-associated flow characteristics, post-peak strain softening, and strain-localization into a shear band with a specific width. The material model will be briefly described in this section.

In the elasto-plastic finite element analysis, the material constants of Toyoura sand are as follow: relative density = 88%, residual friction angle = 33 degree. The calibration of the other elasto-plastic parameter of air-dried Toyoura sand in the elasto-plastic constitutive model was performed using the plane strain compression tests by Tatsuoka et al (1993)[4]. The analysis was performed using a series of finite element mesh of each model experiment, as shown in Figure3. Elements around the weir were consisted of 2mm square mesh. Elements bordering on the weir were boundary elements and the friction was set to be equal to the friction between sand and weir in these elements.

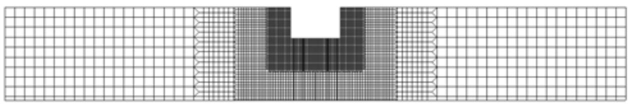

(a) All mesh of 50-0 mesh

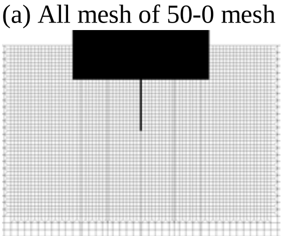

(b) 20-30-M mesh

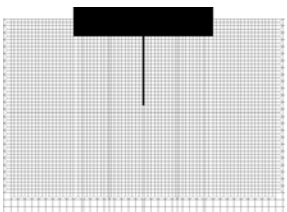

(c) 10-40-M mesh

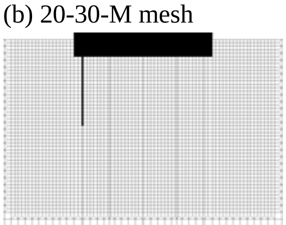

(d) 10-40-L mesh

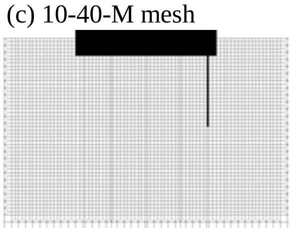

(e) 10-40-R mesh

Figure3 FEM mesh

4.2 The validation of this FEM

Result of model experiments and FEM in each groups are discussed about the effectiveness of FEM and the tendency of seepage failure of foundation of the weir. Figure4 indicates the critical water head of Position group. The critical water head gradually increases with the moving to the downstream end of the weir in Position group which has same creep length. Results of FEM predicted each critical water head well. Figure5 indicates the critical water head of Depth group. The critical water head gradually increases with the increasing the penetration depth of the weir in Depth group which has same creep length. Results of FEM predicted each critical water head well.

Results of FEM which penetration depth of weir was 10mm and the cut-off wall was set at upstream side or middle of the length of weir were computed higher than results of model experiments (10-40-M and 10-40-L). The reason is considered that the continuum model might not hold true when number of particle of sand (the average particle side is 0.16mm) was about 60 at the downstream edge of the weir. Result of FEM which penetration depth of weir was 50mm was computed lower than results of model experiment (50-0). The reason was considered that the friction of the side glass wall influenced the water head of boiling because it was observed that larger sand mass moved during the boiling in the model experiments of 50-0. These discussions indicated that our FEM was effective analysis to compute the critical water head of the foundation of the weir.

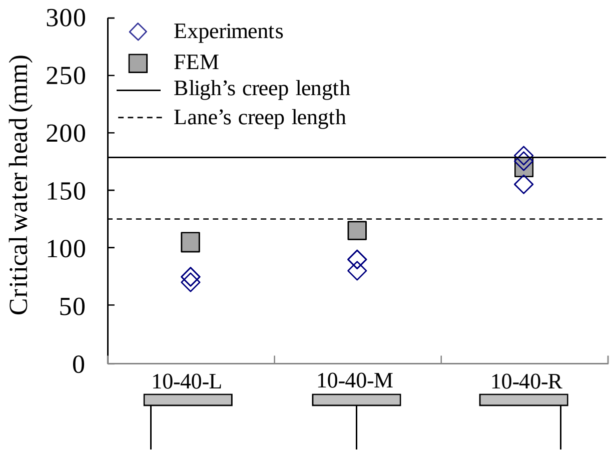

Figure 4 Critical water head of Position group

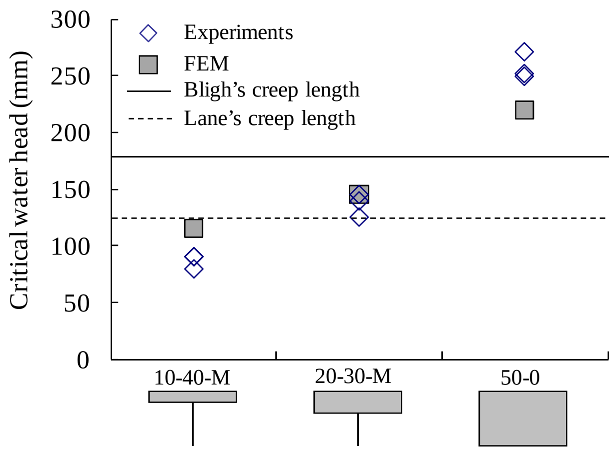

Figure 5 Critical water head of Depth group

5 SEEPAGE FAILURE OF THE FOUNDATION IN DIFERENT RELATIVE DENSITY

5.1 Finite element method and analysis conditions

It was considered that the foundation of the weir had various densities. In this study the effectiveness of our FEM was verified on the seepage failure of the foundation of the weir. The effectiveness of our FEM had been verified on the seepage failure of the ground around the sheet pile by Okajima et al. (2009)[5]. We considered that our FEM was able to be applied to the seepage failure problem in different relative density foundation.

We prepared the set of model cases to estimate the impact of relative density in the seepage failure of the foundation of the weir. Shapes of weirs were 10-40-L, 10-40-M, 10-40-R, 20-30-L, 20-30-M and 20-30-R. The tendency of seepage failure in the difference of the position of the cut-off wall and penetration depth of the weir was checked. Finite element meshes which were indicated in Figure 6 were applied to analyses of 20-30-L and 20-30-R. Conditions of relative density of the foundation were high(85%), middle(50%) and low(15%) in each weir shape.

5.2 Impact of relative density in seepage failure of weir

Critical water heads of finite element analyses was shown in Figure 7. Even when relative density was changed, each difference of critical water heads of the group of penetration depth 20mm and cut-off length 30mm (20-30 group) was much the same difference. On critical water heads of the group of penetration depth 10mm and cut-off length 40mm (10-40 group), each difference of critical water heads in high(85%) and middle(50%) relative density was much the same difference but critical water heads in low(15%) relative density were almost same.

To estimate the seepage failure mechanism of 10-40 group in low(15%) relative density, Figure8 showed the maximum shear strain distribution around the weir of 10-40 group in low(15%) relative density. The contour lines showed ten lines from 0.1 to 1.0 of maximum shear strain. Our elasto- plastic FEM has the frictional hardening-softening functions. When the maximum shear strain reached about 0.1, the frictional function changed from hardening regime to softening regime. We evaluated that the shear band develops in these elements at that time. The concentration of maximum shear strain contour line reached under downstream edge of the weir in 10-40-L and 10-40-M. This indicated that seepage failure progressed in the ground of downstream in 10-40-L and 10-40-M. On the other hand the concentration of maximum shear strain contour line reached under upstream edge of the weir in 10-40-R. The seepage failure of 10-40-R which had shallow penetration depth progressed from upstream. 10-40 group of low(15%) relative density had almost same critical water head, but the mechanism of seepage failure of each weir was different. And critical water heads of 10-40-R in middle(50%) and high(98%) were near to critical water heads of 20-30-R in middle(50%) and high(98%). Critical water heads of 20-30-L and 20-30-M and critical water heads of 10-40-L and 10-40-M were near each other. It indicated that the seepage failure of the foundation of the weir might depend on penetration depth of downstream side of the weir.

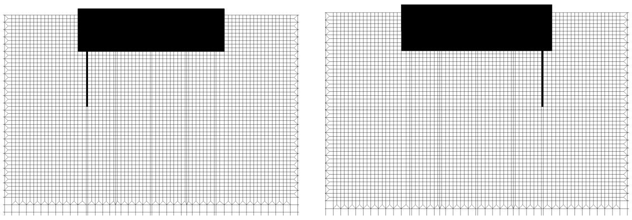

(a) 20-30-L mesh (b) 20-30-R mesh

Figure6 FEM mesh

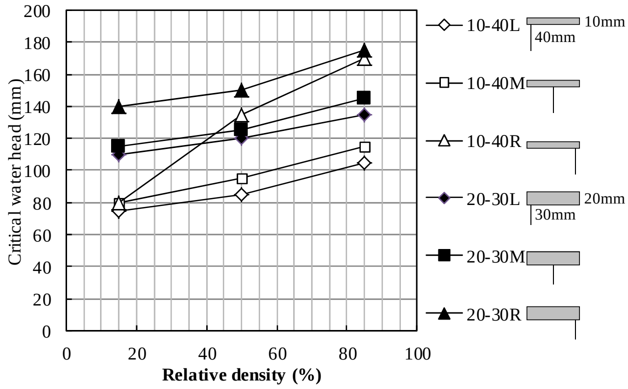

Figure7 Relationship of relative density and critical water head

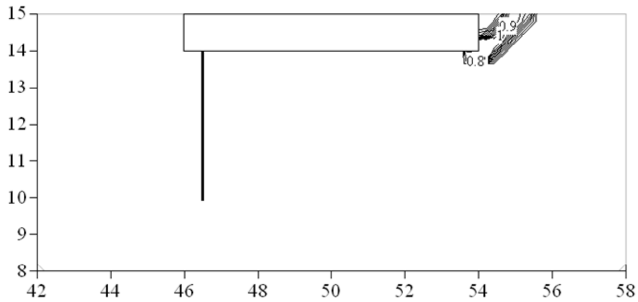

(a) Maximum shear strain distribution at water head 75mm of 10-40-L in low relative density (15%)

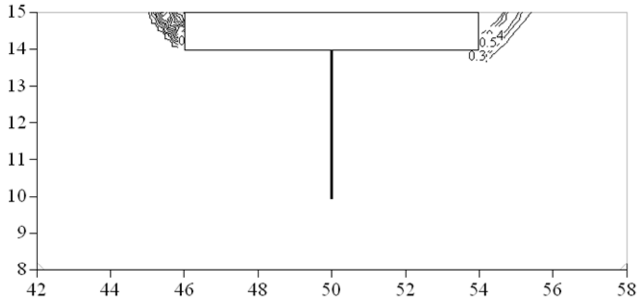

(a) Maximum shear strain distribution at water head 80mm of 10-40-M in low relative density (15%)

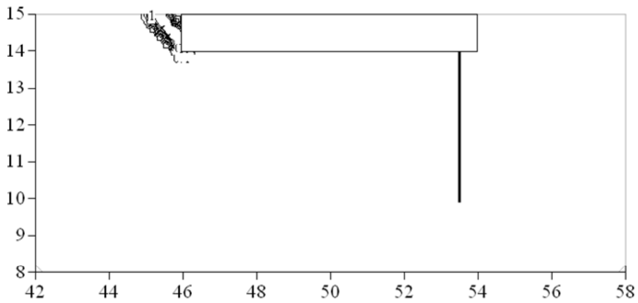

(a) Maximum shear strain distribution at water head 80mm of 10-40-R in low relative density (15%)

Figure8 Maximum shear strain distribution of elasto-plastic FEM

6 RESULT

Creep flow theories were reexamined by model six patterns experiments and finite element analyses that had same creep length by changing the installation position and length of cut-off wall in this study. These critical water heads of model experiments were different from each pattern. It was clear that creep flow theories were not able to predict the critical water head.

Our FEM predicted these critical water heads of model experiments.

We estimate the impact of relative density in the seepage failure of the foundation of the weir. Difference of each critical water head depending on position of cut-off wall was less affected by relative density. When the penetration depth of the weir was shallow, however, difference of each critical water head depending on position of cut-off wall was few by the difference of mechanism of seepage failure.

7 REFERENCES

[1] Bligh, W. G., “The practical design of irrigation works”, London Constable, 1910, pp.162-205

[2] Lane, E.W., “Security from Under seepage Masonry Dams on Earth Foundations”, Trans. ASCE, vol. 100,1935, pp.1234-1351

[3] Tanaka, T. and Kawamoto, O., “Three dimensional finite element collapse analysis for foundations and slopes using dynamic relaxation”, Proc. of Numer. Meth. in Geomech., 1988, pp.1213-1218

[4] Tatsuoka, F., Siddiquee, M. S. A, Park, C. S., Sakamoto, M. and Abe, F., “Modeling Stress-Strain Relations of Sand”, Soils and Foundations, vol.33(2), 1993, pp.60-81

[5] Okajima, K, Tanaka, T, Zhang, S and Komatsu, T, “Model experiments and elasto-plastic finite element analysis about seepage failure of sand behind fixed sheet pile”, Transactions of the JSIDRE, vol.260, 2009, pp.107-112

First International Conference on Geotechnique, Construction Materials and Environment, Mie, Japan, Nov.21-23, 2011, ISBN: 978-4-9905958-0-7 C3051

Shear Deformation and Failure of Sandy Slope According to Pore Pressure Generation due to Rainfall Infiltration

Sasahara K., Kochi University, Sakai N. , NIED

ABSTRACT: Monitoring of surface displacement of slope has been widely adopted as time prediction method of shallow landslide due to rainfall. Modeling of shear deformation according to rainfall infiltration is necessary for establishment of the method. In order to examine the constitutive relation for the model, surface displacement, pore pressure at the base, volumetric water content (hereafter, V.W.C.) and suction, shear strain in the sandy model slope are monitored during artificial rainfall. Analysis of the monitored data shows that surface displacement proceeds at small rate under unsaturated condition first, then increases remarkably with the rise of pore pressure at the base. Unsaturated component of surface displacement of steeper slope is larger than that of gentler slope. It is likely to be due to that shear strain with the increase of suction is larger in steeper slope while shear strain according to the increase of pore pressure is larger in gentler slope.

Keywords: Shallow landslide, Rainfall, Shear strain, Pore pressure, Suction

1. INTRODUCTION

The modeling of shear deformation of steep slope due to rainfall infiltration is necessary for the establishment of time prediction method of shallow landslide due to rainfall. Observations of deformation of the slope under artificial rainfall or specimen under anisotropic condition just before the failure had been implemented by some researchers [1]-[3], and produced the empirical law between time and deformation. The law has been adopted as the time prediction method based on the monitoring surface displacement [2], [3].

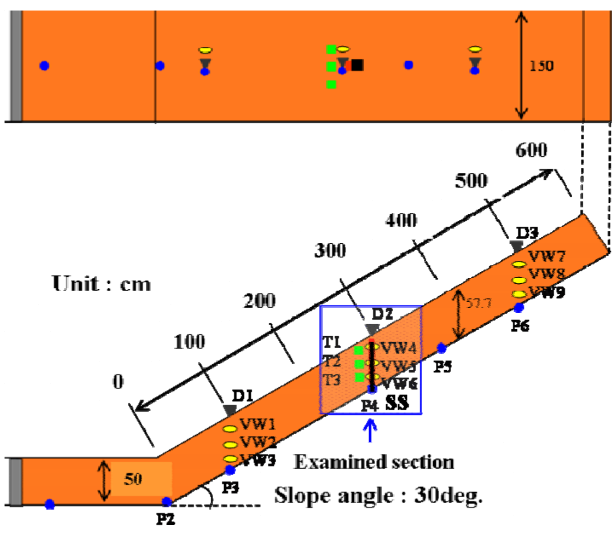

Fig.1 Geometry of model slope and location of monitoring devices

Because this method is empirical one, it does not take the change of stress in the slope into consideration. So it often failed to predict the time of failure of the slope under sudden change of rainfall intensity.

Recently some researches [4], [5] tried to observe slope deformation by Microelectro-mechanical system (MEMS) tilt-meter under the change of geometry of the slope such as cutting works, and other researches [6], [7] observe the deformation of the slope under artificial rainfall. Although they made much efforts to measure the slope deformation, they could not examine the mechanical law of the slope deformation.

In order to examine the constitutive law for the deformation of the slope under rainfall, the monitoring of V.W.C., suction, shear strain, pore pressure, and surface displacement are measured in the sandy model slope under constant rainfall in this paper. And some consideration are made in order to derive the relation between V.W.C., suction and shear strain, or that between shear strain and pore pressure in the slope under rainfall infiltration.

2. METHODOLOGY

2.1 Model slope and monitoring devices

Fig.1 shows the plane and longitudinal section of the model slope and location of monitoring devices with slope angle of 30deg. Model slope is made in a flume of 300cm length, 150cm width, and 50cm height at horizontal section, and 600cm length, 150cm width, and 50 cm depth at slope section (Fig.2). The flume has vertical steel blades of 1cm height located every 50cm in the longitudinal direction at the base of the slope in order to prevent slip between the soil mass and the base. Model slope is made of granite soil (Fig.3). The soil is filled and compacted horizontally at every 20cm thickness due to human stepping on the soil, and is managed to keep

Fig.2 Flume and model slope

void ratio of 1.46~1.52. Water content of the soil layer is 3.7~4.4%. The soil layer thickness is 50cm so that soil depth to gravitational direction is 57.7cm The base and upper boundary of the flume is undrained condition, while the lower boundary is drained condition.

In the model slope, soil moisture sensors (expressed as 'VW' in Fig.1) are installed at the depth of 10, 25, 40cm at 100, 300,500cm from the toe of the slope. They has the accuracy of 0.02 (m^3/m^3). Tensiometers (expressed as 'T' in Fig.1) are installed at the depth of 10, 25, 40cm at 300cm from the toe of the slope. They have accuracy of 1(kPa). Shear strain gauge (expressed as 'SS' in Fig.1) is installed at 300cm from the toe of the slope. It is series of tilt meter at every vertical depth of 9.2cm and tilt meters are connected by bolt and nut. So the meters can incline only to slope inclination direction. Shear strain increment at some depth $\Delta\gamma$ is defined as tan($\Delta\theta$), while $\Delta\theta$ is the inclination increment of the tilt meter (Fig.4). Tilt meter has non-linearity of 0.2 degree which corresponds to that of 0.0035 for $\Delta\gamma$. Groundwater level (hereafter G.W.L.) gauges (expressed as 'P' in Fig.1) with the accuracy of 1cmH_2O are located at the base of the model at 0, 100, 300, 400, 500cm from the toe of the slope. The measurement data

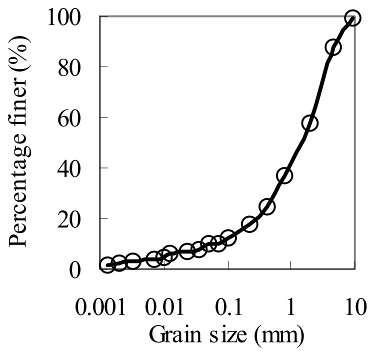

Fig.3 Grain size distribution of granite soil

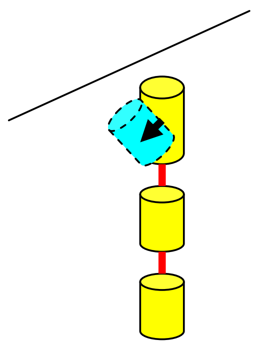

Increase of increment of tilt-meter :$\Delta\theta$

Shear strain increment $\Delta\gamma$ = tan$(\Delta\theta)$

Fig.4 Measurement of shear strain by tilt meter

of the gauge at 100, 300, 500cm are used for the examination in this paper. Extensometers are installed at the surface of the slope. The location is 100cm, 300cm, 500cm from the toe of the slope. It has the non-linearity of 0.1mm

2.2 Experimental conditions

2 types of model slope with different inclination 30deg. (Fig.1), 40deg. are prepared for the examination of the influence of the slope inclination to the relation between shear deformation and rainfall infiltration. The arrangement of measurement devices in the slope of 40deg. are just same with that of 30deg. The difference between the slope of 30deg. and that of 40deg. are soil layer depth to gravitational direction at the slope section of the model. Soil layer depth to gravitational direction of 30deg. is 57.7cm, while that of 40deg. is 65.3cm. Artificial rainfall with the constant intensity of 50 mm/h is sprayed from the rainfall simulator above the model slope until the onset of slope failure.

3. RESULTES OF EXPERIMENTS

Fig.5 shows time variation of V.W.C., suction and shear strain in the slope at 300cm from the toe of the slope, G.W.L. and surface displacement at 100cm, 300cm, 500cm from the toe of the model slope with 30deg inclination. Slope failure occurred at 5150sec. in the model slope of 30deg.. V.W.C. keeps constant just after the start of the experiment, then makes rapid increase earlier with shallower depth, and it continues to be almost constant after rapid rise. After constant value, V.W.C. at 40cm depth increases again at 4300sec. and that at 25cm also increase again at 5000sec., while that at 10cm keeps almost constant. Suction starts rapid decreasing earliest at 25cm at 500sec., then 40cm at 1300sec., and keeps almost constant negative value after that. Suction at 10cm keeps constant just after the start of experiment then makes rapid decrease at 3000sec. then makes second decrease at 6000sec.. Shear strain at each depth is almost zero until 3700sec., then increase rapidly. Shear strain at 4.6cm, 13.8cm, 23cm, and 50.6cm proceeds to positive while that at 32.2cm, 41.4cm proceeds to negative. Negative value may be due to reaction of tilt meter at this depth against large movement of tilt meters at upper or lower location. Time variation of G.W.L. and surface displacement at 100cm is almost same with those of 300cm, 500cm. This fact suggests that shear deformation and groundwater rise at any cross-section from 100cm to 500cm is almost same. G.W.L. continues slight decreases from the start of the experiment until 4000sec., and then makes remarkable increase after almost 4000sec.. Surface displacement also makes no increase until 4000sec., then increases rapidly. Surface displacement and shear strain in the slope makes remarkable increase after around 4000sec when G.W.L. starts rise. It suggests that shear deformation proceeds according to increase of pore pressure in the slope of 30deg..

Fig.6 shows time variation of V.W.C., suction and shear

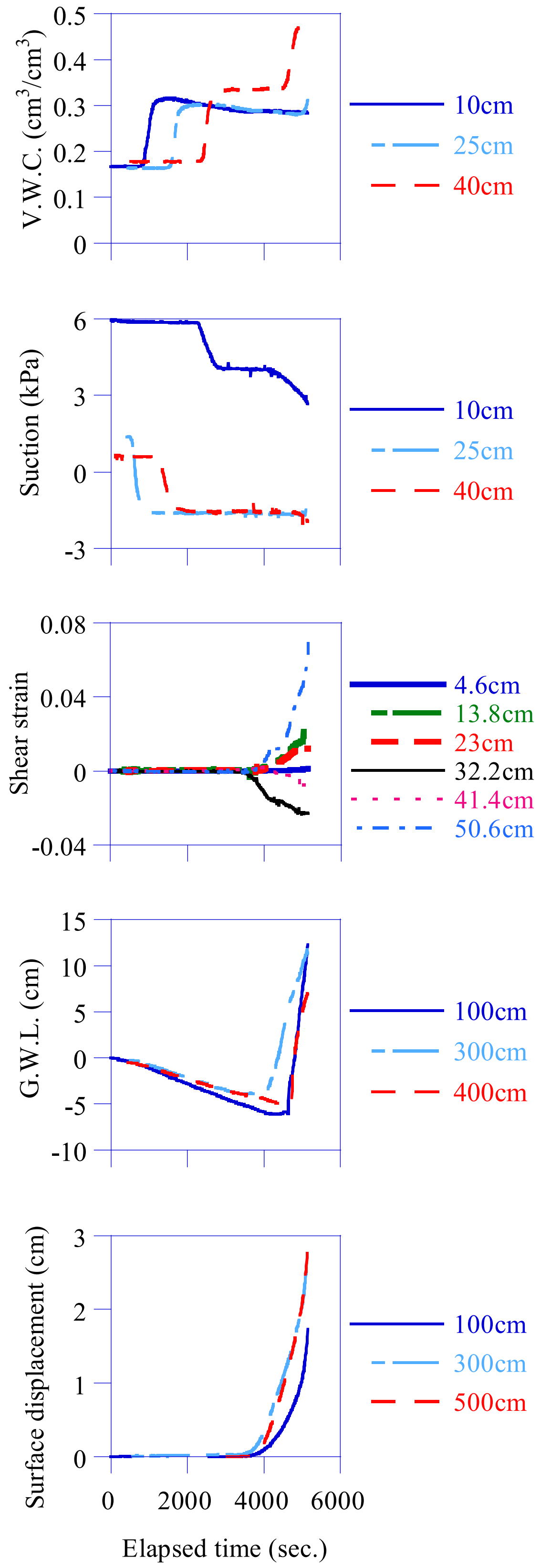

Fig.5 Time variation of V.W.C., suction, shear strain, pore pressure, and surface displacement (30 deg.)

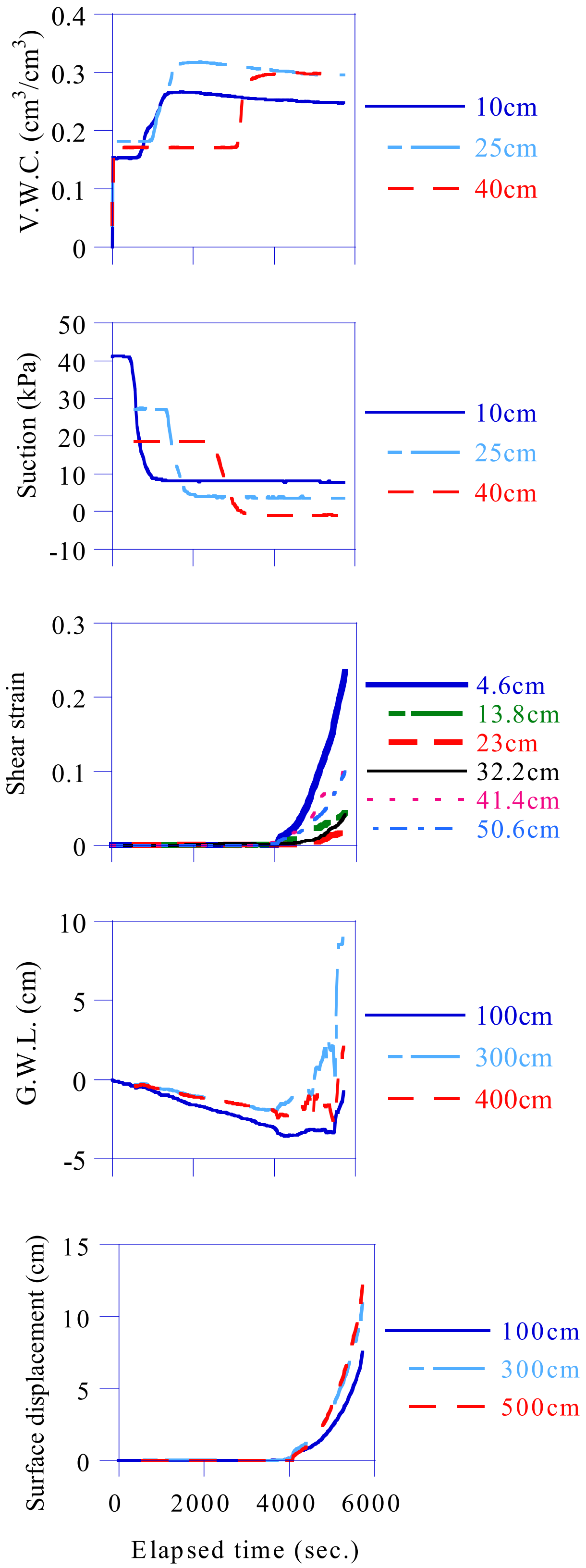

Fig.6 Time variation of V.W.C., suction, shear strain, pore pressure, and surface displacement (40 deg.)

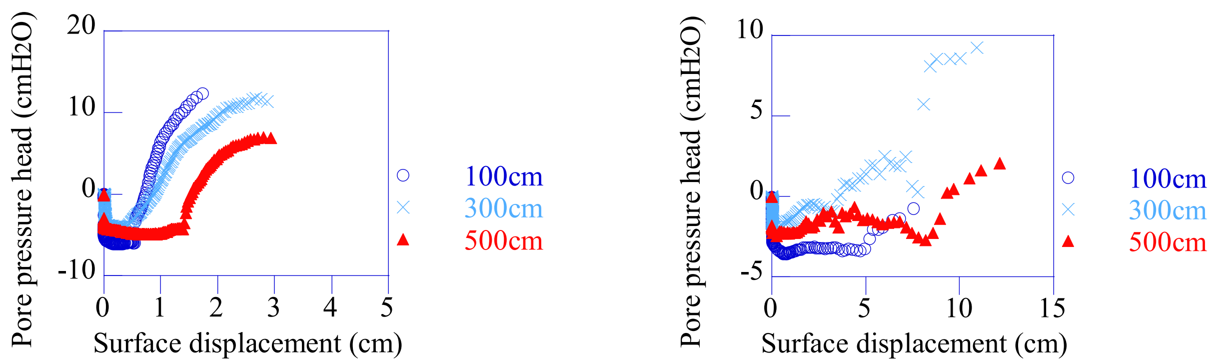

(a) 30deg. (b) 40deg.

Fig.7 Relation between surface displacement and pore pressure

strain in the slope at 300cm from the toe of the slope, G.W.L. and surface displacement at 100cm, 300cm, 500cm from the toe of the model slope with 40deg inclination. V.W.C. starts increase earlier at shallower depth, then keeps almost constant vale within 0.25~0.3. Suction also starts decrease earlier at shallower depth, then keeps almost constant value within 0~10 kPa. Shear strain make little variation until 4000sec., then remarkably increase to positive. G.W.L. keeps negative and continues slight decrease until 4000sec., then increase largely. G.W.L. at 100cm, 500cm is lower than that at 300cm.Surface displacement also shows almost no variation until 4000sec., then rapidly increases. Remarkable increase of shear strain and surface displacement starts around 4000sec. when G.W.L. starts rise also in the case of the model slope of 40deg.. It suggests that shear deformation in the slope of 40deg. also greatly influenced by generation of pore pressure.

4. DISCUSSION

4.1 Surface displacement and pore pressure

Fig.7(a) shows the relation between surface displacement and pore pressure head on the base at 100, 300, 500cm from the toe of the slope of 30deg.. Pore pressure head at the base is equal to G.W.L.. Pore pressure head decreases and then keeps -7~-3 cmH_2O just after the start of the experiment. Surface displacement increases under unsaturated condition with negative pore pressure at this stage. After the surface displacement of 0.5~1.4cm, it increases with the increase of pore pressure head. Surface displacement increment becomes larger as pore pressure head increase. So the relation between surface displacement and pore pressure head can be modified by hyperbolic curve which is often adopted for stress-strain relation of the element of soil. The unsaturated component and all surface displacement are 0.5 and 1.7cm for 100cm, 0.4 and 2.8cm for 300cm, 1.4cm and 2.9cm for 500cm. So the ratios of unsaturated component to all surface displacement are 0.29 for 100cm, 0.14 for 300cm, and 0.48 for 500cm in the slope of 30deg..

Fig.7(b) shows the relation between surface displacement and pore pressure head on the base at 100, 300, 500cm from the toe of the slope of 40deg.. Similar to the relation of the slope of 30deg., pore pressure sudden decreases just after the experiment and keeps -4~0 cmH_2O until surface displacement of 5~8cm. Surface displacement proceeds under unsaturated condition in this stage. Although pore pressure of 300cm fluctuates and rises up to 2cm in this stage, it can be thought negative. Fluctuation of pore pressure may be due to error of measurement. Surface displacement remarkably increases with increase of pore pressure after that. Even though pore pressure at the start of this stage of 100, 500cm is negative, this stage can be thought to be under generation of positive pore pressure. Negative value of pore pressure of -4~0 kPa might mean quasi-saturated condition near the base of the slope. The unsaturated component and all surface displacement are 5 and 7.9cm for 100cm, 7.8 and 10.9cm for 300cm, 8.2cm and 12.2cm for 500cm. So the ratios of unsaturated component to all surface displacement are 0.63 for 100cm, 0.72 for 300cm, and 0.8 for 500cm in the slope of 40deg.. The ratio of unsaturated component is larger in the slope of 40deg. than that of 30deg..

4.2 Suction and shear strain in the slope

Fig.8(a) shows the relation between suction and shear strain at the same depth in the slope of 30deg.. Suction decreases with small increase of shear strain in the soil layer shallower than 23cm. Especially shear strain at 4.6cm is almost zero even after the increase of suction up to 4 kPa. Suction is still positive after the decrease at those depths. At the depth shallower than 23cm, shear strain continues to be almost zero with the increase of suction up to -4~0 kPa of suction, then it proceeds under almost constant suction. Shear strain proceeds to positive at 23, 50.6cm while it proceeds to negative at 32.2, 41.4cm with positive constant suction..

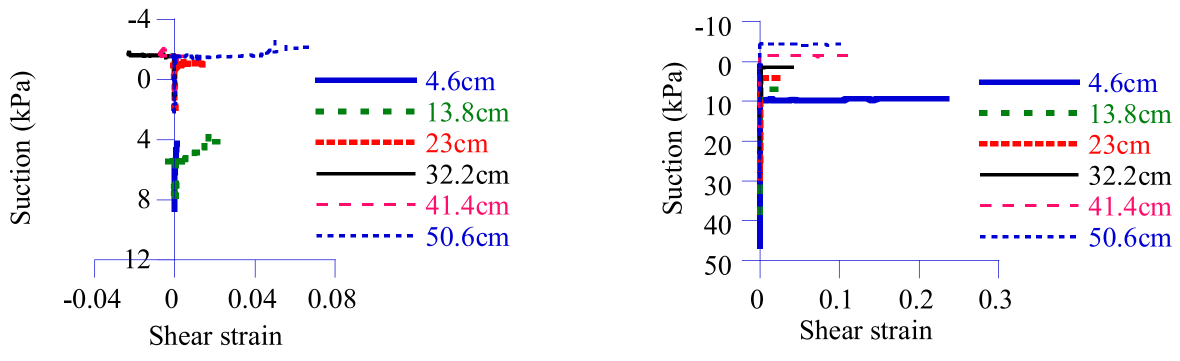

(a) 30deg. (b) 40deg.

Fig.8 Relation between shear strain and suction

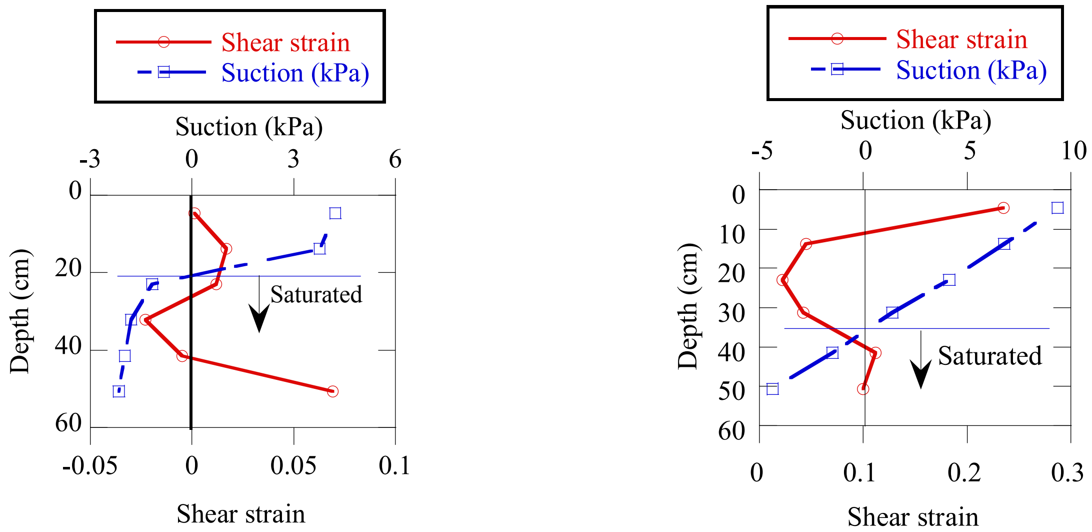

(a) 30deg. (b) 40deg.

Fig.9 Vertical profile of shear strain just before failure

Fig.8(b) shows the relation between suction and shear strain at the same depth in the slope of 40deg.. Shear strain keeps almost zero with the increase of suction at first, then proceeds with almost constant suction at all depths. Shear strain increases under positive suction (unsaturated condition) in the soil layer shallower than 32.2cm while it increases under negative suction at 41.4, 50.6cm. Shear deformation proceeds at unsaturated condition at deeper soil layer in the slope of 40deg. than that of 30deg..

Fig.9(a) shows the vertical profile of shear strain and suction at 300cm from the toe of the slope of 30deg.. Soil layer with negative suction is assumed to be saturated. Shear strain at deeper soil layer is larger than that near surface. Shear strain at 23~41.4cm depth is negative which might mean inverse movement of tilt meter at the depth corresponding to large movement of upper or lower tilt meter. Deeper soil layer is saturated. In the slope of 30deg., shear strain increases largely at saturated soil layer. Fig.9(b) shows the vertical profile of shear strain and suction at 300cm from the toe of the slope of 40deg.. Shear strain is larger near surface where suction is positive, while it is relatively smaller near the base which is saturated. In the slope of 40deg., shear strain increases largely at unsaturated soil layer.

4.4 Shear deformation under different slope inclination

According to the examination as above, shear deformation at saturated layer is larger in the gentler slope while shear deformation at unsaturated layer is larger in steeper slope. In order to compare the contribution of unsaturated component to shear deformation at examined section of the slope under different slope inclination, ratio of unsaturated part of shear area under different slope inclination is calculated from Fig.9. Shear area is defined as sum of shear strain from one depth to other depth, and is derived by the equation below.

$$A = \int_{z1}^{z2} \gamma dz \tag{1}$$

Here, A: shear area, γ : shear strain at some depth, z1, z2: depth (z1<z2). Shear area under unsaturated layer and saturated area in each slope is calculated. The ratio of shear area of unsaturated layer are 0.17 for the slope of 30deg. while it is 0.58 for 40deg.. So contribution of shear deformation at unsaturated layer is larger in the steeper slope. It is same trend with the ratio of unsaturated component of surface displacement that is larger in the steeper slope.

5. CONCLUSION

From the examination as above, the facts as bellows are made clear.

(1) Surface displacement and shear strain in the slope makes remarkable increase at the time of rise of G.W.L.

(2) Surface displacement proceeds at unsaturated condition at first, then increase remarkably with the increase of pore pressure at the base. The relation between surface displacement and pore pressure is hyperbolic just like stress-strain curve of soil element. The ratio of unsaturated component to all surface displacement is larger in steeper slope.

(3) In the slope, shear strain proceeds under almost constant suction after rapid increase of suction. Unsaturated soil layer near surface is thicker in the steeper slope.

(4) Shear strain at saturated zone near bottom is larger than that at unsaturated layer in the slope of 30deg., while shear strain at unsaturated layer near surface is larger in the slope of 40deg..

(5) Contribution of unsaturated shear deformation is larger in steeper slope.

REFERENCES

[1] Saitou M and Uezawa H, “Failure of Soil Due to Creep”, Proc. 5th International Conference on Soil Mechanics and Foundation Engineering, vol.1, 1961, pp.315-318.

[2] Saitou M, “Forecasting the Time of Occurrence of a Slope Failure”, Proc. 6th International Conference on Soil Mechanics and Foundation Engineering, vol.2, pp.537-541.

[3] Fukuzono T, “A New Method for Predicting the Failure Time of a Slope”, Proc. IVth International Conference and Field Workshop on Landslides, 1985, pp.145-150.

[4] Ito K and Toyosawa Y, “Field test of slope failure during slope cutting work”, JSCE Journals, vol.65, no.1, 2009, pp.254-265(in Japanese with English abstract).

[5] Uchimura T, et. al., “Simple monitoring method for precaution of landslides watching tilting and water contents on slopes surface”, Landslides, DOI 10.1007/s10346-009-0178-z., 2009.

[6] Moriwaki H, et. al., “Failure process in a full-scale landslide experiment using a rainfall simulator”, Landslides, vol.1, no.4, 2004, pp.277-288.

[7] Ochiai H, “AFludaized landslide on a natural slope by artificial rainfall”, Landslides, vol.1, no.3, 2004, pp.211-219.

First International Conference on Geotechnique, Construction Materials and Environment, Mie, Japan, Nov.21-23, 2011, ISBN: 978-4-9905958-0-7 C3051

Load Settlement Relationships of Circular Footings Considering Dilatancy Characteristics of Sand

Yusuke Tomita, Graduate Student, Dept. of Architecture, Faculty of Environmental and Urban Eng., Kansai Univ., M. Eng.
Tatsuaki Nishigata, Prof., Dept. of Civil, Environmental and Applied System Eng., Faculty of Environmental and Urban Eng., Kansai Univ., Dr. Eng.
Takeshi Masui, Assoc. Prof., Dept. of Architecture, Faculty of Environmental and Urban Eng., Kansai Univ., Dr. Eng.
Shintaro Yao, Prof. Emeritus, Kansai Univ., Dr. Eng.

ABSTRACT: In order to elucidate the mechanical properties of load-settlement relationships of spread foundations on sand ground, experimental and analytical study on strain hardening and dilatancy of sand is needed. Here we present the theoretical properties which were derived from circular footing model experiment and computer simulation. The model experiment was carried out through vertical loading on circular footing, and used relative density and tank dimensions as parameters. The quantitative relationship between load and settlement was analyzed through FEM simulation with SMP-Cam-Clay model, which is capable of estimating the dilatancy of sand. The results are summarized as follows; In both cases of dense and loose sand models, before reaching the ultimate load, the load-settlement relationship obtained from FEM simulation corresponded with that of obtained from the experiment. After reaching the ultimate load, "Terzaghi's bearing capacity line" corresponded with the load-settlement relationship obtained from the experiment. In the case of medium-dense sand models, some binding effect of a soil tank rectangle was recognized. The effect was considered to be exerted by the positive dilatancy of the sand, which occurred steadily with the settlement progresses.

Keywords: Spread Foundation, Sand Ground, Load-Settlement Curve, Constitutive Equation, Dilatancy

1 INTRODUCTION

Although the quantitative load-settlement relationships of spread foundation have been experimentally well demonstrated on sand ground [1]–[4], the underlying mechanical properties of the relationships still remained to be elucidated. Especially, since little study has been done on the mechanical properties characterized through strain hardening and dilatancy of sand. Here we present the theoretical properties which were derived from circular footing model experiment and computer simulation. The model experiment was carried out through vertical loading on circular footing, and used relative density and tank dimensions as parameters. The quantitative relationship between load and settlement was analyzed through FEM simulation with SMP-Cam-Clay model. In addition, a part of the contents of this paper have been reported in [5], [6].

2 VERTICAL LOADING TEST OF CIRCULAR FOOTING

2.1 Test Pit and Loading Equipment

The model experiments were performed on Toyoura sand, with different relative densities. The Maximum and minimum densities of the sand, as determined by the standard procedure, are given in Table1. The loose sand models were built by pouring sand from containers. The density of the sand models is a unique-function of the height of free fall of sand. Medium-dense and dense sand models were built by vibration provided by an earthquake simulator. The soil tank was made of steel, which made the tank completely resistant to earth pressure. Teflon sheets with double layers of grease were set on the sides of the soil tank, in order to omit the friction caused by the experiment ground [7]. To study the effect of sand dilatancy on mechanical properties of the load-settlement relationship, soil tanks with different volumes were used in the experiments. The short side of the big soil tank was measured to be 400 millimeters in Fig.1-1 which shows the experimental device, whereas that of the small soil tank was 100 millimeters in Fig.1-2 which shows the experimental device. The model footing has a circular cross section with diameter of 20 millimeters, and is 80 millimeters in height. Moreover, the model footing is made of wood, and sandpapers are put on the tip [1]. In the following,

Table1 Specifications of the Experiment Ground

Density of Soil Particles ρ_s	2.558g/cm^3
Maximum Density $\rho_{d\,max}$	1.645g/cm^3
Minimum Density $\rho_{d\,min}$	1.337g/cm^3

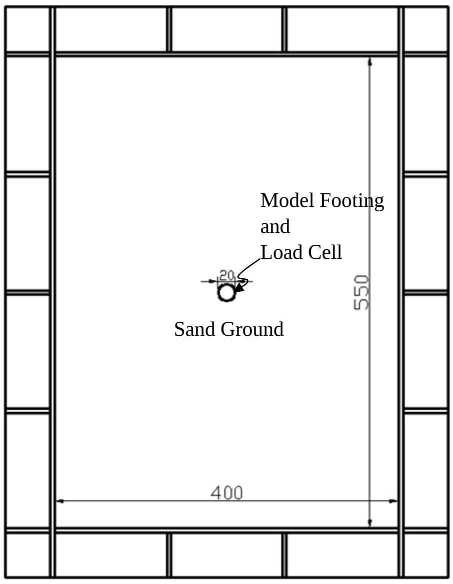

The Ground Plan : ℓ 20B (Unit : mm)

Fig.1-1 Experimental Device (ℓ 20B)

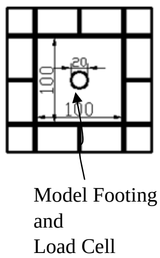

The Ground Plan : ℓ 5B (Unit : mm)

Fig.1-2 Experimental Device (ℓ 5B)

Table2 Experiment Name

Name	Relative Density D_r	Soil Tank
L-20B	20～30%	ℓ 20B
L-5B	20～30%	ℓ 5B
M-20B	50～60%	ℓ 20B
M-5B	50～60%	ℓ 5B
D-20B	80～90%	ℓ 20B
D-5B	80～90%	ℓ 5B

short side length of the soil tank is named ℓ, diameter of the model footing is named B, the soil tank that ℓ is 400 millimeters is named ℓ 20B, and the soil tank that ℓ is 100 millimeters is named ℓ 5B. In other words, ℓ 20B expresses that ℓ is 20 times of B, ℓ 5B expresses that ℓ is 5 times of B. Experiment name is shown in Table2. In Table2, L, M, and D indicate the loose sand ground, the medium-dense sand ground, and dense sand ground, respectively. Also, 20B indicates soil tank ℓ 20B, whereas 5B indicates ℓ 5B. The binding effect caused by the soil tank was treated as a negligible factor throughout the experiment. This was confirmed when the result of separate experiment conducted on dense sand ground using ℓ as 800 millimeters corresponded to that of D-20B [5]. Therefore, the binding effect was also considered to be negligible in the experiments of L-20B and M-20B.

2.2 Loading Procedure

300kN universal testing machine is used as a loading device. By vertical loading to the settlement rate 12.5μm/sec on the model footing, the quantitative load-settlement relationship was determined. In the case of loose sand models and medium-dense sand models, the load measured by load cell installed at the top of the model footing divided by the bottom area of the model footing was defined as the load. In the case of dense sand models, the load measured by load cell installed at the bottom of the soil tank divided by the bottom area of the model footing was defined as the load. In all the experiments, the amount of relative displacement between the soil tank and the loading plate of a universal testing machine was defined as the settlement. In the following, the load is named p, the settlement is named S. In lastly, loading was performed until S reached 10 millimeters.

2.3 Test Results

2.3.1 In the Case of Loose Sand Models

L-20B and L-5B were performed three times, each. As a result, the p-S relationship showed no significant variation. The results of two typical cases are shown by both logarithms indications in Fig.2. In any results of L-20B and L-5B, p steadily increases as the settlement progresses, and both results appear to be consistent. Based on [3], the ultimate load in p-S relationship was defined as a load at the point that shifts from a curve to a straight line. This point corresponds to an inflection point in log p-log S relationship. In any results of L-20B and L-5B, the inflection point was

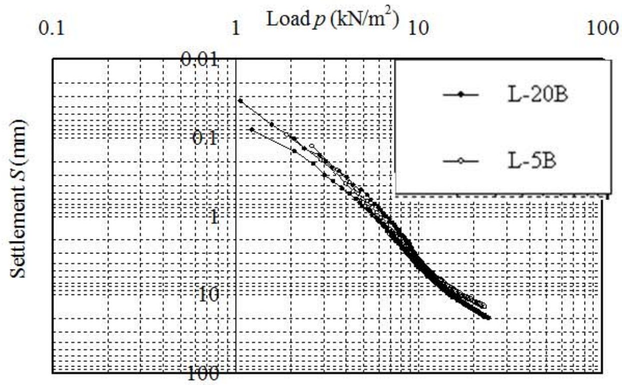

Fig.2 log$p$-log$S$ Relationships (In the Case of Loose Sand Models)

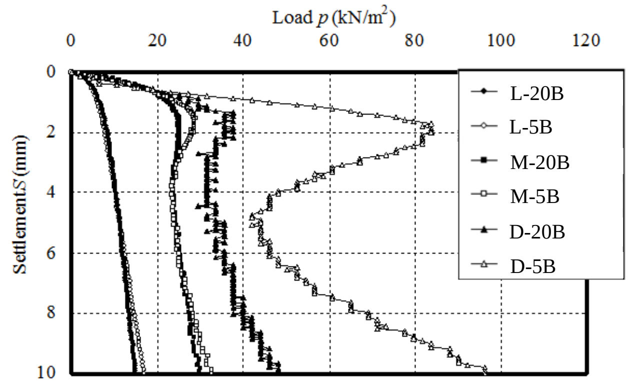

Fig.3 p-S Relationships (Comparison of the Relative Density)

confirmed when S reached 3 millimeters, so the load at this point was defined as the ultimate load. Probably because the loose sand ground under the model footing exhibit contractile behavior, the elevation of sand surface around the model footing did not appear in any results of L-20B and L-5B.

2.3.2 In the Case of Dense Sand Models

D-20B and D-5B were performed three times, each. As a result, the p-S relationship showed no significant variation. The result of a typical case is shown in Fig.3. In any results of D-20B and D-5B, p steadily increases until S reaches about 2.0 millimeters. Both results are almost consistent until S reaches 1.0 millimeters. But the stiffness on settlement of D-5B becomes larger than that of D-20B from 1.0 millimeters to 2.0 millimeters. As a result, p of D-5B is about 2.4 times larger than that of D-20B as S reached about 2.0 millimeters. From 2.0 millimeters to 4.5 millimeters, p steadily decreases as the settlement progresses where the rate of decrease in p of D-5B is about 6 times larger than that of D-20B. In any results of D-20B and D-5B, p then steadily increases again as the settlement progresses, and the stiffness on settlement of D-5B becomes larger than that of D-20B. In addition, in both results of D-20B and D-5B, the ultimate load was confirmed when S reached about 2.0 millimeters. The elevation of sand surface around the model footing appeared when S reaches about 4.5 millimeters in the result of D-5B. In this paper, the failure surface was decided to have reached the sand surface, based on the appearance of the elevation of the sand surface around the model footing [8].

2.3.3 In the Case of Medium-Dense Sand Models

M-20B and M-5B were performed three times, each. As a result, the *p*-*S* relationship showed no significant variation. The result of a typical case is shown in Fig.3. In any results of M-20B and M-5B, *p* steadily increases until *S* reaches about 1.6 millimeters. Both results are almost consistent until *S* reaches 0.8 millimeters. But the stiffness on settlement of M-5B becomes larger than that of M-20B from 0.8 millimeters to 1.6 millimeters. As a result, *p* of M-5B is about 1.2 times larger than that of M-20B at *S* reached about 1.6 millimeters. From 1.6 millimeters to 4.0 millimeters, *p* steadily decreases as the settlement progresses where the rate of decrease in *p* of M-5B is about 3 times larger than that of M-20B. In any results of M-20B and M-5B, *p* then steadily increases again as the settlement progresses, and both results appeared to be consistent. In addition, in both results of M-20B and M-5B, the ultimate load is confirmed when *S* reached about 1.6 millimeters. Such characteristics of the *p*-*S* relationship were similar to that of the *p*-*S* relationship which was derived from D-20B and D-5B. The elevation of sand surface around the model footing did not appear in any results of M-20B and M-5B. Such behavior of sand was similar to what was derived from L-20B and L-5B.

3 THE INFLUENCE OF SAND DILATANCY ON P-S RERATIONSHIPS

3.1 In the Case of Dense Sand Models

In the case of dense sand models, sand ground under the footing seemed to exhibit a continuous behavior with positive dilatancy until *p* reaches the ultimate load, whereas the sand behavior under footing exhibits a discontinuous behavior with a sign of failure surfaces after *p* reached the ultimate load. Therefore, the FEM simulation was performed until *p* reaches the ultimate load, and then the rigid-plastic analysis based on the bearing capacity of Terzaghi's theory was performed [5]. In the following, SD-20B expresses the analysis corresponding to D-20B, and SD-5B expresses the analysis corresponding to D-5B.

3.1.1 In the Case of D-20B

[Until p reaches the ultimate load]

The comparison of the load-settlement relationship obtained from D-20B and SD-20B, and "Terzaghi's bearing capacity line" is shown in Fig.4. Here, "Terzaghi's bearing capacity line" is calculated as D_f *S* in (1), indicating the line that linked q_u as a parameter *S*. In Fig.4, both *p* of SD-20B and D-20B are roughly consistent until *S* reaches about 1.0 millimeter. From 1.0 millimeter to 2.0 millimeters, *p* of SD-20B is larger than that of D-20B.

$$q_u = \alpha c N_c + \beta \gamma_1 B N_\gamma + \gamma_2 D_f N_q \tag{1}$$

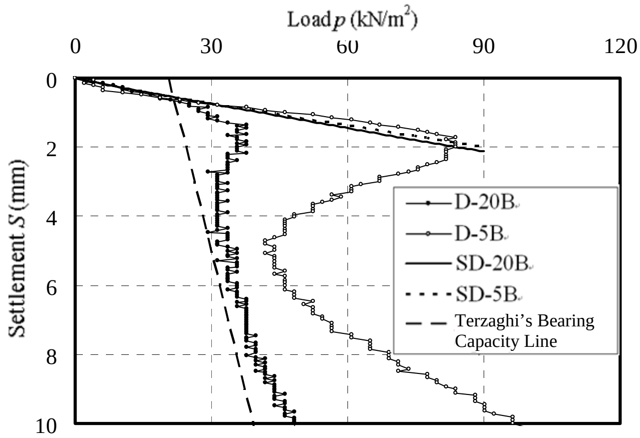

Fig.4 Comparison of the Load-settlement Relationship obtained from D-20B and SD-20B, and "Terzaghi's Bearing Capacity Line"

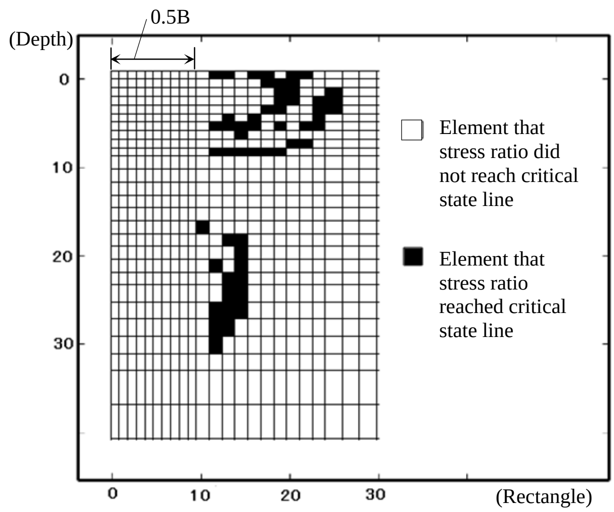

Fig.5 The Distribution of Stress Ratio obtained from SD-20B(Unit：mm)

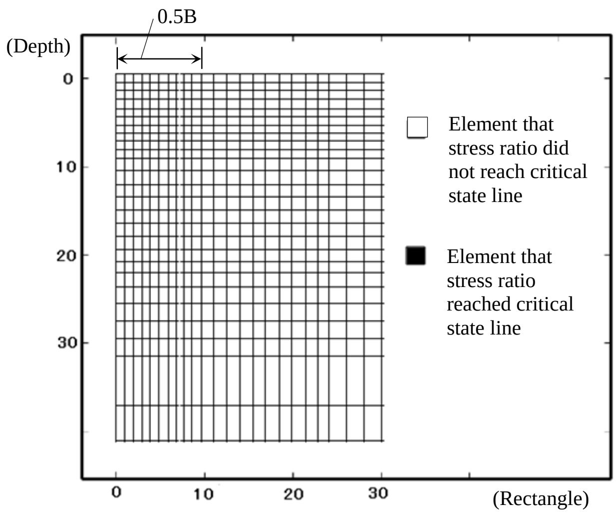

Fig.6 The Distribution of Stress Ratio obtained from SD-5B(Unit：mm)

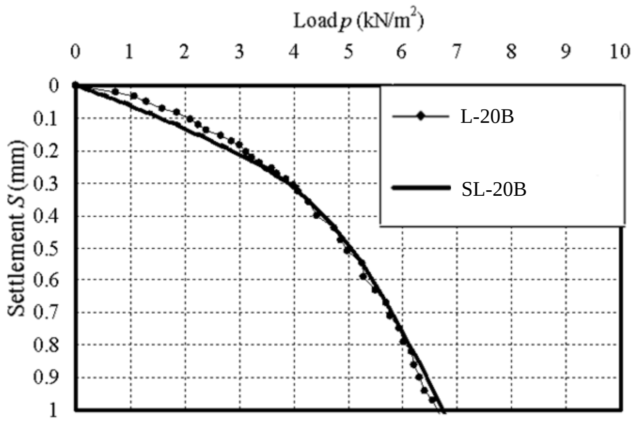

Fig.7 Comparison of the Load-settlement Relationship obtained from L-20B and SL-20B

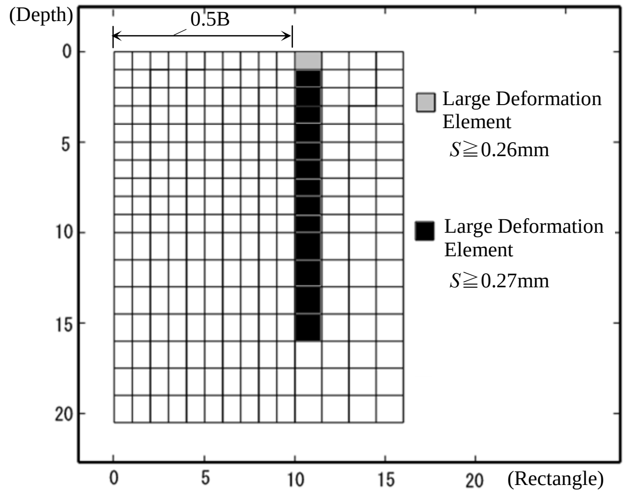

Fig.8 The Distribution of “Large Deformation Element” obtained from SL-20B (Unit：mm)

This is because the progressive failure accompanied by the generation of the failure surface occurs. It can be confirmed from Fig.5 which shows the distribution of stress ratio obtained from SD-20B when S reached about 2.0 millimeters. In addition, the element that stress ratio reached critical state line occurred first when S reached about 1.0 millimeter. In Fig.5, it is confirmed that the element that stress ratio reaching critical state line steadily increases from 1.0 millimeter to 2.0 millimeters. Therefore, because the condition that the boundary of the element changes discontinuous when stress ratio reached critical state line is not considered in the case of SD-20B, p of SD-20B is considered to be larger than that of D-20B from 1.0 millimeter to 2.0 millimeters. From the above, it is considered that sand behavior shifts from a continuous behavior based on SMP-Cam-Clay model to a discontinuous behavior accompanied by the generation of the failure surface when S reached about 1.0 millimeter, and that the sheared mass of sand appears under the footing when S reached about 2.0 millimeters.

[After p reached the ultimate load]

In Fig.4, from 2.0 millimeters to 4.5 millimeters, p decreases slightly as the settlement progresses. When S reached about 4.5 millimeters, the load-settlement relationship is asymptotic to “Terzaghi’s bearing capacity line”. Therefore, sand behavior is considered to result in a total failure at this stage. After S reached about 4.5 millimeters, p increases steadily along “Terzaghi’s bearing capacity line” as the settlement progresses, indicating the sand behavior resulted in a continuous failure.

3.1.2 In the Case of D-5B

[Until p reaches the ultimate load]

The comparison of the load-settlement relationship obtained from D-5B and SD-5B is shown in Fig.4. Because both p of SD-5B and D-5B are roughly consistent until S reaches about 1.0 millimeter, the mechanical properties of the p-S relationship obtained from D-5B is considered to be similar to that of obtained from D-20B. From 1.0 millimeter to 2.0 millimeters, both p of SD-5B and D-5B are roughly consistent throughout. As a result, the ultimate load of D-5B is 2.4 times larger than that of D-20B. To analyze the cause, the comparative studies shown in Fig.5 and Fig.6 were conducted. Fig.6 shows the distribution of stress ratio obtained from SD-5B. In the case of SD-20B, the area recognized as sheared mass of sand appears under the footing. On the other hand, in the case of SD-5B, the area recognized as sheared mass of sand does not appear. In other words, in the case of D-5B, positive dilatancy exerts a marked binding effect of a soil tank rectangle and the dilatancy causes the increase of mean principal stress as a result. Therefore, from 1.0 millimeter to 2.0 millimeters, the ultimate load of D-5B is considered to be 2.4 times larger than that of D-20B.

[After p reached the ultimate load]

In Fig.4, from 2.0 millimeter to 4.5 millimeters, p decreases slightly until p reaches half of the ultimate load. Such characteristic of the p-S relationship is not recognized in the case of D-20B. Because the failure surface appeared at the sand surface when S reached 4.5 millimeters, the effect of positive dilatancy which occurred from 1.0 millimeter to 2.0 millimeters is considered to disappear from 2.0 millimeters to 4.5 millimeters.

3.2 In the Case of Loose Sand Models

In the case of loose sand models, shear failure which occurs and progresses below edge of the footing is considered to have a significant influence on the mechanical properties of the p-S relationship. Therefore, the element that stress ratio reached critical state line and shear strain excelled was defined as “Large deformation element”, and regarded it as a gap element in each step, and the FEM simulation was performed [6]. In the following, SL-20B expresses the analysis corresponding to L-20B, and SL-5B expresses the analysis corresponding to L-5B. In addition, because both results of SL-20B and SL-5B were almost consistent, only the results of SL-20B are described as follows.

[Until p reaches the ultimate load]

The comparison of the load-settlement relationship obtained from L-20B and SL-20B is shown in Fig.7. In Fig.7, both p of SL-20B and L-20B are almost consistent until S reaches about 1.0 millimeter. To investigate the stress condition in the sand ground, the distribution of “Large deformation element” was obtained from SL-20B as shown in Fig.8. In Fig.8,

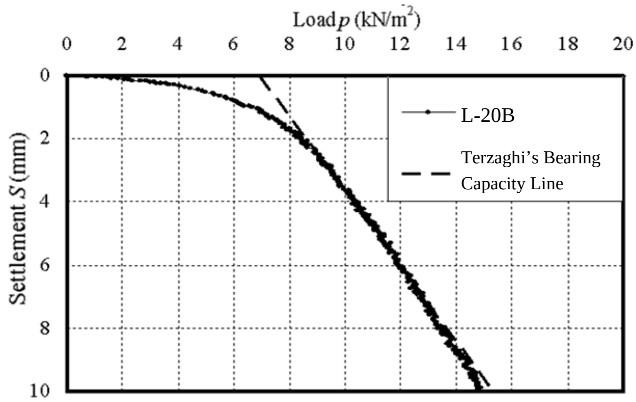

Fig.9 Comparison of the Load-settlement Relationship obtained from L-20B and "Terzaghi's Bearing Capacity Line"

Table3 Comparison of the Ultimate Load by the Relative Density

Experiment Name	The Ultimate Load (kN/m^2)	R_u
L-20B	9.51	0.96
L-5B	9.17	
M-20B	25.01	1.15
M-5B	28.70	
D-20B	35.66	2.35
D-5B	83.91	

"Large deformation element" appears below edge of the footing first when S reached 0.26 millimeters, and after S reached 0.27 millimeters, it appears directly below "Large deformation element" which occurred when S reached 0.26 millimeters. Because both p of SL-20B and L-20B are almost consistent until S reaches about 1.0 millimeter, the sand ground under the footing is considered to exhibit a behavior based on SMP-Cam-Clay model until S reaches about 0.26 millimeters. In other words, sand ground under the footing is considered to exhibit a contractile behavior with negative dilatancy. From 0.26 millimeters to 1.0 millimeters, it is considered that sand ground under the footing exhibits a contractile behavior continuously with negative dilatancy and that shear failure occurs and progresses at the same time below edge of the footing.

[After p reached the ultimate load]

In Fig.7, the p-S relationship obtained from SL-20B showed a good correspondence with that of obtained from L-20B until S reaches 1.0 millimeter. After S reached 1.0 millimeter, the simulation of the p-S relationship was carried out based on "Terzaghi's bearing capacity line," since SL-20B was difficult to perform as p of L-20B approached the ultimate load. Here, the relative density D_r was determined to be consistent with q_u when S reached 3.0 millimeters and the ultimate load of L-20B. The relationship between D_r and internal friction angle ϕ was estimated from [9]. As a result, D_r=59%, ϕ =38.9°, $\gamma_1=\gamma_2$=1.52g/cm^3 were obtained. These values correspond to the constants representing the mechanical properties of the medium-dense sand ground. The comparison of "Terzaghi's bearing capacity line" using these values and the load-settlement relationship obtained from L-20B is shown in Fig.9. In Fig.9, it was obtained the interesting results that "Terzaghi's bearing capacity line" shows a good correspondence with the p-S relationship obtained from L-20B after S reached 3.0mm millimeters.

3.3 In the Case of Medium-dense Sand Models

A comparison of the ultimate load in the case of each sand model is shown in Table3. In Table3, R_u is the ratio of the ultimate load in the case of using ℓ 5B against ℓ 20B. Some binding effect of a soil tank rectangle is recognized on R_u in the case of medium-dense sand model. A binding effect of a soil tank rectangle becomes marked by positive dilatancy as described in Section 3.1.2. Therefore, in the case of medium-dense sand model, because the condition of dilatancy occurrence is located between positive dilatancy and negative dilatancy, some binding effect of a soil tank rectangle recognized on R_u is considered to be exerted by positive dilatancy which occurred steadily as the settlement progresses.

4 CONCLUSIONS

In this paper, we present the theoretical properties of the load-settlement relationship on sand ground, which were derived from circular footing model experiment and computer simulation. To study the effect of sand dilatancy on the mechanical properties of the load-settlement relationship, the model experiment was carried out on relative density and tank dimensions as parameter. The quantitative relationship between load and settlement was analyzed through FEM simulation with SMP-Cam-Clay model, which is capable of estimating the dilatancy. The results are summarized as follows;

1) In the case of dense sand models with large soil tank (D-20B), it is considered that sand behavior shifts from a continuous behavior based on SMP-Cam-Clay model to a discontinuous behavior accompanied by the generation of the failure surface when S reached about 1.0 millimeter, and that the sheared mass of sand appears under the footing when S reached about 2.0 millimeters. When S reached about 4.5 millimeters, sand behavior is considered to result in a total failure. After S reached about 4.5 millimeters, sand behavior is considered to result in a continuous failure.
2) In the case of dense sand models with small soil tank (D-5B), until S reached about 1.0 millimeter, the mechanical properties of the p-S relationship obtained from D-5B is considered to be similar to that of obtained from D-20B. From 1.0 millimeter to 2.0 millimeters, it is considered that positive dilatancy exerts a marked binding effect of a soil tank rectangle and the dilatancy causes the increase of mean principal stress. Accordingly, the ultimate load of D-5B was 2.4 times larger than that of D-20B. From 2.0 millimeter to 4.5 millimeters, the effect of positive dilatancy which occurred from 1.0 millimeter to 2.0 millimeters is considered to disappear. When S reached about 4.5 millimeters, mechanical properties of D-5B are considered to be similar to that of D-20B.

3) In the case of loose sand models with large and small soil tank (L-20B and L-5B), sand ground under the footing is considered to exhibit a behavior based on SMP-Cam-Clay model until S reaches about 0.26 millimeters. In other words, sand ground under the footing is considered to exhibit a contractile behavior with negative dilatancy. From 0.26 millimeters to 1.0 millimeters, it is considered that sand ground under the footing exhibits a contractile behavior continuously with negative dilatancy and that shear failure occurs and progresses at the same time below edge of the footing. After S reached 3.0millimters, the results showed that, with the values correspond to the constants representing the mechanical properties of medium-dense sand ground, "Terzaghi's bearing capacity line" seemed to correspond with the p-S relationship obtained from L-20B.
4) In the case of medium-dense sand models (M-20B and M-5B), some binding effect of a soil tank rectangle was recognized on R_u which shows the ratio of the ultimate load in the case of using ℓ 5B against ℓ 20B. This is considered to be exerted by positive dilatancy which occurred steadily as the settlement progresses, because the condition of dilatancy occurrence is located between positive dilatancy and negative dilatancy.

5 REFERENCES

[1] Rei Morimoto et al, "Large-scale plane strain bearing capacity tests of shallow foundation on sand. (Part 2) ," 24th Japan National Conference of Geotechnical Engineering, 1989, pp.1243-1246

[2] K. Terzaghi, "Theoretical Soil Mechanics," John Wiley & Sons. Inc., 1963, pp118-134

[3] Vesic, A.S. "Bearing Capacity of Deep Foundations in Sand," Highway Research Record, Vol.39, 1963, pp112-153

[4] E. E. De Beer, "Experimental determination of the shape factors and the bearing capacity factors of sand, Geotechnique, Vol.20, No.4, 1970, pp387-411

[5] Yusuke Tomita et al., "Load Settlement Relationships of Circular Footings Considering Dilatancy Characteristics of Dense Sand ," Journal of Structural and Construction Engineering (Transactions of AIJ), No. 646, 2009, pp.2263-2270

[6] Yusuke Tomita et al., "Load Settlement Relationships of Circular Footings Considering Negative Dilatancy Characteristics of Loose Sand ," Journal of Structural and Construction Engineering (Transactions of AIJ), No. 661, 2011, pp.563-570

[7] Wei Li et al., "Measurement of soil Displacement around Pile Tip by Digital Image Analysis," Geotechnical Engineering in Urban Construction, Proceeding of the Sino-Japanese Symposium on Geotechnical Engineering, Beijing, China, 2003, pp.393-400

[8] Naotoshi Kashiwa et al. "Displacement Amplitude Dependence of Effect of Pile Group by Cyclic Lateral Loading Tests on Large Displacement," Journal of Structural and Construction Engineering (Transactions of AIJ), No. 614, 2007, pp.53-60

[9] Yorihiko Osaki, "Architectural Foundation Structure," gihodobooks, 1991

Thermally Modifying Bentonite for Construction Industry

Abdoullah Namdar, Department of Civil Engineering and Earth Resources, Universiti Malaysia Pahang

ABSTRACT – The application of geology in civil engineering make possibility of ground improvement. This paper involve with the thermally modification of construction material based on changing micro and macro characteristics. The heat could modify the soil shape, size and chemical composite as well as crystal structure. In this research work the bentonite subjected to the heat for 6 hours from 100 ºC to 500 ºC in increment of 100 ºC. The different techniques and methods have been used for changing soil micro and macro characteristics. And also the different technique validated this research investigation and the result has been shown that heat has significant affect on controlling geotechnical engineering problem. And in the final author would like suggest that the there is still more scope for continuing this research work on several natural soil and mineral in applying heat for different time and level for approaching better results.

Keyword: Soil characteristics; natural soil; ground improvement; geotechnical problem; soil atomic structure

1. INTRODUCTION

Clay has always played a major role in human life. Clay raw materials are used and their value recognized in many economic branches, agriculture, civil engineering and environmental studies. This is largely because of their wide ranging properties, high resistance to atmospheric conditions, geochemical purity, and easy access to their deposits near the earth's surface and low price.

Clay minerals, the essential constituents of argillaceous rocks, can be classified in seven groups according, to their crystal structure and crystal chemistry. Clay raw materials are divided in the same way into seven groups. An eighth group covers clay ochres and pigments. Further classification is based on the purpose-made technological application. It gives information on the application of clay raw materials or individual clay minerals: in the production of foods, feedstuffs, beverages, paper, rubber, plastics, artificial leather, protective coatings for interior and exterior use, pharmaceutics, cosmetics, paints, pencils, pastels, porcelain, etc [1]. There are many tests have been performed on bentonite for simulating compaction and densities. It is heated on one end while hydration with deionised water takes place by the opposite end to simulate the thermal gradient created by the heat generated by the radionuclide decay and the hydraulic gradient generated by the groundwater coming from the host rock into the bentonite barrier [2-3]. It has been considered the engineering behavior of bentonite enhanced sand (BES) mixtures in relation to their performance as environmental barriers. Data on the swelling and hydraulic conductivity are presented. At low effective stresses the bentonite within BES mixtures swells sufficiently to separate the sand particles. In such states two factors affect the void ratio reached by the bentonite after swelling: the ionic concentration of the pore solution and the bentonite fabric after compaction. Bentonite swelling is very sensitive to the pore solution concentration because increasing concentration suppresses the diffuse double layer component of swelling. Remoulding during compaction can result in a slight reduction in bentonite swelling, probably because of disruption to the cluster-based fabric of bentonite. At high effective stresses the bentonite has insufficient swelling capacity to force the sand particles apart, and the sand pore volume thus limits swelling [4]. Bentonite enhanced sand (BES) mixtures are widely used as barriers to control the movement of liquid from waste disposal facilities because BES can combine relatively high strength and low compressibility with very low hydraulic conductivity. This is achieved by using a mixture that contains sufficient sand to ensure the stability of the compacted mixture and enough bentonite to seal the voids between the sand particles. Other benefits are that compacted BES containing modest amounts of bentonite is fairly resistant to the effects of desiccation, and the bentonite in BES has a high chemical buffering capacity [5-6].

It has been reported on GMZ bentonite as a potential material for the construction of engineered barrier in the Chinese program of geological nuclear waste disposal, for its high montmorillonite content, high cation exchange capacity (CEC) and large specific surface etc. Studies on mineralogy and chemical composition, mechanical properties, hydraulic behavior, swelling behavior, thermal conductivity, microstructure and volume change behavior of GMZ bentonite were performed from 1980s. Based on a review of the former studies, achievements on experimental and theoretic results obtained on compacted GMZ bentonite specimens including basic properties, thermal, hydraulic and mechanical behaviors are presented. Results show the thermal conductivity of GMZ bentonite and the bentonite based mixtures influenced by its dry density, water content, mixture of other materials and degree of saturation etc. Water retention capacity of highly compacted GMZ bentonite decreases as the temperature increases under confined and unconfined conditions. The hysteretic behavior in the water retention curves of the compacted GMZ bentonite is not so significant at 20 or 40 °C. The unsaturated hydraulic conductivity of compacted GMZ bentonite under unconfined conditions is higher than that of under confined conditions. This is possibly induced by the difference in the mechanism of micro-structural changes during hydration under different confining conditions. The compaction curves for GMZ bentonite with different dry densities are clearly step phased. And the optimum water content for GMZ bentonite is about 15%. An exponential relationship between swelling pressure and dry density of highly compacted GMZ bentonite was determined for the prediction of swelling pressure. Furthermore, the void ratio after swelling for unconfined sample also can be predicted using diffuse double layer (DDL) theory [7]. Conceptually the design of high-level radioactive waste (HLW) repositories in deep geological media includes the construction of an engineered barrier around the waste containers constituted by a buffer backfill material [8].

The purpose of the entire this research exercise would be (i) identification under heat bentonite morphology and mechanical properties (ii) and modify bentonite characteristic for innovation of new material could be use for mitigation of geotechnical and geo-environment problems.

2. METHODOLOGY AND EXPERIMENTS

To innovation a new construction material for solving geotechnical and geo-environment problems an investigation on thermally treated bentonite has been executed. The bentonite has been submitted to the heat for 6 hours from 100 ºC to 500 ºC in increment of 100 ºC. The main research attempt was to modifying construction material under laboratory condition. The evaluation of both for the macro and micro of bentonite characteristics based on new research work and previous investigation have been taken systematically trough of laboratory testing. And in the laboratory triaxial, XRF and SEM tests have been conducted.

3. RESULTS AND DISCUSSION

The heat has been affected on soil mechanical behavior based on soil crystal structure and chemical composite and had significant affect on soil mechanical properties in macro and micro scale. In this investigation has been observed that the heat strongly changed soil mechanical properties. From the previous investigation in the table 1 is indicated unit weight, optimum moisture content and natural moisture content of bentonite.

Table. 1 the bentonite mechanical properties [9]

Heat ºC	γ kN/m^3)	OMC (%)	NMC (%)
RT	12.1	42.4	13.43
100	12.2	42.5	9.46
200	12.3	42.77	8.9
300	12.1	42.3	5.3
400	11.6	39.2	2.53
500	11.5	38.8	2.33

Table. 2 the bentonite mechanical properties

Heat ºC	γ (KN/m^3)	C (KN/m^2)	Φ [◦]
RT	12.1	38	0
100	12.2	48	0
200	12.3	56	5
300	12.1	70	10
400	11.6	84	3
500	11.5	98	12

From this research work some other mechanical properties of bentonite has been mentioned in the table 2. The heat is playing in reducing bentonite unit weight and the interesting issue is the bentonite cohesive characteristic is increased linearly and from other hand the internal angle of friction is changing nonlinearly. In overall it is find that the bentonite with new characteristic is with less weight and more bearing capacity. The changing bentonite crystal structure due to heat resulted in improved permeability. It could be suggested that for increasing waterproof of soil foundation thermally treated bentonite could be acceptable material. The soil mechanics experiment result has been shown that the best safe bearing capacity appeared when soil is subjected to 500 ºC heat, and the decreasing unit weight in this level has not affected on final result compare to when bentonite is under less heat level. In the room temperature bentonite has 700.06 kN/m^2 safe bearing capacity, when it is submitted to the heat for 500 ºC has been improved up to 3132.90 kN/m^2, it was understood that the application of heat on soils could helps in modification of construction material for improving earth structure stability and impermeability, and also could used in other industry. The fig 1 is stress-strain relationship of bentonite from triaxial test and the fig 2 is [9] also stress-strain relationship of bentonite from compression tests when subjected to different level of heat. The results of both methods are almost close to each other. When the heat is increased the stress-strain relationship increased but not linear and always increasing of heat not resulted in improving soil bearing capacity in this regard could bring example of bentonite is submitted to the 400 ºC. This investigation was for applying heat on the bentonite up to 500 ºC and has also been limited for 6 hours. For the future investigation could be extend the heat time and level in applying on bentonite, or other material for approaching better or optimizing result. For evaluation of changing bentonite mechanical properties subjected to the heat the chemical element and the morphology of the bentonite have also been investigated.

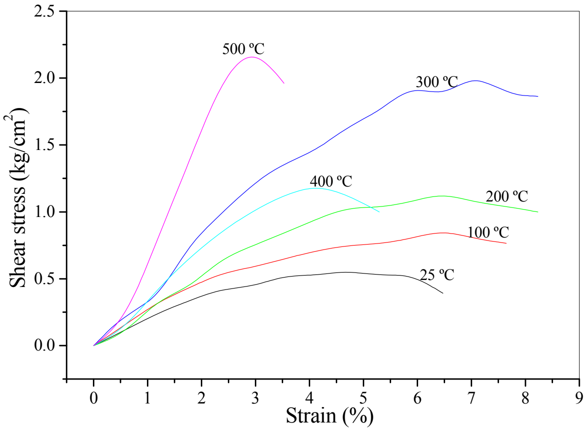

Fig 1 shear stress Vs strain in bentonite clay

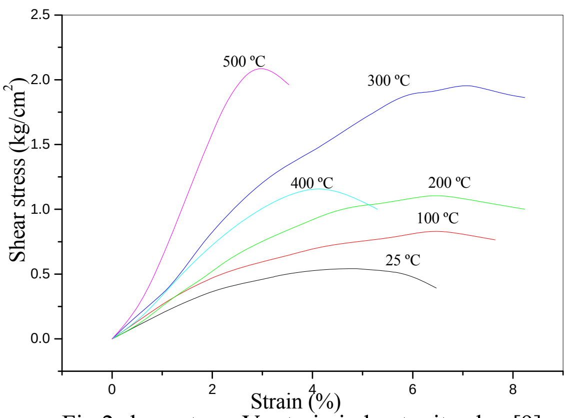

Fig 2 shear stress Vs strain in bentonite clay [9]

Table. 3 Chemical element of the bentonite in different level of heat

Heat ºC		O	Mg	Al	Si	C	K	Ti	V	Fe
25	Wt %	40.71	0.89	8.42	26.97	1.12	1.90	2.68	0.48	16.84
	At %	59.18	0.85	7.25	22.33	0.73	1.13	1.30	0.22	7.01
100	Wt %	40.91	-	8.34	26.79	1.09	1.95	2.97	-	17.95
	At %	59.68	-	7.22	22.27	0.71	1.16	1.45	-	7.50
200	Wt %	43.09	-	8.57	27.26	1.14	2.11	2.82	-	15.01
	At %	61.27	-	7.23	22.09	0.73	1.22	1.34	-	6.12
300	Wt %	36.29	-	8.05	28.17	0.82	1.95	3.03	-	21.69
	At %	55.41	-	7.28	24.50	0.56	1.22	1.54	-	9.49
400	Wt %	40.06	-	8.44	27.98	0.93	1.73	2.50	-	18.36
	At %	58.72	-	7.33	23.36	0.62	1.04	1.22	-	7.71
500	Wt %	39.65	-	9.21	27.67	0.50	1.91	2.27	-	18.79
	At %	58.29	-	8.03	23.17	0.33	1.15	1.11	-	7.91

The table 3 indicated the chemical composite of the bentonite subjected to the heat from 100 ºC to 500 ºC in increment of 100 ºC, and the XRF chemical analysis experiment has been indicated that the Mg and V of the bentonite have been disappeared after applying 100 ºC heat, and the from other hand the remaining elements which are O, Al, C, K, Ti, Si, Fe showing different level in changing heat level, and could be understand that the chemical elements are not responsible for changing soil mechanical properties.

The SEM photographs have clearly revealed that the surface morphology, shape and size of the minerals (figs 3-8). The bentonite under heat for 6 hours from 100 ºC to 500 ºC in increment of 100 ºC selected to study its morphology modification, the result shown that under all conditions results are closely similar (fig 3-8) and also same result is observed about soil chemical composite from the XRF experiment (table 3) it could be expected that the soil crystal structure is main reason in modification of soil mechanical properties. It is observed different color of bentonite at any level of heat is applied. The changing bentonite color during increasing heat is due to modification of crystal structure of bentonite.

It is to be noted that innovation of the better construction material is possible by application of the heat on bentonite. It is interesting to be mention that in the bentonite submitted to the heat for 500 ºC after return to room temperature when mixed with the water to carry out of compaction test the small hydration has been observed. It is due to developed new bentonite characteristic based on changing crystal structure. The modification of crystal structure was responsible for improving bentonite mechanical properties.

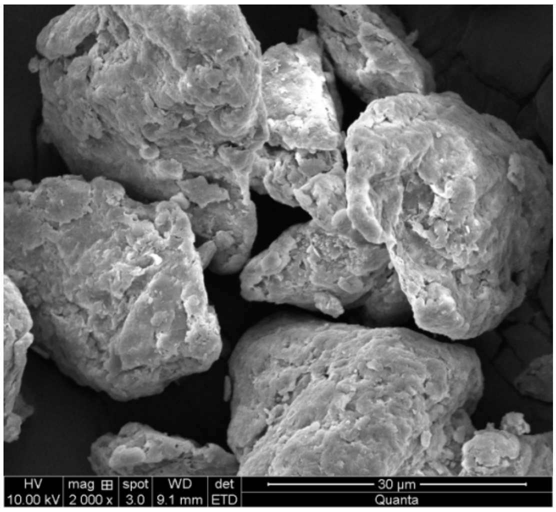

fig. 3 SEM Photo of bentonite at 25 ºC

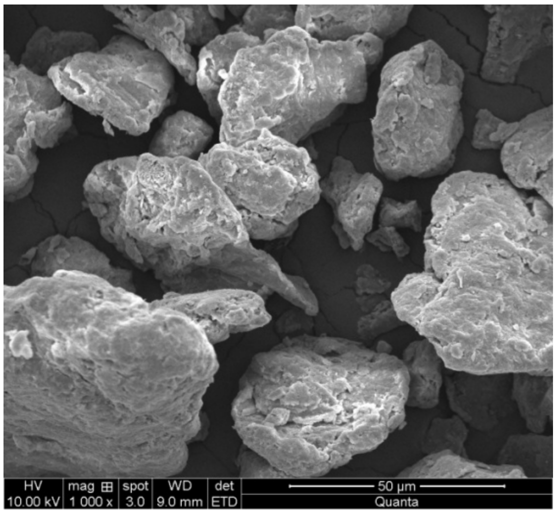

Fig. 4 SEM Photo of bentonite processed under 100 ºC for six hours

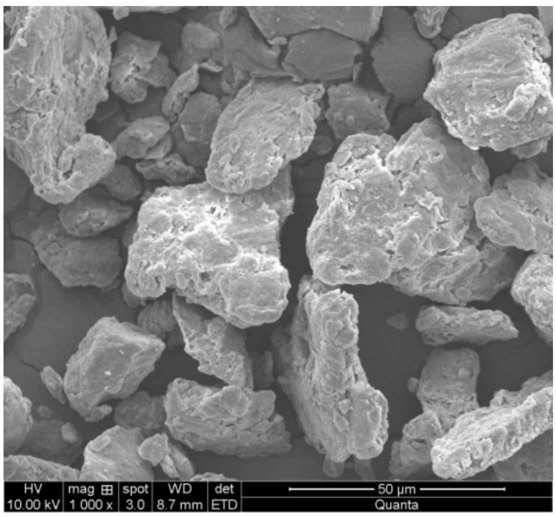

Fig. 5 SEM Photo of bentonite processed under 200 ºC for six hours

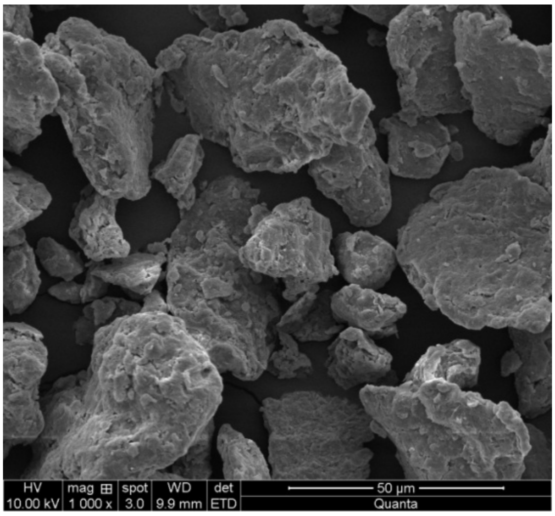

Fig. 6 SEM Photo of bentonite processed under 300 ºC for six hours

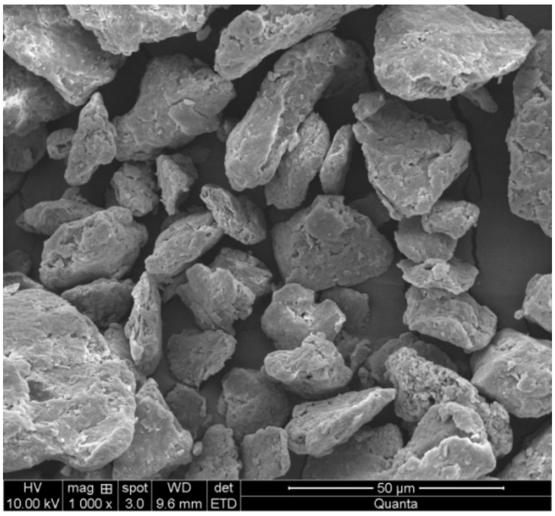

Fig. 7 SEM Photo of bentonite processed under 400 ºC for six hours

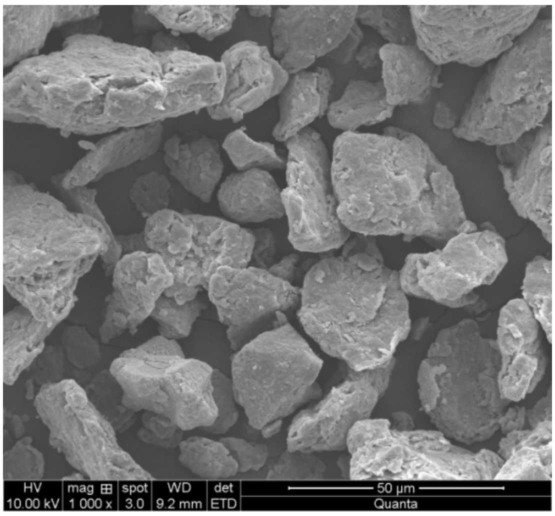

Fig. 8 SEM Photo of bentonite processed under 500 ºC for six hours

4. CONCLUSION

- The validation of the results have been proved by comparing different results
- The bentonite crystal structure was responsible for soil mechanical properties modification
- It could be suggested this method can apply for improving construction material characteristic.
- There is different material could be investigated in applying heat for different time and level for approaching better results

5. ACKNOWLEDGEMENTS

The author would like to express his thanks to faculty of civil engineering, SJCE, Mysore, India, and faculty of earth science of University of Mysore, India for timely guidance.

6. REFERENCES

[1]. Ji i Konta, Clay and man: clay raw materials in the service of man , Applied Clay Science, 10, (4), (1995), pp 275-335.
[2]. Martín, M., Cuevas, J., Leguey, S., 2000. Diffusion of soluble salts under a temperature gradient after the hydration of compacted bentonite. Applied Clay Science 17, 55–70.
[3]. Villar, M.V., Sánchez, M., Gens, A., 2008b. Behaviour of a bentonite barrier in the laboratory: experimental results up to 8 years and numerical simulation. Physics and Chemistry of the Earth 33 (Supplement 1), S476–S485.
[4]. D.I. Stewart, P.G. Studdsb, T.W. Cousens, The factors controlling the engineering properties of bentonite-enhanced sand, Applied Clay Science 23 (2003) 97 – 110.
[5]. Tay, Y.Y., Stewart, D.I., Cousens, T.W., 2001. Shrinkage and desiccation cracking in bentonite – sand landfill liners. Engineering Geology 60, 263 – 274.
[6]. Yong, R.N., 1999a. Soil suction and soil – water potentials in swelling clays in engineered clay barriers. Engineering Geology 54, 3 – 13.
[7]. Wei-Min Ye, Advances on the knowledge of the buffer/backfill properties of heavily-compacted GMZ bentonite, Engineering Geology 116 (2010) 12-20.
[8]. Villar, M.V., Lloret, A. 2008. Influence of dry density and water content on the swelling of a compacted bentonite. Applied Clay Science 39, 38–49.
[9]. Abdoullah Namdar, et al (2011), Bentonite Thermal Behavior in Geotechnical Engineering, Annals of faculty engineering Hunedoara, International Journal Of Engineering, Tome IX, Fascicule 1

7. NOMENCLATURE

Φ (Degree)	= Angle of Friction
C (KN/m^2)	= Cohesive of Soil
OMC (%)	= Optimum Moisture Content
SBC (KN/m^2)	= Safe Bearing Capacity
γ (KN/m^3)	= Unit Weight
NMC (%)	= Natural Moisture Content

First International Conference on Geotechnique, Construction Materials and Environment, Mie, Japan, Nov.21-23, 2011, ISBN: 978-4-9905958-0-7 C3051

Mesh-Free Analysis of Beam on Elastic Foundation

S. M. Binesh, Department of Civil and Environmental Engineering, Shiraz University of Technology, Shiraz, Iran

ABSTRACT: The concept of beam on elastic foundation has been extensively used by geotechnical engineers for foundation design and analysis. However most of the studies on the analysis of beam on elastic foundation are devoted to the mesh based methods. In this paper a mesh-free method is implemented for the analysis of beam on two parameter elastic foundation. The geometry of the problem is modeled by nodes and the displacement field is constructed by radial basis functions. The final system of equations is derived by the substitution of the displacement field into the weak form of the governing equation. The elastic foundation is simulated by the concept of linkage element and there is no need of node or element in the traditional sense. At the end of the paper the results of analysis with the mesh-free method are compared with the results of the finite element analysis.

Keywords: Mesh-Free, Beam, Elastic Foundation

1. INTRODUCTION

There are many geotechnical engineering problems that can be idealized as beams on elastic foundations. This kind of modelling helps to understand the soil-structure interaction phenomenon and predict the contact pressure distribution and deformation within the medium. The most common theory for the beam on elastic foundation modelling is the Winkler approach [1]. However the modelling of soil using the Winkler's theory was considered inadequate in the handling of various problems. The main weakness lies in the fact that it overlooks the shear interaction between the spring elements. Hence the two-parameter models were proposed some decades ago [2-3]. The numerical solution for these two-parameter models are mainly obtained by mesh based methods such as finite element or finite difference method [4].

In this paper a mesh-free method is implemented for the analysis of beam on two-parameter elastic foundation. In the proposed approach the geometry of the beam is modelled by nodes and the displacement field is constructed by radial basis functions. The two-parameter foundation is simulated by a virtual layer consists of two sets of springs with different stiffness coefficients. At the end of the paper the results of analysis with the mesh-free method are compared with the results of the finite element analysis.

2. MESH-FREE METHODS

A new family of numerical methods is developed to get rid of the deficiencies related to mesh definition. These methods are globally coined as mesh-free or mesh-less methods and their main characteristic is their independency to the traditional mesh definition. There are many mesh-free methods such as smoothed particle hydrodynamics (SPH) [5], element free Galerkin method (EFGM) [6], reproducing kernel particle method (RKPM) [7], etc. In this paper the radial basis point interpolation method (RPIM) is used for the analysis of beam on elastic foundation.

2.1 Enriched RPIM

According to the enriched RPIM A field function u(x) can be approximated using both radial and polynomial basis as

$$u(\mathbf{x}) = \sum_{i}^{n} R_i(\mathbf{x}) a_i + \sum_{j}^{m} P_j(\mathbf{x}) b_j = \mathbf{R}^T(\mathbf{x})\mathbf{a} + \mathbf{P}^T(\mathbf{x})\mathbf{b} \qquad (1)$$

where $\mathbf{R}(\mathbf{x})$ and $\mathbf{P}(\mathbf{x})$ are, respectively, the vector of radial and polynomial basis and n is the number of field nodes in the local support domain for point $\mathbf{x}$. Vectors $\mathbf{a}$ and $\mathbf{b}$ are coefficients for $\mathbf{R}(\mathbf{x})$ and $\mathbf{P}(\mathbf{x})$ respectively .

The coefficient vectors $\mathbf{a}$ and $\mathbf{b}$ are determined by enforcing Eq. (1) to be satisfied at all the n nodes within the local support domain. Hence, Eq. (1) can be written as:

$$u(\mathbf{x}) = \mathbf{\Phi}(\mathbf{x})\mathbf{U}_s \qquad (2)$$

where $\mathbf{U}_s$ is a vector of nodal displacements, and $\mathbf{\Phi}(\mathbf{x})$ contains RPIM shape functions for the n local nodes in the support domain. For details the reader is referred to [8].

3. BEAM ON ELASTIC FOUNDATION MODELING

3.1 Beam Modeling

In the present approach, a beam with any arbitrary thickness can be simulated readily. As shown in Fig. 1 two or more parallel sets of nodes may be used to model the beam structure. Considering the variational (weak) form of the total potential energy functional for the beam, the discrete form of equations in mesh-free approach can be written as

$$\mathbf{K_B U_B} = \mathbf{F_B} \qquad (3)$$

where

$$\mathbf{K_B} = \iint_{\Omega} \mathbf{B_B}^T \mathbf{D_B B_B}\, d\Omega \qquad (4)$$

$$\mathbf{F_B} = \iint_{\Omega} \mathbf{\Phi_B}^T \mathbf{b}\, d\Omega + \int_{\Gamma} \mathbf{\Phi_B}^T \overline{\mathbf{T}}\, d\Gamma \qquad (5)$$

where $\mathbf{\Phi}$ and $\mathbf{B}$ are respectively, the shape functions and the gradient of shape functions matrices, $\mathbf{b}$ is the body force vector, $\mathbf{D}$ is the material matrix, Ω is the problem domain, $\overline{\mathbf{T}}$ is the prescribed surface traction and Γ is the boundary along which the surface traction is imposed. It should be noted that subscript B stands for the beam media.

3.2 Elastic Foundation Modeling

In order to simulate the elastic foundation, the concept of linkage element is used [9]. As shown in Fig. 2 the two-parameter foundation can be considered as a layer with two stiffness coefficients along two orthogonal directions (i.e. K_S and K_n). According to Fig. 2, the relative deformation vector δ at point P between the top and bottom surfaces can be related to the displacements of points A and B. Hence it can be written as

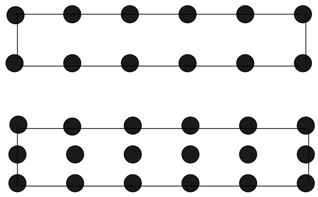

Fig. 1 Mesh-free modeling of beam media

$$\boldsymbol{\delta}=\begin{bmatrix}\delta_S\\ \delta_n\end{bmatrix}=\overline{\boldsymbol{U}}_A-\overline{\boldsymbol{U}}_B=\begin{bmatrix}u_A-u_B\\ v_A-v_B\end{bmatrix} \tag{6}$$

where δ_S and δ_n are respectively, the shear and normal relative displacement at point P. $\overline{\boldsymbol{U}}_A$ and $\overline{\boldsymbol{U}}_B$ are the displacement vectors in the local coordinate n-s at points A and B respectively. However, as the location of point B is fixed, the displacement components of $\overline{\boldsymbol{U}}_B$ (i.e. u_B and v_B) are both zero. Then equation (6) can be re-written as

$$\boldsymbol{\delta}=\begin{bmatrix}\delta_S\\ \delta_n\end{bmatrix}=\overline{\boldsymbol{U}}_A=\begin{bmatrix}u_A\\ v_A\end{bmatrix} \tag{7}$$

where u_A and v_A are respectively, the displacement of point A in the s and n directions.

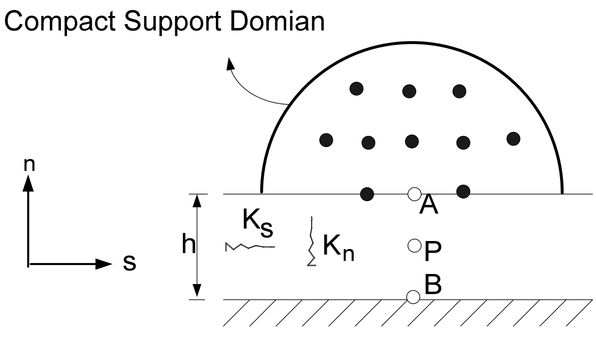

Fig. 2 Foundation modeling by linkage element concept

Considering the relation between local and global coordinate, we have

$$\overline{\boldsymbol{U}}_A=\boldsymbol{L}\boldsymbol{U}_A \tag{8}$$

where $\boldsymbol{L}$ is coordinate transform matrix and $\boldsymbol{U}_A$ is the displacement vector of point A in global coordinate.

As shown in Fig. 2 the field variable (i.e. displacement) at point A can be estimated by its nodal values at the nodes located in the compact support domain of point A. According to Eqs. (2) , (7) and (8) the displacement of point A can be written as

$$\boldsymbol{\delta}=\boldsymbol{B}_f\boldsymbol{U}_{SA} \tag{9}$$

where $\boldsymbol{U}_{SA}$ is the displacement vector composed of displacement at all nodes in the compact support domain of point A and

$$\boldsymbol{B}_f=\boldsymbol{L\Phi} \tag{10}$$

Neglecting the normal strain component in the s direction, the strain vector in the local coordinate can be defined as

$$\boldsymbol{\varepsilon}=\frac{1}{h}\boldsymbol{\delta} \tag{11}$$

where h is the virtual thickness assumed for the foundation layer and $\boldsymbol{\varepsilon}=\begin{bmatrix}\gamma_{ns} & \varepsilon_n\end{bmatrix}^T$, in which ε_n is the normal strain in the n direction, and γ_{ns} is the shear strain. By substituting Eq. (11) into Eq. (9) the relation between strain and nodal displacement can be obtained as

$$\boldsymbol{\varepsilon}=\frac{1}{h}\boldsymbol{B}_f\boldsymbol{U}_{SA} \tag{12}$$

To evaluate the stiffness matrix related to the elastic foundation, the relation between stress and strain in this region is also needed. According to Fig. 2 the relation between stress vector and relative deformation can be written as

$$\boldsymbol{\sigma}=\boldsymbol{D}_f\boldsymbol{\delta} \tag{13}$$

where the stress vector $\boldsymbol{\sigma}$ consists of the normal stress σ_n and the tangential stress τ in the foundation region.

$$\boldsymbol{\sigma}=\begin{bmatrix}\tau & \sigma_n\end{bmatrix}^T \tag{14}$$

Matrix $\boldsymbol{D}_f$ can also be defined as

$$\boldsymbol{D}_f=\begin{bmatrix}K_S & 0\\ 0 & K_n\end{bmatrix} \tag{15}$$

Substituting (11) into (12) gives

$$\boldsymbol{\sigma}=\frac{1}{h}\boldsymbol{D}_f\boldsymbol{\varepsilon} \tag{16}$$

Using the variational principle the stiffness matrix of elastic foundation can be written as

$$\boldsymbol{K}_{\mathrm{f}}=\int_A\left(\frac{1}{\mathrm{h}}\boldsymbol{B}_f\right)\left(h\boldsymbol{D}_f\right)\left(\frac{1}{h}\boldsymbol{B}_f\right)dA \tag{17}$$

Assuming constant virtual thickness for foundation layer, Eq. (17) can be written as

$$\boldsymbol{K}_{\mathrm{f}}=\int_\beta\boldsymbol{B}_f\boldsymbol{D}_f\boldsymbol{B}_f\,d\beta \tag{18}$$

where β is the length parameter along the foundation layer. The final matrix form of equations for the whole system of beam on elastic foundation can be written as

$$[\boldsymbol{K}_B + \boldsymbol{K}_f]\boldsymbol{U} = \boldsymbol{F} \tag{19}$$

where $\boldsymbol{U}$ and $\boldsymbol{F}$ are nodal displacement and nodal force respectively.

4. NUMERICAL STUDY

A typical example is investigated to verify the efficiency of proposed method in this paper. As shown in Fig. 3, a beam with 10 m length and 1 m thickness is assumed. The elastic modulus and Poisson ratio of the beam material are 2 GPa and 0.25 respectively. The normal and shear stiffness modulus are respectively, 15000 and 10000 kN/m^3. Plane strain condition is assumed. Two 500 kN concentrated loads are exerted in a symmetric manner at 2 m distance from each end.

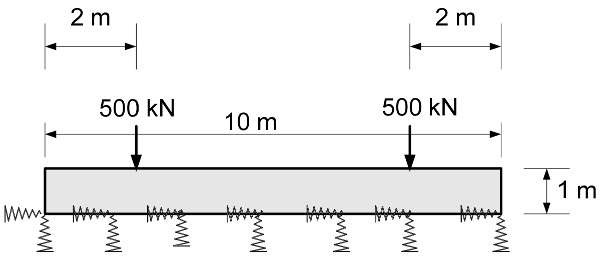

Fig. 3 Typical problem of beam on two parameter elastic foundation

The problem is solved by the finite element program SIGMAW as well as the proposed mesh-free method. The finite element modelling consists of two models; 10 elements model and 40 elements model (Fig. 4). It is obvious that by increasing the number of elements the accuracy of results will also increase. Hence this can be a measure to investigate the accuracy of proposed mesh-free method. As it is depicted in Fig. 5 the mesh-free model is constructed by the same number of nodes as the 10 elements finite element model. The results of analyses are shown for the upper and lower surfaces of the beam in Figs. 6 and 7. Due to the symmetry of the model only the results for one half of the beam are demonstrated. As it is obvious from the figures, the proposed mesh-free method offers acceptable results that are even more accurate than the results of finite element analysis with the same order of nodes.

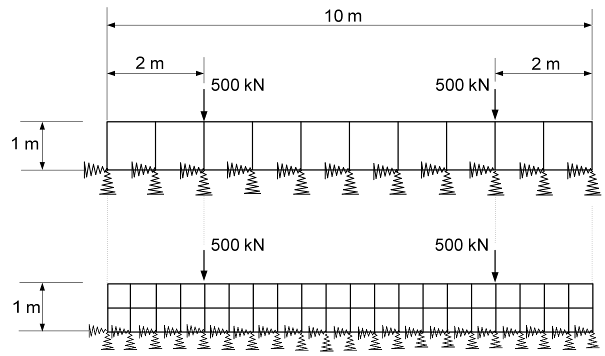

Fig. 4 Finite element models of beam on two parameter elastic foundation using 10 and 40 elements

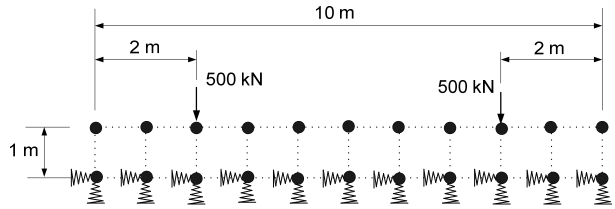

Fig. 5 Mesh-free model for the beam on two parameter elastic foundation

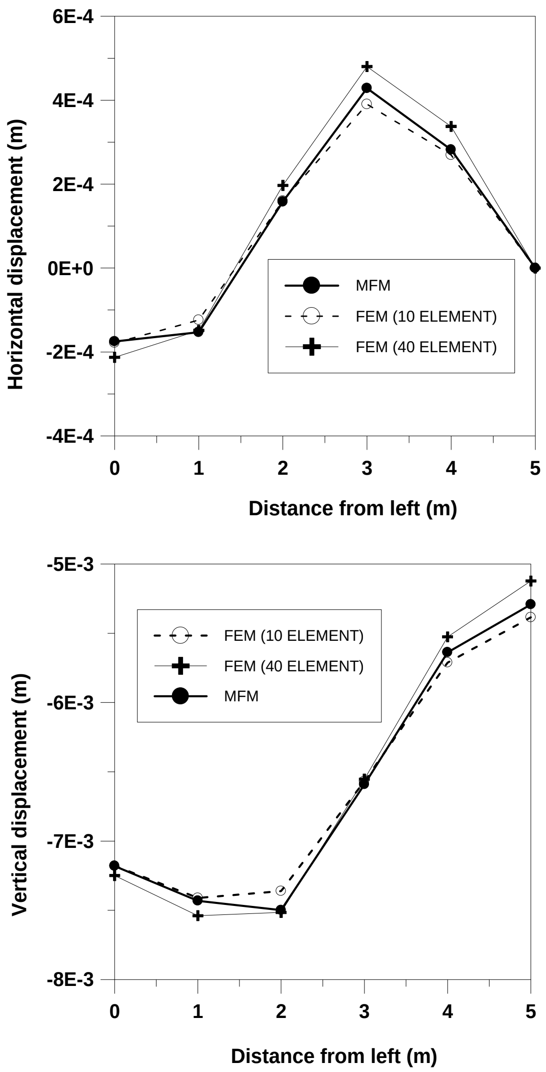

Fig. 6 Horizontal and vertical displacement of the nodes located at the lower edge of the beam

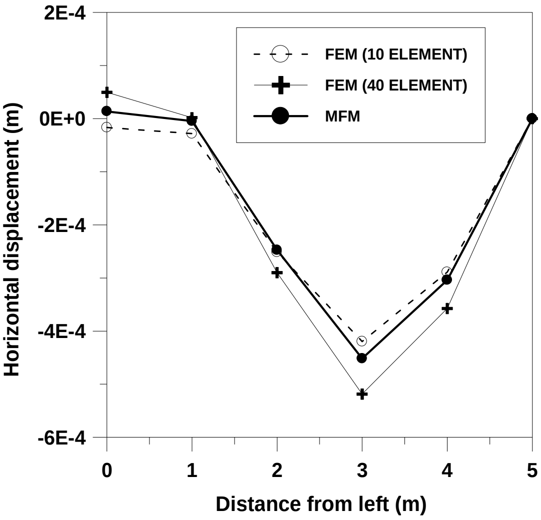

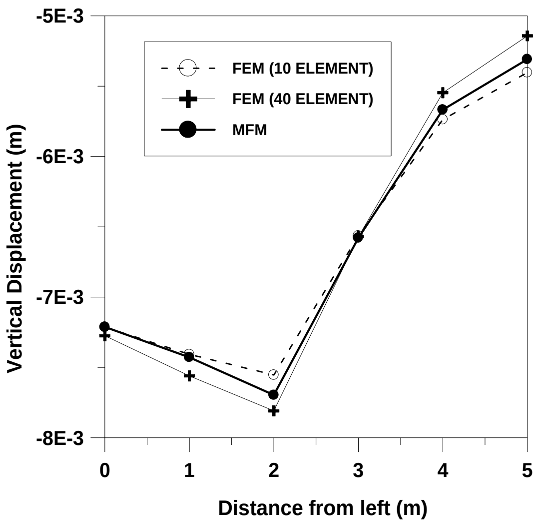

Fig. 7 Horizontal and vertical displacement of the nodes located at the upper edge of the beam

5. CONCLUSION

A mesh-free procedure is implemented for the analysis of beam on two parameter elastic foundation. The elastic foundation is simulated by the linkage element concept and there is no need of node or element in the traditional sense. The thickness of the beam can be readily adjusted and the nodes can be added or omitted easily. Besides all these benefits, the accuracy of results is also acceptable and they are even better than the finite element results with the same order of nodes.

6. REFERENCES

[1] Winkler E., in: Die Lehre von der Elastizitat und Festigkeit, Domonicus, Prague, 1867

[2] Pasternak P.L., "On a new method of analysis of an elastic foundation by means of two foundations constants", (in Russian), Gasudarstvennoe Izdatelstvo Literaturi po Stroitelstvui Arkhitekture, Moscow, USSR, 1954.

[3] Pronk A.C., "The Pasternak foundation- An attractive alternative for the Winkler foundation", Proc. of the 5th Int. Conf. on concrete pavement design and rehabilitation, Purdue Univ. West Lafayette, Indiana, 1993, Vol. 1.

[4] Bowles J.E., Foundation analysis and design, 5th edition, The McGraw-Hill Companies, Inc., 1996, Ch. 9.

[5] Libersky L.D., Petschek A.G., "Smoothed particle hydrodynamics with strength of materials", Proc. of The Next Free Lagrange Conf., 1991, PP. 248-257.

[6] Belytschko T., Lu Y.Y., Gu L., "Element-free Galerkin methods", International Journal for Numerical Methods in Engineering, 1994, Vol.37, PP.229-256.

[7] Liu W.K., Jun S., Zhang Y.F., "Reproducing kernel particle methods", International Journal for Numerical Methods in Fluids, 1995, Vol.20, PP.1081-1106.

[8] Liu, G.R., Meshfree Methods: Moving Beyond the Finite Element Method, CRC Press, Boca, 2003, Ch. 8.

[9] Herrmann L.R., "Finite element analysis of contact problems", ASCE, Journal of Engineering Mechanics Division, 1978, Vol. 104, No. 5, PP. 1043-1057

First International Conference on Geotechnique, Construction Materials and Environment, Mie, Japan, Nov.21-23, 2011, ISBN: 978-4-9905958-0-7 C3051

Frictional Performance of Infilled I-Blocks with Geosynthetic Inclusions

Faisal Hj Ali, Department of Civil Engineering, National Defense University of Malaysia

Md. Zahidul Islam Bhuiyan*, Department of Civil Engineering, University of Malaya

Firas A. Salman, Department of Civil Engineering, University of Malaya

Siau Lian Sang, Managing Director, Soil & Slope Sdn. Bhd.

ABSTRACT: Geosynthetic reinforced segmental retaining walls (GR-SRWs) are in a period of development and have achieved popularity all over the world. Inclusion of geosynthetic layer at the interface has great influence on interface frictional performance of segmental retaining wall units. In this investigation, three (3) types of geosynthetic reinforcements were chosen and used to find out their influences on the interface shear capacity of newly designed and locally produced precast I-blocks. A series of direct shear tests were conducted using a specially designed and fabricated direct shear apparatus to assess the frictional characteristics of the blocks with geosynthetic inclusions. The results presented in this paper report that flexible geosynthetic reinforcements perform well than stiff geosynthetics although decrease the interface shear capacity than no inclusion condition. The presence of geosynthetic layers also minimizes the localized stress concentrations at the interface.

Keywords: *geosynthetics; interface shear; segmental block; retaining wall; reinforced soil*

1. INTRODUCTION

Segmental concrete units (segmental retaining wall units) as the facing element for geosynthetic MSE (mechanically stabilized earth) walls have been frequently used worldwide for about three (3) decades [1]. They have achieved popularity due to many advantages in the fields of geotechnical engineering. In Malaysia, geotechnical engineers have been widely exercising geosynthetic reinforced segmental retaining walls (GR-SRWs) for last decades [2].

Facing stability is an important issue in the current design guidelines [3], [4] and it is related to shear and connection failures. Past research works [5], [6] reported that facing instability basically occurs due to poor connection strength and inadequate connection systems.

In GR-SRW constructions, polymer reinforcements are used to stabilize the backfill soils and facing columns. The presence of geosynthetic layers at the interface might increase or decrease the interface shear capacity of segmental concrete units [1], [7]. It depends on the flexibility of geosynthetic reinforcements as well as block's geometry.

In this investigation, three (3) types of geosynthetic reinforcements were chosen: a knitted polyester (PET) geogrid (flexible), a high density polyethylene (HDPE) geogrid (stiff), and a non-woven polyester geotextile (flexible) those which are mostly used in Malaysia for GR-SRW constructions. Plastic shear pins and natural coarse aggregate (NCA) were used to increase the interface shear capacity of the facing systems "to be published" [8]-[9]. A series of direct shear tests were executed under various normal loading conditions [3], [10]. Test results were presented in the form of shear stress-displacement relationship to compare the effect of different types of polymer reinforcements at interface. Shear capacity envelopes were also drawn using Mohr-Coulomb failure criteria to outline the angle of friction for different inclusions.

2. MATERIALS

2.1 Segmental concrete unit

"I" blocks were used as segmental concrete units in this research. "I" blocks are wet cast concrete units (G30), which have one center web and the tail/rear flange is extended beyond the web (Fig. 1). The rear flange is tapered that allows the blocks to form curve walls. The maximum tapered angle of the "I" block is 11.3 deg. "I" blocks are double open-ended units and provide a larger hexagonal hollow space in conjunction with two units, and the equivalent hole dimensions are about 450 mm in length, 280 mm in width and 300 mm in height. The infill weigh is approximately 93 to 94 kg with the aggregate of bulk density of 1527 kg/m^3.The physical and mechanical properties of the used blocks are outlined in Table 1.

2.2 Granular infill

The hollow cores between the blocks were infilled with 100% crushed limestone aggregate and lightly compacted. The maximum and nominal maximum sizes of the aggregate were 25 and 19 mm respectively. The particle size distribution of the granular infill meets ASTM standard size #57 gradations [11]. The physical properties of infill are given in Table 2.

2.3 Plastic pin

Ultrahigh molecular weight polyethylene (UHMWPE) plastic bars were used in this investigation as flexible connectors because of their toughness and flexibility. UHMWPE has also highest impact strength. The physical and mechanical properties of the plastic bars are given in Table 3.

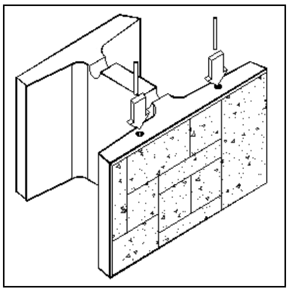

Fig. 1 Schematic of used "I" block

Table 1 Physical and mechanical properties of segmental concrete unit

Property		Value
Dimensions (WxHxL)* in mm		370x300x500
Weight (kg)		41-42
Oven dry density (g/cm^3)		2.17
Water absorption capacity	%	7.1
	g/cm^3	0.16
Moisture content (%)		3.7
Net compressive strength (MPa)		8.0

* W = Width (Toe to heel), H= Height, L= Length (Parallel to the wall face)

Table 2 Physical properties of granular infill

Property	Value
Bulk density (g/cm^3)	1.53
Specific gravity (SSD)	2.63
Void content (%)	42
Coefficient of gradation, Cc	1.15
Fineness Modulus (FM)	7.16

Table 3 Physical and mechanical properties of plastic bar

Property	Value
Yield strength at 23°C (MPa)	22
Modulus of elasticity (MPa)	750
Elongation at break (%)	>300
Notched impact strength (kJ/m^2)	No break
Density (g/cm^3)	0.94
Cross section area (mm^2)	127.66

Table 4 Physical and mechanical properties of inclusions

Property		GX80/30	E'Grid 90R	Rock PEC75
Short term tensile strength T_c (KN/m)	MD	80.0	90.0	75.0
	CD	30.0	-	14.0
MD Tensile strength (KN/m)	5% strain	34.0	45.2	33.8
Strain at MD tensile strength (%)		11.0	11.5	10.0
Weight (Kg/m^2)		0.32	0.55	0.34
Aperture size (mm)	MD	23	240	-
	CD	21	16	
Thickness (mm)	Bond thickness (T_b)	1.40	4.1	2.2
	Rib thickness (T_r)		1.1	

Note: MD = machine direction; CD = Cross-machine direction. Unless noted otherwise, data are from manufacturers' literature.

2.4 Geosynthetic reinforcements

Three (3) different types of geosynthetic reinforcements were used in this study because of their high strength and low creep. Details of the reinforcements are referred as below:

Miragrid GX 80/30 is a knitted uniaxial geogrid prepared from high tenacity polyester yarns, and covered with a black polymeric coating. The major characteristics are good connection capacity with modular blocks and excellent interface friction behavior, and high tensile strength at low creep.

E'Grid 90R is an extruded uniaxial geogrid with elongated apertures. It is made of high density polyethylene (HDPE). The principal characteristics are good gripping capacity with the shear connectors of the modular block units and good creep performance with low strain, and high tensile strength under constant load.

Rock PEC 75 is a non woven needle punched composite geotextile consisting of combination between high tenacity polyester yarns stitched to polypropylene continuous filaments. It provides high tensile strength at low elongation and high water flow capacity in its plane.

Typical application areas of the geosynthetics (Fig. 2) are reinforcement of modular block walls, earth walls, slopes and bridge abutments. Table 4 summaries the physical and mechanical properties of the used geosynthetic reinforcements.

Fig. 2 Photographs of GX80/30, E'Grid 90R, and Rock PEC75 (left to right)

3. TEST METHODOLOGY

3.1 Experimental device

A specially designed and modified large-scale apparatus was used to carry out the shear tests of the "I" blocks. A photograph of the modified test apparatus is illustrated in Fig. 3. It mainly consists of loading frame, hydraulic actuators, and a fabricated electric hydraulic pump. The vertical actuator was mounted with the loading frame using steel rollers to allow block movement during the shear test but in ASTM test protocol the vertical actuator was kept fixing [12]. The vertical and horizontal actuators were capable of applying around 45 tons of surcharge load and 130 tons of push/pull out force respectively and simultaneously. The electric hydraulic pump was connected to the actuators with pressure hoses.

A geosynthetic loading clamp was set with horizontal actuator to apply the tensile load as well as shear load. To hold the geosynthetic layer at back of the blocks, a geosynthetic gripping clamp was mounted for interface shear tests. Two (2) pressure transducers were installed over each hydraulic actuator of 150 mm stroke, and the actuators were calibrated by using load cell against the pressure transducers. Two (2) flow regulators were attached with the pump to control the rate of displacement of horizontal (shear) and vertical actuators.

The shear displacements were measured using of two 50 mm linear variable displacement transducers (LVDTs) with an accuracy of 0.001mm. Pressure transducers and LVDTs reading were continuously measured and recorded during the test by a data logger. The data were recorded at every 10 second interval.

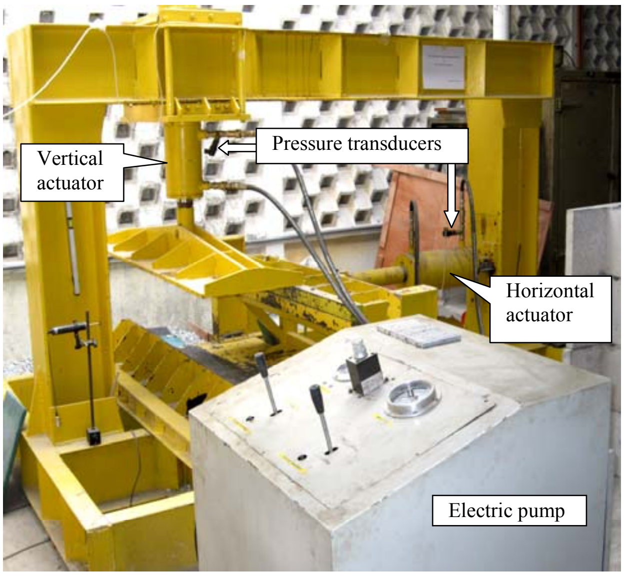

Fig. 3 Photograph of test apparatus

3.2 Interface Shear Tests

Two (2) courses of modular block units were used for interface shear tests. The bottom course consisting of two (2) "I" blocks was installed and braced laterally at the front of loading frame and the hollow space between the blocks was filled up with fresh aggregate, and lightly compacted using a steel rod. Due to tapered rear flange, a small steel plate was used at the back of the bottom course to hold the compacted aggregate. One end of the geosynthetic sample was placed over the bottom course and connected with the plastic shear pins, and then the other end of geosynthetic was gripped to the steel clamp for preventing the slippage of the reinforcement layer during the shear tests. A single "I" block was placed centrally over the running joint formed by the two underlying units to simulate the staggered construction procedure used in the field. The double open-ended space of the top block was filled up with aggregate and two (2) steel plates were used to hold the infilled aggregate of the top block. A photograph of interface shear test arrangement is shown in Fig. 4.

Normal load was imposed only over the top block through stiff rubber mat and simulated an equivalent height of the stacked blocks. The shear load was applied against the top block at a constant rate of 1 mm/min [10]. A steel plate with stiff rubber mat was used with geosynthetic loading clamp to concentrate the shearing load only over the centrally installed top block. A horizontal seating load was applied to the top block to ensure close fitting of the blocks, and after that the load and displacement devices were set to zero. The imposed seating load was 10% of maximum shear strength.
Mohr-Coulomb failure criteria were used to find out interface shear capacity at ultimate strength criterion.

$$V = N \tan\lambda + \alpha. \quad (1)$$

Where:
V = Interface shear capacity (kPa)
N = Normal stress (kPa)
λ = Angle of friction (deg.)
α = V interception (apparent cohesion)

Fig. 4 Photograph of interface shear test showing geotextile sample and gripping system

4. Results and discussion

Fig. 5 and 6 illustrate the typical curves for blocks with geosynthetic inclusions under different normal stresses. From the Figs. 5 and 6, it is also seen that the ultimate shear stresses of the infilled blocks without any geosynthetic inclusion is higher than inclusion conditions.

Among the three (3) types of inclusions, polyester geogrid (flexible) perform well than other types of geosynthetics. This is happened due to its cushion effects, which minimizes the stress concentration at interface and it also allows the aggregate interlocking through the apertures because of its grid structures. Figs 5 and 6 demonstrate that the shear stress behavior of the blocks with HDPE geogrid and polyester geotextile inclusion is quite same for both normal stresses (54 &124 kPa). Even at high normal stress the frictional performance of the blocks with HDPE geogrid inclusion is almost equal to those with polyester geotextile (Fig. 6). Due to the physical structure i.e. thickness and grid structure of HDPE geogrid, blocks can easily move over each others. HDPE geogrid works like a friction reducing layer for its grids, which are stiff and smooth. Its aperture systems also do not give better interlocking mechanism among the aggregates. On the other hand, although, the polyester geotextile provide better cushion at the block's interface but actually it interrupts the aggregates interlocking mechanism fully that reduces the frictional capacity of the blocks with geotextile inclusion.

Fig. 6 shows that the ultimate shear stress of the blocks with polyester geogrid inclusion is almost equal to those without inclusions. At high normal stress, the shear stress drop of the blocks with HDPE geogrid and polyester geotextile is more than those with polyester geogrid at low normal stress (Fig. 5).

Plots of the ultimate interface shear stress against the applied normal stress are presented in Fig. 7. It is seen that, the presence of geosynthetic inclusions reduces the ultimate interface shear capacity of the blocks. Bathurst and Simac [1], and Bathurst et al. [7] observed the same behaviors for different types of blocks with polyester geogrid inclusion. The ultimate interface shear capacity of the blocks with polyester geogrid inclusion is closer to no-inclusion condition because this flexible inclusion improves shear transfer across the block's interface than others. Fig. 7 also reports that the reduction in ultimate shear capacity for the inclusions of HDPE geogrid and polyester geotextile is higher than polyester geogrid inclusion. It is influenced by the physical structures of the used geosynthetics i.e. flexibility and grid patterns.

Table 7 summarizes performance parameters of the tested "I" block with and without geosynthetic inclusions. It is seen that the flexible geosynthetic inclusions give better angle of friction than stiff geosynthetic layer.

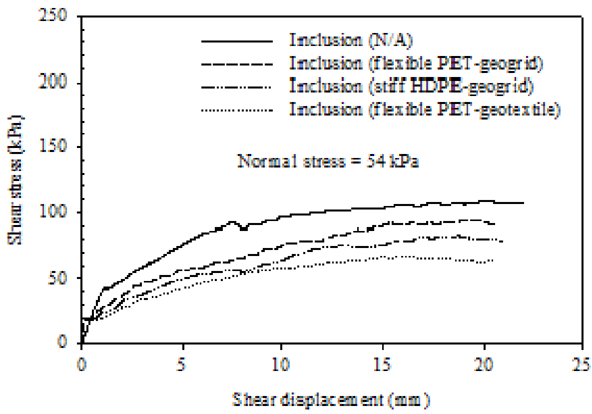

Fig. 5 Shear stress against displacement

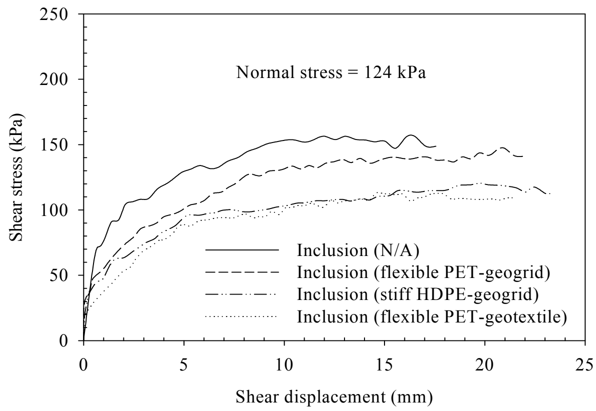

Fig. 6 Shear stress against displacement

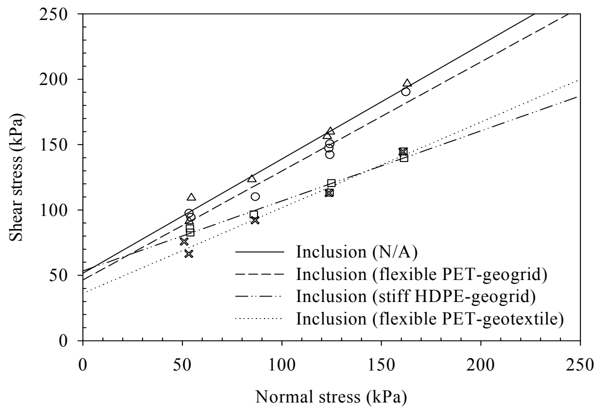

Fig. 7 Ultimate shear capacity for "I" blocks

Table 5 Interface shear parameters for different inclusion conditions

Inclusion	Angle of friction, λ (deg.)	Apparent cohesion, α (kPa)
N/A	41.2	51.6
Flexible PET-geogrid	39.8	46.4
Stiff HDPE-geogrid	28.2	53.4
Flexible PET-geotextile	33.2	36.1

5. Concluding remarks

The presence of geosynthetic layer at the facing unit's (segmental concrete unit) interface reduces the interface shear capacity. It depends on the flexibility of the used geosynthetic samples as well as its grid patterns. The angle of friction of the blocks with polyester geogrid inclusion is higher than those with HDPE geogrid and polyester geotextile inclusions.

6. Acknowledgments

The financial support for this study was provided by a grant (Fundamental Research Grant Scheme - 2010) from the Ministry of Higher Education of Malaysia awarded to the first author. Materials and technical support were provided by Soil & Slope Sdn Bhd (Malaysia).

7. References

[1] Bathurst RJ, and Simac MR, "Geosynthetic reinforced segmental retaining wall structures in North America," in Proc. 5th Int. Conf. on Geotextiles, Geomembranes and Related Products, 1994, pp. 1-41.

[2] Lee CH, "Design and construction of a 9.6m high segmental wall," in Proc. 2nd Asian geosynthetics conference, 2000.

[3] National Concrete Masonry Association (NCMA) "Design manual for segmental retaining walls," Herndon, Virginia, 1997.

[4] Elias V, Christopher BR, and Berg RR, "Mechanically stabilized earth walls and reinforced soil slopes: Design & construction guidelines,"FHWA-NHI-00-043, Washington D.C., National Highway Institute, 2001.

[5] Bathurst RJ, and Simac MR, "Laboratory testing of modular concrete block - geogrid facing connections," in Proc. ASTM Symposium on Geosynthetic Soil Reinforcement Testing, 1993, pp. 32-48.

[6] Soong TY, and Koerner RM, "On the required connection strength of geosynthetically reinforced walls," Geotextiles and Geomembranes, vol. 15, Aug.-Dec. 1997, pp. 377- 393.

[7] Bathurst RJ, Althoff S, and Linnenbaum P, "Influence of test method on direct shear behavior of segmental retaining wall units," Geotechnical Testing Journal, vol. 31, Mar. 2008, pp. 1-9.

[8] Ali FH, Bhuiyan MZI, and Salman FA, "Effects of mechanical connectors on the interface shear capacity of segmental - concrete blocks in-filled with gravel," Int. J. of Civil Engineering and Building Materials, accepted, 2011.

[9] Bhuiyan MZI, Ali FH, and Salman FA, "Frictional behaviour of segmental retaining wall units infilled with recycled concrete aggregate," in Proc. Symposium on business, engineering and industrial applications, accepted, 2011.

[10] ASTM D 6916-03, "Standard test method for determining the shear strength between segmental concrete units," West Conshohocken, PA, USA, ASTM International.

[11] ASTM D 448-03a, "Standard classification for sizes of aggregate for road and bridge construction," West Conshohocken, PA, USA, ASTM International.

[12] ASTM D 6916-06c, "Standard test method for determining the shear strength between segmental concrete units," West Conshohocken, PA, USA, ASTM International

First International Conference on Geotechnique, Construction Materials and Environment, Mie, Japan, Nov.21-23, 2011, ISBN: 978-4-9905958-0-7 C3051

Varying Ground Water Level to Minimise Liquefaction Hazards in Urban Areas

Heitor, A.[1], Oka, F.[2], Kimoto, S.[2], Higo, Y.[2],
[1]Centre for Geomechanics and Railway Engineering, Faculty of Engineering, University of Wollongong,
[2]Dept. of Civil and Earth Resources Eng., Graduate School of Engineering, Kyoto University

ABSTRACT: During a seismic event, the occurrence of liquefaction causes severe ground deformations that compromise the structural integrity of many buried elements. Currently, there are a number of different ground improvement methods that can be adopted to treat the foundations of the newly constructed structures. However, fewer remediation methods have been developed for the treatment of the ground of already existing superstructures. This study explores the performance of a cost-effective remediation technique consisting of inducing ground water level (GWL) depth variation. A 2-D profile of a soil embankment (i.e. river levee) was selected to model the GWL variation effect on the deformations associated with the dynamic loading. The results show that the GWL located at higher depth, minimizes the overall embankment deformations and contribute to a significant reduction in the vertical displacements observed on the top of the embankment.

Keywords: Liquefaction, partially saturated ground, remediation method, GWL variation,

1. INTRODUCTION

In the event of an earthquake, the occurrence of liquefaction is often the main cause of severe ground deformations that compromise the structural integrity of many buried elements of urban superstructures, including buildings, foundation piles, and lifelines. This aspect is of paramount importance, since the vast majority of the largest cities centres in the world that are exposed to frequent seismic events, are located by the coast lines. Furthermore, due to the increasingly urban development pressure, there is a great deal of superstructures now constructed in high liquefaction susceptibility terrains that were part of earlier reclamation schemes. Currently, there are a number of different ground improvement methods that can be adopted to treat the foundations of the newly constructed structures, including soil densification, dynamic compaction or vibroflotation. However, there are few remediation methods developed for the treatment of the ground, on which already existing structures were built. In fact, a large number of old structures, currently erected in high liquefaction susceptibility areas, are without treatment against liquefaction.

The bubble injection method, proposed in [1], is an example of a current existing method for liquefaction remediation of existing structures. In general, this method consists of inducing partial saturation in the ground by injecting air bubbles, which constitutes a very attractive cost-effective liquefaction remediation technique. Conversely, in time the air bubbles will dissolve in the ground water and the recurrence interval of the treatment should be adequately studied. This is the main disadvantage of using this method, since the mechanics of air dissolution in ground water, necessary to establish the recurrence period are still not well understood.

The method proposed in this study is based on similar concept (i.e. inducing partial saturation in the ground) by artificially varying the ground water level (GWL) (i.e. by pumping water). Since the GWL is located at greater depth, the ground above the water level indirectly becomes partially saturated. And because liquefaction is less likely to occur under partially saturated conditions [2], [3], the application of this technique will likely reduce the overall deformations caused by the occurrence of liquefaction. This method has further advantages related to the supply of water, since it involves the continuous pumping of ground water to maintain the GWL at certain depth. By doing so, a steady supply of water can be guaranteed and the water extracted can be either lead to storage facilities or used for other purposes (i.e. agricultural, industrial use).

The study of the effectiveness of this technique was carried out numerically, adopting a 2-D profile of a soil embankment (i.e. river levee). Different GWL depths were superimposed in the ground profile and the effect of the GWL change on the deformations associated with the dynamic loading of 1Hz sinusoidal wave was investigated. The dynamic numerical analysis was conducted adopting a finite element code LIQCA-2D-SF, in which both saturated and partially saturated soil theoretical frameworks were included.

2 ELASTO-PLASTIC SIMPLIFIED MODEL FOR PARTIALLY SATURATED GROUND

The governing equations for gas-fluid-soil coupled problem can be derived from Biot's type theory of water saturated porous media based on the continuum mechanics. Herein, the compressibility of the air is assumed to be very high, or in other words, the three-phase analysis can be simplified into the soil-water coupled two-phase mixture theory [4], [5]. An elasto-plastic model with the effect of suction has been applied to the unsaturated soil using the skeleton stress concept expressed in (1) as follows,

$$\sigma'_{ij} = \sigma_{ij} - \left\{ S_r p^f \delta_{ij} + \left(1 - S_r\right) p^a \delta_{ij} \right\} \tag{1}$$

where S_r is degree of saturation, p^f and p^a are the pore water and pore air pressure, respectively and δ_{ij} is the Kronecker's delta.

In the present model the collapse behaviour is described by the shrinkage of the over consolidation boundary surface due to the decrease in suction, as shown in (2) and (3), as below:

$$f_b = \overline{\eta}^*_{(0)} + M_m{}^* \ln \frac{\sigma'_m}{\sigma'_{mb}} = 0 \tag{2}$$

where σ'_m is the mean effective stress, M^*_m is the stress ratio value at phase transformation, $\overline{\eta}^*_{(0)}$ is the relative stress ratio and σ'_{mb} is isotropic consolidation yield stress, which is given by

$$\sigma'_{mb} = \sigma'_{mbi} \exp\left(\frac{1+e_0}{\lambda - \kappa} v^p\right) \left[1 + S_I \exp\left(-s_d\left(\frac{P_i^C}{P^C} - 1\right)\right)\right] \tag{3}$$

where σ'_{mbi} is initial value of consolidation yield stress σ'_{mb} pre-consolidation pressure, e_0 is the initial void ratio, λ is the compression index, κ is the swelling index, the v^p is the plastic volumetric strain, S_I is the is the ratio of reduction of initial suction, s_d represents the rate of that change, P_i^C is initial suction and P^C is the current suction value. The governing equations and the elasto-plastic model are implemented in the finite element code to consider partial saturation and seepage flow LIQCA-2D-SF [6],[7].

In the numerical analyis the u-p formulation was adopted. For the discretization of the equations of the motion (or equilibrium of the mixture) FEM (Finite Element Method) was used, while for discretization of the continuity equations of the pore fluids (water and gas) FDM (Finite Difference Method) was used. The time discretization is based on Newmark's β method, with β and γ set at 0.3025 and 0.6, respectively. The time increment in the calculation was set to be small enough to guarantee the accuracy of the results without having large computational time (i.e. 0.01 seconds).

3 TWO-DIMENSIONAL NUMERICAL ANALYSIS

To study the influence of the GWL, an embankment-ground system was adopted, typically with a total ground depth of 15m. Three cases with GWL's located at different depths were adopted as follows:

Case1 ; GWL=0.0m

Case 2 ; GWL=-1.0m

Case 3 ; GWL=-3.0m.

The dynamic input motion used was a 1Hz of frequency sinusoidal wave with increasing amplitude, following an arithmetic progression scheme, with maximum amplitude of 250 gal (Fig.1). In the liquefaction analysis the definition of the initial effective is an important step. The profile adopted was composed of saturated and unsaturated domains, which means that two different approaches have to be considered. In the saturated domain the effective stress was calculated using the conventional Terzaghi's effective stress based on the unit weight. Conversely, in the unsaturated domain, the skeleton stress tensor, σ'_{ij}, as defined in (1) was adopted. The horizontal stresses were estimated from the vertical stresses under the at-rest condition, assuming a coefficient of earth pressure at rest K_0 of 0.5 and a Poisson's ratio ν of 0.33. In the unsaturated domain, the increase of the negative pore water pressure (or matric suction) as the depth decrease, was assumed to follow the relationship given by the soil water characteristic curve (SWCC) (Fig.2). At the transition between saturated-unsaturated regions the vertical mesh was refined, so that the change (herein assumed linear for simplicity) of degree of saturation and effective stress could be adequately considered. The dimensions of embankment-ground system used in the analysis were set to be consistent with of a river levee, as in Fig.3. For the boundary conditions it was adopted a horizontal and vertical fixed condition on the base, equal horizontal displacement condition on the lateral boundaries and impermeable boundary on base, lateral and top boundaries (Fig.3). The parameters concerning the soil, the elasto-plastic analysis and the hydraulic properties are representative of Edosakisa sand and were taken from [4], as shown in Table1.

The results were analysed in terms of top vertical displacement and acceleration reduction, as well as in the Effective Stress Decreasing Ratio (ESDR) minimisation. The ESDR is a quantitative indicator of the occurrence of liquefaction and is given as the ratio between the current effective stress value and the initial mean effective stress, as follows:

$$ESDR = 1 - \left(\frac{\sigma'_m}{\sigma'_{m0}}\right) \tag{4}$$

in which σ'_m is the mean effective stress and σ'_{m0} is the initial mean effective stress, and for the unsaturated soil the skeleton stress is used instead of the effective stress .

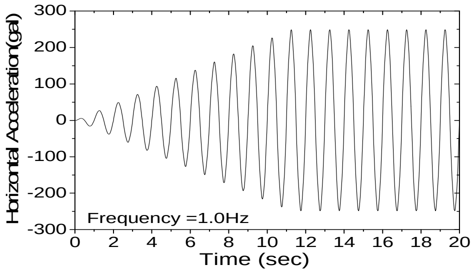

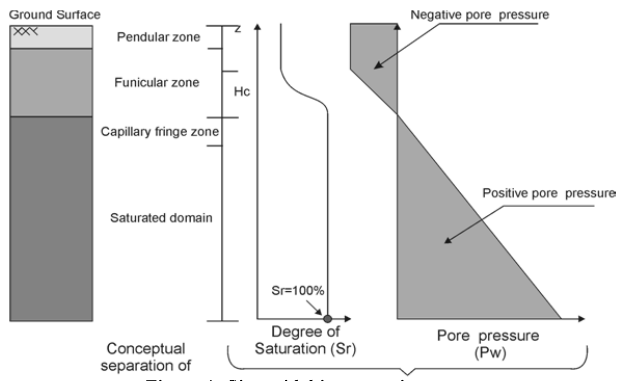

Figure 1: Sinusoidal input motion wave

Figure 2: Unsaturated domain hydraulic model.

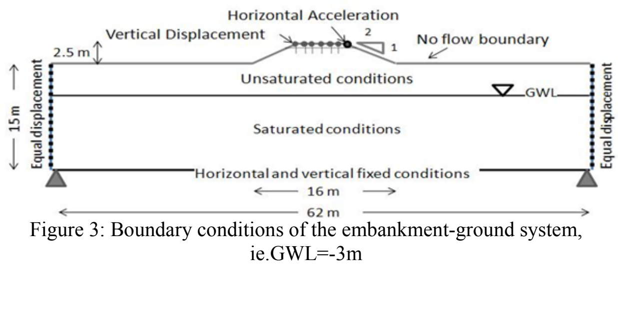

Figure 3: Boundary conditions of the embankment-ground system, ie.GWL=-3m

4 RESULTS AND DISCUSSION

The results show that the GWL located at higher depth, minimizes the overall embankment deformations and contribute to a significant reduction in the vertical displacements observed on the top of the embankment (Fig. 4). In fact, the GWL located at a larger depth yielded smaller vertical displacements on top of the embankment levee. However, the vertical displacements are reduced by a more significant amount for the case with GWL located closer to the surface at -1m depth (i.e. 24% reduction). In the case where GWL was set a deeper level (GWL=-3m) the reduction of the vertical displacements was marginal comparatively to the case with GWL -1m depth (increase of 4%). These results indicate that even small GWL depth changes (i.e. up to -1m depth) are likely to minimise significantly the vertical displacement of the superstructures located on high liquefaction susceptibility areas. In Figs. 5, 6 and 7 are represented the horizontal acceleration time profiles for the top right corner of the embankment levee together with their respective envelopes. In Fig. 7 the envelopes representative of the acceleration profiles for the GWL at different depths are shown together with the acceleration profile for GWL= -3m depth. The decrease in the water level leads to a progressive increase in the peak acceleration, varying from 0.38 m/s^2 for GWL= 0m depth to 0.42m/s^2 for GWL= -3m depth. This tendency is likely to be related with the reduction of the saturated region, that causes a more significant transmission of the dynamic motion to the upper elements located at the level of the embankment. Conversely, after the peak acceleration is reached (i.e. around 2sec) the acceleration values are smaller for the cases where GWL is located at higher depth.

Table 1: Soil and Elasto-plastic parameters

Initial void Ratio: e_0	0.85
Swelling index: κ	0.0018
Compression index: λ	0.006
Permeability: k (m/s)	2.5E-05
Density: ρ (kN/m^3)	19.0
Normalized Shear modulus: $G0/\sigma'_m$	873.28
Quasi Over consolidation ratio: OCR*	1.2
Phase transformation stress ratio: M_m*	0.91
Failure stress ratio: M_f*	1.12
Hardening parameter: B_0*	2200
Hardening parameter: B_1*	30
Dilatancy parameters: D*, n	1.1, 1.5
Elastic modulus of water: K^f (kPa)	2.04E6
Plastic, Elastic ref. strain: $\gamma_{ref}^{P*}\gamma_{ref}^{E*}$	0.005; 0.001
Initial degree of Saturation: S_r	0.6
van Genuchten parameters: α and n'	1.8 , 3.2
Initial suction: P_i^C (kPa)	6.6
Suction parameters: S_I and s_d	0.2 ; 0.2

Fig.8 a) to c) shows the 2D representation of the final values (t=20sec) of ESDR for GWL's located at different depths. ESDR values closer to 1 it suggest that the ratio between the current effective stress (which is decreasing during cyclic loading) and initial effective stress has become very small, which means that liquefaction has occurred.

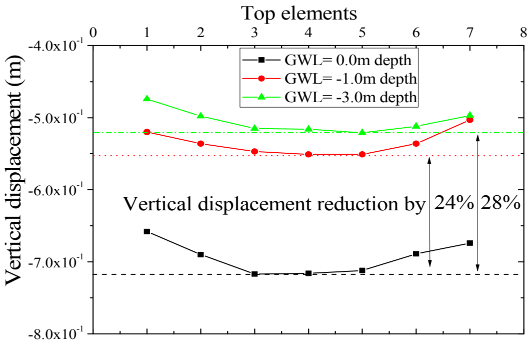

Figure 4: Top Vertical displacement at t=20sec.

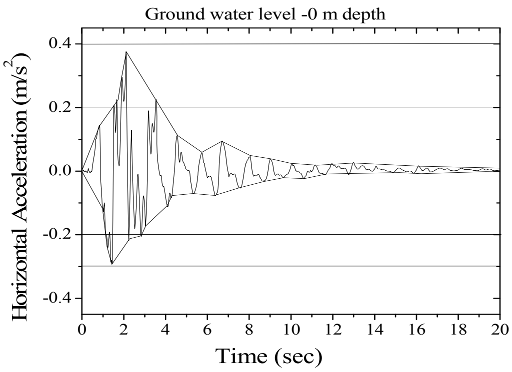

Figure 5: Top horizontal acceleration at the top boundary, t=20sec (GWL= 0m, surface).

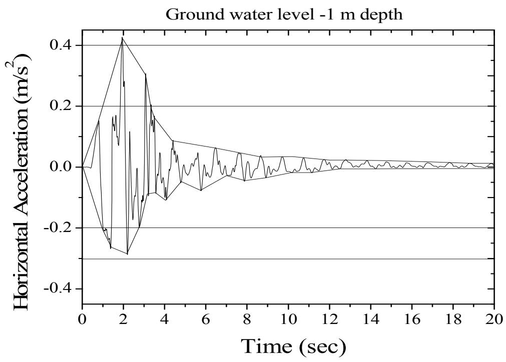

Figure 6: Top horizontal acceleration at the top boundary, t=20sec (GWL= -1m, surface).

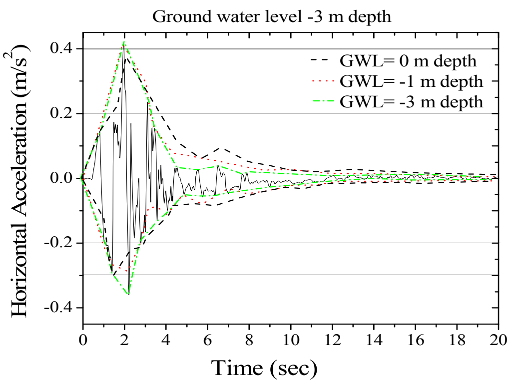

Figure 7: Top horizontal acceleration at the top boundary, t=20sec (GWL= -3m, surface).

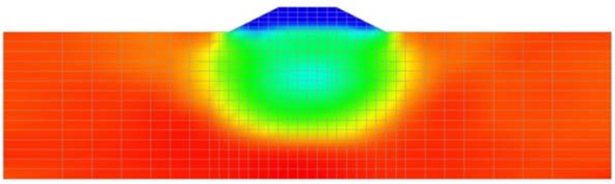

(a) Case 1: GWL = 0.0m

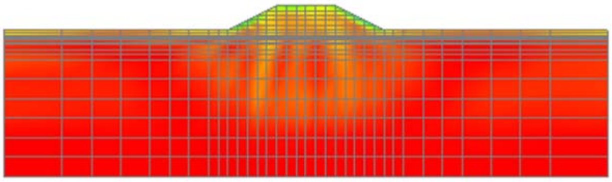

(b) Case2: GWL = -1.0m

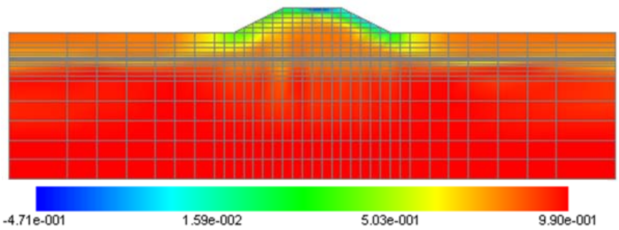

(c) Case3: GWL = -3.0m

Figure 8: 2D representation of ESDR values at t=20sec.

Overall, the increase in GWL depth seems to decrease the area that is affected by liquefaction (i.e. ESDR =0.99).

In all the cases (Fig. 8a to 8c) ESDR values obtained for the unsaturated domain were smaller or even negative, particularly on top of the embankment. In this domain there is nearly no increase in pore water pressure and consequently the effective stress does not decrease during cyclic loading. However, negative ESDR values (i.e. ESDR=-0.471) indicate that effective stress is increasing beyond its initial value this is likely to be related with the definition of effective stress in the unsaturated domain; where matric suction (negative by convention) plays an important role in the shear strength of the soil. Below the embankment levee were obtained smaller values of ESDR this tendency is related to the effective confining stresses acting on the ground, which are higher for the portion below the embankment. Note also that the liquefaction condition closer to the toe of the embankment (Fig 8a) that are likely to cause severe lateral deformations to the embankment structure are considerably minimised for the cases where GWL in located at a deeper level.

5 CONCLUSION

An alternative cost-effective method for liquefaction mitigation inducing GWL variation was investigated. The artificially variation of GWL depth causes the soil to be partially saturated and in turn strengthens the soil against liquefaction hazards. In fact, smaller vertical displacements were observed for the cases where GWL was located at higher depth. Furthermore, even a small variation of GWL, i.e. GWL=-1m depth was enough to produce a vertical displacement reduction of 24% compared with a marginal increase of 4% obtained for GWL located at -3m depth. The peak acceleration values were higher for GWL depths located at deeper levels motivated by the transmission of dynamic motion to the upper unsaturated elements (that typically behaved like dry soil). However, the order of this difference was found to be small.

This study shows that artificially GWL variation can be used as an effective method to control the magnitude of the superstructures deformations caused by the occurrence of liquefaction. In this study a 1Hz sinusoidal input wave was adopted for simplicity. Similar results are likely to be obtained for a real earthquake wave, on which frequency and acceleration contents are quite different. Further studies using real earthquake data are necessary to confirm the present findings. Moreover, the successful application of this methodology lies on an adequate GWL numerical study, so that the best cost-benefit ratio (GWL depth vs. vertical displacement reduction) can be found.

6 ACKNOWLEDGMENT

The Authors wish to acknowledge the financial support given by the Japanese Ministry of Education (Monbugakusho). Thanks are also due to Dr. Kato, Mr. Morinaka and Mr. Sanagawa for assisting with the details of some of the numerical work contained in this study.

7 REFERENCES

[1] Okamura, M. Inexpensive liquefaction countermeasure- soil desaturation by air injection. Tsuchi to kiso-JGS , 54-7, 2006, pp 28 – 30 (Japanese)

[2] Yoshimi Y., Tanaka, K., Tokimatsu, K. Liquefaction resistance of a partially saturated soil. Soils and Foundations, 29-3, 1989, pp. 157-162.

[3] Nakazawa, H., Ishihara, K., Tsukamoto, Y. and Kamata, T. Cases studies on the evaluation of liquefaction resistance of imperfectly saturated soil deposits. In Proc. Of Cyclic Behavior of Soil and Liquefaction Phenomena Conference, Triantafyllidis(ed), 2004, pp. 295-304.

[4] Oka, F.,Yashima, A., Taguchi, Y. & Yamashita, S. –Geotechnique, 49-5,1999, pp.661–680.

[5] Oka, F., Kodaka, T., Kimoto, S., Kato, R. & Sunami, S. Key Engineering Materials, 340-341, 2007, pp.1223–1230.

[6] Kato, R.; Oka, F., Kimoto, S.; Kodaka, T. & Sunami,S. Transaction of JSCE, C, vol65-1, 2009, pp.226-240

[7] The LIQCA Research and Development Group – User's Manual for LIQCA2D04, 2005

First International Conference on Geotechnique, Construction Materials and Environment, Mie, Japan, Nov.21-23, 2011, ISBN: 978-4-9905958-0-7 C3051

Development of a New Type Reinforced Soil Wall

Hara, T. Tsuji, S. Yoshida, M. Ito, S. and Sawada, K., Department of civil engineering, Gifu Unicersity

ABSTRACT: Our aim in this study is to develop a new type of reinforced soil walls as substitute for concrete ones. The structure that piles are inserted into reinforced soil wall body has been studied as the new type structure. In this development, a static loading test, a dynamic centrifuge test and an impact loading test were carried out in order to confirm the practicability of the structure to actual diverse sites. In this paper, the details of the static and impact loading tests are introduced and the practicability of the structure is discussed.

Keywords: Reinforced soil, pile foundation, retaining wall, rockfall protection structure

1. INTRODUCTION

The high ductility of soil structures reinforced by geogrid is well known, as is the possibility of building independent soil structures. The independent reinforced soil structure, which is referred to "Geo-wall" in this paper, has been applied to such diverse structures as rockfall protection walls [1], mud and snow avalanche protection walls [2] and the suchlike. Fig. 1 shows an example of the application of Geo-wall to a rockfall protection wall. Since Geo-wall can be built using existing soil at the construction site if it is compactable one, they are being used ever more frequently as one of economic and CO2 reducible structures.

Fig. 1. Application to a rockfall protection wall.

At present, however, the adoption of the spread foundation for Geo-walls makes the design too wide for application to narrow construction sites, such as beside mountainous road. If a narrow Geo-wall as like as RC structure with pile foundation is achieved, Geo-walls could be widely applied. And it can also be applied as substitute for concrete structures and contribute sustainable development.

Therefore, a new type reinforced soil wall that piles are inserted into the Geo-wall body as shown in Fig. 2, which is referred to "Piled Geo-wall" in this paper, has been developed by authors. The application of piles to Geo-wall in order to improve lateral resistance is a completely new approach, since piles tend to be vertical bearing piles and are applied to soil fillings or as reinforcements to soil fillings on soft ground vertical pile [3]. In this novel approach, an assumption is made regarding the interaction between the pile and Geo-wall, as shown in Fig. 3. The high ductility of the Geo-wall was assumed to make it possible to transmit lateral force to the piles despite large relative displacement between the pile and Geo-wall. The validity of this assumption and practicability of Piled Geo-wall to actual diverse structure were confirmed through three experiments, a dynamic centrifuge model test [4]-[6], a static loading test and an impact loading test.

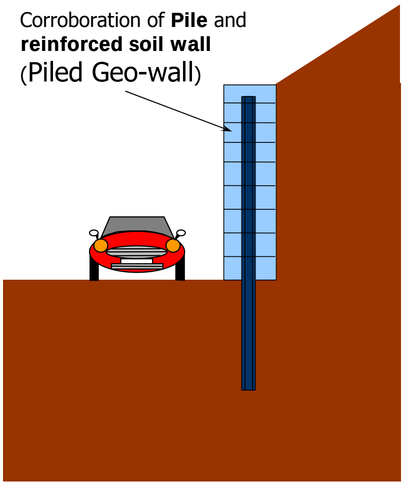

Fig. 2. An image of Piled Geo-wall.

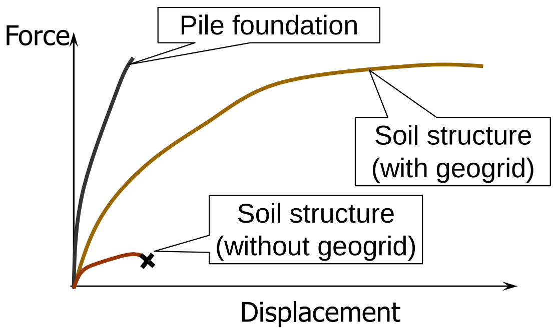

Fig. 3. Interaction between pile and Geo-wall.

In this paper, the details of the static and impact loading tests are introduced and the practicability of the Piled Geo-wall is discussed.

2. STATIC AND IMPACT LOADING TEST

2.1 Geo-walls for Experiments

Three full scale Geo-walls, normal Geo-wall (without pile), Piled Geo-wall-1 (PGW-1) and Piled Geo-wall-2 (PGW-2) were built on an actual field, and, at first, a static loading test was carried out with using the normal Geo-wall and PGW-1 and then an impact loading test was carried out with using all Geo-walls as shown in Fig. 4. Respective structural conditions, measurements and loading conditions are illustrated in each section of experiment. Fig. 5 shows the appearance of the Geo-walls.

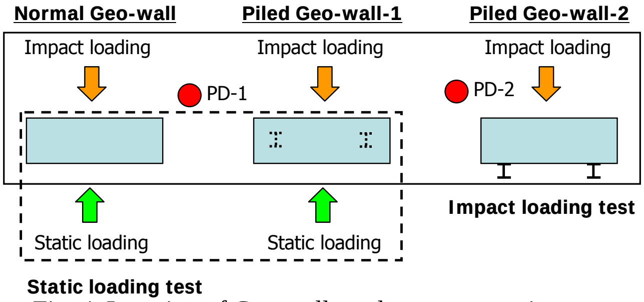

Fig. 4. Location of Geo-walls and respect experiments.

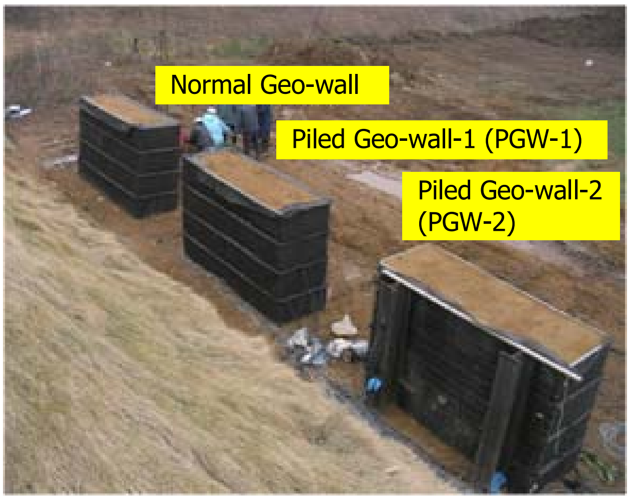

Fig. 5. Appearance of Geo-walls.

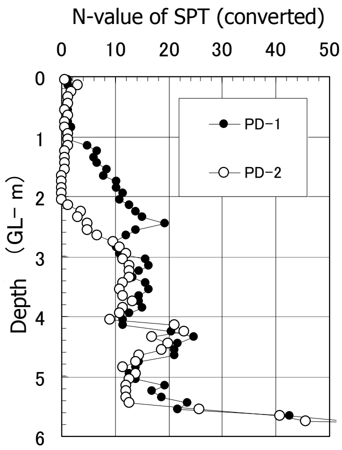

Fig. 6. Results of dynamic penetration tests.

2.2 Ground Condition

The foundation ground consists of three types of sandy silt, soft buried one, medium stiffness and stiffness ones. Fig. 6 shows the results of dynamic penetration test converted to N value of standard penetration test (SPT). The location of the borings, PD-1 and 2, is shown in Fig. 4. The thickness of the soft buried top soil is varied from the place of normal Geo-wall (PD-1) to Piled Geo-walls (PD-2).

2.3 Static Loading Test

A static loading test was carried out in order to confirm the practicability of Piled Geo-wall to earth retaining wall. In this test, two full scale Geo-walls, PGW-1 and normal Geo-wall (without pile), were adopted. Fig. 7 shows the structural summary of the test. Static horizontal load are given by two jacks set at 1.0m in height. And the horizontal load is carried as distributed pressure through an EPS of 0.5m in thickness, a steel plate of 0.12m in thickness and H steel (H200 x 200 x 8 x 12).

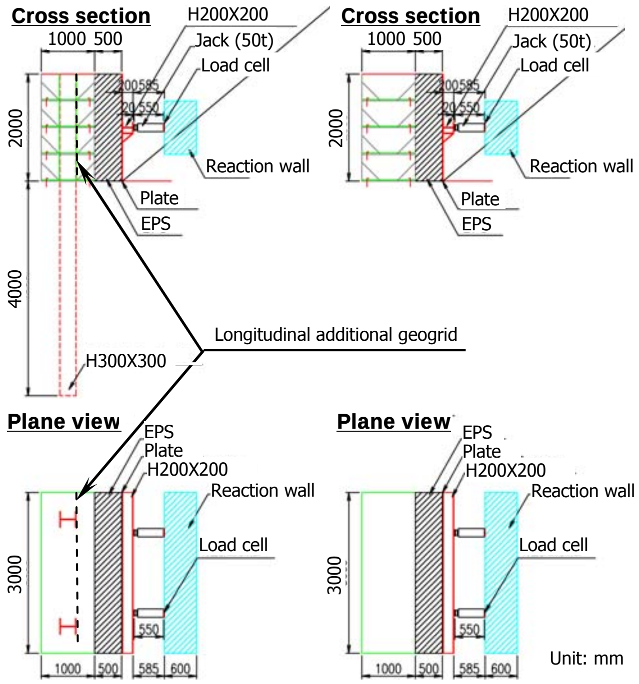

(a) PGW-1 (b) Normal Geo-wall

Fig. 7. Structural summary of static loading test.

The procedure of Geo-walls' building is as follows;

Pile installing (Piled Geo-wall only): H steel piles (H-300x300x10x15) of 6.0m in length are installed in 4.0m into the ground.

Setting of steel face member and installing of geogrid at each layer: steel face members were set on the both side of Geo-wall and a geogrid was installed at one layer. In the construction of Piled Geo-wall, a geogrid with holes located in the piles was installed through the piles, as shown in Fig.8. Fig. 9 shows the tensile stiffness of the geogrid.

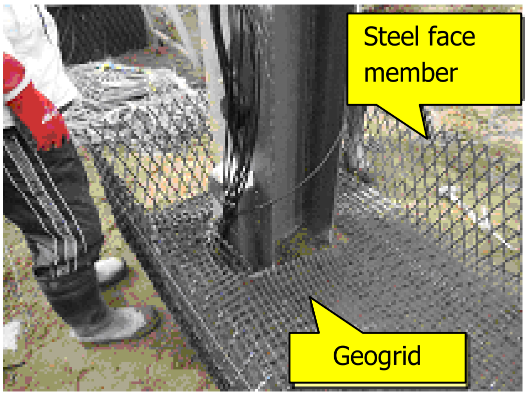

Fug. 8. Installing of steel face member and geogrid.

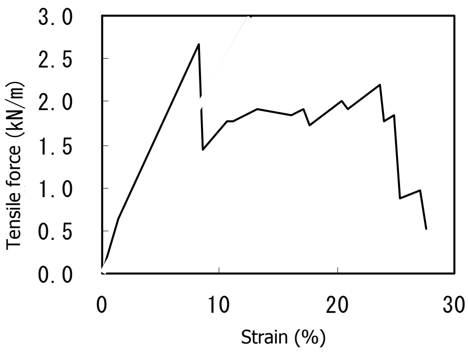

Fig. 9. Tensile stiffness of geogrid.

Installing of longitudinal additional geogrid at each layer (Piled Geo-wall only): the additional geogrid was installed on the loading side of piles, as shown in Fig. 10, in order to transmit the load to the piles from the Geo-wall body smoothly.

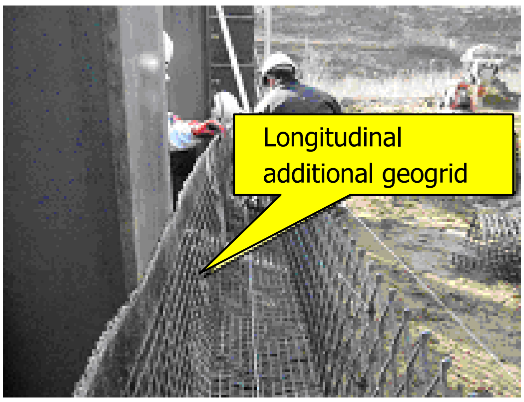

Fig. 10. Installing of longitudinal additional geogrid.

The executions of each layer, 0.5m in thickness, were repeated until that the Geo-walls, 2.0m in height, were completed.

The measurements of strains of geogrids, additional longitudinal geogrids and a pile, earth pressure of the Geo-walls at the loading side, deformation of the Geo-walls and jack pressures were planned. Figure 11 and 12 show the summary of measurements.

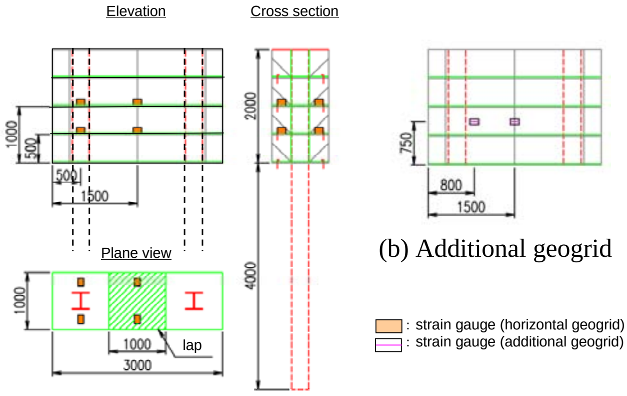

(a) Horizontal installed geogrid

Fig. 11. Measurements of strain in geogrids.

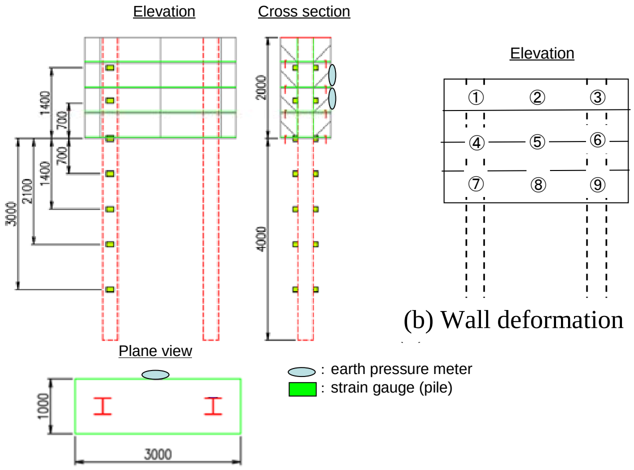

(a) Pile strain and earth pressure

Fig. 12. Measurements of strain of pile, earth pressure and deformation of Geo-wall.

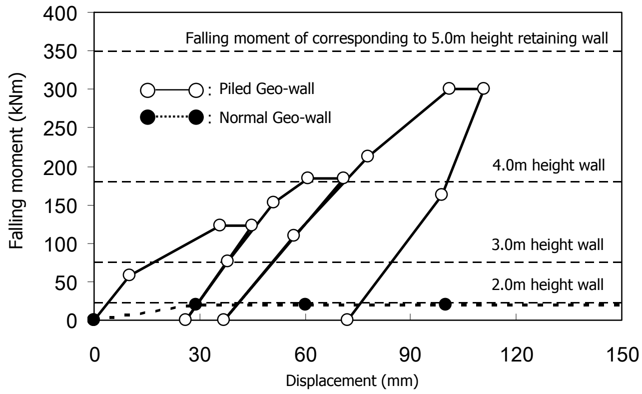

Fig. 13. Response of Geo-walls.

Fig. 13 shows the relationship between falling moment and displacement of center top of the Geo-walls (No.2 of Fig. 12(b)). Where, in order to compare with the active earth pressures loaded to retaining walls with different height, vertical axis is presented by falling moment. According to the results, high resistance characteristics of the Piled Geo-wall can be confirmed from the view point of that the proof strength of Piled Geo-wall is still increasing even if corresponding earth pressure of retaining wall of 4.0m in height is loaded. Against the Piled Geo-wall, because of soft bearing foundation shown in Figure 6, the normal Geo-wall indicated the tendency of falling by corresponding earth pressure of retaining wall of 2.0m in height. Namely, in case of adoption of normal Geo-wall in this site, too wide Geo-wall has to be designed.

Fig. 14 shows the maximum response distribution of pile. According to the results, it can be confirmed that the horizontal load is transmitted to the pile and the pile contributes for improving the lateral resistance of the narrow Geo-wall.

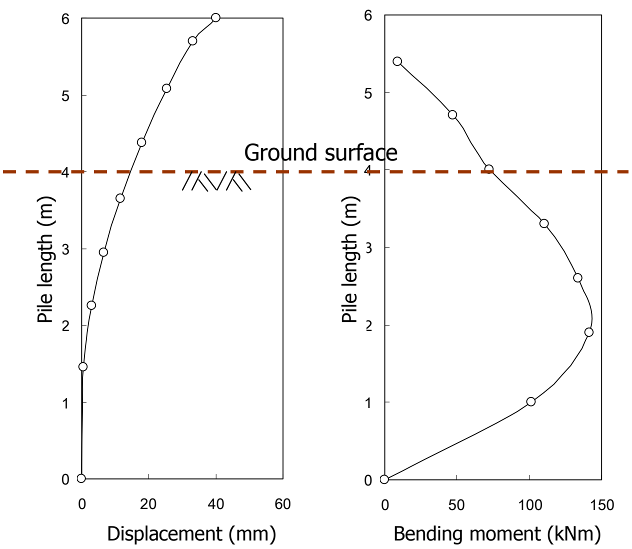

(a) Displacement (b) Bending moment

Fig. 14. Maximum response distribution of pile.

Fig. 15 shows the relationship between horizontal load and strain occurring in longitudinal additional geogrid. According to the results, the strain occurring in the geogrid of the pile side is larger than the center one and the strain depends on the intensity of the horizontal load, thus the geogrid is considered to sufficiently function for transmitting of lateral force to piles from Geo-wall body.

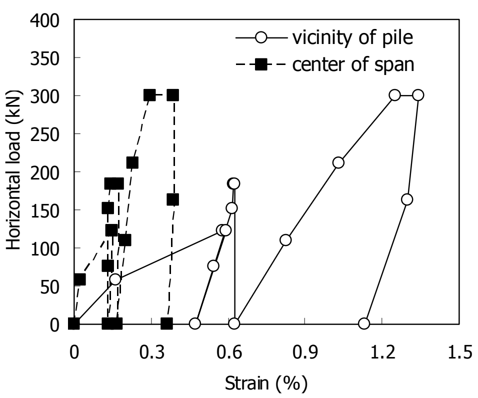

Fig. 15. Strain occurring in additional geogrid.

Fig. 16 shows the responses of the pile and the Geo-wall body at the point of pile top (No.1 of Figure 12(b)). According to the results, large relative displacement of the pile and Geo-wall is occurred though, the lateral force is transmitted to the pile from the Geo-wall and the lateral resistance of the Geo-wall was improved as abovementioned. Namely, the validity of the assumption established previously, “Geo-wall with high ductility can transmit lateral force to piles despite large relative displacement between the pile and Geo-wall as shown Fig. 3”, could be confirmed.

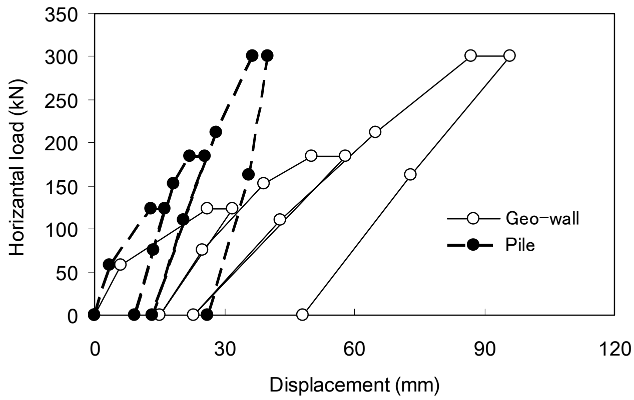

Fig. 16. Response of pile and Geo-wall body.

2.4 Impact Loading Test

An impact loading test was carried out in order to confirm the practicability of Piled Geo-wall to rockfall protection walls. In this test, three actual scale models, the two models of the normal Geo-wall and PGW-1, which are adopted in the static loading test, and a new one (PGW-2) were adopted, as shown in Fig. 4. The piles of PGW-2 are installed at outside of Geo-wall as shown in Fig. 17, are adopted.

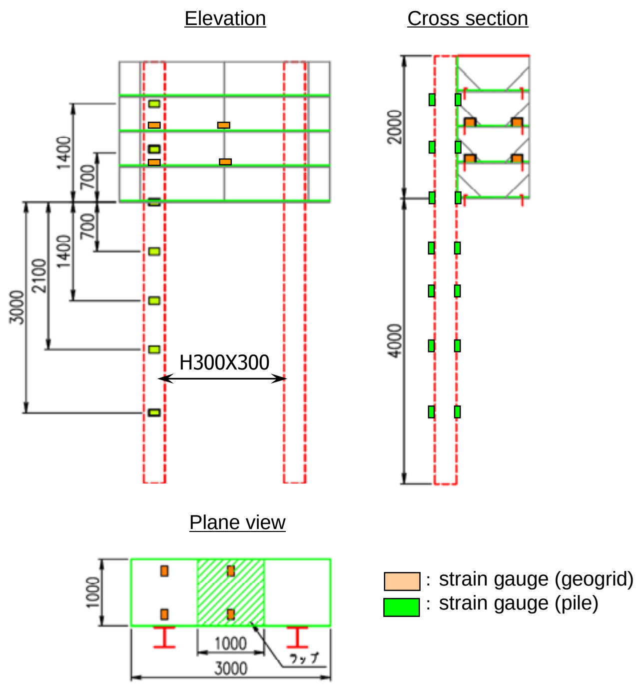

Fig. 17. Structural condition and measurements of PGW-2.

PGW-2 was adopted to confirm the best position of pile installing in case of impact loading, because there considered a possibility that keeping wide energy absorption extent is better than receive the rockfall energy at the center of Geo-wall body as PGW-1. In addition, the loading direction of static and loading tests are different, thus longitudinal additional geogrid of PGW-1 was installed on both sides of the Pile previously. In PGW-2, the additional geogrid was not installed. In this impact test, the impact of 100kJ was loaded to respective Geo-walls as shown in Fig. 18.

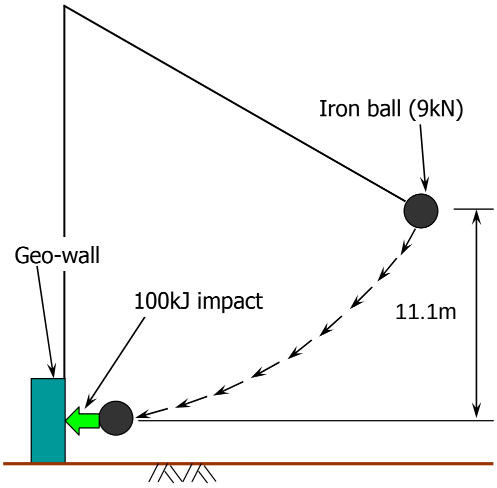

Fig. 18. Impact loading test.

Fig. 19 to 21 show the respective test results.
According to the results, against the collapse of normal Geo-wall, both Piled Geo-walls could receive the impact energy. Namely, the effectiveness of application of piles to improve lateral resistance of Geo-wall could be confirmed.
Note, however, that the deformation of the back side of the Geo-wall (protecting side, road side for instance), one of PGW-2 (piled installed at outside of the Geo-wall) is smaller than one of PGW-1 (piles installed at center of the Geo-wall). Since this result, the possibility that the best position of pile installing is outside of the Geo-wall in impact loading case can be considered. Meanwhile, from Fig. 22 showing responses of piles of the PGW-1 and 2, it is also considered that the resistance of the piles of PGW-1 seems to be smaller than ones of PGW-2. With respect to the result, following reasons can be considered.
- There might be a void in front of resistance surface of the piles of PGW-1 before the impact loading test because of the static loading test implementation.
- In the foundation ground that the piles of PGW-2 were installed, the soft buried soil is comparatively thin, because the piles of PGW-2 were installed at the position closed to vicinity hill of 0.65m.
The best position of pile installing in case of impact loading has to be studied again with considering abovementioned phenomenon in the near future.


Fig. 19. Normal Geo-wall.


(a) Loading side


(b) Back side (protecting side)
Fig. 20. Piled Geo-wall-1 (PGW-1)


(a) Loading side


(b) Back side (protecting side)
Fig. 21. Piled Geo-wall-2 (PGW-2)

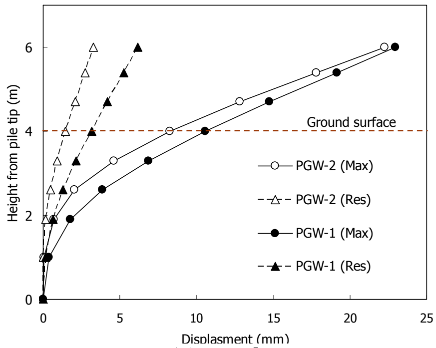

(a) Displacement

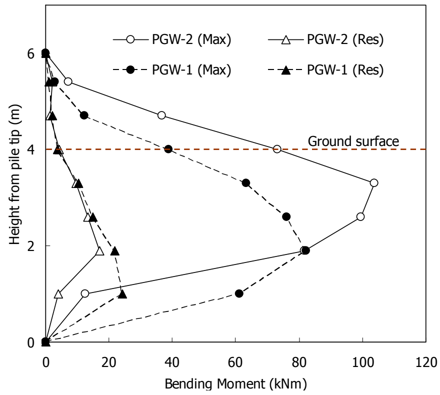

(b) Bending moment

Fig. 22. Response of piles of PGW-1 and 2.

Fig. 23 shows transition of strain occurring in the longitudinal additional geogrid and the pile of PGW-1. According to the results, from the view points of the strain occurring in the geogrid and the timing of occurrence of the strain between the geogrid and the pile, effect of the geogrid to transmit the lateral forces to the piles from Geo-wall could also be confirmed in the impact loading test.

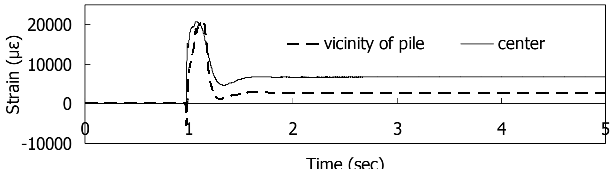

(a) Additional geogrid

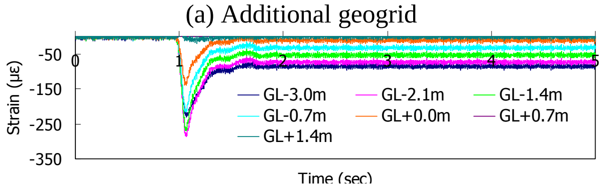

(b) Pile

Fig. 23. Strain of additional geogrid and pile of PGW-1.

3. CONCLUSION AND DISCUSSION ON PRACTICABILITY OF PILED GEO-WALL

Application of piles to Geo-wall: The effectiveness of application of piles to Geo-wall in order to improve lateral resistance of Geo-wall was confirmed from all the tests carried out in this study.

Unification of piles and Geo-wall body: Geo-wall with high ductility can transmit lateral forces to piles despite large relative displacement between the pile and Geo-wall. And adoption of longitudinal additional geogrid is effectiveness to achieve the unification of piles and Geo-wall body. Note, however, that the effect of the relative displacement to the internal quality of the Geo-wall body has to be studied.

Application to retaining walls: High resistance characteristics against static load and dynamic earth pressure could be confirmed from the static loading test as well as the previous carried out dynamic centrifuge model test [4]-[6]. Therefore, application of Piled Geo-wall to retaining walls is sufficiently possible for all ones depending on the tolerable deformation of the Piled Geo-wall and the embankment sustained by Piled Geo-wall.

Application to rockfall protection walls: High performance of Piled Geo-wall to receive rockfall could be confirmed from the impact loading test. Hence, application of Piled Geo-wall to rockfall protection walls would be possible if it is similar target rockfall with the experiment carried out in this study. Further experiments to determine the best position of the pile installing and to study the design for appropriate size of Piled Geo-wall depending on the intensity of rockfall energy are necessary before the widely application.

Design code for the application: Studies on the design method based on numerical simulations of the test results are conducting by authors. Although needed further experiments and studies to solve several issues are remained as abovementioned, a valuable design code for widely use of Piled Geo-wall would be published in the near future.

Expectation of Piled Geo-wall to sustainable development: Piled Geo-wall has possibility to be used as alternative structure of concrete ones with similar size. Therefore, if the development of Piled Geo-wall is achieved, it can be expected that the Piled Geo-wall contribute to sustainable development from the viewpoint of reducible structure of CO2.

4. REFFERENCES

[1] Yoshida, M., Tatsuta, N., Nishida, Y., Inoue, S., Yashima, A., Sawada, K. & Moriguchi, S., "Full-scale field test of reinforced embankment adjacent to steep-slope," Geosynthetics Engineering Journal, Vol.20, 2005, pp. 295-300.

[2] Itou, S., Yokota, Y., Kubo, T. & Arai, K., "Field loading test of the protection embankment retaining wall reinforced with geosynthetics," Geosynthetics Engineering Journal, Vol.15, 2000, pp. 340-349.

[3] Hara, T. & Tsuji, S., "A reinforced soil structure with pile foundation," Geosynthetics Engineering Journal, Vol.23, 2008, pp. 209-214.

[4] Hara, T., Tsuji, S., Yashima, A., Sawada, K., Tatta, N., "Dynamic interaction between pile and reinforcement soil structure – Piled Geo-wall –," in Proc. of Int. Conf. on IS-KYOTO, 2009, pp. 457-463.

[5] Hara, T., Tsuji, S., Yashima, A., Tatta, N., "Dynamic centrifuge model test on Piled Geo-wall," Geosynthetics Engineering Journal, Vol.24, 2009, pp. 257-262.

[6] Hara, T., Tsuji, S., Yashima, A., Sawada, K., Tatta, N. & Otake, Y., "Independent reinforced soil structure with pile foundation," J. of SOILS AND FOUNDATIOS, Vol.50, No.5, 2010, pp. 565-571.

Development of Design Charts for Reinforced Embankment Using Excel Spreadsheet Slope Stability Analysis

K. Ito, M. Z. Hossain and T. Sakai, Graduate School of Bioresources, Mie University

ABSTRACT: The present study is an attempt to develop design chart for reinforced embankment using excel spreadsheet slope stability analysis. The selected reinforcing materials that have been identified for reinforced embankment are composite materials with smooth surface and rough surface made of used cells, stones, wood, concrete and brick. Utilizing simplified available method and equations, the design charts for reinforced embankments have been presented using simple techniques. The most critical slip surface has been identified based on random searching that produced minimum factor of safety. Results for different slope angle with varying reinforcing layers and spacing corresponding to the most critical slip surface are given. It is expected that this study will facilitate in designing and constructing reinforced embankments containing various types of reinforcing materials.

Keywords: Reinforced Embankment, Slope Stability, Composite Reinforcements, Design Charts

1. INTRODUCTION

Compared to conventional soil reinforcing material, composite materials generally exhibit superior behavior in performance and strength. Generally, the conventional reinforcements, used for reinforcing soil, contain only one type of material such as geogrid, geosynthetic or wire mesh etc. It is known that the material used in soil reinforcement applications must be safe against tension failure and adhesion failure for its effective utilization in the field and reliable design of earth structures. For a given situation, single type of material can provide limited reinforcement capability in reinforced soil structures due to its low frictional resistance and poor cohesion. For an optimal response, therefore, different types of reinforcement, that fulfills both the requirements such as possess adequate tensile strength and adequate frictional resistance, is getting considerable attention lately. Thin-reinforced-mortar composite consisting of evenly distributed fine mesh as the reinforcement and cement-sand mortar as the matrix showed enhanced performance because of its synergetic action of mesh with mortar and mortar with soil [1]. In view of the above distinct advantages of composite material, a study is undertaken with the following objectives; a) to present a simplified technique for slope stability analysis using excel spreadsheet and b) to develop design charts for reinforced embankment containing different composite materials in order to facilitate safe and reliable construction using locally available materials.

2. METHODOLOGY

There are several methods for stability analysis of slopes [2-15]. Any method can be used to solve the equilibrium equations of slices and to search for the critical slip surface automatically, by the combined use of spreadsheet iteration method. Here, Jambu's generalized procedure of slices is used [16]. Equations for generalized procedure of slices are given as follows (Fig.1). Fill embankment considered in the present study is shown in Fig.2.

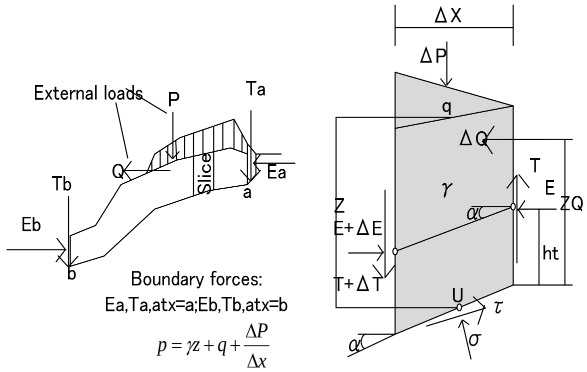

Fig.1 Symbol used in Janbu's generalized procedure of slices

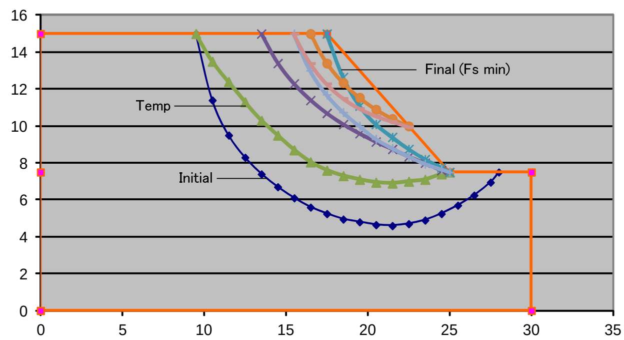

Fig.2 Example of search of critical slip surface

For Vertical equilibrium

$$\sigma = p + t - \tau \tan\alpha \tag{1}$$

For Horizontal equilibrium

$$\Delta E = \Delta Q + (p + t)\Delta x \tan\alpha - \tau\Delta x(1 + \tan^2\alpha) \tag{2}$$

For Moment equilibrium

$$T = -E\tan\alpha_t + h_t\frac{dE}{dx} - z_Q\frac{dQ}{dx} \tag{3}$$

For Limit equilibrium

$$\tau = \frac{c + (\sigma - u)\tan\varphi}{F_s} \quad (4)$$

$$\Sigma\, \Delta E = E_b - E_a \quad (5)$$

$$B = \Delta Q + (p + t)\Delta x \tan\alpha. \quad (6)$$

$$A' = [c' + (p + t - u)\tan\varphi']\Delta x \quad (7)$$

$$n_\alpha = \frac{1+(\frac{1}{F})\tan\varphi' \tan\alpha}{1+\tan^2\alpha} \quad (8)$$

$$A = \frac{A'}{n_\alpha} \quad (9)$$

$$F = \frac{\Sigma A}{E_a - E_b + \Sigma B} \quad (10)$$

$$\Delta E = B - \frac{A}{F} \quad (11)$$

$$E = E_a + \Sigma\, \Delta E \quad (12)$$

$$\frac{dE}{dx} \cong \frac{\Delta E}{\Delta x} = \frac{\Delta E_i + \Delta E_{i+1}}{\Delta x_i + \Delta x_{i+1}}. \quad (13)$$

$$T = -E\tan\alpha_t + h_t\frac{dE}{dx} - z_Q\frac{dQ}{dx} \quad (14)$$

$$\Delta T = T_i - T_{i-1} \quad (15)$$

$$t = \frac{\Delta T}{\Delta x} \quad (16)$$

$$\tau = \frac{A}{F(1+\tan^2\alpha)\Delta x} \quad (17)$$

$$\sigma' = p + t - \tau\tan\alpha - u \quad (18)$$

3. SPREADSHEET AUTOMATED ITERATION METHOD

The spreadsheet approach is shown in Table 1 as an example of 19 slices.

Table 1. Input fundamental properties of slopes

	X	Y	Ytp	hij									Ea = 0
Slice#	9.5	15	15	0	tan a	D X	P	Bo	A'o	n a0	Ao	D Eo	0
1	10.5	11.4	15	3.6	3.6	1	32.4	116.64	19.44	0.162658	119.5148	47.69536	47.69536
2	11.5	9.5	15	5.5	1.9	1	81.9	155.61	49.14	0.362396	135.5974	77.38782	125.0832
3	12.5	8.3	15	6.7	1.2	1	109.8	131.76	65.88	0.583429	112.9186	66.62053	191.7037
4	13.5	7.4	15	7.6	0.9	1	128.7	115.83	77.22	0.727997	106.0718	54.64025	246.344
5	14.5	6.7	15	8.3	0.7	1	143.1	100.17	85.86	0.836967	102.5847	40.99186	287.3358
6	15.5	6.1	15	8.9	0.6	1	154.8	92.88	92.88	0.891017	104.2404	32.74674	320.0826
7	16.5	5.6	15	9.4	0.5	1	164.7	82.35	98.82	0.941189	104.9949	21.78152	341.8641
8	17.5	5.25	15	9.75	0.35	1	172.35	60.3225	103.41	1.000927	103.3143	0.723512	342.5876
9	18.5	4.95	14	9.05	0.3	1	169.2	50.76	101.52	1.01458	100.0612	-6.96237	335.6252
10	19.5	4.8	13	8.2	0.15	1	155.25	23.2875	93.15	1.029776	90.45657	-28.8943	306.7309
11	20.5	4.65	12	7.35	0.15	1	139.95	20.9925	83.97	1.029776	81.54201	-26.0467	280.6842
12	21.5	4.6	11	6.4	0.05	1	123.75	6.1875	74.25	1.015111	73.14472	-36.0076	0
13	22.5	4.7	10	5.3	-0.1	1	105.3	-10.53	63.18	0.955151	66.14659	-48.688	-48.688
14	23.5	4.9	9	4.1	-0.2	1	84.6	-16.92	50.76	0.893659	56.80018	-49.6864	1
15	24.5	5.25	8	2.75	-0.35	1	61.65	-21.5775	36.99	0.78081	47.37386	-48.9061	-47.9061
16	25.5	5.7	7.5	1.8	-0.45	1	40.95	-18.4275	24.57	0.699511	35.12452	-38.6898	2
17	26.5	6.25	7.5	1.25	-0.55	1	27.45	-15.0975	16.47	0.618707	26.62005	-30.4538	-28.4538
18	27.5	6.95	7.5	0.55	-0.7	1	16.2	-11.34	9.72	0.505315	19.23553	-22.4364	3
19	28	7.5	7.5	0	-1.1	0.5	4.95	-2.7225	1.485	0.276801	5.364863	-5.81733	-2.81733

Ytp=I=Xi/slope ratio   P=J=1/2(hij1+hij2) γ

Table 2 Calculation of factor of safety

						S B1			S A1		Fs =		
Calculation of T1						646.5529			1563.479		2.418176		
Col(15)	Col(16)	Col(17)	Col(18)	Col(19)	Col(20)	Col(21)	Col(22)	Col(23)	Col(24)	Col(25)	Col(26)	t	s
DEo / Dx	tana t	ht	T1	D T1	t1	B1	A'1	na1	A1	D E1	E1(Ea = 0)		
		0	0								0		
62.54159	2.4	1.2	−39.419	−39.419	−39.419	−25.2682	−4.21137	0.084389	−49.9043	−4.63107	−4.63107	−1.47831	−1.69705
72.00417	1.266667	1.833333	−26.431	12.98792	12.98792	180.287	56.93275	0.237306	239.9127	81.0748	76.44374	21.52109	53.99784
60.63039	0.8	2.233333	−17.9551	8.475943	8.475943	141.9311	70.96557	0.434163	163.4539	74.33725	150.781	27.70241	85.03305
47.81606	0.6	2.533333	−26.6724	−8.71727	−8.71727	107.9845	71.98964	0.577081	124.7478	56.39691	207.1779	28.50141	94.33146
36.8693	0.466667	2.766667	−32.085	−5.41262	−5.41262	96.38117	82.61243	0.694379	118.9731	47.18165	254.3595	33.01981	114.5735
27.26413	0.4	2.966667	−47.1494	−15.0645	−15.0645	83.84132	83.84132	0.757116	110.7377	38.04744	292.407	33.67198	119.5324
11.25251	0.333333	3.133333	−78.6968	−31.5474	−31.5474	66.57632	79.89158	0.819786	97.45425	26.2756	318.6826	32.24058	117.0323
−3.11943	0.233333	3.25	−90.0753	−11.3784	−11.3784	56.34005	96.58294	0.906292	106.5694	12.2699	330.9525	39.26071	147.2303
−17.9283	0.533333	3.016667	−233.084	−143.009	−143.009	7.857412	15.71482	0.931045	16.87869	0.877485	331.83	6.403602	24.27029
−27.4705	0.433333	2.733333	−208.003	25.08112	25.08112	27.04967	108.1987	0.985251	109.8183	−18.364	313.4659	44.41438	173.669
−31.0271	0.433333	2.45	−197.646	10.35643	10.35643	22.54596	90.18386	0.985251	91.53385	−15.3065	298.1595	37.01949	144.7535
−42.3478	0.366667	2.133333	−90.342	107.3043	107.3043	11.55272	138.6326	0.999973	138.6363	−45.7782	0	57.18797	228.1949
−49.1872	0.266667	1.766667	−73.9139	16.42806	16.42806	−12.1728	73.03684	0.985202	74.1339	−42.8298	−42.8298	30.35341	124.7634
−49.2962	0.2	1.366667	−67.5715	6.342401	6.342401	−18.1885	54.56544	0.952026	57.31506	−41.8903	−84.72	22.79017	95.50043
−43.798	0.1	0.916667	−35.3575	32.21401	32.21401	−32.8524	56.3184	0.875446	64.33113	−59.4556	1	23.69992	102.159
−34.5718	−0.13333	0.6	−20.4764	14.88109	14.88109	−25.124	33.49865	0.81309	41.19917	−42.1613	−41.1613	14.16822	62.20679
−26.4451	−0.36667	0.416667	−21.4519	−0.97545	−0.97545	−14.561	15.88473	0.746867	21.26847	−23.3563	−64.5175	6.752594	30.18848
−18.8358	−0.46667	0.183333	−2.05324	19.39864	19.39864	−24.919	21.35918	0.647903	32.96664	−38.5519	2	9.149566	42.00334
−11.6347	−0.73333	0	−2.06604	−0.01281	−0.02562	−2.70841	1.477315	0.427869	3.45273	−4.13623	−2.13623	1.292148	6.345746

In the field of earth slope protection, the basic materials needed for cement composite constructions are wire mesh, sand, cement and water. The skeletal steel is used in the construction of cement composite frame structures for earth slope protection. A basic description of the constituent materials and construction procedure is given below. After iteration, the solver automatically searches the critical slip surface as shown in light blue color or orange color in Fig.1 and determines the minimum factor of safety [FS less than 1 depending on slope]. Reinforcements for this critical slip surface having minimum FS needs to be calculated for the safe design and construction of embankments.

4. RESULTS AND DISCUSSION

Reinforcements for embankments having slope angle 45 and 60 are calculated and shown in Fig.3. The FS values are greater than one by inserting 3 layers of reinforcements [Fig.4].

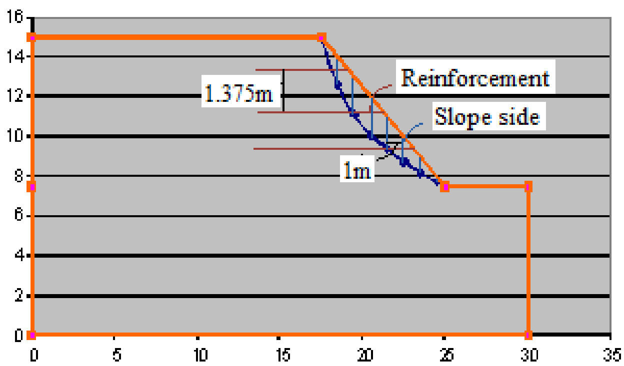

Fig.3a Reinforced slope with 60 angle

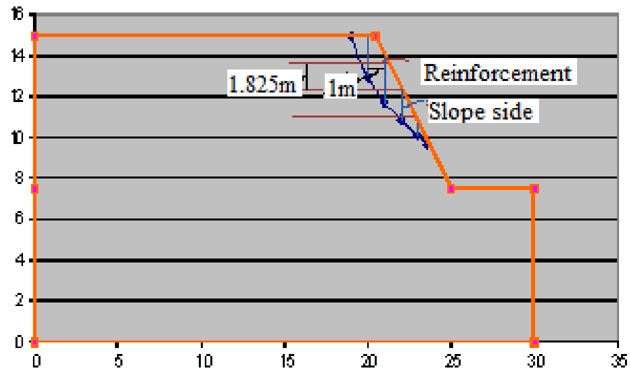

Fig.3b Reinforced slope with 45 angle

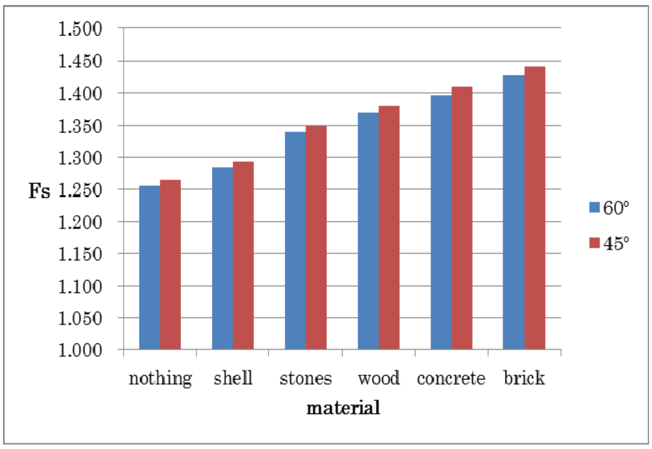

Fig.4 FS vs. types of reinforcements with 3 layers

For safe design, the FS should be more than 1.5 which indicates that the number of layers should be more than three layers. For economic design, it is necessary to minimum number of layers of reinforcements. Considering the both safe and economic design, the number of layers were increased to 4 and FS has been calculated and given in Fig.5. It was observed that the FS values are greater than 1.5 for reinforments containing stones, wood, concrete and brick.

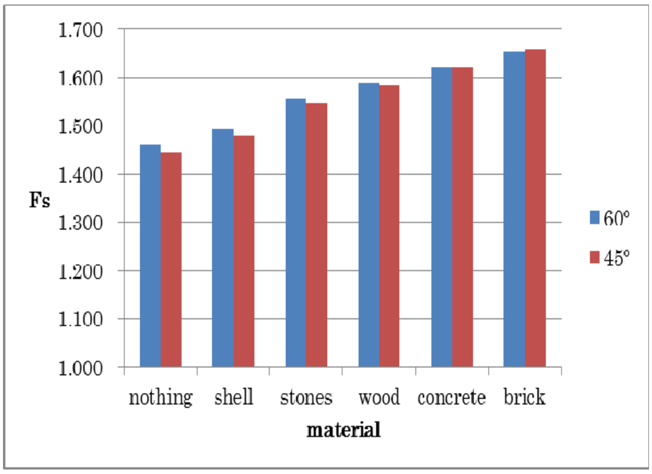

Fig.5 FS vs. types of reinforcements with 4 layers at bottom part

The above FS are obtained when the reinforcements are inserted at the bottom part of the embankment. This was performed for the ease of calculation. However, for the ease of construction, it is necessary to insert the reinforcement uniformly throughout the embankment. Considering the facts above, the FS with 4 layers inserted at 1m interval are calculated and given in Fig.6.

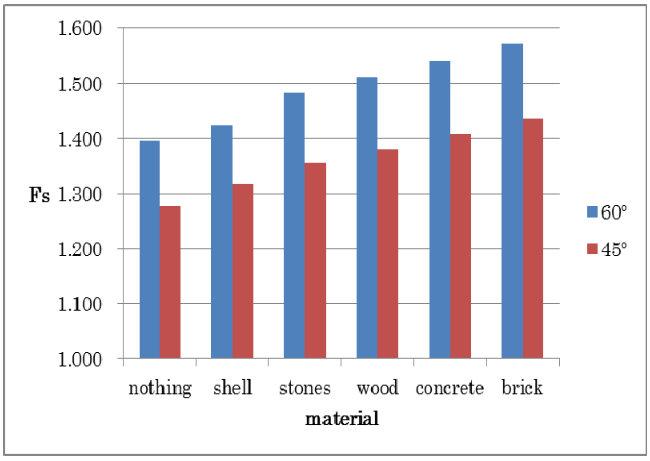

Fig. 6 FS vs. types of reinforcements with 4 layers at uniform distribution

It is observed that the embankments with 60 slopes are giving FS values of more than 1.5 for reinforcements made of wood, concrete and brick only. The embankments with 45 slopes giving lower FS for all the cases. This type of behavior was absolutely obscured in the case of Fig.5 although the numbers of layers were same. This factor needs to be carefully considered during construction reinforced embankments.

5. CONCLUSIONS

Design charts for reinforced embankments containing various types of reinforcements have been presented in this paper. In the process, the powerful spreadsheet techniques are used to render the iterations in the search for critical slip surface and for calculation of minimum factor of safety. A noteworthy feature of the proposed study is that the search for the critical slip surface is non-circular and automatic, despite the fact that the FS is non-explicit. It is expected that the present study will bring the new concept for the design of reinforced slope. The conceptual simplicity, ease of implementation and practical versatility of the proposed perspectives and spreadsheet methods are likely to apply also to other reinforcement and slopes.

6. REFERENCES

[1] M. Zakaria Hossain, "Pullout Response of Cement composite Members Embedded in Soil," ACI Materials Journal, V. 105, No. 2, March-April 2008, pp.116-124

[2] Janbu,N., "Slope stability computation. In Embankment-Dam Engineering," Casagrande Volume,ed.R.C. Hirschfeld and S. J. Poulos .Krieger Pub. Co.,1987,pp.47-86

[3] Bishop, A.W., "The use of the slip circle in the stability analysis of slopes." Geotechnique, 1955,5,7-17

[4] Morgenstern, N.R. and Price,V.E., "The analysis of the stability of general slip surface. Geotechnique,1965,15,79-93

[5] Spencer, E., "A method of analysis of the stability of embankments assuming parallel inter-slice forces." Geotechnique,1967,17,11-26.

[6] Chen,Z. and Morgenstern, N.R., "Extensions to the generalized method of slice for stability analysis.," Canadian Geotechnics Journal, 1983, 20, 104-119

[7] Sarma,S.K., "Note on the stability of slopes." Geotechnique,1987,37, 107-111.

[8] Hoek,E., "General two-dimensional slope stability analysis.In Analytical and Computational Methods in Engineering Rock Mechanics," Ed. E. T. Brown.Allen & Unwin,1987.pp.95-128.

[9] Wright,S.G., Kulhawy,F.G. and Duncan, "J.M.,Accuracy of equilibrium slope stability analysis.Journal of Soil Mechanics and Foundations Division," ASCE,1973,99,783-791.

[10] Fredlund, D.G.and Krahn,J., "Comparsion of slope stability methods of analysis," Canadian Geotechnical Journal,1977,14,429-439.

[11] Skempton, A,W. and Vaughan, P.R., "The failure of Carsington dam," Geotechnique,1933,43,151-173.

[12] Alonso, E.E., Gens, A. and Lloret, A., "The landslides of Cortes de Pallas, Spain," Geotechnique,1933,43,507-521.

[13] Wright,S.G. and Duncan, J.M., "Limit equilibrium stability analyses for reinforced slopes," TRB Paper No.910441,Transportation Resarch Board, Washington DC,1991.

[14] Chen,Z. and Shao,C., "Evaluation of minimum factor of safety in slope stability analysis," Canadian Geotechnical Journal,1988,25,735-748.

[15] Ugai,K. and Leshchinsky,D., "Three-dimensional limit equilibrium and finite element analyses:a comparsion of results," Soils and Foundations,1 995,35,1-7.

[16] Duncan, J.M., "State of the art: limit equilibrium and finite-element analysis of slopes, "Journal of Geotechnical Engineering, ASCE,1996, 122, 577-596.

First International Conference on Geotechnique, Construction Materials and Environment, Mie, Japan, Nov.21-23, 2011, ISBN: 978-4-9905958-0-7 C3051

Numerical Simulation of 2D Crack Growth with Frictional Contact in Brittle Materials

Kai Zhang.[1, 2] Jing-cai Jiang.[2] Qing Yang.[1]

(1. Institute of Geotechnical Engineering, School of Civil Engineering, Dalian University of Technology, Dalian, China)

(2. Department of Civil and Environmental Engineering, The University of Tokushima, Tokushima, Japan)

ABSTRACT: In this paper, the extended finite element method (XFEM) is applied in modeling the 2D crack growth with frictional contact under uniaxial compress load in the rock-like materials. First, the implementation of XFEM is incorporated into a commercial FEM software (ABAQUS) in which the constitutive law of linear elasticity and the criterion of maximum tangential stress (MTS) is adopted. Then a user subroutine is coded and incorporated into ABAQUS to simulate the growth of wing crack with the frictional contact in the crack faces. A series of numerical simulations of 2D plane strain rectangle with central pre-set crack are carried out, and computed results are compared with experimental ones. The effects of inclination and coefficient of the friction of the pre-set cracks on growth of wing cracks are examined. In addition, size effect of materials is also investigated, and these jobs contribute to the understanding of 2D crack growth.

Keywords: Extended finite element method (XFEM); rock-like materials; crack growth; frictional contact; size effect.

1. INTRODUCTION

The discontinuities (e.g. joint, crack, and void) which exist previously or appear during the evolution often control the instability and final failure in the brittle materials. In recent years, a lot of experiments and numerical simulations have been carried on crack growth in brittle materials, such as rock, concrete and so on. It has been widely acknowledged that FEM is one of the effective methods used to model the crack problem because of its good adaptability and scalability. But conventional FEM has many difficulties in dealing with the strong discontinuities, which mostly lead to high density meshes on the crack tip or repeated remeshing as crack grows [1].

The Extend Finite Element Method (XFEM) originally proposed by Belytschko and Black [2, 3] in 1999, is very powerful for discontinuous problems in fracture mechanics. They added discontinuous enrichment function to the finite element approximation to account for the presence of the crack. Later, other researchers improved the method, and applied it in many subjects in fracture mechanics.

Actually, the extended finite element method (XFEM) is an extension of the conventional finite element method based on the concept of partition of unity. It allows the presence of discontinuities in an element by enriching degrees of freedom with special displacement functions. It does not require the mesh to match the geometry of the discontinuities. It allows contact interaction of cracked element surfaces based on a small-sliding formulation and allows both material and geometrical nonlinearity [4].

During the numerical analysis, the contact is a typical nonlinear problem, which not only due to the complicated mechanical model for the contact surface, but also more originate from the special discontinuous constraint of contact surface. The convergent results are difficult to obtain only when the appropriate friction model is chosen. In the simulation of the paper, the penalty method is used to deal with the frictional contact of the crack surfaces during the load process, which can better model the impact on the contact surface when the wing crack grows.

This paper intends to contribute to the understanding of 2D crack growth under uniaxial compress load in brittle material with frictional contact, and a series of numerical modeling are carried out whose results are compared with experimental ones [5]. The effects of inclination and coefficient of the friction of the pre-set cracks on growth of wing cracks are examined.

2. THE XFEM APPROXIMATION

In the classical FEM, the approximation to displacement field $u(x)$ is expressed as [1]

$$\mathbf{u}^h(x) = \sum_{i=1}^{n} N_i \mathbf{u}_i \tag{1}$$

where N_i is the interpolated shape function associate with the node i; $\mathbf{u}_i$ is the classical vectorial DOF(degrees of freedom) at node i. For each computational point (x, y) in the field, N_i should satisfy PU (partition of unit):

$$\sum_{i=1}^{n^e} N_i(x, y) \equiv 1 \cdot \tag{2}$$

The XFEM enriched a standard approximation locally on the crack with discontinuous functions.

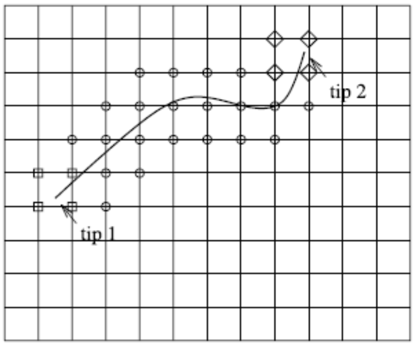

Fig. 1 An arbitrary crack placed on a mesh

$$
\begin{aligned}
\boldsymbol{u}^h(\boldsymbol{x}) &= \sum_{i\in I} N_i(\boldsymbol{x})\boldsymbol{u}_i + \sum_{j\in J} H(x) N_j(\boldsymbol{x})\boldsymbol{a}_j \\
&+ \sum_{k\in K_1} N_k(\boldsymbol{x})\left(\sum_{l=1}^{4} \boldsymbol{b}_k^{l1}\varphi_l^1(r,\theta)\right) \\
&+ \sum_{k\in K_2} N_k(\boldsymbol{x})\left(\sum_{l=1}^{4} \boldsymbol{b}_k^{l2}\varphi_l^2(r,\theta)\right)
\end{aligned} \tag{3}
$$

where I is the set of all nodes in the mesh; J is the subset of nodes which support is intersected by the crack but do not cover any crack tips (e.g. the circled nodes in Fig. 1.); K_1, K_2 is the subset of nodes which support conclude the first and second crack tips (e.g. the squared and diamond nodes in Fig. 1.).

The function $H(x)$ is a "generalized Heaviside" function, in which the discontinuity is aligned with the crack surface Γ_d . $\mathbf{a}_j$ is the corresponding additional DOF for the discontinuity. Given a point in the domain, we denote the vectorial distance $\Delta\mathbf{x}$ between it and the closet point on Γ_d . Also, the normal vector to Γ_d is constructed. The function $H(x)$ is then given by the sign of the scalar product $\Delta\mathbf{x}\cdot e_n$:

$$
H(x) = sign(\Delta\mathbf{x}\cdot e_n) = \begin{cases} 1, \Delta\mathbf{x}\cdot e_n > 0, \\ -1, \Delta\mathbf{x}\cdot e_n < 0. \end{cases} \tag{4}
$$

The set of near-tip functions $\phi_l(r,\theta)$ are a set of additional shape functions which span the exact asymptotic crack-tip fields for a linear elastic material:

$$
\begin{aligned}
\{\varphi_l(r,\theta)\} &= \{\sqrt{r}\sin\left(\frac{\theta}{2}\right), \sqrt{r}\cos\left(\frac{\theta}{2}\right), \\
&\sqrt{r}\sin\left(\frac{\theta}{2}\right)\sin(\theta), \sqrt{r}\cos\left(\frac{\theta}{2}\right)\sin(\theta)\}
\end{aligned} \tag{5}
$$

where (r,θ) are the local polar coordinates at the crack tip. Except this, b_k^l is corresponding additional DOF for the crack tip.

3. FRICTIONAL BEHAVIORS

3.1 Conventional friction theories

Usually, when the inner surfaces of the crack are in contact, the shear force will be transmitted as well as the normal force across the interface. We now consider unilateral contact with friction on the interface.

The crack faces or the interface are assumed as $\Gamma_d = \Gamma_d^- \bigcup \Gamma_d^+$ with the unit normal vector to Γ_d^+ denote by $\mathbf{n}$ in Fig. 2, and in the later modeling flat ellipse is chosen which is close to the real situation of rock-like material. We also introduce the displacement and traction on each face of the crack: $\mathbf{w}^-, \mathbf{t}^-$ on Γ_d^- and $\mathbf{w}^+, \mathbf{t}^-$ on Γ_d^+ [6].

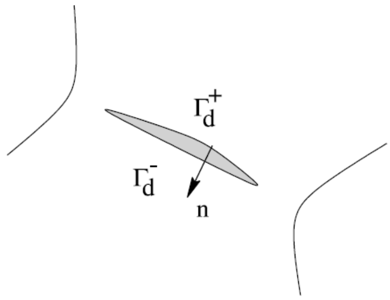

Fig. 2 The crack faces

The frictional model is easily described by using the appropriate form of the displacement and traction on the crack faces. The normal components are expressed in the condition of no contact and in contact:

$$
(\mathbf{w}^- - \mathbf{w}^+)\cdot\mathbf{n} \ge 0, \tag{6A}
$$

$$
\mathbf{t}^+\cdot\mathbf{n} \le \mathbf{0}, \mathbf{t}^-\cdot\mathbf{n} \ge \mathbf{0}, \mathbf{t}^+\cdot\mathbf{n} = -\mathbf{t}^-\cdot\mathbf{n}, \tag{6B}
$$

$$
(\mathbf{t}^+\cdot\mathbf{n})(\mathbf{w}^- - \mathbf{w}^+)\cdot\mathbf{n} = \mathbf{0} \tag{6C}
$$

The tangential component will satisfy the equilibrium:

$$
\mathbf{n}\times(\mathbf{t}^+\times\mathbf{n}) + \mathbf{n}\times(\mathbf{t}^-\times\mathbf{n}) = \mathbf{0}, \tag{7}
$$

so that the standard value of the tangential component can be represented by

$$
p = \left\|\mathbf{n}\times(\mathbf{t}^+\times\mathbf{n})\right\|. \tag{8}
$$

The additional equations depend on whether or not there is friction. When the friction is idealized using a Coulomb law, two contacting surfaces can carry shear stress up to the maximum frictional force before they start sliding relative to each other:

$$
g = \mu|\mathbf{t}\cdot\mathbf{n}|, \tag{9}
$$

where μ is the coefficient of friction.

There is two states (sticking and sliding) and two equations to be satisfied are:

$$
\mathbf{n}\times(\mathbf{w}^+\times\mathbf{n}) = \mathbf{n}\times(\mathbf{w}^-\times\mathbf{n}) \quad \text{if } p < g \text{ (stick),} \tag{10A}
$$

$$
\mathbf{n}\times(\mathbf{w}^+\times\mathbf{n}) - \mathbf{n}\times(\mathbf{w}^-\times\mathbf{n}) \ne 0 \text{ if } p = g \text{ (slide).} \tag{10B}
$$

3.2 Stiffness method for friction

The stiffness method used for friction is a penalty method that permits some relative motion for the surfaces called elastic slip when they should be sticking. While the surfaces are sticking, the magnitude of sliding is limited to the elastic slip and adjusted to enforce this condition.

The stiffness method requires the appropriate selection of an allowable elastic slip γ_i . Using a larger γ_i makes the convergence of the solution more rapid, but brings the bad accuracy. If γ_i is chosen very small, convergence problems may occur. So the value of allowable slip used in the simulation which works very well must provide a conservative balance between efficiency and accuracy.

The allowable elastic slip is given as [4]

$$\gamma_i = F_f \overline{l_i} \tag{11}$$

where F_f is the slip tolerance, and $\overline{l_i}$ is the characteristic contact surface length.

4. NUMERICAL EXAMPLES

4.1 The pre-set of parameters

The models used in the numerical study are rectangle blocks with dimension 240 mm high and 120 mm wide. A pre-existing flaw (25 mm long and 0.5 mm wide) with different inclinations and coefficients of friction is set up in the center of each model. The flaw will close during the loading procedure. The other parameters of the flaw and the parameters of the material see Table. 1 and Table. 2.

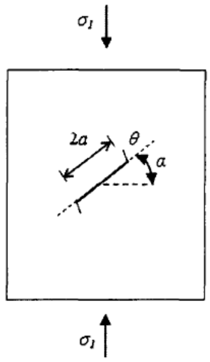

Fig. 3 The model of a flaw under compression
(2a: the length of the flaw, θ: the initial angle)

Table.1 The dimension parameters of the flaw

No.	Inclination α/°	Coefficient of friction μ	No.	Inclination α/°	Coefficient of friction μ
1-1	30	0.5	2-2	45	0
1-2	45	0.5	3-2	45	0.1
1-3	60	0.5	4-2	45	0.3
			5-2	45	0.7

4.2 Modeling and Computing

Before the analysis of the program, we set appropriate loading steps and the number of iteration, which not only enables the convergent results, but also makes a good crack propagation path. During the meshing, the encryption (0.1mm*0.1mm) is made around the crack tip, while normal mesh (5mm*5mm) is chosen in other zones. After each converged load increment the crack propagation criterion is checked. If no crack growth happens, the current crack configuration remains unchanged and the next loading step is applied; otherwise a new crack segment will be inserted with some length (thought as the size of element). Subsequently, the process will continue with the next loading step [8].

Table.2 The parameter of material

Compressive strength /MPa	Tensile strength /MPa	Yonng's modulus /GPa	Possion's ratio
38.5	3.2	5.93	0.14

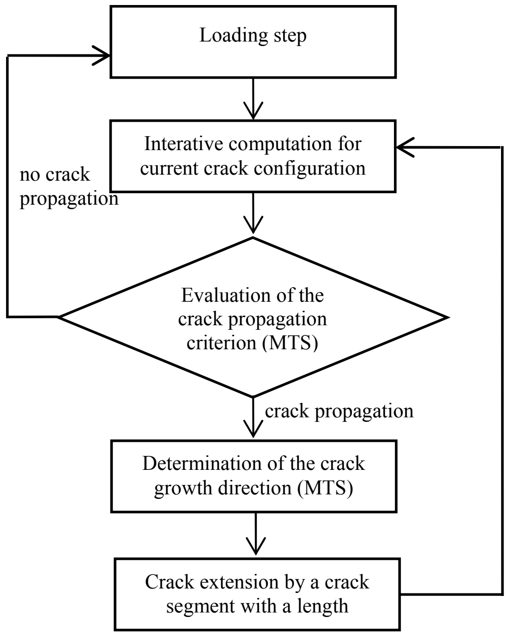

Fig. 4 Algorithm used for crack propagation analyses[8]

4.3 Numerical results

The main findings from the modeling are as follows:

(1) Wing cracks are observed in all the models, which shows mode-I cracking is the main failure mode. Wing cracks appear first with a very short length at the tips of the initial crack, and then become wider and longer with the load increasing, finally towards the direction of the compressive

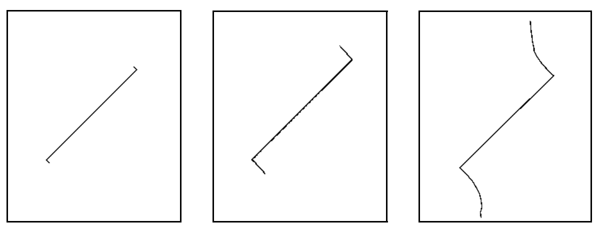

(1) 50 steps (2) 100 steps (3) 200 steps

Fig. 5 The typical propagation path of the wing crack

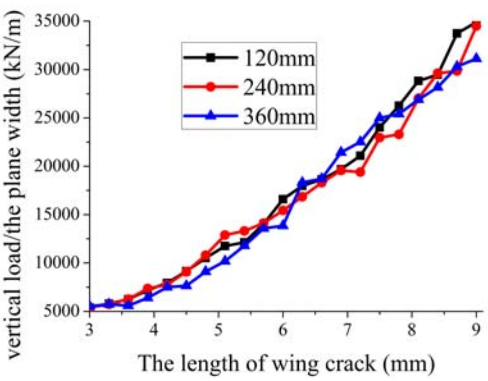

Fig. 6 Curve of the length of wing crack vs. vertical load/the plane width for μ=0.3

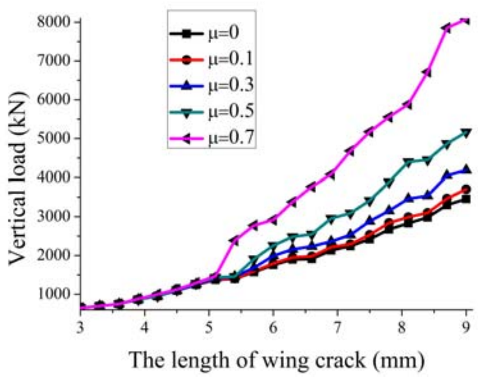

Fig. 7 Curve of the length of wing crack vs. vertical load for β=45°

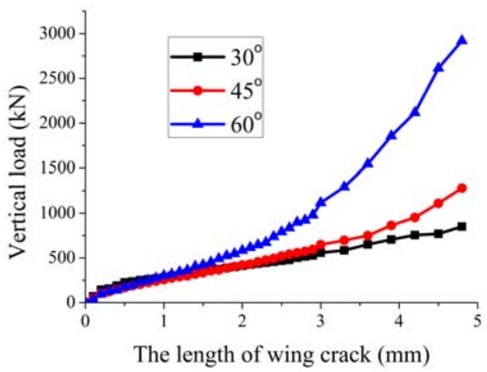

Fig. 8 Curve of the length of wing crack vs. vertical load for μ=0.5

stress. The path of wing crack seems to be similar to the hyperbola lines in mathematics, which are discussed in the previous papers of Yang who is one of this paper's authors.
(2) The crack in the infinite plate will completely keep open or close under the loading, while in the finite plate middle region maybe exist, which means the crack will close partly. Because of the complex in mathematics, it is difficult to obtain the analytical solution of the problem, and the phenomenon is observed in this modeling.
(3) The size has little effect in the vertical load increasing when the wing crack grows, so the model with fixed width and height is able to simulation the real results for different rock mass's situation.
(4) As the increase of the coefficient of the friction, the wing crack propagation will be slowly as the vertical load increase. Fig.7 also shows the crack faces will close when the length of wing crack reaches near 5mm. The curves extend mostly not as the line, which shows the friction over the crack face make the stress around the crack changed, thereby inhabit the propagation of the wing crack.
(5) The length of the wing crack increases nonlinearly as the vertical load increases, in details that increasing rate of crack length for vertical load increase at first and then decrease fast when the length of the wing crack reaches the critical value which means that the stress around the crack is changed due to the propagation of the crack. The initial load decreases as the increase of the inclination of the pre-set crack. The results in Fig. 8 show the difference of the inclination produce the different distribution of the normal and tangential stress.

5. CONCLUSIONS

The mechanism of crack propagation was studied using brittle material with the frictional contact under uniaxial expression and the relationship between the length of wing crack and vertical load was recorded and analyzed. A XFEM technique was used to simulate the propagation of wing cracks in the specimens, and the obtained results were compared with the laboratory test one [5], which shows they were very close to the experimental ones. It proves the accuracy and practicability of the above method in modeling the frictional contact behavior.

6. ACKNOWLEDGEMENTS

This research is supported by the NSFC (Grant No.50979013). The authors are grateful for these supports.

7. REFERENCES

[1] Lu-xian, Li. & Tie-jun, Wang, "The extended finite element method and its applications," Advances in Mechanics, vol.35 (1), 2005, pp. 5-20.
[2] Belytschko, T. & Black, T, "Elastic crack growth in finite elements with minimal remeshing," Int. J. Numer. Meth. Eng. vol.45 (5), 1999, pp. 601-620.
[3] Moes, N., Dolbow, J. & Belytschko, T, "A finite element method for crack growth without remeshing," Int. J. Numer. Meth. Eng, vol.46 (1), 1999, pp. 131-150.
[4] SIMULIA, ABAQUS 6.10: Analysis Users' Manual. 2010.
[5] Shao-hua, G, "The experimental and theoretical investigation on fracture of rock-type materials under compressive loading," Ph.D. Thesis, 2003.
[6] Dolbow, J., Moes, N. & Belytschko, T, "An extended finite element for modeling crack growth with frictional contact," Computer Methods in Applied Mechanics and Engineering, vol.190, 2001, pp. 6825-6846.
[7] Yu-wen, D., Qing-wen, R. & Qin, S. "Extended finite element method of frictional contact problem," Journal of Yangtze River Scientific Research Institute, vol.26 (5), 2009, pp. 45-49.
[8] Dumstorff. P. & Meschke, G. "Crack propagation in the framework of X-FEM-based structural analyses," International Journal for Numerical and Analytical Methods in Geomechanics. vol.31, 2007, pp. 239-259.

First International Conference on Geotechnique, Construction Materials and Environment, Mie, Japan, Nov.21-23, 2011, ISBN: 978-4-9905958-0-7 C3051

Interface Behaviour of Basalt Geosynthetic with Sand Using Direct Shear Device

Md. Bellal Hossain, Md. Zakaria Hossain and Toshinori Sakai
Department of Environmental Science & Technology, Mie University, Japan

ABSTRACT: The suitability of the geosynthetic materials depends on not only the mechanical properties but also the soil-geosynthetic interaction properties. Therefore, this paper attempted to evaluate interface behaviour of basalt type geosynthetic with sand through a series of direct shear tests. In the tests the applied normal stresses were 40-160 kPa. The test results reveal that the shear strength of all sand-geosynthetic interfaces increased with the increasing normal stresses. The geogrid having small apertures and thin ribs shows the maximum interface shear resistance whereas the sand-geotextile interface shows significantly lower shear resistance comparing to that of sand-sand interface. Strain hardening-softening behaviour is clearly observed for the geogrid interfaces, but the geotextile interface shows completely different behaviour. It is also observed that the presence of sand in the apertures of geogrids dominates the dilatancy behaviour of the sand-geogrid interfaces. The average interface efficiency of the sand-geogrid interfaces tested in this study ranges from 0.61 to 0.87.

Keywords: Direct shear tests, Basalt geosynthetics, Interface efficiency, Toyoura Sand.

1. INTRODUCTION

Geosynthetics have been increasingly used in geotechnical and environmental engineering for the last four decades. There are a significant number of geosynthetic types and applications in geotechnical and environmental engineering. Common types of geosynthetics used for soil reinforcement include geotextiles (particularly woven geotextiles), geogrids and geocells. For practical use of geosynthetics as soil reinforcement materials, the suitability of the material should be checked by evaluating not only the mechanical properties but also the soil-geosynthetic interaction properties.

The pullout and the direct shear tests are the two laboratory tests commonly used to measure the corresponding mobilized interaction resistances. With the advancement of soil reinforcement techniques, a number of researches on soil-geosynthetic interaction testing have been performed [1]-[5]. The interface shear resistance of geotextiles against soil results solely from the shear resistance between the geosynthetic surface against soil particles because soil particles are not interlocked with openings. On the other hand, Geogrids are characterized by a combination of longitudinal and transverse ribs. Therefore, the interactions between soil and geogrid refer to the following mechanisms: (1) shear resistance between soil and the surface of the geosynthetic along the reinforcement plane (the ribs, in the case of geogrids); and (2) internal shear resistance of the soil (in the aperture of geogrid). The mechanisms (1) and (2) have been quantified by researchers such as [6], [7].

Practically, the direct shear test is a suitable mean to study the interaction between soil and reinforcement because it can simulate the shear mechanism along a potential failure plane in reinforced earth structure. However, the in-soil interaction behaviour of a geogrid depends on the relative displacement of the geogrid and soil. It is necessary to use an appropriate testing method for estimating the behaviour of reinforced soil structures since the details of the test method may influence the results of direct shear tests. Moreover, the interaction mechanisms between soil and geogrid in direct shear mode are more complicated than sheet-like geosynthetics like metallic strips and geotextiles. Different test methods have been used by different researchers. Mitachi et al. [8] proposed a method to estimate the deformation behaviour of geogrid embedded in soil based on the results of direct shear tests. The study also compared the data calculated from direct shear tests with observed data from pull-out tests. They concluded that the relative displacement of geogrid in any part of the reinforced soil, as well as the pull-out force vs. pull-out displacement relationship, can be predicted by using direct shear test results. Consequently, Nakamura et al. [9] performed a series of direct shear tests changing the configurations of soil and geogrid, roughness of substrate material on which the geogrid is glued, and the distance between the surface of geogrid and the shear plane. They proposed that the test specimen of the geogrid glued on the substrate should be placed under the sand layer and a suitable substrate material should be used taking into account the mode of interaction between soil and geogrid in situ. A similar type of device has been used in this study where the relative position of the geosynthetics against the soil layer remain unchanged which gives the most approximate condition to that in the field.

The shear strength of sand-geosynthetic interfaces has been investigated using direct shear tests by a number of researchers [10]-[12]. These studies used geosynthetic materials such as High density polyethylene (HDPE), poly propylene (PP), Polyester (PET) yarns coated with PVC etc. However, this study focuses on estimating the interface behaviour of Basalt geosynthetic with sand in direct shear mode. The frictional behaviour of sand-sand and sand-steel interfaces is also investigated. Moreover, the interface efficiency is evaluated with the influence of various geometric properties of Basalt geogrids at different applied normal stresses.

2. MATERIALS

As backfill material, air-dry uniform silica sand (Toyoura sand), available in Japan, was used in all direct shear tests conducted throughout this study. Before testing, the physical properties of sand were tested in the laboratory. This sand has no fine content less than 0.075mm with effective diameter D_{10} of 0.01 mm, D_{30} of 0.15 mm, D_{60} of 0.19 mm, the uniformity

Table 1 Geometric properties of geosynthetic

Material (Product No.)	Aperture length (mm)	Aperture width (mm)	Longitudinal rib width (mm)	Transverse rib width (mm)	Percent open area (%)	Mass per unit area (g/m^2)	Ultimate tensile strength (kN/m)	
							Machine direction	Cross direction
GG1(BGA5×5-40)	4.25	3.00	2.00	0.75	45	165	50	40
GG2(BGA10×10-40)	9.00	8.00	2.20	1.00	65	165	50	40
GG3(BGA25×25-40)	21.35	20.35	4.65	3.65	70	350	50	50
GT (B-WF450)	---	---	---	---	---	450	1870	1600

coefficient (Cu) of 15.45, and the coefficient of curvature of the gradation curve (Cc) of 9.89. The particle size distribution of the sand is shown in Fig. 1. The specific gravity, maximum and minimum void ratio are Gs= 2.64, e_{max}= 0.98 and e_{min}= 0.61, respectively. The water content of sand is less than 1%, which corresponds to air-dried conditions.

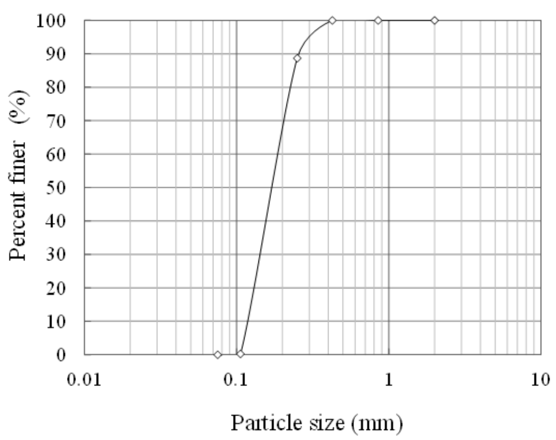

Fig. 1 Particle size distribution curve of sand

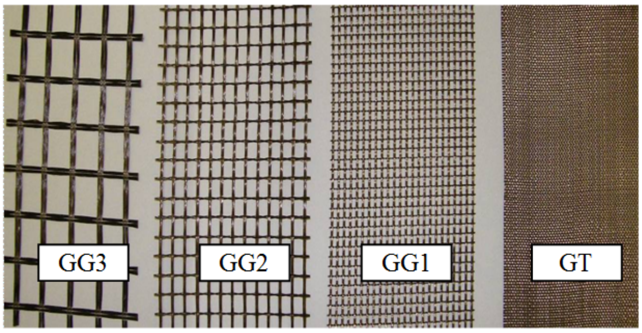

Fig. 2 Geosynthetic specimens used in this study

Four types of geosynthetics made of basalt fiber, including one woven geotextile and three geogrids, were used in this study. This material has excellent property of elasticity and stretch tension with good resistance to acid, alkali, heat and vibration. It has also non-conductive and non-magnetic resistance. Hence, Basalt material is considered to reclining as an alternative to glass fibers, silica fibers and carbon fibers. All geosynthetic materials are manufactured by JCK CO. LTD, Japan. For the purpose of discussion, the geotextile is noted as GT and the geogrids are noted as GG1, GG2 and GG3 as shown in Fig. 2. The physical characteristics of these geosynthetics are listed in Table 1.

3. TEST EQUIPMENT AND PROCEDURES

A direct shear testing equipment which consists of a fixed lower box and a moving upper shear box has been used in this study. In this equipment, vertical load is applied to the backfill material through a loading plate below the lower shear box. A reaction plate is placed on the backfill in upper shear box. The displacement of the loading plate is used to record the vertical displacement of the test specimen. The inside dimension of both shear box is 150mm in length and 100mm in width. The movement of the upper shear box in the horizontal direction is controlled by a set of gears mobilized by an electric motor. Fig. 3 shows a frontal view of the direct

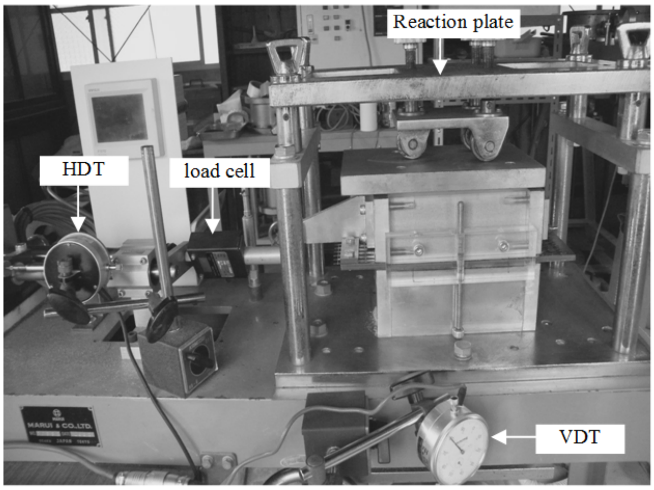

Fig. 3 Direct shear apparatus used in this study

shear device used in this study. The applied shear force, horizontal and vertical displacements were recorded at one second interval throughout the tests. These data were collected using one load cell, and two displacement transducers (one for horizontal, HDT, and other for vertical, VDT) connected to a data-acquisition system which consists of 8-channel micrologger.

The direct shear tests of sand-sand interface were performed prior to the sand-geosynthetic interface tests. A smooth steel plate was used as substrate material on which geosynthetic specimens were placed below the sand layer. To know the frictional behaviour of Toyoura sand with the steel plate, the direct shear tests of sand-steel interface were also performed. The geosynthetic specimen was positioned on the substrate placed on the top of the lower box. Subsequently, the specimen was clamped on the front edge of the steel plate using four aligned bolts and two steel clamping blocks. The sand in the upper shear box was rained using a raining device with two sieves. The dry unit weight of the sand mass in upper box was 1.63 g/cm^3 (15.9kN/m^3), which corresponds to relative density (Dr) of 95% (dense condition). The thickness of the sand layer in upper shear box was 70mm. The specification of this equipment is within the standard of JIS and the Japanese Geotechnical Society (JGS: T941-199X). The detail of this equipment is also available at [13]. The direct shear tests were conducted using normal stresses of 40, 80, 120 and 160 kPa. All shear tests involved applying the normal stress and monitoring the vertical displacement. The shear load was only applied after the vertical displacement had reached equilibrium after applying the normal load. The vertical load is maintained constant during shearing process. A shear displacement rate of 0.5mm/min was used during testing. This rate is in the range recommended in the research manual [14]. The maximum shear strength obtained during the shear process was recorded as the peak shear strength.

4. TEST RESULTS

4.1 Test of sand-sand and sand-steel interfaces

To quantify the shear strength parameters of experimental sand, the direct shear tests are conducted for four different normal pressures. The shear stress versus horizontal displacement and vertical displacement versus horizontal displacement curves from direct shear tests on sand is plotted in Fig. 4(a). A well defined peak and residual shear stress is observed at all normal stress level. Maximum shear resistance mobilized within 3-6mm of shear displacement. Before and after the peak shear stress, hardening and softening behaviour is markedly observed. The volumetric behaviour shows positive dilatancy during shear after a small contraction at initial stage of horizontal displacement. The average peak and residual angle of internal friction of the sand are found to be 34.5° and 25° respectively. The shear stress-displacement and volumetric behaviour of sand-steel interface is shown in Fig. 4(b). Several researchers have already studied the interface behaviour of steel surfaces (rough and smooth) with sand and fine grained soil [15]-[18]. In this study used a smooth steel plate is used as substrate for holding the geosynthetic specimens. Thus, it is important to understand the behaviour of smooth steel surface with sand in case of testing geogrid interfaces, particularly. As shown in Fig. 4(b), small difference between the peak and post peak shear strength of the sand-steel interface is observed for all normal stresses. The average friction angle between sand and smooth steel surface is calculated as 10.5°. All the shear stress lines seem to follow the same line upto yield point which is similar to the findings reported by Kishida and Uesugi [19] on Toyoura sand-steel interface tests. A progressive nature of strain-softening behaviour is also observed after the peak shear stress. From vertical vs. horizontal displacement relationship, only compression behaviour is observed during shearing which is typical of laboratory shearing along smooth interfaces, e.g. [20].

4.2 Test of sand-geosynthetic interfaces

Four types of Basalt geosynthetic materials, including one woven geotextile (GT) and three geogrids (GG1, GG2 and GG3) have been used to evaluate the behaviour of sand-geosynthetic interfaces. These interface tests were performed using the same direct shear equipment which was

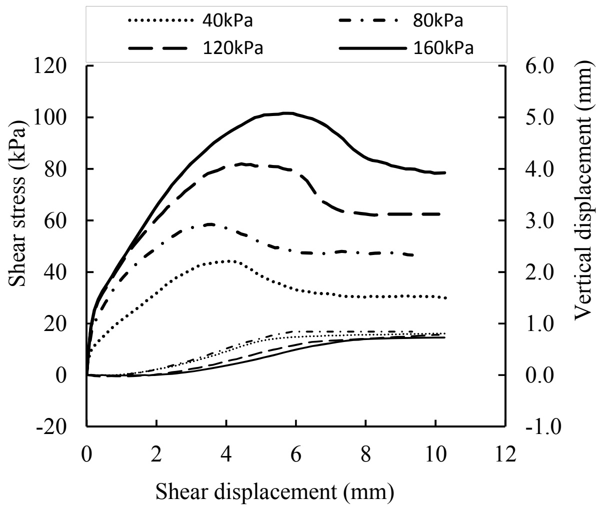

(a)

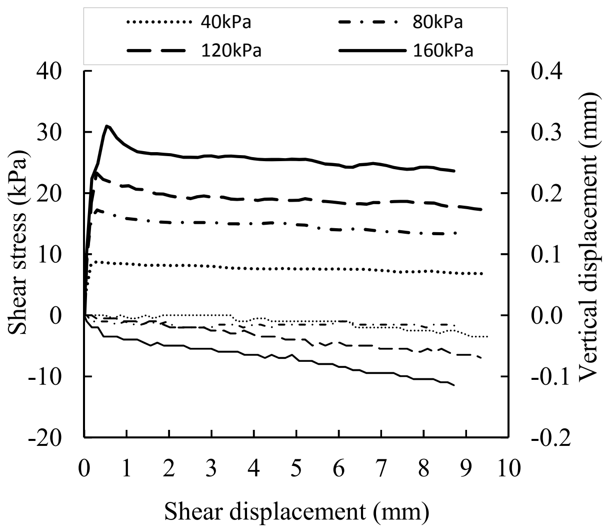

(b)

Fig. 4 Shear stress-displacement and horizontal vs. vertical displacement relationships of (a) sand-sand, (b) sand-steel interfaces

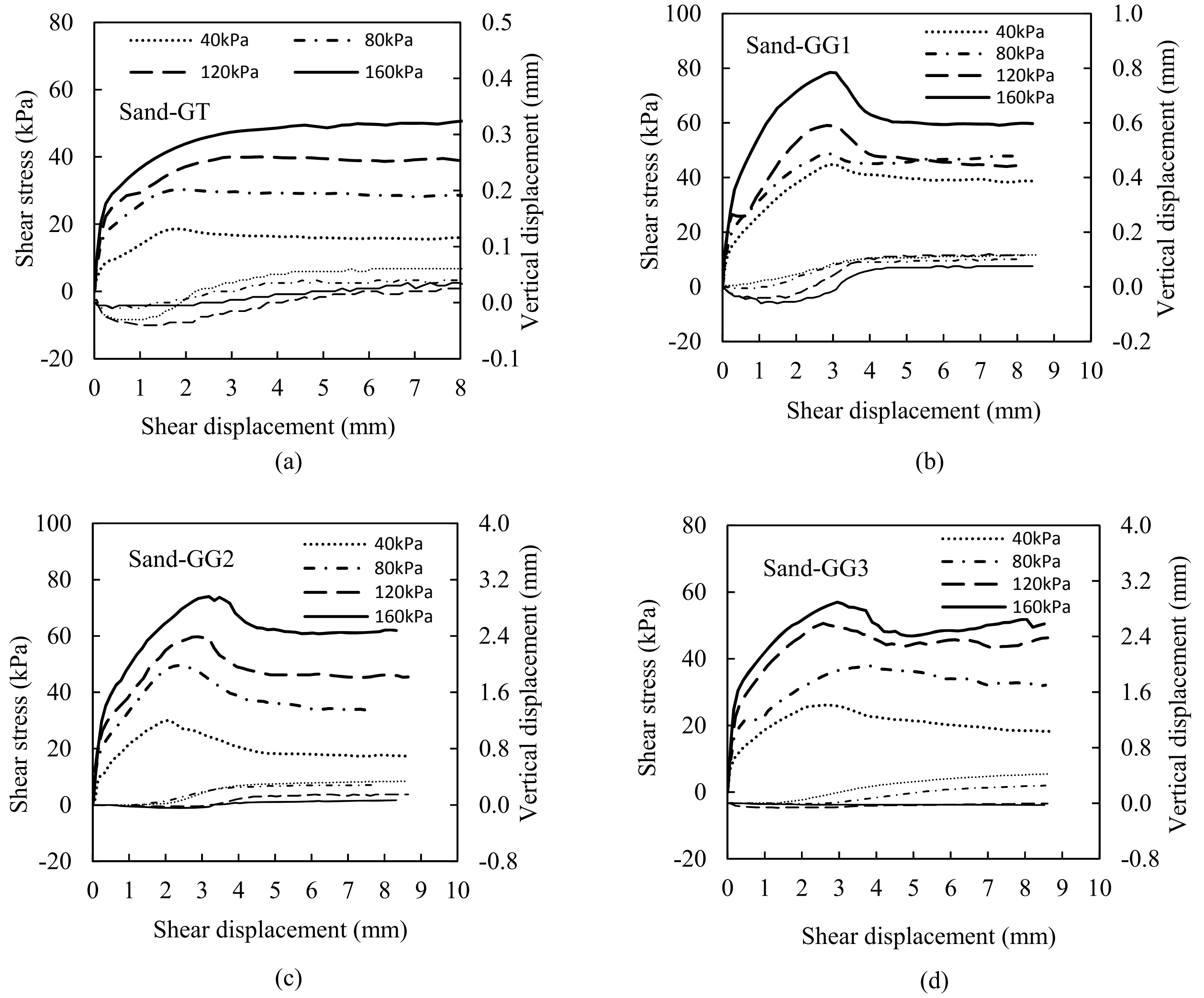

Fig. 5 Shear stress-displacement and horizontal vs. vertical displacement curves for (a) sand-GT, (b) sand-GG1, (c) sand-GG2, (d) sand-GG3 interfaces

used for the direct shear tests on sand and sand-steel interfaces. The results of sand-geosynthetic interface tests are shown in Fig. 5. It shows that the shear strength of all interfaces including the geotextile (GT) and geogrids (GG1, GG2 and GG3) increases with the increase of normal stresses of 40, 80, 120 and 160kPa. At the initial stage of shear loading, all interfaces develop linear shear stiffness before yielding takes place. This may be because of the initial high bonding stress between sand and the surface of geosynthetic materials. From the yield point to maximum shear stress, strain hardening behaviour is observed in all interfaces. The post peak nature of sand-GG1 and sand-GG2 interfaces are similar to that of sand-sand interface which ends up with a constant residual state. In case of sand-GT interface, a slight strain-softening response is seen at lower normal stress (40kPa), but this response disappears with the increase of normal stress and the residual stress becomes equal to the peak shear stress. Though the sand-GG3 interface shows strain softening behaviour after the peak, a slight strain hardening response is seen further for higher normal stresses of 120 and 160kPa. The maximum shear stress obtained from sand-sand interface tests is consistently higher than that obtained from all other interface tests except for sand-GG1 interface at lower normal stress of 40kPa. However, the maximum shear stress is found decreasing with the decrease of geosynthetic area of the geogrids at all normal stresses. Since GG1 has small apertures and thin ribs, large shear stress is exerted from the initial stage of shear due to interlocking between geogrid and sand. On the other hand, as the size of the apertures of GG2 and GG3 is relatively larger than GG1, the shear stress is found relatively low due to less confinement of sand in the apertures as well as less geosynthetic area for effective skin friction.

4.3 Volume change behaviour of the interfaces

The vertical displacement versus shear displacement curves obtained from the direct shear tests on the sand-geosynthetic interfaces are shown in Fig. 5. It shows that the maximum vertical displacement (0.07mm) of sand-GT interface is very small compare to that of sand-sand interface (0.8mm). The behaviour is mostly dilative with a little contractive nature at the initial stage of shearing. The presence of dilation with shearing indicates the presence of some degree of particle rolling and interlocking as dilation is required for the shearing and rearrangement of angular particles. The volumetric behaviour of sand-GG1 interface is seen almost same to sand-sand interface, but the magnitude is different. In case of GG2 and GG3, as shown in Fig. 5(c) &5(d), the volumetric behaviour is almost similar to sand-GG1 interface at lower normal stress. But, exception volumetric behaviour is observed at high normal stress of 160kPa where GG2 and GG3 interfaces show very small changes in volume that is contractive or negative dilatancy in nature. This contractive behaviour has similarities with that of the sand-steel interface. It is interesting to note that the maximum vertical displacement increases with increasing the percent open area of the geosynthetics. The maximum vertical displacements for sand-GT, sand-GG1, sand-GG2 and sand-GG3 interfaces are 0.07, 0.12, 0.34 and 0.44mm respectively. It means that the sand in the apertures of geogrids dominates the dilatancy behaviour of the sand-geogrid interfaces.

4.4 Frictional resistance of the interfaces

The maximum shear stress vs. normal stress values of all six interfaces are presented in Fig. 6. It can be observed that, if

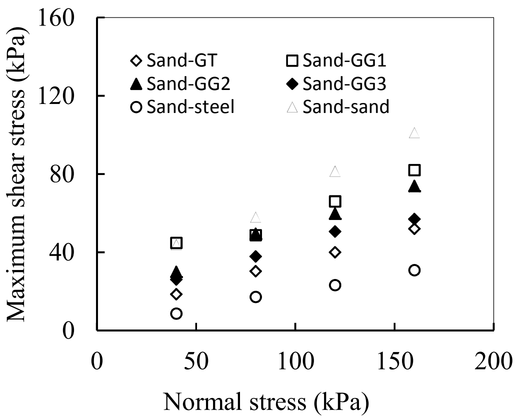

Fig. 6 Maximum shear stress vs. normal stress for all interfaces

linear shear strength envelop is drawn fitting the experiment results it would define a little cohesion intercept. This intercept may be induced probably due to nonlinearity of the shear strength envelop. The sand-sand interface obtained maximum friction angle of 34.5° whereas the minimum friction angle of 10.5° is found for sand-steel interface. The friction angles of sand-GT, sand-GG3, sand-GG2 and sand-GG1 interfaces are obtained as 18.5°, 21.5°, 27° and 29.5°, respectively. It is observed that among all sand-geosynthetic interfaces, the sand-GG1 interface develops the highest frictional resistance whereas sand-GT interface develops the lowest resistance which is about 86% and 54%, respectively, of the sand-sand interface frictional resistance. Although the frictional resistance of sand-GG2 interface is closer to that of sand-GG1 interface, significant difference is observed for sand-GG3 interface. The possible reason of this phenomenon is already discussed in the previous section.

4.5 Interface efficiency

To calculate efficiency of the sand-geosynthetic interfaces, the peak shear strength of Toyoura sand (τ_s) at each normal stress is considered as a reference value. It is to note that the shear strength values are the test values and not the fitted values using Mohr-Coulomb failure criterion. The shear strength values of sand-geosynthetic interfaces ($\tau_{s\text{-}g}$) were normalized using the reference values at the corresponding normal stress level (40, 80,120 and 160kPa). The normalized value is identified as the interface shear strength efficiency or interface efficiency ($E_i = \tau_{s\text{-}g}/\tau_s$). In literature similar relationships have been identified as "bond coefficient" [5], "interface efficiency"[9], and interface shear strength coefficient [14]. The interface efficiency of different sand-geosynthetic interfaces are shown in Table 2.

Table 2 Interface efficiency of sand-geosynthetic interfaces

Interfaces	Normal stress, kPa				Average
	40kPa	80kPa	120kPa	160kPa	
Sand-sand	1.00	1.00	1.00	1.00	1.00
Sand-GG1	1.02	0.84	0.81	0.83	0.87
Sand-GG2	0.68	0.85	0.73	0.75	0.75
Sand-GG3	0.59	0.65	0.62	0.56	0.61
Sand-GT	0.42	0.52	0.49	0.51	0.49

Table 2 shows that the sand-GT interface strength is significantly lower than the shear strength of the sand. Unlike geogrids, the woven geotextile does not allow direct contact between sand particles. Hence, the shear resistance comes only from shear between geosynthetic surface and the sand particles. It is observed that the efficiency of sand-GG1 interface is higher than other sand-geosynthetic interfaces. Although, at 80kPa of normal stress, the efficiency of sand-GG2 interface is little higher than that of the sand-GG1 interface. It is interesting to note that the efficiency of GG1 interface at low normal stress (40kPa) is higher (1.02) than sand. But, this is not exception in the literature. Cancelli et al. [12] reported interface shear strength coefficients ranging from 1.04 to 1.12 for interfaces between HDPE and polypropylene (PP) geogrids against sand, Cazzuffi et al. [13] reported interface shear strength coefficient of 0.97 for sand-HDPE geogrid interface, while Liu et al. [21] found interface shear strength coefficients for sand-PET (coated with PVC) geogrid interface ranging from 0.89 to1.01. For the sand-geogrid interfaces tested in this study, the average interface efficiency ranges from 0.61 to 0.87. However, the interface efficiency of the same geosynthetic would vary depending on the backfill material used in the field. Thus, there is scope for further investigation to evaluate the interface efficiency for different backfill materials like cohesive soils and soil with various admixtures which may increase interface efficiency.

5. CONCLUSION

This study was carried out to evaluate the interface behaviour of basalt geosynthetic with sand by a series of direct shear tests. The main conclusions that can be drawn from this investigation are as follows:

1. The interface shear strength of all sand-geosynthetic interfaces increased with the increasing normal stresses.
2. Strain hardening-softening behaviour is clearly observed for all sand-geogrids (GG1, GG2 and GG3) interfaces which resembles the shear stress-displacement behaviour of the sand. The sand-geotextile (GT) interface shows strain hardening behaviour before peak and almost plastic condition is observed after the peak.
3. Due to small size apertures and thin ribs of GG1, large shear stress is exerted from the initial stage of shear. Since GG2 and GG3 have larger apertures, the shear stress is found relatively low due to less confinement of sand in the apertures as well as less geosynthetic area for effective skin friction.
4. The maximum vertical displacement increases with increasing the percent open area of the geosynthetics which is 0.07, 0.12, 0.34 and 0.44mm for sand-GT, sand-GG1, sand-GG2 and sand-GG3, respectively. It means that the presence of sand in the apertures of geogrids dominates the dilatancy behaviour of the sand-geogrid interfaces.
5. The interface efficiency of sand-GG1 interface is found higher than other sand-geosynthetic interfaces which was even higher (1.02) than sand itself at low normal stress. However, the average interface efficiency of the sand-geogrid interfaces tested in this study ranges from 0.61 to 0.87.

6. REFERENCES

[1] Ingold, TS., "Laboratory pull-out testing of grid reinforcements in sand", Geotech. Testing J.,vol.6, No. 3, 1983, pp. 101-111.

[2] Jewell, RA and Milligan GWE,"Interaction between soil and geogrid", Polymer grid reinforcement, Conference publication, Thomas telfold Limited, London, March 1985, pp. 18-30.

[3] Palmeria E M and Milligan GWE, "Scale and other factors affecting the results of pull-out tests of grids buried in sand", Géotechnique, vol.39, No. 3, 1989, pp. 511-524.

[4] Bergado, D. T., Chai, J.C., Abiera, H. O., Alfaro, M.C., Balasubramaniam, "Interaction between Cohesive-Frictional Soil and Various Grid Reinforcements", Geotextiles and Geomembranes, Vol. 12, No. 4, 1993, pp. 327 – 349.

[5] Bergado D. T., Shivashankar R., Alfaro M. C., Chai JC, Balasubramaniam A. S., "Interaction behaviour of steel grid reinforcements in a clayey sand", Géotechnique, 1993, vol.43, No.4, pp. 589-603.

[6] Alfaro M., Miura N., Bergado D. "Soil-Geogrid Reinforcement Interaction by Pullout and Direct Shear Tests", Geotech. Test. J., 1995, vol.18, No.2, pp. 157-167.

[7] Tatlisoz, N., Edil, TB. and Benson CH., "Interaction between Reinforcing Geosynthetics and Soil-Tire Chip Mixtures", J. Geotech. Geoenviron. Eng., 1998, vol.124, No.11, pp. 1109-1119.

[8] Mitachi, T., Yamamoto, Y. and Muraki, S.,"Estimation of in-soil deformation behavior of geogrid under pull-out loading", Proc., Int. Symp. on Earth Reinforcement , Kyushu Univ., Fukuoka, Japan, vol. 1, 1992, pp. 121–126.

[9] Nakamura T, Mitachi T and Ikeura I, "Direct shear testing method as a means for estimating geogrid-sand interface shear-displacement behavior", Soils and Foundations, vol. 39, No.4, 1999, pp. 1-8.

[10] Cancelli, A., Rimoldi, P., and Togni, S., "Frictional characteristi cs of geogrids by means of direct shear and pullout tests", Proc., Int. Symp. on Earth Reinforcement , Kyushu Univ., Fukuoka, Japan, 1992, pp. 51–56.

[11] Cazzuffi, D., Picarelli, L., Ricciuti, A., and Rimold, P., "Laboratory investigations on the shear strength of geogrid reinforced soils", ASTM Spec. Tech. Publ., 1993, 1190, pp. 119–137.

[12] Bakeer, R. M., Sayed, M., Cates, P., and Subramanian, R., "Pullout and shear test on geogrid reinforced lightweight aggregate", Geotextiles and Geomembranes, vol. 16, No. 2, 1998, pp. 119–133.

[13] Hossain, MZ, "Dilatancy behavior of soil-structure interfaces for farm roads and embankments", Australian Journal of Agricultural Engineering, vol. 2, No. 1, 2011, pp. 12-17.

[14] Ingold, T.S., "The geotextile and geomembranes manual", Elsevier Advanced Technology, ISBN: 1856171981, 1994, pp. 610, U.K.

[15] Kishida, H., and Uesugi, M., "Tests of interface between sand and steel in the simple shear apparatus", Ge´otechnique, vol. 37, No. 1, 1987, pp. 45–52.

[16] Tsubakihara, Y., Kishida, H., and Nishiyama, T., "Friction between cohesive soils and steel", Soil and Foundation, vol. 33, No. 2, 1993, pp. 145–156.

[17] Tejchman, J. and Wu, W., "Experimental and numerical study of sand–steel interfaces", International Journal for Numerical and Analytical Methods in Geomechanics, 19, 1995, pp. 513–536.

[18] Uesugi, M., Kishida, H., and Tsubakihara, Y., "Behavior of sand particles in sand–steel friction", Soils and Foundations, vol. 28, No. 1, 1988, pp. 107–118.

[19] Uesugi, M., Kishida, H., "Influential factors of friction between steel and dry sands", Soils and Foundations, vol. 26, No. 2, 1986, pp 33-46.

[20] Evgin, E. and Fakharian, K., "Effect of stress paths on the behaviour of sand-steel interfaces", Canadian Geotechnical Journal, vol. 33, No. 6, 1996, pp. 853-865.

[21] Liu, C.N., Zornberg, J. G., Tsong C. C., Ho, Y.H. and Lin, B.H., "Behavior of Geogrid-Sand Interface in Direct Shear Mode", Journal of Geotechnical & Geoenvironmental Engineering, vol. 135, No. 12, 2009, pp. 1863-1871.

First International Conference on Geotechnique, Construction Materials and Environment, Mie, Japan, Nov.21-23, 2011, ISBN: 978-4-9905958-0-7 C3051

Effect of Soil Parameters Uncertainty on Seismic Response of Buried Segmented Pipeline

Chaminda Gallage, School of Urban Development, Queensland University of Technology, Brisbane, Australia
Pathmanathan Rajeev, Department of Civil Engineering, Monash University, Melbourne, Australia
Jayantha Kodikara, Department of Civil Engineering, Monash University, Melbourne, Australia

ABSTRACT: Pipelines are important lifeline facilities spread over a large area and they generally encounter a range of seismic hazards and different soil conditions. The seismic response of a buried segmented pipe depends on various parameters such as the type of buried pipe material and joints, end-restraint conditions, soil characteristics, burial depths, and earthquake ground motion, etc. This study highlights the effect of the variation of geotechnical properties of the surrounding soil on seismic response of a buried pipeline. The variations of the properties of the surrounding soil along the pipe are described by sampling them from predefined probability distribution. The soil-pipe interaction model is developed in OpenSEES. Nonlinear earthquake time-history analysis is performed to study the effect of soil parameters variability on the response of pipeline. Based on the results, it is found that uncertainty in soil parameters may result in significant response variability of the pipeline.

Keywords: Buried pipe, soil-pipe interaction, soil parameters, uncertainty, seismic response

1. INTRODUCTION

Buried segmented pipelines are commonly used in many lifeline systems, such as water distribution and gas supply systems, etc. There are several publication and reports that discuss the severe damage to civil life cause by the failure of buried pipelines during or after the high-intensity earthquake [1], [2]. After the Hyogo-Ken Nanbu earthquake of 1995 in Japan, it was reported that gas leakage from buried pipelines occurred at 234 different places; subsequently, fires started primarily due to gas release and electricity sparks. Fires occurred at 531 different places and burnt areas were over 1 km^2 [3]. Another example, the Chi-Chi earthquake of 1999 in Taiwan also caused serious damage to natural gas supply systems. More than 100,000 industrial and residential customers in the disaster area were cutoff from the natural gas supply after the earthquake, and the estimated economic loss of five major natural gas companies was approximately US$ 25 million [4].

During the 1994 Northridge earthquake, several pipelines and aqueducts were broken due to large permanent ground deformation; and during the 1995 Kobe earthquake, around 2000 repairs had to be done in the water distribution system due to significant ground shaking, ground distortion, and liquefaction in the artificial fills constructed near the bay [5]. Due to the serious consequences of lifeline system failure under earthquakes, their seismic performance has been the subject of many research studies. The performance of a pipeline under seismic load depends on type of buried pipe material and joint, end-restraint conditions, soil characteristics, earthquake ground motion, and burial depths etc. In this paper, the effect of soil parameters uncertainty in seismic response of pipeline in longitudinal direction is investigated. The dynamic soil-pipe interaction is developed using Winkler-based approach with nonlinear discrete soil springs in longitudinal and vertical directions. The effect of soil variability in seismic response is modeled using probabilistic approach.

2. PIPELINE CONSIDERATION

A cast iron pipeline of 120 m long with lead caulked pipe joint buried in sandy soil with fixed end condition is considered in this study. The length of pipe segment (l_s), yield strength (f_y), outer diameter (D) and burial depth (H) are 6 m, 250 MPa, 150 mm and 800 mm, respectively. The friction coefficient (δ), depending on the outer-surface characteristics and hardness of the pipe, is taken as 0.8. It is assumed that the pipeline is placed well above the ground water level; therefore, the soil liquefaction is not considered. The change in internal pressure in the pipeline and the live load over the ground surface are neglected.

3. FINITE ELEMENT MODELING OF PIPELINE

Finite element analysis of the pipe-soil system is performed using OpenSEES finite element analysis package [6]. Pipe segment is modeled with elastic beam element and the joint is modeled using zero-length element with nonlinear material model. Also, the soil response in vertical and axial direction is modeled with zero-length element and nonlinear material model. The schematic diagram of pipe-soil system is shown in Fig.1.

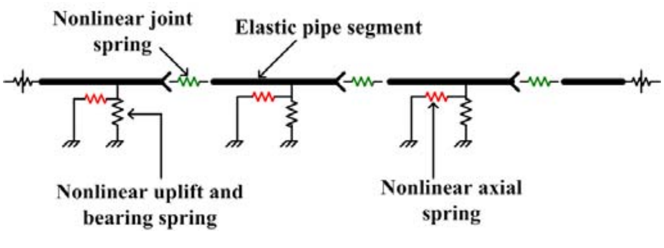

Fig.1. Schematic diagram of pipe-soil system

3.1 Behavioral model for soil spring

The force-displacement behavior of axial soil springs are based upon recommendations in the 1984 ASCE Guideline for Gas and Liquid Fuel Pipelines [7] for non-cohesive backfill. The nonlinear behavior of axial spring is shown in Fig. 2 (right).

A symmetric bilinear-type curve (elastic-perfectly plastic) is employed with a peak force per unit length at the soil-pipe interface, T_u:

$$T_u = \frac{\pi}{2} DH\gamma(1+K_0)\tan(\delta\phi) \tag{1}$$

where γ is the effective unit weight of the soil, ϕ is the angle of internal friction of the sand and K_o is the coefficient of lateral soil pressure at rest. The equivalent "yield" displacement (Δ_t) for the soil spring is typically about 2 mm.

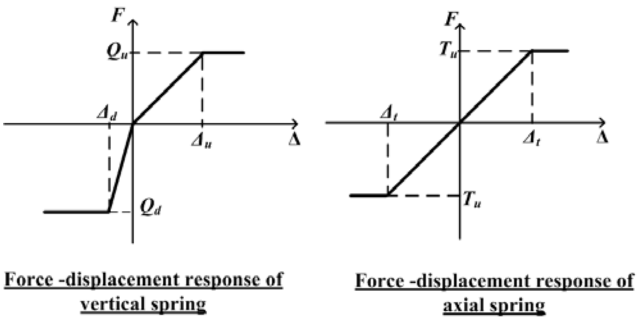

Fig.2. Nonlinear force-displacement behavior of soil springs: vertical spring (left); axial spring (right)

The nonlinear behavior of vertical soil springs is shown in Fig. 2 (left). The upward soil resistance per unit length (Q_u) of the pipe in sandy soil can be determined as:

$$Q_u = N_{qv}\gamma HD \tag{2}$$

$$N_{qv} = \frac{\phi H}{44D} \le N_q \tag{3}$$

$$N_q = \exp(\pi\tan\phi)\tan^2\left(45^0 + \frac{\phi}{2}\right) \tag{4}$$

The corresponding displacement, Δ_u at Q_u can be taken as $0.01H$ for the dense sand.

The vertical bearing soil spring force per unit length (Q_d) can be calculated by:

$$Q_d = N_q\gamma HD + N_\gamma\gamma\frac{D^2}{2} \tag{5}$$

$$N_\gamma = \exp(0.18\phi - 2.5) \tag{6}$$

The displacement, Δ_d , at Q_d is 0.1D for granular soil. A more detailed description of (1) to (6) is provided in the American Lifeline Alliance, ASCE [8].

3.2 Behavioral model for pipe joint

The axial force-deformation relationship considered for the lead caulked pipe joint is based on the study reported in [9]. The force-displacement response is represented by bi-linear relationship as shown in Fig. 3.

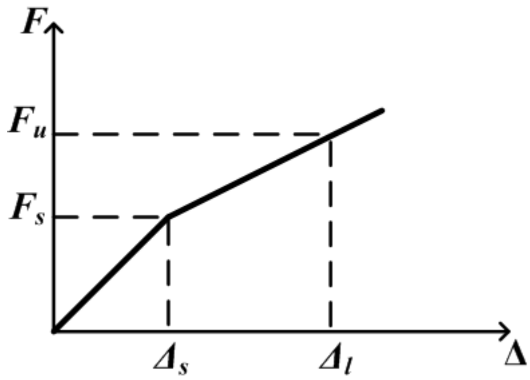

Fig.3. Axial force-displacement behavior of joint spring

There is an initial elastic region until slippage at a relative joint displacement of Δ_s, followed by a linear post-slippage region until leakage at a relative joint displacement of Δ_l. The axial force at slippage, F_s, is based upon a model proposed in [10].

$$F_s = C_a\pi Dd_1 \tag{7}$$

where C_a is the adhesive strength at the pipe/lead interface and d_l is the depth of lead caulking. The average value of C_a is around 1.7 MPa, and d_l for a 150 mm diameter pipe is 55 mm. The initial stiffness of the joint and the joint force at leakage also reported in [9]. For 150 mm diameter pipe the initial stiffness is quite large, resulting in a typical slippage displacement of only about 3.3 μm. The joint force at leakage is equal to twice the slippage force. The slippage displacement at leakages (Δ_l) is taken as 16.5 mm.

4. EARTHQUAKE GROUND MOTION

In order to perform nonlinear time-history analyses, the acceleration time history recorded at El-Centro during Imperial Valley California (1940) is considered. The characteristics of the record are: the magnitude (M_w) is 6.6, source-to-site distances (r) range is 8 km and soil condition is stiff. The maximum acceleration to velocity ratio (A/V) is 1.04, where A is in 'g' and V is in m/s. Fig.4 shows the acceleration time history and acceleration response spectra with 5% damping of El-Centro record.

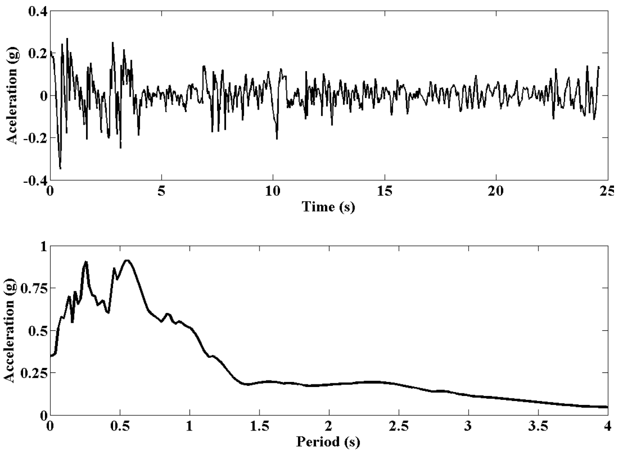

Fig.4. El-Centro acceleration time history (top) and response spectrum (bottom)

5. VARIABILITY IN SOIL PROPERTIES AND THEIR MODELING

It is evidence from section 3.1, that the soil proprieties are one of the performance controlling parameter of pipe-soil system. The force-displacement behavior of soil spring is controlled by the soil parameters. Thus, it is essential to investigate the effect of soil parameters uncertainty in seismic response of buried pipelines. In this study, the soil properties such as internal friction angle and unit weight of soil are considered as uncertain variable. Those variables are assumed be described by lognormal distribution, since they are necessarily positive values. Table 1 shows the list and respective mean values and corresponding 10% coefficient of variation (CV) of the input parameters. Although some studies have reported that a larger variation of the in situ CV, the 10% CV for different soil types including, sand, clay and silt seems to be reasonable [11]. No correlation between internal fraction angle and unit weight is considered.

Table.1 Statistical property of soil parameters

Parameter	Mean	CV (%)	Distribution
Friction angle	35^0	10	Lognormal
Unit weight	16 (kN/m^3)	10	Lognormal

6. TREATMENT OF UNCERTAINITY IN SEISMIC RESPONSE ANALYSIS

Seismic response analysis of the pipeline which incorporates the source of uncertainty considered above can be carried out using random sampling Monte Carlo simulation coupled with the finite element pipeline model. Fig. 5 shows histogram of 500 values of random sampled fraction angle and unit weight of soil.

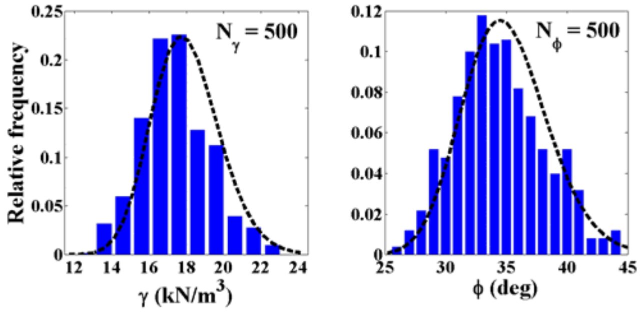

Fig.5. Histogram of sampled soil unit weight (left) and fraction angle (right)

Each randomly generated (γ,φ) pair is input into the finite element model and time history analysis is performed to predict the response. The natural period of the pipeline with mean value of soil property is 0.27 s.

7. RESULTS AND DISCUSSION

Fig.6 shows the axial displacement of pipeline, which has the mean values of the soil properties, at different time in the time history analysis. The displacement is concentrated at the joints and the maximum displacement is occurred at the middle section of the pipeline. The maximum pipe displacement observed at the middle of the pipeline is approximately 24 mm.

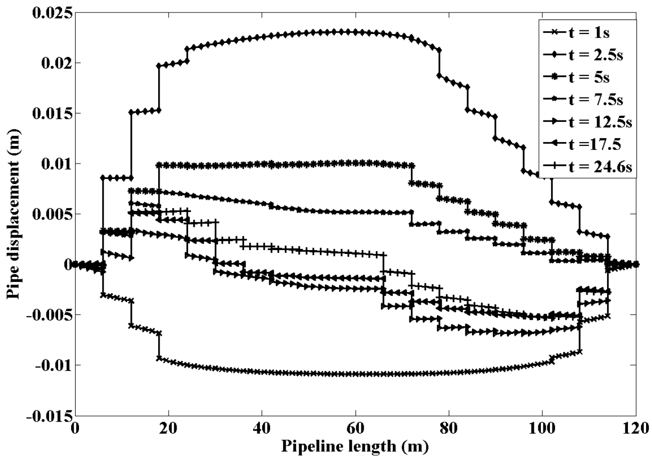

Fig.6. Axial displacement of pipeline at different time in the time history analysis

The maximum relative displacement is observed at the joints which are close to the supports. Fig.7 shows the maximum relative displacement at each joint along the pipeline. The maximum relative displacement at the joints is close to 9 mm which is less than the slippage displacement at leakages. The joint at the middle of the pipeline shows no relative displacement for the mean valued model. The maximum relative displacement is high at the joints close to support and decreases towards the middle of the pipeline.

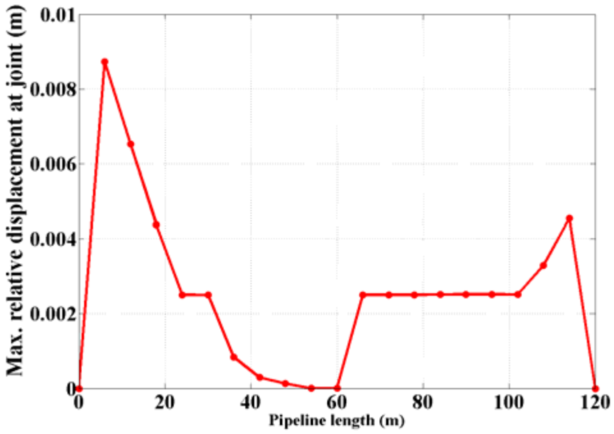

Fig.7. Maximum relative displacement at the joint during time history analysis

To study the effect of single soil parameter on the response, the lower and the upper value among the sampled values of each parameter is selected, while keeping the other one in its mean. Fig. 8 shows the effect of unit weight of soil on the response. For the upper value of the unit weight, the maximum relative joint displacement response is increased in general compare to the mean valued model response and decrease for lower value of the unit weight. It may be due to the fact that the mass of the system is increased with increasing unit weight and consequently the system subjected to higher inertia force, which causes larger displacement in the system. In the case of lower value of unit weight of soil, a few joints at the middle part of the pipeline show no relative displacement.

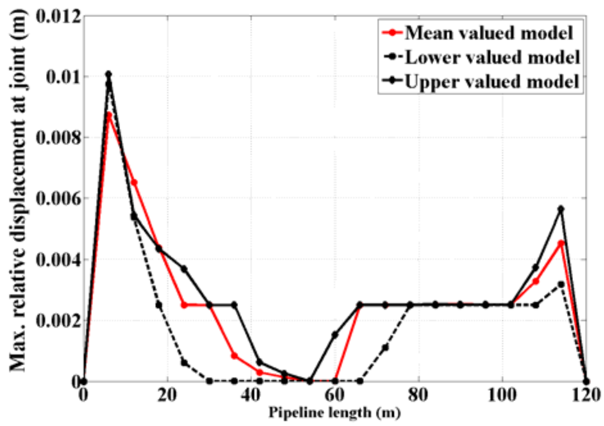

Fig.8. Effect of unit weight on the maximum relative displacement at the joint

Fig.9 shows the effect of internal fraction angle of soil on the maximum relative joint displacement response. For the lower value of the soil fraction angle, the joint displacement is increased and for the upper value of the fraction angel the joint displacement is decreased significantly from the mean valued model. Due to large axial soil fractional forces in the pipe segment, a few joints at each side from the middle section of the pipeline show no relative displacement for upper value of fraction angle. Contrary, the pipeline shows significant increase in relative joint displacement for lower value of frication angle from the mean valued model. Further, the effect of fraction angle on the response of the system is much significant compare to the unit weight of the soil.

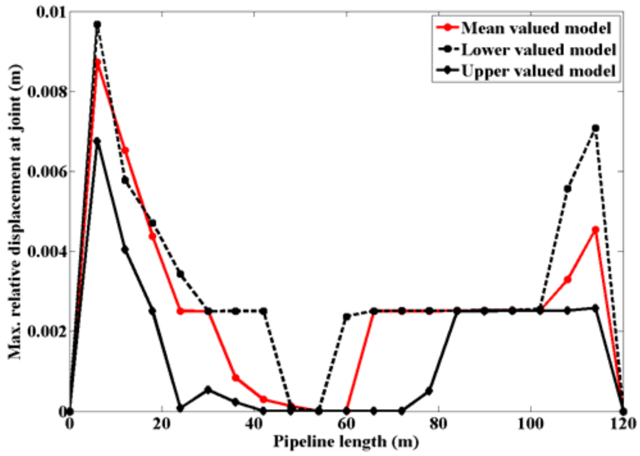

Fig.9. Effect of friction angle on the maximum relative displacement at the joint

Fig. 10 shows the 95% confidence bound and median of the maximum relative joint displacement response from the random sampled model together with the mean-valued model response. The median and mean-valued model responses are essentially the same. But the variability in the response due the uncertainty in the soil properties is significantly high.

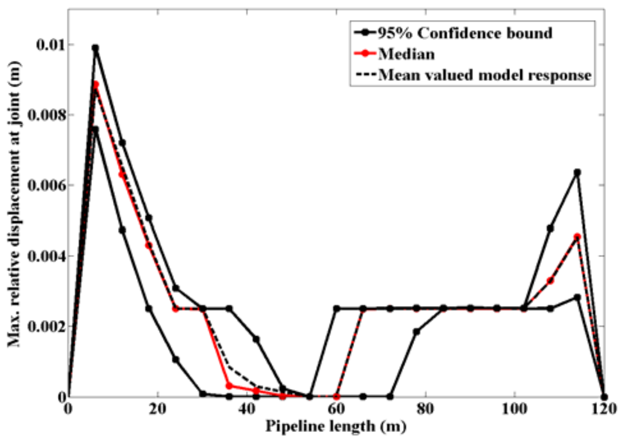

Fig.10. Mean-valued pipeline model response and 95% confidence bound and median of random sampling model response

8. CONCLUSION

The influence of soil parameters uncertainty on the seismic response of buried segmented pipeline is investigated in this paper. A 120 m long pipeline in sandy soil is molded using nonlinear Winkler approach to represent the soil behavior. Random sampling method is used to randomize the soil parameters. The effect of different types of soil is not considered. Within this limitation, the analysis results show that the uncertainty in soil property has significant influence on the displacement response of pipeline. The influence of internal fraction angle is significant compare to unit weight of the soil. The coefficient of variation of joint response is more than 100% in some location. Finally, it is important to consider the variability in soil properties in seismic risk assessment of pipeline.

9. REFERENCES

[1] Ayala G and O'Rourke MJ, "Effects of the 1985 Michoacan earthquake on water systems and other buried lifelines in Mexico", Report No. NCEER-89-0009, National Center for Earthquake Engineering Research, State University of New York at Buffalo, 1989.

[2] Wang L, Shao-ping S and Shijie S, "Seismic damage behavior of buried lifeline systems during recent severe earthquakes in U.S., China and other countries", Technical Report No. ODU Lee-02, Old Dominion University Research Foundation, 1985.

[3] Scawthorn C and Yanev PI, "Preliminary report on Hyogo-ken Nambu, Japanese earthquake" Eng Struct, Vol. 17(3), 1995, pp.146-57.

[4] Chen WW, Shih BJ, Wu CW, "Chen YC. Natural gas pipeline system damages in the Ji-Ji earthquake (The City of Nantou)", In: Proc of the 6th international conf on seismic zonation, 2000, pp ..

[5] Eidinger JM. and Avila EA, Guidelines for the Seismic Evaluation and Upgrade of Water Transmission Facilities. Monograph # 15. Technical Council on Lifeline Earthquake Engineering, American Society of Civil Engineers, 1999.

[6] McKenna F, Fenves GL, Jeremic B and Scott MH,Open System for Earthquake Engineering Simulation, http://opensees.berkely.edu, 2007.

[7] American Society of Civil Engineers, Guidelines for the Seismic Design of Oil and Gas Pipeline Systems Reston, VA, 1984, pp. 473..

[8] American lifelines alliance, Guidelines for the design of buried steel pipe. ASCE, 2001.

[9] Hmadi EI and O'Rourke, MJ, Seismic Wave Effects on Straight Jointed Buried Pipeline. Technical Report NCEER-89-0022, Multidisciplinary Center for Earthquake Engineering Research, New York,1989

[10] O'Rourke TD and Trautmann CH, Analytical Modeling of Buried Pipeline response to Permanent Earthquake Displacements, Report No 08-4, School of Civil Engineering and Environmental Engineering, Cornell University, Ithaca, New York, 1980.

[11] Jones AL Kramer SL and Arduino P, Estimation of uncertainty in geotechnical properties for performance-based earthquake engineering. Technical Report 2002/16, Pacific Earthquake Engineering Research Center, PEER, 2002.

First International Conference on Geotechnique, Construction Materials and Environment, Mie, Japan, Nov.21-23, 2011, ISBN: 978-4-9905958-0-7 C3051

The Sorption Capacity of Cu by SC-Soil from Batch and Column Tests

Arwut Yimtae, Pongsakorn Punrattanasin and Noppadol Sangiumsak
Faculty of Engineering, Khon Kaen University, Thailand

ABSTRACT: This paper presents the sorption capacity of Cu by SC-soil collected from a location in the Northeastern part of Thailand. Copper (Cu) is one of the common heavy metals that have been discharged from industries and from the use in the daily life of human being. The toxic conditions from Cu are always occurred with plants, animals, and human from this metal. The batch equilibrium method was used as a tool to investigate the adsorption value. The results from batch tests can demonstrate the sorption isotherm of the soil. The results showed that the adsorption isotherm well fit both the Langmuir and Freundlich models. The next series of test were evaluated by performing column leaching test. The purpose of the test is to investigate the transportation phenomena of liquid into soil layer. This method is also for the assessment of ground water risk due to pollutant emission from contaminated soil.

Keywords: Copper, Adsorption, Isotherm, Langmuir

1. INTRODUCTION

Due to economic growth during many decades in Thailand especially in the Northeastern part, industrial sector leads many environmental problems. Industries discharged the waste water into river or soil without treatment and care. Copper (Cu) is one kind of heavy metals and toxins that has caused serious health problem to humans and animals [1,2]. There are many methods for remove the heavy metals from the waste water and soil [3,4,5]. Adsorption is one of the most common methods for heavy metal removal because it is an effective and economical technique. This is the main objective that brought about the research to be a choice of improving pollution problem by focusing on the sorption capacity of heavy metal by soil. In this work, the adsorption of Cu by soil found in the Northeastern part of Thailand was studied and investigated by batch and column techniques.

2. MATERIALS AND METHODS

2.1 Adsorbent

The material used as adsorbent was soil collected from one location in the upper part of Northeastern (Fig.1), Thailand. It was excavated at a depth of 50 cm from its surface (Fig.2). The soil was dried at a temperature of 110 ^{o}C for 48 hours and was sieved through sieve No.16. It can be classified by the Unified Soil Classification System (USCS) as SC-Soil. It will then be called SC-Soil throughout this paper. Engineering properties and porous properties of the soil sample are tabulated and shown in Table 1. The porous properties were evaluated by adsorption of nitrogen gas (N_2) at -196 ^{o}C. The specific surface area was calculated by Brunauer-Emmett-Teller (BET) equation. Figure 3 shows the SEM photographs of the soil with different magnifications. As shown in Fig 3, it can be seen that the surface of soil particles are almost rough. Table 2 summarized the compound composition of this soil by using XRF technique.

Fig.1 The aerial view of the location of excavation pit

Fig.2 The collection of soil sample

Table 1. Engineering properties of soil

Soil	SC-Soil
Specific gravity	2.65
Optimum moisture content (OMC), %	18.28
Maximum dry unit weight (γ_d), kN/m^3	16.48
Coefficient of permeability (k), cm/s	0.51 x10^{-6}
Specific surface area (S_{BET}), m^2/g	103
Micropore volume (V_{DR}), cm^3/g	0.040
Total pore volume (V_T), cm^3/g	0.21
Average pore diameter (D_P), nm	8

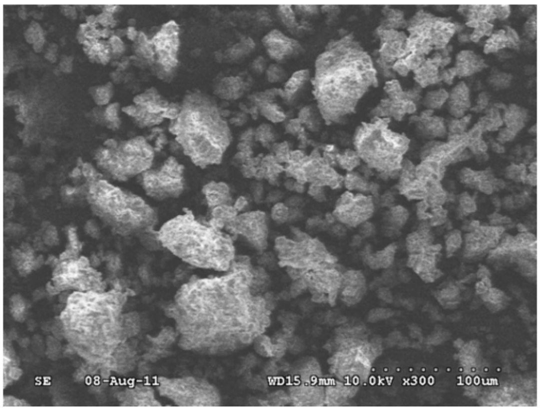

(a) x300

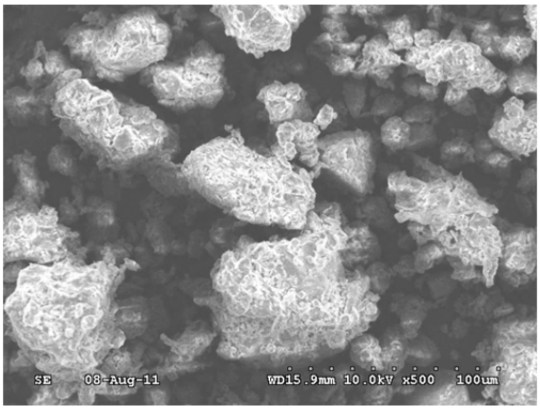

(b) x500

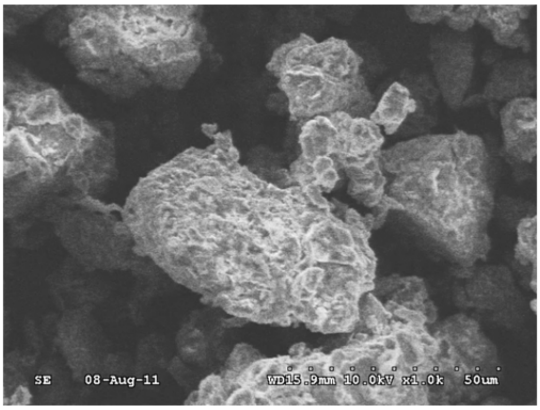

(c) x1000

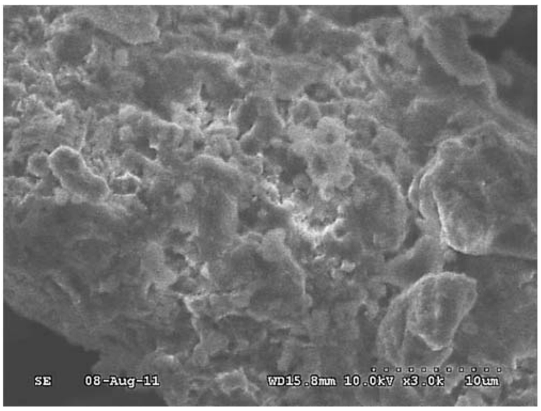

(d) x3000

Fig.3 SEM photograph of SC-Soil at different magnifications

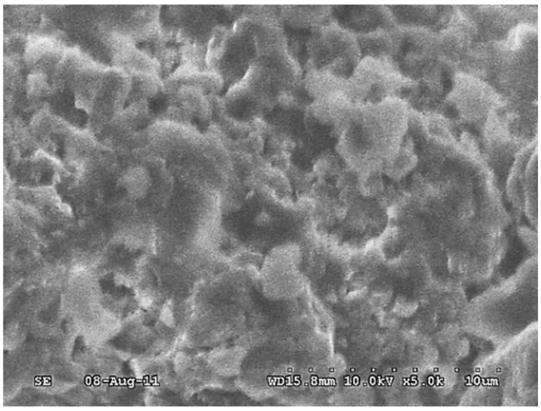

(e) x5000

Fig.3 SEM photograph of SC-Soil at different magnifications

Table 2. Compound composition of SC-soil

	O	Si	Al	K	Ti	Ca	P	Mg
(%)	51.26	36.89	8.62	1.54	0.61	0.39	0.37	0.31

2.2 Heavy Metal Solution

Heavy metal chosen as the adsorbed materials in this study was copper (Cu). It was prepared by dissolving Copper Nitrate ($Cu(No_3)_2$) in distilled water. The solutions were varied with concentrations of 5, 25, 50, 100, 250 and 500 mg/L. Table 3 summarized properties of copper nitrate. Selection of Cu as a heavy metal was based on its low toxicity and also Cu is easily found in all areas and Cu is commonly discharged from various industries.

Table 3. Properties of copper nitrate

Compound	Copper Nitrate
Formula	$Cu(NO_3)_2$
Molecular weight (g/mol)	295.65
Density (g/cm^3)	2.07
Solubility (g/100 ml)	137.8

2.3 Experimental work

In this study, batch and column adsorption tests were carried out to investigate the heavy metal adsorption. The batch test processes can be performed by mixing a 2.5 g of soil with the Cu solution. The initial concentrations were ranged from 5 to 500 mg/L and put it in 120 mL plastic bottle. Then the mixture was shaken by the horizontal shaker with a speed of 130 cycles per minute for 0.5, 1, 3, 6, 12, 24, 48, and 72 hours. After a particular period of the time, the soil was separated from the heavy metal solution by using a 0.45μm filter and diluted it into the solution. Finally, concentration of the residual solution was analyzed by using Atomic Adsorption Spectrometer (AAS) (Fig.4). From the step above, it can be measured the adsorption equilibrium time and the amount of heavy metal adsorbed by soil at equilibrium time (q). The equilibrium amount of heavy metal can be calculated from the following equation:

$$q = \frac{(C_o - C_{eq})V_{sol}}{M_s} \quad (1)$$

Where q is the adsorption capacity of the soil at equilibrium condition (mg/g), C_o is the initial concentration of heavy metal solution (mg/g), C_{eq} is the equilibrium concentration of the solution (mg/g), V_{sol} is the volume of solution (cm^3), and W is the mass of soil (g). After the adsorption volume was determined, the adsorption isotherm can then be investigated. The adsorption isotherm is the relationship between the concentration of the heavy metal solution at equilibrium condition (C_{eq}) and the equilibrium amount of heavy metal adsorbed by soil (q). In this study, the Langmuir and Freundlich models were used to describe the adsorption isotherm.

Fig.4 Atomic Adsorption Spectrometer (AAS)

For column leaching test, the purpose of the test is to investigate the transportation phenomena of liquid into soil layer. The column test is commonly used for the determination of desorption or dissolution rates of contaminants from contaminated soil. This method is also for the assessment of ground water risk due to pollutant emission from contaminated soil. The column leaching procedure used in this study is described briefly in Fig.5. Figure 5 show the schematic drawing of equipment used in the column test. The soil sample was compacted by standard compaction method into the column with a maximum dry density and optimum moisture content. Contaminated water is pumped and put in the top container. The soil column and storage tank are connected each other by system of nut. The flow velocity of contaminated solution and water in the column are adjusted by pressure from pressure pump. In this study flow velocity in the column was about 1 m/day, which corresponds roughly to typical groundwater flow velocity. The advantage of column test compared to the batch technique is that the amount of soil used in the column is much larger than in the batch test and the column technique can simulate the conditions as found in the real field.

In this study, three cycles of column test were done to simulate the infiltration of contaminated solution into the soil. In the first cycle, copper solution was used and the solution was infiltrated into the soil under pressure. The concentrations were measured with different elapsed times. In this cycle, a total time of 144 hours or 6 days were used. The elapsed times of 1, 3, 6, 12, 24, 48, 96 and 144 hours were selected to pick up the sample concentrations. The solutions leaked under the sample were then collected and were sent to the lab to measure the concentration by AAS technique. In the second cycle, the distilled water was used as a solution instead of copper. The purpose of this cycle is to simulate the leaching effect from raining. The adsorption of copper around the soil surface was leached by this water. The remaining concentration can then be measured. The results of this effect are depending on the soil type and its physical and chemical properties. The time used in this cycle is the same as in the first cycle. The last cycle was then performed by using the copper solution again. The purpose of the last cycle is to simulate the repetition of leaking of contaminated solutions into the soil. The amounts of leaking solution from the bottom of the container were then sent to measure the concentration after a particular period of times.

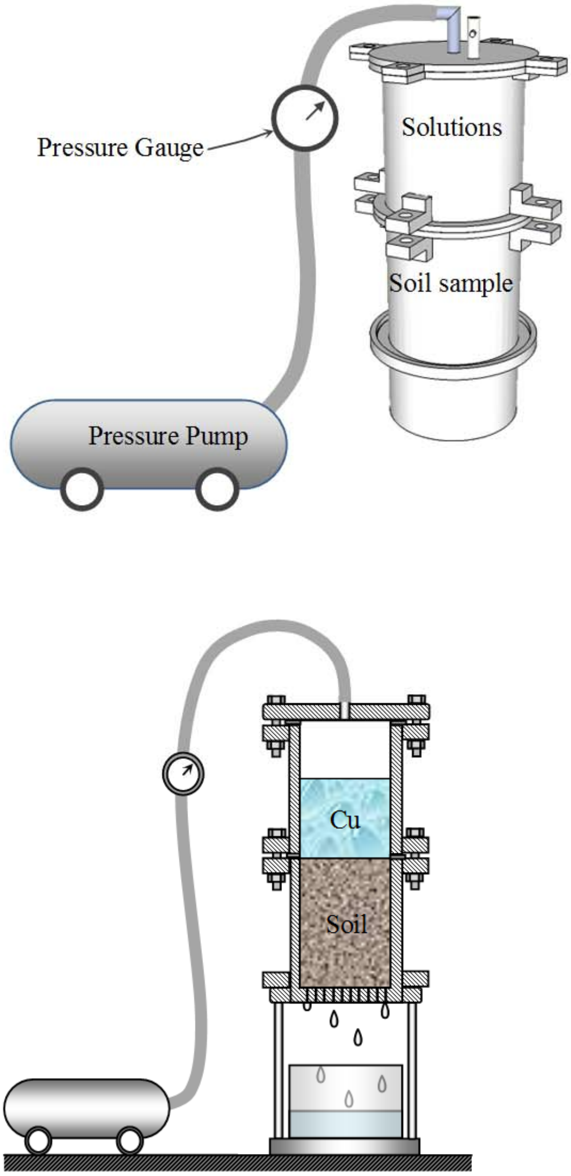

Fig.5 The schematic drawing of column test

3. RESULT AND DISCUSSION

3.1 Adsorption isotherm from batch test

The adsorption of Cu for various concentrations by SC-Soil at different time was shown in Fig 6. The results show the remaining concentration of the heavy metal (C_t) as a function of time. It can be seen that the adsorption took place rapidly at the beginning of the reaction, which the concentration rapidly decreased at the period of 1-3 hours and decline over time until reaching the equilibrium condition within 6-12 hours.

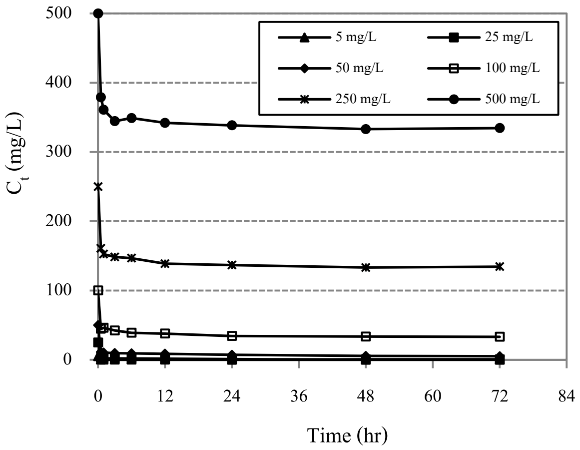

Fig.6 Effect of contact time on Cu adsorption by SC-Soil

Figure 7 showed the adsorption isotherm of Cu. As shown in 6, the amount of adsorption (q) increased with increasing equilibrium concentration (C_{eq}). The adsorption isotherm can be represented by Langmuir and Freundlich adsorption isotherms as shown in Figs 8 and 9, respectively. The consistency of the isotherm describes that the surface of soils was covered with monolayer of the metal particles. Langmuir parameters (β and α) and the coefficient of correlation (R^2) were then summarized in Table 4. Freundlich parameters were summarized in Table 5. Very high coefficient of correlation (R^2) from both models indicated that the adsorption of Cu by soil sample favorable fit both to Langmuir and Freundlich adsorption isotherms.

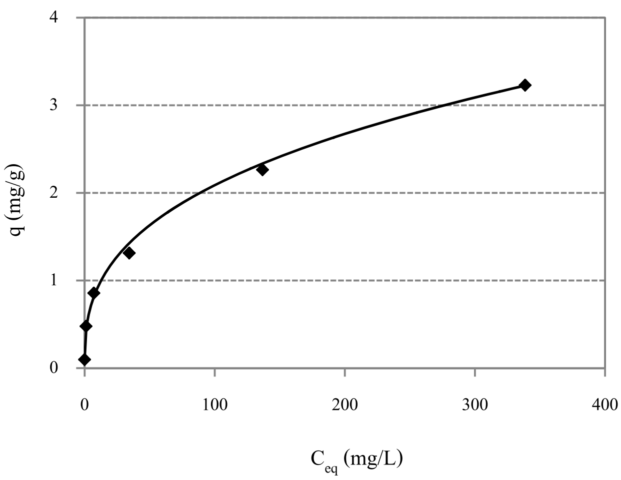

Fig.7 Adsorption isotherm of Cu adsorption by SC-Soil

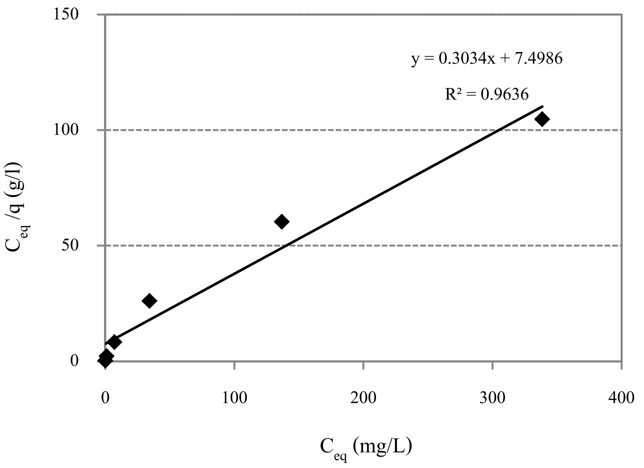

Fig.8 Langmuir adsorption isotherm of Cu

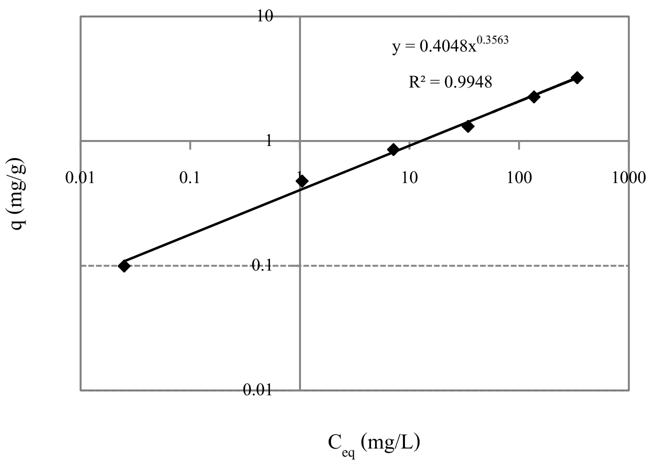

Fig.9 Freundlich adsorption isotherm of Cu

Table 4. Langmuir parameters of soil samples

Soil	β (mg/g)	α (L/mg)	R^2
SC	3.2960	0.0405	0.9636

Table 5. Freundlich parameters of soil samples

Soil	K (L/g)	n	R^2
SC	0.4048	2.8066	0.9948

3.2 The results from column test

The relationship between sorption capacity of Cu and flow rate of polluted solution with a particular time (C_t) are shown in Figs. 10 and 11, respectively. At the first cycle, the initial concentration of 100 mg/l was used. In Fig.10, it can be seen that the measured values of remaining concentration, C_t at a time of 0 hour is approximately 0.9 mg/l. It means that the soil has a high potential to adsorb almost all of the concentration. After a certain period of time, the measured concentrations seem to slightly and slowly increase with time. The reason to explain this phenomenon is that the accumulations of Cu particles on the soil surfaces almost reach the maximum value that soil can offer so that the areas for the adsorption remain smaller. The rate of adsorption found is very slow (1.6 mg/l). In the second cycle (144-288 hours), the distilled water was replaced in the container. The purpose of this cycle is to simulate like a raining occurred above the soil surface. It can be seen in the middle part of Fig.11 that the concentrations of the solution are almost the same as at the end of the first cycle but C_t is not 0. It is indicated that Cu still slightly leaked by the leaching effect of water. In the last cycle (288-432 hours), the copper solution was put into the container again. The measured values of concentration seem slightly increase with time and have a same trend found in the first cycle. It can be said that after leaching by water, the soil can still adsorb copper and the soil did not lost the capacity in adsorbing the copper solution. In Fig. 12, it can be found that the flow rates are in the range of 4-7 cm^3/hr.

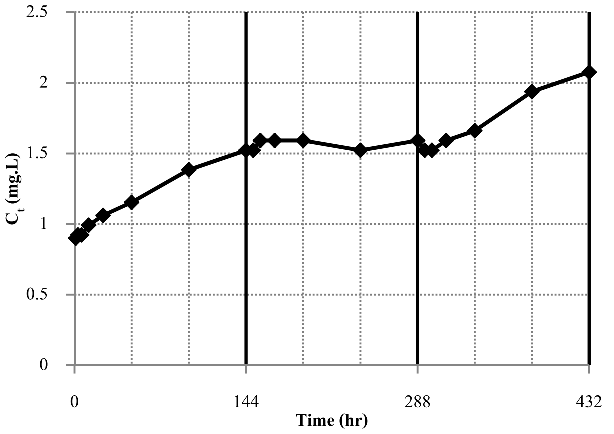

Fig.10 The sorption of Cu at different times by column test

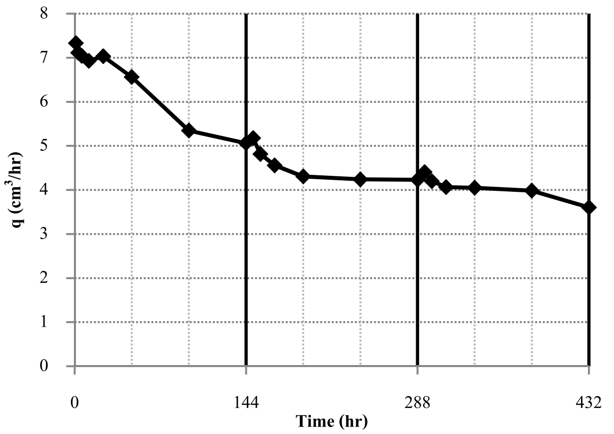

Fig.11 The flow rate of Cu at different times by column test

4 CONCLUSION

In this study, the adsorption capacity of Cu by SC- Soil collected the upper part of Northeastern, Thailand was investigated by performing batch and column leaching tests. The results from batch test indicated that the adsorption reaches the equilibrium time within 6-12 hours. The adsorption capacity increased with increasing initial concentration. Langmuir and Freundlich isotherm models can favorable and well describe the adsorption of this soil. For column leaching test, the purpose of the test is to investigate the transportation phenomena of liquid into soil layer. In this study, three cycles of column test were done to simulate the infiltration of contaminated solution into the soil. In the first cycle, copper solution was used and the solution was infiltrated into the soil under pressure. The concentrations were measured with different elapsed times. In the second cycle, the distilled water was used as a solution instead of copper. The purpose of this cycle is to simulate the leaching effect from raining. The adsorption of copper around the soil surface was leached by this water. The remaining concentration can then be measured. The last cycle was then performed by using the copper solution again. The purpose of the last cycle is to simulate the repetition of leaking of contaminated solutions into the soil.

5 ACKNOWLEDGMENT

This research was funded by Faculty of Engineering, Khon Kaen University. The authors wish to acknowledge and grateful thank to Dr.Arthit Neramittagapong and Ms.Wimomporn Iamamornphonth of the Department of Chemical Engineering, Khon Kaen University.

6 REFERENCES

[1] Mohumed EI Zayat and Edward Smith, “Removal of heavy metals by using activated carbon produced from cotton stalks,” Canadian Journal on Environmental, Construction and Civil Engineering, vol. 1, September. 2010, pp. 71-79.

[2] Y. B. Onundi, A. A. Mamun, M. F. Al Khatib and Y. M. Ahmed , “Adsorption of copper, nickel and lead ions from synthetic semiconductor industrial wastewater by palm shell activated carbon,” International Journal of Environmental Science and Technology, vol. 7(4), 2010, pp. 751-758.

[3] Souag R, Touaibia D, Benayada B and Boucenna A, “Adsorption of heavy metals (Cd, Zn and Pb) from water using keratin powder prepared from Algerien sheep hoofs,” European Journal of Scientific Research, vol. 35, No.3. 2009, pp. 416-425.

[4] Kailas L. Wasewar, “Adsorption of Metals onto Tea Factory Waste: A Review,”IJRRAS, vol. 3(3), June 2010, pp. 303-322.

[5] Tae-Young Kim, Sun-Kyu Park, Sung-Yong Cho, Hwan-Beom Kim, Yong Kang, Sang-Done Kim and Seung-Jai Kim, “Adsorption of heavy metals by brewery biomass,” Korean Journal, Chemical Engineerin, vol. 22(1). 2005, pp. 91-98.

Construction Materials

First International Conference on Geotechnique, Construction Materials and Environment, Mie, Japan, Nov.21-23, 2011, ISBN: 978-4-9905958-0-7 C3051

Green Construction: The Role of Palm Oil Fuel Ash in Concrete

A.S.M. Abdul Awal, Department of Structure and Materials, Faculty of Civil Engineering
Universiti Teknologi Malaysia, 81300 Skudai, Johor, Malaysia

ABSTRACT: The pressing need for the preservation of natural resources and reductions in carbon dioxide emissions together with the ever-rising production volume of concrete to meet the needs of the developing world have fuelled the search for alternative solutions. As the green construction movement begins to hit its stride, recycling of waste and utilization of supplementary cementing materials are gaining promises as efficient and attractive choices in the production of concrete. This paper is a state-of-the-art report on the study and research findings of the behaviour of concrete containing palm oil fuel ash (POFA) as supplementary cementing material. Fresh and hardened state properties including durability aspects of POFA concrete in both indoor and outdoor exposure conditions have been presented and discussed. Along with the typical applications, possible use and potential benefits of the high volume palm oil fuel ash in concrete have also been highlighted in this paper.

Keywords: Supplementary cementing materials, sustainable development, palm oil fuel ash, green construction

1. INTRODUCTION

Over the decades there has been a growing emphasis on the utilization of waste materials and by-products in construction industry. Use of these materials not only helps in getting them utilized in cement, concrete, and other construction materials, but also has numerous indirect benefits such as reduction in land-fill cost, saving in energy and protecting the environment from possible pollution effects. Further, their utilization has shown to improve the microstructure, mechanical and durability properties of mortar and concrete, which are difficult to achieve by the traditional method of concrete construction.

There is no doubt that the inclusion of pozzolanic materials, either naturally accruing or artificially made, as a partial replacement of cement imparts significant enhancements of the basic characteristics of the resulting mass both in its fresh and hardened states. Of all the silicon by-products, pulverized fuel ash or fly ash is widely used globally. Added to this is the fact that fly ash makes significant changes to physical, mechanical and durability properties of concrete that are well documented in national codes and standards. Apart from industrial waste, ashes from agricultural origin like rice husk, coconut husk, corn cob, peanut shell etc. have been identified as supplementary cementing materials in many parts of the world [1]-[4]. One of such pozzolanic materials is palm oil fuel ash, a waste material obtained on burning of palm oil husk and palm kernel shell in palm oil mill plants.

The objective of this paper is to provide a cohesive literature survey on studies published in recent decades, accounting for the contribution or behaviour of palm oil fuel ash (POFA) in concrete, rather than a comprehensive report summary of all the investigations. Being a new member in the ash family, however, POFA has not been studied in all types of concrete works particularly at long-term outdoor exposure conditions. Considering the availability and the inherent quality, significant research findings have been highlighted in regard to the utilization of this ash as a sustainable construction material in concrete.

2. CONCRETE AND ENVIRONMENT

2.1 Waste Materials in Concrete Construction

Concrete is without question one of the oldest and strongest man-made materials in the world where cement as a binding material plays a key role in achieving strength and durability. Portland cement concrete is a fundamental and versatile building material that touches the life of nearly every individual in the modern world. It is difficult indeed to visualize what a comparatively dark age we would be living in without concrete. The economy of many nations is markedly influenced by the cement and concrete industry. It has been estimated that the world-wide consumption of concrete amounts to about one thousand kilogram per person, and this demand is expected to rise in future [5]. However the environmental aspects involved in the manufacture and use of cement, concrete and other building materials are of growing concern. This situation can, however, be improved by effective and efficient utilization of existing materials together with the development of recycled materials generated as industrial or agricultural wastes.

With a given set of constraining conditions waste materials in concrete mixes can be employed in several ways. For many purposes a pozzolan, for example, has been regarded as a substitute for a proportion of cement in a concrete. In some cases, it is preferable to use it as an addition. This involves direct weight addition of pozzolan to cement, replacing part of aggregate (usually sand) in concrete. Another method which Samarin et al. [6] describe as a replacement-addition method that involves replacement of a part of the Portland cement with excess weight of fly ash, replacing also part of the aggregate in order to achieve more economical concrete. According to Dunstan [7], fly ash should be considered to be the 'fourth ingredient' in concrete, that is in addition to the aggregate, cement and water but not as a replacement of the cement. It has also been postulated that only in this way it is possible to obtain the fullest benefits from fly ash, particularly with low lime content. Whatever is the mode of application, all the methods can result in a significant improvement and optimization of certain properties of both fresh and hardened concrete. The strategy of applying pozzolans in concrete, as revised and modified from Hwang [8], is sketched in Fig. 1.

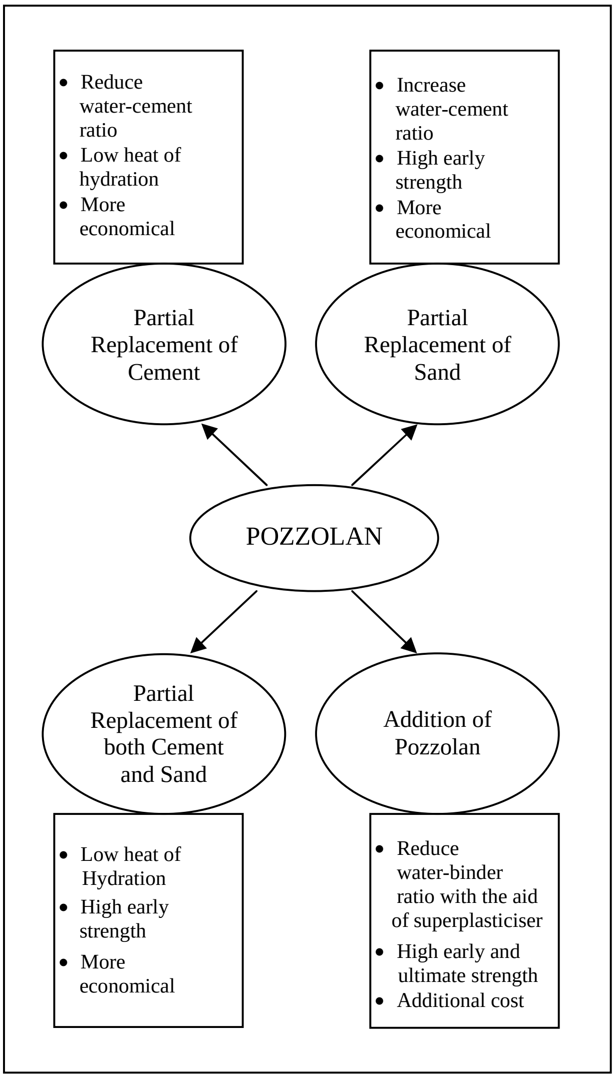

Fig. 1 Strategies of using pozzolans in concrete productions

Although the use of supplementary cementing materials has been increased during the last decades, the amount is still below the satisfactory level. At the same time the data available so far on the performance behaviour of such materials are not ample; the current information can sometimes be confusing regarding their usefulness. In response to growing environmental economic forces it is, therefore, likely that the materials that might have been researched to some extent will require adaptation and further development for full commercial utilization. In this respect, green building practices have all the potentials towards sustainable construction.

2.2 Green Construction and Sustainable Development

There is no single definition of green construction. But, in general green construction or green building refers to a structure using process that is environmentally responsible and resource-efficient throughout a building's life-cycle: from sitting to design, construction, operation, maintenance, renovation and demolition. Green building aims to maximize efficiency in their use of water, energy and other resources to minimize waste, pollution or other contributions to environmental degradation, and to create environments that contribute to health and productivity.

Although the concept of green construction differs from place to place there are fundamental principles that consist of economy, utility, durability and comfort [9],[10]. The essence of green building is thus an optimization of one or more of these principles. As the world population continues to grow, further urbanisation and developments are inevitable. The challenges in civil engineering practices in the near future will, therefore, be to realise projects in harmony with the concept of sustainable development, and this involves the use of high performance materials and products manufactured at reasonable cost with the lowest possible environmental impact. Concrete is, indeed, the most widely used man-made material in the world, and is second only to water as the most utilised substance on the planet. However, the production of Portland cement, an essential constituent of concrete, releases large amount of CO_2 into the atmosphere, i.e. about one ton of CO_2 for every ton of Portland cement produced. As CO_2 is a major contributor to the green house effect and the global warming of the planet, both the developed and developing countries are considering very severe regulations and limitations on CO_2 emissions.

To make a breakthrough the trend toward sustainable construction has pushed the envelope in the area of concrete mix designs by introducing materials that are not only more green but also can create a more superior final product. There are several factors that constitute 'green' and the overall greenness of a new construction can be increased exponentially through synergic actions of innovative construction materials. The first and simplest measure in sustainable construction is the choice of materials with high percentage of recycled content. As a normal practice fly ash, for example, is used to partially replace Portland cement at relatively modest levels of 15 to 25% (by mass). Research workers have demonstrated that fly ashes can suitably be used at much higher replacement levels of between 40 to 60% to produce concrete with good mechanical properties and excellent durability [11]-[14].

2.3 Palm Oil Fuel Ash: A Unique Cement Substitute

The oil palm is a tall-stemmed tree which belongs to palm family *Palmea.* The countries in the equatorial belt that cultivate oil palm are Benin Republic, Colombia, Ecuador, Nigeria, Zaire, Malaysia, Thailand and Indonesia of which Malaysia is the largest producer of palm oil and palm oil products. To date, for instance, there are more than two hundred palm oil mill plants operating in the country that are self sufficient industry as far as energy utilisation is concern. It has been estimated that the total solid waste generated by this industry has amounted to about ten million tons a year [15]. The palm fibre and shell obtained as waste products by the industry are generally used as boiler fuel to produce steam for electricity generation and palm extraction process. The ash produced on burning palm fibre and palm kernel shell is considered to be a waste product, the disposal of which poses enormous problems. As a normal practice this ash, popularly

known as palm oil fuel ash (POFA) is simply disposed of without any commercial return. However, it has been identified that POFA has good pozzolanic properties that can be used as a cement substitute in mortar and concrete mixes [1],[3],[16].
In bulk, POFA is grayish in colour that becomes darker with increasing proportions of unburned carbon. The particles have a wide range of sizes, a typical electron micrograph of POFA being shown in Fig. 2. Physical properties and the chemical analysis of typical ash, illustrated in Table 1, reveal that POFA satisfies the requirements to be pozzolanic and may be classified in between Class C and Class F according to the standard specified in ASTM C6I8-94a. Critical evaluation based on the current literature, however, suggests that the present-day classification system of grouping of ashes into Class N, Class F, and Class C is not adequate to apprise their total usefulness. It should be the performance-oriented criteria rather than the chemical composition alone should be considered for proper representation of ashes of agricultural origin like POFA.

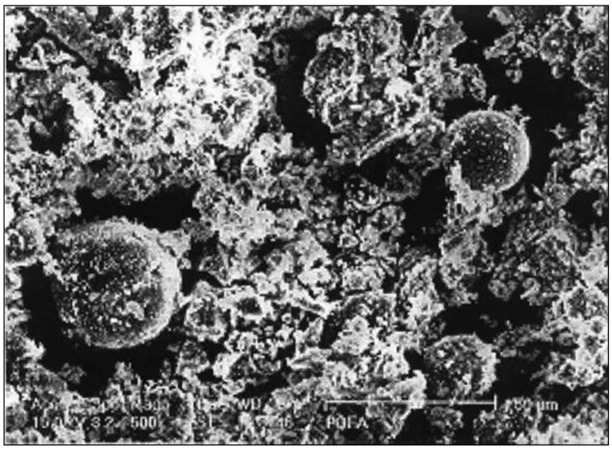

Fig. 2: Scanning electron micrograph of POFA

Table 1: Physical properties and chemical composition of typical palm oil fuel ash

Tests	POFA
Physical Properties	
Fineness - Sp. surface area (m^2/kg)	520
Soundness – LeChatelier method (mm)	1
Specific Gravity	2.22
Chemical Analysis (%)	
Silicon Dioxide (SiO_2)	43.60
Aluminium Oxide (Al_20_3)	11.40
Ferric Oxide (Fe_2O_3)	4.70
Calcium Oxide (CaO)	8.40
Magnesium Oxide (MgO)	4.80
Trioxide (SO3)	2.80
Sodium Oxide (Na_2O)	0.39
Potassium Oxide (K_2O)	3.50
Loss of Ignition (LOI)	18.00
28-day Strength Activity Index with OPC	112

3. FRESH CONCRETE PROPERTIES

3.1 Setting Time of OPC and Palm Oil Fuel Ash

One of the most important properties of cementing materials is setting time that influences the fresh and hardened state properties of concrete. The setting time of OPC as well as of OPC with POFA at various replacement levels are shown in Table 2. Setting times given in the table suggest that like other fly ashes the inclusion of POFA in cement paste retards the setting time; the higher the amount of ash the more is the retarding time. This is to be expected; because when the ash content is high, less is the amount of cement that results in slower setting time. Test results on setting time also reveal that setting time of cement with 60% ash is within the limit as specified in ASTM C150-94. The slight retarding effect with higher amount of ash would, however, be beneficial to concreting in hot weather conditions.

Table 2: Setting time of OPC and palm oil fuel ash

Mix	Setting Time (min)
100% OPC	150
90% OPC + 10% POFA	195
80% OPC + 20% POFA	225
70% OPC + 30% POFA	300
60% OPC + 40% POFA	375
50% OPC + 50% POFA	420
40% OPC + 60% POFA	420

3.2 Workability of Concrete

Concretes with pozzolans usually have an improved workability than those made with un-substituted Portland cement at the same water content though there are exceptions. There are numerous evidences that pulverised fuel ashes improve workability of concrete because of their spherical glassy particles. It has generally been thought that the improvement of workability of concretes incorporating fly ash is due to a ‘ball-bearing’ action of the particles. These fine spherical particles are assumed to reduce the interference between larger particles of the aggregate.
It is interesting to note that unlike fly ash concrete, POFA concrete exhibits higher water demand. To attain the same level of workability, mixes containing 30% POFA required higher water content than those containing only ordinary Portland cement as the binder [16]. Table 3 illustrates that the slump of concrete for all mixes increased with the increase in water-binder ratios. Although the slump of both OPC and POFA concretes using superplasticiser was found to increase reasonably, its response to POFA concrete at low water-binder ratios was not significant. At higher water-binder ratios, however, POFA concrete showed some improvement but the slump values still remained below that of concrete with OPC alone.
No single cause has so far been identified for the lower slump value in POFA concrete. The cohesiveness of the mix due to the higher surface area and high carbon content in the ash could be responsible for the lower slump. Also, unlike typical fly ash particles, the POFA particles seem to be predominantly irregular although some particles with

Table 3: Workability of OPC and POFA concrete

Mix	Type of Concrete	Slump of Concrete (mm) at Water-Binder ratio of				
		0.4	0.45	0.5	0.55	0.6
Without admixture	OPC	0	0	20	30	60
	POFA	0	0	10	10	30
With 1% superplasticiser	OPC	40	50	80	120	180
	POFA	10	30	65	100	165

spherical shape appeared in the scanning electron micrograph as illustrated in Fig. 2. Possibly because of such character, other pozzolanic materials like rice husk ash behave similarly [5],[17].

3.3 Bleeding Characteristics

Over the decades, extensive research has been carried out into the causes and mechanism of bleeding in cement paste and concrete. Among others, the properties of cementing materials largely affect the bleeding characteristics, and, in general, it is decreased by the increase in the fineness of the cement. The bleeding characteristics of concrete containing various amount of palm oil fuel ash have been studied [16] and illustrated in Fig. 3. It can be seen that bleeding in POFA concrete was much lower than in OPC concrete at all levels of replacements. The accumulated bleeding water after 30 minutes, for example, in OPC concrete was 60ml; whereas concrete with 10, 30 and 60% POFA bleeded only 35, 20 and 5ml respectively after the same period of test. Similar observation goes with other pozzolanic materials like rice husk ash and silica fume. The reason for the low bleeding would possibly due to the fact that the extremely fine particles attach themselves to the cement particles, reducing the channels for bleeding, and leaving very little free water available in the fresh concrete for further bleeding [18].

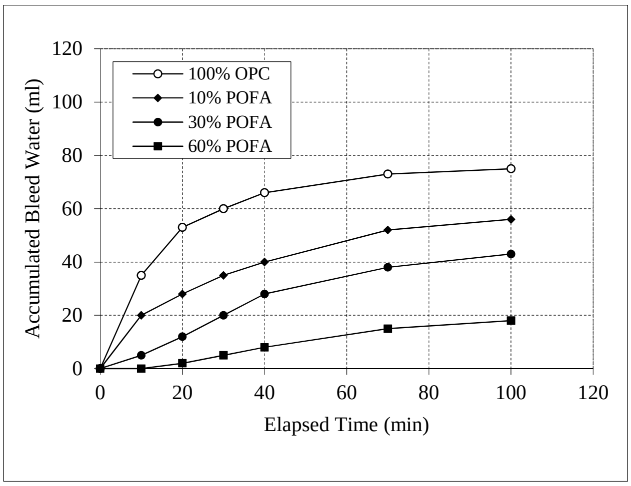

Fig. 3: Bleeding characteristics of OPC and POFA concrete

4. STRENGTH AND DEFORMATION BEHAVIOUR

4.1 Ash Quality and Development of Strength

The hydration of cement paste containing pozzolanic materials is complex in nature, and the factors which are responsible for hardening of concrete with fly ash have, in general, shown to influence the strength of concrete containing palm oil fuel ash. Among others, type and amount of ash, curing of concrete are most critical. Like other fly ashes the fineness of palm oil fuel ash has been shown to influence the strength of concrete [14],[19]. Fig. 4 demonstrates that finer the ash, higher is the development of strength.

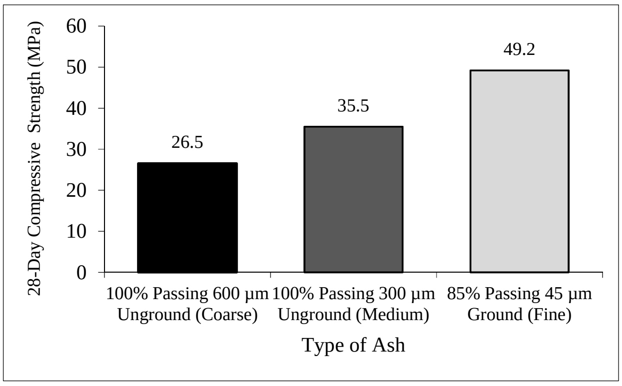

Fig. 4: Effect of fineness of ash on strength of concrete

Although it has been possible to replace 30% OPC by POFA without any loss of strength [16], replacement levels from 10 to 20% have been found to be optimum in producing high strength concrete [19].

4.2 Effect of Curing on Strength Development

There has been a school of thought that the strength development of concrete containing pozzolans at early ages is slower than that of concrete with only Portland cement. Like other typical fly ash concrete POFA concrete has been shown to develop lower strength at early ages [16]; at later ages the compressive strength of POFA concrete has been found to be slightly higher than the OPC concrete (Fig.5).

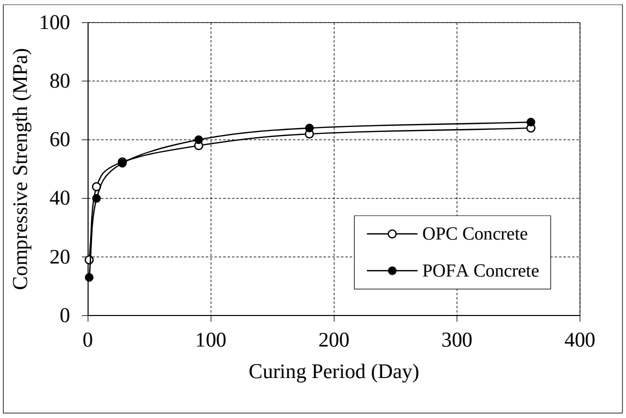

Fig. 5: Strength development of concrete containing POFA

Interestingly POFA concrete has been identified to be highly sensitive to wet curing as the reactions of ash in concrete take a relatively longer time; prolonged weight curing appears to be vital for the development of strength (Fig. 6). Insufficient curing especially during early ages, therefore, seems to be detrimental to the long term strength of POFA concrete. Similar observations have been made by Abdullah et al. [20] on lightweight aerated concrete containing palm oil fuel ash.

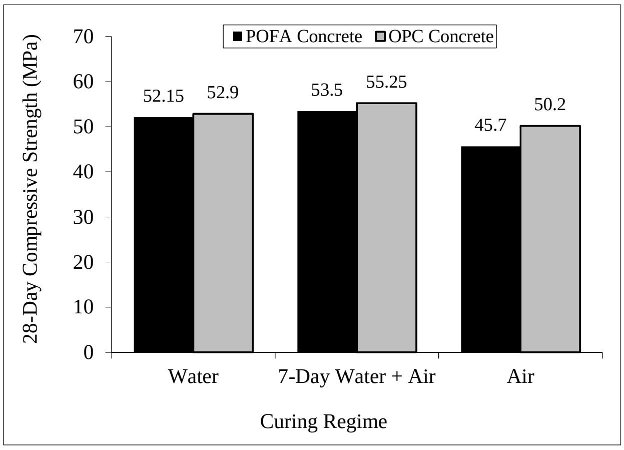

Fig. 6: Effect of curing regime on compressive strength of OPC concrete and concrete with 30% POFA.

4.3 Influence of Admixture

Over the years there have been tremendous advances in the development of chemical and mineral admixtures. The use of chemical admixture particularly superplasticisers of various types in fly ash concrete has been emphasised since the beginning of the wide application of ashes in structural concrete. Although fly ashes impart workability to a certain extent, the use of superplasticiser has been shown to be indispensable for the improvement of strength and long-term durability, especially when the amount of ash is large.

Short-term investigation on the compatibility of POFA concrete with chemical and mineral admixture indicates (Table 4) that superplasticiser has a positive response on the development of strength of concrete.

Table 4: Strength development of concrete as influenced by chemical and mineral admixture

Concrete Mix	Compressive Strength (MPa)		
	1 Day	7 Days	28 Days
Control (100% OPC)	17.55	37.40	46.60
Double Blend (70% OPC+30%POFA)	14.70	35.10	45.50
Double Blend (70% OPC+30%POFA) with 1% superplasticiser	16.85	36.25	50.60
Triple Blend (65% OPC+30%POFA+ 5% Silica Fume) with 1% superplasticiser	16.00	37.15	49.70

Limited data on concrete with silica fume have also shown to influence the strength of concrete by compensating the slower strength gain at early ages although the overall performance of silica fume in POFA concrete was not much satisfactory.

4.4 Modulus of Elasticity

Modulus of elasticity of concrete containing POFA has been studied by several researchers and has been described in different ways. In general, however, it has been shown to be closely associated with the magnitude of the corresponding compressive strength of concrete. Ishida [21] demonstrated that modulus of elasticity of 20% POFA concrete was lower at early ages, but slightly higher than that of control after one year. Concrete containing 30% POFA exhibited similar trend although the compressive strength was a bit lower than that of the control specimen. The observation made is consistent with the short-term research findings of Awal and Hussin [22]. In another experiment Sata et al. [19] found that the ground POFA content up to 30% by weight of cementitious materials had little effect on modulus of elasticity of concretes. With the compressive strength value of about 90 MPa, it was found that ground POFA gave slightly lower modulus of elasticity than those of control specimen. This lower value, as they presumed, was due to the decrease in coarse aggregate content of the concrete mixes. Tangchirapat and Jaturapitakkul [23] experienced it in different ways. Although the use of coarse and fine POFA did not influence the value, the modulus of elasticity of ground POFA concrete increased with the increase of compressive strength, and was found to be about 7% higher than that predicted by ACI 318.

4.5 Shrinkage and Creep

In addition to the deformation due to load, a concrete specimen exhibits other types of deformations – creep and shrinkage. Creep is the deformation when a concrete member is subjected to a sustained load, and shrinkage is the contraction suffered by concrete even in the absence of load. Like that of other pozzolanic materials, the properties of POFA have been shown to influence the shrinkage and creep of concrete. Along with modulus of elasticity, Ishida [21] carried out extensive study on shrinkage behaviour of concrete containing POFA over a period of one year. It has been found that POFA concrete, in general, exhibited more shrinkage value than the concrete with OPC alone. Tangchirapat and Jaturapitakkul [23] also demonstrated that concrete incorporating coarse ash did not have reduced drying shrinkage; however, concrete containing fine palm oil fuel ash exhibited 10-17% lower drying shrinkage than OPC concrete.

Awal and Nguong [14] conducted short-term investigation on shrinkage of concrete containing high volume palm oil fuel ash. The measured values of shrinkage over a period of 28 days, plotted in Fig. 7, reveal that the shrinkage strain of POFA concrete was higher than that of concrete with OPC alone. The magnitude of shrinkage of OPC concrete at 28-day, for instance, was 285 x 10^{-6}. At the same time about 21% higher value of shrinkage i.e. 347×10^{-6} was recorded for the concrete with 50% palm oil fuel ash. The general observations made by Brooks and Neville [24] corroborates

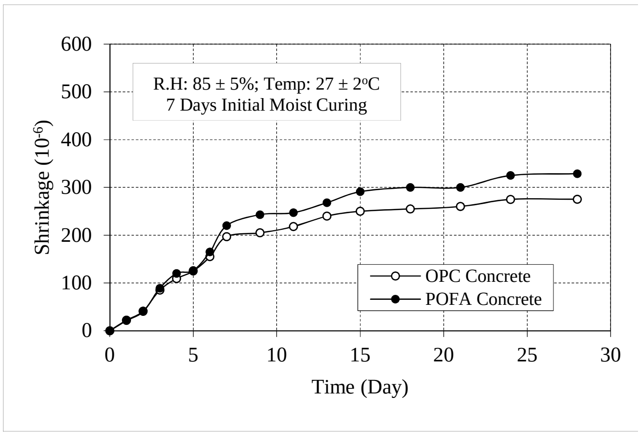

Fig. 7: Drying shrinkage of OPC concrete and high volume POFA concrete

the findings in this study. They have demonstrated that at a constant water-cement ratio, a higher proportion of fly ash leads to higher shrinkage magnitude by some 20%.

Unlike shrinkage, research findings on creep of concrete containing palm oil fuel ash are not many. The observation made by Ishida [21] suggests that the inclusion of POFA in concrete did not influence much of creep properties. The specific creep of concrete containing 30% POFA was found to be 5% lower than that of control at 180 days. The creep co-efficient of POFA concrete, as he observed, was about 11% lower as compared to that of concrete without ash.

5. ASPECTS OF DURABILITY

5.1 Resistance to Heat Rise

The hydration of cement compounds is exothermic i.e. heat is generated within the concrete matrix during hydration. The temperature rise of concrete due to hydration is largely controlled by materials and mix properties, and by environmental factors. Like that of chemical admixture the use of pozzolanic materials in reducing heat of hydration in concrete is well established.

Experimental investigation conducted by Awal and Hussin [25] on resistance to heat rise demonstrates that the partial replacement of OPC by POFA is advantageous particularly for mass concrete where thermal cracking due to excessive heat rise is of great concern. The development of temperature due to heat liberation by the hydration process was measured at the mid-depth of concrete blocks. Fig. 8 reveals that during the initial period, the temperature rise for both OPC and POFA concrete was almost equal. With time, a two-fold effect of the partial replacement of OPC by POFA can be detected. Firstly, concrete with POFA reduced the total temperature rise and secondly, it delayed the time at which the peak temperature occurred. Although the initial mixing temperature of both the mixes was approximately the same, considerably more heat was evolved from OPC concrete during the first day i.e. within twenty four hours after casting. The peak temperature of 36.7°C, as obtained for OPC concrete, was recorded at 20 hours. On the other hand, the

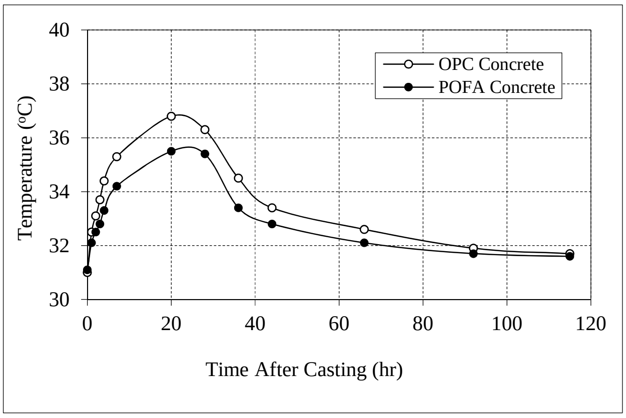

Fig. 8: Development of temperature in OPC and POFA concrete

highest temperature of 35.4°C was monitored in concrete with 30% POFA at 28 hours of casting.

5.2 Resistance to Chloride Penetration

Concrete, either plain or reinforced, can be harmfully affected by chloride action. To protect from chlorides less permeable concrete and adequate cover thickness are generally considered. In addition to these precautions, however, utilisation of special cements and particularly incorporation of pozzolanic materials have been proved to be useful in minimizing the harmful effects.

Investigation on the resistance to chloride ion revealed (Fig. 9) that the depths of penetration of chloride ions in concrete containing 30% POFA was much lower than in concrete with OPC alone [26]. The pozzolanic behaviour of the ash causing a decrease in permeability resulting from the refinement of pore structure of the cement matrix has been attributed for the higher resistance to penetration of chloride ion into concrete.

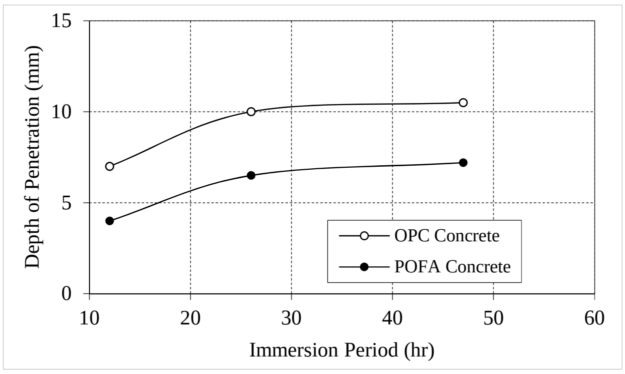

Fig. 9: Chloride penetration in OPC and POFA concrete

5.3 Resistance to Sulphate Attack

Among all chemicals, sulphates are the most significant in view of their attack on concrete. Sulphate attack on concrete is a complex phenomenon that involves a series of primary and secondary chemical reactions, some of which are interrelated. The inclusion of pozzolanic materials in increasing the resistance to sulphate attack is well recorded in the literature. Many pozzolans have been found that can effectively double the service life of a concrete when exposed to sulphate attack [27]. Although the composition of pozzolan that influences the resistance of concrete to sulphate attack is not fully understood, but in general terms it appears that low-calcium fly ashes have been reported to be effective mineral admixtures for combating sulphate attack on concrete [28]. The results on the expansion of mortar bars prepared from ordinary Portland cement and the one blended with POFA have been presented in Fig. 10.

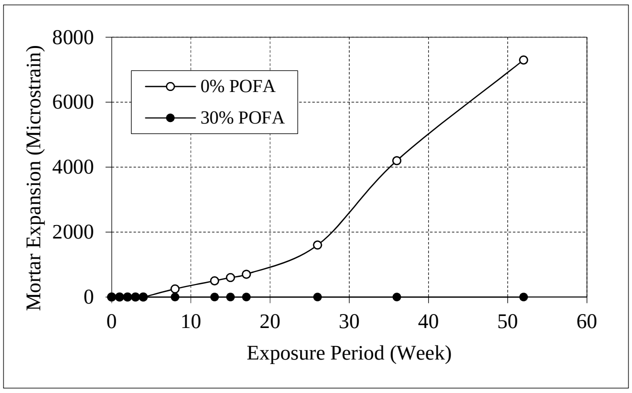

Fig. 10: Expansion of mortar bars due to exposure in 10% sodium sulphate solution

5.4 Resistance to Acid Attack

Cement based materials are subjected to acidic environment in a variety of ways. The resistance of concrete to acid attack can be increased either by artificial surface treatment [29] or by incorporating suitable pozzolans [18],[30]. Like concrete with other fly ashes of low-lime content, POFA concrete exhibited a commendable resistance to acid attack [26]. Concrete specimens exposed to hydrochloric acid solution for a period of 1800 hours demonstrated (Fig. 11) that at all periods of immersion the loss of weight of OPC concrete was higher than that of concrete with 30% POFA. The pozzolanic behaviour as well as its low CaO content had been characterized for the resistance to such acidic environment.

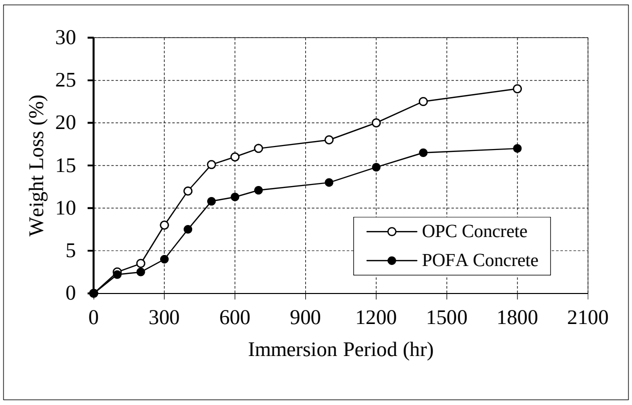

Fig. 11: Comparative weight loss of OPC and POFA concrete specimens immersed in 5% hydrochloric acid solution

5.5 Alkali-Silica Reactivity

The alkali-silica reaction, in its simple meaning, is an internal chemical reaction between the hydroxyl ions derived from the alkalis and certain forms of reactive silica present in the aggregate of a concrete mass. The use of supplementary cementing materials such as fly ash, slag and silica fume is one of the most popular solutions proposed to suppress the expansion due to alkali-silica reaction [31],[32].

The extent of research in fly ash and alkali-aggregate reaction has proliferated in the past decades. Despite higher alkali content, laboratory tests following the South African accelerated mortar bar test method demonstrated that POFA has a good potential in suppressing expansion due to alkali-silica reaction [33]. Inevitably, the fineness of POFA and its pozzolanic behaviour, identified responsible for its unique resistance to other aggressive chemicals, acted in favour of its effectiveness in preventing expansion owing to alkali-silica reactivity.

5.6 Performance in Marine Environment

The use of concrete in marine structures goes back to the ancient Romans and Greeks. Since that time numerous marine structures have been built using concrete, and many of the structures made with pozzolans are still in good condition. However, the history of concrete in marine environments demonstrates that no construction materials are perfectly durable to sea water which presents one of the most corrosive natural environments in the world. Most importantly concrete in the marine conditions differs from the concrete in other environments in that, under water, the material is continuously exposed to the action of complex sea water, and above water, to spray or airborne salt and other mechanical load [34]-[36]. With the increasing marine activities, the use of pozzolanic materials such as fly ash, silica fume, and natural pozzolans in concrete contribute to the formation of a denser binder which inhibits the migration of the sea water into concrete. Indeed, due to the higher pozzolanicity, the performance of these materials in marine environment have been well marked [37]-[40]. The durability performance study of concrete containing palm oil fuel ash in marine environment was carried out [41], [42] by installing the concrete specimens in sea under the jetty of Marine Police Station along Johor Straits near the Malaysia-Singapore ‘causeway’. Table 5 illustrates the performance behaviour of concrete at various exposure periods.

Results summarised in Table 5 reveal that all the concrete specimens had an overall very satisfactory appearance at all ages of inspection. The strength data obtained here in, on the whole, suggest that the performance of concrete containing palm oil fuel ash in sea is quite satisfactory. Penetration data, given in the table also reveal that at all periods of exposure the depth of penetration of chloride ions into OPC concrete was higher than in concrete with POFA. No significant differences in carbonation, however, have been noticed in OPC and POFA concrete specimens. At early exposure periods, the depth of carbonation was almost zero. At later ages, only a small amount of carbonation in both OPC and POFA concretes was detected.

Table 5: Characterization of ageing performances of concrete exposed to marine environment

Tests	Exposure Period	Types of Concrete	
		OPC	POFA
Visual Observation	2 years	Almost intact with few bore holes on the surface of the concrete specimen	Same as OPC concrete
Compressive Strength (MPa)	6 months	56.8	58.1
	1 year	59.9	59.5
	2 years	60.7	61.9
Flexural Strength (MPa)	6 months	6.85	7.70
	1 year	6.95	7.00
	2 years	6.90	7.50
Chloride Penetration (mm)	6 months	21.0	13.5
	1 year	23.5	17.0
	2 years	28.0	20.5
Carbonation (mm)	6 months	0.0	0.5
	1 year	1.5	1.5
	2 months	2.0	1.5

6. CONCLUDING REMARKS

While the whole world is going green, the construction industry in both the developed and developing world is also going green. Indeed, the sustainable development has become the core of green technology i.e. transition or transformation of all activities towards greener future through green actions. Due to the increased interest in green building concepts and practices, more supplementary cementing materials are expected to be seen in the market. The experimental findings and the observations made so far, suggest that the inherent pozzolanic properties of palm oil fuel ash have resulted in significant quality improvements including enhancement of strength and durability. These high performance characteristics have positioned POFA as a suitable material when resistance to aggressive chemical environments and long-term strength characteristics are called for. It remains, however, for the construction industry to adopt and advance the material technology to its full utilization towards the green concrete construction.

7. ACKNOWLEDGEMENTS

The author wishes to acknowledge the technical support received from the Department of Structure and Materials, Faculty of Civil Engineering, Universiti Teknologi Malaysia. The ‘research university grant’ acquired from the Research Management Centre (RMC) of the university (Code: Q.J130000.7122.01J81) is also gratefully acknowledged.

REFERENCES

[1] Tay JH, “Ash from oil-palm waste as concrete material”, J. of Materials in Civil Engineering, , vol. 2, no. 2, 1990, pp. 94-105.

[2] Nimityongskul P and Daladar TU, “Use of coconut husk, corn cob and peanut shell as cement replacement, In Proc of the International Symposium on Urban Housing Issues on Environment and Technology, Asian Institute of Technology, Thailand,1993, pp. 353-362.

[3] Salihuddin RS, Relationships Between Engineering Properties and Microstructural Characteristics of Mortar Containing Agricultural Ash, PhD Thesis, Universiti Teknologi Malaysia, 1993.

[4] Hossain MZ, Sakai T and Awal ASMA, “SEM images and chemical analyses of palm oil fuel ashes for their likely pozzolanic properties in concrete”, In Proc. of 1st International Conference on Recent Advances on Concrete Technology, Arlington, USA, 2007, pp.95-100.

[5] Siddique R. Waste Materials and By-Products in Concrete, Springer-Verlag Berlin Heidelberg, 2008.

[6] Samarin A, Munn RL, Ashby JB, “The use of fly ash in concrete – Australian experience”, In Proc. of the 1st International Conference on Fly Ash, Silica Fume, Slag and other Mineral By-Products in Concrete, Montebello, Canada, ACI Publication SP-79, vol.1, pp.143-172.

[7] Dunstan MRH, “Fly ash as the ‘fourth ingredient’ in concrete mixtures”, In Proc. of the 2nd International Conference on Fly Ash, Silica Fume, Slag and Natural Pozzolans in Concrete, Madrid, ACI Publication SP-91, vol. 1, pp. 171-199.

[8] Hwang CL, “The role of pozzolans and blast furnace slag on the properties of high-performance concrete”, In Proc. of R.N. Swamy Symposium on Real World Concrete, 5th CANMET/ACI International Conference on Fly Ash, Silica Fume, Slag and Natural Pozzolans in Concrete, 1995, pp. 197-208.

[9] Jepsen MT, Green Concrete, XVII Symposium on Nordic Concrete Research, Reykjavík, Denmark, 1999.

[10] http://en.wikipedia.org/wiki/Green_building

[11] Malhotra V, “CANMET investigations dealing with high-volume fly ash concrete”, Advances in Concrete Technology, 2nd ed., CANMET, Ottawa, 1994, pp. 445-482.

[12] Sirivivatnanon V, Cao HT, Khatri RP and Bucea L, Guidelines for the Use of High Volume Fly Ash Concretes, Technical Report TR95/2, Division of Building, Construction and Engineering, CSIRO, Australia, 1995.

[13] Anon, Handbook on High-Volume Fly Ash Concrete Technology, International Centre for Sustainable Development of Cement and Concrete, CANMET, Ottawa, 2005.

[14] Awal ASMA and Nguong SK, “A short-term investigation on high-volume palm oil fuel ash (POFA) concrete”, In Proc. of the 35th Conference on Our World in Concrete and Structures, Singapore, 2010, pp. 185-192.

[15] Rashid M and Rozainee M, "Particulate emissions from a palm oil mill plant – a case study", Jurnal Teknologi, Universiti Teknologi Malaysia, vol. 22, December, 1993, pp. 19-24.
[16] Hussin MW and Awal ASMA, "Palm oil fuel ash: a new cement substitute", JURUTERA, Monthly Bulletin of the Institution of Engineers Malaysia, no. 11, 1998, pp. 40-46.
[17] Habeeb GA and Mahmud HB, "Experimental investigation on the mechanical properties of Grade 40 concrete incorporating rice husk ash", In Proc. of the 7th Asia Pacific Structural Engineering and Construction Conference and 2nd European Asian Civil Engineering Forum, vol. 2, 2009, pp. 678-682.
[18] Malhotra VM, Carette GG and Sivasundaram V, "Role of silica fume in concrete: a review", Advances in Concrete Technology, 2nd ed., CANMET, Ottawa, 1994, pp. 915-990.
[19] Sata V, Jaturapitakkul C and Kiattikomol K, "Utilization of palm oil fuel ash in high-strength concrete", J. of Materials in Civil Engineering, vol.16, no. 6, 2004, pp. 623-628.
[20] Abdullah K, Hussin MW and Awal ASMA, "Effect of curing regime on properties of lightweight concrete containing palm oil fuel ash", In Proc. of the International Conference on Building Science and Engineering, Johor Bahru, 14-15 December, 2009.
[21] Ishida T, Creep and Shrinkage of Concrete Containing Palm Oil Fuel Ash, M. Eng Thesis, Universiti Teknologi Malaysia, 1999.
[22] Awal ASMA and Hussin MW, "Strength, modulus of elasticity and shrinkage behaviour of POFA concrete", Malaysian Journal of Civil Engineering, vol.21, no. 2., 2009, pp. 125-134.
[23] Tangchirapat W and Jaturapitakkul C, "Strength, drying shrinkage, and water permeability of concrete incorporating ground palm oil fuel ash", Cement and Concrete Composites, vol. 32, 2010, pp. 767-774.
[24] Brooks JJ and Neville AM, "Creep and shrinkage of concrete as affected by admixtures and cement replacement materials", Creep and Shrinkage of Concrete: Effect of Materials and Environment, ACI Publication SP-135, 1992, pp. 19-36.
[25] Awal ASMA and Hussin MW, "Effect of palm oil fuel ash in controlling heat of hydration of concrete", Procedia Engineering-ELSEVIER, In Proc. of the 12th East Asia-Pacific Conference on Structural Engineering and Construction , vol. 14, 2011, pp. 2650 -2657.
[26] Awal ASMA and Hussin MW, "Durability of high performance concrete containing palm oil fuel ash", In Proc. of the 8th International Conference on Durability of Building Materials and Components, Vancouver, Canada, 30 May - 3 June, 1999, pp. 465-474.
[27] Harboe EM, "Long time studies and field experiences with sulphate attack", In Proc. of the George Verbeck Symposium on Sulphate Resistance of Concrete, ACI Publication SP-77, 1982, pp. 1-20.
[28] Hussin MW and Awal ASMA, "Influence of palm oil fuel ash on sulphate resistance of mortar and concrete", In Proc. of the 6th CANMET / ACI International Conference on Fly Ash, Silica Fume, Slag and Natural Pozzolan in Concrete, Bangkok, ACI Publication SP-178, vol.1, 31 May - 5 June, 1998, pp. 417-430.
[29] Chandra S and Ohama Y, "History interactions and current status of the polymers in concrete", In Proc. of the V. Mohan Malhotra Symposium on Concrete Technology: Past, Present and Future, 1994, pp. 483-506.
[30] Mehta PK, "Rice hull ash cement - high quality, acid-resisting", ACI Journal, May, 1975, pp. 235-236.
[31] Hobbs DW, "Deleterious expansion of concrete due alkali-silica reaction: Influence of PFA and slag", Magazine of Concrete Research, vol. 38, 1986, pp. 191-205.
[32] Swamy RN, "Alkali-aggregate reactions - The bogeyman of concrete", In Proc. of the V. Mohan Malhotra Symposium on Concrete Technology: Past, Present and Future, ACI Publication SP-144, 1994, pp. 105-139.
[33] Awal ASMA and Hussin MW, "The effectiveness of palm oil fuel ash in preventing expansion due to alkali-silica reaction", Cement and Concrete Composites, vol. 19, no. 4,1997, pp. 367-372.
[34] Browne RD and Baker AF, "The performance of structural concrete in a marine environment", Developments in Concrete Technology-1, Applied Science Publishers Ltd., London, 1979, pp. 111-149.
[35] Marshall AL, Marine Concrete, Blackie and Son Ltd., London, 1990.
[36] Al-Rabiah AR, "Concrete durability consideration for the King Fahad Causeway – a case study", In Proc. of the 4th International Conference on Structural Failure, Durability and Retrofitting, Singapore, 1993, pp. 199-205.
[37] Hoff GC, "Concrete for offshore structures", Advances in Concrete Technology, 2nd ed., CANMET, Ottawa, 1994, pp. 83-123.
[38] Mehta PK, "Concrete in the Marine Environment, Elsevier Science Publishers Ltd, 1991.
[39] Malhotra VM, Carette GG and Bremner TW, "Performance of high-volume fly ash concrete at Treat Island, Maine, In Proc. of the 6th International Conference on Durability of Building Materials and Components, Omiya, Japan, 1993, pp. 1011-1020.
[40] Roper H, Sirivivatnanon V and Baweja D, "Long-term performance of Portland and blended cement concretes under marine conditions", In Proc. of the 3rd International Conference on Durability of concrete, Nice, France, ACI Publication SP-145, 1994, pp. 331-351.
[41] Hussin MW and Awal ASMA, "Influence of palm oil fuel ash on strength and durability of concrete", In Proc. of the 7th International Conference on the Durability of Building Materials and Components, Stockholm, Sweden, 1996, pp. 291-298.
[42] Awal ASMA and Hussin MW, "Concrete in marine environment: influence of palm oil fuel ash on strength and durability", In Proc. of the Civil and Environmental Engineering Conference - New Frontiers and Challenges, Bangkok, Thailand, 1999, pp. 11149-11156.

First International Conference on Geotechnique, Construction Materials and Environment, Mie, Japan, Nov.21-23, 2011, ISBN: 978-4-9905958-0-7 C3051

Behavior of Collapsible Loessic Soil After Interparticle Cementation

Arrua P., Aiassa G., Eberhardt M., Alercia Biga I., Grupo de Investigación y transferencia en Geotecnia, Estructuras y Fundaciones (GIGEF), Facultad Regional Córdoba, Universidad Tecnológica Nacional. Argentina

ABSTRACT: The water content, shape and roughness of soil particles are related to the strength and stiffness of loessic soil samples in remolded state. When soil sample are in undisturbed stage, the cementation level between particles by the presence of water-soluble carbonates, govern the macroscopic behavior. Soil stiffness depends on the rigidity of the link. To control the mechanical collapsible behavior usually compaction and stabilization is made with cementations agents. This work presents the hydration process of cement without mixing water and how geotechnical index and parameter are modified. The variables that influence the resistance have been evaluated by unconfined compression tests. Results showed that resistance depend with the initial water content of hydration. Optimal conditions for generation cementing bridges are established.

Keywords: micrograph, hydration, strength, unconfined compressive

1. INTRODUCTION

In the construction of geotechnical structures, the improvement of soil properties is very common in Argentine [1]-[4]. Many studies in the literature are related to the use of cement in the improvement of engineering properties of soils[5]-[8] . The compacted soil and soil mixtures must be constructed with local soil, so soil behavior is relevant to design. The Córdoba city is located in the geographical center of Argentina. Loess soils are usually found in arid or semiarid climates and their physical and chemical characteristics depend on their geological origin [9]. In nature the loess has an open structure, low unit weight, highly dependent on external conditions. The purpose of the addition of cementing agents is to stabilize the silty loess due to lack of technical qualities for application in construction works. Environmental conditions such as temperature and humidity significantly influence the strength characteristics of soil-cement mixtures [10]. The amount of cements incorporated, is generally related to the strength and stiffness assigned to the material at the stage of design, however this definition may be inadequate if the environmental conditions during the stage of hydration are not considered in the final strength of material [11], [12]. This paper presents the chemical composition, principal geotechnical properties, particles size and relation between different kinds of loess in Argentine. An electron microscope has been used to establish the chemical composition of local cement. Different samples have been built to study the behavior of loess-cement mixtures. To quantify the stress strain relation, unconfined compression test have been made. Time of curing, temperature of curing, initial water and cement contents, are the variables that govern behavior. The results allow establishing the roughness and sphericity of the particles. It also identifies the link between them. The results showed that stress-strain curves modify its initial elasticity modulus with variations of cement content.

2. MATERIALS

2.1 Loessic soil

Loess is non stratified aeolian deposit, and probably most abundant Quaternary deposit on land [13]. It consists of silt with some small fraction of clay, sand and carbonate. The deposits are up 30 m in thick en the Missouri and Rhine Rives Valleys, more than 180 m thick in Tajikistan, 330 m thick in northern China [14] and 2-80 m thick in Argentine. The most important deposit in Latin America is located in central area of Argentine.

These kinds of soils have been deposited during the Upper Pleistocene and Holocene and cover much of the province of Córdoba. Reference [15] has been described how, light yellow or brown in color, some times with a reddish or grey tinge. Usually, most researchers agree that the material originates from the Andes Mountains, with volcanic mineralogy agents. Recent contributions on the knowledge of the origin and evolution of the loess are presented in [9] and [16]. Locally, the soil has got mineral content from Small Hills of Córdoba Province. Grain-size distribution includes fine sand (1%-10%), silt (50%-80%) and clay (2%-15%) that have been deposited by wind action in areas of low energy. Fig. 1 presents typical grain size distribution. The chemical compositions of loess are mainly SiO_2, Al_2O_3, Fe_2O_2 y CaO. Chemical compositions of the soil from different regions of Argentina are shown in Table I. Note that close similarity exists between those loess, except for the percentages of CaO (which reflect the influence of locally degradation of Cordoba Small Hills). However the chemical composition is remarkably uniform, suggesting a common regional source. In natural conditions the water content (%) ranges from 12.7 to 23.0, the dry unit weight (kN/m^3) is 12.5 to 13.5, Specific gravity is 2.66 to 2.67, Atterberg limits are: liquid limit 23% – 30% and plasticity index 4.2% – 4.9%. Dynamic Cone Penetration Index [mm/blow] is 18–24, for Mohr-Coulomb failure criterion the friction angle in triaxial test (CD) is 27º – 30º, and cohesion [kN/m^2] in triaxial test (UU) is 15 – 40. Poisson modulus rages from 0.3 to 0.35, and elasticity modulus from unconfined compression test (MN/m^2) is 1.5–8. From oedometer test, the secant modulus for 100kPa in MN/m^2 is 2.0 – 7.0. Usually yield pressure in oedometer test (a: vertical direction; b: horizontal direction) is (a) 60kPa –

280kPa, (b) 100kPa – 180kPa.

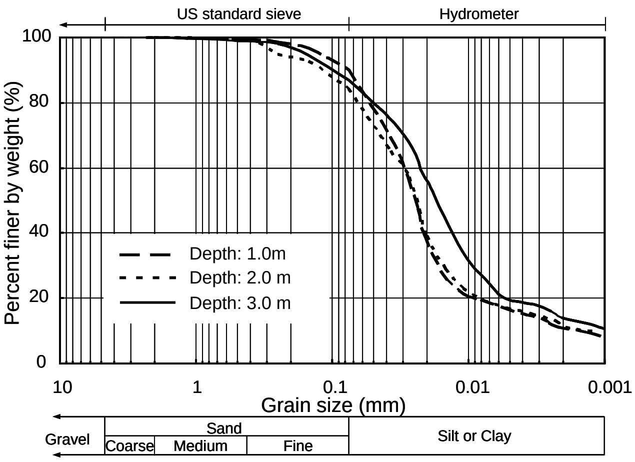

Fig. 1. Gradation result for loess soil

2.2 Cement

The chemical composition of Normal Portland Cement CP40 and particle morphology have been determined by a LEO 1450 VP Energy Dispersive Spectroscopy analysis (EDS) and Scanning Electron Microscope (SEM). The results shows that ordinary cement manufactured in Malagueño-Córdoba have SiO_2: 15.42%, Al_2O_3: 4.60%, Fe_2O_2: 3.35%, CaO: 65,71%, MgO: 2.79%, K_2O: 1.97%, Na_2O: 0.59%, SO_3: 5.10%, TiO_3: 0.47%. The most important difference with soil is content of SiO_2 and CaO.

2.3 Soil cement mixtures

The mixtures were designed to evaluate the performance in Unconfined Compression (UC). A review of literature about the testing of laboratory samples of soil-cement indicates that test results are highly dependent on sample preparation. This work includes variations in cement content, time of curing, temperature of curing, initial water content and compaction level.

The cement contents (C.c.) used, expressed as a percentage of the dry soil weight, were: 2.5%, 5.0%, 7.5%, 10% and 15%. The soil was dried in an oven at 105 ºC for 24 hours, was sieved and recovering the material passing sieve #40. Water was added in the proportions established at each case as mixing water. The samples were generated by compaction in the mold at constant dry unit weights (approx. 14 kN/m^3). The manufacture of the samples was performed in three equal layers scarification between them. Were classified and arranged in different curing conditions. Variable temperatures were taken from -20°C to 120°C.

Table I: Oxides soil components

SiO_2	Al_2O_3	TiO_3	Fe_2O_2	CaO	MgO	K_2O	Na_2O	H_2O	Reference
58.35	16.64	---	6.69	8.98	2.75	2.82	2.11	---	Soil used in this work. Cordoba City
67.22	14.35	---	6.81	5.16	2.13	2.93	1.41	---	Córdoba City [17]
59.20	13.60	---	4.30	6.50	1.10	2.20	3.10	---	Provincia de Córdoba [18]
59.86	17.40	---	4.80	3.08	1.17	1.70	1.97	6.04	Baradero, La Plata [13]
62.70	15.00	---	6.00	2.80	1.90	1.88	1.40	4.32	Miramar. Buenos Aires [13]
57.16	17.28	---	5.43	2.83	1.67	3.68	8.35	---	Buenos Aires [15]
66.01	16.22	0.88	5.30	2.85	1.62	1.90	1.97	3.14	La Pampa [19]
59.00	17.00	---	5.87	3.05	2.55	1.56	1.38	5.80	Valles Preandinos subtropicales; Provincia de Tucumán [20]
---	14.00	0.80	4.60	0.09	1.50	3.00	1.90	---	Llanura Chaco Oriental [21]

3 SHAPE AND COMPOSITION OF PARTICLE

The shape and connection between particles are an inherent soil characteristic that play a mayor role in macroscopic mechanical properties. The morphology describes at large scale the level platy or sphericity, and texture in smaller scales reflect the local roughness.

In this work, the chart from [22] is used to compare individual grains for visual estimation of roundness and sphericity. The chart from [23] is used for shape characterization. The particle morphology, roughness and roundness have been determined by a LEO 1450 VP Scanning Electron Microscope (SEM) and the components of loess soil with an Energy Dispersive Spectroscopy analysis (EDS).

The microscopic morphology of loess was shown in Fig. 2. It could be seen from these SEM results that the surface of loess material are subrounded and rounded with 0.7 sphericity coefficient and a 0.5 to 0.7 roundness coefficient. The size particles distribution is homogenous. The silt particles are the biggest and the smaller size are clay particles. Fig. 2 shows the zone to zoom and analyzed in Fig. 3. The cement presence affects the structure inherent of soil, because small particles stick to larger particles in stable connections. SEM photos of loess, cement, soil cement mixture at C.c: 2.5% and 15% are also shown in Figs. 3. Fig. 3(a) shows that particle size taken in consideration for comparison with mixtures, has size in upper limit of silty soil (~< 75μm and ~< 45μm). It can be seen that particle has angular and subangular shape with some small silty particles. Also appears some clays particles. The Fig. 3(b) presents Portland cement particles. It shows that predominant grain sizes are smaller than silt and with size between ≈1μm to ≈10 μm. It could be seen from these SEM that sphericity coefficient is 0.3 to 0.5 and roundness coefficient is 0.3-0.5. From SEM photo, it is found that the particles of cement are smaller than loessic soil.

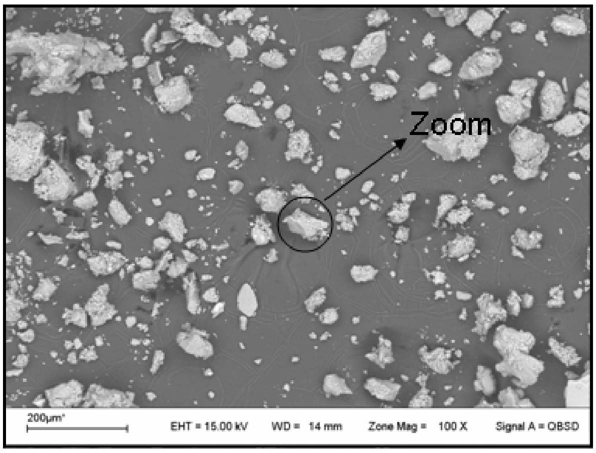

Fig. 2. SEM morphology of loess

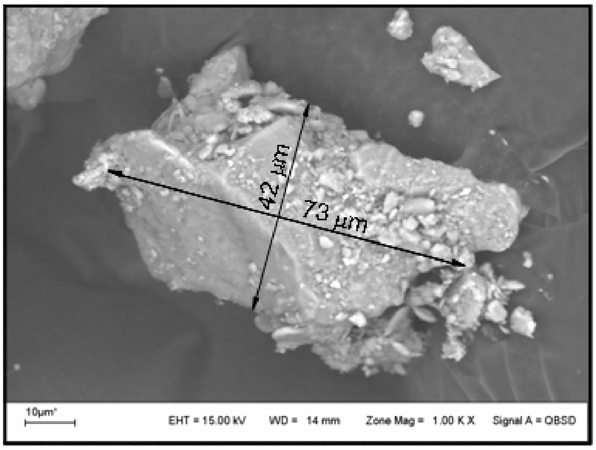

(a)

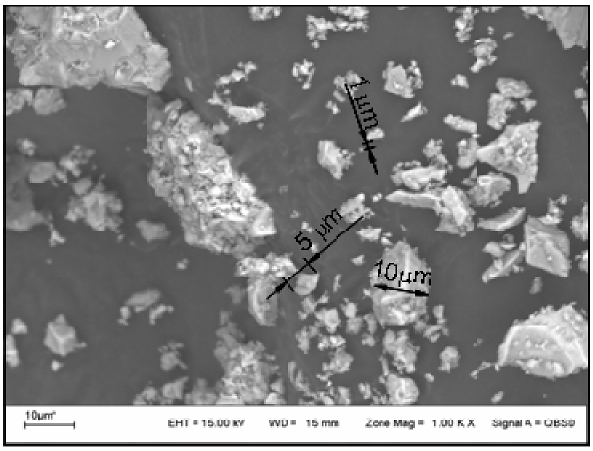

(b)

Fig. 3. SEM photos. (a) Natural loess soil. (b) Normal Portland cement

As shown in Fig. 4 mixture after 21 cementation days with cement content of 2.5% do not shows relevant difference with Fig. 3(a). When the cement content is low, stick on the cement particles some of silty soil, forming clusters that fail to establish links with others silt.

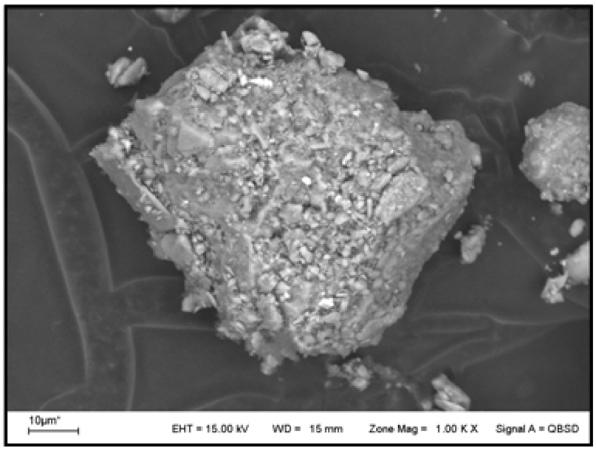

Fig. 4. SEM photo of mixture C.c.: 2.5%

There are cementation between smaller particles and big silt particles, but we do not find cementation between big silty particles. The low cement content may be responsible for the links absence.

Fig.5 shows the SEM for a cement content of 15%. When the cement content are high (15 % of C.c.) were able to establish stable cementation and links between different silt particles. This phenomenon may be responsible for increased stiffness and strength of mixtures samples. The ellipses areas indicate links between silt and hydrations products.

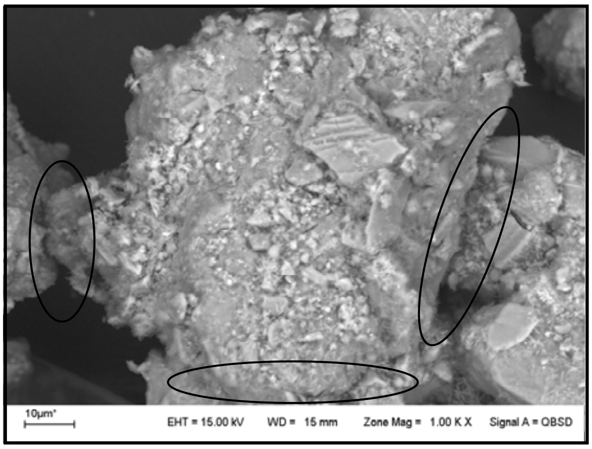

Fig. 5. SEM photo of mixture C.c.: 15%

Analysis of Energy Dispersive Spectroscopy is presented in a schema three dimensional (Fig. 6). It shows the mineral level present in cement, loessic soil and a mixture of soil cement with C.c: 15%.

The figure shows that the content of Si decreases with increasing of cement content (C.c), while calcium (Ca) decreases with decreasing of cement content. The content of Ca are 35.50%, 12.91% and 5.34% for cement, mixture soil-cement (15% of Cc), and loess respectively. The content of Si are 5.46%, 18.63% and 22.78% for cement, mixture soil-cement (15% of Cc), and loess respectively.

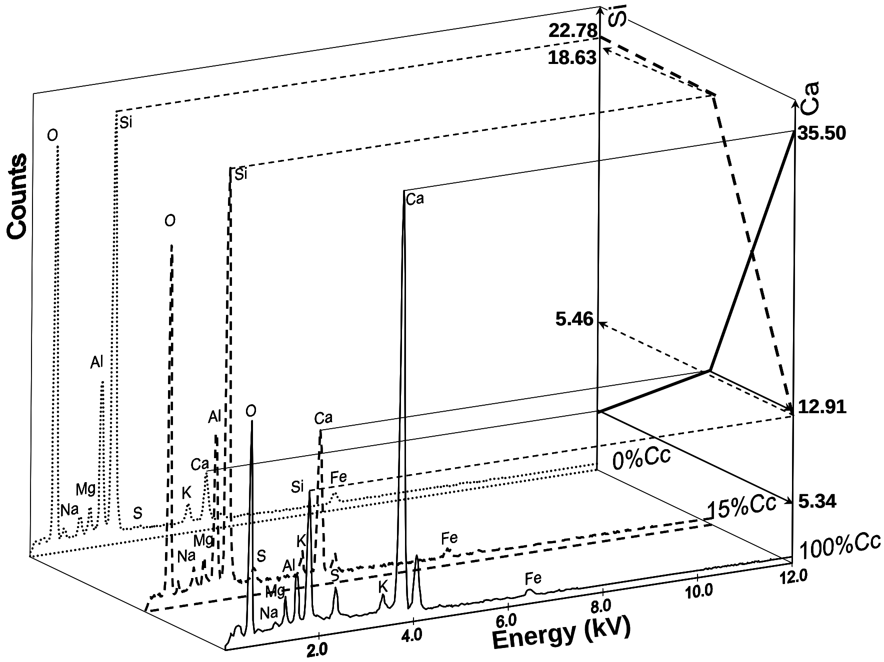

Fig. 6. Energy Dispersive Spectroscopy test (EDS). Variation of Si and Ca

4 MECHANICAL TEST

For unconfined compression tests (UC) a mechanical press was used, instrumented with a load cell with a capacity of 50kN and a digital comparator for recording displacements with a precision of 0.001 mm, to a constant deformation rate of 2.4 mm/min. UC tests is used to evaluate the stress–strain characteristics and the stiffness properties of the Soil-Cement-Mixture (SCM).

Fig. 7 shows the typical failure of specimens with C.c: 15% and natural loess soil (C.c: 0%). The addition of cement, causes an increase stress and strength. SCM samples have a typical inclined failure plane (α_f) for defining cohesion and friction angle in Mohr-Coulomb failure criterion. In loess samples without cement addition (C.c: 0%) there is an increase of sectional side due to material ductility. The failure stress is considered as maximum stress reached before softening in stress-strain curve. It does not take into account the level of deformation reached.

The results obtained from 5 UC tests with unit weight: 14 kN/m^3, time of curing: 14 days, temperature of curing: 20 ºC, and initial water content: 21 % is shown in Fig. 8.

The tendency on stress-strain curves show that the initial modulus increases with increasing of cement content. The tendencies are not linear and deformation reaches 2.5%. Cement content of 2.5% have a unconfined compressive strength of 270 kPa, but a cement content of 15% can increase resistance to 9628 kPa. Cementation, cohesion and suction level, modify cohesive parameter from Mohr-Coulomb failure criterion. (Fig.2 (b)), it grows to 1564 kPa for C.c: 15%, 1463 kPa for C.c.: 10%, 987 kPa for C.c: 7.5%, 208 kPa for C.c: 5.0%, 71.95 kPa for C.c: 2.5%. For each C.c specified in paragraph 2.3, has been modified water content. This allows establishing its influence in the development of resistance. The specimens were built to 14 kN/m^3 dry unit weight.

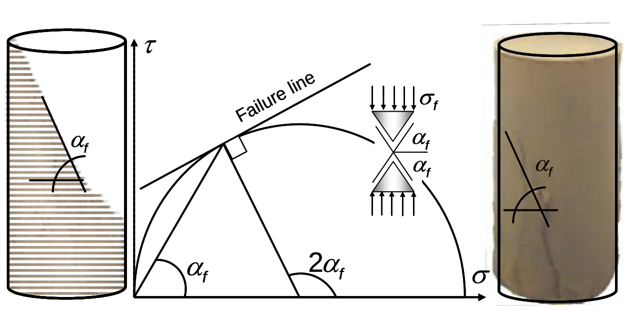

(a) (b) (c)

Fig.7: Typical failure. (a) Soil-cement (C.c.: 15%) (b) Theoretical behavior model (c) Natural loess soil

Fig. 9 shows the maximum compressive strength of concrete mixtures and the initial water content. Samples built with Cc: 2.5%, presents a maximum resistance to wi = 19%, for Cc: 5.0% at wi = 23%, Cc: 7.5% at wi = 19%, Cc: 10.0% at wi = 21 %, and Cc: wi = 15% to 23%. The results show that the peaks of resistance are obtained for water contents between 19% and 23%, average 21%. Outside this interval, the unconfined compressive strength decreases significantly. This behavior can be associated with deficiency or excess in available water in the soil matrix during the hydration process.

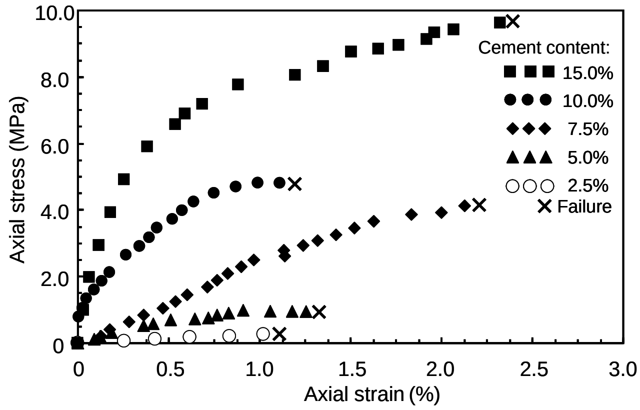

Fig.8: Stress-strain curves unconfined compression test

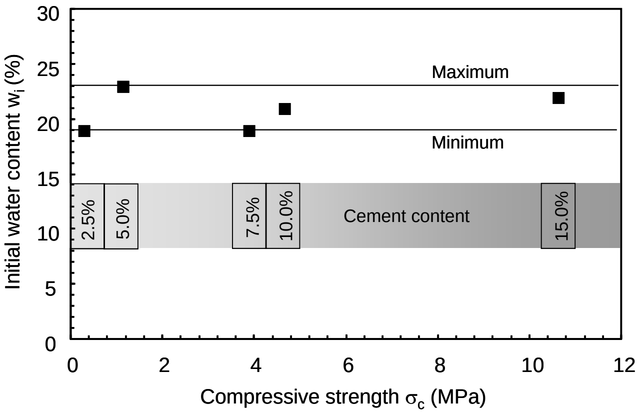

Fig. 9: Maximum compressive strength for different initial water content

A cement content of 9% has been defined to study the curing time influence and curing temperature influence. Fig. 10 presents the relationship between unconfined compressive strength and curing time, with 21% initial water content and 20 °C curing temperature.

At early ages less than 15 days, developed the most important percentage of resistance, which reaches 3.5 MPa. In semilogarithmic scale, the relationship between curing time and the resistance is linear.

After 15 days, there is a strength improvement less than 20% of the maximum strength.

Fig. 11 presents results that relate to the curing temperature and unconfined compressive strength. The samples were stored during the curing period in different environmental conditions. The samples were cured in an oven, refrigerator and laboratory environment. Temperature was controlled.

For temperatures below 0 °C, the maximum strength reached is 2.0 MPa. The optimum is between 20 ºC and 30 ºC. The results showed that unconfined compressive strength decrease (40%), for temperature extreme conditions (100 ºC).

Decreased resistance to low and high temperatures may occur by inhibition of water available for hydration during freezing effect or vaporization effect respectively.

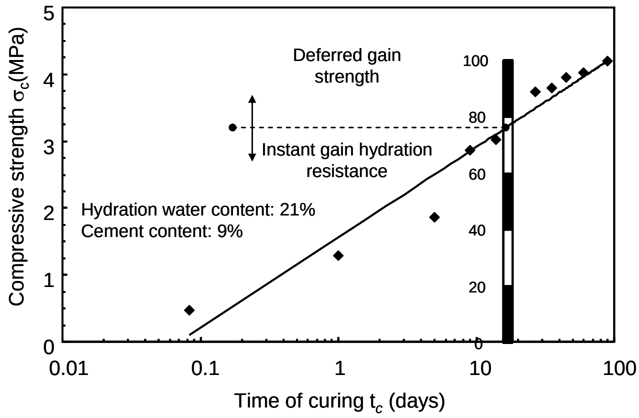

Fig. 10: Compressive strength and time or curing

This phenomenon prevents the hardening material generation and the cement links between particles. The lowest resistance obtained for tests, is presented for low temperatures. Possibly because of increased volume of water during freezing, and decrease in water available for hydration.

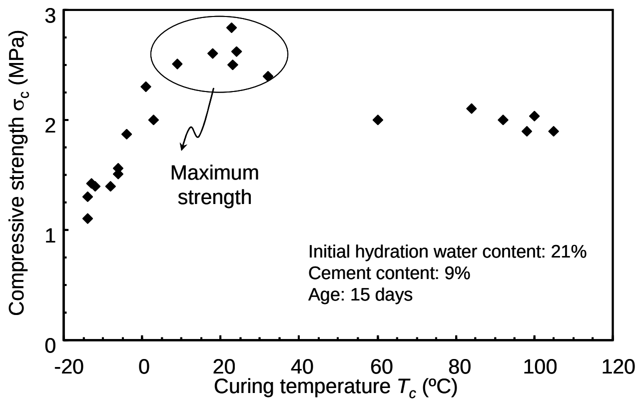

Fig. 11: Compressive strength vs. temperature of curing

5 CONCLUSION

This paper has presented a study on loess material and normal Portland cement and revised the importance of interparticle bridges and their influence on the mechanical performance of the material. Water content, unit weight, cements content, time of curing and temperatures of curing have been studied. The principal results are as follows:

- The unconfined compression shows a maximum independent of cement content when initial water content range is 19% to 21% (hydration water).
- The temperature range that triggers the hydration of cement and improves the unconfined compressive strength ranges from 20 ºC to 30 °C.
- Extreme temperatures (high or low) will reduce strength of samples in 60%.
- 80% of unconfined compression strength is achieved

during the first 15 days of hydration.

- Mixtures with Cc: 7.5% or higher have appropriate physical and mechanical properties for use in various civil infrastructures. Highlights the possibility of making bricks for building houses.

6 ACKNOWLEDGMENT

This work was partially funded by the National University Technological, Regional Córdoba Faculty (Argentina), by the National Agency of Scientific and Technological Promotion of Argentina and Ministry of Science and Technology (Government of Córdoba). The authors thank the staff of GIGEF.

7 REFERENCES

[1] Arrúa, P; Aiassa, G. Eberhardt, M. and Alercia, I. 2011. Estabilización de suelos loessicos mediante la incorporación de un aglomerante mineral. 14th Pan-American Conference on Soil Mechanics and Geotechnical Engineering. Toronto, Ontario, Canadá 2 - 6 October 2011 (to be published).

[2] Eberhardt, M.; Arrúa, P.; Aiassa, G. y Terzariol, R. 2011. Optimización de las obras de cierre para el control de inundaciones en el noreste pampeano. Revista de Geología Aplicada a la Ingeniería y el Ambiente. ISSN: 1851-7838. Junio 2011 Nº26. pp. 29-36.

[3] Aiassa, G. y Arrúa, P. 2007. Diseño de mezclas de suelo compactado para la construcción de terraplenes. Revista EIA. ISSN:1794-1237. Vol. 7 pp. 51-69.

[4] Aiassa, G.; Arrúa, P. and Eberhardt, M. 2011. Geotechnical and hydrogeological considerations for landfill site selection in the Argentina loess region. International Journal of Earth Sciences and Engineering. ISSN: 0974-5904. Vol. 4, No 1, pp.1-12.

[5] Lachemi M., Hossain, K., Shehata, M., Thaha W. 2008. Controlled low strength materials incorporating cement kiln dust from various sources. Cement & Concrete Composites 30, pp. 381–392.

[6] Piattoni Q., Quagliarini E., Lenci S. 2011. Experimental analysis and modelling of the mechanical behaviour of earthen bricks. Construction and Building Materials 25, pp.2067–2075

[7] Bahar R., Benazzoug M., Kenai S. 2004. Performance of compacted cement-stabilised soil. Cement & Concrete Composites 26: pp. 811–820.

[8] Li Chen, Deng-Fong Lin. 2009. Stabilization treatment of soft subgrade soil by sewage sludge ash and cement. Journal of Hazardous Materials 162: 321–327.

[9] Zárate, M.A. 2003. Loess of southern South America. Quaternary Science Reviews. PERGAMON. 22: 1987-2006.

[10] Shan B., Wang C., Dong Q., Tang L., Zhang G., and Wei J., 2010. Experimental study on improving collapsible loess with cement. Global Geology, 13 (2) pp. 79-84.

[11] Altun S., Sezer A., Erol A., 2009. The effects of additives and curing conditions on the mechanical behavior of a silty soil. Cold Regions Science and Technology 56, pp.135–140.

[12] Ying Xia Yu, Yu Feng Jiao, Bin Liang, Wei Zhang. 2011. Experimental Research on the Mechanical Properties of Compacted Cement Soil in Collapsible Loess Area and Engineering Application. J. of Advanced Materials Research. Volumes 250 – 253, pp. 421-424.

[13] Sayago J., Collantes M., Karlson A., Sanabria J. 2001. Genesis and distribution of the Late Pleistocene and Holocene loess of Argentina: a regional approximation. Quaternary International, 76/77: 247-257.

[14] Mitchell, J.K. and Soga, K. 2005. Fundamentals of Soil Behavior, 3rd ed. Jhohn Wiley & Sons, Hoboken, New Jersey, USA

[15] Teruggi M. 1957. The Nature and Origin of Argentine Loess. Journal of Sedimentary Petrology 27 (3): 322-332.

[16] Bidegain J., Rico Y., Bartel A., Chaparro M. and Jurado S. 2009. Magnetic parameters reflecting pedogenesis in Pleistocene loess deposits of Argentina. Quaternary International, Vol 209, pp. 175-186.

[17] Arrúa, P.; Aiassa, G. and Eberhardt, M. 2011. Loessic soil stabilized with cement for civil engineering applications. International Journal of Earth Sciences and Engineering. ISSN: 0974-5904 (to be published)

[18] Ricci J. 1966. El loess de Río Tercero y el probable origen de los mallines (Córdoba). Terceras Jornadas Geológicas Argentinas, Bahía Blanca.

[19] Arens, P. 1969. Algunos paisaje geoquimicos de la región pamepeana, Reunión Argentina de la Ciencia del Suelo, Santa Fe, Argentina, Actas V.

[20] Camino, M., 1988. Estratigrafía y evolución paleoambiental durante el Cuaternario del Valle de La Sala. Unpublished Thesis, Facultad de C. Naturales, Universidad de Tucumán, Tucumán, Argentina.

[21] Morras, H., 1996. Composición y evolución de la fracción limo grueso de suelos del Chaco meridional argentino. Congreso Geológico Argentino, Actas XIII Vol. IV: 263-265.

[22] Krumbein W., and Sloss L. 1963. Stratigraphy and Sedimentation, 2nd ed. W.H. Freeman, San Francisco.

[23] Powers M. 1953. A new roundness scale for the sedimentary particles. Journal of Sedimentary Petrology, Vol. 23, pp.117-119.

First International Conference on Geotechnique, Construction Materials and Environment, Mie, Japan, Nov.21-23, 2011, ISBN: 978-4-9905958-0-7 C3051

A Study on Hardened Soil Brick Using Liquid Type and Powder Type Hardening Agent

Jin, Sung Ki. Jung, Seung Yong. Kim, Tae Ho., Overseas Business Team, EGE(Expert Group for Earth & Environment) Co. Ltd.

ABSTRACT: The study is to produce hardened soil bricks, blocks, boundary stones, or other objects. It uses hardening agent (liquid- or powder-type) made with eco-friendly ingredients. Contrarily to the traditional bricks, baked in the furnace, it is possible to make hardened soil bricks and blocks from site soil, whose particles are unevenly distributed, without applying heat to them. Therefore, a purpose of this study is to provide a method of the hardened soil brick production which is able to reduce costs and meet the demanding quality standard by utilizing the site soil. To achieve this, laboratory mixing test and uniaxial compression test have been performed regarding specimen that mixes liquid and powder type hardening agent with the site soil not meeting the standard of grain-size distribution. Input percentage of chemical components for the agents is also evaluated by XRF. Through the tests, improvement effect on the hardening agents may be verified, and moderate mixing ratio of them may be drawn.

Keywords: Hardened Soil Brick, Powder Type Hardening Agent, Liquid Type Hardening Agent, OMC(Optimum Moisture Content), Maximum Dry Density(γ_{dmax})

1. INTRODUCTION

Lately, the demands for economical and satisfactory methods of road base treatment and brick production have been increasing in developing countries such as China, Southeast Asian countries, and African countries. The fundamental reason for that is the short supply of quality sand and crushed stone in some regions or the financial difficulty to supply them.

Currently, the road bases in developing countries are treated with concrete, but a technology to utilize the site soil is needed to reduce the expenses for the disposal of surplus soil and the treatment itself. On the other hand, bricks are produced by the conventional method, of which the site clay is collected with human hand then put in a mechanical former to shape clay bricks, and then the clay bricks are dried under the sun and burned in the furnace. Bricks produced in this way vary in quality since the heat a brick receives in the furnace differs depending on the spot it is placed. Also, the method caused deforestation when firewood is used to operate the furnace and resulted air pollution when fossil fuel is used.

Other than burned clay brick, cement brick is out in the market. The approximate cement - sand - crushed stone ratio for cement brick production is 1:2:4. There are two ways to decide the quantity of water added, which have a great impact on the solidity of brick. One follows the approximate cement-to-water ratio of 1:10. The other is to go by the call of the site engineer. It is done by grabbing the mixture of aggregate, cement, and water with his fist and judges the O.M.C. (Optimum Moisture Content) by the sensation in his hand, which gives rise to varied quality. Also, if cement is used by itself, heavy metal eruption is possible and the strength is increased limitedly unless crushed stones are added. To prevent these problems, the additives are mixed with the cement. There are two different kinds of typical hardening agent, liquid type and powder type. The liquid type is suitable for sandy soil, and the powder type clayey soil. For these agents, input percentage of chemical components is evaluated by XRF(X-ray fluorescence) analysis in order to survey the harmful components.

This paper presented two different ways for the production of the hardened soil bricks, which is elastic, economical, and eco-friendly and exceeds by far the target strength, 8 N/mm2 (81.6kg/cm^2), with high durability and no heavy metal eruption. The first of the two ways mentioned is to mix cement and sandy soil and add a little quantity of liquid type hardening agent. The second is to mix clayey soil and cement and add power-type hardening agent.

A purpose of this study is to provide a method of the hardened soil brick production and the road base treatment, which is characterized by the aggregate of the site soil, cement, and the hardening agent mixed by the agitator, vibrated, pressed by oil pressure, and molded. Another purpose is to present the materials and mixing ratio of liquid and powder type hardening agents for the production of soil brick and the road treatment using the site soil (sandy soil, clayey soil) which is unevenly distributed.

2. FIELD OF STUDY AND METHOD

2.1 Experimental Method

Considering the unfavorable condition for the site soil quality in some countries, soil sampling for this study was conducted at Jebudo beach in Incheon-si, Korea, the silt and sand sample of which does not meet the standard of grain size distribution, Coefficient of Uniformity (Cu), of 4 to 6 [4].

The quality control standard was established according to the result of the tests done to different types of hardening agents for road base treatment and brick production. Strength test and pre-mixture test was performed identically to each type, and then the agents which satisfy the criteria from those tests were tested in detail. Two different types of hardening agent, in broad, were developed and the improvement to each soil type accordingly was shown after a series of tests. The first is liquid type which is mainly composed of chemicals, and the other powder type which is mainly mineral materials [2]-[3]-[7].

2.2 Used Hardening Agents

2.2.1 Liquid type hardening agent

Liquid type hardening agent used for this study is inorganic, and Sodium silicate (Na_2SiO_3), Magnesium chloride ($MgCl_2$), Potassium chloride (KCl), Calcium chloride ($CaCl_2$), and Sodium carbonate (Na_2CO_3) are the additives for the hardening agent. The chemical reaction formulas among the additives are as follows:

$$CaCl_2 + Na_2SiO_3 \rightarrow CaSiO_3 + 2NaCl \quad (1)$$

$$KCl + Na_2SiO_3 \rightarrow KSiO_3 + 2NaCl \quad (2)$$

$$MgCl_2 + Na_2SiO_3 \rightarrow MgSiO_3 + 2NaCl \quad (3)$$

$$H_2O + Na_2SiO_3 \rightarrow SiO_2H_2O + 2NaCl \quad (4)$$

The by-products of this process, which are Calcium silicate ($CaSiO_3$), Potassium chlorate ($KSiO_3$), Magnesium silicate($MgSiO_3$), and Silicon dioxide Hydrate(SiO_2H_2O), are assumed to complexly react to the main component of normal cement such as SiO_2, Al_2O_3, CaO, and Fe_2O_3, with the chief ingredient of site soil like SiO_2, Al_2O_3, Fe_2O_3, CaO to cause solidification [1].
The Input Percentage of the Component of Liquid Type Hardening Agent is as Table Ⅰ.

Table Ⅰ. The Input Percentage of the Component of Liquid Type Hardening Agent

Description	**SiO_2**	**CaO**	**MgO**	**Na_2O**	**K_2O**
Percentage(%)	50.08	3.02	3.08	2.25	4.08
Description	**SO_3**	**Cl**	**CHO**	**Others**	
Percentage(%)	1.68	18.61	16.50	0.70	

The Standard Mixing Ratio for Liquid Type Soil Brick which satisfies the target strength of 8N/mm^2 (81.6 kg/cm^2) for hardened soil brick in this study is specified in Table Ⅱ below.

Table Ⅱ. The Standard Mixing Ratio for Liquid Type Soil Brick

Description	**Liquid Input (kg/m^3)**	**Cement Input (kg/m^3)**
Sandy Soil	1.5	400

2.2.2 Powder type hardening agent

Silica Fume which is used for powder type hardening agent in this study is micro-fine powder that is the by-product of producing silicon and ferrosilicon alloys in electric arc furnace. Although it is essential in the production of high-strength concrete, the use for it as an additive to the hardening agent for brick is very insignificant. One of the physical properties of silica fume is that its particles are very minute. Above 95% of its particles is less than 1 micrometer in size. When silica fume is added to cement slurry, the fine particles of silica fume fill the space between cement particles and this phenomenon is called Micro Filling. Because Micro Filling substitutes the pores bigger than 1 micrometer in size to innumerable microscopic pores, using silica fume increases the coherent force among soil particles and the strength of solidified body. Also, silica fume, which has a high percentage of amorphous Silicon Dioxide (SiO_2), turns into highly reactive pozzolan material in soil. It chemically reacts to Calcium Hydroxide ($Ca(OH)_2$), the product of chemical reaction between Portland cement and water(H_2O), and forms the binder called Calcium Silicate Hydrate(C-S-H). This binder especially improves the strength of solidified body. Its high amorphous Silicon Dioxide (SiO_2) content and minuscule particles cause silica fume to be highly reactive especially in the early phase. Furthermore it is known that powerful dispersing agent or chemical admixture, known as the water reducing agent, increases effectiveness of silica fume [5]. The chemical equation for powder type hardening agent of this study shows Pozzolanic reaction and as follows. Particularly silica fume, SiO_2, is artificially supplied to promote formation of the Calcium Silicate Hydrate(C-S-H) binder [5]-[6].

C_3S, C_2S(in cement) $+H_2O \rightarrow Ca(OH)_2 + H_2O$ (5)

↓

Add SiO_2 to the product (6)

↓

The formation of C-S-H(Calcium Silicate Hydrate) (7)

The Input Percentage of the Component of Powder type hardening agent is as Table Ⅲ.

Table Ⅲ. The Input Percentage of the Component of Powder type hardening agent

Description	**SiO_2**	**Al_2O_3**	**Fe_2O_3**	**CaO**	**MgO**
Percentage(%)	90.09	1.05	1.43	1.33	1.77
Description	**Na_2O**	**K_2O**	**SO_3**	**Cl**	**Others**
Percentage(%)	0.50	2.76	0.68	0.13	0.26

The Standard Mixing Ratio for Powder Type Soil Brick which satisfies the target strength of 8N/mm^2 (81.6kg/cm^2) for hardened soil brick in this study is specified in Table Ⅳ below.

Table Ⅳ. The Standard Mixing Ratio for Powder Type Soil Brick

Description	**Cement (kg/m^3)**	**Silica Fume (kg/m^3)**	**Lignosulfonate (kg/m^3)**
Clayey Soil	520	26 (5% of Cement Weight)	1.3 (0.25% of Cement Weight)

3 RESULT

3.1 Result of Soil Property Test

Table Ⅴ. Result of Soil Property Test

Description		Sand		Silt	
Depth (m)		0.30	0.30	0.30	0.30
Moisture Content (%)		1.4	1.1	29.7	29.4
Density, ρ_s (g/cm^3)		2.692	2.694	2.697	2.697
Liquid Limit (%)		NP	NP	27.9	29.1
Plastic Index		-	-	2.1	2.7
D Compaction	γ_{dmax} (t/m^3)	1.62	-	1.60	-
	OMC (%)	18.0	-	17.0	-
USCS		SP	SP	ML	ML

The average Uniform Coefficient (Cu) of the site soil samples for this study was recorded 2.89 for sandy soil and 2.56 for clayey soil, which means the soil particles are unevenly distributed. According to the compaction test, sandy soil sample showed Maximum Dry Density (γdmax) of 1.62 t/m^3, and Optimum Moisture Content (O.M.C) of 18.0%. Also, clayey soil sample showed Maximum Dry Density (γdmax) of 1.60 t/m^3, and Optimum Moisture Content (O.M.C) of 17.0%.

The result of grain-size distribution test for sand and silt is shown in Fig. 1 and 2. The result of compaction test for sand and silt is also shown in Fig. 3 and 4.

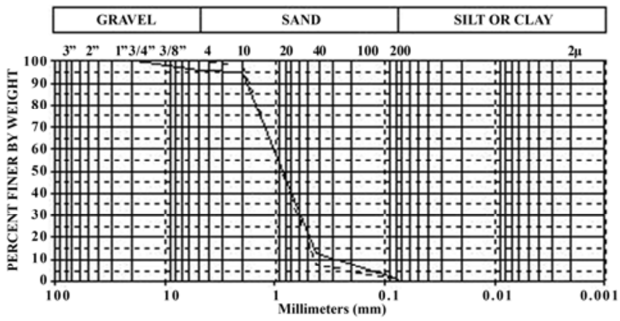

Fig. 1 Grain-Size Distribution Curve (Sand)

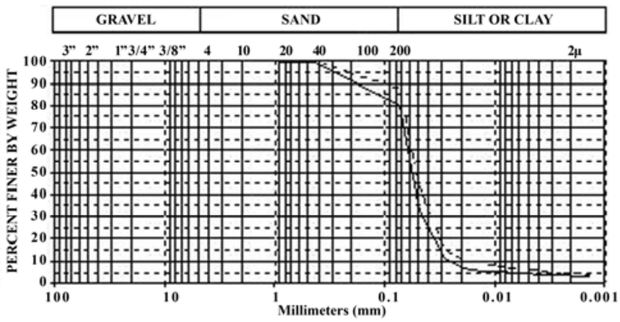

Fig. 2 Grain-Size Distribution Curve (Silt)

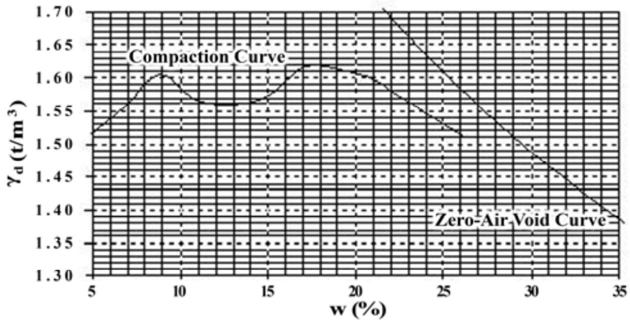

Maximum Dry Density (γ_{dmax})	1.62	t/m^3
Optimum Moisture Content (OMC)	18.0	%

Fig. 3 Result of Compaction Test (Sand)

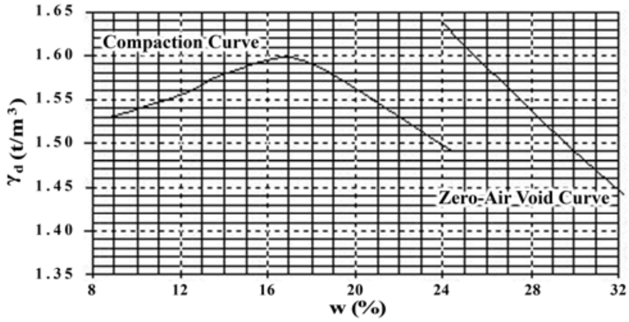

Maximum Dry Density (γ_{dmax})	1.60	t/m^3
Optimum Moisture Content (OMC)	17.0	%

Fig. 4 Result of Compaction Test (Silt)

3.2 Result of the Uniaxial Compression Strength Test

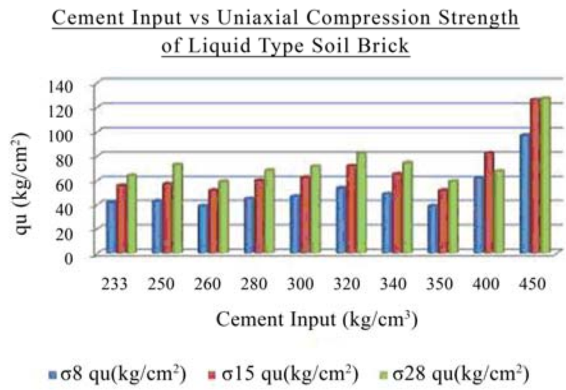

Fig. 5 Cement Input vs. Uniaxial Compression Strength of Liquid Type Soil Brick

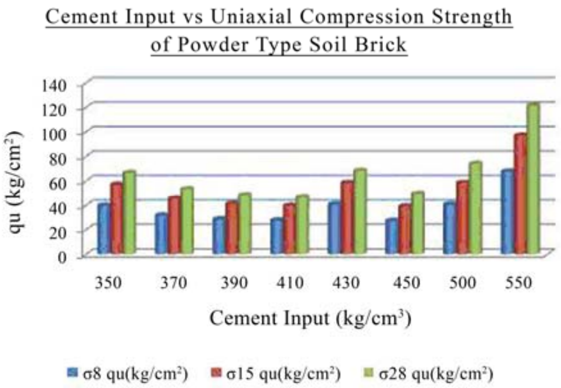

Fig. 6 Cement Input vs. Uniaxial Compression Strength of Powder Type Soil Bricks

According to the uniaxial compression strength test carried out to soil brick specimen, liquid type hardening agent is more effective to sandy soil sample, and powder type to silt soil sample. As for liquid type sand brick, the maximum strength was yielded when the input of the agent was 2.5kg/m^3, and as for powder type clay brick when the input of the mineral-consisting powder type agent reaches 8% of the total cement weight. Also, the mixture is to be compacted to -2% of Optimum Moisture Content(O.M.C.) in the case of liquid type sand brick, and +2% of O.M.C. in the case of powder type silt brick. The optimum mixing ratio for liquid type sand brick is 2.5kg/m^3 of liquid hardening agent and 400kg/m^3 of cement. The optimum mixing ratio for powder type sand brick is when the input of powder type mineral additive is 8% of the total cement weight, and the cement input is 520kg/m^3, and this satisfies the strength standard for cement brick as shown in Fig. 5 and 6 above [8].

4 CONCLUSION

Liquid type hardening agent used for this study is inorganic, and Sodium silicate (Na_2SiO_3), Magnesium chloride ($MgCl_2$), Potassium chloride (KCl), Calcium chloride ($CaCl_2$), and Sodium carbonate (Na_2CO_3) are used as the additives for the hardening agent.

The by-products of this process, which are Calcium silicate ($CaSiO_3$), Potassium chlorate ($KSiO_3$), Magnesium silicate($MgSiO_3$), and Silicon dioxide Hydrate(SiO_2H_2O), react complexly with the main components of normal cement such as SiO_2, Al_2O_3, CaO, and Fe_2O_3 and cause the solidification.

1. Silica Fume and lignosulfonate are used for powder type hardening agent as the main additives.

Also, silica fume turns into highly reactive pozzolan material in soil and forms the binder called Calcium Silicate Hydrate(C-S-H). When it is mixed with cement and acts both as water reducing agent and binder for strength increase.

2. Sodium silicate and various additives are used for liquid type hardening agent.

These materials act with the normal cement and cause the strength increase.

3. For sandy soil, the standard mixing ratio for liquid type soil brick which satisfies the target strength of 8N/mm^2 (81.6 kg/cm^2) for hardened soil brick in this study is specified as follows; Liquid Input: 1.5(kg/m^3), Cement Input: 400(kg/m^3)

4. The input percentage of the component of liquid type hardening agent is as follows; SiO_2: 50.08(%), CaO: 3.02(%), MgO: 3.08(%), Na_2O: 2.25(%), K_2O: 4.08(%), SO_3: 1.68(%), Cl: 18.61(%), CHO: 16.50(%), Others: 0.70(%)

The input percentages of the component of powder type hardening agent are as follows; SiO_2: 90.09(%), Al_2O_3: 1.05(%), Fe_2O_3: 1.43(%), CaO: 1.33(%), MgO: 1.77(%), Na_2O: 0.50(%), K_2O: 2.76(%), SO_3: 0.68(%), Cl: 0.13(%), Others: 0.26(%)

5. For clayey soil, the standard mixing ratio for powder type hardening agent which satisfies the target strength of 8N/mm^2 (81.6kg/cm^2) is specified as follows; Cement: 520(kg/m^3), Silica Fume : 26(kg/m^3)(5% of Cement Weight). Lignosulfonate : 1.3(kg/m^3)(0.25% of Cement Weight)

5 REFERENCES

[1] Moon Han Kim, “Study on Development of Soil Cement Brick and validity for its application”, Journal of the Architectural Institute of Korea, Volume 24, No. 94, 1980, pp 25-32.

[2] Korea Institute of Industry and Technology Information, “Study on optimum treatment of by-product gypsum”, 1998.

[3] Ministry of Construction and Transportation, “Study on the reuse of the casting foundry fly ash - Final Report of Research and Development Project for 1996”, 1998.

[4] Sang Kyu Kim, “Soil Mechanics - Theories and Applications”, Cheong Moon Gak Publishers, 1992.

[5] Korea Concrete Institute, “Concrete Structures”, 1995.

[6] Silica Fume Association, “Sillica Fume User's Manual”, U.S. FedDeperal Highway Administration, 2005.

[7] Byung Sik Chun, “A Study on the Surface Soil Stabilization on Marine Clay by the Hardening Agent”, Journal of Ocean Engineering and Technology, Volume 15, No. 1, 2001, pp 92-97.

[8] Korean Standards Association, “Korean Industrial Standards - Concrete Brick(KS F 4004)”, 2003.

[9] “The Deep Mixing Method(Principle, Design, Construction)”, Coastal Development Institute of Technology, Japan, 2002, pp 37-50.

The Effect of Salt Content in Soil on the Sorption Capacity of Heavy Metals

Lerd Kerdchaiyaphum and Pongsakorn Punrattanasin
Research Center for Environmental and Hazardous Substance Management and Department of Civil Engineering
Faculty of Engineering, Khon Kaen University, Thailand
Email: lerdkerd@gmail.com, ppunrattanasin@gmail.com

Abstract
In the Northeastern part of Thailand, saline soil can be easily found in abundance in all areas. Salts can be directly extracted from the topmost layer of soils. This study aimed to determine the sorption values of contaminations on soil with a variety of salt content. A soil sample in this study was collected from Khon Kaen University. The soil is known as loess or silty fine sand (SM). The amount of contaminations adsorbed in soil was measured using the batch equilibrium test. Chemical analyses were performed with an Atomic Absorption Spectrophotometer (AAS). The equilibrium conditions required are around 48 hours of shaking between loess with heavy metals. The results also show the adsorption isotherm and the maximum adsorption capacity of soil with different contents of salts.

Keywords: Contaminations, Saline soil, Sorption value, Isotherm, Loess

1. Introduction

Due to technologies in the Northeastern part of Thailand growth during many decades, industrial has been increased. The results in a discharge of waste into environmental over the limit. The environmental problems are severe and difficult to resolve. One result is leakage of heavy metals in contaminated water and soil [2]. Heavy metals are some of the deposit in the soils. Because soils are heterogeneous, numerous studies have focused on the interaction of several heavy metals with different soil constituents [4]. The Northeastern region of Thailand covers an area of 168,855.50 km^2. The top most soil layer found in all areas in loess layer or wind-deposited soil (Fig.1). The thickness of loess ranges from a few meters to more than six meters. In the Northeastern part, saline soil can be also easily found in abundance in all areas, especially in the top and middle parts. Thus, this research aims to investigate the effect of salt content in soil on the adsorption capacity of heavy metals by the loess.

2. Material description

The material used in this study is loess which is collected and excavated from Khon Kaen University. The soil can be classified as silty find sand (SM) in the Unified Soil Classification System (USCS). The basic, index and engineering properties of the loess are tabulated in Table 1.

Figure 1. Loess deposit in the Northeastern part of Thailand.

Table 1. Loess properties.

Properties	Loess
Soil classification (USCS)	SM
Specific gravity	2.60
Natural dry unit weight (kN/m^3)	15.30
Natural water content (%)	5-12
Liquid limit (%)	16.0
Plastic limit (%)	13.0
Plasticity Index (%)	3.0
Optimum moisture content (%)	10.0
Maximum dry unit weight (kN/m^3)	21.1
Coefficient of Permeability (cm/s)	2.80×10^{-6}

Heavy metals chosen in this study was only copper (Cu), zinc (Zn) and nickel (Ni) which was obtained by dissolving nitrate. Tables 2, 3 and 4 summarized properties of copper nitrate, zinc nitrate and nickel nitrate, respectively. Selections of Cu, Zn and Ni as heavy metals were based on its low toxicity and relative ease involved in handling, disposal and also all are easily found in all areas. All three are the common heavy metals which are discharged from various and common industries [1].

Table 2. Properties of copper nitrate.

Compound	Copper Nitrate
Formula	$Cu(NO_3)_2$
Molecular weight (g/mol)	295.65
Density (g/cm^3)	2.07
Solubility (g/100 ml)	137.8

Table 3. Properties of zinc nitrate.

Compound	Zinc Nitrate
Formula	$Zn(NO_3)_2$
Molecular weight (g/mol)	297.49
Density (g/cm^3)	2.065
Solubility (g/100 ml)	137.8

Table 4. Properties of nickel nitrate.

Compound	Nickel Nitrate
Formula	$Ni(NO_3)_2$
Molecular weight (g/mol)	290.79
Density (g/cm^3)	2.05
Solubility (g/100 ml)	94.2

3. Experimental methodology

In this study batch adsorption test is designed as a tool to study the equilibrium adsorption of soil suspensions with contaminants [5]. In batch adsorption test, chemical solution and disaggregated state are brought into contact [3]. The main objective of this test is to find the adsorption capacity of heavy metals by loess and to find the effect of salt content in soil on the sorption capacity of heavy metals.

3.1 Batch adsorption test

The equilibrium contact time was firstly determined and investigated by batch adsorption test. Soil sample was loess (SM). This sample was washed to clear as much as contaminant away first after that, sized it by taking through by the sieve No. 200. Heavy metals used in the experiment were Copper Nitrate, Zinc Nitrate and Nickel Nitrate with the concentration of 100, 200, 300, 400 and 500 mg/L. A constant mass of oven soil powder of 2.5g and 50 ml of metal solution were added into a set of 120 ml plastic bottles (Fig 2.). The soil solution ratios were then shaken at 150 rpm for 0.5, 1, 3, 6, 12, 24, 48 and 72 hours by using a horizontal shaking machine (Fig 3.). After particular shaking time the solutions were filtrated though 0.45μm of filter to separate the soil and liquid solution. Liquid solution was then analyzed the chemical concentration by using Atomic Absorption Spectrophotometer (AAS) (Fig 4.).

Figure 2. Soil and solution.

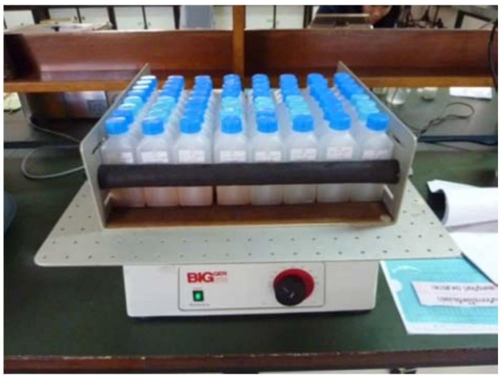

Figure 3. Shaking soil and solution.

Figure 4. Atomic Absorption Spectrophotometer (AAS).

3.2 Salt content on the adsorption test

The salt was mixed with loess with different contents. The salt contents were starting from 10% up to 90% by weight of soil. Heavy metals used in the experiment were the same as in the previous section. A constant mass of oven soil powder of 2.5g, percentage of salt by weight of soil and 50 mg/L of metal solution were added into a set of 120 ml plastic bottles. The soil solution ratios were then shaken at 150 rpm for 48 hours by using a horizontal shaking machine. After that, the experiment was the same as batch adsorption test.

4. Experimental result

4.1 Bath adsorption test

Batch adsorption test were carried out with the aim of observing the equilibrium contact time of copper, zinc and nickel by loess. The results are shown in Figs. 5-7 for contact time of copper, zinc and nickel by loess, respectively. The equilibrium sorption of copper, zinc and nickel were found in the 48 hours. After achieving equilibrium condition if soil solution was kept in still state, it would not cause any sorption or leaching.

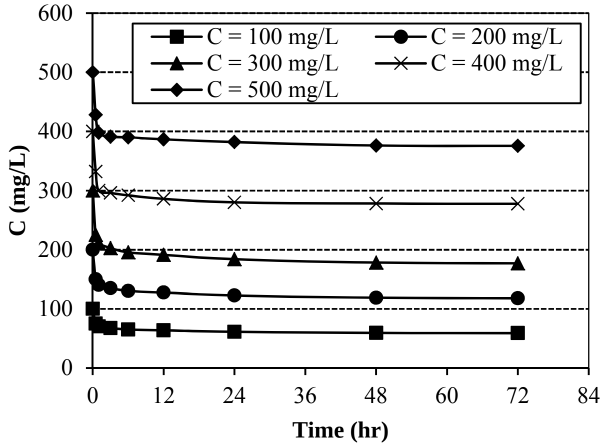

Figure 5. Sorption capacity of copper by loess.

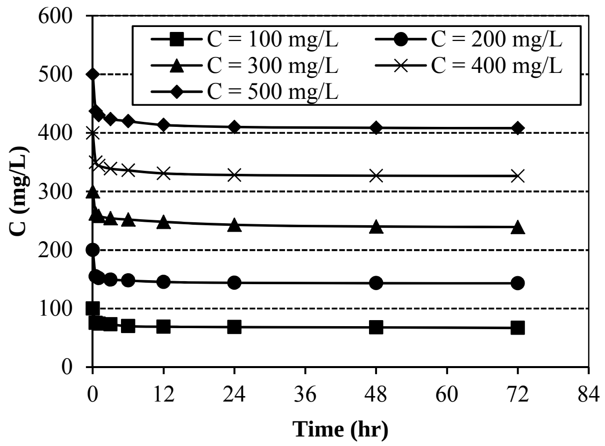

Figure 6. Sorption capacity of zinc by loess.

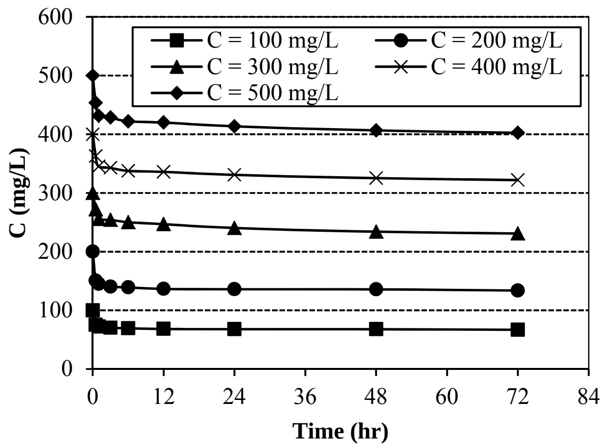

Figure 7. Sorption capacity of nickel by loess.

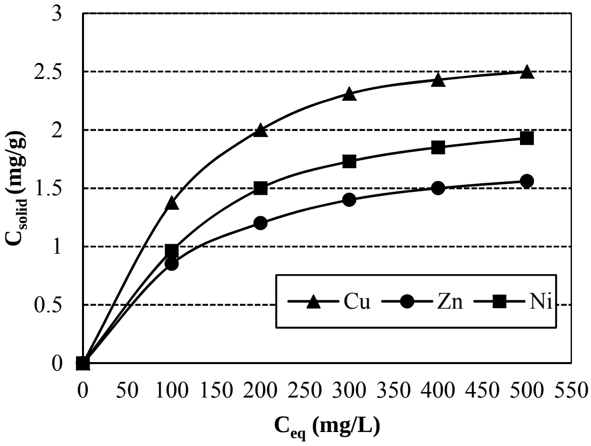

Figure 8. The sorption isotherm of zinc, copper and nickel by loess.

After that, the results of chemical analyzed were plotted between the adsorbed concentration of soil (C_{solid}) versus the equilibrium concentration of liquid (C_{eq}) in order to see the highest tendency that soil can adsorption. For loess with all three solutions, the curves are in Fig. 8. All results show the non linear relationship between C_{solid} and C_{eq} thus the non linear models were implied in the analysis. The result will be plotted at the graph for find the slope and the intercept form to compare with Langmuir (Fig. 9). Langmuir sorption isotherm has been developed on the concept that a solid surface possesses a finite number of sorption sites and mathematically expressed as

$$C_{solid} = \frac{\alpha\beta C_{eq}}{1+\alpha C_{eq}} \tag{1}$$

where α = the adsorption constant related to the binding energy (L/mg) and β = the maximum amount of contaminant that can be absorbed by the solid (mg/g). To determine the values of α and β, a relationship of C_{eq} versus C_{eq}/C_{solid} is plotted. The determined values of α and β based on the calculation from Figs. 9 and 10 for different isotherms are shown in Table 5. It was found that the copper has the highest sorption capacity by considering the α and β values from its isotherm.

Table 5. Langmuir isotherm parameter

Soil	Solution	α (L/mg)	β (mg/g)	Correlation Coefficient (R^2)
Loess	Copper	0.0085	3.132	0.997
	Zinc	0.0078	1.976	0.999
	Nickel	0.0067	2.543	0.995

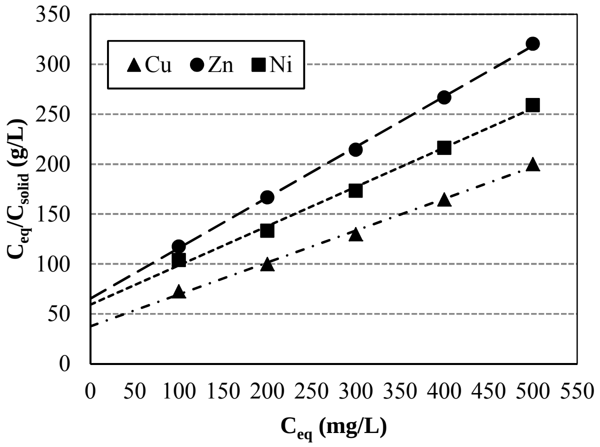

Figure 9. Langmuir isotherms of toxic metals by loess.

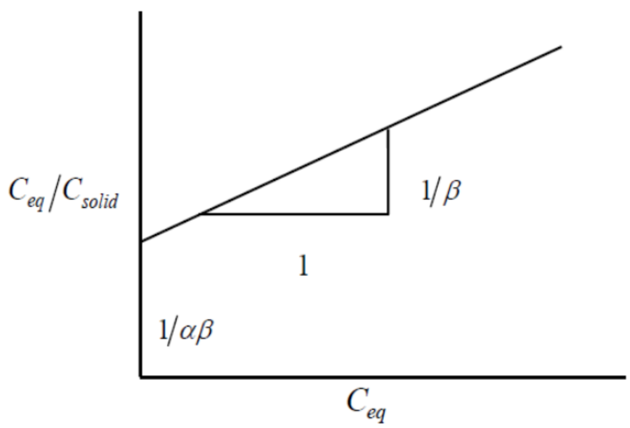

Figure 10. Langmuir isotherm's parameters.

4.2 Salt content on the adsorption capacity

The results of chemical analysis of soil with heavy metals with different contents of salt were plotted between the equilibrium concentration of liquid (C_{eq}) versus the percentage of salt in order to see the highest tendency that soil can adsorption. The results are shown in Figs.11-13. The sorption capacities of toxic metals by loess mixing with salt were found that the percentage of salt staring from 60% by weight can provide the equilibrium concentration of liquid (C_{eq}). The sorption capacities of heavy metals in loess mixing with salt ranked from the highest were copper, nickel and zinc, respectively.

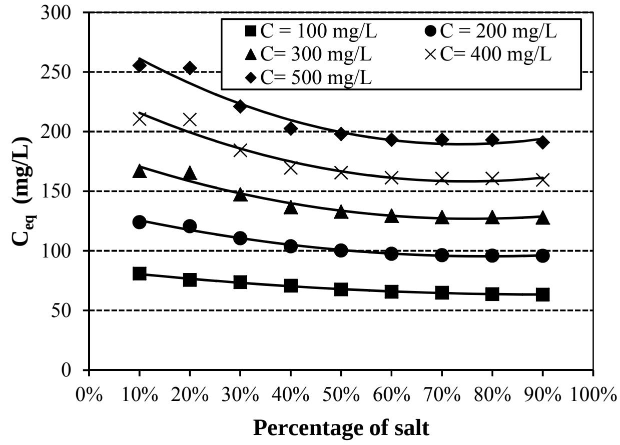

Figure 11. Sorption capacity of copper by loess mixing with salt.

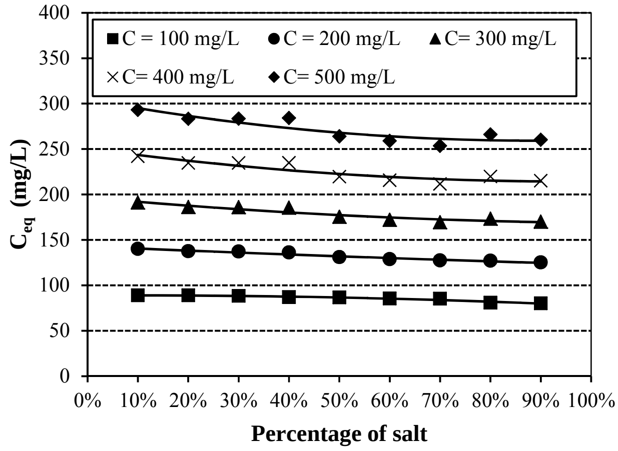

Figure 12. Sorption capacity of zinc by loess mixing with salt.

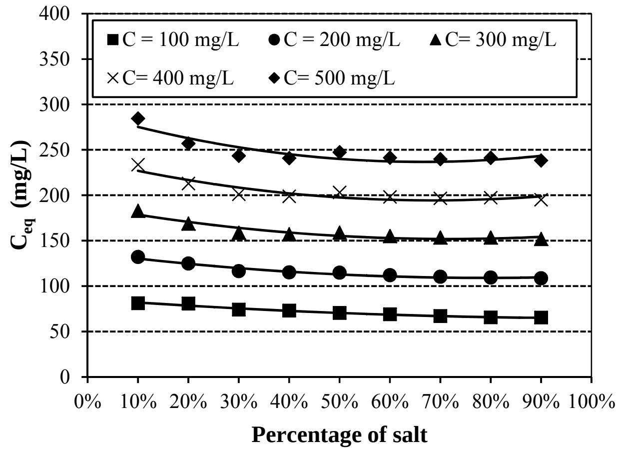

Figure 13. Sorption capacity of nickel by loess mixing with salt.

Then, the results of chemical analyzed of loess mixed salt were plotted between the adsorbed concentration of soil (C_{solid}) versus the percentage of salt. The salt was mixed with loess. It was found that a salt content starting from 60% by weight can provide the highest sorption capacity. The results are shown in Figs.14-16. The sorption capacities of heavy metals in loess ranked from the highest were copper, nickel and zinc, respectively.

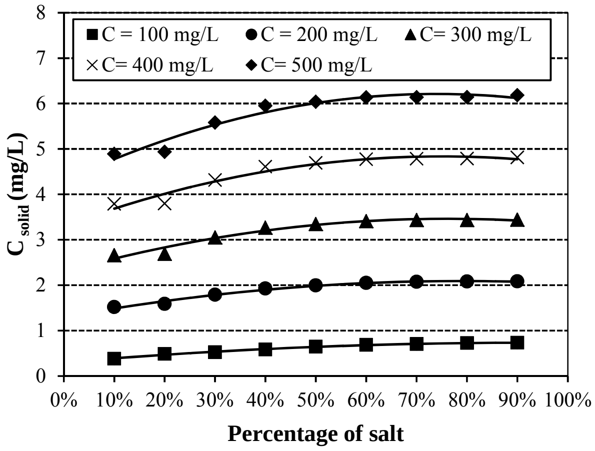

Figure 14. The relationship between C_{solid} and percentage of salt from the test of copper.

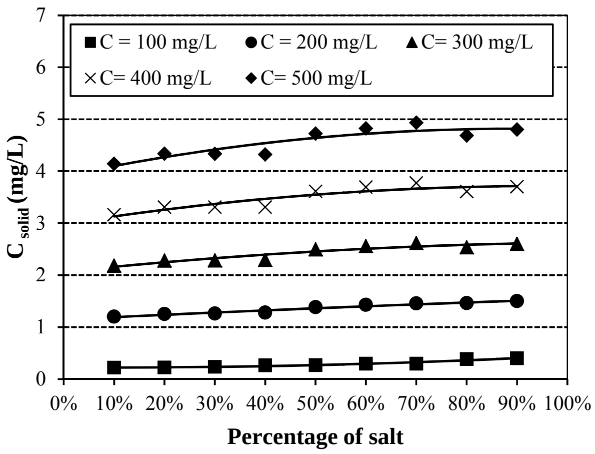

Figure 15. The relationship between C_{solid} and percentage of salt from the test of zinc.

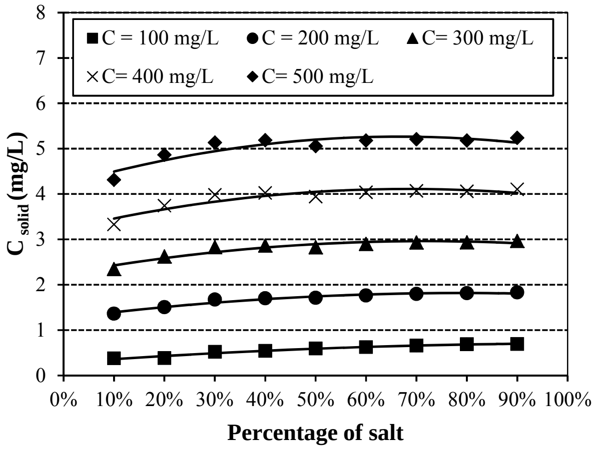

Figure 16. The relationship between C_{solid} and percentage of salt from the test of nickel.

5. Conclusions

This research presents sorption values of contamination on loess which can be found in the top most layers in Khon Kean University. A possible method of reducing the amount of toxic in the river is also proposed by adding and mixing the salt content into the original soil. Batch adsorption test can give an estimate for maximum possible amount of contaminant that can adsorbed by soil. The following conclusions are results in this study from batch adsorption test;

1) The equilibrium sorption of copper, zinc and nickel were found in the 48 hours.
2) The sorption capacities of heavy metals in loess ranked from the highest were copper, nickel and zinc, respectively. The highest sorption capacity by considering the α and β values from Langmuir isotherm.
3) The salt was then mixed with the loess from Khon Kaen University in order to investigate the effect of salt content starting from 60% by weight can provide the highest sorption capacity. The sorption capacities of heavy metals in loess ranked from the highest were copper, nickel and zinc, respectively.

6. Acknowledgment

This research was funded by Research Center for Environmental and Hazardous Substance Management, Khon Kaen University. The authors wish to acknowledge and grateful thank to Asst. Prof. Dr. Arthit Neramittagapong and Miss Wimonporn Iamamornphonth of the Department of Chemical Engineering, Khon Kaen University.

7. References

[1] Alloway, B.J., 1995. "Heavy metal in soil", 2nd ed. Blackie academic and professional.

[2] Bedient, P.B., Rifai, H.S. and Newell, C.J. 1994. "Groundwater Contamination", Prentice-Hall.

[3] Fetter, C.W. 1999. "Contaminant Hydrogeology", Prentice-Hall.

[4] Selim, H.M. and Sparks, D.L., 2001. "Heavy metals release in soils", Liwis Publishers.

[5] Tanchuling, M.A. 2005. A study on sorption and dispersion of heavy metals in clay using column leaching test. *Ph.D. Thesis*, Tokyo Institute of Technology, Tokyo, Japan.

Manufacture of Housing Construction Materials with Jute Polymer Composite (Jutin)

Mubarak A. Khan*, Fahmida Parvin, Jahid M M Islam, Md. Zakaria Hossain[1]
Institute of Radiation and Polymer Technology
Bangladesh Atomic Energy Commission, P. O. Box 3787, Dhaka 1000, Bangladesh
[1]Department of Environmental Science and Technology, Mie University, Japan

ABSTRACT

With jute fiber (hessian cloth) reinforced unsaturated polyester (USP) resin along with additives; composites were prepared by simple hand lay-up technique at room temperature (25°C). The prepared composite has been given shape of corrugated tin, so termed as "JUTIN" (jute + tin). The mechanical properties (such as tensile and bending properties) of the composites were measured with the extent of jute contents (20-40%wt) and found highest at 30% fiber content. To improve the fiber-matrix adhesion, jute fiber is subjected to chemical treatment with curing and coupling agent, and physical treatment with UV radiation of different intensities. Composite made of chemically modified jute fabrics shows better mechanical performances than that of the untreated or UV treated composites. The two treatments together provide synergistic effect on the properties of the composite. The treated composites also show the best of charpy impact strength. Storage and loss modulus as well as cantilever tests of the composites were performed.About35%weight of the composite is for jute.The tensile strength of the composite is 147MPa, bending strength is 150MPa and impact strength is 68 $kJm^{-2}$and will be stable more than 50 years.

Keyword: Jute, Composite, Natural Fiber, Jutin, Constriction materials

1. INTRODUCTION

Among destructive and terrifying natural calamities, earthquakes measuring intensity morethan 5.0 on the Richter scale can cause immense damage to the buildings and structures, dams, bridges, railways, communication systems etc [1]. Earthquakes are common in Japan, one of the world's most seismically active areas. The country accounts for about 20 percent of the world's earthquakes of magnitude 6 or greater. Recently a temblor struck the region of the Pacific where a magnitude-9.0 quake hit on March 11, triggering a huge tsunami. At least 23,000 people were killed or left missing in those disasters, which destroyed hundreds of homes, offices and factories in northeastern Japan.As the occurrence of earthquakes is unpredictable, there is an ardent need to design and construct the buildings and structures to reduce the damages, thus saving precious human lives. Conventional heavy andbrittle building materials such as stones, bricks, mortar, granite etc. do not absorb shock waves but they amplify them, causing more destruction. The material of construction to be used in earthquake prone areas should be such that they absorb & reduce seismic energy [1].

Jute has high cellulose content and low micro-fibril angle which are desirable properties of a fiber to be used as reinforcement in polymer matrices. Jute is one of the most common natural fibers having high tensile modulus and low elongation at break. If the low density (1.45 g/cm^3) of this fiber is taken into consideration, then its specific stiffness and strength are comparable to respective quantities of glass fiber [2, 3]. In spite of these above-mentioned advantages, jute fiber – like other natural fibers – exerts some difficulties while used as reinforcement in non-polar polymer matrices. Being polar and hydrophilic in nature, jute fiber exhibits poor interfacial adhesion with hydrophobic polymer matrices. To overcome these kinds of bottlenecks, many attempts, such as physical and chemical treatments, lead to changes in the surface structure and surface energy of the fibers.Such an effort was made to prepare a composite with improved mechanical properties using radiation induced jute-urethane polymer system. The resin matrix was prepared under gamma radiation using urethane acrylate in the presence of N-vinylpyrrolidone, ethyl hexyl acrylate and trymethylol propane triacrylate. Some additives such as acetic acid, acrylamide, urea, talc, and titanium oxide were incorporated into the formulation [4]. In this context, hessian cloth (jute product) was coated with urethane pre-polymer with different formulations in the presence of plasticizers under UV radiation. Tensile properties of the composites were found to increase. It is also indicative that simulated weathering and soil degradation tests show the biodegradable nature of the prepared composites [5]. A good correlation was found between composite impact damping and yarn toughness for the jute-epoxy composites [6]. Two monomers such as 2-hydroxy ethyl methyl acrylate (HEMA) and 2-ethyl hexyl acrylate (EHA) were successfully used as novel coupling agents for jute fabric (hessian cloth) polypropylene composite. The mechanical properties of the resulting composites increased as a result of surface treatment of the jute fabrics [7]. Polyester resin was used as matrix material for composite fabrication. The mechanical properties (tensile and bending strengths) of the surface modified jute fabrics reinforced polyester composites improved significantly [8]. The unsaturated polyester resin is quite useful for industrial and civilian world. As a low-cost, rigid, high strength-to-weight material, one can find its products in the form of mechanical parts, pipes, tanks, electronic gears, etc.They can be cured to give insoluble, infusible solid plastics through a free radical curing process. Organic peroxides are employed as free radical initiators while tertiary aromatic amines and some organic metal salts, such as cobalt naphthenate, are used as curing promoters if needed Tertiary aromatic amine and cobalt naphthenate can significantly reduce the decomposition temperature of peroxides via chemical reduction processes [9]. The objective of this research work is to prepare low cost light weight, durable, earthquake and cyclone tolerance housing materials and so on likewise products with sustainable local technology.

2. MATERIALS AND METHODS

2.1. Materials

Jute fabric was used as the reinforcing agent. The matrix polymer was a commercial unsaturated polyester resin (EPOLAC G-153ALX) containing 1.5% cobalt napthenate solution, 6% cobalt catalyst as promoter, and 36% styrene as diluent. Methyl ethyl ketone peroxide (MEKP) and wax were used as curing agent and mold releasing agent respectively. REOLOSIL fumed silica (aerosealpowder)was used as filler. A substituted aromatic tertiary amine was used as coupling agent.

2.2. Methods

Surface Modification

Hessian cloth was cut into rectangles (12 ×10 cm^2) and temporarily fixed in a long square sized plate (50 ×50 cm^2) where UV radiation could be given together to six equal sized rectangular samples. Then the samples were subjected to UV radiation (254–133 nm) using an irradiator (UV minicure Me-200, ISTTechnik, Germany), which delivers apower strength of 2 kW. The speed of the manicure was 4 meter/minute for each pass of the substrate under the lamp by maintaining different UV radiation intensities expressed by number of passes.

2.3.Composite Fabrication

Composites were fabricated using a simple hand lay-up technique. The working surfaces were treated with releasing waxes to facilitate easy removal of samples from the mold surfaces. Cobalt napthenate(catalyst) and MEKP (curing agent) were mixed thoroughly with USP at various formulations before each operation. At the beginning of fabrication, a gel coat with 2% MEKP was uniformly brushed into the finished side of the male and female parts of the mold. After 1h, when curing of gel coat was completed, each layer of the fiber was pre-impregnated with formulations made of USP. The impregnated jute samples were then placed one over another as a sandwich. This sandwich was placed into a mould. Both parts of the mold were tightened by screw-bolt and allowed 3 h for total curing (composite fabrication). The composites were cut into rectangular pieces of equal size (120×100×3mm^3) for different tests. All results are taken as the average of five samples for each testing.

2.4.Mechanical Tests

The tensile and bending strength of the composites were measured according to DIN 53455 and DIN 53452 standard methods by a universal testing machine (Hounsfield S Testing Series, UK) with an initial clamp separation of 20 mm and a cross-head speed of 10 mm/min. Charpy impact strength of the composite was determined by an impact tester (MT-3016) according to the DIN EN ISO 179 standard in the flat wise, unnotched mode. The test samples were conditioned at 25°C and 50% relativehumidity for several days before testing and all the tests were performed under the same conditions.The result of each test is taken as the average value of five samples

3. RESULTS AND DISCUSSION

The effect of jute content (%wt) on the mechanical properties of the resulting composites is studied here and shown in Figures 1 and 2. It was found shows poor mechanical properties due to poor fiber population and low load transfer capacity to one another. levels of fiber content (such as 20%), the composite As a result, stress gets accumulated atcertain points of the composites and highly localized strains occur in the matrix. At intermediate levels of loading (30%), the population of the fibers is just right for maximum orientation and the fibers actively participate in stress transfer. So, the mechanical properties of the composite reaches maximum. At high levels (suchas 40%) of jute content, the non homogeneous fiber matrix adhesion becomes prominent which leads to agglomeration among the fibers and stress transfer gets blocked [10]. As a result, the mechanical properties of the composite again decreased. The composite of the optimized jute content (30%w/w) showed 205% increase in tensile strength (TS), 141% in tensile modulus (TM), 226% in bending strength (BS) and 195% in bending modulus (BM) than that of the resin based composite.

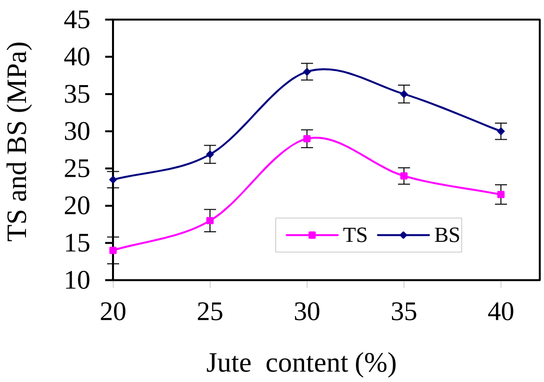

Fig.1 Effect of jute content on tensile and bending strength of composite

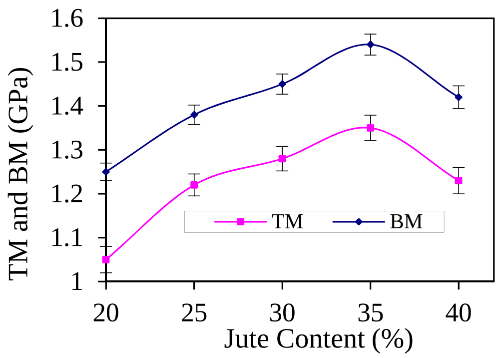

Fig. 2. Effect of jute content on tensile and bending modulus of composites

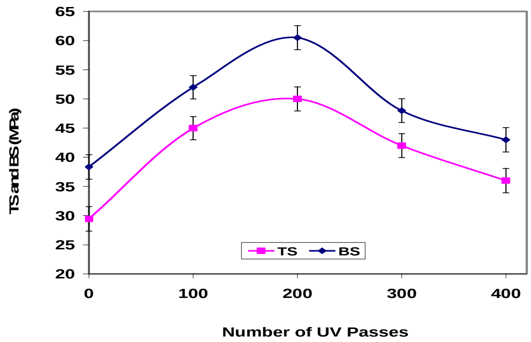

Fig.3 Effect of UV radiation on tensile and bending strength of jute-based composites

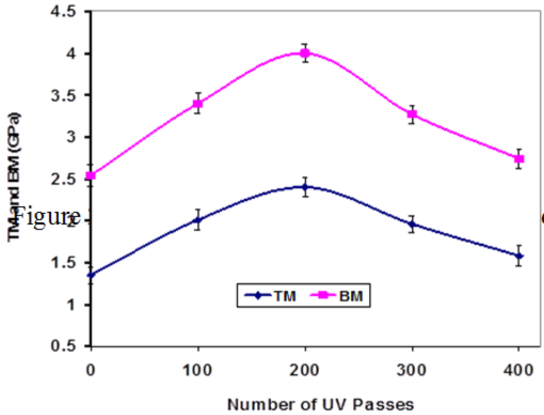

Fig.4. Effect of UV radiation on tensile and bending modulus of composites

The effect of UV radiation on the mechanical properties of jute based composites was investigated and presented in Figures 3 and 4. Jute content in the UV treated composite is maintained at about 30%. The UV intensities of different passes (200-400 pass) were exposed to jute surfaces.1 UV pass indicates 1 metre of UV exposure in the machine. It was found that UV intensity of 200 pass showed the highest mechanical properties. Mechanical properties, such as tensile and bending properties increase up to 200 pass, which gives 68% increase in TS, 78% in TM, 58% in BS, and 57% in BM relative to untreated jute-based composites. The TS, BS, TM and BM of the control composite were found 29.45 MPa, 38.35 MPa, 1.35 GPa and 2.54 GParespectively. The increase of mechanical properties of the composite with increasing UV radiation may be due to the intercross-linking between the neighboring cellulose molecules, which results in the strength of jute fabrics. It is observed from Figures 3 and 4 that mechanical properties of the composite increase with UV pretreatment up to a certain limit and then decrease due to the two opposing phenomena, namely, photo cross-linking and photo degradation that take place simultaneously under UV radiation. At lower doses, free radicals are stabilized by a combination reaction and, as a result, photo cross-linking occurs. The higher the number of active sites generated on the polymeric substrate, the greater the grafting efficiency. But at higher radiation, the main chain may be broken-down and polymer may degrade into fragments and, as a result, mechanical properties were found to decrease after certain UV doses. An intense radiation results in a loss of strengths and a reduced degree of polymerization is observed [10].

Jute fabrics were further treated with a coupling agent (0.1 to 2.0 %) at the stage of pre-impregnating the fibers with USP resin to show its effect on to the composites. Figs 5 and 6 show the effect of coupling agent on the properties of the composites.

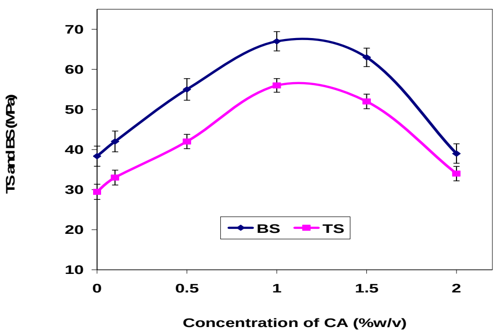

Fig. 5. Effect of coupling agent on tensile and bending strength of composites.

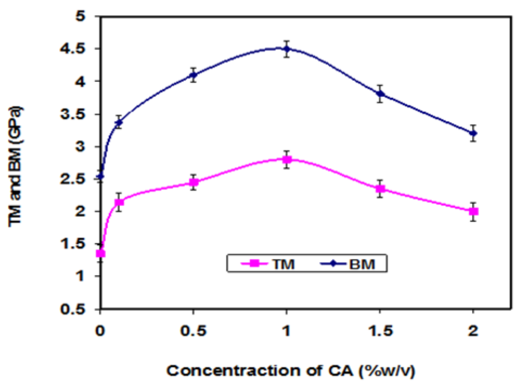

Fig. 6. Effect of coupling agent on tensile and bending modulus of composites

The coupling agent with a concentration of 1.0 % performed the best of mechanical properties. It is also indicative that coupling agent treated composite showed much better mechanical properties than that of the control composite. It was found that 1.0% coupling agent treated composite showed 90, 74.7, 77.77 and 57.48% higher TS, BS, TM and BM values than that of the control composite.

Table 1 shows the synergistic effect of the two treatments – coupling effect and UV treatment – on the properties of the composite. It was found that TS, BS, TM and BM values of UV+CA treated composite were 96 MPa, 117 MPa, 4.2 GPa and 5.5 GPa respectively. The values are about 226, 205, 211and 116% higher than that of the control composite. The free radical and cross linking mechanisms of the two effects (UV +CA) may be mainly responsible for the increase of mechanical properties of the composite.

Table 1.The effect of UV+CA on the properties of composite

Sample	Properties			
	TS (MPa)	BS (MPa)	TM (GPa)	BM (GPa)
UV+CA treated composite	96 ± 2.2	117± 2.5	4.2 ± 0.11	5.5 ± 0.15

The charpy impact strength (IS) of the control and treated composites were studied here. The IS values of UV, CA and UV+CA treated and control composites were found 35, 39 and 44 and 20 kJ/m^2 respectively. The effect of glass fiber (GF) in the mechanical properties of UV + CA treated jute fabrics composites was investigated and is shown in Figures 7and 8.

The weight fractions of glass fiber content in the jute/GF hybrid composites varied from 5 to 100%. The incorporation of glass fiber into jute fabrics up to 75% helps the hybrid composites show better mechanical properties over the other treated composites. The values of TS, BS, TM, BM and IS of the hybrid composites at 75% GF content were found 140 MPa, 150 MPa, 6.55 GPa, 7.12 GPaand 68 kJ/m^{2}respectively. The incorporation of GF increases the reinforcement of jute fibers into the matrix. In a hybrid composite, the mechanical properties of composites are mainly dependent on the modulus and percentage elongation at break of individual reinforcing fibers. The increase in mechanical properties through the addition of glass fiber to jute can be explained on the basis of higher modulus and elongation at break of the glass fiber [11], whereas the extensibility of glass is low compared to the jute fiber.

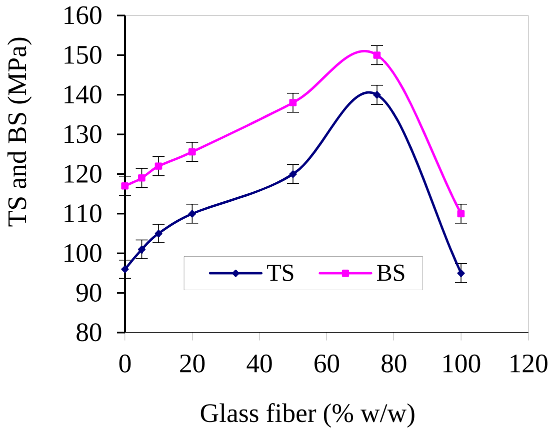

Fig. 7. The effect of glass fiber content on tensile and bending strength of jute/GF hybrid composite

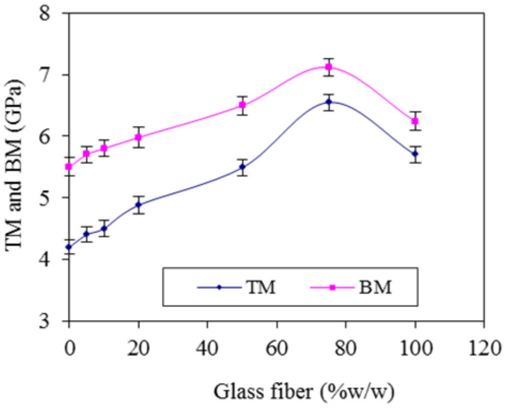

Fig. 8. The effect of glass fiber content on tensile and bending modulus of jute/GF hybrid composite

4. Comparative Studies

Figures 9 and 10 shows the comparative data of different treatments on the properties of jute and jute/GF based composites. It was found that the glass fiber on the UV + CA treated jute based composite performed the best mechanical properties.

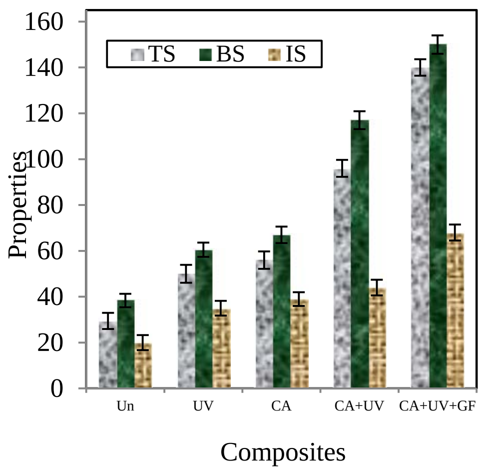

Fig. 9. The effect of different treatments on the strength of composites

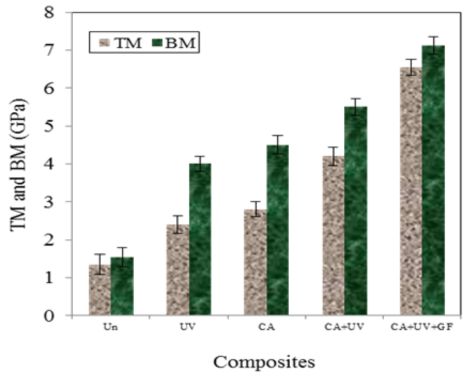

Fig.10. The effect of different treatments on the modulus of composites

5. Aging properties of Composite (JUTIN)

5.1. Thermal aging

Table 2.The effect of thermal aging on tensile strength of JUTIN

Sample	Room temp.	Tensile strength (MPa) 15 days			
		0ºC	4ºC	50ºC	70ºC
Jutin	96	116±2.0	99.8±1.9	93±1.82	78±1.8

The JUTIN was subjected to undergo different temperature treatments at 15 days time periods to investigate the effect of thermal aging on tensile strength of JUTIN. It was found that the strength of composite increases with the decrease of temperature. The TS decreased to about 19.0 and 3.0 % at aging temperature of 70ºC and 50ºC respectively. Whereas, the incat 4ºC and 0ºC, TS increased about 4.0 and 21.0% respectively.

5.2. Water aging

There is very negligible amount of water uptake (<1%) within 3 months. There is no change in mechanical properties within 3 months.

5.3. Normal weathering aging

The mechanical properties increased up to 7-10% within 6 months and remain unchanged up to 12 months.

5.4. Acceleratedweathering aging

To study the weathering effect on the mechanical properties of Jutin, the samples of jutin were exposed under simulated weathering tester from Q-panel Co. (model QUV, USA). The weathering testing was performed in alternating cycles of sunshine over 4h (65º±2ºC) and condensation for 2h (45º±2ºC). This aging test was carried out for 600 h.Owing to this test the losses of mechanical properties more or less zero up to 300 hours and about 10% up to 600 h.

6. Conclusion

The tensile strength of the prepared composites composite is 150 MPa, bending strength is 147 MPa and impact strength is 68 kJm^{-2} and It will be stable up to 50 years. This jute-based polymer composite shows extra-ordinary features which are very promising to make jute based polymer composite as a effective alternative of metallic or plastic materials. It is rust proof, saline resistant, lightweight, heat resistant, sound proof, environmental friendly, Very low thermal expansion, and damaged area can be sealed very easily. In contrast, lightweight jute made composite boards fixed on steel frames with bolts & nuts are more flexible allowing lateral movements of the structures. They absorb and reduce seismic energy. The usage of natural fiber (jute) based products in post disaster management of rehabilitation & rebuilding, would become cost competitive compared to other building materials. Thus, all the properties of composite claim its position as an ideal building material.

REFERENCES

[1] Soumitra Biswas, Atul Mittal & G Srikanth, Gujarat Earthquake - Composite Materials towards Re-building & Rehabilitation

[2] Bogoeva-Gaceva G., Avella M., Malinconico M., Buzarovska A., Grozdanov A., Gentile G. and Errico M.E. (2007). Natural fiber eco-composites.*Polymer Composite*;**28**: 98-107.

[3] Joshi S.V., Drzal L.T., MohantyA.K.andArora S. (2004). Are natural fiber composites environmentally superior to glass fiber reinforced composites? *Composites:Part A*; **35**: 371-376.

[4] Khan M.A., Ali K.M. I., Balo S.K. and Ahmad, M.U. (1998). Effect of additives reinforcement of radiation induced jute urethane polymer composites. *Journal of Applied Polymer Science*; **67**:79-85.

[5] Khan M.A., Uddin M.K. and Ali K.M.I. (1997). Degradable jute plastic composite.*Polymer Degradation and Stability*; **55**:1-7.

[6] Gassan J. and Bledzki A. K. (1999). Possibilities for improving the mechanical properties of jute/epoxy composites by alkali treatment of fibers.*Composites Science and Technology*; **59**:1303-1309.

[7] Khan M.A., Hinrichsen G. and Drzal L.T. (2001). Influence of novel coupling agents on mechanical properties of jute reinforced polypropylene composites. *Journal of Materials Science Letters*; **20**:1711-1713.

[8] Mohanty A.K, Khan M.A. and Hinrichsen G. (2000). Influence of chemical surface modification on the properties of biodegradable jute fabrics-polyester amide composites. *Composites:Part A*; **31**:143-150.

[9] Khan M.A., Ganster J. and Fink H. P. (2004). Natural and man-made cellulose fiber reinforced hybrid polypropylene composites.5th Global Wood and Natural Fiber Composites symposium, in Kassel, Germany, April 27-28.

[10] KuangW. and Richardson, A. (2007).A New Amine Promoter for Low-temperature Cure of MEKP Initiated Unsaturated Polyester Resin Systems. *Composites Research Journal;* **1**(4): 9-13.

[11]Abdullah-Al-Kafi, Abedin M. Z, Beg M. D. H, Pickering K. L and Khan M. A (2006).Study on the Mechanical Properties of Jute/Glass Fiber-reinforced UnsaturatedRadiation Polyester Hybrid Composites: Effect of Surface Modification by Ultraviolet Radiation. *Journal of Reinforced Plastics and Composites*; 25: 575-588.

[12] Khan, M. A. and Hasan, M. M. (2004). Surface Modification of Natural Fibers by Photo-grafting and Photo-curing, In: Mital, K. L. (ed.), Polymer Surface Modification: Relevance to Adhesion, VSP, Vol. 3, pp. 263–283.

First International Conference on Geotechnique, Construction Materials and Environment, Mie, Japan, Nov.21-23, 2011, ISBN: 978-4-9905958-0-7 C3051

Evaluation of Strength of Granulated Construction Waste Sludge with Quicklime and its Application to Soil Structure

Makoto Kobayashi, Department of Civil Engineering, Toyota National College of Technology,
Hiroaki Nakamura and Hideaki Mizuno, Taihei Sangyo Co., Ltd

ABSTRACT: In this study, the strength characteristics of granulated construction waste sludge mixed with quicklime were examined to identify an efficient improvement method for the effective use of such waste sludge. The tests results indicate that it is possible to estimate the strengths of improved sludge based on mixing ratio of quicklime and dried sludge. Furthermore, appropriate curing is necessary when using the sludge because the increased strength of the improved soil depends on minimal water content, which can easily increase due to saturation from rainfall. An in situ investigation into applications of soil structures using improved soil are also described in this paper, specifically, the counterweight fill for preventing slope failure and forming dike for a reservoir.

Keywords: granulated construction waste sludge, quicklime, soil structure, unconfined compression strength

1. INTRODUCTION

According to the white paper on Land, Infrastructure, Transport and Tourism in Japan[1)], construction waste should be reduced, recycled and reused to establish a sound material-cycle for our society. The recycling rate of construction waste sludge (CS) has been lower than that of other construction waste. The primary reasons for this problem are as follows[2), 3)]: 1)the characteristics of CS are extremely complicated because it is generated by the addition of water, regardless of the type of soil used, and 2)the treatment cost of CS is higher than that of construction generated soil, since it is classified as industrial waste. It is necessary to find an appropriate improvement method to raise the recycling rate of waste sludge.

The properties and performance of CS treated with cement and lime have been studied[4), 5)]. With cement treated soil, hexavalent chromium is generated, negating some of the advantages of the resulting high strength. With this shortcoming in mind, the characteristics of the soil stabilized by lime should be investigated to use it as an alternative to cement treated soil. CS treated with quicklime is known for being slow in developing an acceptable strength. However, the improved sludge should maintain the cone index just after improvement at a value above 800kN/m^2 that classified the second type of improved soil. To identify the amount of quicklime that provides the most improvement in the CS, the unconfined compression strength should be tested after quicklime are mixed and cured.

The improved CS is being considered for use as constructing embankments and back filling[6)].Therefore, it is important to examine the variation in the strength of the improved soil when the degree of saturation is increased by rainfall.

In this study, to evaluate the performance of granulated construction waste sludge mixed with quicklime (improved soil), cone penetrating tests and unconfined compression tests were conducted. The improved soils were produced with CS from various construction sites mixed with different quantities of quicklime. The relationships between the cone index and the unconfined compression strength just after improvement were identified. Unconfined compression tests were carried out to investigate the strength characteristics increase resulting from curing. Based on these tests, a method of describing the unconfined compression strength was developed based on the ratio of quicklime and dried sludge.

Furthermore, laboratory tests and in situ test were conducted to examine the variation in the strength of the improved soil when the degree of saturation was increased. Additionally, the use of improved soil to form counterweight fill to prevent slope failure and to construct a reservoir dike were observed and discussed.

2. GRANULATED CONSTRUCTION WASTE SLUDGE WITH QUICKLIME

2.1 Improvement technology

Fig. 1. The plant of treatment

The treatment plant is shown in Fig. 1. The improvement method was as follows: 1) the CS collected in the pit was dredged by backhoe and put on the belt conveyor to the treatment plant. 2) On the belt conveyor, the CS was vibrated and the quantity was averaged by a gate in the plant. 3) Then, the quicklime was added to the CS and mixed by a paddle mixer. The amount of quicklime added was determined based on the water content of the CS. No tests were done to identify the CS properties before improvement. This choice was made to increase the efficiency of improved soil production. On the other hands, not reviewing the properties of the CS before improvement makes it difficult to obtain consistent properties in the produced improved soils.

2.2 Specimen

Improved soil was allowed to cure for 1day, and then, a sample was compacted into a mold. This was followed by carrying out the method for determining the cone index of compacted soils: JIS A 1228:2000. The specimen created for the unconfined compression test was formed into a cylinder 10cm high and 5cm in diameter. It was then wrapped in vinyl. Curing was done following one of two methods in this study. The first method was standard curing while wrapped. The second method was to cure the sample without wrap, natural drying, in order to allow the water content to decrease with time. Table 1. lists the test cases in this study, and for each case it lists the test code, the weight of quicklime relative to the volume of CS, the initial water content of the improved soil, and the weather conditions at improvement.
The permeability of the improved soil for test case CS38 was $k=9.3\times10^{-7}$(cm/sec). This implies that it should be difficult to saturate a soil structure constructed using improved soils.

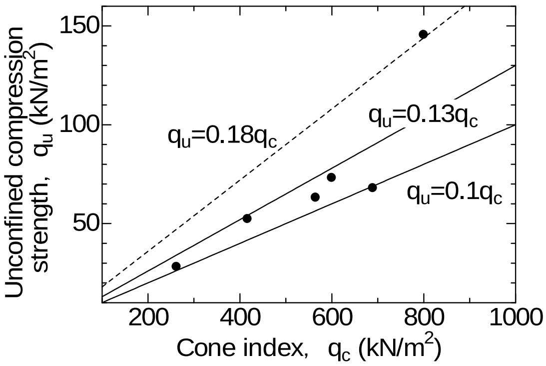

Fig. 2. Relationships between unconfined compression strength and cone index shortly after soil improvement

3 UNCONFINED COMPRESSION STRENGTH

3.1 Relationships between unconfined compression strength and cone index just after improvement

The cone penetration test conducted to identify the quality of the improved soil. Accordingly, it was also important to investigate the relationships between the cone index and the unconfined compression strength just after treatment. This relationship is shown in Fig. 2.
For test cases with a lower cone index, the compression strength was represented by $q_{u\,lml} = (0.1\sim0.13)\times q_c$. The other cases can be expressed by $q_{u\,lml} = 0.18q_c$. This result implies the cone index will be representative of the unconfined compression strength[7].
For test cases with high water content, a smaller unconfined compression strength was obtained. This was due to over compaction during the compaction process. This is why two versions of the estimation formula were required.

4 INCREASING STRENGTH WITH CURING

4.1 Standard curing

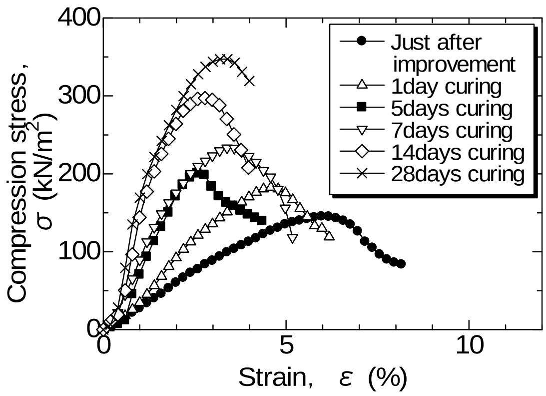

Fig. 3. Stress-strain curve for test case CS18 with standard curing

The stress-strain curves obtained from the unconfined compression tests for test cases CS18 and CS30-1 are shown in Figs.3 and 4, respectively. The longer the curing was allowed to occur, the smaller the strain at the peak strength. This implies that the improved soil will become a brittle material after lime stabilization. The modulus of deformation

Table 1. Test code and condition of specimen as well as weather conditions

Test code	Weight of quicklime against the volume of CS (kg/m^3)	Initial water content of improved soil (%)	Weather condition at improvement	
			Amount of precipitation (mm)	Average daily temperature (degree centigrade)
CS18	18	28.6	3.0	20.7
CS24	24	28.5	24.5	16.6
CS30-1	30	28.3	0.0	19.5
CS30-2	30	36.2	0.0	14.0
CS38	38	41.2	0.0	12.0
CS44	44	38.2	0.0	8.4

for test case CS18 after 28 days was $10MN/m^2$, showing an increase since just after improvement the value was $2.5MN/m^2$. In test case CS30-1, the modulus of deformation also increased by 4 time after quicklime stabilization.

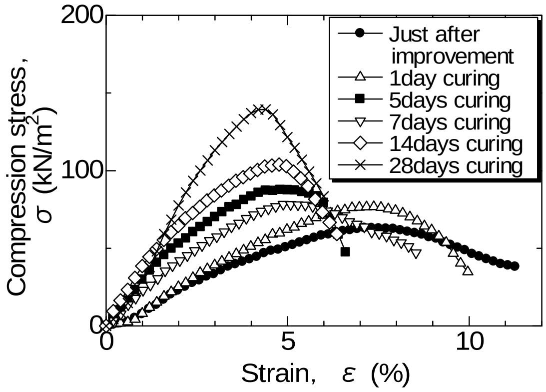

Fig. 4. Stress-strain curve for test case CS30-1 with standard curing

The change in the unconfined compression strength in relation to the curing period for in each test case in this study is shown in Fig. 5. It is clear that the improvement in the soil strength from the addition of the quicklime was slow-acting, so that the curing continued a full 84 days after improvement. The variations in the water content of the specimens during the curing process are shown in Fig. 6. A steady decrease in the water content over time was not indicated in spite of the fact that the pore water should be spent not only on hydration but also the pozzolanic reaction of the improvement mechanism. As can be seen from the Fig.5, after 28days of curing the strength of the improved soil doubled. However, the figure also implies that a small amount of quicklime is enough to improve the CS.

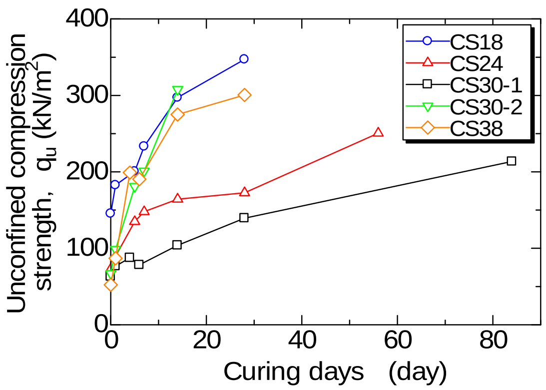

Fig. 5. Variation in the unconfined compression strength relative to curing period.

In order to analyze the unconfined compression strength of improved soil after 28 days curing (q_{u28}), first an increment ratio relating q_{u28} to $q_{u\ ini}$ was defined. The term $q_{u\ ini}$ indicates the unconfined compression strength just after improvement, as identified using the one index. Second, the mixing ratio quicklime to dried CS (Lime content: LC) was defined, because it could be regulated in the treatment plant with easily additional soil tests. The increment ratio of strength was assumed by means of the relationships shown in Fig. 7. In this figure, the rough relationships between increment ratio of strength and mixing ratio of quicklime were obtained as follows:

$$q_{u\ 28}/q_{u\ ini} = 10^{\{(0.25\sim0.33)\times Lc\}} - (0.5\sim0.8) \qquad (1)$$

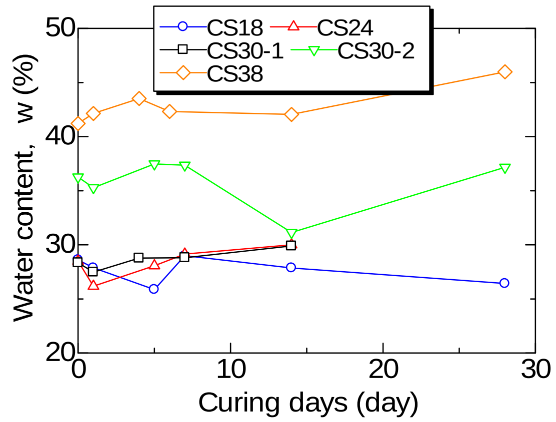

Fig. 6. Variation into water content vs curing period

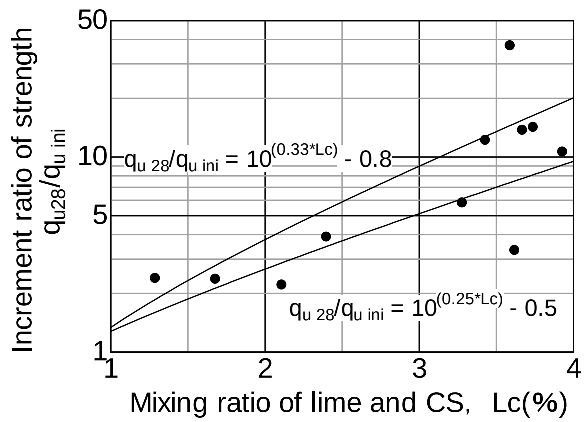

Fig. 7. Relationships between increment ratio of strength and lime content

It is difficult to manage the lime content relative to several properties of the CS while the treatment plant is producing improved soil at a rate of more than $500m^3$/day from a diverse selection of construction sites. As a result of these tests, however, the strength of the improved soil at 28 days can be roughly estimated using the cone index, lime content, and water content of CS.

4.2 Curing with natural drying

The stress-strain curves obtained by the unconfined compression tests are shown in Fig. 8. The peak strength after curing for 5 days was 8 times the initial strength. These specimens suffered brittle fracture after peak strength was achieved.

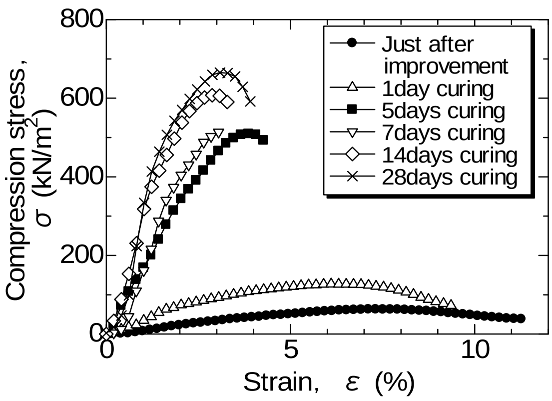

Fig. 8. Stress-strain curve for test case with CS30-1 for curing with natural drying

The relationships between the unconfined compression strength and the length of the curing time are shown in Fig. 9. In this figure, not only is the increment of strength observable, but also the sudden decrement of strength in the cases of CS30-2 and CS38. Fig. 10 shows the change in the water content of the specimens during the curing process. In all test cases, the water content decreased until about the tenth day before stabilizing. This indicates that the changes in the compressive strength were not caused by lime stabilization but rather by increase the friction between soil particles that comes with a decrease in the water content.

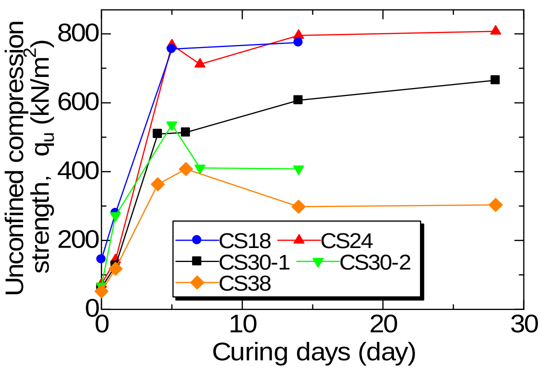

Fig. 9. Variation in unconfined compression strength relative to curing time

If the above mentioned theory is correct, it is important to investigate the unstable mechanism during rainfall, which will increase the volume of void water. To test this condition, samples were submerged in water before compression testing to test the strength when saturated. Using a specimen (CS38) that had cured for 28 days, the unconfined compression test was conducted after the specimen had been submerged for 24hours. The variation in the stress-strain curve obtained by this test is shown in Fig. 11. The effect of submergence was a marked decrease in the peak strength when the sample was cured by natural drying. This was due to the increased water content lubricating the motion of the soil particles. Namely, it implies that the compression strength of improved soil cured by natural drying increases with the increase of friction of the surface, which dependent on the moisture levels. However, the permeability of these materials is lower than that of general soil when used for soil structures, so only the surface of the structure made with improved soil will become unstable due to rainfall.

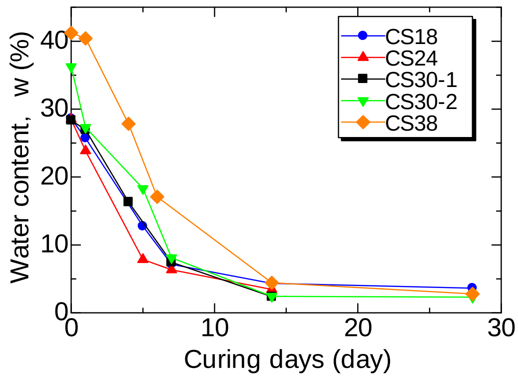

Fig. 10. Variation in water content with curing

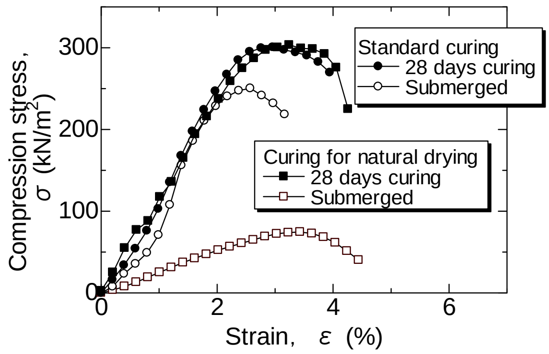

Fig. 11. Stress-strain curve when the sample is submerged

5 APPLICATION TO SOIL STRUCTURE

5.1 The counter weight fill for slope failure

Cracks in the slope surface were observed at a ceramic material mine where the site had been reclaimed by using construction generated soil, as shown in Fig. 12. Identifying the cause of this phenomenon was complicated because of the following: 1) ground water was existent in the slope and 2) the load on the slope was increased due to the construction of an embankment at the crest of the slope.

To solve these problems, improved soil was used to form a counterweight fill at this site. Also, the slope angle was changed to a gentler 1:2.0, or 26.6 degree. Lastly, a drainage conduit was inserted into the slope in order to lower the ground water level.

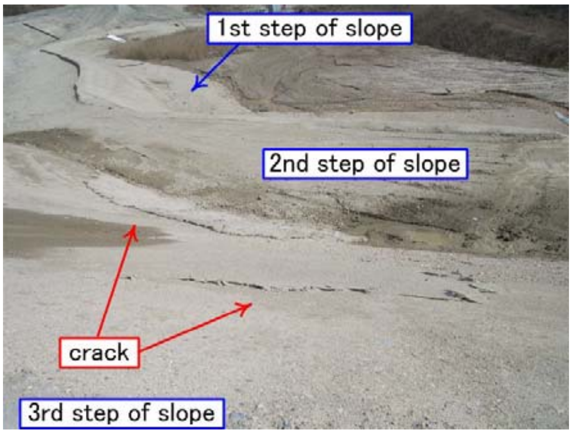

Fig. 12. Observed cracks in slope

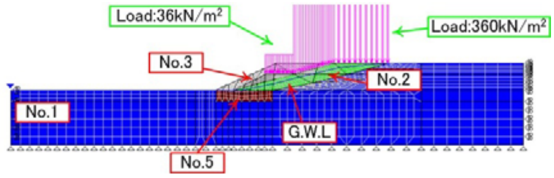

(a) Analysis model at sliding

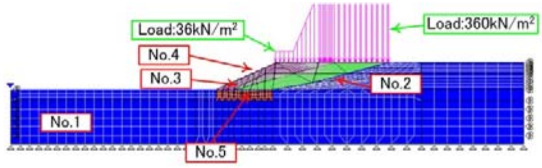

(b) Analysis model of countermeasure
Fig. 13. Analysis model of the ground

To examine the effectiveness of the countermeasure to the landslide, FEM analysis was performed. In this analysis, the shear strength reduction method (SSRM)[8] was used to investigate the critical slip circle of the slope. The analysis model and the parameters of the ground material are shown in the Fig. 13 and Table 2, respectively. The results of unconfined compression tests with CS30-1, which examined the long term strength, were used to estimate the cohesion of the improved soils. In addition, the result of a triaxial compression tests was used to identify the internal friction angle of the improved soil. The internal friction angle of Improved Soil 1 was used in the model, with a measure of underestimation to account for the ground water present in the slope. Other parameters for the ground materials were decided by analysis, which continued until similar deformation was obtained.

The results of the FEM analysis, which expressed the distribution of the maximum strain increment obtained by SSRM, are shown in Fig. 14. The critical slip surface was confirmed through the upper side of the embankment made by the construction generated soil and down to the toe area of slope. Furthermore, the largest strain was generated in the base ground at the toe area of the embankment. This indicates that the crack was caused by differential settlement of the foundation. After countermeasures were installed using improved soil, however, there was no definite slip circle in the slope.

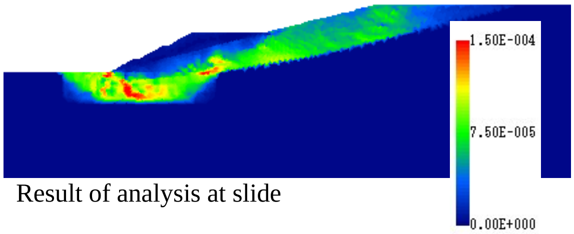

(a) Result of analysis at slide

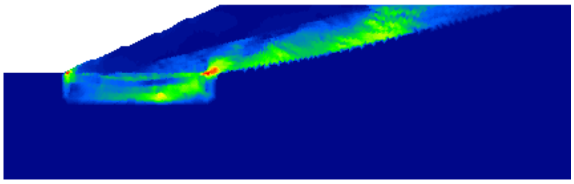
(b) Result of analysis after countermeasure
Fig. 14. Distribution of maximum strain

5.2 Dike of regulating reservoir

The improved soil was also suitable for constructing a dike for a regulating reservoir because of its low permeability, as already mentioned in 2.2. The photo of dike under construction is shown in Fig. 15. In the 2 years since construction, no remarkable deformation has been observed. Further observation is continuing, watching for changes, including deformation and collapse.

Table 2. Parameter of ground material for FEM analysis

Material No.	Model	Young's modulus (kN/m^2)	Cohesion (kN/m^2)	Internal friction angle (degree)	Constitutive law
1	Base ground	2×10^5	-	-	Elastic
2	Construction generated soil	8×10^2	1.0	24	Elastic-perfectly plastic Mohr-Coulomb
3	Improved soil 1	1.5×10^4	30.0	20	Elastic-perfectly plastic Mohr-Coulomb
4	Improved soil 2 (for countermeasure)	1.5×10^4	200.0	24	Elastic-perfectly plastic Mohr-Coulomb
5	Base ground under toe of slope	4×10^2	1.0	20	Elastic-perfectly plastic Mohr-Coulomb

Fig. 15. Dike of the regulating reservoir during construction

6 CONCLUSION

In this study, a series of soil test were carried out to estimate the performance of granulated construction waste sludge when mixed with quicklime. Furthermore, a case study of the improved soil when used in two soil structures was described. The conclusions of this study as follows:

1) The estimated strengths of improved soil can be estimated based on the mixing ratio of lime to dried sludge and the cone index of the improved soil just after treatment.

2) The improved soil must be cured to fully strengthen the sludge since the increased strength of improved soil depends on a low water content and can easily be reduced with saturation by rainfall.

3) The improved waste sludge is applicable for some soil structure, for instance, as counterweight fill to prevent slope failure and forming a dike for a reservoir. The granulated construction waste sludge has a low permeability and large strength while being easily formable.

7 REFERENCE

[1] Ministry of land, infrastructure, transport and tourism(2009): White paper on land, infrastructure, transport and tourism in Japan, pp. 93-94.

[2] Kamon, M. (2008):Current status and recycling strat-egies of construction sludge, Waste Management Research, Vol.19, No.3, pp.122-130.

[3] Sakamoto, H. (2008): Approaches to construction sludge recycling in the construction industry, Waste Management Research, Vol.19, No.3, pp.138-145.

[4] Ogawa, N., Akimoto, K, Seki, S. and Yoshinari, S., (1995): An attempt on effective use of construction sludge (part1), The 30th japan national conference on soil mechanics and foundation engineering, pp.2221-2222.

[5] Umemoto, K., Kirikoshi, S., Fujisaki, K. and Ohhara, T., (1995): An attempt on effective use of construction sludge (part3), The 30th japan national conference on soil mechanics and foundation engineering, pp.2225-2226.

[6] Onodera, Y., Yoshida, H., Tajika, H., Miyakawa, M. and Saito, K. (1999): Mechanical properties of stabilized gravelly soft soil, -Backfill mate-rials of pipeline with stabilized soil by lime-, Monthly report of civil engineering research in-stitute, No.556, pp.32-41.

[7] Ogawa, N, Kirikoshi, N, Hisano, K. and Yamamoto, H., (1995): An attempt on effective use of construction sludge (part4), The 30th japan national conference on soil mechanics and foundation engineering, pp.2227-2228.

[8] Ukai, K., (1990): Availability of shear strength reduc-tion method in stability analysis, Tsuti-to-kiso JSSMFE, Vol. 1, No.38. pp.67-72.

First International Conference on Geotechnique, Construction Materials and Environment, Mie, Japan, Nov.21-23, 2011, ISBN: 978-4-9905958-0-7 C3051

Analysis of Enhanced Strength and Deformation Resistance of Some Tropical Geomaterials through Application of In-situ Based Stabilization Techniques

Kogi SK & Ndeda M., Materials Testing & Research Department, Ministry of Roads, Nairobi, Kenya
Mukabi JN & Wekesa S., Research & Development Department, Kensetsu Kaihatsu Limited, Nairobi, Kenya

ABSTRACT: In this paper, some aspects of OBRM (Optimum Batching Ratio Method) and OPMCS (Optimum Mechanical & Chemical Stabilization) in-situ based stabilization techniques, which have been scientifically developed and successfully applied for the design and construction of runway and highway pavement structures in East and Central Africa, are introduced through experimental data analysis.
Quantitative analyses are carried out to show how the improved mechanical stabilization and reduction in voids (densification) by accelerated particle agglomeration, through the application of OBRM and OPMC respectively, contribute significantly to the enhancement of bearing capacity, strength and deformation resistance of the composite geomaterials.
It is then demonstrated, through comparative analysis of the enhanced geotechnical engineering properties in respect to the cost aspect ratio and enhanced geotechnical engineering properties, that these techniques are highly cost-time-maintenance-effective whilst contributing to environmental conservation due mainly to the reduction in the quantities required for construction and length of access roads to borrow pits in comparison to the conventional and traditional methods of design and construction.

Keywords: OBRM, OPMCS, Geomaterial, Strength and deformation resistance, Design and construction

1. INTRODUCTION

1.1 Geomaterial Constraints in Design and Construction

In most parts of the world and, developing countries in particular, engineers are constantly faced with the major challenges of designing, constructing and maintaining pavement structures with limited financial resources. On the other hand, for the fulfillment of the acceptable construction standards, traditional design and construction practices require high-quality geomaterials which are usually expensive and mostly involve long haulage distances thereby increasing the period of construction and, most of all, the project cost. Due to these constraints, engineers are often forced to seek alternative designs that are innovative enough to allow for the use of substandard geomaterials, which, in singularity, are mostly deficient in mechanical stability and other geo-properties but are, however, readily available for the construction of most layers of the pavement and other geo-structures such as embankments and bridge abutments.

1.2 Brief Introduction of OBRM and OPMCS Technologies

In their natural state, most geomaterials are usually deficient in one or more of the particle fractions required. Consequently, mechanical stabilization plays an important role in achieving a pavement structure which, under loading conditions, is appreciably resistant to shear and deformation. In developing the Optimum Batching Ratio Method (OBRM), [1] considered that; such geomaterials would have a particle size distribution that tends towards a correctly proportioned ratio that would yield optimum density and adequate strength to resist stress-induced deformation.

(1) Optimum Batching Ratio Method (OBRM)

The OBRM is a mechanical stabilization method that was odeveloped on geo-scientific basis. Based on this method, the blending of two otherwise structurally inferior geomaterials with different characteristics can be achieved at optimum proportionate levels thereby enhancing the vital geotechnical engineering properties such as mechanical stability, bearing capacity, strength and deformation resistance [1], [2].

(2) Optimum Mechanical and Chemical Stabilization (OPMCS)

OPMC is the combination of optimum mechanical batching (OBRM) and optimum chemical mixing of, and into geomaterials with varying properties [3], [4].
These methods have been practically applied for the design and construction of various civil engineering projects in East and Central Africa and have been proven to: 1) promote cost-effective use of otherwise relatively inferior geomaterials, whilst ensuring the achievement of sound geotechnical engineering structures; 2) contribute immensely to environmental conservation through the reduction in use of borrow and/or extruded geomaterials; 3) provide partial solutions to problematic soils, and; 4) realize significant reduction in the requirements of chemical stabilizers.

2. METHODS OF TESTING AND ANALYSIS

2.1 Laboratory and In-situ Testing Testing

Details of the standard and innovative laboratory and in-situ testing regimes and methods are discussed in [5]-[9].
Experimental testing was undertaken on soil samples from, and in-situ, in five different countries in East and Central Africa namely; Southern Sudan, Ethiopia, Burundi, Tanzania and Kenya.

2.2 Full Scale Experimental Testing Sections

Full-fledged field experimental sections with varying pavement structural configurations were designed and implemented as reported in [6]-[10].

2.3 Main Analytical Functions Adopted

The fundamental theories and concepts adopted for the comprehensive analysis are discussed in detail in [4], [10], whilst some of the basic functions are introduced in this section. The analytical functions were derived to characterize

the impact of environmental factors on the performance of the road pavement, evaluate the change in the intrinsic material characteristics influenced by the nature, mode and degree of stabilization coupled with the reciprocal impact and intensity of loading [4] and [10], [11].
The relations applied for comprehensive Quality Control (QC) of OBRM and OPMC stabilized ground and geomaterials are also proposed in [11].

(1) *Analysis of Mechanical Stability, Bearing Capacity, Shear Strength and Deformation Resistance*

The analyses for mechanical stability, strength and deformation resistance were made based on various equations [1]–[4] and [10]. Some of the principle relations adopted in the analysis of this Study are presented in (1) ~ (11).
Quantitative analysis of the contribution of enhanced mechanical stability due to OBRM stabilization was undertaken by applying (1) to (5).

$$M_S^f = A_{MS} \exp^{-1.16\eta} \tag{1}$$

when $\eta \geq 0.5$

$$M_S^f = M_S^{ideal} - \left[A_{MS} \exp^{-1.16\eta} - M_S^{ideal}\right] \tag{2}$$

when $0 < \eta < 0.5$

$$B_C = A_{BC} - A_{GI}\eta \tag{3}$$

when, $\eta \geqq 0.5$

$$B_C = B_C^{ideal} - \left[A_{BC} - A_{GI}\eta - B_C^{ideal}\right] \tag{4}$$

when, $0 < \eta < 0.5$

$$B_C = \delta \exp^{A_{BN} M_S^f} \tag{5}$$

where, M_S^f is the Mechanical Stability (MS) factor, and for this case, A_{MS} is the MS constant=178.6, η is the gradation index=$log0.01P/log(d/d_{max})$, M_S^{ideal}=100% for non-stabilized geomaterial, B_C is the bearing capacity factor, A_{BC} is the B_C constant=130, A_{GI} is the grading index constant=60, B_C^{ideal}=100% for non-stabilized geomaterial, δ=B_C-M_S correlating constant=24.7 and A_{BN} =B_C-M_S constant=0.014.
The contribution of particle agglomeration in enhancing strength and elastic modulus due to cementation is quantitatively analyzed from (6).

$$q_{max} = A_q ln a_f + q_{max}^i \tag{6}$$

where, q_{max} is the maximum shear strength, $A_q = 1.06$ is a material constant and a_f is the agglomeration factor computed from the level of OPMC related factors.
On the other hand, the effective angle of shearing resistance Φ' is computed as:

$$\Phi' = A_\Phi a_f^2 + B_\Phi a_f + \Phi'_i \tag{7}$$

where, $A_\Phi = 0.05$ and $B_\Phi = 0.95$ are geomaterial constants. Based on UCS testing of OPMC specimens, Φ' is determined from (8).

$$\phi' = \frac{A_{Nf}(q_u)_{\max} + A_{\phi f}}{B_{\phi f}} \tag{8}$$

where, $(q_u)_{max}$ values are expressed in kN/m^2 and A_{Nf}, $A_{\phi f}$, $B_{\phi f}$ are experimentally determined geomaterial constants.
On the other hand, under triaxial conditions considering that q_{max}= $(\sigma'_a - \sigma'_r)_{\max}$ and $P'_f = 1/3(\sigma'_a + 2\sigma'_r)$ then,

$$\phi' = Sin^{-1}\left[\frac{q_{\max}}{2p'_f + 1/3 q_{\max}}\right] \tag{9}$$

The elastic stiffness E_{max} of OPMC stabilized Geomaterial taking into account the particle agglomeration effects, is quantitatively analyzed from:

$$E_{max} = A_{EM} a_f^2 + B_{EM} a_f + E_{max}^i \tag{10}$$

where, $A_{EM} = 62.4 \; and \; B_{EM} = 690$ are geomaterial constants. E_{max} is measured and/or expressed in MPa.
Estimation of the linear elastic range or initial yield surface is made from (11).

$$(\varepsilon_a)_{ELS}^{ij} = \frac{(\varepsilon_a)_{50}^{ij}}{\left\{\phi_{ELS}^{ij}(\varepsilon_a)_{\max}^{ij} + A\right\}}, (\%) \tag{11}$$

where, ϕ_{ELS} is a function of the deformation modulus E_{50} with respect to the initial (Elastic) modulus, E_{max} and A is a constant depending on the physical properties of the geomaterial.

3. ANALYSIS AND DISCUSSIONS OF TEST RESULTS

3.1 Tabulated Summary of Some Typical Test Results

Tables 1 and 2 present a tabulated summary of some typical results based on laboratory and in-situ experimental testing reported in this Study. Table 1 is a summary of the basic physical and mechanical parameters for non-stabilized geomaterials, while part of the measured shear strength and elastic modulus data is presented in Table 2.
The results in table 1 show that: 1) the basic physical and mechanical lateritic soils from different countries vary drastically (the same was observed for lateritic materials sampled from different locations in the same country); 2) the relatively fine graded Kenyan lateritic gravel exhibits rather superior bearing capacity, shear and deformation resistance properties when compared to the relatively coarse graded one from Burundi; attributable to the superior mechanical stability of the former [10]; and, 3) the degree of influence of MDD and OMC depends on properties of the geomaterial.

Table 1 Summary of basic physical and mechanical geo-properties of non-stabilized geomaterial

Country of Origin	Loca-tion	Geomaterial	Basic Physical Parameters							Mec. Stab.	Consolidat-ion		Bearing Capacity	Shear Properties		Elastic Modulus
		Type of material	*Compaction Characteristics*			*Densification / Atterburg Properties*			Clay Activity	M_S (%)	δ^f_{CSR}	*CSR*	CBR	q_u (MPa)	Φ' (°)	E_{max} (MPa)
			MDD (Kgf/cm^3)	OMC (%)	FMC (%)	VRe	G_S	PI (%)	A_C	Sieve	UCS/CUTC	UCS/CUTC	CBR/DCP	UCS/DCP	CUTC	CUTC/UCS DCP
South-ern Sudan	Juba	Lateritic Quartzic Wearth. Gravel	2141	7.4	6.0	0.17	2.75	17.5	0.42	14.2	46.1	1.565	30	0.71	26.7	392
	Jonglei	Sandy Clay	1650	19.6	32.8	0.86	2.62	25	0.64	-18	28.1	1.494	2.6	0.087	23.6	18.8
Ethiopia	Addis	Highly Weathered Clayey Gravel	1640	20.3	11.9	0.42	2.21	18	0.46	-12	47.6	1.569	21	0.51	28.3	345
	Addis	Volcanic Ash	1678	16.7	9.9	0.38	2.13	8	0.28	71.2	48.2	1.571	67	1.62	29.5	1883
	Addis	Graded Crushed Basaltic Ag.	2322	7.8	5.7	0.18	2.73	0	0	105	57.3	1.594	108	2.62	37.3	3403
Burundi	Bujum-bura	Coarse Graded Lateritic Gravel	2120	6.9	12.5	0.35	2.79	10	0.42	32.7	41.7	1.551	39	0.94	27.8	478
Tanza-nia	Songwe	Pozzolanic	1780	14.5	12.6	0.26	2.03	6.4	0.16	61	48.3	1.571	58	1.40	29.8	1467
Kenya	Isiolo	Fine Graded Lateritic Gravel	1486	19.1	15.3	0.36	2.36	11	0.53	53.3	45.3	1.562	52	1.23	28.6	1216

Table 2 Summary of shear strength and elastic modulus of OBRM and OPMC stabilized geomaterials

Country of Origin	Loca-tion	*Type of material*	*OBRM1*		*OBRM2*		*OPMC1*		*OPMC2*		*OPMC3*		*OPMC6*	
			q_u MPa	E_{max} (MPa)	q_u MPa	E_{max} (MPa)	q_u MPa	E_{max} (MPa)	q_u MPa	E_{max} (MPa)	q_u MPa	E_{max} (MPa)	q_u (MPa)	E_{max} (MPa)
South-ern Sudan	Juba	Lateritic Quartzic Wearth. Gravel	1.21	1187	1.93	3029	2.66	3422	3.11	5201	4.26	5861	8.13	7492
	Jonglei	Sandy Clay	0.27	125	0.52	301	1.28	1244	1.66	1880	2.59	3388	2.83	3504
Ethiopia	Addis	Highly Weathered Clayey Gravel	0.63	669	0.96	681	1.71	1568	2.21	3190	2.72	3452	3.35	3736
	Addis	Volcanic Ash	1.86	2823	2.35	3085	2.72	4942	3.36	5356	4.75	6108	6.13	6730
	Addis	Graded Crushed Basaltic Ag.	3.21	3676	3.96	3981	4.93	6195	5.95	6654	7.65	7321	9.88	8069
Burundi	Bujum-bura	Coarse Graded Lateritic Gravel	1.35	1923	1.79	2356	2.26	4606	2.64	4886	3.12	5207	6.48	6874
Tanza-nia	Songwe	Pozzolanic	2.86	3518	4.67	4239	6.11	6721	7.25	7173	8.69	7685	11.74	8615
Kenya	Isiolo	Fine Graded Lateritic Gravel	1.74	2913	2.30	3239	2.97	5110	3.87	5651	4.71	6089	5.63	6516

It can further be noted from Table 1 that the Mechanical Stability (MS) is higher for the Kenyan gravel than the Burundi one. It can therefore be inferred that MS is the contributing factor to the enhanced shear and deformation resistance properties. A graphical summary of part of the results presented in Table 2 is made in Fig. 3.4.

3.2 Shear Strength

(1) OBRM Characteristics

A typical graphical representation of OBRM shear strength characteristics is presented in Fig. 3.1.

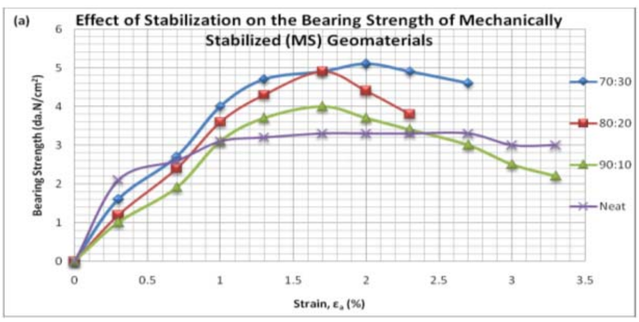

Fig. 3.1. Graphical representation of OBRM shear strength characteristics of geomaterials sampled from the swampy Sudd Plains in Jonglei, Southern Sudan.

In this case, the Optimum Batching Ratio (OBR) was 70:30 in percentage terms of relatively expansive Sandy Clay : Sand. The original sand content in the sandy clay was approximately 12%. This exercise was part of the Basic Design (BD) study for pad foundations for oil drilling rigs.

It can be noted from this figure that, as the batching proportionate tends towards to an optimum value, the shear strength is enhanced accordingly notwithstanding the inferior quality of the base material.

(2) OPMCS Characteristics

The OPMCS shear characteristics for specimens subjected to varying modes of stabilization, soaking and curing conditions are depicted in Fig. 3.2. The testing regime was specifically designed to investigate the rate of particle agglomeration for different batching ratios and types of chemical agents. OPMC-co implies the geomaterials that were batched at ratios of OBRM, i.e., 50:25:25; Lateritic-Quartzic Gravel : Coarse Aggregate : Fine Aggregate with an addition of 20% by weight of Portland Cement (PC), while OPMC-cl refers to similar OBRM ratios but with an addition of 14% PC and 6% Hydrated Lime (HL).

Analysis of the OPMC stabilized Juba gravel indicates that the following derivations can be made: 1) the development of most strength and deformation resistance is realized within the first three days (also ref. to Fig. 3.3); 2) It can be noted that, in this case, the OPMC-cl attains the commonly specified strength of $q_u \geq 30kgf/cm^2$ after only three days of curing while the OPMC-co will have attained 65% of the required strength within the same period, and; 3) the inclusion of lime seems to accelerate the particle agglomeration mechanism by a significant magnitude. This mode of stabilization can therefore be effectively applied for geo-structures that require enhanced development of bearing capacity, strength and deformation resistance within a short period of time hence reducing the construction time.

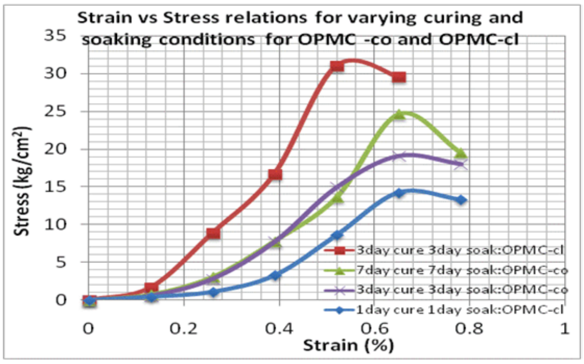

Figure 3.2 OPMC-cl and OPMC-co Stress – strain relations for varying curing and soaking conditions for specimens constituent of geomaterials sampled in Juba, Southern Sudan.

3.3 Initial Deformation Resistance (Elastic Modulus)

The investigation results on the influence of curing period in relation to the initial deformation resistance are graphically plotted in Fig. 3.3 for the two modes of stabilization introduced in this Study. It can be observed that: 1) as the curing period prolongs, the development of the elastic modulus mildly tends towards a residual state; 2) in general, the rate of strength and deformation resistance is higher for the OPMC-cl specimens compared to the OPMC-co ones; and, 3) the addition of lime enhances the rate of development of the deformation resistance immensely.

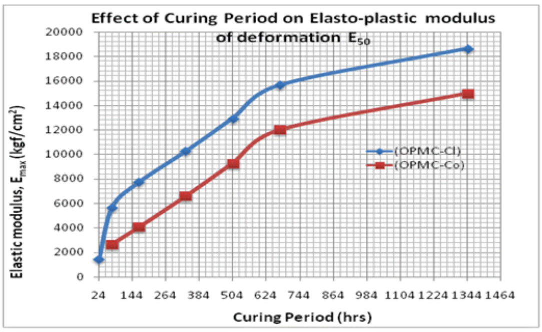

Figure 3.3 Effect of curing period on the elastic modulus of OPMCS geomaterials – Juba, Southern Sudan.

3.4 Graphical Summary of OBRM/OPMCS Shear Characteristics

The graphical summary of OBRM/OPMCS shear characteristics subjected to different modes of stabilization for varying tropical geomaterials sampled from a number of countries in East and Central Africa is presented in Fig. 3.4.

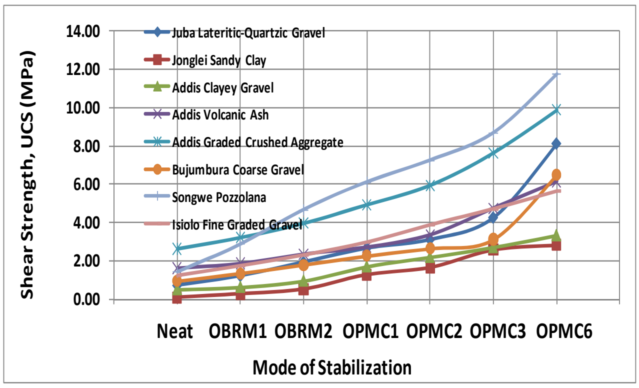

Figure 3.4 Summary of shear strength enhancement based on different modes of stabilization for varying tropical geomatrials

It can be derived from Fig. 3.4 that: 1) response to the mode of stabilization depends on the intrinsic properties of the geomaterial; 2) the magnitude and rate of increase in the shear strength varies with the mode of stabilization; 3) the rates of increase in the magnitude of shear strength are virtually uniform for the Addis Graded Crushed Aggregate and Songwe Pozzolana; and, 4) shear strength enhancement is dependant upon the degree/level and mode of stabilization.

3.5 Combination of OBRM/OPMCS and Geogrid Reinforcement

The quantitatively analyzed effects of soil particle agglomeration on the Unconfined Compressive Strength (UCS) for varying modes of stabilization are depicted in Figure 3.5. The results were adopted in the Detailed Design (DD) of the runway pavement, aprons, taxiway and parking for the Isiolo Airport located in the North Eastern Province of Kenya, which is to be upgraded to international standards [8].

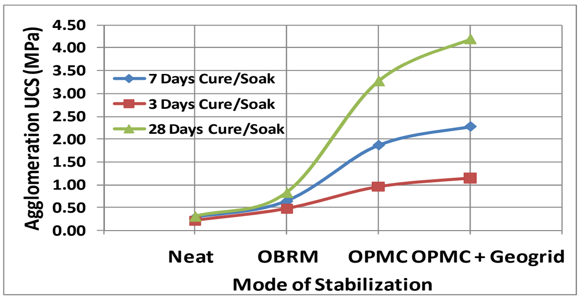

Figure 3.5 Enhanced strength resulting from particle agglomeration for varying modes of stabilization [12].

It can be noted from this figure that: 1) the UCS is significantly enhanced as the soil particles agglomerate progressively with time particularly for the cemented geomaterial, 2) soil particle agglomeration is dependent on the mode of stabilization, 3) the effects of geogrid reinforcement are more noticeable with increased agglomeration possibly due to the influence of confinement in increasing the degree of interlocking of particles culminating in reduction of voids ratio and, 4) the degree of soil particle agglomeration is higher under OPMC stabilization in comparison to geogrid reinforcement thus further confirming the theory that, in comparison to other influencing factors, cementation processes have greater impact on agglomeration mechanisms .

4. CONTRIBUTION OF OBRM/OPMCS TO ENVIRONMENTAL IMPACT MITIGATION

In this Study (ref. to Fig. 4.1) as well as [6]-[10], the results have shown that through the application of the OBRM and OPMCS technologies: 1) reduction of volume of materials used by approximately 40% is achieved in most cases; 2) less disturbance of land for borrow pits; 3) reduced amounts of disposable soil during construction; 4) reduced risk of collapse of geo-engineering structures and; 5) environmentally friendly due to; utilization, as much as possible, of locally available material and reduction of dust, distances (lengths of access roads) to borrow pits, geomaterial quantities required and land acquisition, among other factors. Whilst developing these methods, comprehensive appraisals and environmental assessments that would lead to sustainable development with minimal negative environmental impacts, were undertaken [11].

The example depicted in Fig. 4.1 was part of the design for Wau~Abyei Trunk road constructed in the northern oil fields of Southern Sudan.

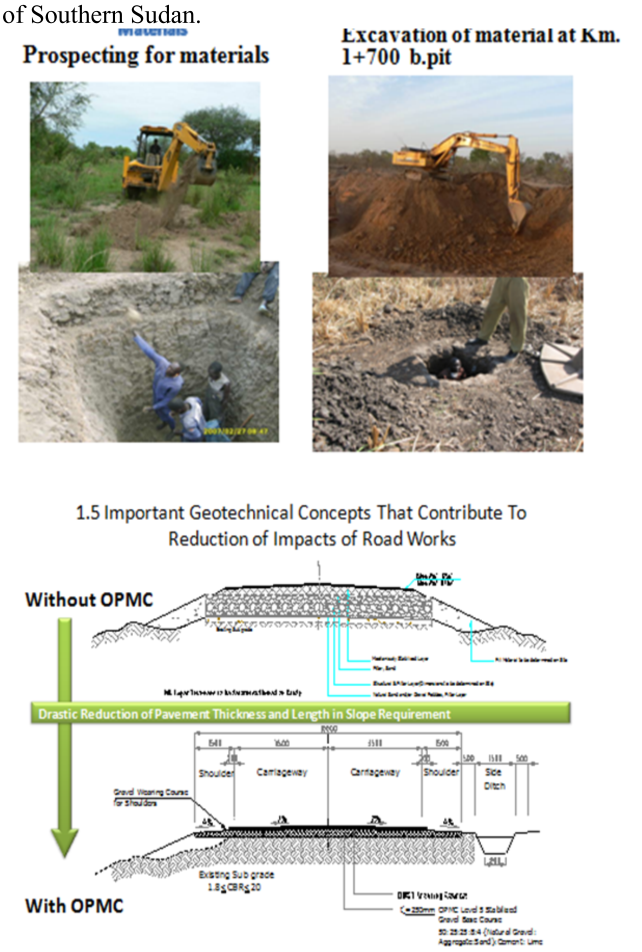

Figure 4.1 Contribution of OPMCS to reduction of environmental impacts of road works [11].

A summary of the approach, considerations and contribution of OBRM and OPMCS from an environmental and geotechnical engineering perspective are discussed in [11].

5. EVALUATION OF CONSTRUCTION AND MAINTENANCE REQUIREMENT RATIOS

The comparative evaluation and analysis of the construction and maintenance requirement ratios expressed in terms of enhanced structural soundness, cost and time savings, was undertaken for the recently constructed Songwe International Airport located in the Southern part of Tanzania [8].

The results of three varying design options are shown in Figs. 5.1 ~ 5.6. OPTION1 (Reviewed) is the design that adopted the OBRM/OPMCS technologies reported in this Study.

5.1 Quantitative Analysis of Structural Performance

Figs 5.1 and 5.2 clearly show that the OBRM/OPMCS technologies significantly enhanced the structural capacity and deformation resistance of the pozzolanic geomaterials exhibiting far more superior geo-properties of the composite pavement structure in comparison to the other designs.

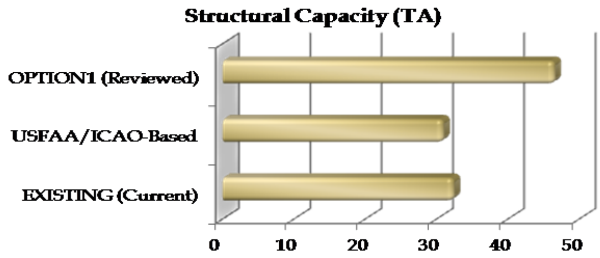

Figure 5.1 Quantitative derivation of OBRM/OPMCS enhanced structural capacity performance.

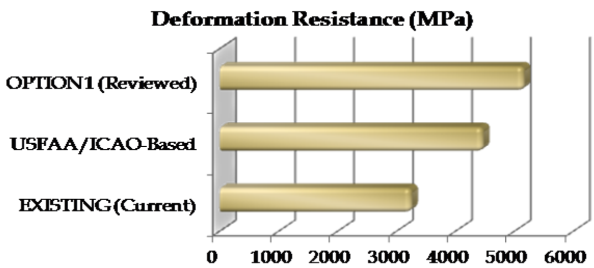

Figure 5.2 OBRM/OPMCS enhanced initial deformation resistance analysis in terms of elastic stiffness measured in in-situ in MPa.

5.2 Cost Aspect Ratio for Construction

The cost aspect ratio was computed mainly on the basis of: 1) reduction in the material quantities required; 2) reduction in construction time; 3) enhancement ratio of the structural and mechanical components in relation to the achievement of a sound geo-structure, and; 4) maintenance requirement ratio.

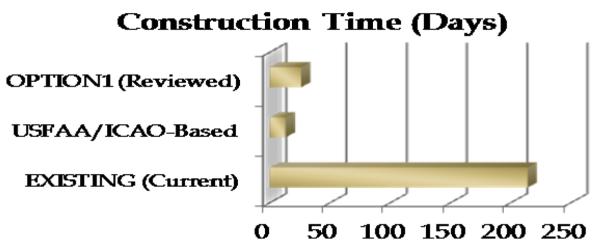

Figure 5.3 Reduction in construction time due to application of OBRM/OPMCS technologies.

As can be inferred from the results depicted in Figs. 5.1~5.5, application of OBRM/OPMCS ensures the achievement of the stipulated objectives by an appreciable margin.

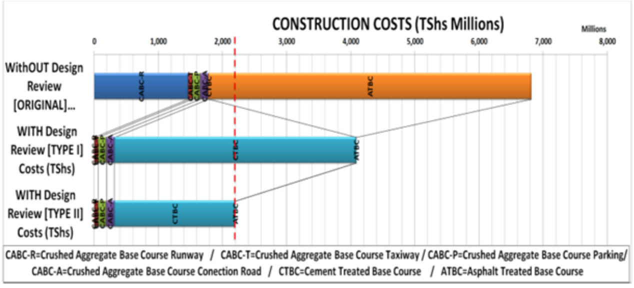

Figure 5.4 Significant reduction in construction cost as a result of OPMCS (shown in blue: approx. 40% reduction).

5.3 Maintenance Requirement Ratio (MRR)

The computation of the MRR was made from (12) based on the results of the SCDR [8] model by adopting the T_A over an initial reference loading period N_t and Design Life, (*DL=20years*).

$$MRR = \frac{T_A^{\{N_t=DL\}}}{T_A^{\{N_t=2.2\}}} \times f_{SC}^{d\{N_t=10\}} \times \frac{T_A^{\{N_t=0.5DL\}}}{T_A^{\{N_t=2.2\}}} \times \left[\frac{N_t=0.5DL}{N_t=DL}\right] \times F_S \tag{12}$$

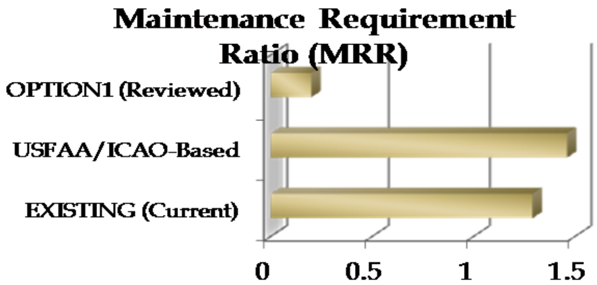

Figure 5.5 Analytical results of the Maintenance Requirement Ratio (MRR).

5.4 Summary of Overall Performance

A summary of the overall performance of the three pavement structures based on the varying designs is presented in Fig. 5.6. It can be noted that OBRM/OPMCS excels in all cases.

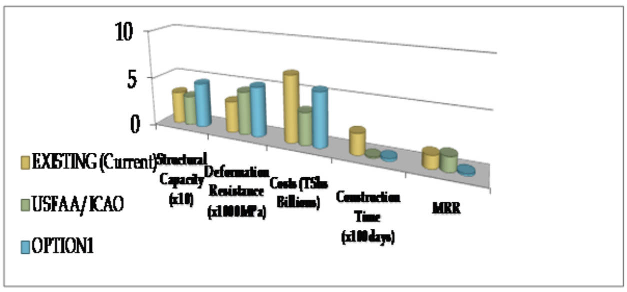

Figure 5.6 Summary of performance of the varying designs and technologies

6 CONCLUSIONS

The analysis of the performance of some recently developed in-situ based stabilization techniques have been reported in this paper for varying tropical geomaterials from five different countries of the East and Central African Region.

It has been demonstrated in all cases that the OBRM/OPMCS technologies contribute significantly to not only the enhancement of the geotechnical engineering properties that are vital in design, but also in achieving immense construction cost and time savings as well as minimum maintenance requirements.

7 ACKNOWLEDGEMENT

The authors wish to extend their sincere appreciation to the Japan International Cooperation Agency (JICA), Katahira & Engineers International, Japan and Urban Tone Corporation, Japan, for sponsoring most of the research for this Study. Acknowledgement is also extended to the Materials Testing & Research Department of the Ministry of Roads, Kenya, the Tanzania Airports Authority, and the KGS for their support.

8 REFERENCES

[1] Mukabi, J.N, "Theoretical and empirical basis for a method of determining the optimum batching ratio for mechanical stabilization of Geomaterials", Procs. 14th IRF road World Congress, Paris, 2001, CD.

[2] Mukabi, J.N & Shimizu, N, " Strength and deformation characteristics of mechanically stabilized road construction materials based on a new batching ratio method", Procs. 14th IRF Road World Congress, Paris, 2001, CD-ROM.

[3] Mukabi JN, Kimura Y, Shimizu, N, Mwangi SN, Omollo A, Njoroge BN, " Evaluation of some Kenyan Geomaterial properties for embankment design based on a quasi-empirical approach", Procs. 15th Int. Conf. on SMGE, Istanbul, 2001, pp2159-2166.

[4] Mukabi JN, "Case Study Analysis of OPMC improved foundation ground, pavements and geo-structures employing the GECPRO model", to be published in Procs. Of ISSMGE International Symposium on Ground Improvement (IS-GI), Brussels, 2012.

[5] Mukabi JN, "Innovative laboratory and in-situ methods of testing in geotechnical engineering, to be published in the Proc. of the Int. Conf. of the Inst. of Engineers Kenya , Nairobi, 2013.

[6] Kensetsu Kaihatsu Limited, Juba River Port Access Road Pavement Design, Engineering Report No. SST1, submitted to Japan International cooperation Agency, JICA, vide Katahira & Eng. Int., Japan, 2007.

[7] Kensetsu Kaihatsu Limited, A Comprehensive Engineering Report on the Study, Design and Construction of Drilling Pad Foundations in Jale, Jonglei State, Southern Sudan, submitted to White Nile Oil Exploration Company, London, England, 2007.

[8] Kensetsu Kaihatsu Limited, Songwe Airport Pavement Design Review Engineering Report No. SAT 09T1, submitted to Tanzania Airports Authority, Government of the Republic of Tanzania, 2011.

[9] Kensetsu Kaihatsu Limited, Isiolo Airport Pavement Design, Engineering Report No. ISAT 0211/O2, submitted to Kenya Airports Authority, Government of Kenya, Nairobi, 2011.

[10] Mukabi JN, Kimura Y, Murunga PA, Njoroge BN, Wambugu J, Sidai V, Onacha K., Kotheki S, Ngigi A, "Case example of design and construction within problematic soils", in Procs. Int. Geotechnical Conference on Geotechnical Challenges in Megacities, Geomos, Moscow, 2010, vol. 2, pp 1172-1179.

[11] Mukabi J.N., Toda, T. & Shimizu, N, "Application of a new mechanical stabilization technique in reducing the cost and impact of rural road construction, Procs. 23rd World Road Congress, Paris, 2007, CD-ROM.

[12] Wekesa S, Mukabi JN, Sidai V, Kotheki S, Okado J, Ogallo J, Amoyo G, Ngigi L, "Quantitative analysis to verify the theory of soil particle agglomeration and its' influence on strength and deformation resistance of geomaterials", Procs. 15th ARC on SMGE, Maputo, 2011, pp. 330-335.

First International Conference on Geotechnique, Construction Materials and Environment, Mie, Japan, Nov.21-23, 2011, ISBN: 978-4-9905958-0-7 C3051

Further Developments in the Swelling Model of Expansive Clays under ASTM 4546 and CBR Testing

Moshe Livneh. Civil and Environmental Engineering Department, Technion-Israel Institute of Technology

ABSTRACT: The prediction of heave for pavements based on expansive subgrades requires knowledge of the percentage expansion expected at each depth at which the absorption of water takes place until equilibrium moisture is obtained under a controlled suction state. This heave prediction necessitates knowledge of the swell-pressure characteristics of the given clay stratum, data that are usually obtained from laboratory tests on undisturbed clay samples. It has been demonstrated in regard to 352 local undisturbed samples under ASTM 4546 testing that a general swelling model can be employed that predicts the percentage of swell under a given vertical pressure exerted on clay characterized by basic parameters. The present paper, too, deals with the development of the general swelling model, but this time for 674 local CBR remolded samples soaked in water and subjected to swell under a given surcharge pressure for a period of 4 days. The paper concludes with a comparison of these two general models.

Keywords: CBR, expansive-clay, heave, suction, swell.

1. INTRODUCTION

A considerable proportion of roads and railways are based on swelling-clay subgrades. Thus, it is important to assess the rates of heave expected to occur as a result of clay activity in any given alternative that defines the design solution for pavement or railway-bed structures. This assessment is based on a swelling model that links the rate of vertical swell with the clay's characteristics, combined with the rate of the swell pressure (i.e., rate of the vertical pressure to obtain a zero rate of vertical swell).

The reliability of the aforementioned heave assessment depends on, among other things, the reliability of the swelling model (also known as the general swelling model) used in the prediction. This swelling model refers to undisturbed samples subjected to ASTM 4546 Method B testing for rates of vertical swell and ASTM 4546 Method C testing for rates of vertical swell pressure. Thus, it is only natural to have an interest in updating this model with the accumulation of additional test results over time. This paper presents such an update, while comparing its output with previous results.

In addition, it is important to determine the rate of the remolded vertical swell ratio, defined as the ratio of the vertical swell rate obtained in remolded clayey samples to the vertical swell rate obtained in natural (undisturbed) clayey samples. Obviously, this definition refers to equal conditions of moisture, density, and consistency limits for both remolded and undisturbed materials. The rate of the remolded vertical swell ratio is reflected in the heave prediction for the clayey horizontal strips that were processed and compacted on site. The rate of the remolded vertical swell ratio is determined, obviously, by conducting specific vertical swell and swell-pressure tests on undisturbed and remolded samples for a given project. This paper, however, concentrates on the development of an additional swelling model for local CBR remolded samples soaked in water and subjected to swell under a given surcharge pressure for a period of four days. This additional swelling model is based on the same regression analysis used for the development of the general swelling model referred to above. Finally the paper concludes with a comparison of the these two models, one for undisturbed samples tested according to ASTM 4546, and the second for compacted samples in CBR molds after four days of soaking in water.

2. OLD GENERAL SWELLING MODELS

The first Israeli general swelling model was published in 1969 [1]. This model introduces a statistical relationship between the swell pressure (Po), in kPa, and the following parameters characterizing the undisturbed clay samples: liquid limit (LL) in percentages, moisture content (W) in percentages, and dry density in kN/m^3. The general formulation of this model is as follows:

$$\log (Po/98.07)=a_o+a_{LL}\times LL+a_W\times W+ a_D\times(D/9.81) \quad (1)$$

In (1), a_o, a_{LL}, a_W, and a_D denote the regression coefficients of four independent variables. Their values are given in the row labeled "[1]" in Table I. In this row, the coefficient of determination (R^2), taken from [1], is also presented. Table I also contains the regression coefficients published in 1985 [2]. These coefficients were determined for the same 125 samples as in [1] through a semi-statistical analysis, which assumed that the ratio a_W/a_D had a fixed value of 0.04. Obviously, no value can be determined for R^2 in such an analysis.

Table I: Regression coefficients of (1) and its R^2

Ref.	Regression coefficients of (1)				R^2
	a_W	a_W	a_{LL}	a_o	
[1]	0.6650	–0.0269	0.0208	*–2.1320	0.36
[2]	1.0000	–0.0400	0.0200	–2.0000	---
[N]	0.6582	–0.0248	0.0202	–1.8823	0.38

* The value of a_o published in [2] as a quotation from [1] is surprisingly different: –1.868.

For the current study, a new multiple linear regression analysis in the form of (1) was performed for the same 125 undisturbed samples. The results are listed in the row labeled "N" in Table I. This analysis yielded a standard error (SE) of 0.48. The significance of this value is that 68 percent of all predictions from (1), together with the data of row "N" of Table 1, are expected to be accurate within a range of $10^{-0.48}$ (i.e., 1/3) to $10^{0.48}$ (i.e., 3) times the value calculated. Similarly, 95 percent of these predictions are expected to be accurate within 0.1 up to 9 times the calculated value. Both these ranges indicate the existence of an extensive dispersion characterizing the measurement results, as do the low value obtained for R^2. In addition, it is important to emphasis that the results listed in row "N" in Table I are not fully identical with those obtained by [1]. Fig. I shows the gaps associated with these outputs.

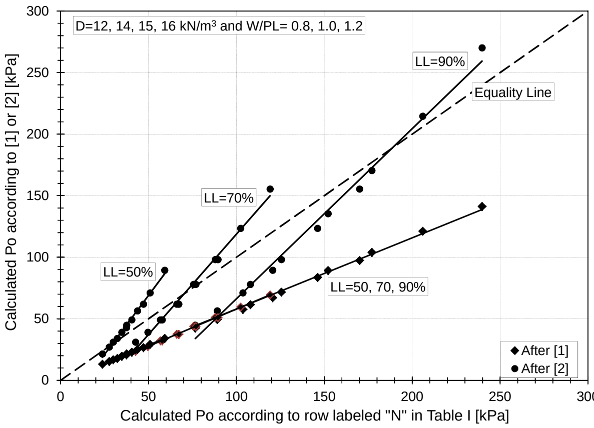

Figure 1. Display of the gaps in swell-pressure outputs following (1) and the coefficients of Table I for the data shown

In Fig. 1, PL=20%, 25% and 30% for LL=50%, 70% and 90%, respectively. For these data, the figure shows that the gap between the current regression and the original regression described in [1] is substantial. The ratio obtained for the original regression outputs to the current regression outputs is about 0.6. It is possible that this inexplicable gap may be due to the existence of possible typing errors in the data published in [1]. As for the regression presented in [2], the gap obtained is not constant, and the ratio varies from 0.6 up to 1.3.

In contrast to [1], the predictions of vertical swell rates (Sp) are given for the first time in [2]. For these predictions, Sp (in percentages) depends on the applied vertical pressure, Pp (in kPa), and the defined characteristics of the undisturbed clay samples. The formulation of the relevant equation is as follows:

$$Sp=-3.683\times(Po/98.07)\times\log(Pp/Po) \qquad (2)$$

In (2) the value of Po is determined from both (1) and the data of the row labeled "[2]" in Table I. Here it is important to note that the factor of -3.683 that appears in the equation is determined after the analysis of a series of empirical relationships reported in the technical literature. The value of this factor, unfortunately, did not receive any verification from requested local laboratory tests, and hence this also is an indication of its weakness.

3. NEW GENERAL SWELLING MODELS

Reference [3] presents the new swelling model, based on a multiple linear regression performed on 352 new local swelling test results obtained for undisturbed samples taken from different sites in Israel. The regressive equation obtained is as follows:

$$Sp=-20.926+9.304\times\log(LL)-1.948\times W/PL+ +4.250\times(D/9.81)-2.352\times\log(Pp/98.07) \qquad (3)$$

For this regression, the R^2 value obtained is 0.36, and the SE value is 1.49%. In other words, 68 percent of all predictions from (3) are expected to be accurate within ± 1.49%, and 95 percent of these predictions are expected to be accurate within ± 2.98%. Fig. 2 depicts (3) graphically for the clay data shown in the figure. For comparison purposes, this figure also includes a graphical representation of (2) for the same clay. Finally, the figure indicates that (3) leads to excessive values for the swell pressure.

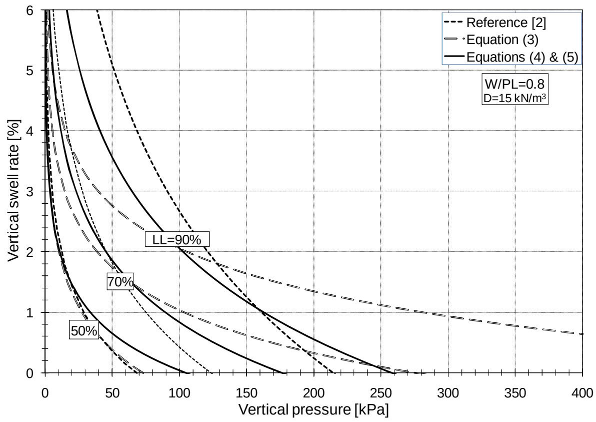

Figure 2. Graphical comparison of three calculated variations of ASTM vertical swell rates with vertical pressure for the data shown

The same 352 undisturbed samples were also used to determine the direct dependence of the variables in the same manner described in (1) and (2). This was performed with the Excel-Solver command, leading to the following two equations:

$$\log(Po/98.07)=-3.256+1.540\times\log(LL)- -0.537\times W/PL+0.738\times(D/9.81) \qquad (4)$$

$$Sp=-1.872\times(Po/98.07)\times\log(Pp/Po) \qquad (5)$$

The SE value associated with the development of these two equations is 1.45%, which is lower than that associated with the development of (3): i.e., 1.49%. In addition to this advantage, another advantage of the model formulated in (4) and (5) is that they produce reasonable swell-pressure values similar in principle to those obtained from the equations in [2]. For this issue, see also the numerical example in Fig. 3. All these facts serve as a necessary justification for replacing the LL independent variable by log(LL), and the W independent variable by W/PL.

Furthermore, it is worthwhile examining the justification for using (4) and (5), in which the LL independent variable has been replaced by log(LL) and the W independent variable by W/PL in the following way. First, there is need to formulate two new equations with the aid of the Excel-Solver command for the 354 new undisturbed samples. This formulation, which is obviously based on the same structure as (2) and (3), leads to the following two equations:

$$\log(Po/98.07)=-0.8936+0.0100\times LL-$$
$$-0.01576\times W+0.5251\times(D/9.81) \quad (6)$$
$$Sp=-1.4836\times(Po/98.07)\times\log(Pp/Po) \quad (7)$$

It should be noted that (6) and (7) yield an SE value of 1.52%. A graphical comparison of (4) and (5) (in which the independents variables are, among others, log (LL) and W/PL) with (6) and (7) (in which the independents variables are, among others, LL and W) is presented in Fig. 3 for the data shown. This graphical representation also contains the two equations given by [2].

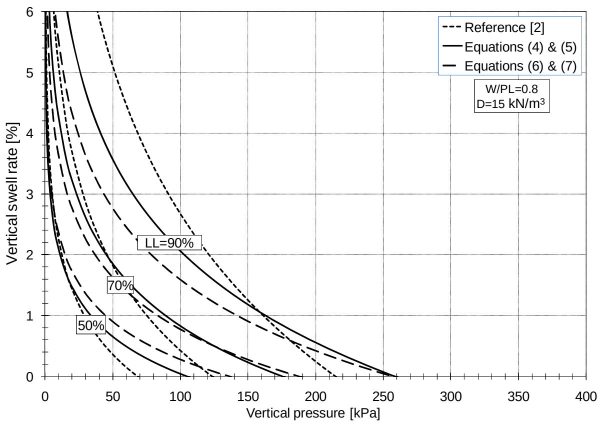

Figure 3. Additional graphical comparison of three calculated variations of ASTM vertical swell rates with vertical pressure for the data shown

Figure 3 indicates that the use of the independent variables of log (LL) and W/PL leads unexpectedly to a stronger effect of the liquid limit on the vertical swell rate than that of the independent variable of LL and W. In fact, this result is more nearly similar to the original equations presented by [2]. Finally, it is also important to note that the preference for replacing W with W/PL arises from the fact that the acceptable characteristic of the moisture state that determines, among other properties, the intensity level of the swelling potential is W/PL [5].

In addition, the preference for the independent variables of log (LL) and W/PL on LL and W, respectively, also derives from the following comparison of the SE values: 1.45% associated with (4) and (5), and 1.52% associated with (6) and (7). Finally, it can be concluded from the comparisons presented in Fig. 2 and Fig. 3 that (4) and (5) are the most appropriate to serve as the updated equations to define the general swelling model in relation to the older equations described in [2]; this is due to the fact that (4) and (5) yield higher results than do (6) and (7), thus giving the former pair of equations the benefit of the factor safety.

4. NEW CBR GENERAL SWELLING MODEL

Reference [4] describes several predicting models of the vertical swell rates measured in local CBR molds. The samples of these molds are soaked in water and subjected to swell under a given surcharge pressure for a period of 4 days. Obviously, these vertical swell rates are related to compacted (remolded) material. At this juncture it is important to note that all the CBR swelling models of [4] do not belong to the same formulation family of the new general swelling models as expressed in (4) and (5). Thus, there is a need to formulize a new CBR general swelling model with a similar formulation of the above equations. Performing the Excel-Solver command on the local 674 samples led to the following two equations:

$$\log(Po/98.07)=-0.8002+0.8625\times\log(LL)-$$
$$-0.9370\times W/PL-0.0711\times(D/9.81) \quad (8)$$
$$Sp=-6.0347\times(Po/98.07)\times\log(Pp/Po) \quad (9)$$

where Sp denotes the CBR vertical swell, in percentages; Pp denotes the vertical surcharge pressure, in kPa; LL denotes the liquid limit, in percentages; PL denotes the plasticity limit, in percentages; W denotes the water content, in percentages; and D denotes the dry density, in kN/m^3.

The SE value obtained for these two equations is 1.406%. Here it should be noted that these two equations lead, contrary to what was expected, to decreased values of Sp with increasing values of D. This behavior stems from the way the CBR test is conducted. As we know, the CBR molds are soaked in water for four days, an operation that does not ensure the complete saturation of the sample, unlike in the standard ASTM 4546 testing.

In the CBR mold, the sample saturation occurs only at its top, the depth of this saturated strip depending on the rate of the water flow. When the dry density of the sample increases, the rate of flow deceases, thus leading to decreasing thickness of the top of the swelling strip. Therefore, the combination of this thickness reduction, which acts to decrease Sp, and the increasing potential for swelling that occurs with increased dry density creates the final balanced phenomenon in accordance with the weighting influence of these two magnitudes. As noted, this final phenomenon consists of a decline in the rate of heave of the sample and, hence, in the rate of vertical swell. In any case, the impact of D input on Sp output in (8) and (9) is secondary as will be demonstrated later in this section.

To illustrate the issue of differences in the depth of the saturation in the CBR molds after four days of soaking, Fig. 4 presents the relationship between the difference in moisture content of the top 1 inch of the sample from that of the total sample (both after four days of soaking in water) as seen with the ratio of the molding water content to the plasticity limit of the clay. This figure refers to swellings of clay samples taken from seven different locations in the area of Israel's major airport.

Fig. 4 shows that the difference in wetting after soaking the CBR samples in water depends on the ratio of the molding moisture content of the clay to its plasticity limit. With an increasing moisture-content ratio, the rate of the difference in wetting indicates a decrease. In the same manner, Fig. 5 depicts the relationship between this difference in wetting and the sample's dry density multiplied by the expression (1+PL/100). The figure refers to the same clay samples as in Fig. 4. With an increasing rate of dry density, the rate of the difference in wetting is also shown to increase; however, this occurs only when the upper swelling thickness apparently decreases.

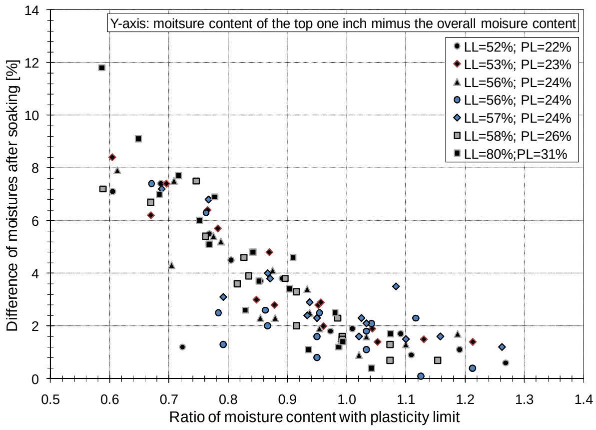

Figure 4. Difference in moisture content of the top 1 inch from that of the total sample (both after 4 days of soaking) with the ratio of molding water content to the plasticity limit of the clay

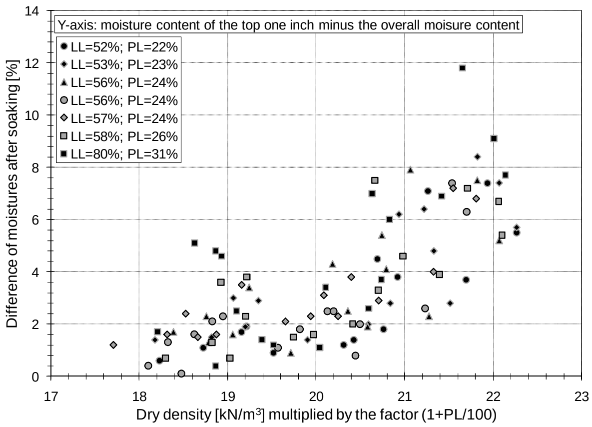

Figure 5. Difference in moisture content of the top 1 inch from that of the total sample (both after 4 days of soaking), with dry density multiplied by (1+PL/100)

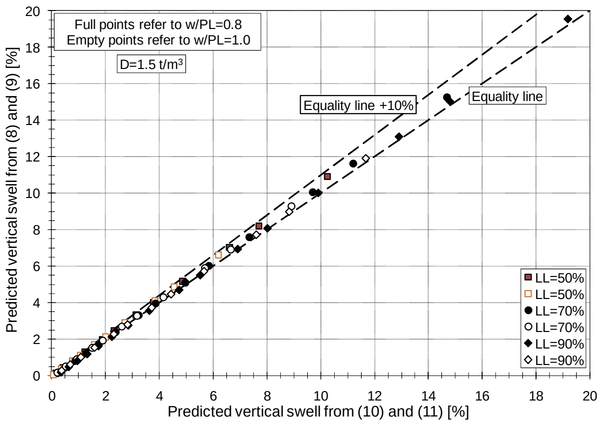

Figure 6. Comparison of rate of vertical CBR swell according to (8) and (9) with that according to (10) and (11) for the data shown in the figure

Now, in order to neutralize the opposite effect of the dry-density input on the output of the vertical swell calculated value, it is necessary once again to implement the Excel-Solver command. This time, implementation should be without the dry-density variable; such an implementation leads to the following two equations:

$$\log(Po/98.07)=-1.0099+0.93023\times\log(LL)-0.9409\times W/PL \quad (10)$$

$$Sp=-5.5283\times(Po/98.07)\times\log(Pp/Po) \quad (11)$$

The value of SE obtained for these two equations, 1.409%, is very similar to that obtained for the previous two equations. Also, the difference in the predictions of the vertical swelling rate, which derived from (8) and (9) minus that derived from (10) and (11), is low. For the numerical examples of Fig. 6, this difference is about 10% or less for the range of a 2% vertical swell rate and higher.

5. COMPARISON OF CBR AND ASTM MODELS

Fig. 7 presents a graphical comparison of the swelling models calculated from the outputs of the Excel-Solver command performed on the test results of (a) 674 CBR samples as expressed in (10) and (11) and (b) 352 undisturbed samples of the ASTM testing as expressed in (4) and (5), the latter serving as the local general swelling model. This comparison includes the old general swelling model taken from [2]; i.e., (1) and (2) together with the data of row "N" in Table I.

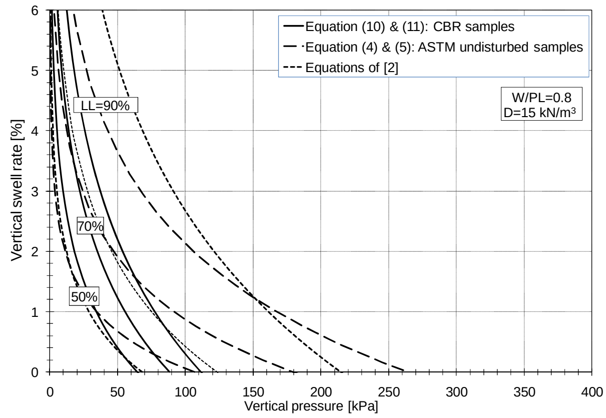

Figure 7. Graphical comparison of CBR swelling model obtained from (10) and (11) with that of ASTM obtained from (4) and (5), including [2]

The aforementioned comparison refers to a dry density of 15 kN/m^3 and a ratio of moisture content to plasticity limit of 0.8. Fig. 7 shows that the predicted swell-pressure rates of the CBR remolded samples obtained from (8) and (9) are lower than those of the undisturbed ASTM samples obtained from (4) and (5). Here, it is important to note that the acceptance of this finding should be of a limited nature, as the behavior of the CBR swelling model beyond the surcharge pressure rates of 10 up to 20 kPa stems from the fact of their being in the extrapolation zone of the experimental data. To recall, surcharge pressure rates of 10 up to 20 kPa were applied in the CBR tests of [4].

Fig. 8 presents a variation of the ratio of measured vertical CBR swell to the predicted vertical ASTM swell according to

(4) and (5) with the variation in measured vertical CBR swell. The figure contains ratio values for three suction levels for which the vertical swell rate was calculated using (4) and (5). The logic of including two suction levels together with 0.0 kPa is the possibility that after four days of soaking in water, the CBR sample will not reach a full saturated state, thus leading to a residual suction value in the sample. To recall, a residual suction value of 30 kPa exists in a clayey subgrade when, covered by a standard asphalt pavement, it reaches an equilibrium state of excess moisture absorption [5], [6].

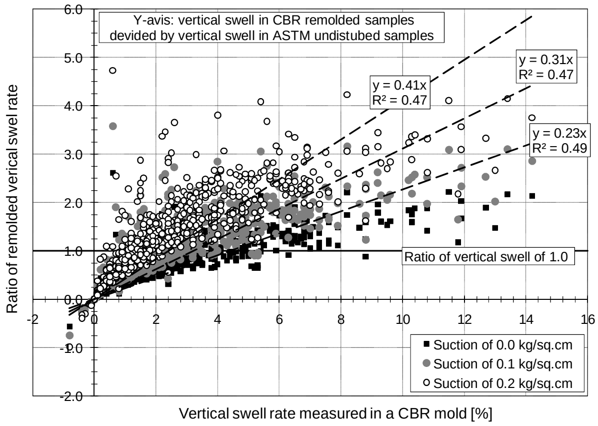

Figure 8. Variation in the ratio of the measured vertical CBR swell to the predicted vertical ASTM swell according to (4) and (5) with the variation in measured vertical CBR swell

Fig. 8 shows that the value of the slope of the line of variation decreases with the increase in the suction level. This fact indicates an increase in the frequency of cases in which the swell ratio (as defined previously) is greater than 1.0. For a suction value of 0.0 kPa, the majority of the measured points is below the swell ratio of 1.0. Finally, the conclusion to be derived from Fig. 8 is that the vertical swell rates of remolded samples are higher than those of the undisturbed samples, provided that the final suction level in these two kinds of samples is identical.

6. COMPARISON OF CBR SWELLING MODELS

As stated in Section 4, all the CBR swelling models of [4], which are based on the swelling results of 674 remolded samples, do not belong to the same formulation family of new general swelling models as expressed in (3) or (4) and (5). Thus, it is interesting to compare these models with that developed in the present paper in Section 4. The two existing models of [4] are these:

$$Sp=47.2124\times[(0.0423\times LL-0.001662\times Pp)/\ln(D/9.81)]^{Q}$$
$$Q=0.0078\times W^2-0.1617\times W+2.6491 \quad (12)$$

$$Sp=72.0419+0.1216\times LL-0.02822\times Pp$$
$$-8.9911\times\ln(D/9.81)-0.4665\times W \quad (13)$$

For the CBR swelling model expressed in (12), the value obtained for R^2 was 0.680, and that obtained for SE was 1.40%. In the same manner, the value obtained for R^2 was 0.655 for the CBR swelling model expressed in (13), and 1.45% for that obtained for SE. What is interesting to note is that the standard error value of (12) is lower than that obtained for (10) and (11); i.e., SE=1.41%. Can one then conclude that the CBR swelling model expressed in (12) is the most appropriate one for implementation?

In order to examine the likelihood of (12) and (13) compared with that of (10) and (11), Fig. 9 depicts a graphical comparison of CBR swelling models obtained from (12) and (13) with that obtained from (10) and (11) for the data shown in the figure. This figure clearly indicates a non-physical compatibility of (12) being able to serve as a basic functional equation for developing a forecasting model for the vertical swell rates. The swell-pressure rates obtained from (12) in the extrapolation zone are completely unrealistic. Moreover, (12) does not allow for vertical swell rates to be negative (i.e., to be changed from heave to deflection) for surcharge pressure values greater than the swell-pressure values. Thus, the conclusion given in [4], that the impact of surcharge pressure values on the rates of the vertical swell is only of minor intensity, does not comply with reality. Obviously, this conclusion stems from the use of an inappropriate basic functional equation for the conditions of the given problem, and therefore its validity is very questionable.

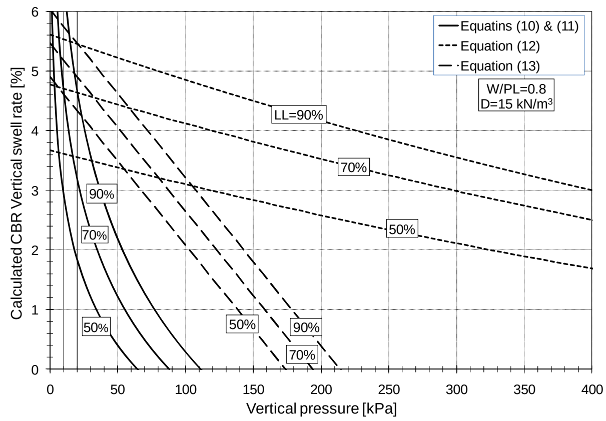

Figure 9. Graphical comparison of CBR swelling models obtained from (12) and (13) with that obtained from (10) and (11) for the data shown in the figure

Fig. 9 also indicates the non-physical compatibility of (13) to serve as a basic functional equation for developing a forecasting model for vertical swell rates. The linear variation of the rate of vertical swell with the rate of the vertical surcharge pressure as specified by (13) and shown in that figure has no reference in the technical literature, which presents a wide range of laboratory test results for this purpose. In addition, (12) and (13) indicate that increasing the dry density variable decreases the expected rate of the CBR vertical swell. To recall, the same phenomenon is characterized by (8) and (9). However, for (13) these deceased rates are not negligible, 0.6% or more for a dry-density increase of 1.0 kN/m^3. As for (12), this decreased rate is, in contrast to (13), negligible, about 0.1% for the same dry density increase of 1.0 kN/m^3.

Together with the above-mentioned reservations concerning the CBR swelling models of (12) and (13) in [4], it should be noted that the gaps between the families of the three CBR swelling models shown in Fig. 9 are reduced for the zone of actual vertical surcharge pressure applied in the CBR vertical swell measurements (i.e., 10 to 20 kPa). The conclusion is, again, that the choice of a basic functional equation to insert into a statistical analysis of any measured data is critical, especially for use in predicting values that are outside the actual measurement range; that is, in the range of extrapolation. Therefore, the selection of a calculative model from a number of calculative alternatives only on the principle of minimum standard error (SE) or maximum coefficient of determination (R^2) is seriously questionable.

7. SUMMARY AND CONCLUSION

A summary of all the developments described in the preceding sections is shown in Table II for the ASTM undisturbed samples and in Table III for the CBR remolded samples. The data in these two tables are given for the following independent variables: log(LL) and W/PL; i.e., instead of LL and W. When the principle of a minimum standard error (SE) is applied to the 352 ASTM undisturbed samples, the preferred solution is given by (4) and (5).

Table II: Summary of SE for the ASTM undisturbed samples

Section No.	Eqns. No.	Samples' Number	Analysis Method	SE %
3	3	352	Linear Regression	1.49
3	4, 5	352	Excel-Solver	1.45

Table III: Summary of SE for the CBR remolded samples

Section No.	Eqns. No.	Samples' Number	Analysis Method	SE %
---*	---*	674	Linear Regression	1.63
4	10, 11	674	Excel-Solver	1.41

* Taken from another local study [7].

Table III refers only to the equations that do not contain the dry density independent variable. This table indicates, again, that when the principle of a minimum standard error (SE) is applied, the preferable solution is that of (10) and (11) as derived from the Excel-Solver command. Again, for this case, the application of the above principle is legitimate, as the basic functional equations are compatible with the physical behavior of the swelling phenomenon.

It is clear that the preference for (12) taken from [4], for which the SE value is 1.40% (i.e., less than the 1.41% specified in Table III), is unacceptable, because the basic functional equation of (12) that is used in the implementation of the statistical analysis of the reported measured data does not represent the actual physical behavior of the variation in the vertical swell rate with the vertical surcharge pressure rate. As noted, the use of inappropriate basic functional equations is particularly severe in the extrapolation zone of the measured data. To conclude, the analysis of the measured CBR vertical swell rates of the 674 remolded samples presented in this paper can be used as an example of permissible and forbidden operations in order to determine models for any measured data.

Another point to which attention need to be paid is the preference for replacing the LL and W variables with log (LL) and W/PL, respectively, as discussed in Section 3. This section shows that the equations corresponding to (4) and (5), namely (6) and (7), lead to an SE of 1.52%, compared with the 1.45% listed in Table II (see also Section 3). In addition, as obtained from Fig. 3, the effect of the variation in the LL independent variable on Sp is more severe when the independent variables are log (LL) and W/PL. This finding stems from the comparison with the variation in the LL independent variable with Sp as calculated from the two equations given in [2].

Finally it should be added that the analysis of the CBR samples cannot be used to determine the ratio of the rate of remolded vertical swell with the rate of undisturbed vertical swell, defined as the remolded vertical swell ratio. It is well known that the final moisture state reached in a swell test conducted according to ASTM 4546 on undisturbed samples is characterized by the presence of zero suction, while that for a swell test conducted on remolded samples according to the CBR procedure is characterized by the presence of a suction value greater than zero. Because of these different suction values, it is not possible to include the above two series of experimental results (i.e., the ASTM and the CBR results) into one basket of results. Thus, in order to evaluate the rate of the remolded vertical swell ratio, it is necessary to conduct a series of tests according to ASTM 4546 on remolded samples from the same source of clay in parallel with the undisturbed samples.

8. ACKNOWLEDGMENT

The statistical analysis of the data referred to in [4] was enabled after obtaining all the raw data from Dr. Michael Divinsky, former chief geotechnical statistician of the National Company for Roads in Israel (PWD), to whom thanks are due.

9. REFERENCES

[1] Komornik, A., and David, D., "Prediction of Swelling Pressure of Clays," *Journal of Soil Mechanics and Foundation Division*, Vol. 95, No. SM1, 1969, pp. 209-225.

[2] Wiseman, G., Komornik, A., and Greenstein, J., "Experience with Roads and Buildings on Expansive Clays," *Transportation Research Record* 1032, 1985, pp. 60-67.

[3] Livneh, M., "Additional Updates in the General and Local Swelling Model," *Traffic and Transport, Journal of the Israel Section for Traffic and Transportation*, No. 98, March 2011, pp. 38-44 (in Hebrew).

[4] Ishai, I., Sahar, I., and Divinsky, M., "A Practical and Rational Model for Swell Prediction of Clayey Subgrades Using the CBR Test," Paper submitted to the *2004 Annual Meeting of the Transportation Research Board*, unpublished, 2004.

[5] Kassiff, G., Livneh, M., and Wiseman, G., *Pavements on Expansive Clays*, Jerusalem Academic Press, 1969.

[6] Wiseman, G., Livneh, M., and Uzan, J., "Performance of a Full-Depth Asphalt Pavement on Expansive Clay Subgrade," in *Proc. of the 3rd Conf. of the Road Engineering Association of Asia and Australia*, Taipei, Taiwan, 1981, pp. 747-760.

[7] Livneh, M., "On the Updated Development of the General Swelling Model," in *Proc. of the 7th Conf. on Civil Engineering* (CD Proc.), Israel Association of Engineers for Construction & Infrastructures, Tel Aviv, 2011 (in Hebrew).

First International Conference on Geotechnique, Construction Materials and Environment, Mie, Japan, Nov.21-23, 2011, ISBN: 978-4-9905958-0-7 C3051

The Effect of Clay, Lime and Rice Husk Ash Contents on the Sorption Capacity of Cu, Ni and Zn by Soils

Pongsakorn Punrattanasin and Noppadol Sangiumsak
Research Center for Environmental and Hazardous Substance Management, Khon Kaen University and Department of Civil Engineering, Faculty of Engineering, Khon Kaen University, Thailand

ABSTRACT: Copper (Cu), nickel (Ni) and zinc (Zn) are the common heavy metals that have been discharged from industries. The toxic conditions are always occurred with plants, animals, and human from these metals. This paper presents the sorption of Cu, Ni and Zn by soils collected from three different locations in the upper part of Northeastern, Thailand. Then the new method was used to increase the sorption capacity of Cu, Ni and Zn by the soils. Clay, lime and rice husk ash were then selected and used as the additional materials to improve the sorption capacity. The soils were mixed with different ratios of the additional materials. Batch equilibrium method was used as tools to investigate the adsorption value. The results showed that the adsorption fit to Langmuir Isotherm Model. All additional materials can dramatically improve the sorption capacity of Cu Ni and Zn by soils.

Keywords: Heavy metals, Adsorption, Isotherm

1. INTRODUCTION

Rapid growth of industries and communities in every part of Thailand including Northeastern leads to the environmental problem especially waste water and contaminated soil. Many houses and industries discharged the waste water into river or soil without treatment. This resulted in an accumulated of toxins in soil and water. Heavy metals are one kind of the toxins that has caused serious health problem to humans and animals. They cause damage to the kidney, liver, reproductive system [1], nervous system and ultimately death [2]. Ministry of Industry Thailand has enacted laws to limit the amount of heavy metal in discharged waste water from industries. There are many methods for remove the heavy metals from the waste water such as a reduction process, magnetic ferrites treatment, ion exchange, reverse osmosis, and chemical oxidation and reduction, membrane separation, coagulation, flotation, filtration, evaporation etc. [3,4,5]. Adsorption is one of the most common methods for heavy metal removal because it is an effective and economical technique. In this work, the adsorption of Cu, Ni and Zn by soils found in the upper part of Northeastern, Thailand was investigated and also the method of improvement of the adsorption by mixing soils with clay, lime and rice husk ash was studied. The objective of this study is to find the effect of additional materials on the sorption capacity of soils.

2. MATERIALS AND METHODS

2.1 Adsorbent

The materials used as adsorbent were soils collected from three different locations in the upper part of Northeastern, Thailand. They were excavated at different depths ranging from 20-50 cm from the soil surface. The soils were dried at a temperature of 110 ^{o}C for 48 hours and were sieved through sieve No.16. They can be classified by the Unified Soil Classification System (USCS) as CL, SM and ML. They will then be called CL-Soil, SM-Soil and ML-Soil, respectively throughout this paper. Engineering properties and porous properties of the soil samples are tabulated and shown in Table 1. The porous properties were evaluated by adsorption of nitrogen gas (N_2) at -196 ^{o}C. The specific surface area was calculated by Brunauer-Emmett-Teller (BET) equation. Figs.1 to 3 graphically show the SEM photographs of CL-Soil, SM-Soil and ML-Soil, respectively. As shown in Figs 1 to 3, it can be seen that the surface of soil particles are almost rough.

Table 1 Engineering properties of soil

Soil	CL-Soil	SM-Soil	ML-Soil
Specific gravity	2.64	2.60	2.67
Optimum moisture content (OMC), %	19.81	12.74	18.48
Maximum dry unit weight (γ_d), kN/m^3	15.70	18.34	15.60
Coefficient of permeability (k), cm/s	0.59 x10^{-6}	4.9 x10^{-6}	8.6 x10^{-6}
Specific surface area (S_{BET}), m^2/g	74	6	15
Micropore volume (V_{DR}), cm^3/g	0.029	0.002	0.006
Total pore volume (V_T), cm^3/g	0.11	0.03	0.05
Average pore diameter (D_P), nm	6	17	12

2.2 Additional Materials

The additional materials used to mix with soil for improve the adsorption capacity in this study were rice husk ash, lime and clay. Rice husk ash and clay were taken from the local brick manufacturing plant and from Roi-Et Green Power Plant, respectively. The lime or calcium oxide (CaO) was bought from a construction material shop. All of the additional material were dry at a temperature of 110 ^{o}C and were then sieved through sieve No. 16. Figs.4 to 6 show the SEM photographs of rice husk ash, lime and clay, respectively.

2.3 Heavy Metal Solutions

Heavy metals chosen as the adsorbed materials in this study were Cu, Ni and Zn. They were prepared by dissolving Copper Nitrate ($Cu(No_3)_2$), Nickel Nitrate ($Ni(No_3)_2$) and Zinc Nitrate ($Zn(No_3)_2$) in distilled water. The solutions were varied with concentrations of 5, 25, 50, 100, 250 and 500 mg/L.

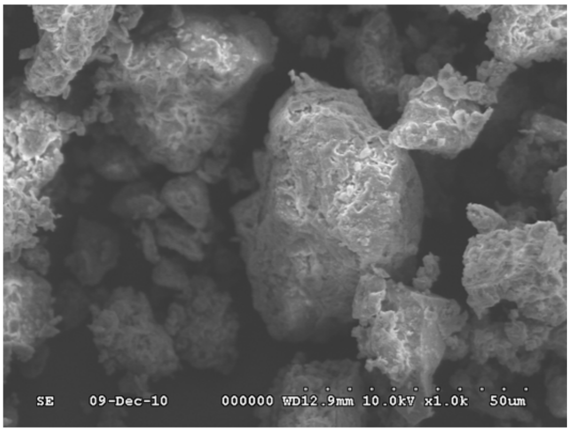

Fig.1 SEM photograph of CL-Soil

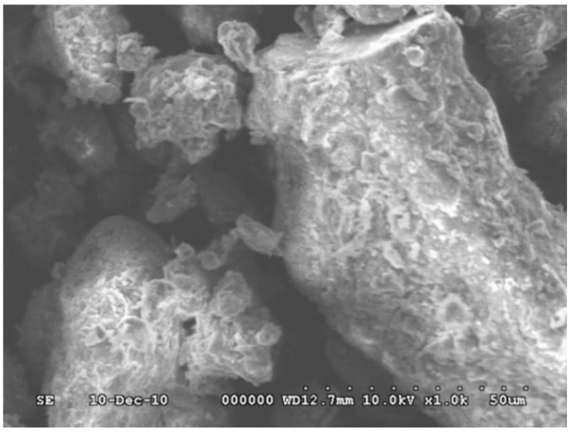

Fig.2 SEM photograph of SM-Soil

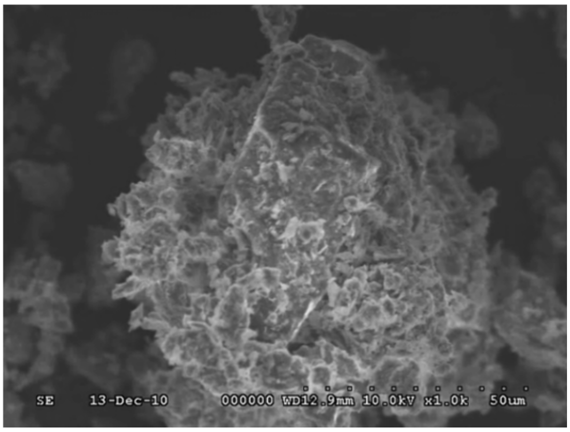

Fig.3 SEM photograph of ML-Soil

2.4 Experimental work

In this study, batch adsorption test was carried out to investigate the heavy metal adsorption. The test processes can be performed by mixing a 2.5 g of soil with the Cu, Ni and Zn solutions. The initial concentrations were ranged from 5 to 500 mg/L and put it in 120 mL plastic bottle. Then the mixture was shaken by the horizontal shaker with a speed of 130 cycles per minute for 0.5, 1, 3, 6, 12, 24, 48, and 72 hours as shown in Fig.7. After a particular period of the time, the soil was separated from the heavy metal solution by using a 0.45μm filter and diluted it into the solution. Finally, concentration of the residual solution was analyzed by using Atomic Adsorption Spectrometer (AAS) (Fig.8). From the step above, it can be measured the adsorption equilibrium time and the amount of heavy metal adsorbed by soil at equilibrium time (q). The equilibrium amount of heavy metal can be calculated from the following equation:

$$q = \frac{(C_o - C_{eq})V_{sol}}{M_s} \tag{1}$$

Where q is the adsorption capacity of the soil at equilibrium condition (mg/g), C_o is the initial concentration of heavy metal solution (mg/g), C_{eq} is the equilibrium concentration of the solution (mg/g), V_{sol} is the volume of solution (cm^3), and W is the mass of soil (g). After the adsorption volume was determined, the adsorption isotherm can then be investigated. The adsorption isotherm is the relationship between the concentration of the heavy metal solution at equilibrium condition (C_{eq}) and the equilibrium amount of heavy metal adsorbed by soil (q). In this study, the Langmuir Isotherm Model was used to describe the adsorption isotherm which represented by the following equation:

$$q = \frac{\alpha\beta C_{eq}}{1+\alpha C_{eq}} \tag{2}$$

Where $\propto$ is Langmuir constant related to the energy (L/mg), β is the adsorption capacity (mg/g).

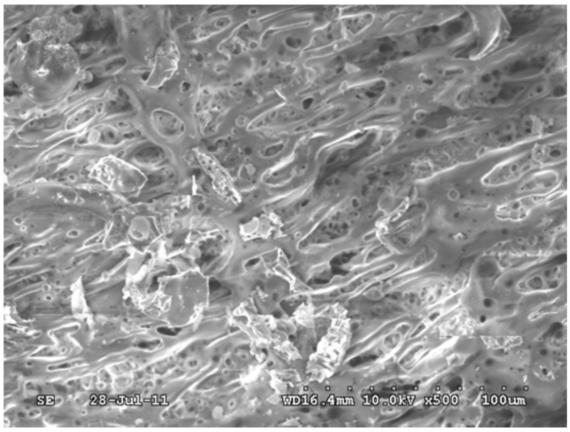

Fig.4 SEM photograph of rice husk ash

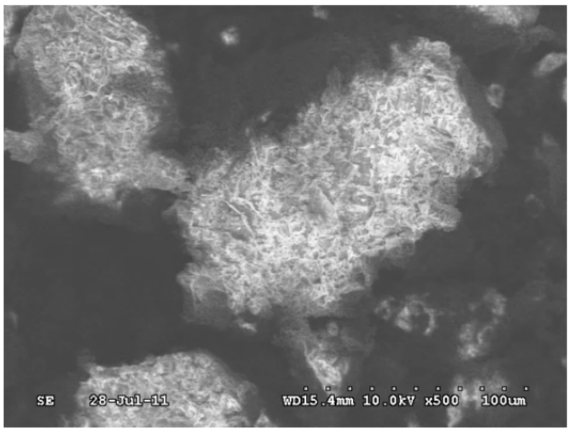

Fig.5 SEM photograph of lime

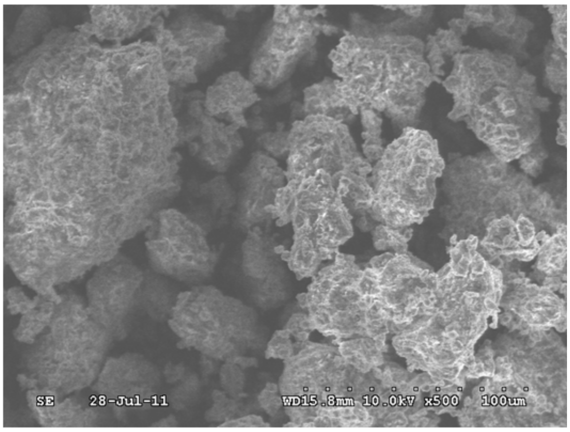

Fig.6 SEM photograph of clay

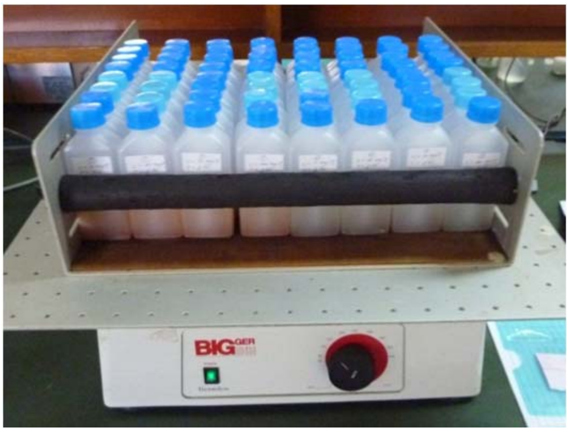

Fig.7 Shaking the mixture of soil and heavy metal solutions

Fig.8 Atomic Adsorption Spectrometer (AAS)

3. RESULT AND DISCUSSION

3.1 Equilibrium time of adsorption

The adsorptions of Cu, Ni and Zn for an initial concentration of 100 mg/L by CL-Soil, SM-Soil and ML-Soil at different time were shown in Figs.9 to 11. The results show the remaining concentration of the heavy metal (C_t) as a function of time. It can be seen that the adsorption took place rapidly at the beginning of the reaction, which the concentration rapidly decreased at the period of 1-3 hours and decline over time until reaching the equilibrium condition within 6-12 hours. The same trend of results was also found when performing the tests with Cu, Ni and Zn for all soils.

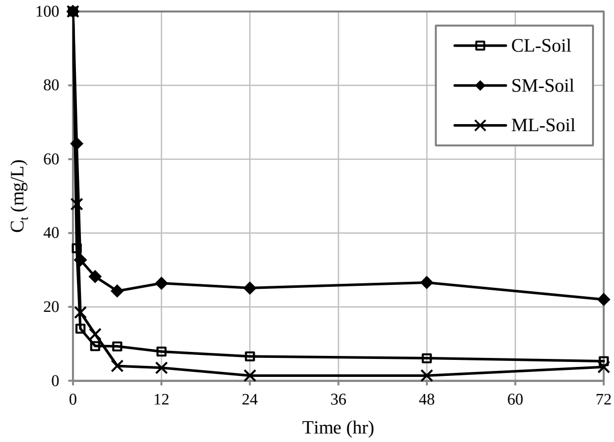

Fig.9 Effect of contact time on Cu adsorption by CL-Soil, SM-Soil and ML-Soil

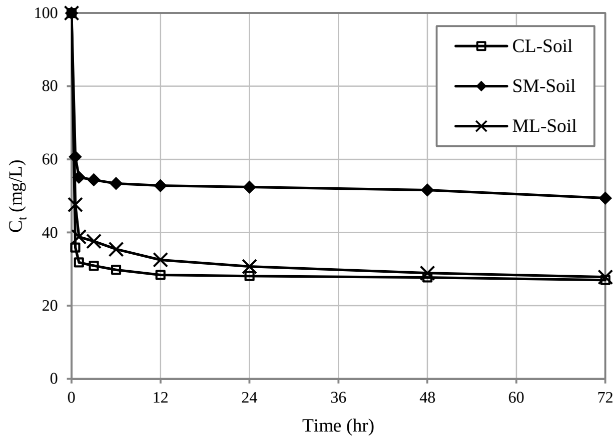

Fig.10 Effect of contact time on Ni adsorption by CL-Soil, SM-Soil and ML-Soil

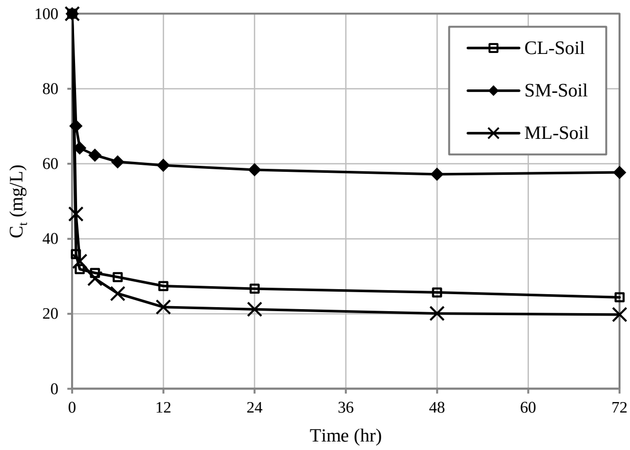

Fig.11 Effect of contact time on Zn adsorption by CL-Soil, SM-Soil and ML-Soil

3.2 Adsorption Isotherm

Figs.12 to 14 showed the adsorption isotherm of Cu, Ni and Zn for different soil samples (CL-Soil, SM-Soil and ML-Soil). As shown in Figs.12 to 14, the amount of adsorption (q) increased with increasing equilibrium concentration (C_{eq}). The adsorption isotherm can be represented by Langmuir adsorption isotherm except the adsorption of Cu by ML-Soil (as showed in Fig. 12). The consistency of the Langmuir isotherm describes that the surface of soils was covered with monolayer of the metal particles [5]. Langmuir parameters (β and α) and the coefficient of correlation (R^2) were then summarized in Table 2. As shown in Table 2, SM-Soil has the lowest adsorption capacity (β) when performing the tests with Cu, Ni and Zn compared to CL-Soil and ML-Soil. This can be explained from the results that SM-Soil has the lowest specific surface and the lowest surface roughness than CL-Soil and ML-Soil (data shown in Table 2 and Figs.1-3). Very high coefficient of correlation (R^2) indicated that the adsorption of Cu, Ni and Zn by all soil samples favorable fit to Langmuir Isotherm. When comparing the adsorption of each heavy metal, it can be seen that the adsorption capacity was in the order of Cu>Ni>Zn.

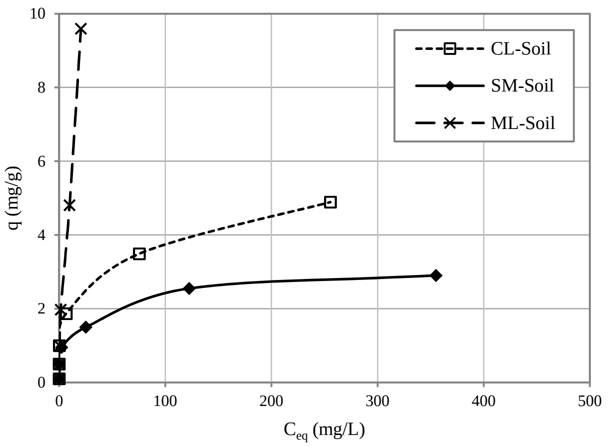

Fig.12 Adsorption isotherm of Cu adsorption by CL-Soil, SM-Soil and ML-Soil

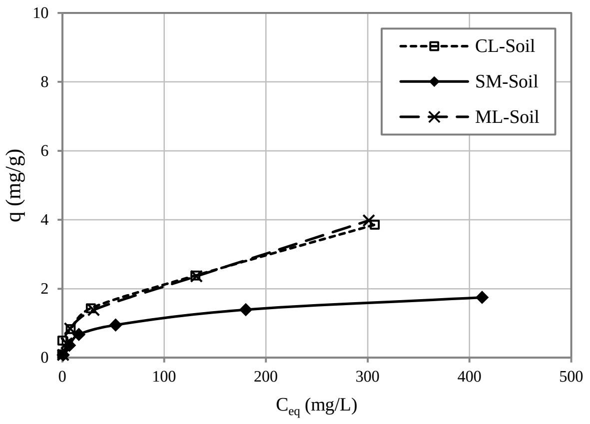

Fig.13 Adsorption isotherm of Ni adsorption by CL-Soil, SM-Soil and ML-Soil

Table 2 Langmuir parameters of soil samples

Solution	Soil	Langmuir Parameters		
		β (mg/g)	α (L/mg)	R^2
Cu	CL-Soil	4.8876	0.1466	0.9858
	SM-Soil	2.9343	0.1161	0.9948
	ML-Soil	1.1723	1.3225	0.8507
Ni	CL-Soil	3.8805	0.0371	0.9310
	SM-Soil	1.8423	0.0296	0.9903
	ML-Soil	4.3048	0.0198	0.9354
Zn	CL-Soil	3.0285	0.0332	0.9855
	SM-Soil	1.2240	0.0610	0.9985
	ML-Soil	2.6323	0.1684	0.9992

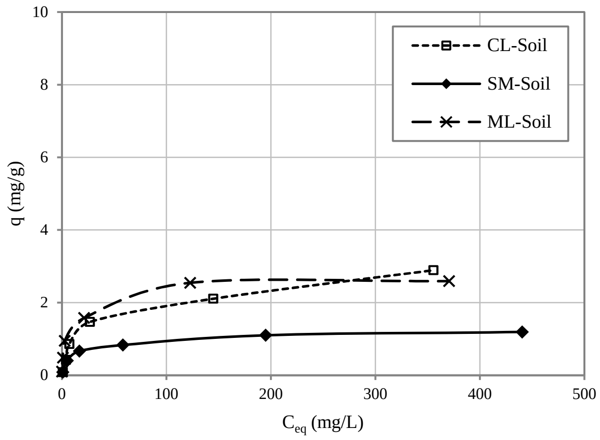

Fig.14 Adsorption isotherm of Zn adsorption by CL-Soil, SM-Soil and ML-Soil

3.3 Effect of the additional material on the adsorption of heavy metals

Because the SM-Soil has the lowest adsorption of heavy metal (as already shown in details in the previous section), this soil was chosen as a representative of all soils to find the method of improvement of the adsorption capacity. The SM-soil was replaced with the rice husk ash, lime and clay at the amount of 0, 20, 40, 60, 80 and 100% by weight. The effects of the three additional materials on the adsorption capacity of Cu, Ni and Zn are presented in Figs.15 to 17, respectively. As presented in Figs.15 to 17, all the additional materials especially lime can dramatically improve the adsorption capacity of heavy metals (q). The adsorption capacity increased with increasing amount of rice husk ash and clay content. While using 20% of lime in the replacement, the results showed the maximum adsorption capacity of Cu and Ni. In case of Zn, the adsorption almost reached the maximum when 40% of lime was used in the replacement. It was possible to conclude that the proper amount of lime which should be used to replace SM-Soil was 20% for increasing the adsorption capacity of Cu and Ni and 40% for adsorption capacity of Zn. The optimum content and the recommended amount of rice husk ash, lime and clay using to mix with SM-Soil are summarized in Table 3. The recommended contents may not be the optimum contents. The optimum contents were the amount of the additional material that provided the maximum adsorption capacity. The recommended contents were evaluated by the consideration both the volume of replacement and the adsorption capacity.

4 CONCLUSION

In this study, the adsorption capacities of Cu, Ni and Zn by three kinds of soil (CL, SM and ML) collected from three different locations in the upper part of Northeastern, Thailand were investigated. Further, the new method was introduced to improve the adsorption capacity of soil by mixing the soil with rice husk ash, lime and clay. The result indicated that the adsorption reaches the equilibrium time within 6-12 hours. The adsorption capacity increased with increasing initial concentration. Langmuir isotherm model can favorable describe the adsorption. The adsorption capacity of all soil was in the order of Cu>Ni>Zn. The SM-Soil provided the lowest adsorption capacity because the specific surface area and roughness were the important factors which affected on the adsorption. From the improvement of the adsorption capacity, rice husk ash, lime, and clay can increase the adsorption capacity of the SM-Soil. Lime showed the highest performance for improvement of Cu and Zn adsorption while the highest performance for improvement of Ni was found by rice husk ash. The recommended contents of lime was 20% by weight of soil in the replacement for adsorption of Cu and Ni and 40% by weight of soil in the replacement for adsorption of Zn. For the rice husk ash, the recommended content was 60% by weight of soil for adsorbing the Ni.

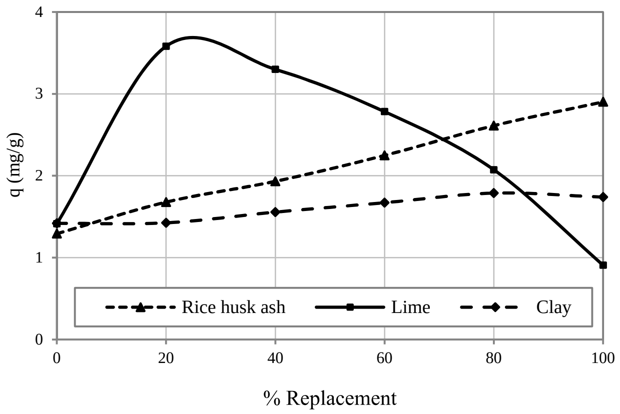

Fig.15 Effect of the additional material on Cu adsorption by SM-Soil

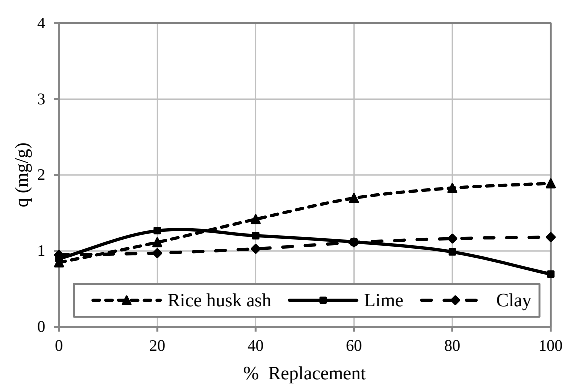

Fig.16 Effect of the additional material on Ni adsorption by SM-Soil0

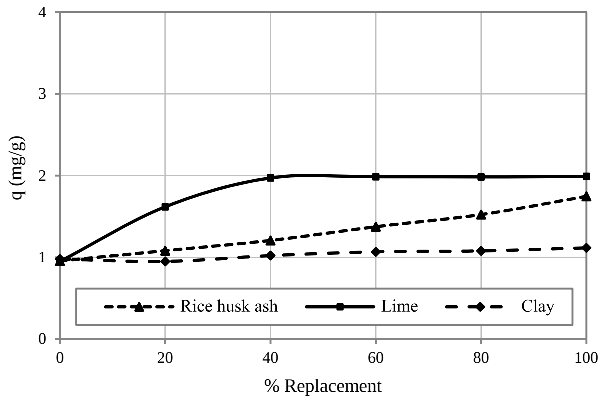

Fig.17 Effect of the additional material on Zn adsorption by SM-Soil

Table 3 The optimum contents and the recommended amounts of rice husk ash, lime, and clay using to mix with SM-Soil

Additional materials	Heavy metals	Optimum content (%)	Increasing of q (%)	Recommended Amount (%)
RHA	Cu	100	225	-
	Ni	100	223	60
	Zn	100	183	-
Lime	Cu	20	253	20
	Ni	20	141	20
	Zn	100	210	40
Clay	Cu	100	126	-
	Ni	100	125	-
	Zn	100	114	-

5 ACKNOWLEDGMENT

This research was funded by Research Center for Environmental and Hazardous Substance Management, Khon Kaen University. The authors wish to acknowledge and grateful thank to Dr. Arthit Neramittagapong, Dr. Yuvarat Ngernyen and Miss Wimonporn Iamamornphonth of the Department of Chemical Engineering, Khon Kaen University.

6 REFERENCES

[1] Mohumed EI Zayat and Edward Smith, "Removal of heavy metals by using activated carbon produced from cotton stalks," Canadian Journal on Environmental, Construction and Civil Engineering, vol. 1, September. 2010, pp. 71-79.

[2] Y. B. Onundi, A. A. Mamun, M. F. Al Khatib and Y. M. Ahmed , "Adsorption of copper, nickel and lead ions from synthetic semiconductor industrial wastewater by palm shell activated carbon," International Journal of Environmental Science and Technology, vol. 7(4), 2010, pp. 751-758.

[3] Souag R, Touaibia D, Benayada B and Boucenna A, "Adsorption of heavy metals (Cd, Zn and Pb) from water using keratin powder prepared from Algerien sheep hoofs," European Journal of Scientific Research, vol. 35, No.3. 2009, pp. 416-425.

[4] Kailas L. Wasewar, "Adsorption of Metals onto Tea Factory Waste: A Review,"IJRRAS, vol. 3(3), June 2010, pp. 303-322.

[5] Tae-Young Kim, Sun-Kyu Park, Sung-Yong Cho, Hwan-Beom Kim, Yong Kang, Sang-Done Kim and Seung-Jai Kim, "Adsorption of heavy metals by brewery biomass," Korean Journal, Chemical Engineerin, vol. 22(1). 2005, pp. 91-98.

First International Conference on Geotechnique, Construction Materials and Environment, Mie, Japan, Nov.21-23, 2011, ISBN: 978-4-9905958-0-7 C3051

The Effect of Temperature on the Sorption Capacity of Copper by Soils

Noppadol Sangiumsak[1] and Pongsakorn Punrattanasin[2]
Department of Civil Engineering, Faculty of Engineering, Khon Kaen University, Thailand
E-mail: g_noppadol@hotmail.com[1], ponpun@kku.ac.th[2]

ABSTRACT: Copper is a common heavy metals which is discharged from various industries. In previous studies, it can be seen that soil is a potential adsorbent to remove heavy metal from waste water. This paper presents the effect of temperature on the sorption capacity of Copper by soils found in the upper part of Northeastern, Thailand. The experiments were done by using batch equilibrium test method. The adsorptions were tested and measured at temperatures between 30 to 50 degrees of Celsius and the initial concentrations of heavy metals are in the range of 100 to 1000 mg/L. The results from the experimental study showed that the adsorption isotherms of the soils can be satisfactorily described by Langmuir model. It is also found that temperature plays an importance role to the sorption capacity of the heavy metals by soils. Higher temperature of heavy metal solutions can make the higher sorption capacity.

Keyword: Adsorption, Heavy metal, Soil, Temperature

1. INTRODUCTION

Rapid growth of industries and municipalities in Thailand has led to increase the environmental problem. A large amount of waste water has been discharged from houses and industries into river or soil without treatment. The waste water often contaminated with toxins. One kind of the toxins is heavy metals. Various industries such as mining, plating, dyeing, and metal processing released the waste water contaminated with heavy metal [1]. The heavy metals may be found in soils, water, sediments and plants [2]. The heavy metals cause damage to the kidney, liver, reproductive system [3] and nervous system [4]. There are many methods for remove the heavy metals from the waste water such as a reduction process, magnetic ferrites treatment, ion exchange, reverse osmosis, chemical oxidation, membrane separation, coagulation, flotation, filtration, evaporation etc. [5,6,7]. Adsorption is one of the most common methods for heavy metal removal because it is an effective and economical technique. Many studies demonstrated that soil is a potential adsorbent to remove heavy metal from waste water [8,9,10,11].

The objective of this study is to investigate the effects of temperature on the adsorption capacity of Cu by soil found in the upper part of Northeastern, Thailand. The adsorptions were done at temperatures ranging from 30 ^{o}C to 50 ^{o}C.

2. MATERIALS AND METHODS

2.1 Adsorbent

Four soil samples collected from different locations in the upper part of Northeastern, Thailand were used as the adsorbent. They were excavated at different depths ranging from 20-50 cm from soil surface. The soils were dried in the oven at a temperature of 110 ^{o}C for 48 hours and then were sieved through sieve No.16. The results from sieve analysis and Atterberg limits test demonstrated that the soil samples can be classified as CL, ML, SM and SM-SC by the Unified Soil Classification System (USCS). They will be named according to their kind throughout this paper as CL-Soil, ML-Soil, SM-Soil and SM-SC-Soil, respectively. Engineering properties and porous properties of the soil samples are tabulated and shown in Table 1. The porous properties were evaluated by adsorption of nitrogen gas (N_2) at -196 ^{o}C. The specific surface area was calculated by Brunauer-Emmett-Teller (BET) equation. Figs.1 to 4 graphically show the SEM photographs of CL-Soil, ML-Soil, SM-Soil and SM-SC-Soil, respectively. As shown in Figs 1 to 4, it can be seen that the surface of all soil particles are almost rough.

Table1 Characteristics of soil samples

Characteristics	CL-Soil	ML-Soil	SM-Soil	SM-SC-Soil
Specific gravity	2.64	2.67	2.66	2.62
Coefficient of permeability (k), cm/s	0.59 $\times10^{-6}$	8.6 $\times10^{-6}$	9.6 $\times10^{-6}$	14.9 $\times10^{-6}$
Specific surface area (S_{BET}), m^2/g	74	15	103	54
Micropore volume (V_{DR}), cm^3/g	0.029	0.006	0.040	0.021
Total pore volume (V_T), cm^3/g	0.11	0.05	0.21	0.11
Average pore diameter (D_P), nm	6	12	8	8

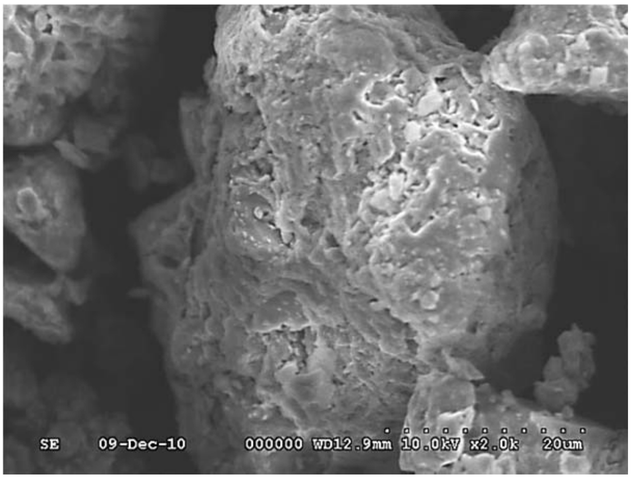

Fig.1 SEM photograph of CL-Soil

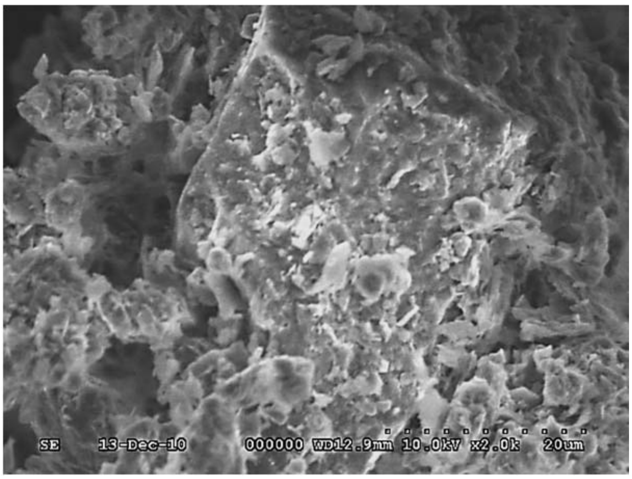

Fig.2 SEM photograph of ML-Soil

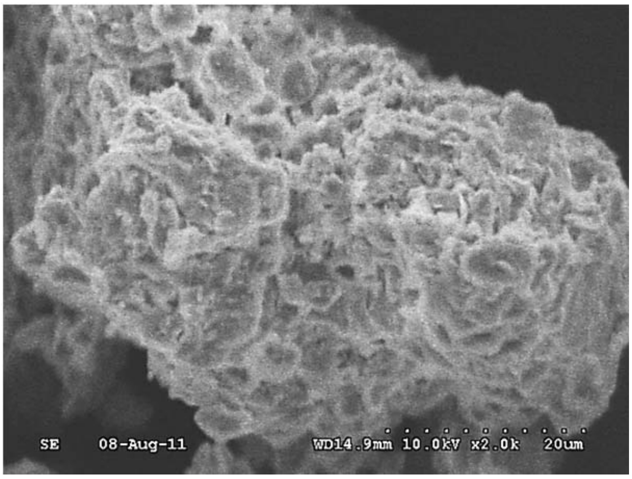

Fig.3 SEM photograph of SM-Soil

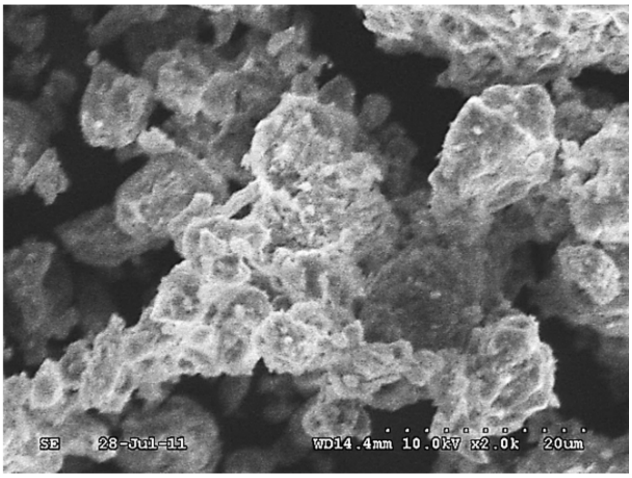

Fig.4 SEM photograph SM-SC-Soil

2.2 Heavy Metal Solutions

Cu is one kind of the most heavy metals, which generally found in the discharged wastewater from industries and houses. It was then chosen as the adsorbed materials in this study. The solution of Cu was prepared by dissolving copper nitrates ($Cu(NO_3)_2$) in distilled water. The concentration of Cu solution was varied with concentrations of 100, 250, 500 and 1000 mg/L. The properties of copper nitrates used are summarized in Table 2.

Table 2 Properties of copper nitrate

Properties	Copper Nitrate
Formula	$Cu(NO_3)_2$
Molecular weight (g/mol)	295.65
Density (g/cm^3)	2.07
Solubility (g/100ml)	137.8

2.3 Experimental work

In this study, the adsorption of Cu with respect to contact time, initial concentration and temperature was experimentally investigated. The test process can be done by mixing a 2.5 g of soil with Cu solution. The initial concentrations are ranged between 100 to 1000 mg/L. The temperature of the mixtures was controlled at 30 ^oC , 40 ^oC and 50 ^oC by putting in the water bath as shown in Fig. 5. The contact times were from 1 to 48 hours. After a particular period of the time, the soils were separated from the Cu solution by using a 0.45μm filter and the solution were then diluted to limit a concentration not exceed 5 mg/L. Finally, concentration of the residual solution was analyzed by using Atomic Adsorption Spectrometer (AAS) (Fig.6). From the step above, it can be measured the adsorption equilibrium time and the amount of heavy metal adsorbed at equilibrium time. The amount of heavy metal adsorbed can be calculated from the following equation:

$$q = \frac{(C_o - C_{eq})V_{sol}}{M_s} \qquad (1)$$

Where q is the adsorption capacity of the soil at equilibrium condition (mg/g), C_o is the initial concentration of heavy metal solution (mg/g), C_{eq} is the equilibrium concentration of the solution (mg/g), V_{sol} is the volume of solution (cm^3), and M is the mass of soil (g).

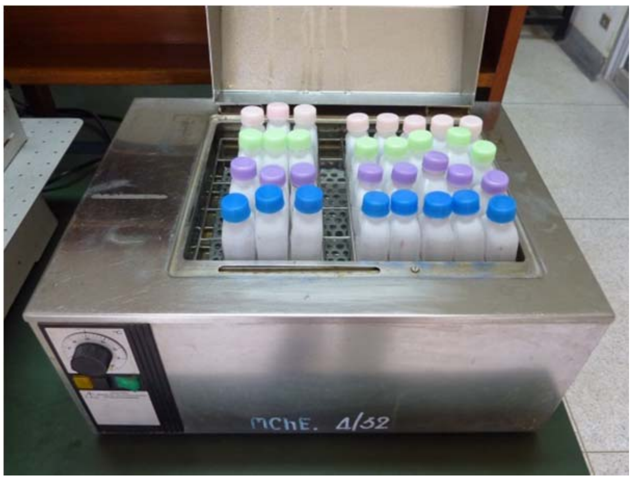

Fig.5 Temperature control of the adsorption

Fig.6 Atomic Adsorption Spectrometer (AAS)

After the adsorption volume was determined, adsorption isotherm was investigated. The adsorption isotherm is the relationship between the concentration of the heavy metal solution at equilibrium condition (C_{eq}) and the equilibrium amount of heavy metal adsorbed by soil (q). In this study, the Langmuir isotherm model was used to describe the adsorption isotherm which represented by the following equation:

$$q = \frac{\alpha \beta C_{eq}}{1 + \alpha C_{eq}} \qquad (2)$$

Where α is Langmuir constant related to the energy (L/mg), β is the adsorption capacity (mg/g)

3. RESULT AND DISCUSSION

3.1 Equilibrium time of adsorption

The adsorptions of Cu at different times and different temperatures for an initial concentration of 500 mg/L by CL-Soil, ML-Soil, SM-Soil and SM-SC-Soil were shown in Figs.7 to 10, respectively. The Figures show the remaining concentration of the heavy metal (C_t) as a function of time. It can be seen that the adsorption occurred rapidly at the time of 1 to 3 hours. The adsorption rate gradually decreased and eventually reached the equilibrium. It can be said that the adsorptions reached equilibrium within 6 hours for CL-Soil and SM-SC-Soil and within 24 hours for SM-Soil. For ML-Soil, it seems that the adsorption still increased after 48 hours. It was found that the temperature greatly affected on the adsorption of Cu by all soil. The adsorption increased with increasing temperature. However, it can be observed that the equilibrium times did not depend on temperatures.

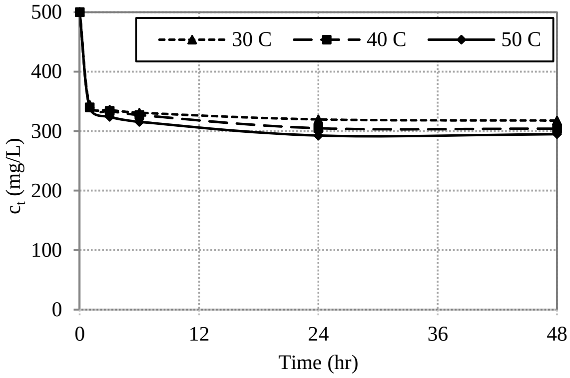

Fig.7 Adsorption of Cu by CL-Soil at different temperatures

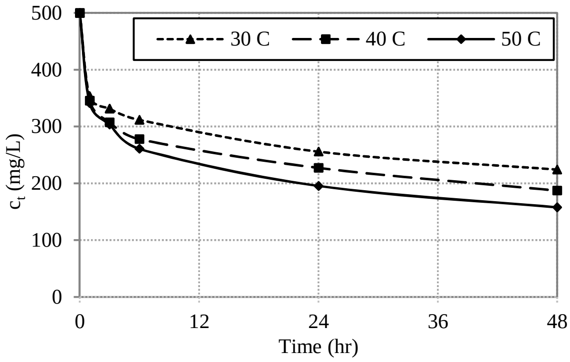

Fig.8 Adsorption of Cu by ML-Soil at different temperatures

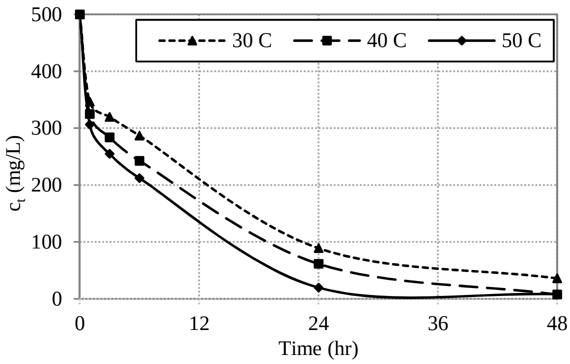

Fig.9 Adsorption of Cu by SM-Soil at different temperatures

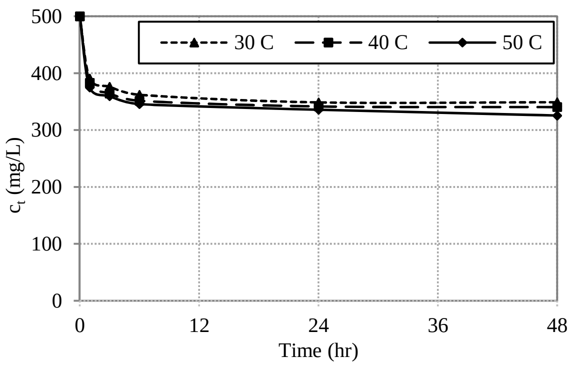

Fig.10 Adsorption of Cu by SM-SC-Soil at different temperatures

3.2 Adsorption isotherm

Figs.11 to 14 show the adsorption isotherm of Cu for CL-Soil, ML-Soil, SM-Soil and SM-SC-Soil, respectively. As shown in Figs.11 to 14, the adsorption capacity (q) increased with increasing equilibrium concentration (C_{eq}). For CL-Soil, ML-Soil and SM-SC-Soil, the increasing rate of q gradually decreased and converged to the maximum value. In next step, the relationships of C_{eq} versus C_{eq}/q were plotted as shown in Figs.15 to 18 to determine the values of α and β. The values of α and β can be determined from the slope and interception (β =1 /slope, $\alpha = 1/c\beta$ where c = interception). It can be found that the adsorption isotherm of CL-Soil, ML-Soil and SM-SC-Soil soils can be represented by Langmuir Adsorption Isotherm. The consistency of the Langmuir Isotherm describes that the surface of soils was covered with monolayer of the metal particles [1]. SM-Soil show different character of the adsorption isotherm. The increasing rate of q with respect to C_{eq} of SM-Soil negligible decreased so that Freundlich Isotherm is more proper than Langmuir Isotherm in describing the adsorption of SM-Soil. Langmuir parameters (β and α) and the coefficient of correlation (R^2) were summarized in Table 3. The last column of Table 3 shows the increasing value of β when the temperature increased from 30°C to 40°C and 50°C. The improvement can be calculated from the following equation:

$$\text{\% Increasing of } \beta = \frac{(\beta_T - \beta_{30})}{\beta_{30}} x100 \qquad (3)$$

Where β_T and β_{30} are the β values at temperature T and at temperature of 30 °C, respectively. The temperature of 30 °C is the representative normal temperature in the Northeastern, Thailand. As shown in Table 3, the adsorption capacity (β) significantly increased with increasing temperature. The effect of temperature occurred with ML-Soil and SM-SC-Soil. It can be found that the increasing of β can reach up to 25.6% when the temperature increased from 30°C to 50°C. The results of adsorption of CL-Soil, ML-Soil and SM-SC-Soil show a very good result from the high value of R^2. This indicated that the adsorption of Cu by these soils well fit to Langmuir Isotherm Model. Although the adsorption isotherm is not fit to Langmuir Isotherm, it can see from Figs. 9 and 13 that the adsorption of Cu by SM-Soil was still very high.

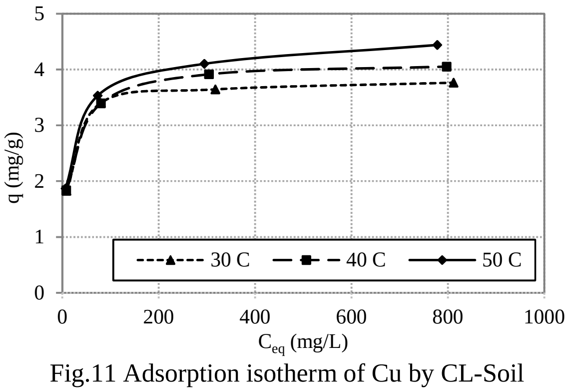

Fig.11 Adsorption isotherm of Cu by CL-Soil at different temperatures

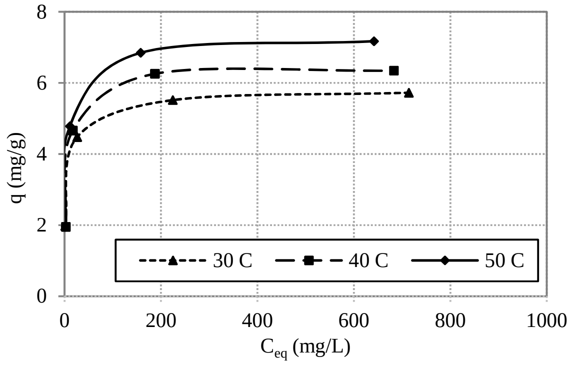

Fig.12 Adsorption isotherm of Cu by ML-Soil at different temperatures

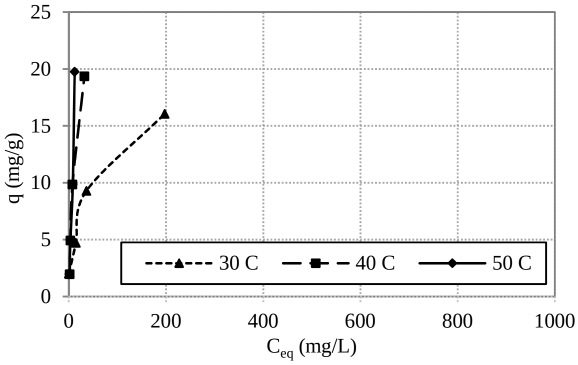

Fig.13 Adsorption isotherm of Cu by SM-Soil at different temperatures

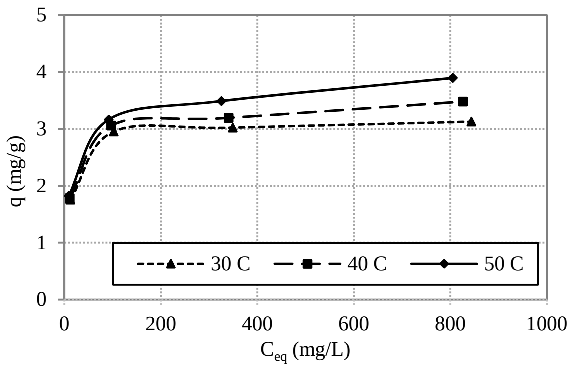

Fig.14 Adsorption isotherm of Cu by SM-SC-Soil at different temperatures

4 CONCLUSION

In this study, the effects of temperature on the adsorption capacity of Cu by four different kinds of soils (CL, ML, SM and SM-SC) found in the upper part of Northeastern, Thailand were investigated. The experiments were done by using batch equilibrium method. The temperature was varied over the range of 30 to 50 °C. The results revealed that the adsorption occurred very rapid at the period of 1 to 3 hours and reach to the equilibrium condition with different times. The equilibrium condition occurred within 6 hours for CL-Soil and SM-SC-Soil and occurred within 24 hours for SM-Soil. The temperature do not affect to the equilibrium time. The adsorption of CL-Soil, ML-Soil and SM-SC-Soil fit to Langmuir Adsorption Isotherm very well. The adsorption capacity significantly increased with increasing temperature. For the ML-Soil and SM-SC-Soil, the adsorption capacity of Cu increased up to 25.6% when the temperature increased from 30°C to 50°C.

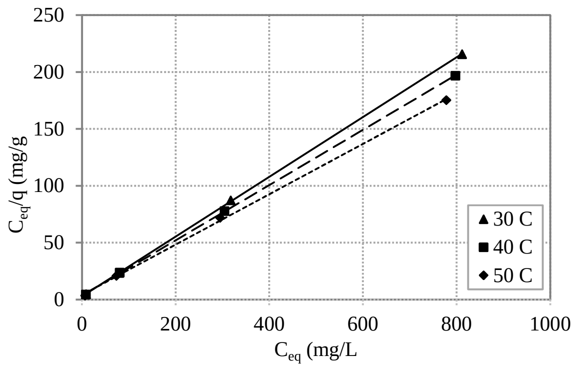

Fig.15 Langmuir Adsorption Isotherm of CL-Soil at different temperatures

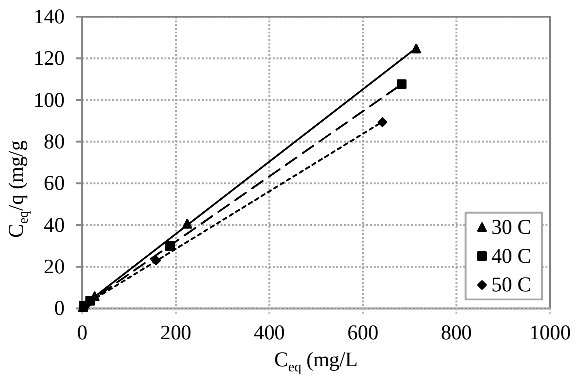

Fig.16 Langmuir Adsorption Isotherm of ML-Soil at different temperatures

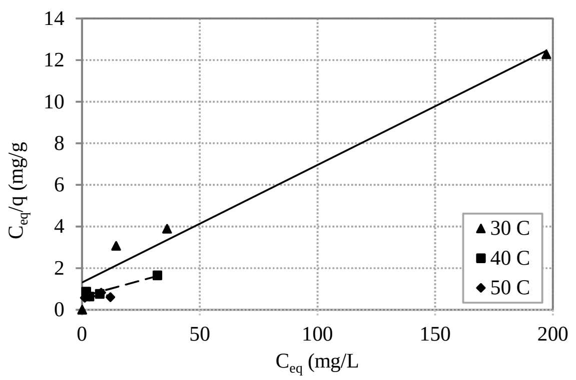

Fig.17 Langmuir Adsorption Isotherm of ML-Soil at different temperatures

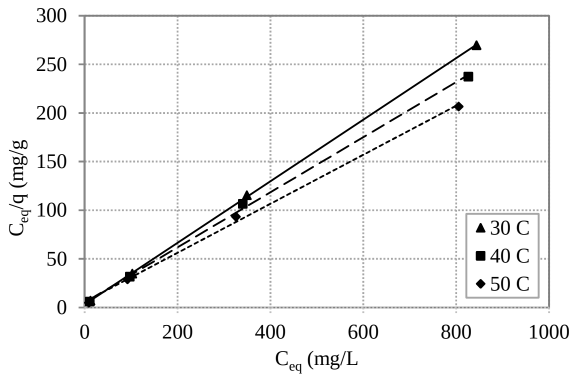

Fig.18 Langmuir Adsorption Isotherm of ML-Soil at different temperatures

Table 3 Summarized of Langmuir parameters of soil samples

Soil	Temp.	Langmuir Parameters			% Increasing of β
		β (mg/g)	α (L/mg)	R^2	
CL	30 °C	3.81	0.09	1.0000	0
	40 °C	4.12	0.07	0.9999	8.2
	50 °C	4.52	0.05	0.9993	18.8
ML	30 °C	5.76	0.16	0.9999	0
	40 °C	6.40	0.18	1.0000	11.0
	50 °C	7.24	0.15	1.0000	25.6
SM	30 °C	17.70	0.04	0.9647	0
	40 °C	32.36	0.05	0.9114	-
	50 °C	144.93	0.01	0.0918	-
SM-SC	30 °C	3.16	0.10	0.9999	0
	40 °C	3.53	0.06	0.9990	11.7
	50 °C	3.97	0.04	0.9982	25.6

5 ACKNOWLEDGMENT

This research was funded by Faculty of Engineering, Khon Kaen University. The authors wish to acknowledge and grateful thank to Dr. Arthit Neramittagapong, Dr. Yuvarat Ngernyen and Miss Wimonporn Iamamornphonth of the Department of Chemical Engineering, Khon Kaen University.

6 REFERENCES

[1] Tae-Young Kim, Sun-Kyu Park, Sung-Yong Cho, Hwan-Beom Kim, Yong Kang, Sang-Done Kim and Seung-Jai Kim, “Adsorption of heavy metals by brewery biomass,” Korean Journal, Chemical Engineering, vol. 22(1). 2005, pp. 91-98.

[2] A. Dube, R. Zbytniewski, T. Kowalkowski, E. Cukrowska, B. Buszewski, “Adsorption and Migration of Heavy Metals in Soil,”Polish Journal of Environmental Studies, vol. 10, No. 1, August 2000, pp. 1-10.

[3] Mohumed EI Zayat and Edward Smith, “Removal of heavy metals by using activated carbon produced from cotton stalks,” Canadian Journal on Environmental, Construction and Civil Engineering, vol. 1, September. 2010, pp. 71-79.

[4] Y. B. Onundi, A. A. Mamun, M. F. Al Khatib and Y. M. Ahmed , “Adsorption of copper, nickel and lead ions from synthetic semiconductor industrial wastewater by palm shell activated carbon,” International Journal of Environmental Science and Technology, vol. 7(4), 2010, pp. 751-758.

[5] Souag R, Touaibia D, Benayada B and Boucenna A, “Adsorption of heavy metals (Cd, Zn and Pb) from water using keratin powder

prepared from Algerien sheep hoofs," European Journal of Scientific Research, vol. 35, No.3. 2009, pp. 416-425.
[6] Kailas L. Wasewar, "Adsorption of Metals onto Tea Factory Waste: A Review,"IJRRAS, vol. 3(3), June 2010, pp. 303-322.
[7] Jihyun Lim, Hee-Man Kang, Lee-Hyung Kim and Seok-Oh Ko, "Removal of Heavy Metals by Sawdust Adsorption: Equilibrium and Kinetic Studies,"Environmental Engineering Research, vol. 13, No.2, March 2008, pp. 79-84.
[8] Saad A. Al-Jlil, "Removal of Heavy Metals from Industrail Wastewater by Adsorption using Local Bentonite Clay and Roasted Date Pits in Saudi Arabia, " Trends in Applied Sciences Research, vol. 5(2), 2010, pp. 138-145.
[9] Islem Chaari, Mounir Medhioub and Fakher Jamoussi, "Use of Clay to Remove Heavy Metals from Jebel Chakir Landfill Leachate,"Journal of Applied Science in Environmental Sanitation, vol. 6, No.2, June 2011, pp. 143-148.
[10] Chuangcham U and Charusiri P, "Adsorption of Heavy Metals from Landfill Leachate in Soil: A Case Study of Kham Bon Landfill, Khon Kaen Province, NE Thailand,"Proceedings of The International Symposia on Geosciences and Environments of Asian Terranes(GREAT 2008), 4^{th} IGCP516 and 5^{th} APSEG,2008, pp. 501-505.
[11] M. Ali Awan, Ishtiaq A. Qazi and Imran Khalid, "Removal of Heavy Metals through Adsorption Using Sand,"Journal of Environmental Sciences, vol. 15, No.3, 2003, pp. 413-416.

First International Conference on Geotechnique, Construction Materials and Environment, Mie, Japan, Nov.21-23, 2011, ISBN: 978-4-9905958-0-7 C3051

Experimental Investigation for Nitrate Reduction Using Iron Powder in Porous Media

Shimada H, Inoue K, Ihara I, Suzuki K and Tanaka T, Graduate School of Agricultural Science, Kobe University

ABSTRACT: This paper assessed the potential of iron powder as a nitrate reduction and retardation material in porous media. Under saturated and unsaturated flow conditions, column experiments were conducted in silica sand with a mixture of two kinds of iron powders. Experimental breakthrough curves were analyzed using temporal moments not only to estimate the retardation factor and the degradation rate but to quantify mass recovery fractions associated with nitrate and ammonium ions. The results showed the increase of the amount of iron powder resulted in the increase of the degradation rates and the retardation factor estimates. Moreover, the production of ammonium occurred by nitrate reduction was confirmed. A mixture of iron powder with soil has a potential to reduce the concentration of nitrate by the reduction of nitrate to ammonium and to retard a nitrate.

Keywords: Nitrate, Reduction, Iron Powder, Column Experiments

1. INTRODUCTION

Excessive nitrate concentrations in groundwater are related to land use activities including pastoral farming market gardening, application and leaching of nitrogenous fertilizers and industrial and sewage waste disposal [1]. Overloading agricultural soils with nitrogen leads to rising nitrate concentration in groundwater, while enhancing crop growth by the application of nitrogen gives economic benefits in many parts of the world. Protection of groundwater from nitrate contamination is an often overlooked health concern. The immediate health concern is the reduction of nitrate to nitrite in the digestive tract by nitrate-reducing bacteria. Nitrite is readily absorbed into the blood where it combines with the hemoglobin that carries oxygen, leading to the form of methemoglobin, which is unable to transport oxygen, and the physical stress. When severe enough, nitrate poisoning is life threatening because of suffocation, which is called methemoglobinemia, or blue baby syndrome, in infants [2],[3]. Nitrate released to the environment can also increase eutrophication levels in rivers or lakes.

In general, nitrate can readily be transported beneath the soil zone without ion exchange or adsorption to soil surface. Therefore, high concentration of nitrates can be found in shallow groundwater systems, especially in sandy aquifers [4],[5]. There has been developed many processes for removing nitrate from water, including biological denitrification, separation with ion exchange or reverse osmosis and reduction by chemical reductants [6]. However, almost all treatment processes are performed after groundwater extraction by wells or drains, which is the primary technology to treat contaminated groundwater [7], and have a markedly different property from the reduction of nitrate concentrations at a source in a contaminated site. In addition, at a vast contaminated site groundwater extraction might be ineffective [8]. This ineffectiveness has been led to the development of alternative and unique approaches towards groundwater cleanup [9]-[11].

At present, reduction of nitrate using zero-valent iron (Fe^0 or ZVI) is a highly exergonic reaction and is expected to be an alternative for nitrate removal from water [6]. ZVI has been used to remediate contaminated groundwaters by placing large quantities of granular metal to act as a permeable barrier [12]. Although nitrate reduction using ZVI is a rapid reaction if the solution pH remains within an acidic range [13], the formation of passivating scales on the ZVI over time may limit its long-term reduction potential since nitrate reduction by ZVI is a corrosive process. Previous work has demonstrated the ability for ZVI to reduce nitrate in batch experiments, with nearly stoichiometric recovery of nitrogen as ammonium [14],[15]. However, only a few studies have been reported the reduction of nitrate and in column experiments [16].

The present work is aiming to evaluate the reduction of nitrate and nitrate transformation to ammonium ions by ZVI in columns where a sandy soil is homogeneously mixed with ZVI and to quantify the retardation of nitrate onto soil and/or ZVI surfaces. Temporal moment approaches are applied to estimate the retardation factor and the degradation constant based on the experimental breakthrough curves (BTCs) in columns. Specifically, the effect of the weight ratio of ZVI to sandy soils on the degree of the retardation and degradation of nitrate is of concern to explore the possible use of ZVI in a field.

2. MATERIALS AND METHODS

2.1 Materials

For column experiments, silica sand with a low uniformity coefficient of 1.25 was selected in order to simulate a sandy aquifer having a relatively high hydraulic conductivity. Silica sand of interest has 0.050 cm and 2.68 g/cm^3 of physical properties such as the mean particle size and the particle density, respectively. A ZVI powder in hand warmer and a commercial ZVI powder with a high reduction property were used to compare the degree of nitrate reduction and retardation and were referred to as Material 1 and Material 2, respectively.

2.2 Column experiments

In column experiments, ZVI powder of concern was mixed with soil in order to examine the relation between the amount

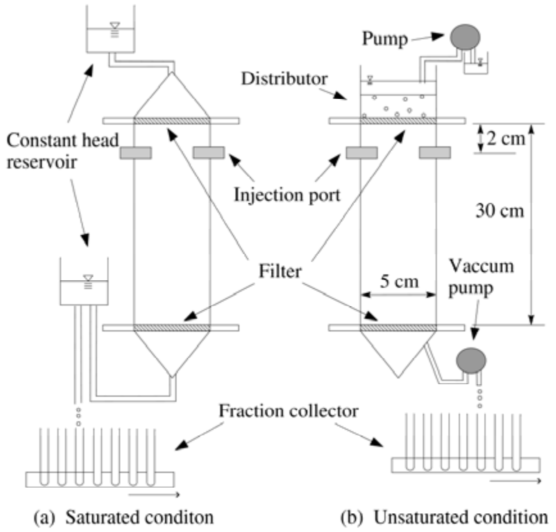

Fig. 1 Schematic diagram of experimental column system

of ZVI powder and the degree of reduction of nitrate. From the practical viewpoint, mixture ratios of ZVI powder were set to 0%, 7.5%, 15% and 30% by weight. These soils with ZVI powder were completely saturated before packing to avoid the entrance of air and were filled into the column, which has 30 cm in length and 5 cm in diameter, in increments of 2.5 cm. Each layer was compacted to adjust the dry density prior to filling the next layer. The porosity can be estimated in each experiment indirectly from the measurements of the particle density and the dry soil bulk density, resulting in approximately 0.41 of the porosity in flow field for both materials. In Fig. 1, the detailed column design is illustrated.

After packing, as shown in Fig. 1(a), water was applied to the column up to a specific level controlled by constant head reservoirs at the top and bottom of the saturated media, while maintaining the saturated condition of porous media. Steady saturated flow field was established in the column when fluctuations in the observed drainage rate from the bottom reservoir became negligible. A volume of 40 cm^3 KNO_3 solution under saturated condition was applied to the top of the column to produce a pulse input with an initial concentration of 1.5×10^{-4} g/cm^3 of NO_3-N. Prescribed solute source condition was designed to clarify the transient concentrations of NO_3-N and to effectively provide the parameter identification relevant to solute transport using temporal moment approaches, which will be stated in the following subsection. Pore water samples at the end of the column were taken at specific intervals using a fraction collector. Nitrate ion in the pore water samples was analyzed by capillary electrophoresis (G1600A, Agilent technologies, USA). The basic anion buffer and a fused silica capillary with 104 cm in length and 50 μm internal diameter were obtained from Agilent technologies. The temperature controlled cartridge for fused silica was set at 15 °C. The concentration of ammonium ion was determined by the indophenol blue method using a spectrophotometer (HACH, DR-4000).

To investigate the impact of water content on the nitrate behavior, column experiments under unsaturated conditions were carried out in a similar manner but a different pulse volume of 20 cm^3. As shown in Fig. 1(b) in unsaturated experiments, instead of constant head reservoir, suction was applied at the bottom of the column to keep the moisture content inside the column uniform while water was sprinkled over the top of the medium until the outflow from the bottom of the column equaled the volume of the water input. Prior to an application of solute pulse, samples were adjusted to steady state water flow condition.

2.3 Temporal moment analysis

Consider a sorbing and degradable chemical moving through a homogeneous medium at a steady, uniform, flow rate. Assuming linear, equilibrium sorption and first-order kinetic degradation for the solute, the governing transport equation can be written as

$$R\frac{\partial c}{\partial t} = \alpha_L v_p \frac{\partial^2 c}{\partial x^2} - v_p \frac{\partial c}{\partial x} - \lambda c \tag{1}$$

where c is the concentration of solute, x is the coordinate, t is the time, R is the retardation factor estimate, v_p is the average pore water velocity, α_L is the dispersivity, and λ is the degradation rate [17].

Temporal moment analysis is convenient to use, as there is no need to solve the transport model in real time and degrees of spreading and asymmetry [18]. The n-th order temporal moments are defined as

$$M_n = \int_0^\infty t^n c(x,t)dt \tag{2}$$

The nomalized temporal moments μ_n at a location x, are defined as

$$\mu_n = \frac{M_n}{M_0} = \frac{\int_0^\infty t^n c(x,t)dt}{\int_0^\infty c(x,t)dt} \tag{3}$$

Equations (2) and (3) are used to obtain experimental temporal moments from concentration BTCs. Das and Kluitenberg [17] derived theoretical first temporal moment using Laplace formation of Eq. (1). By setting the experimentally determined moments equal to the theoretical moments, we can estimate the dispersivity and the retardation factor [19].

$$\alpha_L = \frac{\xi_p}{2}\frac{\mu_2}{\mu_1^2} \tag{4}$$

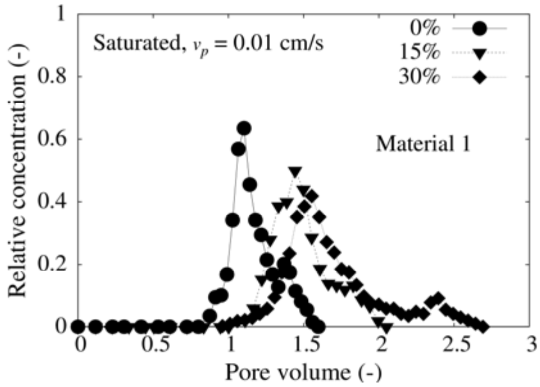

Fig. 2 Representative BTCs for different mixture ratios of ZVI powder in hand warmer under saturated condition

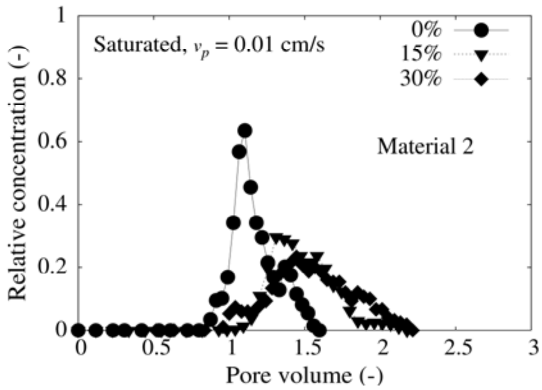

Fig. 3 Representative BTCs for different mixture ratios of commercial ZVI powder under saturated condition

$$R = \frac{(\mu_1 - 0.5t_0)\sqrt{v_p^2 + 4\alpha_L v_p \lambda}}{x} \quad (5)$$

where ξ_p is the distance between the source and the observation location and t_0 is the pulse duration. In all experiments, t_0 was set to 30 seconds.

The mass fraction of solute that is collected in the effluent during column experiment is summed up to provide an estimate of the mass recovery fraction (MRF) [17].

$$\mathrm{MRF} = \frac{\int_0^\infty Q(L,t)c(L,t)dt}{\int_0^\infty Q(0,t)c(0,t)dt} \quad (6)$$

where Q is the volumetric flow rates and L is the length of the soil column. MRF allows to obtain the degradation rate [17].

$$\lambda = \frac{1}{\mu_1}\ln\left(\frac{1}{\mathrm{MRF}}\right) \quad (7)$$

3 RESULTS AND DISCUSSION

3.1 Effect of ZVI powder on nitrate retardation

Representative BTCs under different mixture ratios of ZVI powder as a function of pore volume for Materials 1 and 2 are shown in Fig. 2 and Fig. 3, respectively. Pore volume is calculated as

$$\text{Pore volume} = \frac{q_w t}{\theta L} = \frac{v_p t}{L} \quad (8)$$

where q_w is the water flux and θ is the volumetric water content. When solutes travel without the adsorption onto the soil particle, or the retardation, the pore volume becomes the unity and increases with the increase of the degree of retardation.

As shown in Fig. 2 and Fig. 3, observed BTCs exhibit the shift of the peak concentration at the corresponding pore volume toward a larger pore volume with the increase of the amount of ZVI powder. A slight tailing of the BTCs can also be seen in Fig. 2 and Fig. 3, except for the case of 0% of the mixture ratio. These results imply that the influence of a mixture of ZVI powder and soil, in a practical situation, degradation of nitrate concentration is expected due to the reaction of nitrate with ZVI powder as a travel time of nitrate from ground surface to groundwater becomes longer. Thus, for the purpose of the retardation and the reduction of nitrate, the use of ZVI powder might be effective in soils.

In order to quantify the degree of adsorption of nitrate onto ZVI powder, the retardation factor is employed as a measure and is estimated based on Eq. (5). The relation between the mixture ratio of ZVI powder and the retardation factor estimates for Materials 1 and 2 are shown in Fig. 4 and Fig. 5, respectively. The retardation factor estimates tend to increase with increasing the percentage of ZVI powder and are within the range of approximately 1.3 to 1.6 under saturated condition. It is indicated that the opportunity of adsorption of nitrate to ZVI powder increases as the amount of ZVI powder becomes larger. On the other hand, under unsaturated condition, the retardation factor estimates range from approximately 1.0 up to 1.2, indicating that the degree of adsorption under unsaturated condition is lower than that under saturated condition. This is because a less water content and a higher pore velocity may lead to decrease the course of transport under unsaturated condition in comparison with solute pathways under saturated condition.

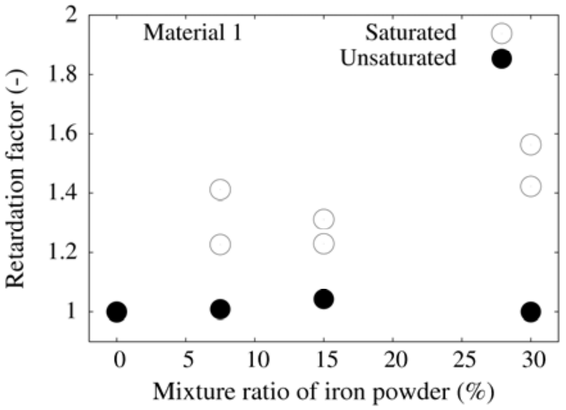

Fig. 4 Relation between the mixture rario of ZVI powder in hand warmer and the retardation factor estimates

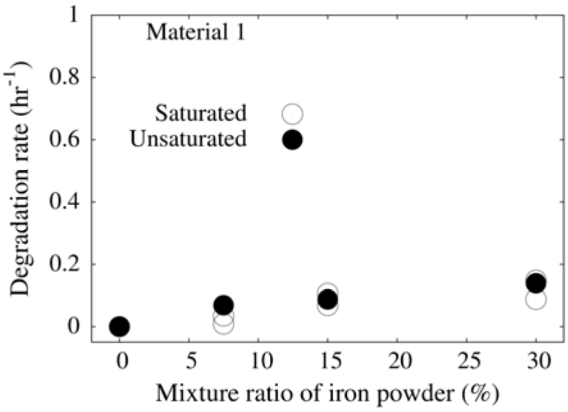

Fig. 6 Relation between the mixture rario of ZVI powder in hand warmer and the degradation rate

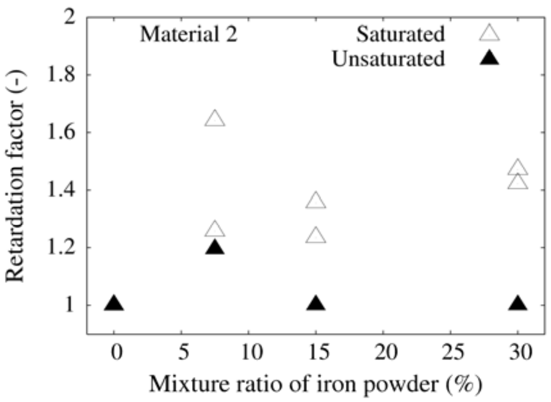

Fig. 5 Relation between the mixture rario of commercial ZVI powder and the retardation factor estimates

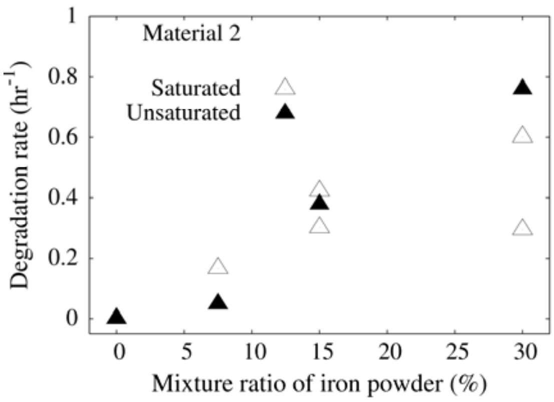

Fig. 7 Relation between the mixture rario of commercial ZVI powder and the degradation rate

The values of retardation factor between two kinds of ZVI powder, as seen in Fig. 4 and Fig. 5, vary with a similar tendency. In addition, the retardation factor estimates for both materials are almost the same values corresponding to the same mixture ratio of ZVI powder. These results show that there is no difference in the degree of adsorption between two materials.

3.2 Effect of ZVI powder on nitrate reduction

To quantify the effect of ZVI powder on nitrate reduction during a transport, degradation rate estimates are plotted as a function of mixture ratio of ZVI powder for Materials 1 and 2 in Fig. 6 and Fig. 7, respectively. Regardless of water content, the degradation rate increases as the amount of ZVI powder increases for both materials, suggesting that the increase of the amount of ZVI powder is expected to contribute nitrate reduction. As stated in the preceding section, under saturated condition, the opportunity of adsorption of nitrate to ZVI powder increases with increasing the amount of ZVI powders and may enhance the nitrate reduction in the duration occurring adsorption phenomena. On the contrary to this, as seen in Fig. 4 and Fig. 5, retardation factor estimates are little change in the range of approximately 1.0 to 1.2 regardless of the mixture ratio of ZVI powder under unsaturated condition. However, the degradation rates exhibit a little difference between saturated and unsaturated conditions at the same amount of ZVI powder as seen in Fig. 6 and Fig. 7. This may attribute to the presence of air under unsaturated condition, enhancing a prompt oxidation of ZVI powder, since corrosion process may induce the nitrate reduction [15].

As for the case of Material 1, the degradation rate estimates are in the range of approximately 0.09 hr^{-1} to 0.15 hr^{-1} in Fig. 6, when pH ranges from 7 to 9 in this study. The results are in good agreement with a previous study. Alowitz and Scherer [9] reported the degradation rate of approximately 0.13 hr^{-1} at pH 8. In the comparison with two kinds of ZVI powder, although the retardation factor estimates have similar values, the degradation rates hinge on the material of interest. In the case of Material 2 as shown in Fig. 7, the estimate of degradation rate at 7.5% of the mixture ratio is about 2 times larger than that of Material 1 in Fig. 6. At 30% of the mixture ratio, the degradation rate of Material 2 becomes about 4 times larger than that of Material 1. These results show that

Table 1 MRF by mixture ratio of ZVI powder

Nitrogen species	Condition of water content	Mixture ratio of ZVI powder (%)						
			Material 1			Material 2		
		0	7.5	15	30	7.5	15	30
NO_3-N	Saturated	1.000	0.976	0.924	0.930	0.939	0.853	0.795
NH_4-N	Saturated	0.000	0.003	0.000	0.005	0.038	0.044	0.090
NO_3-N	Unsaturated	1.000	0.990	0.985	0.978	0.992	0.951	0.893
NH_4-N	Unsaturated	0.000	0.003	0.009	0.000	0.010	0.048	0.109

commercial ZVI powder is more effective than ZVI powder in hand warmer from the point of view of nitrate reduction.

3.3 Mass recovery fraction

In the process of nitrate reduction, the product of ammonium and relevant mass recovery are of important. Table 1 lists the MRFs for different mixture ratios of ZVI powder estimated from Eq. (6) in order to compare the total amount of NO_3-N leaching from the bottom of the column with the total amount of NH_4-N yielded by NO_3-N reduction. The reaction of nitrate reduction can be described by Eq. (9) [16].

$$NO_3^- + 10H^+ + 4Fe^0 \rightarrow NH_4^+ + 3H_2O + 4Fe^{2+} \qquad (9)$$

As seen in Table 1, the MRF of NO_3-N decreases with the increase of the mixture ratio of ZVI powder, resulting in the increase of the MRF of NH_4-N, particularly in Material 2. Interestingly, the loss of NO_3-N does not necessarily correspond to the production of NH_4-N, especially in the media mixed with Material 1. It appears that a part of nitrate or ammonium ion may strongly adsorb to ZVI powder and remain in the column, consequently leading to the unbalance of the total MRFs of NO_3-N and NH_4-N.

Moreover, the MRF of NH_4-N of Material 2 is about 10 times larger than that of Material 1 at the same mixture ratio, indicating the property of commercial ZVI powder in terms of nitrate reduction to ammonium. On the contrary to this, nitrate is slightly converted to ammonium by the reaction between nitrate and Material 1. Hence, single application of Material 1 becomes less effective in the nitrate degradation.

3.4 Effect of ZVI powder on dispersivity

The spread of the nitrate in soils is also important in a field application of ZVI powder. The dispersivities of nitrate are also estimated from Eq. (4), and are shown as a function of mixture ratio of ZVI powder for Materials 1 and 2 in Fig. 8 and Fig. 9, respectively. As seen in Fig. 8 and Fig. 9, the longitudinal dispersivities range from approximately 0.16 cm to 0.70 cm and slightly increase with increasing the mixture ratio of ZVI powder because of the influence of the mixture of ZVI powder and soil. The longitudinal dispersivity at maximum mixture ratio of ZVI powder is about 3 times larger than the case without ZVI in porous media. Therefore, the effect of the mixture of ZVI powders in field soils on nitrate dispersion may be relatively lower.

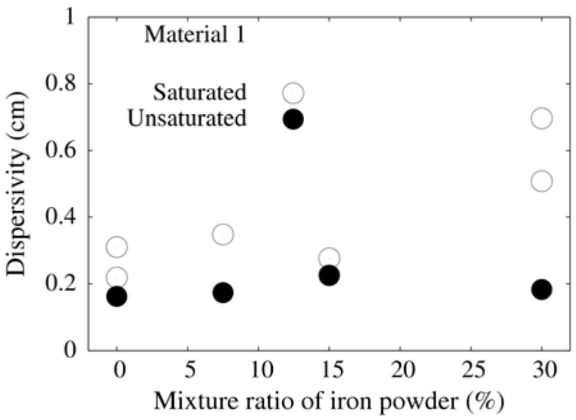

Fig. 8 Relation between the mixture ratio of ZVI powder in hand warmer and the dispersivity

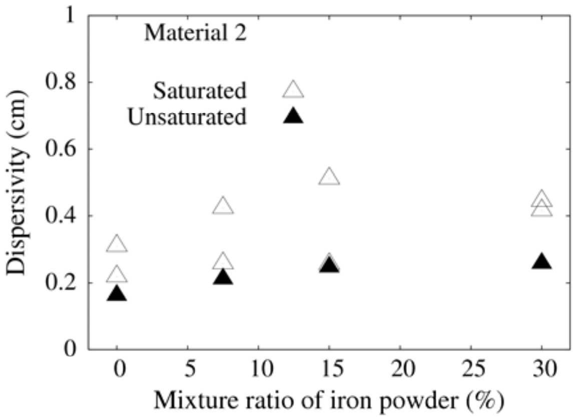

Fig. 9 Relation between the mixture ratio of commercial ZVI powder and the dispersivity

4 CONCLUSIONS

This paper assessed the potential of zero-valent iron (ZVI) powders as a nitrate reduction and retardation material in porous media. Under saturated and unsaturated flow conditions, column experiments were conducted in silica sand with a mixture of two kinds of ZVI powders. Experimental breakthrough curves were analyzed using temporal moments not only to estimate the retardation factor and the degradation rate but to quantify mass recovery fractions associated with nitrate and ammonium ions. The findings of this study are drawn as follows:

1) The retardation factor estimates under saturated condition were slightly larger than those under unsaturated condition regardless of the kinds of ZVI powders.

2) The increase of the amount of ZVI powder resulted in the increase of the degradation rate regardless of the water content. The degradation rates of commercial ZVI powder were larger than those of ZVI powder in hand warmer, indicating that commercial ZVI powder is more effective in the reduction of nitrate to ammonium.

3) According to the results of the mass recovery fraction, it was confirmed that ammonium was produced by reduction of nitrate in the presence of ZVI. The degree of production of ammonium increased with increasing the amount of ZVI powder, especially for commercial ZVI powder.

4) The longitudinal dispersivities slightly increased with increasing the mixture ratio of ZVI powder.

5 ACKNOWLEDGMENT

The work reported here was supported by the Nippon Life Insurance Foundation.

6 REFERENCES

[1] Schepers JS, Varvel GE and Watts DG, “Nitrogen and water management strategies to reduce nitrate leaching under irrigated maize,” J. Contam. Hydrol., 20, 1995, pp. 227–239.
[2] Knobeloch L, Salna B, Hogen A, Postle J and Anderson H, “Blue-babies and nitrate-contaminated well water,” Environ. Health Perspect, 108(7), 2000, pp. 675–678.
[3] Sandor J, Kiss I, Farkas O and Ember I, “Association between gastric cancer mortality and nitrate content of drinking water: ecological study on small area inequalities,” Euro. J. Epidemiol., 17, 2001, pp. 443–447.
[4] Jansen DM, Buijze ST and Boogaard HL, “Ex-ante assessment of costs for reducing nitrate leaching from agricultural-dominated regions,” Environ. Monitor. Software, 14, 1999, pp. 549–565.
[5] Schröder JJ, Aarts HFM, van Middelkoop JC, Schils RLM, Velthof GL, Fraters B and Willems WJ, “Permissible manure and fertilizer use in dairy farming systems on sandy soils in The Netherlands to comply with the Nitrates Directive target,” Euro. J. Agronomy, 27, 2007, pp. 102–114.
[6] Bennet P, He F, Zhao D, Aiken B and Feldman L, “In situ testing of metallic iron nanoparticle mobility and reactivity in a shallow granular aquifer,” J. Contam. Hydrol. 116, 2010, pp. 35–46.
[7] Mackay DM and Cherry JA, “Groundwater contamination: pump-and-treat remediation,” Environ. Sci. Technol., 23(6), 1989, pp. 630–636.
[8] Travis CC and Doty CB, “Can contaminated aquifers at Superfund sites be remediated?,” Environ. Sci. Technol., 24(10), 1990, pp. 1464–1466.
[9] Alowitz MJ and Scherer MM,“Kinetics of nitrate, nitrite, and Cr(VI) reduction by iron metal,” Environ. Sci. Technol., 36(3), 2002, pp. 299–306.
[10] Maeda M, Ihara H and Ota T, “Deep-soil adsorption of nitrate in a Japanese Andisol in response to different nitrogen sources,” Soil Sci. Soc. Am. J., 72(3), 2008, pp. 702–710.
[11] Inoue K, Ihara I, Yoshino A and Tanaka T, “Assessment of the use of hand warmer for nitrate retardation in porous media,” J. Water Environ. Technol., 8(4), 2010, pp. 355–362.
[12] Jeen S-W, Gillham RW and Przepiora A, “Predictions of long-term performance of granular iron permeable reactive barriers: field-scale evaluation,” Environ. Sci. Technol., 23(6), 1989, pp. 630–636.
[13] Ruangchainikom C, Liao C-H, Anotai J and Lee M-T, “Characteristics of nitrate reduction by zero-valent iron powder in the recirculated and CO2-bubbled system,” Water Res., 40, 2006, pp. 195–204.
[14] Murphy AT, “Chemical removal of nitrate from water,” Nature, 350, 1991, pp. 223–225.
[15] Cheng IF, Muftikian R, Fernando Q and Korte N, “Reduction of nitrate to ammonia by zero-valent iron,” Chemosphere, 35(11), 1997, pp. 2689–2695.
[16] Westerhoff P and James J, “Nitrate removal in zero-valent iron packed columns,” Water Res., 37, 2003, pp. 1818–1830.
[17] Das BS and Kluitenberg GJ, “Moment analysis to estimate degradation rate constants from leaching experiments,” Soil Sci. Soc. Am. J., 60, 1996, pp. 1724–1731.
[18] Valocchi AJ, “Validity of the local equilibrium assumption for modeling sorbing solute transport through homogeneous soils,” Water Resour. Res., 21(6), 1985, pp. 808–820.
[19] Pang L, Goltz M and Close M, “Application of the method of temporal moments to interpret solute transport with sorption and degradation,” J. Contam. Hydrol., 60(1-2), 2003, pp. 123–134.

First International Conference on Geotechnique, Construction Materials and Environment, Mie, Japan, Nov.21-23, 2011, ISBN: 978-4-9905958-0-7 C3051

Using Spatial Moments in Conjunction with Image Processing to Estimate Macrodispersion in Stratified Porous Formations

Suzuki K., Inoue K. and Tanaka T., Graduate School of Agricultural Science, Kobe University
Kobayashi A., Faculty of Environmental and Urban Engineering, Kansai University

ABSTRACT: Laboratory dye tracer experiments with a pulse source were conducted under saturated unidirectional flow conditions in a two-dimensional and vertically placed water tank. In tracer experiments, homogeneous and stratified porous formations, which were comprised by a few combinations with three types of soil particles, were of concern to examine the effect of variation of pore structure on macrodispersion phenomena. A new methodology using spatial moment analysis linked with image processing of a dye tracer behavior was developed to estimate macrodispersivities both in longitudinal and lateral directions. These results demonstrated that the ratio of the longitudinal macrodispersivity to the longitudinal microdispersivity ranged from about 2 to about 40. Moreover, it is indicated that the layering of stratified porous formations had an effect on the degree of longitudinal and transverse macrodispersions.

Keywords: macrodispersion, stratified porous media, image processing, spatial moment.

1. INTRODUCTION

The movement of groundwater in porous media is subject to convection and dispersion, independently of any material being transported [1]. Advection and forced-advection are due to bulk movement of groundwater caused by regional movement in the aquifer and by some man-made disturbance such as pumping wells, respectively, while natural convection is relevant to differences in density. Dispersion results from the irregular movement of water in porous formations where tortuosity of flow paths is induced. On a larger scale, these irregularities are due to the presence of zones of different hydraulic conductivities. It is progressively accepted that dispersion of solutes by groundwater is governed by large-scale spatial heterogeneity of natural formations [2],[3]. The scale effect in solute transport through porous media is strongly associated with the heterogeneity and has been the topic of significant theoretical and numerical experiments. As for layered media, Güven *et al* [4] conducted deterministic analysis of dispersion in a perfectly stratified aquifer of finite thickness and suggested that the time-dependent dispersivity approached an asymptotic limit in time. Black and Freyberg [5] used Monte Carlo simulations to estimate the impact of hydraulic conductivity uncertainty on concentration uncertainty in a perfectly stratified aquifer. Fadili *et al* [6] employed a Lagrangian particle tracking to investigate the behavior of concentration and statistical moments of the transported tracer plume in multilayered media. The scale effect in solute transport in a stratified aquifer has also been studied under field conditions. Sudicky *et al* [7] observed the transitional values of both longitudinal and transverse dispersivities. Güven *et al* [8] demonstrated that the results of a single-well tracer test could be interpreted without a scale-dependent dispersivity.

Although significant work has been performed through field efforts, relatively few controlled laboratory efforts have been reported. Recently, a few of the dye tracer experiments combined with an image processing technique have been studied to quantify the behavior of dye tracers [9],[10], which have been used for a long time to trace water flow and solute movement in aquifers. McNeil *et al* [11] performed intermediate-scale laboratory experiments in heterogeneous porous media and characterized the spatial distribution of solute concentrations using image analysis methods, providing concentration distributions and longitudinal dispersivity in a corresponding porous formation. However, the variation of longitudinal and transverse macrodispersivities corresponding to the heterogeneity was not described.

The objectives of this study are to investigate the transport behavior of dye tracer in homogeneous and stratified porous formations under saturated conditions, to estimate transport parameters including the longitudinal and transverse dispersivities and dispersion coefficients and to assess macrodispersion phenomena. An image processing technique is used in conjunction with spatial moments for the reliable parameter estimation and is applied to a flow field with a layered formation.

2. TRACER EXPERIMENTS

2.1 Dye tracers and experimental apparatus

Dye tracing is widely used to characterize water flow and solute transport behavior in porous media. Previous work demonstrated that colored dye tracers could be successfully used to monitor solute transport in a porous medium confined in a transparent container [12]. In this study, a dye tracer, Brilliant Blue FCF, with the initial concentration of 0.4 mg/cm^3 is employed. The specific gravity of dye tracer is 1.0001 measured using the specific gravity meter and can be therefore regarded as almost the same as that of water. Although the initial concentration of dye tracer is determined to be low enough to avoid density-induced flow effects, there is no denying that the effect of gravity on solute transport during the course of movement.

Tracer experiments are carried out in a two-dimensional and vertically placed water tank with the dimensions of 62 cm

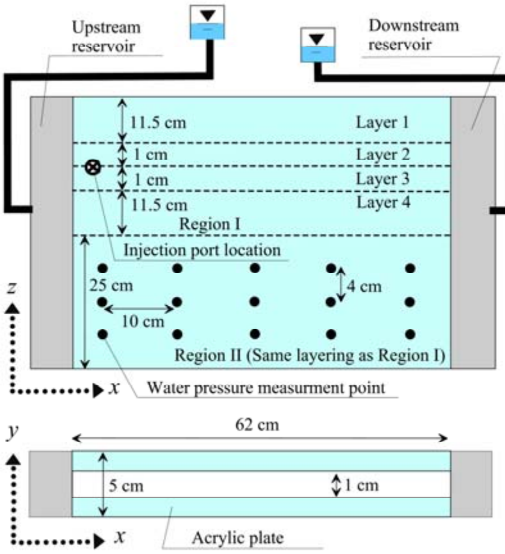

Fig.1 Schematic diagram of experimental apparatus.

width, 50 cm height and 1 cm thickness. The water flow tank contains silica sand to form transparent quasi two-dimensional solute transport phenomena and consists of two acrylic plates with 2 cm thickness. Schematic diagram of experimental apparatus is shown in Fig.1. Constant head water reservoirs connected to the upstream and downstream ends of the water tank are used to control the hydraulic gradient. One transparent acrylic plate allows for the observation of migrating dye tracer and for the measurement of the piezometric head at 20 observation points using manometers.

In tracer experiments, in order to elucidate the effect of the layering on the degree of macrodispersion, ten stratified porous formations are of interest and are comprised using three types of soil materials. Physical properties of soil materials, referred to as K4, K5 and K6, are shown in Table 1. For the base case, each soil material is filled in all Layers 1 through 4 shown in Fig.1 and comprises a homogeneous porous formation, providing "Single type formation" as Cases K4, K5 and K6. In two-layered porous formations, Layers 1 and 2 are filled with soil material K4 as the upper layer, while soil material K5 or K6 comprise the lower layer including Layers 3 and 4. As Cases K4-5 and K4-6, these two types of porous formations are referred to as "Step type formation". As one possible Step type formation, all three materials comprise flow fields where soil materials K4, K5 and K6 are filled with Layer 1, Layer 2 and 3, and Layer 4, respectively. In the same manner except for the use of two types of soil materials, soil material K4 comprises the top and bottom layers and the middle layer consists of material K5 or K6, referred to as "Convex type formation" and as Cases K4-5-4 and K4-6-4. In Convex type formation, soil material is switched to another material in order to create two different flow fields as "Concave type formation". In Table 2, experimental cases and corresponding layering formations

Table 1 Properties of soil materials.

	Material		
	K4	K5	K6
Mean particle size (cm)	0.085	0.050	0.030
Uniformity coefficient (-)	1.80	1.25	1.31
Hydraulic conductivity (cm/s)	0.751	0.268	0.0571
Dry density (g/cm^3)	2.68	2.68	2.68

Table 2 Experimental cases.

Case	Layer number				Type of stratified porous formation
	1	2	3	4	
K4		K4			Single
K5		K5			Single
K6		K6			Single
K4-5	K4		K5		Step
K4-6	K4		K6		Step
K4-5-6	K4	K5		K6	Step
K4-5-4	K4	K5		K4	Convex
K4-6-4	K4	K6		K4	Convex
K5-4-5	K5	K4		K5	Concave
K6-4-6	K6	K4		K6	Concave

using three soil materials are summarized as well as the assigned name of stratified porous formations of concern.

2.2 Experimental procedure

Materials are completely washed and saturated before packing to remove organic chemicals attached to the particle surface, to avoid entering the air and to conduct experiments under the saturated condition. In the process of creation of homogeneous and heterogeneous flow field formations, water flow tank is filled with water and material of interest from bottom to top in 5 cm layers to achieve uniform packing. In this process, saturated material is funneled using an extended funnel. Each layer is compacted prior to filling the next layer, resulting in 0.41 ± 0.02 of the porosity for all materials. The porosity of each material can be estimated indirectly from measurements of the particle density and the dry soil bulk density.

After packing, water is applied to the flow tank under a specific hydraulic gradient controlled by constant head water reservoirs at the upstream and downstream sides, while maintaing saturated condition of porous media. A steady saturated flow field is established in the flow tank when fluctuations in the observed drainage rate, which is effluent from the constant head water reservoir, and piezometer readings can become negligible.

After reaching steady state flow conditions, in order to simulate a pulse type source, dye tracer with the volume of 5 cm^3, which makes flow paths visible, is uniformly injected along the whole thickness of the flow tank. Tracer injection requires approximately 20 seconds so as not to possibly induce complications in the flow field, resulting in cylindrical source having a height of 1 cm and a radius of approximately 1.2 cm. In an injection system, a needle is inserted through the injection port with 0.05 cm of the radius on the face of acrylic

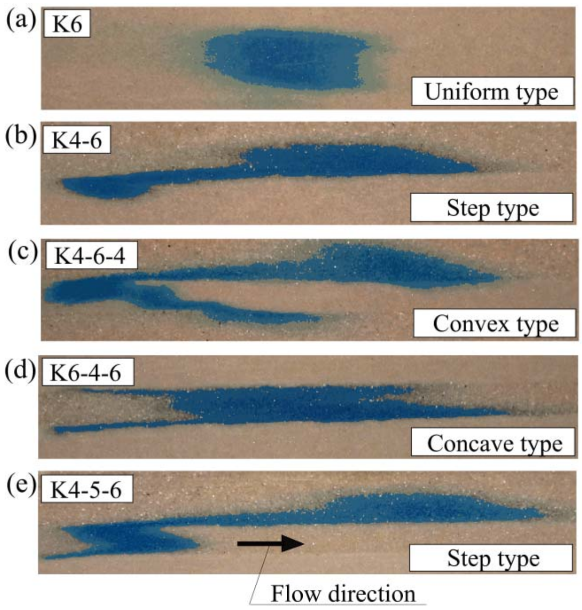

Fig.2 Image examples of dye tracer transport.

plate in order to create a two-dimensional transport state. During the experiment, the profiles of tracer migration are periodically recorded using a digital camera. The distance between the digital camera and the experimental flow tank is set at approximately 40 cm. A time series of images can then be processed and analyzed through image analysis for parameter estimation. Several experimental cases are repeatedly conducted under various hydraulic gradient conditions within approximately one order range of Reynolds number.

2.3 Transport process and image calibration

Fig.2 exhibits some images associated with dye tracer distributions in porous media. Data recorded by the digital camera successfully indicate different intensities in dye tracer distributions, suggesting different concentrations of the dye tracer. Moreover, the tracer experiments may be regarded as effectively two-dimensional since dye tracer is injected across the full 1 cm thickness of the flow tank.

In order to establish the relationship between the image intensity of a pixel and dye tracer concentration, a calibration is conducted. Under identical experimental conditions, a known concentration of dye tracer is injected into a corresponding porous formation without a hydraulic gradient. The spread of dye is captured by the digital camera. The same procedure is repeated using different concentrations of dye tracer, providing the relation between the image intensity and dye tracer concentration as shown in Fig.3 where calibration formulas are also shown and are specific to the experimental configuration. The concentration of the dye is proportional to the pixel brightness over the range of 0 mg/cm^3 to 0.4 mg/cm^3 as seen in Fig.3.

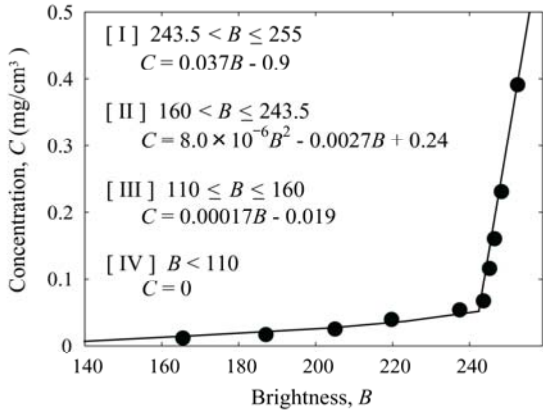

Fig.3 Relation between the image brightness and the dye tracer concentration.

2.4 Spatial moment approach

A commonly used measure of dilution is the spatial moments of the concentration spatial moments of aqueous concentrations distributed in space in porous media and are calculated from snapshots of tracer plume at given times as follows [13].

$$M_{ij}(t) = \int_{-\infty}^{\infty}\int_{-\infty}^{\infty} C(x,z,t)x^i z^j dxdz \qquad (1)$$

where x and z are the Cartesian coordinates, C is the solute concentration, t is the time, M_{ij} is the spatial moments associated with the distribution of tracer plume at a certain time, and i and j are the spatial order in the x and z coordinates, respectively.

The tracer brightness distribution can be converted to a concentration distribution by the calibration, providing an analogy between Eq.(1) and Eq.(2).

$$M_{ij}(t) = \int_{-\infty}^{\infty}\int_{-\infty}^{\infty} H(x,z)B(x,z,t)x^i z^j dxdz \qquad (2)$$

where $H(x,z)$ is the area per unit pixel and $B(x,z,t)$ is the brightness at a corresponding pixel.

The centroid of plume concentration distribution is calculated as the normalized first order spatial moment by the following equation.

$$x_c = \frac{M_{10}}{M_{00}}, \quad z_c = \frac{M_{01}}{M_{00}} \qquad (3)$$

where x_c and z_c are the cetroid locations of plume concentration distribution in the x and z coordinates, respectively. The liquid phase second order spatial moments are also computed as follows.

$$\sigma_{ij} = \begin{pmatrix} \sigma_{xx} & \sigma_{xz} \\ \sigma_{zx} & \sigma_{zz} \end{pmatrix} = \begin{pmatrix} \dfrac{M_{20}}{M_{00}} - x_c^2 & \dfrac{M_{11}}{M_{00}} - x_c z_c \\ \dfrac{M_{11}}{M_{00}} - z_c x_c & \dfrac{M_{02}}{M_{00}} - z_c^2 \end{pmatrix} \quad (4)$$

where σ_{ij} is the second order spatial moments.
Longitudinal and transverse macrodispersivities from spatial moments of the distributed tracer plume are calculated as [10]

$$A_L = \frac{1}{2}\frac{\sigma_{xx}}{\xi_c}, \quad A_T = \frac{1}{2}\frac{\sigma_{zz}}{\xi_c} \quad (5)$$

where A_L is the longitudinal macrodispersivity, A_T is the transverse macrodipersivitity and ξ_c is the travel distance of the center of tracer plume in the mean flow direction at time t. Furthermore, the longitudinal and transverse dispersion coefficients are estimated based on the relation between the flow velocity of dye tracer and the dispersivity as the following equations.

$$D_L = |v| A_L, \quad D_T = |v| A_T \quad (6)$$

where D_L is the longitudinal dispersion coefficient and D_T is the transverse dispersion coefficient.
An advantage of spatial moment analysis in conjunction with an image technique is that the underlying physical model is not needed unlike other techniques such as fitting advection and dispersion equation. This point may lead to the cost reduction related to labor sampling of other conservative chemicals such as NaCl and KBr.

3 RESULTS AND DISCUSSION

3.1 Microdispersion coefficient estimates

Estimates of longitudinal and transverse microdispersion coefficients in single layer formations of Cases K4, K5 and K6 are shown in Fig.4 as a function of Reynolds number, which is expressed as follows [1]

$$Re = \frac{v d_{50}}{\nu} \quad (7)$$

where Re is the Reynolds number, v is the seepage velocity, d_{50} is the mean particle size and ν is the kinematic viscosity. Harleman and Rumer suggested that a nonlinear relation between dispersion coefficients and Reynolds number as follows [14] .

$$D_L / \nu = b_L Re^{f_L}, \quad D_T / \nu = b_T Re^{f_T} \quad (8)$$

where b_L, b_T, f_L and f_T are constants, which depend on particle shape. The best fittings based on Eq.(8) with the empirical constants of 2.48 of b_L, 0.66 of f_L, 0.257 of b_T and 0.53 of f_T. In this figure, empirical relations suggested by Harleman and Rumer [14] are also depicted for the normalized longitudinal dispersions with the constants 0.66 of b_L and 1.20 of f_L and for the transverse dispersions with the constants 0.036 of b_T and 0.70 of f_T. Both longitudinal and transverse dispersion coefficients increase not only with the Reynolds number in flow fields but with the mean particle size. This tendency is quite natural in solute transport phenomena in homogeneous porous media [1], indicating the validity of the methodology applied herein. On the other hand, the fitting curves obtained in this study provide larger values compared to the empirical relations because the difference between physical properties including the uniformity coefficient and the mean grain size of materials in tracer experiments employed in this study and other literature may affect a porous formation, and result in a wide variety of tortuous pathways during the course of tracer migration.

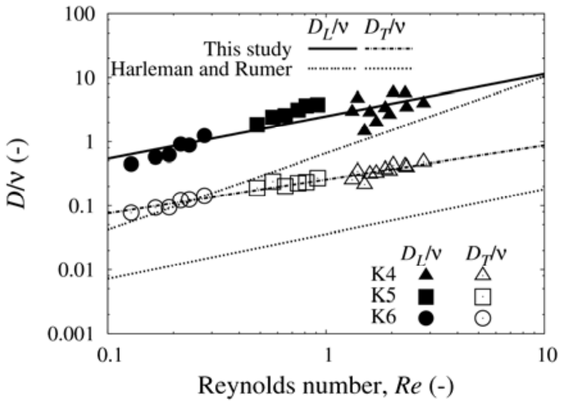

Fig.4 Variation of normalized longitudinal and transverse dispersion coefficients as a function of Reynolds number.

3.2 Macrodispersivity estimates

As stratified porous formations of Step, Convex and Concave type formations, as well as Single type formation, longitudinal and transverse macrodipersivites in each formation are plotted in Fig.5 as a function of Reynolds number. Longitudinal macrodispersivites in multilayered porous media are larger than those in single layers of Cases K4, K5 and K6. This is attributed to the distribution of hydraulic conductivity comprising flow fields and is one evidence occurring macrodispersion phenomena.
As for Step type formations, longitudinal macrodispersivities in Case K4-6 are larger than those in Case K4-5. Moreover, longitudinal macrodispersivites in Case K4-5-6 are lower values than those in Case K4-6. It is inferred that larger difference of hydraulic conductivity between neighboring layers results in larger values of longitudinal macrodispersivity. On the other hand, the difference of transverse macrodispersivities is relatively small despite of the stratified porous formation. This is because the flow direction is parallel to the layers and the vertical component

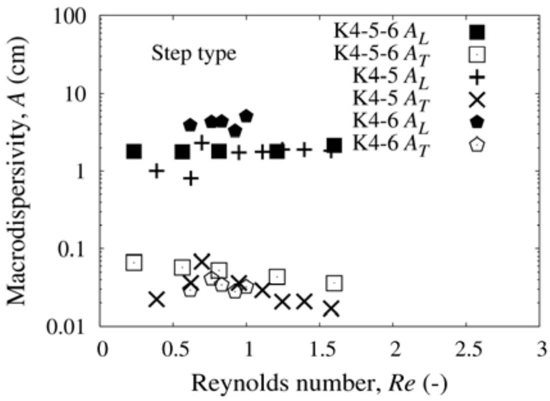

Fig.5 Variation of longitudinal and transverse macrodispersivities as a function of Reynolds number in Step type formation.

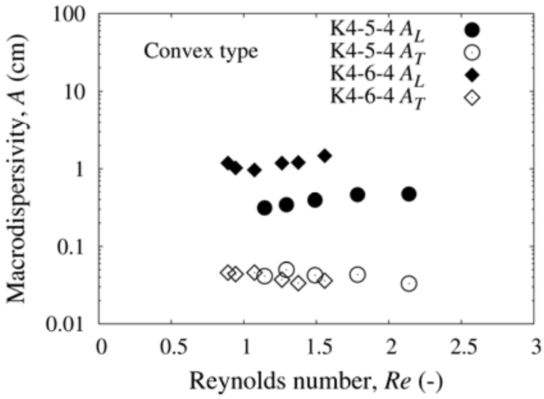

Fig.6 Variation of longitudinal and transverse macrodispersivities as a function of Reynolds number in Convex type formation.

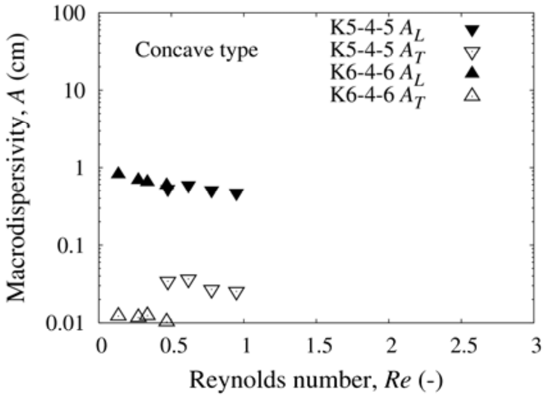

Fig.7 Variation of longitudinal and transverse macrodispersivities as a function of Reynolds number in Concave type formation.

of flow velocity is almost zero in this experimental field. As for Convex type formations, the same tendency as the results of Step type formation appears for longitudinal and transverse macrodispersivity estimates as seen in Fig.6.

On the other hand, unlike the results of Step and Convex type formations, Concave type formations where the soil material having the largest hydraulic conductivity comprises the middle layer in three layers present a unique tendency as shown in Fig.7. Whereas a little difference of the longitudinal macrodispersivity estimates between Cases K5-4-5 and K6-4-6 appears, transverse macrodispersivity estimates depend on the soil materials comprising the top and bottom layers. A few studies [15], [16] mentioned a solute transfer across a discontinuity such as a layered formation and suggested a probability expression as follows

$$P_1 = \frac{\sqrt{D_1}}{\sqrt{D_1} + \sqrt{D_2}}, \quad P_2 = 1 - P_1 = \frac{\sqrt{D_2}}{\sqrt{D_1} + \sqrt{D_2}} \tag{9}$$

where D_1 is the transverse dispersion coefficient in a layer in which tracer exists, D_2 is the transverse dispersion coefficient in the neighbor layer, P_1 is the transfer probability that a tracer remains in the same layer in which tracer exists and P_2 is the transfer probability that a tracer goes into the neighboring layer.

As seen in Fig.4, Case K4 has the largest value of transverse macrodispersion coefficient among flow fields of Single type formation. Therefore, according to the expression of Eq.(9), tracers migrating in the K5 or K6 layer may tend to travel toward the K4 layer. Hence, as shown in Fig.7, in Concave type porous formations employed herein, it appears that the difference of hydraulic conductivity between layers does not affect on the variation of longitudinal macrodispersivity estimates but on transverse macrodispersivity estimates.

3.3 Macrodispersivity vs. microdispersivity

As for results in stratified porous formations, Fig.8 exhibits the variation of the transverse macrodispersion coefficient as a function of Reynolds number. Additionally, for the purpose of comparison between macrodispersion and microdispersion coefficient estimates, transverse dispersion coefficients in Single type formation in Cases K4, K5 and K6 are also plotted. Transverse macrodispersion coefficient estimates in Step and Convex type formations are larger than those estimated in single layers K4, K5 and K6. This is because tracers migrating in K5 or K6 layer may tend to flow into the K4 layer as aforementioned above. Opposite to this result, transverse macrodispersion coefficient estimates in the Concave type formation of Case K6-4-6 are smaller than those estimates in single layers K4, K5 and K6. This also attributes to the difference of hydraulic conductivity between two layers. In Concave type formations, tracers located in the top and bottom layers have a certain possibility to flow into the middle layer, which has the largest hydraulic conductivity. Therefore, the degree of transverse dispersion may tend to decrease as tracers move. However, as shown in Fig.8, one of the Concave type formations, Case K5-4-5, leads to almost the same values of transverse macrodispersion coefficients as those in Single type formations. According to Eq.(9), the transfer possibility of tracers depends on the transverse dispersivity. There is a small difference between not only

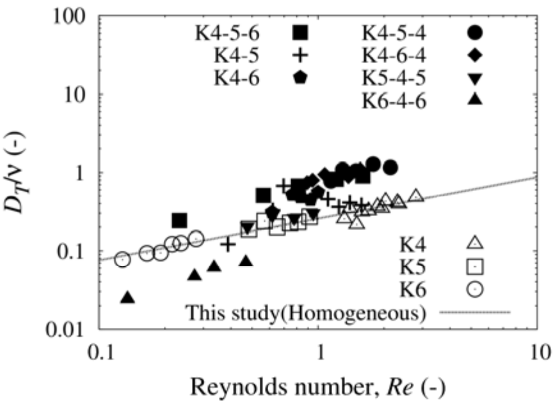

Fig.8 Variation of normalized transverse dispersion coefficients as a function of Reynolds number.

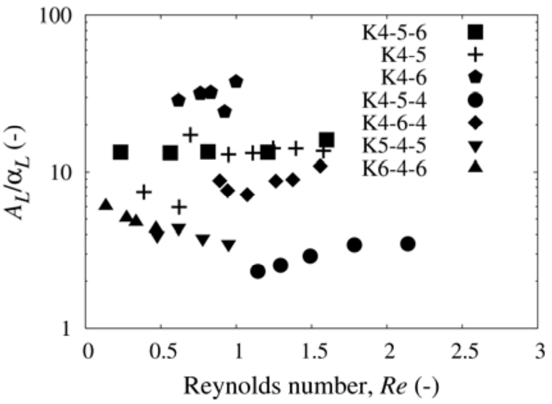

Fig.9 Variation of normalized longitudinal macrodispersivities as a function of Reynolds number.

transverse dispersivities but the values of hydraulic conductivity in soil materials K4 and K5, resulting in similar values of Case K5-4-5 to the results of Single type formation. Fig.9 demonstrates that the variation of the longitudinal macrodispersivities divided by the microdispersivity (α_L=0.135cm), which is an estimate in Single type formation of Case K4, as a function of Reynolds number. Regardless of stratified porous formations, the ratio of the longitudinal macrodispersivity to the longitudinal microdispersivity exceeds 1, and ranges from about 2 to about 40. Moreover, there is a marked difference between estimated values of A_L/α_L in stratified porous formations. In Step type formation the values of A_L/α_L are larger than those in Convex and Concave type formations due to the difference of the degree of transverse dispersion induced from the layering comprising stratified formations.

4 CONCLUSION

In the present study, the behavior of macrodispersion in stratified porous formations has been assessed. Macrodispersion coefficient and microdispersivity have been estimated based on spatial moments in conjunction with image processing. The following findings have been clarified.

1. Image processing is a non-intrusive approach and can directly characterize the solute movement in porous media.
2. Transverse macrodispersion coefficient estimates in Step and Convex type formations are larger than those in Single type formations. Contrary tendency is seen in Concave type formation due to the effect of the layering comprising stratified formations.
3. Regardless of stratified porous formations, the ratio of the longitudinal macrodispersivity to the longitudinal microdispersivity exceeds the unity, and ranges from about 2 to about 40.
4. The layering of stratified porous formations has an impact on longitudinal and transverse macrodispersion.

5 REFERENCES

[1] Bear J, Dynamics of fluids in porous media. Dover Publications.

[2] Dagan G, "Time-dependent macrodispersion for solute transport in anisotropic heterogeneous aquifers," Water Resour. Res., 24(9), 1988, pp. 1491–1500.

[3] Gelhar LW, Welty C and Rehfeldt KR, "A critical review of data on field-scale dispersion in aquifers," Water Resour. Res., 28(7), 1991, pp. 1955–1974.

[4] Güven O, Moltz, JM and Melville JG, "An analysis of dispersion in a stratified aquifer," Water Resour. Res., 20(10), 1984, pp. 1337–1354.

[5] Black TC and Freyberg DL, "Stochastic modeling of vertically averaged concentration uncertainty in a perfectly stratified aquifer," Water Resour. Res., 23(6), 1987, pp. 997–1004.

[6] Fadili A, Abaou R and Lenormand R, "Dispersive particle transport: identification of macroscale behavior in heterogeneous stratified subsurface flows," Math. Geol., 31(7), 1999, pp. 793–840.

[7] Sudicky EA, Cherry JA and Frind EO, "Migration of contaminants in groundwater at a landfill: a case study 4. A natural-gradient dispersion test," J. Hydrol., 63, 1983, pp. 81–108.

[8] Güven O, Falta RW, Moltz, JM and Melville JG, "Analysis and interpretation of single-well tracer test in stratified aquifers," Water Resour. Res., 21(5), 1985, pp. 676–684.

[9] Schincariol R and Schwartz FW, "An experimental investigation of variable density flow and mixing in homogeneous and heterogeneous media," Water Resour. Res., 26(10), 1990, pp. 2317–2329.

[10] Inoue K, Takenouti R, Kobayashi A, Suzuki K and Tanaka T, "Assessment of a UV excited fluorescent dye technique for estimating solute dispersion in porous media," J. Rainwater Catchment Systems, 17(1), 2011, pp. 1–9.

[11] McNeil JD, Oldenborger GA and Schincariol RA, "Quantifying imaging of contaminant distributions in heterogeneous porous media laboratory experiments," J. Contam. Hydrol., 84, 2006, pp. 36–54.

[12] Flury M and Flühler H, "Tracer Characteristics of Brilliant Blue FCF," Soil Sci. Soc. Am. J., 59(1), 1995, pp. 22–27.

[13] Tompson AFB and Gelher LW, "Numerical simulation of solute transport in three-dimensional, randomly heterogeneous porous media," Water Resour. Res., 26(10), 1990, pp. 2541–2562.

[14] Harleman DRF and Rumer RR, "Longitudinal and lateral dispersion in an isotropic porous media," J. Fluid Mech., 16, 1963, pp. 385–394.

[15] Hoteit H, Mose R, Younes A, Lehmann F and Ackerer P, "Three-dimentional modeling of mass transfer in porous media using the mixed hybrid finite elements and the random-walk methods," Math. Geol., 34(4), 2002, pp. 435–456.

[16] Uffink GJM, "A random-walk method for the simulation of macrodispersion in a stratified aquifer," Proc. IAHS symposia, 65, 1985, pp. 26–34.

First International Conference on Geotechnique, Construction Materials and Environment, Mie, Japan, Nov.21-23, 2011, ISBN: 978-4-9905958-0-7 C3051

The Novel Technology of Desertification Control and Ecological Restoration with an Hydrolysis Polyurethane(W-OH)

Weimin Gao[1], Zhiren Wu[2], Zhishen Wu[3], Kentaro Iwashita[4], Hirondo Inagaki[2], Caiqian Yang[5]
1. Graduate School of Engineering, Ibaraki University, Hitachi, 3168511, Japan
2. JCK Co. Ltd., Anjo, Aichi, 446-0071 Japan
3. Department of Urban and Civil Engineering, Ibaraki University, Hitachi, 3168511 , Japan
4. Department of Urban and Civil Engineering, Meijo University, Nagoya, 468-8502, Japan
5. International Institute for Urban Systems Engineering, Southeast University, Nanjing, 211189, China

ABSTRACT: A novel hydrolysis polyurethane(W-OH) is an eco-type solidification material that is used in desertification control. This paper presents a new method for the ecological treatment of desertification using W-OH and discusses the large-scale production technology of W-OH. Solidification of W-OH is by a cross-linking reaction between W-OH and water in a broad proportion. The reaction is rapid (2 to 20 min). The resulting material is elastic with large water holding properties. A sand-fixing layer can be formed by spraying an aqueous solution of W-OH on a sand surface. We find that the resulting sand-fixing layer has good elasticity, suitable porosity, excellent capability of holding water, heat and fertilizer, and it can supply a stable and suitable environment for vegetation. Moreover, the degradation period of W-OH can be controlled by adding different concentrations of a hindered amine light stabilizer (HALS or the W-US as product name). The degradation of the sand-fixing layer can be modified according to the local environmental conditions. The degradation products are non-toxic and do not present an environmental hazard. Construction of W-OH desertification control is simple: it does not require large mechanical equipment and is suitable for large-scale construction.

Key words: W-OH organic composite material; W-US; Chemical-biological sand fixation; Desertification control; Ecological restoration

1. INTRODUCTION

Currently, there are three major methods to combat desertification [1]: the physical and mechanical method, the chemical method and the biological method. The physical and mechanical method consists of placing a sand trap, such as a grass grid, on the sand surface. While the sand trap is beneficial in the prevention of sand-shifting, it is also plagued by many problems, such as the labor associated with installation, low efficiency in the prevention of desertification, and poor biological-environmental compatibility, among others [2]–[4]. As the sand trap ages, the material degrades and gradually rots. The trap loses its function when sand particles begin to shift with the wind. The physical and mechanical method is thus not suitable for large-scale use and is not a viable solution for desertification [5], [6].

Chemical sand fixation is essentially a specialized mechanical sand-fixing method. Critical development of chemical sand fixation methods has taken place over the past 80 years. With improvements in the chemical industry, many new organic and inorganic sand-fixing materials have been developed and applied in desertification control [7], [8]. However, this method has the same inherent problems as mechanical sand fixation: the sandy soil is only fixed for a short term and thus does not provide a reliable solution to desertification. On exposure to UV radiation and wind/sand erosion, the materials gradually degrade and eventually disappear. Additional limitations include high costs and complex construction. Moreover, the fixed surface is unsuitable for plants growth and typically harmful to the environment [9].

Biological sand fixation not only controls desertification but also improves microclimate conditions, restores the environment and provides additional benefits in areas with relatively high rainfall. Biological sand fixation is a fundamental solution for the problem of desertification. However, because of the poor climate and hydrological conditions often found in areas at risk for desertification, it is impossible for plants to survive and grow. Therefore, it is necessary to study a novel control technology for improving the growth environment and survival rate of plants under extreme desertification conditions [10], [11].

The development of chemical-biological integrated sand fixation technology is a current trend in the field of desertification control. However, it is difficult to combine existing chemical sand-fixing materials with a biological solution due to their poor durability and plant affinity. Therefore, such methods have not been applied for large-scale desertification prevention and control. In this paper we introduce a novel hydrophilic polyurethane(W-OH) sand stabilizer. The material is prepared with ethylene oxide (EO) and propylene oxide (PO) random copolyethers, excess modified 4, 4’-diphenylmethane diisocyanate and other functional materials. Solidification is obtained by a cross-linking reaction between W-OH and water in a broad proportion. The reaction is quick and is completed within the range of 2 to 20 min. The resulting solid is elastic, with great water-holding capability. A sand-fixing layer is formed by spraying W-OH aqueous solution on the sand surface. The thickness of the layer is between 1and 5 cm, with a porosity between 8 and 25%(by volume percent). The layer is robust enough to prevent erosion caused by sand and wind. The sand-fixing layer is characterized by good elasticity, suitable porosity and excellent capability of preserving water, heat and fertilizer. Therefore, it provides a stable and good environment for the growth of vegetation. The degradation period can be controlled from 1 to 20 years by using different concentrations of a hindered amine light stabilizer(HALS or W-US as the product name). Therefore, the method of combating desertification with W-OH proves to be a sustainable technique [12]–[15].

2. The characterization of W-OH

2.1 Physical and chemical characteristics of W-OH

W-OH is a light yellow, oily liquid. Water is used as a solidifying agent. W-OH is soluble in water at a broad range of concentrations. Solidification is achieved using a cross-linking reaction between W-OH and water. The reaction is quick, ranging from 2 to 20 min. W-OH has many potential applications, including use in soil stabilization and sand fixation, and as a waterproofing agent in irrigation ditches or a dust proof layer. Recent research on soil stabilization and sand fixation has resulted in many technological breakthroughs. In the work presented here, we stress that W-OH has many excellent properties, such as ① Excellent durability: the resulting solid is resistant to UV irradiation for up to 20 years, and this property can be controlled by adjusting the components of W-OH; ② Good mechanical properties and high adhesive forces with other materials such as sand and soil; ③ Fast solidification with a large range of water concentrations, and the resulting solid is very elastic with great water holding capacity; ④ Good resistance to acid and alkaline erosion, hydrolysis and salt corrosion; ⑤ Is environmentally friendly.

2.2 Solidifying characteristics of W-OH

W-OH can be dissolved in water, emulsified and dispersed homogeneously. The solidification proceeds over several minutes following the introduction of water. As shown in Fig. 1, when the concentration of W-OH is less than 3%(by weight percent), the cross-linking reaction forms a very weak solid due to the low cross-linking density and low molecular weight of the solidified W-OH. Therefore, a concentration of at least 3% of the sand-fixing material in water is necessary for sand fixation. With an increase in temperature from 5 to 30℃, molecular motion is accelerated and the viscosity of the cross-linking reaction increases. However, this is accompanied by a decrease in the cross-linking density and a corresponding decrease in the viscosity and the strength of the solidified W-OH. By comparing the solidification conditions

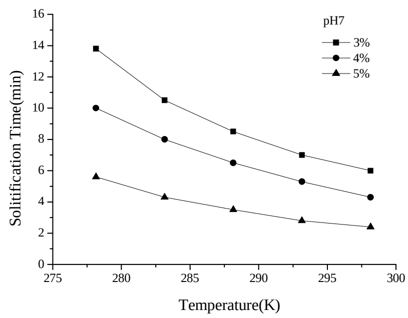

Fig.1 Relationship between the solidifying time of W-OH and temperature

at 5℃ and 30℃, we see that the time for solidification decreases by more than 50%, from 19 min to 7 min at a concentration of 3% sand-fixing agent, from 12 min to 2.2 min at a concentration of 4% sand-fixing agent, and from 8 min to 2 min for a concentration of 5% sand-fixing agent. Therefore, the solidification time and final strength of the material is a function of reaction temperature and W-OH concentration.

2.3 Safety of W-OH

W-OH uses water as solidifying agent. On completion of the W-OH and water reaction, all of the W-OH present is consumed. W-OH contains no heavy metal ions. The safety of W-OH was measured and certified by public authorization, with respect to both plant and animal toxicity. The graph in Fig. 2 shows the results of the W-OH fish toxicity test. Results from both fish and mouse toxicity tests demonstrate that W-OH is an environmentally friendly material and does not harm living organisms. This is a prerequisite for any material used in desertification control.

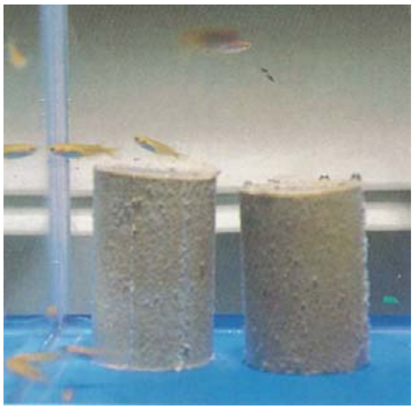

Fig. 2 Security test

3. The mechanism and construction technology of sustainable decertification control with W-OH

3.1 The mechanism of sustainable decertification control with W-OH

The work presented here is a novel conception of sustainable desertification control with W-OH and we aim to further develop and study this technology. Sustainable desertification control relies on a combination of chemical sand fixation and organic biological sand fixation. Desertification control and ecological restoration can be divided into two stages: first, chemical sand fixation with W-OH, followed by biological sand fixation. The schematic diagram illustrating the mechanism of sustainable sand fixation and vegetation using W-OH is shown Fig. 3. W-OH is sprayed on a sand surface that has been treated with seed and fertilizers. Several minutes later, a sand-fixing layer is formed on the sand surface and the objective of chemical sand fixation is achieved. However, chemical sand fixation only addresses the stability of the soil and sand dune, and with chemical fixation alone, it is impossible to achieve sustainable biological sand fixation and complete ecological restoration.

The sand-fixing layer with W-OH has a thickness of more than 1 cm and porosity of approximately 20%. This layer presents a suitable environment for plant germination and growth. Thus, the second stage of sustainable biological sand fixation can be achieved in the presence of W-OH. The degradation period of the W-OH sand-fixing layer can be controlled according to the local environmental conditions. It has been found that plants can germinate one week after spraying W-OH aqueous solution, and the sand-fixing layer degrades completely after 2 to 3 plant life cycles. In this way, the natural transition between chemical sand fixation and biological sand fixation is achieved.

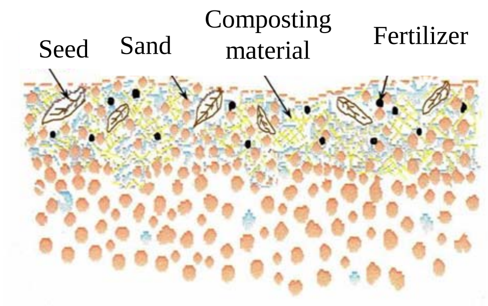

a. Distribution of seed and fertilizers

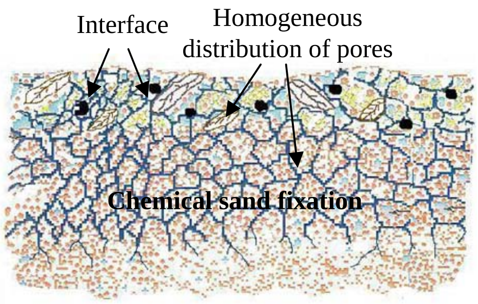

b. W-OH spraying-solidifying

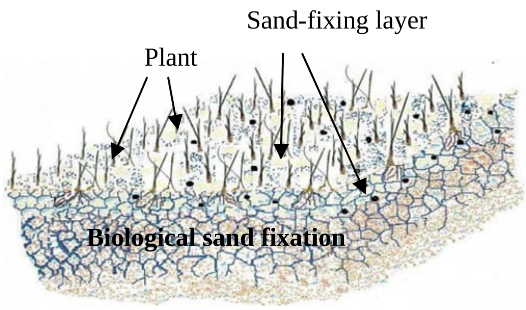

c. Sustainable biological sand fixation and ecological restoration

Fig. 3 The mechanism of sustainable sand fixation and vegetation with W-OH

3.2 The construction technology

The construction technology of sustainable decertification control with W-OH is simple and convenient without any large mechanical equipment. It is very important for application in desertification control due to dismal and remote desert. The construction technology with W-OH is mainly clarified into two stages. The first stage is land consolidation which includes mixture of seed, composting material and fertilizers with sand, spraying the mixture on the sand surface, land grading and filling, followed by spraying water. The second stage is spraying W-OH on the sand surface with a special equipment of Y type. It contains two pumps and tunnels for transporting W-OH and water respectively, and W-OH and water mixes at nozzle and then the solution is sprayed on the sand surface. The concentration is controlled by adjusting water pump.

The technology needed for desertification control with W-OH consists solely of spraying equipment, which is suitable for large-scale application. The concentration of W-OH can be controlled form 2% to 7%, according to the needs of a specific application. This technology benefits from simple equipment and construction processes.

4 Properties of the W-OH sand-fixing layer

4.1 Appearance of the sand-fixing layer

As a result of low viscosity prior to solidification, W-OH can easily penetrate into the sand on spraying, and a sand-fixing layer forms after few minutes. Fig. 4 shows the appearance of the sand-fixing layer. The sand-fixing layer is characterized by good elasticity and sufficient porosity, which is necessary for plant growth. Fig. 5 shows the layer thickness and initial porosity of the sand-fixing layer as a function of the amount of W-OH that is sprayed. If the amount of W-OH is too low, the thickness of the sand-fixing layer will be too thin to achieve proper sand fixation. Therefore, the spraying quantity is set to more than 3 L/m^2. When the amount of W-OH sprayed on the sand is 3 L/m^2, the thickness of the sand-fixing layer is approximately 1.4 cm with an initial porosity of 20%. The sand-fixing layer not only fixes sand but is also suitable for plant growth. The thickness of the sand-fixing layer increases linearly with the quantity of W-OH that is sprayed. However, with an increased quantity, the initial porosity decreases due to the higher concentration of the sand-fixing material in the sand, and the smaller pore size. When the quantity of W-OH sprayed on the sand is 10 L/m^2, the thickness of the sand-fixing layer is approximately 3 cm, and the porosity decreases to 8%. These results demonstrate that the thickness and porosity of the W-OH sand-fixing layer can

Fig. 4 Appearance of the sand-fixing layer with W-OH

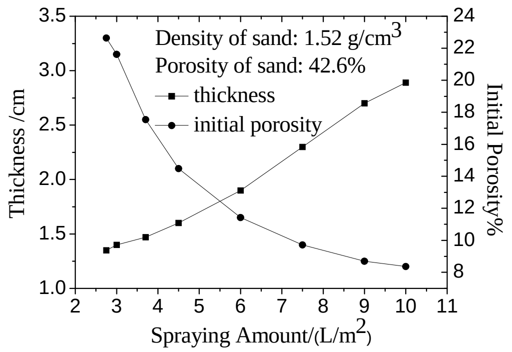

Fig. 5 Relationship between thickness and initial porosity of the sand-fixing layer and the spraying amount of W-OH

be controlled according to the needs of the local condition by adjusting the quantity of the W-OH solution sprayed.

4.2 Performance of compressive stress and wind erosion resistance

The sand-fixing layer is an elastic material. When the concentration of W-OH is increased, the molecular weight of the solidified W-OH network increases, the cross-linking density increases, the intensity solidified W-OH increases, and the adhesion between the solidified network and sand particles is enhanced. Therefore, the compressive stress of the sand-fixing specimens increases linearly with increasing concentration of W-OH. As the concentration increases from 3% to 7%, the compressive stress enhances from 0.37 MPa to 1.27 MPa (Fig. 6). The linear formula is shown in Eq. 1, with R^2 equal to 0.97. Therefore, the sand treated with W-OH has adequate mechanical properties to withstand strong wind/sand erosion and an adverse desert environment.

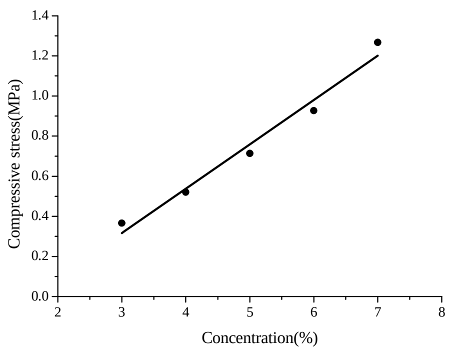

Fig. 6 Relationship between compressive stress of the sand-fixing specimens and concentrations of W-OH

$$Y=0.17576X - 0.22588 \quad R^2=0.97 \tag{1}$$

The objective of the wind tunnel test was to study wind erosion resistance. The specimens were made by spraying W-OH on sand that was contained in a rectangular sand table with dimensions of 32 cm×40 cm×4.5 cm. Concentrations of W-OH set by 2%、2.5%、3%、3.5%、4%、4.5%、5%、6% and 7%. The prepared sand-fixing specimens were placed into the testing section of the wind tunnel and subjected to wind-sand flow under various certain velocities and angles. The velocity was measured and controlled by the pilot tube, and a sand sampler with multiple tubes was used to measure sand flow. The testing parameters were set with a wind/sand flow velocity of 10 m/s for 30 min, 15 m/s for 20 min, 20 m/s for 10 min or 25 m/s for 8 min and angles of 0°, 30° or 60°. The result demonstrated that W-OH sand-fixing specimens had excellent wind/sand erosion resistance. The resulting solidified network can withstand strong wind/sand erosion at a high speed of 25 m/s without deformation or surface damage. This implies that layers fixed with W-OH can withstand wind erosion exceeding grade 8 and are completely suited for use in desert control.

4.3 Performance of durability and water retention

It is well known that a desert environment is characterized by strong sunshine, UV radiation, low annual precipitation and high water evaporation. As a result, it is prerequisite for W-OH sand-fixing material to have good durability and water retention, especially under UV radiation. The durability of W-OH was studied under accelerated aging test conditions with UV radiation. Degradation was inhibited by the inclusion of W-US. Fig. 7 shows the results of W-OH durability tests using different concentrations of W-US. Tests demonstrate that W-OH durability is significantly improved by the inclusion of W-US. The decomposition rate of the sand-fixing layer is decreased by 80% when a W-US

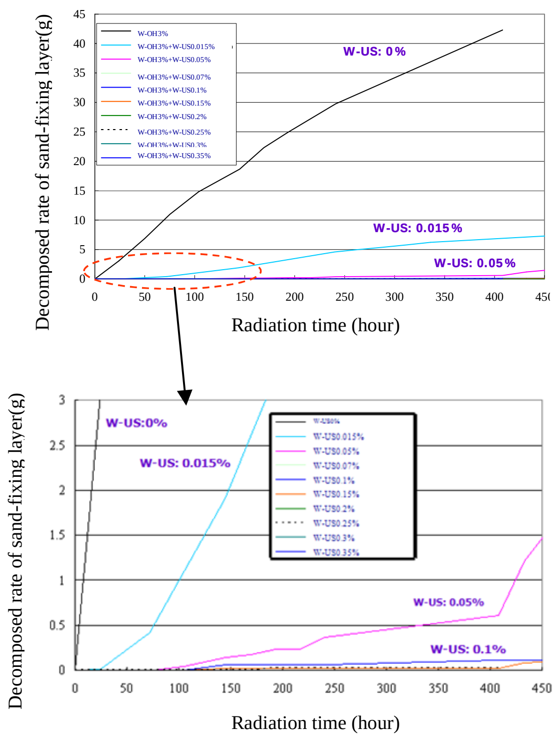

Fig. 7 Relationship between W-OH durability and concentration of W-US

concentration of 0.015% is used and 96% for a W-US concentration of 0.05%. When the W-US concentration is increased to 0.1%, the degradation of the sand-fixing layer with W-OH is almost completely inhibited. Based on the UV radiation intensity found around Qinghai Lake, China, which is 600~720 kJ/cm^2/a and an experimental UV radiation intensity of 1000 w/m^2, the UV radiation duration of 140.6~166.7 hours in our accelerated aging test is equivalent to one month in the desert near Qinghai Lake. The service life of W-OH without the inclusion of W-US is only one and a half months. The service life is increased to over 10 months with the inclusion of 0.015% W-US, and to 6 years and 8 months with the inclusion of 0.05% W-US. When the W-US concentration is increased to 0.1%, the lifetime increases to 22 years and 8 months, or essentially no degradation in the strong UV radiation region around Qinghai Lake.

A super water absorbent resin (SAP or W-BW as product name) was added to improve the water retention of the W-OH sand-fixing layer. It was mixed in the aqueous W-OH solution and sprayed on the sand surface. The results are shown in Fig.8. Water retention capacity can be improved by 28~35％ with the addition of 0.06~0.5％ W-BW. By increasing the concentration of W-BW to 0.7%, the water retention capacity increases. However, when the concentration of W-BW is larger than 0.7%, the water retention capacity increases only slightly. Thus, water retention capacity can be improved by 50％ with 0.5~1％ W-BW, and 0.7% is the ideal concentration of W-BW for improved water retention.

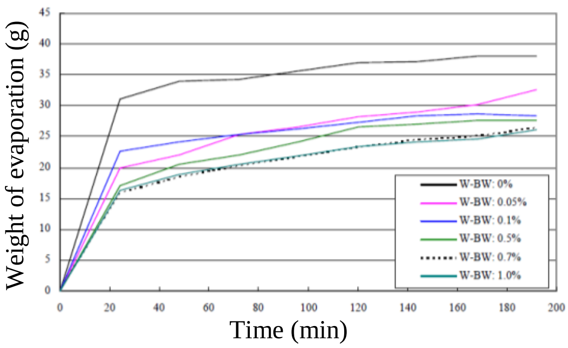

Fig. 8 Performance of water retention of W-OH sand-fixing layer

4.4 Effect of sand fixation on vegetation

To determine how the sand fixing layer affects vegetation, Toyoura sand with a density of 1.56 g/cm^3 was placed into a mold with the dimensions of 30 cm × 30 cm × 5 cm and compacted by hand. The prepared sand model was 4.5 cm thick, with a porosity of 40%. A concentration of 3% aqueous W-OH solution with varying concentrations of W-US was prepared and homogenously sprayed on the sand surface homogeneously. The concentrations of W-US used in this test were 0%, 0.05% and 0.1%, and this experiment was developed by JCK Co. Ltd, Japan. The seeds germinated one week after W-OH sand treatment. Two weeks later, the

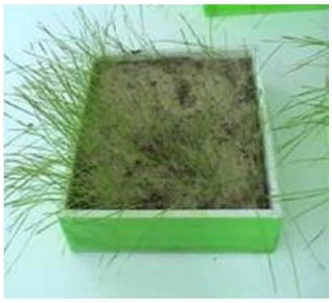

a. W-US 0%

b. W-US 0.05%

c. W-US 0.1%

Fig.9 Effect of sand fixation on vegetation.
(After one month growth)

relative germination rate was greater than 80%, indicating a favorable environment for growth. Vegetation growth continued to improve with time. Fig. 9 illustrates the growth conditions after one month. The W-US additive had no effect on vegetation.

5. Demonstration of sand fixation study with W-OH

The W-OH treatment was applied to sand dunes and vegetation in Qinghai China. More than 5 demonstration sites were built. The effect of sand fixation on vegetation are better observed in actual application. Fig. 10 shows an experiment conducted near around Qinghai Lake, supported by the NEDO Program. The demonstrations were performed over 2 years, with constructed areas of 6600 m^2 and 33000 m^2, respectively. Weather in this region, which is considered a mobile dune, is characterized by high UV radiation, strong wind and extremely low precipitation. Therefore, traditional organic sand-fixing materials readily degrade and are not very effective. Our experiments demonstrated that W-OH was a good sand-fixing material, effective in both sand

a. Beginning

b. One year later

Fig. 10 Demonstration of vegetation and sand fixation of a sand dune around Qinghai Lake, China

fixation and vegetation growth, even under high UV radiation and other adverse conditions. Vegetation growth proceeded well over the one year treatment and the vegetation coverage increased from 0 to over 50%. Results were verified by a separate demonstration in Wudaoliang, along the Qinghai-Tibet Railway. In this experiment, the vegetation growth was healthy after a two-year treatment, with vegetation increasing from 0 to over 40%. In addition, the W-OH treatment showed excellent UV radiation resistance [16].

6 CONCLUSION

W-OH is a solidification material with hydrophilic polyurethane being the fundamental ingredient. W-OH reacts with water at a broad proportion, resulting in a solidified network after 2 to 20 min. A 3% W-OH concentration is necessary for sand fixation. The solid formed does not dissolve in water and boasts large water-holding and water retention capacity. A sand-fixing layer can be formed by spraying aqueous W-OH solution on the sand. With a spraying amount of 3 L/m^2, the resulting sand-fixing layer has a thickness of 14 mm and a porosity of 20%. The sand-fixing layer has good elastic properties and mechanical durability, withstanding wind erosion higher than grade 8. The UV degradation resistance and water retention can be greatly improved adding W-US and W-BW to W-OH. Moreover, the UV degradation period can be controlled for a period of 1 to 20 years by adjusting the concentration of the W-US additive. Therefore, the layer formed provides a good environment for vegetation. The technology for the construction of a W-OH layer is simple and does not require large mechanical equipment, making it convenient for large-scale applications. The effects of sand fixation on vegetation growth were also verified by field demonstration. In conclusion, the W-OH-based technology has the potential to be one of the most important and efficient methods for application in desertification control and ecological restoration.

7 ACKNOWLEDGMENTS

This work was financial support by the China-Japan Cooperation Projects of International Science and Technology (2010DFB54170). The authors also gratefully expressed their thanks to Water Conservancy and Hydroelectric Scientific Research Institute of Qinghai Province, for their participating in building demonstrations.

8 REFERENCES

[1] UNEP, "United Nations Convention to Combat Desertification," Nairobi, Kenya, 1994, 35.
[2] Jian J, Li HJ, Dai XA, "Research on Land Sandy Desertification Using Remote Sensing Taking Qinghai Lake Area as an Example," GEO-INFORMATION SCIENCE, 8(2), 2006, pp.116-120.
[3] Wang LL, Qin ZY, Qin NS, "Climate Change and Its Impact on Desertification around Qinghai Lake," PLATEAU METEOROLOGY, 21(1), 2002, pp. 59-65.
[4] Dirk G, Zvi YO, "Aeolian dust erosion on different types of hills in a rocky desert: wind tunnel simulations and field measurements," Journal of Arid Environments, 37, 1997, pp. 209-229.
[5] Zhang TH, Zhao HL, Li SG, Li FR, Shirato Y, Ichiro Taniyama TO, "A comparison of different measures for stabilizing moving sand dunes in the Horqin Sandy Land of Inner Mongolia, China," Journal of Arid Environments, 58, 2004, pp. 203–214.
[6] Li FR, Kang LF, Zhang H, Zhao LY, Shirato Y, Taniyama I, "Changes in intensity of wind erosion at different stages of degradation development in grasslands of Inner Mongolia, China," Journal of Arid Environments, 62, 2005, pp. 567–585.
[7] Dong ZB, Chen GT, He XD, Han ZW, Wang XM, "Controlling blown sand along the highway crossing the Taklimakan Desert," Journal of Arid Environments, 57, 2004, pp. 329-344.
[8] Ren J, Tao L, Liu XM, "Effect of different microhabitats and stand age on survival of introduced sand-fixing plants," Journal of Arid Environments, 51, 2002, pp. 413-421.
[9] FUJIYOSITAKAO, "Integrated areas to prevent the desertification, Chemistry and Industry," Chemical Society of Japan, 61(2), 2008, pp. 103-107.
[10] Yang J, Wang F, Fang L, Tan TW, "Synthesis, characterization and application of a novel chemical sand fixing agent-poly(aspartic acid) and its composites," Environmental Pollution, 49(1), 2007, pp.125-130.
[11] Z. Dong, L. Wang, S. Zhao, "A potential compound for sand fixation synthesized from the effluent of pulp and paper mills," Journal of Arid Environments, 72, 2008, pp. 1388–1393.
[12] Wu ZR, Iwashita K, Wu ZS, Inagaki H, "Research on Sand Dune Fixation and Green Vegetation of a Novel Chemical Material and Construction Method of Demonstration Areas Around Qinghai Lake," The Report of METI NEDO Project: H19 NO. 0710002, July 2007-Feb.2009, 2009
[13] Gao WM, Wu ZR, Wu ZS, Yang CQ, Li RJ, Dong ZB, "Study on Resistance of Wind/sand Erosion Based on a Solidifying Composite Material of Hydrophilic Polyurethane," Journal of the Japan Society of Material Science, 60(9), accepted, 2011
[14] Wu ZR, Iwashita K, Wu ZS, Inagaki H, "Experimental study on evaluation and control of ultraviolet resistance of sand stabilized with organic slurry containing hydrophilic polyurethane," Journal of the Japan Society of Material Science, 57(11), 2008, pp. 1167-1172.
[15] Wu ZR, Wu ZS, Iwashita K, Gao WM, Inagaki H, "UV Irradiation Degradation Control of Sand Stabilized with Organic Slurry Containing Hydrophilic Polyurethane," Journal of the Japan Society of Material Science, 60(3), 2011, pp. 235-239.
[16] Wu ZR, "Development of mobile sand-fixing and vegetation technique with Hydrophilic Polyurethane," Ph.D.Thesis, 2011.3.

First International Conference on Geotechnique, Construction Materials and Environment, Mie, Japan, Nov.21-23, 2011, ISBN: 978-4-9905958-0-7 C3051

Migration of Radioactive Materials through Porous Media: Theory and a Solution for an Unsteady State Problem

Hamza K.I., Civil Engineering Department, Faculty of Engineering, Fayoum University, Fayoum, Egypt

ABSTRACT: Groundwater constitutes a major natural resource for freshwater supply. Transport of pollutants in porous media is subjected to different processes; they can sorbed onto the surface on the mineral, sorbed by organic carbon, undergo chemical reactions …etc. The flow of water is under hydraulic gradient, while transport of solute ions is under concentration gradient. In this paper, a mathematical development of a two-dimensional numerical model to simulate density-dependent leachate migration of radioactive materials in a leaky aquifer system is presented. Various transport processes such as advection, dispersion, diffusion, sorption and retardation with the concept of reference density are considered. The model can be used to predict the equiconcentration and equipotentional lines for various cases with different hydraulic and geometric parameters. The influence of the half live time of leaching materials on plume migration is examined, and results show that decreased of pollutant transport will occur under such conditions.

Keywords: Concentration, Density-dependent, Migration, Reactive, Reference density, half live time.

1. INTRODUCTION

Groundwater contamination includes any deterioration of the quality of the underground water. Methods of contamination to pertinent of the physical environment include wastewater disposal practices (both at land surface or deep formulation or aquifers). Land disposal sites of solid waste can be sources of groundwater contamination because of leachate generated by water percolating through the bodies of refuse, or by refuse materials decomposition.

Many materials dissolve in water, whereas others may be carried with the water in suspension. Reactive materials released into groundwater, in connection with nuclear power productions, by accidents, from landfills, or from nuclear waste repositories, pose a pollution problem that requires special attention.

Many studies have been conducted to simulate flow and pollution of groundwater. Reference [16] applied the finite element theory to approximate the nonlinear equations for velocity and pressure. The solution for concentration was used to update the density profile assumed in the flow equation and a new estimate for velocity and pressure was obtained. Iteration between the flow and transport equations was preformed until convergence was achieved.

Reference [21] employed a two-dimensional hybrid finite-element method and integrated finite-difference method to simulate the fluid-density dependent saturated or unsaturated groundwater flow and transport of solute in porous media (pressure based model). The simulation may be employed for areal and cross-sectional modeling of saturated groundwater flow systems, and for cross-sectional modeling of unsaturated flows.

Reference [6] simulated the evolution of the Chloride plume at an abandoned landfill in a shallow sand aquifer at the Canandian Force Base Borden, Ontario. A high- resolution grid was used to obtain an accurate simulation and a consistent flow field. The simulation was nonunique to some extent because a longitudinal spreading similar to that produced by the longitudinal dispersivity may also be produced by an increasing source function.

Reference [9] developed a two-dimensional finite element model for solute transport in leaky aquifer systems to simulate pollution migration in heterogeneous anisotropic porous media. The model was capable of predicting pollutant migration in leaky aquifers under steady and transient flow conditions with point and/or line source of pollutions. Reference [7] derived an analytical solution for the advection-dispersion equation with rate-limited desorption and first-order decay. The model equations represent one-dimensional, steady state groundwater flow through homogeneous isotropic aquifer. It was found that the larger desorption and decay rates and the smaller the distribution coefficient, the faster the rate of contaminant removal from the aqueous and sorbed phases.

Reference [17] presented a two-dimensional cross sectional finite difference model which can simulate density dependent pollutant migration from dumped disposal sites in multilayer leaky aquifers using the concept of reference density. They found that high equiconcentration lines did not move significantly after 2000 days, while low equiconcentration lines continued to advance with time.

Reference [18] developed a numerical model to study the mixed convection processes below a saline disposal basin located between a recharge and discharge zone. Numerical simulations are performed in cross-section using the 2-D density dependent model SUTRA [21]. Both homogenous and heterogeneous aquifer systems were studied and the effects of anisotropy were considered. The movement of salt to the underlying groundwater system from Lake Tutchwwop, a saline disposal complex in north-central Victoria was modeled in cross-section [19]. Density-dependent flow was simulated due to salinity contrast between the hypersaline bain waters and the regional groundwater.

Reference [10] introduces a two-dimensional cross section finite difference model, which can simulate scale dependent dispersion for the transport of the dissolved substances in groundwater aquifers. The dispersivity coefficient was taken to

be dependent on the travel distance of the solute from an input source.
A series of column experiments was undertaken to explore the influence of colloid input concentration (2, 1, 0.5, and 0.25 times a reference concentration, colloid size (negtivelly changed 3.2 and 1.0 μm quartz sands) on transport and deposition [5]. They found that for a given input concentration, decreasing the sand size and increasing the colloid size resulted in increased mass retention in the sand near the column inlet and lower relative concentrations in the effluent. A finite-element code COMSOL was used by [8] to model dispersion in two-dimensional artificial packed beds. The steady state incompressible Navier-stokes equation along with the convection diffusion equation was solved to obtain an interesting analysis of the effect of porosity and heterogeneity on dispersion coefficient.
In this paper, the finite element model of incompressible fluid flow in porous media developed by [11] was extended to model dispersive of reactive materials in a leaky aquifer system. The flow and transport equations are coupled, using the reference density approach with the elimination of the intermediate step of calculating velocities. The developed model is a two-dimensional fluid density-dependent finite element model for reactive materials (2D-FERM). Leachate migration of reactive materials in leaky aquifer system is simulated. Governing equations, including flow and transport equations, are coupled using a new approach with replacing fluids with different densities by hypothetical fluid (reference density approach). The dispersion coefficients are considered to be velocity dependent, and their components values are updated in each iteration. The (2D-FERM) model is then used to predict the shape of equiconcentration and equipotential lines in leaky aquifer system.

2. VARIABLE CONTAMINATION PATTERNS

The complex variable to be considered in evaluating the potential of contamination to spread in groundwater calls for selected concepts. A usual concept centers on two opposing tendencies of the movement of contaminants in the ground. One is the tendency of the contaminant to move with groundwater, and the other is for contaminates to be retarded or degraded by mechanisms of attenuation. Different contaminants attenuate to varying degrees by: (1) dilution with water; (2) decay with time or some other degradation mechanism, and (3) sorption on the earth materials [1]. For example, chlorides may attenuate only by dilution, but certain radioactive nuclides attenuate effectively by a combination of dilution, decay with time, and sorption on clays [2].
Questions center on the extent to which one can rely on sorption, dilution, and/or decay to allow contaminants to disappear or reach a harmless levels some distance from points of water use. In some cases contaminates do not extended more than a few meters from waste sites, whereas in other cases, they may extend for long distances in the direction of groundwater flow.

3. REFERENCE DENSITY APPROACH

The density of water in natural aquifer systems ranges from 998.2 Kg/m^3 at 20^{o}C for freshwater to greater than 1,345 Kg/m^3 as reported for the salado brine of New Mexico. Reference [12] set a classification for saline water, ranging from slightly saline to brine. He divided the salty water into four groups on the basis of total dissolved solids as slightly saline, moderately saline, very saline, and brine.
The density of the flowing groundwater varies according to its concentration. As such, piezometric heads at various nodes would not indicate the actual pressures unless associated with indigenous water density. On the other hand, ignoring the effect of density variation may result into false or misleading conclusions, with specific reference to sensitive problems where small variations in fluid density affect the flow and transport regimes considerably. Leaching from dumped disposal sites is a good example for such cases. In such situations, it is more convenient to employ the concept of reference density. Various densities are unified to the freshwater density and equivalent freshwater heads are evaluated. Finally, one reference density for the whole domain is defined and all the piezometric heads are evaluated in terms of freshwater heads.

4. GOVERNING EQUATIONS

The governing equations describing the radioactive materials transport in groundwater under unsteady state conditions are as in [4]:
1. The general Darcy equation for groundwater flow:

$$q = -\frac{k}{\mu}(\nabla P + \rho g\,\nabla Z) \qquad (1)$$

where,
q is the specific discharge vector (LT^{-1}),
k is the intrinsic permeability tensor (L^2),
μ is the dynamic viscosity (ML^{-1}T^{-1}),
P is the pressure (M L^{-1}T^{-2}),
ρ_f is the fresh water (reference) density (ML^{-3}),
ρ is the fluid density (ML^{-3}),
g is the gravitational acceleration (LT^{-2}),
Z is a space coordinates (L).

Substitution of $h = \frac{p}{\rho_f g} + z$, $K = \frac{k \rho_f g}{\mu}$, and $\rho_r = \frac{\rho}{\rho_f} - 1$ into "(1)," yields

$$q = -K(\nabla h + \rho_r \nabla Z) \qquad (2)$$

where,
h is the equivalent hydraulic head (L),
K is the hydraulic conductivity tensor (LT^{-1}),
ρ_r is the relative density (L^0).

2. The mass balance equation for the fluid can be written as:

$$\frac{\partial n\rho}{\partial t} = -\nabla.\rho q + R\,\rho_{re} \qquad (3)$$

where,

n is the effective porosity (L^o),

t is the time (t),

R is a recharge rate per unit volume of aquifer medium (T^{-1}),

ρ_{re} is the density of the recharge water (ML^{-3}).

3. The hydrodynamic dispersion equation or the mass balance equation for the pollutant can be written as:

$$\frac{\partial nC}{\partial t} = -\nabla.(Cq - nD_h.\nabla C) + (1-n)K_d\,\rho_b\frac{\partial C}{\partial t} - (1-n)\rho_b K_s F - n\lambda C + RC_r \qquad (4)$$

where,

C is the pollutant concentration (ML^{-3}),

nC is the quantity of the pollutant increased within a control box (ML^{-3}),

D_h is the hydrodynamic dispersion coefficient (L^2T^{-1}) which can be calculated as in [3]:

$$D_{xx} = \alpha_l\frac{V_x^2}{|V|} + \alpha_t\frac{V_z^2}{|V|} + D_d^*,$$

$$D_{zz} = \alpha_t\frac{V_X^2}{|V|} + \alpha_l\frac{V_z^2}{|V|} + D_d^*, \text{ and}$$

$$D_{xz} = D_{zx} = (\alpha_l - \alpha_t)\frac{V_xV_z}{|V|} \qquad (5)$$

where,

α_l is a longitudinal dispersivity (L),

α_t is a transversal dispersivity (L),

V_x is pore-velocity in x direction (LT^{-1}),

V_z is pore-velocity in z direction (LT^{-1}),

$|V|$ is magnitude of the resultant velocity (LT^{-1}),

D_d^* is the coefficient of molecular diffusion (L^2T^{-1}),

C_{re} is the recharged water concentration (ML^{-3}),

K_d is the distribution coefficient,

ρ_b is the bulk density of the porous medium (ML^{-3}),

K_s is the degradation rate constant of the water (T^{-1}),

λ is equal to 1/T, where T is the half live time (T).

F is the mass of pollutant on the solid per unit mass of bulk dry porous medium which is defined as $F = K_d C$.

4. A constitutive equation relating fluid density to contaminant concentration can be expressed as:

$$\rho = \rho_o + a(C - C_o) \qquad (6)$$

where,

C_o is the reference concentration (ML^{-3}),

a is a known constant (L^o) called coefficient of fluid density change which can be calculated as:

$$a = \frac{\rho_{max} - \rho_o}{C_{max} - C_o} \qquad (7)$$

where, ρ_{max} is the maximum water density corresponding to the maximum concentration C_{max}.

5. BOUNDARY CONDITIONS

Consider the idealized leaky aquifer domain as shown in Fig. 1. A line source of pollutant, represent the dumped disposal site, is placed at the bottom of the aquitard. The aquifer is recharged by freshwater entering at the left boundary B4 and by downward leakage through the upper boundary B1, where the water table is higher than the aquifer piezometric head. Water, entering into the system, flows out of the system through the right boundary B2.

The downward flux through upper boundary B1 is governed by Darcy's equation. The concentration below the pollutant source will be set equal to the source concentration, C_{max}. Solute particles are assumed to move only vertically through the aquitard. Along the remaining part of boundary, the concentration is set equal to freshwater concentration. The right boundary B2 allows for advective transport of pollutant ions only, i.e., the concentration gradient is set equal to zero. This boundary is subject to hydrostatic pressure distribution. The pressure distribution along B2 is not constant but varies as contaminant concentration increases when the leachate plume approaches boundary. The piezometric head at this boundary is transformed into equivalent freshwater head, and its value is updated as the simulation proceeds according to the new concentrations at this boundary. The bottom boundary B3 is impermeable, i.e., the normal flux through it for both fluid and pollutant ions are equal to zero. The left boundary B4 is located where the concentration is assumed to be constant and equal to freshwater concentration, C_f. The pressure along this boundary is hydrostatic. Therefore, the boundary conditions can be written as follow:

- On the top boundary B1

$$q_z = K_z^{\backslash}\left[\frac{W.T. - P.H.}{b} + \rho_r\right]$$

$C = C_{max}$ below the pollution source,

$C = C_f$ otherwise

where, $K_z^{\backslash}$ is the vertical hydraulic conductivity for the aquitard (m/s), b is the aquitard thickness (m), W.T. is free water table elevation (m), P.H. is the piezometric head throughout the aquifer, and ρ_r is the relative density.

- On the right boundary B2

$h = h_s$

$$\frac{\partial C}{\partial x} = 0$$

where, h_s is the piezometric head at the right boundary.

- On the bottom boundary B3

$q_z = 0$

$$\frac{\partial C}{\partial z} = 0$$

- On the left boundary B4

$h = h_o$

$C = C_f$

where, ho is the piezometric head at the left boundary.

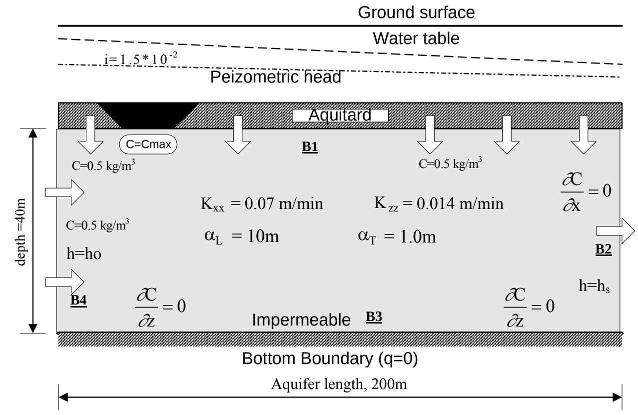

Figure 1: Idealized leaky aquifer system and boundary conditions

6. MATHEMATICAL DERIVATION OF THE (2D-FERM) MODEL

Because the contaminant transport problem is a nonlinear one, and the velocity field and hence the dispersion coefficients depend upon concentration distribution, Galerkin's procedure is well suited for the problem [15]. The Galerkin finite element technique is therefore adopted. Triangular elements are used with linear interpolation functions, $<N> = <N_i\ N_j\ N_k>$.

Application of the Galerkin technique with Gauss's theorem to the fluid mass balance equation in two-dimensions yields:

$$\int_{A^e} \frac{\partial < N >^T}{\partial X} \left[\frac{1}{nq}(\rho q_x)\right] dA^e + \int_{A^e} \frac{\partial < N >^T}{\partial z} \left[\frac{1}{nq}(\rho q_z)\right] dA^e$$
$$+ \int_{A^e} < N >^T \frac{\partial C}{\partial t} = \int_{L^e} < N >^T \frac{(\rho q_n)}{nq} dL^e \quad (8)$$

Similarly, the two dimensional hydrodynamic dispersion equation can be written as:

$$\int_{A^e} \frac{\partial < N >^T}{\partial X} \frac{1}{nR} \left[n\left(D_{xx}\frac{\partial C}{\partial x} + D_{xz}\frac{\partial C}{\partial z}\right) - q_x C\right] dA^e$$
$$+ \int_{A^e} \frac{\partial < N >^T}{\partial z} \frac{1}{nR} \left[n\left(D_{xz}\frac{\partial C}{\partial x} + D_{zz}\frac{\partial C}{\partial z}\right) - q_z C\right] dA^e$$
$$- \int_{A^e} < N >^T \frac{(1-n)\,\rho_b\, K_s\, K_d\, C}{nR} dA^e - \int_{A^e} < N >^T \frac{n\,\lambda\, C}{nR} dA^e$$
$$+ \int_{A^e} < N >^T \frac{\partial C}{\partial t} dA^e = \int_{L^e} \frac{< N >^T}{nR} (n\, D_h\, \Delta C - qC)_n\, dL^e \quad (9)$$

Equations (8) and (9) can be written symbolically in the matrix form as:

$$[F_h]\{h^{k+1}\} = \{A\} \quad (10)$$

$$[F_C]\{C^{k+1}\} = \{B\} \quad (11)$$

Where $[F_h]$ and $[F_C]$ are the coefficient matrices, $\{h^{k+1}\}$ and $\{C^{k+1}\}$ are the unknown hydraulic heads and concentrations at the new time level k+1, k is the time level, and {A} and {B} are the known vectors which contain the effect of boundaries. Equations (10) and (11) constitute the 2D-FERM model.

7. MODEL APPLICATIONS

To determine the shape of equiconcentration and equipotential lines in a leaky aquifer, the model is applied to the system shown in Fig.1. A study domain, 200x40m in area and overlain by a semi-pervious layer 5m thick, was chosen. The aquifer hydraulic conductivities in the x and z directions, K_{xx} and K_{zz}, were taken as 0.07 m/min and 0.014 m/min, respectively. The vertical hydraulic conductivity of the upper semi-pervious layer, $K_z^{\backslash}$, was set to equal $2.8\text{x}10^{-3}$ m/min. The slope of the hydraulic gradient is assumed to be $1.5\text{x}10^{-2}$. Reference [20] indicated that values of longitudinal dispersivity, α_L, which have been reported in field investigations range from 6.0m to 150.0m. Lateral dispersivity, α_T, has usually been taken to be 10-30% of the longitudinal values [14]. Owing to the scale behavior of dispersion, no generally valid values for longitudinal dispersivities can be given [13]. Values between 0.1 and 500.0m can be found in the literature. The Longitudinal and transversal dispersivities, α_L and α_T, are taken as 1.0m and 0.1m, respectively. The effect of molecular diffusion was neglected. Model parameters are given in Table 1.

Table 1: Model parameters for the study case

Freshwater density, ρ =1000 kg/m^3
Groundwater concentration, C_f = 5000 mg/l
Contaminate concentration, C_{max} = 500000 mg/l
Dynamic viscosity, μ =0.001 kg/(m.s)
Maximum density of recharge water, ρ_{max} =1035 kg/m^3
Coefficient of fluid density change, a = 0.707
Water compressibility = $4.5\text{x}10^{-10}$ Pa^{-1}
Soil compressibility = $1.0\text{x}10^{-8}$ Pa^{-1}
Porosity, n = 0.3
Hydraulic conductivity, K_{xx}= 0.07 m/min
Hydraulic conductivity, K_{zz}= 0.014 m/min
Longitudinal dispersivity, α_L = 10.0m
Transversal dispersivity, α_T = 1.0m
Acceleration due to gravity, g = 9.81 m/s^2
Molecular diffusivity, D^o = 0.0

A contaminant source is provided at the bottom of the aquitard in the range of 16<x<48m. Below the pollution source, the concentration was set equal to the maximum concentration, C_{max}. Otherwise, the concentration was set equal to the freshwater concentration; C_f. The effective porosity of 0.3 was employed throughout the aquifer. In the aquitard it was set to equal 0.4. A Dirichet type boundary condition was used at the top and the left boundaries, while a Neumann type boundary condition was assumed at the remaining boundaries. The application of Neumann type boundary condition for transport at an exit boundary is acceptable only when the plume meets the boundary at right angle; this condition is satisfied here, as the exit boundary is located away from the contamination source. Flow, through the upper semi-confining layer (aquitard) was simulated by the one-dimensional form of Darcy's equation. The hydraulic gradient through the aquitard was calculated by

dividing the difference between the water table above the aquitard and the piezometric head below it by its thickness. The study domain was represented by finite-element grid has 390 nodes, defining 696 triangular elements, on a rectangular spacing. The time step was constant at 20 days. Figure 1 presents the study domain and hydraulic parameters of this run . The convergence criterion, ε, was set equal to $1x10^{-3}$. The matrix solver does not need iterative procedures because it is solved by a modified Gauss elimination method, and incorporating the banded matrix to reduced the storage space.
The simulation was carried out after 5 and 10 years of continuous leaching. Fig. 2-a and Fig. 2-b present the corresponding equiconcentration and equipotential lines, respectively. Equiconcentration line 0.3 of the maximum concentration (50.0 kg/m^3) advanced 85m measured from the left boundary after 5 years of leaching while equiconcentration line 0.1 advanced 119m, and reached a maximum depth of about 22m after the same period of time as shown in Fig. 2-a. After 10 years of continuous leaching as shown in Fig. 2-b, equiconcentration line 0.3 advanced 116m from the left boundary, while equiconcentration line 0.1 traveled a distance of 176m and reached a maximum depth of about 30m.
The freshwater recharge from the left and top boundaries mixes with denser polluted water before discharging from the right boundary. The bottom boundary represents no-flow boundary. The aquifer, initially, was assumed to contain freshwater, therefore contour lines of equivalent freshwater head were vertical and orthogonal to the top and bottom boundaries with equal distances for the equal head intervals, as shown near the right boundary (Fig. 2-a).
Transient and steady states distributions of equivalent freshwater heads were obtained by simulating the coupled flow and solute transport using the developed model. Contours of equivalent freshwater heads were distorted, as shown in Figs. 2-a, and b, except in the right part of the domain where its pollutant concentration was relatively low. In the upper left side, where the pollutant source was placed and the fluid densities were high, values of the equivalent freshwater head was also high. It was noticed that the effect of pollutant concentration on the fluid density was considerable and increased with time.

Reactive materials are defined with their half live times (time at which the materials loss 50% of their concentration). The developed model was used to simulate behavior of these materials with a half live time of 2000 days. The hydraulic and geometric parameters were kept the same as in the previous case. Fig. 3-a, and Fig. 3-b present the shape of equiconcentration lines after 5 and 10 years, respectively. Equiconcentration line 0.1 advanced 67m, and reached a maximum depth of about 10.5m after 5 years of leaching, as shown in Fig. 3-a. After 10 years, as shown in Fig. 3-b, equiconcentration line 0.3 advanced 68m beyond from the left boundary, while equiconcentration line 0.1 advanced about 89m and reached a maximum depth of about 15.5m.
It was found that higher equiconcentration lines (0.7 and 0.9 of maximum concentration) reach the steady state condition earlier than the low equiconcentration one (0.1 and 0.3 relative concentration). In case of reactive materials the plume occupied smaller area than the non-reactive materials.

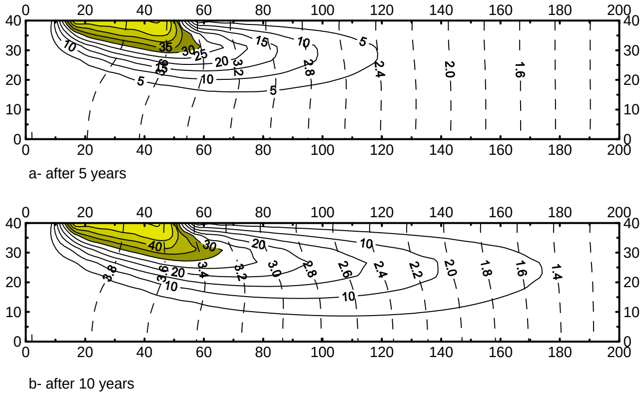

Figure 2: Equiconcentration and equipotential lines (without radioactive materials)

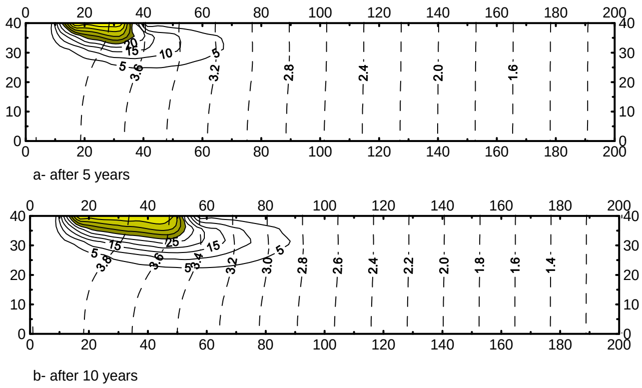

Figure 3: Equiconcentration and equipotential lines (with radioactive materials)

8. CONCLUSIONS

Transport phenomenon in groundwater involves several processes which are driven by density variation, convection and dispersion. The flow of water in the aquifer is under hydraulic gradient, while the transport of solute ions is under concentration gradient. The dependency of the dispersion coefficients, in the hydrodynamic dispersion equation, on the velocity of fluid and concentration distribution makes the problem nonlinear, and hence requires numerical solutions.
Mathematical development of a two-dimensional finite-element model to simulate density dependent leachate migration of reactive materials in leaky aquifers is presented. The concept of reference density, which employed in the model, increased accuracy (over pressure based models) in representation of the transport process. The flow and transport equations are coupled with the elimination of the intermediate step of calculating velocities. The numerical scheme is stable and convergent.

The applied model is stable and the proposed numerical scheme converges under different flow and boundary conditions. It was found that low equiconcentration lines (0.1 and 0.3) continued to move for a long period of time after the pollution source was placed, while higher equiconcentration lines attained the steady state after about earlier than the low equiconcentration lines in most of the cases. Overlapping the equiconcentration lines on the equipotential lines indicated that high concentrations were associated with higher potential heads. The half live time for leachting materials is the most important parameter such that it predominates the migration process.

9. REFERENCES

[1] Anderson, J. R., and Dornbush, J. N., "Influence of sanitary on groundwater quality", Journal of American Water Works Association AWWA, Vol. 59, April 1967.

[2] Bagchi, A., "Design of natural alternation landfill", Journal of Environmental Engineering Division, ASCE, Vol. 109, No. 4, Aug., 1983.

[3] Bear, J., "Hydraulics of Groundwater", New York, McGraw-Hill-Book Co., 1979.

[4] Bear, J., and Verruijt, A., "Modeling Groundwater Flow and Pollution", Redial Publishing Company, Dordrecht, Holland, 1987.

[5] Bradford, S.A. and Bettahar, M, "Concentration Dependent Transport of Colloids in Saturated Porous Media", Journal of Hydrology, 82: Issue 1-2, 99-117, 2006.

[6] Frind, E.O. and Hokkanen, G.E., "Simulation of the Bordon plume using the alternating direction Galerkin technique", Water Resources Research, 23(5): 918-930, 1987.

[7] Fry, V.A., Istok, J.D., and Guenther, R.B., "An analytical solution to the solute transport equation with rate-limited desorption and decay", Water Resources Research 29(9) 3201-3208, 1993.

[8] Garmeh, G. Johns, R.T., and Lake, L.W., "Pore-scale Simulation of Dispersion in porous Media", SPE J. Dec., 559-567, 2009.

[9] Hamza, K.I., "A two-dimensional finite element model for solute transport in groundwater", M. Sc. thesis, Faculty of Engineering, Cairo University, Egypt, 1993.

[10] Hamza, K.I., "Scale-dependent dispersion model in porous media", Proceedings of the International Conference on Geoenvironment 2000 (ICG200), Sultan Qaboos University, Muscat, Sultanate of Oman, March, 4-7, 2000.

[11] Hamza, K.I. "A Two-dimensional finite element model for pollutant transport out of dumped disposal sites: (2D-FEPT)", Dirasat, an International Journal for Engineering Science, University of Jordan, Jordan, 31(1): 82-96, April 2004.

[12] Krieger, R. A., Hatchett, J.L. and Poole, J.F., "Preliminary Survey ofthe Saline-Water Resources of the United States", U.S. Geological Survey, Water Supply Paper no. 1374, 1957, 172 pp.

[13] Kinzelbach, W., "Groundwater Modeling". Elsevier, New York, 333 PP, 1986.

[14] Pickens, F.J. and Grisak, E.G., "Scale-dependent dispersion in stratified granular aquifers", Water Resources Research, 17 (4): 1191-121, 1980.

[15] Pinder, G.F., "A Galerkin finite-element simulation of groundwater contamination on long island", Water Resources Research, 9(6): 1657-1669, 1973.

[16] Segol, G., Pinder, G.F., and Gray, W.G., "A Galerkin finite element technique for calculating the transient position of the saltwater front", Water Resources. Research, 11(2): 343-347, 1975.

[17] Sherif, M.M., and Singh, V.P., "Leachate migration in multilayer aquifers", Proceedings of the International Conference, "Transport and Reactive Processes in Aquifers", Rotterdam, Netherlands, 1994.

[18] Simmons, C.T. and Narayan, K.A., "Mixed convection processes below a saline disposal basin", Journal of Hydrology, 194: 263-285, 1997.

[19] Simmons, C.T. and Narayan, K.A., "Modeling density-dependent flow and solute transport at the Lake Tutchewop saline disposal complex, Victoria", Journal of Hydrology, 206: 219-236, 1998.

[20] Volker, R.E. and Rushton, K.R., "An assessment of the importance of some parameters for seawater intrusion in aquifers and a comparison of dispersive and sharp-interface modeling approaches", Journal of Hydrology, 56: 239-250, 1982.

[21] Voss, C.I., "SUTRA- A Finite Element Simulation Model for Saturated-Unsaturated Fluid Density Dependent Groundwater Flow with Energy Transport", U.S. Geol. Surv., Water Resources. Invest. Rep., 84-4262, 406pp, 1984.

First International Conference on Geotechnique, Construction Materials and Environment, Mie, Japan, Nov.21-23, 2011, ISBN: 978-4-9905958-0-7 C3051

Fundamental Study on Ecosystem Support Canal using Porous Concrete

Masuma Yoshihiro, Graduate School of Integrated Arts and Sciences, Kochi University

Hasegawa Yuki, Graduate School of Integrated Arts and Sciences, Kochi University

MD.ROKUNUZZAMAN, Graduate School of Integrated Arts and Sciences, Kochi University

Yamada Toshio, Water Environment Section, Kaihatsu Concrete Co., Ltd.

Kassai Hirofumi, Water Environment Section, Kaihatsu Concrete Co., Ltd.

Sato Shushi, Faculty of Agriculture, Kochi University

ABSTRACT: This research aimed to enhance the compressive strength of porous concrete as well as to develop the porous concrete that can support and improve the ecosystem preservation by itself. Several porous concrete specimens were prepared for the measurement of mechanical properties. As a result, it was confirmed that the radius of coarse aggregate affected significantly to mechanical properties of porous concrete under the same unit weight of cement. It was also revealed that strengths at age 28 days were stable despite of different sizes of coarse aggregate. The bio-adhesive ability of porous concrete specimen was evaluated against water bugs and adhesive algae. Every porous concrete specimen was soaked in same environmental condition at the bottom of actual concrete canal. From this experiment, it was confirmed that preference environment for some specific species of water bugs are possible to be supplied when the porosity and the size of coarse aggregate would be adjusted.

Keywords: Porous Concrete, Ecosystem Support, Biodiversity, Bio-adhesive

1. INTRODUCTION

In Japan, previous improvement programs on agricultural facilities were mostly executed focused to the functions of water use and structural safety, and they were not considered enough against nature and ecosystem. As a result, various ecosystems were lost or damaged seriously, it is necessary to make actions for conservation and recovery of ecosystem now a day.

From such background, Land Improvement Act was revised in 2001 in Japan. In the law above, "consideration to make the harmony with environment" was provided as the principle of every project. However, existing technology that has such consideration against environment is not established completely including the evaluation of its effect yet. It is necessary to analysis from the viewpoint of general judgment containing the quantitative evaluation on the influence to ecosystem.

Concrete materials are mainly used for the agricultural hydraulic structures such as canal and head works due to their low permeability and structural safety. On the other hand, there are a lot of studies concerns to porous concrete that gives newly function such as environmental consideration. Up to now, porous concrete becomes to be famous material for revetment of river bank in order to support the recovery of vegetation at the river embankment. However, this material has not used frequently because of its low strength and durability.

This research aimed to expand the utilization of porous concrete that has both high strength as well as the special function that is called as "bio-adhesive ability". The former point, to improve the compressive strength of porous concrete as high as structural material, was examined from the viewpoint of strengthening. The latter point, to observe the relationship between the different types of porous concrete and inhabited creatures, was examined from the viewpoint of colonized living things.

2. METHOD AND PROCEDURE

2.1 Evaluation on Compressive Strength of Porous Concrete

Cylindrical porous concrete specimens were placed using different grain size of coarse aggregate; No.5 (13 – 20mm), No.6 (5 – 13mm) and No.7 (2.5 – 5mm). Fundamental mixture proportions of porous concrete are shown in Table I. Amount of mortar was adjusted to be constant in order to examine the influence of grain size of coarse aggregate to compressive strength. Using the biaxial forcing mixer, concrete was mixed under dry condition for 1 minute and additional 3 minutes after adding the water. Water amount was finely adjusted with confirming the adhered mortar condition around the aggregate particles. Porosity of porous concrete were varied with changing the packing amount into mold, and 6 types of porous concrete were placed in this experiment. Three numbers of cylindrical specimens for each type were tested for measuring the compressive strength. Handy vibrator was used for the compaction. Standard curing, sunk in 20 ℃ water, was applied and measured the compressive strength at age 14 and 28 days.

Here describes the measurement method on porosity of porous concrete as follows. Firstly, volume of specimen (V_1) was measured. The specimen was soaked into water for 24 hours in order to absorb the water, measure the weight in water (W_1). Secondly, the specimen was put out to atmosphere where the temperature and relative humidity were controlled into constant condition of 20℃ and 60%, respectively. Wait until the weight into stable. Furthermore, set the same specimen for 24 hours in atmosphere under the same temperature and relative humidity condition was measured as W_2. Total porosity was calculated using (1) is shown below;

$$\text{Total porosity } At\ (\%) = (1-((W_2-W_1)/\rho)/V_1) \times 100 \qquad (1)$$

where ρ is the density of water.

2.2 Summary on Bio-adhesive Characteristic Experiment of Porous Concrete

Porous concrete specimens sizing of 230mm length × 230mm width × 60mm height for bio-adhesive characteristic experiment were made by same process described at previous section. Details of the specimens are shown in Table II. All the specimens were set in actual open channel for agricultural placed in Kochi University, and were studied for the evaluation of bio-adhesive ability such as number of water bugs and amount of attached algae. Concrete specimens were mentioned to be sunk in the water all the time. Water bugs settled in porous concrete specimen were collected on the tray fulfilled with water. Gathered water bugs were investigated as follows; identify the species using technical book of water creatures [1]-[4], divided into each species and counted their number. However, bugs less than 1mm of body length were excluded to count.

Algae were gathered with shaving from one surface (downstream side) of specimen. Suspensions were collected, filtrated with glass filter and measured the wet weight, dry weight and chlorophyll a (call "chl.a" here after). Dry weight was measured after the treatment of drying 24 hours with 60℃. Absorptiometer was utilized for the measurement of chl.a.

3 RESULTS AND DISCUSSION

3.1 Compressive Strength of Porous Concrete

Relation between compressive strength and porosity was shown in Fig.1. Under the same porosity condition, compressive strength was higher as the larger particle diameter of coarse aggregate. It was considered that specific surface of coarse aggregate was decreased when using the larger sizes of coarse aggregate, and the thickness of mortar binder surrounding the coarse aggregate particle in unit volume became increased. Moreover, relationship between compressive strength and porosity made with coarse aggregate No.5 and No.6 showed similar value and tendency despite the thickness of mortar between coarse aggregate No.5 and No.6 were different. It was revealed that developed

Table I Fundamental Mixture Proportions of Porous Concrete

Grain size	No.5	No.6	No.7
Particle diameter (mm)	13 - 20	5 - 13	2.5 - 5
Cement (kg/m^3)	221	221	221
Admixture (kg/m^3)	39	39	39
Sand (kg/m^3)	233	233	233
Gravel (kg/m^3)	1548	1540	1537
Water (kg/m^3)	57	57	57
Porous diameter (mm)	2.0 - 14.6	0.8 - 9.5	0.4 - 3.7

Table II Porous Concrete Specimens detail

Crashed stone size	Particle diameter (mm)	At (%)
No.5	13~20	22.3
		29.4
No.6	5~13	22.2
		25.7
No.7	2.5~5	18.9
		20.5
		22.7

compressive strength would be stable and enough when the

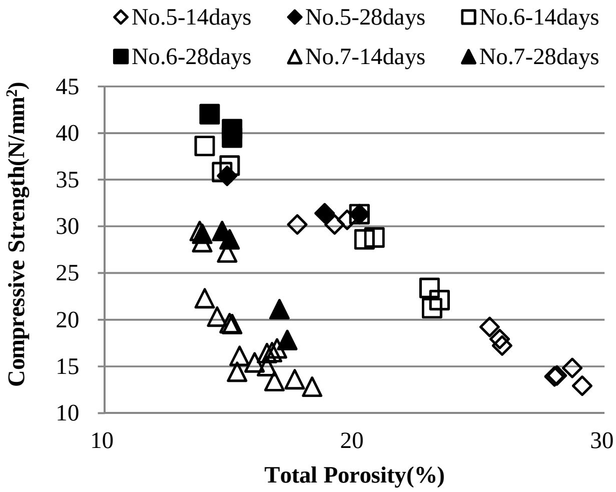

Fig.1 Relation of Compressive Strength and Porosity

thickness of mortar was insured to be standardized.

On the contrary, compressive strength was declined as the increment of porosity of porous concrete. The main cause of this result was occurred due to the reduction of cement amount in unit weight. Comparing the strength development of age from 14 to 28 days, each increment of compressive strength were evaluated as 7.9% in No.5, 10.0% in No.6, and 2.5% in No.7. From this result, it was clarified that strength development of No.7 was smaller than those of No.5 and No.6. It meant that strength of No.7 was close to stable condition while it was age 14 days.

All the porous concrete could gain higher than 20 N/mm^2, as high and stable as normal concrete. It meant that porous concrete could be useful for the member of structure if the relationship between compressive strength and porosity was clarified enough.

3.2 Bio-adhesive Characteristic Experiment of Porous Concrete

3.2.1 Species Number and Population Size of Water Bugs

Generic names and species gathered from porous concrete specimen were shown in Table III. Twenty three of generic names and twenty six of species were confirmed, and the dominant species was *Asellus hilgendorfi*. Second, third and fourth dominants were *Ectopria*, *Stenelmis* and *Ephemeroptera*, respectively. The change with time of population size gathered from the specimen was shown in Fig.2 a). The larger population size was confirmed when size of coarse aggregate was bigger. It was considered that various lengths of body of water bugs were easy to enter to the void of porous concrete surface when the diameter of porosity was large enough. On the other hand, there was a sharp drop in population size of water bugs during May 21st of 2010 to July 18th of 2010. Several times of torrential rainfall were generated before July 18th of 2010, the water bugs were estimated to be washed away or evaded due to violent water flow and muddy water.

Change with time of species number in each specimen was shown in Fig. 2 b). Lots of species were confirmed and variation of population sizes was larger at the beginning of the experiment. However, species number was getting stable as the time went on. It meant that water bugs suited to the environment established with porous concrete were selected with the time passage, and particular species were becoming to be the dominant. Judging from the investigation result in 2011 and 2010, different species were confirmed. Then it was suggested that observed species in the past data would be happened to reach to the specimen from upstream. Further observation will be necessary whether existing species as a dominant were climax species or not. Much population of *Ephemeroptera* and *Ptilodactylidae* were confirmed in the

Table III Species List of Water Bugs

Order	Scientific Name
Ephemeroptera	*Baetis* sp.
	Ecdyonurus sp.
	Cinygmula sp.
	Ephacerella longicaudata
	Uracanthella punctisetae
	Caenis sp.
Trichoptera	*Leptocerus* sp.
	Hydroptila sp.
	Molanna moesta
	Ecnomidae sp.
	Nippoberaea gracilis
	Goerodes sp.
	Goera japonica
Plecoptera	*Nemoura* sp.
Diptera	*Conchapelopia japonica*
	Psychodidae sp.
	Chironomus samoensis
Hemiptera	*Aphelocheirus vittatus*
	Aphelocheirus nawae
Coleoptera	*Ectopria opaca*
	Ectopria opaca
	stenelmis sp.
	stenelmis sp.
Odonata	*Calopterygidae* sp.
	Gomphidae sp.
Isopoda	*Asellus hilgendorfi*

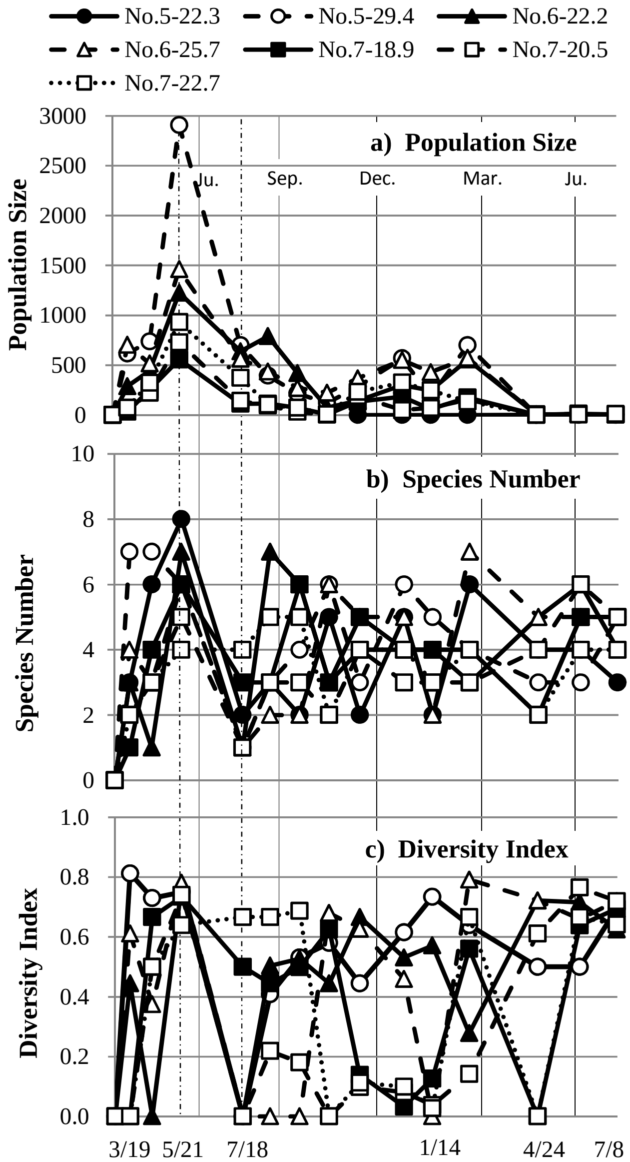

Fig.2 Change with Time of Result for Water Bugs

porous concrete of No.5 and No.7, respectively. Moreover, specimen of lower porosity showed highly number of each species. Therefore, it was suggested that coarse aggregate of No.5 and No.7 might create the preference environment for *Ephemeroptera* and *Ptilodactylidae*, respectively.

Diversity index for each types of specimen was calculated. Simposon's formula shown at (2) was chosen to get the diversity index. This formula aims to see the balance between the species number and population size of biotic community, shown as follows;

$$D = 1 - \sum_{i=1}^{S} P_i^2 \quad (2)$$

where P_i is proportion of individual number of species (i) to all individual number of communities, and S is the species number of objective community. If one species was extremely superior to other species, diversity index would be very small. In this study, the population size of *Asellus hilgendorfi* was too much, therefore, this dominant was excluded from the calculation of this index. Change with time of diversity index was shown in Fig. 2 c). Diversity indexes were varied in all specimens during the initial period of this experiment. However, they came to be stable and similar value in all specimens since May of 2011. We confirmed in 2011 that some newly species were colonized that made permanent resident. That could be one reason of stabilization of that index described above.

3.2.2 Bio-adhesion of Algae Grew on the Porous Concrete

Adhesion of algae was confirmed in all porous concrete specimens, the name of species was shown in Table IV. Identified algae were mostly the same kind of diatom (*Bacillariophyceae*), maximum species number was obtained at 22.7% porosity of porous concrete using coarse aggregate No.7. Change with time of quantity variation of chl.a and dry weight was shown in Fig. 3 a) and b), respectively. Quantity of chl.a and dry weight showed same tendency with the results of water bugs, these values came to be stable as time passing by. There was no relationship between the quantity of chl.a and dry weight; calculated correlation coefficient was almost zero. Here showed the result of relationship between time and ratio (quantity of chl.a / dry weight) in Fig. 3 c). Assuming that quantity of chl.a was an indicator of living algae as well as dry weight was that of both living and dead algae, variation of this ratio was very large in most of all specimens. However, in 18.9% porosity of porous concrete specimen using coarse aggregate No.7, this ratio was stable comparatively. It was suggested that this type of porous concrete would be good adhesion ability against diatom. The reason was considered that smaller particles of aggregate gave larger specific surface and possible to give better condition for the growth of this algae.

4 CONCLUSION

The results in this study were concluded as follows;

1) Larger particle lead higher compressive strength when each porous concrete was used same amount of cement.

2) Higher porosity of porous concrete generated its compressive strength to be lower when each porous concrete was used same amount of cement.

Table IV Species List of Algae

class	Scientific Name
Bacillariophyceae	*Coscinodiscus* sp.
	Melosira sp.
	Cyclotella meneghiniana
	Hysrosera whampoensis
	synedra sp.
	Fragilaria sp.
	Naviculaceae sp.
	Cymbella tumida
	Gomphonema sphaerophorum
	Rhoicosphenia abbreviata
	Surirella sp.
	Nitzschia trybionella
	Bacillaria paradoxa
	Cocconeis placentula
Chlorophyceae	*Cladophora* sp.

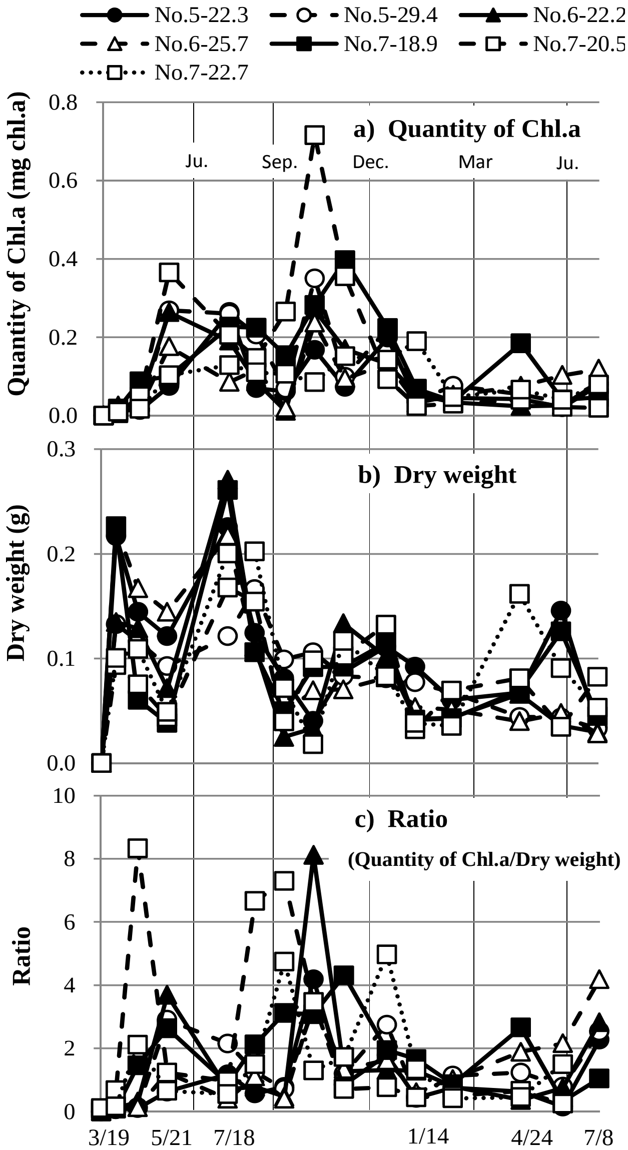

Fig.3 Change with Time of Result for Algae

Strength of porous concrete was close to stable condition while it was age 28 days.
4) Possibility that coarse aggregate of No.5 and No.7 might create the preference environment for *Ephemeroptera* and *Ptilodactylidae*, respectively.
5) Possibility that 18.9% porosity of porous concrete using coarse aggregate No.7 would be good adhesion ability against diatom.

Therefore, porous concrete was appeared to be possible using structure that has enough strength, various pores and holes of pores. In addition to, it is considered that the preference environment for specific creatures is able to be created for adjustment of aggregate size and porosity. However, benthos was main target at this experiment. So, this study will be necessary to pay attention to higher order stage of creature for evaluating ecosystem support.

5 ACKNOWLEDMENT

We are grateful to Mr. Mima Masanori, Mr. Masatsugu Naoki, Mr. Ishikawa Naoya, Mr.Sakai Takehiro, Ms. Matsuoka Mayu, Mr. Haga Masahiro and members of Water Use and Environmental Engineering laboratory in Kochi University, for their kindly cooperation on experiment.

6 REFERENCES

[1] Kawai T, Tanida K, Aquatic insects of Japan : manual with keys and illustrations, Tokaidaigakusyuppankai, 2005..
[2] Maruyama H, Takai M, Tanida K, Illustrated book of aquatic insect larva. Zenkokunosonkyoikukyokai, 2000.
[3] Yamagishi T, Introduction to the Freshwater Algae, UchidaRokakuho, 1999.
[4] Hori T, An illustrated atlas of the life history of algae, vol. 1, Uchidarokakuho. 1994.

First International Conference on Geotechnique, Construction Materials and Environment, Mie, Japan, Nov.21-23, 2011, ISBN: 978-4-9905958-0-7

Alternative Employment of Crushed Shell Particles in Capillary Barrier of Soil

Nakafusa S., Japan Atomic Power Company, Tokyo, Japan
Kobayashi K., Tobishima Corporation, Chiba, Japan
Morii T., Niigata University, Niigata, Japan
Nishimura T., Ashikaga Institute of Technology, Tochigi, Japan

ABSTRACT: Capillary barrier is a tilting soil layer system which is composed of a finer soil layer underlain by a coarser soil layer. Water which infiltrates into the soil is suspended just above an interface between the soil layers and flows downward along the interface, with the result that a vertical movement of water into deeper soil layers below the interface stops within some length along the interface. As the water diversion in the capillary barrier is brought out by a sharp contrast in water retention capacity between the finer and coarser soils, any material which can provide the sharp contrast in water retention capacity can be alternatively employed in the capillary barrier system. A coarse-grained material of crushed shell particles is selected as an alternative candidate for the lower layer soil of the capillary barrier, and its water retention capacity is measured to examine a practical effectiveness of the crushed shell particles in the capillary barrier system.

Keywords: Capillary barrier, Water retention capacity, Crushed shell particles, Fishery byproduct waste

1. INTRODUCTION

Capillary barrier is a tilting soil layer system which is composed of a finer soil layer underlain by a coarser soil layer. Water which infiltrates into the soil is suspended just above an interface between the soil layers and flows downward along the interface, with the result that a vertical movement of water into deeper soil layers below the interface stops within some length along the interface [1]-[5]. Because of this excellent diversion of infiltration water, the capillary barrier of soil has been successfully employed in a top cover of waste landfill. The capillary barrier of soil can be also adopted as effective measures for slope protection of natural soil or earth embankment [4]- [6]. As the water diversion in the capillary barrier is brought out by a sharp contrast in water retention capacity between the finer and coarser soils, any material which can provide the sharp contrast in water retention capacity can be alternatively employed in the capillary barrier system.

In the study, a coarse-grained material of crushed shell particles is selected as an alternative candidate for the lower layer soil of the capillary barrier, and its water retention capacity is measured to investigate a practical effectiveness of the crushed shell particle. There are two reasons for selecting the crushed shell particles: the coarse-grained material of crushed shell particles is environmentally friendly one same as gravel which is usually employed in the capillary barrier of soil; a better employment of shell will offer some possible solution to a recycling of fishery byproduct waste.

Firstly geotechnical features of the capillary barrier of soil are briefly introduced, and some study conducted to determine the length of water diversion of the capillary barrier of soil is given in the paper. Then the crushed shell particles are sieved into three groups, 9.5-4.75 mm, 4.75-2.0 mm and ones smaller than 2.0 mm in particle diameter, and their soil-water characteristic curves (SWCC) are measured by a pressure membrane method using a SWCC apparatus. An effect of mass densification of the crushed shell particles caused by effective confining pressure on the SWCC is also examined. In constructing the capillary barrier system, an inclusion of the finer soil particles in the upper layer into the coarser soil in the lower layer should be avoided in order to keep the sharp contrast in water retention capacity between the finer and coarser soils. To find a solution to this problem in constructing the capillary barrier system, lastly, a degree of the inclusion of sand particles into the crushed shell particles is investigated by tapping a soil column in the laboratory.

2. WATER DIVERGENCE BY CAPILLARY BARRIER

2.1 Soil Water Movement in Capillary Barrier System

In the capillary barrier system, water which infiltrates into the soil is suspended just above the interface between the soil layers due to a physical difference in the water retention characteristics of the finer and coarser soils. When the interface between soils has an inclination as shown schematically in Fig. 1, the suspended water flows downward along the interface. This water flow downward along the interface between soil layers gradually accumulates its mass of flow due to continuous infiltration from the soil surface, and, at some length along the interface, water percolates

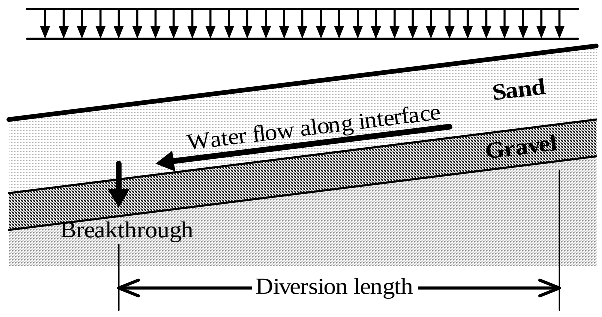

Fig. 1 Schematic diagram of water flow downward along an interface between soil layers in capillary barrier system.

vertically into the coarser soil layer. A horizontal distance from the beginning of water flow to this percolation or breakthrough into the coarser soil layer is called a divergence length, and is one of important design parameters to determine a structural configuration of capillary barrier system and to select a suitable combination of the finer and coarser soils [1], [2]. In this chapter the divergence length of capillary barrier is investigated based on a field measurement of soil moisture in slope soil [6] and a series of laboratory soil box test.

2.2 Field Experiments to Determine Water Divergence

The capillary barrier soil was constructed in the natural sand slope as shown in Fig. 2, and volumetric moisture content in the soil layers was measured together with rainfall intensity for about four months. Dry densities of the sand layer and gravel layer were 1.38 and 1.67 Mg/m^3, respectively. A completely-permeable polypropylene net was placed over the compacted gravel layer so that the finer sand particles did not fall into nor clog void formed in the gravel layer. Inclination of the interface between the sand and gravel layers was 19.7 degrees in average. Fig. 3 shows grain size distribution curves of sand and gravel. The sand is classified into "Sand" with less-5 % fine and coarse fractions; the gravel, commercially available, is siliceous with mean particle size of 5 to 6 mm. Relationships of negative pore pressure h with the volumetric moisture content of the sand and gravel were measured by a laboratory soil column test, and are plotted in Fig. 4. The SWCC's in the figure are determined using van Genuchten

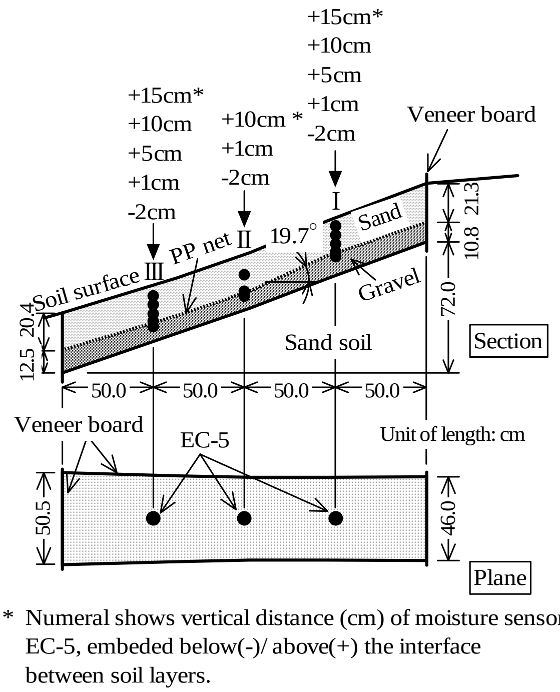

* Numeral shows vertical distance (cm) of moisture sensor, EC-5, embeded below(-)/ above(+) the interface between soil layers.

Fig. 2 Configuration of capillary barrier soil constructed in the natural sand slope. Numerals show vertical distances (cm) of the moisture sensor, EC-5, embedded below (-)/ above (+) the interface between sand and gravel.

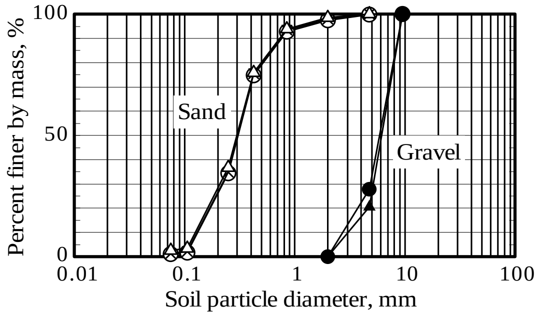

Fig. 3 Grain size distributions of sand and gravel employed in the capillary barrier soil slope.

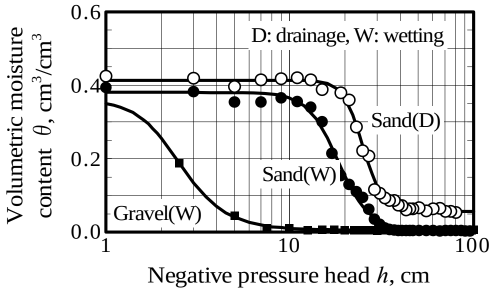

Fig. 4 Soil-water characteristic curves of sand and gravel measured by laboratory soil column tests and estimated by using van Genuchten equation.

equation [8]. It is found in Fig. 4 that an air entry value of the sand, h_a, is about 16 cm, and a water entry value of gravel, h_w, about 1 cm.

The volumetric moisture contents measured in the sand and gravel layers are given in Fig. 5. The upper, central and lower figures show the measurement at the position Ⅰ, Ⅱ and Ⅲ in the slope shown in Fig. 2, respectively. The precipitation is given by an inverse bar with the right vertical axis of the figure. It's found that the volumetric moisture content measured in the sand layer increases rapidly after rainfall and then decreases slowly, in a successive way from shallow to deep depth in the soil. But in the gravel layer, as opposed to the sand layer, there can be seen only very small or negligible change after rainfall event. It may be understood that this is exactly due to the water diversion by the capillary barrier for long time duration.

2.3 Estimation of Length of Water Divergence

Comparing the upper figure with the central and lower ones in Fig. 5, there can be notified some difference in the soil moisture changes measured in the gravel layer (denoted by "-2" in Fig. 5 which shows the depth of the moisture sensor embedded as shown in Fig. 2). That is, although the low moisture content of soil is maintained in the upper position of the slope during four-month measurement, the soil moisture contents measured in the central and lower positions of the slope increase with a small amount immediately after rainfall. It may be possible to think that this difference in the soil moisture changes indicates the percolation or breakthrough of the water flow along the interface into the gravel layers.

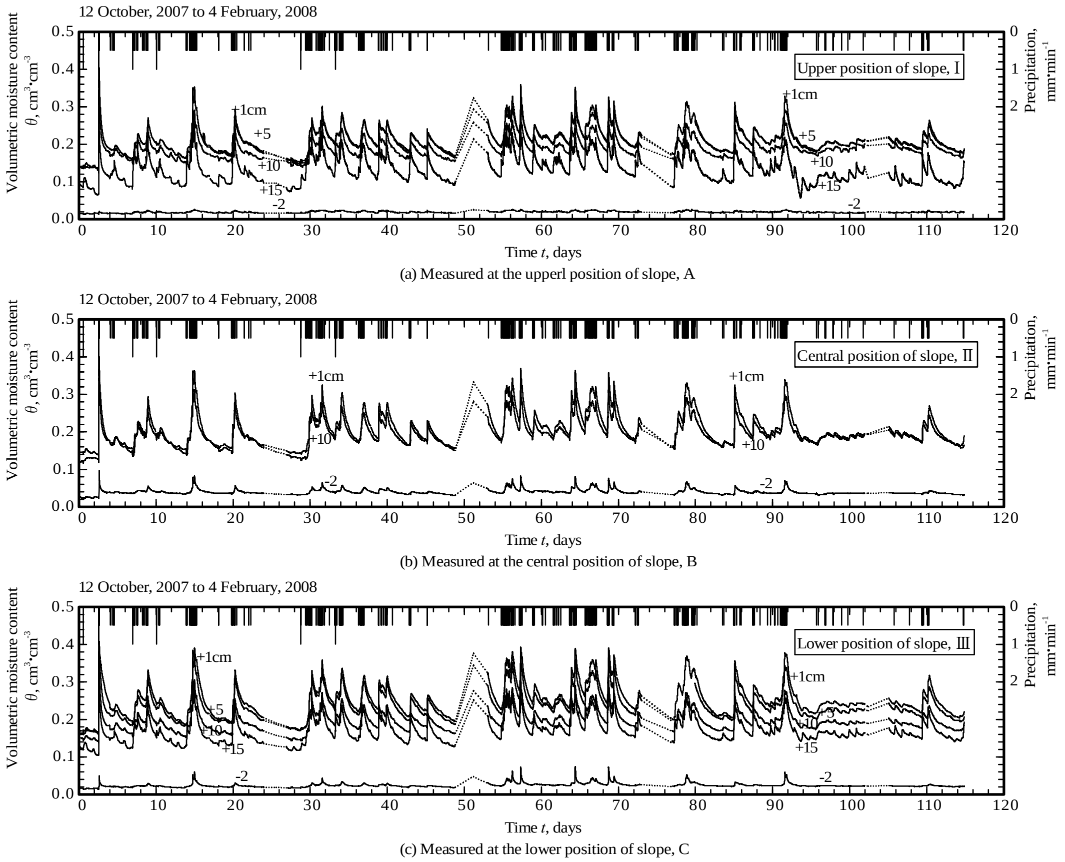

Fig. 5 Volumetric moisture content in the sand and gravel layers and the precipitation measured during 12 October, 2007 to 4 February, 2008. Note that numerals show the vertical distances of the moisture sensor, EC-5, embedded below (-)/ above (+) the interface between soil layers in cm. Some dotted lines are interpolated linearly because of lack of data.

Based on this observation and taking account of the location of measurement points shown in Fig. 2, the divergence length of the capillary barrier is estimated to be around 100 cm.

Some equations have been proposed to estimate the divergence length of capillary barrier by several researchers such as Ross [1], Kung [9], and Steenhuis, Parlange and Kung [7]. Among these, the equation by Steenhuis, Parlange and Kung is effectively adaptable [2], [3]. In the case where an infiltration rate, q, is much smaller than a saturated hydraulic conductivity of sand (the upper finer soil), K_s, the equation of the divergence length, L, is given by

$$L \le \frac{K_s}{q}\tan\phi\left[\alpha^{-1} + \left(h_a - h_w\right)\right] \qquad (1)$$

where φ is the slope angle of the interface, h_a and h_w are the air entry value of sand and the water entry value of gravel, respectively, as explained in 2.2. α is an exponential constant describing the relationship between the negative pressure head, h, and an unsaturated hydraulic conductivity, K, of sand near saturation.

Estimating K from the soil characteristic curve of sand in Fig. 4 by van Genuchten equation and plotting K with h, α near saturation can be estimated to be 0.084 cm^{-1} [6]. Introducing K_s=8.2×10^{-3} cm/s which was determined by a laboratory permeability test, φ=19.7 degrees given in Fig. 2, h_a=16 cm and h_w=1 cm determined in Fig. 4 into (1) and assuming that q is approximately equal to an average value of precipitation, 0.5 mm/min, then about 99 cm is calculated as a value of L. This L corresponds fairly well to the horizontal length of the slope from the most upper position to the central position Ⅱ where the soil moisture was measured, which is around 100 cm as explained in the preceding paragraph. Fig. 6 shows this good comparison of the diversion length observed in the field with one estimated by (1) by using a double circle.

In order to observe directly the breakthrough of water flow along the interface and to determine the diversion length, a series of the laboratory soil box test was carried out. The soil box with an acrylic front panel, 100 cm in length, 50 cm in height and 5cm in depth, was placed on a horizontal floor and gravel was compacted into the layer of 10 cm thickness, and then the sand into 10 cm thickness above the gravel layer in the soil box. The completely-permeable polypropylene net was placed over the compacted gravel layer as same as in the field experiment. After gauze sheet was spread over the soil surface to protect soil erosion by rainfall droplet, one side of the soil box was lifted so that the interface between sand and gravel layer had the inclination, then rainfall was supplied onto the soil surface. Rainfall was simulated by emitting needles attached to the base plate of water reservoir with constant head of water. To keep the acrylic front panel clean, the emitting needles were placed so that the rainfall droplet

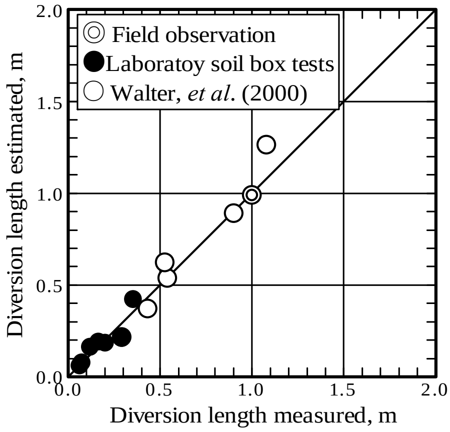

Fig. 6 Comparison of the diversion length measure in the field and the laboratory with one estimated by Steenhuis, Parlange and Kung [7].

did not fall along the front panel. Intensity of rainfall was regulated by adjusting the head of water in the water reservoir.

The divergence lengths which were observed under different condition of the inclination and the rainfall intensity are compared with ones estimated by (1) in Fig. 6 by using black circles. Laboratory results published by Walter, et al. [2] are also plotted by single circles. It may be found that (1) can be well employed to estimate the diversion length of capillary barrier. Because it is known that the diversion length reaches theoretically as long as 5 to 50 m under a proper combination of soil particle size [1], a continuing examination in the range of larger diversion length will be required.

3 ALTERNATIVE EMPLOYMENT OF CRUSHED SHELL PARTICLES

3.1 Water Retention Characteristics of Crushed Shell Particles

As the water diversion in the capillary barrier is brought out by a sharp contrast in water retention capacity between the finer and coarser soils, any material which can provide the sharp contrast in water retention capacity may be alternatively employed in the capillary barrier system. In this chapter, a coarse-grained material of the crushed shell particles is selected as an alternative candidate for the lower layer soil of the capillary barrier, and its water retention capacity is measured to examine a practical effectiveness of the crushed shell particles in the capillary barrier system.

Being washed and oven-dried, the shells of clams, *Meretrix lusoria* and *Ruditapes philippinarum*, were crushed and sieved into three groups, that is A: 9.5-4.75 mm, B: 4.75-2.0 mm and C: ones smaller than 2.0 mm in particle diameter, as shown in Fig. 7. The SWCC's of three groups of the crushed shell particles were measured by the pressure membrane technique using a thin porous membrane [10] in the SWCC apparatus. The crushed shell particles were compacted into a steel mold and saturated with de-aired water. Then a specimen of the crushed shell particles compacted in the steel mold was loaded with matric suction from 0 to about 200 cmH_2O step by step. After this drying process, the matric suction was inversely decreased to 0 cmH_2O to follow a wetting process. During the drying and wetting processes, water mass drained from the specimen and absorbed into the specimen, respectively, was successively measured by using a burette of the SWCC apparatus. The SWCC's of the crushed shell particles A, B and C are given in Fig. 8. Dry densities of the specimen of crushed shell particles A, B and C were 1.00, 1.19 and 1.27 Mg/m^3, respectively. It's found in Fig. 8 that

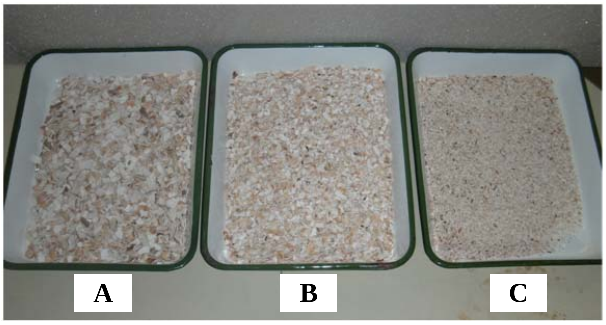

Fig. 7 Crushed shell particles sieved into A: 9.5-4.75 mm, B: 4.75-2.0 mm and C: ones smaller than 2.0 mm in particle diameter.

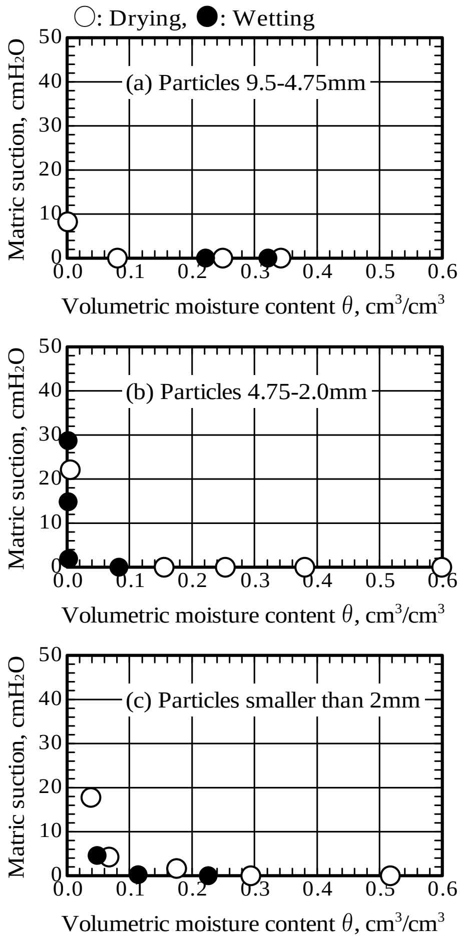

Fig. 8 Water retention characteristics of the crushed shell particles measured by the pressure membrane method.

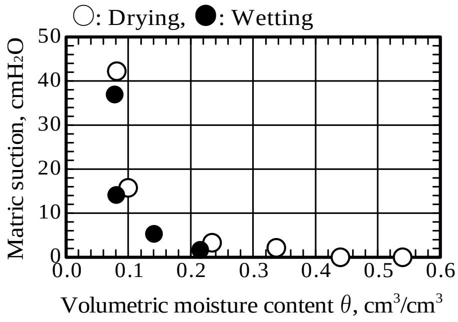

Fig. 9 Water retention characteristics of the crushed shell particles smaller than 2 mm in particle diameter under the confining pressure of 50 kPa. Dry density of the specimen was 1.37 Mg/m^3.

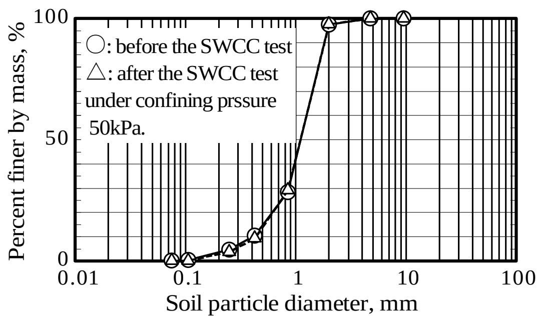

Fig. 10 Grain size distributions of the crushed shell particles smaller than 2 mm in particle diameter measured before and after the SWCC test under the confining pressure of 50 kPa.

the water entry value of the crushed shell particles is sufficiently smaller than that of gravel in Fig. 4 even in the group C, the crushed shell particles smaller than 2 mm in particle diameter. As shown in (1), the smaller the water entry value is, the larger the divergence length becomes. This leads to a practical evaluation that the crushed shell particles can be preferably adopted as the alternative of gravel usually employed in the capillary barrier system.

Because the coarser material is overlain by the finer material in the capillary barrier system, a possible increase of dry density of the coarser layer may cause a change of its water retention characteristics. Fig. 9 shows the SWCC of the crushed shell particles C measured under the confining pressure of 50 kPa which corresponds to about 3 to 4 m thickness of the upper sand layer. There can be seen, in Fig. 9, some small increase of the water entry value. As there is not any change in the grain size distribution of the crushed shell particle before and after the measurement of the SWCC as shown in Fig. 10, it may be thought that the small increases in the water entry value of the crushed shell particles under the confining pressure were caused by mass densification of the specimens. In Fig. 9, the water entry values of the crushed shell particles are found to be about 1 to 2 cm. These are sufficiently small comparatively with that of gravel shown in Fig. 4, which does not reject a practical adoption of the crushed shell particles as the alternative of gravel usually used in the capillary barrier system.

3.2 Sand Particle Inclusion into Crushed Shell Particles

In constructing the capillary barrier system, an inclusion of the finer soil particles in the upper layer into the lower coarser soil layer should be avoided to keep the contrast of water retention characteristic between both the layer soils sharp. Although a chemical sheet was employed for a technical convenience in the field experiment described in the preceding chapter, its use should be avoided in constructing the capillary barrier system from an environmentally-conscious point of view as well as a long-term durability. To investigate the effectiveness of the crushed shell particles as the effective alternatives of gravel, the degree of inclusion of sand particles into the crushed shell particles were examined by a tapping soil column test in the laboratory. Two combinations of gravel overlain by the sand and the crushed shell particles overlain by the sand were tested and compared. The grain size distributions of the sand and gravel are given in Fig. 3. The group C of the crushed shell particles was selected in the test because of the preferable reason mentioned in the preceding section, and its grain size distribution is shown in Fig. 10.

Firstly gravel and the crushed shell particles were poured and lightly compacted into two 1,000cc-graduated glass cylinders 35cm in height and 6.8cm in inner diameter to form the same height of cylindrical volume as shown in Fig. 11(a). Then the sand was poured above the cylindrical volumes of gravel and the crushed shell particles so both the heights of the cylindrical volume in the graduated glass cylinder reach the same. After being placed on a horizontal desk, the graduated glass cylinder was tapped around its base cyclically, continuously and lightly by a wood hammer with horizontal amplitude of 5 cm. Fig. 11(b) shows the cylindrical volumes in the graduated glass cylinders after the cyclic tap 100 times. A higher line given in Fig. 11(b) shows the initial height of the cylindrical volume before the cyclic tap. In the case of gravel overlain by the sand, the left-hand side in Fig. 11(b), a large amount of the sand particles fell down into the lower volume of gravel, and the initial height of the cylindrical volume lowered to a position denoted by a dotted line. Contrary to this, the cylindrical volume of the crushed shell particles overlain by the sand keep its initial height almost the same after the cyclic tap 100 times, and the interface between the sand and the crushed shell particles was clearly observed. Both of these observations suggest less inclusion in the case of the crushed shell particles overlain by the sand than in the case of gravel overlain by the sand. Although the grain size of the crushed shell particles C is smaller than gravel as shown in Fig. 3 and Fig. 10, the water entry value of the crushed shell particles is very small compared to gravel as shown in Fig. 8 and Fig. 9 and, furthermore, small inclusion of the finer soil particles from the upper layer in constructing the capillary barrier system can be well expected as observed above. It may be thought that these special features make the crushed shell particles attractive as the alternative of gravel in the capillary

(a) Gravel (left) and the crushed shell particles (right) poured and lightly compacted in the glass cylinder. A solid line shows the height of both the lower cylindrical volumes.

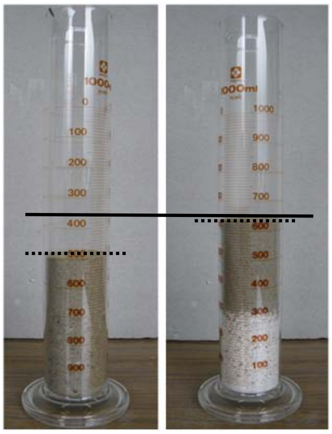

(b) Cylindrical volumes in the glass cylinders after the cyclic tap 100 times. The left-hand side is gravel overlain by sand, and the right-hand side the crushed shell particles overlain by sand. A solid line shows an initial height, and dotted lines show the height after the cyclic tap.

Fig. 11 Inclusion of the sand particles in the upper layer into gravel and the crushed shell particles in the lower layer observed in the tapping soil column test.

barrier system.

4 CONCLUSIONS

Geotechnical features of the capillary barrier of soil were briefly introduced, and the study conducted to determine the length of water diversion of the capillary barrier was summarized in the paper. Soil moisture changes in the gravel layer were well compared those in the sand layer to confirm a practically excellent divergence of infiltration water along the tilting interface between the sand and gravel layers. The divergence length of the water flow along the interface was estimated using the soil properties determined by the laboratory tests and the structural configuration of the capillary barrier of soil. Fairly good correspondence of the divergence length between the observation and the estimation indicated a practical effectiveness of the equation proposed by Steenhuis, Parlange and Kung [7].

Because the coarse-grained material of the crushed shell particles is the environmentally-conscious one same as gravel which is usually employed in the capillary barrier system and a better employment of shells will offer some possible solution to the recycling of fishery byproduct waste, the effectiveness of the crushed shell particles as the alternative of gravel was investigated by a series of the pressure membrane test and the tapping soil column test in the laboratory. It was found that the water entry value of the crushed shell particles smaller than 2.0 mm in particle diameter was extremely small even under the confining pressure. It's also found in a series of the tapping soil column test that the inclusion of the sand particles in the upper layer into the lower layer could be well eliminated by using the crushed shell particles. As the inclusion of the sand particles into the lower coarse-grained layer is one of important problems to be solved in constructing the capillary barrier system, the result of the tapping soil column test will support attractive employment of the crushed shell particles in the capillary barrier system.

5 ACKNOWLEDGMENTS

The present study is supported by the Grant-in-Aids for Scientific Research (B), No. 22380127, and Scientific Research (C), No. 22560507, made by the Ministry of Education, Science, Sports and Culture of Japan.

6 REFERENCES

[1] Ross B., "The diversion capacity of capillary barriers," Water Resources Research, 26(10), 1990, pp. 2625-2629.
[2] Walter M. T., Kim J.-S., Steenhuis T. S., Parlange J.-Y., Heilig A., Braddock R. D., Selker J. S. and Boll J., "Funneled flow mechanisms in a sloping layered soil: Laboratory investigation," Water Resources Research, 36(4), 2000, pp. 841-849.
[3] Smesrud J. K. and Selker J. S., "Effect of soil-particle size contrast on capillary barrier performance," Journal of Geotechnical and Geoenvironmental Engineering, 127(10), 2001, pp. 885-888.
[4] Tami D., Rahardjo H., Leong E.-C. and Fredlund D. G., "A physical model for sloping capillary barriers," Geotechnical Testing Journal, 27(2), 2004, pp. 173-183.
[5] Rahardjo H., Krisdani H. and Leong E.-C. "Application of unsaturated soil mechanics in capillary barrier system," Proceedings of the Third Asian Conference on Unsaturated Soils, Nanjing, China, 2007, pp. 127-137.
[6] Morii T., Takeshita Y., Inoue M. and Matsumoto S., "Alternative measures for soil slope stability using capillary barrier of soil," Proceedings of the Fourth Asia-Pacific Conference on Unsaturated Soils, Newcastle, Australia, 2009, pp. 319-324.
[7] Steenhuis T. S., Parlange J.-Y. and Kung K.-J., "Comment on 'The diversion capacity of capillary barriers' by Benjamin Ross," Water Resources Research, 27(8), 1991, pp. 2155-2156.
[8] Stephens D. B., "Characterizing hydraulic properties," Vadose Zone Hydrology, CRC Press, Inc., 1996, pp. 183-187.
[9] Kung K.-J. S., "Preferential flow in a sandy vadose soil 2, Mechanism and implications," Geoderma, 46, 1990, pp. 59-71.
[10] Nishimura T., Toyota T. and Koseki J., "Evaluation of apparent cohesion of an unsaturated soil," Proceedings of the Fourth Asia-Pacific Conference on Unsaturated Soils, Newcastle, Australia, 2009, pp. 109-114.

A Novel Statistical Approach for Investigating the Significant Factors that Influence the Performance Score of the Turkish Method

Kshama S. Roy, Faculty of Engineering and Applied Science, Memorial University of Newfoundland, Canada

Kamrul Islam, Civil and Environmental Engineering, University of Alberta, Canada

Md. Shams Arafat, Department of Civil Engineering, Bangladesh University of Engineering and Technology, Dhaka, Bangladesh.

ABSTRACT: This article addresses a statistical approach to evaluate the effectiveness of Turkish Method for seismic vulnerability assessment of low to medium rise reinforced concrete frame (RCF) buildings. Design of Experiment (DOE) methodology is extensively used to investigate the most important factors that affect the performance score given by the Turkish method using non-commercial software Design Expert 7.1.3. A 2^{10-3} Fraction Factorial Design is used to determine the factors that significantly influence the performance score. The results show that pounding effect, topographic effect, plan irregularity, area of the ground floor, number of frames in X and Y direction and the interaction between the number of frames in X and Y direction are the most significant factors. Finally a linear regression model is developed for computing the performance score to compare with the performance score given by the Turkish Method.

Keywords: Fractional Factorial Design, DOE, Turkish Method, Seismic Vulnerability.

1. INTRODUCTION

Recent years the world has seen some severe threats imposed by several earthquakes in different countries. Those earthquake events have caused serious disruption in normal way of livings including deaths, economic loses and damage of infrastructures. Most recent earthquakes in Japan (2011), New Zealand (2010, 2011), Mexico (2011), Indonesia (2010, 2011), China (2010), and Haiti (2010) have brought attention to researchers to predict the severity of damage of infrastructures [1]. Many cities of the different countries of the world contain a significant number of vulnerable buildings under considerable seismic risk. Seismic risk assessments of those buildings are gaining more attention to assess correctly the degree of risk to which such critical structures may be subjected to in the event of an earthquake. Various vulnerability assessment procedures are found in the literature while those procedures are based on building plan, foundation, structural system, structural and non-structural components, and structural performance [2-4]. Vulnerability assessment using those procedures show accurate and realistic performance of a building if the building was built according to proper building design code and architectural features. Recent years, Bangladesh has seen the construction boom of multi-storied (mainly 6 stories and above) reinforced concrete frame (RCF) buildings in the capital city of Dhaka where standard building codes are not followed properly. Most of these buildings have open parking space in the ground floors resulting in soft story construction. Some of them have structural irregularities. Seismic vulnerability assessment of existing buildings of Dhaka city is, therefore, of major importance. According to the opinion of a German earthquake expert (Dorka, 2005) of the University of Kassel, Germany, Turkish method of seismic risk assessment may be applicable for a developing country like Bangladesh [5]. The Turkish method, based on the statistical analysis of observed earthquake damages of RCF buildings in Turkey and related building attributes is expected to provide reasonable results for assessment of buildings in Bangladesh [6, 7]. Turkish method is a two level seismic risk assessment procedure considering a significant number of factors [6]. It gives a performance score for each building being assessed considering the factors. But as it uses a lot of empirical equations and tables for determining the score, it is difficult to find the most significant factors that affect the score. The main aim of this study is to develop a statistical approach using Design of Experiment (DOE) methodology to investigate the significant factors of Turkish method described by Ozcebe,G. *et al.* (2003) [6] and to develop a linear regression equation for determining the performance score to compare with the results given by the Turkish Method.

2. TURKISH METHOD

The Turkish seismic vulnerability assessment method for buildings consists of two-level evaluation: (i) level one – walk down evaluation and (ii) level two - measurements at ground level and basement.

The walk down evaluation procedure consists of taking notes of different external features of the building. Buildings are then described as belonging to high risk, moderate risk or low risk. After level 1 survey, buildings falling into the moderate and high risk levels can be subjected to more detailed level 2 surveys to determine their performance scores. Details of Level 1 and Level 2 Survey procedures can be found in [8]-[9]. Once the vulnerability parameters of a building are obtained from two-level surveys and its location is determined, the seismic performance scores for survey levels 1 and 2 are then calculated (Sucuoglu *et al.,* 2003) [10].

A general equation for calculating the seismic performance score (PS) can be formulated as follows:

PS = (Initial Score) - Σ (Vulnerability parameter) x (Vulnerability Score)

The detailed procedures for vulnerability scoring are given by Sucuoglu *et al*., 2003 [10].

3. DOE METHODOLOGY

Design of experiment (DOE) and statistical techniques are widely used to optimize process parameters and to develop a mathematical relationship between the input parameters and the output variables. It involves the study of any given system by a set of independent variables (factors) over a specific region of interest (levels) and provides a straightforward technique with linear graphs to determine the relationship (interactions) between the considered factors, which can be used for practical experimentation. By using DOE, it is possible to investigate the experimental process, to screen the important variables (or factors), to build a mathematical model with prediction and even to optimize the responses where necessary. Among the different techniques in design of experiment method, Fractional factorial design is one of the common DOE techniques for experimentation which is used in this study.

4. EXPERIMENTAL PROCEDURE

4.1 Strategy of experimentation

For performance score of the building, basically Level 2 survey is important as it also incorporates the Level 1 survey result. So to find the factors that affect the performance score, factors for Level 2 survey are chosen as factors for DOE and the response, the performance scores are found by giving the factors as inputs in the program. The levels of the factors are chosen on the basis of the survey that was done in the ward 75, 76 and 77 of the old town of Dhaka city which is the capital of Bangladesh [8]. The runs for the fractional factorial design are run by the Microsoft Excel software program and then the data are analysed by the non-commercial software, Design Expert 7.1.3.

4.2 Factors and Response of Interest and their levels

Ten (10) parameters of the Level 2 survey of Turkish method are used as factors here. The factors are A) Pounding effect, B) Topographic effect, C) Plan irregularity, D) Area of the ground floor, E) Area of the above floor, F) No of frames in X direction, G) No of frames in Y direction, H) Column dimension _x, I) Column dimension _y and J) No of columns. Performance score is used as Response. Among the ten factors A) Pounding effect, B) Topographic effect and C) Plan irregularity are considered as categorical factors and others are considered as numeric factors. For the categorical factors the high and low levels are "yes" and "no" respectively. But for the other factors the levels are shown in Table 1.

4.3 Experimental Design

As ten (10) factors and two levels are considered, 2^{10} = 1024 runs were required if full factorial design was used. So to minimize the runs, 2^{10-3} fractional factorial design is used. So 2^{10-3} =128 runs are required for the experiment for finding the important factors that affect the performance score. Though seven effects are sacrificed for doing the 2^{10-3} fractional factorial design, the main factor and the two factor interactions are kept free from aliases. So it is a Resolution V design that means two factors

Table I: Levels for Numeric Factors

Factor	Name	Low Actual	High Actual	Low Coded	High Coded
D	Area of the ground floor	500 ft^2	3000 ft^2	-1.0	+1.0
E	Area of the above floor	400 ft^2	5000 ft^2	-1.0	+1.0
F	No of frames in X direction	2	20	-1.0	+1.0
G	No of frames in Y direction	2	20	-1.0	+1.0
H	Column dimension _x	3 in	40 in	-1.0	+1.0
I	Column dimension _y	3 in	40 in	-1.0	+1.0
J	No of columns	4	50	-1.0	+1.0

interactions are aliased with three factors interaction

and single factor is aliased with four factors interaction. However "Sparsity of effects" principle is used, so three factors interactions and above are considered negligible

5. ANALYSIS OF RESULTS

After giving the input data in the Design-Expert 7.1.3, the significant effects and interactions are determined by using Effects list and half-normal plot. From the effects list, factors A, B, C, D, F, G and the interaction between F and G are found having maximum contribution. So these are used as models.

5.1 Statistical Testing (ANOVA analysis)

The name ANOVA (Analysis of variance) stems from a partitioning of the total variability in the response variable into components that are consistent with a model for the experiment. ANOVA is used to determine the significant factors and their interaction. The model was checked (checking the assumption of ANOVA, the R^2 and adjusted R^2 and also lack of fit) and found that model with natural log transformation gives the higher R^2 as well as high insignificant lack of fit values. So the results given here are the results obtained after natural log transformation. The ANOVA table is given in the Fig. 1.

The calculation in Fig 1shows that MS (treatment) is larger than MS (residuals) which results a larger F

ANOVA for selected factorial model

Analysis of variance table [Partial sum of squares - Type III]

Source	Sum of Squares	df	Mean Square	F Value	p-value Prob > F	
Model	2.48	7	0.35	185.91	< 0.0001	significant
A-Pounding	*0.080*	*1*	*0.080*	*42.06*	*< 0.0001*	
B-Topographic	*0.059*	*1*	*0.059*	*30.77*	*< 0.0001*	
C-Plan irregul	*0.21*	*1*	*0.21*	*112.78*	*< 0.0001*	
D-Area of grou	*0.18*	*1*	*0.18*	*92.01*	*< 0.0001*	
F-No of frames	*0.86*	*1*	*0.86*	*451.80*	*< 0.0001*	
G-No of frame	*0.86*	*1*	*0.86*	*453.46*	*< 0.0001*	
FG	*0.25*	*1*	*0.25*	*129.00*	*< 0.0001*	
Residual	0.22	115	1.903E-003			
Cor Total	2.70	122				

Std. Dev.	0.044	R-Squared	0.9188
Mean	4.12	Adj R-Squared	0.9139
C.V. %	1.06	Pred R-Squared	0.9072
PRESS	0.25	Adeq Precision	52.918

Fig. 1: ANOVA table for selected factors

value (>> 1) (test static). Moreover p-value is << 0.05 for all the factors (A, B, C, D, F, G) and also for the interaction of F & G. So all the selected effects are highly significant which indicates that the six factors, A, B, C, D, F, G and the interaction FG have the significant effect on the response (performance score).

Again the value of R-squared is 0.9188 which is near to 1. That means the model is good enough and 91.88% of variability of data can be explained by the model. The "Pred R-Squared" of 0.9072 is in reasonable agreement with the "Adj R-Squared" of 0.9139. "Adeq Precision" measures the signal to noise ratio. A ratio greater than 4 is desirable. In this model, the ratio of 52.918 indicates an adequate signal. So, this model can be used to navigate the design space.

5.2 Assumption of ANOVA

a) All samples are random samples from their respective populations.
b) All samples are independent of one another.
c) Departures from group mean are normally distributed for all groups.
d) All groups have equal variance.

5.3 Checking the Adequacy of the Model

5.3.1 Normality and Constant Variance Assumption

To verify the normality assumption, that the error is normally distributed, we can use a normal probability plot of the standardized residuals as shown in the Fig. 2 and Fig. 3.

The normal plot of residuals shows that except some points, most of points follow a straight line which means that the residuals are normally distributed. The points are following an S –shape curve after the transformation. So we have to check the other residual plots. From Fig. 2, the plot of Residuals Vs Predicted looks like well scattered. The randomly scattered plot indicates the constant range of residuals across the graph.

5.3.2 Randomness and Checking for Goodness-of-Fit

In the Fig. 4, most of the data are randomly scattered which indicates the sequence of run was random. In Fig. 5, the plot shows that the data points are split evenly by the 45^0 line means no transformation. It also shows that the model provides accurate values even though most of the Effects are discarded.

5.3.3 Box-Cox plot

In the Box-Cox plot, the current line (blue line) is between the ranges (the red lines) and near the best value line (the green line). This recommends for no transformation. So, we can conclude that the assumptions of ANOVA are satisfied.

5.4 Regression Model (Model Equation)

The model equation is given in terms of coded unit in the Fig7. In the equation 4.12 is the overall average of the effects and 0.026, 0.022, 0.042, 0.038, 0.084, 0.084 and 0.045 are the effects of A, B, C, D, F, G and FG consecutively in terms of coded factors. So from the above equation in coded factors, it can be seen that F and G have the largest effect on performance score.

5.5 Model Graphs and Interpretation

The Fig. 8 shows the effect of F on performance score when all others are fixed at high level. This shows that F has significant effect on score and the score increases gradually as the F increases from 2 to 20. The Fig. 9 shows the effect of G on score when all others are fixed at high level. This shows that G has a significant effect on score. As the G increases from 2 to 20, the score also increases significantly. In both Fig. 10 and Fig. 11, interaction between F and G are showed when all other factors are at low level (Fig. 10) and when all others are at high level (Fig. 11). In the Fig. 14, the score (response) increases slightly with the changes of F from 2 to 20 when G is low (2), the red line. But score increases significantly with the changes of F from 2 to 20 when G is high (20), the black line. Again in the Fig. 11, score increases very slightly with the changes of F from 2 to 20 when G is low (2), the red line. But score increases significantly with the changes of F from 2 to 20 when G is high (20), the black line. Also it is clear that the performance score (response) is also higher when all the other factors are at low level.

The cube plot in Fig 12 also shows that performance score is maximum when A, B, C, D are minimum and F and G are maximum.

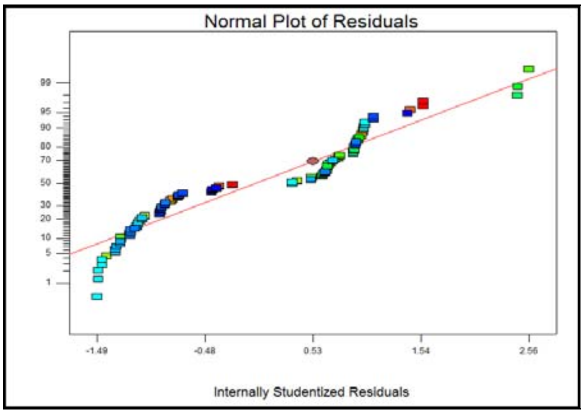

Fig. 2: Normal Plot of Residuals

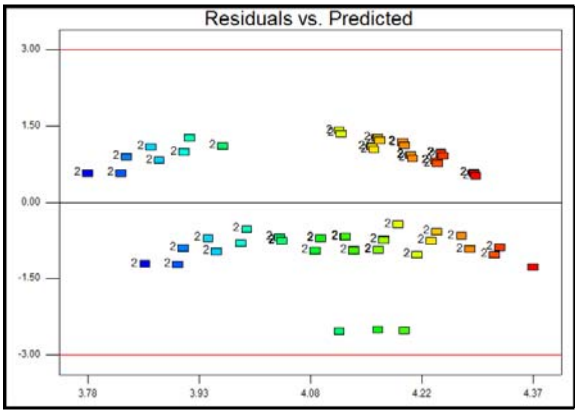

Fig. 3: Residuals vs Predicted

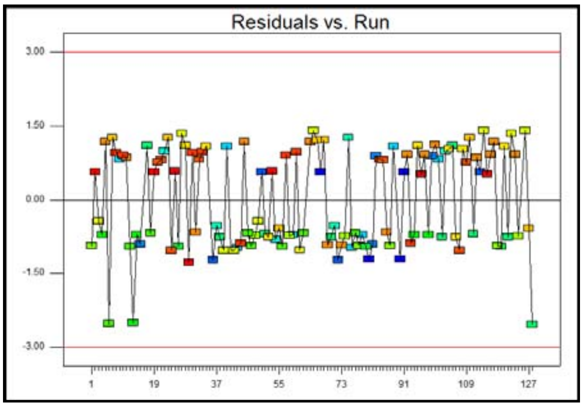

Fig. 4: Residuals vs. Run

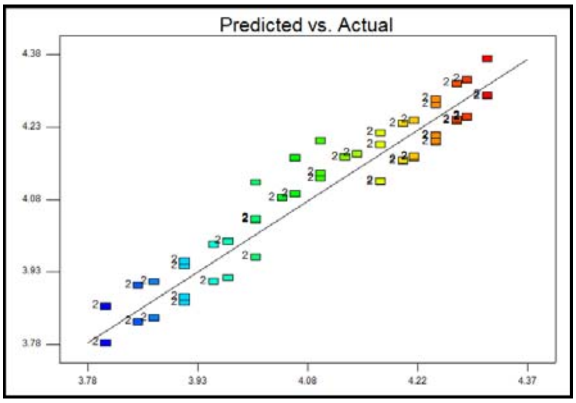

Fig. 5: Predicted vs. Actual

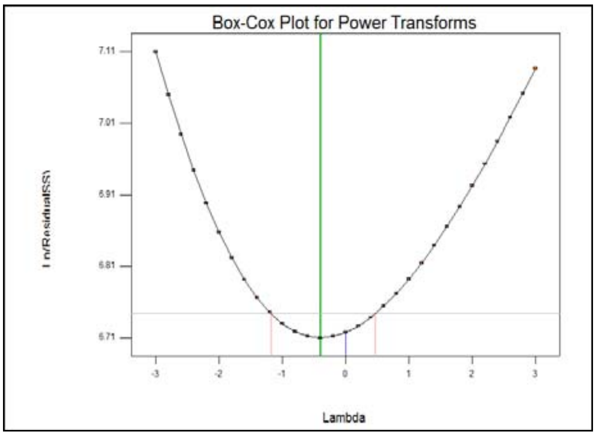

Fig. 6

Final Equation in Terms of Coded Factors:

Ln(Performance score) =
+4.12
-0.026 * A
-0.022 * B
-0.042 * C
-0.038 * D
+0.084 * F
+0.084 * G
-0.045 * F * G

Fig. 7

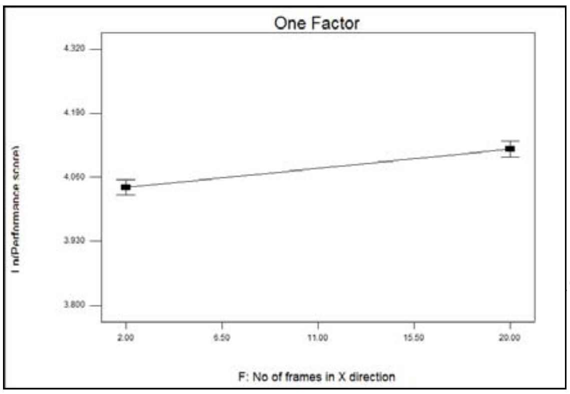

Fig. 8: Box-Cox Plot

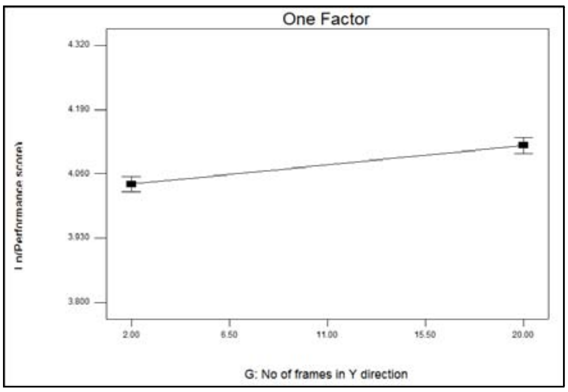

Fig.9: Model equation

6.0 MODEL VALIDATION

After developing an appropriate model, several runs were conducted that were not in the initial runs and each of the time the performance score found by the optimization chart was almost similar to the performance score obtained from the program. This proves that the model developed can give almost same result as the program.

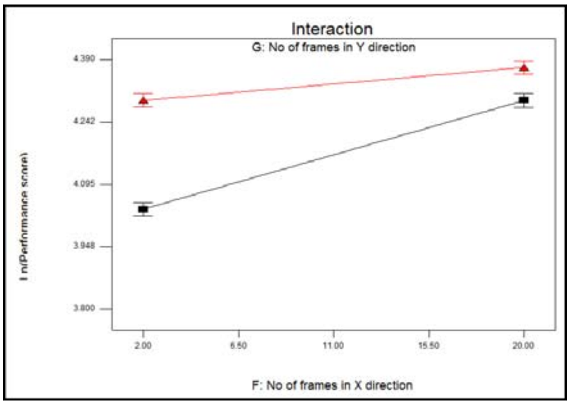

Fig. 10: Interaction graph between F and G

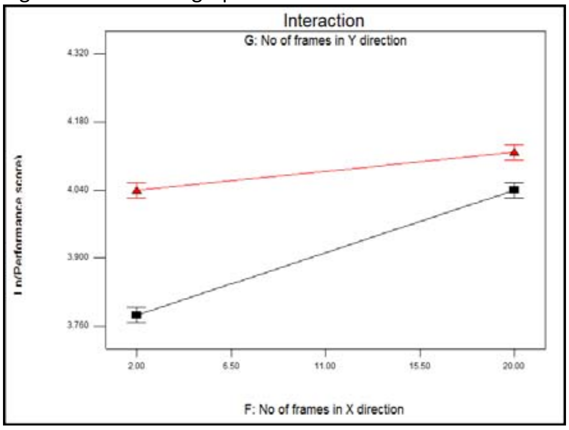

Fig. 11: Interaction graph between F and G

7.0. CONCLUSION

The paper gives a linear model to calculate the performance score of the Turkish method. It also describes clearly that Pounding effect, Topographic effect, Plan irregularity, Area of the ground floor, Number of frames in X and Y direction and the interaction between the number of frames in X and Y directions are the most significant factors for performance score of the Turkish Method. The model equation developed by ANOVA can be used to compare the performance score of the Turkish Method to the score obtained from the program.

The paper also shows the adequacy of the model equation by various diagnostic plots which are all in agreement with the model equation. The R^2 value obtained from the ANOVA result for this model is also good which indicates good fitness of the model. The predicted R^2 and adj R^2 are also found in reasonable agreement. Finally, few test runs are also performed to check the accuracy of the optimum solution and achieved responses are also found to be in good agreement with predicted response.

8. REFERENCES

[1]http://earthquake.usgs.gov/earthquakes/eqinthenews/

[2]Hassan, A.F., Sozen, M.A. Seimic vulnerality assessment of low-rise buildings in region of infrequent earthquake. ACI Structural journal 1997; 94(1): 31-39

[3] Gulkan, P.and Sozen, M.A. Procedure for determining seismic vulnerability of building structures. ACI Structural journal 1997; 96(3): 336-342

[4] Kircher,C. Reitherman, R.K., Whitman, R.V., and Arnold,C. Estimation of Earthquake lossess to buildings. Earthquake Spectra, EERI 1997; 13(4): 703-720

[5] Dorka, U. (2005) *Personal Communication*.

[6] Ozcebe, G., Yucemen, M. S., Aydogan, V., and A. Yakut (2003) "Preliminary Seismic Vulnerability Assessment of Existing Reinforced Concrete Buildings in Turkey- Part I: Statistical Model Based on Structural Characteristics, Seismic Assessment and Rehabilitation of Existing Buildings, NATO Science Series IV/29, 29-42.

[7] Ahmed, M. Z., Islam, M. K., Ahsan, R. and Ozcebe, G (2007) " Seismic Vulnerabilty Assessment Methods: A Possible Application to Bangladesh", First Bangladesh Regional Science Association (BRSA) Conference, Dhaka.

[8] Ahmed, M.Z., Islam, K., Roy, K. S., Arafat, M. S. and Al-Hussaini, T.M. (2010) "Seismic Vulnerability Assessment of RCF Buildings in Dhaka City", in Proc. 3rd Int. Earthquake Symposium, Dhaka, Bangladesh.

[9] Roy, K. S., Islam, K. and Arafat, M. S. (2010) "Seismic Risk Assessment of Existing Low-rise Buildings in Unplanned Urban Regions of Dhaka City" in Proc. 2nd Int. Conf. on Construction in Developing Countries (ICCIDC-2), Cairo, Egypt.

[10] Sucuoglu, H. and Yazgan, U. (2003) "Simple Survey Procedures for Seismic Risk Assessment In Urban Building Stocks", Seismic Assessment and Rehabilitation of Existing Buildings, 97-118, NATO Science Series, IV/29, Editors: S.T. Wasti and G. Ozcebe, Kluwer.

First International Conference on Geotechnique, Construction Materials and Environment, Mie, Japan, Nov.21-23, 2011, ISBN: 978-4-9905958-0-7 C3051

Ultimate Strength and Fatigue Life of Concrete Structural Elements Reinforced with Carbon Fiber Sheet

HIDENORI Tanaka, Environmental and Urban Engineering, Gunma National College of Technology
YUTAKA Toi, Institute of Industrial Science, University of Tokyo

ABSTRACT:Continuum Damage Mechanics(CDM) was applied to evaluate the mechanical behavior of concrete structural elements reinforced with carbon fiber sheet(CFsheet) under quasi-static and cyclic loading. A constitutive equation for elasto-plastic damageable solids is formulated by using Drucker-Prager's equivalent stress and identified by the uniaxial compressive and tensile experimental results for concrete , tensile results for CFsheet. And then finite element analyses are carried out for real-scale cantilever reinforced concrete slabs and concrete blocks with CFsheet. Finally It was concluded that the application of CDM for concrete structural ultimate strength and fatigue durability comparing the experimental data and the calculation by 2-dimensional finite element method (FEM) was very useful.

Keywords: Ultimate strength, Fiber sheet, Fatigue life
Concrete, Damage Mechanics

1. INTRODUCTION

Concrete is a standard brittle material in civil engineering. Reinforced concrete structures with steel bar resisting tension have been used for the infrastructures such as buildings, bridges and tunnels, due to its durability and economy. In recent years, special attention has been paid to CF sheets to resist against earthquake repair damage and prevent separation failure[1]-[3].The CF sheets is of light weight(1/5 of steel),high strength (10 times of steel),high rigidity and high durability as well as easy to construct. Considering future development of CF sheets, it is important to establish the analytical evaluation of the strength and durability of concrete structural members reinforced with CF sheets.

The elasto-plastic model, the smeared crack model and the discrete crack model considering cracking in concrete have been proposed as the analytical model for reinforced concrete (RC) structures[4]. On the other hand, there has been much progress in the application of CDM[5] to metal materials. The mechanical deterioration is represented by the internal state variable D called damage variable and the strain energy release rate Y conjugate with D in damage mechanics. It is expected as a branch of mechanics essentially applicable to fatigue fracture and residual life prediction as well as static and dynamic strength analysis at the material test and structure level. The validity of the application of damage mechanics to concrete structures has been recognized through the researches on reinforced concrete rigid frames[6],short fiber-reinforced concrete[7] and high-strength concrete[8].

The development of the analysis program based on damage mechanics and its experimental validations are conducted in the present study for the purpose of establishing the method for ultimate strength and lifetime evaluation of the concrete structural members reinforced with CFsheet. In the application of damage mechanics models to concrete and the CFsheet, the two-dimensional elasto-plastic damage constitutive equation is formulated by using Drucker-Prager's equivalent stress in order to consider the difference between the tensile and the compressive strength of concrete. The formulated constitutive equation is implemented in the two-dimensional finite element program. The material constants are identified by using the material test results under uniaxial tension and compression and applied to the ultimate strength and fatigue life analysis.

2. FORMULATION AND IDENTIFICATION OF ELASTO-PLASTIC DAMAGE CONSTITUTIVE EQUATION

2.1 Elasto-Plastic Damage Constitutive Equation

The dissipation potential for the growth of plastic strains, which is the sum of the plastic potential and the damage potential is expressed by the following equation:

$$F = F_p\left(\overline{\sigma}, \gamma; D\right) + F_D\left(Y; p, D\right)$$
$$= \overline{\sigma_{eq}} - \gamma - \sigma_y + \frac{S_1}{\left(S_2+1\right)\left(1-D\right)}\left(\frac{Y}{S_1}\right)^{S_2+1} \qquad (1)$$

Where F_p is the potential for the growth of plastic strains,which is a function of the effective stress $\overline{\sigma}$,the plastic hardening parameter γ and the scalar damage variable D . F_D is the potential for the evolution of damage, which is a function of the strain energy release rate Y ,the equivalent plastic strain p and the damage variable D .

In the formulation of the constitutive equation, the yield function is assumed as follows:

$$f = F_p = \overline{\sigma_{eq}} - \gamma - \sigma_y = 0 \qquad (2)$$
$$\overline{\sigma_{eq}} = \sigma_{eq} / \left(1-D\right) \qquad (3)$$
$$\sigma_{eq} = \alpha I_1 + \left(J_2^{'}\right)^{1/2} \qquad (4)$$

Where the following notations are used: $\overline{\sigma_{eq}}$;effective Drucker-Prager's equivalent stress, σ_y ;the yield stress, α ;the material parameter, I_1 ;the first invariant of stress and $J_2^{'}$;the second invariant of deviatoric stresses.

The yield function given in equation(2) is assumed as the plastic potential.

Finally, The relation between the effective stress increment and the strain increment were derived [9],[10]:

$$d\overline{\sigma} = \overline{C} d\varepsilon$$

$$= C\left[1 - \frac{\frac{\partial F_p}{\partial \overline{\sigma}}\left(\frac{\partial F_p}{\partial \overline{\sigma}}\right)^T C}{H + \left(\frac{\partial F_p}{\partial \overline{\sigma}}\right)^T C \frac{\partial F_p}{\partial \overline{\sigma}} - \frac{\overline{\sigma_{eq}}}{1-D}\frac{\partial F_D}{\partial Y}}\right] d\varepsilon \quad (5)$$

Where $\overline{C}$ is the effective stress-strain matrix considering the elasto-plastic damage. The relation between the stress increment and the strain increment is expressed by the following equation:

$$d\sigma = (1-D)d\overline{\sigma} - \overline{\sigma}dD = D_{epd}d\varepsilon \quad (6)$$

Where D_{epd} is the tangential stress-strain matrix considering the elasto-plastic damage, which relates the stress increment with the strain increment.The damage evolution equation as given by the following equation is used in the present study[5].

$$dD = \left(\frac{Y}{S_1}\right)^{S_2} dp \quad (7)$$

Where S_1 and S_2 are the material constants. It is assumed that the damage evolves with an increase of the equivalent plastic strain. The strain energy release rate Y is a function of Young's modulus E and equivalent stress σ_{eq} as expressed by the following equation:

$$Y = \frac{\sigma_{eq}^{\ 2}}{2E(1-D)^2} \quad (8)$$

2.2 Identification of Material Patrameters

The material constants of concrete used in the constitutive equation have been determined as shown in Table 1 by the curve-fitting technique for the uniaxial compressive test results given by displacement measuring method (Fig.1) and tensile results by using strain gauge method. In this study, the plus sign means tensile and minus means compressive respectively. Fig.2 and Fig.3 show the stress-strain curves of compression and tension. In Fig.2, one of the stress-strain curves for experiment sharply dropped after peak. It would be occurred by shear fracture due to eccentric loading after peak. ε_{pd} and D_{cr} in Table 1 are the damage plastic strain threshold and the critical damage at crack initiation respectively. When the equivalent strain exceeds ε_{pd}, the damage evolves according to equation (7). And the damage variable reaches D_{cr} ,the material fractures and the stress is released. The experimental results were shown until the tensile strength in Fig.3. The post peak behavior after tensile strength could not be obtained because of brittle fracture of concrete and strain gauge's breaking.

The material constants of the CFsheet has been determined as shown in Table 2 from the tensile test result given in Fig.4.

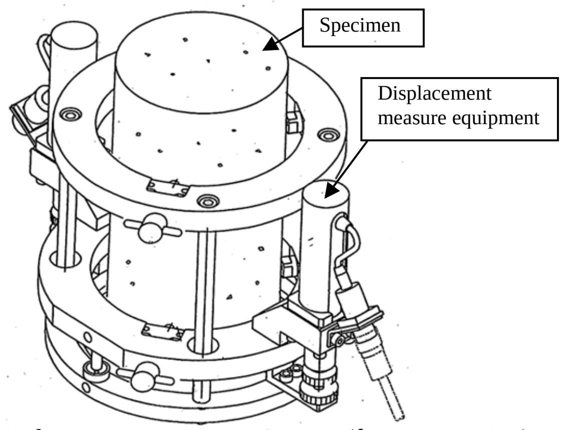

Fig.1 Displacement measure equipment (for compression)

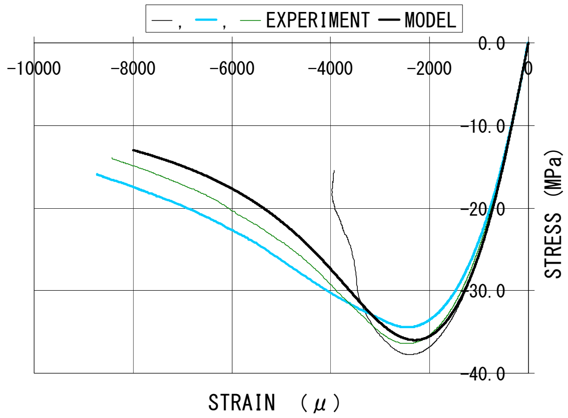

Fig.2 Compressive stress-strain curves for concrete

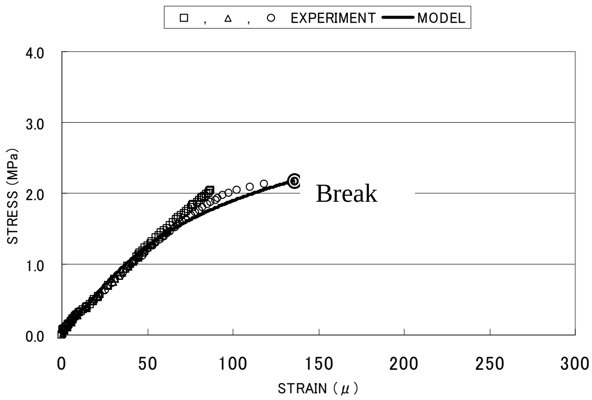

Fig.3 Tensile stress-strain curves for concrete

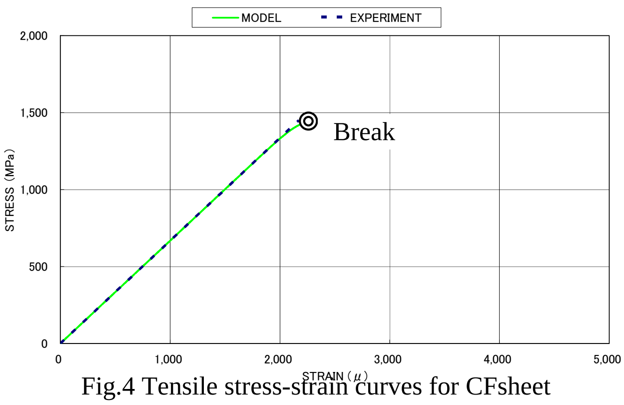

Fig.4 Tensile stress-strain curves for CFsheet

Table 1 Material constants for concrete

E (Young's modulus)	29.7×10^3 MPa
ν (Poisson's ratio)	0.17
α (equivalent stress)	0.72
σ_y (yield stress)	0.75 MPa
K (plastic hardening)	40.0 MPa
n (plastic hardening)	0.215
S_{p1} (damage parameter)	0.215×10^{-3} MPa
S_{p2} (damage parameter)	1.55
ε pd (damage threshold)	0.00
Dcr (critical damage)	2.75×10^{-5}

Table 2 Material constants for CFsheet

E (Young's modulus)	668.0×10^3 MPa
ν (Poisson's ratio)	0.2
α (equivalent stress)	0.0
σ_y (yield stress)	1200.0 MPa
K (plastic hardening)	1950.0 MPa
n (plastic hardening)	0.0955
S_1 (damage parameter)	0.055 MPa
S_2 (damage parameter)	1.755
ε pd (damage threshold)	0.00
Dcr (critical damage)	0.0146

3. STATIC AND CYCLIC LOADING TESTS FOR RC STRUCTURAL MEMBERS

The real size clamped RC Slab structure used in the experiments is schematically shown in Fig.5.

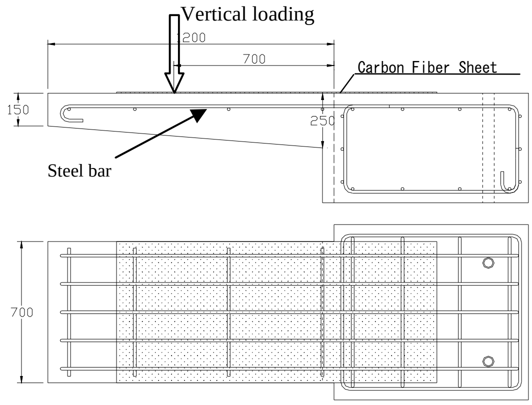

Fig.5 Test specimen(unit;mm)

This structure is a part of the bridge which has been constructed in the early of 1970's. It needs some repair and reinforce to use as a bridge. The static and cyclic loading test as a traffic load was carried out, and the ultimate strength and the affect of the strength after 2-millions cyclic loading were evaluated from this test and numerical analysis.

The 2-dimensional FEM model for this structure is described in Fig.6,and the damage(cracking) distribution by numerical analysis is shown in Fig.7.In this Fig., The cracking was initiated at the static loading P=32.8(kN).

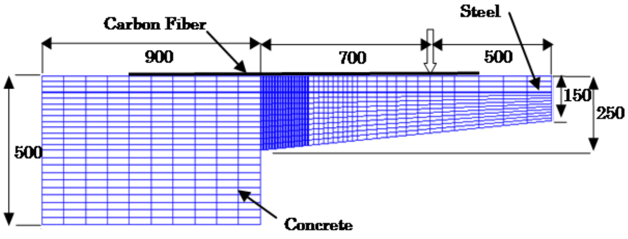

Fig.6 FEM model for clamped RC structure (unit;mm)

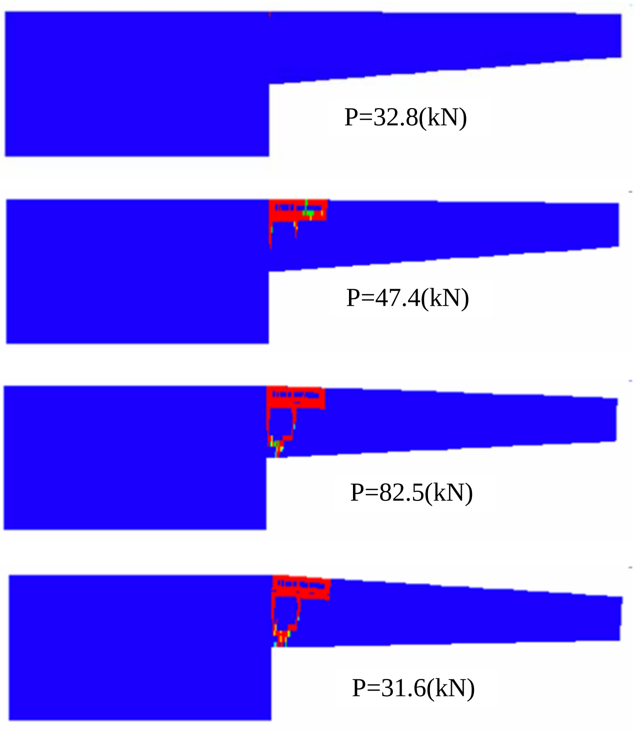

Fig.7 Cracking distribution by FEM

Fig.8 Specimen before test

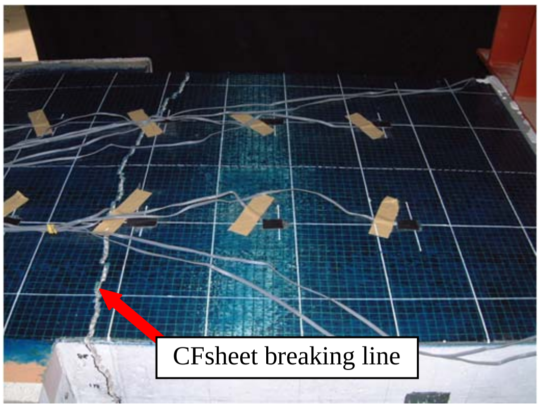

Fig.9 CFsheet fracture after test

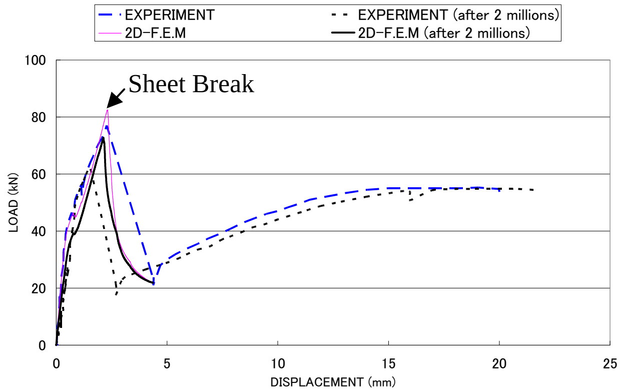

Fig.10 Relationship between load and displacement

Fig.8 and Fig.9 are specimen before and after quasi-static loading test, respectively. The CFsheet breaking mode was found as a final fracture mode. The relationship between load and displacement at loading- point is shown in Fig.10.The concrete cracking under the CFsheet as well as the vertical crack at the root have corresponded well with the experimental result as shown in Fig.7 and Fig.9.The number of vertical cracks at the root is one in the experiment and is two in the analysis. This difference is probably due to the modeling of the steel bars, which is considered as the equivalent layer area model.

The experimental observation for the load-displacement curve, in which the brittle fracture behavior with a sudden load drop takes place after the fracture of the CHsheet, has also well been simulated as shown in Fig.10.The calculated ultimate load of 82.5(kN) has agreed well with the experimental value of 77.0(kN)[11].

The result of same ultimate load after 2-millions cyclic loading expressed the sine curve which has 28.3(kN) of amplitude and 2(Hz) of frequency as a design traffic load is also shown in Fig.10.The calculated ultimate load of 72.7(kN) has agreed well with the experimental value of 61.8(kN). It was found that the ultimate strength due to affection of pre-cyclic load., which may reduce about 12% the ultimate strength more than that of intact specimen by numerical analysis. And the experimental result was approximately 20%bigger than the numerical results.

4. ADHESIVE FRACTURE OF CONCRETE BLOCK REINFORCED WITH CFSHEET

In this Section, The adhesive fracture mode such as de-lamination , surface detachment between the CFsheet, epoxy resin and concrete were discussed.

4.1 A New Constitutive Equation for shear behavior

Most of ultimate strength of concrete structures reinforced with the CFsheet have been determined by adhesive fracture mode between the CFsheet, epoxy resin and concrete surface.

Therefore, A new equivalent stress was introduced to evaluate the mode as follows[12];

$$\sigma_{eq} = \alpha I_1 + \left(J_2^{'}\right)^{1/2} + \beta\langle\sigma_{\max}\rangle + \delta\left|\tau_{\max}\right| \qquad (9)$$

Where the following notations are used: β and δ ;the material parameter, $\langle\ \rangle$;Macaulay's brackets, $\sigma_{\max}$; maximum principle stress, $\tau_{\max}$; maximum shear stress. another parameters are same in equation(4).

β and δ were determined by the adhesive strength test shown in Fig.11. In this test, the adhesive length was changed 20,40,80(mm) (refer to Table 3).

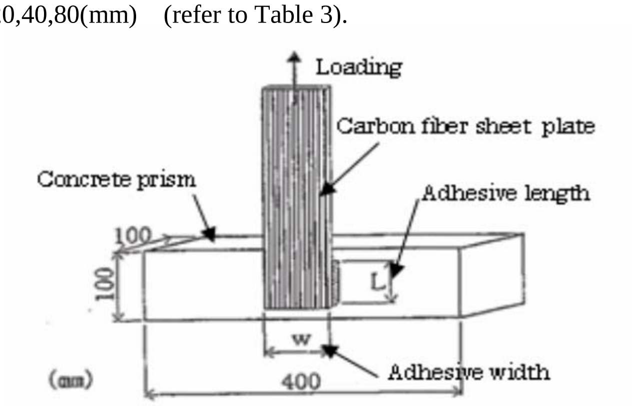

Fig.11 Adhesive strength test

Table 3 Test cases

CASE	Adhesive length L (mm)	Adhesive width W (mm)
CASE1	80	80
CASE2	40	80
CASE3	20	80

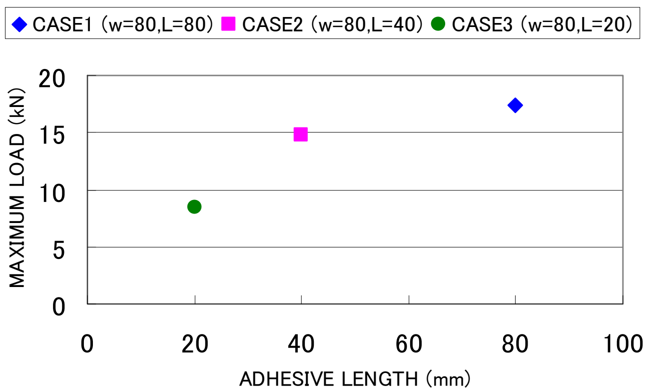

Fig.12 Maximum load and adhesive length

Table 4 Material property

E (Young's modulus)	30,000 (MPa)
ν (Poisson's ratio)	0.17
α (plastic potential)	0.85
β (plastic potential)	0.035
δ (plastic potential)	0.01
σ_y (yield stress)	1.50 (MPa)
σ_f (fatigue limit stress)	1.875 (MPa)
K (plastic hardening)	45.0 (MPa)
n (plastic hardening)	0.175
S_{pf1} (damage parameter)	9.25×10^{-4} (MPa)
S_{pf2} (damage parameter)	1.55
S_{e1} (damage parameter)	4.25×10^{-3} (MPa)
S_{e2} (damage parameter)	5.375
ε_{pD} (damage threshold)	0.00
D_{cr} (critical damage)	7.45×10^{-2}

The relationship between maximum load and adhesive length is shown in Fig.12. The load becomes bigger corresponding to the adhesive length, but the relation is nonlinear. It was found that there is a certain effective length of the CFsheet to resist the shear deformation.

4.2 Adhesive Fracture Analysis Under Cyclic Loading

The damage evolution would be hypothesized following equation. The plastic damage is adopted the former relation of equation(10) and the elastic damage is adopted the later relation of equation(10),respectively.

$$dD=\left(\frac{Y}{S_{pf1}}\right)^{S_{pf2}}dp \quad , \quad dD=\left(\frac{Y}{S_{e1}}\right)^{S_{e2}}de \qquad (10)$$

Where S_{pf1} and S_{pf2} are material constants regarding plastic fatigue and dp is the increment of equivalent plastic strain. S_{e1} and S_{e2} are material constants regarding elastic fatigue . de is the increment of equivalent elastic strain[12].

The CFsheet and epoxy resin were hypothesized as linear elastic material in this section[12]. The applied cyclic loading ,which has 5(Hz) of frequency for CASE3 and the 2-dimensional model for FEM are shown in Fig.13 and Fig.14. Finally, the material property was shown in Table 4

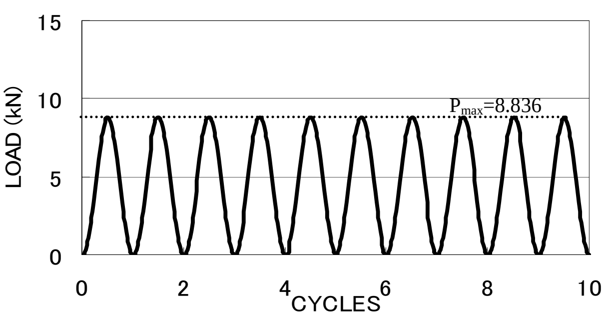

Fig.13 The applied cyclic loading (for CASE3)

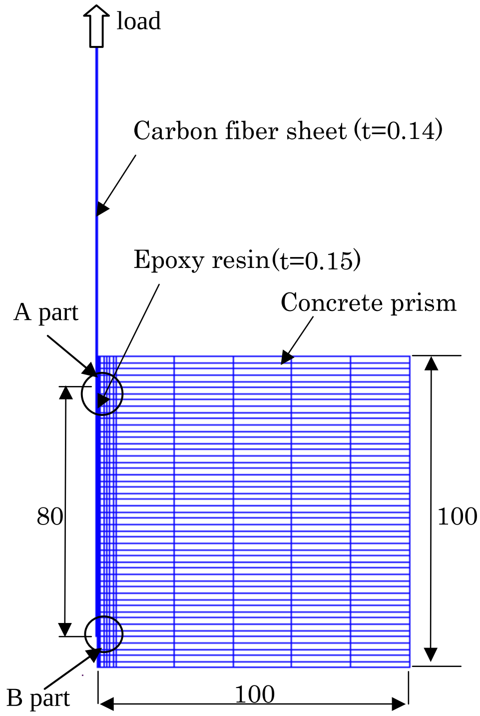

Fig.14 2-dimensional model for FEM(unit;mm)

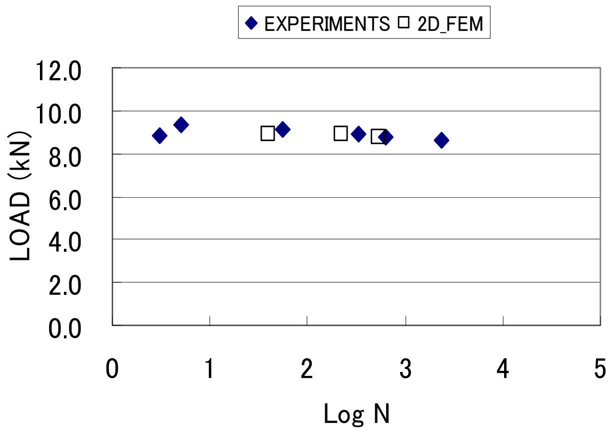

Fig.15 Relation fatigue fracture number and P_{max}(CASE2)

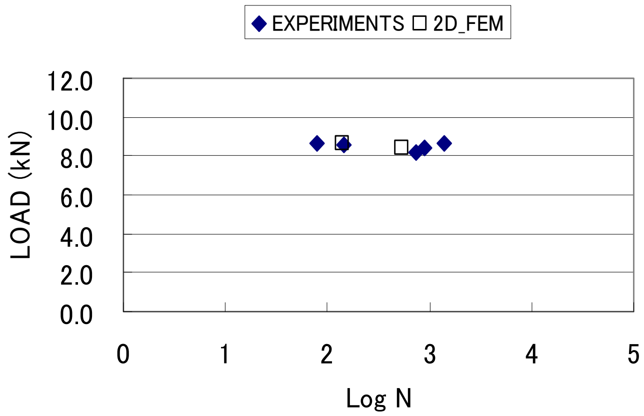

Fig.16 Relation fatigue fracture number and P_{max}(CASE3)

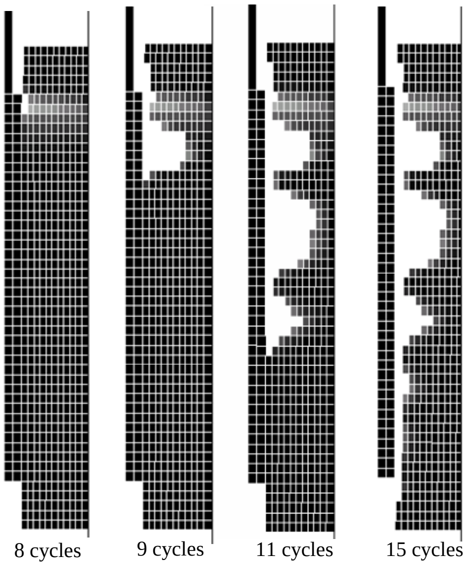

Fig.17 Damage distribution(CASE1)

The relationship between cyclic fracture number and maximum load is shown in Fig.15 and Fig.16.In both cases , the analytical results are a good agreement comparable with the experimental results. Finally, the damage distribution is shown in Fig.17.It was found that the adhesive fracture would be evolved from the root (A part) to the tip (B part) corresponding to cyclic number. In Fig.17, the white area reveals the evolution of de-lamination or adhesive fracture. Herein, the damage zone is enlarged to show up the detachment from concrete surface.

5. CONCLUSION

In this study, the 2-dimensional FEM implementing the elasto-plastic damage constitutive equation based on CDM has been applied to the damage and fracture analysis of the RC structural member and the block reinforced with CFsteet. The following conclusions have been obtained:

(1) The stress-strain relations of the concrete and the CFsheet have been successfully identified by the elasto-plastic damage constitutive equation using Drucker-Prager equivalent stress.

(2) The calculated damage zones have corresponded well with the experimental crack propagation in the RC slab from which it is seen that the damage mechanics model is valid for the damage evaluation of the concrete structural member reinforced with the CFsheet.

(3) The adhesive fracture mode has been identified by an another equivalent stress and which has corresponded well with experimental fatigue fracture number. The validity of present analysis has especially been demonstrated by the fact that adhesive fracture has well been simulated.

(4) The repair and the maintenance to increase the lifetime are important technologies for concrete structures. The quantitative evaluation of the chemical aging, the mechanical damage accumulation due to earthquakes and fatigue and their coupling behaviors is necessary for the appropriate maintenance. Therefore, CDM will be a valid method to evaluate the lifetime and the deterioration of ultimate ability of concrete structures.

6. ACKNOWLEDGMENT

The authors appreciate Penta-Ocean Construction Co., Ltd. for corporation in testing the specimens, Nippon Steel Composite Co., Ltd. for providing the CFsheet.

7. REFERENCES

[1] Liu,Yuqing.et al.," Nonlinear Finite Element Analysis of Reinforced Concrete Members Strengthened with Carbon Fiber Sheets," Proceedings of the Japan Concrete Institute,Vol.20,No.3,1998,pp.1-6.

[2] Murata,K.et al.," Research of Mechanics Characteristics of RC Beam Strengthened with Carbon Fiber Sheets under Dynamic Load," Proceedings of the 47th Science Council of Japan Materials Research Conference,2003,pp.215-216.

[3] Abe,T.et al.," Research of Mechanics Characteristics of RC Beam Strengthened with CFS and its Rehabilitation Effect," Proceedings of the 53rd National Congress of Theoretical & Applied Mechanics,2004,pp.215-216.

[4] Polak,M.A.,Vecchio,F.J.," Nonlinear Analysis of Reinforced-Concrete Shells," Journal of Structural Engineering, ASCE Vol.119,No.12, 1993,pp.3439-3462.

[5] Lemaitre,J.," A course on Damage Mechanics ,Second Edition," Springer,1990.

[6] Cipollina,A.et al.," A Simplified Damage Mechanics Approach to Nonlinear Analysis of Frames," Computers and Structures,Vol.54,No.6,1995,pp.1113-1126.

[7] Peng,X.,Meyer,C.," A Continuum Damage Mechanics Model for Concrete Reinforced with Randomly Distributed Short Fibers," Computers and Structures,Vol.78,No.4,2000,pp.505-515.

[8] Al-Gadhig,A.H.,Baluch,M.H.," Damage Model for Monotonic and Fatigue Response of High Strength Concrete," International J. of Damage Mechanics,Vol.9,2000,pp.57-78.

[9] Toi,Y. et al.,"Element-Size Independent Elasto-Plastic Damage Analysis of Framed Structures, "Transaction of the Japan society of Mechanical Engineering, Series A ,Vol.67,No.653,2001,pp.8-15.

[10] Toi, Y.,Lee,J.G.," Element-Size Independent Elasto-Plastic Damage Behaviors of Framed Structures, "ICCSA2005,Lectures Notes in Computational Science 3483,Springer,2005,pp.1055-1064.

[11] Tanaka H,Toi Y. et al.," Damage and fracture analysis of brittle structural elements reinforced with carbon fiber sheets "JOURNAL OF ENVIRONMENT AND ENGINEERING,Vol.3,No.1,2008,pp111-122

[12] Hidenori TANAKA,Yutaka TOI,"Adhesive Failure Analysis of Structural Elements Reinforced with Carbon Fiber Sheets,"Transaction of the Japan society of Mechanical Engineering, Series A ,Vol.72,No.724,2006,pp.198-204.

First International Conference on Geotechnique, Construction Materials and Environment, Mie, Japan, Nov.21-23, 2011, ISBN: 978-4-9905958-0-7 C3051

Development of Functional Carbon Nanotubes -Asphalt Composites

Tatsuo SHIRAKAWA, Akio TADA and Noriyasu OKAZAKI
Department of Civil & Environmental Engineering, Kitami Institute of Technology

ABSTRACT: The purpose of this study is to prepare asphalt composites containing CNTs and to elucidate the characteristic properties of CNTs-dispersed asphalt composites. In the present study, such composites were prepared using several types of asphalt emulsions as a binder. As a result, both nonionic and anionic emulsions kept dispersed state, when combined with as-prepared CNTs. However, cationic emulsions failed to keep dispersed state. But after several additional systematic experiments, it was found that cationic emulsion successfully retained an adequate dispersion state, when as-prepared CNTs were treated with acid solution and the following incremental addition of the pretreated CNTs. The three types of CNTs-asphalt composites demonstrated higher performances in both penetration and microwave-absorption tests than asphalt composites including carbon black powder instead of CNTs, when the mass percentage of all carbon materials was the same.

Keywords: carbon nanotubes -asphalt composites, asphalt emulsion, acid treatment, penetration test, absorption of microwave

1. INTRODUCTION

In recent years, nanocarbon materials such as carbon nanotubes (CNTs) and carbon nanofibers (CNFs) have been attracting much global attention as potential fillers for improving the mechanical and electrical characteristics of cement mortars in many countries [1]. However, there has not been much investigation into the application of nanocarbon materials for asphalt pavement [2].

CNTs are well known for their superior performances in mechanical, thermal, and electrical performance [3]. A CNT has a very high aspect ratio and so it probably acts as a bridge between grains of sand, suggesting that CNTs-enriched asphalt have the potential to reinforce asphalt pavement. Moreover, CNTs are highly electro-conductive and therefore CNT-enriched asphalt will surely absorb microwave and increase in temperature. Often, the resulting temperature is high enough to melt solid asphalt into liquid asphalt that can combine grains of sand and gravel. This novel form of asphalt manipulation may provide a new way to pave roads with asphalt.

CNTs are thought to be too expensive to use as construction materials. Recently, however, a new production process, which will possibly lower the cost of CNTs, has been reported [4]. The process, which was named direct methane reforming (DMR) process, can provide CNTs as a by-product of hydrogen production from natural gas using catalysts. In this process catalyst materials remain in as-prepared CNTs and so the purification is necessary to obtain CNTs of high purity. Especially, CNTs for the uses of a lithium ion battery, electronic devices, etc. should be of higher purity. CNTs have a variety of uses. For some uses, CNTs of not so high purity will serve their purpose. A paving material is one example. In this case CNTs are used as a filler of high mechanical strength due to their high aspect ratio.

The purpose of this study is to prepare new asphalt composites containing CNTs and to elucidate the characteristic properties of CNTs dispersed asphalt composites. Since asphalt is not fluid at ordinary temperatures, it does not act as a binder of aggregate. Therefore, asphalt is usually heated at elevated temperatures to lower the viscosity before its use. Another methods of fluidizing without heating are the addition of a solvent to asphalt and the emulsification of asphalt with water using surface-active agents. Asphalt emulsions, namely, colloidal dispersions of asphalt particles in water have low viscosity and so are easily mixed with aggregate even at ordinary temperatures. Asphalt emulsions were made by emulsifying high-viscosity asphalt into water with the aid of surface-active agents. The mixture of asphalt-emulsion and aggregate became very strong, because the aggregate became bound together with asphalt after water was removed off.

In order to disperse CNTs into a liquid, surface-active agents are frequently used. Although surface-active agents that are used in asphalt emulsions are not common to those of CNTs, the former agents could be act as the latter agents. If so, asphalt emulsions, which are inexpensive, are suitable materials for adding of CNTs. In this study, such composites were prepared using several types of asphalt emulsions instead of conventional asphalt which needs preheating.

2. EXPERIMENTAL

2.1 Materials

a) Asphalt emulsions as binders

As asphalt binders, cationic, anionic and nonionic asphalt emulsions were used (Table 1) [5]. All asphalt emulsions were provided by Nichireki Corporation. It is noteworthy that the pH of every asphalt emulsion is different; cationic emulsion is acidic, nonionic emulsion is neutral and anionic emulsion is alkaline.

b) Carbon fillers

CNTs and carbon black are used as carbon fillers (Table 2) [6]. The CNTs were produce by the direct methane reforming reaction using an iron catalyst [4].

An industrial carbon black sample was provided by Tokai Carbon Corporation. Its arithmetical mean particle size (the

Table 1 Characteristics of asphalt emulsions

Emulsion type		Viscosity (B type) 25°C (cP)	pH	Reduction of mass during evaporation (wt%)
Cationic	For permeation	50.2	1.93	67.06
	Tuck coat	19.9	2.40	50.49
	For mixing MK-2（JIS K 2208）	178.9	4.66	57.70
Nonionic	For mixing MN-1（JIS K 2208）	35.5	6.90	56.60
Anionic		525.0	12.89	65.05

Table 2 Bulk density measurements of carbon fillers

No.	Carbon filler	Bulk density (g/cm^3)	Ratio to the density of sample A
A	As-prepared CNTs	0.0289	1.00
B	As-prepared CNTs after milling	0.1048	3.63
C	Acid treated CNTs (HCl)	0.1503	5.20
D	Acid treated CNTs (HNO_3)	0.1517	5.25
E	Carbon black produced by the DMR method	0.1030	3.57
F	Industrial carbon black	0.3380	11.7

primary particles) was 28nm [7]. Another carbon black sample also was produced by the direct methane reforming reaction using another iron catalyst. The as-prepared CNTs were treated with dilute solution of hydrochloric acid (HCl) or nitric acid (HNO3) followed by filtering with suction.

2.2 Preparation of carbon filler-asphalt composites

CNTs or carbon black of 0.40g was added into an asphalt emulsion of 40g and then mixed using a magnetic stirrer. The resulting samples were dried in a dry oven maintained at 70°C until constant weight was reached.

2.3 Penetration test

The penetration test (JIS K 2208) was adopted as a standard test of hardness evaluation of asphalt materials.

2.4 Absorption of electric magnetic wave

The microwave-absorption ability of the filler-emulsion composites was evaluated by measuring a rise in the surface temperature. This is because microwave absorbed by a sample is converted into thermal energy to result in a temperature rise. Every sample was irradiated with microwave of 500W for 10 seconds. The temperature measurements were done with a radiation thermometer.

Fig. 1 Agglomeration on cationic emulsion surface

3. RESULTS AND DISCUSSIONS

3.1 Dispersion of carbon fillers into asphalt emulsions

Table 3 summarizes the dispersibility of the carbon fillers to different types of asphalt emulsions.

3.1.1 Effects of asphalt emulsions

a) Nonionic emulsion

The two types of carbon black samples became dispersed in the nonionic emulsion by stirring in a short time. And as-prepared CNTs also became dispersed in the nonionic emulsion by stirring in over 5min.

b) Anionic emulsion

In the case of anionic emulsion that has higher viscosity than nonionic emulsion, both CNTs and two types of carbon black samples also dispersed, although the necessary time for stirring was longer than in the case of nonionic emulsion.

c) Cationic emulsion

In the case of the cationic emulsions, however, the degree of dispersion depended on both the kind of a carbon-filler and the type of an asphalt emulsion.

The two types of carbon black samples were dispersed in both MK-2 emulsion (JIS K 2208), which is frequently used for surface treating of wearing course and modified asphalt emulsion for tuck coat layer.

On the other hand, it was difficult to disperse the as-prepared CNTs were not dispersed instantly; CNTs particles stayed for a while in the upper zone of the MK-2 emulsion and modified-asphalt emulsion (Fig. 1).

This suggests that the wettability of the CNTs by the cationic asphalt emulsion is not good.

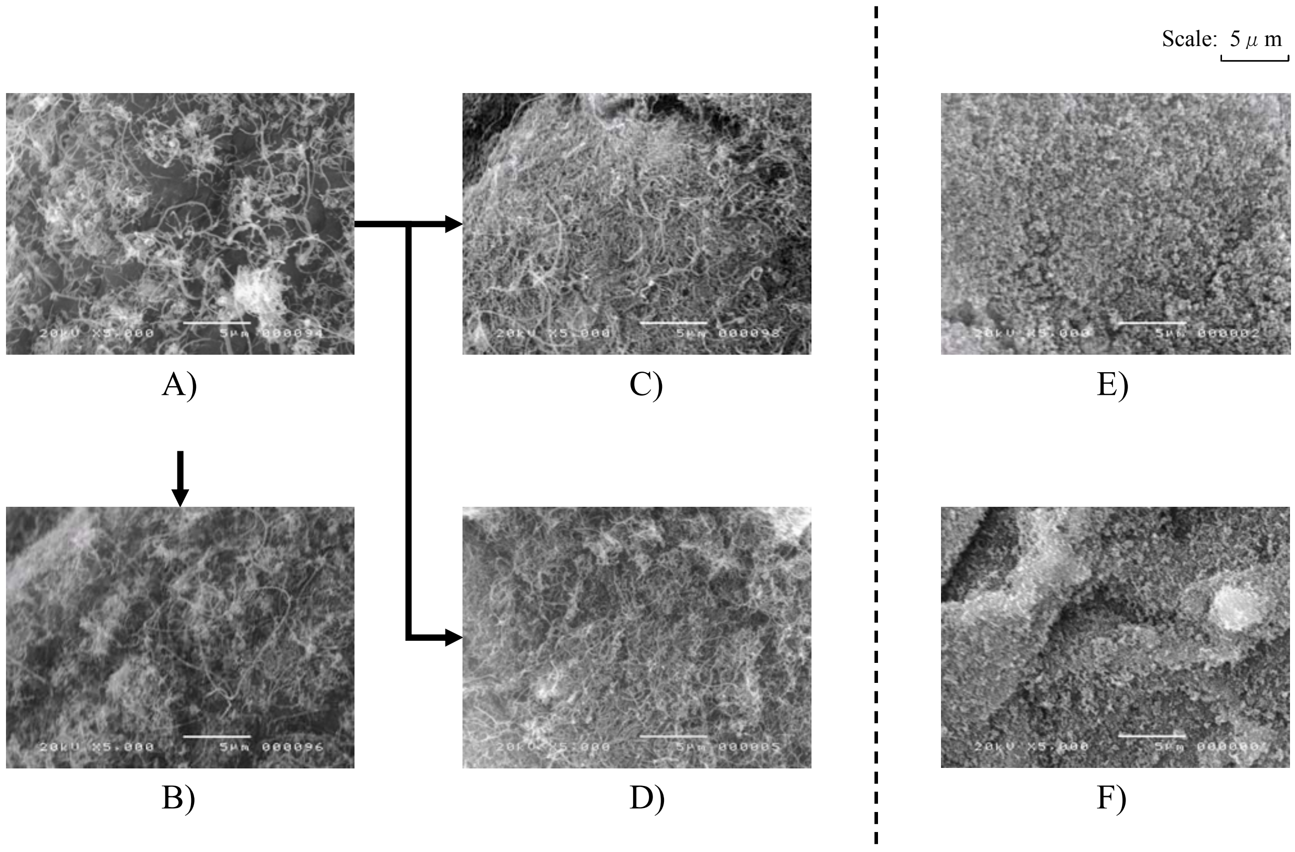

Fig. 2 Effects of milling or acid treatment on as-prepared CNTs (SEM: 5,000 times)

3.1.2 Effects of CNTs-addition methods

a) MK-2 emulsion

Although carbon black samples added at once was dispersed into MK-2 emulsion regardless of the quantity, CNTs failed to disperse when a large quantity of CNTs was added at one time. However, the same quantity of CNTs was managed to disperse when the CNTs were subdivided into several parts and adding incrementally all the parts by repeating the following step; a part of CNTs is added and then stirred until well-dispersed state is achieved.

b) Modified asphalt emulsion

In the case of modified asphalt emulsion, as-prepared CNTs hardly dispersed in spite of adopting the same addition method as in the case of MK-2 emulsion, although carbon black samples added at once were dispersed regardless of its quantity.

3.2 Microscopic gathering states of carbon fillers

a) The SEM images of acid-solution treated CNTs

Figure 2A shows an image of as-prepared CNTs and this image demonstrates that the bulk density of the CNTs is low. Figure 2B shows an image of as-prepared CNTs that were mechanically milled prior to SEM examination. Figures 2C and 2D are an image of the CNTs that were treated with dilute hydrochloric acid (HCl) and dilute nitric acid (HNO_3) respectively. As seen in Figs. 2C and 2D, the bulk density of the acid-solution treated CNTs seems to have increased, and there are a few tangles of the fibers. This situation seems to be a good condition to scatter the CNTs in asphalt emulsion, resulting in a good dispersion. Figures 2E and 2F show the images of homemade carbon black and industrial carbon black respectively. The shape of their samples is clearly different from that of CNTs (seen in Figs. 2A-2D). The former is spherical, while the latter is fibrous.

3.3 CNTs and their acid-solution treatment

a) SEM images of carbon fillers

Figure 2 shows a scanning electron microscopy (SEM) image of as-prepared CNTs with a magnification of 20,000. A secondary electron is discharged from iron particles attached on tops of the CNTs and whitens with the SEM image. Each iron particle was a constituent of the iron catalysts used for producing the CNTs, clearly indicating that catalysts remain in the as-prepared CNTs.

A result of the analysis with the energy dispersion type fluorescence X-ray analyzer (XRF-EDX) revealed that as-prepared CNTs included a catalyst (iron: 4.3wt%).

In Fig. 2, the CNTs (diameter: ~100nm) flex in the shape of a fiber and grow up while twisting and tangling. When the CNTs twist up, a cavity occurs in the CNTs. As a result, the bulk density of the CNTs is low.

b) Acid–solution treatment of CNTs

As a result, the bulk density of the CNTs shrinks. Therefore, it is thought that preprocessing to reduce the amount of

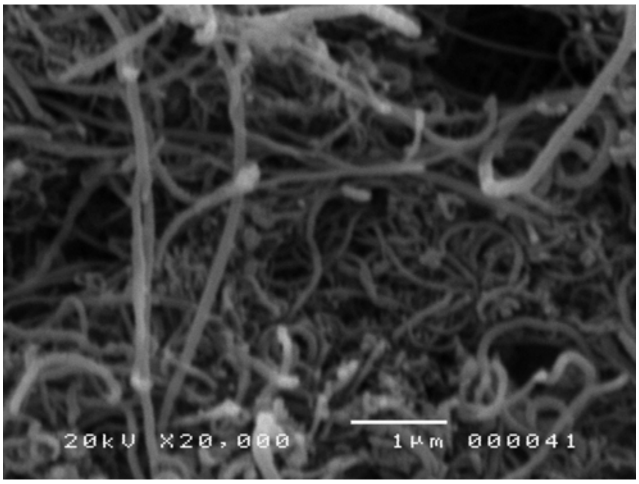

Fig. 3 SEM image of as-prepared CNTs (20,000 times)

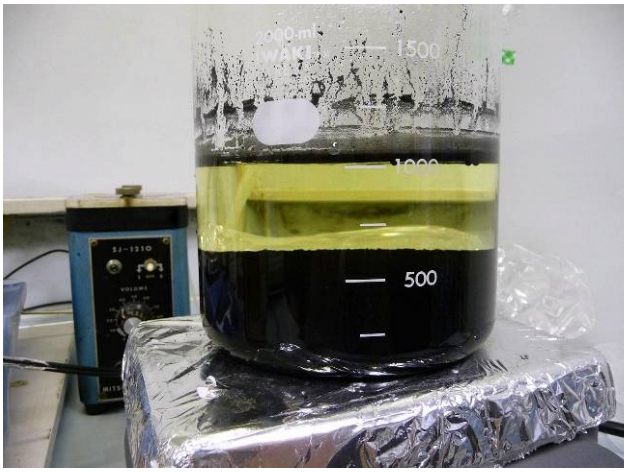

Fig. 4 Treatment of as-prepared CNTs with a dilute hydrochloric acid solution

remaining catalyst is important. An acid–solution treatment of the CNTs was carried out in anticipation of the improvement in degree of their dispersion. When the as-prepared CNTs contact the acid solution (Fig. 4), every iron particle in the residual catalyst (fine particles of iron) is dissolved into the solution.

Two specimens of the acid-solution treated CNTs samples were measured by the XRF-EDX method and it was found that the concentration of residual catalyst (iron) was 2.0wt% and 1.7wt% respectively. The concentrations are almost as in half as that of as-prepared CNTs, indicating that the acid-solution treatment is useful to improve the purity of the CNTs.

c) Bulk density

Table 2 lists the results of measuring the bulk density of the same samples shown in Fig. 2. The bulk density of as-prepared CNTs increased after milling or treating with the acid-solution. This change in density probably occurs because the bulky agglomerate of as-prepared CNTs was disentangled and compacted.

3.4 Degree of dispersion of acid-solution treated CNTs in emulsions

a) Nonionic and anionic emulsions

The CNTs became dispersed in the nonionic emulsion after stirring in a short time, indicating the affinity of both filler with the liquid is very high. In the case of anionic emulsion that has higher viscosity than nonionic emulsion, both CNTs needed longer time than in nonionic emulsion to reach a similarly state of dispersion.

b) Cationic Emulsions

In the case of the emulsion of MK-2 or tuck coats, acid-solution treated CNTs fairly dispersed when a large quantity of the CNTs was added at one time. And the degree of dispersion became good when the CNTs were added incrementally.

In the case of modified-asphalt emulsion, acid-solution treated CNTs hardly dispersed when a large quantity of the CNTs was added at one time. However, the CNTs fairly dispersed when the CNTs were added incrementally.

3.5 Improved dispersibility of acid-solution treated CNTs into cationic emulsions

The acid solution dissolved iron particles in as-prepared CNTs, releasing ferric ions (Fig. 4). In the same manner, the cationic emulsions, which are strong acid, probably dissolves iron particles in as-prepared CNTs.

The ferric ions will interact with a surface-active agent that contributed to stabilize the cationic emulsions and take away its important role, resulting in the agglomeration. The reason as-prepared CNTs failed to disperse is that the ferric ions released from the residual catalyst in as-prepared CNTs.

This change in bulk density probably occurs because the bulky agglomerate of as-prepared CNTs was disentangled and compacted.

3.6 Characteristics of CNTs -asphalt composites

a) Penetration test

Figure 5 shows the results of penetration test (JIS K 2208) for CNTs-emulsion composites. Apparently a CNTs-emulsion composite was more greatly stiffened by adding CNTs than carbon black of the same mass concentration. In other words, CNTs can give the same penetration degree as carbon black samples with a lesser quantity of addition.

b) The absorption of microwave by CNTs-emulsion composites

The experimental results are shown in Fig. 6 in which surface temperature was plotted as a function of time on a semi logarithmic graph. Except the anionic emulsion, the surface temperature of CNTs-emulsion composites increased with time, indicating that microwave was absorbed by those composites.

3.7 Strong points of CNTs-asphalt emulsions

The above-mentioned results clearly show that CNTs are potential filler for reinforcing as well as for giving

Table 3 Dispersibility of carbon fillers in asphalt emulsions

Emulsion type		pH	As-prepared CNTs		Acid treated CNTs (with HCl or HNO_3)		Industrial carbon black
			Addition at once	Incremental addition	Addition at once	Incremental addition	Addition at once
Cationic	For permeation	1.93	Poor	Poor (Agglomerate)	Poor	Fair	Fair
	Tuck coat	2.40	Poor	Fair	Fair	Good	Good
	For mixing MK-2（JIS K 2208）	4.66	Poor	Fair	Fair	Good	Good
Nonionic	For mixing MN-1（JIS K 2208）	6.90	Excellent	--	Excellent	--	Excellent
Anionic		12.89	Good	--	Good	--	Good

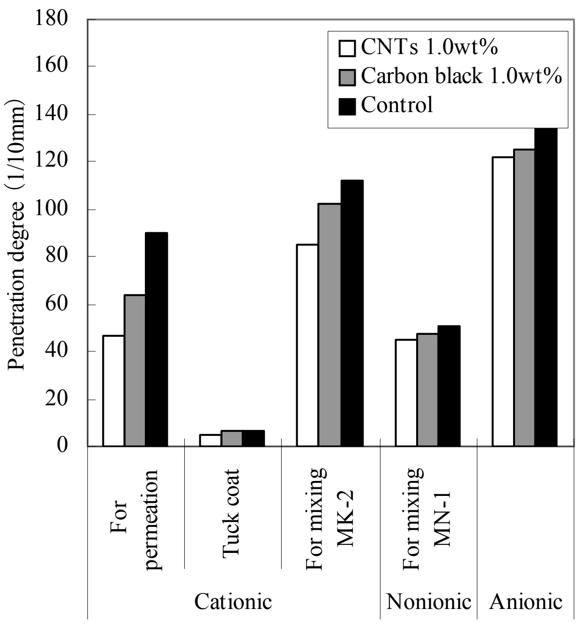

Fig. 5 Results of penetration tests

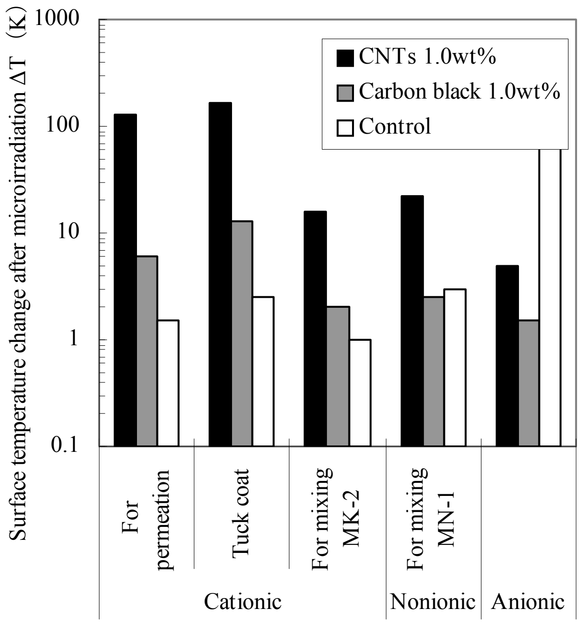

Fig. 6 Temperature change of carbon fillers by microwave irradiation

microwave-absorbing property to conventional asphalt. This is probably the first study about CNTs-asphalt emulsions. Asphalt emulsions, of which viscosity can be easily controlled by the addition of surfactants, are a suitable binder for asphalt pavement.

Civil structures of many countries need to renew old facilities. To renew of civil structures, it has been proposed that the implementation of new paving materials and methods ought to be adopted for performance enhancement and life cycle extension. The present study suggests that microwave heating to lower asphalt viscosity for partial repairs may be a promising construction technique. This will contribute to the ease of pavement construction, improvements in safety, and asphalt heating energy reduction. Thus, CNTs-asphalt emulsions will be greatly useful for construction fields.

4. CONCLUSIONS

The main conclusion to be drawn from the above results is as follows.

(1) In order to take advantage of the essential functions of the CNTs involved in asphalt, the CNTs should be dispersed into asphalt emulsions.
(2) As for both nonionic and anionic asphalt emulsions, as-prepared CNTs easily dispersed. For cationic emulsions, however, as-prepared CNTs failed to disperse. This problem was managed to solve by pretreating the CNTs with the acid solution and adding incrementally the pretreated CNTs.
(3) The CNTs-asphalt composites showed not only higher stiffness (higher performance in the penetration test) than carbon black-asphalt composites but also a new function,

namely, the ability of microwave absorption, when compared under the same conditions (mass concentration of the each carbon material, measuring method, etc.).

5. ACKNOWLEDGMENT

A part of this study was supported by Grants-in-Aid for Young Scientists (B), JSPS (No.23760401).

6. REFERENCES

[1] MANZUR T, YAZDANI N. "Strength Enhancement of Cement Mortar with Carbon Nanotubes Early Results and Potential" Transportation Research Record, No.2142, 2010, pp.102-108.
[2] Shirakawa T, Tada A, Okazaki N, Iwahashi T, Kohata N. "Development of Construction Materials Using Advanced Nanocarbon Provided in a Hydrogen Manufacturing Process Subsidiary" Journal of JSCE Global Environment Engineering Research, Vol. 18, Aug.2010, pp. 81-88.(in Japanese)
[3] Wu Z, Chen1 Z, Du X, Logan J M, Sippel J , Nikolou M, Kamaras K, Reynolds J R, Tanner D B, Hebard A F, Rinzler A G. "Transparent, conductive carbon nanotubes films", Science, Vol.305, Aug. 2004, pp.1273-1276.
[4] Tada A, Matsunaga T, Okazaki N. "Direct methane reforming process and its applications", Transactions of the Materials Research Society of Japan, Vol.33, No.4, Dec. 2008, pp. 1059-1062.
[5] AEMA, MS-19 Basic Asphalt Emulsion Manual, Asphalt Institute, 2008.
[6] Gridley P F, Vallerga B A. "Carbon black reinforcement of asphalts in paving mixtures", ASTM Special Technical Publications, No.724, 1980, pp.110-128.
[7] Yamaguchi K, Sasaki I, Nishizaki I, Meiarashi S, Moriyoshi A. "Effects of film thickness, wave-length, and carbon black on photo degradation of asphalt", Journal of the Japan Petroleum Institute, Vol.48, No.3, 2005, pp.150-155.

First International Conference on Geotechnique, Construction Materials and Environment, Mie, Japan, Nov.21-23, 2011, ISBN: 978-4-9905958-0-7 C3051

Hydraulic Character of Estimation Method on Roughness Coefficient of Concrete Canal

KOICHIRO OTAGAKI, EHIME University, United graduate school of agricultural sciences

KOJI SAI, KOCHI University, Faculty of agriculture

KENICHI FUJISAWA, NIPPON JIKKOU Co. Ltd

SHINSUKE MATSUMOTO, SHUSHI SATO, KOCHI University, Faculty of agriculture

ABSTRACT: The agricultural concrete canals are approximately 450 thousand km in Japan. Recently, aging and deformation of them is becoming a subject to solve, it is necessary to preserve their functions appropriately. Estimation method of hydraulic performance of concrete canal by roughness coefficient was aimed in this research. Hydraulic roughness coefficients of concrete canal were estimated under several hydraulic conditions in the experiment. Roughness coefficient was calculated using measured data of water surface slope. Reynolds number and Froude number were particularly focused in this study. As a result, roughness coefficient was varied enormously with the differences of hydraulic conditions. Especially, Reynolds number and Froude number represent the characteristics of water flow had strong negative correlation with roughness coefficient. It was also suggested that the shape transformation at the downstream of the canal affected to roughness coefficient.

Keywords: Concrete canal, Hydraulic performance, Flow transmissibility, Roughness coefficient, Stock management

1. INTRODUCTION

Agricultural concrete canals are important infrastructure for stable food production. In Japanese agricultural area, aging and drops of function of canals were observed as recent problems, establishment of appropriate maintenance and management scheme is required for the preservation of these facilities. To solve this subject, it is necessary to evaluate quantitatively its present performance as well as to choose the optimum countermeasures against the factor of performance declination.

Main performances of agricultural concrete canal are Hydraulic, Water utilization, Structural safety, and Social safety. Particularly, hydraulic performance is very important as it is affected to the water supply to farmland constantly.

In general, roughness coefficient in Manning mean velocity formula was used as an index of hydraulic performance. Roughness coefficient is well known as a barometer of water conduction. On the other hand, Manning equation is used in canal design and roughness coefficients of various materials are defined in public guideline [1], [2]. Roughness coefficient was also used for evaluation of surface condition of canal [3].

According to some previous studies [4], it was reported that the values of roughness coefficient varied due to hydraulic conductive conditions of canal. To establish evaluation method of hydraulic performance, it is important to verify the relationships among roughness coefficient, hydraulic condition and canal surface condition.

This study aimed to establish the prescribed method on hydraulic performance of agricultural concrete canal. Through the various experiment under several hydraulic conditions, roughness coefficient was estimated quantitatively. Moreover, some of the subjects on the estimation of this coefficient were extracted.

2. METHOD AND PROCEDURE

2.1 Outline of experiment

For the estimation of roughness coefficient, the hydraulic experiments were conducted using slope variable canal system. In the experiment, two patterns of canal surface conditions were examined; one is the surface covered with polyurethane coating and acrylic board and the other one is the surface of concrete flume. The roughness coefficient was calculated using observed data of water surface profiled at each surface condition. The outline of experiment is shown in Fig. 1. Hydraulic conditions were set up by changing cross sectional average velocity and canal slope under the condition of constant water quantity. Water surface profiles were observed at intervals of 1m by point gauge (KENEK Co. PH-340). The observed points of water surface profile of P_0 to P_7 were shown in Fig.1. In the each measurement point of P_0 to P_7, mean depth were obtained by calculation the average of the three points in cross direction that shown in Fig.2.

2.2 Calculation method of roughness coefficient

In this study, the roughness coefficient was estimated by solving fundamental equation of non-uniform flow using observed data of water surface profiles. The fundamental equation of non-uniform flow is described as follow;

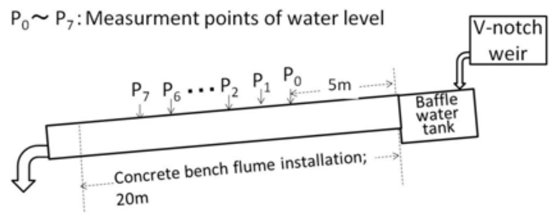

Fig. 1 Overview of experimental channel and measurement points of water depth.

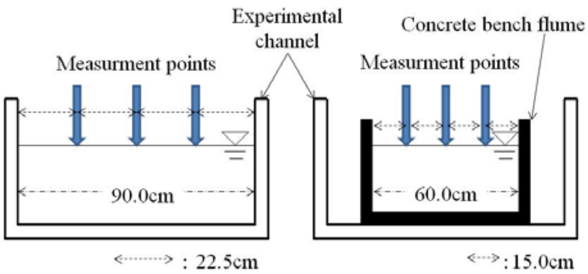

Fig. 2 Measurement points of water depth in transverse section.

$$\frac{dh}{dx}=\frac{i-\dfrac{n^2Q^2}{\{bh/(b+2h)\}^{4/3}b^2h^2}}{1-\dfrac{\alpha Q^2}{gb^2h^3}} \qquad (1)$$

where x is the direction of downward, h is water depth(m), Q is water quantity(m^3/s), α is flow coefficient(=1), g is gravitational acceleration(m/s^2), b is canal breadth(m), i is canal bottom slope, and n is roughness coefficient(s/m$^{1/3}$).

The estimation procedure of roughness coefficient is as follows; using fluctuated value of n, water depth h_c were calculated by integrating the Equation(1) in Δx=1(m). Evaluation function concerning observed water depth h_0 and calculated water depth h_c. The evaluation function is described as follows;

$$E=\frac{1}{N}\sum_{i=0}^{N}\frac{\left(h_{0,i}-h_{c,i}\right)^2}{h_{0,i}} \qquad (2)$$

where, N is number of data, h_0 is observed water depth(m), h_c is calculated water depth(m) and i is a number of data.

Thus, the value of n is changed, and the above operation is repeated. Finally, the value of n which outputs the smallest evaluation function is defined as appropriate values of roughness coefficient.

On the other hand, convenient method for the estimation of roughness coefficient of actual agricultural concrete canal is, in general, solving Manning's formula [5]. Therefore, roughness coefficient was also estimated from Manning's formula by assumption of water flow in the experiment was uniform flow. Energy gradient in the formula was calculated as follows;

$$I=I_w+F_r^{\,2}\left(I_0-I_w\right) \qquad (3)$$

where, I_0 is canal bottom slope, I_w is water surface slope which is average of gradients of P_0 to P_7 in the Fig.1and F_r is Froude number described as ($=v/\sqrt{gh}$).

3 RESULTS AND DISCUSSIONS

3.1 Result of estimated roughness coefficient.

Estimated roughness coefficient obtained from experiment under several canal surface conditions of polyurethane coating and concrete flume were shown in Table 1 and 2, respectively. In these tables, n_1 is calculated by the fundamental equation of non-uniform flow, and n_2 is calculated by Manning's formula. It was difficult to observe when Froude number is 0.4 or higher because of unstable water surface. Therefore, all the latter results are discussed when the Floude number was smaller than 0.4.

As a result, the estimated roughness coefficient changed greatly under the different hydraulic conditions even though the surface condition of canal was same. Results of roughness coefficient shown in Table 1 and 2 clarified that large values comparing with the designed values were confirmed when they were estimated under the most of all hydraulic conditions.

3.2 Estimation method of roughness coefficient

Comparison result on estimation methods of roughness coefficient were examined based on the Figure 3. In this figure, the relations between n_1 and n_2 ($=n_2-n_1$) and water surface slope were appeared. The results show that the differences between n_1 and n_2 increased as the slope of water surface become steep. These results suggested that estimation method by Manning's formula might be uncertain under the condition of non-uniform flow. Therefore, it needs to pay attention to hydraulic condition and form and slope of the canals when using this equation.

3.3 Influence of hydraulic conditions to estimated roughness coefficient.

In the same condition of canal bottom slope, estimated roughness coefficient changed as water velocity was varied. This result suggests that flow condition of canal has affected enormously to the estimation of roughness coefficients.

Figure 4 shows the relation between hydraulic mean radius and roughness coefficient. There is a high correlation between hydraulic mean radius and roughness coefficient. On the other hand, it wasn't confirmed the large difference between polyurethane coating and concrete flume. As a result, roughness coefficient is affected by hydraulic conditions extremely. Moreover, it was suggested that estimated roughness coefficient could not express the exact loss of water flow due to surface condition.

3.4 Influence of hydraulic parameters to roughness coefficient

To examine with considering the mechanical resemblance of flow, relationships between roughness coefficient and non-dimensional hydraulic parameter, Floude number F_r and Reynolods number R_e, were evaluated.

Table 1 Hydraulic conditions and estimated values of roughness coefficient in case of experiment using experimental channel.

Experimental conditions	Channel slope ($\times 10^{-3}$)	Water velocity(m/s)	Mean depth(m)	Hydraulic radius(m)	Froude number	Reynolds number	n_1	n_2
(1)	0.00	0.080	0.222	0.150	0.05	10288	0.0764	-
(2)	0.00	0.099	0.181	0.130	0.07	10958	0.0574	-
(3)	0.00	0.126	0.127	0.100	0.13	11962	0.0359	-
(4)	1.75	0.086	0.208	0.143	0.06	10511	0.0729	0.1125
(5)	1.75	0.109	0.165	0.121	0.09	11247	0.0522	0.0796
(6)	1.75	0.152	0.112	0.090	0.15	12278	0.0307	0.0440
(7)	3.49	0.090	0.198	0.138	0.07	10673	0.0676	0.1620
(8)	3.49	0.119	0.150	0.113	0.10	11521	0.0468	0.1067
(9)	3.49	0.185	0.097	0.080	0.19	12628	0.0204	0.0572
(10)	5.24	0.098	0.183	0.131	0.07	10926	0.0597	0.1813
(11)	5.24	0.133	0.134	0.104	0.12	11829	0.0379	0.1144
(12)	5.24	0.257	0.070	0.061	0.33	13290	0.0095	0.0438

Table 2 Hydraulic conditions and estimated values of roughness coefficient in case of experiment using concrete bench flume.

Experimental conditions	Channel slope ($\times 10^{-3}$)	Water velocity(m/s)	Mean depth(m)	Hydraulic radius(m)	Froude number	Reynolds number	n_1	n_2
(1)	0.00	0.111	0.247	0.135	0.07	12851	0.0576	-
(2)	0.00	0.140	0.197	0.119	0.10	14145	0.0422	-
(3)	0.00	0.189	0.146	0.098	0.16	15765	0.0296	-
(4)	0.00	0.202	0.123	0.087	0.20	16586	0.0252	-
(5)	1.75	0.118	0.232	0.131	0.08	13194	0.0575	0.0758
(6)	1.75	0.151	0.181	0.113	0.11	14589	0.0423	0.0521
(7)	1.75	0.185	0.131	0.091	0.19	16308	0.0258	0.0318
(8)	1.75	0.244	0.109	0.080	0.24	17183	0.0224	0.0235
(9)	3.49	0.126	0.217	0.126	0.09	13585	0.0512	0.1082
(10)	3.49	0.164	0.167	0.107	0.13	15032	0.0356	0.0753
(11)	3.49	0.236	0.116	0.084	0.22	16870	0.0232	0.0434
(12)	3.49	0.297	0.092	0.070	0.32	17908	0.0184	0.0300
(13)	5.24	0.137	0.200	0.120	0.10	14037	0.0464	0.1215
(14)	5.24	0.183	0.150	0.100	0.15	15621	0.0306	0.0807
(15)	5.24	0.286	0.096	0.073	0.31	17757	0.0137	0.0431

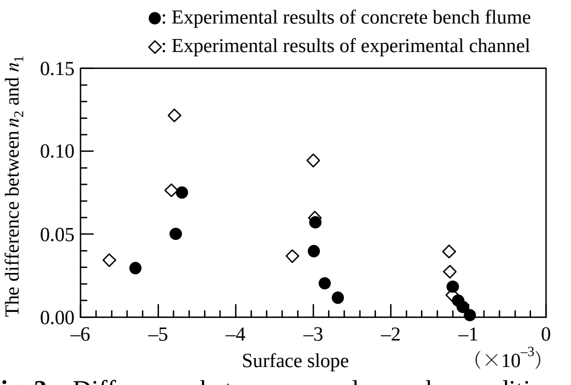

Fig. 3 Differences between n_1 and n_2 under conditions of each water inclination.

Reynolds number is described as follows;

$$R_e = \frac{vR}{\upsilon} \quad (4)$$

where ν is kinematic viscosity coefficient(m^2/s). Figure 5 shows the relationship between Froude number and roughness coefficient, Figure 6 shows the relation between Reynolds number and roughness coefficient. From the results of Figure 5 and 6, both Froude number and Reynolds number has highly negative correlation with roughness coefficient. Correlation coefficient between Froude number and roughness coefficient on concrete flume is 0.93, and on the polyurethane coating is 0.90. Correlation coefficient between Reynolds number and roughness coefficient on concrete flume is 0.99, furthermore, on polyurethane coating is 1.00.

From the results of these experiments, extremely large roughness coefficients were observed when Froude number was within the small value. These results may cause by influence of back water or drop down of water due to the shape change at the end of canal. Hydraulic conditions were changed by heading-up gate at the end of the canal. However, equation (1) is representing the water slope caused of surface roughness friction; the variation of water surface due to the

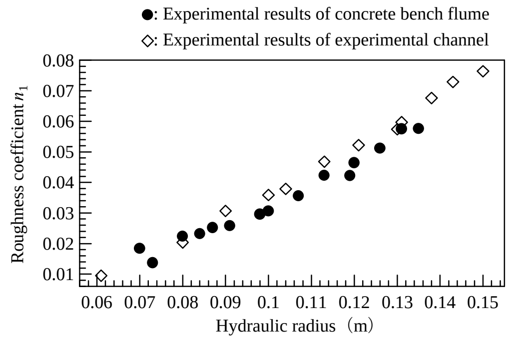

Fig. 4 Relationship between hydraulic radius and roughness coefficient.

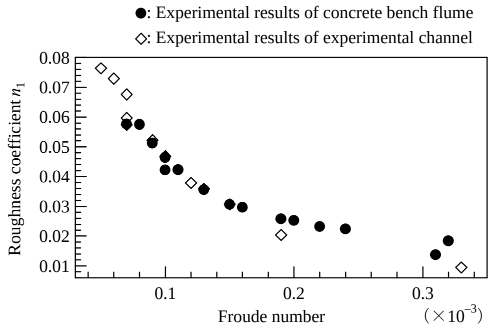

Fig. 5 Relationship between Froude number and roughness coefficient.

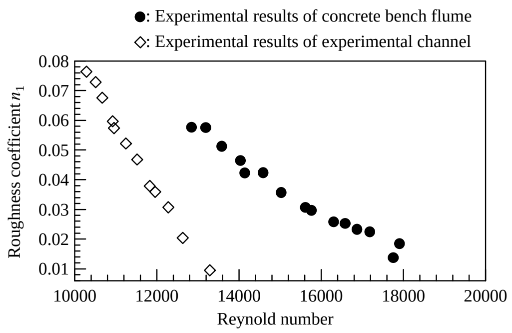

Fig. 6 Relationship between Reynolds number and roughness coefficient.

formation changes of cross-section of canal was not considered well in the experimental data. Therefore, apparent roughness coefficient increased while the flowing spot of low Froude number where the flow was strongly affected by the lower stream. That is why the roughness coefficient cannot be estimated accurately. Further examinations concerned to the variation characteristic of estimated roughness coefficient will be necessary from the viewpoint of various hydraulic conditions.

It is very difficult to exclude the influence of downstream on canal experiment. However, Figure 5 shows that hydraulic conditions of the range over 0.3 of Froude number conduct the values of roughness coefficient become stable.

For establishment of estimation method of roughness coefficient, an appropriate experimental condition must be investigated in the future.

4 CONCLUSION

As the fundamental study for achieving the verification of hydraulic performance on agricultural concrete canals, the influence of hydraulic conditions and parameters to roughness coefficient were studied quantitatively. The results of experiments are concluded as follows;

(1) Using the convenient estimation method of roughness coefficient according to Manning's formula, the difference between measured and estimated roughness coefficient increased as the increment of water surface gradient. However, this simple equation is available for the practical use. Therefore, it is necessary to define the appropriate hydraulic conditions for using this equation.

(2) Estimated roughness coefficients had varied enormously as the differences of hydraulic conditions such as velocity and hydraulic mean radius.

(3) Roughness coefficient value had strong relationship with Froude number and Reynolds number.

(4) In the case of estimating roughness coefficient on experiment canal in finite length, roughness coefficient may be estimated at excessive values due to the change of the form at the end of canal by weir board.

From this study, the roughness coefficient of canals changed widely due to hydraulic condition. Hereafter, from the viewpoint of hydraulic, it is absolutely necessary to find out characteristic of changing the value of roughness coefficient and appropriate hydraulic conditions for estimation. Furthermore, it is important to accumulate data of roughness coefficient obtained several surface conditions of canal to establish estimating method of roughness coefficient.

5 ACKNOWLEDGMENTS

A part of this study was supported by JSPS KAKENHI (23380143) (Grant-in-Aid for Scientific Research (B), A representative; Professor S. Matsumoto). Also a part of this paper is based on the discretionary spending from president of Kochi University in 2008 and 2009, and discretionary spending from president of faculty of agriculture of Kochi University in 2010.

6 REFERENCES

[1] JAPAN SOCIETY OF CIVIL ENGINEERS, "The collection of hydraulic formulas", Maruzen, 1986.

[2] "Design guideline of Land improvement projects federation, canal design", Ministry of Agriculture, Forestry and Fisheries society of irrigation, Drainage and rural engineering ,2001, pp.152-207

[3] HORACE W. KING and ERRNEST F. BRATER "*Handbook of Hydraulics,* 5th", McGraw-Hill Book Co. Inc., 1963, p.7-18.

[4] TAKASHI KATO, SHINYA HONMA, KITAMURA KOJI and IMAIZUMI Masayuki, "Deterioration of Irrigation Canals and Change in Roughness Coefficient", Report of the NIRE, No.275, 2008, pp. 183-193.

[5] TAKESHI TAKEMURA, HAJIME TANJI, YOSHINOBU ARARAGI, "Study on a method to estimate coefficients of roughness," Journal of Japanese society of irrigation, DRAINAGE AND RURAL ENGINEERING, 2001, pp. 25-28.

First International Conference on Geotechnique, Construction Materials and Environment, Mie, Japan, Nov.21-23, 2011, ISBN: 978-4-9905958-0-7 C3051

Na-bentonite as Rock Containment Barrier against Heavy Metals and Acid Leachates

Angelica Naka[1], Takeshi Katsumi[2], Toru Inui[3], Giancarlo Flores[4], and Takehiro Ohta[5]

ABSTRACT: Contamination by acid rock drainage (ARD) is recognized as one of the most serious environmental problems facing mining and some specialized construction industries, such as in the case of road and rail transport. These activities involve excavation and transport of large amount of rocks and sediments, so if they contain heavy metals of natural origin, a proper disposal is necessary to prevent the oxidation of sulfide minerals, and the subsequent release of acid leachates with high metal concentrations. The use of Na-bentonite as rock containment barrier seems to be a possible solution since previous studies have found that it has large specific surface area and low hydraulic conductivity. However, since the long-term performance of this mineral when exposed to ARDs is not widely understood, the aim of this research is to investigate its long-term barrier performance against these acid leachates. For this purpose chemical and physical parameters, such as metal attenuation capacity and hydraulic conductivity on natural and artificial ARD were evaluated.

Keywords: acid rock drainage, geosyntehtic clay liner, bentonite, metal sorption, hydraulic conductivity

1. INTRODUCTION

The need to control natural contamination by metals and metalloids coming from mine tailings and rock disposal sites represents a current challenge for the mining industry and construction companies in many countries such as Japan [1]. In the past, remediation technologies were focused on physical covers to reduce the production of acids by limiting infiltration of water and oxygen [2]. However, recent researches have suggested that potentially toxic elements, particularly As, Se, and in some cases Ni, and Zn are mobile even under neutral pH-conditions [2], [3]. Moreover, the reductive dissolution of As-bearing minerals has resulted in the release of As [3].

As a result, disposal of excavated rocks with potential of acid rock drainage (ARD) from construction and mining is moving towards storage of hazardous materials in lined containment facilities [4]. To this effect, the use of geosynthetic clay liners (GCLs), which usually contain Na-bentonite, seems to be a good solution, since previous studies have suggested that Na-bentonite has a relatively large specific surface area, high metal sorption capacity, self-healing capacity, and low hydraulic conductivity, and is available in many parts of the world [5], [6], [7].

GCLs have been commonly used in landfills. Nowadays, their potential use in mining operations is being tested [2], [4], [8] since it is not a simple matter of transferring the technology from landfill applications to rock containments with potential of ARD generation [9], due to the extreme range in leachate properties. Therefore this research aims to investigate the barrier performance of Na-bentonite when exposed to ARDs (natural and artificial) with different metal composition and pH values through batch sorption tests and 9-month hydraulic conductivity tests.

2. MATERIALS

Na-bentonite was obtained from a needle-punched geosynthetic clay liner (Bentofix® NSP 4900), which is a fiber-reinforced GCL. This GCL contained powered sodium bentonite sandwiched between woven and non-woven geotextiles, and had a unit mass of 4670 g bentonite/m^2. Bentonite within this GCL had a water content, specific gravity, and smectite content of approximately 10.0%, 2.85, and 80%, respectively.

Nine different natural rock leachates obtained from different parts of Japan were used. Four of them were liquid samples, collected from four ore deposits (Kaminosawa, Okunosawa, Honko and Tateishi) of Kamikita mining complex (Aomori Prefecture) on July 2010. The other five rock drainage samples were obtained after leaching test using rocks from excavated sites and natural ground located in Yamanashi, Hyogo, Miyagi (2 samples) and Tokyo. The rocks from excavated sites and natural ground were crushed under 2 mm diameter and dried in the oven at 105±5 °C for 1 day, and 150 grams of these material were mixed with 1.5 L of distilled water in a 2 L plastic bottle with hermetic cap and placed in an incubator shaker at 100 rpm for 40 days at 20°C. The pH, EC, and ORP were monitored periodically. Before conducting sorption tests, the mixtures were centrifuged and filtrated, and the metal contents were analyzed by ICP-MS (Agilent 7500ce). Some chemical properties of the natural drainage from mines and excavated rocks and natural ground from different sites of Japan are summarized in Table 1. These values were considered as the initial conditions.

An artificial ARD was prepared in the laboratory based on the drainage composition of a Pb-Zn-(Cu) deposit located in Cerro de Pasco, Peru [10]. Metal composition is presented in Table 2. GR grade $FeSO_4 \cdot 7H_2O$, $Al_2(SO4)_3 \cdot 16H_2O$, $CuSO_4 \cdot 5H_2O$, $ZnSO_4 \cdot 7H_2O$, $Na_2HAsO_4 \cdot 7H_2O$, $PbCl_2$, K_2SO_4, Na_2SO_4, $CaSO_4$, and $MgSO_4$ were mixed, and then the pH was adjusted to 3 using H_2SO_4. EC was 1195 mS/m.

[1]Graduate Student, Graduate School of Global Environmental Studies, Kyoto University, Japan
[2]Professor, Graduate School of Global Environmental Studies, Kyoto University, Japan
[3]Associate Professor, Graduate School of Global Environmental Studies, Kyoto University, Japan
[4]Lecturer, Graduate School of Engineering, Kyoto University, Japan
[5]Senior Researcher, Disaster Prevention Technology Division, Railway Technical Research Institute, Japan

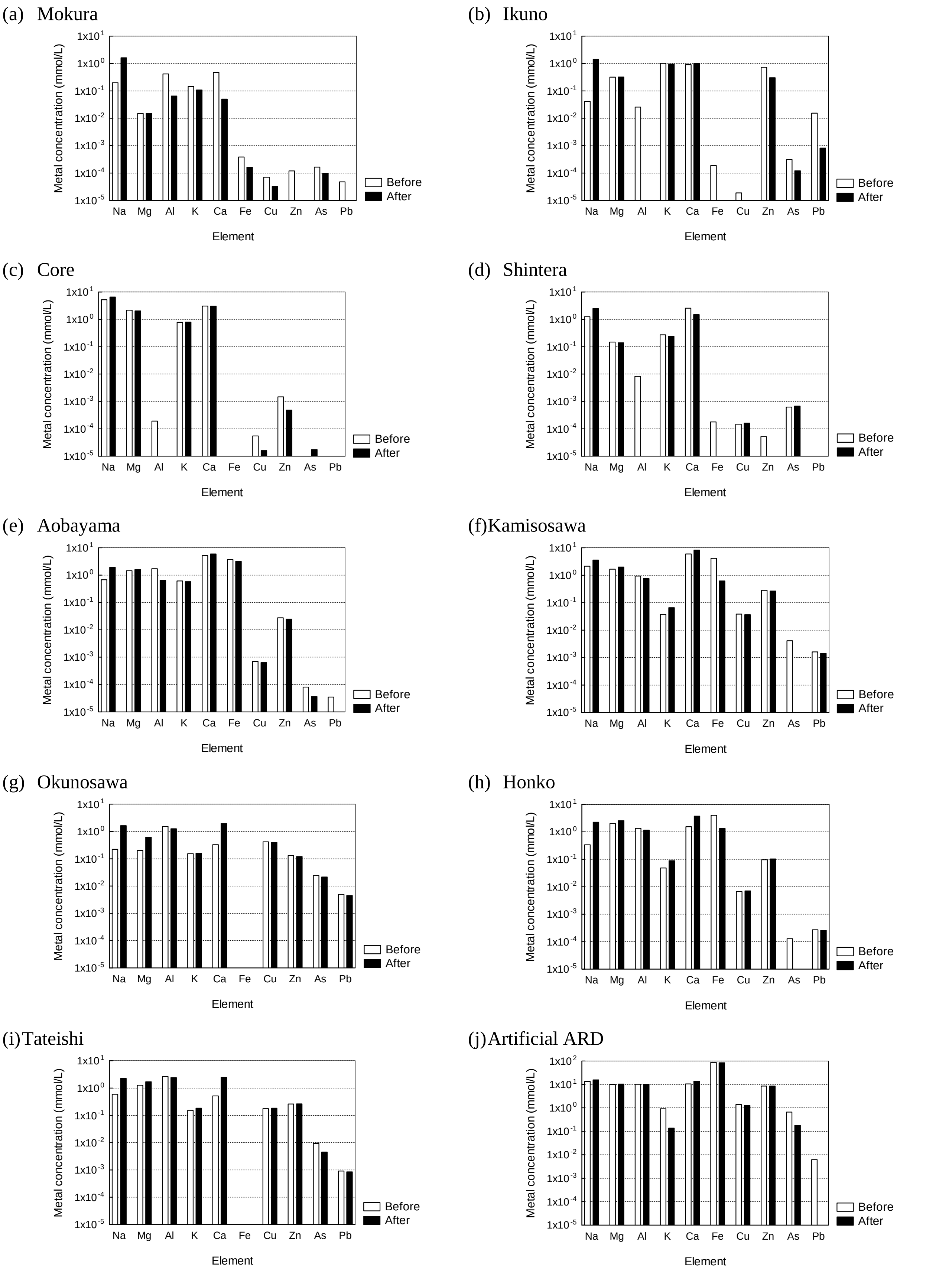

Fig. 1. Metals sorption on bentonite: (a) Mokura, (b) Ikuno, (c) Core, (d) Shintera, (e) Aobayama, (f) Kaminosawa, (g) Okunosawa, (h) Honko, (i) Tateishi, (j) Artificial ARD

Table 1. Profile and chemical characteristics of natural ARDs from Japan

Identification	Place	Type	pH	EC (mS/m)	ORP (mV)
Kaminosawa	Aomori	Liquid	2.37	297	10
Okunosawa	Aomori	Liquid	1.23	1227	81
Honko	Aomori	Liquid	2.55	208	48
Tateishi	Aomori	Liquid	1.80	620	69
Mokura	Yamanashi	Altered volcanic rock	7.70	9.52	156
Ikuno	Hyogo	Altered volcanic rock	5.16	57.2	262
Aobayama	Miyagi	Mud sediment	3.33	213	354
Shintera	Miyagi	Mud sediment	8.09	51.6	140
Core	Tokyo	Mud sediment	6.25	182.1	205

3. SORPTION TEST

The chemical performance of bentonite was studied through batch sorption tests. Sorption test is a quick method that provides information about bentonite performance regarding metal affinity, metal sorption capacity and involved mechanism. For this test, 10 different ARDs (9 natural and 1 artificial ARD) were used.

Sorption tests were conducted using 0.1 g of bentonite in 50 mL of solution for the natural ARDs and 0.2 g bentonite in 50 mL of solution for the artificial ARD (higher amount in the latter case because of higher metal concentration). Samples were taken after 24 hours on an incubator shaker at 100 rpm and 25^{o}C. After shaking, every mixture was centrifuged and filtered using a filter with a 0.22-μm pore size. The concentrations of Fe, Cu. Zn, Al, As, Pb, Na, Ca, Mg, and K before and after the sorption tests were analyzed by ICP-MS (Agilent 7500ce).

The reduction in the concentration values of 10 metals after the addition of bentonite is presented in Fig. 1. In some cases, the reduction was small, which suggests that the solid-liquid ratio was low, but enough to detect sorption. Results led to a better understanding of sorption capacity of bentonite against heavy metals in a metal complex system (natural leachates from excavated rocks and mines and artificial ARD). Due to the release of Na, K, Ca, and Mg, cations present in Na-bentonite, it can be inferred that the mechanism involved is probably ion exchange.

Sorption test results usually represent ideal conditions and, therefore, to evaluate field application of bentonite, additional tests, such as hydraulic conductivity test, become necessary.

Table 2. Artificial ARD composition

Metal	Concentration (mg/L)
Al	259.2
Fe	4330.2
Cu	86.9
Zn	493.1
As	49.1
Pb	2.9
K	31.8
Na	413.9
Ca	397.0
Mg	214.0

4 HYDRAULIC CONDUCTIVITY TEST

Nine-month hydraulic conductivity tests were conducted on GCL following the procedures described in ASTM D 5084 “Standard Test Methods for Measurement of Hydraulic Conductivity of Saturated Porous Materials Using a Flexible Wall Permeameter” and ASTM D 7100 “Standard Test Method for Hydraulic Conductivity Compatibility Testing of Soils with Aqueous Solutions”, using a falling headwater–constant tailwater system. Fig. 2 shows a typical diagram for this system, which consists of a flexible-wall permeameter with a cell pressure of 30 kPa and an average hydraulic gradient of 85–95 at constant room temperature of 25°C. The GCL (specimen) was placed between filter papers, geotextiles, and plastic caps and was confined by a latex membrane on the sides. The thickness of the GCL was measured regularly using a cathetometer, while the EC, pH, effluent volume, and metal content by ICP were measured periodically (results of effluents not shown).

Table 3. Testing conditions for hydraulic conductivity test

Sample	Prehydration solution	Permeant solution
Sample 1	ARD	ARD
Sample 2	Distilled water	ARD
Sample 3	Distilled water	Distilled water

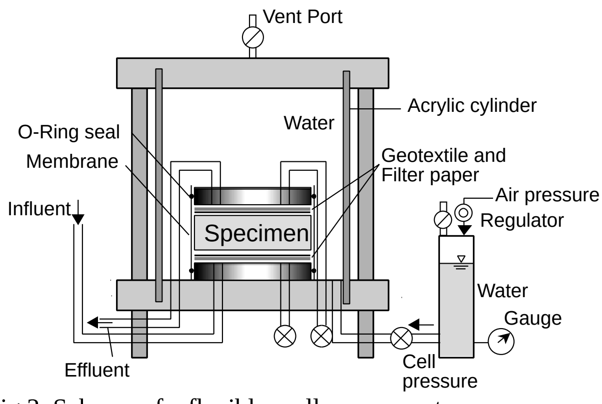

Fig 2. Scheme of a flexible-wall permeameter

For hydraulic conductivity tests, the artificial ARD was used because its composition is critical in terms of metal concentration and pH values compared to the natural ARDs.

Because waste rock containment is expected to last long, hydraulic conductivity, pH and EC changes, and metal release over time were monitored for nine months. Before ARD permeation, two types of prehydration were performed using either ARD (Sample 1) or distilled water (Sample 2). For the prehydration process, GCLs were placed into containments with the corresponding permeant solution for seven days and 30 kPa of pressure was applies. As a control, a test with distilled water prehydrated and permeated GCL was also conducted (Sample 3).

The results of the hydraulic conductivity test are presented in Fig. 3. The hydraulic conductivity of GCL permeated with distilled water (control) was constant, with an average of 1.4×10^{-11} m/s. The hydraulic conductivity value of the GCL prehydrated with water and permeated with ARD was around 1.1×10^{-10} m/s, and the hydraulic conductivity of the GCL prehydrated and permeated with artificial ARD, around 5.0×10^{-10} m/s. The hydraulic conductivity of GCL prehydrated with water and permeated with ARD was five times lower than the one of ARD prehydrated and permeated GCL, which suggests that water prehydration positively impacts on hydraulic conductivity.

Hydraulic conductivity values of GCLs permeated with the natural ARDs have not been determined yet, but can be probably predicted, considering that hydraulic conductivity values may be a function of EC, pH, or swell volume. For example, according to a relationship between hydraulic conductivity and swell volume presented in [7], at a 8.5 mL/2 g bentonite of swell volume obtained for the artificial ARD (results presented in [6]), the expected hydraulic conductivity value should be $3.6\text{x}10^{-10}$ m/s. This value is close to the experimental value ($5.0\text{x}10^{-10}$ m/s) with a 72% accuracy and confirms the relationship between the hydraulic conductivity and free swell index reported in the literature. Relationships between parameters are still under investigation and, thus constitute part of the future research.

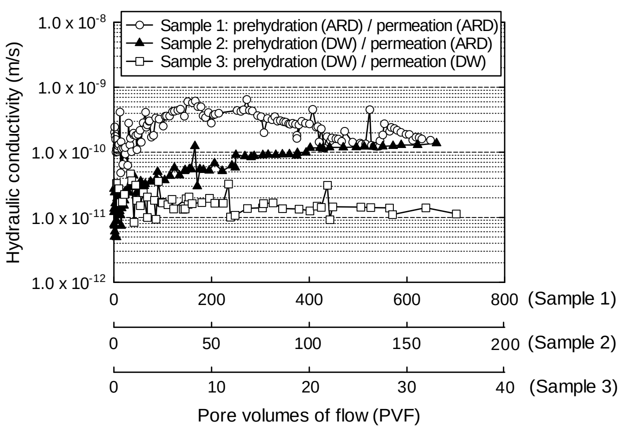

Fig. 3. Hydraulic conductivity change of each condition

4 CONCLUSIONS AND FUTURE RESEARCH

From natural rock leachates and mine drainage it was observed that these minerals have the capacity to sorb heavy metals even when they are in combination (complex metal mixture).

Nine-month hydraulic conductivity tests showed that permeability changes over time, especially due to precipitation (physical clogging). The hydraulic conductivity remained low during the test duration and was approximately 5 times lower when GCL was prehydrated with water before ARD permeation ($1.1\text{x}10^{-10}$ m/s) than the case in which prehydration and permeation were done using ARD ($5.0\text{x}10^{-10}$ m/s).

Considering that bentonite inside GCLs has the potential to retain heavy metals present in solution, showing relatively low hydraulic conductivity under even extreme conditions, with availability in many parts of the world, GCLs seem to provide an alternative for barriers against rock leachates with high heavy metal content.

Future research will be done on the relationship between parameters such as EC, pH, swell volume or metal sorption capacity and hydraulic conductivity in order to predict field application of GCLs.

5 ACKNOWLEDGMENTS

The Nikkei Scholarship granted by The Nippon Foundation (Nippon Zaidan) has been provided to the first author's postgraduate study. The authors express deep gratitude to Mr. Atsushi Takai and Dr. Zhenze Li (Kyoto University), and Takuya Urakoshi and Tomokazu Ishihara (Railway Technical Research Institute) for their helpful discussions and constructive comments and suggestions.

6 REFERENCES

[1] Ohta, T., Enomoto, H., and Tokunaga, T., 2006. Evaluation and prediction of pollution caused by acid water exuded from mud sediment in urban ground, IAEG 2006, No.265, pp.1-9.

[2] Lange, K., Rowe, R. K., and Jamieson, H., 2010. The potential role of geosynthetic clay liners in mine water treatment systems, Geotextiles and Geomembranes, Vol.28, No.2, pp.199-205.

[3] Rowe, R. K., 2006. Some factors affecting geosynthetics used for geoenvironmental applications, 5th International Conference on Environmental Geotechnics, London, pp.43-69.

[4] Lange, K., Rowe, R. K., and Jamieson, H., 2007. Metal retention in geosynthetic clay liners following permeation by different mining solutions, Geosynthetics International, Vol.14, No.3, pp.178-187.

[5] Shackelford, C. D., Sevick, G. W., and Eykholt, G. R., 2010. Hydraulic conductivity of geosynthetic clay liners to tailings impoundment solutions, Geotextiles and Geomembranes, Vol.28, No.2, pp.149-162.

[6] Naka, A., Li, Z., Inui, T., Katsumi, T., and Mogami, H., 2010. Heavy metals retention in geosynthetic clay liners and its potential role in acid rock drainage treatment, Geosynthetics Engineering Journal, Japan Chapter of International Geosynthetics Society, Vol.25, pp.233-240.

[7] Katsumi, T., Ishimori, H., Ogawa, A., Yoshikawa, K., Hanamoto, K., and Fukagawa, R., 2007. Hydraulic conductivity of nonprehydrated geosynthetic clay liners permeated with inorganic solutions and waste leachates, Soils and Foundations, Vol.47, No.1, pp.79-96.

[8] Lange, K., Rowe, R. K., and Jamieson, H., 2009. Diffusion of metals in geosynthetic clay liners, Geosynthetics International, Vol.16, No.1, pp.11-27.

[9] Hornsey, W. P., Scheirs, J., Gates, W. P., and Bouazza, A., 2010. The impact of mining solutions/liquors on geosynthetics, Geotextiles and Geomembranes, Vol.28, No.2, pp.191-198.

[10] Wibkirchen, C., Dold, B., Friese, K., and Glaber, W., 2005. Hydrogeochemistry and sediment mineralogy of Lake Yanamate - an extremely acidic lake caused by discharge of acid mine drainage from the Pb-Zn-(Cu) deposit, Cerro de Pasco (Peru), Securing the Future, pp.1013-1022.

First International Conference on Geotechnique, Construction Materials and Environment, Mie, Japan, Nov.21-23, 2011, ISBN: 978-4-9905958-0-7 C3051

The Comparison of Monotonic Behaviors of Two Different Calcareous Sands

R. Rezvani, M.Sc. Student, School of Civil Engineering, Iran University of Science and Technology
H. Shahnazari, Assistant Professor, School of Civil Engineering, Iran University of Science and Technology
H. Salehzadeh, Assistant Professor, School of Civil Engineering, Iran University of Science and Technology
Y. Dehnavi, Ph.D. Candidate, School of Civil Engineering, Iran University of Science and Technology

ABSTRACT: Investigating the behavior of calcareous soils has been extended during recent decades and the differences between the mechanical behaviors of various calcareous soils due to their local geological effects were mentioned by previous researchers. This paper is containing an experimental investigation on the monotonic behaviors of two originally different calcareous sands. These sands were obtained from northern coast of Persian Gulf, including Hormuz Island (HI) and Bushehr Port (BP). The testing program was consisted of two main parts: a series of isotropic compression (IC) tests to high stress levels (up to 1.5 MPa), and a series of drained isotropically consolidated (CID) tests on reconstituted specimens. Grain size analyses were carried out prior to and following of the tests to quantify the amount of particle breakage of used sands. The effects of drastic parameters such as density and confining pressure on compressibility and shearing response of the soils were also investigated. The results showed that particle breakage occurred during shearing and this phenomenon affected the mobilized friction angle.

1. INTRODUCTION

Carbonate deposits which are located in tropical and subtropical areas, cover approximately 40% of the ocean floor [1]. Investigating on the mechanical behaviors of the carbonate soils has been extended in a rapid rate in recent years due to the existence of these deposits at many petrochemical reserves and hydrocarbon industries such as Persian Gulf. These reasons have encouraged many researches to investigate the geotechnical behaviors of calcareous sands [2]–[6]. Previous researches have showed that there are many differences between the behaviors of calcareous and terrigenous sands [7]–[9]. The most important of these differences are related to the compressibility and the potential of particle breakage of calcareous sands under applicable pressures. Not only carbonate sands behave different in comparison of terrigenous sands, but also various types of calcareous sands have significant different behavior in their response to the shearing loading due to their locations and origins [9].

Particle breakage is one of the important features of calcareous sands and has a chief role on the mechanical behaviors of these sediments. For example, particle breakage reduces the dilation response of the sands and mobilized friction angle [9]. Many researchers try to quantify the amount of particle breakage of soils [10]–[12]. In some methods, increasing of passing percentage of only one size in gradation curves of soils is analyzed which in some conditions may not be appropriate. Hardin (1985) used overall gradation curves of soils to measure the particle breakage with a good accuracy [13].

In this study, mechanical behaviors of two originally different carbonate soils were investigated. The soils are obtained from northern coast of Persian Gulf. Experimental research was consisted of two series of triaxial tests including a series of isotropic compression (IC) tests and a series of drained isotropically consolidated (CID) tests on reconstituted specimens. In the isotropic compression tests, confining pressure was increased up to 1.5 MPa to investigate the compressibility of the sands under high pressure. To measure the amount of particle breakage of the soils, the grain size distribution analyses were carried out before and after the tests. Samples were prepared in various densities (i.e., loose, medium and dense) and consolidated under different confining pressures to investigate the effects of these important parameters on the shearing response of used sands.

2. SOIL CHARACTERIZATION

The carbonate sands were obtained from the north of Persian Gulf, Hormoz Island (HI) and Bushehr Port (BP). Hormuz Island is located in the north of the famous Hormuz Strait. Another soil was obtained from Bushehr Port which is one of the most important and strategic commercial harbours of Iran. Fig. 1 shows the origins of the used carbonate sands in this study.

Grain size distribution tests showed that both carbonate sands are well graded (SW). It can also be inferred that HI sand is coarser than BP sand (Fig. 2).

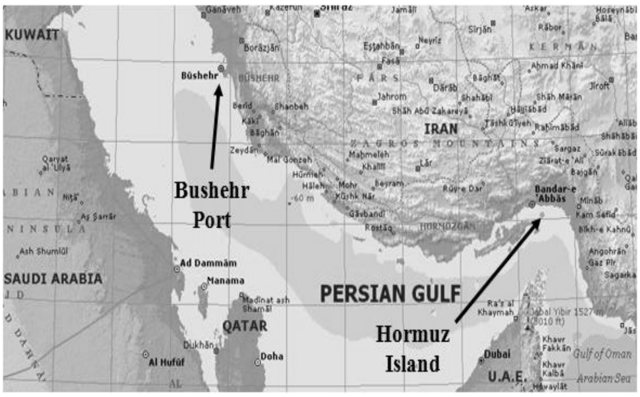

Fig.1. Location of Hormuz Island and Bushehr Port in Persian Gulf

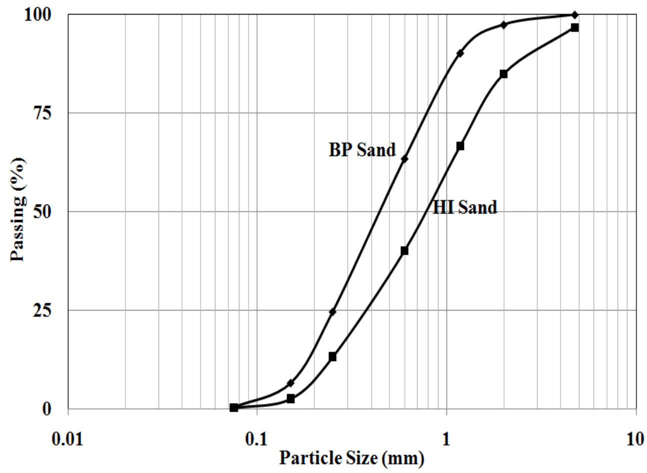

Fig.2. Grain size distribution of the used sands

Also, Carbonate content tests using British Standard 1377, were conducted on the used sands. The results showed that HI and BP sands contain more than 53 and 44 percentages of carbonate calcium, respectively. Table.1 shows some physical properties of the carbonate sands.

Table.1. Physical properties of the carbonate sands

Physical Property	Soil Type	
	HI	BP
Grain Shape	Angular	Subangular
D_{50} (mm)	0.78	0.43
C_u	8.33	7.87
C_c	1.54	0.84
γ_{min} (kN/m^3)	14.48	13.21
γ_{max} (kN/m^3)	17.01	15.69
G_s	2.764	2.709
Carbonate Content (%)	53.78	44.58

Figs. 3 and 4 show the FESEM micrographs for HI and BP soils. Microscopic photographs present that both types of soils are dominated by thin-walled mollusk and echinoderm plate fragments and thick-walled foraminifera.

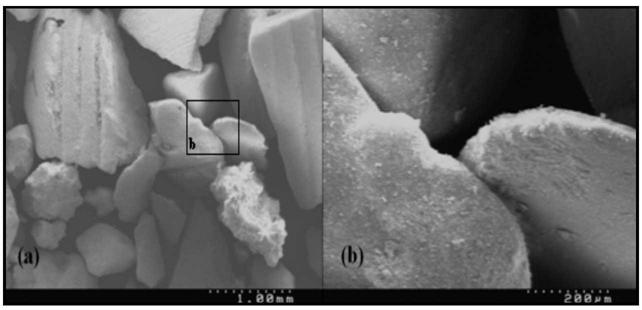

Fig.3. FESEM micrograph for the HI sand;
a: Angular particles of soil; b: Close-up view of the particles

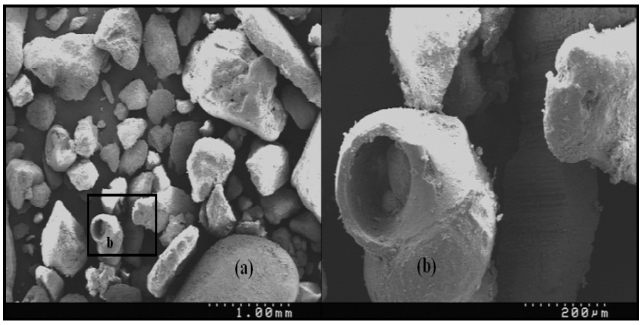

Fig.4. FESEM micrograph for the BP sand;
a: Subangular particles of soil; b: Close-up view of the particles

3. SAMPLE PREPARATION

In this study, the specimens were prepared by the air-pluviation method. The dry sand was spread into the mold which was fixed on the base pedestal of the triaxial apparatus and lined with a rubber membrane. To acquire the desired density the mold was then tapped. The diameter and the height of the specimen were 70 mm and 140 mm, respectively. Saturation procedure contained flushing CO_2, exuding de-aired water and applying a back pressure of 200 kPa under an effective pressure of 10 kPa to the specimens. Following this procedure, all specimens achieved high saturation conditions, and the B-values greater than 0.95 insured the high quality of all the specimens. Afterward, samples were isotropically consolidated under desired pressures. The loading part of tests was conducted at strain control condition with the rate of 0.5 mm/min in drained condition.

The tests were performed by the ELE International Corporation Triaxial apparatus, located in Geotechnical Engineering Research Center of Iran University of Science and Technology (GERC-IUST). Data Acquisition system contained a PC machine which converting input signals to bits through a DASH-12 analogue to digital converter (ADC). The procedure of testing was managed and recorded with a geotechnical software called DataSystem7 (DS7). Table.2 shows the list of tests carried out in this study.

To measure the amount of particle breakage by the Hardin method, grain size distribution test was carried out. This method supposed that particle breakage ceases when the gradation curve of the soil reaches to the stable condition. This condition was achieved when all particles become smaller than 0.074 mm (sieve No. 200). According to the Hardin method, grain crushing of the soil is defined as the ratio of variation of grading curve to its all possible variations:

$$B_r = \frac{B_t}{B_p} \tag{1}$$

In which, B_r is the relative breakage of the soil, B_t (total breakage) is the area between the initial and the final grading curves and B_p (breakage potential) is the area between the original grain size distribution curve and the vertical line for U.S. sieve No. 200 (Fig.5).

Table.2. List of tests

Test Type	Soil Type	Confining Pressure (kPa)	Relative Density Condition
IC*	HI	100	Loose
IC	HI	400	Loose
IC	HI	600	Loose
IC	HI	1000	Loose
IC	HI	1500	Loose
IC	BP	100	Loose
IC	BP	400	Loose
IC	BP	600	Loose
IC	BP	1000	Loose
IC	BP	1500	Loose
CID**	HI	100	Loose
CID	HI	200	Loose
CID	HI	400	Loose
CID	HI	600	Loose
CID	HI	100	Medium
CID	HI	200	Medium
CID	HI	400	Medium
CID	HI	600	Medium
CID	HI	100	Dense
CID	HI	200	Dense
CID	HI	400	Dense
CID	HI	600	Dense
CID	BP	100	Loose
CID	BP	200	Loose
CID	BP	400	Loose
CID	BP	600	Loose
CID	BP	100	Medium
CID	BP	200	Medium
CID	BP	400	Medium
CID	BP	600	Medium
CID	BP	100	Dense
CID	BP	200	Dense
CID	BP	400	Dense
CID	BP	600	Dense

* Isotropic Compression
** Drained Isotropically Consolidated Triaxial

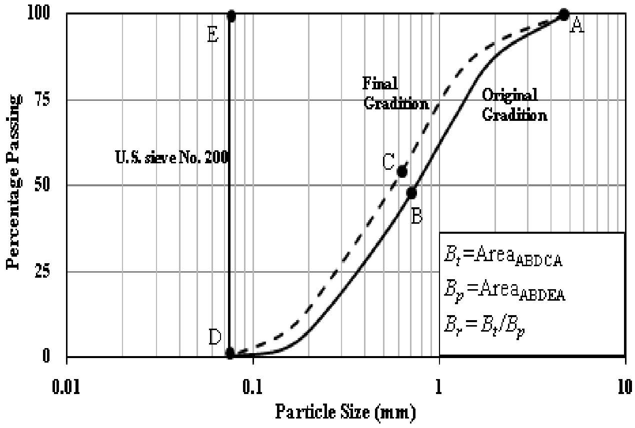

Fig.5. Definition of particle breakage based on Hardin method (1985) [13]

4. ISOTROPIC COMPRESSION TEST

Isotropic compression (IC) tests were performed on the specimens of HI and BP calcareous sands which were prepared in loose conditions. The confining pressure was increased up to 1.5 MPa and the volume change was measured.

Fig. 6 shows the variation of void ratio of the two carbonate sands under isotropic compression. It can be seen that the BP sand has more compressibility than the HI sand. Particle breakages of the samples were measured in isotropic compression tests under various confining pressures. The results showed that the BP sand has a higher particle breakage potential than the HI sand. Particle breakage of the BP samples is insignificant until the pressure of 600 kPa. Afterward, this parameter increases intensely. For the HI sand, the main particle breakage occurs beyond 1000 kPa (Fig.7). Hyodo et al (1999) and Kwag et al (1999) reported this parameter for Aio, Dogs Bay, Amami and Quiou sand about 3000, 1000, 4000 and 900 kPa, respectively in medium and dense conditions [14], [15]. So, it can be concluded that, the particle strength of the HI sand is higher than that of the BP sand.

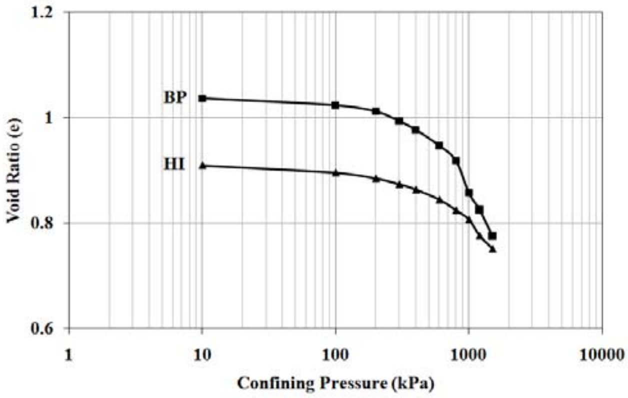

Fig.6. Isotropic compression behavior of carbonate sands in loose conditions

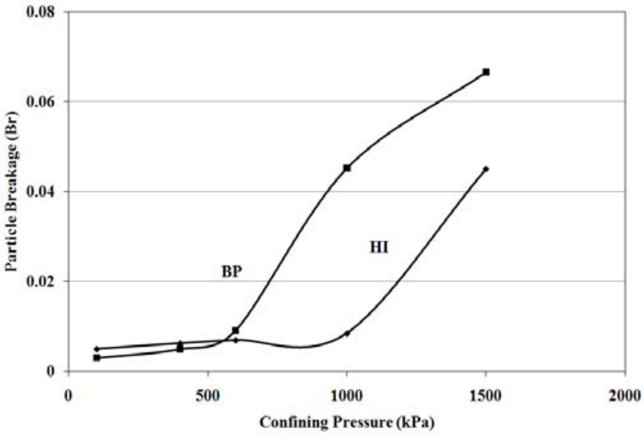

Fig.7. Particle breakage of samples in isotropic compression tests in loose conditions

5. DRAINED ISOTROPICALLY CONSOLIDATED TRIAXIAL TEST

A series of monotonic drained isotropically consolidated triaxial (CID) tests were carried out to investigate the shearing behaviors of two originally different carbonate sands. Several specimens in different relative densities (i.e., loose, medium and dense) were tested under various confining pressures including 100, 200, 400 and 600 kPa. The strain-controlled loading was applied at the rate of 0.5 mm/min and terminated when the axial strain reached to 20%. In the theory of soil mechanics, the response of the used calcareous sands to the drained shearing loading contains two stages. At the first stage, samples tend to contract and the overall volume of samples reduces (i.e., contactive behavior). Continuing the loading causes the dilation response of the specimens (i.e., dilative behavior). In this stage the volume of the samples increases.

In this study, the results showed that the BP sand had more tendency to volume change than the HI sand. In addition, at high confining pressures, there was no dilation phase in both HI and BP sands and only contractive phase occurred. Figs 8 to 11 show the drained shearing response of the HI and BP sands in loose condition under varied confining pressures between 100 and 600 kPa. The deviatoric stress in this study was calculated based on the following relation:

$$q = \sigma_1 - \sigma_3 \qquad (2)$$

It can be inferred from the Figs 8 and 9 that the shearing strength of the HI sands is higher than that of the BP sands.

Figs 10 and 11 illustrate the volume change of HI and BP sands. As it was seen during the isotropic compression tests, the BP samples showed more volume change than the HI sand in similar loading conditions. For the HI sand, specimens which were consolidated under 100 and 200 kPa had both contractive and dilative phases but in higher confining pressures only contraction was observed. For the BP sand, only the specimen under the confining pressure of 100 kPa had both contractive and dilative responses and the others showed no dilation and the volume decreases during the deviatoric loading.

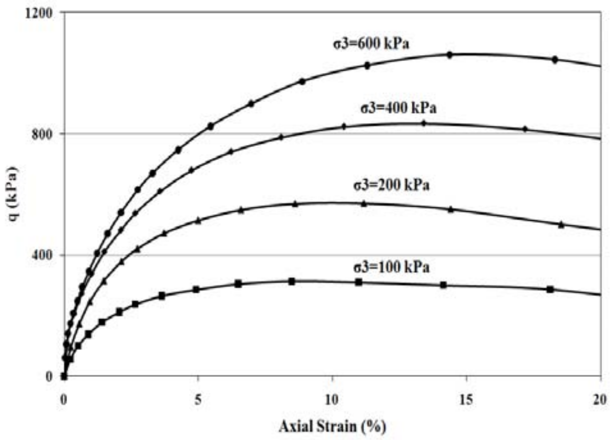

Fig.8. Effect of confining pressure on the shearing strength of the HI sand in loose conditions

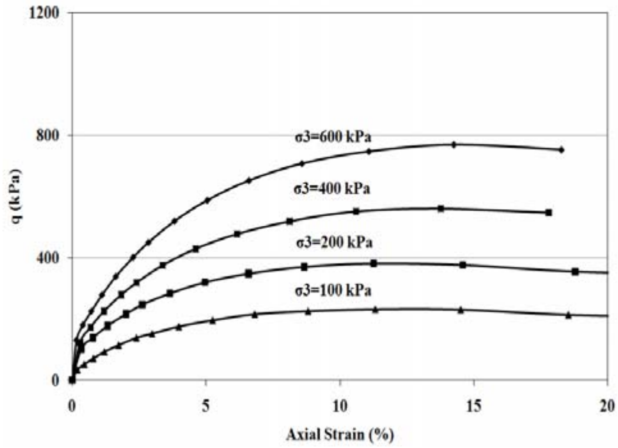

Fig.9. Effect of confining pressure on the shearing strength of the BP sand in loose conditions

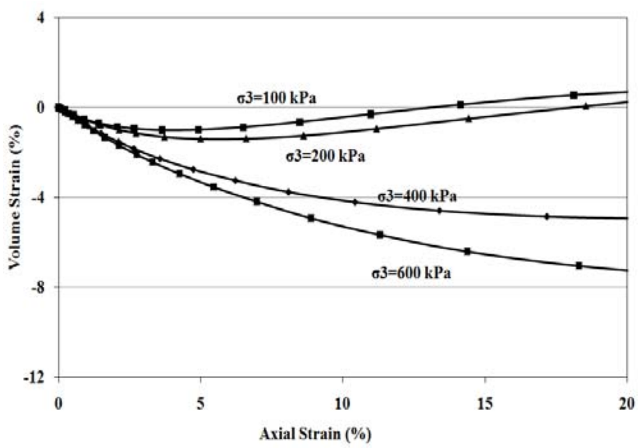

Fig.10. Effect of confining pressure on the volume change of the HI sand in loose conditions

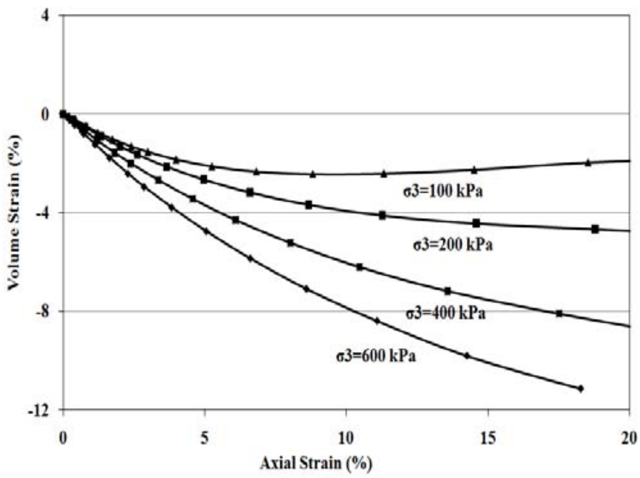

Fig.11. Effect of confining pressure on the volume change of the BP sand in loose condition

The Mohr-Coulomb failure analysis was used to find the mobilized friction angle of the specimens in different relative densities (i.e. loose, medium and dense). Figs 12 and 13 show the variation of mobilized friction angle of the HI and BP sands in drained triaxial tests. Obviously, increasing the confining pressure causes the decrement of mobilized friction angle which was observed in this study too. The maximum change in mobilized friction angle of the HI sand which took place in loose conditions was 9.46^0 but for the BP sand the amount of this parameter was 12.3^0 and occurred in dense conditions. The higher amount of variation in mobilized friction angle of the BP sand can be related to the higher amount of particle breakage of the BP sand in comparison to HI sand which resulted in strength reduction.

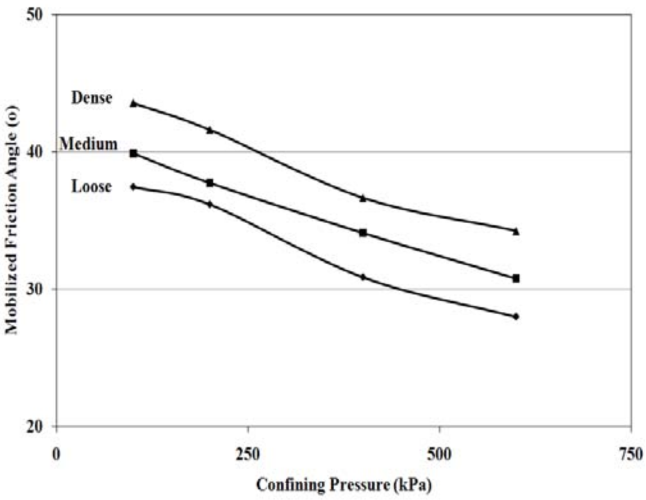

Fig.12. Variation of mobilized friction angle of the HI samples in drained triaxial tests

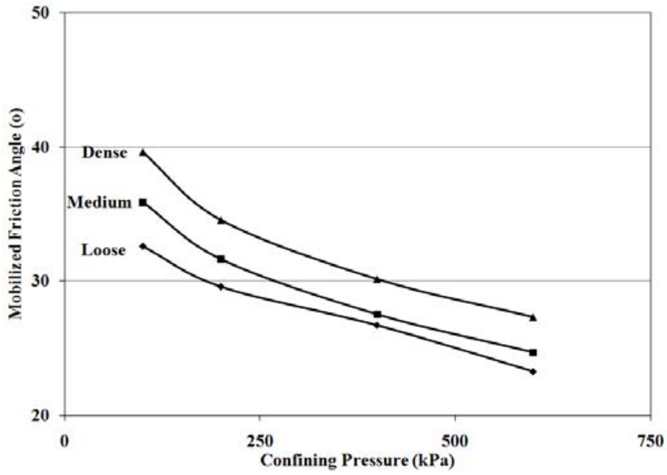

Fig.13. Variation of mobilized friction angle of the BP samples in drained triaxial tests

6. CONCLUSION

Experimental investigations were conducted to study the monotonic shearing behaviors of two calcareous sands. The two originally different calcareous sands were obtained from the north coast of Persian Gulf. Experimental investigation contained a set of isotropic compression tests (CI) and a set drained isotropically consolidated triaxial (CID) tests. Following results from the tests can be concluded:

1) Initial tests about the physical properties of the used carbonate sands showed that the HI sand is coarser and has greater maximum and minimum density. These differences resulted from the different origins of the HI and BP sands with different geological characteristics.
2) Isotropic compression tests showed higher compressibility index for the BP sand. In these tests, the void ratio of the BP samples decreased at a higher rate than that of HI samples.
3) It can be inferred from the isotropic compression tests that the yielding stress of the HI and BP sands are about 1000 and 600 kPa, respectively. Beyond these pressures the amount of particle breakage increases intensely.
4) Different behaviors in shearing response of the used carbonate sands were observed. The HI samples showed more dilation than the BP ones. At high confining pressures only contractive phase could be seen in both sands.
5) Particle breakage of the used sands caused to have more reduction in mobilized friction angle by increment of the confining pressure. Comparison between the HI and BP sands, demonstrated that the BP sand has a higher reduction in mobilized friction angle that was resulted from higher particle breakage.

7. REFERENCES

[1] Holmes, A. "Principles of physical geology", Sunbury-on- Thames, Nelson, London, 1978, pp730.

[2] Kaggwa, W. S., Poulos, H. G., and Carter, J. P. "Response of carbonate sediments under cyclic triaxial test conditions", Engineering for Calcareous Sediments, Proc. Int. Conf. on Calcareous Sediments, Jewell and Andrews, eds., Balkema, Rotterdam, Perth, Australia, 1988, pp. 97-107.

[3] Airey, D.W., "Triaxial Testing of Naturally Cemented Carbonate Soil", Journal of Geotechnical Engineering, 1993, 119(9): 1379-1398.

[4] Salehzadeh, H., “The behaviour of non-Cemented and artificially cemented carbonate sand under monotonic and reversed cyclic shearing, University of Manchester”, U.K., 2000, Ph.D.

[5] Hasanlourad, M., Salehzadeh, H., and Shahnazari, H., "Dilation and particle breakage effects on the shear strength of calcareous sands based on energy aspects", International Journal of Civil Engineering, 2008, 6(2): 108-119

[6] Dehnavi, Y., Shahnazari, H., Salehzadeh, H., and Rezvani, R., "Compressibility and Undrained Behavior of Hormuz Calcareous Sand", Electronic Journal of Geotechnical Engineering, 2010, Vol. 15.

[7] Datta M., Gulhati, S. K. and Rao, G. V., "Crushing of calcareous sands during shear", Proceedings 11th Annual Offshore Technology Conference, Houston, 1979, pp. 1459-1460

[8] Coop, M. "The mechanics of uncemented carbonate sands", Geotechnique, 1990, 40(4): 607-626.

[9] Brandes, H. "Simple Shear Behavior of Calcareous and Quartz Sands", Geotechnical and Geological Engineering, 2011, 29(1): 113-126.

[10] Leslie, D.D., "Shear Strength of Rockfill", Physical Properties Engineering Study No. 526, South Pacific Division, Corps of Engineers Laboratory, Sausalito, Calif., Oct., 1975, pp. 124.

[11] Marsal, R. J., "Discussion of Shear Strength", Proceedings of the 6th International Conference on Soil Mechanics and Foundation Engineering, Montreal, 1965, Vol. 3, pp. 310-316

[12] Morrison, M.J., Mcintyre, P.D., and Sauls, D.P., "Lab- oratory test results for carbonate soils from offshore African", Proceedings of the International Conference on Calcareous Sediments, Perth, Western Australia, 1988, Vol. 2, pp.777-784.

[13] Hardin, B. O., "Crushing of Soil Particles", Journal of Geotechnical Engineering, 1985, 111(10): 1177-1192.

[14] Hyodo, M., Aramaki, N., Nakata, Y., Inoue, S., Hyde and A.F.L. "Particle crushing and undrained shear behaviour of sand", Cupertino, CA, ETATS-UNIS, International Society of Offshore and Polar Engineers, 1999.

[15] Kwag, J., Ochiai, H. and Yasufuku, N., "Yielding stress characteristics of carbonate sand in relation to individual particle fragmentation strength", Engineering for calcareous sediments, Edited by KA Al-Shafei. AA Balkema, Rotterdam, the Netherlands, 1999, 79–87.

First International Conference on Geotechnique, Construction Materials and Environment, Mie, Japan, Nov.21-23, 2011, ISBN: 978-4-9905958-0-7 C3051

Soaking Effect on Strength and Performance of Fine Grained Soil Stabilized with Recycled Gypsum

Aly Ahmed[1], Keizo Ugai[2] and Taira Jinno[3]
[1]Civil Engineering Department, Beni-Suef University, Beni-Suef, Egypt
[1, 2,3]Civil and Environmental Engineering Department, Gunma University, Japan

ABSTRACT: The use of recycled gypsum as a stabilizer material in ground improvement projects has been initiated in Japan recently since the disposing of gypsum wastes in landfill sites has many environmental problems. As the use of recycled gypsum in soil stabilization applications has many environmental and economical benefits, it has many challenges since gypsum is soluble material. Therefore, it's essential to investigate the behavior of stabilized soil with recycled gypsum under soaking conditions. Recycled gypsum was mixed with Furnace cement type B with different ratios and various percentages of this admixture content were used. Cylindrical stabilized soil specimens were prepared and subjected to different numbers of soaking periods. The soaked specimens were tested for compressive strength, volume change and soil deterioration to investigate the effect of soaking conditions on their strength, durability and performance. Results showed that the increase of admixture content has a positive effect on the strength increase and durability improves. The early soaking days have a negative effect on strength and durability compared to the later soaking days. The increase of admixture content is associated with the increase of percentage of soil soluble deterioration. The use of Furnace cement as a solidification agent to prevent the solubility and to improve the durability of stabilized soil with recycled gypsum is recommended. The influence of soaking conditions on strength, durability and performance for specimens stabilized with the investigated limits of recycled gypsum in this study is limited. Generally, stabilized soft clay soil with recycled gypsum, which is treated with Furnace cement, has an acceptable durability as well as a good performance against the actions of soaking conditions.

Keywords: Recycled gypsum; Soaking; Durability; Strength

1. INTRODUCTION

Gypsum waste plasterboard is a serious problem in Japan since 1.6 million tons of gypsum wastes are generated annually. The disposing of gypsum wastes in ordinary landfill sites is not permitted in Japan according to Japanese environmental regulations [1-4]. It must send to controlled landfill sites to avoid the negative effect on the environment and then the cost of their disposing increases [2]. Therefore, investigations to produce recycled gypsum from gypsum waste plasterboard and then to use as a stabilizer material in ground improvement projects have been conducted recently in Japan [1-3; 5-7]. In fact the use of recycled gypsum as a stabilizer material has many economical and environmental advantages but it has many challenges since gypsum is a soluble material. The solubility of gypsum is considered one of the most challenges for the application of recycled gypsum, produced from gypsum wastes, in ground improvement projects. The solubility of gypsum results a negative effect on both strength and durability since the bonding between soil and gypsum is destroyed when water is introduced. To avoid such negative effects, the additives of solidification agent such as cement is essential to prevent the solubility of gypsum as well to improve both strength and durability of soil stabilized with recycled gypsum. The effect of soaking conditions on soil stabilized with recycled gypsum has not been reported in literature up to the knowledge of authors. So, it is essential for geotechnical engineers to have knowledge about the effect of soaking conditions on the performance of soil stabilized with recycled gypsum to facilitate the use of recycled gypsum as a stabilizer material in ground improvement projects. The influence of weathering or environmental conditions in terms of freezing-thawing and wetting-drying cycles on the performance of soil stabilized with recycled gypsum have been conducted [9-11]. The influence of freezing-thawing cycles on the durability of silty sand soil stabilized with recycled gypsum was investigated. Different contents of recycled gypsum-cement admixture were mixed with tested soil in dry state; subsequently the optimal moisture and dry density for each sample were determined. The 7 days cured sample was subjected to different numbers of freezing-thawing and wetting-drying cycles and then tested for compressive strength and durability. Results showed that the actions of freezing-thawing had a significant effect on strength and durability decrease especially in the early cycles compared to the actions of wetting-drying cycles. Samples stabilized with only recycled gypsum did not survive against the actions of freezing-thawing and wetting-drying cycles. The additives of furnace cement improved the durability and strength. The performance and durability of stabilized samples were enhanced with the increase of both recycled gypsum and furnace cement contents [9-10]. The performance of soft clay soil stabilized with recycled gypsum against the actions of wetting-drying cycles was studied. For that purpose soft clay soil was mixed with different contents of Bassanite and cement and then cylindrical stabilized soil specimens were molded. Stabilized soil specimens were subjected to different numbers of wetting-drying cycles to investigate their effect on strength and durability. Results showed that the early cycles had a negative effect on durability and strength compared to the later cycles. Bassanite and cement contents had a significant effect on the improvement of strength and durability. As mentioned above, the main negative point for using recycled gypsum in ground improvement projects is the solubility of gypsum when water is introduced. So, the influence of soaking conditions on soil stabilized with recycled gypsum is considered the appropriate test in such case.

This paper investigates the influence of soaking conditions on the strength and durability of very soft clay soil stabilized with recycled gypsum and furnace slag cement type B. For that purpose, recycled gypsum was mixed with furnace slag cement type B with different ratios and then different percentages of this admixture were added to tested soil. The effect of admixture content and ratio on the performance and strength of tested soil subjected to different soaking times is investigated.

2. MATERIALS AND METHODS

Three different materials are used in this research: very soft clay, recycled gypsum and furnace cement type B. Soft clay soil was brought from some construction site at Gunma Prefecture in Japan. The initial water content for soil sample was determined by an oven drying soil sample according to ASTM specifications [12] and the average value was found 160%. Properties for tested soil sample are presented in Table 1. According to unified soil classification, USC, system, the tested soil can be classified as clay soil with high plasticity (CH).

Table 1. Properties of tested soil

Property	Value	Property	Value
Specific gravity, Gs	2.46	Plasticity index	38.50
Water content, Wc %	160	D60, mm	0.040
Liquid limit, LL %	100	D50, mm	0.022
Plastic limit, PL %	61.5	D30, mm	0.008

Recycled gypsum used in this research was produced from gypsum waste plasterboard by heating process. All procedures for producing recycled gypsum from gypsum waste plasterboard were presented in details in previous work [7]. Based on chemical analysis results for the produced gypsum, the content of $CaSO_4.1/2H_2O$ in the produced recycled gypsum was found 92.6%. The recycled gypsum was mixed with furnace cement at different ratios of 1:1, 2:1 and 3:1 for using this admixture as a stabilizing agent to improve the performance and strength of tested soil. Four different percentages of these admixtures of 0, 7.5, 15 and 22.5 % were mixed with tested soil to investigate their influence on the performance of tested soil subjected to soaking conditions.

Furnace slag cement type B used in this research was brought from some cement company in Tokyo, Japan. This cement type is mainly produced from waste materials and by-product of Portland cement manufacture. It has 30 to 60% of blast furnace slag in its compositions in accordance JIS R5211 specifications [4]. It is important to evident that the main purpose of using cement in this study is not only to improve the strength of tested soil but also to prevent the solubility of recycled gypsum as mentioned before. Furnace cement was added to recycled gypsum with different ratios of 1:1, 2:1 and 3:1, respectively.

Cylindrical soil specimens with 50 mm in diameter and 100 mm in height were prepared. Firstly, recycled gypsum was mixed in dry state with furnace cement at the investigated different ratios of 1:1, 2:1 and 3:1, respectively. Subsequently, soft clay soil sample was mixed with the desired gypsum-cement admixture contents of 0, 7.5, 15 and 22.5% according to testing program. The mixing process was done by using an automatic mixer and mixing process was prolonged for a certain time to ensure the gypsum-soil mixture to be uniform. Secondly, the tested soil was placed in three layers in special plastic mould, which is made for this purpose. Each layer was compacted statically with efforts equal to the efforts used in the standard compaction test. It is important to evident that samples were compacted with their original water content to simulate field conditions. Samples were extracted from moulds after 24 hours. More attentions were taken during sample preparation and extraction to produce homogenous samples. For each test two to three specimens were used and the average was considered. The extracted samples were wrapped in polyethylene plastic sheet and then kept in the controlled room at temperature 21±1 °C for a certain time until required for the testing according to testing schedule. The molded samples were cured for 3, 7 and 28 days before to subject for soaking. For soaking test, the cured specimens were soaked in water for different interval times of 0, 4, 7, 15 and 30 days and then tested for unconfined compression. The main target of soaking test is to investigate the influence of soaking condition on the stability of soil stabilized with recycled gypsum in terms of strength, performance, durability and solubility. Besides, the effect of curing time on the performance and strength of stabilized soil specimens subjected to soaking condition is investigated. Volume change and soil deterioration for tested soil samples were reported after each soaking time.

3. RESULTS AND DISCUSSIONS

Aforementioned, the solubility of recycled gypsum is considered the main negative point for the use of recycled gypsum in ground improvement projects. This property results in deterioration for the developed bonding between soil particles and gypsum and then the strength declines. The use of any solidification material to prevent the solubility of gypsum is essential needed to improve the performance and strength of soil stabilized with recycled gypsum. Fig. 1 shows the influence of curing time on strength ratio for samples stabilized with 15% content of gypsum-cement admixture and subjected to different soaking periods. Strength ratio is defined as the ratio between the strength of sample subjected to specified soaking time to the strength of identical un-soaked sample. This figure indicates that the strength ratio increases with the increase of soaking time in case of soaked samples subjected to curing time of 3 and 7 days. The increase of strength ratio in these cases is attributed to the following reason. The chemical reaction between gypsum-cement admixture and clay particles may need more time to achieve the optimal strength, which might be more than 7 days. Subsequently, the exposition of stabilized soil specimens in this case for soaking helped the specimens to gain more additional curing. This additional curing time promotes the reaction between gypsum-cement admixture and clay particles to complete and then the strength ratio increased with the increase of soaking time. After 30 days soaking, the exposition of specimens which cured for 3 and 7 days for more soaking times has no significant effect on the strength ratio increase. This is attributed to most of the reaction between clay particles and admixture is already completed within the 30 days of soaking. Thus there is no more improvement in strength is developed. Besides, the soaking of specimens for long time weakens the developed cementations between soil particles. On the contrary for samples cured for 28 days, the strength ratio decreases with the increase of soaking time for specified time and after that the prolonged soaking time more than 15 days has insignificant effect in strength ratio. The decrease of strength ratio with the increase of soaking time in this case is attributed the stabilized specimens after 28 days curing became almost in dry state. Subsequently, the exposition of dry specimens for soaking destroyed the developed bonding force between soil particles and then the strength decreased as presented above.

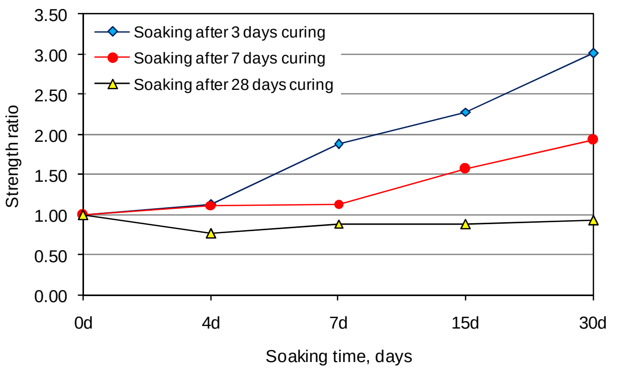

Fig. 1. Effect of curing time on strength ratio for stabilized soil specimens subjected to different soaking times.

The effect of admixture content and ratio on the durability of stabilized soil specimens subjected to different soaking times is presented in Figs. 2 and 3, respectively. Durability index is defined as the ratio between the strength of sample cured for 28 days and then subjected to a specified soaking time to the strength of identical un-soaked sample. The durability index reduces with the increase of soaking time for all samples stabilized with different contents and ratios of gypsum-cement admixtures. It is clear that, the durability index decreases significantly up to 15 days soaking and afterward the durability improves. This result is related to the effect of early soaking times have a significant effect on durability reduction compared to the later soaking times. This result is attributed to the following reasons. Firstly, the rate of water absorption in the early soaking time is greater than that occurred in the later soaking time. Subsequently, the reduction in durability increased with the increase of water absorption rate. The penetration of water to stabilized soil specimens results in disturbance for the developed cementation between soil particles which results in change in soil structure and then the durability reduced. This result agrees in concept with the results presented in the previous works for studying the effect of wet-dry cycles and soaking conditions on soil stabilized with different materials [10,13-15]. Secondly, the structure of stabilized specimens subjected to soaking after a specified time, which is 15 days in this case, may be able to rearrange itself again and accommodates with the new environment. Subsequently, the durability improved slightly after 15 days soaking due to the additional gain of curing for stabilized specimens during soaking time [10, 16]. This figure also indicates that, the admixture content has a significant effect on the improvement of durability. This result is attributed to the increase of gypsum-cement admixture content in soil mixture developed enough hardening between soil particles which able to improve the durability. The increase of admixture ratio is associated with the decrease of durability as presented in Fig. 3. It is attributed to the increase of admixture ratio means that the decrease of cement proportion in admixture content. It is well-known that the presence of cement in admixture content is considered the main responsible factor to resist the actions of soaking condition as well as improving the durability since gypsum is soluble material.

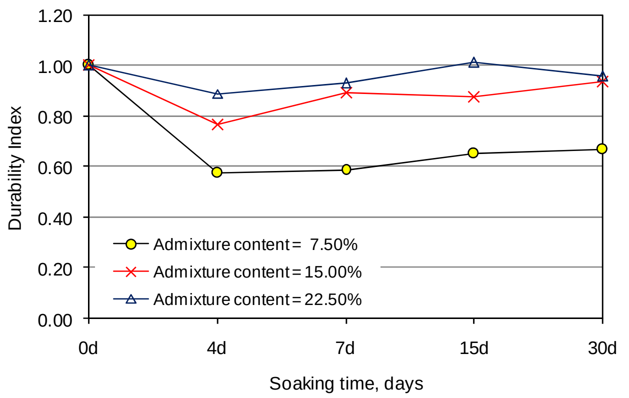

Fig. 2. Effect of admixture content on durability index for stabilized soil specimens subjected to different soaking times.

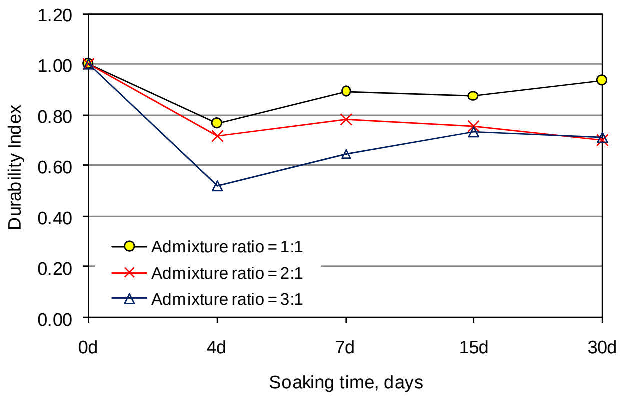

Fig. 3. Effect of admixture ratio on durability index for stabilized specimens subjected to different soaking times.

Deformation change in this study referred to settlement or swelling. It is the difference between the displacement measurements for the height of tested soil before and after to subject for soaking. The positive value means swelling while the negative value means settlement. The deformation change was measured by using a micrometer through two fixed points along the height of tested sample. The influence of admixture content at admixture ratio 1:1 on the deformation change of stabilized specimens cured for 28 days and then subjected to soaking condition is presented in Fig. 4. The effect of soaking conditions on the swelling reduces after 15 days soaking and then the samples start gradually to settle. It is attributed to the presence of cement in the admixture content resists the swelling phenomena because cement has a shrinkage property. Besides, the presence of cement in soil-gypsum mixture is solidified the activity of recycled gypsum to swell. Subsequently, the chemical reaction between recycled gypsum and clay particles, which causes the swelling, is constrained and then the swelling is reduced with the increase of soaking time. It is observed from Fig. 4 that, the effect of soaking conditions on volume change for soil stabilized with recycled gypsum-cement admixture is not significant since the maximum deformation change among all tested samples was found less than 1.50 %. This proves that the use of recycled gypsum, which is solidified with furnace slag cement, in ground improvement projects within the investigated limits in this study is durable against the effect of soaking actions in term of deformation change.

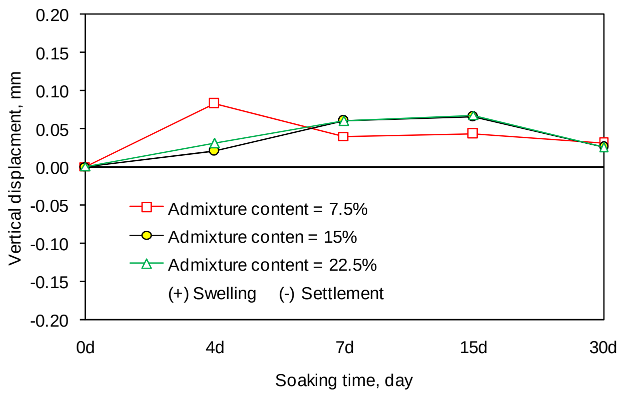

Fig.4. Effect of admixture content on deformation change for stabilized soil specimens subjected to soaking conditions.

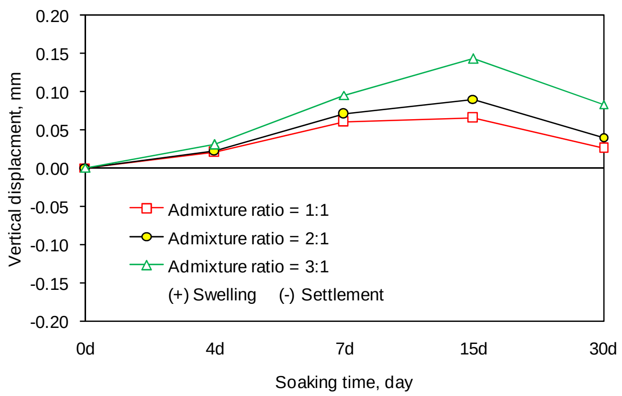

Fig.5. Effect of admixture ratio on deformation change for stabilized soil specimens subjected to soaking conditions.

The effect of admixture ratio on the deformation change of stabilized specimens is presented in Fig. 5. As observed in case of admixture content, the swelling reduces gradually after 15 days of soaking for all different investigated admixture ratios. This result is attributed to most of reactions between gypsum-cement admixture and clay soil particles are almost completed and afterward the potential of gypsum to swell is declined. It is obvious from this figure that, the increase of admixture ratio increases the swelling. It is attributed to the increase of admixture ratio means that the increase of recycled gypsum proportion in soil mixture and then the tendency of samples to swell is promoted.

The percentage of soluble soil deterioration particles for stabilized soil specimens with recycled gypsum was determined based on the dry soil mass before and after soaking. It is defined as the difference between the initial and final dry soil masses for soil sample before and after soaking divided by the initial soil mass before soaking. Fig. 6 shows the effect of admixture content on the percentage of soluble soil deterioration for stabilized soil specimens subjected to soaking conditions. The increase of soaking time increases the percentage of soluble soil deterioration up to 15 days soaking. Thereafter the percentage of deteriorated soil keeps constant and there is no more soil deteriorated from specimens. This result is related to most of water absorption is occurred in the early soaking times. Water absorption is considered the major factor responsible about the increase of the percentage of soil deterioration due to the change of soil structure. This figure indicates that, the increase of admixture content is associated with the increase of the percentage of soil deterioration. This result due to the increase of admixture content in soil mixture increases the chance or possibility of gypsum particles to dissolve in water since the amount of gypsum in soil mixture is high and then the percentage of soil deterioration is increased.

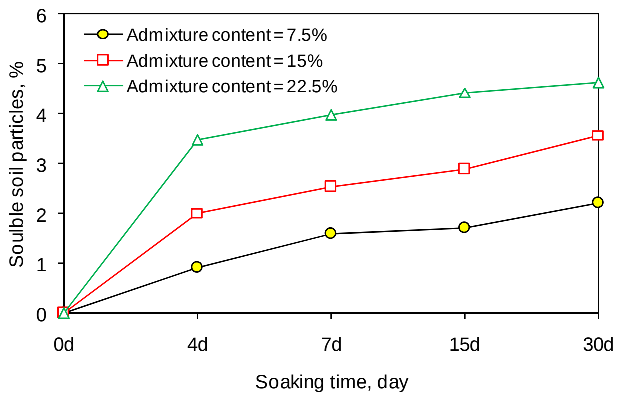

Fig.6. Effect of admixture content on the deterioration of soluble soil from specimens subjected to soaking conditions.

Fig. 7 shows the effect of admixture ratio on the percentage of soluble soil deterioration for stabilized soil specimens subjected to soaking conditions. The same behavior obtained in case of admixture content is also obtained in the case of admixture ratio. The increase of soaking time is associated with the increase of the percentage of soil deterioration from tested soil samples. It is obvious from this figure that, there is no much difference between the effects of admixture ratios investigated herein on the percentage of soil deterioration. This result may be related to the suggested proportions of cement in admixture content is enough to resist the actions of soaking condition. It is important to evidence that the tested specimens did not subject for brushing process as in case of wetting-drying test. This means that the target of the addition of cement in this case is only to prevent the solubility but it is not to improve the strength. It is well-known that the increase of cement proportion in admixture content is associated with the increase of strength. While in case of soil deterioration, the stabilized specimens did not subject to any external stresses except their own weight. Thus, the minimum suggested ratio of gypsum to cement which is 3:1 is capable to prevent the solubility of gypsum as well as to reduce the percentage of soil deterioration.

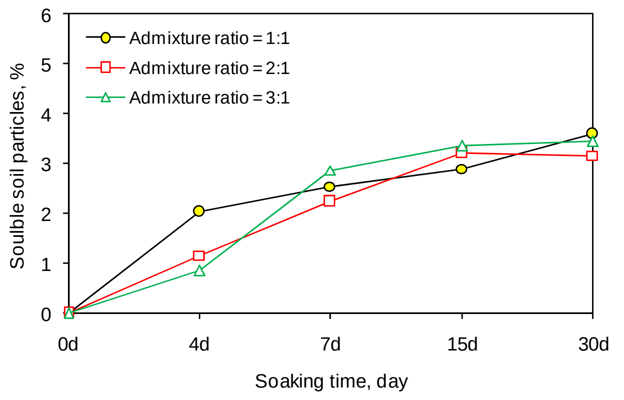

Fig.7. Effect of admixture ratio on the deterioration of soluble soil from specimens subjected to soaking conditions.

4. CONCLUSIONS

Based on experimental results, the conclusion points can be drawn as follows:

1. Both of admixture content and ratio have significant effect on the improvement of durability, strength and performance of soil stabilized with recycled gypsum. The durability index decreases with the increase of admixture ratio.
2. The early soaking time has a negative effect on the durability compared to the later soaking times and after 15 days soaking the durability improved with the increase of soaking time.
3. The early curing times of 3 and 7 days have a positive effect on the improvement of durability and strength compared to the later curing time of 28 days.
4. The effect of soaking conditions on the deformation change for stabilized soil specimens is not significant since the maximum deformation percentage was found less than 1.50 %. This indicates that the investigated limits of recycled gypsum which is solidified with furnace cement for the enhancement of very soft clay soil is durable against the actions of soaking in term of volume change.
5. Increasing soaking time increases the percentage of soluble soil deterioration up to 15 days soaking and beyond that time the percentage of the deteriorated soil is reduced.
6. There is no much difference between the effects of admixture ratios on the percentage of the deteriorated soil for specimens subjected to different soaking times.
7. Furnace slag cement type B within the investigated proportions in this study is recommended to use as a solidification agent for soft clay soil stabilized with recycled gypsum.

5. ACKNOWLEDGMENT

Funding of this research is provided through a grant from Japan Society for the Promotion of Science, JSPS to Dr. Ahmed with ID No.: P10377. The authors appreciate the financial support from this organization.

6. REFERENCES

[1] Ahmed, A., Ugai, K., and Kamei, T., “Laboratory and field evaluations of recycled gypsum as a stabilizer agent in embankment construction” Journal of Soils and Foundations, vol. 51, December 2011, (In Press).

[2] Ahmed, A., Ugai, K., and Kamei, T., “Environmental evaluation for clayey soil stabilized with gypsum waste plasterboard in Japan” In the Proceeding of the International GeoHunan 2011 Conference, June 9-11, Hunan, China, GSP, ASCE, 2011, vol. 217, June 2011, pp. 9-17.

[3] Kamei T. and Shuku T., “Unconfined compressive strength of cement-stabilized soils containing Bassanite produced from waste plasterboard. Geotechnical Society Electronic J., vol. 2, March, 2007, pp. 237-244. (In Japanese)

[4] Kamei T. and Horai H., "Development of solidification technology for fluorine contaminated Bassanite using Portland blast-furnace (B) cement.” Japanese Geotechnical J., vol. 4, Jan. 2008, pp. 91-98. (In Japanese).

[5] Kamei, T., Kato, T., and Shuku T., “Effective use for bassanite as soil improvement materials -Recycling of waste plasterboard-.” Geotechnical Society Electronic J., vol. 2, March 2007, pp. 245-252 (In Japanese)

[6] Ahmed, A., Ugai, K., and Kamei, T., "Application of gypsum waste plasterboard and waste plastic trays to enhance the performance of sandy soil" In the Proceedings of Geo-Shanghai 2010 International Conference, Geotechnical Special Publication, Ground Improvement and Geosynthetics, ASCE, vol. 207, June 2010, pp. 165-173.

[7] Ugai, K., Ahmed, A., “Evaluation of using gypsum waste plasterboard in ground improvement.” In the Proceeding of the National Workshop on Recycling Waste Plasterboard, Memorial Hall, Chuo University, Tokyo, Japan, March 2009, pp. 9.

[9] Ahmed A., Ugai K. and Kamei T., " Durability of Fine Grained Soil Stabilized with Gypsum Waste Plasterboard” In the Proceedings of 6th International Congress on Environmental Geotechincs 2010, New Delhi, India, 8-12th November, vol.2, pp. 1469-1477.

[10] Ahmed A. and Ugai K., “Environmental effects on durability of soil stabilized with recycled gypsum” Journal of Cold Regions Science and Technology, vol. 66, May 2011, pp. 84-92.

[11] Kamei T., Ahmed A. and Ugai K., “Environmental effects on durability of soil stabilized with recycled gypsum” In the Proceedings of 2011 Pan-Am CGS Geotechnical Conference, October 2-6, 2011, Toronto, Canada, p.10.

[12] Bowles, J.E., “Engineering properties of soils and their measurement.” Text Hand book, 4th Edition, McGraw-Hill, New York, Inc. 1992, 241pp.

[13] Oti, J., Kinuthia, J., Bai J., “Engineering properties of unfired clay masonry bricks.” Engineering Geology J., vol. 107, 2009, pp. 130–139

[14] Masato, M., Hiroshi, T., Koji, K., “An experimental study on the durability of fiber-cement-stabilized mud by repeated cycle test of drying and wetting. Journal of the Mining and Materials Processing Institute of Japan, vol. 121, February 2005, pp. 37-43 (In Japanese)

[15] Khattab, S.A.A., Al-Juari, K.A.K., Al-Kiki, I.M.A., "Strength, durability and hydraulic Properties of clayey soil stabilized with lime and industrial waste lime. Journal of Al-Rafidain Engineering, vol. 16, January 2008, pp. 102-116.
[16] Bin-Shafique, S., Rahman, K., Yaykiran, M., Azfar, I., "The long-term performance of two fly ash stabilized fine-grained soil subbases". J. Resources, Conservation and Recycling, vol. 54, 2010, pp. 666-672.

First International Conference on Geotechnique, Construction Materials and Environment, Mie, Japan, Nov.21-23, 2011, ISBN: 978-4-9905958-0-7 C3051

Heat Control of Pavement Surface Temperature Using Oyster Shell Lime

Satoru Ishiguro, Department of Bioresources, Mie University, Tsu, Japan

Masayoshi Yamanaka, Asahidoboku Co. Ltd., Yokkaichi, Japan

ABSTRACT: The developed heat reflective pavement is an open-graded asphalt concrete in which voids in the upper part of the pavement are filled with a cement mortar containing oyster shell lime. In this study, the heat reflecting pavement using the oyster shell lime was constructed in an open place, and the temperature reduction of the pavement surface was evaluated experimentally by taking measurements in summer. The temperature reduction effects of the heat reflecting pavement were also investigated by laboratory tests. The results show that the maximum surface temperature of the pavement fell by about 12°C compared with that of an asphalt concrete pavement. It was found that the temperature reduction effect was particularly due to the increasing reflectance of the solar radiation on the pavement surface, which was indicated in the results of spectral reflectance tests.

Keywords: Heat reflecting pavement, Oyster shell lime, Pavement surface temperature, Laboratory irradiation test, Spectral reflectance

1 INTRODUCTION

Asphalt concrete pavements generally tend to absorb solar radiation heat because they are black, and the temperature can rise to a maximum of 60°C or above at the surface in daylight in summer. The high temperature of the asphalt concrete pavement will affect the durability of the pavement as well as the heat island phenomenon in urban areas.

In Mie Prefecture, oyster farming is prosperous and discharges a large quantity of oyster shell. Some of the shells are pulverized in a factory after removing salt and utilized as oyster shell lime. Fig. 1 shows piles of oyster shell gathered at a factory site located in Toba city, Mie Prefecture. The factory produces 6,000 tons of oyster shell lime per year.

In this study, a heat reflecting pavement using oyster shell lime has been developed. The reduction of the pavement surface temperature was evaluated by both laboratory tests and field experiments.

Fig. 1 Oyster shell piles gathered at a factory site located in Toba city, Mie Prefecture.

2 MATERIALS AND PAVEMENT STRUCTURE

2.1 Pavement structure

A cross section of the pavement tested in this study is shown in Fig. 2. The thickness of the pavement is 50 mm. The heat reflecting pavement is an open-graded asphalt concrete in which voids in the upper part of the pavement are filled with a cement mortar containing oyster shell lime. A maximum aggregate size of 13 or 20 mm is used for the open-graded asphalt concrete pavement. Fig. 3 shows the pavement surface patterns. The beautiful patterns are produced by grinding the pavement surface after the filling mortar has hardened. The results of a skid resistance test and a wheel tracking test show that the pavement has a good skid resistance and plastic deformation resistance.

2.2 Materials

The oyster shell is a waste product from oyster farming. To form the lime, the oyster shells are pulverized into a fine particle size of less than 2 mm and used as the filling mortar in this study. In the filling mortar mixture, Portland cement and the pulverized oyster shells are used as a binder and a fine aggregate, respectively. As the oyster shell lime is lighter in

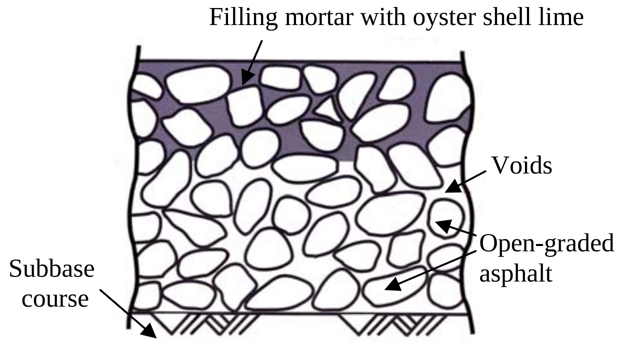

Fig. 2 Cross section of the pavement.

Fig. 3 Pavement surface patterns.

color than the commonly used Portland cement, its inclusion in the mortar subsequently produces a mortar which is lighter in color. Consequently the surface of the open-graded asphalt filled with the mortar increases the solar reflectance which results in a lower surface temperature.

3 EXPERIMENTS AND RESULTS

3.1 Field experiments

The pavements were constructed at the company site of the branch office located in Ise city, Mie Prefecture in June 2009. The temperature measurements were conducted in mid-August 2009. Fig. 4 shows a plan view of the pavements constructed at the outdoor testing site to monitor the surface temperature in summer. The pavements are 50 mm thick and placed on an asphalt binder course. An open-graded asphalt concrete with maximum aggregate size of 20 mm was used for the heat reflecting pavement. A dense-graded pavement was constructed around the heat reflecting pavement as a control. After the filling mortar in the heat reflecting pavement has hardened, the surfaces of the heat reflecting pavement were subject to water jet, grinding, and shot blasting treatments. The surface temperature was measured by thermocouples attached to the pavement surfaces and recorded by a data logger at 1 minute intervals. Temperatures at depths of 25 and 50 mm from the surface were also measured by thermocouples embedded at the same position in the pavement. The air temperature and solar radiation were monitored at the same time.

The temperature change of the heat reflecting pavement surfaces are shown in Fig. 5. There was no rainfall during this period. The black dense-graded asphalt rises to a maximum of 60°C at the surface, whereas it is not more than 50°C for the heat reflecting pavement. The surface temperature of the heat reflecting pavement on a fine day was up to 12°C lower than that of the dense-graded pavement. The temperature reduction of pavement surface results from the higher solar reflectance of the surface filled with the mortar of a lighter color. The maximum surface temperatures of the pavements and the temperature differences are summarized in Table I. Furthermore, results from tests conducted in August 2010 showed that the surface temperature difference between the pavements was about 10°C. A decrease of the temperature difference is partly because of the variation in the surface colors of aged asphalt.

Table I Maximum temperature of the pavement surfaces

	Dense-graded asphalt (°C)	Heat reflecting pavement (°C)	Temperature difference (°C)
2009.8.11	54.3	45.0	–9.3
2009.8.12	61.0	49.1	–11.9
2009.8.17	60.0	48.0	–12.0
2009.8.18	57.1	45.6	–11.5

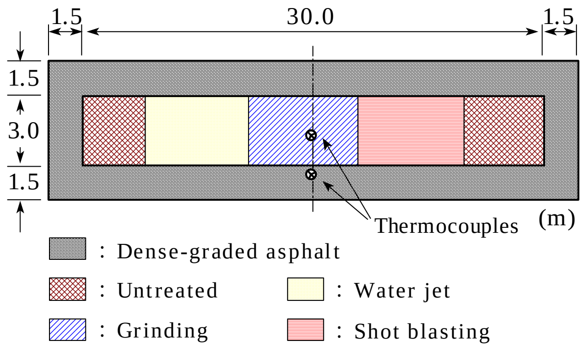

Fig. 4 Plan view of the pavement and surface treatments.

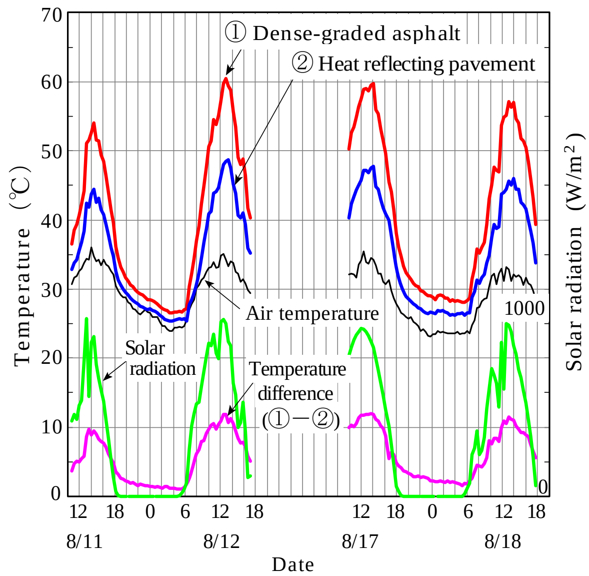

Fig. 5 Temperature changes on the pavement surface.

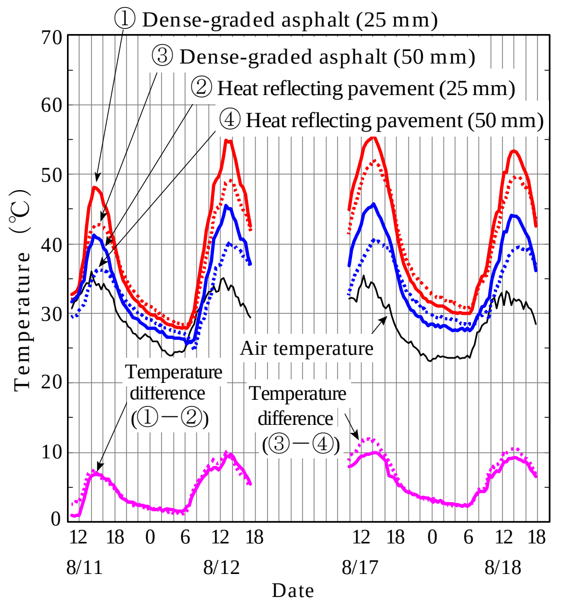

Fig. 6 Temperature changes at depths of 25 and 50 mm.

The temperature changes at depths of 25 and 50 mm are shown in Fig. 6. The maximum measured daily internal temperatures of the heat reflecting pavement fell about 10°C compared with those of the dense-graded asphalt. The results of the field experiments show that the maximum temperature of heat reflecting pavement decreases both on the surface and below the surface under summer sunlight irradiation, and this acts to reduce the urban heat island effect.

Fig. 7 shows a thermal image of the pavement taken by an infrared camera on August 17. Fig. 8 shows the corresponding visible image. The temperature differences between the heat reflecting pavement and the dense-graded pavement are visually apparent in Fig. 7. The surface of the heat reflecting pavement filled with the mortar is significantly lighter in color than the dense-graded pavement as shown in visible image (Fig. 8). Consequently, this leads to an increase in the solar reflectance and a lower surface temperature.

3.2 Laboratory irradiation tests

Laboratory irradiation tests were also carried out to evaluate the temperature reduction of the heat reflecting pavement using the oyster shell lime. Specimens of five different material types were used: a dense-graded asphalt, an open-graded asphalt filled with a cement paste without oyster shell lime, a (2:1) heat reflecting pavement, a (3:1) heat reflecting pavement, and an open-graded asphalt filled with a mortar containing coral sand. The numbers in parentheses represent the oyster shell lime and cement mix mass ratio for the filling mortar. The (2:1) heat reflecting pavement is the same as tested in the field experiments.

Fig. 9 shows a schematic of the arrangement for the lamp irradiation tests. The specimens are 30 × 30 × 5 cm in size, and the surface temperatures were measured by a thermocouple embedded in the middle of the specimen. The specimens were irradiated by a 150 W lamp for the first 3 hours and subsequently placed in a room at constant temperature. The room temperature was approximately 27–28°C during the measurement.

Fig. 10 shows the surface temperature changes of the specimens in the irradiation test. The difference at the highest temperature between the dense-graded asphalt and the (2:1) heat reflecting pavement was 12.4°C, and this value was the almost same as the result of the field experiments exposed to natural sunlight. The highest temperature of the open-graded asphalt filled with cement paste was 47.6°C; 5.1°C higher than that of the (2:1) heat reflecting pavement. The pavement surface filled with cement paste is darker in color than the surface filled with the mortar containing oyster shell lime. The difference of the surface temperature is partially due to the variation in surface colors.

Fig. 11 shows the surface temperature changes of the specimens for different types of filling mortar. The highest temperature of the specimen filled with mortar containing coral sand is 43.9°C and is only 1.5°C higher than that of the (2:1) heat reflecting pavement. It seems that coral sand is lighter in color and thus effective as a filling mortar. The highest temperature of the (3:1) heat reflecting pavement is

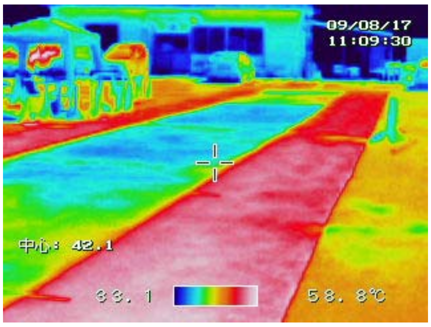

Fig. 7 Thermal image of the pavement.

Fig. 8 Visible image of the pavement.

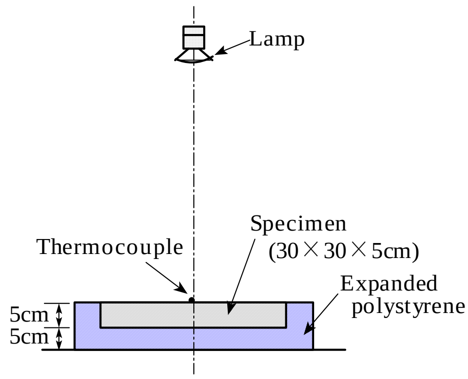

Fig. 9 Arrangement for the lamp irradiation tests.

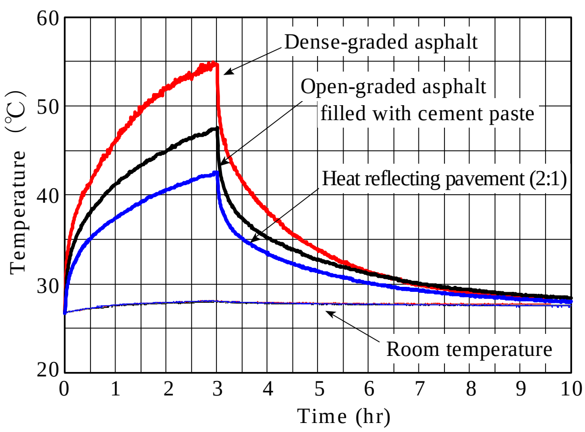

Fig. 10 Surface temperature changes in the irradiation test.

about 1°C lower than that of the (2:1) heat reflecting pavement. The results show that a filling mortar with a high shell lime content achieves a slightly higher solar reflectance.

3.3 Spectral reflectance tests

A spectral reflectometer is used to evaluate the solar reflectance of the pavements. Specimens of four different material types were used: a dense-graded asphalt, a (2:1) heat reflecting pavement, cement paste, and cement mortar containing oyster shell lime. The specimens are 30 × 30 × 20 mm in size.

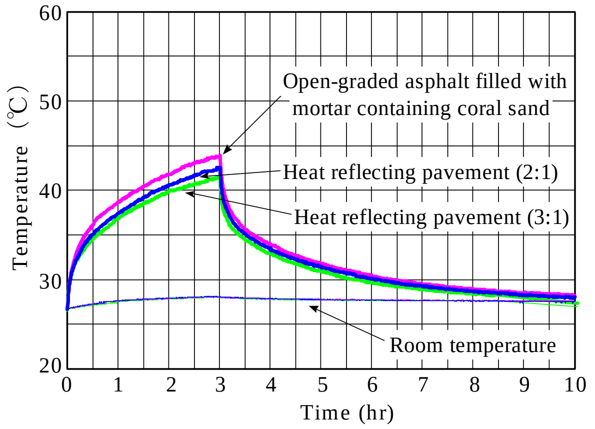

Fig. 11 Surface temperature changes of the specimens with different types of filling mortar.

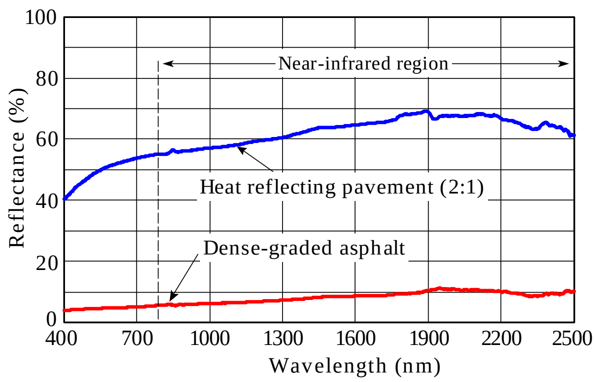

Fig. 12 Spectral reflectance of the pavements.

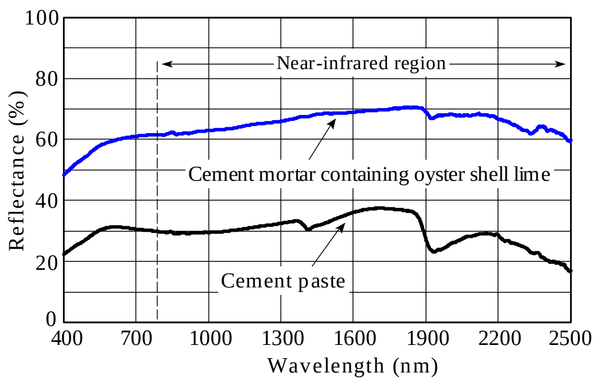

Fig. 13 Spectral reflectance of the cement mortar and cement paste.

Fig. 12 shows the spectral reflectance of the pavements. The spectral reflectance in the near-infrared region is 0.05–0.11 and 0.55–0.7 for the dense-graded asphalt and heat reflecting pavement, respectively. The spectral reflectance of heat reflecting pavement is significantly different from that of the dense-graded asphalt. In order to reduce the pavement surface temperature, the results show that it is necessary to increase the spectral reflectance, or solar reflection. Fig. 13 shows the spectral reflectance of the hardened cement mortar and cement paste. The spectral reflectance in the near-infrared region is 0.2–0.38 and 0.6–0.7 for the cement paste and cement mortar, respectively. The values confirm that the cement paste is darker in color and has a lower reflectance compared with the cement mortar with oyster shell lime.

4 CONCLUSIONS

A heat reflecting pavement using oyster shell lime has been developed and the temperature reduction effect was evaluated by both laboratory tests and field experiments. The results of this study are summarized as follows.

1) The surface temperature of the heat reflecting pavement is up to 12°C lower compared with the dense-graded pavement. This is particularly due to the increase in the reflectance of solar radiation on the pavement surface.

2) The measured spectral reflectance in the near-infrared region was 0.05–0.11 and 0.55–0.7 for the dense-graded asphalt and heat reflecting pavement, respectively.

3) The heat reflecting pavement and the open-graded asphalt filled with mortar containing coral sand are lighter in color and have a higher solar reflectance.

4) The beautiful patterns were produced by grinding the pavement surface after the filling mortar has hardened.

5) A large quantity of oyster shell is discharged from oyster farming each year. Heat reflecting pavements using oyster shell are environmentally friendly and contribute to promoting the effective use of a wasted resource.

5 ACKNOWLEDGMENT

The first author wishes to express his gratitude for the financial support of the Japan Society for the Promotion of Science.

6 REFERENCES

[1] The Society of Heating, Air-Conditioning and Sanitary Engineers of Japan, Heat Island, Ohmsha Ltd., 2009, pp. 25-39.

[2] Japan Society of Civil Engineers, Evaluation Technology of Eco-friendly Pavement, Pavement Engineering Library 4, 2007, pp. 83-153.

[3] Ishiguro, S. & Yamanaka, M. Research on Heat Reflection Pavement Using Cement Mortar Containing Crushed Oyster Shell (in Japanese), Proceedings of the Japan Concrete Institute, Vol. 32, No. 1, 2010, pp. 1367-1372.

First International Conference on Geotechnique, Construction Materials and Environment, Mie, Japan, Nov.21-23, 2011, ISBN: 978-4-9905958-0-7 C3051

Buckling Behavior of Composite Triangular Plates

T. Farsadi, Aerospace Engineering Department, Sharif University of Technology, Tehran, Iran
P. Amani, Aerospace Engineering Department, Sharif University of Technology, Tehran, Iran
E. Heydarnia, Aerospace Engineering Department, Amirkabir University of Technology, Tehran, Iran

ABSTRACT: This paper is to do a brief research on the buckling behavior of composite triangular plates with various edge boundary conditions and in-plane loads. It may be regarded as a right and simple numerical method for the analysis of composite triangular thin plate using the natural area coordinates. Previous studies on the solution of triangular plates with different boundary conditions were mostly based on the Rayleigh-Ritz principle which is performed in the cartesian coordinate. In this method, the energy functional of a general triangular plate is derived and the Rayleigh-Ritz method is utilized to derive the governing eigenvalue equation for the buckling problem. The geometry is presented in a natural way by mapping a parent triangle and the integrals are evaluated analytically. The polynomial terms L_1^i, L_2^j, L_3^k in the area coordinates are employed to interpolate plate deflection and L_1^a, L_2^b, L_3^c are used to enforce the prescribe boundary conditions. Therefore, the admissible basic functions given are $L_1^{(i+a)}, L_2^{(j+b)}, L_3^{(k+c)}$. In this approach, the convergence is always assured due to the completeness of interpolating polynomials. Extensive buckling factors are presented for several selected right-angled triangular plates of various edge support conditions and subjected to composite thin plates under various in-plane compressive and shear loads and results are compared with other available data..

Keywords: Triangular plate - Composite Material - Area Coordinate - Buckling - Rayleigh-Ritz Principle

1 INTRODUCTION AND BRIEF REVIEW

In many engineering applications, it is very important to predict buckling behavior of triangular plates. Buckling phenomenon is critically dangerous to structural components because the buckling of composite plates usually occurs at a lower applied stress and generates large deformation. This led to a focus on the study of buckling behavior in composite materials. The use of composite materials in place of more traditional isotropic materials has increased dramatically over the past decades in areas such as the aerospace industry. With the wide use of composite plate structures in modern industries, dynamic and static analysis of plates of complex geometry becomes an important part of engineering design. Composite plates have been widely used due to their excellent high strength-to-weight ratio, modulus-to-weight ratio and the controllability of the structural properties with variation of fiber orientation. The problem regarding buckling of plates under various shapes and boundary conditions has been studied in some famous classic and academic reference text books [1,2] and some of numerous literature works [3-6].

It is interesting to note that buckling of triangular plates has received far less attention than their rectangular counterparts. Woinowsky-Krieger [7] derived the exact buckling load for a simply supported equilateral triangular plate under an isotropic in-plane compressive load. Burchard [8] studied the buckling of simply supported right-angled triangular plates under uni-axial compression. There are several research investigated the buckling of isosceles triangular plates under various loading conditions. Wakasugi [9,10] investigated the buckling of simply supported and clamped equilateral triangular plates. Conway and Lissa [11] searched the buckling of equilateral triangular plates subjected to isotropic in-plane compression. Tan et al. [12] and Tan [13] employed the finite element method to study the buckling of general triangular plates. In the recent years, Wang and Liew [14] utilized their pb-2 Rayleigh-Ritz method to investigate the buckling of isosceles and right-angled triangular plates under isotropic in-plane compressive load.

The basic aim of this research is to study and formulate the effect of plate geometry aspect ratio and fiber orientation to determine critical value of buckling load factor for a composite triangular plate of various boundary conditions and various in-plane (compression and shear) loads by using an approximate-analytical solution for first critical mode predominantly.

2 THEORETICAL ANALYSIS AND FORMULATION

2.1 Area-coordinate

In this section, the use of triangular coordinates to define the interior of a triangular area is briefly described. This description is important when formulating triangular finite elements. The triangle in Fig. 1 is defined by coordinates (x_i, y_i) of its vertices in the coordinate system $O(x, y)$. Cartesian coordinates are usually employed to describe any point (x_0, y_0) on a rectangular area. They are, however, difficult to use when the boundary and the interior of a triangular area need to be defined. In order to define a triangular area, the coordinates (x_0, y_0) can be expressed in the following way,

$$\begin{cases} x = x_1 L_1 + x_2 L_2 + x_3 L_3 \\ y = y_1 L_1 + y_2 L_2 + y_3 L_3 \end{cases} \quad (1)$$

where L_1, L_2, L_3 are triangular coordinates. The values of the triangular coordinates range between 0 and 1 when the following constraint is used,

$$L_1 + L_2 + L_3 = 1 \quad (2)$$

[#] Corresponding author (Touraj-Farsadi),
E-mail: touraj.farsadi@gmail.com, Tel: +905375213780

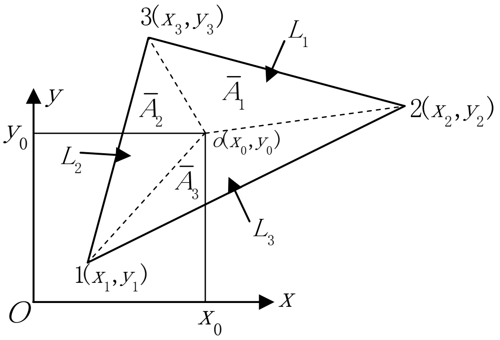

Fig. 1. Area coordinates in arbitrary triangular plate

Equation (1) together with (2) can be used to define any point (x_0, y_0) in the triangle. The coordinates L_1, L_2, L_3 represent dimensionless areas of triangles $\bar{A}_1, \bar{A}_2, \bar{A}_3$ as depicted in Fig. 1. These coordinates can be expressed as follows:

$$\begin{cases} \bar{A}_1 + \bar{A}_2 + \bar{A}_3 = A \\ L_i = \dfrac{\bar{A}_i}{A}, \quad i = 1,2,3 \end{cases} \tag{3}$$

where *A* is the area of the triangle defined as,

$$2A = \begin{vmatrix} x_1 & x_2 & x_3 \\ y_1 & y_2 & y_3 \\ 1 & 1 & 1 \end{vmatrix} \tag{4}$$

When constraint (2) is accounted for, the triangular coordinates can be solved from (5) as follows,

$$L_i = \frac{1}{2A}\left(a_i + b_i x + g_i y\right), \qquad i = 1,2,3 \tag{5}$$

Where a_i a coefficient that depends on is coordinates x_j, y_k of the three nodes in the coordinate system $O(x, y)$. The coefficients can be expressed as follows:

$$\begin{cases} a_i = x_j y_k - y_j x_k, \quad b_i = y_j - y_k, \\ g_i = x_k - x_j, \qquad j,k = 1,2,3 \end{cases} \tag{6}$$

In the latter equation and below *j*, *k* and *i* form a cyclic permutation.

Thin plate theory is used in the present analysis. However, to obtain the strains differentiation operator with respect to Cartesian coordinates needs to be carried out. This is done as follows,

$$\begin{cases} \dfrac{\partial}{\partial x} = \displaystyle\sum_{i=1}^{3} \frac{\partial}{\partial L_i}\frac{\partial L_i}{\partial x} = \frac{1}{2A}\sum_{i=1}^{3} b_i \frac{\partial}{\partial L_i} \\ \dfrac{\partial}{\partial y} = \displaystyle\sum_{i=1}^{3} \frac{\partial}{\partial L_i}\frac{\partial L_i}{\partial y} = \frac{1}{2A}\sum_{i=1}^{3} g_i \frac{\partial}{\partial L_i} \\ \dfrac{\partial^2}{\partial x^2} = \dfrac{\partial}{\partial x}\dfrac{\partial}{\partial x} = \displaystyle\frac{1}{4A^2}\sum_{i=1}^{3}\sum_{j=1}^{3} b_i b_j \frac{\partial}{\partial L_i}\frac{\partial}{\partial L_j} \\ \dfrac{\partial^2}{\partial y^2} = \dfrac{\partial}{\partial y}\dfrac{\partial}{\partial y} = \displaystyle\frac{1}{4A^2}\sum_{i=1}^{3}\sum_{j=1}^{3} g_i g_j \frac{\partial}{\partial L_i}\frac{\partial}{\partial L_j} \\ \dfrac{\partial^2}{\partial x \partial y} = \dfrac{\partial}{\partial x}\dfrac{\partial}{\partial y} = \displaystyle\frac{1}{4A^2}\sum_{i=1}^{3}\sum_{j=1}^{3} b_i g_j \frac{\partial}{\partial L_i}\frac{\partial}{\partial L_j} \end{cases} \tag{7}$$

All expressions remain polynomial in the area coordinates and can be easily integrated.
In other words,

$$\begin{Bmatrix} \dfrac{\partial}{\partial x} \\ \dfrac{\partial}{\partial y} \end{Bmatrix} = [T_1] \begin{Bmatrix} \dfrac{\partial}{\partial L_1} \\ \dfrac{\partial}{\partial L_2} \\ \dfrac{\partial}{\partial L_3} \end{Bmatrix}, \quad \begin{Bmatrix} \dfrac{\partial^2}{\partial x^2} \\ \dfrac{\partial^2}{\partial y^2} \\ \dfrac{2\partial^2}{\partial x \partial y} \end{Bmatrix} = [T_2] \begin{Bmatrix} \dfrac{\partial^2}{\partial L_1^2} \\ \dfrac{\partial^2}{\partial L_2^2} \\ \dfrac{\partial^2}{\partial L_3^2} \\ \dfrac{2\partial^2}{\partial L_1 \partial L_2} \\ \dfrac{2\partial^2}{\partial L_2 \partial L_3} \\ \dfrac{2\partial^2}{\partial L_1 \partial L_3} \end{Bmatrix} \tag{8}$$

Where,

$$[T_1] = \frac{1}{2A}\begin{bmatrix} b_1 & b_2 & b_3 \\ g_1 & g_2 & g_3 \end{bmatrix} \tag{9}$$

$$[T_2] = \frac{1}{4A^2}\begin{bmatrix} b_1^2 & b_2^2 & b_3^2 & b_1 b_2 & b_2 b_3 & b_3 b_1 \\ g_1^2 & g_2^2 & g_3^2 & g_1 g_2 & g_2 g_3 & g_3 g_1 \\ 2b_1 g_1 & 2b_2 g_2 & 2b_3 g_3 & (b_1 g_2 + g_1 b_2) & (b_2 g_3 + g_2 b_3) & (b_3 g_1 + g_3 b_1) \end{bmatrix} \tag{10}$$

$[T_1]$ and $[T_2]$ are transfer matrices.

2.2 The displacement vector field

For the displacement field in L_1, L_2 and L_3 the area coordinate system is used for the function as follows,

$$\begin{cases} w = w_u w_v \\ w_u = w_u(L_1, L_2, L_3), \quad w_v = w_v(L_1, L_2, L_3) \end{cases} \tag{11}$$

$w_u(L_1, L_2, L_3)$ is taken as the product of the boundary equations and the internal line/curved support equations and $w_v(L_1, L_2, L_3)$ is a polynomial in the area coordinates with an undetermined coefficient that the holder of the displacement field is expanded. The $w_u(L_1, L_2, L_3)$ function is defined,

$$w_u = L_1^a L_2^b L_3^c \tag{12}$$

Where the value *a, b, c* depending on the free, simply supported or clamped boundary conditions are 0, 1 or 2. $w_v(L_1, L_2, L_3)$ shape function includes terms with unknown coefficients y_{ijk} as follow:

$$\begin{aligned} & w_{vI} = \sum_{i=0}^{p}\sum_{j=0}^{p}\sum_{k=0}^{p} y_{ijk} L_1^i L_2^j L_3^k, \\ & i + j + k = p, \quad 0 \le i, j, k \le p \end{aligned} \tag{13}$$

So that the polynomial order *p* and *i, j, k*, respectively, display the correct coordinates L_1, L_2, L_3, varies from zero to *p*. $w_v(L_1, L_2, L_3)$, shape function can be demonstrated with uncertainty factor that is just an index as follows. Such a display of computer programming is essential for the shape function, $w_v(L_1, L_2, L_3)$

$$w_{vI} = \sum_{I=1}^{N} \Upsilon_I L_1^i L_2^j L_3^k \tag{14}$$

Where " *I* " is number of sentences and *N* is the count of sentences. Performing some mathematical operations can be shown that a simple choice for the *i, j, k* using the following equation,

$$\begin{aligned} & i = I - jN - kN^2 - 1 \\ & j = INT\left[\frac{I - 1 - kN^2}{N}\right] \\ & k = INT\left[\frac{I - 1}{N^2}\right] \end{aligned} \tag{15}$$

second shape function is obtained by,

$$w_{vJ} = \sum_{J=1}^{N} \Upsilon_J L_1^e L_2^f L_3^g \tag{16}$$

where,

$$\begin{aligned} & e = J - fN - gN^2 - 1 \\ & f = INT\left[\frac{J - 1 - eN^2}{N}\right] \\ & g = INT\left[\frac{J - 1}{N^2}\right] \end{aligned} \tag{17}$$

and the Count sentences is possible by the following equation:

$$N = \frac{1}{2}(p + 1)(p + 2) \tag{18}$$

and thus specifying the order of the polynomial *p* and the number of sentence can get symbols *i, j, k* with number of sentence" *I* ".

2.3 The Rayleigh-Ritz Method

The Rayleigh-Ritz method consists of assuming that some desired deflection pattern can be approximated by a linear combination of deflection functions, each of which satisfied the rigid boundary conditions of the problem, and then finding the coefficients governing this linear combination by minimizing the total energy of the deformed body and the in-plane loads. Clearly, a proper choice of the deflection expression is important to ensure good accuracy for the final solution. The total energy is the sum of the strain energy of the plate, *U*, and the potential energy of the in-plane loads, *V*.

3 GOVERNING SYSTEM EQUATIONS OF PRESENT SYSTEM

In this paper, an elastic, composite, flat and thin triangular plate is used. The edges of the plate may be free, simply supported or clamped supported. The boundary of this plate defined by the equations $L_1 = 0, L_2 = 0, L_3 = 0$ and the boundary conditions are provided by choosing *a, b, c*. It is noteworthy that even if *x* and *y* axes are not coincided with the main purpose, there is no limit to the formulation. The problem at hand is to determine the elastic buckling load of such a general triangular plate subjected to an in-plane compressive and shear load.

In accordance with established stiffness procedures, the vector of infinitesimal buckling strains consists of two parts. (i) the linear flexural strain e_L , and (ii) the nonlinear flexural strain e_N , that are given by,

$$\begin{aligned} \{e_L\} &= \{e_{Lx}, e_{Ly}\}^T \\ &= \left[\left(\frac{\partial w}{\partial x}\right)^2, \left(\frac{\partial w}{\partial y}\right)^2\right]^T \\ \{e_N\} &= \{e_{Nx}, e_{Ny}, e_{Nxy}\}^T \\ &= \left[\frac{\partial^2 w}{\partial x^2}, \frac{\partial^2 w}{\partial y^2}, \frac{2\partial^2 w}{\partial x \partial y}\right]^T \end{aligned} \tag{19}$$

Infinitesimal buckling Linear and Nonlinear strains in an area coordinate system are defined,

$$\begin{aligned} \{\hat{e}_L\} &= \{e_{L1}, e_{L2}, e_{L3}\}^T \\ &= \left[\left(\frac{\partial w}{\partial L_1}\right)^2, \left(\frac{\partial w}{\partial L_2}\right)^2, \left(\frac{\partial w}{\partial L_3}\right)^2\right]^T \\ \{\hat{e}_N\} &= \{e_{N1}, e_{N2}, e_{N3}, e_{N12}, e_{N23}, e_{N31}\}^T \\ &= \left[\frac{\partial^2 w}{\partial L_1^2}, \frac{\partial^2 w}{\partial L_2^2}, \frac{\partial^2 w}{\partial L_3^2}, \frac{\partial^2 w}{\partial L_1 \partial L_2}, \frac{\partial^2 w}{\partial L_2 \partial L_3}, \frac{\partial^2 w}{\partial L_3 \partial L_1}\right]^T \end{aligned} \tag{20}$$

Between vectors $\{e_L\}$, $\{\hat{e}_L\}$ and $\{e_N\}$, $\{\hat{e}_N\}$ using the relationship between Cartesian coordinates and the area coordinates are expressed as the following:

$$\begin{aligned} \{e_L\} &= [\ ]\{\hat{e}_L\} \\ \{e_N\} &= [\ ]\{\hat{e}_N\} \end{aligned} \tag{21}$$

So that transfer matrix $[T]$, $[R]$ with fixed array is calculated and available in (8).

3.1 Strain Energy

Adopting the classical thin plate theory, the strain energy U due to bending is given in the matrix form, by,

$$U = \int_A \frac{1}{2}\{e_N\}^T [D] \{e_N\}\, dA \tag{22}$$

Where "D" is the standard matrix of elastic constants transformed to the local element coordinate system and is given by,

$$[D] = \begin{bmatrix} d_{11} & d_{12} & 0 \\ d_{12} & d_{22} & 0 \\ 0 & 0 & d_{66} \end{bmatrix} \tag{23}$$

Where,

$$\begin{cases} d_{11} = \dfrac{t^3}{12}\dfrac{E_1}{(1-v_{12}v_{21})}, d_{12} = \dfrac{t^3}{12}\dfrac{v_{12}E_2}{(1-v_{12}v_{21})} \\ d_{22} = \dfrac{t^3}{12}\dfrac{E_2}{(1-v_{12}v_{21})}, d_{66} = \dfrac{t^3}{12}G_{12} \end{cases} \tag{24}$$

In the above expressions, E_1, E_2, v_{12}, v_{21}, and G_{12} are elastic constants dependent on the physical characteristics of the plate material. For the composite material,

$$[T] = \begin{bmatrix} \cos^2 q & \sin^2 q & -2\cos q \sin q \\ \sin^2 q & \cos^2 q & 2\cos q \sin q \\ \cos q \sin q & -\cos q \sin q & \cos^2 q - \sin^2 q \end{bmatrix} \tag{25}$$

and elastic constant matrix is obtained by,

$$[D] = [T][D][T]^T \tag{26}$$

By transfer elasticity matrix into area-coordinate and substituting (21) and (26) into (22), the strain energy U due to bending in area coordinate is given by,

$$U = \int_A \frac{1}{2}\{\hat{e}_N\}^T [\hat{D}] \{\hat{e}_N\}\, dA \tag{27}$$

where,

$$[\hat{D}] = [R]^T [D] [R] \tag{28}$$

function W using the following (11), (12), (13) and (14) are available,

$$\begin{cases} w_I = w_u w_{vI} = \langle \Phi_I(L_1, L_2, L_3) \rangle \{\Psi_I\}, \\ \Phi_I = L_1^{a+i} L_2^{b+j} L_3^{c+k} \end{cases} \tag{29}$$

and for second shape function,

$$\begin{cases} w_J = w_u w_{vJ} = \langle \Phi_J(L_1, L_2, L_3) \rangle \{\Psi_J\}, \\ \Phi_J = L_1^{a+e} L_2^{b+f} L_3^{c+g} \end{cases} \tag{30}$$

By substituting (29) and (30) into (27), strain energy in area-coordinate is given by,

$$U = \{\Psi\}^T \int_A \frac{1}{2}\{P\}^T [\hat{D}] \{P\}\, dA \{\Psi\} \tag{31}$$

In other words,

$$U = \frac{1}{2}\sum_I \sum_J K_{IJ} \Psi_I \Psi_J \tag{32}$$

So that,

$$K_{IJ} = \int_A \{P\}_I^T [\hat{D}] \{P\}_J\, dA \tag{33}$$

where,

$$\{P\}_{I(6\times1)} = \begin{Bmatrix} (a+i)(a+i-1)L_1^{(a+i-2)}L_2^{(b+j)}L_3^{(c+k)} \\ (b+j)(b+j-1)L_1^{(a+i)}L_2^{(b+j-2)}L_3^{(c+k)} \\ (c+k)(c+k-1)L_1^{(a+i)}L_2^{(b+j)}L_3^{(c+k-2)} \\ 2(a+i)(b+j)L_1^{(a+i)}L_2^{(b+j-1)}L_3^{(c+k-1)} \\ 2(b+j)(c+k)L_1^{(a+i-1)}L_2^{(b+j)}L_3^{(c+k-1)} \\ 2(c+k)(a+i)L_1^{(a+i-1)}L_2^{(b+j)}L_3^{(c+k-1)} \end{Bmatrix} \tag{34}$$

$\{P\}_{J(6\times1)} = \{P(a,b,c,e,f,g)\}$ is obtained similarly.

Provided that the arrays of matrix $\{P\}$ if the exponent is characteristics a negative, to be chosen as absolutely zero.

3.2 Potential energy

The potential energy V of the orthotropic in-plane compressive and shear load can be expressed in the matrix form, as,

$$V = \int_A \frac{1}{2}\{e_L\}^T [N] \{e_L\} dA \tag{35}$$

While $[N]$ contains the in-plane compressive and shear loads in the manner,

$$[N] = \begin{bmatrix} N_x & N_{xy} \\ N_{xy} & N_y \end{bmatrix} \tag{36}$$

In the above expressions, N_x , N_y and N_{xy} are in-plane compressive and shear load. By conversion load matrix into area-coordinate and substituting (21) and (36) into (35), the potential energy V due to bending in area-coordinate is given by,

$$V = \int_A \frac{1}{2}\{\hat{e}_L\}^T [\hat{N}] \{\hat{e}_L\}\, dA \tag{37}$$

where,

$$[\hat{N}] = [R]^T [N] [R] \tag{38}$$

function W using the following (11), (12), (13) and (14) are available,

$$\begin{cases} w_I = w_u w_{vI} = \langle \Phi_I(L_1,L_2,L_3) \rangle \{\Psi_I\}, \\ \Phi_I = L_1^{a+i} L_2^{b+j} L_3^{c+k} \end{cases} \tag{39}$$

and,

$$\begin{cases} w_J = w_u w_{vJ} = \langle \Phi_J(L_1,L_2,L_3) \rangle \{\Psi_J\}, \\ \Phi_J = L_1^{a+e} L_2^{b+f} L_3^{c+g} \end{cases} \tag{40}$$

By substituting (39) and (40) into (37), strain energy in area-coordinate is given by,

$$V = \{\Psi\}^T \int_A \frac{1}{2}\{Z\}^T [D] \{Z\}\, dA \{\Psi\} \tag{41}$$

In other words,

$$V = \frac{1}{2}\sum_I \sum_J G_{IJ} \Psi_I \Psi_J \tag{42}$$

So that,

$$G_{IJ} = \int_A \{Z\}_I^T [D] \{Z\}_J \, dA \tag{43}$$

where,

$$\{Z\}_{I(3\times 1)} = \begin{Bmatrix} (a+1) L_1^{(a+i-1)} L_2^{(b+j)} L_3^{(c+k)} \\ (b+j) L_1^{(a+i)} L_2^{(b+j-1)} L_3^{(c+k)} \\ (c+k) L_1^{(a+i)} L_2^{(b+j)} L_3^{(c+k-1)} \end{Bmatrix} \tag{44}$$

$\{Z\}_{J(6\times 1)} = \{Z(a,b,c,e,f,g)\}$ is obtained similarly.

It can be shown that when integrating polynomials in L_1, L_2 and L_3 over a triangle area A, the following relation holds,

$$\int_A L_1^a L_2^b L_3^c \, dA = \frac{a!\,b!\,c!}{(a+b+c+2)!} 2A \tag{45}$$

3.3 Total Energy

Finally, with the function of both strain energy and the potential energy of the total energy is written as,

$$\begin{aligned} \Pi &= U - V \\ &= \{\Psi\}^T \int_A \frac{1}{2}\{P\}^T [D] \{P\}\, dA \{\Psi\} - \\ &\quad \{\Psi\}^T \int_A \frac{1}{2}\{Z\}^T [D] \{Z\}\, dA \{\Psi\} \end{aligned} \tag{46}$$

In other words,

$$\Pi = \frac{1}{2}\sum_I \sum_J \left(K_{IJ}\Psi_I\Psi_J - G_{IJ}\Psi_I\Psi_J \right) \tag{47}$$

3.4 Linear buckling analysis

Linear buckling technique allows one to obtain just the critical load and the corresponding deformed shape of the modeled structure. To obtain this result, the condition of neutral equilibrium between external loads and internal reactions is searched, solving the equation,

$$\left([K] - \lambda [K_G]\right)\{\Psi\} = \{0\} \tag{48}$$

$[K]$ is the stiffness matrix calculated in small-displacements range, $[K_G]$ is the geometric stiffness matrix corresponding to a reference load, "λ" is the eigenvalue, that is the load factor to multiply to the reference load to obtain the critical value. As is written, the equation system appears as an eigenvalues determination problem, then for found some values of "λ",

$$\det\left([K] - \lambda [K_G]\right) = 0 \tag{49}$$

4 SOME NUMERICAL RESULTS AND VALIDATION

Although the Rayleigh-Ritz method in area-coordinate presented in this paper can be used to study buckling of general triangular plates, we will concentrate our analysis on right-angled orthotropic plates subjected to in-plane compressive and shear load with various boundary conditions. To describe the Boundary conditions in a composite thin plate, we use letters *F* for free, *S* for simply supported and *C* for clamped edges. Consider an orthotropic triangular plate with length *a*, a vertex angle α_0, uniform thickness *t*, the modulus of elasticity E_1, E_2, and Poisson's ratio v_{12}, v_{21}, as shown in Fig. 2. This figure shows the selected right-angled composite triangular thin plate studied in this paper.

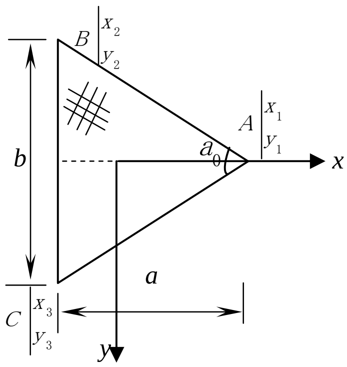

Fig. 2. Composite right-angled triangular plate

4.1 Validation

As the Rayleigh- Ritz method used in this study is an approximate numerical approach, convergence and comparison studies are essential to ensure the correctness and convergence of the buckling results.

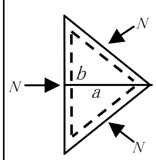	**Table. I.** Comparison of the buckling factor ($\lambda_{cr} = \frac{\bar{N}b^2}{\pi^2 D}$) of the isotropic triangular plate			
	b/a	1	$2/\sqrt{3}$	2
	Ref [14]	45.827	52.637	98.696
	Present work	46.142	52.666	99.000

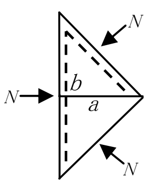

Table. II. Comparison of the buckling factor ($\lambda_{cr} = \frac{\bar{N}b^2}{\pi^2 D}$) of the isotropic triangular plate

b/a	1	$2/\sqrt{3}$
Ref [14]	6.609	8.371
Present work	6.626	8.386

4.2 Results

The buckling loads are expressed in terms of non-dimensional parameter, $\lambda = \frac{\bar{N}b^2}{E_2 t^3}$, where $\bar{N}$ is the critical buckling compressive or shear loads.

Figure.3 present the buckling factors for right-angled triangular plates for different combinations of edge conditions, fiber orientations and width-to-height ratios, b/a = 0.5, 1, 1.5 and 2.

5 BRIEF CONCLUDING REMARKS

This paper presents a research about the buckling of composite triangular plates. The total energy functional for a general composite triangular plate is derived, and the eigenvalue equation for elastic buckling of the plate is obtained through the application of the Rayleigh-Ritz method. To this end, computer code has been developed to simulate the buckling behavior of the composite triangular plate model. Convergence and comparison studies are carried out to verify the validity and accuracy of the solution method. Extensive first-known buckling solutions for several selected right-angled composite triangular plates are presented in the paper. The influence of the fiber orientation on the buckling behavior of the plates is examined. We find that the fiber orientation and width-to-height ratios are most effective in buckling behavior of the composite triangular plates.

6 REFERENCES

[1] Ugural A.C., "Stresses in Plates and Shells" , 2nd., WCB/McGraw-Hill, 1999.

[2] Timoshenko S., Woinowsky-Krieger S., "Theory of Plates and Shell", 2nd ed., McGraw-Hill, 1959.

[3] Tung T.K., Surdenas J., "Buckling of rectangular orthotropic plates under biaxial loading", Journal of Composite Materials, Vol.21, No.2, 1987, pp. 124-128.

[4] Wang, J. T.S., Biggers S.B., Dickson J.N., "Buckling of composite plates with a free edge in edgewise bending and compression", AIAA journal, Vol.22, No.3, 1984, pp. 394-398.

[5] Farshad M., Ahmadi G., "Perturbation solution to the problems of general orthotropic rectangular plates", Iranian Journal of Science and Technology, Vol.1, No.2, 1971, pp. 147-162

[6] Whitney J.M., Leissa A.W., Biggers S.B., Dickson, J.N., "Analysis of a simply supported laminated anisotropic rectangular plate" , AIAA journal, Vol.8, No.1, 1970, pp. 28-33.

[7] Woinowsky-Krieger, S. "Berechnung der ringsum frei aufliegenden gleichseitigen dreiecksplatte", Ing. Archiv, 1933. 4, 54-262.

[8] Burchard, W., "Beulspannungen der quadratichen platte mit schragseife under druck bzw. Schub", Ing Archiv. 1937, 21(107), 332-348.

[9] Wakasugi. S., " Buckling of a simply supported equilateral triangular plate", Trans. Japan. Soc. Mech. Eng. 1960, 26, (164), 538-544.

[10] Wakasugi. S., " Buckling of a clamped equilateral triangular plate under uniform compression", Trans. Japan. Soc. Mech. Eng. 1961, 27 (179), 1010-1017.

[11] Conway. H. D. and Leissa. A. W., "A method for investigating certain eigenvalue problems of the buckling and vinration of plates", J. Appl. Mech. 1960, 27, 557-558.

[12] Tan, H. K. V., Bettess, P., Bettess, J. A. "Elastic buckling of isotropic triangular flat plates by finite elements. Appl. Math. Modelling 7, 311-316 (1983).

[13] Tan, H. K. V., "Elastic buckling of isotropic triangular flat plates by finite elements", Proc. Inst. Civil Engineers 77, 13-21(1984).

[14] Wang , C. M., Liew, K. M., "Buckling of triangular plates under uniform Compression" . Eng. Struct. 16, 43-50 (1994)

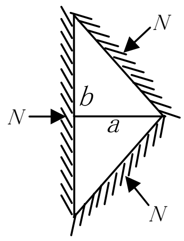

(a) (CCC)

(b

(c) (SFS)

(d

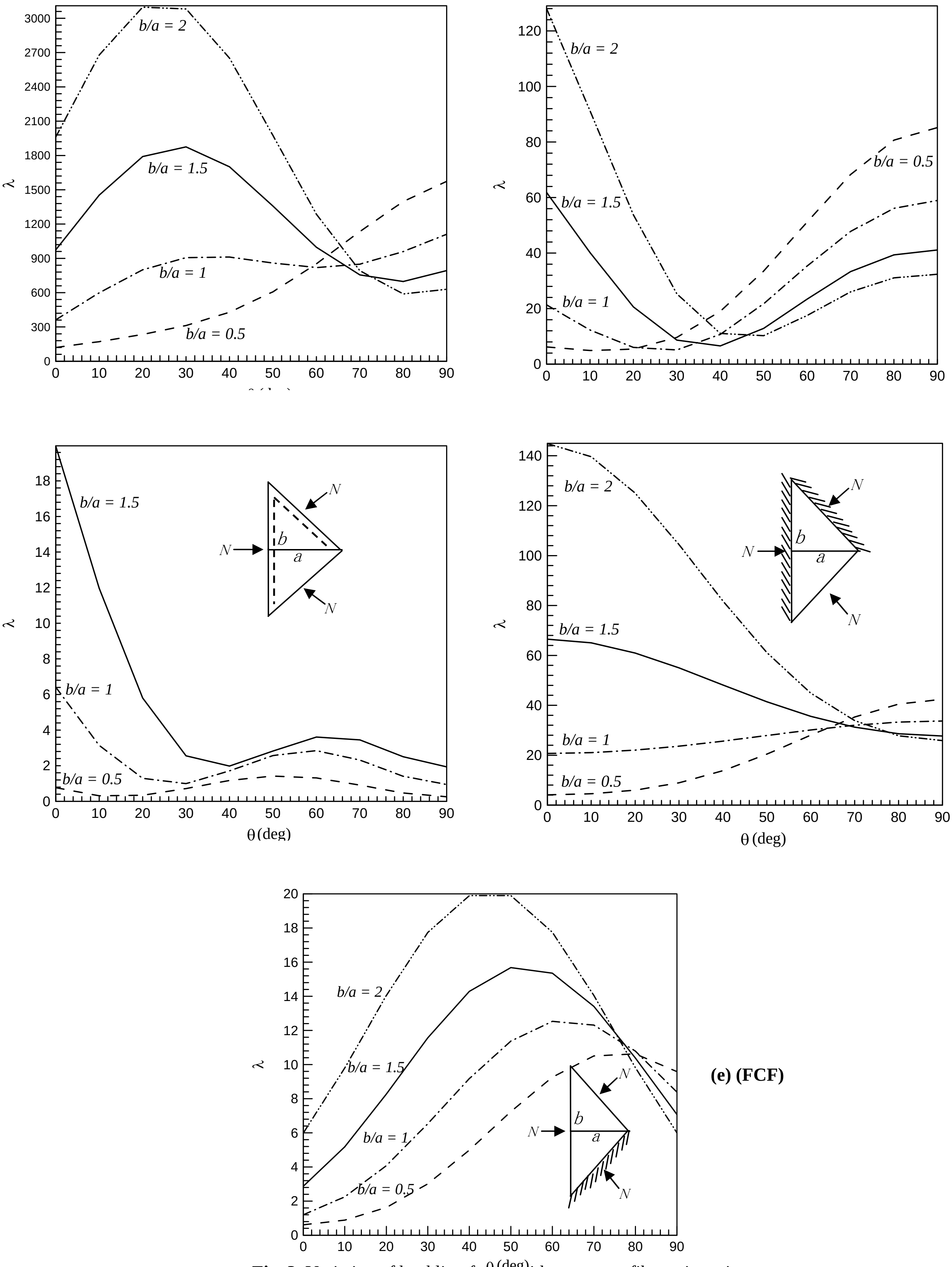

Fig. 3. Variation of buckling factor with respect to fiber orientation
for different width-to-height (b/a) and different boundary conditions

First International Conference on Geotechnique, Construction Materials and Environment, Mie, Japan, Nov.21-23, 2011, ISBN: 978-4-9905958-0-7 C3051

Durability of Cement Treated Highway Materials

Sukolrat J., Klummeng A., Anuvechsirikiat S., Department of Highways, Thailand

ABSTRACT: Department of Highways, Thailand has used cement modification to improve highway materials to overcome the problems of scarcity of suitable materials. The modification increases strength of local materials, which are not conformed the standards for base courses and subbase courses in highway structures. In some routes, cracks in road structures have been observed on pavement constructed on cement modified structures which may result from excess cement content. In order to prevent such problem, durability of cement modified materials should be one parameter to be concerned in addition to the strength to avoid excess cement content in the design. The paper presents durability test result of cement modified materials from six differrent locations categorised as modified crushed rock and soil cement. The tests include wetting and drying test, slake durability test, and wheel track test to observe the performance in different durability testing. The results show that cement content required for the modification can be decreased to obtain satifactory durability, and materials' suitability can be evaluated. A simple design chart for the cement content selection can be used to pre defined the suitable materials for cement modfication.

Keywords: Cement treared materials, highway materials, durability, design chart

1. INTRODUCTION

Land transportation is one important mode for both domestic and international transportations. Thus, roadway is essential for supporting economic and social development. With the increasing usages of roads, new construction projects, road widening and maintenance are required. With such circumstance, road construction materials, conformed the qualification standards, are insufficient. Many standardised materials need to be haulled from remote quarries costing over budget for the project. Besides, the haulage also affects on service life reduction and pollutions. Modification of engineering properties for local materials is one alternative way to overcome such problems.

Most widely technique used for material modifiaction in Thailand is cement modification. They have been used in roads construction for more than 30 years. Main purpose for such modifiaction is to strengthen materials for use as basecourse and subbase course. Recently, the pavement recycling technique has been used for reconstructed deterirated pavement structure with cement mixing method. However, reflective cracks occur on pavement surface in some routes after construction and the more damages developed. Fig. 1 presents cracks on asphaltic pavement over cement modified crushed rock base.

The cause of cracks and failures of pavement on cement modified materials structure may occur from inappropriate quantity of cement use, the quality control and quality assurance during construction, and suitable design criteria. In current design, the modified materials are subjected to strength increment by cement content. Without consideration for durability the materials may be unsuitable for road structure. This paper will present appropriated cement content for modification by considering traffic capacity, durability of cement modified materials, relationship between cement content, strength of material and durability.

Fig. 1 Block cracks on asphaltic pavement

2. CURRENT SITUATION

Unsuitable aggregate is not allowed to use for road structure to avoid undesired road performance. Currently, lack of road construction materials has been underlined. So, it is necessary to promote use of local materials for road structure with property improvement such as strength and durability to ensure its performance for road standards.

Cement modified base course can increase ability for traffic load transferring, and decrease fatigue in sub base course. The modification can also decrease possibility for cracks in pavement surface. Moreover, high strength increment in base course can decrease vertical deflection in sub base course and tensile strain in pavement surface on both dry and wet conditions; hence, decrease opportunities in cracking and raveling. Besides, the base course can distribute traffic load in larger area to underneath structures [1].

Normally, cement modified soil can be categorised into 5 groups depending on cement content as follows [2]:

2.1 Cement Modified Silty Clay

This type of modification was use in less cement which is approximately 1-3 %. The objective is to modify silty clay surface course, which contains high moisture and very soft, to improve its strength and skid resistance.

2.2 Cement Modified Granular Soil

Cement modified granular soil require less cement content of 1-3 %. The cement can reduce plasticity and water absorption. Although both cement modified silty clay and cement modified granular soil requires less cement content, the modification can improve properties clearly.

2.3 Soil Cement

Soil cement has been designed for improve soils' compressive strength and durability, so more cement content is required. Normally, 5 % cement content is used for well grade soil. In the case that soil with high PI, lime is first added to decrease its plasticity.

2.4 Plastic Soil Cement

Cement content in this kind of material should be enough for increasing flow ability. The modified soil is always used for lining purpose i.e. ditch linings or side slope linings. Plastic soil cement should be high workability. Normally it is also used as grouting materials in concrete pavement repair.

2.5 Cement Treated Soil Slurry

Cement treated soil slurry contain cement, sand and water. This material is the mixture of high water content with added some admixtures for good workability. Normally it is used as grouting material in concrete pavement repair similar to plastic soil cement.

Soil cement was firstly use in the United States in accordance to cooperation research of South Carolina State Highway Department and Portland Cement Association (PCA) to set up soil cement specification standard for designing and testing including moisture density test (ASTM D558/AASHTO T134), wetting and drying test (ASTM D559/AASHTO T135), and freeze and thaw test (ASTM D560/AASHTO T136). All tests were used for samples prepared with standard Proctor test to optimize cement content at optimum moisture content and maximum dry density. Unconfined Compressive Strength test (UCS) and sample preparation and curing followed ASTM D1632 and ASTM D1633 [1].

Department of Highways, DOH, Thailand firstly applied cement stabilization technique for road construction in 1965. According to the standards, highway's base course structure such as crused rock requires strength in term of CBR more than 80%. However, in NortheasternThailand, there has been sign of lack for suitable materials for road construction. Consequently, cement modified soil is one option for materials used for highway's structure.

The problem of soil cement modification in practice is micro cracks [1]. Along with cement hydration, the structures are always affected by volumetric shrinkage resulting in reflective cracks on road surface. The spacing between cracks is approximately about 2.4-6 meters with crack width of less than 3 mm. Normally, cracks are very small and do not affect to traffic load capacity, and water cannot penetrate to lower structure. However, excessive cement content will accelerate cracks causing damages for flexible road pavement.

3. STUDY FOR DURABLE PROPERTIES FOR HIGHWAY MATERIALS

3.1 Highway Materials

Highway materials used in the research have been collected from 6 different areas around Thailand. They can be classified, according to highway's standard as crushed rock and soil aggregate. Fig. 2 shows samples used in this study.

a) Crushed Rock CR1 b) Crushed Rock CR2

c) Crushed Rock CR3 d) Soil Aggregate AG1

e) Soil Aggregate AG2 f) Soil Aggregate AG3

Fig. 2 Samples used in the study

From compositions of each sample, CR1 is mainly composed of grey limestone. CR2 is basalt with high porosity. CR3 is taken from reclaimed base course which limestone is major composition. For aggregates, AG1 comprises conglomerate and breccias which contain quartz. AG2 is a mixture of sand and brown lateritic soil. AG3 mainly composes clay and silt being weathered from mudstone.

Table 1 shows engineering properties of the samples including gradation, liquid limits, plasticity index, optimum moisture content, maximum dry density, CBR, swelling index, and specific gravity. According to AASHTO classification, CR1 can be classified as A-2-6(0) while CR2 and CR3 are both A-1-a(0). Aggregates AG1, AG2, and AG3 can be classified as A-2-6(2), A-2-4(0), and A-2-4(0) respectively.

Table 1 Engineerimg properties of samples

ID	Sieve Analysis (%Passing)										Plasticity		Compaction		Lab CBR		GS
	1"	3/4"	1/2"	3/8"	#4	#10	#20	#40	#100	#200	LL%	PI%	OMC %	ρ_{dmax} (g/cm^3)	CBR%	Swell%	
CR1	96.4	95.9	81.1	69.6	49.3	28.1	16.5	10.9	5.8	2.0	28.8	22.3	6	2.4	80	0	2.78
CR2	100	99.1	87.6	74.2	51.7	27.4	16.0	9.9	4.6	2.5	NP	NP	12	2.2	96	0	2.82
CR3	98.8	90.9	78.6	68.9	49.7	30.6	18.8	11.4	1.8	1.1	NP	NP	6	2.3	92	0	2.52
AG1	96.7	91.0	78.5	60.0	33.0	12.8	6.4	3.2	0.9	0.3	39.3	27.3	9	2.2	31.5	0	2.63
AG2	96.9	92.9	79.8	55.9	41.0	30.9	25.5	18.2	3.0	0.7	28.7	4.3	7.5	2.3	22.5	0	2.70
AG3	94.1	88.4	82.4	75.2	60.0	44.3	28.2	18.1	6.5	3.4	29.5	10.1	10	2.1	22	0	2.64

Strength of materials can be seen from CBR value. All crushed rock samples show value of more than 80% while aggregates show value of 20-30%. According to DOH's standard for crushed rock base course materials, CR1 has high liquid limit and plasticity index. CR2 contains high proportion of fine material (finer than #200). CR3 has gradation off specification. Aggregates from three locations show that AG1 has high liquid limit while AG2 has high fine particle content.

3.2 Strength of Cement Modified Materials

Samples are modified with cement. Crushed rock samples are mixed with Portland cement Type 1 at 1%, 2%, 3%, and 4% by weight, while soil aggregates are mixed with cement content of 2%, 4%, 6%, and 8%. The samples are mixed at OMC obtained from modified compaction tests. Samples are prepares in 4" proctor mold then cured for 7 days and subjected for unconfined compression test. Fig.3 presents results of unconfined compressive strength with respect to cement content for modified samples showing that higher cement content results in higher strength as the effect of cement hydration process.

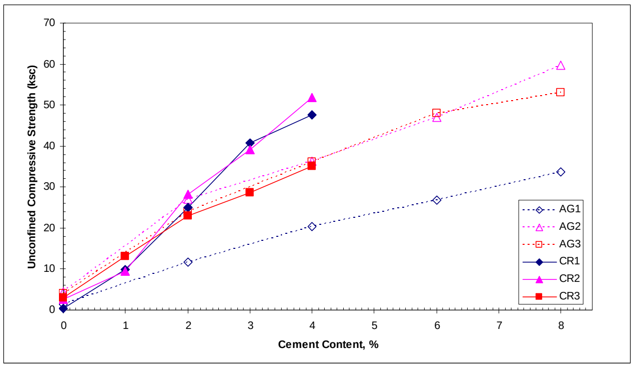

Fig.3 Compressive strength of cement modified samples

3.3 Durability Test

Department's standard is bound to strength of materials for cement modified samples for pavement structure used. However, durability is also a vital factor affecting performance of cement treated materials. Two types of durability tests are carried out for each material: slake durability and wetting-drying durability.

Slake durability test were performed on samples mixed at the same cement content for strength test. After curing for 7 days, samples are broekn down into pieces about 40-60 g each. The test follows ASTM 4644-08 for slake durability index. Fig.4 shows slake durability results for cement treated samples in term of slake durability index and cement content. The figure shows that the higher the cement content, the higher durability index as aggregates are stongly cemented.

Wetting amd drying test is one well-known method to obtained durability. Samples were prepared under the same cement content as strength test and were compacted using 4" proctor mold and cured for 7 days. The test follows ASTM D559-0. Fig.4 shows test result from wetting and drying test for cement modified samples. Loss of weight is decreased as the cement content incrases. From the figure, CR2 shows high loss of weight during wetting and drying cycle showing that baslt with high pososity has difficulty in cement modification.

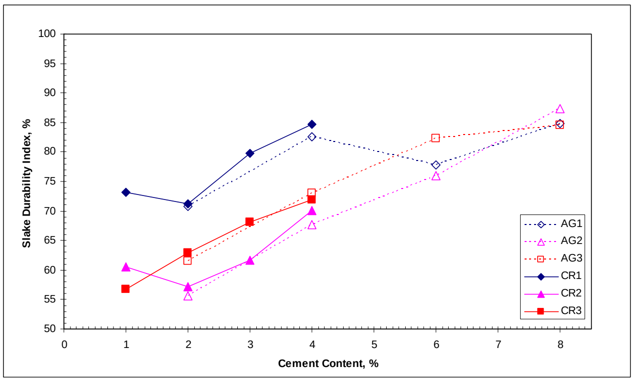

Fig.4 Slake durability test for cement modified materials

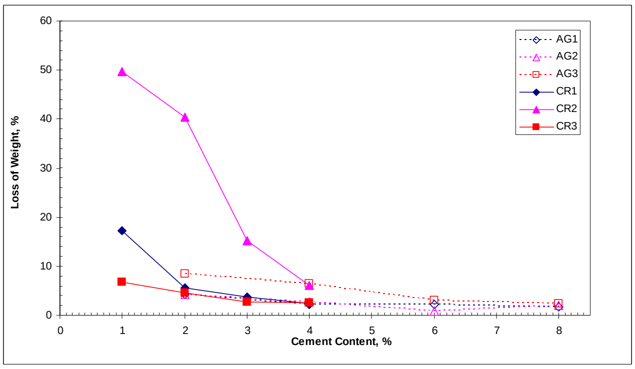

Fig.5 Wetting and drying test for cement modified materials

4. PROPOSED DESIGN CRITERIA FOR DURABILITY IN CEMENT MODIFICATION

Durability of cement modified materials is one factor controlling performance of pavement structure. The application for durability in cement modified materials has been developed [3],[4]. From test results, samples can be grouped under durability criteria as Fig.6. The figure shows relationship of loss of weight and unconfined compressive strength.The loss is increased as the strength increased. With the criteria from [3] and [4], the minimum cement content of CR1, CR2, and CR3 are 2%, 3% and 1%, respectively. The minimum cement content of AG1 and AG3 is 3% and AG2 requires at least 2% cement content.

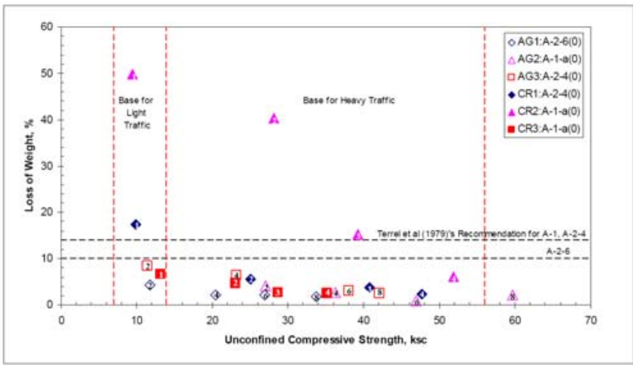

Fig.6 Relationship between loss of weight and strength

Sample CR2 is clearly unsuitable for use as pavement structure as showing high loss of weight. This material requires high cement content for durability concept. In addition, from the framework in Fig.6, for the pavement structure design to sustain heavy traffic volume, strength of cement modified materials can be possibly reduced to 14ksc (1.4MPa) for being in suitable durability range comparing to the strength of 17.5ksc (1.75MPa) for current DOH's design standard.

Although wetting and drying test is a good indicator for material's durability, one disadvantage is testing time. Hence, slake durability tends to be an alternative as it takes less time. From test result, durability from both tests can be plotted as Fig.7.

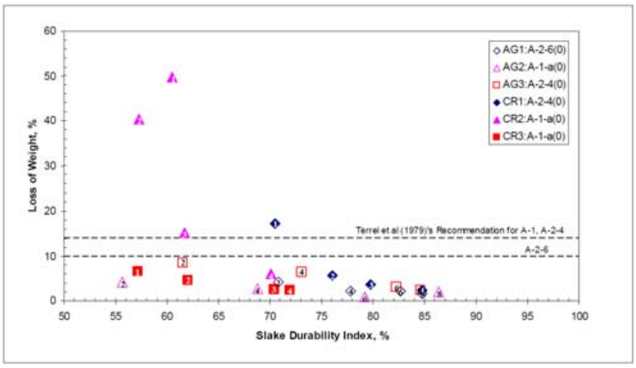

Fig.7 Loss of weight and slake durabilty index of samples

The result shows slake durability index can indicate the suitability of materials for cement modification. CR1, CR2, and CR3 shows that slake durability index of modified samples should be at least 70% and AG1, AG2, and AG3, should have more than 55% slake durability index. This means that the cement content should be high enough for increasiin slake durability index to the recommended values.

5. PERFORMANCE TESTS FOR CEMENT MODIFIED MATERIALS

Performance of cement treated samples can be observed from repeatitive load test. Wheel track testing was used for observing rutting depth of modified mateials. Samples were prepared for CR1 at 0%, 1%, 2%, and 3% cement content, and AG1 at 0%, 2%, 4%, and 8%. Sample dimension is 305x305x100 mm and it was repetitively loaded under 20 kN as shown in Fig.8.

Fig.8 Wheel track testing and rutting depth

Both samples, CR1 and AG1, have high resistivity for rutting when the cement contents increases as shown in Fig.9-10. At 10,000 passes, CR1 without cement modification shows rutting depth of 6mm compared to 0.5mm with cement content only 1%. In the same trend, rutting depth of AG1 is decreased from 11mm to 0.5mm when 2% cement is added to the samples. The test result implies that under repetitive load condition, small amount of cement used for modification is enough for resisting rutting on pavement structure.

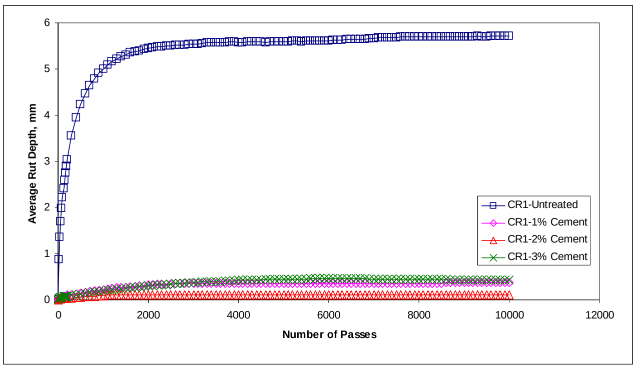

Fig.9 Rutting depth of sample CR1 against number of passes

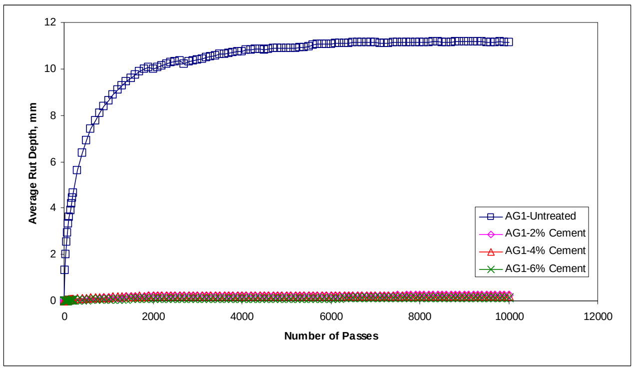

Fig.10 Rutting depth of sample AG1against number of passes

6. CONCLUSIONS

Cracks in cement modified structure have been reflected onto asphaltic pavement when the cement content of such modified materials is not appropriate, quality of materials and quality control during construction are not suitable.

In accordance with durability concept, effect from unsuitable cement content can be underlined. The result from wetting and drying test can be related to unconfined compressive strength, normally used for design by the department. The proposed design is to create guide for cement content required for modification to obtain both enough strength and durability. The study shows that, although CR2 can obtain high strength from modification, it is no durable. So, the engineer can make judment that CR2 may be inappropriate for use as cement modified structure as high cement content will be required for durability.

The result from wheel track test indicates that with small cement content for modification, about 1-2%, can prevent rutting on structure. Consequently, the engineer can possibly decrease cement content to optimise compression strength and durability properties because decreasing in cement content can help to decrease possibility for reflective cracks damages to the asphaltic structure.

Alternatively, in consideration of durability test, slake durability test is quicker test than wetting and drying test. The result shows the same trend on both methods. However, the relationship between results from both tests requires more databases to obtain strong relationship for higher confidence.

7. REFERENCES

[1] PCA, “Soil-Cement Information”, www.cement.com, 2003.
[2] Ruenkrairerksa T, “Material modification and problems in Thailand”, Department of Civil Engineering, KMITT, Bangkok, 1996.
[3] Terrel, R. L., Barenberg, E.J., Mitchell, J.M. and Thomson, M.R., “Soil Stabilization in Pavement Structures”: A User’s Manual, Vol.2: Mixture Design Considerations, FHWA Report IP 80-2, Washington D.C., 1979.
[4] Ingles, O.G. and Metcalf, J.B., “Soil Stabilization Principle and Practice”, Butterworths Pty. Limited, Sydny-Melbourne-Brisbane, Australia, 1972.

First International Conference on Geotechnique, Construction Materials and Environment, Mie, Japan, Nov.21-23, 2011, ISBN: 978-4-9905958-0-7 C3051

Porous Geopolymer Concrete

Tawatchai Tho-in, Vanchai Sata, and Prinya Chindaprasirt
Sustainable Infrastructure Research and Development Center, Dept. of Civil Engineering
Khon Kaen University, Khon Kaen 40002, Thailand

ABSTRACT: This paper presents the use of fly ash based geopolymer as cementitious materials in porous concrete. Porous geopolymer concretes (PGC) were made of fly ash (FA), alkali activators of sodium silicate (NS) and sodium hydroxide (NH) solution, and coarse aggregates. The PGC mix proportions used of FA to coarse aggregate of 1:8 by weight, constant NS/NH ratio and liquid alkaline/FA (L/A) ratio at 0.50 and 0.45, respectively. Crushed lime stone with 4.5-9.5, 9.5-12.5 mm diameter and three concentrations of NH solutions at 10, 15, and 20 M were used. The curing temperature of 60°C for 48 h was used to activate the geopolymerization. The results show that fly ash based geopolymer binder could be used to made porous concrete with compressive and splitting tensile strength range from 9.0-13.7 MPa and 1.1-1.8 MPa, respectively. The void content of PGC increased from 24.2 to 31.0% for water permeability coefficient from 1.09 to 2.58 cm/s.

Keywords: Porous concrete, geopolymer, sodium hydroxide, fly ash, coarse aggregates

1. INTRODUCTION

Porous concrete or pervious concrete is a special concrete which has relatively high water permeability as comparing with conventional due to interconnected pore structure. Typically porous concrete has void content between 18 to 35%, with compressive strengths of 2.8 to 28.0 MPa [1]. Porous concrete is traditionally used in parking areas, areas with light traffic, pedestrian walkways, tennis courts, greenhouse, and other civil engineering and architectural applications [2-4]. In addition, it has environmental benefits such as thermally insulating, acoustic absorption, and water purification [5-6]. Porous concrete mixture is composed of cementitious materials, coarse aggregate, little or no fine aggregates, water, possibly admixtures. Generally, cementitious material used in porous concrete is Portland cement.

Recently, the other form of cementitious materials in term of geopolymer or alkali-activated cementitious materials has developed. This cementitious material obtained from the geoplymerization reaction of alumino-silicate oxide from source materials with high alkali solution [7]. The source materials should be rich in silicon (Si) and aluminum (Al) from geological origin or by-product materials such as clays, metakaolin, fly ash, bottom ash, and slag. The high alkali solutions are usually sodium or potassium based solutions. Many researchers [8-9] found that fly ash based geopolymer can be developed as an alternative Portland cement with many excellent properties such as high early strength, excellent mechanical properties, and good resistance in acid and sulfate attacks. Furthermore, its use involves a lesser amount of green house gas and environmental friendly material compared to the conventional Portland cement [10]. This study focuses on application of fly ash based geopolymer for making porous concrete. Lignite fly ash, sodium silicate and sodium hydroxide solution, and coarse aggregate were used to produce porous geopolymer concrete (PGC). The compressive strength, splitting tensile strength, void content, and water permeability of PGC were tested.

2. EXPERIMENTAL DETAILS

2.1 Materials

Lignite fly ash (FA) from Mae Moh Power plant in north of Thailand with mean particle size of 50 µm, Blaine fineness of 2250 cm^2/g, and retained on sieve #325 at 45% was selected as source materials. The particle shape of FA was mainly spherical with the main chemical composition of 36.8% SiO_2, 15.2% Al_2O_3, 19.7% Fe_2O_3, and 19.4% CaO. Three concentrations viz., 10, 15, and 20 M of sodium hydroxide solution (NH) and sodium silicate solution (NS) with 15.32% Na_2O, 32.87% SiO_2 and 51.81% water were used as alkali activator. Crushed lime stone with 4.5-9.5 and 9.5-12.5 mm diameter (assigned as CS and CM, respectively) were used. The properties of all aggregates are showed in Table 1.

Table 1. Properties of aggregates

Properties	Aggregates (mm.)	
	4.5 – 9.5 (CS)	9.5 – 12.5 (CM)
Specific gravity	2.72	2.71
Water absorption (%)	0.21	0.21
Unit weight (kg/m^3)	1590	1570
Abrasion resistance (%)	31.1	33.2
Fineness modulus	6.06	7.00

2.2 Mix proportion and mixing

All PGC were made with fly ash to coarse aggregate 1:8 by weight. The NS/NH ratio and the liquid alkaline/FA (L/A) ratio were kept constant at 0.50 and 0.45, respectively. The typical mixture consisted of 221 kg/m^3 FA, 33 kg/m^3 NS, 66 kg/m^3 NH, and 1768 kg/m^3 coarse aggregate. All of PCG mix proportions are shown in Table. 2. The symbol of S-PGC15 concrete was PGC with CS aggregate and NH concentration of 15 M.

The PGC were mixed in control room at 22-25 °C. First of all, FA was mixed with NH for 5 minutes in a pan-type mixer.

Then, coarse aggregate was added and mixed for 4 more minutes. Finally, NS was added and mixed for a last minute. After mixing, fresh PGC were cast in cylindrical specimens with 100 mm in diameter and 200 mm in height and compacted using a vibrating table. The PGC specimens were wrapped with a thin plastic sheet and kept in the controlled room at 25°C for 1 hour. After that, they were placed in the oven for heat curing at 60°C for 48 hours. After the heat curing, the specimens were put in the laboratory to cool down and demoulded the next day. The specimens were wrapped with vinyl sheet and stored in the controlled room at 23±2°C and 50% RH until the testing age. Fig. 1 shows PGC specimens after demoulding.

Table 2. PGC mix proportions

Concrete	Materials (kg/m^3)				
	FA	NS	NH	CS	CM
S-PGC10	221	33.0	66.0	1768	-
S-PGC15	221	33.0	66.0	1768	-
S-PGC20	221	33.0	66.0	1768	-
M-PGC10	221	33.0	66.0	-	1768
M-PGC15	221	33.0	66.0	-	1768
M-PGC20	221	33.0	66.0	-	1768

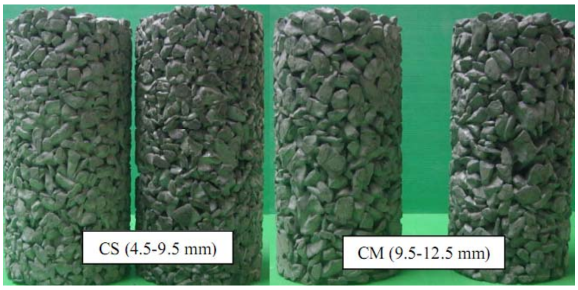

Fig.1 Porous geopolymer concrete specimens

2.3 Testing details

2.3.1 Compressive and splitting tensile strength

The compressive strengths of PGC were determined at 7 days in accordance with ASTM C39 [11]. Before testing, the cylindrical specimens were capped at both ends with a sulfur capping compound to level the loading surface. The splitting tensile strengths at 7 days were measured by performing in accordance with ASTM C496 [12].

2.3.3 Void content

The total void ratio of PGC was determined by taking the difference between the weight of the cylinder sample in saturated under water and air dry sample [13]. The equation used to calculate this value is shown in equation (1).

$$V_C = [1-(W_2 - W_1)/\rho_W V)]\times 100 \quad (1)$$

Where: V_C is the void content of PGC (%), W_1 is the saturated under water weight of the sample (kg), W_2 is the following 24h exposure in air dry weight of sample (kg), ρ_W is the density of water (kg/mm^3), and V is the volume of the sample (mm^3).

2.3.4 Water permeability

The water permeability of PGC was determined using the constant head method following Darcy's Law [14, 15]. Fig. 2 shows the schematic diagram of the experimental test set-up. The coefficient of water permeability (k) is calculated as shown in equation (2).

$$k = \frac{QL}{HAt} \quad (2)$$

Where: k is coefficient of water permeability (cm/s), Q is quantity of water collected (cm^3) over time t (s), L is the length of specimen (cm), H is the water head (cm), and A is the cross sectional area of the specimen (cm^2).

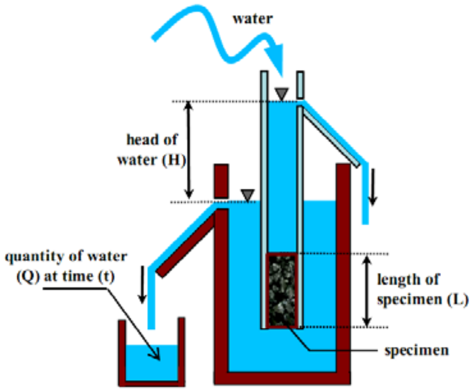

Fig. 2 Water permeability test set-up.

3. RESULTS AND DISCUSSION

3.1 Compressive and splitting tensile strength

The density, compressive strengths, and splitting tensile strength of PGC are shown in Table 3. Because of the high porosity of PGC, the density of all PGC ranged from 1750 to 1860 kg/m^3 which were lower than conventional concrete by about 25%. The compressive strengths of PGC were lower than those of normal Portland cement concrete. However, the fly ash geopolymer could be applied to produce porous concrete with acceptable compressive strength of 9.0 to 13.7 MPa. The splitting tensile strengths varied between 0.9 and 1.4 MPa.

Table 3. Compressive and splitting tensile strength of PGC

Concrete	Density (kg/m^3)	Compressive strength (MPa)	Splitting tensile strength (MPa)
S-PGC10	1860	13.6	1.6
S-PGC15	1800	13.7	1.8
S-PGC20	1810	11.9	1.5
M-PGC10	1840	11.4	1.2
M-PGC15	1800	12.0	1.4
M-PGC20	1750	9.0	1.1

Fig. 3 shows the relationship between NH concentration and the compressive strengths of PGC with CS and CM aggregates. At same NH concentration, the PGC containing CS aggregate had compressive strength higher than those of CM aggregate. For example, the compressive strength of S-PCG15 was 13.7 MPa, while M-PGC15 was 12.0 MPa. This is due to the PCG with small size of coarse aggregate was due the larger specific surface area of CS particle as comparing with the CM which helped in higher contract area of the aggregate particles and paste, resulted in high bonding and compressive strength [16].
The effect of NH concentrations between 10 and 20 M on PGC compressive strengths showed that the optimum NaOH concentration to produce good strength PGC was 15 M. Because of the formation of gel depended on the concentration of alkali OH ion, the low NH concentration resulted in a weak chemical reaction, and the compressive strength was low. An increase in alkali concentration enhanced strength development of geopolymer, but excess hydroxide ion concentration caused aluminosilicate gel precipitation at early stage, resulting in lower strength geopolymer [17, 18]. A maximum compressive strength of 13.7 MPa were obtained at S-PGC15 concrete.

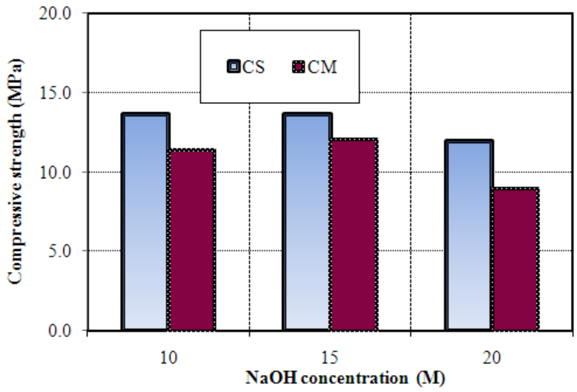

Fig. 3 Compressive strength of PCG

The effects of NH concentrations and aggregate sizes on splitting tensile strength of PGC are shown in Fig. 4. The results had the same direction of the compressive strength. The PGC containing CS aggregate had the splitting tensile strength higher than those of CM aggregate. The use of 15 M NH in PGC had the highest splitting tensile strength. Similar to the compressive strength, S-PGC15 concrete gave the maximum splitting tensile strength at 1.8 MPa. The ratio of splitting tensile to the compressive strength ranged from 10.6 to 13.0% with the average of 12.0%. These ratios were slightly higher than 10% for the conventional concrete. This was probably due to the stronger interfacial transition zone between aggregate and gepolymer binder compared to that of Portland cement binder [19].

3.2 Void content and water permeability

From this study, the void content of PGC varied between 24.2 and 31.0% with average value of 26.8% depended on coarse aggregate size and NH concentration. The relatively high void contents of PGC led to high water permeability coefficients which ranged from 1.09 to 2.56 cm/s. All of void contents and water permeability coefficients of PGC are summarized in Table 4.

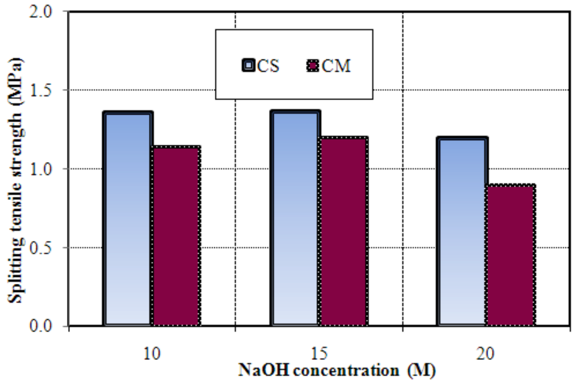

Fig. 4 Splitting tensile strength of PGC

Table 4. Void content and water permeability of PGC

Concrete	Void content (%)	Water permeability coefficient (k) (cm/s)
S-PGC10	24.2	1.16
S-PGC15	25.3	1.09
S-PGC20	27.4	2.00
M-PGC10	24.9	1.73
M-PGC15	28.0	1.79
M-PGC20	31.0	2.58

The influence of coarse aggregate sizes and NH concentrations on void content of PGC are shown in Fig. 5. It was showed that the PGC containing CS aggregate had lower void content than those of CM aggregate for all concentrations of NH. Since, the small size of CS aggregate had the unit weight higher that of CM aggregate, it had lower void between its particles. In addition, it was found that the M-PGC20 concrete with the highest void content of 31.0% had the lowest density of 1750 kg/m^3, and, oppositely, the S-PGC10 concrete with the lowest void content of 24.2% had the highest density of 1860 kg/m^3.
The relationship between NH concentration and water permeability coefficient of PCG with CS and CM aggregate are shown in Fig. 6. The trend here was similar to the void content results. At the same NH concentration, lower values of water permeability coefficient were achieved in PGC using small aggregate size. Also, the water permeability coefficient of PGC obtained from different NH concentration. Thus, the relationship between void content and water permeability of PGC could be fitted in exponential curve as shown in Fig. 7.

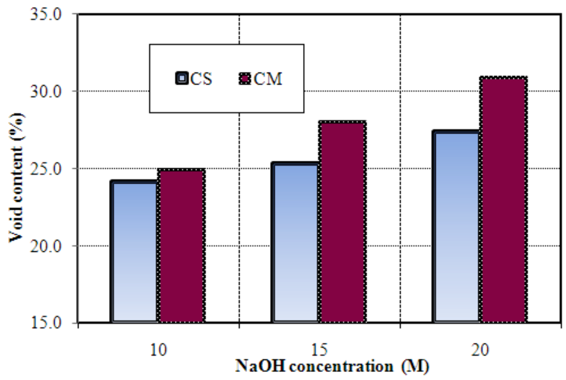

Fig. 5 Void content of PGC

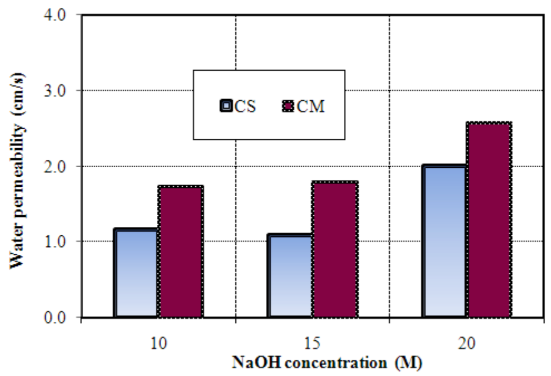

Fig. 6 Water permeability of PGC

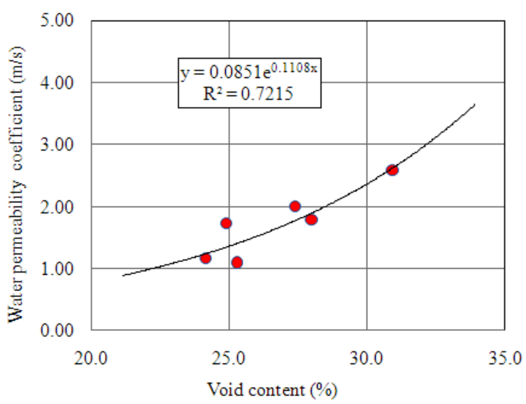

Fig. 7 Relationship between void content and water permeability coefficient of PGC

4 CONCLUSION

From the test results, the following conclusions can be drawn as follow:

1. Fly ash based geopolymer could be used as cementitious materials for making porous concrete with acceptable compressive strength of 9.0 to 13.7 MPa.
2. The compressive and splitting tensile strengths were optimum with PGC containing small aggregate size and NH concentration of 15 M.
3. The void content of PGC ranged from 24.2 to 31.0%. This high porosity leaded to a high water permeability coefficient at 1.09 to 2.58 cm/s.

5 ACKNOELEGMENT

This work was supported by the Higher Education Research Promotion and National Research University Project of Thailand, Office of the Higher Education Commission, through the Advanced Functional Materials Cluster of Khon Kaen University.

6 REFERENCES

[1] ACI committee 522, Pervious Concrete, Report No. 522R-10, American Concrete Institute, Detroit, USA, 2010 P.38.

[2] Schaefer VR, Wang K, Sulieman MT, Kevern JT. ”Mix design development for pervious concrete in cold weather climates.” Final Report, Iowa Department of Transportation, National Concrete Pavement Technology Center, Iowa Concrete Paving Association, February 2006, P.67.

[3] Scholz M, Graboweiki P. “Review of permeable pavement system,” Bulid. Environ., 2007;42:3830-36.

[4] Tyner JS, Wright WC, Cobbs PA. “Increasing exfiltration from pervious concrete and temperature monitoring,” J. Environ. Manage., 2009;90:2636-41.

[5] Park AB, Tia M. “An experimental study on the water-purification properties of porous concrete,” Cem. Concr. Res., 2004;34:177-184.

[6] Kim HK, Lee HK. “Acoustic absorption modeling of porous concrete considering the gradation and shape of aggregate and void ratio,” J. Sound Vib., 2010;329(7):866-79.

[7] Davidovits J. “Geopolymer: inorganic polymeric new materials,” J Therm Anal 1991;37:1633-56.

[8] Hardijito D, Wallah SE, Sumajouw DMJ, Rangan BV. “On the development of fly ash based geopolymer concrete,” ACI Mater J., 2004;101(6):467-72.

[9] Bakharev T. “Resistance of geopolymer materials to acid attack,” Cem Concr Res., 2005;35:658-670.

[10] Duxson P, Provis JL, Lukey GC, van Deventer JSJ. “The role of inorganic polymer technology in the development of ‘green concrete,” Cem Concr Res., 2007;37:1590-7.

[11] American Society for Testing and Materials (ASTM) C 39/C 39M-01. Standard test method for compressive strength of cylindrical concrete specimens: 2003.

[12] American Society for Testing and Materials (ASTM) C 496-96. Standard test method for splitting tensile strength of cylindrical concrete specimens: 2003.

[13] Park AB, Tia M. “An experimental study on the water-purification properties of porous concrete,” Cem Concr Res., 2004;34:177-184.

[14] Japan Concrete Institute, Proceedings of the JCI Symposium on Design, Construction and Recent Applications of Porous concrete (2004) pp.1-10.

[15] Park SB, Lee BJ, Lee J, Jang YI. “A study on the seawater purification characteristics of water-permeable concrete using recycled aggregate,” Resour Conserv Recy., 2010;54:658-65.

[16] Al-Oraimi SK, Taha R, Hassan HF. “The effect of the mineralogy of coarse aggregate on mechanical properties on high-strength concrete,” Constr Build Mater., 2006;20:499-503.

[17] Somna K, Jaturapitakkul C, Kajitvichyanukul P, and Chindaprasirt P. “NaOH-activated ground fly ash geopolymer cured at ambient temperature,” Fuel., 2011;90:2118-24.

[18] Lee WK van Deventer JSJ. “The effect of inorganic salt contamination on the strength and durability of geopolymer,” Colloids Surf A., 2002;211:115-26.

[19] Sarker PK. “Bond strength of reinforcing steel embedded in fly ash-based geopolymer concrete,” Mater Struct., 2011;44(5):1021-30.

First International Conference on Geotechnique, Construction Materials and Environment, Mie, Japan, Nov.21-23, 2011, ISBN: 978-4-9905958-0-7 C3051

Design and Fabrication of Composite Technology for Earth Slope Protection

Md. Toriqul Islam , Department of Sustainable Social Systems, Mie University
Md. Zakaria Hossain, Department of Environmental Sci. and Tech., Mie University
Masaaki Ishida, Department of Sustainable Social Systems, Mie University

ABSTRACT: This paper presents the design and fabrication of composite technology for earth slope protection. The selected structures that have been identified for earths slope protection are skeletal frame of soil anchoring, earth reinforcements, hill cover and slope surface lining. Design sketches of various composites along with fabrication procedure are depicted. Some examples of practical applications of this composite technology have been demonstrated using simple techniques. Based on the cost of required materials and labor, the cost of fabrication per unit area of composite structure has been calculated. It is concluded that the required cost of the composite structure was U$ 60 dollar per square meter.

Keywords: Composite structure, Design, Fabrication, Slope protection, Application.

1. INTRODUCTION

Composite technology consists of sand-cement mortar reinforced with wire mesh are used in the construction of various structures [1]. It has also been used for making linings to bridge arches, swimming pools, flumes, aqueducts, thin shell structures and low-cost farm structures [2]. Research and development work on this material in Japan, however, are not so many. Only a few research institutions in Japan like Building Research Institute, Tokyo Institute of Technology, Nihon University including the Mie University and Kyoto University have applied the composite techniques but mostly limited to demonstration only [3-7]. In view of the above distinct advantages of this material, it may be effective to utilize this technology for earth slope protection in the hilly country like Japan. Understanding the facts stated above, a study was undertaken in the Division of Environmental Science and Technology, Mie University, Japan with the following objectives. i) to identify the structures that can be made with composite technology for earth slope protection, and ii) to present the fabrication process and cost estimation of composite structures for earth slope protection.

2. MATERIALS AND METHODS

In the field of earth slope protection, the basic materials needed for composite constructions are wire mesh, sand, cement and water. The skeletal steel is used in the construction of composite frame structures for earth slope protection. A basic description of the constituent materials and construction procedure is given below.

2.1 Constituent Materials

Wire mesh: As given above, there were different types of meshes used in composite works. It is one of the most essential components of composite especially for slope surface protection works. The wire meshes must be easily handled and flexible enough to be bent around sharp corners and unevenness of the slope surface. The main function of the wire mesh in slope surface protection is to act as a lath providing the form and to support the mortar during the hardened state of composite. The wire meshes absorb the tensile stresses on the structure which the mortar, on its own, would not be able to withstand. In the project special types of steel wire mesh (galvanized metal mesh) having 2.0 mm wire diameter with center to center wire spacing of 50 mm were used. The mesh (**Fig.1**) has been folded for the ease of transportation and can easily be spread during construction. It has been coated with zinc to protect from rusting according to the Japan Industrial Standard (JIS G3552).

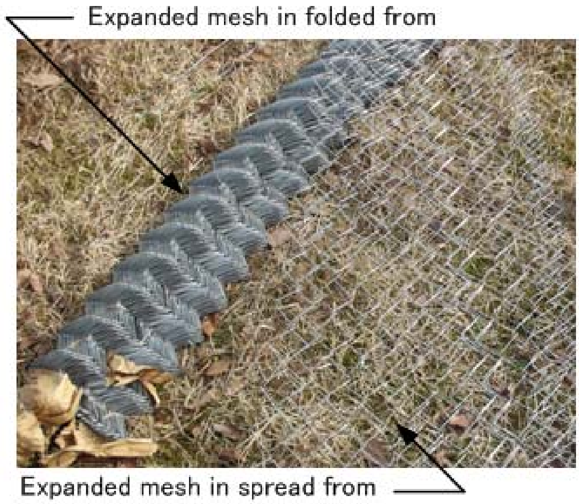

Fig. 1 Mesh used for composite technology for slope protection

Cement: The ordinary Portland cement is the most commonly used in Japan among several types of cement available commercially. In the present study, the ordinary Portland cement (JIS R5210) was used throughout the research work. This type of cement is adequate for application in earth slope protection where special conditions do not prevail.
Sand: For composite work, well graded coarse sand is commonly used. In the present study, the river coarse silica sand is used. The sand is passing through 5.0 mm sieve and the fineness modulus of it is 2.5.
Water: Water plays a vital role on the resulting hardened state of composite. Sea water or water with any impurities such as acids, soluble salts and any organic matters are not at all suitable for mixing mortar as they may increase the risk of corrosion or interfere the setting time of cement and finally

the strength of the composite. In this study tap water was used for making the cement mortar.

2.1 Construction Procedure

Placement of wire mesh: For placement of wire mesh, no skeletal steel frame is needed for the composite work in earth slope protection. The slope is cleaned after removing the trees, grass and any other element before placing the mesh. An example of this procedure is shown in **Fig.2**.

Fig. 2 Cutting of trees and cleaning of the slope before pacing the mesh (Sasagatake mountain, Iga city, Mie)

Following the shape of the slope surface, one layer of wire mesh was placed on the slope spreading from the top to bottom of the slope. The mesh was tied by the hook or anchored pin with the slope. The most common size of the anchored pin was 13-16 mm in diameter and 20-400 mm in length depending on the position slope. The placement procedure of the wire mesh is shown in **Fig.3**. The anchoring pin used to fix the wire mesh on the slope is shown in **Fig.4**.

Fig. 3 Placement of wire mesh on the slope surface (Sasagatake mountain, Iga city, Mie)

2.2 Preparation of Mortar

In order to obtain the desire strength of the structures, it is very important to select the suitable proportion of the cement to sand ratio.For the composite in building works, the proportion of cement to sand generally varies from 1 part of cement to 1.5 to 2 parts of sand by weight. However, for the composite in slope protection, the proportion of cement to sand is taken as 1 part of cement to 3 to 5 parts of sand by weight. This provides the strength of more than 15 N/mm^2 which is considered enough for slope protection. The water to cement ratio used was in the order of 0.45 depending upon the dryness of sand. In the mixing process the sand and cement were firstly mixed uniformly. The water was added gradually part by part in order to obtain the required workability on the mortar mix.

Fig. 4 Anchored pin for fixing the mesh on the slope

Plastering: The plastering technique employed in this study was done by spraying the mortar by a particular form of gun which is supplied with compressed air. As part of an overall apparatus, that includes a pump and an air compressor, which enables spray applications to be effected remotely from the mortar supply for the in-situ composite of slope surface. The spray pattern of the gun is adjustable. Controlling the mortar supply and air pressure helps to reduce the problems associated with excessive spray formation and rebound of the applied mortar. For stiff mixes, the mortar normally remains in position after placing.

Curing: The objective of curing is to keep the mortar saturated and to promote the hydration of cement. There are several methods of curing. In this research the moist curing was followed for about one week. After that the composite structure is cured for long time with the moisture that usually comes from soil.

3. Results and discussion

The sketches of various composite structures identified for slope surface protection are given in **Figs.5-12**. Based on the cost of the materials and labors, the cost of construction of composite for slope surface protection has been estimated and given in Table 1. The shape the edge of a composite structure used for earth slope protection is shown in **Fig.5**. Both the upper and lower edges have vertical portions (flanges) of 30 cm or more depending on the field conditions. Due to these two vertical portions of flanges, the edge of composite structures would be fixed on the slope and prevent water entry just underneath the composite layer. According to the need, however, one can make the structure without any flanges or the flanges can be made with variable sizes. The cross-sectional view of the composite structure showing the mortar, mesh and the anchored pin is given in **Fig.6**. The length of the anchored pin ranges from 200 to 400 mm with diameter of 13 to 16 mm depending on the slope conditions and position of the pin. The anchored pin is used to hold the mesh on the surface of the earth slope during construction and to facilitate the composite structures to be remained on the slope during on-service. The average thickness of the composite structures used for slope protection is usually 6 to 7 mm. However, this may be little bit thicker due to the unevenness of the surface of the slope. A part of the completed composite structures for slope surface protection is shown in **Fig.7**. This figure also shows a portion of the mesh and the application technique of the mortar on the mesh.

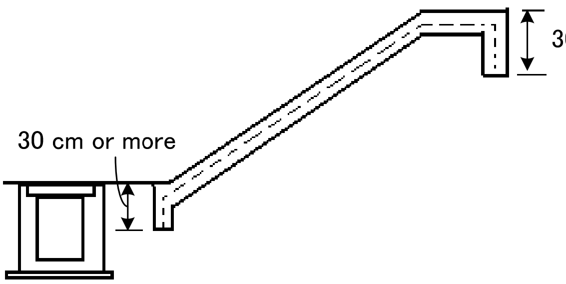

Fig. 5 Shape of the edge of composite for slope protection

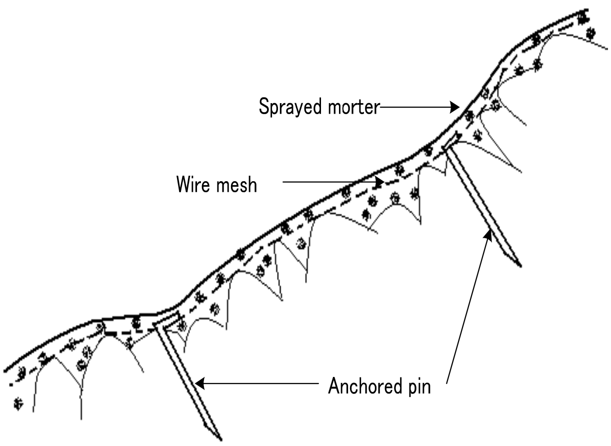

Fig. 6 Cross-sectional view of composite and the anchored pin used for slope protection work

Fig. 7 A part of completed composite for slope protection (Sasagatake mountain, Iga city, Mie)

Another item of composite that has been made for use in slope surface protection is the composite frame structures (**Figs.8-12**). Traditional structures made of brick are neither strong nor suitable for mass use in slope protection works. Concrete made frame structures are found to be expensive and intricacy in construction. Because of high adaptability of composite to various structural forms and ease in construction and economy; the composite technology can be applied in making not only the complete layer on whole surface of the slope as shown in **Fig.7** but also be employed in constructing frame structures especially for large scale slope or the like. The sketches of composite frame structure having joint at the vertical column is shown in **Fig.8** and the completed structure having joint in vertical frame is shown in **Fig.9**. For the case of the joint in vertical frame, the joint is usually made at a distance of $b/2$ from the nearest frame that has ground anchor and the next ground anchor is made at a distance of b between the two frames (**Fig.8**).

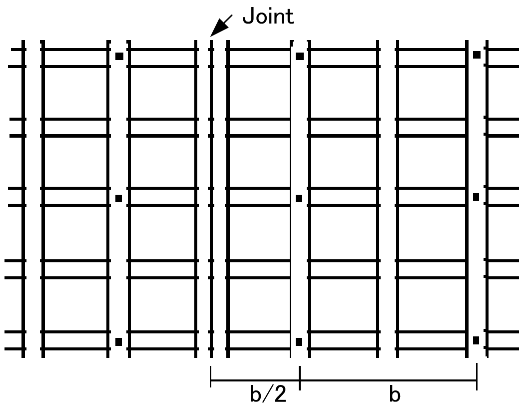

Fig. 8 Sketches of composite frame with vertical joint for slope protection

On the other hand, for the joint in horizontal frame, it is usually made at the mid-section of the frame with the distance $d/2$ from the center of the nearest frame as shown in **Fig.10**. In this case usually, the ground anchor is provided at all intersectional points of the frame (**Fig.10**).

Fig.9 Completed composite frame with vertical joint for slope protection (Sasagatake mountain, Iga city, Mie)

The completed structure having joint in horizontal frame is shown in **Fig.11**. This technique of composite structure for earth slope protection allows greeneries between the frames, and thus conserves the environment. Therefore, the composite technology for the earth slope protection can be treated as the environmentally friendly technology and the composite can be termed as environmentally friendly material, especially when dealing with the earth slope.

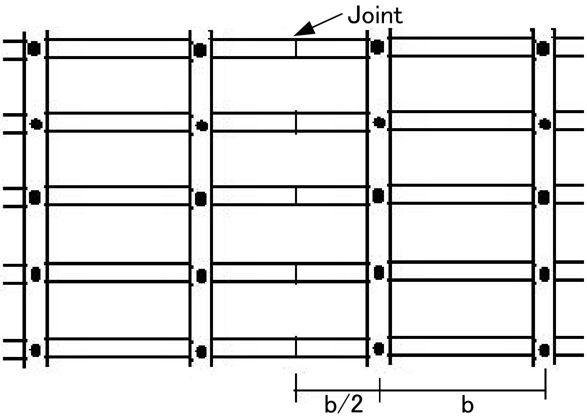

Fig. 10 Sketches of composite with horizontal joints for earth slope protection

Fig. 11 Completed composite frame with horizontal joints for earth slope protection (Sasagatake mountain, Iga city, Mie)

The design of the horizontal and vertical frames along with the placement of mesh, skeletal steel and ground anchor is shown in **Fig.12**. Usually, the placement of skeletal steel and the mesh in the vertical frame is done firstly then the placement of skeletal steel and the mesh in the horizontal frame is performed. As can be seen in this figure that themesh of the vertical frame is cut at the mid-section of the two horizontal meshes and then bent it outside. This facilitates the ease of placement of mortar and the aesthetics of the structures. The ground anchor is provided at the position close to the skeletal steel instead of the center of the intersection in order to clamp and hook the frame to be remained in its position during casting and on-service.

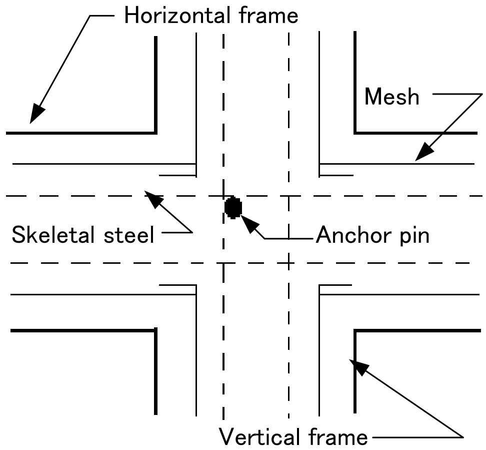

Fig. 12 Method of processing the intersection point of the composite frame

The cost of different items used for the construction of composite structures for earth slope protection is summarized in Table 1.

Table 1 Calculation of the cost of composite structure for earth slope protection

Items	Cost (Yen)	Cost (US$)
Price of mortar per cubic meter (cement:sand=1:4)	15200.0	126.67
Mortar per square meter with thickness 7 cm, (1 cubic meter×0.7)	1064.0	8.87
Wire mesh (dia.2mm, cc opening 50mm) per square meter	230.0	1.92
Anchor pin and spacer, tools etc. per square meter	206.0	1.72
Mortar mixing, spraying, labors etc. per square meter	3000.0	25.00
Total cost composite structure per square meter	4500.0	37.5

Note: 1US$=￥75 (4500yen=60US$), Sept.01, 2011

The cost given in Table 1 is calculated based on the costs of materials and labors. Though it has not been the prime objective of the studies to compare the cost of composite structures with other varieties of materials, it can, however, be emphasized that the composite structures are relatively cheaper than those made with traditional materials like timber, steel and such other materials.

3. CONCLUSION

Composite structures that have that have been indentified and constructed in this research study are some of the examples that can be constructed for earth slope protection using composite technology. Results obtained have demonstrated that the utility and economy can both be achieved using very simple techniques using locally available materials. It is expected that the observations made here in this study will bring the new concept in gaining wide acceptance of composite for the construction of strong, durable and cost-effective composite structures for earth slope protection.

4. ACKNOWLEDGEMENT

The author is grateful to Mr. Morimoto of Yamaichi Construction Company Ltd. for supplying some information during preparation of this manuscript. This research is partly supported by the Research Grant No. 18580243 with funds from Grants-in-Aid for Scientific Research given by the Japanese Government. The writer gratefully acknowledges these supports. Any opinions, findings, and conclusions expressed in this paper are those of the authors and do not necessarily reflect the views of the sponsor.

5. REFERENCES

[1] Naaman AE, "Composite and Laminated Cementitious Composites," Techno Press 300. Ann Arbor, Michigan, 2000.
[2] Awal ASMA, Composite: "A unique material of construction and its use in agriculture," Bangladesh J, of Agric. Engg., Vol.1, No.2, 1987, pp.35-40,
[3] Hossain, MZ. and Hasegawa, T. " A Study on Pre- and Post-Cracking Behavior of Composite Plates," J. of Composite,vol. 27, No. 2, 1997, pp. 127-142.
[4] Hossain, MZ and Inoue S, " Compression Behavior and Buckling Analysis of Composite Elements Using the Finite Element Method," Journal of Composite, Vol.30, No.2, 2000, pp.147-166.
[5] Hossain, MZ, Sakai, T and Paramasivam, P " Bearing Capacity of Thin Cementitious composites Reinforced with Different Types of Meshes," Journal of Composite, Vol.36, No.3, 2006, pp.833-848.
[6] Ohama, Y and Shirai, A " Flexural behavior of polymer composite with steel fibers," J. of Composite, Vol.14, No.3, 1984, pp.205-210.
[7] Shirai, A and Ohama, Y " Improvement in flexural behavior and impact resistance of composite by use of polymers," J. of Composite, Vol.20, No.3, 1990 pp.257-264.

First International Conference on Geotechnique, Construction Materials and Environment, Mie, Japan, Nov.21-23, 2011, ISBN: 978-4-9905958-0-7 C3051

Study of Slump Testing for Hydraulic Plastic Grout

Hiroyasu ISHII[1], Kenichi HORIKOSHI[1] and Masaki KITAZUME[2]
1) Technology Center, TAISEI Corporation, 2) Tokyo Institute of Technology

ABSTRACT: Hydraulic plastic grout, which consists of cement, water, admixtures and a plasticizing agent, has different properties in its fresh state than other fluid construction materials such as mortars and concretes. This brings specific benefits in civil construction, especially in void filling and foundation work, because its plasticity endures flow even under the influence of gravity.

In this research, the authors mainly focus on a conventional quality test used on fluid materials in their fresh state, the slump test. Although this is a very useful method and is used in various evaluations of fluid materials, including hydraulic plastic grout, the measured deformation (slump, flow) of hydraulic plastic grout is very small due to its plastic property and small specific gravity.

This paper begins with a review of hydraulic plastic grout to indicate how it is used in practice. Then a simple modified slump test is presented in which an additional vertical burden is applied to the top surface of a hydraulic plastic grout sample. The slump and flow values obtained through the method are presented and studied analytically to obtain a typical property, the yield stress.

Keywords: Hydraulic plastic grout, Slump test, Void filling, Yield stress

1. INTRODUCTION

Hydraulic plastic grout consists of cement, water, admixtures and plasticizing agent and has plastic properties in the fresh state. The grout can be injected under pressure and endure flow even under gravitational force. This makes it effective for civil construction work such as void filling and foundation work since it does not leave major voids. That is, the properties of the grout are quite different from those of conventional fluid materials like mortars and concretes [1]. (Fig. 1, 2)

This type of grout has been used to fill the tail void during tunnel boring machine (TBM) tunneling. Other recent applications have demonstrated the effectiveness of the material in other areas, as described in the following section. The use of hydraulic plastic grout is expected to expand as it comes into use for repair work and remediation work related to foundations.

In these various applications, past and future, different grout plasticity may be used according to the purpose of the grout as well as working conditions. This means that slump tests will play a key role in on-site quality control.

Until now, the cylinder flow test (JHS A313) and the table flow test (JIS R 5201) have been used to measure slump, just as for mortar or concrete. The authors, however, take the view that the present use of slump tests for hydraulic plastic grout needs further study due to the lack of consideration of its different properties from conventional materials.

In this paper, a review of hydraulic plastic grout is given to shown how it works in actual applications. Then a simple modified slump test is presented in which an additional vertical burden is applied to the top surface of the hydraulic plastic grout being measured. Slump and flow values obtained using this modified method are presented. Through an analytical study, a characteristic property of the grout, yield stress, is estimated.

2. USE OF HYDRAULIC PLASTIC GROUT

2.1 Site operations

The components of a hydraulic plastic grout, generally consisting of cement solution, admixture solution and plasticizing agent, are prepared and supplied separately before mixing altogether for use. Each solution is so thin that it can be transported through supply piping at a relatively low pumping pressure. This is one of key benefits of hydraulic plastic grout as compared with conventional materials like mortars and concretes, which have high viscosity and require much higher pumping pressures.

The solutions are mixed together in the supply piping immediately before injection. The mixed hydraulic plastic grout gains plasticity in seconds. The level of plasticity depends on the mix proportion, the cement content, the type

Fig. 1 Hydraulic plastic grout

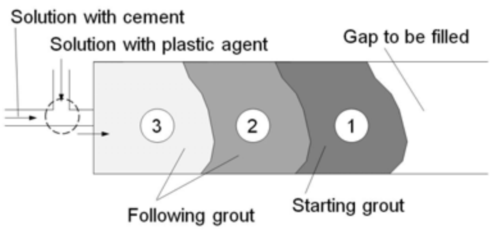

Fig. 2 Schematic diagram of hydraulic plastic grout during injection

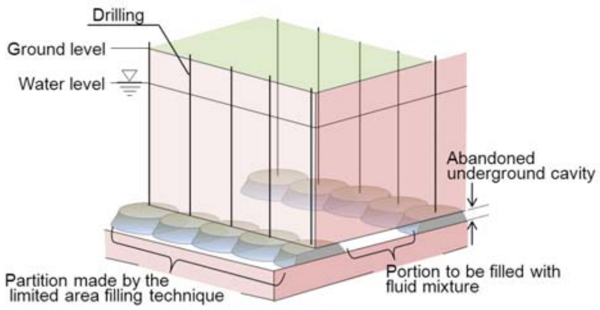

Fig. 3 Schematic diagram of limited volume filling technique applied to abandoned underground cavity [2]

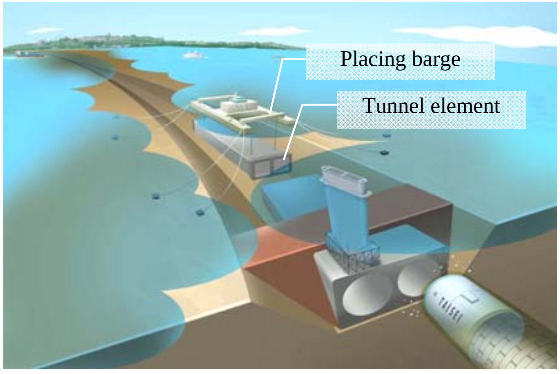

Fig. 4 Birds-eye view of immersed tunnel crossing the Bosphorus strait.

of plasticizing agent and other factors. Typical properties are 1,000–10,000 N/m^2 vane shear strength and 140–160 mm of cylinder flow value.

Injection work can take from minutes to hours depending on the work plan. After injection, the grout is left to harden by cement hydration. Typical unconfined compressive strength is 0.8–1 N/mm^2.

The major benefit of hydraulic plastic grout is that good filling can be achieved without leaving major voids. This is because the mix proportion is intentionally prepared so that bleeding will be negative, and also the grout undergoes significant deformation under gravity during and after injection.

2.2 Conventional Use

The original use of hydraulic plastic grout was to fill the tail void, meaning the gap around the segments, during tunneling by boring machine. Its advantages in this application are good filling, early age strength, and the possibility of pumping long distances through piping along the tunnel. A number of different mixtures and methods have so far been implemented by construction firms in Japan.

Repair work and remediation work around foundations and retaining walls are among other typical applications. Gaps sometimes form below or behind structures as a result of consolidation settlement, seismic effects and seepage washout. Hydraulic plastic grout is very suitable for filling these voids.

Another application that takes advantage of the properties of hydraulic plastic grout is the filling of limited volumes. This technique has been developed for use in the filling of abandoned underground cavities [2]. The hydraulic plastic grout is used only to form partitions within the cavities, which are too large and complex in shape to be filled with a fluid material in one step. Each partition formed by placing a hydraulic plastic grout barrier is a limited region that can then be filled with a different fluid mixture. (Fig. 3)

2.3 Recent Applications

A recent application is in filling the space between immersed tunnel elements and their prepared foundations for a 1.4 km length of immersed tube tunnel crossing the Bosphorus Strait in Turkey [3] (Fig. 4). This is one of the main structures forming the Marmaray Project in Istanbul, which is a full upgrading of the present commuter rail system and includes a 13.4 km underground section.

As part of tunnel construction work, any space between the foundation and the immersed tunnel element has to be filled after each element is immersed and placed on the seabed. Various conditions of the entire work led to hydraulic plastic grout being chosen as the most suitable material for filling the space under all 11 immersed elements [4].

Full scale injection tests were carried out in advance of actual site work. These test injections were performed in the space between a model slab and a stone foundation positioned in a 9 m-diameter water tank. A mound with a height of 300 mm was intentionally formed on the stone foundation so as to observe how the grout performed with such undulations. (Fig. 5)

Grout was injected over the whole area from only one injection valve. After it had set, its surface was found to be fully flat without major voids, as indicated in Fig. 6. It was confirmed that one injection point could be used to inject up to 6 m in distance.

For the actual work, injection valves were positioned along two lines spaced 5 m apart, as illustrated in Fig. 7. Valves in both lines were spaced at 8 m and they were offset from each other in the two lines. This gave a valve-to-valve spacing of 6.6 m. Injection took place in order from one end of the element, using approximately 30 valves per tunnel element. The injection valves were used as arrival valves for grouting from the preceding valve; arrival of the grout was mostly confirmed by opening neighboring valves and allowing grout to escape.

3 SLUMP TEST FOR HYDRAULIC PLASTIC GROUT

3.1 Application of Slump Test

Slump tests (or flow tests) are a well-known method of evaluating the consistency of construction materials such as mortars, concretes, and various kinds of grout. The material to be tested is placed in a vessel, of which several sizes and shapes are used according to sample composition or fluidity.

The cylinder flow test (JHS A 313; cylinder dia. = 80 mm,

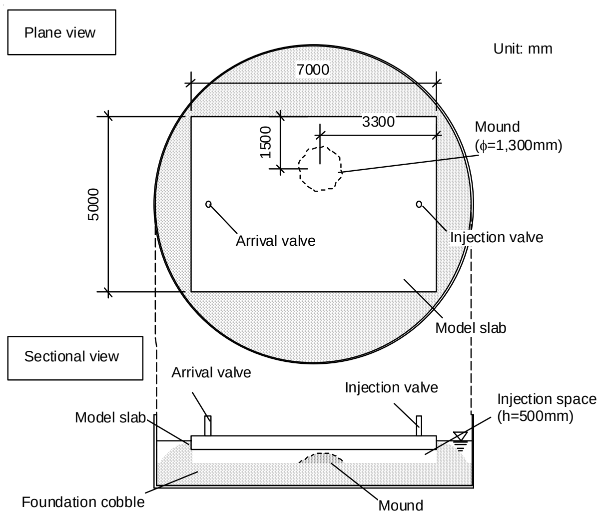

Fig. 5 Plane and sectional view of full-scale model test

Fig. 6 Surface and section of solidified hydraulic plastic grout after test injection

height = 80 mm) and the table flow test (JIS R 5201; cone upper dia. = 60 mm, lower dia. = 80 mm, height = 60 mm) are in common use for measuring hydraulic plastic grout. Although both measure the diameter of the sample material after it has slumped, the former allows the grout to flow under gravity only, while in the latter the grout is tamped 15 times. A target flow value of 160–180 mm was set for the mixture developed as a limited volume fill material [2].

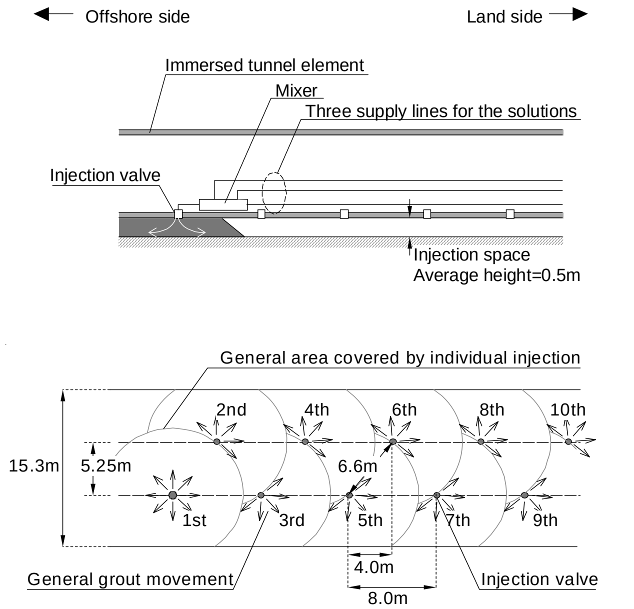

Fig. 7 Injection sequence for construction of immersed tunnel foundations

Although these tests work efficiently as checks on the quality of grout, the authors raise two concerns for further consideration:

- The higher yield stress as well as the lower unit weight of hydraulic plastic grout as compared with mortars and concretes mean that deformation is generally poor during flow tests.
- Although tamping 15 times as stipulated in the table flow test effectively results in a larger deformation, the flow value obtained is merely an index and does not directly represent the viscous property of the grout.

In order to modify the conventional procedures to take into account these two concerns, there are two possible approaches that will enhance the deformation without tamping. One is to use a larger scale and the other is to apply an additional burden to the grout. In this study, the latter approach is employed to examine its applicability and benefit.

3.2 Theoretical Approach

After the first simple theoretical analysis relating slump to yield stress carried out by J. Murata [5], a number of studies using similar methods have been published for mortars and concretes as well as for mineral and industrial suspensions [6]–[9]. This study refers to an analytical model developed for cylindrical geometry and which was generalized in dimensionless form [8]. The model described below is based in part on this conventional one, but a burden is newly added to enhance grout deformation.

Conventional slump theory

Figure 8 is schematic diagram of the deformation and stress state at each stage. Initially, the pressure, $P|_{z,0}$, at any given height, z, can be approximated as

$$P\big|_{z,0} = z\rho g \tag{1}$$

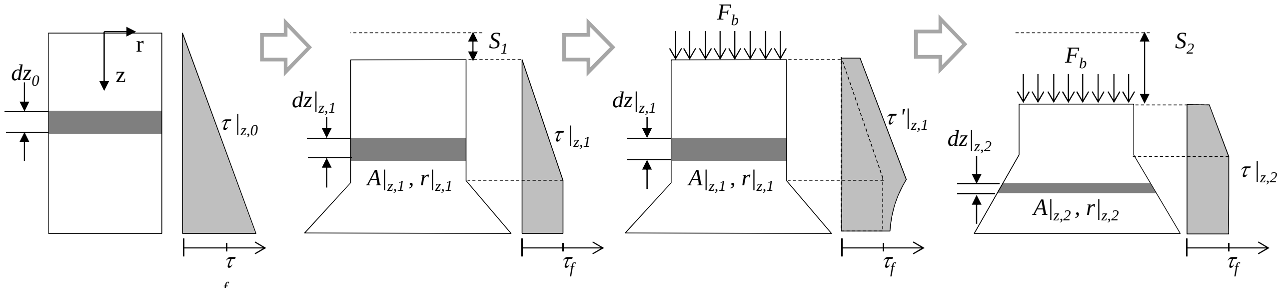

a) Initial state b) Conventional slump c) Applying a burden d) Enhanced slump

Fig. 8 Schematic diagram of deformation and stress state at each stage

where ρ represents specific gravity of the sample. The maximum shear stress, $\tau|_{z,0}$, is, assuming an ideal elastic solid, equal to half the pressure.

$$\tau|_{z,0} = 0.5z\rho g \tag{2}$$

As illustrated in Fig. 9, the initial shear stress is distributed linearly from 0 at the top to a maximum at the base. Toward the top of the sample, the stress experienced may be less than the yield stress; without yielding, no deformation takes place. On the other hand, lower down in the sample, stress may exceed the yield stress; flow then occurs until the stress falls to the yield value.

$$A|_{z,1} = A_0 \cdot \tau|_{z,0} / \tau_f \tag{3}$$

where A_0 $A|_{z,1}$ represents the cross-sectional area of the cylindrical specimen in the initial state and in conventional slump, respectively. With the height divided into thin elements of thickness dz, the volume conservation assumption gives the following equation.

$$dz_0 \cdot A_0 = dz_1 \cdot A|_{z,1} \tag{4}$$

where dz_0 and dz_1 are the element thickness in the initial state and in the conventional slump state, respectively.

Accordingly dz_1 can be specified and slump, S_1, can be numerically calculated by accumulating dz_0–dz_1.

$$S_1 = \sum (dz_0 - dz_1) \tag{5}$$

Twice the value of r_1, derived from S_1, at the bottom is specified as the flow value.

<u>*Enhanced slump theory*</u>

A burden, F_b, is applied in the conventional slump state, as illustrated in Fig. 8(c). Based on same simplifications and assumptions used above, pressure, $P'|_{z,1}$, and shear stress, $\tau'|_{z,1}$, at any given height can be assumed as the following.

$$P'|_{z,1} = P|_{z,1} + F_b / A|_{z,1} \tag{6}$$

$$\tau'|_{z,1} = 0.5P'|_{z,1} \tag{7}$$

In elements where the shear stress exceeds the yield stress, additional deformation takes place. The stress balance and volume conservation give the following equations.

$$A|_{z,2} = A|_{z,1} \cdot \tau'|_{z,1} / \tau_f \tag{8}$$

$$dz_{z,1} \cdot A|_{z,1} = dz_{z,2} \cdot A|_{z,2} \tag{9}$$

Accordingly dz_2 can be specified and the enhanced slump, S_2, can be numerically calculated by accumulating dz_1–dz_2.

$$S_2 = S_1 + \sum (dz_1 - dz_2) \tag{10}$$

Twice the value of r_2, derived from S_2, at the bottom is specified as the flow value.

Table 1 Mix proportion of hydraulic plastic grouts used for the slump tests (for 1 m^3)

Solution		M1	M2
A	Oridinal portland cement (kg)	320	240
	Solution B (L)	60	60
	Admixture (L)	2	2
	Water (L)	246	309
B	Bentonite (kg)	45	35
	Water (L)	552	516
C	Sodium Silicate (L)	20	20

3.3 Laboratory Tests

In order to investigate the actual slump value obtained by the proposed enhanced method, slump tests were conducted with both slump and flow values were recorded.

The two mixtures tested here were typical hydraulic plastic grouts. Their mix proportions are summarized in Table 1. Two tests were conducted for each mix. This allowed slump to be measured with two different yield stresses for the same mixture; the setting time caused cement hydration to increase the yield stress of the grout.

The cylinder used for the slump tests had a height of 80 mm and a diameter of 80 mm. The cylinder was first filled with the hydraulic plastic grout. It was then lifted away, allowing the grout to collapse under its own weight. The slump height and flow diameter of the grout were measured as a conventional method.

In order to measure the enhanced slump, a burden was applied using a specially fabricated cup and small lead balls. After the conventional measurement of slump as described above, these were placed on top surface of the grout to

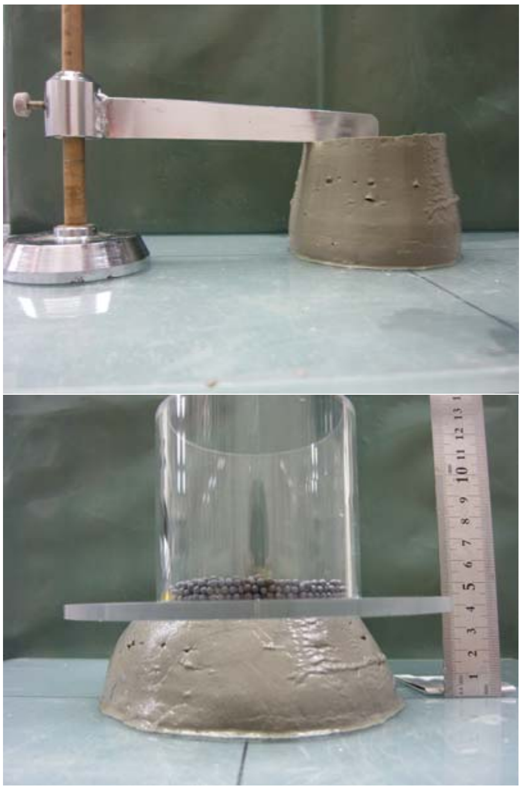

Fig. 9 The conventional slump test and the enhanced test with a burden applied using a specially fabricated cup and small lead balls

Table 2 Results of conventional slump and enhanced slump

Mix. & Time	Conventional		Enhanced	
	Flow (mm)	Slump (mm)	Flow (mm)	Slump (mm)
M1 15 min.	105 x 103 Ave. 104	25	F_b=2.5N 122 x 113 Ave. 118	38
M1 60 min	93 x 91 Ave. 92	16	F_b=4.0N 124 x 121 Ave. 123	40
M2 30 min.	118 x 112 Ave. 115	35	F_b=4.0N 142 x 142 Ave. 142	48
M2 120 min	96 x 97 Ave. 97	18	F_b=4.0N 133 x 131 Ave. 132	43

Note: F_b=2.5 N and 4.0 N corresponds to 498 N/m^2 and 796 N/m^2 against the cross-sectional area of the cylindrical specimen in the initial state.

increase grout deformation. The additional slump caused by a particular burden was measured.

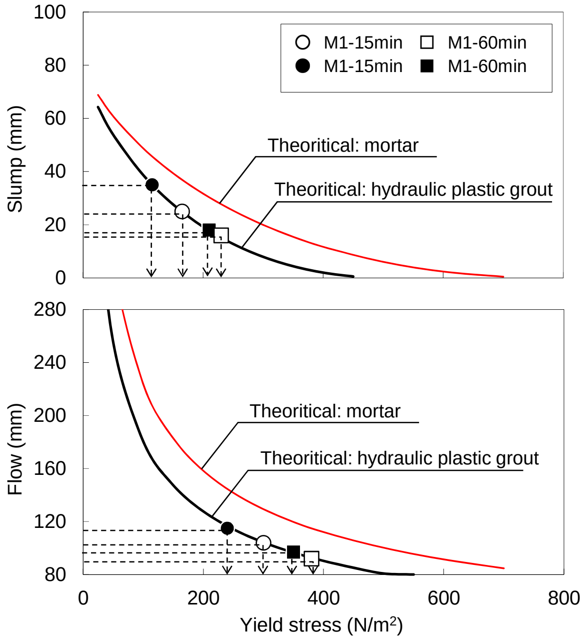

Fig.10 Relationship of yield stress against conventional slump and flow value

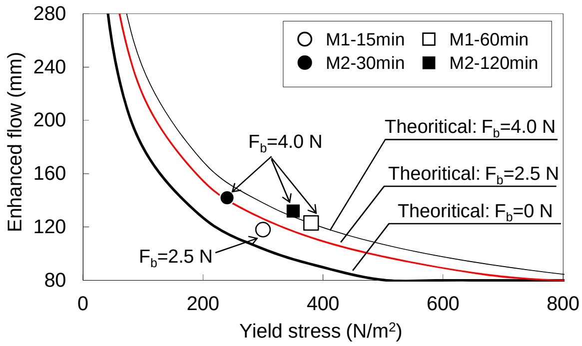

Fig.11 Relationship of yield stress against enhanced flow value

3.4 Results and Discussions

Test results

Figure 9 shows hydraulic plastic grouts undergoing the two forms of slump testing. Under enhanced deformation (lower photo), the grout has expanded in diameter almost linearly from top to bottom. This infers that all of the grout reached yield in respect of the theory given in the section above. Four test results are summarized in Table 2, where a burden of 2.5 N was applied to grout M1 for 15 minutes and a burden of 4.0 N was applied in the remaining cases to M1 for 60 minutes, to M2 for 30 minutes, and to M2 for 120 minutes.

Theoretical calculation for conventional slump

Conventional slump and flow was first calculated theoretically. The results are plotted in a relationship of grout yield stress against slump and flow in Fig. 10. In addition to the results using the actual specific gravity of 1.3, another calculation using a specific gravity of 2.0, corresponding to typical ordinary mortar, is shown for reference purposes in the same figure. It is inferred from this figure that:

- The conventional slump measurement is applicable to hydraulic plastic grout for yield stresses of up to approximately 500 N/m^2. For other cases, no effective deformation occurs and slump and flow values are identified as zero.
- This range of yield stress for the reference results extends to 700 N/m^2 due to the greater shear stresses in the specimen resulting from its higher specific gravity.

This relationship between yield stress and conventional slump and flow value was then used to identify the yield stress of the tested specimen, as indicated in the diagram by the arrows. Clear differences are found between the estimated yield stress values given by the slump and flow values. The reason for this cannot be explained and is to be examined in further work.

Theoretical calculation for enhanced slump

The relationships between yield stress and the enhanced flow value are plotted in Fig. 11 based on the theory described in the section above. One line in the figure represents the result with a burden of zero, which is equivalent to the conventional slump test. The others are results for burdens of 2.5 N and 4.0 N, corresponding to the tests conditions. It can be inferred from this figure that, whereas the conventional slump test is applicable up to a yield stress of 500 N/m^2, this can theoretically be extended to as much as 800 N/m^2 with the enhanced test. The measured flow values summarized in Table 2 are plotted in the same diagram, where the estimated yield stress in Fig. 10 was employed. The plot with F_b = 4.0 N generally matches the calculated results for the corresponding burden. The enhanced flow caused by the F_b = 2.5 N burden lies below this curve, and matches the theoretical results well. This indicates that the diagram can be used just as Fig. 10 was, to evaluate the yield stress from flow values.

Although further verification is preferred though tests on different mixtures of hydraulic plastic grout, this study suggests that the proposed enhanced slump test is an effective way to estimate the viscosity of hydraulic plastic grouts more precisely and over a wider range than the conventional slump test.

4 CONCLUSION AND REMARKS

This paper first summarizes the properties and uses of hydraulic plastic grout, and then proposes an enhanced slump test that provides better estimates for this material, which differs from conventional materials to which slump tests are applied, like mortars and concretes.

Hydraulic plastic grout is a material particularly suited for repair and remediation work. Usage may be expected to increase as the proportion of such types of work increases in comparison to new construction. The authors aim to carry out further studies of this beneficial material, looking into its properties, methods of estimating them, and its site application.

5 REFERENCES

[1] Miki G., Uechi H. and Shimoda, K., “New backfill material and its grouting system,” Journal of the Society of Materials Science, Japan, Vol.31, No.341, 1982, pp.138-143. (in Japanese)

[2] Sakamoto A. et al., “Development and applications of limited area filling techniques for abandoned underground cavities”, Journal of Japanese Society of Civil Engineer, Vol.62, No.3, 2006, pp. 546-557. (in Japanese)

[3] Ingerslev L.C.F.et al., “Marmaray project: requirements for the design and construction of the Bosphorus tunnel,” Proc. of International Tunneling Association (ITA) World Tunnel Congress, Istanbul, 2005, pp. 1269-1275.

[4] Ishii H. et al., “Construction of immersed tunnel foundations using hydraulic plastic grout”, Proc. of 14th Asian Regional Conference on Soil Mechanics and Foundation Engineering, May 2011, CD-ROM.

[5] Murata J., “Flow and deformation of fresh concrete”, Materiaux et Construction, 1984, pp.117-129.

[6] Aaron W. Saak et al., “A generalized approach for the determination of yield stress by slump and slump flow”, Cement and Concrete Research, No.34, 2004, pp.363-371.

[7] S. Clayton et al., “Analysis of the slump test for on-site yield stress measurement of mineral suspensions”, Journal of Mineral Processing, Vol.70, 2003, pp. 3-21.

[8] N. Pashias and D. V. Boger, “A fifty cent rheometer for yield stress measurement”, Journal of Rheology, Vol.40, No.3, 1996, pp. 1179-1189.

[9] W. R. Schowalter and G. Christensen, “Toward a rationalization of the slump test for fresh concrete: Comparisons of calculations and experiments”, Journal of Rheology, Vol. 42, No. 4, 1998, pp. 865-870.

Behavioral Comparison of Coarse Aggregate from Various Quarry Sites of Pakistan, Effect on Hardened Concrete, Economics and Environment

Faisal Malik [1], Dr. S. Muhammad Jamil PhD [2]

[1]Graduate Researcher, School of Civil and Environmental Engineering, National University of Science and Technology, Islamabad, Pakistan.
[2]HOD, Department of Geotechnical Engineering, National University of Science and Technology, Islamabad, Pakistan.

ABSTRACT: Coarse aggregate quarry sites are available in different regions of Pakistan. Lack of geotechnical data of these sites has led to a biased practice of using crushed stone either from "Margallah" or "Sargodha", located in the North of the country. Common practice of using these quarry sites is leading to enormous transportation cost, for projects towards South of the country. This practice adversely affects the project economics. Seven coarse aggregate quarry sites were identified, in various parts of the country. The material from each site was tested for thirteen different tests as per ASTM/BS to include Specific Gravity and Absorption, Shape, Chemical Composition through X-Ray Fluoresce (XRF), Microfines, Characterization of Microfines through X-Ray Diffraction (XRD), Clay lumps and friable Particles in Aggregate, Loss Angeles (LA) Abrasion, Aggregate Crushing Value, Aggregate Impact, Sodium Suphate Soundness and Compressive Strength of Concrete. It revealed that basic constituent of six quarry sites was lime stone (sedimentary rock) against Sargodha quarry site where it is igneous, and show indifference properties. The analysis led to 60% cost effect solution towards the South. The study also generated comprehensive database for the construction industry. Over reliance on existing known sources will be reduced, which is depleting the Magallah hills resulting into big environmental issue.

Keywords: Coarse aggregate, Concrete, Pakistan, Margallah, Quarry sites

1. INTRODUCTION

Since up to approximately 80 percent of the total volume of concrete consists of aggregate, aggregate characteristics significantly affect the performance of fresh and hardened concrete and have an impact on the cost effectiveness of concrete [1]. Relative density is not necessarily related to aggregate behavior. However, it has been found that some aggregates compounds of shale, sandstone, and chert that have somewhat low specific gravity may display poor performance, particularly in exposed concrete in northern climates [2]. Aggregate porosity (absorption) may affect durability as freezing of water in pores in aggregate particles can cause surface popouts [3]. Aggregate characteristics of shape, texture, and grading influence workability, finishability, bleeding, pumpability, and segregation of fresh concrete and affect strength, stiffness, shrinkage, creep, density, permeability, and durability of hardened concrete [4]. Shape is related to three different characteristics: sphericity, form, and roundness [5]. Research shows that there is a clear relationship between shape, texture, and grading of aggregates and the voids content of aggregates [6]. Coatings, the layers of material covering the surface of aggregate, can increase the demand for water and can impair the bond between paste and particles. Sometimes these coatings are formed by materials that can interact chemically with cement, negatively affecting concrete [7]. Soundness, according to Forster [8], is the aggregate resistance to weathering that primarily includes resistance to freezing and thawing, and to a lesser extent, resistance to wetting and drying; and heating and cooling. A sound aggregate has a satisfactory durability factor when used in properly mature concrete with enough air void content [9]. Pakistan has coarse aggregate quarry sites through its length and breadth. However proper developed quarry sites are restricted in Northern or central region of the country which are contributing the construction activities in the country. Detailed characterization of coarse aggregate even for the northern quarry sites is not available. Comprehensive testing mechanism was This study has not only yielded coarse aggregate characterization database as per ASTM/BS but also identified 3 new quarry sites towards the West and South of the country. Identification of three quarry sites has resulted in cheaper coarse aggregate in South of country and lowering reliance on the Northern quarry sites thus slowing environmental issues linked to depleting Northern quarry sites.

2. IDENTIFICATION OF COARSE AGGREGATE QUARRY SITES

Emphasis was laid on identification of new coarse aggregate quarry site towards the South of the country, evaluating its material and engineering properties also drawing comparison with existing quarry sites. The locations of under study coarse aggregate deposits are shown in Fig 1.

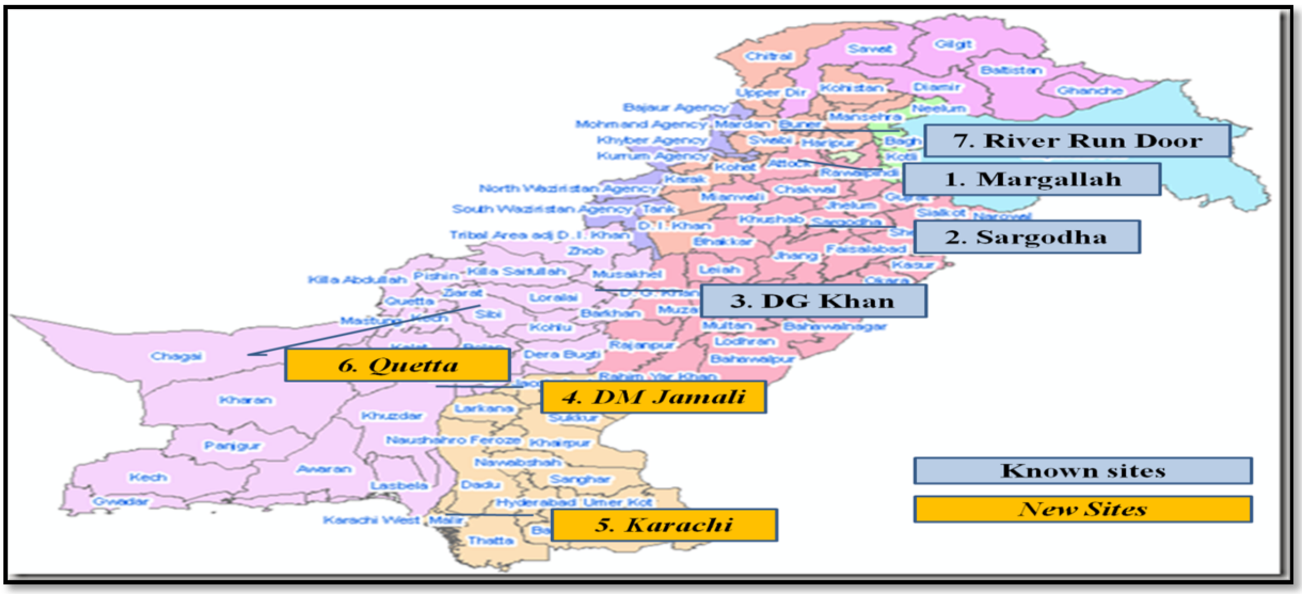

Fig 1. Locations of Under Study Coarse Aggregate Deposits

3. EXPERIMENTAL PROGRAM

3.1 Specific Gravity and Absorption

The test was to ascertain specific gravity and percent absorption to for material characterization. The test was conducted as per ASTM C 127-88[10]. The results are shown in Fig 2.

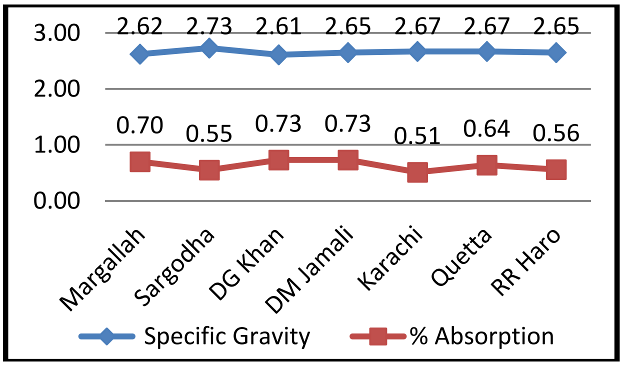

Fig 2. Specific Gravity and Absorption

3.2 Shape

The test was conducted as per BS 812 105.1/2 1998[11]. The results are shown in Fig 3.

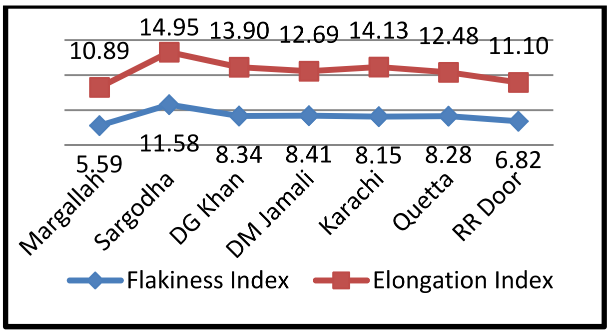

Fig 3. Elongation and Flakiness Index

3.3 Mineral Structure through X ray Florescent (XRF)

The test was selected to indentify basic material constituents of coarse aggregate. It was conducted as per ASTM C 295 [12] and revealed indifference value for six sites indicating lime stone. The results are in Fig 4.

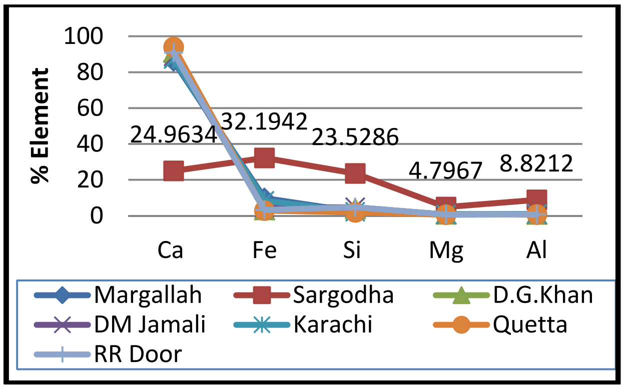

Fig 4. Mineral Structure through XRF

3.4 Percentage of Microfines

The test was conducted as per ASTM C 117-95 [13]. The results are shown in Fig 5.

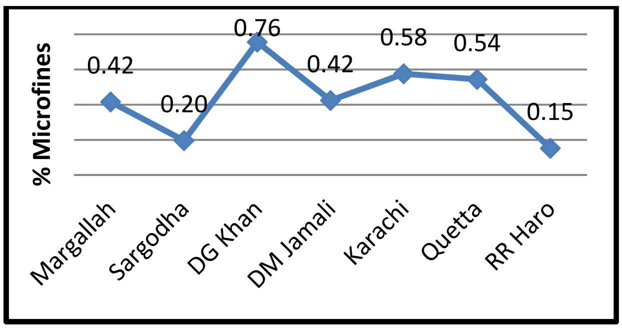

Fig 5. Percentage of Microfines

3.5 Characteristics of Microfines through X-Ray Diffraction (XRD)

The test aimed at microfines characterization to know if any quarry site contain deleterious microfine or otherwise. The results are shown table 1. The tests result of XRD, given in table shows, indifference value for six sites indicating crushed stone dust i.e. no undesired microfines.

Table 1: Characteristics of Microfines

Site	Compound
Margallah	Calcium Carbonate, Ca C O_3, Calcite, syn
Sargodha	Calcium, Ca, beta - phase
DG Khan	Calcium Carbonate, Ca C O_3, Calcite, syn
DM Jamali	Calcium Carbonate, Ca C O_3, Calcite, syn
Nooriabad Karachi	Calcium Carbonate, Ca C O_3, Calcite, syn
Sohrab Quetta	Calcium Carbonate, Ca C O_3, Calcite, syn
RR Doar	Calcium Carbonate, Ca C O_3, Calcite, syn

3.6 Clay Lumps and Friable Particles in Aggregates

The test was selected to know if any deleterious material attached with coarse aggregate from any quarry site, which minute and with the allowable limit of ASTM. The test was conducted as per ASTM C 142-78 [14]. The results are shown in Fig 6.

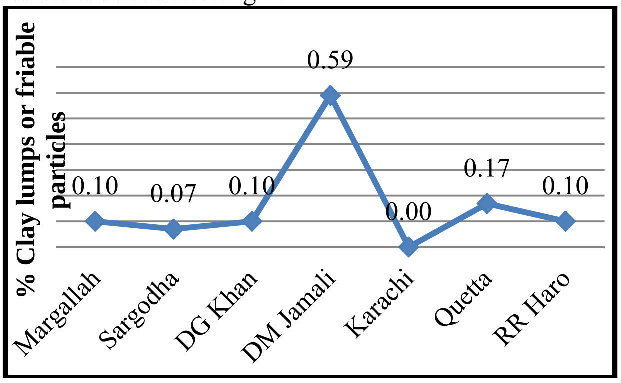

Fig 6. Percentage of Clay Lumps and Friable Particles

3.7 Abrasion and Impact in the LA Machine

The test was aimed at finding the material strength and conducted as per ASTM C 131-96 [15]. The results are shown in Fig 7.

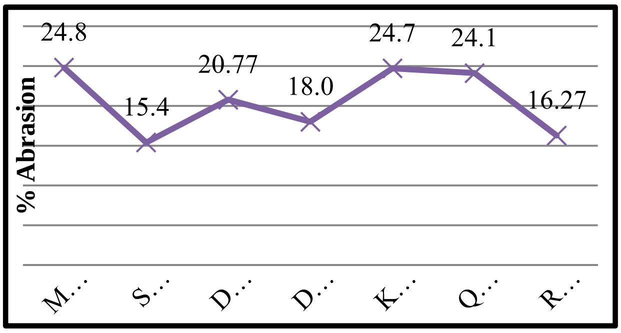

Fig 7. Abrasion & Impact in LA Machine

3.8 Aggregate Crushing Value (ACV)

The test was aimed at identifying material behavior against external forces. The test was conducted as per BS 812-110 [16]. The results are shown in Fig 8.

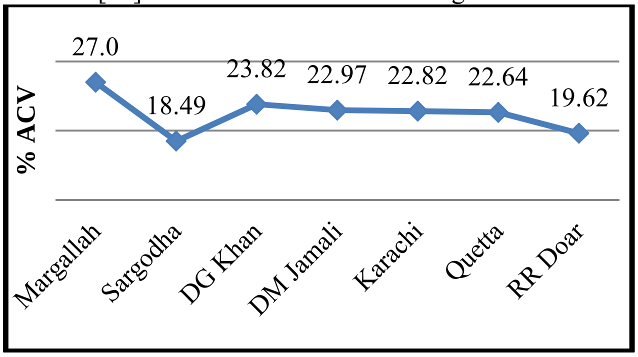

Fig 8. Aggregate Crushing Value (ACV)

3.9 Aggregate Impact Value (AIV)

The test was aimed at identifying material behavior against impact. The test was conducted as per BS 812-112 [17]. The results are shown in Fig 9.

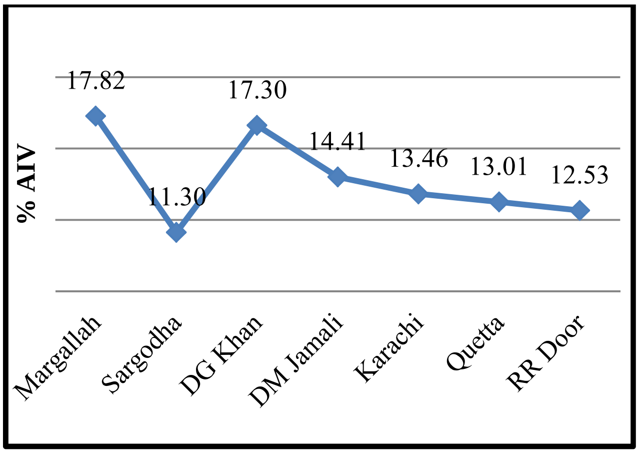

Fig 9. Aggregate Impact Value (AIV)

3.9 Soundness of Aggregate by Use of Sodium Sulphate

The test was aimed to find the material strength against chemical reaction. The test was conducted as per ASTM C 88-90 [18]. The results are shown in Fig 10.

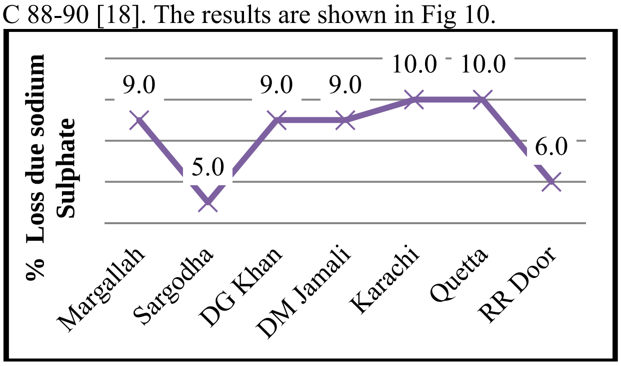

Fig 10. Soundness of Aggregate by Use of Sodium Sulphate

3.10 Compressive Strength of Concrete

The concrete mixes were prepared using coarse aggregate from seven different sources and remaining variables as constant with the cement: sand: coarse aggregate ratio of 1: 2: 4 (by weight) respectively, cement content (201.7 kg/cum) and water cement ratio of 0.5. The course and fine aggregates were used in SSD condition. The fine aggregate used was taken from lawncepur quarry located in the Northern region. The cement used was Fauji cement (type 1, Portland cement). The water used was normal tap water without any undesired colour. The test was conducted as per ASTM C 39-96 [19]. The results are shown in Fig 11.

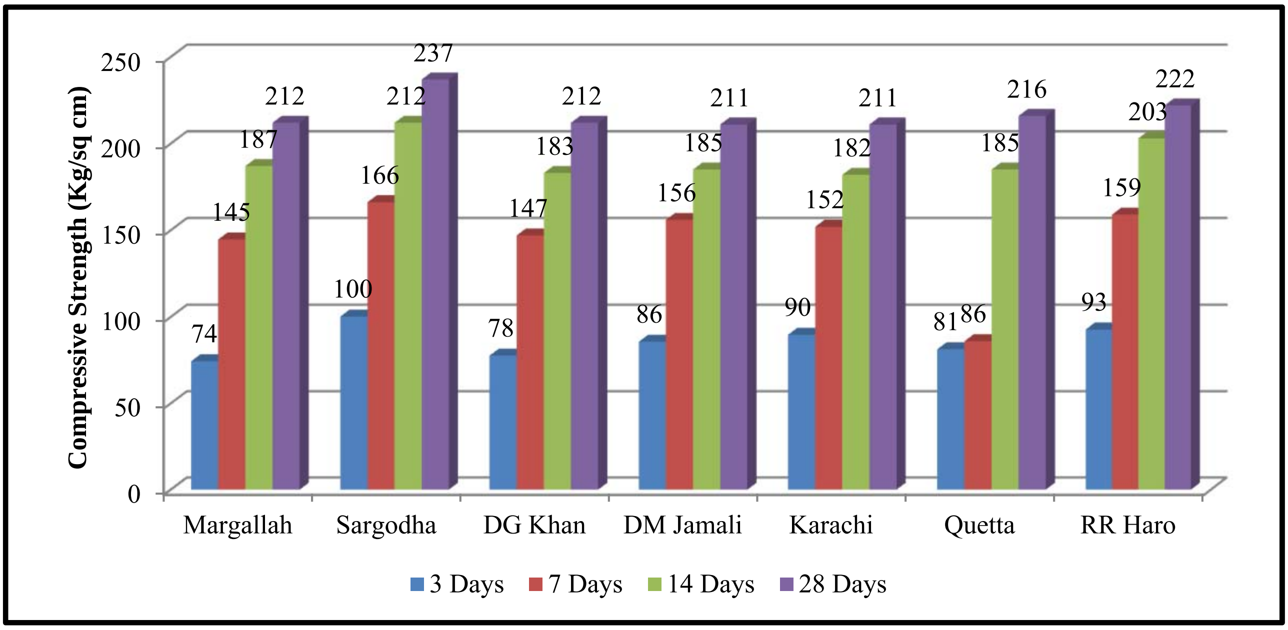

Fig 11. Compressive Strength of Concrete

4. TEST RESULTS AND DISCUSSIONS

4.1 Petrographic Analysis

The test led to conclusion, that out of seven coarse aggregate quarry sites, six i.e. (Maragllah, DG Khan, DM Jamali, Nooriabad Karaachi, Quetta and River Run River Doar Abbottabad), limestone as basic rock constituents and the seventh site (Sargodha) has Basalt as basic rock. Both rock types exhibit satisfactory material, engineering behavior, thus can be used for construction purposes.

4.2 Basic Material Characteristics

Test results of specific gravity, absorption, microfines and clay lumps support each other, and follow laid down limits. It also indicate, specific gravity as basic property if an aggregate has higher values for it (within allowable limits), the aggregate behavior will be better.

4.3 Material Strength Characteristics

Results of Loss Angeles abrasion test, Aggregate Crushing Value and Aggregate Impact Value tests follow same trend and support one another results, indicating sufficient physical strength for aggregates under consideration. Depending upon project importance, any one of three test may be conducted that will lead to strength parameters.

4.4 Concrete Compressive Strength

Compressive strength of concrete based on the aggregate from quarry sites also indicates that the strength and behavior is quite satisfactory.

4.5 The Result

Series of test result show that three minimal exploited site towards the west of country can be used with significant degree of confidence in construction industry, reducing dependence on depleting coarse aggregate source.

5. ECONOMICAL IMPACT

5.1 Demand and Supply

Pakistan is self-sufficient in primary aggregates and there are significant regional imbalances in consumption, which require balance in inter-Pakistan movements of aggregates. Present reliance/share of aggregate quarry sites is given Fig 1. Consequently there is substantial and increasing movement of aggregate in the Pakistan straining the economy and raising construction cost.

5.2 Haulage vs. Cost

Transporting aggregates, and the effects of aggregates transport, aggregate products are generally used with hundreds of kilometers in Pakistan as compared to UK where it is within a thirty-mile radius of the quarry from which they have been extracted. One clear example of haulage is from D.G Khan to interior/South Sind, involving one way distance of 400 - 800 kms with approximate haulage cost of Rs (6000 – 18000)/400 cft. Cost Effect is reflected in table 2.

Table 2. Cost Effect of Transportation

Region of Use	Material Cost of Crush (Rs/Cum)	Transportation Cost (Rs/Cum)	Total Cost of Crush (Rs/Cum)
DG Khan	420	470	890
Sukhur	420	1325	1745
Hyderabad	420	1782	2202

5.3 Cost Effectiveness

Coarse aggregate cost comparison from the existing arrangement to the proposed arrangement is upto 60% cost effective. Comparison is given in table 3.

Table 3. Cost Effectiveness as result of study

Region/place of Use	Cost of Local Crush (Rs/Cum)	Cost of DG Khan Crush (Rs/cum)	%age Decrease
Sukhur	890 (DM Jamali)	1745	49 %
Hyderabad	890 (Nooriabad)	2202	60 %

5.3 Recommended Regions of Supply

The experimental study of the sites towards the south of Pakistan has revealed that there is no significant difference in crush from Margallah / Sargodha / DG Khan and Nooriabad Karachi / DM Jamali / Quetta. Based on study three new quarry sites were indentified with acceptable range of material properties. Hence coarse aggregate from the later sites can be used with same confidence for engineering purposes. Therefore redistribution of supply regions recommended specially effecting towards the South of the country. This will also reduce the project cost considerably. New suggested areas of coarse aggregate supply from particular quarry site are given in Fig 12.

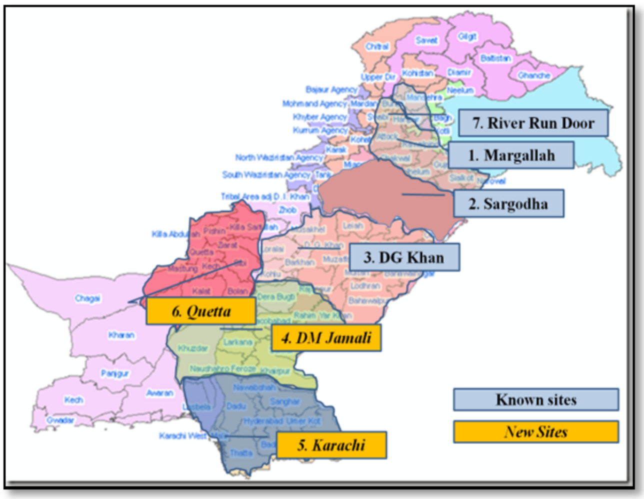

Fig 12. Recommended Regions of Supply

5.4 Benefits Visualized

- Reduction in cost of construction by minimizing the transportation cost of crush.
- Minimizing the dependence of construction projects on a specific source of crush.
- Development of local economy.
- Indirect Cost savings from vehicle/roads wear and tear.

6. ENVIRONMENTAL ISSUE

6.1 The Issue

Margallah hills coarse aggregate quarry site mainly comprises of sandstone and shale, which is very suitable for construction of building and bridges. It is the main supplier of limestone for the construction, and well known/exploited in construction industry. Over reliance on one quarry site for coarse aggregate is/will lead to environmental issue. Margallah is point incase. The issue is due to effects of Mining and crushing Margallah hills. That is why the beautiful Margallah hills are being eaten away causing large scale environmental degradation and air pollution. Based on the interpretation of the aerial photographs and studying other relevant data, it can be concluded that if the present quarrying remain continue, very soon the western side of the Margalla hills will be diminishes [20].

6.2 Envisaged effect of study to the issue

The study led to identification of three new sources of coarse aggregate towards the South of country. As and when these sources are exploited, the trickledown effect will relieve Margallah, Sargodha and DG Khan, from ever increasing mining activity. Probability study indicates that 20-30% decrease in demand from Margallah, Sargodha and DG Khan, resultantly the decreased mining activity. Although additional measure will be required to avoid the environmental damage, yet this study will help in delaying the issue.

7 CONCLUDING REMARKS

Based on laboratory investigations and data analysis, following conclusions are drawn:

- Total seven coarse aggregate sites were selected for aggregate characterization, to include Maragllah, Sargodha, DG Khan, and River Run River Doar Abbottabad towards the north and center while DM Jamali, Nooriabad Karachi, and Quetta were selected towards south of Pakistan. This will allow development of three new coarse aggregate quarry sites towards South of the country.
- Aggregate characterization procedure devised/adopted has given details of physical, engineering and petrographic properties of coarse aggregate thus all inclusive database has been created.
- Out of seven coarse aggregate quarry sites, six i.e. (Maragllah, DG Khan, DM Jamali, Nooriabad Karaachi, Quetta and River Run River Doar Abbottabad), limestone as basic rock constituents and the seventh site (Sargodha) has Basalt as basic rock. Both rock types exhibit satisfactory material, engineering behavior, thus can be used for construction purposes.
- Coarse aggregate cost comparison from the existing arrangement to the proposed arrangement is upto 60% cost effective.
- Exploiting new sources in the light of study will result, 20-30% decrease in demand from Margallah, Sargodha and DG Khan, resultantly the decreased mining activity – environmental hazard.

REFERENCES

[1] Hudson, B. “Modification to the Fine Aggregate Angularity Test,” Proceedings, Seventh Annual International Center for Aggregates Research Symposium, Austin, TX, 1999.

[2] Legg, F.E. Jr., Aggregates, Chapter 2, Concrete Construction Handbook, ed. Dobrowolski, J. McGraw-Hill, 1998

[3] Helmuth, R.A., “The Nature of Concrete,” ASTM Special Technical Publication No. 169C, Philadelphia, 1994

[4] Lafrenz, J.L., “Aggregate Grading Control for PCC Pavements: Improving Constructability of Concrete Pavements by Assuring Consistency of Mixes,” Proceedings, Fifth Annual International Center for Aggregates Research Symposium, Austin, Texas, 1997.

[5] Galloway, J. E. Jr., “Grading, Shape, and Surface Properties,” ASTM Special Technical Publication No. 169C, Philadelphia, 1994, pp. 401-410.

[6] De Larrard, F., “Concrete Mixture Proportioning: A Scientific Approach,” London, 1999.

[7] Mather, B., “Shape, Surface Texture, and Coatings,” ASTM Special Technical Publication No. 169A, Philadelphia, 1966

[8] Forster, S.W., “Soundness, Deleterious Substances, and Coatings,” ASTM Special Technical Publication No. 169C, Philadelphia, 1994.

[9] Mather, B., “Durability: Freezing and Thawing,” Proceedings, Seventh Annual International Center for Aggregates Research Symposium, Austin, Texas, 1999.

[10] ASTM C 29 Test Method for Bulk Density (“Unit Weight”) and Voids in ggregate, Philadelphia, PA: American Society for Testing and Materials, 1997.

[11] British Standards Institution, “Methods for determination of particle shape," BS-812-105: Part 1 and 2, 1989

[12] ASTM C 295, Standard Guide for Petrographic Examination of Aggregates for Concrete, Philadelphia, PA: American Society for Testing and Materials, 2003

[13] ASTM C 117, Standard Test Method for Materials Finer than 75 µm (No. 200) Sieve in Mineral Aggregates by Washing, Philadelphia, PA: American Society for Testing and Materials, 1995.

[14] ASTM C 142-78, Standard Test Method for clay lumps and friable particles in aggregate, Philadelphia, PA: American Society for Testing and Materials, 1984

[15] ASTM C 131-96, Standard Test Method for degradation of small size coarse aggregate, by abrasion and impact in the Loss Angelus Machine, Philadelphia, PA: American Society for Testing and Materials, 1984

[16] British Standards Institution, “Methods for determination of aggregate crushing value (ACV)," BS-812-110, 1990.

[17] British Standards Institution, “Methods for determination of aggregate impact value (AIV)," BS-812-112, 1990

[18] ASTM C-88-90, Standard test method for soundness of aggregate by use of sodium sulphate or magnesium sulphate, Philadelphia, PA: American Society for Testing and Materials, 1990.

[19] ASTM C-39-96, Standard test method for compressive strength of cylindrical concrete specimen, Philadelphia, PA: American Society for Testing and Materials, 1996.

[20] The Effect of Mining on Geomorphology (Detection of Changes by Using Remote Sensing Techniques) by: Falak Nawaz

First International Conference on Geotechnique, Construction Materials and Environment, Mie, Japan, Nov.21-23, 2011, ISBN: Article Number 148

Methods for execution of concrete piles in corrosive and destructive marine environments, based on study of the Persian Gulf marine installations

Nasser Arafati[A]. Abdol Hossein Fazli[b]. Seyed Mehdi Mousavi[c]. Department of civil engineering, Tafresh University, Tafresh, Iran

A: Associate professor. b&c: Research Student

ABSTRACT: Marine environments include ions and corrosive gases and are the place of marine living things, which are harmful for construction materials. Hydrostatic pressures and high temperature changes, which are current in most of the coastal areas and marine structures, are able to accelerate destruction of construction materials. Marine structures and port installations existing in ports are considered as important infrastructural installations that due to their concrete or metal nature are exposed to decay and destruction arising from being in marine environments. Concrete piles, which are executed in sea beds or in coasts, are affected by corrosive factors and the factors decreasing stability. Therefore methods and materials should be used to confront these factors. Undoubtedly Persian Gulf is one of the most corrosive and risky environments of the world for execution of concrete structures and concrete piles.

This research tries to investigate the optimum methods for execution of concrete piles and also concrete technology of these piles in Persian Gulf in details. In order to access this aim the geotechnical experiences of the piles and foundations executed in Persian Gulf were used and finally some proposals for execution of such structures in destructive environments without any problem were offered.

Keywords: marine environment, displacement concrete piles, Persian Gulf, pile concrete technology, driven piles, Concrete Materials

1. INTRODUCTION

Generally, ease of use of driven piles in marine environments caused their more extensive application as compared with drilled shafts. Using driven piles in marine environments was started since Neolithic times. The first residents of the globe used to utilize such piles for construction of their houses on water in flood plains and different types of bridges on rivers.
For execution of driven piles different methods have been used since that time up to now [1]. In the past very simple and time-consuming methods and equipment were used but nowadays precise and very quick and modern methods and equipment are employed.
Modern equipment can be employed by contractors to ensure safe, quick and adequate installation of driven pipes. Global Positioning Systems (GPS) aid in survey and accurate layout of pile locations. New hammers are capable of energy adjustments and monitoring to provide the required hammer performance while protecting the piles from damage. Instruments can be used during testing and installation to confirm the design and pile load capabilities.
In addition to the problems related to common piles, piles problems in marine environments include the problems arising from the corrosive water environment. Some of these problems are:
Liquefaction of saturated sands during pile installation, settlement around piles, heave, buoyancy and hydrostatic pressure [1],[2].
One of the most important problems we encounter in marine environments is splash zone effect and a more important problem is the severe corrosive effect of some of the marine environments on piles.
At present one of the most corrosive marine environments of the world is Persian Gulf in the south of Iran. Because of the abundant amount of salts and ions existing in this environment, concrete piles are under severe decay and destruction.
Very corrosive climatic conditions, insufficient knowledge of the executive personnel, weakness in construction stages, application of improper and low quality materials, etc. are some of the factors of different types of destruction of concrete structures in Persian Gulf marine environments.
Current regulations of concrete production and piles execution, which have been considered for execution in the other points of the world, are not suitable for such an environment and create a lot of problems. There are a lot of samples of problems occurred in such structures in 1990s.

1.1 general descriptions of exposure conditions

Persian Gulf is one of the most corrosive and aggressive environments for concrete structures particularly concrete piles; drilled piles and driven piles. As it is shown in "Table.1" In comparison with other seas in the world, Persian Gulf has more chloride ions than others. This content surely increases durability risk in these environments, also jeopardize reinforcements to corrosion. Temperature difference between night and day is about 25-35 centigrade,"Fig.1" and humidity difference is high too,"Fig.2". [3, 4]
Thus executing method and concrete technology of piles and other concrete structures is unique in this Gulf.

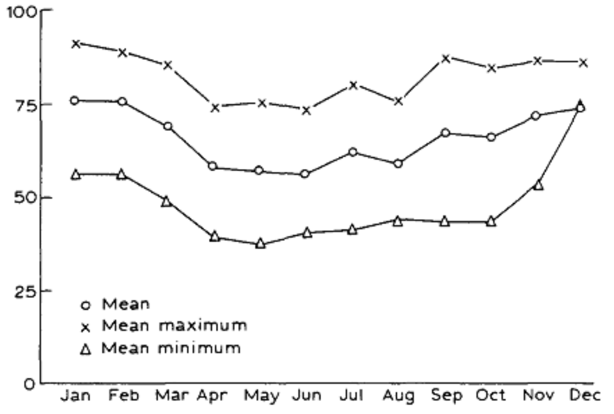

Fig.1.Montly relative Humidity averages

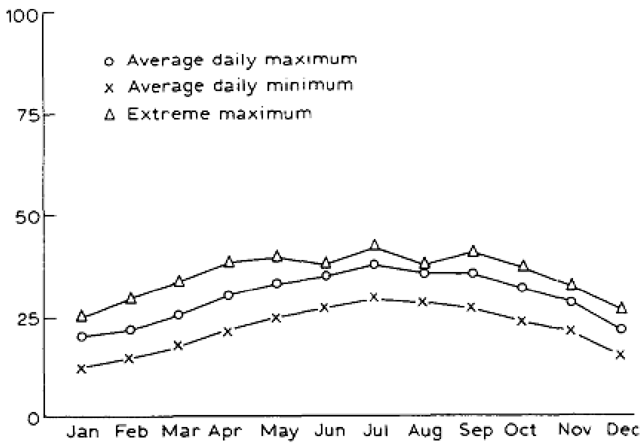

Fig.2.Montly Temperature

ions	Baltic sea	Atlantic sea	North sea	Mediterranean sea	Persian Gulf
K++	180	430	400	420	450
Ca++	190	410	430	470	430
Mg++	600	1500	1330	1780	1460
So4-	1250	2540	2780	3060	2720
Na+	4980	9950	11050	11560	12400
Cl-	8960	17830	19890	21380	21450
Salt Content	16200	32600	35900	38700	38900

Table 1: ions content in world seas.

1.2 Pile selection:

Due to high corrosion risk for steel piles, pre stressed or pre tensioned concrete piles are recommended for this environments [5]

Quality control, efficient increased strength and durability, sufficient curing, manufacturing precision are advantages of pre stressed and pre tensioned driven piles in comparison with drilled piles in these environments.

Table 2: ions content in world seas.

2. Backgrounds

Reinforcement's corrosion is usually most considerable issue in deteriorated marine concrete structures, induced chloride ion affects on durability of concrete structures in severe exposures. Chloride ions which penetrate through cracks or voids or diffusion through matrix cause to onset of pitting corrosion when their concentration at the steel surface exceeds a critical threshold value. This threshold depends on several factors, such as pH of concrete, steel potential and presence of micro voids in the cement paste [6, 7, 8, and 9]. One procedure to prevent or delay the corrosion is covering piles with epoxy resins [10], since piles are more risky in tidal/splash zones, epoxy resins can protect piles from connection between seawater and concrete layer.
Another way is providing cathodic prevention by means of sacrificial anodes [6],[11]. Often cathodic protection cost is higher than strengthed concrete which has optimum strength and durability, so high cost of this method is one of the disadvantages of this method. Contractors prefer to increase material quality and quality control instead of using cathodic protection.
Chloride ions influx through cracks that exist on concrete cover of piles. After considerable time, corrosion starts when ions connected to reinforcements, thus preventing penetration of chloride ions is important step in piles and marine concrete structures. In addition chloride penetration increases voids [18] thus deterioration risk arises consequently.

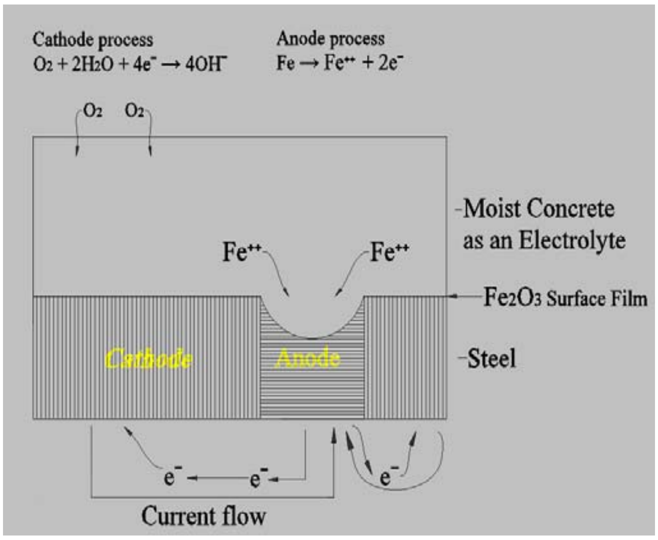

Fig 3

Fig.3, *"illustrate the electrochemical process of steel corrosion in moist and permeable concrete .The galvanic cell constitutes an anode process and a cathode process. The anode process cannot occur until the protective or the passive iron oxide film is either removed in an acidic environment (e.g., carbonation of concrete) or made permeable by the action of CL- ions. The cathodic process cannot occur until a sufficient supply of oxygen and water is available at steel surface. The electrical resistivity of concrete is also in the presence of moisture and salt*", Mehta et al [11]

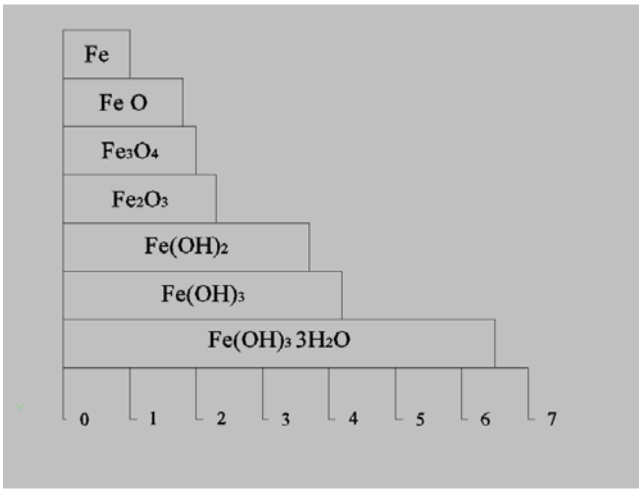

Fig.4

Fig.4, "*shows that depending on the oxidation state, the corrosion of metallic iron can result in up to six times increase in the solid volume"*, Mehta et al [11]

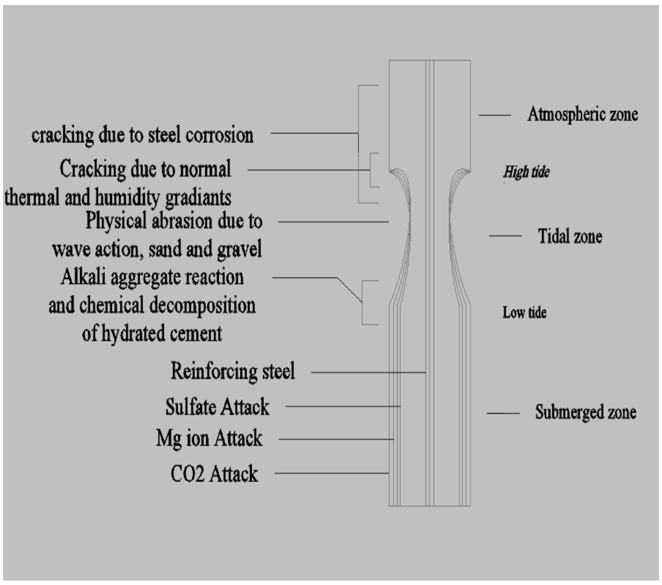

Fig. 5

Fig.5: Diagrammatic representation of reinforced concrete cylinder exposed to seawater (From Mehta, P.P., *Performance of Concrete in Marine Environment*, ACI SP-65, pp.1_20, 1980) [23].

"*The type and severity of attack on a concrete sea structure depends on the conditions of exposure. The sections of structure that remain fully submerged are rarely subjected to frost action or corrosion of embedded steel. Concrete at this exposure condition will be susceptible to chemical attacks. The selection above the high-tide mark will be vulnerable to both frost action and corrosion of the embedded steel. The most severe deterioration is likely to take place in the tidal zone because here the structure is exposed to all kinds of physical and chemical attacks" Mehta et al* [11].

3. Materials

3.1 Cement and replacements

There was a view that cements type (V) is suitable and also more durable than type(I) ,(II).but experiences in concrete structures and concrete piles in Persian Gulf shows that structures which are made of cement type (V) has more deterioration than structures which are made of cement type (I),(II) [1].Also M. Naderi showed that concrete prisms which contains cement type(I) has more chloride penetration resistance than concrete prism which contains cement type (II) [10]. Using type (V) reduces durability of concrete considerably. Moreover references [13],[14] prove this claim that replacing fly ash by 15% cement content increase strength and durability of concrete structures and moreover it is proven that it can increase initiation time to corrosion,15% fly ash and w/b=0.4 can delay corrosion initiation until 60 years [15].

As reference [16] shows, replacing calcium chloride by 2-4% cement content , that is used as setting accelerator was recognized as a corrosion cause in pre stressed tendons. So it is prohibited to replacing calcium chloride as cement replacement or hardening accelerator.

Although voids and entrained air can increase permeability and consequently decrease durability but according Haynes, H. H, air entrain by 2-6 % doesn't increase permeability[15], and it is recommended for concrete piles in Persian Gulf. It can reduce cracks which are caused by temperature gradients and also it can increase workability and slump (consequently it will be easier to compacting and casting successfully).

According to A.Shayan experiments, replacing Glass powder as a pozzolanic material reduces chloride ion penetration [19] utilization this material in concrete is highly recommended in casting marine piles and marine structures.

Coastal concrete structures in Netherland that made by cements with blast furnace slag showed no corrosion after 30 years. Although it is possible that corrosion initiated after 20 years but no corrosion detected in 88% of 64 structures [21]

3.2 Aggregate

Aggregates contain 60-80 % concrete volume and are considered as inactive material in concrete structures but it is not allowed to neglect effect of aggregate types on marine structures especially which are in severe exposure and aggressive environments. Aggregates are cause of abnormal dimensional stability and durability depletion.

A.Shayan experiments, which is a comparison between non-reactive, slowly reactive, highly reactive behavior in seawater proves this claim that it is not allowed to utilize highly reactive aggregates and it is suggested not to use slowly reactive aggregates in high temperature [20].Expansion of highly reactive is recognized as deterioration cause in marine concrete structures in south of Iran and Persian Gulf shores.

Limestone and non-reactive dolomite aggregates or sufficiently high level of other forms of carbonate calcium have desirable corrosion properties R.E.Melchers *et al* [10]. Limestone favorable corrosion properties can observe in Escambia Bay Bridge, piles in tidal zones didn't have any significant corrosion after 30 years [20].

It is highly recommended to rinse aggregate before use. It lets concrete to reduce alkalinity and consequently reduce expansion of pile thus it will be easier to reduce surface cracks.

3.3 Water Quality

Due to delicacy of piles, it is not allowed to use sea water for producing concrete, although concrete prism which is made by sea water can reach up to 90% of compression strength of ordinary water (edible), but it isn't recommended to use seawater or any salty water.

4. Execution and design notice

Reducing w/b is the most important element to have durable, strengthen, corrosion protected, and any other desirable issues. As Woosuk [15] showed, lowering w/b about 0.05 is more effective than 13mm (1/2 inch) increment of cover thickness. It means that the piles with 51mm(2inch)clear cover and w/b=0.35 act better than the piles with 76mm(3inch) cover and w/b=0.4 .In marine splash/tidal exposures, Woosuk et al [15], showed that service life of piles with w/b=0.3 concrete mixture and 51mm (2 inch) clear cover is more than 100 years.

Thermal gradient during steam curing, transporting by inexperienced performers, using improper driving hammer, inadequate driving, should be controlled by executors to prevent premature cracks.

Protecting pile by covering epoxy resin that is a method to prevent of corrosion needs highly experienced workers to isolate piles completely from moisture.

5. Conclusion

As it was observed, with due attention to the very especial conditions of the Persian Gulf with a view to both very corrosive environment and abundant number of coastal constructions it was tried to present the best method for piles selection and execution with use of the most recent researches and executed samples. In brief the results were as follows:

-Use of pre-stressed or pre-tensioned driven piles
-Covering piles with epoxy resins for splash zones
-Using cement type (1) or (2)
-Replacing fly ash by 15% cement or even higher
-Not using calcium chloride
-Aid entrain by 2-6%
-Using glass powder as a pozzolanic material
-Using non-reactive aggregates
-Using limestone and non-reactive dolomite aggregates of carbonate calcium
-Rinsing aggregate before use
-Not using marine water for concrete production
-Reducing w/b
-Employment of experienced and trained personnel

Using the above-mentioned method causes much increase in life of the piles executed in the Persian Gulf environment, in such a way that with execution of these methods corrosion is started much later. In such conditions we can make sure of the confident performance of the executed structure during its lifetime.

In addition to increment of piles execution quality, another preference of execution of the above-mentioned methods is economizing of construction and execution activities of such resistant to corrosion piles, which is another positive factor for encouragement of contractors for execution of these methods.

6. References

[1]Foundatioun Engineering:In the wet design and counstruction of civil works projects,U.S Army corps of engineers,No:1110-2-565

[2] R.J Jardine, Review of technical issues relating to foundations and geotechnics for offshore installations in the UKCS, First published 2009,Imperial college London

[3] Concrete in Hot countries, office of the deputy for technical affairs bureau of technical affairs and standards, No: 184

[4] A.R. A1-Rabiah, Rasheeduzzafar, Roger Baggott, Durability Requirements for Reinforced Concrete
Construction in Aggressive Marine Environments, *Marine Structures* 3 (1990) 285-300

[5] Joseph e. Bowles, Foundation analysis and design, fifth edition, Mc-Graw hill

[6] Luca Bertolini, Elena Redaelli, Throwing power of cathodic prevention applied by means of sacrificial Anodes to partially submerged marine reinforced concrete piles:
Results of numerical simulations

[7] L. Bertolini, B. Elsener, P. Pedeferri, R. Polder, Corrosion of Steel in Concrete.
Prevention, Diagnosis, Repair , Wiley-VCH, Weinheim, 2004.

[8] C.L. Page, Corrosion and protection of reinforcing steel in concrete, in: C.L.
Page, M.M. Page (Eds.), Durability of Concrete and Cement Composites, Woodhead Publishing Ltd., Cambridge, 2007, pp. 156–186.

[9] A. Bentur, S. Diamond, N. Berke, Steel Corrosion in Concrete: Fundamental and Civil
Engineering Practice, E&FN Spon, London, 1997.

[10] R.E. Melchers, C.Q. Li , Reinforcement corrosion initiation and activation times in concrete structures exposed to severe marine environments, Cement and Concrete Research

[11] p.k.mehta,p.j.m.monteiro, concrete microstructure, prosperities and material, chapter5

[12] M. Naderi and S. A. K. Mousavi, Investigation of Some Properties and Durability of Concrete in the Urumie Lake.
[13] K. Lau, A.A. Sagues, L. Yao, R.G. Powers, Corrosion performance of concrete cylinder piles, Corrosion 63 (4) (2007) 366–378.
[14] A.A. Sagues,Modeling the effects of corrosion on the lifetime of extended reinforced concrete structures, Corrosion 59 (10) (2003) 854–866.
[15] Woosuk Ahn, Darrell Joque, and Amfinn Rusten , A Study on Corrosion Resistance of Prestressed Marine Concrete Piles, corrosion 2003,page nomber03239
[16] Building research establishments news, Her Majesty's Stationanery Office, London, Winter 1979
[17] Haynes, H. H., "Permeability of Concrete in Sea Water" Performance of Concrete in Marine Environment, ACI SP-65, edited by Malhotra, V. M., ACI, Detroit, MI, August 1980, pp. 22-38.
[18] C. Ftikos, G. Parissakis, A study on the effect of some ions contained in seawater on hydrated cement compounds, in: J.M. Scanlon (Ed.), Katharine and Bryant Mather International Conference on Concrete Durability, American Concrete Institute,1987, pp. 1651–1665, S P (100).
[19] Ahmad Shayan, Aimin Xu, Performance of glass powder as a pozzolanic material in concrete: A field trial on concrete slabs, Cement and Concrete Research 36 (2006) 457–468 December 2005
[20] A. Shayan ,A. Xu, G. Chirgwin, H. Morris, Effects of seawater on AAR expansion of concrete, Cement and Concrete Research, 40 (2010) 563–568
[21] J.G. Wiebenga, Durability of concrete structures along the North Sea coast of the Netherlands, American Concrete Institute SP65 (1980) 437–452.
[22] A.A. Sagues,Modeling the effects of corrosion on the lifetime of extended reinforced concrete structures, Corrosion 59 (10) (2003) 854–866.
[23] Mehta,P.P. , Performance of Concrete in Marine Environment, ACI SP-65,pp.1_20,1980

First International Conference on Geotechnique, Construction Materials and Environment, Mie, Japan, Nov.21-23, 2011, ISBN: 978-4-9905958-0-7 C3051

Fundamental Study on Particle Size Distribution of Coarse Materials by Image Analysis

G.H.A.J.J. Kumara, K. Hayano and K. Ogiwara, Department of Civil Engineering, Yokohama National University, Japan

ABSTRACT: Particle size distribution of materials is usually evaluated by sieve analysis tests. In this research, an image analysis technique using ImageJ is proposed to evaluate particle size distribution of coarse material. On particular conditions, some difference of particle gradation curves determined by sieve analysis and image analysis were observed. Based on the results, several aspects related to image analyzing are discussed in this paper. They include appropriate evaluation of particle diameter in image analysis, minimization of shadow effects appeared in image, effects of number of particles adopted for sieve analysis and image analysis and so on.

Keywords: coarse materials, ImageJ, image analysis, particle size distribution, sieve analysis

1. INTRODUCTION

Characterization of quality of materials is important to ensure good use of resources from environmental and economic perspectives. Particle size distribution of materials is one of the widely used tests in geotechnical engineering to evaluate quality of materials. Sieve analysis test has been the main method to determine particle size distribution of coarse materials for many decades. However, recently, some researchers including Fernlund (1998) [1], Mora et al. (1998) [2], Kwan et al. (1999) [3], Banta et al. (2003) [4], Fernlund (2005a) [5] and Fernlund (2005b) [6] used some image analyzing techniques to evaluate particle shape characteristics including particle size distribution.

In general, image analysis uses 2-D images. Banta et al. (2003) [4] studied particle gradation curves by 2-D images of 4.75-25mm size limestone and found that image analysis gave good results. However, mass of individual particles were measured using a balance to compare gradation curves by two methods. It was a time consuming process since the mass of individual particles were measured. Kwan et al. (1999) [3] used 2-D images of coarse aggregates to study particle shape characteristics. However, rather than gradation curves, particle shape characteristics like flakiness and elongation of aggregates were discussed. Fernlund (1998) [1] studied particle form on sieve analysis with 32-64mm size railroad aggregates using 2-D images. Moreover, the difference of gradation curves determined by mass and no. of particles in hand sieve analysis tests were also studied and found that gradation curve determined by no. of particles underestimate that of by mass.

Mora et al. (1998) [2] compared gradation curves determined by image analysis method and sieve analysis test using 2-D images. However, rather than using area of particles measured directly from 2-D images, mass of particles were evaluated from 2-D images with some assumptions. The gradation curve overestimated gradation curve determined by sieve analysis test. Therefore, a size correction factor was assigned to get same gradation curves as that of by sieve analysis test. Therefore, it is not clear whether the assumptions in evaluating mass affected the difference or image analysis had some effects on gradation curves.

On the other hand, Fernlund (2005a) [5] measured all three axes of particles of 10-50mm size granite while manually changing positions of particles. 2-D images of same particles were taken twice to measure three axes. Gradation curve determined by image analysis were compared with that obtained by Danish Box. The results showed that 2-D images when particles placed on the most stable location gave good results. However, it was a time consuming process due to the fact that location of particles had to be changed twice to obtain images to measure all three axes.

As mentioned in literature, usually, gradation curves were determined based on mass by image analysis techniques than using direct measurement of area of particles measured from 2-D images. However, mass (or volume) cannot be measured directly from 2-D images. Moreover, it was seen that image analysis using direct measurement of area of particles gave different results than sieve analysis. The difference of results would have been due to several issues such as evaluation of particle diameter, shadow effects appeared in image, effects of difference of number of particles between sieve analysis and image analysis and so on. However, they have not been fully understood. Therefore, during this research, issues mentioned here were examined using an image analysis technique named ImageJ.

During this research, it was discussed how area of particles can be used to obtain gradation curves of coarse materials varying from 2-19mm size as well as how no. of particles or random selection of particles from the main sample affect gradation curve.

2. METHODOLOGY

Gravels ranging from 2-19mm were used for the experiments. They are Andesite, originally produced in Yamanashi prefecture in Japan.

2.1 Sieve analysis

Sieve analysis test was done according to JIS A 1204 [7]. JIS requirement for the materials used is 1.5kg. However, to obtain high accuracy for gradation curve, additional sieves such as 6.7, 11.2 and 13.2mm were added in addition to 2, 4.75, 9.5 and 19mm sieves required by JIS method. Moreover, sieve analysis test were conducted with hand shaking.

2.2 Image capturing process

Particles were arranged manually such a way that particles stand on their most stable positions. However, particles were arranged without touching or overlapping to obtain good quality images.

Particles were placed on transparent sheet during initial analysis as shown in Fig. 1. Transparent sheets were used as lights were applied from both bottom and top of the sheet to eliminate shadow effects. The main light is back light. Top light was applied to strengthen back light effect with a reflective sheet placed as shown in Fig. 1. However, as it was difficult to apply same light arrangement when the size of the sheet becomes large with higher no. of particles, white or black color sheets were used on the table.

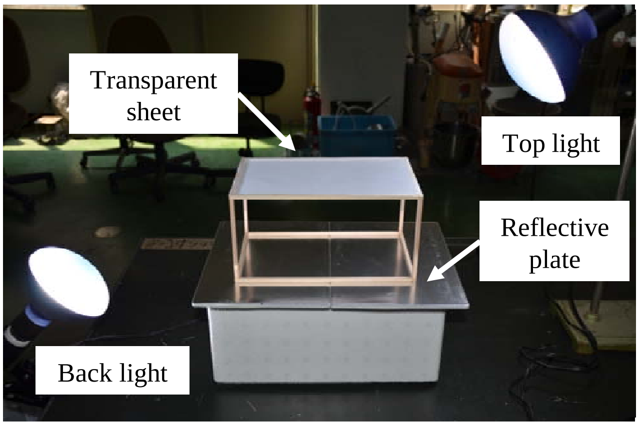

Figure 1: Image capturing process

In Series A, whether there is any effect due to randomly selection of particles were examined such a way that particles were placed on sheets varying from small size to large size as discussed in section 3.2 and given in Table 1. Moreover, shadow effect was evaluated using black color sheets in Series B as given in Table 2. Then, gradation curves determined with white color sheets in Series A were compared with that of by black color sheets in Series B.

Sieve analysis tests relevant to the sample used for image analysis were done as given in Table 3.

Table 1: Image analysis – Series A

Case	No. of particles	Particle placed sheet
1	3300 x 1 image	Transparent
2	1100 x 3 images	White
3	100 x 33 images	White

Table 2: Image analysis – Series B

Case	No. of particles	Particle placed sheet
1	1100 x 3 images	Black
2	3300 x 1 image	Black

Table 3: Details of sieve analysis tests

Case	No. of particles
a	100
b	3300

Images were captured by a Nikon D7000 camera. The camera can measure up to 16 million pixels.

2.3 Image analysis

All the images captured were evaluated in ImageJ software. ImageJ can read many image formats including TIFF, GIF, JPEG, BMP, DICOM and FITS. JPEG images were used during this research. It can calculate area and pixel value statistics of user defined selections. Moreover, it can measure distance and angle as well. It supports standard image processing functions such as contrast manipulation, sharpening, smoothing, edge detection and median filtering. More details on ImageJ can be found in Ferreira and Rasband (2011) [8].

In ImageJ, it can convert original images into binary images. It assumes that binary images have black objects and white background. However, black background with white objects can also be obtained. Binary images are very important to make some process like *Erode*, *Dilate*, *Open*, *Close-*, *Fill Holes*, *Watershed* and so on. *Erode* removes pixels from the edge of black objects while *Dilate* adds pixels to the edges of black objects. *Open* performs an erosion operation followed by dilation while *Close-* performs a dilation operation followed by erosion. *Fill Holes* fills holes in objects. Moreover, *Watershed* separates or cuts touching particles. However, during this research, particles were arranged such a way that they didn't touch each other. More details on different processes can be read on The Image User Guide given by Ferreira and Rasband (2011) [8].

Image analysis process conducted is shown in Fig. 2. As shown in Fig. 2, firstly, pixel is converted into mm using a scale factor. Then, images captured were converted into binary images. Figs. 3 - 7 show some of images and their binary images of samples with 100, 1100 and 3300 particles. Depending on quality of the images judged by the operator, no. of steps of *Dilate*, *Fill Holes* and *Erode* process were decided. Moreover, no. of steps of *Dilate* and *Erode* were always made equal to make there is no addition or removal of pixels from the real particles.

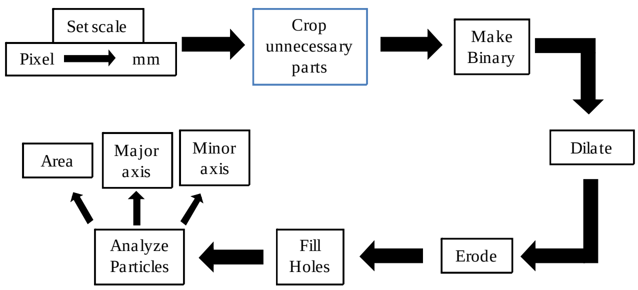

Figure 2: Image analysis process

Since particles are in irregular shapes, during image analysis, *Bounding Rectangle* and *Fit Ellipse* were used to find areas enclosed by individual particles. *Bounding Rectangle* gives the smallest area of a particle enclosed by a rectangle while *Fit Ellipse* gives that of by an ellipse. Area, major axis and minor axis were measured during image analysis though many shape characteristics including roundness, perimeter, area fraction and so on can be measured. More details on image processing techniques available can be found in Ferreira and Rasband (2011) [8].

Figure 3 (a): Image with 100 particles

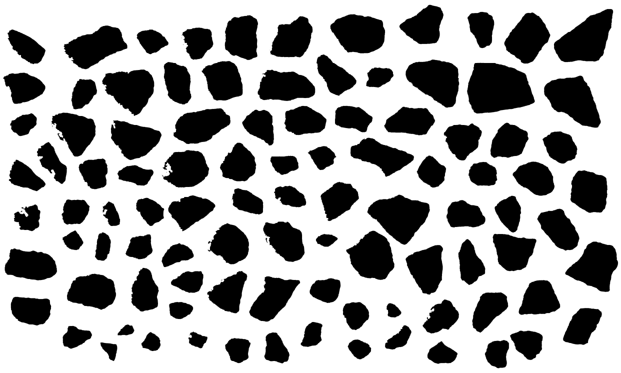

Figure 3 (b): The binary image of Fig. 3 (a) image

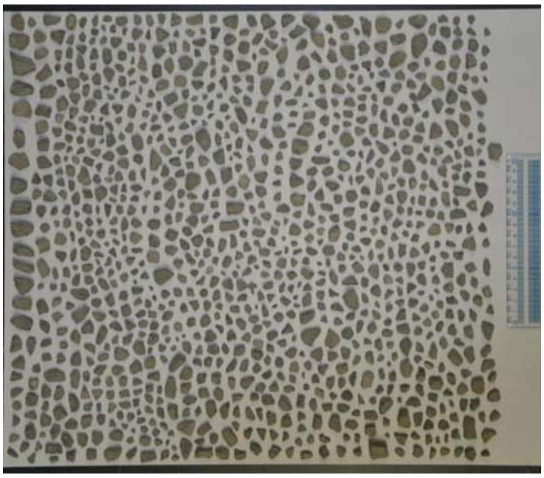

Figure 4 (a): Image with 1100 particles on white sheet

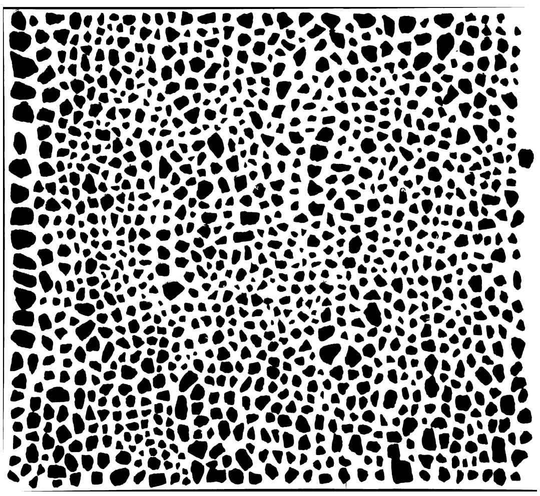

Figure 4 (b): Binary image of Fig. 4 (a)

Figure 5 (a): Image with 1100 particles on black sheet

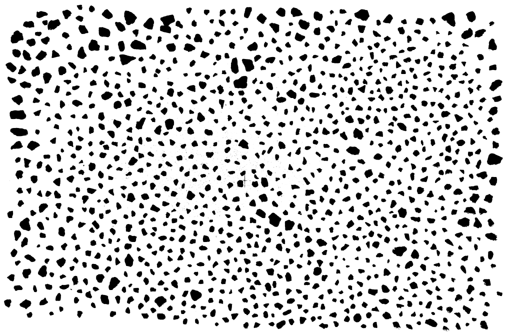

Figure 5 (b): Binary image of Fig. 5 (a)

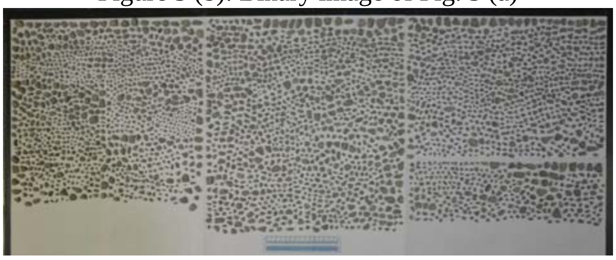

Figure 6 (a): Image with 3300 particles on white sheet

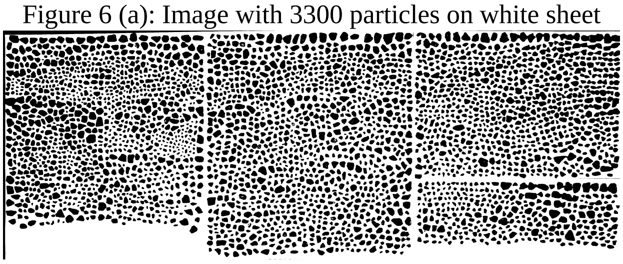

Figure 6 (b): Binary image of Fig. 6 (a)

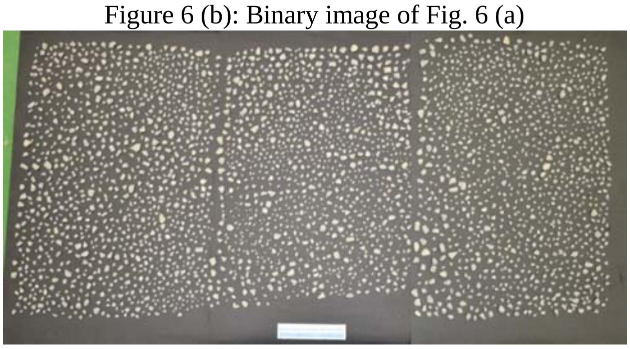

Figure 7 (a): Image with 3300 particles on black sheet

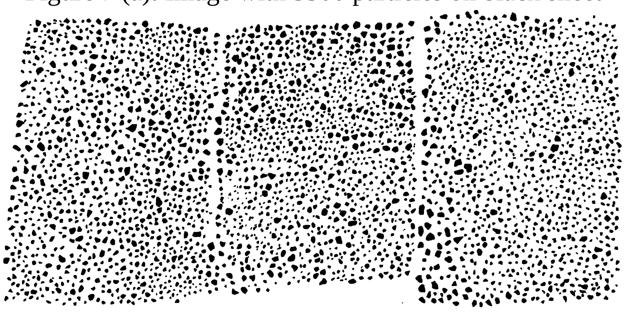

Figure 7 (b): Binary image of Fig. 7 (a)

3. RESULTS AND DISCUSSIONS

Sieve analysis tests use mass when evaluating cumulative curve of particle size distribution whereas image analysis can use either area of particles or no. of particles.

Some researchers including Banta et al. (2003) [4], Mora et al. (1998) [2] and Cheng (2000) [9] used mass determined from volume of particles instead of area of particles. The assumptions in determining volume from 2-D images would result in some errors. On the other hand, if mass of particles are measured individually like in Banta et al. (2003) [4], that would be time consuming. Moreover, area of particles can easily be determined from 2-D images. As a main objective of this research is to reduce time in determining gradation curve, image analysis was done with area of particles.

3.1 Effect of fitting shape on the evaluation of particle diameter

As shown in Fig. 8, effect of shape of particles was analyzed using three different shapes such as sphere, rectangle and ellipse. In this case, 100 no. of particles were randomly selected by the operator and used. Diameter, width and minor axis were used respectively for sphere, rectangle and ellipse as the grain size, *D*. Though JGS standard needs large amount of materials for sieve analysis (1.5kg which equals to 3300 particles for this material), sieve analysis were conducted for the same samples of 100 particles used for image analysis for comparison purposes. As it can be seen in Fig. 8, minor axis of ellipse gives the closest results to that of by sieve analysis test among the shapes considered. It can also be seen that if rectangle or sphere shapes is used, gradation curves would overestimate that of by sieve analysis tests. Therefore, hereafter, particles were analyzed using minor axis of ellipse shape during the research.

As particles are placed on the sheets with their most stable positions, it can be observed that 2-D images have longest and intermediate axis while the shortest axis is perpendicular to the plane of images. Therefore, it can be concluded that intermediate axis (minor axis on 2-D images) should be examined when comparing the results with sieve analysis tests. Effects of three axes were discussed in Fernlund (2005a) [5] and Fernlund (2005b) [6]. As discussed in Fernlund (2005a) [5] and Fernlund (2005b) [6], intermediate axis in 2-D images should give good results.

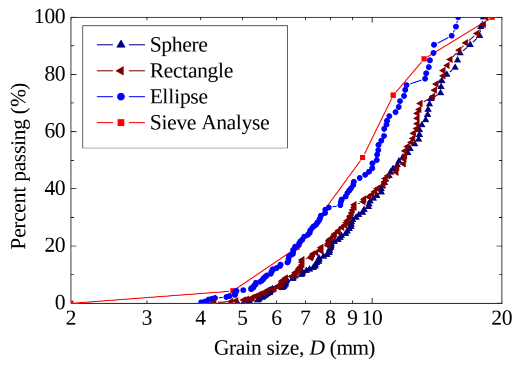

Figure 8: Effect of fitting shape on the evaluation of particle diameter

3.2 Effects of random selection of particles

JGS standard requires minimum amount of materials depending on the material's maximum particle size. It was found that JGS standard requirement is equivalent to 1.5kg which equals to approximately 3300 particles for the gravels used in this research. However, when the operator takes small sample (e.g. 100 particles) from the sample (3300 particles), it is not clear whether the operator gets 100 particles which would represent whole sample appropriately. When there is large no. of particles available, there might be some segregation and that would result in the operator getting coarser particles at initial stages.

The effect of random selection from a sample of 3300 particles on the gradation curve was evaluated using many samples of 100 particles and the results are shown in Fig. 9 (a). In this case, 10 samples each with 100 particles were randomly taken from the main sample of 3300 particles. As shown in Fig. 9 (a), initially selected samples overestimate gradation curve determined by sieve analysis test while later selected samples underestimate gradation curve evaluated by sieve analysis test. However, it should be noted that light arrangement and particle placed sheet were different in these cases than in previous cases. Moreover, it can be seen that gradation curve determined by sieve analysis test stands at the middle of gradation curves determined by image analyses.

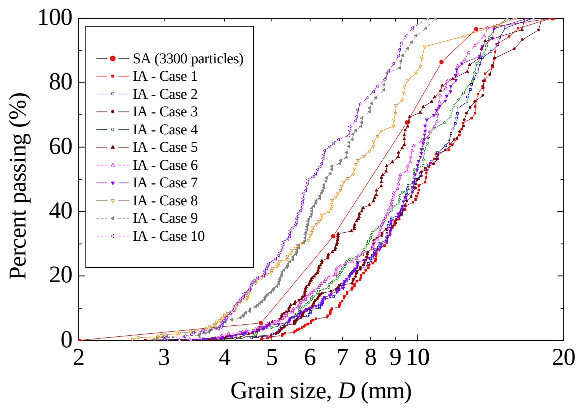

Figure 9 (a): Effects of random selection of particles

Then, in the next analysis, the operator intentionally tried to get a good sample to represent the main sample (3300 particles). All the particles (3300) were placed in 33 samples each with 100 particles and analyzed individually. In these cases, compared to cases in Fig. 9 (a), the operator purposely tried to select good samples of 100 particles than just randomly selecting like in Fig. 9 (a) since it was observed in Fig. 9 (a) that when particles are randomly selected, the operator tends to get coarser particles initially. The purpose was to evaluate whether the operator can select a sample which would represent the main sample appropriately. Even then, there is some difference between the randomly selected samples and the main sample as shown in Figs. 9 (b) – (d).

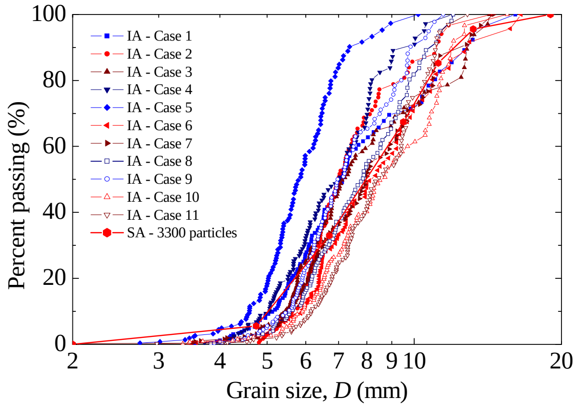

Figure 9 (b): Effects of random selection of particles – Cases 1- 11

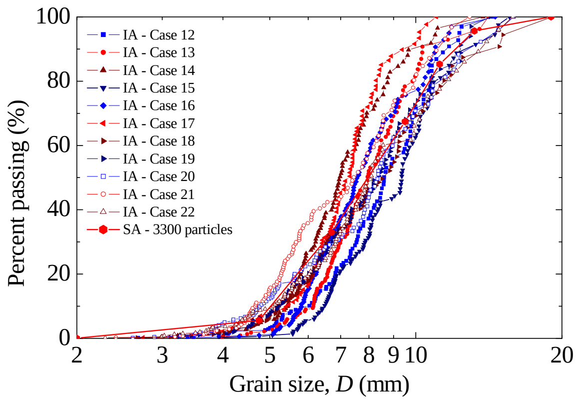

Figure 9 (c): Effects of random selection of particles – Cases 12- 22

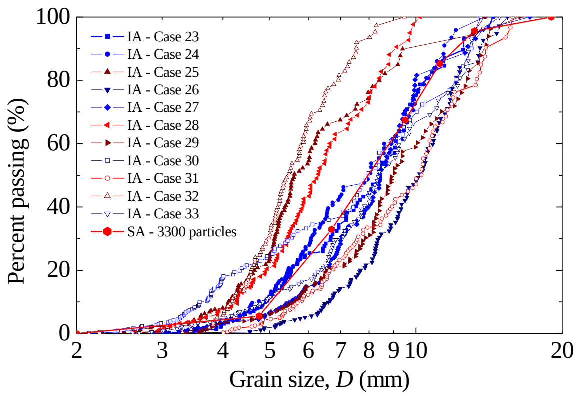

Figure 9 (d): Effects of random selection of particles – Cases 23- 33

As seen in Figs. 9 (b) – (d), it can be concluded that even when the operator intentionally tries to take particles to represent the main sample, there is still some difference among particle sizes in each small samples. However, it can be seen that gradation curve determined by sieve analysis test stands at the middle of gradation curves determined by image analyses. Therefore, it could be argued that if all the particles used for sieve analysis test is considered for image analysis, results could be good.

Since taking many images as high as 33 to cover all the particles would take some time, it was considered taking less no. of images with all the particles. As given in Tables 1 and 4, to cover all the particles, it needs a very large size sheet. However, shadow effects on particles closed to the boundary of the sheet could be a problem for very large sheets.

Table 4: Details of the size of the sheets

Case	Size of sheet	No. of images
1	20 x 13.2 cm	33
2	77 x 51.3 cm	3
3	130 x 86 cm	1

Fig. 10 shows gradation curves related to Case 2 where three images with 1100 particles each were analyzed. As it can be seen in Fig. 9 and Fig. 10, scattering of data become less when no. of particles in images are increased.

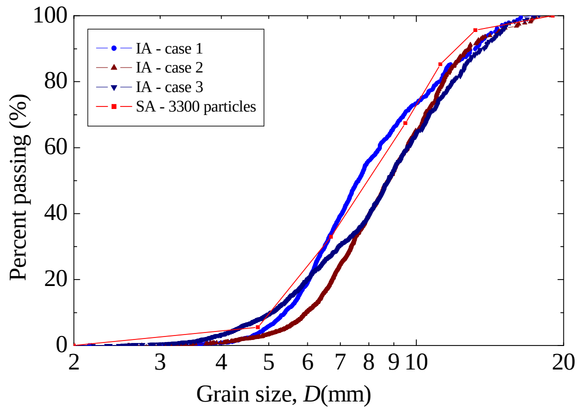

Figure 10: Gradation curves with 1100 particles

It can be seen in Fig. 11 that images with less no. of particles gives better gradation curves. As shown in Fig. 11, in all cases (Series A), gradation curves by image analysis overestimated gradation curve determined by sieve analysis test. It could be assumed that the overestimation of gradation curve determined by samples on large sheets could be due to shadow effects. Moreover, as shown in Fig. 11, it can be observed that 33 images covering all the particles give a gradation curve very similar to that of by sieve analysis test.

Error between D_{50} of gradation curves determined by image analysis and sieve analysis test, e, was determined as given in (1). It was found the errors are 1.1, 7.3 and 8.8% for Cases 1, 2 and 3 respectively. The error was always positive, i.e. image analysis always overestimates the gradation curve determined by sieve analysis. Therefore, it could be concluded that when very high accuracy needed on gradation curves, particles should be placed on a small sheet such that shadow effects, probably at the edges of the sheets, won't be significant.

$$e = \frac{(D_{50,IA} - D_{50,SA})}{D_{50,SA}} x\,100\,(\%) \qquad (1)$$

where $D_{50,IA}$ is D_{50} of gradation curve determined by image analysis while $D_{50,SA}$ is that of by sieve analysis test.

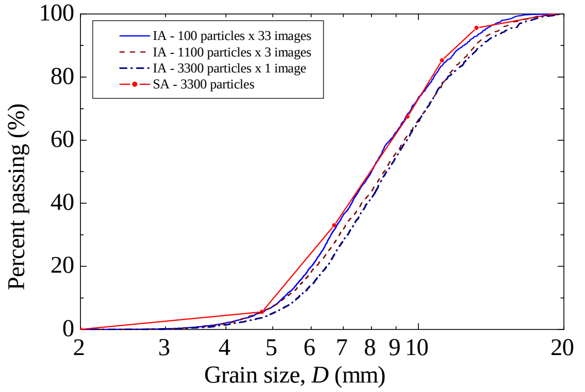

Fig. 11: Gradation curves with different no. of particles

3.3 Effects of color of particle placed sheet

It was also examined whether there is any effect of color of particle placed sheets on the gradation curves by light effects in Series B as given in Table 2.

Fig. 12 shows results of gradation curves determined when particles were placed on black color sheets. It can be observed that trend of gradation curves in Fig. 12 is similar to that of Fig. 11 in which gradation curves by image analysis overestimate that of by sieve analysis test. Moreover, images with less no. of particles give better gradation curves. However, in Fig. 12, gradation curve determined by images with 100 particles are also included for comparison purposes though that was determined with transparent sheet as given in Table 1.

Moreover, it was determined the error, *e*, are 3.2 and 5.0% for Cases 1 and 2 respectively. Table 5 describes comparison of errors with white and black color sheets. It can be observed that black color sheets give better results compared to white color sheets, perhaps black color sheets have less effect from lights than white color sheets.

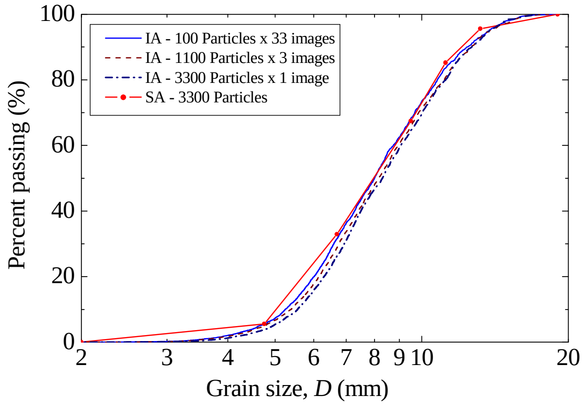

Figure 12: Effects of color of particle placed sheet

Table 5: Details of error of D_{50} between SA and IA

No. of images	Error, *e* (%)	
	White sheet	Black sheet
3	7.3	3.2
1	8.8	5.0

4. CONCLUSION

Particle size distribution curve of coarse materials (2-19mm) were evaluated using image analysis, ImageJ. 2-D images of particles were used in image analysis. Gradation curves by image analysis were compared with that of by sieve analysis test. Finally, the following conclusions were made,

Since area of particles gives accurate gradation curves as that of by sieve analysis test, image analysis technique used was simple and less time consuming than sieve analysis test. Moreover, it was also simple as mass from volume of particles are no need to be evaluated.

As particles were in irregular shapes, ellipse shape was better to represent them properly than spheres or rectangle shapes. When the shape of particles was represented by sphere or rectangle, gradation curves overestimate that of by sieve analysis test.

Shadow effects can be eliminated with proper light arrangements. That's to say, if two lights are used symmetrically, that would eliminate shadow effects very much.

All the particles should be considered to obtain accurate gradation curves as taking a random sample from a large sample of particles would not necessary represent the whole sample.

The errors of D_{50} were 7.3 and 8.8% with white color sheets while they were 3.2 and 5.0% with black color sheets for cases of 1100 and 3300 particles respectively. Therefore, it can be concluded that black color sheets were better than white color sheets to place particles. That's to say, shadow effects on black color sheets should be less than that of white color sheet.

Error of D_{50} between two methods was 1.1% for images with 100 particles on a transparent sheet. Moreover, they were 3.2 and 5.0% for particles 1100 and 3300 respectively when black color sheets were used. Therefore, when very high accuracy on gradation curve is needed, small sheet should be used to place particles to eliminate shadow effects.

5. REFERENCES

[1] Fernlund JMR, The effect of particle form on sieve analysis: a test by image analysis, Engineering Geology, Vol. 50, 1998, pp. 111-124.

[2] Mora CF, Kwan AKH and Chan HC, Particle size distribution analysis of coarse aggregate using digital image processing, Cement and Concrete Research, Vol. 28, No. 6, 1998, pp. 921-932.

[3] Kwan AKH, Mora CF and Chan HC, Particle shape analysis of coarse aggregate using digital image processing, Cement and Concrete Research, Vol. 29, 1999, pp. 1403-1410.

[4] Banta L, Cheng K and Zaniewski J, Estimation of limestone particle mass from 2D images, Power Technology, Vol. 132, 2003, pp. 184-189.

[5] Fernlund JMR, Image analysis method for determining 3-D size distribution of coarse aggregates, Bull Eng Geol Environ, Vol. 64, 2005a, pp. 159-166.

[6] Fernlund JMR, Image analysis method for determing 3-D shape of coarse aggregate, Cement and Concrete Research, Vol. 35, 2005b, pp. 1629-1637.

[7] JIS A 1204, Test method for particle size distribution of soils, 2009, pp. 115-123 (in Japanese).

[8] Ferreira T and Rasband W, The ImageJ user guide 1.44, 2011.

[9] Cheng K, Optical Gradation for Crushed limestone aggregates, PhD Dissertation, West Virginia University, 2000.

Environment

First International Conference on Geotechnique, Construction Materials and Environment, Mie, Japan, Nov.21-23, 2011, ISBN: 978-4-9905958-0-7 C3051

CALIBRATION AND SIMULATION OF RUNOFF MODELS FOR DEVELOPING WATERSHED RESPOND KNOWLEDGE AT TROPICAL AREA

Arien Heryansyah, Zulkifli Yusop. Faculty of Civil Engineering, Universiti Teknologi Malaysia

ABSTRACT: Knowledge of environmental respond at watershed level is crucially important for good, scientifically and economically accepted strategic planning design. Since most of the South East Asian countries are tropical developing areas with short and few historical data are available but rapidly change of land utilization, modeling approach is the only way to establish the knowledge of watershed responds to system change. Because, rainfall runoff modeling can be use for flood mitigation, for water supply design, for controlling non-point source pollution, or for evaluating the watershed with reasonable data requirement. However, the models need specific local calibration therefore they valid on specific locations and condition only. In this study a watershed tank model at several locations will be calibrated simultaneously then evaluated according to their applicability, simplicity and possibility to become regional tropical watershed runoff model. Simple regional scale of watershed model and better understanding of watershed respond to land use change for strategic planning were expected as the result of the study.

Keywords: Tank model, land use change, tropical region, calibration.

1. INTRODUCTION

Development and sustainability are sometimes usually considered as two words that contradict. Development is to meets the needs of the present, while sustainability is to preserve the ability of future generations to meet their own needs. However by using a lot of experience, data and local wisdom, development and sustainability can be synergized. But at developing country, hydrology and environment data are always insufficient, or for short period only. A water related development can have a significant impact on health, quality of life, economic development, natural resource, and threatening the long-term viability of communities. On the other word, it is too many risks to conduct development and impossible to synergize development and sustainability at developing country without establish new way to interpret short period of data.

Land uses change rapidly due to development, population or economic pressure. As a hydrological unit, land uses has important role in water related development. Interpretation of flood and drought of short period data without proper understanding of the land uses pattern will cause design malfunction: under or over estimate. As long as land use pattern is considered in the interpreting the data and design, the short period of data will not a barrier anymore. In this case, modeling approach is proposed to become tools for designer or decision maker as well as new hydrological and environmental data observation station. Modeling can be used for learning, and observe the impact of changing condition, especially land use.

2. LITERATURE REVIEW

Hydrological runoff model have been developed from a need to analyze and solve specific hydrological problems, such as to obtain useful outcome of the modeling exercise, to evaluate variation of state-variables over space and time, and to understand internal flow processes. According to suitable solution for those problems, hydrological model was differentiated into distributed and lumped model. Normally, distributed modeling associated with physically based parameter and they are necessary if variation of state-variables over space and time are more important rather than direct relationship between rainfall and discharge. On the other hand, lumped model is more appropriate if the focus is good agreements between calculated and discharge without neglect basic hydrological processes, such as evapotranspiration (ET), infiltration, and water movements in the soil. Calibrated parameters are used more often, as a consequence of simplification.

The lumped model is suitable in the typical application of a hydrological model on simulation of discharges under stationary catchments conditions [1]. The most famous of the lumped model is Tank Model. It was broadly use for simulated rainfall-discharge relation in various watershed condition [2]. Tank model also can be used as specific tools, such as for evaluating the retention capacity of watershed. Another researcher use diffusive tank model with 10 minutes interval for flood analysis [3] or for run off analyses in paddy field [4]. Watershed modeling that thank model as basis has succeeded to give right figure to decision maker at Cidanau Watershed [5].

Areal Non-points Source Watershed Environment Response Simulation model, ANSWERS, is one of famous distributed (grid based) hydrological model. Its primary application was envisioned to be planning and evaluating various strategies for controlling nonpoint source pollution from intensively cropped areas [6]. Similarly, [7] proposes Hydrological Similar Unit (HSU), a kind of distributed type modeling, to take into consideration land use contribution on hydrological processes. And recently, [8] succeeds to identify hydrological processes at landscape zone at sub tropic area. All these three models employ land use role in hydrological processes but these models were considered to be complex and required a lot of data.

However, all the models valid on specific locations only and they need calibration for each location. Model applications at tropical area are should be more simple and required less complicated data. Therefore in this study, the same hydrologic model on several watersheds will be evaluated according to their applicability, simplicity, and reasonability relationship between model parameter and physical based parameter. On top of that, a kind of regional model for tropical area was expected to be established.

2 STUDY AREA

The research was conducted at two watershed at Java Island (Cidanau and Citarum watershed) and two watershed at Sumatra Island (Krueng Aceh and Musi Watershed). Cidanau, Citarum, and Musi are located on South hemisphere, while Krueng Aceh Watershed is located on Northern Hemisphere as presented on Fig.1. They are considered to be representing tropical region.

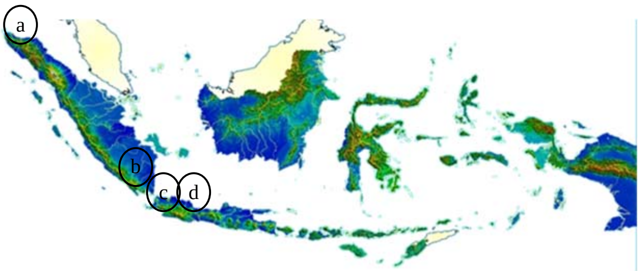

Fig 1. Study area: (a) Krueng Aceh; (b) Musi; (c) Cidanau; and (d) Upper Citarum Watershed

3 METODOLOGY

Collect the rainfall, discharge and land use data from several Watershed / Sub watershed are the first step of this research. Then continued with water balance analysis, model development, calibration, sensitivity analysis and simulation. Water balance was conducted to understand the hydrological cycle (1) and to verify the hydrologic data.

$$Rainfall = Discharge + ET + Storage \qquad (1)$$

Four layer lumped tank model was employed. This lumped tank model modeling replicated five typical hydrological processes at tropical area, i.e. evapotranspiration, infiltration, surface flow, inter flow, and base water flow. Each process was represented by calibrated parameter in calibration step such as CR for coefficient of runoff (surface, inter, and base flow), and CP for coefficient of percolation.

Calibration was conducted using automatic trial and error. It generates random value for CR and CP of each land use type, and then calculates values for the watershed proportionally with land use. The optimum values were evaluated using Model Efficiency (*ME*) and Mean Relative Error (*MRE*). Bias Error (*BE*) was calculated also to express the balance condition between observed and calculated discharge.

Table 1. The land use scenario of each watershed

Condition	Watershed	1	2	3	4	5	6	7
Existing	Cidanghiang	21.0%	25.9%	0.0%	8.3%	41.8%	3.0%	0.0%
	Mandalawangi	6.4%	12.9%	0.0%	56.2%	24.4%	0.1%	0.0%
	Peusar	7.5%	34.4%	9.0%	36.1%	11.0%	1.8%	0.2%
	Cidanau	6.8%	31.5%	8.2%	41.1%	10.2%	2.0%	0.3%
	KruengAceh	56.9%	0.2%	0.0%	0.3%	37.6%	4.7%	0.2%
	Keleker (Musi)	3.7%	0.0%	1.4%	85.7%	1.8%	7.3%	0.1%
	Upper Citarum	15.5%	20.6%	0.0%	5.4%	48.1%	10.3%	0.1%
SLU-1	Cidanghiang	33.9%	25.9%	0.0%	1.9%	35.3%	3.0%	0.0%
	Mandalawangi	22.6%	12.9%	0.0%	48.0%	16.3%	0.1%	0.0%
	Peusar	10.5%	34.4%	9.0%	34.6%	9.5%	1.8%	0.2%
	Cidanau	9.6%	31.5%	8.2%	39.7%	8.8%	2.0%	0.3%
	KruengAceh	87.5%	0.2%	0.0%	0.0%	7.3%	4.7%	0.2%
	Keleker (Musi)	10.7%	0.0%	1.4%	80.4%	0.0%	7.3%	0.1%
	Upper Citarum	64.3%	20.6%	0.0%	0.0%	4.7%	10.3%	0.1%
SLU-2	Cidanghiang	1.7%	25.9%	0.0%	14.8%	48.2%	9.4%	0.0%
	Mandalawangi	1.5%	12.9%	0.0%	57.8%	26.0%	1.8%	0.0%
	Peusar	5.4%	34.4%	9.0%	36.8%	11.7%	2.5%	0.2%
	Cidanau	4.9%	31.5%	8.2%	41.7%	10.8%	2.6%	0.3%
	KruengAceh	0.2%	0.2%	0.0%	53.3%	37.6%	8.5%	0.2%
	Keleker (Musi)	0.0%	0.0%	1.4%	88.9%	1.8%	7.8%	0.1%
	Upper Citarum	1.0%	20.6%	0.0%	15.1%	48.1%	15.1%	0.1%
SLU-3	Cidanghiang	0.0%	25.9%	0.0%	15.3%	48.8%	10.0%	0.0%
	Mandalawangi	0.0%	12.9%	0.0%	58.3%	26.5%	2.3%	0.0%
	Peusar	5.1%	34.4%	9.0%	36.9%	11.8%	2.6%	0.2%
	Cidanau	4.7%	31.5%	8.2%	41.8%	10.9%	2.7%	0.3%
	KruengAceh	3.9%	0.1%	0.0%	0.3%	90.5%	4.9%	0.2%
	Keleker (Musi)	0.0%	0.0%	1.4%	78.8%	12.3%	7.3%	0.1%
	Upper Citarum	0.5%	6.1%	0.0%	5.4%	57.8%	30.0%	0.1%
SLU-4	Cidanghiang	0.0%	0.0%	0.0%	15.3%	61.7%	22.9%	0.0%
	Mandalawangi	0.0%	0.0%	0.0%	58.3%	33.0%	8.7%	0.0%
	Peusar	5.1%	30.8%	9.0%	36.9%	13.6%	4.4%	0.2%
	Cidanau	4.7%	28.2%	8.2%	41.8%	12.5%	4.3%	0.3%
	KruengAceh	11.5%	0.0%	0.0%	23.0%	60.3%	4.9%	0.2%
	Keleker (Musi)	0.0%	0.0%	1.4%	64.8%	22.7%	11.0%	0.1%
	Upper Citarum	0.0%	10.9%	0.0%	19.9%	48.1%	20.4%	0.6%
SLU-5	Cidanghiang	0.0%	0.0%	0.0%	0.0%	61.7%	38.3%	0.0%
	Mandalawangi	0.0%	0.0%	0.0%	0.0%	33.0%	67.0%	0.0%
	Peusar	5.1%	30.8%	9.0%	28.6%	13.6%	12.7%	0.2%
	Cidanau	4.7%	28.2%	8.2%	34.2%	12.5%	11.9%	0.3%
	KruengAceh	53.1%	4.0%	0.0%	26.8%	3.5%	12.3%	0.2%
	Keleker (Musi)	0.5%	0.0%	1.4%	54.3%	1.8%	41.9%	0.1%
	Upper Citarum	5.8%	1.3%	0.0%	5.4%	53.0%	34.4%	0.1%
SLU-6	Cidanghiang	0.0%	0.0%	0.0%	0.0%	0.0%	100.0%	0.0%
	Mandalawangi	0.0%	0.0%	0.0%	0.0%	0.0%	100.0%	0.0%
	Peusar	5.1%	30.8%	9.0%	23.6%	7.3%	24.0%	0.2%
	Cidanau	4.7%	28.2%	8.2%	29.7%	6.8%	22.2%	0.3%
	KruengAceh	56.9%	15.4%	0.0%	3.4%	14.9%	7.7%	1.7%
	Keleker (Musi)	0.5%	0.0%	0.4%	43.8%	1.5%	53.7%	0.1%
	Upper Citarum	0.5%	20.6%	0.0%	10.3%	28.9%	38.7%	1.1%
SLU-7	Cidanghiang	29.4%	0.0%	0.0%	0.0%	67.6%	3.0%	0.0%
	Mandalawangi	62.6%	0.0%	0.0%	0.0%	37.3%	0.1%	0.0%
	Peusar	30.9%	34.4%	9.0%	12.7%	11.0%	1.8%	0.2%
	Cidanau	28.2%	31.5%	8.2%	19.7%	10.2%	2.0%	0.3%
	KruengAceh	60.7%	0.0%	0.0%	0.3%	37.8%	0.9%	0.2%
	Keleker (Musi)	3.8%	0.0%	1.5%	36.5%	50.7%	7.6%	0.0%
	Upper Citarum	15.5%	10.9%	0.0%	0.6%	48.1%	24.7%	0.1%
SLU-8	Cidanghiang	93.8%	0.0%	0.0%	0.0%	3.2%	3.0%	0.0%
	Mandalawangi	99.2%	0.0%	0.0%	0.0%	0.7%	0.1%	0.0%
	Peusar	40.4%	34.4%	9.0%	12.7%	1.6%	1.8%	0.2%
	Cidanau	36.8%	31.5%	8.2%	19.7%	1.6%	2.0%	0.3%
	KruengAceh	56.9%	4.0%	0.0%	16.2%	22.5%	0.2%	0.2%
	Keleker (Musi)	25.7%	0.0%	0.4%	17.5%	50.0%	6.3%	0.1%
	Upper Citarum	29.9%	20.6%	0.0%	0.6%	38.5%	10.4%	0.0%

Note: (1) Forest, (2) Paddy Field, (3), Swamp Forest, (4) Plantation, (5) Upland Area, (6) Settlements, and (7) Open water

Sensitivity analysis was used to identify the most influence land use and/or parameter, while simulation used for understanding the land use management. Seven types of land uses such as forest, swamp forest, paddy field, plantation, upland area, and settlements, and open water were considered suitable to represent most frequent land use at tropical area.

Several reasonable scenarios were developed to learn how to manage the watershed using land use change. They are based on the change of forest into plantation, upland, or settlement as worst scenario; compensate housing area using lake (open water) as moderate scenario; maintain forest and upland as conservative scenario. The land use change scenarios are presented on Table 1.

4 RESULTAND DISCUSSION

The water balance analysis shows that the watersheds have almost similar water balance pattern, and reasonable water movement (Table 2). The watersheds with negative storage mean water shortage occur during dry season. Most of them located at near the coastal area, such as Peusar, Cidanau, and Krueng Aceh Watershed. On the other hand, several spring locations were found at the downstream of watershed with positive storage. It means the storage, in this case groundwater, was released at downstream area.

Table 2. The water balance analysis

(Sub) Watershed	Rainfall	Discharge	ET	Storage
Cidanghiang	2607.0	14%	51%	35%
Mandalawangi	3664.7	35%	42%	23%
Peusar	6531.8	44%	66%	-10%
Cidanau	19937.5	48%	59%	-6%
Krueng Aceh	822.0	52%	72%	-24%
Keleker (Musi)	2706.9	68%	12%	21%
Upper Citarum	3001.2	68%	59%	-27%

The optimum calibrated parameters for each land use were evaluated using several assumptions, such as general understanding of hydrological processes, and physical characteristic of the land uses. Runoff coefficient first layer should be higher than second layer, as well as percolation coefficient at first and second layer. Then runoff coefficient of forest should be lower than paddy field, plantation, or upland area. And also, runoff settlement area and open water should be higher than plantation, or upland area. Optimum and evaluated parameter are presented on Table 3.

Tabel 3. The Optimum and evaluated parameter

Parameters	1	2	3	4	5	6	7
CR_O	7.13E-04	1.17E-03	2.25E-03	2.44E-03	3.95E-02	4.36E-02	6.10E-01
CR_1	9.75E-06	1.91E-05	1.72E-04	4.43E-04	4.43E-04	6.53E-03	6.04E-01
CR_2	9.16E-06	6.18E-06	6.12E-06	6.07E-06	2.82E-06	2.09E-06	4.77E-07
CR_3	9.07E-06	6.12E-06	6.06E-06	6.01E-06	9.16E-07	3.86E-07	1.65E-07
CP_1	1.68E-02	6.45E-03	3.61E-06	1.06E-06	7.78E-07	1.07E-12	3.71E-13
CP_2	1.37E-02	3.63E-05	1.19E-06	4.77E-07	5.29E-08	8.27E-13	1.40E-13

Note: (1) Forest, (2) Paddy Field, (3), Swamp Forest, (4) Plantation, (5) Upland Area, (6) Settlements, and (7) Open water

The model performance for almost all the watersheds are sufficient, as presented on Table 4. Only one watershed (Upper Citarum) has very low performance. Probably it caused by improper interpretation of land use classification. At upper Citarum watershed, paddy field is dominant land use since it occupies more than 20% of total area in addition to 39% of upland paddy field. For paddy field dominant watershed, detail information about cropping pattern is required to replicate the water loss in form of ET during a year. However, since there are at least 3 paddy field dominant watersheds with sufficiently good performance such as Cidanau and Krueng Aceh, the model was considered to be suitable for land use change simulation.

Table 4. The model performance

(Sub) Watershed	ME	MRE	BE
Cidanghiang	0.4432	0.4371	-0.1340
Mandalawangi	0.4525	0.2588	0.1066
Peusar	0.5660	0.3719	0.0358
Cidanau	0.6720	0.5280	0.0329
KruengAceh	0.5891	0.3535	0.1869
Keleker (Musi)	0.5667	0.6700	-0.1064
Upper Citarum	0.1845	0.4637	0.5232

Sensitivity analysis result is presented on Table 5. Forest, paddy field, plantation and upland are considered as most influencing land use, while runoff coefficient at 1st and 3rd layers are consider as most influencing parameter. It means watershed manager should be thinks deeply before change the fraction of the most influencing land use. On the other words, the most influencing land uses are required to be maintained or to be increased to prevent water resources problem. This is in line with the opinion of naturalists and conservative. However in term of engineering view of point there are possibilities to manage the land use using structure also. To convert forest into others is acceptable as long as keep the runoff coefficient, especially at 1st and 3rd layers, at the same level with forest.

Table 5. The result of sensitivity analysis

Parameter	Land Use	Changing Frequency
Runof Coefficient-1	Forest	4
Percolation Coefficient-1	Forest	16
Runof Coefficient-3	Forest	18
Runof Coefficient-0	Open Water	6
Runof Coefficient-1	Open Water	15
Runof Coefficient-1	Paddy Field	8
Percolation Coefficient-1	Paddy Field	12
Runof Coefficient-3	Paddy Field	17
Runof Coefficient-2	Plantation	3
Runof Coefficient-1	Plantation	11
Runof Coefficient-3	Plantation	11
Runof Coefficient-3	Settlements	5
Runof Coefficient-0	Settlements	6
Runof Coefficient-1	Swamp Forest	4
Runof Coefficient-0	Upland	14
Runof Coefficient-3	Upland	14
Runof Coefficient-1	Upland	16

Simulation result as presented on Table 6 and Table 7 show that Forest has important role to reduce the maximum discharge and increase the minimum discharge. Contrary, settlement has inverse role of forest. They show also that in some case (Cidanau), convert forest into plantation also can maintain the maximum discharge at existing level. On top of that, better understanding of watershed management in term of land use change, especially minimum and maximum discharge, were expected to be achieved.

Tabel 6. The impact of land use change on minimum discharge.

Minimum Discharge (m^3/s)	Existing	SLU-1	SLU-2	SLU-3	SLU-4	SLU-5	SLU-6	SLU-7	SLU-8
Cidanghiang	0.1	0.1	0.2	0.2	0.0	0.0	0.0	0.1	0.1
Mandalawangi	1.0	0.9	0.8	0.9	0.1	0.0	0.0	1.2	1.6
Peusar	0.6	0.6	0.5	0.5	0.4	0.4	0.4	0.8	0.9
Cidanau	0.2	0.2	0.2	0.2	0.2	0.1	0.1	0.4	0.6
Krueng Aceh	1.4	2.2	0.2	0.1	0.5	1.7	1.1	1.8	1.8
Keleker (Musi)	0.0	0.0	0.0	0.0	0.0	0.0	0.0	0.0	0.0
Upper Citarum	0.3	0.8	0.2	0.1	0.0	0.1	0.1	0.3	0.5

Tabel 7. The impact of land use change on maximum discharge.

Maximum Discharge (m^3/s)	Existing	SLU-1	SLU-2	SLU-3	SLU-4	SLU-5	SLU-6	SLU-7	SLU-8
Cidanghiang	6.9	4.3	8.1	19.5	26.1	31.1	45.0	5.7	3.4
Mandalawangi	16.6	7.9	14.5	30.0	35.0	56.8	69.0	6.0	4.4
Peusar	174.7	166.3	194.9	197.9	205.5	221.7	243.1	130.7	121.5
Cidanau	576.5	915.5	1086.9	1098.1	1139.7	1165.2	1197.4	456.7	355.3
Krueng Aceh	680.8	252.3	1242.0	1070.5	765.8	369.4	1519.6	318.7	320.3
Keleker (Musi)	43.0	31.9	89.7	90.6	93.0	93.7	97.8	32.7	22.2
Upper Citarum	5.5	4.0	7.8	9.8	16.2	9.1	24.0	6.8	3.2

5 ACKNOWLEDGMENTS

This research was a part of the Research University Program of Universiti Teknologi Malaysia, 2011. I wish to express my sincere gratitude to Dean of Water research Alliance for his support in conducting this research. I also wish to thank to my colleges Dr Yanuar and Prof Rizaldi at Bogor Agricultural University for their continuous advises and other kinds of assistance.

6 CONCLUSION

The results of this study are summarized as follows:

- Calibration and simulation of runoff model were done with sufficient performance.
- This lumped tank model work properly on at least 2 sites near to equator in this study area. Therefore this model can be proposed as regional model on tropical region.
- Better watershed management was expected to be achieved since impact of land use on minimum and maximum discharges are understood.

7 REFERENCES

[1] Refsgaard J.C and Knudsen J, Operational validation and intercomparison of different types of hydrological models, Water Resources Research, 1996: 32 (7), 2189-2202

[2] Sugawara, M. On the Analysis of the Runoff Structure of Several Japanese Rivers. Japanese Journal of Geophysics, 1961: Vol. 4, No. 2.

[3] Hayase, Y., Kadoya, M., Diffusive tank model for flood analysis and its fundamental characteristics: runoff analysis by the diffusive tank model in low-lying drainage basin. Trans. Jpn. Soc. Irrigat., Drainage and Reclam. Eng., 1993: 165, 75–84 (in Japanese).

[4] Chen, R.S., and Pi, L.C. Diffusive tank model application in rainfall-runoff analysis of upland fields in Taiwan. Agricultural Water Management, 2004: 70, 39–50.

[5] Heryansyah Arien., Goto Akira., Mizutani Masakazu., and Yanuar Muhammad JP. Development of Watershed Water Quality Model in Indonesia, Transactions of JSIDRE, 2007: No.251 (Vol.75-5), 97-105.

[6] Bouraoui, F. and T. A. Dillaha. ANSWERS-2000: Runoff and sediment transport model. Journal of Environmental Engineering, ASCE, 1996: 122(6):493-502.

[7] T. Karvonena, H. Koivusaloa, M. Jauhiainena, J. Palkob, K. Weppling c. A hydrological model for predicting runoff from different land use areas. Journal of Hydrology 217, 1999: 253–265.

[8] Yang, Y., Xiao, H., Wei, Y., Zhao, L., Zou, S., Yin, Z., Yang, Q., Hydrologic processes in the different landscape zones of Mafengou River basin in the alpine cold region during the melting period, Journal of Hydrology, 2011. Published Online.

First International Conference on Geotechnique, Construction Materials and Environment, Mie, Japan, Nov.21-23, 2011, ISBN: 978-4-9905958-0-7 C3051

Effect of Geological Succession on Macrophyte and Microbiota in Aquifer Ecosystem in Urban Coastal Zone

Kazuhito MURAKAMI* and Akiko INOUE-KOHAMA**

*Dept. of Life and Environmental Sciences, Chiba Institute of Technology, 2-17-1 Tsudanuma, Narashino, Chiba 275-8588 Japan
**Dept. of Environmental Information Engineering, Tohoku Institute of Technology, 35-1 Kasumicho, Yagiyama, Sendai, Miyagi 982-8577 Japan

ABSTRACT: This study was conducted to investigate the effect of geological succession of sediment on macrophyto and microbiota in aquifer ecosystem. The research field was selected as Yatsu Tidal Flat where located in urban coastal zone in Tokyo Inner Bay. This tidal flat has been registered under Wildlife Protection Area of Japan in 1988 and the Ramsar Convention in 1993, and just as the tidal flat that was left from reclamation of waterfront zone of urban area. It is very important to obtain some information about these ecosystem characteristics of such nature left in urban area, because creation of artificial tidal flat is recognized as one of important enterprises to construct urban ecosystem. In recent years, a large chlorophyceae, *Ulva* spp. (mainly *Ulva pertusa* and *Ulva japonica*) which is recognized as a biotic indicator of eutrophicated sea area, has become observed in Yatsu tidal flat, and it is considered that *Ulva* spp. give a large effect to water quality. *Ulva* spp. has high absorbent potential of nutrient salts at its growth phase, so this macrophyte is considered to place the microbiota such as zooplankton and phytoplankton under its control. In the first place, the geological succession as muddy to sandy occurred because of water quality change as fresh water to sea water. This water change resulted from the decrease of drainage with the sewer system service in basin area, and lead oligotrophication of the sediment. *Ulva* spp. is one of the biological indicater for sea water and sandy sediment and eutrophicated environment. Because of the irregular growth of *Ulva* spp., the quantity of phytoplankton decreased drastically, and the dominant species of phytoplankton and zooplankton transited from ideal to unsuitable food organisms for macrobenthos which is important food for the migratory birds, and the production potential of this aquifer ecosystem became in fragility.

Keywords: urban coastal zone, macrobenthos, macrophyte, geological succession, Yatsu tidal flat

1. INTRODUCTION

Tidal flat is located in the boundary zone between land and sea area. Therefore, the environmental factors are changing periodically and very rapidly, according to supply of fresh water from river and tide action. On the other hand, the algal production speed and rate, such as diatoms and/or flagellums on surface of sediment that is forming bio-film, is very high, because of much nutrient salts are supplied from both land and sea areas. Unique and precious ecosystem is constituted, and birds and fishes gather to take feed at the same time. Tidal flat is very important place as familiar nature, for not only wild lives in tidal flat but also human in surrounding area. And it is the place where for recreation, and to obtain marine resources [1]. Although the area is decreased by reclamation because of tidal flat is shallow sea and therefore it is easy to reclaim, the importance of wetland including tidal flat is indicated recently, and Ramsaor Convention whose purpose is to protect migratory is adapted at the year 1971. Eleven wetlands are registered for the convention in Japan [2].

Yatsu Tidal flat where is registered under Ramsaor Convention, is reclaimed its circumference, and shut out from Tokyo Inner Bay for over 20 years. And environment of this tidal flat is terrifically changed, for instance decrease of inflow load and pure water originate in domestic wastewater by improvement of public sewerage system. Furthermore, it is recognized apprehensions in recent years that there is possibility to occur the runoff of sediment by tidal current. From analysis for the environmental succession and factors of this unique tidal flat, some essential suggestions for construction artificial tidal flat in urban area is expected to be obtained.

In this paper, the study was conducted to investigate the effect of geological succession of sediment on macrophyto and microbiota in aquifer ecosystem.

2. OUTLINE OF YATSU TIDAL FLAT

In the extreme end of the Tokyo Inner Bay, an un-reclaimed Tideland of 40 ha is left which is now called as Yatsu Tidal Flat (Yatsu Higata) as shown in Fig.1. Sea water comes in and out with the ebb and flow of the bay. Large numbers and different kinds of shorebird and migratory bird come here each season. They are giving tremendous relaxation to the community in the midst of the urban area. Yatsu Tidal Flat was designated as an official site of Ramsar Convention (Convention on Wetlands of International Importance Especially as Waterfowl Habitat) in 1993.

In 1898, it was a shoal beach and was used for salt manufacturing. In 1924, Keisei Rail Road (Keisei Dentetsu) reclaimed the area and made a play land Yatsu Play Land (Yatsu Yu-en). The remaining shore served for swimming and clam fishing. The community had great fun out of it. In 1979, Tokyo Bay Reclamation project encroached the shore and Yatsu Tidal Flat came to be in danger of land development. Groups and community people stood against for its protection (Fig.2). In 1984, the conservation of the Yatsu Tidal Flat was then included in the construction project of local area public facility. Later in 1988, Yatsu Tidal Flat was designated as the Natural Wildlife Protection Area. In 1982, Yatsu Play Land was closed due to the opening of the Tokyo Disney Land in the nearby town. In 1993, Yatsu Tidal Flat was designated as the Ramsar Site by The 5th Conference of the Contracting Parties to the Convention on Wetlands. In 1994, Observation Center was opened. In 1996, Yatsu Tidal Flat joined to The East Asian and Australasian Shore Bird Reserve Network in The 6th Conference in Brisbane, Australia. In 1997, Narashino City enacted The Day of Yatsu Tidal Flat for celebration of Yatsu Tidal Flat conservation. In 1998, Narashino City and Brisbane City Council agreed to The Affiliation Agreement of their Wetland Conservation.

In Yatsu Tidal Flat, during the flow tide, the tidal flat is in the water (0.8m depth in average), and during ebb tide, the tidal flat appears. The tidal flat is connected to Tokyo Inner Bay through two canals, and the water flows in and out. So many shorebirds gather and feed themselves, and so many creatures are inhibiting such as crabs and invertebrates on which the birds live. Throughout a year, many kinds of birds are seen in Yatsu Tidal Flat. Seasonally there comes huge number of seasonal migratory birds. For the shorebirds flying between Siberia and Australia, Yatsu Tidal Flat is their important intermediate rest place after and before their long journey [3].

3. RECENT PLOBLEMS IN YATSU TIDAL FLAT

Since 1983, *Ulva* sp., a marine macrophyte (chlorophyceae) which forms the green tide with its irregular growth, has been observed and increased in its individual number. The occupied zone in Yatsu Tidal Flat has expanded, that is, 6.8 ha in 1995, 13 ha in 1993, 20 ha in 2000, and 40 ha (completely occupied) after 2005 (Fig.3) [4]. The main species of *Ulva* spp. was identified as *U.pertusa* and *U.japonica*. The reasons of this phenomenon, an eutrophication of water quality, increasing of seawater supply, and sediment succession from mud to sand have been reported (Fig.4) [5].

Ulva spp. is recognized as one species of large green algae that like sand or sandy-mud sediment condition rather than mud sediment condition [6][7]. That is, it is thought that growth of *Ulva* spp. is brought about by existence of sufficient nutrient salts and progress of chlorinization of water and sandification of sediment in this tidal flat. From these outcomes, the rise of a ratio (sand / mud) and that of (sea water / fresh water) can be considered as one of reasons for the irregular growth of *Ulva* spp..

Sediment condition of the area where *Ulva* spp. is much grown (ORP : -200～-250mV) is presenting the black reduction state compared with the sediment of the area where *Ulva* spp. is not observed (ORP : -50～-100mV). So, in such reduction area, there cannot be observed any macrobenthos

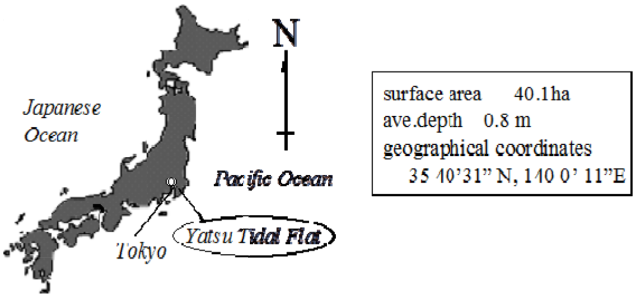

Fig.1 Location of Yatsu Tidal Flat

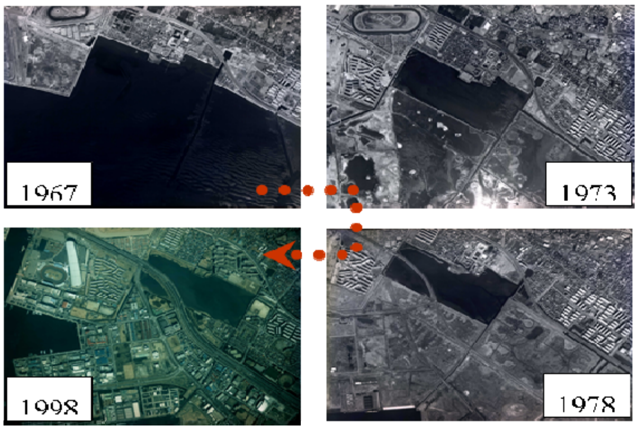

Fig. 2 Succession of environmental condition around Yatsu Tidal Flat

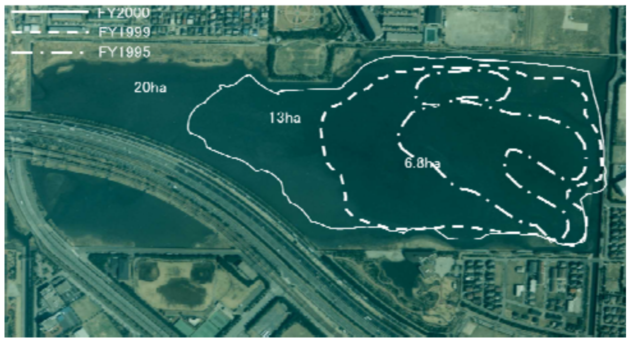

Fig.3 Succession of occupied zone by *Ulva* spp.

Fig.4 *Ulva* spp. multiplicated in Yatsu Tidal Flat

that is supporting a tidal flat ecosystem as main predator [8]. It is considered that *Ulva* spp. decayed and made anaerobic Sediment state after its irregular growth. In comparison with 1984 and 1995, the total species number of macrobenthos has increased from 13 to 39, however, the total individual number has clearly decreased, and no living point was also observed [9]. That is, it is suggested that biological production mechanism has been changing from "large quantity of small species" condition to "small quantity of large species" condition, namely, change to brittle bio- production state.

Thus, a change of phytoplanktonic flora which plays an important role on food chain of the tidal flat ecosystem as the primary producer, and that of zooplanktonic fauna as the primary consumer leads a change of macrobenthic fauna as the food source of the migratory birds. The decrease of migratory birds attracts very few customers who visit to Yatsu Tidal Flat to relax, and this leads decay of recreational function, that is, the ecosystem service.

4. GEOLOGICAL SUCCESSION IN YATSU TIDAL FLAT

In Yatsu Tidal Flat, the mud area has decreased from 20 ha to 15 ha, sandy-mud area has increased from 10 ha to 18 ha, and Ignition Loss (I.L.) of sediment, that indicates the quantity of organic matters in sediment, has also been decreased (Fig.5). Moreover, although the thickness of the mud layer in Yatsu Tidal Flat was 25-200cm in 1984, it is decreased rapidly 0-50cm in 1995. This means sediment condition of Yatsu Tidal Flat is changing from mud to sand, and it was suggested at the same time that flow out of sediment, especially mud layer from this tidal flat to Tokyo Inner Bay.

The amount of inflow load that is flown from its basin area to Yatsu Tidal Flat is decreased 16.8% for these 12 years from 1983 to 1995 (Fig.6), and the diffusion of the sewerage system in basin area is 85.3% in 2010. The decrease is because of the amount of drainage inflow from the household decreased with improvement of public sewerage system of a basin area. Furthermore, improvement of public sewerage is not only reduction of inflow loads, but also brought about the result of reduction of the amount of fresh water supply. Chloride ion concentration in Yatsu-Funadamari located in most inner part of Yatsu Tidal Flat continues rising (Fig.7). This phenomena namely means the water quality in Yatsu Tidal Flat is changing from fresh water to sea water.

At Yatsu Tidal Flat, the inflow loads has decreased as improvement of public sewerage system that is started since 1990. As the result, water quality has changed from fresh water to sea water and sediment condition has also changed from mud to sand, and it is caused the irregular growth of *Ulva* spp., which is the indicator of eutrophicated state. That is, as shown in figure 6, at the first step of succession, a tidal flat just like tideland lake is formed artificially with reclamation and development of its circumference, and the water quality became fresh water and sediment condition became muddy, in gradually. So it is formed ecosystem that

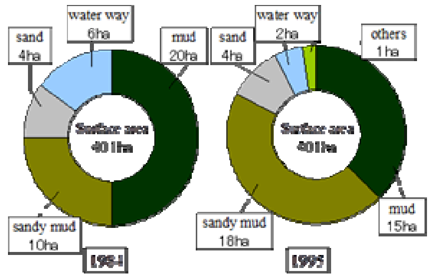

Fig.5 Comparison of sediment quality in 10 years

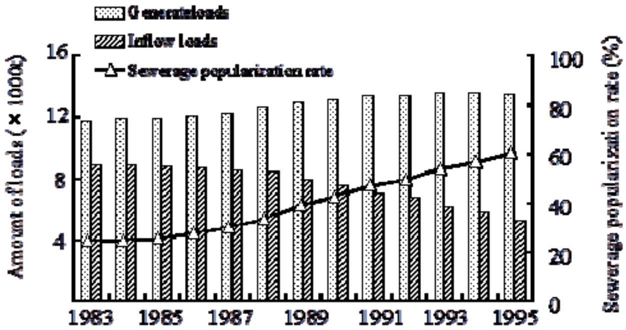

Fig.6 Change of popularization of sewerage and amount of loads

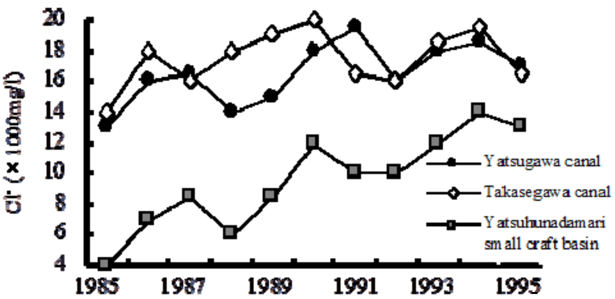

Fig.7 Change of chloride ion concentration

has high-bio-production potential. However, in recent years, supply of fresh water and organic matter from land area has decreased with improvement of public sewerage system, so chloronization of water quality and sandification of sediment condition have progressed, and bio-production potential has reduced. Moreover, tide action becomes more influence, such as flow out of sand from Yatsu Tidal Flat. From these outcomes, it was made clear that Yatsu Tidal Flat has been changing to the foreshore tidal flat again with remaining the topographical characteristics as tideland lake.

5. SUCCESSION OF MICROBIOTA

Regarding to phytoplanktonic flora which plays an important role on the food chain as the primary producer of the tidal flat ecosystem, microscopic observation has been conducted for several years (Fig.8). As results obtained from the observation, the following outcomes were obtained. 1) As quality of phytoplanktonic flora, seasonal change of species composition of phytoplankton is not so large and its species number was 50-60 species through a year, 2) As quality of phytoplanktonic flora, individual numbers of phytoplankton was larger in summer and smaller in winter, and supplied from Tokyo Inner Bay to Yatsu Tidal Flat throughout two channels, called Yatsu river in the eastern side and Takase river in the western side, with the ebb and flow of the bay, 3) The diversity index, calculated by Shannon Index, of phytoplankton is larger in winter and smaller in summer, and the possibility of simplisation of phytoplanktonic flora was occurred by outflow from Yatsu Tidal Flat to Tokyo Inner Bay, 4) Unique ecosystem has been constructed in this enclosed tidal flat because of its closure circumstance which greatly influencing to phytoplanktonic flora.

The macrobenthos mainly observed in Yatsu Tidal Flat were Cinidaria, Mollusca, Annelida, Arthropoda and Lophophorata. As biotic indicator of organic polluted condition, Annelida was much observed in mud sediment zone. Macrobenthic fauna is considered poor in un-polluted environment and rich in polluted environment in general [10] . But in further polluted environment, the species and individual number of macrobenthos become to decrease, and macrobenthic fauna become poor again as a result. This tendency is not only in case of macrobenthos but also in most of biotic indicator, for example, phytoplankton, water glass, and so on. The wealthy nature means a state that co-exist with many species, many individuals, and without one or some dominant species. Yatsu Tidal Flat was considered to be in the state which environmental condition is shifting from the further polluted condition to the polluted condition with the progress of sandy sediment and seawater. Yatsu Tidal Flat is considered to indicate succession from mud sediment tideland to sandy tideland like other tidal flat in Tokyo Inner Bay. Macrobenthic fauna is very diverse in sand tideland, so the macrobenthic fauna in Yatsu Tidal Flat is considered to become more diverse year by year (Fig.9). On the other hand, *Ulva* spp. has become observed to be growing irregularly. This large green algae is considered to beat macrobenthos such as Annelida because of its large leaf body and sedimentation which leads anaerobic condition. From these phenomena, ecosystem balance is considered to be not in good condition [11].

Increase in the amount of pollutants that flows into Yatsu Tidal Flat has been resulted from the concentration of population, the increase of factories and the expansion of reclaimed land. And water plant and macrobenthos, especially Annelida in tideland is very useful to purify the organic pollutants with their prey-predation interaction [12][13]. It is important to protect macrobenthos from extermination because of its usefulness for purification of organic polluted sediment, especially in tidal flat ecosystem. In addition, Tokyo Inner Bay is recognized as a famous sea area where the Blue Tide (Aoshio, anaerobic water bodies) occurs frequently. In fact, a large scale Aoshio occurred 3 times in summer in 2000. This anaerobic water bodies flew into Yatsu Tidal Flat and influenced greatly not only to macrobenthos but also to other creatures in this enclosed tidal flat. Furthermore, EDCs are also considered to be one of environmental factors that give large effect [14]. So, further study about the effect of environmental factors on macrobenthic fauna is necessary for the environmental improvement of not only Yatsu Tidal Flat but also any nature left in urban area.

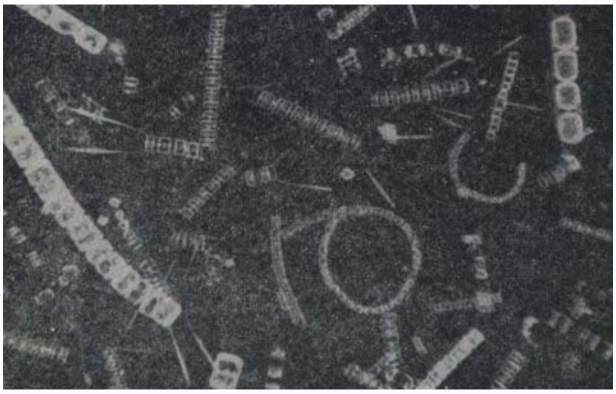

Fig.8 Plankton observed in Yatsu Tidal Flat

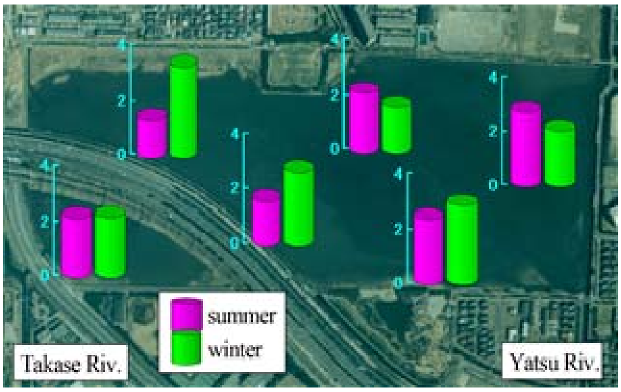

Fig.9 Diversity index (H’) of macrobenthos

Fig.10 Sandbank located near the mouth of Yatsu river which disappeared after the Tohoku Region Pacific Coast Earthquake in 11 March 2011.

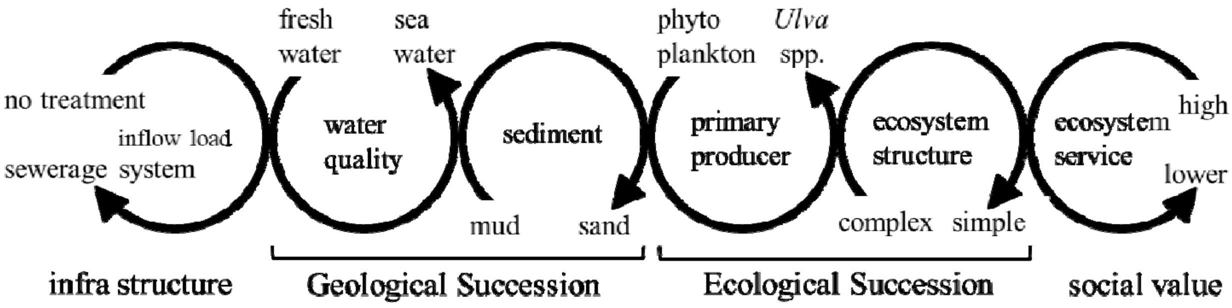

Fig.11 Relationship between geological and ecological succession in Yatsu Tidal Flat

6. EFFECT OF TOHOKU REGION PACIFIC COAST EARTHQUAKE

The Tohoku region Pacific Coast Earthquake which occurred at 11 March 2011 gave large influence not only to the pacific coast but also to the coastal zone of Tokyo Inner Bay. Yatsu Tidal Flat is not exception as same as Sanbanze and Banzu Tidal Flat where also located in Chiba prefecture side of Tokyo Inner Bay. The liquefaction of sediment in Yatsu Tidal Flat was observed. The promenadea walk was damaged and the microtopography of ebb water route in tidal flat was changed with an uplift of sediment. For example, a sandbank located near the mouth of Yatsu river was disappeared after the earthquake (Fig.10). It is considered that micro particle sand was ejected from underground and sedimental condition in the tidal flat became more sandy. However, in Yatsu Tidal Flat, the water flow, especially ebb tide, is very fast (about 2m/s in the canal) [15] and the sand particle was immediately flush out to Tokyo Inner Bay. *Ulva* spp. was also damaged temporary but it grew and occupied the tidal flat surface again. Further continuous investigation should be necessary to estimate the geological succession effect on the tidal flat ecosystem structure and function (Fig.11).

7. CONCLUSIONS

The investigation of the effect of geological succession of sediment on macrophyto and microbiota in aquifer ecosystem was conducted in this study. The results obtained are summarized as follows.

1) As a result of inflow loads has decreased with improvement of public sewerage system, water quality has changed from fresh water to sea water and sediment condition has also changed from mud to sand, and bio-production potential has reduced, in Yatsu Tidal Flat, the artificial tideland lake.

2) There is the inherent clockwise flow occurred by tidal action is made clear, and the relationship between the clockwise flow and sediment condition was suggested.

3) The phenomenon of sand spill is occurred by tide action in the east area of Yatu Tidal Flat was made clear.

4) It is considered that Yatsu Tidal Flat has been changing to the foreshore tidal flat again with remaining the topographical character as tideland lake.

5) Because of the irregular growth of *Ulva* spp., the quantity of phytoplankton decreased drastically, and the dominant species of phytoplankton and zooplankton transited from ideal to unsuitable food organisms for macrobenthos which is important food for the migratory birds, and the production potential of this aquifer ecosystem became in fragility.

6) Further continuous investigation should be necessary to estimate the geological succession effect on the tidal flat ecosystem structure and function.

8. REFERENCES

[1] Kurihara Y, "Ecology and Ecotechnology in Estuarine-Coastal Area," Tokai University Publishers, 1988.
[2] Yamashita H, "Ramsar Convention and Wetland in Japan," Shinzansha Scitech, 1993.
[3] Yatsuhigata Nature Observation Center, "Welcome to Yatsuhigata (tidal flat)," Narashino City, 1998.
[4] Murakami K, Ishii Y, Taki K, Hasegawa A, "Succession Characteristics of Tideland Lake located in Tokyo Inner Bay," J. of Coastal Engineering, vol.47, Nov.2000, pp.1121-1125.
[5] Sugiyama K, "Sea Shore Biotope," Shinzansha Scitech, 2000.
[6] Notoya M, "Utilization of *Ulva* spp. and Environmental Restoration," Seizando, 1999.
[7] Murakami K, Ishii T, Taki K, Ishii Y, Tatsumoto H, "Material Circulation and Species Composition in Tidal Flat Microcosm System," Conference papers on 6th International Conference on the Mediterranean Coastal Environment (MEDCOAST'03), vol.2, Oct.2003, pp.825-830.
[8] Murakami K, Takano H, Katayama Y, Ogino Y, Mori T, Nagafuchi O, Komai Y, Seiki T, "relationship between Macrobenthic Fauna and Sediment Condition in the Seto Inland Sea," MEDCOAST99-EMECS99 Joint Conference, Land-Ocean Interactions: Managing Coastal Ecosystems, vol.1, Oct.1999, pp.111-122.
[9] Environmental Agency of Japan, Chiba Prefecture, Narashino City, "Environmental Research Report of Yatsu Tidal Flat," 1996.
[10] Rhoads DC, Morse JW, "Evolutionary and Ecologic Significarse of Oxygen deficient Marine Basins," Lethaia, vol.4, 1971, pp.413-428.
[11] Ishii Y, Murakami K, Ishii T, Tatsumoto H, Taki K, "relationship between Ecological Balance and Environmental Factors in Natural Tidal Flat left from Reclamation," Proc. Civil Eng. Ocean, JSCE, vol.17, Oct.2001, pp.129-134
[12] Inamori Y, Kimura M, Sudo R, "The Role of Benthos and Conservational Measure in Tideland," J. of Water and Waste, vol.36, Jan.1994, pp.15-20.

[13] Kohama A, Enari K, Tamaki S, Nakayama M, “Evaluation of the Amount of Nitrogen and Phosphorus Absorption by the Aquatic Plant (Zizania latifolia),” J. of Japanese Society of Water Treatment Biology, vol.39, Jun.2003, pp.59-66.
[14] Murakami K, Imatomi Y, Komai Y, Nagafuchi O, Seiki T, Koyama T, “Relationship between Annelida and Sedimental Environment in Seto Inland Sea,” J. of Japanese Society of Water Environment, vol.21, Nov.1998, pp.757-764.
[15] Yauchi E, Hayami T, Ishii Y, Tatsumoto H, “Environmental Dynamics of Tokyo Bay Act on Yatsu Tidal Flat,” Environmental Information Science. Extra, Papers on Environmental Information Science, vol.17, Nov.2003, pp.327-330.

First International Conference on Geotechnique, Construction Materials and Environment, Mie, Japan, Nov.21-23, 2011, ISBN: 978-4-9905958-0-7 C3051

BioClean and Liquid Biofertilizers a New Way to the Green Area

Sittisak Uparivong, Department of Biotechnology, Faculty of Technology, Khon Kaen University, Thailand.

ABSTRACT: The one selection to solve the problems of severely damaged by the tragic earthquake and tsunami is presenting a new way to green area planet. The aim is to be creating a pilot project to support green area for environmental places living. BioClean and liquid biofertilizer projects are attempting to be a new way for the natural balance of combined green area. This generation of bioclean had produced by the donation of various flowers during the graduated ceremony of khon kaen university since 2010, and adding the 18 zymogenic synthetic microorganisms (18 ZSMs) with molasses as substrate. Furthermore, the liquid biofertilizers had produced as similar processes as bioclean excepting differential raw materials by using the previous research product of liquid biofertilizers, which were produced by using vegetables, fruits, herbal crops, etc. Results of microorganism population of bioclean and liquid biofertilizer products were 1.0 x 10^8 to 8.0 x 10^{12} cfu/ml, which mainly serviced for environmental and agricultural sections, respectively. Including, the both products were presented focus on supporting to the green area for living places and related to climate change. The service result of project products was activated on the event of “Temples Big Cleaning Day 2011” by servicing for cleaning and the green area at the two temples near khon kaen university, which satisfactory result obtained 50% excellence, 30% good and 20% fair by the board of ten committee’s considerations.

Keywords: BioClean, liquid biofertilizer, 18 zymogenic synthetic microorganism (18 ZSMs), temple, green area

1. INTRODUCTION

BioClean is an original brand name of liquid bioextracted flowers since 2003 [10]. BioClean was produced as the similar processes as the production of liquid biofertilizers by fermenting various biomaterials. The difference between bioclean and liquid biofertilizers was the differential raw materials, which liquid biofertilizers were produced by using various combined biomaterials such as; vegetables, fruits, some herbaceous crops, etc., while bioclean was produced by using the diversities of odoriferous flowers (donated various flowers from a graduated ceremony of khon kaen university since 2010) in order to solving the odour problem of liquid biofertilizers that responded by users. The target project of this generation of bioclean was mainly used to service for the example communities of environmental and healthy living to the two temples of adulkaewmordee temple and nonmuang temple at nearly to the regions of khon kaen university in order to servicing for reducing odour treatment such as; on floor temples, sewerage, bathroom/lavatory, wastewater treatment, water quality treatment etc., and liquid biofertilizer services were mainly used to encourage for green area and along the main road of khon kaen university. Furthermore, bioclean could be applied for agricultural sectors as the similar as liquid biofertilizers. Thus, the utilization of liquid biofertilizers were to solve the problem of decay soil by increasing organic biofertilizers into soil land, and to increase quality organic agricultural productions [1], and to quality better life and health safety, and to respond the policy for agricultural products safety to kitchen of the world [3]. The board of 18 zymogenic synthetic microorganisms (18 ZSMs) were consisted of 9 bacteria, 6 fungi and 3 yeast species. The 18 ZSMs was originally selected by Prof.Dr.Chaitat Pairintra at khon kaen university to our research project of “Improvement of the Theparuge’s Liquid Biofertilizer Product” since 2002 [2].

2. MATERIALS AND METHODS

2.1 Materials

The raw materials were used to produce this generation products as 1). To produce bioclean (version 2011) was utilized the donated various flowers during the graduated ceremony of khon kaen university in 2010. 2). To produce liquid biofertilizers (version 2011) were utilized the previous research stocks of original microorganism seeding of liquid biofertilizer biotech-1 and liquid biofertilizer biotech-2 which had been produced by using organic biomaterials such as; vegetables, fruits, herbaceous crops, etc. since 2004-2005 [3]-[5]. 3). The original microorganism seeding of liquid biofertilizer biotech-1 or liquid biofertilizer biotech-2 were produced by the group of 18 zymogenic synthetic microorganisms (18 ZSMs) that was transferred from the microorganism seeding product of a liquid biofertilizer KKU-1 [2]. 4). Molasses was supplied from a sugar cane factory at the local area of udon thani near khon kaen provinces.

2.2 Equipments

The biofermentor equipments utilized to produce this generated products of bioclean and liquid biofertilizers were supported by the previous research equipments such as; a 300-L biofermentor model BT-1 equipped with a stirrer motor ½ hp [2], a 500-L liquid biofermentor model BT-1 equipped with a motor 1 hp and/with/or/without a compressor air supply [3], a 500-L liquid biofermentor model BT-2 equipped with a stirrer motor 1 hp and/with/or/without an air pump supply [5], and a 500-L liquid biofermentor model BT-3 equipped with a stirrer motor 1 hp and/with/or/without an air pump supply [7], as shown in Fig.1.

2.3 Methods

The method to produce bioclean was produced as the same processes method as the production of liquid biofertilizers but excepting only the differential raw materials [8]-[11]. This generation of bioclean (2011) was used variously donated

Fig.1 Liquid biofermentors.

flowers as mention above while liquid biofertilizers were utilized the previous research stocks of original liquid bio-extract of vegetables, fruits, some herbaceous crops, etc., the 3 step processes methods as;

The first step of preparation of original liquid bio-extract (OLB), the all raw materials of variously donated flowers were cleaned and cut into small pieces for fermenting as the ratio as "small pieced flowers : molasses : liquid biofertilizer microorganism seeding (LBMS) of liquid biofertilizer biotech-1 or biotech-2" = 3 : 1 : 1 or 3 : 1 : 2 (w/v), and clean water within biofermentors such as; 75.7, 113.55, 151.4 liters (20, 30, 40 gallons) or more etc., during the retention time of 1 week.

The second step of fermentation, the LBMS product from the first step process was fermented with molasses and clean water as the ratio as "LBMS : molasses : clean water" = 1 : 1 : 40 or 2 : 1 : 40 (v/v) within liquid biofermentors such as; 500, 1000, 1500 liters equipped with/or/without a stirrer motor to produce the fermented liquid bioproduct during the retention time of 2 weeks.

The third step of filtration, the fermented liquid bioproduct (FLB) from the second step process was filtered to obtain the final products as so called "BioClean" or "Liquid Biofertilizers" depending on the differential types of raw materials.

The methods to utilization of bioclean and liquid biofertilizers (including 18 ZSMs) are aimed to the two way of utilization for environmental and agricultural sections as;

1). For agriculture, using the dilution ratio of liquid biofertilizer product at 1:2000 by spraying or pouring to the growth crops every 5-7 days, and the dilution ratio of 1:500 to the plant trees and green area for lively places.

2). For environment, using the dilution ratio of bioclean product at 0.05% (1:2000) for floor cleaning, and the concentration ratio of 70-80% for reducing odour treatment of bathroom/ lavatory/ toilet/ wc./ sewerage etc., and the concentration ratio of 0.05% for wastewater treatment and water quality treatment.

The methods to quality testing of bioclean and liquid biofertilizers were investigated before servicing to the temples and the green area at the regions of khon kaen university as; 1). For agricultural testing, the both products were tested by cultivating for various crops such as; water convolvulus, flowers, etc., 2). For environmental and healthy testing, the both products were tested by treating for sanitary systems such as; reducing odour treatment for bathroom/ lavatory/toilet/wc., sewerage, wastewater treatment and water treatment, including water quality treatment for goldfish and nile tilapiafish living, etc.

2.4 Analysis Methods

The analysis composition of bioclean and liquid biofertilizer products were supported investigation by a laboratory of faculty of agriculture of khon kaen university, and referred to the previous analysis methods of the composition of liquid biofertilizers such as; pH, EC, %OM, N, P, K, Na, Ca, Mg, etc., as in [2]-[7]. Microorganism biomass populations were determined by the method of standard plate count (agar powder, peptone, bacteriological *HIMEDIA RM001*). The quality standard of both products were determined by impact testing for agricultural, environmental and healthy impact assessments. For agricultural testing, the quality of both products were evaluated the growth rate of crops by pots/ fields testing such as; water convolvulus, some flower, etc. For environmental and healthy impact assessments, the quality of both products were evaluated by field testing at sanitary systems such as; reducing odour treatment for bathroom/lavatory/toilet/wc./sewerage at general households etc., and quality testing for the efficiency of water treatment such as; DO, BOD, COD, TKN, etc., at a pond treatment of nonmuang temple near khon kean university.

The analysis methods to evaluate the satisfactory services rating of both products of bioclean and liquid biofertilizers during temples big cleaning day at wat adulkaewmordee and wat nonmuang, and green areas and along main road at the region of khon kaen university, were evaluated by surveying the applied checklist forms of academic service center of khon kaen university, the evaluated methods as following; 1). Evaluation of satisfactory services rating by general persons/ home/shop owner/or/members were evaluated by surveying at around the regions of the both temples. 2). Evaluation of satisfactory services rating by persons and monks were evaluated by surveying at the both temples. 3). Evaluation of satisfactory services rating by the board of expert committees were evaluated by inviting the expert board of ten committee's considerations.

3 RESULTS AND DISCUSSION

3.1 Properties products of BioClean and Liquid Biofertilizers

The products of bioclean and liquid biofertilizers of biotech-1 and biotech-2 (2011) were contained into bottom and tank containers such as; 1-L, 10-L, 20-L, etc., as shown in Fig. 2. The results of effective microorganism populations of bioclean and liquid biofertilizers biotech-1, 2 obtained 1.0 x 10^8 to 4.0 x 10^{12} cfu/ml and 1.0 x 10^8 to 8.0 x 10^{12} cfu/ml after the retention time more than 7-8 day respectively, which be more than the standard products (10^7-10^8 cfu/ml), the properties of both products obtained such as; pH = 3.76, EC = 4.31 ds/m, N = 0.018 ppm, P = 25 ppm, K = 561 ppm, Na = 73 ppm, Ca = 254 ppm and Mg = 200 ppm for bioclean, and pH = 3.45-4.19, EC = 3.00-5.43 ds/m, N = 0.025-14 ppm, P = 28-38 ppm, K = 881-1023 ppm, Na = 108-225 ppm, Ca = 175-271 ppm and Mg = 0.50-142 ppm for liquid biofertilizers biotech-1, 2, as shown in Table 1, and as similar results as the previous research products of bioclean and liquid biofertilizers, as in [2]-[11].

Fig. 2 BioClean and Liquid biofertilizer biotech-2 (2011).

Table 1
Properties products of bioclean and liquid biofertilizers biotech-1, 2.

Product Sample (2011)[a]	pH_w	EC (ds/m)	OM (%)	Total N (ppm)	Total P (ppm)	Total K (ppm)	Total Na (ppm)	Total Ca (ppm)	Total Mg (ppm)
BioClean (donated flowers)	4.32 (1:5)[b]	2.50		10	26	598	82	205	131
BioClean	3.76	4.31		0.018	25	561	73	254	200
Liquid biofertilizer Biotech-1	4.19 (1:5)[b]	3.00		14	28	811	108	271	142
Liquid biofertilizer Biotech-2	3.45	5.43	1.43	0.025	38	1023	225	175	0.50

[a]The generational products were produced since 2011.
[b]The pH_w (1:5).

3.2 Quality Testings of Products

The quality products of bioclean and liquid biofertilizers biotech-1, 2 were satisfyingly evaluated by quality testing before distributing to general users at the pots/fields tests. For agricultural testing, the both products of bioclean and liquid biofertilizers were satisfactory the growth rate of various crops such as; water convolvulus, flower, etc. during 45 days [2]-[11]. For environmental and healthy testing, the both products were satisfactorily evaluated by testing for sanitary systems such as; reducing odour treatment for the bathroom/ lavatory/ toilet/ wc./ sewerage of distributed general households by responding feedback users, and the efficiency bioclean of pond treatment was 61.90% and 89.80% during the retention time of 7 day and 14 day, respectively at a pond treatment of wat non muang near khon kaen university, including water quality treatment by using the dilution ratio of 0.05% bioclean for goldfish and nilefish healthy living.

3.3 Services Rating of Temples Big Cleaning Day

The both products of bioclean and liquid biofertilizers were serviced to the two temples of wat adul kaew mordee and wat non muang near the regions of khon kaen university, as shown in Fig. 3, on the event of “Temples big cleaning day” by using the dilution ratio of bioclean at 1:2000 for floor cleaning, 70-80% for thin coating sewerage/toilet/wc., 0.05% for wastewater treatment or water quality treatment, and using the dilution ratio of liquid biofertilizer biotech-1, 2 at 1:500 for the temples plant trees and green area. The overview services to the both temples were satisfactory results which obtained 44.4% excellence, 33.3% good, 22.2% fair for wat adulkaewmordee, and 50% excellence, 30% good, 20% fair for wat nonmuang after services respectively, which considered by invited the expert board of ten committee’s considerations.

Fig. 3 The Two Temples Big Cleaning Services.

3.4 Services Products to Green Area

The utilization of liquid biofertilizers biotech-1, 2 was serviced in order to being liquid biofertilizers for the green area living and the plant trees along the main road at the regions of khon kaen university by using at the dilution ratio of 1:500, as shown in Fig. 4. The overview services of liquid biofertilizer products were satisfactory for green area living place during May-August, 2011.

Fig. 4 Service of liquid biofertilizer biotech -1 (v.2011) at along the main kku road to the green area living.

4 CONCLUSION

1). BioClean services to the temples

BioClean (v.2011) services from the board of 18 zymogenic synthetic microorganisms (18 ZSMs) could be reduced odour treatment for sanitary systems and communities healthy living places to the pilot temples with satisfactory services.

2). Liquid biofertilizers services to the along main road and the green area

Liquid biofertilizers biotech-1, 2 (v.2011) services from the board of 18 zymogenic synthetic microorganisms (18 ZSMs) could be much more enriched to the plentiful trees of along main road and green area for environmental places living and related to climate change with satisfactory services.

5 ACKNOWLEDGMENT

This research was financially supported by grants from the academic service center of khon kaen university, Thailand. Acknowledgements are extended to the expert board of ten committee's considerations to Mr. Boonyarit Sombutlai, Mr. Rachaporn Patawanit, Mr. Soontorn Sarapanich, Asst. Prof. Dr. Araya Ahromrit, Asst. Prof. Dr. Somsak Pitaksanurat, Assoc. Prof. Dr. Sirinda Yunchalard, and Assoc. Prof. Dr. Pinit Wangsomnuk, Pol. Sub. Lt. Suwith Nampan, Pra Petcharat Kachapanyo, Pra Veerasak Jantemduang.

6 REFERENCES

[1] Pairintra, C. et al. 1991. Zymogenic synthetic soil and crop "Agricultural in the Next New Century". ISBN 974-55-251-3.

[2] Uparivong, S., Prachankanchana, S. and Pairintra, C. 2002. Product development on liquid biofertilizer of the theparuge's agricultural community. J. of Academic Service Center Khon Kaen University. 11 (3): 37-41.

[3] Uparivong, S. et al. 2004. Production of liquid biofertilizer to kitchen of the world. In Proc. The 16th Annual Thai Society for Biotechnology "Innovative Biotechnology: The Opportunity for Kitchen of the World". Phitsanulok, 12-15 December.

[4] Uparivong, S. 2005. The production of liquid biofertilizer. In Proc. Asian Wetland Symposium 2005. Innovative Approaches to Sustainable Livelihood. Bhubaneswar, India, 6-9th February.

[5] Uparivong, S. et al. 2006. Liquid biofertilizer fermentor and microorganism biofermentor of model BT-2. In Proc. Int. Conf. on TISD2006 Technology and Innovation for Sustainable Development Conference. Khon Kaen, Thailand, 25-26 January.

[6] Uparivong, S. 2006. 18 Zymogenic synthetic microorganism of liquid biofertilizer Biotech-3 for agricultural and environmental. In Proc. The 18th Annual Thai Society for Biotechnology. Biotechnology : Benefits & Bioethics. Bangkok, Thailand. 2-3 November.

[7] Uparivong, S. 2007. The development of biofermentor BT-3. In Proc. IAEC2007 International Agricultural Engineering Conference. Theme : Cutting edge technologies and innovations on sustainable resources for world food sufficiency. Asian Institute of Technology (AIT), Bangkok, Thailand, 3-6 December.

[8] Uparivong, S. 2009. BioClean. In Proc. Int. Conf. on Innovations in Agricultural, Food and Renewable Energy Productions for Mankind. The 10th Annual Conference of Thai Society of Agricultural Engineering. 1st-3rd April 2009. Surasammanakhan, Suranaree University of Technology, Nakhon Ratchasima. pp. 173-175.

[9] Uparivong, S. 2009. Utilization of liquid bioferilizer for mandkinds. In Proc. XXXIII CIOSTA CIGRV Conference 2009. Technology and Management to Ensure Sustainable Agriculture, Agro Systems, Forestry and Safety. WORKSHOP IUFRO. Forestry Utilization in Mediterranean Countries with Particularly Respect to Sloping Areas. 17-19 June 2009. Reggio Calabria, Italy. pp. 1391-1395.

[10] Uparivong, S. 2010. BioClean a new friendly environmental cleaning product. In Proc. Int. Conf. Workshop on "Livelihood and Health Impacts of the Climate Change: Community Adaptation Strategies" 24-25 August 2010 Pullman Raja Orchid Hotel, Khon Kaen, Thailand. pp. 122-128.

[11] Uparivong, S. 2010. BioClean for environmental biotechnology of canteens and green area. In Proc. Int. Conf. on Biotechnology for Healthy Living. The 22nd Annual Meeting of the Thai Society for Biotechnology. TSB2010 October 20-22, 2010. Prince of Songkla University, Trang Campus, Trang Province, Thailand. pp. 849-857.

First International Conference on Geotechnique, Construction Materials and Environment, Mie, Japan, Nov.21-23, 2011, ISBN: 978-4-9905958-0-7 C3051

Massive Point Cloud Acquisition on a Soil Surface Using a Stereo Camera

Masafumi NAKAGAWA, Anna NAKANISHI, Hirotaka ENDO and Kenta OCHIAI,
Department of Civil Engineering, College of Engineering, Shibaura Institute of Technology

ABSTRACT: Point cloud data can describe natural objects such as soil. Massive point cloud data acquisition is required for geographic information systems (GISs) and remote sensing to generate environment maps, including surface models. For the contactless measurement of landslides, we believe that a stereo system has some advantages, because it can acquire high spatial resolution data in real time. Therefore, we propose massive point cloud acquisition from soil surfaces using a stereo camera without markers. Although soil surfaces are difficult candidates for image processing, we have verified in indoor experiments simulating landslides that our procedure with constraints can measure a soil surface using a stereo camera. We have also tried to develop a temporal stereo measurement application based on the above procedure. Although our experiments were conducted indoors, we have confirmed that our procedure can be used as a 3D measurement system without markers for moving soil surfaces.

Keywords: Landslide, Stereo measurements, Image matching, Point cloud, Point-based rendering

1. INTRODUCTION

A set of points with geometric X, Y, and Z values is called point cloud data. When point cloud data are registered with a color image taken from a digital camera, each point in the point cloud can hold color information. Because the data can be represented without topological relationships between points, the point cloud can describe natural objects such as soil, rubble and trees. Massive point cloud data acquisition is required for geographic information systems (GISs) and remote sensing to generate environment maps, including surface models and elevation models. Developers of autonomous construction robots are also studying point cloud data acquisition in outdoor environments [1].

Stereo cameras and laser scanners are general survey instruments for acquiring point cloud data in an outdoor environment. The stereo camera can acquire massive point clouds using consumer cameras. Data from a scene can be acquired at 15 or 30 frames per second. However, measurements depend on the density of available feature points in an image. Soil surfaces are difficult to measure correctly, because there are generally few feature points for image processing on the surface. On the other hand, a laser scanner can acquire massive point clouds and does not require feature points. A current high-end scanner can acquire approximately one hundred thousand points per second. However, data acquisition for one scene requires from a few seconds to a few minutes. Thus, in the current state, there are no available 3D measurement systems without markers for moving soil surfaces.

We believe that a stereo system has advantages for soil surface measurement, because it can acquire data in real time. Therefore, we propose massive point cloud acquisition from soil surfaces with homogeneous textures using a stereo camera without markers. In addition, we try to develop a temporal stereo measurement application to represent landslides.

2. METHODOLOGY

In general, when massive point cloud data are acquired with a stereo camera, long processing times are required. In addition, when the measured object is a soil surface, the homogeneous textures in images cause high error rates because of mismatching in the stereo matching step. When landslide animation is generated with temporal point cloud data, 3D soil motion representation is unstable because of the above errors. On the other hand, automated point cloud modification can be achieved with hole-filling approaches [2, 3, 4], although they require long times for massive point processing and error point detection before the modification. Generally, error point detection also requires long processing times. Therefore, we focus on performance improvement to reduce processing time and errors. First, we propose a stable stereo matching procedure based on a coarse-to-fine approach to reduce processing time and mismatching in stereo matching. Second, we propose a temporal stereo matching methodology using some constraints to improve stability in tracking moving surfaces.

2.1 Massive point cloud acquisition from a soil surface

Figure 1 shows our procedure to acquire massive point cloud from soil surfaces. It consists of three components: edge density image generation for feature point distribution; correlation coefficient matching with an epipolar constraint using a circular template; and coarse-to-fine image matching using a spatial constraint with iterative surface model generation.

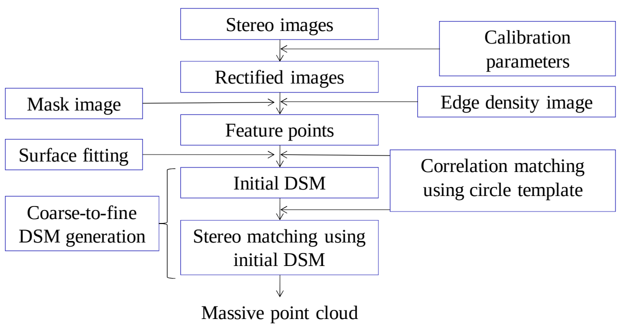

Fig. 1 Stereo matching with coarse-to-fine DSM generation

We extract points with high likelihoods of features from a base stereo image to achieve an accurate matching, because the use of suitable points for image matching can improve matching success rate. First, an edge density image is generated from an edge image taken from the base image. Each pixel in this edge density image expresses the complexity of an edge. Then, feature points with higher edge densities are selected from the edge density image as suitable feature points to generate the initial digital surface model (DSM).

In coarse-to-fine matching in image space, fine matching generally uses higher-resolution stereo images and initial values generated with lower-resolution stereo images [5]. This procedure achieves faster processing and stable matching. However, when there are only a few suitable points for features in an image (e.g., a sand surface), unsuitable points selected for image matching cause many matching errors. Therefore, in this research, coarse-to-fine matching in 3D space is applied to stereo matching, as shown in Fig. 2. First, 3D coordinate values are acquired with correlation matching using only feature points extracted from the edge density image. In our procedure, the sum of absolute difference (SAD) methodology is applied to correlation matching. Second, coarse 3D shaped data are generated as an initial DSM with spatial interpolation such as bilinear interpolation or cubic spline interpolation. Then, corresponding full points in the stereo reference image are searched for under the DSM constraint, as described later.

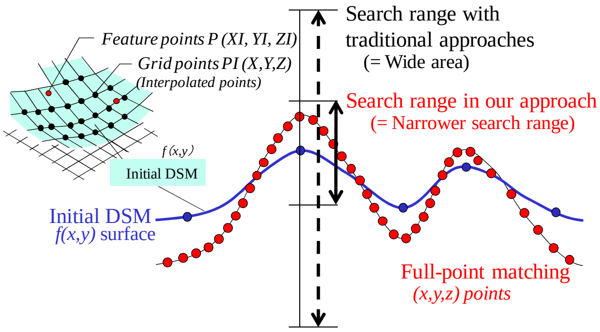

Fig. 2 Coarse-to-fine DSM generation

2.2 Moving soil surface tracking

The tracking of a moving soil surface is processed using temporal stereo image matching in the two steps of stereo matching and temporal image matching. Our temporal stereo matching consists of a clockwise matching flow and an anticlockwise matching flow, as shown in Fig. 3. Temporal stereo images extracted at times t0 and t1 are arranged in a vertical direction in the figure. Image coordinate values x and y are translated to A_* or B_*.

In the clockwise matching flow, the corresponded point (A_{Rt1}) is detected in the right image at time t1 after image matching in the right image at time t0. In the anticlockwise matching flow, the corresponded point (B_{Rt1}) is detected in the right image at time t1 after image matching in the left image at time t1. When A_{Rt1} is equal to B_{Rt1}, image matching is successful. If A_{Rt1} is different from B_{Rt1}, this result can be rejected as a matching error.

In addition, three constraints are implemented to reduce mismatching. The first constraint is an epipolar constraint. When stereo images are rectified using camera calibration parameters, the search range can be limited to the horizontal direction of feature points. The second constraint is the DSM constraint, which makes the search range narrower along the epipolar line. The third constraint is a motion constraint. This constraint depends on objects. For example, when a sand flow such as a landslide is an object, a search region in the image can be limited to downward from the initial feature point, because the sand flow moves downward.

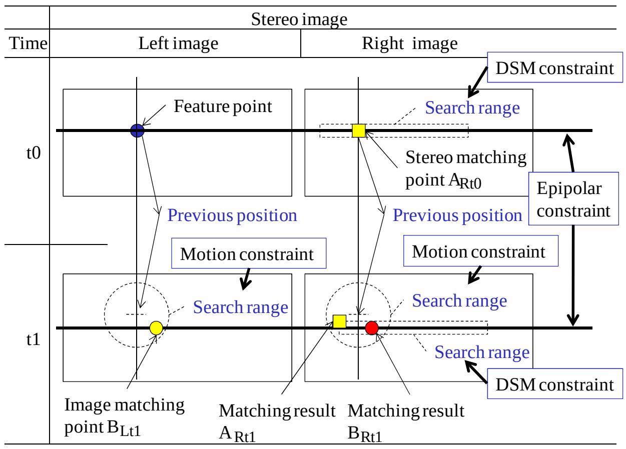

Fig. 3 Our matching methodology with mismatching rejection using temporal stereo images; A_{Rt0}, A_{Rt1}, B_{Lt1} and B_{Rt1} indicate image coordinate values (i.e., A_{Lt1} is an image coordinate value in the left image at time t1)

3 EXPERIMENT

We conducted an indoor experiment, as shown in Fig. 4. We first prepared a stereo camera consisting of two digital cameras controlled by a PC. These cameras were assembled and calibrated to satisfy the required measurement accuracy, as shown in Table. 1.

Fig. 4 Experimental environment

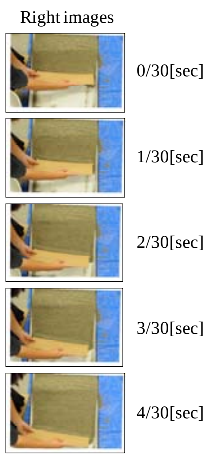

Fig. 5 Acquired sequence images

Table. 1 Stereo camera specification

Camera	Nikon D300
Focus length	35 mm
Baseline	15 cm
Distance from camera to object	150 cm
Measurement accuracy	0.20 mm(RMSE)
Image size (still capture mode)	1072 × 712 pixel
Image size (30fps mode)	640 × 426 pixel

We also prepared sand of approximately 1 mm particle size in a tray as the measured object. The stereo camera then captured this sand object. In this operation, we inclined the sand tray from 30° to 45° to create a sand flow to simulate a landslide. Sequenced stereo images were acquired at 30 frames per second using the stereo camera, as shown in Fig. 5.

4 RESULTS

Feature extraction, 3D measurement and temporal image matching were conducted in our experiment for massive point cloud acquisition on a soil surface using a stereo camera. First, a result for feature extraction in the initial DSM generation is shown in Fig. 6. The left image shows a color image used as input data, the center image shows an edge density image taken from a region selected manually in the input data, and the right image shows the result of the masking procedure on the edge density image. These results show that feature points can be extracted from higher edge density values indicated as white areas in the edge density image.

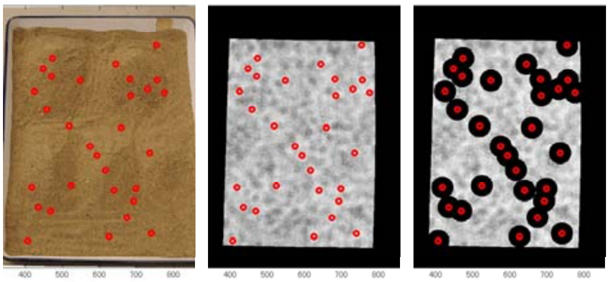

Fig. 6 Result for feature extraction for initial DSM generation

Second, 3D measurement results after stereo matching are shown in Fig. 7. The left image shows a result of the traditional approach without coarse-to-fine DSM generation in stereo matching, and the right image shows a result with our methodology.

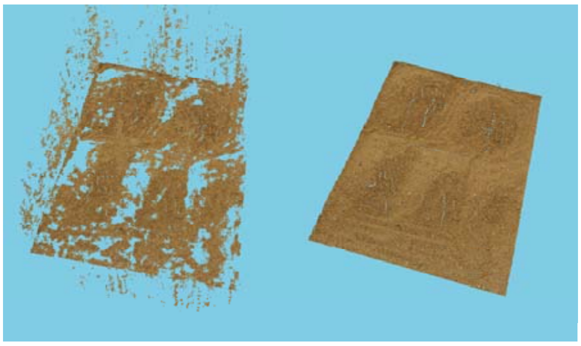

Fig. 7 Comparison of our approach with the traditional approach for 3D measurement results

Finally, Fig. 8 shows a result of temporal image matching using 58 frames taken at 30 frames per second on the left image coordinates. The blue line shows a tracking result using 390 distributed feature points on the moving sand surface.

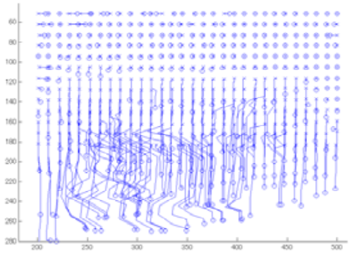

Fig. 8 Result of temporal image matching

5 DISCUSSION

The stereo measurement accuracy was 0.20 mm, as described above. Thus, our approach should be considered in terms of performance improvement in matching success rate and processing time. In addition, corresponding feature points from images selected manually are hard to use as true values for validation, because it is difficult to find objects manually in soil surfaces with homogeneous textures. Therefore, some performance comparisons of our approach with traditional approaches are included in our validations.

Although soil surfaces with homogeneous textures are also difficult candidates for image processing, we have verified that our procedure with constraints can measure a soil surface using a stereo camera in indoor experiments simulating landslides, as follows.

First, we have verified the accuracy of the matching procedure. Figure 9 shows a comparison of our approach with the traditional approach in 3D measurement results projected onto the Z-plane. The left image shows the result for the traditional approach, and the right image shows the result for our approach. With the traditional approach, the result includes some matching errors, shown as holes in the left image. On the other hand, the results for our approach show no holes, as shown in the right image.

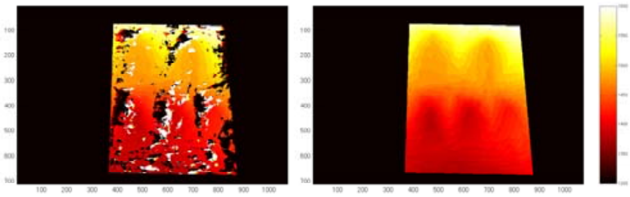

Fig. 9 Comparison of our approach with the traditional approach for 3D measurement results projected onto the Z-plane

We have subtracted the results from our approach from the results of the traditional approach, and calculated absolute subtracted values to measure the matching error, as shown in

Fig. 10. The subtracted values in 3D space are colored as matching error values with an index from 0 mm to 60 mm; the white region indicates a matching error of more than 60 mm. The results can clearly be classified as correctly matched or mismatched.

In addition, we have counted the pixels taken from the region selected in the input image to compare our approach with the traditional approach as errors. The number of pixels taken from the region selected in the input image was 279,818 points. Of these, 181,720 points are within a 5 mm gap, and 196,347 points are within a 10 mm gap.

This numerical comparison indicates that the matching success rate for the traditional approach in 3D data generation is from 60% to 70%, while our approach can reduce mismatching error by between 30% and 40%.

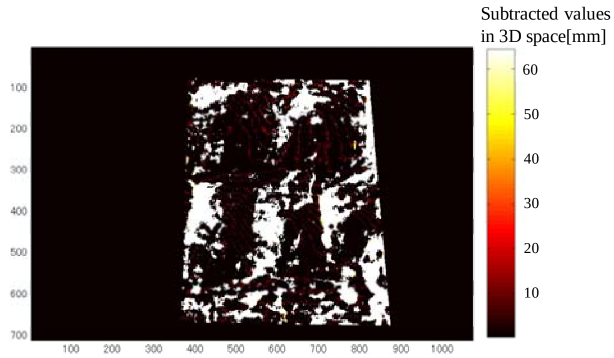

Fig. 10 Subtracted 3D measurement result projected onto the Z-plane

Second, we have compared the processing time for our approach with that for the traditional approach, as shown in Table. 2. The search range could be narrowed from 800 mm to 100 mm in our experiment. As a result, although the performance comparison depends on the parameter settings, such as the range for matching, Table. 2 shows that our approach performed about 10 times faster than the traditional approach.

Table. 2 Processing time comparison of our approach with the traditional approach in processing time

Measured points : 280,000 Intel Core i7 2.80 GHz ／Single-core／MATLAB	Traditional approach Stereo matching from Z = 1100 mm to Z = 1900 mm	Our approach Stereo matching with initial DSM ± 50 mm
Edge density image generation	-----	25 s
Initial DSM generation	-----	3 s
Stereo matching (Sub-pixel matching)	2247 s	195 s
Total	2247 s	223 s

Third, we have compared the performance for our approach with that for the traditional approach for temporal stereo measurement and tracking. The 3D feature tracking results for the moving sand surface are shown in Fig. 11. The blue lines indicate the 3D feature tracking results of 390 points on the moving sand surface in 58 frames, and the Z-axis is the depth direction from the stereo camera. We have verified that matching errors given by the traditional approach have been rejected automatically with our approach.

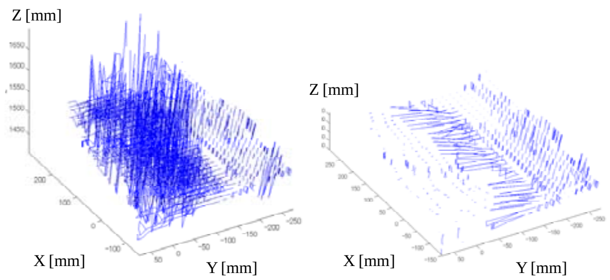

Fig. 11 Comparison of our approach with the traditional approach for 3D feature tracking results of moving sand surface shown as blue lines; the left image is the result for the traditional approach, while the right image is the result for our approach

6 CONCLUSION

We have proposed massive point cloud acquisition from soil surfaces with homogeneous textures using a stereo camera without markers. Although soil surfaces are difficult candidates for image processing, we have verified that our three-component procedure can measure a soil surface using a stereo camera in indoor experiments simulating landslides. We have also developed a temporal stereo measurement application based on the above procedure. Although our experiments were conducted indoors, we have confirmed that our procedure can be used as a 3D measurement system without markers for moving soil surfaces.

7 REFERENCES

[1] Shiegru Sarata, Niriho Kiyachi, Kazuhiro Sugawara, “Measuring and Update of Shape of Pile for Loading Operation by Wheel Loader”, The 25th International Symposium on Automation and Robotics in Construction. ISARC, pp. 113–118, 2008.

[2] Wei, Z. Shuming, Gao. Hongwei, Lin., “A robust hole-filling algorithm for triangular mesh”, The Visual Computer, 23(12): 987-997, 2007.

[3] Zoltan, C.M. Radu, B.R. Michael, B., “On Fast Surface Reconstruction Methods for Large and Noisy Point”, Robotics and Automation, ICRA '09, IEEE International Conference: 3218 -3223, 2009.

[4] Lars, L., Karsten, M. & Paul R., “Splat-based Ray Tracing of Point Clouds”, Journal of WSCG, Vol.15, Issue: 1-3: 51-58, 2007.

[5] Masafumi NAKAGAWA, Ryosuke SHIBASAKI, “Development of Methodology for Refining Coarse 3D Urban Data Using TLS Imagery”, International Society for Photogrammetry and Remote Sensing, 2004.

First International Conference on Geotechnique, Construction Materials and Environment, Mie, Japan, Nov.21-23, 2011, ISBN: 978-4-9905958-0-7 C3051

Estimation of Earthquake Ground Motion in Padang, Indonesia

R.R. Rusnardi. J. Kiyono. Y. Ono., Graduate School of Engineering, Kyoto University, Japan., Department of Urban Social Systems and Civil Engineering, Tottori University, Japan

ABSTRACT: Several powerful earthquakes have struck Padang during recent years, one of the largest of which was an M 7.6 event that occurred on September 30, 2009 and caused more than 1000 casualties. Following the event, we conducted a questionnaire survey to estimate the shaking intensity distribution during the earthquake. About 500 residents of Padang were interviewed. The residents received explanations for each item on the questionnaire from the interviewers, and answers were filled in directly on the answer sheets. From this survey we produced a map of the shaking intensity distribution in Padang. In addition to the questionnaire survey, we performed single observations of microtremors at 110 sites in Padang. The results enabled us to estimate the site-dependent amplification characteristics of earthquake ground-motion. We also conducted a 12-site microtremor array investigation to gain a representative determination of the soil condition of subsurface structures in Padang. From the dispersion curve of array observations, the central business district of Padang corresponds to relatively soft soil condition with Vs_{30} less than 400 m/s, the predominant periods due to horizontal vertical ratios (HVSRs) are in the range of 2.0 to 4.0 s, and the seismic intensity obtained is upper 5 (5+) in the JMA_i scale. By making these observations, we can obtain a relationship between soil types, predominant periods and seismic intensities.

Keywords: peak ground acceleration, seismic intensity of the Japan Meteorology Agency, Padang Earthquake, microtremor observations.

1. INTRODUCTION

Seismic intensity is one of the simplest and most important parameters for describing the degree of ground shaking during an earthquake. Sometimes it has a strong correlation with the human response to ground shaking, observations of damage, and earthquake effect. In this study, we adopt the seismic intensity scale of the Japan Meteorology Agency (I_{JMA}) scale, an instrumental seismic intensity that was first adopted in Japan after the 1995 Kobe earthquake. Its scale runs from 0 to 7, with ten classes including lower 5, upper 5, lower 6 and upper 6. We propose the use of the instrumental I_{JMA} to make initial and fast estimations of damage following a seismic event.

The city of Padang, located on the west coast of Sumatra in western Indonesia, lies close to the Sumatran subduction zone that is formed by the subduction of the Indo-Australian Plate beneath the Eurasian Plate. Relative motion of the plates occurs at a rate of about 50 to 70 mm/year and this is the main source of subduction-related seismicity in the area [1]. Based on our catalog, seven giant earthquakes have occurred in this region since records began: 1779 (Mw 8.4), 1833 (Mw 9.2), 1861 (Mw 8.3), 2004 (Mw 9.2), 2007 (Mw 7.9 and 8.4) and 2009 (Mw 7.6). The hypocenter of the Padang earthquake that occurred on September 30, 2009 was located in the ocean slab of the Indo-Australian Plate at -0.81°S, 99.65°E and at a depth of 80 km. It produced a high degree of shaking and the tremor was felt in the Indonesian capital, Jakarta, about 923 km from the epicenter. The tremors also were felt in neighboring countries such as Malaysia and Singapore [2]. The earthquake caused landslides and collateral debris flows in the hills surrounding Lake Maninjau. A major landslide in Gunung Nan Tigo, Padang Pariaman completely destroyed some villages and forced road closures.

This 1900-km-long active strike-slip fault zone that runs along the backbone of Sumatra poses seismic and fault hazards to a dense population distributed on and around the fault zones [3]. The Sumatran Fault is highly segmented. It consists of 20 major geometrically defined segments and the slip rate along the fault increase to the northwest, from about 5 mm/yr [3]. This fault also has generated large destructive earthquakes, e.g., 1892 (Mw 7.1), 1943 (Mw 7.6) and 2007 (Mw 6.4). These faults are capable of generating strong ground motion in the future that would greatly affect vulnerable structures. According to our catalogs, the Sumatran Fault produces a very high annual rate of earthquakes, many of which occur in the shallow region under the island of Sumatra (**Fig. 1**).

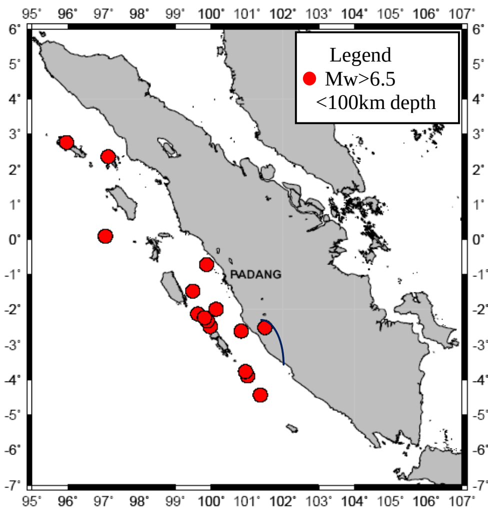

Fig.1 Seismicity of Sumatra Island from 2005 to 2010, Mw>6.5, <100km depth, and Padang city

2. REGIONAL GEOLOGY AND RECENT EARTHQUAKES

The city of Padang, with a population of 856,814 people as of 2008, is the capital of West Sumatra province. The location of the city center is at 100.38°E, 0.95°S. The main part of Padang is situated on an alluvial plain between the Indian Ocean and the mountains. For the most part, the mountainous area is formed of Tertiary sedimentary rocks with outcrops of metamorphic rocks seen in some places. The alluvial plain spreads along the base of the mountains and is roughly 10 km wide in the east-west direction and 20 km wide in the north-south direction.

The topography of the Padang region (**Fig.4(a)**) is very similar to the tsunami-damaged area of Miyagi Prefecture in Japan, that was inundated by as much as 4-5 km from the coast after the March 11, 2011 Mw 9.0 Tohoku earthquake off the east coast of Honshu. In Padang, about 600,000 people live in the coastal area (covering about 60 km^2). The population density is very high, about 8500 people/km^2. The city is located on the coast of the Indian Ocean between the Sumatran Fault and the Sunda Trench Fault. Both faults are active with slip rate ranging from 10 to 27 mm/year [3]. According to our catalog, 2995 events with a magnitude greater than 4 occurred in this region from AD 1779 to 2010. The seven giant earthquakes mentioned previously have all been strongly felt here. For example, the source of the 2009 Padang earthquake was located in the ocean slab of the Indo-Australian Plate.

It produced extensive shaking and severe damage to houses and buildings in Padang and Padang Pariaman, because its epicenter was about 60 km offshore from Padang (**Fig. 2(a)**). As the Padang earthquake was an intra-slab earthquake at intermediate depth with a comparable magnitude, the event did not generate a tsunami of significance [4]. Due to this earthquake, 1117 people were reported killed, 1214 severely injured, 1688 slightly injured, and 3 were left missing in West Sumatra. The earthquake also destroyed many houses, buildings and infrastructure (heavily damaged houses numbered 114,797, with 67,198 moderately damaged and 67,837 slightly damaged). In Padang, 5458 buildings sustained damage [5]. This event occurred at the end of the working day, just 15 minutes after offices and schools closed; if it had struck earlier, the number of causalities would definitely have been higher as a result of building collapses. Several hours after Padang earthquake, 1st October 2009, Sumatran fault line generated Mw7.1 and 10km depth. Due to this earthquake destroyed many houses and building (heavily damaged houses numbered 600, with 550 moderately damaged). **Fig.2(a)** shows Padang earthquake and Kurinci earthquake.

There are four accelerometers in Padang. Three were donated by Engineers Without Borders Japan (EWBJ) and installed in 2008, and the other was installed by the Indonesian Government's Bureau of Meteorology, Climatology and Geophysics (BMKG). However, only one ground motion record is available for the Padang earthquake. Due to an electric power cut during the earthquake, only the BMKG device recorded the time history of the earthquake. The observed record shows about 20 s of strong shaking with a peak ground acceleration (PGA) of 0.3 g and a predominant period of 0.5 s (**Fig. 2(b)**). response spectra at law period is greater then Indonesia code for rock condition (0.83g) (Fig.2b).The location of this station is a mountainous suburb about 12 km in from the coast. The subsurface condition at this station is rocky; the average shear wave velocity for the upper 30 m of the subsurface here, V_{s30}, is 1200 m/s [6].

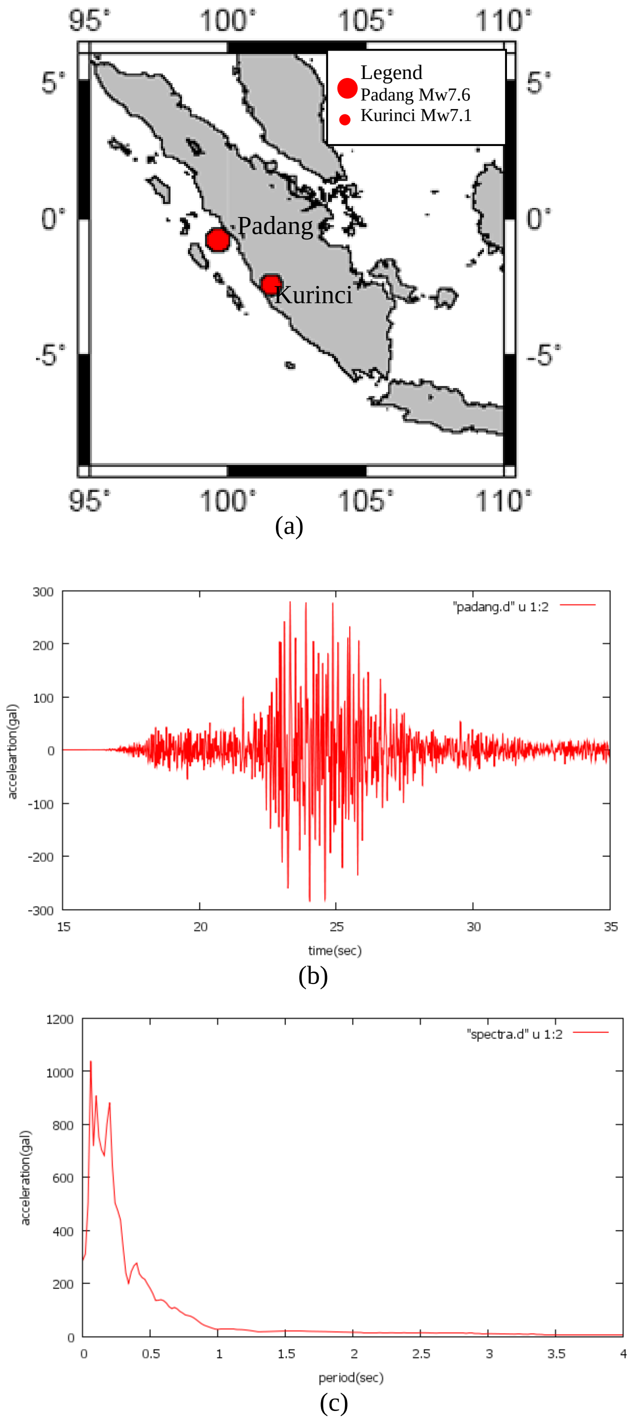

Fig.2 Seismicity and time series. (a) two giant earthquake in Padang and Kurunci, (b) time series of Padang earthquake, (c) response spectra due to Padang earthquake.

The paucity of measured ground motion information for this earthquake results in a need for transforming observed data (seismic intensity) into parameters that are more useful for engineering purpose (e.g., engineering ground-motion measures)[7]. From seismic intensity, we can evaluate historical earthquakes, assess seismic hazard and damage, correlate different intensity scales, and rapidly assess the severity of ground shaking [8]. In additional, we performed a 12-site microtremor array observations to determine the shear velocity of subsurface structures at several districts in Padang. From these observations, we obtained relationship between soil types, predominant period and seismic intensity.

3. DAMAGE FROM THE 2009 PADANG EARTHQUAKE

The city of Padang covers an area of about 695 km^2 and is divided into 11 districts: B. T. Kabung, K. Tangah, Kuranji, L. Begalung, L. Kilangan, Nanggalo, P. Barat, P. Selatan, P. Timur, P. Utara, and Pauh. 51.0% of the land is forested, 28.52% is used for farming, 9.54% for housing and 7.1% for rice fields [9]. The population of more than 857,000 is increasing by 2% per year. The K. Tangah district has the highest population and most extensive area compared with the other districts in the city.

The central business area of Padang is close to the coast and consist of several districts: P. Barat, P. Utara, P. Selatan and P. Timur, B.T. Kabung, K. Tangah. The downtown area is utilized as a center of political and commercial activities. Although the Padang earthquake affected all districts of the city, the major damage occurred downtown, because about 80% of population lives near the coast.

The majority of houses in the city are one- and two-storey non-engineered structures. These structures are typically built of confined masonry, with reinforced-concrete (RC) frames acting as confinement for the brick masonry walls. There are three general categories of houses in Padang: permanent houses (RC), semi-permanent houses (mix of RC and wood) and traditional houses (wood). Unfortunately, no detailed damage statistics are available for each type of building, so we cannot classify the category of the house.

This earthquake also affected lifelines in Padang. The strong ground shaking destroyed public water distribution pipes leading to 2,906 reported leakage points in total [10]. Damage to pipelines forced the cessation of water delivery to consumers for several weeks.

4. SITE CHARACTERIZATION BY MICROTREMOR OBSERVATION

4.1 SINGLE OBSERVATIONS

A microtremor is a very small ground motion that can be recorded on the ground surface. It can be produced by a variety of excitations (e.g., wind, traffic, breaking sea waves). A full microtremor record can be described by one vertical and two horizontal components. Our analysis was conducted using the recorded microtremor. First, the horizontal and vertical spectrum ratios (HVSR) were computed for all sites (**Fig. 3)**. The peak period of the HVSR is known to correspond to the resonant period of the site. This method postulates the shape of the Fourier spectrum [11].
Equation. (1) shows the method used to calculate HVSR using the observed records.

$$HVSR= \sqrt{\frac{F_{NSi}(\omega)^2+F_{FWi}(\omega)^2}{F_{UDi}(\omega)^2}} \tag{1}$$

where $F_{NSi}(\omega)$ and $F_{UDi}(\omega)$ denote the Fourier amplitude of the NS, EW and UD components of each interval, respectively, and ω is the frequency.

We performed 110 single site surveys that sampled every district of the city of Padang. These observations were carried out in November 2008, September, November, and December 2009 and January 2010. The locations of observations are plotted in **Fig.3**. Microtremor was measured using a GPL-6A3P sensor. The two horizontal (NS and EW) and the vertical (UD) components were recorded simultaneously for 10 minutes with a 100 Hz sampling frequency.

We estimated the distribution of the peak periods of the HVSRs for all sites in Padang using the ordinary kriging technique (**Fig.3**). From single observations, we obtained a predominant period of 2.0 to 4.0 s in the central business district and less than 1.0 s in the mountainous areas. These results indicate an affect related to the thickness of alluvium in the coastal area of Padang city, which decreases in thickness inland.

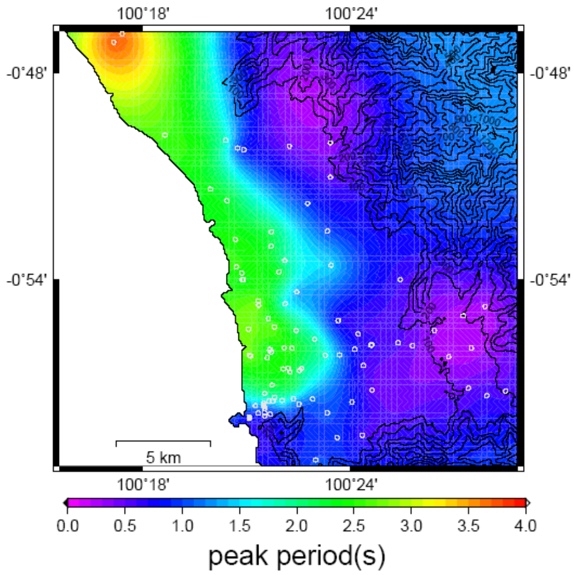

Fig. 3 white circles are single observation sites, result HVsRS ratio

4.2 MICROTREMOR ARRAY OBSERVATIONS

The velocity of surface waves is well known to vary as a function of frequency (or period) due to dispersion. Since dispersion is a function of subsurface structure, the substructure can be estimated from a Rayleigh wave dispersion curve. We carried out microtremor array investigations using 12 sites at several districts in Padang (**Fig.4(a)**). Dispersion curves were calculated using the SPAC method [12] to obtain a velocity structure from the microtremor recordings. An outline of the procedure follows. It is necessary to simultaneously record microtremors with an instrument array of at least three stations. The dispersion of a measured surface wave is a response to the subsurface structure directly below the array, and the estimation of the subsurface structure causing the dispersion is determined by means of inversion of Rayleigh waves. The basic principles of the SPAC method assume that the complex wave motions of microtremors are stochastic processes in time and space. A spatial autocorrelation coefficient for a circular array can then be defined when the waves composing the microtremor (i.e., the surface waves) are dispersive. Hence, the spatial autocorrelation is a function of phase velocity and frequency. Rayleigh wave records were measured for the 12-array observation sites using the SPAC method and inversion analysis was undertaken on the observed dispersion curves to estimate the soil profiles. In the inversion analysis, the Particle Swarm Optimization (PSO) algorithm was adopted to solve the non-linear optimization problem [13]. The basic procedures of PSO are outlined below.

We estimate the subsurface structure of the model by solving a nonlinear minimization problem with the fitness function below.

$$v_{id}^{t+1} = \omega\, v_{id}^{t} + c_1 r_1 (p_{id}^{t} - x_{id}^{t}) + c_2 r_2 (p_{gd}^{t} - x_{gd}^{t}) \tag{2}$$

$$x_{id}^{t+1} = x_{id}^{t} + v_{id}^{t+1} \tag{3}$$

where v_{id}^{t} is particle velocity of the i^{th} component in dimension d in the interaction, x_{id}^{t} is the particle position of the i^{th} component in dimension d in interaction, c_1 and c_2 are constant weight factors, p_i is the best position achieved by particle i, p^g is the best position found by the neighbor of particle i, $r_1$and r_2 are random factors in the [0,1] interval and ω is the inertia weight. Before performing the inversion analysis, the subsurface structure was assumed to consist of horizontal layers of elastic and homogeneous media above a semi-infinite elastic body. The shear wave velocity and thickness of each layer are the parameters determined by the inversion analysis. The results enable us to determine the condition of shallow subsurface structures [14]. The outline of the SPAC method for the phase velocity calculation of Rayleigh waves follows. The spatial autocorrelation function is defined as

$$\emptyset(r,\theta,\omega) = \overline{u(0,0,\omega,t) * u(r,\theta,\omega,t)} \tag{4}$$

where $\overline{u(t)}$ is the average velocity of the wave in the time domain, and the harmonic waves of frequency ω of the microtremor have the velocity wave forms $u(0,0,\omega,t)$ and $u(r,\theta,\omega,t)$, observed at the center of the array $C(0,0)$ at point $X(r,\theta)$ on the array.

The spatial autocorrelation coefficient ρ is defined as the average of the autocorrelation function $\emptyset$ in all directions over the circular array:

$$\rho(r,\omega) = \frac{1}{2\pi\emptyset(0,\omega)} \int_0^{2\pi} \emptyset(r,\theta,\omega)d\theta \tag{5}$$

where $\emptyset(0,w)$ is the SPAC function at the center $C(0,0)$ of the circular array. By integration of the Equation. 5 we obtain

$$\rho(r,\omega) = Jo\left(\frac{\omega r}{c(\omega)}\right) \tag{6}$$

where $Jo(x)$ is the zero-order Bessel function of the first kind of x, and $c(\omega)$ is the phase velocity at frequency ω. The SPAC coefficient $\rho(r,\omega)$ can be obtained in the frequency domain using the Fourier transform of the observed microtremors.

$$\rho(r,\omega) = \frac{1}{2\pi} \int_0^{2\pi} \frac{Re[S_{Cx}(\omega,r,\theta]}{\sqrt{S_C(\omega).S_X(\omega,r,\theta)}} d\theta \tag{7}$$

where $S_c(\omega)$ and $S_x\,(\omega,r,\theta)$ are the power densities of the microtremor at sites C and X respectively, and $S_{CX}(\omega,r,\theta)$ is the cross spectrum between ground motions at these two sites. Thus the SPAC coefficients may be obtained by averaging the normalized coherence function defined as the spectrum between points C and X in the direction θ. From the SPAC coefficient $\rho(r,\omega)$, the phase velocity is calculated for every frequency from the Bessel function argument of Equation. 6, and the velocity model can be inverted**.**

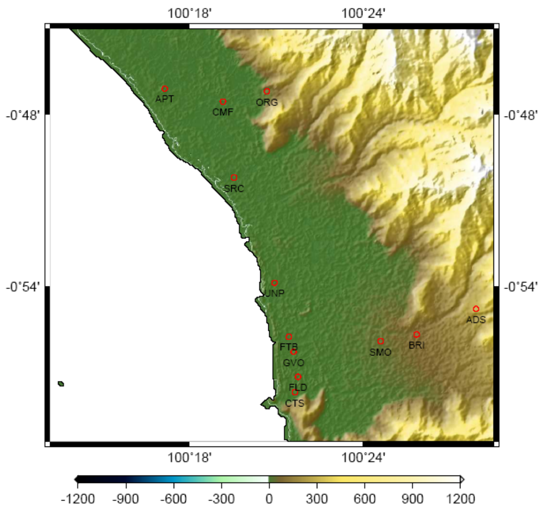

Altitude

(a)

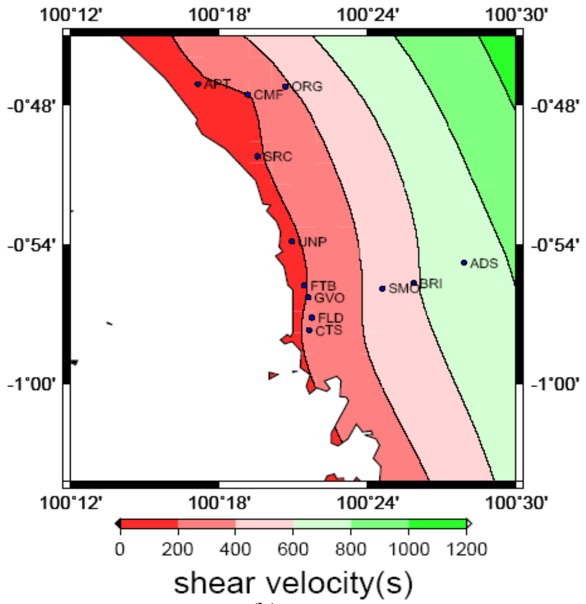

(b)

Fig.4 Observation sites and distribution of average shear wave velocity, (a) Array observation sites, (b) Contour of V_{s30} (m/sec)

5 SHAKING CHARACTERISTICS BY QUESTIONNAIRE SURVEY

5.1 Survey Outline

Seismic intensity has been used to quantify the severity of the ground shaking based on the observed or felt effect in a limited area [7]. The method was originally developed by [15] and has been widely applied to the development of seismic macro or micro zoning maps in Japan since 1970. The method has also been applied in India and Indonesia by Honda in 2005. It has been useful for estimating seismic shaking in a limited area and for determining intensity distributions over local areas [7]. The original questionnaire sheet was written in Japanese; however, it was translated into Indonesian, for its application to Aceh. The questionnaire has 35 items that cover recognition of shaking, location, shaking duration, possibility of movement, structural damage, swinging of hanging objects, and 27 other items.

For the 2009 Padang earthquake, some sentences were modified to make it more relevant for local people while not changing the original topics covered by the questionnaire. People living near the observation points were interviewed using the questionnaire [15]. The questionnaire survey was conducted from December 24 to 31, 2010, three months after the main shock. The survey was carried out in all districts of Padang by distributing and completing 500 questionnaires through a direct interview process with residents of the city. The interviewers explained each item of the questionnaire to residents, discussed the responses given, and documented the answers on the standard answer sheets.

5.2 Estimation of JMA Intensity

The calculation of the seismic intensity determined by the questionnaire is described as:

$$IQ \;= \frac{1}{N_e}\sum_i^{n_q}\beta_i(m_i) \quad (8)$$

where m_i is chosen by a respondent for the ith question (e.g., i=12 and m_{12}=12), $\beta_i(m_i)$ is a seismic coefficient, n_q is the number of effective questions of each questionnaire and N_e is the number of responses from all questions. To obtain the JMA intensity (I_{JMA}), the result from Equation. 8 is inserted into Equation.

$$I_{JMA=2.958\ x\ (I_Q-1.456)^{0.547}} \quad (9)$$

Finally, to obtain the JMA intensity (I_{JMA}) for each district, the calculation for each questionnaire is averaged as follows.

$$I_{JMA} = \frac{1}{N}\sum_{i=1}^{N} I_{JMA(i)} \quad (10)$$

where N is number of questionnaires in one location, and $I_{JMA(i)}$ is the seismic intensity for each questionnaire.

The results of the questionnaire survey conducted to estimate the shaking intensity distribution in Padang during the earthquake are summarized in mapped. The results of the questionnaire survey conducted to estimate the shaking intensity distribution in Padang during the earthquake are in mapped. The seismic intensity (I_{JMA}) for the suburbs and downtown were lower 5 (5^-) and upper 5 (5^+) respectively (**Fig.5**). A JMA seismic intensity, I_{JMA}, value of 5^- corresponds to 4.5< I_{JMA} <5.0 and 5^+ equates to 5.0< I_{JMA} <5.5. A value of 5^+ corresponds to very strong ground motion where many people are considerably frightened and find it difficult to move. Non-engineered structures sometimes collapse, walls crack, and gravestones and stone lanterns overturn. A value of 5^- corresponds to strong ground motion. Many people are frightened and feel the need to hold on to something stable. Occasionally, less earthquake-resistant buildings suffer damage to walls, and windows may break and fall. The distribution of various intensity values came from differences in the subsurface structural conditions of each district.

5.3 SHAKING CHARACTERISTICS

By comparing the results of the 500 questionnaires of the seismic intensity survey with microtremor observations (110 single-site observations and numerous other 12-site array observations), we found a correlation, in which the subsurface area or site is seen to correspond to the soft soil condition (which we here define as V_{s30}<400 m/s) that exceeds the predominant period. This area corresponds to the thick alluvium in the coastal area of Padang.

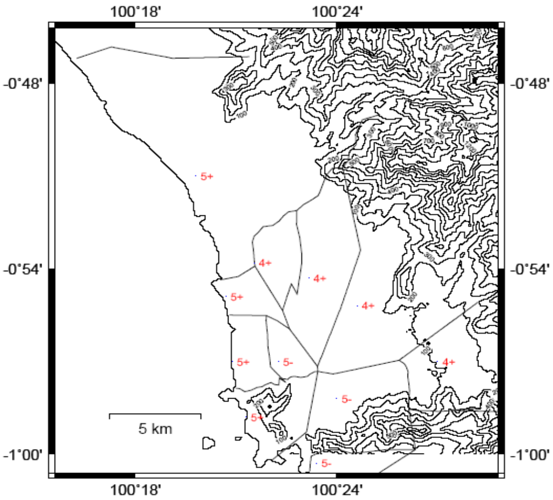

Fig.5 Average seismic intensity

The thickness of the alluvium gradually decreases in a landward direction from the coast. As a result, greater seismic intensities are observed in the coastal area and the value decreases from coastal to mountain areas. Important information from respondents' answers were collated. The area was divided in two by considering subsurface structure condition: shear velocities V_{s30}<400 m/s, corresponding to soft soil (area 1), and V_{s30}>400 m/s, corresponding to the engineering bedrock conditions (area 2).
The structural type, the age of building, and the number of floors in each of the two areas were found to be generally the same. However, the shaking duration was significantly different.
In area 1, 96% of respondents said that the duration of shaking was longer than 2minutes, but in area 2, only 39% of respondents felt the duration of shaking to be longer than 2 minutes. These observations support the existence of a thick alluvial layer that caused the prolonged shaking that most people living in the coastal area felt during the earthquake.

6 CONCLUSIONS

Our survey conducted in Padang consisted of (1) microtremor observations (single and 12-channel arrays) made before and after the earthquake of September 30, 2009, and (2) a questionnaire survey of 500 people in the Padang area. The central part of the city, consisting of the four districts, P. Utara, P. Barat, P. Selatan and P. Timur, experienced greater seismic intensities (5+) compared with other areas (districts) of Padang.
According to microtremor observations, downtown Padang is underlain by soft soil conditions (V_{s30}<400 m/s). Consistent results concerning the soil condition were found based on predominant period observations and the questionnaire survey. In both cases, the coastal area was determined to have a soft soil conditions (V_{s30}<400 m/s), a longer predominant period, and a greater seismic intensity.
Padang has a thick alluvial layer in the coastal area (with a predominant period between 2.0 and 4.2 s) that thins toward the mountains (with a predominant period less than 2.0 s). The subsurface geology also changes slowly from soft soil in the coastal area to rocky conditions in the mountains. The seismic intensity decreases from the coastal area (5+) to mountains (4+).
These results provide critical information for making shaking maps, updating hazard maps, and developing disaster prevention countermeasures in Padang.

REFERENCES

[1] Prawirodirjo, L., Y. Bock, J.F. 2000, *One Century of Tectonic Deformation along the Sumatran Fault from Triangulation and Global Positioning System Surveys*, J. of Geophysical research, 105, 28, 343-28,363.
[3] Natawidjaja and Wahyu Triyoso 2007. The *Sumatran Fault Zone-from Source to Hazard*, J. of Earthquake and Tsunami, Vol. 1 No. 1, 21-47.
[4] EERI 2009. *The M_w 7.6 Western Sumatra Earthquake of September 30, 2009*, Special report.
[5] BNPB 2009. *Total Damage Report and Verification for West Sumatra due to Padang Earthquake*, BNPB report, 2009
[6] Rusnardi, J. Kiyono, Y. Ono. 2010, *Seismic Hazard Analysis for Indonesia*, Proc. of International Symposium on a Robust and Resilient Society against Natural Hazards and Environmental Disasters and the third AUN/SEED-Net Regional Conference on Geodisaster Mitigation, pp.317-325.
[7] Tselentis. G-Akis and LaurentiuDanciu. 2008. *Empirical Relationship between Modified Mercalli Intensity and Engineering Ground-motion Parameters in Greece*, bull. Of the Seismological Society of America, vol.98, No.4, pp.1863-1875
[8] Wald, D.J., V. Quintoriano, T.H. Heaton, H. Kanamori, C.W. Scrivner, and C.B Worden (1999). TriNet"ShakeMaps": R*apid Generation of Peak Ground Motion and Intensity Maps for Earthquake in southern California*, Earthquake Spectra 15, no. 3, 537-555.
[9] Pemerintah kota Padang. availableat at www.Padang.go.id (Padang local government website).
[10] Padang spring water agency, www.pdampadang.co.id
[12] Aki, K. 1957. *Space and Time Spectra of Stationary Stochastic Waves, with Special Reference to Microtremor*, Bull. Earth. Res. Inst., Vol. 35, No. 3, 415-456.
[13] Keneddy, J. and Eberhart, R. C. (1995), *Particle Swarm Optimization*, Proc. Of IEEE International conference on Neural Networks, Vol.4,pp.1942-1948.
[14] Ono, Y., Kiyono, J., Rusnardi, P. R. and Noguchi, T. 2010. *Microtremor Observation in Padang City, Indonesia to Estimate Site Amplification of Seismic Ground Motion*, Proc. of International Symposium on a Robust and Resilient Society against Natural Hazards and Environmental Disasters and the third AUN/SEED-Net Regional Conference on Geodisaster Mitigation, pp.386-391.
[15] Otha, Y., Goto, N., and Ohashi, H., (1979). *A questionnaire Survey for Estimating Seismic Intensity*, full. Fac. Eng., Hokkaido University 92, 241-252 [in Japanese]

First International Conference on Geotechnique, Construction Materials and Environment, Mie, Japan, Nov.21-23, 2011, ISBN: 978-4-9905958-0-7 C3051

Groundwater Contamination Due to Irrigation of Treated Sewage Effluent in the Werribee Delta

Hiroyuki II, Masanobu TANIGUCHI, Ataru SATOH, Faculty of Systems Engineering, Wakayama University, Japan
Graeme ALLINSON, Matt KITCHING, George CROATTO, Bruce SHELLEY, Department of Primary Industry, Victoria, Australia

ABSTRACT: The Werribee River, groundwater and Melbourne's treated sewage effluent (or recycled water) are used for irrigation water in the Werribee Delta. Groundwater beneath the Werribee delta may be contaminated by the recycled water. The mixing ratios of the sea, river and recycled waters in groundwater were calculated from water chemistry and isotopic ratio. Inland of the Werribee Delta the river mixing ratio was very high (70 %) and sea and recycled water mixing ratios were low. At the delta area, some borehole water had a high river mixing ratio, and others a low river mixing ratio and high recycled water ratio (over 60 %). Overall, at the delta area, half of the groundwater had a high mixing ratio of recycled water. The marine origin for Cl^- in the groundwater was very limited, and was only found at the seaward boundary of the delta area. Origin of NO_3^- for groundwater was recycled water and fertilizer at the delta.

Keywords: Oxygen isotope, Recycled water, Sewage irrigation, Estimation of groundwater origin

1. INTRODUCTION

1.1 Study area and Purpose

The Werribee delta area at the west of Melbourne, Victoria, Australia is important for growing vegetables for the city of Melbourne. However, because of small amount of precipitation in the area (average 500 mm per year [1]), the Werribee River, groundwater and recently treated sewage waters from Melbourne (recycled water) have been used for irrigation water. The groundwater used in the delta area is pumped up from 6 to 30 m in depth. A decline of approximately 2m in the aquifer level, and increasing salinity (varied from 2500 to 9000 EC) led to bans and restrictions on ground water use in 2003, in part to mitigate saline intrusion [1]. In 2004 the use of recycled water from Melbourne's Western Treatment Plant began. Approximately 90 % of the irrigators had signed on to receive recycled water in 2008. Although average salinity of recycled water was 2000 EC and less than groundwater EC, groundwater contamination caused by irrigation water is a concern because the recycled water contains trace elements and high nitrogen concentrations. Therefore, in this study, origin of the groundwater was estimated using water chemistry including isotopes and influence of recycled water on groundwater was clarified.

1.2 Recharge area

The upper catchment of the Werribee area consists of Silurian sandstone and mudstone, Devonian granite, Permian glacial tillite, older Tertiary basalt and recent alluvial sand; the middle stream area consists of Pliocene basalt; and the lower stream area consists of recent alluvial sediments [2]. The basement of the middle to lower stream area is Tertiary sediment covered with basalt lava and recent alluvial sediments [3]. The Tertiary sediments are composed of sand, clay and gravel including older volcanics and have high water permeability. The recharge area of delta groundwater was thought to be from the mid-catchment to delta area.

2. METHOD

Sea, river, borehole, recycled and rain waters were studied from 2007 to 2010. Sea water was sampled at the delta coast. Borehole waters were sampled from the middle stream area to the delta area. The Werribee River and its surrounding river waters were sampled. Recycled waters were sampled from irrigation supply channels and drains in the delta. Rain water was sampled at Werribee. Temperature, pH ORP and EC values were measured on site using a portable instrument (HORIBA, pH meter D-54, 55). Samples for anion and cation analysis were filtered through 0.45μm filters and were measured using liquid ion chromatography (DIONEX, DX-ICS, AQ-1500 and ICS-1600). Also HCO_3^- was measured by an acidic titration. Trace elements in the samples were analyzed by ICP-MS (Ultramass ICP-MS, Varian Australia). The oxygen and hydrogen stable isotope ratios of water samples were measured using a mass spectrometric system (Finnigan Mat Delta Plus), followed by the CO_2-H_2O and H_2-H_2O equilibration technique using platinum catalyst. The measured isotopic ratio was calculated using equation (1).

$$\sigma = (R_x / R_{st} - 1) \times 1000 \qquad (1)$$

where R_x is the stable isotopic ratio of x, and R_{st} the stable isotopic ratio of st

3 RESULTS

Groundwater sampled from the boreholes at the delta is thought to be derived from the recycled water, the sea and upper stream recharge water. To estimate the origin of delta groundwater, sea, recycled, and river waters were analyzed. Geologically, the upper Werribee River catchment consists of hard impervious rock, and the mid–catchment is thought to be the recharge area for delta groundwater. River water in the mid-catchment was thus regarded as the recharge water from the upper catchment in data analysis.

3.1 Character of water chemistry for sea, recycled water and rivers

Fig.1, 2 and 3 show the NO_3^-, F^-, and Cl- concentrations of sea water sampled in Port Philip Bay, recycled water from delta drains and channels, and river water sampled at the Werribbe River, Little River, Skelton River, Lerderderg River, Pykes Creek, and Toolern Creek (excluding the lower stream area). The recycled water has extremely high concentrations of NO_3^- (over 100 mg/l). The mixing ratio changes with sampling site and sampling time and so NO_3^- concentration is variable. A high NO_3^- concentration value (100 mg/l) was adopted as the recycled water concentration for data analysis. As the NO_3^- concentration of the river and sea waters, and most groundwater at the delta were very low, the main source of NO_3^- is thought to be treated sewage effluent. A low NO_3^- concentration value (0 mg/l) was adopted as the sea and river water NO_3^- concentration for data analysis. So, NO_3^- was a good indicator of mixing ratio of recycled water because sea and river water concentration were 0 mg/l. However, NO_3^- for groundwater is contaminated by fertilizer at a farm land and contamination must be considered for determining mixing ratio using NO_3^-.

F^- in the recycled water was much higher than in sea and river waters. The origin of F^- for the recycled water was thought to be derived from sewage and F- is stable. So, F^- was also a good indicator of mixing ratio of recycled water. However, as F^- concentrations for recycled and river water were variable, F^- was not used for data analysis.

The sea water had an extremely high concentration of Cl^- (19000 mg/l), relative to the recycled water (450 mg/l), and the river water (50 mg/l). Generally, Cl- was stable and then Cl^- was a good indicator of mixing ratio of sea water.

Fig.4 shows that Oxygen isotopes for the Werribee River and its surrounding river waters, channel water (recycled water before irrigation), and drain water (after irrigation). From the figure, oxygen isotopes were -3.3 per mil for the recycled water and -5.8 per mil for the middle catchment river water. Oxygen isotopes were generally 0 per mil for the sea water. -5.8 per mil for average oxygen isotope of rain water at the delta area was in agreement with those for the middle catchment river water and then oxygen isotope for the catchment area was thought to be -5.8 per mil. Since the isotopic ratio of oxygen for each type of water was different and oxygen isotopic ratio was stable when water reacts with minerals at the low temperature condition, the oxygen isotopic ratio was a good indicator to determine mixing ratios.

3.2 Estimation method of mixing ratio

First, because the Cl^- concentration of the sea was extremely high relative to other waters, Cl^- was used for determining the mixing ratio of sea water. The mixing ratio between sea and river water (recharged water) was calculated using equation (2).

$$Msea1 = (Cl\text{-}sam-50)/(19000-50)*100\% \qquad (2)$$

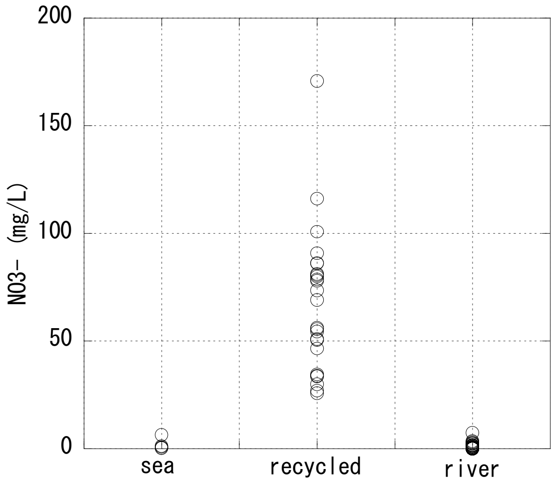

Fig.1 NO_3^- concentration for the sea, recycled and river waters

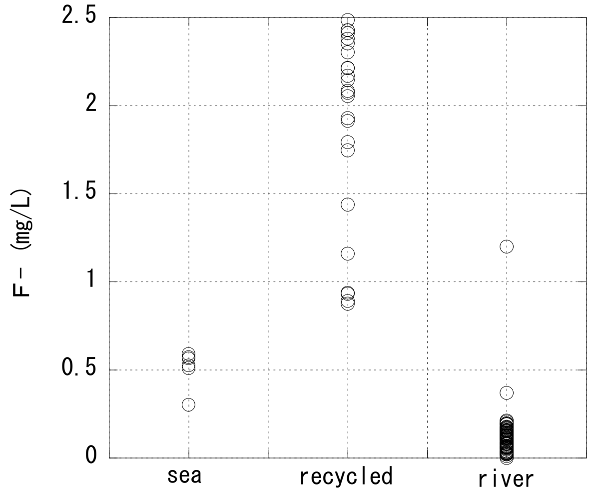

Fig.2 F^- concentration for the sea, recycled and river waters

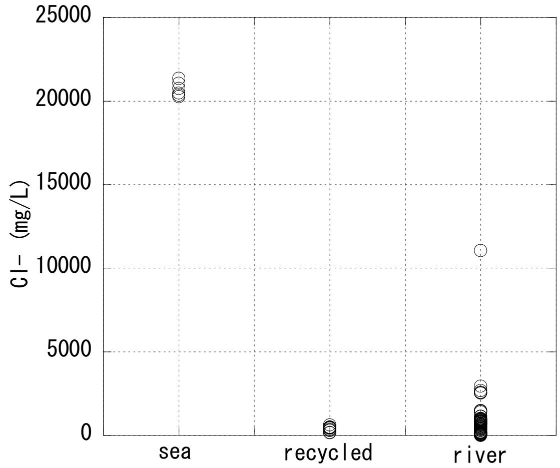

Fig.3 Cl^- concentration for the sea, recycled and river waters

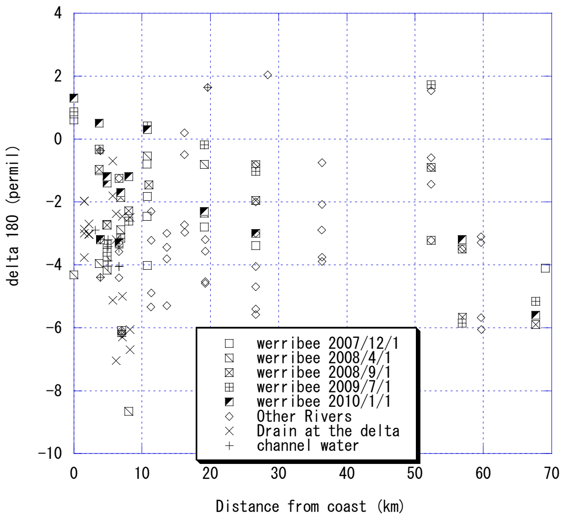

Fig.4 Delta 18O for recycled and river waters

where Cl-sam is the Cl^- concentration of borehole water. The mixing ratio between the sea and recycled water was calculated using equation (3).

$$Msea2 = (Cl\text{-}sam-450)/(19000-450)*100\% \qquad (3)$$

The actual value is between the Msea1 and the Msea2. The difference between the Msea1 and the Msea2 was very small and the average value was adopted.
Nitrate (NO_3^-) is also an important indicator because the sea and river concentrations are very low relative to the recycled water, and NO_3^- concentration is very sensitive to the mixing ratio of the recycled water. The mixing ratio between the recycled water and river water (recharge water) was calculated using equation (4).

$$Mrecy= NO_3^-sam/100*100\% \qquad (4)$$

where NO_3^-sam is NO_3^- concentration of borehole water. If Mrecy was less than 100 %, the Mrecy value was adopted as a mixing ratio of the recycled water. However, when the Mrecy value was over 100 %, the Mrecy value cannot be used. In that case, the groundwater is thought to be contaminated by nitrogen fertilizer from farm land on the delta. When both the Msea and Mrecy values can be derived, all mixing ratio of sea, recycled, and river waters can be determined. The accuracy of this process was confirmed by isotope values. The difference between the calculated groundwater oxygen isotopic ratio from the determined mixing ratio of sea (0 per mil), recycled water (-3.3 per mil), and river water (-5.8 per mil), and the measured isotopic ratio was compared. When the difference between both the isotopic ratios was less than 2 per mil, the mixing ratio was fixed. When the Mrecy is over 100 % or the difference is over 2 per mil, mixing ratio cannot be determined and the limited values only were used.

3.3 Estimation results of mixing ratio

Fig.5 shows the mixing ratios of the sea, river and recycled waters for borehole water in December 2007, April 2008, July

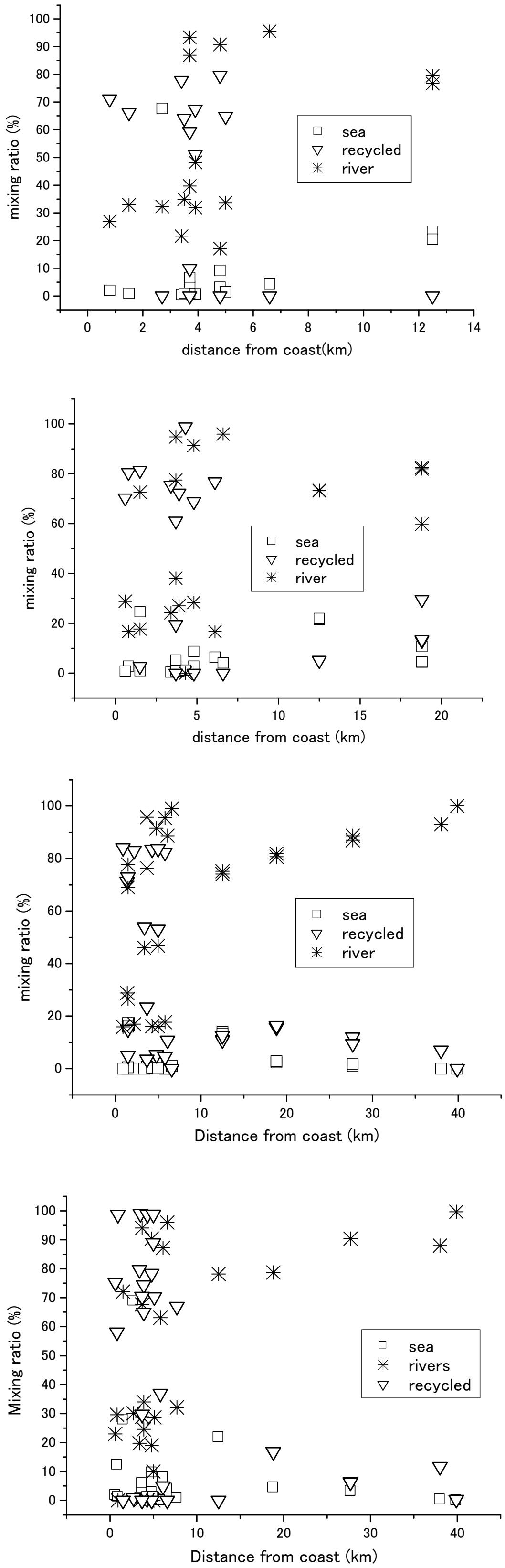

Fig.5 Mixing ratios of the sea, river and recycled waters for borehole water in December 2007, April 2008, July 2009 and January 2010.

2009 and January 2010. The river mixing ratio increased with the distance from the coast. Inland, where the distance from the coast is over 10 km, the river mixing ratio was very high (70 %), and the sea and recycled water mixing ratios were low. In the delta area, where the distance from the coast is less than 10 km, there were two types of borehole waters. One had high river mixing ratio and the other low river mixing ratio. In the low river mixing case, the recycled water ratio was high (over 60%), suggesting direct surface water intrusion. Some borehole values indicated high mixing ratio of the sea water in the delta area. Overall, in the delta area, half of groundwater has high mixing ratio of the recycled water.

On the other hand, inland area over 10km distance from the coast, the analyzed mixing ratio of sea and recycled water were very low. Inland area, recycled water was not used and far from the sea. Therefore, the analyzed results were in agreement with the actual phenomenon.

Fig.6 shows the mixing ratios of sea, river and recycled waters for borehole water with depth at the delta. The mixing ratio was not clearly divided by depth. The recycled water ratio was always high at the delta, although some borehole water has low mixing ratio of the recycled water. The sea mixing ratio increased with depth.

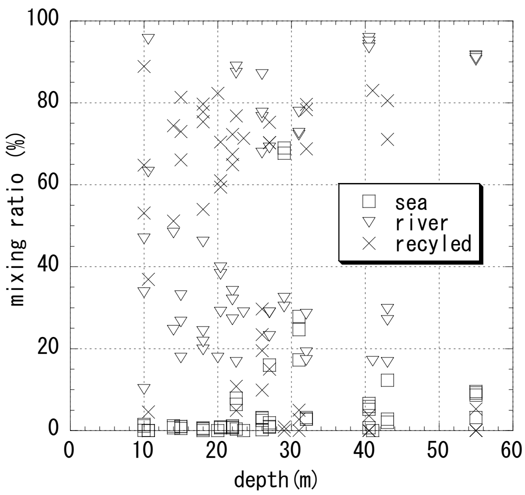

Fig.6 Mixing ratios of sea, river and recycled waters for borehole water with depth at the delta.

3.4 Cl^- and NO_3^- origin for borehole water

Fig.7 shows Cl^- and NO_3^- concentrations with distance from the coast for borehole water. Although Cl^- concentration increased towards the coast in Fig.7, the sea water mixing ratio did not increase close to the coast. The increase of Cl^- in the borehole water was not thought to be caused by salt of marine origin. NO_3^- concentration increased near the coast (Fig 7) and the recycled water mixing ratio increased towards the coast. As the recycled water was only used for irrigation in the delta area and some borehole waters at the delta area had high NO_3^- concentration, initially the origin of NO_3^- in some borehole water was thought to be the recycled water. However, on the calculation of the Mrecy, the Mrecy value for some borehole was over 100 % and so some borehole water is thought to be contaminated by nitrogen fertilizer from farm land on the delta.

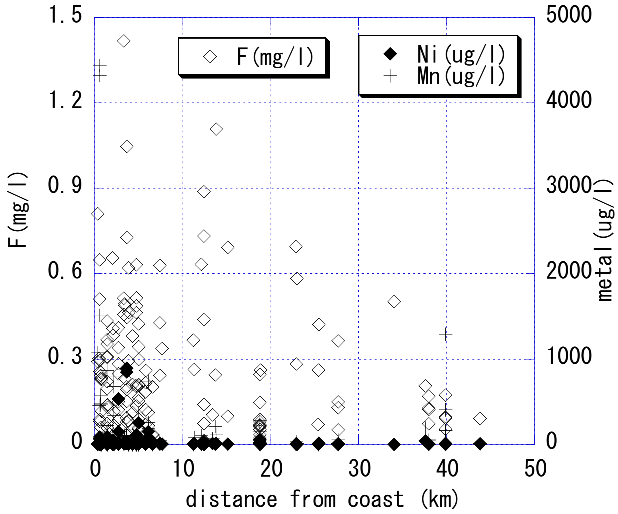

Fig.7 Cl^- and NO_3^- concentrations of borehole water with distance from coast.

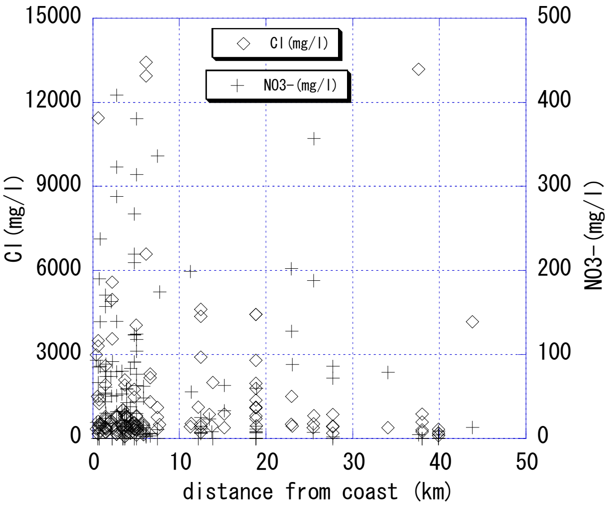

Fig.8 Relationship between F^- and trace element concentrations in the borehole water.

In the mid-catchment area, the low mixing ratio of the recycled water was in agreement with low concentration of NO_3^- concentration for borehole water. Initially, the source of NO_3^- in the borehole water was thought to be the recycled water. However, as the recycled water is not used in the mid-catchment area, the NO_3^- concentration for rivers was very low, and some high NO_3^- concentration borehole water was found in that area, the high NO_3^- concentration is thought to be caused by nitrogen fertilizer [4] .

3.5 Origin of F- and metal

Fig.8 shows the relationship between F^- and trace element concentrations of the borehole water. The F^- concentration for the borehole water increased near the coast and reached 1.5 mg/l at the delta area. The F^- concentrations for the sea and river waters were 0.5 mg/l and less than 0.3 mg/l, respectively. On the other hand, F^- concentration for the recycled water was high (1 to 2.5 mg/l). Therefore, mixing of recycled water was thought to be important for high F^- concentration. However, upstream of the delta area, F^- concentration for the borehole water was also above 0.5 mg/l; in this case the increase of F^- was caused by contact with sediments. Overall, F^- origin of the borehole water was thought to be sewage or sediments.

At the delta area, borehole waters with high Ni and Mn concentrations were found. Fig.9 shows Ni and Mn concentrations for the sea, recycled and river waters. Both metals were low for recycled and sea water and high for the river waters. The high Ni and Mn concentrations in borehole water are thought to derive from river water which infiltrated near the delta area (because river water recharge ratio was high at the delta and surrounding area).

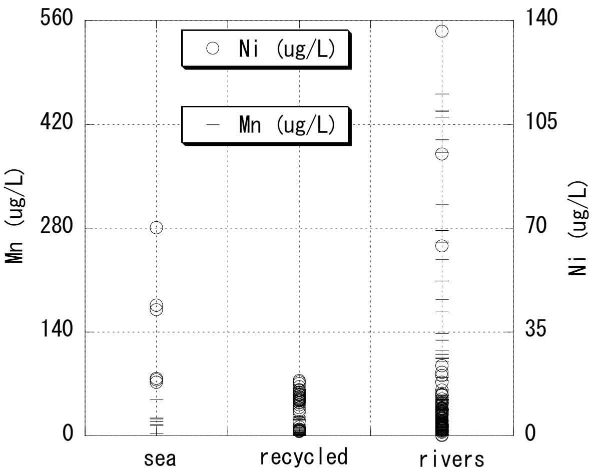

Fig.9 Ni and Mn concentrations for sea, recycled and river waters.

4 CONCLUSION

The mixing ratios of the sea, river and recycled waters in borehole water were calculated from water chemistry and isotopic ratios. Inland, the river mixing ratio was very high (70 %), and the sea and recycled water mixing ratios were low. At the delta area, some borehole water had a high river mixing ratio, and others low river mixing ratio with high recycled water ratio (over 60 %). Overall, at the delta area, half of groundwater has high mixing ratio of the recycled water.

The origin of each analyte for borehole water was estimated by considering the mixing ratios of the samples. The marine origin for Cl^- in borehole water was very limited and was only found in the delta area. The origin of NO_3^- for borehole water at the delta is thought to be recycled water and/or fertilizer. In the mid-catchment area, fertilizer was the only NO_3^- source. The origin of F^- in borehole water is thought to be recycled water in the delta area, and sediments in the mid catchment.

The high Ni and Mn concentration in borehole water is thought to derive from river water which has infiltrated into the aquifer near the delta area.

5 REFFRENCE

[1] Department of Primary Industry, Victoria, “Atlas of Western Irrigation Futures”, Southern Rural Water, Victoria, Australia, 2009. pp1-36.

[2] Condon MA, “The Geology of the Lower Werribee River, Victoria” Soil Mechics, 4th ed. vol. 63, Proc. Royal Society Victoria, Australia, 1951, pp. 1–25.

[3] John L, “Port Philiip Region Groundwater Resources- Future Use and Management” Department of water Resources Voctoria, Australia. 1992. pp1-116.

[4] Commonwealth Scientific and Industrial Research Organisation, “Groundwater Nutrient and Toxicant Inputs to Port Phillip Bay”, Technical Report No.13, Victoria, Australia, 1993. pp1-63.

First International Conference on Geotechnique, Construction Materials and Environment, Mie, Japan, Nov.21-23, 2011, ISBN: 978-4-9905958-0-7 C3051

Process of Invading the Alien Plant Species into the River Ecosystem

Michiko Masuda[1], Yumie Ito[1], Fumitake Nishimura.[2], [1]Department of Civil Engineering, Nagoya Institute of Technology, [2]Department of Environmental Engineering, Kyoto University.

ABSTRACT: A lot of alien plant species invaded the fluvial environment. Up to now, some researchers pointed out that the disturbance by the flood help the invasion of alien plants. But there are a few studies how alien plants invade into the river ecosystem. Because grand-scale experiment was difficult, considering the flood control and water utilization of the river, the alien invasion had not been examined. Fortunately, we have a chance to experiment how the alien species invaded by using the park where the buried seed was removed. At the construction of the park, *Sicyos angulatus* must be removed from this area. This species make a lot of burial seed population, then the planner of the park removed soils 2m in depth and brought into clean soils from deeper area. As a result three of the following became clear, 1) the vegetation of the river was maintained by seeds flow out, 2) the seeds were supplied with rising of the river, 3) the duration of the seed emerging at alien plant species are longer than that at native plant species. The character that the seeds are able to emerge anytime and anywhere like the alien plants species are advantageous at the fluvial environment where rising of the river sometimes occurs. It was shown that the seed emergence occurred in a short term like native plant species missed the occupation chance. This pattern was remarkably admitted in spring in autumn.

Keywords: Seed emergence, Invading plant, Germination characteristics, Native plant.

1. INTRODUCTION

The river law of Japan was revised in 1997. A past river law was aiming at the flood control and the water utilization. However, environmental preservation was added to the purpose in 1997. Law revision is received, and "Multi-natural river-making" has been done as a stream management that considers the environment. "Multi-natural river-making" means the river is managed for maintenance and the creation of a native habitat of the living thing that the river originally maintains and various river spectacles. The protection of the habitat of wildlife and the approach of the aquatic conservation are performed on the many site of "Multi-natural river-making". Many “Multi-natural river-makings” constructions are promoted after 1997, and restoration of natural condition is expected [1].

In “Multi-natural river-making", first of all, it is necessary to recover vegetation. Vegetation is recovered because of making the habitat of other living things, and leading to the recovery of the ecosystem. Three methods are given to the vegetative restoration [2]. First, it is a method of leaving to the seed scatter of around natural vegetation. Second, it is a method of transplanting and sowing suitable plant species. Third, it is a method of utilizing seed bank around there. If an appropriate seed source to surroundings doesn't exist, the first technique cannot be used. In the second technique, it is a problem that the selection of an appropriate plant is difficult. The third method is being paid attention to as a method of making use of the potential, natural recovery power in the region [3]. However, the fluvial environment is a hard disturbance area, and the transportation power of earth and sand is also large. Therefore, the examination which technique was suitable had not been done.

Moreover, another big problem exists for the vegetative restoration of the fluvial environment. It is a disturbance of biodiversity by the invasion of the alien plants. Rising forms the bare land in the river area. The bare land is formed frequently. The bare land can be invaded at any time by the plant with a life history of ruderal species. The invasion of an alien plants have been diminishing the biodiversity at the river condition. Especially, the alien plant that invades the fluvial environment brought in to Japan by the seed medium. Therefore, genetic diversity is very high which adjusts easily to the each invading environment [4]. Moreover, many alien plants brought in exotic area without their disease or natural enemy at all. Therefore, the activities of them tend to be high more than native species [5].

The Ministry of Land, Infrastructure and Transport that had such a problem founded the vocational training center named “The School in the Yada River Waterside” using “Multi-natural river-making” in Yada river at central Japan. It gropes for shape that the biodiversity can be maintained when the diversity of the river is created in this facilities, and vegetation restoration is done. Then there were seeds of *Sicyos angulatus,* the species notorious alien species, in this area. So to recover the rich biodiversity of the river, all the surface soil with burial seeds was buried under the depth of 2m, and the buried soil under the 2m depth of there with no seed bank was covered over there.

Then, it was investigated how the vegetation restoration of the river was done in the “Multi-natural river-making”. 1) Where is the seed supplied when the buried seed doesn't exist? 2) When do the seeds of many kinds of species invade into the bared area? 3) Is there a difference in the method of the invasion in the alien and native species? It was paid attention to these three points, and analyzed.

2. MATERIALS AND METHODS

2.1 Study site

The study was carried out on a left bank of the Yada River at Joganji, Nagoya City (35^{o} 12’ 58’’N, 136^{o} 55’ 2’’E, altitude 9 m). Yada river is a urban river in the Shonai River water system of the extension 23km and 115 km^{2} in the valley area. The putting substitution construction of the river channel was done in 1932. Today’s Yada River is a circle belt placed between Shonai river and Yada River until the beginning of the Showa era. Because this region had frequently received the flood damage, Yada River put up to a present river channel and was substituted by repair work.

At the study area, the biotope creation business was done in 2008. This biotope is named “The School in the Yada River Waterside”. It is a place of the activity of children's environmental study and nature experiences now.

2.2 Vegetation area analysis

The region was made land with a cleared surface as a business in 2007, and the buried seed was removed from this area. Then, it took 8 pictures of the entire study area from April to December in 2007. We divided the study site 200 meshes (2m x 2m) using the pictures. The class of each vegetation rate of four ranks was installed, and we analyzed it at the time of passing. The rank of the vegetation rate ranging 0~9% is assumed as A, and 10~89% is assumed as B and 90~100% is assumed as C. The part of starting constructing was assumed D rank, and excluded from the analysis. We divided each mesh into the three categories depending on a place, the outside, the inside, and the waterside, and analyzed it at the invasion season using Tukey-Kramer test.

2.3 Seedlings emergence census

The biotope was made in the investigation place at February in 2008, where all the buried seeds were removed from the soil within 2m in depth. For seedling emergence census, 10 quadrats (80 x 50 cm) were set at every 5 m in waterside part, low water bed part, and high water bed part on the hydrophilicity shore protection slope. The total area was $12m^2$. The species of emerging seedlings was identified by comparison with the seedling specimen which had been prepared by germinating the collected seed under laboratory conditions. The recorded seedlings were checked by pigment ink. Census was carried out from April 5’2008 to May 20’2009 at 2 weeks intervals except for the summer and winter season when no emergence was observed in the preliminary inspection. Unidentifiable seedlings constituted only less than 1% of the total seedlings recorded during the study period except grass family. Using this data, it was compared the duration of seedling emergence between alien and native plants by Mann-Whiteney test.

3. RESULTS

3.1 Spatial patterns of seedling emergence

In April 2007, there was no vegetation area in the study site. The invasion of the plant body started gradually in May, and the vegetation rate of all the meshes exceeded 10% in July (Fig. 1). Vegetation area was increasing from May to August, and was decreasing from September to November.

In order to clarify the invasion part of the bared area by the seedling, the study area was divided study site into three sections, I is water site part (upper edge in Fig. 1), II is inside part (all the mesh except outline mesh in Fig. 1), III is outside part (edge mesh except upper edge in Fig. 1). It was compared the time that each part reached B rank by Tukey-Kramer test. There were some significant differences among three parts. I part was occupied by invading plants earliest (t = -7.55, P < 0.001 compared II, t = -5.05, P < 0.001 compared III). And II part was invaded by plants later than III part (t = -3.08, P < 0.01). It was also compared the time that each part reached C rank by Tukey-Kramer test. There was no significant difference between I part and III part. But II part was the latest area occupied by invading plants among all parts. There were significant differences between II part and I, III parts (t = -3.08, P < 0.01 compared I, t = -5.14, P < 0.001 compared III).

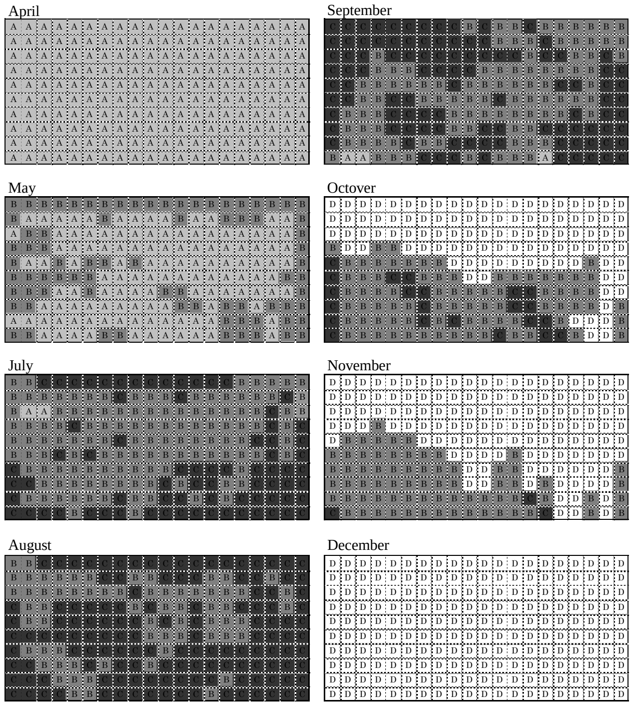

Fig. 1. Seasonal patterns of invade bared area by seedling emergence. Each rank showed vegetation rate, A rank is 0~9% A, B rank is 10~89% B, C rank is 90~100% C. Upper side is water area. D rank is construction part D

3.2 Temporal patterns for seedling emergence

The temporal patterns for each species were shown in Fig. 2-4. Fig. 2 showed the patterns of high water bed part seedling emergence that over three seedlings were observed. Here it was observed the significant difference of seedling emergence duration in spring between alien and native plants (U=22, N=21, P<0.05 in spring). But there is no significant difference of seedling emergence duration in autumn between alien and native plants (U=28.5, N=16, P=0.87). Fig. 3 showed the patterns of low water bed part seedling emergence that over three seedlings were observed in the census quadrats. Here also it was observed the significant difference of seedling emergence duration in

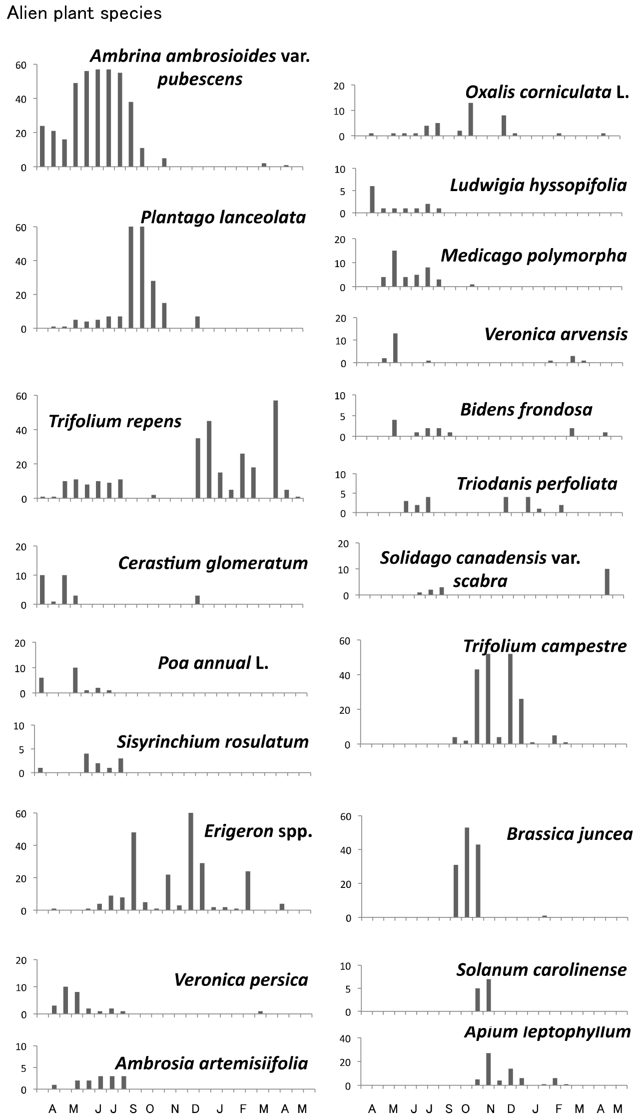

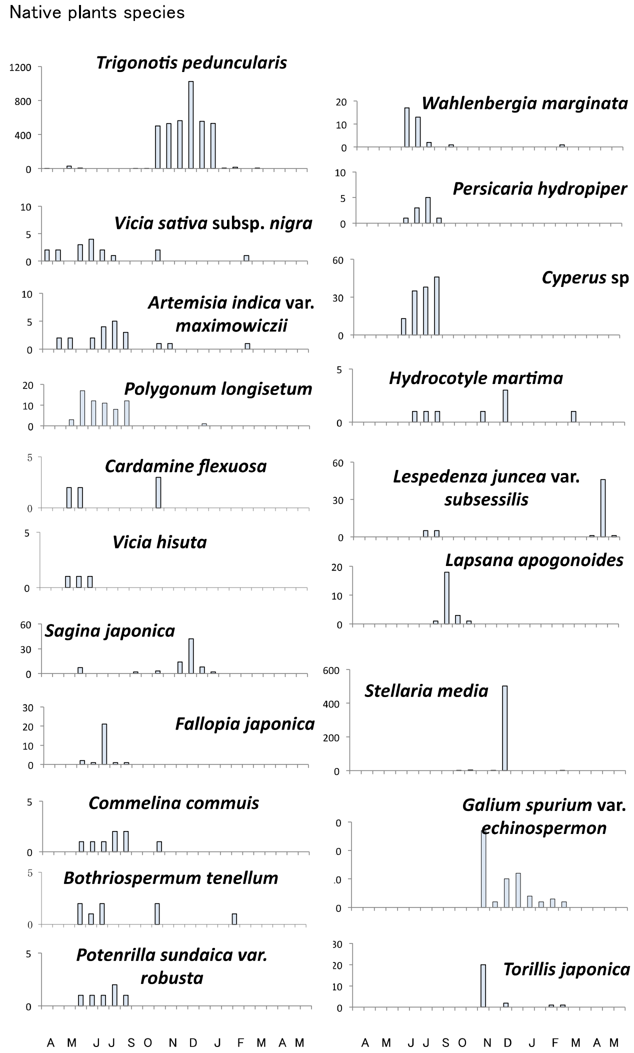

Fig. 2. Seasonal patterns of seedling emergence from April 2008 to May 2009 at high water bed part. Shaded histogram showed alien plants, open histogram showed native plant

spring between alien and native plants (U=8, N=15, P<0.05). And also, there was no difference in autumn in low waterside bed (U=10, N=12, P=0.305). Fig. 4 showed the patterns of seedling emergence that emerged four seedlings at waterside part in census quadrats. Most species emerged in spring or autumn. There was no difference of seedling emergence between alien and native plants (U =36, N=22, P=0.103 in spring, U=8.5, N=11, P=0.274).

In high water bed part, 35 alien species were observed in 10 quadrats, and total seedling number was 2232. And 35 native plant species were observed and total seedling number was 4753 (90% of the seedlings emerged in autumn). Total native seedling number is superior to those of alien plants. And the vegetation survey was done where more than 50% vegetation cover was some alien plants. This shows that the established rate of the seedling of the alien plant is higher than that of a native plant. Though it was from a month to 2 months that emergence of the native plant species in spring, alien plants seedling emerged in the study site during 2 to 4 months. Especially seedlings of *Erigeron* species were emerged from April 2008 to May 2009 except August 2008.

In low water bed part, seedlings of 39 alien plants species and 35 native plants species were observed. And the number of seedlings was almost same, total seedling number of alien plant species was 2891 and that of native plants is 2614. Almost of observed seedlings of native plants emerged in autumn. Compared with native plants, the seedlings of alien plants emerged both in spring and autumn. In the low water bed part, seedlings of *Trifolium repens* emerged very long time from April 2008 to April 2009 except August and September. Compared with alien plants, native plants emergence occurred in spring or in autumn. The short time emergence patterns of native species were observed. More

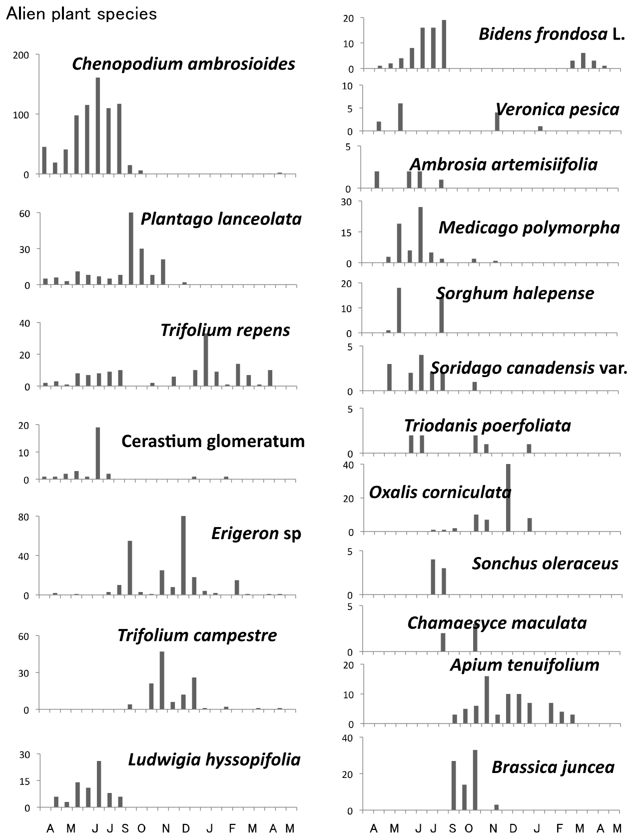

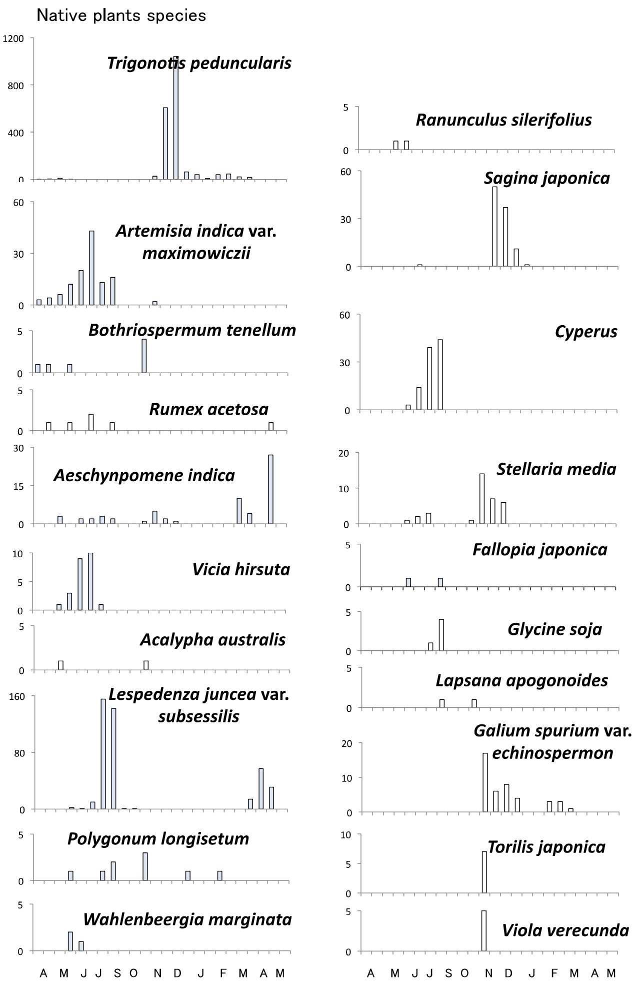

Fig. 3. Seasonal patterns of seedling emergence from April 2008 to May 2009 at low water bed part. Shaded histogram showed alien plants, open histogram showed native plant seedling emergence.

than 80% of the vegetation cover was composed by alien plants in spring 2009.

In waterside part, the seedlings of 36 alien plants species and 49 native plants species were observed. The total seedling numbers were 4333 in alien and 3458 in native plants. In this part, the more than 50% vegetation cover was composed of native plants. The kinds of alien plants species is lower than that of native plants species compared with the other parts. Alien plants emerged through a year, especially *T. repens* and *Erigeron* species, there was not serious invasion by alien plants observed.

4. DISCUSSION

Recently, the weed risk assessment (WRA) is paid attention as a risk evaluation system of the species before alien species intentionally introduces into Japan. In Australia the operation results of the WRA system have exceeded ten years [6]. Because the damage of the exoticism to biodiversity has become the largest problem worldwide, the WRA begins to be used also in Japan [7]. In the WRA, there is a check item concerning the item concerning a character of ruderal strategy. Actually, the invasion of alien species with ruderal strategy become a big problem in Japan.

Especially the invasion of alien species in the river system where continuous disturbance of each rainfall occurred is the serious problem [8].

From 1997 many biotopes have been constructed everywhere in river by using “Multi-natural river-makings” by the Ministry of Land, Infrastructure and Transport. In every biotope there is the problem of alien species more or less. *Eragrostis curvula*, *Coleopsis lanceorata* and *S. angulatus* invade biotopes and cause a serious situation to modify vegetation [9]. These plants were positively introduced for preventing sand erosion and greening in the slope. The seeds amount of *E. curvula* was 30689 kg per year from 1991 to 2000 in Japan (from the Ministry of Agriculture, Forestry and Fisheries materials). The regeneration of these species has succeeded and a huge amount of seeds have been supplied by Rising water level. It is known that it depends whether the alien species can invade on existing plant varieties [10] [11].

The biotopes by using “Multi-natural river-makings” had no vegetation cover when biotope constructions were completed. And there was no seed bank in the new biotopes, because the necessity for preventing the alien species invasion was requested in The Invasive Alien Species Act from 2005. There are many burial seeds of invasive alien

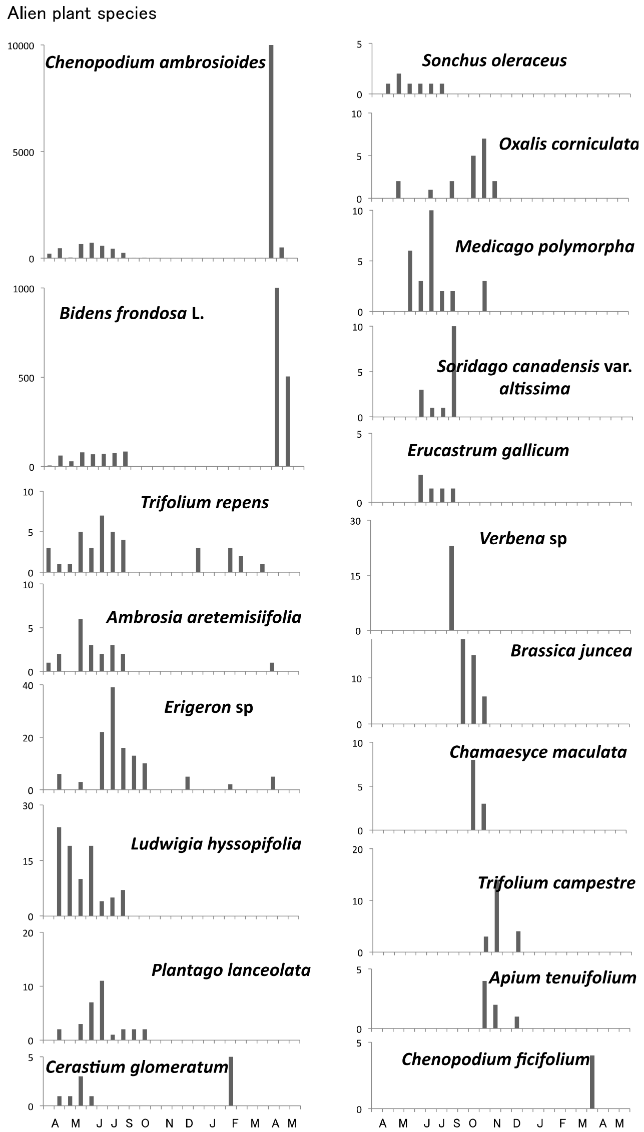

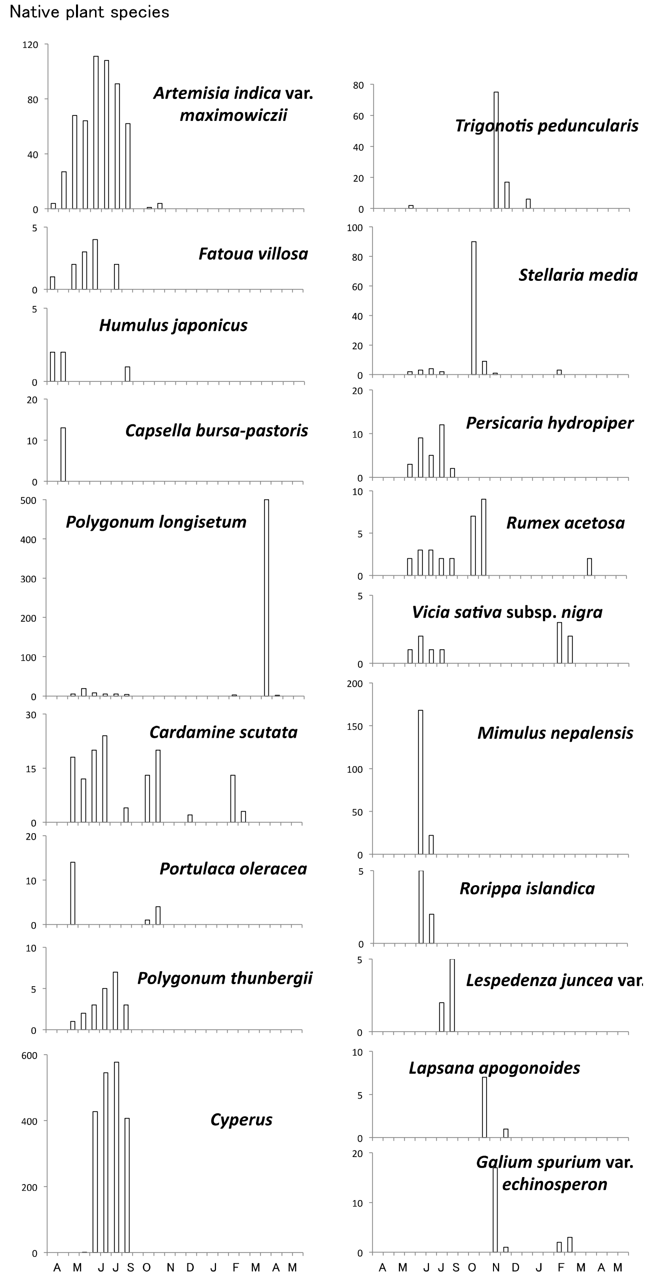

Fig. 4. Seasonal patterns of seedling emergence from April 2008 to May 2009 at waterside part. Shaded histogram showed alien plants, open histogram showed native plant seedling emergence.

plants species in every river. Then the construction must be done without many burial seeds.

Where is the seeds carried when the construction of the biotopes without burial seeds was done? A rising of river always transports the seeds. Fig. 5 shows the line of seeds dispersal where the seeds of *L. juncea* var. *subsessilis* emerged along the water level of the rising. Always seeds have been transported by rainfall. But the intensity of plant invasion was different according to the season. In Japan, summer season is too hot when the survival rate of seedlings is low. And also winter season is too cold when the seedlings cannot survive for freezing [12]. Most emergences occurred in both spring and autumn. The seeds of native species emerged very short duration in spring, and relative long duration in autumn. Compared with native species, the alien species emerged for very long time both in spring and

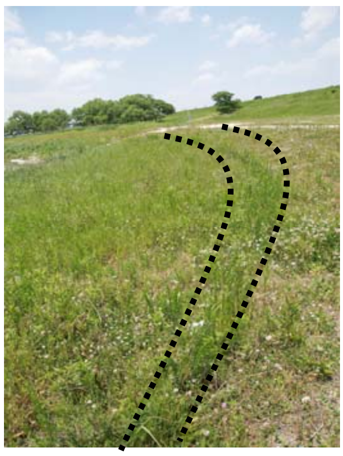

Fig. 5. Seedlings line of *Lespedeza juncea* var. *subsessilis.* The dark green color plants grows along to the dashed line.

autumn. In the disturbing area as river, the long time emergence is very advantageous strategy. Then it is necessary to complete biotope construction in summer if we hope so that native plants may become dominant species. After summer, the seedlings of both alien and native species emerged for long time, from 2 to 4 months. The native plants have an opportunity to dominate in the biotopes. The current biotope constructions were often completed in March for the accounting system of Japan. Then most of the new biotopes were occupied by alien plants species. The study shows the reason of the alien plants invasion. Alien plants can easily invade a new bared area because of the possession of the ability extended germinating periods. And results also suggest that the construction of biotope by using "Multi-natural river-making" should be finished until summer. When the construction was finished until summer, there would be a same chance to invade in both alien plants and native plants.

5. CONCLUSION

1) In the river system, seeds were mainly carried when the river rises. The seeds were carried from the embankment slope to the high water bed part and low water bed part by the rainfall.

2) In spring the amount of seedlings of alien plants was larger than that of native plants at bared area. In autumn the amounts of seedling of both native plants and alien plants at open area.

3) There are some differences of invasion methods between alien and native species. The strategy of alien plants is longtime seedlings emergence in spring. The strategy of native plants is the short time seedling emergence to survive in spring, and the long time seedling emergence to find safe site in autumn.

6. ACKNOWLEDGMENT

We wish to thank the member of Ministry of Land, Infrastructure and Transport Shonai River Office for research support and permission to work in the river. We also thank the members of our laboratory for their assistance in the field works.

7. REFERENCES

[1] Shimatani Y, "Conservation and restoration of the River environment," Kashima-shuppan, 2000.

[2] Van der Valk AG, Pederson RL, "Seed Banks and the Management and Restoration of Natural Vegetation," Ecology of Soil Seed Banks, Leck, Parker, Simpson, Eds. Academic Press, 1989, pp. 329-346.

[3] Imahashi M, Washitani I, "Examination of possibility of a river flood meadow restoration that uses seed bank," Conservation Ecology Research, vol. 1, 1996, pp.145-146.

[4] Masuda M, "Invasion of alien plant: Status of *Coreopsis lanceolata* L. in Japan," Annual Journal of Engineering, Ehime University, vol. 21, Mar. 2000, pp.245-251.

[5] Washitai I, "Management of alien plants," Conservation Ecology Research, vol. 5, 2000, pp. 184-185.

[6] Pheloug PC, Williams PA, Halloy SR, "A weed risk assessment model for use as a biosecurity tool evaluating plant introduction," Journal of Environmental Management, vol. 57, 1999, pp. 239-251.

[7] Nishida T, "Weed risk assessment-mainly in Australia and New Zealand," Ecology of Agriculture and Weed, Plant Species Biology Society, Ed. Bunichisogo, 2007, pp.121-136.

[8] Myers JH, Bazely DR, "Ecology and control of introduced plants," The Press Syndicate of the University of Cambridge, UK, 2003.

[9] Ministry of Environment, "List of regulated living organisms under the Invasive alien species act," materials of Ministry of Environment, 2011.

[10] MacDougall AS, Boucher J, Turkington R, Bradfield GE, "Patterns of plant invasion along an environmental stress gradient," Journal of Vegetation Science, vol. 17, 2006, pp. 47-56.

[11] Maskell LC, Bullock JM, Smart SM, Thompson K, Hulme PE, "The distribution and habitat associations of non-native plantspecies in urban riparian habitat," Journal of Vegetation Science, vol. 17, 2006, pp. 499-508.

[12] Masuda M, Washitani I. "A comparative ecology of the seasonal schedules for 'reproduction by seeds' in a moist tall grassland community," Functional Ecology, vol. 4, 1990, pp. 169-182.

First International Conference on Geotechnique, Construction Materials and Environment, Mie, Japan, Nov.21-23, 2011, ISBN: 978-4-9905958-0-7 C3051

Recent Meandering pattern of the Irrawaddy, MYANMAR

Mayumi MATSUMOTO and Shigeko HARUYAMA
Department of Environmental Science & Technology, Mie University, Japan

ABSTRACT: In the lower and middle river basin of the Irrawaddy, the river is very easy to reform channels and channel beds on the part of meandering direction during severe monsoon seasons. We measured meandering index regarding to topography, and revealed change rate of meandering index during last 60 years. We classified four zones considering to geomorphologic units, as following; Zone A in the middle basin of the Irrawaddy, Zone B and Zone C in the lower basin of the Irrawaddy, Zone D in delta. In our research result, Zone A and D are stable channels, while Zone B and C are unstable channels and easily to move the meandering pattern.

Keywords: Meandering index, channel change, river gradient, Irrawaddy

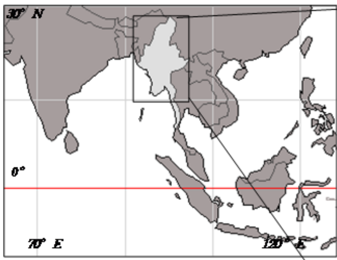

Fig.1 Location of Myanmar in southeast Asia

Fig.2 Location of the Irrawady river basin in Mynanmar

Length	2010km
Basin	415700km^2(Bender,1983)
Discharge	13000m^2/s(at Saiktha)
	max 32,600m^3/s
	min 2300m^3/s

(River regime cofficient: 14.2)

Table.1 Profile of the Irrawaddy

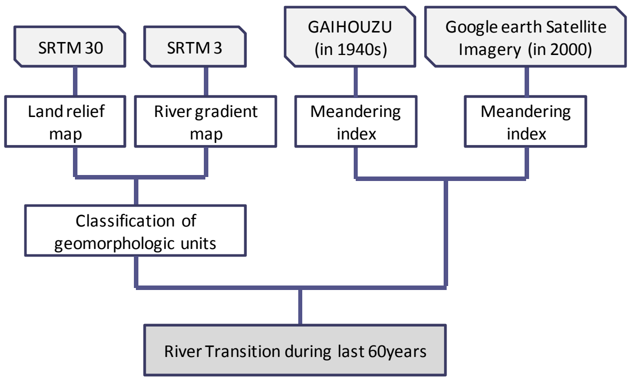

1. INTRODUCTION

Flood plain formations result from the long-term cumulative action of the flow, erosion and depositional process and the meander process will be considered in this paper. It should be convenient that the surface geomorphology and geomorphologic process are clarified in the engineering work for the conservation the flood plain because the flow properties and sediment transport are constructed the flood plain topography. However, in many high energy, fluvial regimes from individual floods should be so great in this paper. The influence of recent and contemporaneous flooding in sculpting the flood plain cannot be ignored Schumm and Lichty(1963). Even in the fluvial system, cumulative changes in channel pattern and flood plain morphology are often great enough to require their incorporation into engineering design and long-term environmental changes. The evolution of channel plan form commonly depends sensitively on local boundary conditions. This is particularly true of flood chute development, meander cutoffs, creation and abandonment of braided-channel anastomoses. The fluvial behavior suggests that even the retail process should be predictive for future long period. Flood plain morphology is generally classified by the associated channel plan form each type Lewin(1987). Nanson and Croke(1992) also classify flood plains by the combination of sedimentary environment and formative process. The Irrawaddy delta has the common flood plain morphology, in monsoon Asia. Yonechi and Win Maung(1986) defined present an outline of the anastmosing river of the upper Irrawaddy and quantitative features of channel patterns. However, in the middle and lower basin of the Irrawaddy, has not been clarified by channel pattern changes. The channel patterns of this study area is classified, has been impacted by the several channel pattern changes and heavy rainfall epoch.(Fig.1, 2 and Table.1)

2. OBJECTIVE AND METHODOLOGY

A fluvial process of the Irrawaddy river should be discussed with the recent environmental changes caused by vegetation changes. Therefore, we try to analyze a lateral migration in the lower and middle basin of the Irrawaddy, where is flowing from Mandalay intermountain basin to the mouth of river. Therefore, we propose the following methodology, as shown in Fig.3. In our experiments, the river gradient classification map of the Irrawaddy and land relief structure map, were prepared by using SRTM elevation data.

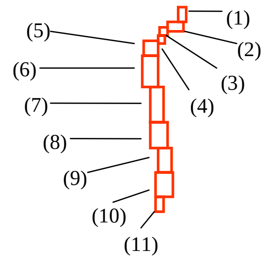

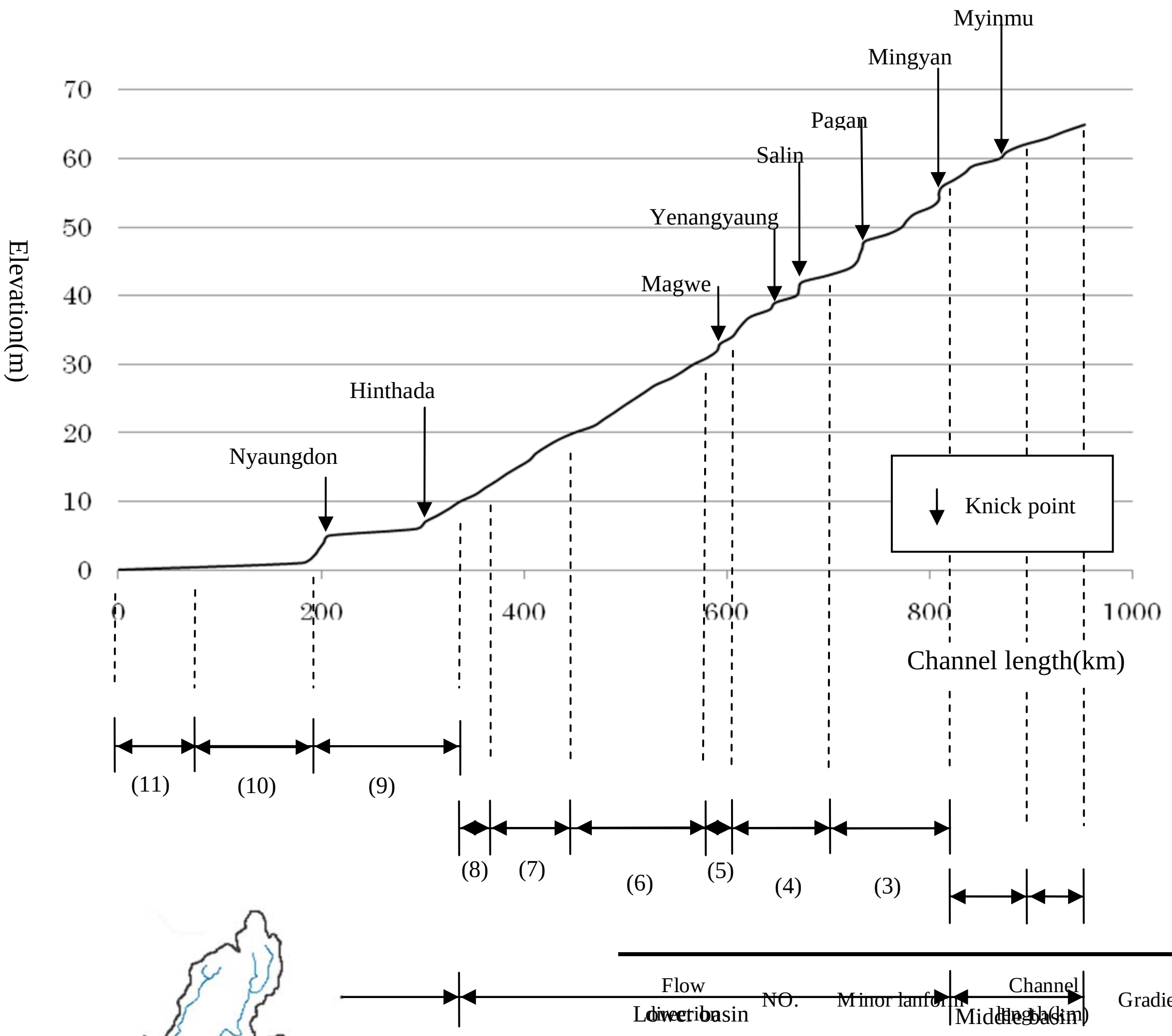

ologic units by river gradient and knick points with village name

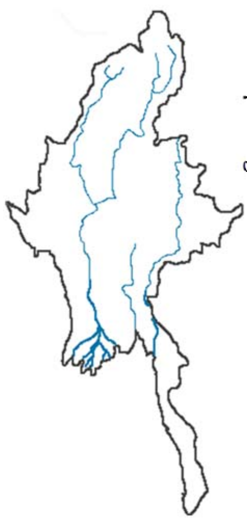

Flow	NO.	Minor lanform	Channel length(km)	Gradient
middle basin	(1)	Valley plain Ⅰ	898～952	1/16,000
	(2)	Valley plain Ⅱ	814～898	1/14,000
lower basin	(3)	Hilly area Ⅰ	707～814	1/9,000
	(4)	Hilly area Ⅱ	605～707	1/11,000
	(5)	Hilly area Ⅲ	573～605	1/10,000
	(6)	Gorge	438～573	1/12,000
	(7)	Small valley plain	366～438	1/12,000
	(8)	Top of alluvial fan	337～366	1/15,000
delta	(9)	Inland of delta	197～337	1/23,000
	(10)	Front of delta	78～197	1/38,000
river mouth	(11)	Estuary	0～78	0

(2) (1)

Table.2 Legend(Fig.4) and river gradient

Next the GAIHOUZU provided by the Japanese army in the 1940s were prepared. Then, satellite imagery taken in 2000s were prepared for geomorphological land classification along the Irrawaddy. Moreover, the authors measured a meandering index of river condition in 1940s and 2000s, and we used the definition in Suzuki's method Suzuki(1998), to quantify a river formation and recent channel changes. Finally , we compared the index in 1940s with the index in 2000s.

2.1 SRTM

A digital elevation model(DEM) is important ancillary data to extract geomorphological information by remote sensing. Especially, Shuttle Reader Topography Mission(SRTM) data are suitable for analyzing topographical units. SRTM acquired on the flight in 2000. SRTM-3 data(90m spatial resolution) and SRTM-30 (900m spatial resolution) were used to generate a river gradient map

2.2 MEANDRING INDEX

Suzuki(1998) defined the meandering index is expressed as follows.

$$\text{(a) Meandering Index(MI)} = \frac{\text{channel length}}{\text{downvalley length}}$$

We measured MI between Mandalay intermountain basin and the mouth of river, with calculation intervals in the each 5km of the main Irrawaddy, considering to the suitable for meandering index in our study. The MI was defined by Suzuki's method.

3. RESULTS

3.1 Geomorphologic units

Results in our experiments are as follows. Geomorphologic units were divided in eleven sections and eight knick points between Mandalay intermountain basin and the river mouth for 1,000km. In the view of the geomorphology, delta has two knick points and inclination of river bed is the gentlest, such as river gradient of (9)inland of delta is 1/23,000, (10)front of delta is 1/38,000 and (11)estuary is 0m area above sea level. There are the knick points showing remarkable convex curves refer to Fig.4. In the lower basin, there are five knick points.The knick points are showing the convex curves of the river bed inclination in hilly area between (3)hilly area Ⅰ and (5)hilly areaⅢ. These areas are steeper than the other area, especially (3)hilly area I is the steepest area that gradient is 1/9,000. The river gradients in the lower basin are 1/11,000 in (4)hilly areaⅡ, 1/11,000 in (5)hilly areaⅢ, their are steep. The inclination of other area, such as (6)gorge, (7)small valley plain and (8)top of the alluvial fan are gentler than hilly area. The terminal knick points has concaved curve in the middle basin on (2)valley plain Ⅱ.The river gradient of (1)valley plain Ⅰ is 1/16,000, and (2)valley plain Ⅱ is 1/14,000. The river inclination is gentle again.

3.2 Comparing the meandering index between the 1940s and 2000s

We measured MI of 1940s and 2000s in our study. We revealed the above two MI value and eleven sections by lanking of the geomorphologic units, refer to Fig.6.We calculated the average of meandering index per eleven sections, and calculated change rate of MIs between 1940s and 2000s. The river deposition, erosion and equilibrium systems should be defined by river bed formation. These systems are important factor for considering to channel changes. There are four segments between Zone A and Zone D. Zone A is (1)valley plain Ⅰ and (2)valley plain Ⅱ. Zone B is (3)hilly area Ⅰ, (4)hilly area Ⅱ and (5)hilly area Ⅲ. Zone C is (6)gorge, (7)small valley plain and (8)top of the alluvial fan. Zone D is (9)inland of delta, (10)front of delta and (11)estuary, considering to geomorphologic units.

Zone A; Zone A is showing a erosional system. MI of (1)valley plain Ⅰ is 1.20, and (2)valley plain Ⅱ is 1.06. The change rate of MI between the valley plain Ⅰ and Ⅱ, are 0.0% and Zone A is the gentlest river slope.

Zone B; Zone B where the Irrawaddy joints the Chindwin river that is tributary of the Irrawaddy, is high change rates of the MI, such as (1)hilly area Ⅰ is -6.1 % and (2)hilly area Ⅱ is 8.0%, that are the highest degree in the other zones. Zone B is showing a erosion and deposition system, in the same area.

Zone C; In the Zone C, the value of MI is the lowest all of the zones. The MI of (6)gorge is 1.06, (7)small valley plain is 1.08, and (8)top of alluvial fan is 0.99, because the river channel is linear or straight. Zone C is showing a equilibrium system. The change rates of the MI of (6)gorge is -1.09%, (7)small valley plain is 1.08% and (8)top of the alluvial fan is 0.99%, these degrees are the lowest in other zones.

Zone D; MI of (9)inland of delta is high degree of 1.29 in 1940s and 1.33 in 2000s, and change rate of meandering index is also high 3.0%. (10)Front of delta is most meandering area that meandering degree of 1.43. Change rate of MI of (10)front of delta and (11)estuary, are 0.7% and 0.0% in respectively. Zone D is showing a deposition system.

4. CONCLUSION

The change rate of MIs in Zone B and Zone C are high, and the inclinations of river bed are steep. Especially Zone B is the highest degree of change rate and river inclination. Zone B and Zone C have indicated that the river channel are unstable that the channel moves easily the meandering patterns, especially Zone B is the most easily moving the meandering pattern, because river inclination are steep. While change rate of MI in Zone A and D, are very low, and the river inclination in gentle. In Zone A and D, change rate of MI are low, and suggested that their channels are stable. In this study, change rate of MI is usually affected by inclination of river bed. Change rate of MI originated of flood occurrence.

5. REFERENCES

[1] Harbans. Lal. Chibber(1934): THE GEOLOGY OF BURMA, *Macminllan and co*, pp1-308

[2] Henry. Benedict. Medlicott, William. Thomas. Blanford, Valentine. Ball, F.R. Mallet (1965) : A manual of the geology of INDIA and Burma, *the government of India*, pp1-30

[5] J. Lewin(1978): Meander development and flood plain sedimentation: A case of study from mid-Wales, *Geological Journal*, vol.13 , 25-36

[6] S. A. Schumm and R. W. Lichty(1963): Channel widening and flood plain construction alon Cimarron River in southwestern Kansas, *US Geological Survey professional Paper*, 352-D, pp71-88

[7] G. C. Nanson and J. C. Croke(1992): A genetic classification of flood plains, *Geomorphology*,

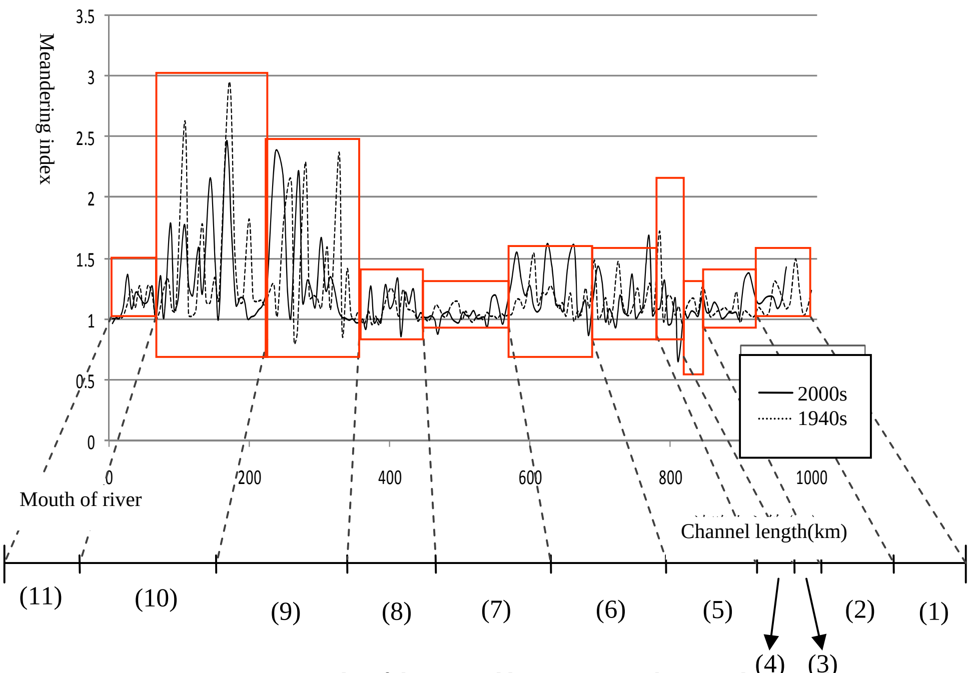

FIg.6 Measurement results of the Irrawaddy mainstreams by meandering index

Table.3 River transition during last 60 years

Flow direction	Zone	Minor lanform	Meandering index (1940s)	Meandering index (2000s)	Change rate of Menadering index(%)	System
Middle basin	Zone A	Valley plain Ⅰ	1.20	1.20	0.0	Erosion
↓		Valley plain Ⅱ	1.06	1.06	0.0	
Lower basin	Zone B	Hilly area Ⅰ	1.15	1.08	-6.1	Erosion and Deposition
		Hilly area Ⅱ	1.12	1.21	8.0	
		Hilly area Ⅲ	1.25	1.29	3.2	
	Zone C	Gorge	1.06	1.04	-1.9	Equilibrium
		Small valley plain	1.08	1.11	2.8	
↓		Top of alluvial fan	0.99	0.97	-2.0	
Delta	Zone D	Inland fo delta	1.29	1.33	3.1	Deposition
↓		Front of delta	1.42	1.43	0.7	
River mouth		Estuary	1.13	1.13	0.0	

[3] Frits van der Leeden(1975) : Water Rseources of the World,Water Information Center,189Kimura S, J. of Computer Science, vol. 1, Aug. 1987, pp. 23-49.

[4] A. D. howerd(1996): Modelling Channel Evolution and Flood plain Morphology, *Flood plain processes*, Malcolm. G.Anderson, Des. E. Walling, Paul D. Bates, pp15-62

[8] Fumio Yonechi, Win Maung(1986):Subdivision on the anastomosing river channel with a proposal of the Irrawaddy type, *The science reports of the Tohoku University. 7th series*, *Geography*, 36(2), pp102-113

[9] Shigeru Kobayashi (2006) : The making of modern Japan in relation to East Asia countries: A perspective on the study of Japanese military and colonial maps, *E-journal*

GEO,vol.1(1)52-66
[10] Seiichiro Asano, Masashi Toyota, Satoshi Kitamura, Goro Tomidokoro, Naoki Sugihara(2008) : The changes of river channel characteristics in the Chikuma basin by means of cross section drawings and aerial photographs, *Journal of Japan Applied Survy Technology,* vol.15, pp109-115
[11] Ryusuke Suzuki(1998) : Kensetsu gijyutusya no tameno tikeizu dokuzu nyuumon, *kokon syoin*,(2), pp223-294

First International Conference on Geotechnique, Construction Materials and Environment, Mie, Japan, Nov.21-23, 2011, ISBN: 978-4-9905958-0-7 C3051

Physical and Chemical Properties of Tsunami Deposit in Northeast Area in Fukushima Prefecture after Tohoku-Kanto Earthquake

FUJIKAWA, T., OKAZAWA, H., NAKAMURA, T., TAKEUCHI, Y. and KOMAMURA, M.
Faculty of Regional Environment Science Tokyo University of Agriculture

ABSTRACT: The damage by tsunami deposit generated by an earthquake on 11 March 2011 widely extended in the coastal area of Tohoku distinct. From the field research and the measurements in Minamisoma city it in northeast area of Fukushima prefecture, two kinds of tsunami deposits, sandy and muddy type deposits were observed. The muddy deposit whose particle size was small was distributed the area which is relatively far from a shoreline. The particle density of this deposit was small and the organic matter content was very large. The sandy deposit whose particle size was large observed in the area near the shoreline. The particle density of the deposit was very large and the hydraulic conductivity of the deposit was large although their bulk density was large. From the approximation of the shape of the tsunami inundated area and the bulk density and the thickness of the deposits, the amount of the deposit was estimated 124,000 m^3 in volume and 193,000 Mg in dry mass. The comparison between the two areas whose distance is 3,000 m suggested that the condition of the deposit (e.g. the thickness of the deposit) was different even if the areas were adjoining.

Keywords: tsunami deposit, particle size distribution, particle density, organic matter content, electric conductivity, total amount of deposit

1. INTRODUCTION

The effect of the large tsunami, which was generated by an earthquake on 11 March 2011, extended in wide region of Tohoku distinct, Japan. From the GIA report ([1]), the estimated area of tsunami inundated field reached 560,000,000 m^2, and many farming areas and farmlands were included in the inundated area. MAFF reported the result that the damaged farmlands were 240,000,000 m^2 in area. Quick reconstruction and restoration of the damaged farmland have been strongly expected.

The effect of tsunami on farmland is classified in three categories, (i) damage by soil salinization caused by infiltration of sea water into the soil, (ii) deterioration of the soil physical, chemical and biological properties by deposition and (iii) erosion of surface soil by tsunami ([2]), and these effects are combined in some cases. The damage by tsunami deposition would be large especially in the coastal area. To select the method of reconstruction of the damaged farmland by tsunami deposit, information about not only the amount of the deposits but also its properties is considered to be very important. The change of the properties of the soil below the deposit is also needed to be understood before the treatment of damaged farmlands because the deposition of earth and sand could compress the surface soil of the farmland and the chemical materials eluted from the deposit could infiltrate into the soil,

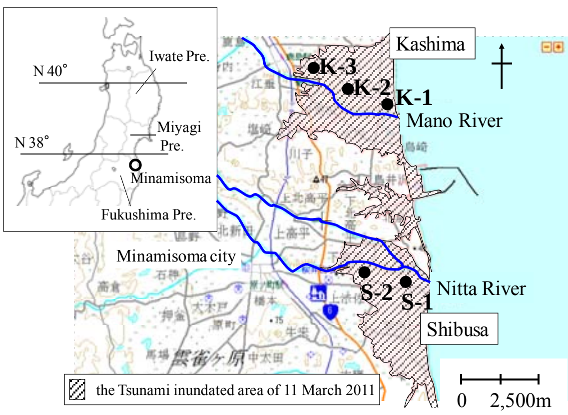

Fig. 1 Research Sites in this study

The purpose of this study is to clarify physical and chemical properties of tsunami deposit and farmland soil below it in northeast area in Fukushima prefecture where the damage of the tsunami brought by the Tohoku-Kanto earthquake was serious.

2. SITES AND METHODS

2.1 Research Sites

The field research was carried out in two areas, Kashima and Shibusa in Minamisoma city located in northeast part of Fukushima prefecture (Fig.1). The shoreline of these areas runs north and south, the wave direction of tsunami was west. The tsunami reached 3,200 m in Kashima and 2,500 m in Shibusa. Three sites in Kashima (K-1, K-2 and K-3) and two sites in Shibusa (S-1 and S-2) were selected for the measurements. These sites had been used as paddy fields before the tsunami event. At each site a sampling pit, which is 0.35 m (K-1 and S-1) or 0.25 m deep, 0.50 m wide and 0.50 m long, was dug to investigate the profile of the deposit and the soil.

The field survey was conducted on 17 June 2011, 3 months after the tsunami event. The total amount of precipitation between the tsunami event and the survey was calculated to be 230 mm from AMeDAS data in [3].

2.2 Sampling and Measurements

Thickness of the deposit was measured by observation of the profile of the sampling pit. Disturbed and undisturbed samples were taken from the profile. The undisturbed sample was taken by the 100 cm^3 core sampler with 5.0 cm in diameter and 5.1 cm in height.

Particle size distribution was determined by hydrometer method (< 0.106 mm) and sieving (> 0.106mm) after decomposition of organic materials by hydrogen peroxide (referring JIS A 1204). Water content and bulk density of the sample was measured by oven dry (105 °C, 24 hours) with the disturbed and undisturbed sample, respectively. Particle density of the disturbed sample was determined by pycnometric method (JIS A 1202). Ignition loss, which indicated the content of organic matter, was calculated from the difference between the weight of the oven dried sample and that of the sample heated to 800 °C for 3 hours in a muffle furnace. Saturated hydraulic conductivity of the undisturbed sample was determined by falling-head method. A water extract was obtained from 4 g of the sample with 20 g deionized water (1:5 method) and electric conductivity (EC) of this extracts was measured. Concentrations of chloride ion and sulfuric ion were analyzed by IC (detector: CDD-10Avp, SHIMADZU) for the extracts filtrated by 0.22 μm filter. The measurements of particle size distribution, EC and anion concentration were made for the samples only in Kashima. The replication of the measurement was one for particle size distribution, EC and anion concentration and two for other properties.

3 RESULTS AND DISCUSSION

3.1 Thickness of the Tsunami Deposit

In Kashima the thickness of the tsunami deposit decreased with distance from the shoreline as some literature ([4]-[6]) reported (Table 1). Muddy deposit was observed in at K-3 whose distance from shoreline was most large. The observations of such muddy deposit (such as, surface muddy deposit layer or muddy caps in [7] - [9]) have been also reported. The thickness of the deposit in coastal area became larger because the large fall of velocity of the tsunami in this area promoted the deposition of including earth and sand carried from sea bed. In Shibusa, on the other hand, the surface deposit layer of S-2, which is closer to the shoreline, was thicker than that of S-1. Some reports ([4],[10]) observed no clear relationship between the distance from a shoreline and the thickness of tsunami deposit and it is explained in term of the change in water flow velocity and direction by microtopography ([5], [11]), deposition and erosion by the outflow or the second and third inflow ([12], [13]). When the tsunami ran up to the field so fast and the water volume of tsunami is so large, the deposition may not occur at the coastal area because of its large transport ability. The thickness at S-1 was different from the average of those of K-1 and K-2 although the distance of S-1 from the shoreline is close to the average of those of K-1 and K-2. It is suggested that the condition of the deposit considerably largely varies between two areas whose distance is only 3,000 m.

3.2 Particle Size Distributions of the Deposit in Kashima

The particle size distributions of the surface deposit (0 – 0.05 m depth) at each measurement site in Kashima shown in Fig.2(a). The deposit at K-3, whose distance from the shoreline is largest, was smaller (D_{50} = 0.04 mm) than those at K-1 (D_{50} = 0.2mm) and K-2 (D_{50} = 0.3 mm). And especially, the sand fraction at K-3 was remarkably smaller. However, the particle size of the deposit of K-2 was larger than that of K-1, and a clear relationship was not observed between the distance from the shoreline and the particle size. These results of the relationships between the distance and the particle size agree with that obtained in [9], [14]. In [14] it was found that the coarse fraction (very coarse and coarse sand) of the deposit decreased with the distance although the range of the fine fraction (fine sand) with the distance was narrow. It is considered to be effective to clarify the spatial variability of the particle size classified into two or three parts (e.g. course fraction, fine fraction and muddy fraction).

The particle size of the deposit increased with depth at K-1 as [8] and [9] reported. This particle size distribution in the direction of depth is considered to be a result of the difference of the settling velocity related with the particle size as shown in Stoke's law. This particle size distribution in the direction of depth would become clearer with the passage of the time because the surface deposit will roll up and settle again and again in the ponding condition after heavy rain. The deposit at K-1 surface included about 10 % of fine fraction (< 0.1 mm), which suggested that the muddy deposit was mixed in the deposit at coastal area even if the deposit was judged to be sand deposit by observation.

Table 1 Location and thickness of the tsunami deposits at the research sites

	Kashima			Shibusa	
Site name	K-1	K-2	K-3	S-1	S-2
Longtitude	37°41´29″	37°41´49″	37°41´59″	37°38´15″	37°38´28″
Latitude	141° 0´28″	140°59´46″	140°58´51″	141° 0´56″	140°59´55″
Distance from shoreline (m)	300	1300	2700	700	2200
Thickness of deposit (m)					
maddy deposit	-	-	0.05	-	0.05
sandy deposit	0.25	0.10	-	0.05	0.05

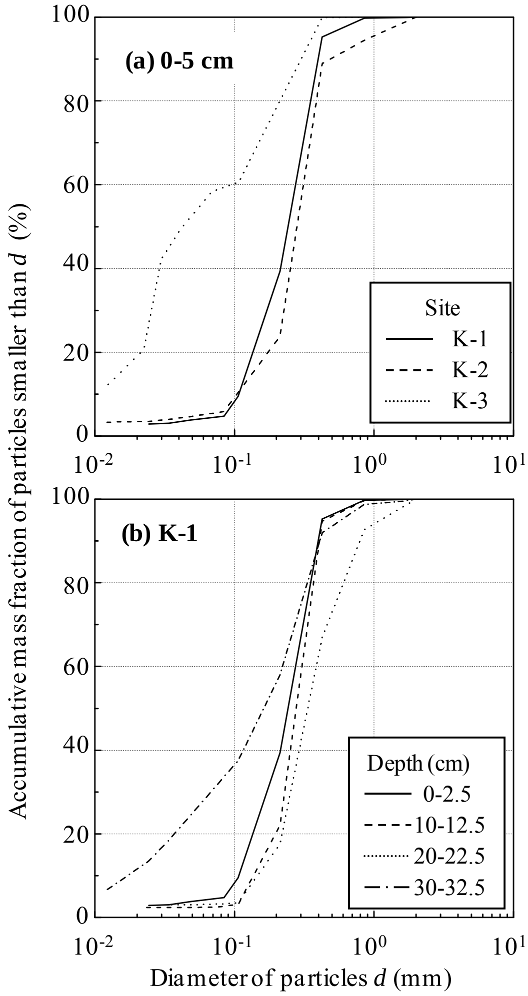

Fig. 2 Particle size distributions of deposit

3.3 Water Content and Bulk and Particle Densities of the Deposit

The water content of the deposit tended to be smaller than that of the paddy soil below the deposit (Table 2). Especially the sandy deposit in the surface layer was dry, of which water content was about 10%. The bulk density of the sandy deposit of K-1 surface layer was 1.6 Mg m^{-3}, which is 1.8 times as large as those of the muddy deposits at K-3 and S-2 (about 0.9 Mg m^{-3}). The increase of the bulk density was not confirmed from the measured values of the bulk density and the effect of compaction by the deposit on the farmland surface soil was not recognized since. It is considered that the influence of compaction by the deposit is comparatively small because the soil type of the surface of paddy fields in this area is heavy clay and the drainage before the tsunami event had already consolidated the surface soil. On the other hand, the influence of compression by the deposit can increase with time because of the iteration of drying and wetting ([15]). Since bulk density of soil, which is related to the water infiltration and retention, is one of the important properties for the agriculture,

Table 2 Water content, densities and ignition loss of the deposits

	Sampling depth* (m)	Deposit/ soil type**	Water content (%)	Bulk density (Mg m^{-3})	Particle density (Mg m^{-3})	Ignition loss (%)
Kashima						
	0-0.05	sandy	10.0	1.59	2.95	2.1
K-1	0.10-0.15	sandy	13.0	1.69	2.93	0.7
	0.20-0.25	sandy	13.9	1.66	3.03	0.9
	0.30-0.35	paddy	26.3	1.24	2.61	9.8
	0-0.05	sandy	3.6	1.35	3.01	1.5
K-2	0.10-0.15	paddy	27.3	1.21	2.55	11.0
	0.20-0.25	paddy	24.6	1.36	2.61	8.5
	0-0.05	muddy	24.6	0.87	2.24	25.6
K-3	0.05-0.10	paddy	25.8	0.97	2.51	12.1
	0.20-0.25	paddy	27.5	1.12	2.59	12.2
Sibusa						
	0-0.05	sandy	7.7	1.28	2.79	3.6
S-1	0.10-0.15	paddy	31.5	1.15	2.49	13.0
	0.20-0.25	paddy	26.4	1.28	2.45	13.9
	0.30-0.35	paddy	13.7	0.99	2.70	17.0
	0-0.05	muddy	13.7	0.90	2.56	19.6
S-2	0.05-0.10	sandy	23.4	1.14	2.65	6.7
	0.20-0.25	paddy	17.0	1.03	2.59	11.1

* depth from the surface of the deposit
** sandy : sandy deposit, muddy : muddy deposit, paddy : paddy soil before tsunami inundation

further measurements are needed to clear effect of the compaction of surface soil by the tsunami deposit.

The particle density of the particle of a sandy deposit was 2.8 - 3.0 Mg m^{-3}, which was larger than that of general soil of farm land in Japan (2.5 - 2.7 Mg m^{-3}), while that of muddy deposit was smaller (2.2 Mg m^{-3}). The large particle density of the sandy deposit can be due to the content of metal or heavy metal. The content of cadmium and chrome in the deposit sampled after the 2004 Indian Ocean tsunami is reported in [16], [17]. They insisted that the source of the heavy metal was not only lithogenic but also anthropogenic in [17], in other word, the metal content of the deposit varies with the condition of industry of the neighbor areas. The analysis of the content of metal of the deposit is necessary also in this area. The small particle density of muddy deposit is interpreted as the high content of organic material. The ignition loss of the muddy deposit was 25 % and higher than those of sandy deposit and paddy soil (Table 2). The organic matter included in the muddy deposit could contain the microorganisms living in the ocean. Some kind of the microorganisms may have toxicity against human health. Microbiological analysis of the deposit will be expected before the removal and disposal of the deposit to restore the farmland. The ignition loss of the surface deposit at K-1 (0-0.05 m) was higher than that of the deposits collected from deeper layers (0.10 - 0.15, 0.20 - 0.25 m) at K-1. This result supports the discussion that the deposit in surface layer of K-1 included the muddy component even if that site is closer to the shoreline.

3.4 Hydraulic conductivity of the deposit

The saturated hydraulic conductivity of a sand deposit was 10^{-4} - 10^{-3} m s^{-1}, which was about ten times as large as that of surface soil of paddy field (Fig.3). The relative large value of the saturated conductivity of the paddy soil may be due to the mixing of organism materials (compost, rice straw, etc.) or sandy soil brought from another place for the improvement of physical properties of the surface soil. The hydraulic conductivity of the muddy deposit was, conversely, smaller than that of the sandy deposit, and that of the deposit at the S-2 surface was about 10^{-7} m s^{-1}. Since the bulk density of the muddy deposit was very small, the pore volume of the deposit was thought to be rationally larger even if the particle density of it was small. This contradiction can be explained by the smaller pore size of the muddy deposit which is formed by small particles included in the deposit. The hydraulic conductivity of K-3 was smaller than that of sandy deposit but 10 times large as that of the deposit of S-2 surface. There were some cracks brought by drying process on the surface at K-3 and there is a possibility that the downward infiltration of rainfall water is promoted through such surface cracks.

3.5 EC and Cation Contents of the Deposit in Kashima

The value of electric conductivity of the deposit sampled in Kashima was 0.39 - 0.13 S m^{-1} for the sandy deposits and about 1.3 S m^{-1} for the muddy deposit (Table 3). The EC value of muddy deposit at K-3 was very large. These values of EC are relatively higher compared to that of the paddy soil under the deposit (0.04 - 0.29 S m^{-1}). The EC of the paddy soil below the deposit may be increased by the infiltrated water

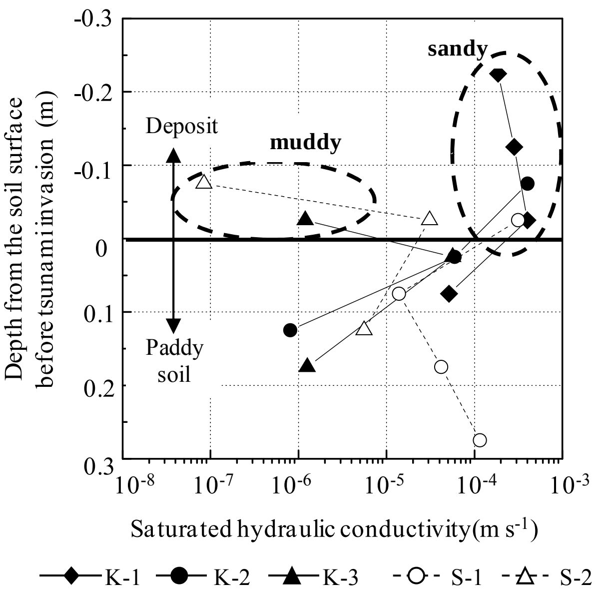

Fig. 3 Distributions of saturated hydraulic conductivity

which contented the high salinity affected by the deposit. From the result of the analysis by IC, both Cl^- and SO_4^{2-} concentrations of the extracted water decreased with depth. The ion contents with dry material were estimated by the water content of the deposits and the ion concentrations of the extracted water. The estimated Cl^- and SO_4^{2-} contents of sandy and muddy deposit were 0.5 % and 0.05 % for sandy deposit, 3 % and 0.2 % for muddy deposit, respectively. These estimated value agree with the result of [17], which reported the Cl^- and SO_4^{2-} content of the tsunami deposit are 0.03 - 3.4 % and 0.05 - 3.5 %, respectively.

In [2] it is described that salt leeching is needed when the Cl- content is larger than 0.1 % for paddy field and 0.05 - 0.07 % for upland field. In this area the contents of both the deposit and the soil are exceeded that standard, and leeching process will be needed before the field is used as a agricultural land when the removal of the deposit has completed.

3.6 Estimation of the Amount of the Deposit in Kashima

The total amount of the deposit in Kashima was estimated by the measured value of the depth and the bulk density of the deposits (Fig. 4). The shape of the area, the bulk density of the deposit and the relationships between the distance from the shoreline and the thickness of the deposits were approximated by the assumption described below.

1) This area is approximated by the trapezoid whose upper base is 2,100 m, bottom base is 4,500 m and height is 2,900 m.
2) The bulk density of the deposit is assumed 1.66 Mg m^{-3} for sandy deposit and 0.88 Mg m^{-3} for muddy deposit, respectively.
3) The thickness of the deposit is expressed by the function of only the distance from the shoreline. And the thickness of the sandy deposit decreased and that of the muddy deposit increased linearly with the distance.
4) Only the sandy deposit exited at K-1 (300 m from the shoreline) and the muddy deposit at K-3 (2,700 m) and the thickness of these deposits are 0.25 m at K-1, 0.05 m at K-3,

Table 3 EC and Cl^- and SO_4^{2-} contents of the deposits

	Sampling depth (m)	Extracted water			Dry soil base	
		EC (S m^{-1})	Cl^- (ppm)	SO_4^{2-} (ppm)	Cl^- (mg g^{-1})	SO_4^{2-} (mg g^{-1})
K-1	0-0.05	0.25	1070	422	5.6	2.2
	0.10-0.15	0.39	750	82	4.5	0.5
	0.20-0.25	0.25	750	80	4.2	0.4
	0.30-0.35	0.17	460	33	3.0	0.2
K-2	0-0.05	0.21	590	57	3.9	0.4
	0.10-0.15	0.13	410	50	2.2	0.3
	0.20-0.25	0.04	100	4	0.6	0.0
K-3	0-0.05	1.28	4830	309	28.4	1.8
	0.05-0.10	0.29	680	132	4.5	0.9
	0.20-0.25	0.14	370	65	2.3	0.4

respectively.

5) The deposit at K-2 surface (0 - 0.05m) was assumed to be a mixture of the sandy and muddy deposit. The mixing ratio was calculated by interior division of the assumed bulk density of sandy and muddy one and the measured bulk density of the deposit at K-2 surface (0 - 0.05m). The mixing ratio of the sandy deposit at K-2 was calculated to be 0.60 and the thickness of the sandy deposit in the surface was determined 0.03 m and that of muddy deposit was 0.02 m. The deposit of 0.05 – 0.10 m at K-2 is assumed to be the sandy deposit.

The relationship between and the distance from the shoreline (*x* m) and the width of the area (*Y* m) was obtained:

$$Y = -0.828x + 4500 \quad (1)$$

from the assumption 1) and relationships between *x* and the amount of the thickness of the deposit (y_1 m: sandy, y_2 m: muddy) :

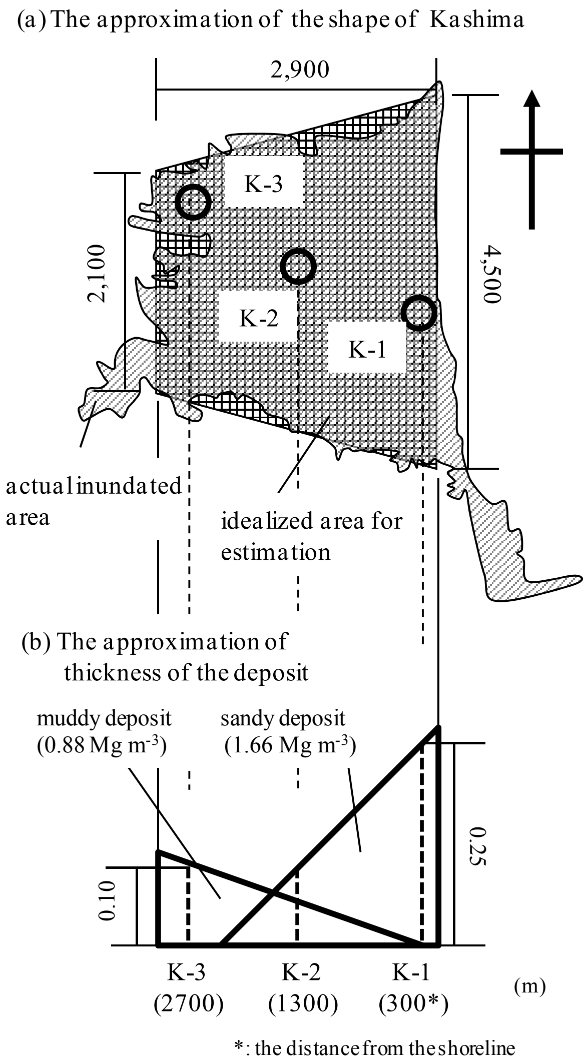

Fig. 4 Schematic diagram for estimation of the amount of the deposit

$$y_1 = -0.00017x + 0.30 \quad (x < 1770) \quad (2)$$

$$y_2 = 0.0000021x - 0.08 \quad (x < 370) \quad (3)$$

from the assumption 3) – 5).

By multiplication of the area and the thickness of the deposit, the total volume of the deposit was estimated 124,000m^3 (sandy deposit: 106,000 m^3, muddy deposit: 18,000 m^3). The total dry mass which was estimated by the multiplication of the volume and the bulk density of the deposit was 193,000Mg (sandy deposit: 176,000Mg, muddy deposit: 17,000Mg). To be the estimation result more precisely, further measurements of the thickness and density of the deposit in the area. The information of wave height and speed of tsunami which affect the amount of tsunami deposit is effective to estimate the amount of the deposit more accurately ([13]). On the other hand, no clear tendency between the distance and the thickness was observed in Shibusa. To estimate the total amount of the deposit in this area it is necessary to investigate more about the microtopography of this area and the sea base in front of this area because not only microgeographical features of the ground but also the spatial variability of properties of seabed can affect the amount and the properties of the deposit.

After the removal of the deposit, salt leeching is needed before the planting of the damaged farmland ([2]). If the amount of the deposit is so small that the change of the chemical and properties is negatively small, the mixture of the deposit into the surface soil and upside down tillage are available to restore the farmland. The Cl^- content of the paddy soil at K-2 (0.20 – 0.25m) was smaller than the standard of the leeching. At this site, only the removal of the deposit can be enough for the restoration of the farmland without leeching. But it is also reported that the peak of the ion concentration moves downward ([10], [17]) with time. The removal of the deposit including toxic substances is expected to be completed as soon as possible to prevent the contamination of the soil below the deposit.

4 CONCLUSION

To clarify the physical and chemical properties of the tsunami deposit caused by Tohoku-Kanto earthquake on 11 March 2011, the field research and the measurements of these properties were done in Minamisoma city located in northeast region of Fukushima prefecture. Two kinds of deposits, sandy and muddy type deposits were observed. The sandy deposit whose particle size was large observed in the area near the seashore. The maximum thickness of the deposit was 0.25 m and decreased with the distance from the shoreline. The particle density of the deposit exceeded 2.8 Mg m^{-3}, which indicated the possibility of the content of metal and / or heavy metal in it. The hydraulic conductivity of the deposit was large although their bulk density was large. The rapid infiltration is likely to promote the downward transfer of these toxic materials into the farmland soil. The muddy deposit whose particle size was small and the density was small is distributed the far area from a shoreline. The maximum thickness of the deposit was 0.05 m. The particle density of this deposit was small and the organic matter content was very large, which suggested that the dried and small particle of the deposit injured human with microorganism or its products including in the deposit. The cation concentrations of the extract water of this deposit absorb was large which indicated the possibility that the anion absorption of it was also large. From the approximation of the shape of the area and the bulk density and the thickness of the deposits, the amount of the deposit was estimated 124,000m^3 in volume and 193,000 Mg in dry mass. The thickness of the deposit in Shibusa whose distance from Kashima is about 3,000 m, however, did not increase with the distance from the shoreline and it is suggested that the condition of the deposit was different among the location.

5 REFERENCES

[1] The Geospatial Information Authority of Japan (GIA), "About the total tsunami inundated area (rough estimated value) (5th report)", http://www.gsi.go.jp/common/000059939.pdf , 2011 (in Japanese)

[2] Ministry of Agriculture, Forestry and Fisheries (MAFF), Manual for salt leaching", http://www.maff.go.jp/j/press/nousin/sekkei/pdf/110624-01.pdf ", 2011 (in Japanese).

[3] Japan Meteorological Agency (JMA), "AMeDAS", http://www.jma.go.jp/jp/amedas_h/, 2011 (in Japanese)

[4] Nishimura Y. and Miyaji N., "Tsunami deposit from the 1993 southwest Hokkaido earthquake and 1640 Hokkaido Komagatake Eruption, Northern Japan", Pegeoph, Vo. 144, 1995, pp.719-733

[5] Peters R., et al., "Distribution and sedimentary characteristics of tsunami deposits along the Cascadian magin of western North America", Sed. Geol., vol 200, 2007, pp.372-386l

[6] Matsumoto D., et al., "Thickness and grain-size distribution of 2004 Indian Ocean tsunami deposits in Periya Kalapuwa Lagoon, eastern Sri Lanka", Sed. Geol., vol 230, 2010, pp.95-104

[7] Richmond B. M., et al., "Deposit, flow characteristics, and landscape change resulting from the September 2009 South Pacific tsunami in Samoan islands", Earth-Sci. Rev., vol. 107, 2011, pp.38-51

[8] Morton R. A., et al., "Physical criteria for distinguishing sandy tsunami and storm deposit using modern examples", Sed. Geol., vol 200, 2007, pp.184-207

[9] Gelfenbaum G. and Jaffe B., "Erosion and sedimentation from the 17 July, 1998 Papa New Guinea Tsunami", Pure appl. Geophys., vol. 160, 2003, pp.1969-1999

[10] Mcleod M.K., et al., "Soil salinity in Aceh after the Decmber 2004 Indian Ocean tsunami", Agric. Water Manag., vol. 97, 2010, pp.605-613

[11] Dawson A. G. and Stewart I., "Tsunami deposit in the geological record", Sed. Geol., vol 200, 2007, pp.166-183

[12] Nakayama F. and Shigeno K., "Inflow and outflow facies from 1993 tsunami in southwest Hokkaido", Sed. Geol., vol. 187, 2006, pp.139-158

[13] Goto K. and Fujino K., "Problems and perspectives of the tsunami deposits after the 2004 Indian Ocean tsunami, Jour. Geol. Soc. Japan, vol. 114, No.12, pp.599-617 (in Japanese with English abstract)

[14] Moore A. L., et al., "Landward finding from multiple sources in a sand sheet deposited by the 1929 Grand Banks tsunami, Newfoundland", Sed. Geol., vol 200, 2007, pp.336-346

[15] Hulugalle N. R., et al., "Physical properties of tsunami-affected soils in Aceh, Indonesia: 2 1/2 years after the tsunami", Catena, vol. 77, 2009, pp.224-231

[16] Szczuciński W., et al., "Contamination of tsunami sediments in s coustal zone inundated by the 26 December 2004 tsunami in Thailand", Environ. Geol., vol. 49, 2005, pp.321-331

[17] Szczuciński W., et al., "Effects of rainy season on mobilization of contaminants from tsunami deposits left in a coastal zone of Thailand by the 26 December 2004 tsunami", Environ. Geol., vol. 53, 2007, pp.253-264

First International Conference on Geotechnique, Construction Materials and Environment, Mie, Japan, Nov.21-23, 2011, ISBN: 978-4-9905958-0-7 C3051

Changes in Bottom Ssediment Caused by Construction of the Airport Island in Ise Bay, Japan.

Maki OYAGI[1], Motohiro KAWASE[2] and Akihiko YAGI[1]

[1]Dept. of Engineering, Aichi Institute of Technology
[2]Dept. of Human Science, Aichi Mizuho University

ABSTRACT: In order to investigate the impact on the marine environment from the construction of the Chubu International Airport Island in Ise Bay, Japan, we made careful observations to clarify the actual seawater, bottom sediment condition and the composition of benthic fauna at some stations located from east to south of the airport island. Grain size compartment, moisture percentage, ignition loss, carbon, nitrogen, phosphorus and sulfur were measured. The ignition loss values in surface sediment in 2003 averaged 150% times higher than that of data in 2007. The benthic fauna revealed the species and number of individuals were very few. Organic matter increases, the species structure of the benthos is made poor. The average number of individuals and species compared before and after the Airport construction clearly showed a remarkable decrease after the construction. This phenomenon might reflect the ongoing progress of eutrophication and oxygen depletion around the airport island sea.

Keywords: Bottom sediment, Airport Island construction, Carbon, Nitrogen, Benthic fauna

1. INTRODUCTION

The Chubu International Airport Island was constructed along the east coast of Ise Bay where fishing grounds have been especially excellent. However, the Oceanographic Soiety of Japanese Environmental Issues Commission warned that this sea area environment would be negatively impacted by constructing the airport island [1]. On the other hand, the Central Japan International airport Co., Ltd. and Aichi prefecture reported that an environmental assessment in connection with the airport island construction revealed minor damage to fishing grounds [2]. After the airport island (580 ha) was built, the other side area (130 ha) of the airport island was developed. After the airport opening in 2005, the investigation near the airport island has been continually carried out every year by Aichi Prefecture and the Central international airport Co., Ltd. [3]-[5]. Originally, the Tokoname City open sea is going sea area, while the fresh water in the Kisosansen River is mixed with seawater, which reading tends to stagnate on the south side in the airport island.

When diving fishermen who have been enaged in fishing in these sea areas, were asked why the shellfishing decreased so shaphy recently, they agreed to coorerate with the present study by assisting with the core sampling of the bottom sediments. This study the purpose of our study is to clarify the effect of large structure of the coastal zone on the nearby sea area environment for water quality, bottom sediments and the benthos.

2. Methods

2.1 Study site

The study site was located on the Ise Bay sea area between the Chubu International Airport Island and Chita Peninsula. Seven sampling points were selected: very shallow sea area; A1 (4 m depth), A2 (3 m depth), A3 (5 m depth), A4 (7 m depth) and shallow area; B1 (11 m depth), B2 (11 m depth), B3 (13 m depth), where water quality and sea sediment were examined. Observations were conducted twice a year (2002, 2004, 2005, 2006 and 2007) and three times in 2003, respectively.

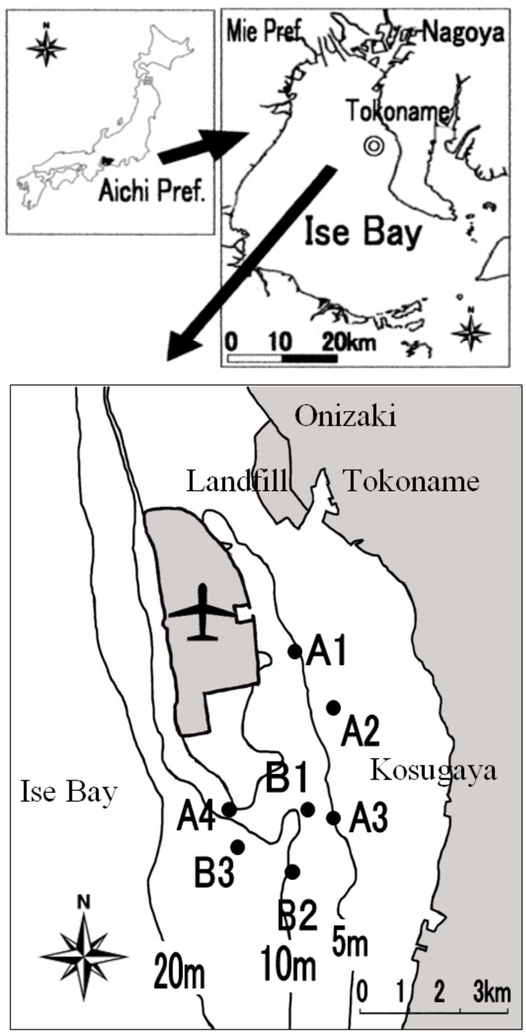

Fig.1 Study site

2.2 Sampling and analysis

Sediment core samples, three acrylic pipes (5 cm in diameter and 50 cm in length), were taken from the each location with two divers, and two core samples of three cores were subdivided into 1 to 2.5 cm-thick sections with a knife by extruding sediment core vertically.

Ignition loss (I.L.: 650℃), total nitrogen (TN), total organic carbon (TOC) and total sulfur (TS) were analyzed with a CHNS analyzer (Perkin Elmer CHNS/O analyzer 2400). The grain size was analyzed using the test method for particle size distribution of soils (JIS A 1204) and was fractionated to six (75 µm or less, 75 to 125 µm, 125 to 250 µm, 250 to 500 µm, 500 to 2 mm, 2 to 4 mm).

Bottom sedimentation rate was estimated by applying the ^{210}Pb method using the bottom sediment cores sample in 2004 and was 0.5 cm y^{-1} in the surrounding area [7]. Furthermore, 0.06～0.76 g cm^{-2} y^{-1} of the sedimentation rates were reported by the applying ^{210}Pb method of ten stations in Ise Bay [8].

Therefore, it was necessary to analyze sediment sample in 1-cm to 2.5-cm-thick sections vertically in order to clarify the environmental change around the airport island.

Macrobenthos was collected by the quadrat method (25 cm square, 25 cm depth), and the sediment was separated by a sieve (φ1 mm). The kind and number of the mollusks were obtained.

3 RESULTS AND DISCUSSION

3.1 Particle size distribution.

Organic matter contents of in B1, B2 and B3 were high ratio of silt-clay fraction and those of B1, B2 and B3 were 39-40%, 31-41% and 20-28%, respectively (Table 1). The silt-clay fraction was big for B2 and B3 in 0-1 cm layer in the pole surface sediment, and with deepening form 1-2 cm layer to 2-3 cm layer this fraction became clearly small tendency.

In spite of shallow A1, the silt-clay fraction was relatively large with 11-13% and then it was indicated that the sea water was easy to stagnate.

3.2 Ignition loss, carbon, nitrogen, phosphate, sulphur

In case of the mean of surface layer (0-1 cm) for carbon and nitrogen ratio (C/N) from September, 2004 to October, 2005, the values of more than 10, less than 7 and the middle were stations of B2 (11)- B3 (13)- A4 (16), stations of A2 (7)-A1 (6) and stations of B1 (9)-,A11 (9), respectively. From this fact, the decomposition of the organic substance seems to progress at sites (B2, B3), where the depth is great, and the site A4 in the pole shallow sea area. At the site with the shallow depth, the influence or the comparatively new sediment was strong, suggesting that B1 and A2 were in between. As for the C/N value, on the other hand, in light of the result from September 2004 to October 2005, a clear difference was recognized between the surface layer (0-1 cm) and the layer beneath. The C/N value has become smaller, suggesting that, under autochthonous production, the sediment seems to immediately deposit on this very surface, causing at least a temporary disturbance with a typhoon. The sites where the stratified structure was clearly recognized were B1, B2, B3, A3 and A4, and A1 and A2 estimated that the disturbing (about 0～7cm) of sedimentary layer occurs in the shallow site coastal from the vertical distribution of C/N,

In order to show the poor oxygen condition of the bottom sediments, the total sulfur was determined.

The ignition losses for B1, B2 and B3 with great depth were high concentrates and the total sulfur was also high with the maximum value of 1～5 mg g^{-1} (Fig. 2). The total sulfur of the surface in the pole surface of 0～2 cm layer tended to be high. Furthermore, the value total sulfur of about 0.3~0.7 mg g^{-1} , of total sulfur was measured in the relatively shallow sea area of A4, where bottom mud evidenced a hydrogen sulfide smell.

In addition, red tide was appeared in the investigation sea areas in July 2005. All bottom core samples to the laboratory turned black within around 6 hours. It showed that a remarkable reduction condition had occurred in that bottom area.

Table 1 The particle size distribution

station	depth (cm)	75 μ m>	75-125 μ m	125-500 μ m	500 μ m-2mm	2-4mm	>4mm
A1	0-1	4.52	5.89	87.50	2.10	0.00	0.00
	1-2	5.75	7.17	85.47	1.30	0.32	0.00
	2-3	6.34	4.81	85.64	2.82	0.39	0.00
A2	0-1	2.72	0.87	92.07	3.04	0.74	0.56
	1-2	3.11	0.88	90.72	3.36	0.37	1.57
	2-3	2.96	0.95	90.50	4.92	0.68	0.00
A3	0-1	3.13	2.11	79.92	14.84	0.00	0.00
	1-2	2.69	1.30	75.15	20.40	0.45	0.00
	2-3	2.95	1.37	72.91	20.92	1.86	0.00
A4	0-1	1.80	0.30	85.89	11.16	0.86	0.00
	1-2	1.76	0.00	83.18	13.93	0.54	0.59
	2-3	1.77	0.00	82.41	13.32	2.50	0.00
B1	0-1	30.21	9.06	44.80	8.30	3.59	4.05
	1-2	24.10	10.48	50.60	9.24	4.81	0.77
	2-3	26.97	13.73	45.55	6.66	3.43	3.66
B2	0-1	38.29	7.73	35.33	14.14	1.75	2.75
	1-2	22.66	12.11	49.92	12.80	1.96	0.55
	2-3	18.66	12.29	47.83	12.86	2.31	6.04
B3	0-1	16.87	11.88	66.76	3.43	0.73	0.33
	1-2	14.22	9.78	70.17	3.70	1.69	0.44
	2-3	13.94	6.40	73.72	3.22	1.63	1.09

3.3 IL Comparison around the airport construction

Ignition loss in 2003 and 2007 in the surface layer (at 0-2.5 cm depth) from the result of the dating which corresponds to about 5 years was compared at each point (Fig. 3). The 2003 value corresponds from 1999 to 2003, and the 2007 value to that from 2003 to 2007. This 5 cm thickness was equivalent to approximately 5 years from a result of the measurement of the sedimentation rate. At deep areas of B1, B2 and B3, the 2003 value is remarkably higher than in 2007, averaging 150%. 112% was obtained at A2, A3 and A4 site in very shallow sea. Beside, TS4 data showed the most remarkably changed value of 190% despite the shallow depth. It appeared at a place especially where the influence on the deep bottom sediments of the construction airport island started in November, 2000 was remarkable.

In this way, the progress of the bottom mud pollution clealy changed at A1 in very shallow sea and also at A4 where the sea bed had a convex shape.

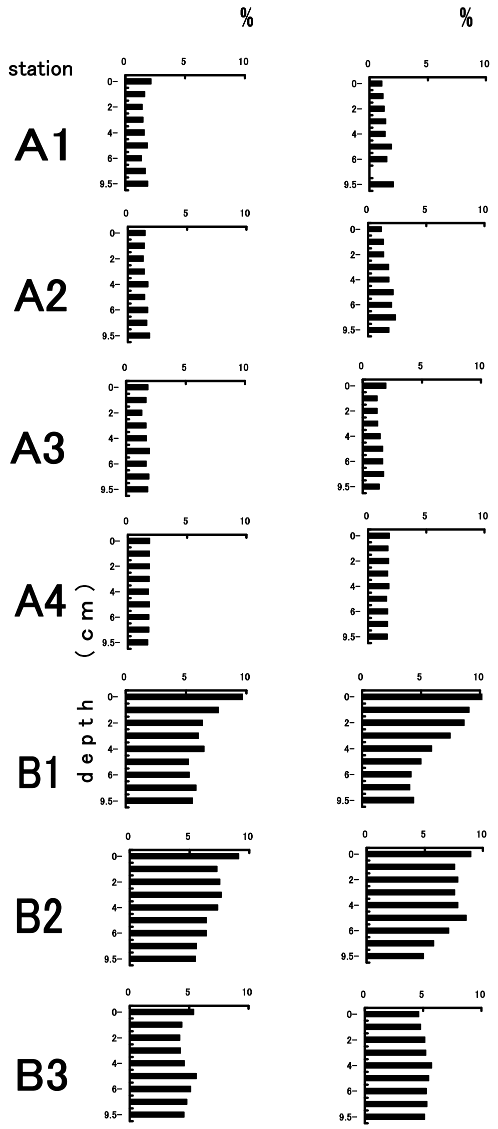

Fig.2 Ignition loss in vertical distribution

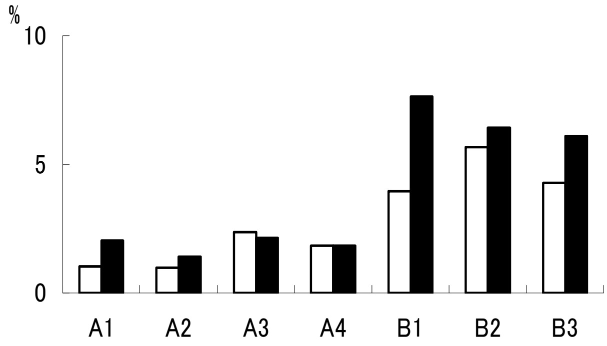

Fig.3 Ignition loss of surface layer (0-2.5 cm depth) in 2003 (white bar) and in 2007 (black bar)

4 ACKNOWLEDGMENT

The authors wish to thank the Himaka Island Fishermen's Union for their valuable field assistance. This study was supported by the 13th Pro Nature Fund, a grant for Japan-Related Research Project 2006 from the Sumitomo Foundation, the Aoi Umi fund 2009 from the Oceanographic Society of Japan.

5 REFERENCES

[1] The oceanographic society of Japanese environmental issues commission "For construction of artificial islands Central International Airport" (in Japanese), Journal of Oceanography, vol.8, 1999, pp. 349-357.

[2] Central Japan International air port Co., Ltd. and Aichi prefecture "The environment assessment's brief about the construction project of the Central Japan International Airport and the constructed project of the airport island area land for development (abstract)" (in Japanese) , 1998, 269pp.

[3] Central Japan International airport Co., Ltd. and Aichi prefecture "Annual report of environmental monitoring results (2002) about the construction project of the Central Japan International Airport, the constructed project of the airport island area land for development and the constructed project of the other side of the airport island " (in Japanese), 2003, 442 pp.

[4] Central Japan International Airport Co., Ltd. and Aichi prefecture "Annual report of environmental monitoring results (2003) about the construction project of the Central Japan International Airport, the constructed project of the airport island area land for development and the constructed project of the other side of the airport island" (in Japanese), 2004, 426 pp.

[5] Central Japan International Airport Co., Ltd. and Aichi prefecture "Annual report of environmental monitoring results (2004) about the construction project of the Central Japan International Airport, the constructed project of the airport island area land for development and the constructed

project of the other side of the airport island" (in Japanese), 2005, 464 pp.

[6] The ministry of the environmental water quality beau, "Marine environmental monitoring guidelines", The ministry of the finance Printing beau, 1997, 136pp.

[7] Saijo Yatsuka, Hisayoshi Terai, Maki Umemura, Akihiko Yagi, Mariko Nagano, Yoshihisa Kato, Motohiro Kawase, Yasuo Matsukawa and Katsuyuki Sasaki, "Degradation of seawater and sediment quality and benthic fauna composition caused by construction of the Chubu international airport island in Ise bay, Japan" (in Japanese), 2008, Oceanography in Japan, 17(4), 281-295.

[8] Lu, X. and E. Matsumoto (2005): Recent sedimentation rates derived from ^{210}Pb and ^{137}Cs methods in Ise Bay, Japan. *Estuarine, Coast. Shelf Sci.*, **65**, 83-93.

First International Conference on Geotechnique, Construction Materials and Environment, Mie, Japan, Nov.21-23, 2011, ISBN: 978-4-9905958-0-7 C3051

Proposal of simple measurement method for evaporation rate by using oxygen isotopic ratio in the Inawashiro Lake

Satoshi Miyahara[1)], Hiroyuki Ii[2)]
1)Graduate School of Systems Engineering, Wakayama University
2)Faculty of Systems Engineering, Wakayama University

ABSTRACT: The purpose of this study is to develop simple method for estimating evaporation rates of water using oxygen isotopic ratio. From the laboratory test, strong negative correlation between average humidity and $\delta^{18}O$ change per unit evaporation rate was observed and humidity was clarified to be important parameter. We can calculate evaporation rate from the amount of change of the $\delta^{18}O$ during evaporation, the amount of change of the $\delta^{18}O$ per unit evaporation rate estimated empirically determined under each humidity condition and humidity.
The amount of evaporation per year in the Inawashiro lake in Fukushima was estimated to be 670 mm/year from the relation between humid and evaporation rate and the estimated value was in agreement with the calculation result of previous research, 600mm/year. Therefore, the simple estimation method is effective for estimation of evaporation rate of an actual lake or a pond especially in a dried area because the measurement error is small under the low humid condition.

Keywords: evaporation rate, oxygen isotopic ratio, humidity, the Inawashiro lake

1. INTRODUCTION

Recently, water shortage is caused by climate change such as Global warming. Therefore, estimation of amount of evaporation for dam, reservoir and irrigation water is important for preservation of water resources.

There are various methods to calculate an amount of evaporation such as Thornthwaite method (Thornthwaite, 1948) and the Penman method (Penman, 1948), etc.

The relation between evaporation and isotope is discussed [1], [2]. The estimation method of evaporation rate using isotopic ratio was made by Allison et al. [3] or Gibson et al. [4]. However the method included many parameters such as humidity, partition coefficient, oxygen isotopic ratio of vapor, kinetic isotope effect, resistance of diffusion, and so on shown in expression (1) [5], [6] and then the some parameter is very difficult to measure or estimate. Therefore, estimation method of evaporation rate to calculate from isotope is very difficult because evaporation rate is controlled by many parameters.

$$\frac{d\,\delta_L}{d\ln f}=\frac{h_A(\delta_L-\delta_A)/(1+\delta_L)-\varepsilon^*}{(a-h_A)(a\cdot\alpha_{vap-liq}\cdot e_{i,L}/e+e_i/e)} \qquad (1)$$

δ_L : isotopic ratio of water
f : ratio of water that remains for the first water
δ_A : isotopic ratio of vapor
h_A : humidity
a : water activity
ε^* : $a\varepsilon+\triangle\varepsilon$ (ε : equilibrium vapor pressure ratio, $\triangle\varepsilon$: amount of change equilibrium vapor pressure ratio)
$\alpha_{vap-liq}$: partition coefficient
$e_{i,L}$: diffusion resistance of heavy water in water
e : diffusion resistance of steam in atmospheric (Constant)
e_i : diffusion resistance of heavy water in atmospheric

However, if there is some effective parameter to determine evaporation rate using isotope, we can estimate evaporation rate from limited parameter to measure easy.

Therefore, the purpose of this study is to develop simple method for estimating evaporation rates of water using oxygen isotopic ratio and finding effective parameter for calculation of evaporation rate [7]–[9]. Then, we can estimate the oxygen isotopic ratio of residual water when the evaporation rate of water reaches 1%.

2. EXPERIMENT AND ANALYSIS

In laboratory test, amount of average evaporation of day, temperature, humidity, and saturation deficit were measured and then the relation of oxygen isotopic ratio of water and their parameters was analyzed.

Table-1 shows the environmental condition and the actual measurement value of the test.

The 33 evaporation tests were performed between 2005 and 2010 in the drying chamber with uniform temperature, the refrigerator with low temperature and the rooftop of the building in the Wakayama University. Figure-1 shows the pictures of evaporation experiment. The water used for the experiment was tap water of Wakayama University.

Both of the 5L (170 mm in the diameter, 300mm in the height, and 75 mm in the mouth diameter) and the 2L (126 mm in the diameter, 245 mm in the height, and 75 mm of mouth in the diameter) bottles were used for checking influence of difference of water volume on the relation between isotopic ratio of water and evaporation rate under the experiment.

Figure-2 shows the flow of the experiment. The quantity of water is measured at the intervals of several days during evaporation period and then 20 ml water was sampled from the residual water for clarify relation between evaporation rate and the oxygen isotopic ratio.

After the carbon dioxide equilibrium method, the oxygen isotopic ratio of the sampled water was measured with mass spectrometer (Finnigan Mat Delta Plus). The measurement error of oxygen isotopic ratio ($\delta^{18}O$) is ±0.1‰. The temperature and humidity were every hour measured and the data was memorized with the storage meter (Sato meter factory SK-L200TH). Moreover, the temperature and the humidity of the outdoor experiment period were used the

Tab.1 Environmental condition and actual measurement value of the evaporation experiment

	Vessel	Evaporation Place	Average Temperature (℃)	Average Humidity (%)	Saturation Deficit (g/m^3)	Amount of average evaporation of day(mm/day)	Start Date	End Date
1	5L	indoor	8.8	68.7	2.3	0.8	2007/11/8	2008/4/11
2			9.9	65.3	2.7	0.7	2005/12/15	2006/4/28
3			19.3	74.3	3.6	1.4	2008/4/21	2008/7/9
4			23.8	74.6	4.7	1.4	2008/7/11	2008/9/17
5			24.8	47.3	11.2	3.6	2008/10/22	2008/12/1
6			24.9	42.3	12.5	3.5	2008/12/15	2009/1/23
7			29.9	41.1	17.2	3.5	2005/11/3	2005/12/5
8			24.6	68.0	6.3	2.0	2009/4/25	2009/8/5
9			24.9	39.8	13.1	3.3	2009/11/19	2010/1/28
10			10.4	73.4	2.1	0.6	2006/7/4	2007/1/4
11		outdoor	7.8	60.0	2.8	0.7	2007/11/22	2008/4/8
12			13.1	62.1	3.7	1.0	2006/10/24	2007/1/4
13			24.7	66.5	6.7	0.7	2007/6/11	2007/10/29
14			27.2	67.5	7.5	1.5	2008/7/1	2008/9/17
15			23.9	65.5	6.6	2.4	2009/4/30	2009/8/27
16			7.1	59.9	2.6	0.6	2007/11/22	2008/3/11
17			24.7	66.5	6.7	0.7	2007/6/11	2007/10/29
18			13.0	61.9	3.7	0.9	2006/10/24	2007/1/4
19	2L	indoor	9.0	69.0	2.3	0.8	2007/11/8	2008/2/27
20			19.8	72.8	3.9	1.4	2008/4/21	2008/6/23
21			24.8	74.8	4.9	1.4	2008/7/11	2008/9/17
22			24.9	53.8	9.7	5.5	2008/10/22	2008/11/18
23			24.9	42.1	12.6	5.7	2008/12/15	2009/1/22
24			24.7	59.2	8.3	3.6	2009/4/25	2009/6/5
25			25.0	42.6	12.5	4.2	2009/11/19	2009/12/21
26		outdoor	7.1	59.9	2.6	0.8	2007/11/22	2008/3/11
27			27.6	67.6	7.6	1.9	2008/7/1	2008/8/29
28			21.7	63.5	6.1	2.2	2009/4/30	2009/8/3
29			7.1	59.9	2.6	1.0	2007/11/22	2008/3/11
30			17.2	64.5	4.5	2.3	2009/10/9	2009/11/9
31			17.2	64.5	4.5	2.6	2009/10/9	2009/11/9
32		Refrigerator	4.6	25.3	4.6	0.4	2009/7/24	2010/3/8
33			5.5	89.6	0.6	0.2	2008/7/14	2009/1/20

【drying chamber】

【refrigerator】

【rooftop in the Wakayama University】

Fig.1 pictures of evaporation experiment

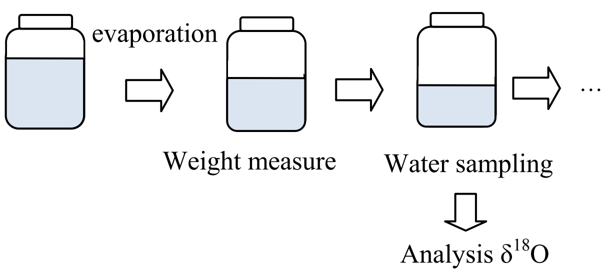

Fig.2 Flow of the evaporation experiment

meteorological data of Wakayama City of the Meteorological Agency.

3. RESULT

3.1 Factor in which it affect oxygen isotopic ratio

Figure-3 shows relationship between the amount of change of the $\delta^{18}O$ per unit evaporation rate and each amount of average evaporation of day, saturation deficit, average temperature and average humidity.

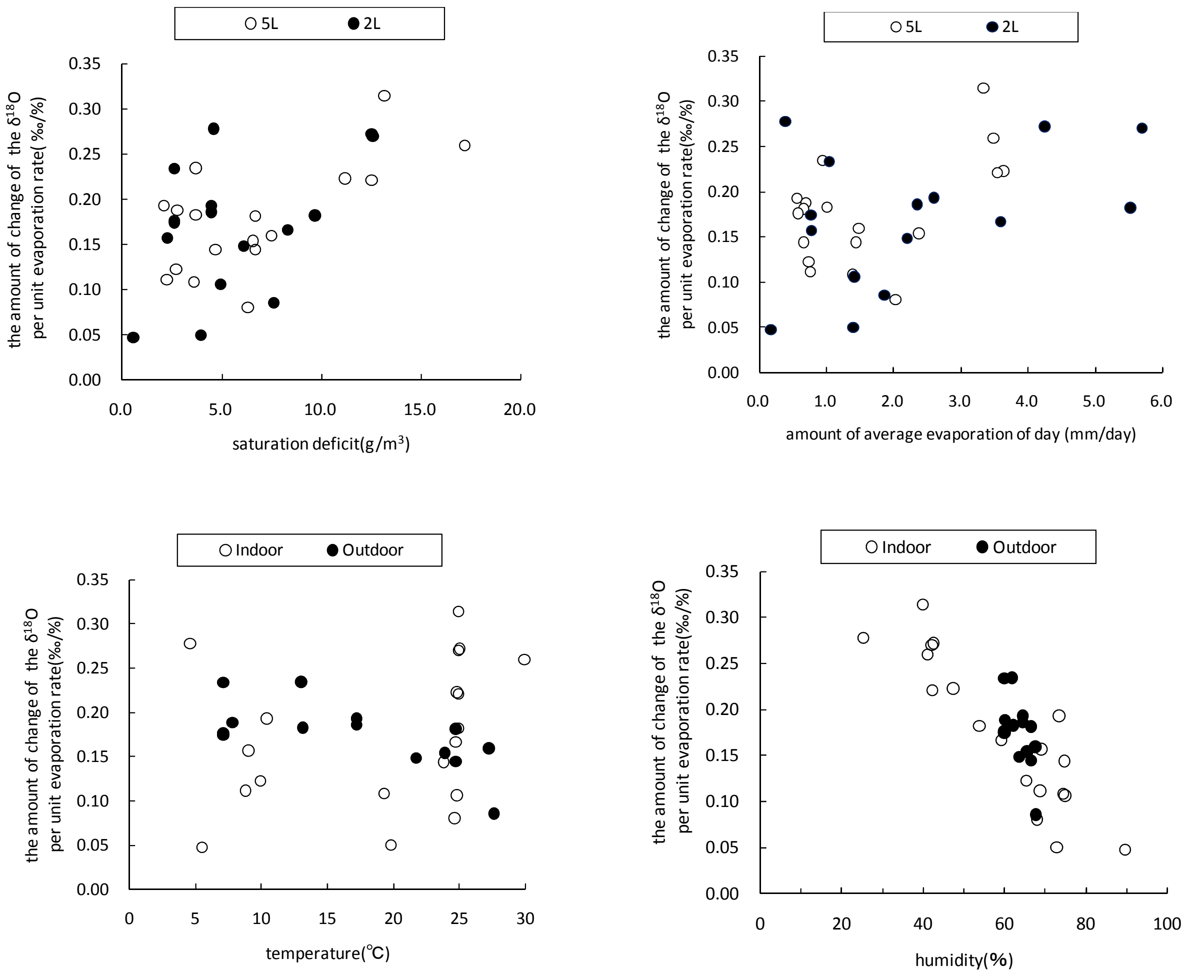

Fig.3 relationship between the amount of change of the $\delta^{18}O$ per unit evaporation rate and each amount of average evaporation of day, saturation deficit, average temperature and average humidity

From the test, negative correlation (R= -0.84) between the average humidity and the amount of change of the $\delta^{18}O$ per unit evaporation rate was found. In particular, the amount of change of the $\delta^{18}O$ per unit evaporation rate is sensitive to humidity under the low humidity condition and then change of the $\delta^{18}O$ per unit evaporation rate of residual water is large during evaporation process under a dry area.

The results of the outdoor experiments were not greatly different from the indoor laboratory results.

Big differences between outdoor and indoor conditions were wind and air volume because temperature and humidity were controlled or measured under the both indoor and outdoor experiments. Therefore, humidity condition was more important than wind and air volume condition.

3.2 Variation of the amount of change of the $\delta^{18}O$ per unit evaporation rate

Figure-4 shows the monthly variation of the amount of change of the $\delta^{18}O$ per unit evaporation in summer (2008.4～2008.7) and in winter(2008.12～2009.1). The humidity was high in summer and low in winter and then, the amount of change of the $\delta^{18}O$ per unit evaporation rate increased from -0.1 to 0.3 ‰ / % as humidity decreased from 80 to 40 %. Therefore, the humidity change accompanying seasonal change was clarified to affect apparently the amount of change of the $\delta^{18}O$ per unit evaporation rate.

Figure-5 shows relationship of the amount of change of the $\delta^{18}O$ per unit the amount of change of evaporation rate and humidity. The amount of change of the $\delta^{18}O$ per unit the amount of change of evaporation rate changed from 0.2 to -0.2 ‰ / % with evaporation rate under the condition of more than 60 % humidity. And then, the amount of change of the $\delta^{18}O$ per unit the amount of change of evaporation rate changed greatly as humidity increased.

On the other hand, under the condition of less than 60 % humidity, the amount of change of the $\delta^{18}O$ per unit the amount of change of evaporation rate kept uniform although evaporation rate changed and then it was in agreement with the equation (1).

3.3 Verification of the measurement method in the Inawashiro lake in Fukushima

The amount of evaporation per year in the Inawashiro Lake in Fukushima was estimated from the relationship of the amount of change of the $\delta^{18}O$ per unit the amount of change of evaporation rate and humidity.

Figure-6 shows distribution of $\delta^{18}O$ of the water in the Inawashiro Lake and rivers surrounding the lake. The area

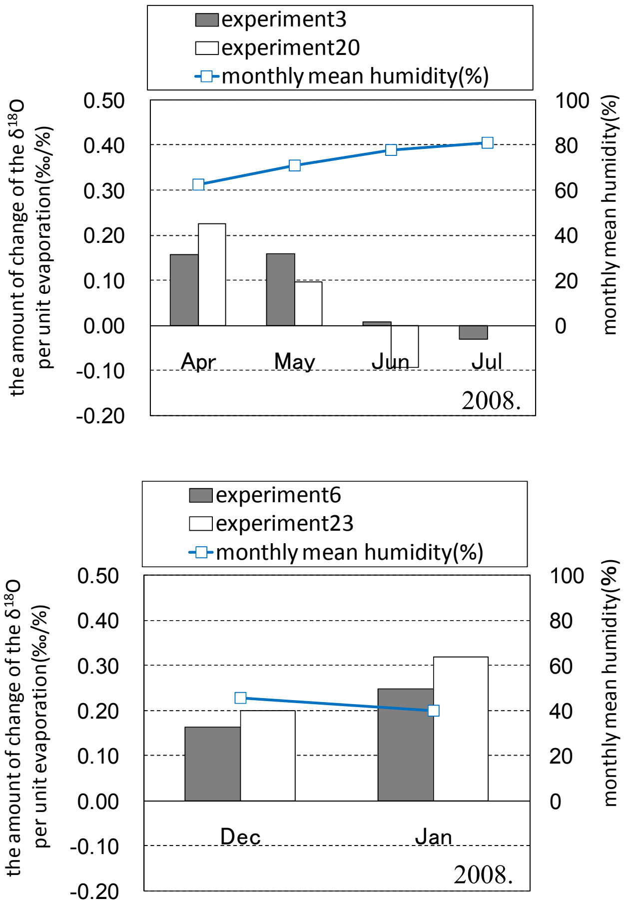

Fig.4 monthly variation of the amount of change of the δ^{18}O per unit evaporation

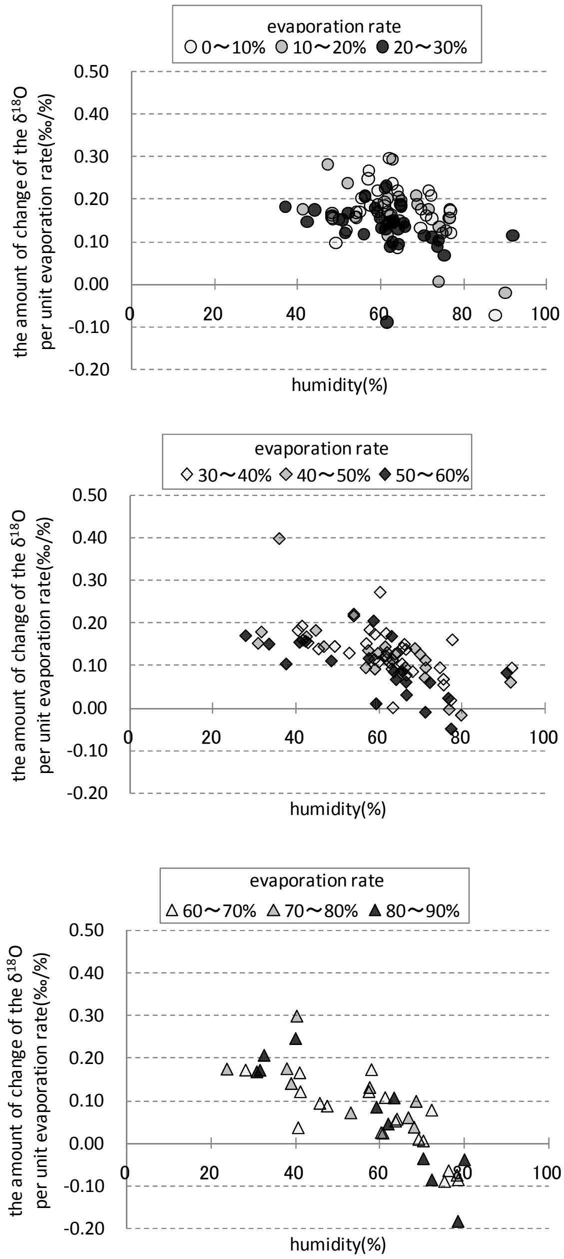

Fig.5 relationship of the amount of change of δ^{18}O per unit the amount of change of evaporation rate and humidity

is 103 km^2. Pondage is 3.9 billion m^3. Maximum depth is about 94 m. The surrounding length is 55 km. It is amount 10300 million m^3 / year of the inflow during the year to the lake. The detention period is estimated by dividing the amount of reservoir during year by the amount of the inflow, and the estimated value is about 3.7 years.

As the δ^{18}O value of the lake was -9.3 ‰ and the δ^{18}O value of the inflow rivers was -10.3 ‰, the δ^{18}O of water increased from -10.3 ‰ to -9.3 ‰ by evaporation process [8].

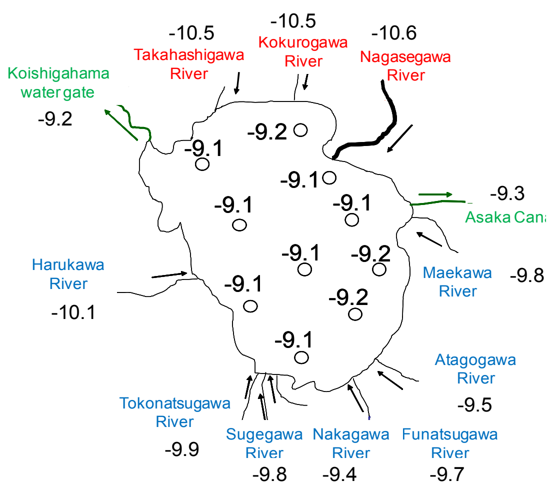

area: 103 km^2

pondage: 3.9 billion m^3

amount of the inflow during the year to the lake: 10300 million m^3 / year

detention period: 3.7year

average humidity: 74%

δ^{18}O of lake before evaporation: -10.3‰

δ^{18}O of lake after evaporation: -9.3‰

Fig.6 distribution of δ^{18}O of the water in the Inawashiro Lake and rivers surrounding the lake

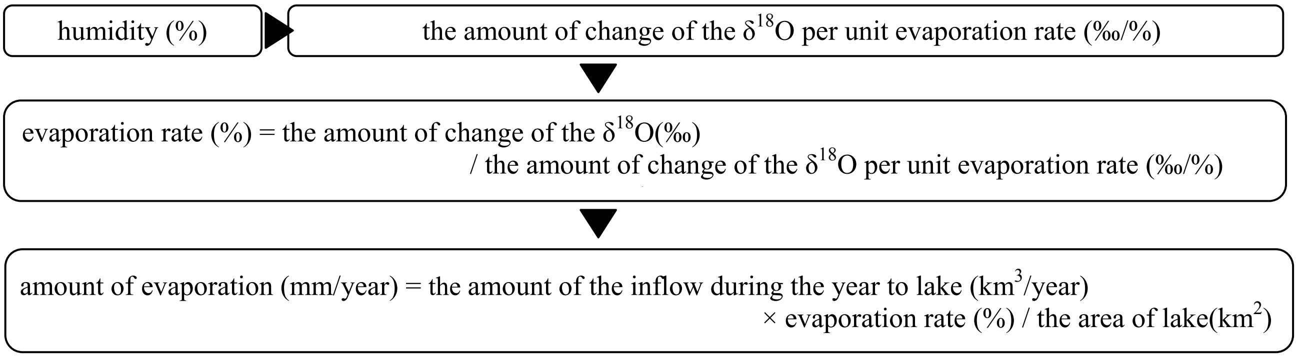

Fig.7 flow of the calculation of the amount of evaporation

The amount of change of the $\delta^{18}O$ evaporation process was 1 ‰.

Also the amount of evaporation of the lake was calculated from the method of Jacobs (1975) with the aerodynamical technique and the estimated value was 600 mm/year [10].

In the Inawashiro Lake, the average humidity for a year was 74 %. And then, the amount of change of the $\delta^{18}O$ per unit evaporation rate with 74 % humidity was adopted.

Figure-7 shows a flow of the calculation of the amount of evaporation.

1) The amount of change of the $\delta^{18}O$ per unit evaporation rate is determined from the figure-5 and average local humidity.
2) The evaporation rate is calculated from the amount of change of the $\delta^{18}O$ and the amount of change of the $\delta^{18}O$ per unit evaporation rate (‰ / %)
3) The amount of evaporation for a year was calculated from the amount of the inflow during the year to lake, evaporation rate, and the area of lake.

The amount of change of the $\delta^{18}O$ per unit the amount of change of evaporation rate was calculated from relationship between the amount of change of $\delta^{18}O$ per unit the amount of change of evaporation rate and humidity. And then, the amount of change of the $\delta^{18}O$ per unit evaporation rate with 74 % humidity, average humidty in the Inawashiro Lake was 0.15 ‰ / % under the evaporation rate 0〜10 %.

The evaporation rate was calculated from the amount of change of the $\delta^{18}O$ and the amount of change of the $\delta^{18}O$ per unit evaporation rate. Therefore, evaporation rate in the Inawashiro Lake was calculated to be 6.7 % from 1 ‰, the amount of change of the $\delta^{18}O$ and 0.15 ‰ / % , the amount of change of the $\delta^{18}O$ per unit evaporation rate shown in expression (2).

$$1\ (‰) / 0.15\ (‰ / \%) \fallingdotseq 6.7\ (\%) \qquad (2)$$

The amount of evaporation for a year was calculated from the amount of the inflow during the year to lake, evaporation rate, and the area of lake. Therefore, the amount of evaporation for a year in the Inawashiro Lake was calculated to be 670 mm / year from 10300 million m^3/ year, the amount of the inflow during the year to lake and 6.7 %, evaporation rate and 103 km^2, the area of the lake shown in expression (3).

$$10300 \text{ million } (m^3 / \text{year}) \times 6.7\ (\%) / 103\ (km^2) = 670\ (mm / \text{year}) \qquad (3)$$

The estimated value was about 670 mm / year in agreement with the calculation result of the previous research using the method of Jacobs, 600 mm / year.

However when the evaporation rate in the lake exceed 10%, evaporation rate in the lake can be not calculated using only 0.15 ‰ / % because of the amount of change of the $\delta^{18}O$ per unit the amount of change of evaporation rate changed with evaporation rate under the condition of more than 60 % humidity. Therefore, if evaporation rate in the lake exceed 10 %, the amount of change of the $\delta^{18}O$ per unit the amount of change of evaporation rate needs to use depending on the evaporation rate.

4 CONCLUSION

The purpose of this study is to develop simple method for estimating evaporation rates of water using oxygen isotopic ratio. From the empirical results, negative correlation (R= -0.84) between the average humidity and the amount of change of the $\delta^{18}O$ per rate of unit evaporation was clarified. And the amount of change of the $\delta^{18}O$ per unit the amount of change of evaporation rate changed with evaporation rate under the condition of more than 60 % humidity.

The amount of evaporation per year in the Inawashiro lake in Fukushima was estimated to be about 670 mm / year from the relation between humid and evaporation rate and the estimated value was in agreement with the calculation result of the previous research using the method of Jacobs, 600 mm / year.

Therefore, the simple estimation method using only oxygen isotopic ratio and humidity is effective for estimation of evaporation rate of an actual lake or a pond.

And when evaporation rate in the lake exceed 10 %, we can estimate the evaporation rate from the amount of change of the $\delta^{18}O$ per unit the amount of change of evaporation rate changed with evaporation rate.

5. REFERENCES

[1] Machida I, Kondoh A: Stable Isotope Ratios of Natural Water in Japan －The Analysis by Using Environmental Isotopes Database, J. Japan Soc. Hydrol.＆ Water Resour. Vol.16，No.15, pp556-569, 2003.

[2] Yoshimura K, Fujita K, Kurita N, Abe O: International Workshop on Isotopic Effects in Evaporation, -Revisiting the Craig-Gordon Model Four Decades after its Formulation - Participation report, Journal of Japan Society of Hydrology & Water Resources.19, pp.420-423, 2006.

[3] Allison, G.B., Brown, R.M. and Fritz, P : Estimation of the isotopic composition of lake evaporate., Jour, of Hydrol. , 42, pp.109-127, 1979.

[4] Gibson, J.J., Edwards, T.W.D., Bursey, G.G. and Prowse, T.D. : Estimating evaporation using stable isotopes: quantitative results and sensitivity analysis for two catchments in northern Canada, 24, pp.79-94, 1993.

[5] Fontes, J. –ch. and Gonfiantini, R.: Comportment isotopique an cours de levaporation de deux basins Sahariens, Earth Plan.Sci. Letters, 3, pp.277-374, 1967.

[6] Pupezin, J., Jancso, G. and Van Hook, W.A.: Vapor pressure isotope effect in aqueous systems. I, Jour. Phys. hem. , 76, pp.743-762.

[7] Miyaji K, Okada S, Ii H, Nagabayashi H: Proposal of simple measurement method for evaporation rate by using oxygen isotopic ratio in the Inawashiro Lake., Annual Journal of Hydraulic Engineering., Vol.52, pp.289-294, 2008.

[8] Miyaji K, Ii H, Miyahara S: Proposal of method for estimating the evaporation rate in lake by using oxygen isotopic ratios and humidity. , Annual Journal of Hydraulic Engineering., Vol.53, pp.331-336, 2009.

[9] Miyahara S, Ii H: Proposal method for estimating evaporation rates of water using characteristic of change of oxygen isotopic ratio, Japan Geoscience Union Meeting 2011.

[10] Watanabe A: The role of heat of the Inawashiro Lake, Tenki, 30 (3), pp.137-142, 1983.

First International Conference on Geotechnique, Construction Materials and Environment, Mie, Japan, Nov.21-23, 2011, ISBN: 978-4-9905958-0-7 C3051

Landslide Susceptibility Mapping using Logistic Regression Model With Neighborhood Analysis: A Case Study in Mizunami City

Wang Liangjie. Sawada Kazuhide. Moriguchi Shuji., Department of Civil Engineering, Gifu University, Yanagido 1-1, Gifu, 501-1193, Japan

ABSTRACT: Landslides which affect human lives and economic losses are always attracted a lot of concerning in modern society. In order to identify the potential hazardous areas related to landslides, three methods have been used, such as qualitative or knowledge-based method, deterministic method and quantitative-based method. Geographical information system (GIS) technology and high computing ability provide a convenient tool to deal with landslide triggering factors and make the quantitative-based method achieve effectively.

In this study, Landslide-related factors such as topographical elevation, slope angle, slope aspect, topographical wetness index (TWI) and stream power index (SPI), were employed in the landslide susceptibility analysis. The logistical regression was used to obtain the relationships for landslide susceptibility between landslides and causative factors. The distributions of observed landslides were used to evaluate the performance of the susceptibility map. The approaches described in this paper showed us that the logistical regression and neighborhood can be used as simple tools to predict the potential landslide locations. And this map will be helpful for city planning, infrastructure construction and agriculture developments in the future.

Keywords: Landslide, Susceptibility map, Logistic regression, GIS

1. INTRODUCTION

Landslides which cause the loss of human life and the damage to the social economy were attracted a lot of attention over the last decades. According a previous study Schuster (1996) [1], landslides will increase in the next decades due to continued deforesting and the changing climatic patterns in landslide-prone areas. In order to identify the landslide-related area, there are three main approaches to assess the landslide susceptibility: qualitative methods, deterministic methods and quantitative methods. In the late 1970s, qualitative approaches were widely applied by engineering geologists to evaluate landslide. Deterministic approaches focus on slope geometry, shear strength data, and pore-water related data (Netra et al., 2010) [2] but lack of taking climatic and human induced factors into accounted. Nowadays, the rapid developments of computer technology and geographic information system (GIS) provide a convenient tool to deal with landslide triggering factors and make the quantitative-based method achieve effectively. Among a lot of quantitative methods, logistic model was recognized as the suitable approach to assess landslide susceptibility because it is free of data distribution and can handle a variety of datasets (Nandi et al., 2009) [3].

In this study, neighborhood analysis "seed cell approach" proposed by (Suzen and Doyuran., 2004) [4] and logistic model were applied to create the relationship between landslides and controlling factors with GIS in Mizunami city ,Gifu prefecture where is well know for landslide hazards.

2. DATABASE CONSTRUCTION

In order to detect the landslide-related factors, some prior knowledge and experiments should be prepared. The main factors include three aspects such as topographic factors water-related factors and human being activity factor are applied in this study. The approach mentioned is based on the assumption that past environmental conditions at the time of landslides can be keys to evaluation the potential sites for landslide in the future. Then, all the landslide-related factors were created and store in the spatial database by using a GIS software with the pixel size or mesh 10×10m.

2.1 Landslide Related Factors

The first database is topographic factors. We create digital elevation model (DEM) derive from a triangulated irregular network (TIN) using elevation points from GSI (Geological Survey of Japan AIST) with spatial resolution 10m. The parameters such as elevation, slope angle, aspect, plan curvature, profile curvature were constructed from DEM. The second database is water-related factors. Those parameters were also obtained from DEM. The topographical wetness index (TWI) and stream power index (SPI) are important parameters of wetness and stream power [5] (Moore et al., 1991) and these are defined as following formulas.

$$TWI = \log_e(A/b\tan\alpha) \tag{1}$$

$$SPI = A\tan\alpha/b \tag{2}$$

Where A (m^2) is the upstream area, b is the size of the mesh expressed as m. and α is the slope gradient. The third database is the human actively factors. The proximate to the highway was used to indicate the human actives induce the landslides. The table 1 shows the significant of the all parameters related to landslides and their spatial distribution patterns are shown in Fig.1.

2.2 Landslide Inventory and Neighborhood Analysis

The landslide inventory map of the study area was downloaded from the organization of NIED (National

Table 1 Landslide causative factors

Data type	Factors	Significance
	Elevation	Climate, Vegetation
	Slope	sub-surface flow velocity
	Aspect	Evapo-transpiration
Topographic	Plan curvature	Converging, soil water content ,soil characteristics
	Profile curvature	Erosion ,Geomorphology
	Tangent curvature	Erosion and deposition
	Solar radiation	Weathering soil moisture
	Flow length	Run off velocity, run off volume
	Flow direction	Runoff velocity. potential energy
	Flow accumulation	Runoff velocity and potential emerge
Water-related	Stream power index	Erosive power of water flow
	Distance to rivers	Susceptible to hill slope undercutting
	Topographic wetness index	Soil water content
Anthropogenic	Distance to highway	Landslide triggering by road construction and vibration

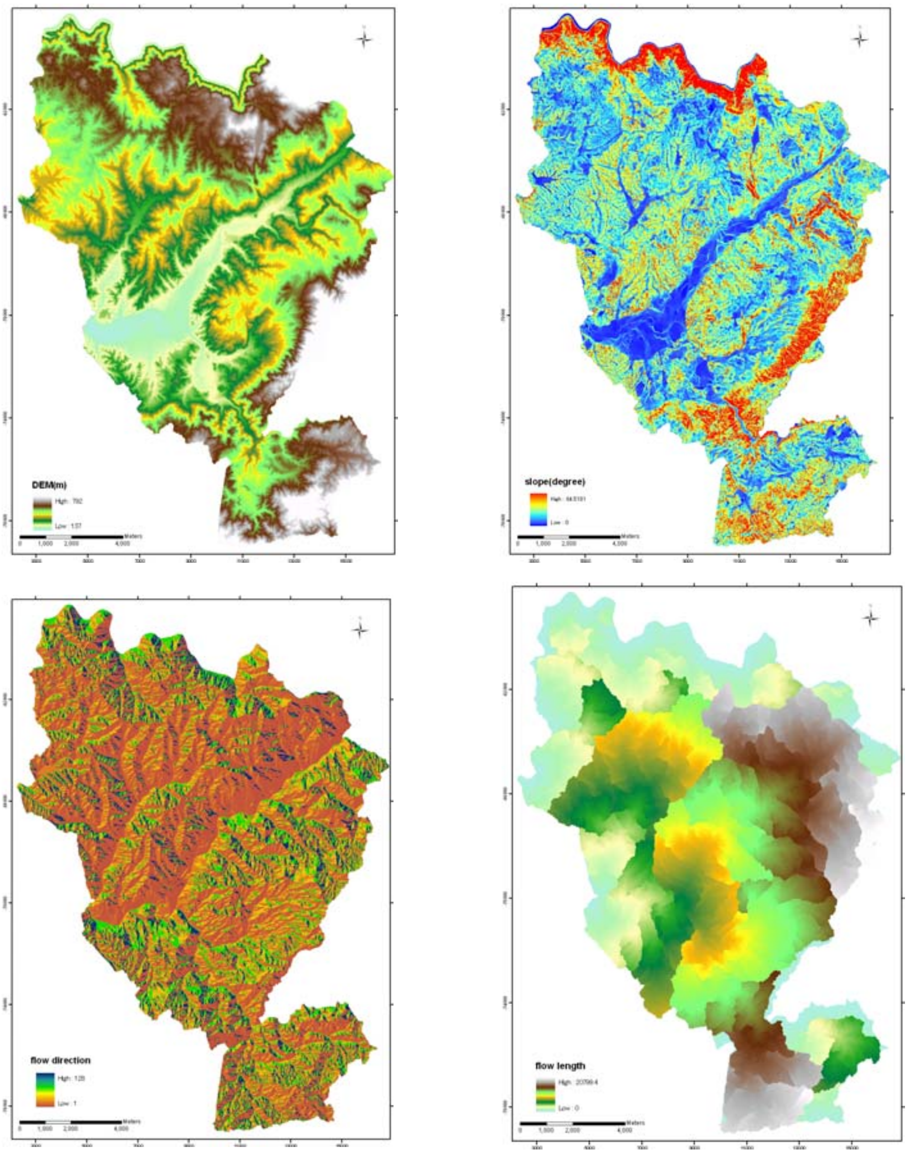

Fig.1. Distribution of landslide causative factors

Research Institute for Earth Science and Disaster Prevention). The sizes of landslides rage from 0.00002 km^2 to 1.2 km^2, which cover 13.6% of the study area. According to Varnes's (1978) definition, mass movement like soil slides, debris slides, rock slides and debris flows are incorporated into the term landslides.

Neighborhood analysis is a spatial analysis tool used to identify the "seed cells" which represent the undestroyed morphologic conditions before the landslides occurred (Suzen and Doyuran., 2004) [4]. These "seed cells" can be extracted from the boundaries of landslides by buffering zone to the landslides. Former studies show us that the buffer zones should be range from 100m to 150m. In this study, 120m buffer zone is chose to be the "seed cells".

3 LANDSLIDE SUSCETIBILITY MAPPING

3.1 Logistic Regression Model

Logistic regression model is applied to establish the relationship between a dependent variable and independent variables (Atkinsm and Massari., 1998) [6]. This model is careless about the distribution pattern of the independent variables. Most of the topographic factors don't have normal distributions. Therefore, logistic regression model could get better results comparing other mathematic models. The predicted values range from 0 to 1 can be defined as landslide hazard index. The index can be expressed as following formula.

$$P = 1/(1+e^{-z}) \tag{3}$$

$$z = b_0 + b_1 x_1 + b_2 x_2 + \ldots + b_n x_n \tag{4}$$

Where P is the probability of landslide occurrence (landslide hazard index), z is the linear logistic mode, b_0 is the intercept of the model, n is the number of landslide causative factors, b_n is the weight of the each factor and x_n is the landslide causative factors.

Our purpose of this research is to propose a model that could be applied in some place where people could not easily get access to or some cities which lack of basic datasets (land cover dataset or digital geological dataset). In this study, most of the landslide-relative factors derive form the DEM that could be easier get from nowadays spatial technology. The causative factors are continuous that would avoid the occurrence of huge redundant data.

3.2 Landslide Points Sampling

Former studies show us that it is the best sampling pattern if the ratio of landslide points to landslide free points is equal to 1(Suzen and Doyuran.,2004) [4]. For this purpose, the ratio is equal to 1 between "seed cells" points that used to extract the attributes from the landslide-causative factors and the random landslide-free points. All of the 11266 points were chosen to create the relationship between landslides and causative factors in logistic regression model. The model would lose his statistic significance if there are no validate points used to identify the efficient of the result. Therefore, the 3518 landslide points occurred in the past were employed to validate the accuracy of the landslide hazard index map. Fig.2 show us the distribution of landslide points, "seed cells" and landslide free points in Mizunami city.

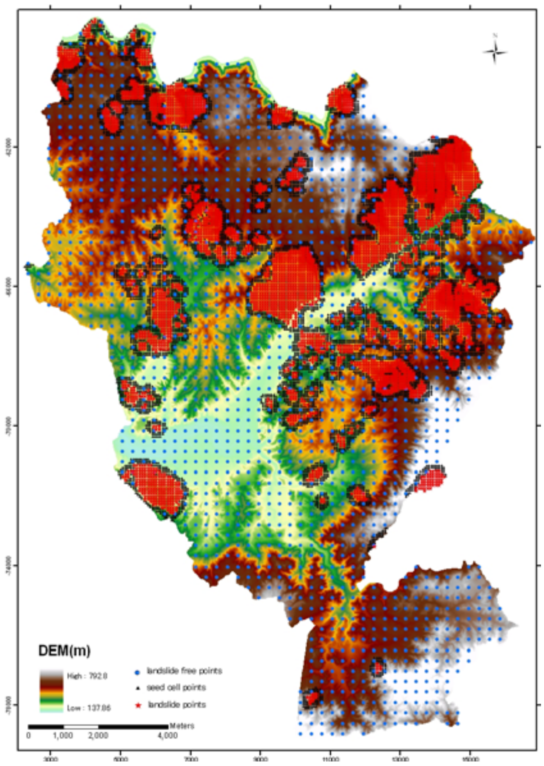

Fig.2. Distribution of sampling points

3.3 Model Results and Validation

The forward stepwise logistic regression model was applied in this study. The probability for stepwise was range from 0.05 to 0.1. And then, $\chi 2$ value of the Hosmer and Lemeshow Test, Cox & Snell R Square and Nagelkerke R Square were applied to evaluate the effectiveness of training datasets. The table 2 shows that the result of the model had statistic significance and the independent variables could explain the dependent variables in this model. During the process of model calculation, the Wald value decreed from 565.8 to 5.3 in all 8 steps. The distance to highway which had the highest value of Wald value implied that this landslide-related factor was the most significant value for explaining landslide occurred, followed by distance to rivers, flow length, elevation, slope angle, solar radiation, and flow accumulation. The relationship between the causative factors and landslide could be shown in table 3. According to table 3, slope angle, flow length and solar radiation were positive relationship with the occurrence of a landslide whereas flow accumulation, distance to highway, elevation and distance to rivers indicated negative relate to the occurrence of a landslide.

Using the weights shown in table 3, the landslide hazard index (LHI) of landslides was calculated (Fig.3).

Table 2 Statistics of logistic regression model with landslide causative factors

Hosmer and Lemeshow Test			-2 Log likelihood	Cox & Snell R^2	Nagelkerke R^2
χ^2	Sig.	Sig.			
173.664	8	.000	14598.819	0.286	0.315

Table 3 Coefficients of the logistic regression model for the seven landslide-related factors

Independent variables	Coefficient
Slope angle	0.01877
Flow length	0.00006
Flow accumulation	-0.000003
Solar radiation	0.000002
Distance to highway	-0.00007
elevation	-0.00289
Distance to rivers	-0.00044
Constant	-0.19102

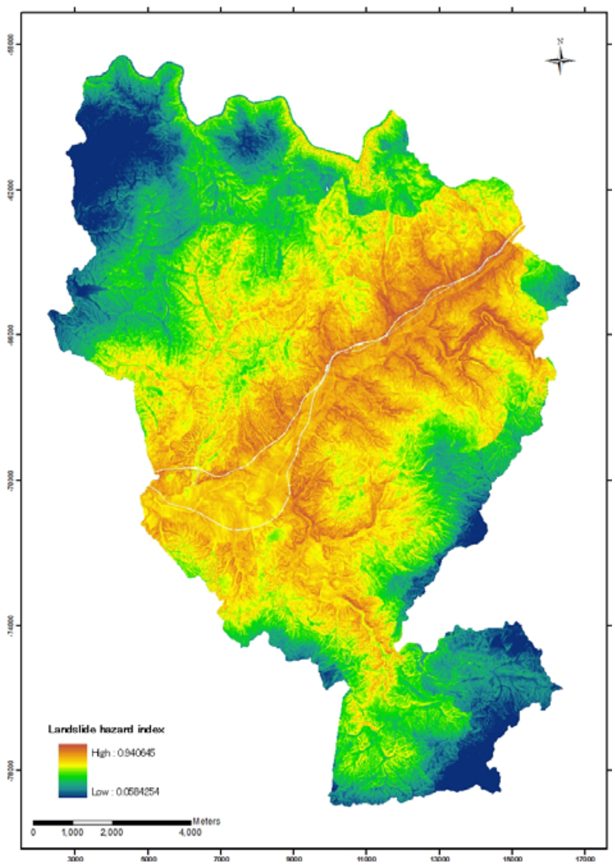

Fig.3. Landslide hazard index map

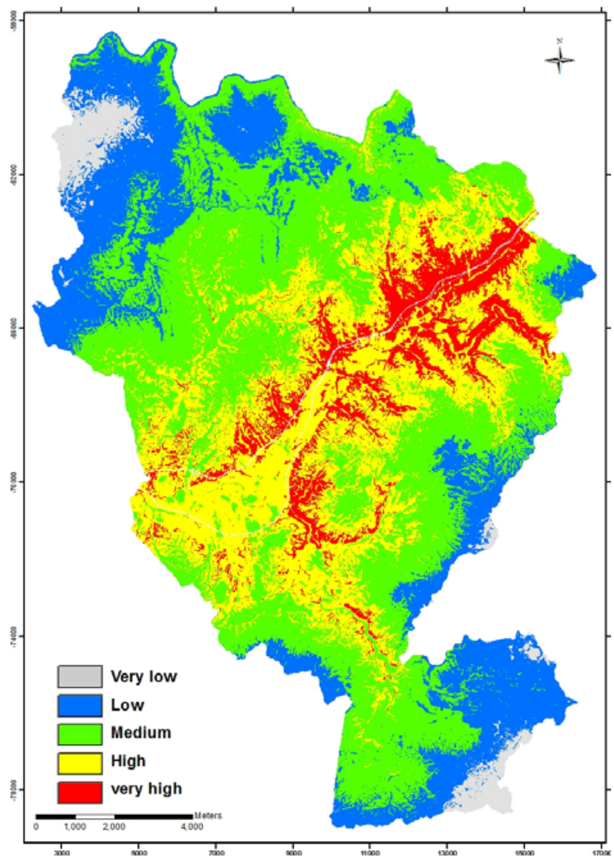

Fig.4. Reclassified landslide susceptibility map

The landslide hazard index decreased from 0.94 to 0.06. If the value is close to 1, it indicates landslides are more likely happen in this area.

The accuracy of the logistic regression model of landslide susceptibility was evaluated by calculating relative operative characteristic (ROC) and percentage of observed landslides points in various susceptibility categories [3] (A.Nandi and A.shakoor., 2009). The area under ROC cure (AUC) value which represents the quality of the probabilistic model by describing its ability to predict the occurrence or non-occurrence of an event was applied in this paper (Yesilnaca and Topal., 2005) [7]. The value of AUC is range from 0.5 to 1. If the AUC value close to 1, that means high accuracy of prediction model and if the AUC value close to 0.5 which indicates the inaccuracy of the model (Fawccett. 2006) [8]. In this study, we obtained the AUC value was 0.69, which implied the reliable correlation between causative factors and landslides. Also the observed landslide points were used to identify the accuracy of the landslide probility map. We divided the landslide hazard index map into five chasses: very low ($0.05<LHI\leq0.1$), low ($0.1<LHI\leq0.3$), medium ($0.3<LHI\leq0.5$), high ($0.5<LHI\leq0.7$) and very high ($LHI\geq0.7$).

From fig.5, 9.55% of observed landslide points were found in very high susceptibility class. 6.76% of the landslide points occur in the areas with very low and low susceptibility classes. Near 60% of the landslide points were concentrated in the area with high susceptibility class. The hypothesis of the method was that a landslide would occur in area with at least medium values of susceptibility or high and very high susceptibility values (Bai et al., 2010) [9]. 93.2% of landslide points appeared in the area with susceptibility classes from medium to very high. Among the whole Mizunami city, 12% of the study area was designated as very high susceptibility zone which had the approximately equal percentage of the former landslide area (covering 13% of the study area) indicated that the dividing approach was appropriate in Mizunami city.

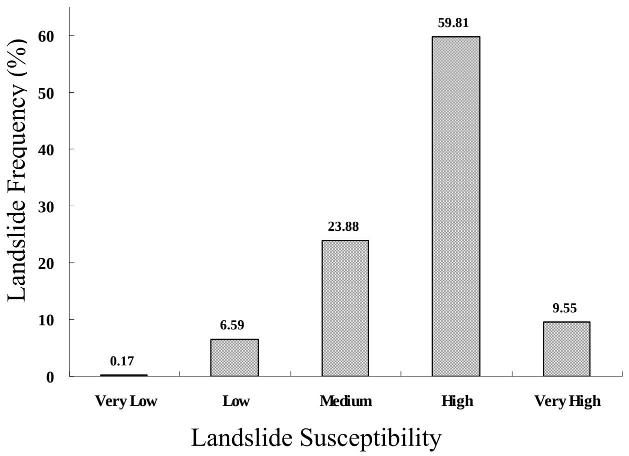

Fig.5. percentages of observed landslide points falling into different susceptibility categories

4 CONCLUSION

Landslides are very complexity phenomenon in the nature world. The reasons cause landslides appearance are hardly be understood. Although some landslide causative factors could be obtained by exploiting advanced spatial technology, some factors remain unknown. There are many quantitative methods used to create the relationship between landslides and causative factors. And then the landslide susceptibility maps are applied for mitigating the geo-hazard in the world. In this paper, logistic regression model which is simple and careless about the distribution pattern of the independent variables was closed to build the landslide susceptibility map by using GIS tools. Most of the causative factors were derived from DEM which was easier acquired nowadays. Seed cells which extracted from the boundaries of landslides were employed to represent undestroyed geomorphologic conditions. The seed cells points were entered into the logistic regression model as training datasets and the observed landslides points were applied as the test dataset to evaluate the accuracy of the model. The results of landslide susceptibility analysis showed us that 70% of the observed landslides points were located in high and very high susceptibility categories. The model seems to be reliable in Mizunami city. The accuracy and prediction ability of the landslide susceptibility map could offer us crucial information for city planning, infrastructure construction and agriculture developments in the future or in other area with similar conditions.

5 REFERENCES

[1] Schuster, R., Socioeconomic significance of landslides. In: Turner, A.K., Schuster, R.L. (Eds.), Landslides: Investigation and Mitigation, Special Report, vol. 247. National Academic Press, Washington, DC, 1996, pp. 12–36.

[2] Netra, R. R., John, R.G., John, D.V., Assessing susceptibility to landslide: Using models to understand observed changes in slopes. Geomorphology, 2010, 122 (4), 25–38.

[3] Nandi, A., Shakoor, A., A GIS-based landslide susceptibility evaluation using bivariate and multivariate statistical analyses. Engineering Geology, 2009, 110, 11–20.

[4] Süzen, M.L., Doyuran, V., Data driven bivariate landslide susceptibility assessment using Geographical Information Systems: a method and application to Asarsuyu catchment, Turkey. Engineering Geology, 2004, 71, 303-321.

[5] Moore, I.D., Grayson, R.B., Ladson, A.R., Digital terrain modeling – a review of hydrological, geomorphological, and biological applications. Hydrological Processes, 1991, 5, 3-30.

[6] Atkinson, P.M., Massari, R., Generalized linear modeling of susceptibility to landsliding in the central Apennines, Italy. Computers and Geosciences, 1998, 24, 373-385.

[7] Yesilnacar, E., Topal, T., Landslide susceptibility mapping: a comparison of logistic regression and neural networks methods in a medium scale study, Hendek region (Turkey). Eng. Geol. 2005, 79, 251-266.

[8] Fawcett, T., An introduction to ROC analysis. Pattern Recognition Letters, 2006, 27, 861-874.

[9] Bai, S.B., Wang, J., Lü, G.N., Zhou, P.G., Hou, S.S., Xu, S.N., GIS-based logistic regression for landslide-susceptibility mapping of the Zhongxian segment in the Three Gorges Area, China. Geomorphology, 2010, 115, 23-31.

First International Conference on Geotechnique, Construction Materials and Environment, Mie, Japan, Nov.21-23, 2011, ISBN: 978-4-9905958-0-7 C3051

The Evaluation of the River Environment and Water Quality by Image Analysis in the Yamato River Basin in Japan

Masanobu TANIGUCHI, Hiroyuki II, Tatemasa HIRATA
Department of Environmental Systems, Faculty of Systems Engineering, Wakayama University

ABSTRACT: Amounts of attached algae and the river bed area were estimated by image analysis in the Yamato River Basin and then natural cleaning effect of nitrogen in the river was evaluated. The image analyze method has been developed since 2009. The Yamato River Basin has 1070 km^2 areas and it is difficult to understand the distribution of plant, sand place, depth and attached algae. The 75% BOD value (Biochemical Oxygen Demand) annually in the Yamato River was the worst of all Japanese rivers managed by the Japanese government. BOD values, ammonia nitrogen and anion surfactant concentrations were high in winter and low in summer and they decreased with temperature. Therefore, it is important to understand amount of natural cleaning effect and the cleaning place. As a result, many adhesion algae lives in less than 30cm depth, the amount of adhesion seaweed was calculated by divided color by based color plus-minus 20% each RGB color code. So, the rate of decrease of nitrogen was about 0.4 mg/l per km in summer, it occurred in less than 30cm depth.

Keywords: evaluation, water quality, image, the Yamato River

1. INTRODUCTION

The Yamato River was mainly polluted by sewage water and industrial effluent and has a major water pollution problem in Japan. The catchment consists of 37% mixture of coarse fragment, sand and clay, 36% granitic rock, 8% alternate layer. 2,000,000 people live in the Yamato River catchment. The amount of water demand in the catchment was larger than the amount of effective water supply, and then the amount of shortage water was provided from the neighboring catchments. The cause of the wastewater pollution was overdue development of sewage systems in recent decades. The 75% BOD value (Biochemical Oxygen Demand) annually in the Yamato River was the worst of all Japanese rivers managed by the Japanese government. Because of this, governments carried out a cleaning campaign to improve the water quality in the Yamato River from 1985 to 2005.(Yamato River construction office, 2005) However the 75% BOD value was still bad and exceeded the allowable limits set by the Japanese environmental quality standard.(Ministry of Land, Infrastructure and Transport, 2004) Therefore, the origin of the river water and the groundwater was analyzed using environmental isotopes and the chemical composition of the Ishikawa River of the Yamato River basin, and the character of the water quality was investigated using field survey data from 1999 to 2005 in the Yamato River. (Hiroyuki II et al, 1999) Moreover, a decrease in water temperature caused an increase in BOD values, ammonia nitrogen and anion surfactant concentrations because these concentrations were high in winter and were low in summer (Masanobu Taniguchi et al, 2002 and 2005). In this research, we developed the image analysis software, and evaluated the river environment and water quality by the image analysis.

2. STUDY AREA AND METHOD

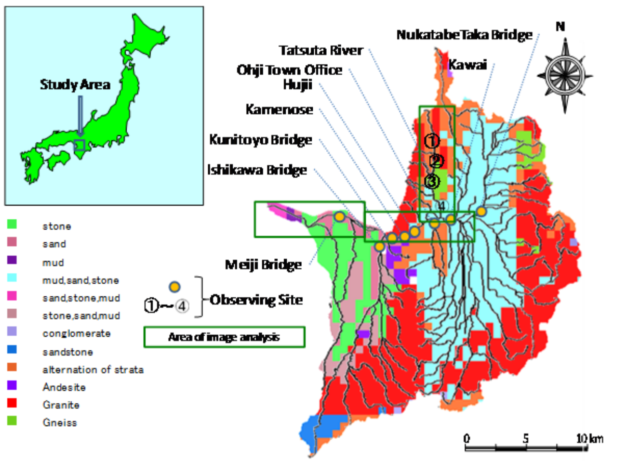

Fig. 1 the geological information of study area and observing site

Figure 1 shows the geological information of study area and observing site. The surround red area is mountain area composed of granite. The Nara basin consists of mad, sand and stone. The river bed of the Yamato River Basin consists of weathering granite. Where river bed is sand, the river water is easy to permeate and then plants and algae or other micro life grow. In this study, the distribution of sand area is important, and rate of sand area and living algae area is estimated by image analysis.

Long term concentrations were analyzed using data from the fixed observing station of the National Land and Transportation Ministry from 2006 to 2009 and data of a field survey by Wakayama University from 2010 to 2011.

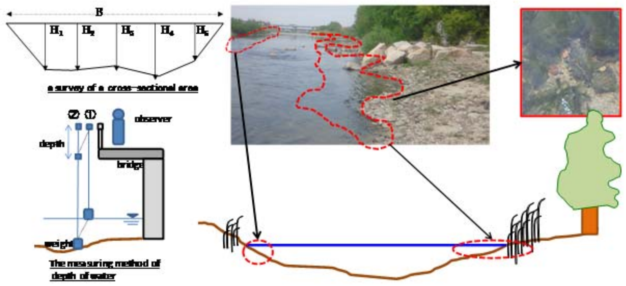

Fig. 2 Survey Method

The river width and depth is measured at 3 sites in the middle stream of the Yamato River, the lower stream of the Tatsuta River and the lower stream of Ishikawa River in 2010. The algae's living place is related by the water depth, distribution of shallow place is important. So, we measure the perpendicular of rivers, because color become dark depend on depth, it is possible that the distribution of depth is divided by color. The algae and sand distribution is made by fixed color comparing survey photographs and the Aerial photographs.

3. WATER QUALITY OF ANNUAL CHANGE

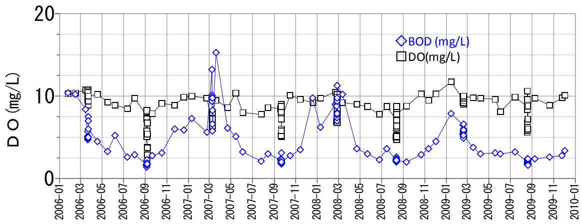

Fig.3 A time series of BOD and DO concentration

Figure 3 shows a time series of BOD and DO concentration from 2006 to 2009. The graph used data of Ministry of Land, Infrastructure and Transport. One day intensive measurement of DO is performed in winter and summer. DO concentration doesn't decrease in winter but decreases about 4mg/L in summer. BOD values were the maximum in winter and the minimum in summer almost generally. BOD means amount of organic compounds and is defined as amount of used oxygen for decomposition of organic compound. In the Yamato River, the domestic sewage flow into the river all the year round, it is need to consider the influence of decomposition of organic compound. So reaction of using oxygen is active by living things in summer, DO decrease in summer.

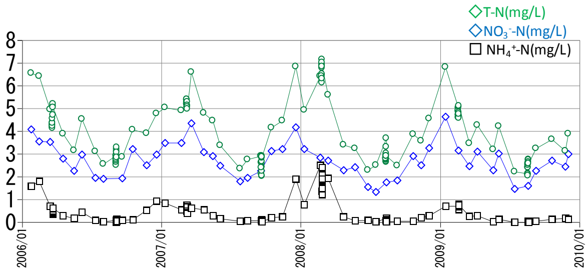

Fig.4 A time series of T-N, NO_3^-N and NH_4^+-N concentrations

Figure 4 shows a time series of T-N, NO_3^--N and NH_4^+-N concentrations from 2006 to 2009. T-N is high in winter and is low in summer as well as the BOD concentration. And Nitrate nitrogen concentration increased regularly in winter in the same way as the BOD concentration. And Ammonia nitrogen concentration increased regularly in winter in the same way as the BOD concentration. Ammonia nitrogen concentration is nothing in summer mostly in every year.

4. NITROGEN OF FLOW DIRECTION CHANGE

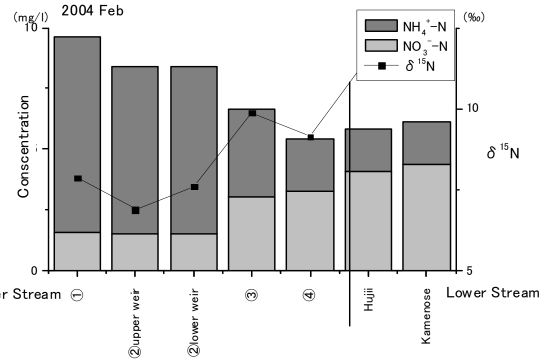

Fig. 5 Relation between nitrogen isotope ratio and nitric acid and ammonia nitrogen in February 2004

Figure 5 shows the relationship between nitrogen isotopic ratio for nitrate and ammonia nitrogen in February 2004. There is a big city on the upper stream of the Tatsuta River and domestic sewage directly flows into the river.

Most domestic sewage was only treated in combined-type private sewage treatment systems. Sampling points with a bed and lateral walls of a river covered with concrete are the point 1 and 2 in the Tatsuta River shown in Fig.5. At these points, the river was always over 1m in depth. However, the bed and lateral walls at the point 3 and 4 in the lower stream of the Tatsuta River were not covered with concrete but the bed was alluvial sediments. In the point 3 and 4, the river had a very natural form. Thus there were many plants on the river bed and the river maintained just a few cm to a few tens of cm in depth. The total inorganic nitrogen concentration of all areas in February was higher than those in July. In February, ammonia nitrogen / inorganic nitrogen (ammonia nitrogen + nitrate nitrogen) ratios at all points were higher than those in July. Each total inorganic nitrogen concentration in point 1 and 2 areas was found to be higher than those in the point 3 and 4 areas, although each nitrate nitrogen concentration in point 1 and 2 areas was lower than those in the point 3 and 4 areas.

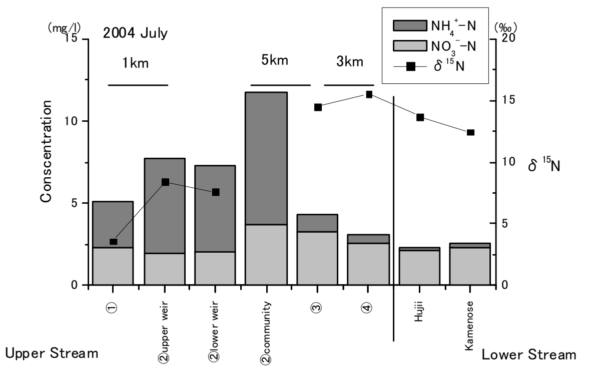

Fig. 6 Relation between nitrogen isotope ratio and nitric acid and ammonia nitrogen in July 2004

Figure 6 shows the relationship between nitrogen isotopes, nitrate and ammonia nitrogen in July 2004. Sample points are from the upper stream to the lower stream of the Tatsuta River and Yamato River's main stream. The total inorganic nitrogen concentration of all areas in February is higher than those in July. In February, ammonia nitrogen / inorganic nitrogen (ammonia nitrogen + nitrate nitrogen) ratios at all points are higher than those in July. Each total inorganic nitrogen concentration in the point 1 and 2 areas is found to be higher than those in the point 3 and 4 areas, although each nitrate nitrogen concentration in the point 1 and 2 areas is lower than those in the point 3 and 4 areas. Also, each ammonia nitrogen concentration in the point 1 and 2 areas is higher than those in the point 3 and 4areas. In both winter and summer season, $\delta^{15}N$ increased down the stream and in particular, the $\delta^{15}N$ change from the point 1 to 4 areas is large. When plants consumed nitrate nitrogen, the $\delta^{15}N$ of nitrate is thought to increase.

Generally, organic compounds in an anaerobic condition were decomposed to ammonia by bacteria. The reaction formula is given by the following equation (1).

$$(CH_2O)_{106}(NH_3)_{16}H_3PO_4 = 53CH_4 + 53CO_2 + 16NH_3 + H_3PO_4 \qquad (1)$$

Nitrification in an aerobic condition is shown by the following equation (2).

$$NH_4^+ + 1.86O_2 + 1.98HCO_3^- = (0.0181 + 0.0024)C_5H_7NO_2 + 1.04H_2O + 0.98NO_3^- + 1.88H_2CO_3 \qquad (2)$$

Generally Ammonia changes into nitrate in aerobic conditions and then finally organic compounds change into nitrate. These reactions depend on activity of living organisms. Temperature is important for the activity of the organisms. However nitrate nitrogen concentration did not change with temperature. Nitrate acid was consumed by photosynthesis or denitrification and the biological activities of photosynthesis or denitrification were also dependent on temperature.

Nitric acid is an intermediate substance between decomposition and photosynthesis and denitrification process.
Therefore, in high-temperature conditions organic compounds easily change into nitrate by aerobic bacteria and nitrate is consumed by denitrification or photosynthesis. On the other hand, in low-temperature conditions, organic compounds are stable.

Denitrification reaction is shown by the following equation (3).

$$(CH_2O)_{106}(NH_3)_{16}H_3PO_4 + 84.8NO_3^- + 84.8H^+ = 106CO_2 + 42.4N_2 + 16NH_3 + H_3PO_4 + 148.4H_2O \qquad (3)$$

Photosynthesis reaction is shown by the following equation (4).

$$106\,CO_2 + 16NO_3^- + 16H^+ + H_3PO_4 + 122H_2O = (CH_2O)_{106}(NH_3)_{16}H_3PO_4 + 138O_2 \qquad (4)$$

When the photosynthesis reaction and denitrification reaction occurred, Nitrogen was removed in the water.

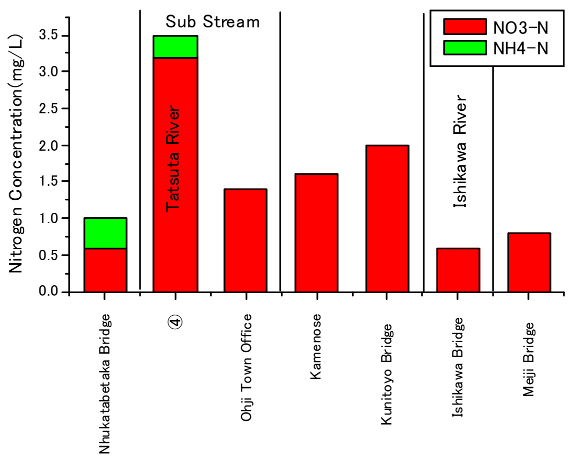

Fig.7 Relation between nitrate nitrogen and ammonia nitrogen in July 2011

Figure 7 shows relation between nitrate nitrogen and ammonia nitrogen concentration in July 2011. Both nitrate nitrogen and ammonia nitrogen concentration in 2011 is lower than those in 2004. However, ammonia nitrogen is shown in the lower stream of Tatsuta River, because domestic sewage flows into the river yet. So, it is thought that organic compound decomposed to ammonia in the Tatsuta River. The nitrate nitrogen concentration of Meiji Bridge decreased from upper stream. In the Yamato River, the ammonia nitrogen is noting, so it is estimated to occur the nitrification. Therefore, it is estimated that the nitrate acid is an intermediate substance through both decomposition and photosynthesis and denitrification process in the Yamato River of middle stream to lower stream. In order to estimate amount of the nitrogen change process of organic compound of decomposition to photosynthesis or denitrification, it considered that relation between chromaticity and water quality.

5. RERATION BETWEEN CHROMATICITY AND WATER QUALITY

The river chromaticity changes with amount of floating material, like as phytoplankton, soil, leftover food and humic acid etc. Chlorophyll a is a coloring matter of the cell of photosynthesizes vegetation. Then amount of phytoplankton increases with Chlorophyll a.

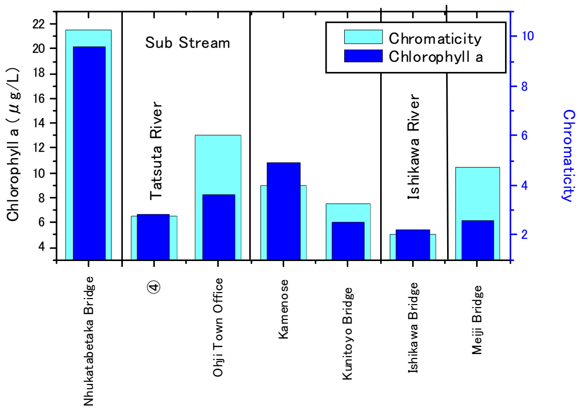

Fig.8 Relation between chromaticity and chlorophyll a in July 2011

Figure 8 shows relation between chromaticity and chlorophyll a in July 2011. The chromaticity is high in Algae living place. The chlorophyll a tends to change as same as chromaticity. The chromaticity and chlorophyll a in the Tatsuta River is lower than the other upper stream. However the chromaticity and chlorophyll a in the Nukatabetaka Bridge is high, the several algae are found in the place. There is a river purification facility in the place.

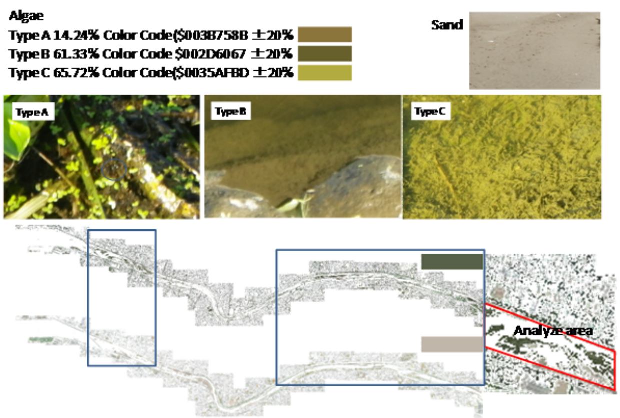

Fig.9 the outline of image analysis

Figure 9 shows the outline of image analysis. If algae occur or the states of a river bed differ, it is possible that the distribution of sand and algae is decided by photograph. In order to fix the color of algae and sand, the survey photograph and the Aerial photographs are compared. The average of color and the near color of plus-minus 20% are used, because the photograph includes some error.

Table 1 Result of Image analysis

Site	Yamato Riv.(Low)	Yamato Riv.(Mid)	Tatsuta Riv.	②	④
Sand	17%	15%	2%	7%	2%
Algae	19%	41%	55%	43%	39%

Table 1 shows result of Image analysis. The used data is analyzed by Google's data, in objective rough calculation.

It is unknown picture date, it is trial calculate. In this result, algae living place is estimated shown by blue line area in Figure 9, 19% of lower stream is algae's living place. The middle stream of the Yamato River is 41%, Tatsuta River is 55%. Comparing survey photographs and the Aerial photographs, it is estimated that algae's living place area is average 46% of calculated area, the range is 14% to 65%.

6. CONCLUSION

Amounts of attached algae and the river bed area were estimated by image analysis in the Yamato River Basin and then natural cleaning effect of nitrogen in the river was evaluated. The image analyze method has been developed since 2009. BOD values, ammonia nitrogen and anion surfactant concentrations were high in winter and low in summer and they decreased with temperature. Therefore, it is important to understand amount of natural cleaning effect and the cleaning place. As a result, many adhesion algae lives in less than 30cm depth, the amount of adhesion algae was calculated by divided color by close to based color plus-minus 20% each RGB color code. So, it occurred in less than 30cm depth, distribution of algae's living place is estimated.

7. REFFERENCES

[1] Yamato River construction office, http://www.yamato.kkr.mlit.go.jp/YKNET/index.html

[2] Ministry of Land, Infrastructure and Transport, Japan, Present condition of water quality of all Japanese first class rivers in 2004, p82

[3] Masanobu Taniguchi, Hiroyuki Ii, Tatemasa Hirata, Masataka Nishikawa, Yumi Ogawa, 2005. Decompose process of sewage organic material using nitrogen isotope and load analyze in Yamato River. The 11th Committee on Technology of River, JSCE, pp35-40(in Japanese)

[4] Masanobu Taniguchi, Hiroyuki Ii, Tatemasa Hirata, Analysis of organic nitrogen compound in domestic sewage in Yamato River using a social experimental test, 2010, vol. 30, Part 10, p. 1587–1590, Stuttgart, April 2010

First International Conference on Geotechnique, Construction Materials and Environment, Mie, Japan, Nov.21-23, 2011, ISBN: 978-4-9905958-0-7 C3051

Distribution of Oxygen and Hydrogen Stable Isotopic Ratios and Estimation of the Spring Water Origin in the Kushiro Moor

Natsuki Kawabe. Hiroyuki Ii., Graduate school of Wakayama University, Wakayama University

ABSTRACT: The purpose of this study is to clarify groundwater movement in the Kushiro Moor comparing the oxygen and hydrogen stable isotopic ratios for stream river waters around the Kushiro Moor with those for spring waters in the Kushiro Moor and estimating the origin of spring waters in there. The $\delta^{18}O$ values of stream water range from -8.0 to -11.5 ‰ relatively high in the east including Kushiro, north and the south Hokkaido. On other hand, the $\delta^{18}O$ values range from -11.5 to -14.0 ‰ relatively low in the central and the northeast Hokkaido. The springs in the Kushiro Moor were divided into low $\delta^{18}O$ values group and high $\delta^{18}O$ values group. Their origins are found to be divided into at least two areas at the north and southeast of the moor.

Keywords: oxygen and hydrogen stable isotopic ratios, Kushiro Moor, spring water, water cycle

1. INTRODUCTION

Hokkaido is a northern Japanese island. Its area accounts for more than 20% of the whole of Japan and about 80,000 km^2. In 1980, the Kushiro Moor, the largest wetland in Japan was registered in the Ramsar Convention as valuable ecosystems [1]. As the Kushiro Moor has some spring inside, then even in winter there is no freezing place which plays an important role in providing some living place for birds in winter. In order to preserve the wetlands it is necessary to understand the water cycle in a wide area including the origin of spring waters.

Although groundwater-dependent rate is low, 2.9 percent in Hokkaido at present, however it may increase with global warming and then it is important to estimate groundwater flow [2].

Isotopic ratios of precipitation vary with region. Therefore, comparing the isotope ratios of precipitation and groundwater, the origin of ground water is estimated. Isotopic ratios measurements of precipitation need water sampling throughout the year, so it is difficult to take a number of measuring points. Isotope ratio of small watershed stream water can be regarded as an average value of precipitation from the previous study [3].

We can estimate the origin of spring comparing the isotope ratios of spring water with stream water. Isotopic ratios of the stream water vary with the distance from the coast, altitude, and prevailing winds. A precipitation isotopic ratio for any place can be estimated from the altitude and distance from the coast by the local calculation formula in the Kii Peninsula [3] and the Yakushima Isalnd [4]. Therefore, the purpose of this study is to estimate the origin of spring water in the Kushiro Moor and to determine the local formula for the Hokkaido area.

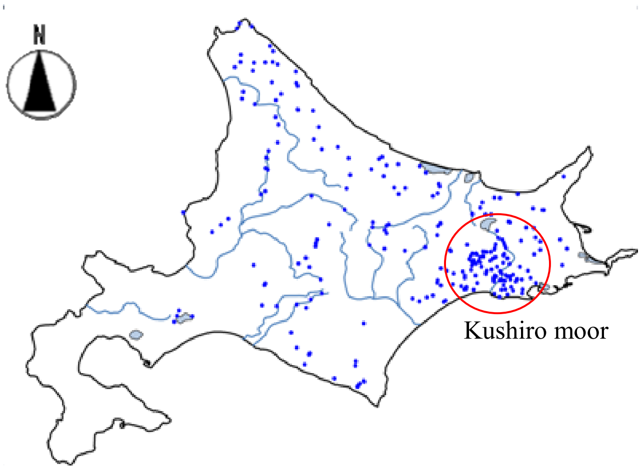

Fig1.Sampling point

2. SUMMARY OF SAMPLE COLLECTION

The study area is the whole area of Hokkaido including the Kushiro Moor. Localities of water samples are shown in Fig.1. The sampling days were in Jun. 13, 2005 to Jun. 18, 2005, Oct. 7, 2005 to Oct. 8, 2005, Sep. 26, 2006 to Sep. 28, 2006, Apr. 27, 2007 to Apr. 30, 2007, Jul. 9, 2007 to Jul. 13, 2007, Sep. 9, 2008 to Sep. 16, 2008, Sep. 11, 2009 to Sep. 17, 2009, Apr. 28, 2010 to Mar. 4, 2010 and Sep. 5, 2010 to Sep. 12, 2010.

There is the Sarobetsu wilderness and a lot of lowlands in the north region. In the northeast region, there is the Saroma Lake that is biggest brackish lake in Japan. In the east region, there are the Kushiro Moor and the Masyu Lake and spread to lowland in the whole. There are the volcanic highlands in the central region, including the Asahi Peak that is the highest peak in Hokkaido. In the south region, there is the Tokachi Plain, and Hidaka Mountains are running around west of this plain. The west region is composed of peninsula and dotted volcanic terrain [5].

Above all, the Kushiro Moor is about 36km length from north to south and about 25km wide from east to west and the total area is 189.2 km^2. Fig.2 shows the sampling points around the Kushiro Moor. In the Kushiro Moor, many springs can be seen around the Chiruwatsunai River located in the north-Kushiro Moor. Therefore, sampling of spring and river waters in the Kushiro Moor was performed intensively.

In this study, river waters, spring waters, ground waters, and hot spring waters were collected in the whole Hokkaido.

To prevent sampling water from contamination, stream water sampling was selected because stream water is thought not to

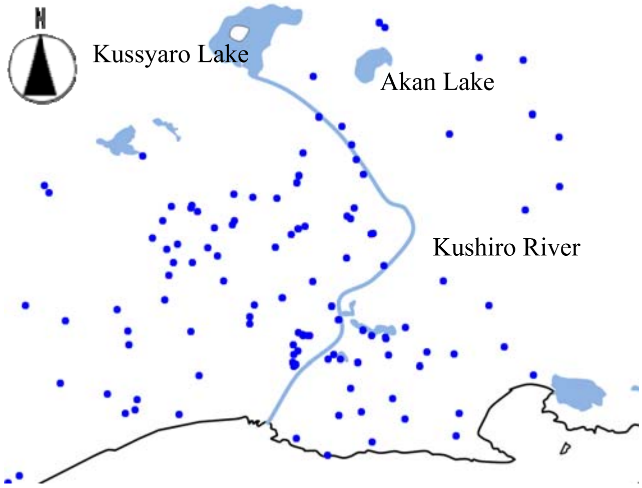

Fig2.Sampling point around the Kushiro Moor

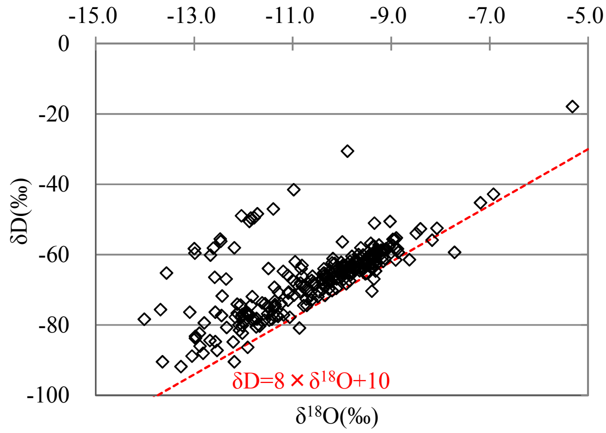

Fig3.Relationship betweenδ^{18}O and δD in Hokkaido

be contaminated and mixing of another place origin water by artificial influence.

Water was sampled with a 100ml polyethylene bottle with double seals and the value of pH, EC (electrical conductivity), ORP (redox potential) and temperature values were measured in the field using simple portable sensor.

3. ANALYTICAL METHODS

Dissolved major ions of sampled waters were measured by ion chromatography, DX-ICS, AQ-1500 and ICS-1600 (Dionex Ltd.). The measured cations are Li^+, Na^+, NH_4^+, K^+, Mg^{2+} and Ca^{2+}. And the measured anions are F^-, Cl^-, Br^-, NO_3^-, PO_4^{3-}, and SO_4^{2-}.

The sampled waters were passed through the 0.45μm pore diameter membrane filter in order to remove impurities such as organic matter. Carbon dioxide (CO_2), carbonic acid (H_2CO_3), bicarbonate (HCO_3^-) and carbonate ion (CO_3^{2-}), such as all carbonate material in water samples was measured by an acidic titration using 0.02N sulfuric acid.

The oxygen and hydrogen stable isotope ratios of water samples were measured by the mass spectrometric system using the CO_2-H_2O and H_2-H_2O equilibration technique with platinum as a catalyst. The mass spectrometric systems were composed of Finnigan Mat Delta Plus and WECs + GEO20-20 mass spectrometer. Oxygen isotope ratios are defined as the 18O / 16O and hydrogen isotope ratios are defined as D / H (2H / 1H). δ^{18}O and δD values are defined as the following equation (1).

$$\sigma = (R_x / R_{st} - 1) \times 1000 \qquad (1)$$

Rx：stable isotopic ratio of x，Rst：stable isotopic ratio of st

4. RESULTS AND DISCUSSION

4.1 Wide distribution of stable isotopic ratios

Relationship between oxygen and hydrogen isotope ratios for sampled water is shown in Fig.3. The oxygen isotope values ranged from -14.0 ‰ to -5.3 ‰ and hydrogen isotope values ranged from -92 ‰ to 18 ‰. The relationship between oxygen and hydrogen isotopic ratios for precipitation, meteoric line is defined by the equation (2)

$$\delta D = 8 \times \delta^{18}O + 10 \qquad (2)$$

Most of precipitation is on the meteoric line but the sampled water in the whole Hokkaido area was divided into two groups shown in Fig.3. One was on the meteoric line and the other was separated from the meteoric line. The separation from the meteoric line was caused by origin of precipitation [6].

Fig.4 and Fig.5 show the distribution of the δ^{18}O and δD in the whole Hokkaido. δ^{18}O and δD values were the nearly same tendency in the north region and around the Kushiro Moor. Low δ^{18}O and δD values are distributed in the northeast region and the boundary between the northeast and the central region. In the central region, the Tokachi Mountains and high altitude areas show low values.

Generally, δ^{18}O and δD values decrease with increasing altitude and then it is called altitude effect. And δ^{18}O and δD values decrease with increasing distance from the coast and then it is called inland effect.

4.2Estimation of the spring waters origin in the Kushiro Moor

Relationship between oxygen and hydrogen isotopic ratios for the Kushiro area is shown in Fig.6. The oxygen isotope values ranged from -12.0 ‰ to -7.0 ‰ and hydrogen isotope values ranged from -79 ‰ to 43 ‰. Fig.6 shows the linear relationship between $\delta^{18}O$ and δD. Fig.7 shows the distribution of the $\delta^{18}O$ values around the Kushiro Moor and the detail distribution of spring points. The oxygen isotope values ranged from -12.0 ‰ to -7.0 ‰. The most of water values ranged from -10.0‰ to -9.0‰ around the Kushiro Moor. Increasing distance from the coast, $\delta^{18}O$ values decrease about 1.0‰. The $\delta^{18}O$ values for the Kushiro Moor were thought to decrease about 1.0‰ with increasing distance from the coast by the inland effect.

Relationship between $\delta^{18}O$ values and altitude is shown in Fig.8. The $\delta^{18}O$ and δD values decreased with increasing altitude. The isotope altitude effect of the Kushiro Moor is -0.23‰/100m for $\delta^{18}O$ and -1.37‰/100m for δD by the previous study [7]. The altitude effect result of this study is

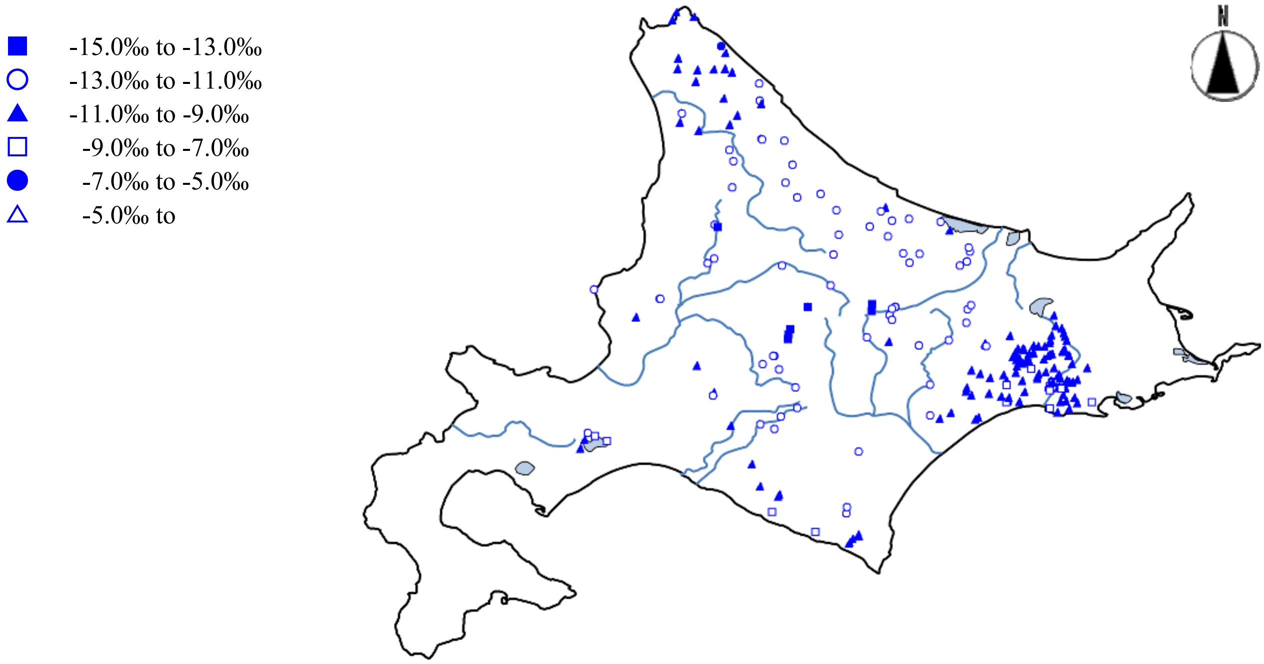

Fig4. Distribution of oxygen stable isotopic ratios

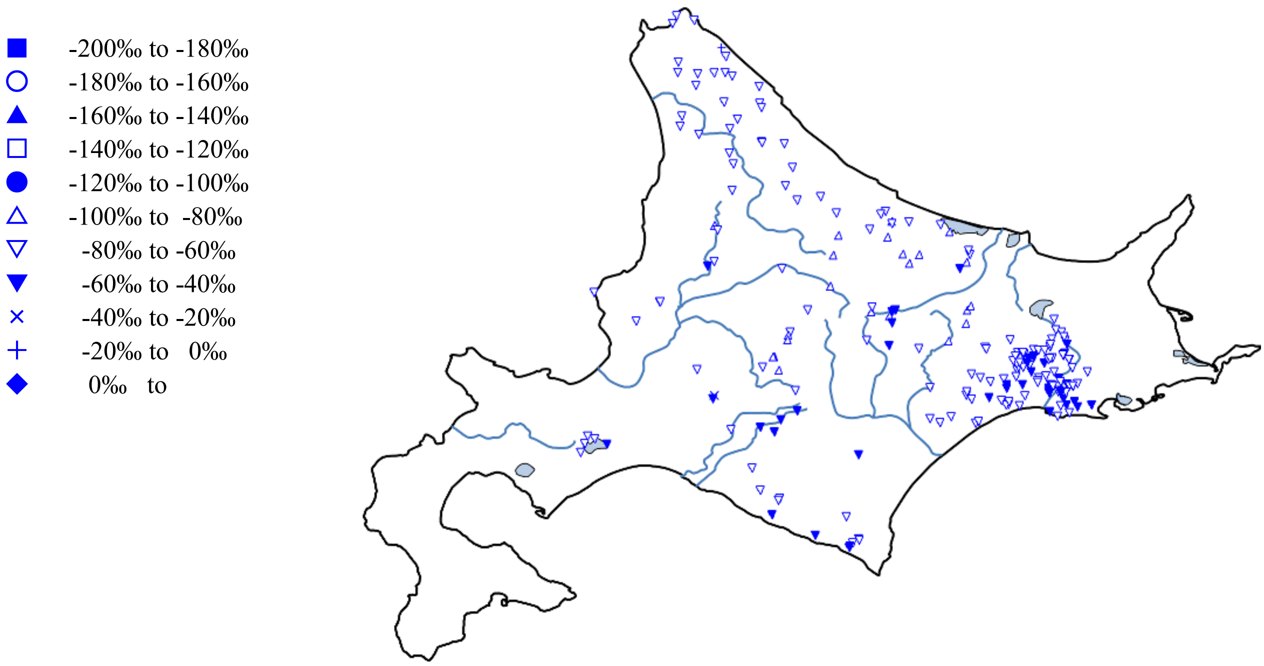

Fig5. Distribution of hydrogen stable isotopic ratios

-0.26‰/100m for $\delta^{18}O$ and -2.02‰/100m for δD.
The difference between both results was thought to be caused by difference of sampling season and sampling points.
The right side figure shown in Fig.7 shows the spring waters around the Chiruwatunai River. The spring waters are classified into three groups. The first group consists of S-01(-10.3‰) with relatively low $\delta^{18}O$ values and is located around the top of the Kirakotan Cape. Second group consists of S-16(-8.5‰) and S-35(-8.1‰). The second springs are located in the upper Chiruwatunai River, and show high values compared with stream water around there. Third group consists of S-34(-6.9‰) and S-36(-7.1‰). The third springs are located in same area of second group but show very high values. The $\delta^{18}O$ values of the stream water around there are about 9.3‰.
The first springs group with oxygen isotopic ratio, about -10.0 ‰ was thought to be derived from the forest area at the north of 10 to 20km from the Kushiro-Moor because the isotopic ratios of the stream water at the A area shown in the Fig.7 were in agreement with those in the spring water.
Then, Fig.8 shows Hexa diagram representing major ions concentration to compare the spring waters and river water.

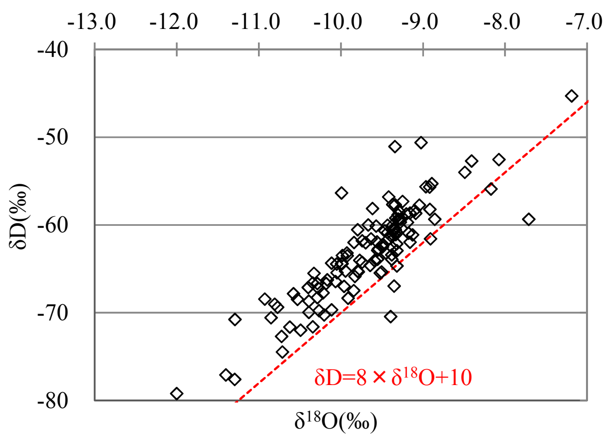

Fig6.Relationship betweenδ18O andδD around The Kushiro Moor

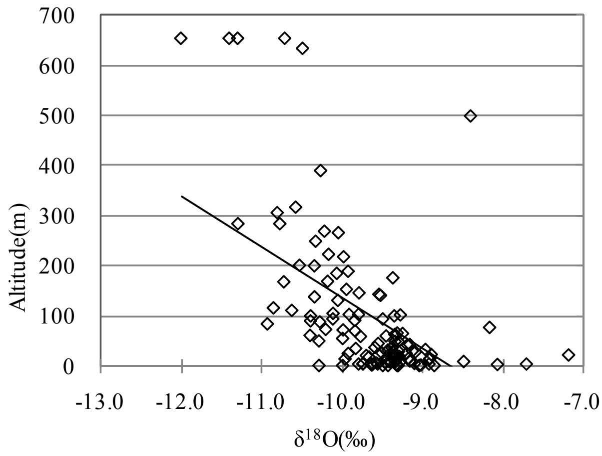

Fig8. Relationship betweenδ18O and Altitude

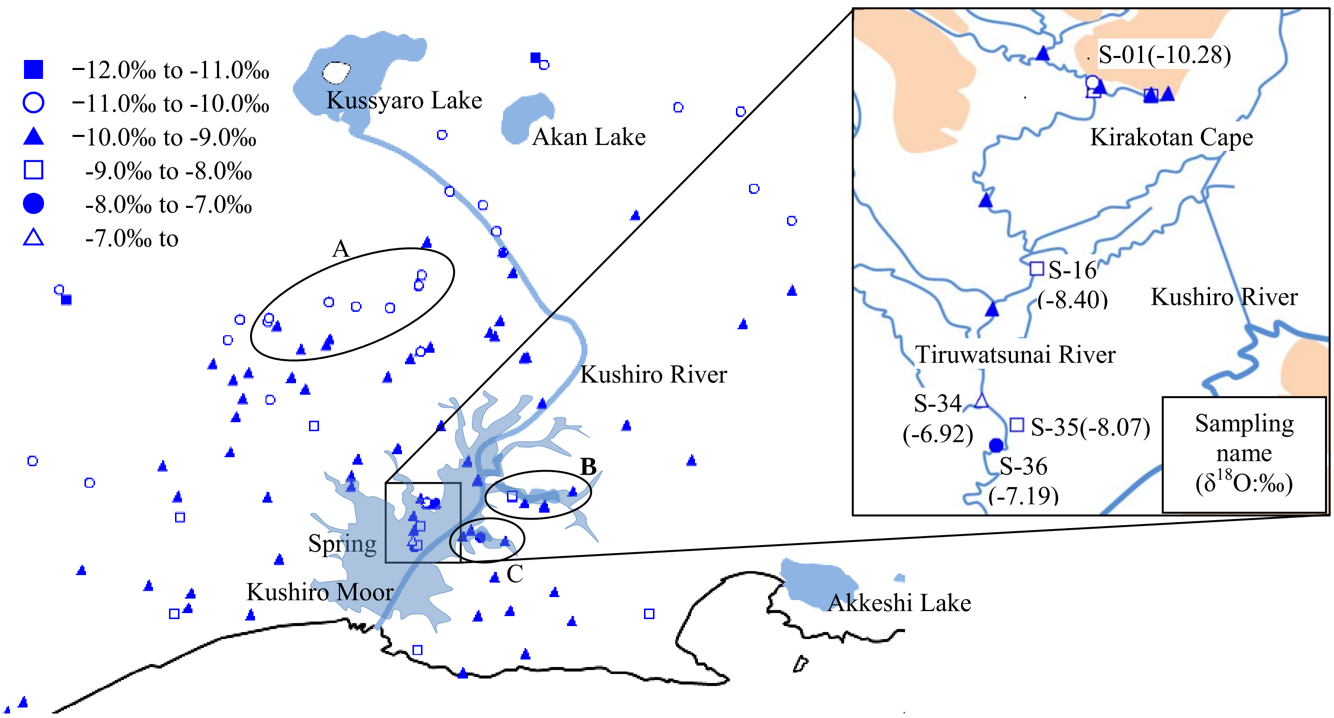

Fig7. Distribution of oxygen stable isotopic ratios around the Kushiro Moor and Spring point around the Chiruwatunai River

As both the A area and the first spring group (S-01) have same character with low values of Mg^{2+} and high values of HCO_3^- and $Na^+ + K^+$, the first spring group is also thought to be derived from the A area.
Although the character of major ions for the A area and the first spring water is same, total concentration of the spring water is higher than those of the A area because generally recharge water is added by ions from sediments or rocks during migration.
The stream waters with oxygen isotopic ratio of the second spring group were found in two areas, the B area and C area near the Toro Lake located on the east side of 5km or 6km away from the Kushiro Moor shown in Fig.7.
The second spring group (S-16 and S-35) was divided by into two groups by the main ions. S-16 is characterized by high values of HCO_3^- and Ca^{2+} and is similar to those of all stream water in the B area and some river water in the C area. On the other hand, S-35 is characterized by high values of HCO_3^- and $Na^+ + K^+$ and is not similar to stream waters in both the B and C area.
The third group with very high values about -7.0‰ was characterized by high values of HCO_3^- and $Na^+ + K^+$. Although the isotopic ratio for the third spring group is high, its Cl^- concentration is low and then sea water mixing is not

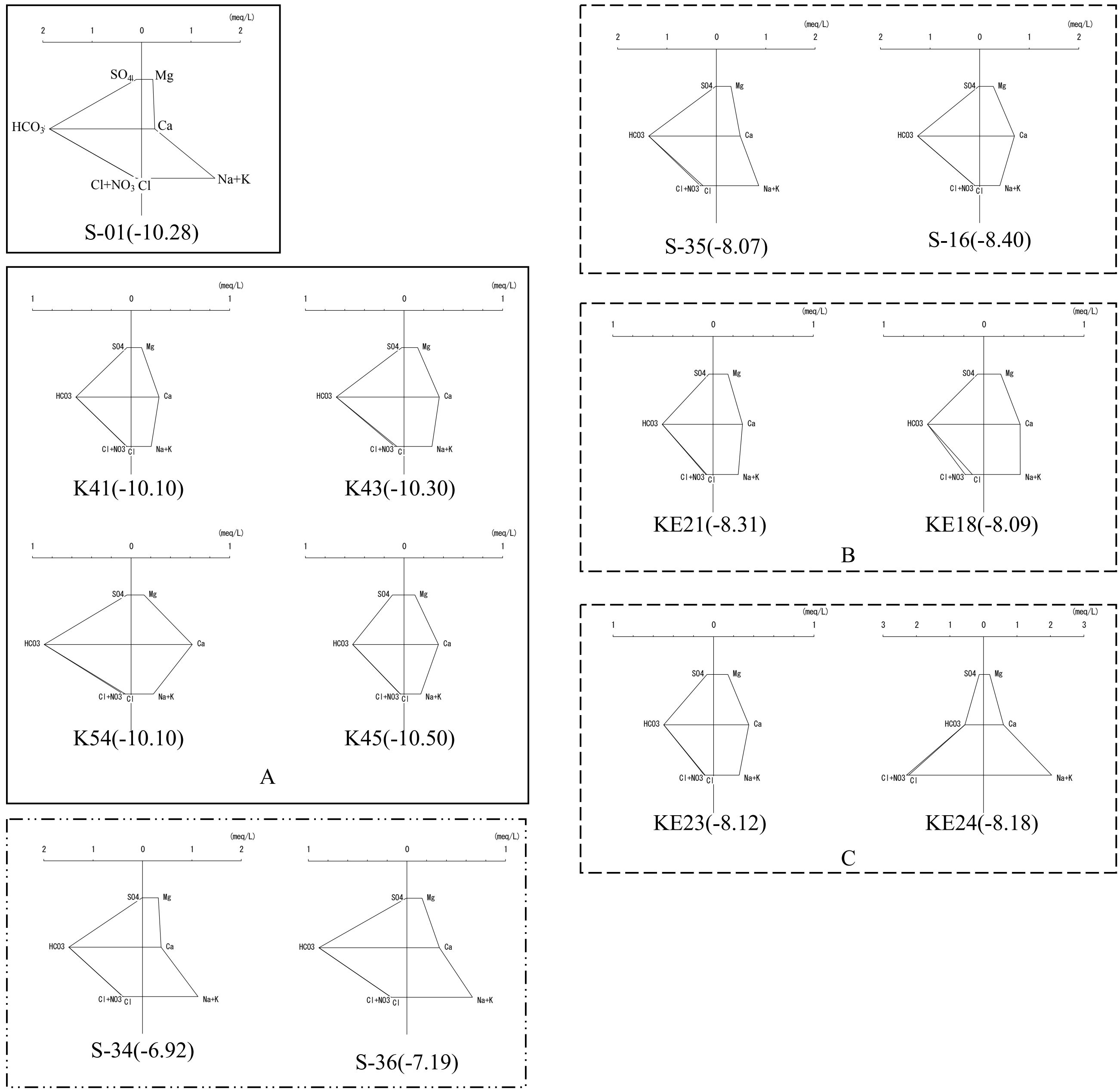

Fig9. Hexa diagram : Sampling name($\delta^{18}O$:‰)

thought to increase isotopic ratio for the third spring.
Although the river water with -7.0 ‰ outside of the Kushiro Moor was not found, Stream water with high isotopic ratio may exist in the southeast and southwest in the Kushiro Moor because there is an inadequate area for sampling and the previous study showed high isotopic ratio in there.

5. CONCLUSIONS

The precipitations in the whole Hokkaido area were divided into two groups by oxygen isotopic ratio. One was on the meteoric line and the other was separated from the meteoric line. The separation from the meteoric line was caused by the condition of precipitation origin.
Oxygen and hydrogen stable isotopic ratios in the north region and around the Kushiro Moor were high.
Low $\delta^{18}O$ and δD values are distributed in the northeast region and the boundary between the northeast and the central region. In the central region, high altitude areas show low values. The $\delta^{18}O$ values decrease with altitude and distance from coast and then altitude effect and inland effect of isotope can be observed.
Low $\delta^{18}O$ values and high $\delta^{18}O$ values spring waters were found in the Kushiro Moor and there were classified into three groups by oxygen isotopic ratio.
The first spring group with oxygen isotopic ratio, about -10.0 ‰ was thought to be derived from the forest area at the north of 10 to 20km from the Kushiro-Moor. Because the isotopic ratios of the stream water at this area were in agreements with the spring water. And both of them have same character with low values of Mg^{2+} and high values of HCO_3^- and $Na^+ + K^+$.
The stream waters of the second spring group, about 8.0‰ were found in two areas, near the Toro Lake located at the east of 5 km or 6 km away from the Kushiro Moor.
Major ions of the one spring in the second group are similar to those of stream water in those areas. On the other hand, major ions of the other spring in the second group are not similar to stream waters in those areas.
The third group with very high values about -7.0‰ was characterized by high values of HCO_3^- and $Na^+ + K^+$. Although the river water with -7.0 ‰ outside of the Kushiro Moor was not found, stream water with high isotopic ratio may exist in the southeast and southwest in the Kushiro Moor with inadequate for sampling.

6. REFERENCES

[1] Kushiro Nature Restoration Committee, “Comprehensive Plan Natural regeneration Kushiro,” 2005

[2] Kenzo HIROKI, “Integrated Water Resources Management for better groundwater management,” Journal of Japanese Association of Hydrological Sciences, Vol.40, No.3, 2010, pp.85-93

[3] Masahide Ishizuka,Yumi Sone, Hiroyuki Ii and Tatemasa Hirata, “Effect of enriched early rainwater on mesoscale isotopic distribution in surface water on the Kii Peninsula, Japan,” Water Resources Research, Vol.42, W12410, doi:10.1029/2004WR003810, 2006

[4] Kyohei Yokota, Hiroyuki Ii and Masanobu Taniguchi,”Effects of altitude and distance from castline of oxygen stable isotope for precipitation in the Yakushima Island,” Environmental Engineering Research,Vol.47, 2010pp.667-677

[5] Editorial Board of the Hokkaido region, “Geology of Japan 1 Hokkaido Region,” Kyoritsu publication, 1990

[6] CHITOSHI MIZOTA and MINORU KUSAKABE, “Spatial distribution of 6D-6^{18}0 values of surface and shallow ground waters from Japan, south Korea and east China,” Geochemical Journal, Vol,.28, 1994, pp.387- 410

[7] National Institute for Rural Engineering, “Estimation of groundwater recharge area as measured by isotopic,” http://www.nkk.affrc.go.jp/library/newpanel/pdf/nouchimizu/panel%2010.pdf

First International Conference on Geotechnique, Construction Materials and Environment, Mie, Japan, Nov.21-23, 2011, ISBN: 978-4-9905958-0-7 C3051

A Debris Flow and Its Risk Analysis Related to the 2008 Wenchuan Earthquake

Yange Li[1], Guangqi Chen[2], Chuan Tang[3], Lu Zheng[1]

[1]Department of Civil and Structural Engineering, Kyushu University, Fukuoka, Japan
[2]Department of Civil and Structural Engineering, Kyushu University, Fukuoka, Japan & Visiting Professor of Institute of Earthquake Science, Beijing, 100036, China
[3]State Key Laboratory of Geo-Hazard Prevention, Chengdu University of Technology, Chengdu, China

ABSTRACT: On August 14, 2010, an intense and prolonged rainfall triggered debris flow in Hongchun gully, Yingxiu town, the epicenter of the Wenchuan earthquake. The event transported huge material sediment to the watercourse of the Minjiang River and formed a natural dam, resulting in flash flood in the new reconstruction Yingxiu town. In order to predict the run out distance and extent of the hazard area of such kind of debris flows, we develop an approach from the earthquake-induced landslides recognition to the numerical simulation of the debris flow in this study. At first, we determined the initial material sediment by aerial photography identification and field investigation. And then, a two-dimensional numerical model was used to simulate the transport process of the debris flow. The raster grid network of digital elevation model generated from GIS was used for the finite difference mesh. The results from the numerical simulation showed a good agreement with the actual movement and deposition distribution of Hongchun gully debris flow.

Keywords: debris flow; aerial photography identification; two-dimensional numerical model; GIS

1. INTRODUCTION

The Wenchuan earthquake (Ms=8.0), with a focal depth of 12-15 km, throughout an area of about 50, 000km^2, was triggered by the reactivation of the Longmenshan fault (LMSF) zone at eastern margin of the Tibetan Plateau, adjacent to the Sichuan Basin on May 12th, 2008. The earthquake led to more than 69,225 fatalities, 374,640 persons injured, about 17,393 persons missing, 5,362,500 collapsed homes and 21,426,600 homes that were badly damaged by April 25th, 2009 according to official statics (Cui et al., 2009, Tang et al., 2011a).

The latest data from aerial photographs and satellite images shows over 56,000 landslides occurred after the earthquake (Dai et al., 2011). The majority of landslides were concentrated in the hanging wall part of the Yingxiu-Beichuan fault and Pengguan fault, northwest part of earthquake zone. Consequently, a great deal of loose sediment was induced which in turn promoted heavy debris flows during subsequent typhoons and heavy rains. The most outstanding example was a severe debris flow hazard occurred in Hongchun gully, Yingxiu town, epicenter of the Wenchuan earthquake on August 14, 2010. The event transported huge sediment material to the water course of the Minjiang River and produced a natural dam, which then changed the course of the river and resulted in flash flood in the new constructive Yingxiu town. The flood claimed 13 lives, with a further 59 listed as missing. About 8,000 local residents were rapidly evacuated from their homes.

More recently, a giant debris flow burst on August 8, 2010 in Zhouqu City, which is also in the earthquake-affected area, that claimed 1,434 lives with a further 331 listed as missing. This catastrophic debris flow was following an intense local rainstorm and led to the destruction of more than 5,500 houses along its flow path. All the events and previous researches (Cannon et al. 2001; Dong et al.2009; Tang et al., 2011b) showed strong earthquakes play a major role in contributing to the accumulation of sediment supply on hillslope and in channels. Bovis and Jakob (1999) and Jakob et al. (2005) highlighted the importance of sediment supply on the frequency and magnitude of debris flows.

In order to predict the run out distance and extent of the hazard area of such kind of debris flows, we develop an approach from the investigation of earthquake-induced landslide to the numerical simulation of the debris flow in this study. At first, we determined the initial material sediment by aerial photography identification and field investigation. Four large scale landslides were identified by using the object-based remote sensing technique and they were thought as the main loose material of the debris flow, their volume was estimated by the scale of the landslides. And then, we used a two-dimensional numerical model to simulate the transport process of the debris flow. In the model, the debris and water mixture was assumed to be a uniform continuous, incompressible and unsteady Newtonian turbulence fluid. The raster grid network of digital elevation model generated from GIS was used for the finite difference mesh.

2. STUDY AREA AND DATA SOURCE

The Hongchun gully is situated on left bank of Minjiang River and in Northeast region of the Wenchuan County, Sichuan Province, China (Fig. 1). The study area is situated in the transitional mountainous belt between the Sichuan Basin and the Western Sichuan Plateau and the gully-mouth is located at 31°04'01"N and 103°29'33"E. The geological main structure and the strike of the rock strata in this area show a NE-SW orientation. The Yingxiu-Beichuan fault just runs through the Hongchun gully.

The study area is situated in the typical humid subtropical, monsoon climate zone. The annual average precipitation over a period of 30 years is 1,253 mm, with a highest recorded annual precipitation of 1,688 mm in 1964. On average, 70% of the annual precipitation is largely concentrated in the period from June to September. The maximum recorded rainfall intensity was 269.8mm/day in 1964.

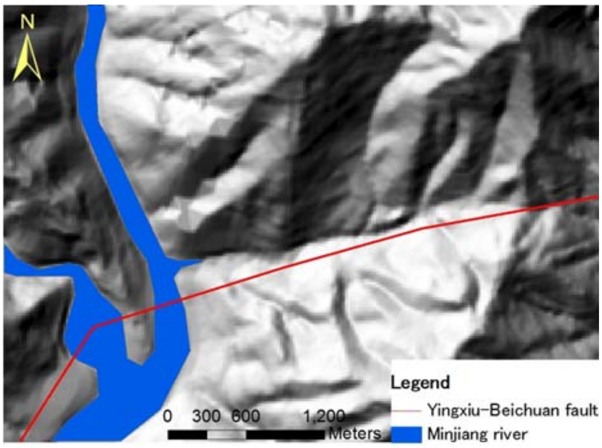

Fig. 1 Hongchun gully of Yingxiu town

The Hongchun gully has a catchment area of 5.35 km^2 and a channel length of 3.55 km. The upslope elevation of the gully is more than 1,700m asl and the gully mouth is at 880m asl, The highest part of the debris flow source area is at 2,168 m asl. In the source area, mainly granitic rocks are exposed, which are deeply fractured and highly weathered, and massive coseismic landslides were developed on the slope.

On August 14, 2010 at 3:00 A.M., triggered by an intense rainfall, numerous debris flows occurred near Yingxiu. The Hongchun gully debris flow was the most catastrophic one. It deposited mud, debris, and rocks onto the G213 national road and the Dujiangyan-Wenchuan highway. The alluvial fan of debris flow was located on the region of under-construction transition settlement building of Yingxiu town. It travelled across Minjiang River and caused a natural debris dam of 10 m height, 100 m in length across the river, and 150 m in width along the river. The dam caused a change of the river course and flooded the newly reconstructed Yingxiu Town (Fig. 2).

Fig. 2 The blocked Minjiang River and new Yingxiu town in flood by Hongchun gully debris flow

The basic data utilized in the study included a 20m × 20m grid digital elevation model (DEM) and an aerial photograph with a spatial resolution of 0.3m (Fig. 3), which was taken on May 20, 2008 by the Ministry of Land and Resources (MLR) after the Wenchuan earthquake occurred.


Fig. 3 Aerial photograph of Hongchun gully

3. CAUSE ANALYSIS OF THE HONGCHUN GULLY DEBRIS FLOW

Debris flows are triggered by a combination of three essential factors: sufficient available loose material, surface runoff, and steepness of the drainage channels on the slopes (Takahashi 1981). Therefore based on field investigation, the cause of debris flow in Hongchun gully can be explained as the following 3 factors:

3.1 Triggering rainfall

Debris flows usually occur at a combination of high accumulated rainfall and very high rainfall intensity (Crosta 1998). On 12 August a total of accumulated rainfall of 162.1 mm in 33 h was recorded from 17:00 P.M. until 02:00 A.M. on 14 August. The rainfall intensity that induced the debris flows occurred between 02:00 and 03:00 A.M.; 16.4 mm/h rainfall intensity was recorded during that time period. However, the peak hourly rainfall was 19.9 mm recorded between 17:00 and 24:00 hours two days before the landslide. Previous studies in the Longmenshan area (Tan and Hen 1992) have reported rainfall that initiates debris flows to have intensities greater than 30-50 mm/h with a total rainfall of at least 80-100 mm. Lan et al. (2003) examined rainfall amount 110 mm/day as the rainfall threshold for the occurrence of past landslide events in the Xiaojiang watershed, south western China. Comparing the triggering rainfall parameter with the rainfall condition in Hongchun gully, it indicates that although the antecedent precipitation of this event is higher than record, the trigger rainfall intensity is about 50% reduced. After the Wenchuan earthquake, debris flow susceptibility is increased by a large precipitation event.

3.2 Sediment supply conditions

The comparison between pre-earthquake and post-earthquake cases indicates that the strong earthquake has modified the conditions and debris flow is more easily induced after earthquake by a smaller rainfall (Lin et al. 2003; Tang et al. 2009). It can be observed by remote sensing analysis of the aerial photographs taken on May 18, 2008, after the 2008 Wenchuan Earthquake that an abundance of landslide debris was presented on the slopes. Therefore, the slopes are very susceptible to debris flows under heavy rainfall conditions.

3.3 Topography

The average vertical of the Hongchun gully is 358‰, and the upstream is 538‰. Slope steepness is a fundamentally important factor influencing the occurrence of debris flows because most debris flows initiate as shallow landslides or as eroded rill or gullies on large landslide deposits. Since the original area and pass channels of the Hongchun gully are straight, the confluence of rainfall water became quick. The highest part of the debris flow source area is at 2,168 m asl. and the gully mouth is at 880m asl. The large elevation difference gave the rainfall water large kinetic energy transformed from potential energy to initiate the loose sediment material to failure

4. LANDSLIDE RECOGNITION

Landslide inventory is the most important procedure for related disaster prevention. Landslide mapping by field investigations is a challenging task in vast and inaccessible mountainous terrain. Visual interpretation of remote sensing data is time and labour consuming. So far there have only been a few attempts at automating the mapping of landslides by pixel-based methods, which likely fail as DN values alone and do not characterise geomorphic processes such as landslide (McDermid and Franklin, 1994). Recently Barlow et al. (2006) achieved good detection accuracy by treating landslide as an object and only considering the knowledge that landslides are quite large. Moine et al. (2009) used high resolution earth observation data without DEM, could recognize small landslides, eventually ruling out the possibilities of classifying landslide types. Tapas R. Martha et al. (2010) used the algorithm developed in Definiens Developer software based on high resolution satellite data and a DEM, achieved 76.4% landslide recognition accuracy in five different landslide classed in a terrain featuring spectrally identical land use/cover units. In our research, a multi-step approach was presented as following to recognize and classify landslides accurately.

4.1 Image segmentation

An important step before characterising diagnostic attributes of features of interest, such as landslides, is the creation of objects/segments that alone or in a group demarcate the boundary of the given feature. This is done using image segmentation, which is a process of dividing the image into objects or regions based on the homogeneity of the pixel values. These segments ideally correspond to real-world objects. Image segmentation can be done in different ways, using techniques such as density slicing, split and merge (Kerle and de Leeuw, 2009).

In this research, we employ an edge-based segmentation algorithm which is very fast and only requires one input parameter, scale level. It is the regularization parameter, if it is small, then a lot of boundaries are allowed and a “fine” segmentation results. As it is increases, coarser and coarser segmentations result. By suppressing weak edges to different levels, the algorithm can yield multi-scale segmentation results from finer to coarser segmentation.

Landslides pose a particular challenge to image segmentation, as land cover variability (e.g. partial vegetation), and illumination variations as a function of terrain characteristics, often result in spectrally diverse features. It is not practical to attempt outlining landslides as single segments for the first time, and some post-segmentation merging processing is needed also due to the typical size variability of landslides in an image (Martha et al., 2010).

We partitioned the image into segments by grouping neighbouring pixels with similar feature values. In order to ensure the features of interest are not grouped into segments represented by other features and to ensure that a feature of interest is not divided into too many small segments (over-segmentation), we firstly choose a small scale level 30, to avoid the wider boundaries between segments which some features of interest will lose.

Then segmentation merging is processed to resolve the over segmentation problem. It used the Full Lambda-Schedule algorithm which is created by Robinson, Rdding and Crisp (2002). The algorithm iteratively merges adjacent segments based on a combination of spectral and spatial information. Merging proceeds if the algorithm finds a pair of adjacent regions, i and j, such that the merging cost $t_{i,j}$ is less than a defined threshold lambda value:

$$t_{i,j} = \frac{\frac{|O_i| \cdot |O_j|}{|O_i| + |O_j|} \cdot \|u_i - u_j\|^2}{legnth(\partial(O_i, O_j))} \quad (1)$$

Where: O_i is region i of the image; O_i is the area of region i; u_i is the average value in region i; u_j is the average value in region j; $\|u_i - u_j\|$ is the Euclidean distance between the spectral values of regions i and j; $legnth(\partial(O_i, O_j))$ is the length of the common boundary of O_i and O_j. In this research, we find the merge scale 93 can best represent the landslide body. Fig. 4 shows the segmentation result.

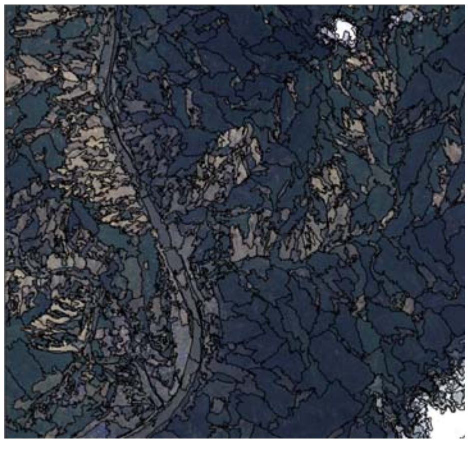

Fig. 4 Image segmentation result

After segmentation, the spatial, spectral, texture and colour attributes were calculated for each object.

4.2 Image classification

Bare rock or debris exposed after the earthquake, giving a bright appearance in the image, although at times mixed with remaining or dislodged vegetation. The Normalized Difference Vegetation Index (NDVI), a simple graphical indicator that can be used to analyse remote sensing measurements, typically but not necessarily from a space platform, and assess whether the target being observed contains live green vegetation or not, is sensitive to low levels of vegetation cover, has been successfully used by previous works (Barlow et al., 2006; Schneevoigt et al., 2008) to discriminate landslides from vegetated features. Therefore, we used NDVI as a first criterion to identify landslide candidates, and separate them from other areas such as forest land, orchards and crop land. An NDVI of 0.15, a value close to the statistical mode of the image NDVI, was found to be useful for discriminating landslide candidates from vegetation cover. Since NDVI is used as a cut-off criterion, objects with similar or lower than the NDVI threshold, such as rock outcrops, roads, water bodies and river beds, are likely to be classified as landslides candidate (Fig. 5).

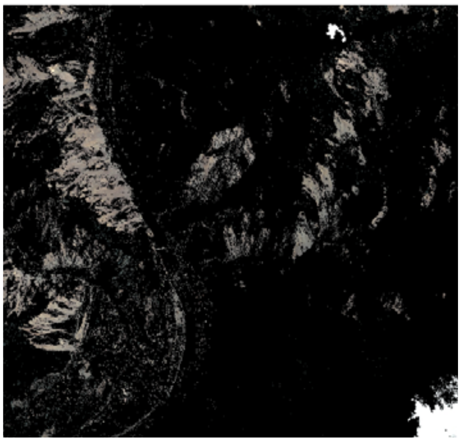

Fig. 5 Landslides candidate recognized by NDVI calculation

In order to classify the landslide candidates, the training samples need to be assigned. Different landslide type shows different spectral characteristic. For example, comparing with rocky landslides, debris flow shows relatively darker appearance. So we divide the landslides into three categories when selecting the training samples. Meanwhile, considering the landslide and some resident have similar spectral features, in order not to miss the landslide area, we take the conservative thinking which is not defining the resident area in the image at first. Then all the landslides will be recognized as well as some mis-classified resident area included. Finally the three kinds of landslides were merged within ArcGIS.

The more features and training samples are selected, the better the results are from supervised classification. However, selecting an overwhelming number of training samples will cause poor performance during classification and previewing classification results. In our case, 30 rock slides, 38 debris flows, 30 debris slides, 10 river objects were selected in total as the training samples for supervised classification.

The K Nearest Neighbour algorithm was used for the classification. The algorithm considers the Euclidean distance in n-dimensional space of the target to the elements in the training data, where n is defined by the number of objects attributed used during classification. This method is generally more robust than a traditional nearest-neighbour classifier, since the K nearest distances are used as a majority vote to determine which class the target belongs to. The K Nearest Neighbour method is much less sensitive to outliers and noise in the dataset and generally produces a more accurate classification result comparing with traditional nearest neighbour methods. In this case, we define the K Parameter as 3 that it means there are 3 neighbours will be considered during classification. Fig. 6 gives the classification result.

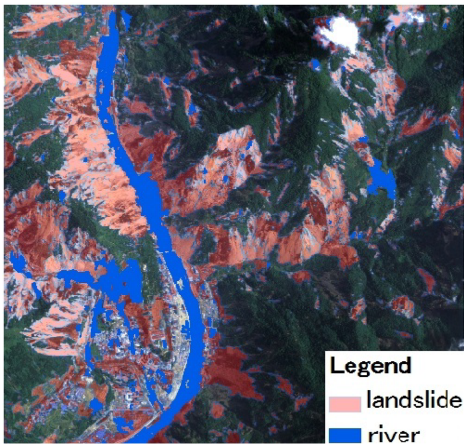

Fig. 6 Image classification of Hongchun gully

4.3 Post classification

As shown in Fig.6, we can see almost all of the landslides were identified, although some resident area was also included. In order to improve the classification results, the non-landslide objects are eliminated by the assumption that landslide will not occur for the slope gradient less than 9° and it is processed in ArcGIS. A total of 73 landslides were semi-automatically detected in the entire area, with a surface area of 1.0 km^2 in the Hongchun catchment area.

Fig. 7 Landslide recognition of Hongchun gully

Meanwhile, we can see some objects with blue colour were mis-classified as river, they were rectified manually (Fig. 7).

5. TWO-DIMENSIONAL NUMERICAL MODEL OF DEBRIS FLOW

Based on the conservation of mass and the momentum of the flow, many researchers have proposed mathematical models of the debris flow. Some of them are 2D models (Takahashi et al., 1992; Chen and Lee, 2000; Ghilardi et al., 2001; Denlinger and Iverson, 2001; Wang et al., 2006). In this study, the debris and water mixture is assumed to be a uniform continuous, incompressible, unsteady Newtonian fluid. The numerical solution using a finite-difference formulation based on the DEM grid was detailed depicted in the previous literature (Wang et al., 2006).

The proposed approach has been used to simulate the Hongchun gully debris flow. Furthermore, the grid networks in GIS are used as the grids of finite-difference method.

When making DEM analysis in GIS, each cell has eight possible flow directions (Fig. 8). The flow direction of a cell is expressed in degrees: left = 0, up = 90, right = 180, down = 270; and the diagonals: 45, 135, 225 and 315. Within a cell, overland flow is routed along one flow direction. The flow direction is the maximum downslope direction, which is determined from the raster-based DEM.

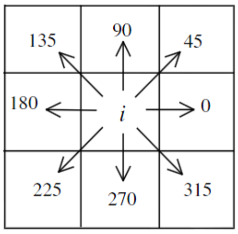

Fig. 8 Possible flow direction in a grid cell

Since only a 20m DEM map is available for generating grids, the area is divided into 200×170 grids by using ArcGIS9.3. The rheological parameters are assumed as constant (Tang et al., 2011b) and listed in Table. 1.

Table. 1 Rheological parameters

ρ_d	α	β	μ	$\tan\varphi$
2050 kg/m^3	1.25	1.0	0.11	0.6

where, ρ_d is the density; α and β are the momentum correct factors; μ is the kinematic viscosity; and $\tan\varphi$ is the friction.

The photo interpretation can only provide information on the landslide surface area, so a relational model between the landslide area and its average thickness is required to determine the volume of the landslide debris. Combining with the identification result and field investigation, we finally selected four landslides: H1, H2, H3, H4 as the main loose source material of the debris flow (Fig.9). Information concerning coseismic landslide thickness was derived from the data in the report: "The investigation report on debris flow hazard in the Hongchun gully of the Yingxiu town after the Wenchuan earthquake", published by the Guanghan Institute of Geological Engineering Investigations of Sichuan Province. The area for the above 4 landslides are separately 7,688 m^2, 5,137 m^2, 2,002 m^2, 4,567 m^2 , and there average depth are separately defined as 4m, 3m, 1m and 1m.

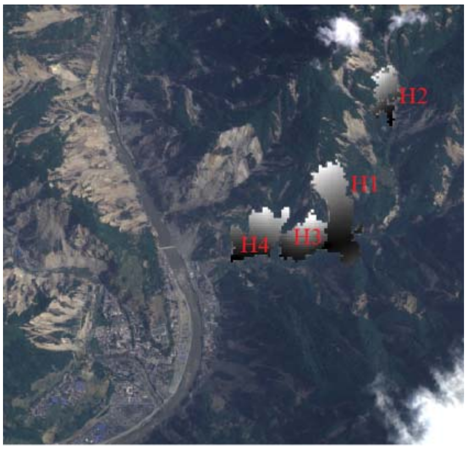

Fig. 9 Loose material identified for the debris flow

The movements of the debris flow are illustrated in Fig. 10(a)-(d) for different time. It can be seen that the river is blocked in Fig. 10(d). The distribution of the maximum depth of the whole flow is shown in Fig. 11.

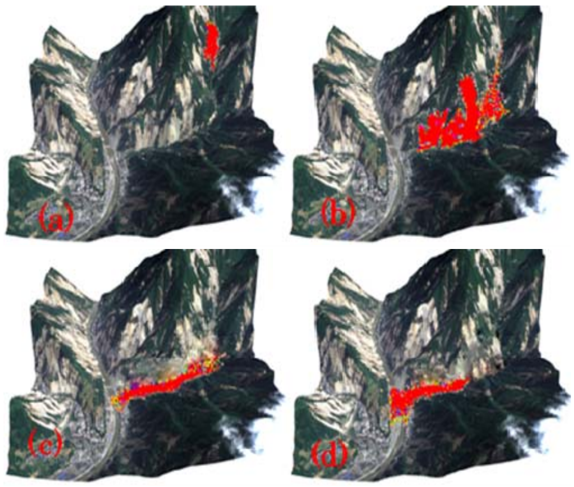

Fig.10 The movement of the debris flow

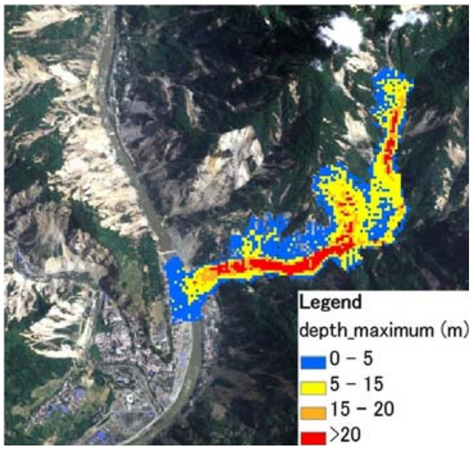

Fig.11 The distribution of the maximum depth of Hongchun gully debris flow

6. CONCLUSION

A strong earthquake not only cause directly damage on constructs but also can result in a series of natural disasters such as landslide, debris flow and flooding. These secondary disasters occur as chain disasters after a strong earthquake. For mitigation of such kind of risk, apart from engineering measures, we have proposed an approach from the earthquake induced landslides investigation to the numerical simulation of the debris flow.

In the first stage, a multi-step segmentation approach has been used to recognize and classify landslides accurately. Firstly, we divided the image into objects based on homogeneity of pixel values through edge-based segmentation algorithm. Then to ensure the features of interest are not over-segmentation, the merge segmentation based on the Full Lambda-Schedule algorithm was used to improve the delineation of feature boundaries. After segmentation, spatial, spectral, texture and colour attributes were calculated for each object. Next NDVI index was used to separate the landslide candidates from vegetation. Finally, supervised classification using the K Nearest Neighbor algorithm was applied to the entire image and the mis-classified objects were rectified by expert-driven knowledge. Another achievement of this study was detection of complex failure mechanism for different kinds of landslides. Considering the spectral characteristic for the landslides in different sites shows different appearance in the image, such as debris flow shows relatively darker brightness than rocky landslide, we separately chose the landslide samples in three categories according to the visual spectral value, and last they were merged together after the classification. Results showed almost all of the landslides were identified as well as some resident area included.

Based on the image interpretation, a depth-averaged 2D numerical model incorporating the grid in ArcGIS used as the finite difference mesh was employed to simulate the debris flow in Hongchun gully. The simulation can show us a real propagation process of the debris flow, the potential inundation area can be derived and the maximum depth in the flow gully was calculated.

7. ACKNOWLEDGMENT

This study has received financial support from Grants-in-Aid for Scientific Research (Scientific Research (B), 22310113, G. Chen) from Japan Society for the Promotion of Science and the Research Fund of the State Key Laboratory of Geo-Hazard Prevention of China (SKLGP2009Z004). The financial supports are gratefully acknowledged.

8. REFERENCES

[1] Barlow J, Franklin S & Martin Y, "High spatial resolution satellite imagery, DEM derivatives, and image segmentation for the detection of mass wasting processes," Photogrammetric Engineering and Remote Sensing, vol. 72, no. 6, Jun, 2006, pp. 687-692.

[2] Bovis MJ & Jakob M, "The role of debris supply conditions in predicting debris flow activity," Earth Surface Processes and Landforms, vol.24, no.11, Oct 1999, pp.1039-1054.

[3] Cui P, Zhu Y, Han Y, Chen X & Zhuang J, "The 12 May Wenchuan earthquake-induced landslide lakes: distribution and preliminary risk evaluation," Landslides, vol. 6. no. 3, Jun 2009, pp. 209-223.

[4] Chen H, Lee CF, Numerical simulation of debris flows. Can Geotech, 2000, J37:146-160.

[5] Crosta G, Regionalization of rainfall thresholds: an aid to landslide hazard evaluation. Environ Geol, 1998, 35:131-145.

[6] Cannon SH, Kirkham RM & Parise M, "Wildfire-related debris flow initiation processes, Storm King Mountain, Colorado," Geomorphology, vol.39, Aug 2001, pp.171-188.

[7] Dai F, Xu C, Yao X, Xu L, Tu X & Gong Q, "Spatial distribution of landslides triggered by the 2008 Ms 8.0 Wenchuan earthquake, China," Journal of Asian Earth Sciences, vol. 40, no. 4, Mar 2011, pp. 883-895.

[8] Dong JJ, Lee CT, Tung YH, Liu CN, Lin KP & Lee JJ, "The role of the sediment budget in understanding debris flow susceptibility," Earth Surf Process Landforms, vol.34, no.12, Aug 2009, pp.1612-1624.

[9] Ghilardi P, Natale L, Savi F, Modeling debris flow propagation and deposition. Phys Chem Earth , 2001, 26:651-656.

[10] Jakob M, Bovis M & Oden M, "The significance of channel recharge rates for estimating debris-flow magnitude and frequency," Earth Surface Processes and Landforms, vol.30, no. 6, Jun 2005,pp.755-766.

[11] Kerle N & de Leeuw J, "Reviving legacy population maps with object-oriented image processing techniques". IEEE Transactions on Geoscience and Remote Sensing, vol. 47, no. 7, Jul 2009, pp.2392-2402.

[12] Lan HX, Wu FQ, Zhou CH & Wang LJ, "Spatial hazard analysis and prediction on rainfall-induced landslide using GIS," Chinese Science Bulletin, vol. 48, no. 7, 2003, pp. 703-708.

[13] Lin CW, Shieh CL, Yuan BD, Impact of Chi-Chi earthquake on the occurrence of landslides and debris flows: example from the Chenyulan River watershed, Nantou, Taiwan. Eng Geol, 2003, 71:49-61.

[14] McDermid GJ & Franklin SE, "Spectral, spatial, and geomorphometric variables for the remote sensing of slope processes," Remote Sensing of Environment, vol. 49, no. 1, 1994, pp. 57-71.

[15] Moine M, Puissant A & Malet JP, "Detection of landslides from aerial and satellite images with a semi-automatic method. Application to the Barcelonnette basin (Alpes-de-Haute-Provence, France)." In: Malet, JP, Remaitre A & Bogaard, T (Eds.), Landslide Processes: From Geomorphological Mapping to Dynamic Modelling. CERG, Strasbourg, France, 2009, pp. 63-68.

[16] Martha TR, Kerle N, Jetten V, van Westen CJ & Kumar KV, "Characterising spectral, spatial and morphometric properties of landslides for semi-automatic detection using object-oriented methods". Geomorphology, vol. 116, Mar, 2010, pp. 24-36.

[17] Robinson, D. J., Redding, N. J., and Crisp, D. J. Implementation of a fast algorithm for segmenting SAR imagery, Scientific and Technical Report, 01 January 2002. Australia: Defense Science and Technology Organization.

[18] Schneevoigt NJ, van der Linden S, Thamm HP & Schrott L. "Detecting Alpine landforms from remotely sensed imagery. A pilot study in the Bavarian Alps". Geomorphology, vol. 93, Jan 2008, pp. 104-119.

[19] Tang C, Zhu J, Qi X & Ding J, "Landslides induced by the Wenchuan earthquake and the subsequent strong rainfall event: A case study in the Beichuan area of China," Engineering Geology, article in press, 2011a.

[20] Tang C, Zhu J, Li WL, Rainfall triggered debris flows after Wenchuan earthquake. Bull Int Assoc Eng Geol, 2009, 68:187-194.

[21] Tang C, Zhu J, Ding J, Cui XF, Chen L & Zhang JS, "Catastrophic debris flows triggered by a 14 August 2010 rainfall at the epicenter of the Wenchuan earthquake," Landslides, accepted, 2011b.

[22] Takahashi T, Estimation of potential debris flows and their hazardous zones. J Nat Disaster Sci 1981, 3:57-89.

[23] Tan WP, Hen QY, "Study on regional critical rainfall induced debris flow in Sichuan Province," Journal of Catastrophology, vol. 7, Feb 1992, pp.37-42 (in Chinese).

[24] Wang CX, Esaki T, Xie MW, Qiu C. "Landslide and debris-flow hazard analysis and prediction using GIS in Minamata-Hougawachi area, Japan," Environmental Geology, vol. 51, no. 1, Oct 2006, pp.91-102.

First International Conference on Geotechnique, Construction Materials and Environment, Mie, Japan, Nov.21-23, 2011, ISBN: 978-4-9905958-0-7 C3051

Impact Analysis of Water Price Reform of Zhangye, China

Atsushi Koike, Dept. of Civil Eng., Kobe University, Japan,
Zhongmin Xu and Kang Wang, CAREERI, Chinese Academy of Sciences, China
Bunei Itoga, Regional Futures Research Center, Japan

ABSTRACT: The Hei River Basin is located in northwest region of China. This region belongs to arid zone, and water resources are one of the main limiting factors of harmonizing the development of ecology, economy and society. Due to the economic growth and the population increase, water consumption has grown rapidly since 1970s in the middle reaches especially in the Zhangye district. The rapid increase of water demand in the middle reaches has degraded the ecosystems of the whole watershed. Water pricing is very important instrumentally in balancing water supply and demand. Appropriate water price is a very effective countermeasure in changing the social behavior towards water resource conservation, promoting economic efficiency and investment in more efficient equipments. The aims of this study are to analyze the comprehensive impacts of Water Price Reform of the Zhangye district by using an operational Computable General Equilibrium (CGE) model based on building a social accounting matrix (SAM).

Keywords: Water Demand Management, Water Price Reform, Computable General Equilibrium model, Zhangye, China

1. INTRODUCTION

The Hei River Basin is one of the major grain producing regions in China. The water shortage is mainly caused by the drastic population growth and the development of the irrigation area in the middle basin over the past decades. Water saving measures have to be taken to improve the irrigation system efficiency both on-farm and in the main canal system including water-saving measures, efficiency improvement and reuse of water. On the other hand, institutional management, water pricing and agricultural sector adjustment will play an important role in balancing demand and supply [15].

Water management includes water supply management and water demand management (WDM). WDM refers to the activities that aim to reduce water demand, improve water use efficiency and avoid the deterioration of water resources. Demand management offers sustainable water management solutions in the face of increasing water scarcity and growing conflicts over water use [6], [12]. For the Hei River Basin, the WDM measures consist of both technical and non-technical measures. Since irrigated agriculture uses 80% of the available fresh water, and the efficiency of this water use is very low, large quantities of water are wasted. Considerable economies can be realized if agricultural water is used in a more efficient way. Furthermore, water pricing and institutional reform can help to control water demand and implement water saving [15].

Appropriate pricing of water (i.e., implementing an increasing block rate pricing structure) has proven to be a very effective measure in changing the public behavior towards water conservation and promoting economic efficiency and investment in new equipment [10].

However, the reform of water price will take impacts in regional economic system. The data on direct water consumption reveal that the amount of water consumed directly by the primary industry (agriculture, forestry, livestock, and fishery) is much greater than that consumed by the industrial and service sectors, with agricultural consumption exceeding 2 billion m^3, and the latter only consuming a small fraction of this amount (approximately 55 million m^3). This finding confirms the well-known fact that agriculture is the main consumer of water resources in Zhangye district, and is responsible for 94% of the total water consumption in the region. In comparison, the volume of water consumed directly by the industrial and service sectors is nearly negligible. However, when indirect water is considered, it becomes obvious that water consumption by the industrial and service sectors increased greatly. This is often unnoticed in analysis that focuses exclusively on the lower values for direct water consumption by these sectors. This means that although these sectors use only a small amount of water directly in production, in order to produce the inputs (generated by other sectors) that they incorporate into their production processes, a high consumption of water is necessary. Thus, it appears that the industrial and service sectors also consume large amounts of water indirectly. In this sense, indirect consumption seems to make up a significant part of the water consumption in the study area [17]. Therefore, water pricing will impact not only the agricultural sector but also other sectors.

Water resources are the fundamental components which drive the evolution of ecological-economic system. Therefore, we should evaluate the impacts of water price reform before it was implemented. The aims of this study are to analyze the comprehensive impacts of Water Price Reform of the Zhangye district by using an operational Computable General Equilibrium (CGE) model based on building a Social Accounting Matrix (SAM).

In this study, we build the SAM for water price reform and the CGE model based on the SAM. And, three water price reform scenarios are considered. We present the results from simulation experiments that we performed with the model to analyze the effects of each water price reform scenario.

2. STUDY SITE

The Hei River Basin spans Qinghai, Gansu and Nei Mongol, and is located in the arid zone of northwestern China. This is the second largest inland river basin in China. It covers an area of approximately 130,000 km2. Its upper reaches source from the boundary district of Gansu and Qinghai, and its lower reaches end to the desert in the western part of Inner Mongolia. Administratively, the basin includes a county of Qinghai Province located in the upstream region of the Hei River Basin; a city and counties of Gansu Province, all of which lie in the midstream region, namely Zhangye district, Minle district, Shandan district, Linze district and Gaotai district, respectively; and a county (within the Ejina Oasis with the location in the downstream region of the basin) in the Inner Mongolia [9] (Fig.1).The study site is Zhangye district, located in the middle reaches of the Hei River, is 42,000 km2 in size and has a population of 1.264 million, including a rural population of 9.11 million and an urban population of 3.53 million. The climate of this region is arid, with annual precipitation ranging from approximate 100 to 300 mm, and potential annual evapotranspiration reaching 2,000 mm.

Although located in one of the driest zones in the world, Zhangye district consists of many oasis ecosystems that are mainly watered by the Hei River. Water use in this city accounts for about 93% of all water use from the river, with 94% of this water used for agriculture. According to the Zhangye Statistical Yearbook [4], the irrigated area in Zhangye district was about 68,667 ha in the 1950s, but by 2002, it expanded to approximate 266,000 ha, including 212,000 ha of farmland and 41,000 ha of forest and grassland. As a result of irrigated farming, Zhangye district has become an important center of Gansu Province for the production of commodity grains.

Since the Chinese national economic reforms that began in 1978, new industrial sectors have arisen, such as mining (including coal production), production of building materials, electric power, metallurgy, machinery assembly, transportation, and services. In recent years, Zhangye district has experienced considerable economic growth as a result of these changes. The gross domestic product (GDP) was 837.3 million US$ in 2001, which was 8% greater than that in 2000. In 2002, 2003, and 2004, the GDP increased to 916.8, 1013.1, and 1206.7 million US$, respectively, representing annual increases of 10%, 11%, and 12%, respectively, over the values in the previous year [8].

Expanding agriculture and rapid economic growth have resulted in excessive use of the region's water resources. According to GPBWR (2003) [7], in 2002, the annual available water resources were 2.05 billion m^3, including 1.63 billion m^3 surface water and 0.42 billion m^3 groundwater while the actual annual water utilizations were 2.42 billion m^3, of which 90% was consumed by the socio-economic systems, and of this amount, 96% was used for agriculture. Ecological and environmental water demands are severely restricted for the excessive water use in socio-economic systems. As a result, the city seems to have locked into an environmental-economic dilemma through increasing dependency on the scarce water resources and further erosion of environmental quality [16].

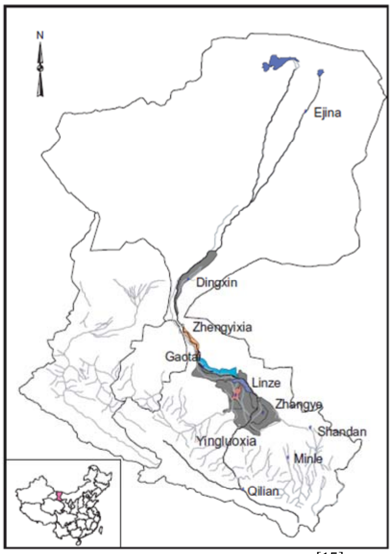

Fig.1 Hei River Basin [15]

3. CGE Model for Water Price Reform

3.1 Computable General Equilibrium model

A Computable General Equilibrium (CGE) model is a general equilibrium model that implements the textbook description of an economy. There are utility-maximizing consumers whose decisions determine the demand for goods and supply of labor. There are profit-maximizing producers whose decisions determine the supply of goods and the demands for primary factors (labor, capital, and land) and intermediate inputs. There is international trade. There is a government which collects taxes and tariffs; may set exchange rates; and provides transfers, subsidies, and services. Finally, there are market-clearing conditions specifying supply-demand balance, which will determine equilibrium prices. The model is a "general equilibrium" because all domestic supplies, demands, prices, and incomes are determined simultaneously within the model. It is computable because the model solves empirically for all endogenous variables in a highly non-linear system of simultaneous equations.

Changes in policy alter demand through changes in prices. The wide scope of the model makes it especially useful for evaluating projects that have broad effects, changing incomes in many sectors through intersectoral linkages. When there is a generating many ripples in the economy, a general equilibrium framework are the appropriate tool of analysis [3]. The CGE model can consider the complex relationships in economic system, and it has been a popular tool in policy analysis. Water issues are important also in the world. Numerous state and regional economic impact studies of water management have been conducted. [Peter Berck, 1990] employ CGE procedure to investigate the reallocation of water in the San Joaquin Valley [11]. and [Chang K. Seung, 1997] investigate the economic impacts of transferring surface water from irrigated agriculture to recreational use at the Stillwater National Wildlife Refuge in Churchill Country, Nevada[5]. [Alexander Smajgl, 2006] develop a conceptual framework of water reform and generates an Applied General

Equilibrium (AGE) model to investigate the impacts of potential water reform scenarios for an irrigation area with features of the Lower Burdekin [1]. [Okuda and Hatano, 2005] provides water-rights transaction model at China's province level applying general equilibrium theory, in which sets a virtual water-rights market for YRB [13]. We built the Social Accounting Matrix (SAM) [2] of Zhangye district and used an operational CGE model to analyze the impacts of water price reform of Zhangye district. And this study analyzes the impact on the Zhangye economy by water price reform methods by using the CGE model.

The CGE model explains all of the payments recorded in the SAM. The model therefore follows the SAM disaggregation of factors, activities, commodities and institutions. It is written as a set of simultaneous equations, many of which are nonlinear.

3.2 Features of CGE Model for Water Price Reform

Fig.2 shows the Framework of the CGE model for water price reform. Continues line shows flow of goods and factors, and it shows money flow in opposite sense. Dash line shows the flow of tax, subsidy, saving and transfer.

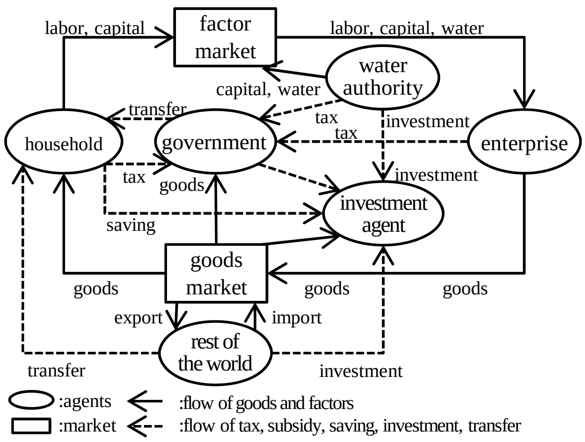

Fig.2 Framework of the CGE model for water price reform

In this CGE model, agents are presented by household, water authority, government, rest of the world, investment agent and ten enterprises. And there are factor market and goods market. Enterprises are "agriculture", "forestry", "livestock", "fishery", "agriculture, forestry and fisheries service (agriculture service) ", "mining", "manufacture", "electricity", "construction", "others".

The household income is composed of returns to labor and capital, as well as transfers from government and the rest of the world. And it is supposed that transfers to households from government are proportionate to government income. Household expend on saving, consumption of commodity and tax. The households consume the domestic consumer goods. It is assumed that each household maximizes its utility function subject to consumption expenditure constraint. The utility functions are defined as Cobb-Douglas functions.

The water supply authority (water authority) holds water and capital, and earns factor incomes. Water authority expend to tax and saving

It is supposed that government revenue is composed of value added tax, household tax and direct tax of water authority. Government expenditures are divided into transfer to household, consumption and saving.

Each producer is assumed to maximize its profits, defined as the difference between revenues earned and the cost. Profits are maximized subject to a production technology; the structure of which are shown in fig.3.

Value added (V) is composed of water (W), labor (L) and capital (K) by the Cobb-Douglas function. Domestic production (DP) is a combination of value added and intermediate (X), which are characterized as strict complements according to Leontief function. In other words, zero-value substitution elasticities are assumed for intermediate inputs and value added. It is assumed that input coefficients of intermediate goods are fixed. Domestic production is transformed to domestic goods (D) and export (E) by CET (constant elasticity of transformation) function and export price is domestic consumer goods price. Domestic consumer goods are obtained to compose of domestic goods and import (M) by CES (constant elasticity of substitution) function and import price is fixed the price of rest of the world. The import price is the price paid by domestic users for imported commodities. And, the export price is domestic consumer goods price. In Zhangye district, most of import and export is transaction between Zhangye district and other national region. In this model, we assumed that the import price is fixed the price of rest of the world. In this model, foreign saving and transfer to household from rest of the world are fixed. The fact that all items except imports and export are fixed mean that, in fact, the trade deficit also is fixed. Model detail is in appendix.

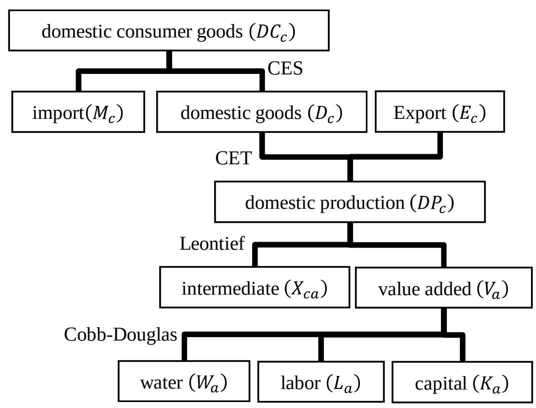

Fig.3 Framework of Production Technology

3.3 Definition of Welfare Loss

The change in welfare is defined as the change in equivalent variation (EV). The EV is an estimate of the hypothetical variation in the household income, which would have produced the same change in the utility of the representative consumer, at fixed prices.

Amount of water saving is defined as the amount of water using without water price reform minus the amout of water using with water price reform.

3.4 Scenario Definition

The primary water price is different in each activity as fig.4. The primary price – also called benchmark – is compared with each scenario which is described in this section. Three scenario conditions are summarized in table 2.

Scenario1 means that the amount of the water price charge for construction, mining, manufacture, electricity and others are larger than the amount of price charge for agriculture, forestry, livestock, fishery and agriculture service

Scenario2 means that the amount of the water price charge for construction, mining, manufacture, electricity and others are less than scenario1, and the amount of price charge for agriculture, forestry, livestock, fishery and agriculture service is larger than sccenario1.

Then, water supply with water price reform doesn't exceed the present water authority income. The price that the water supply exceeds the income of water authority is unfeasible.

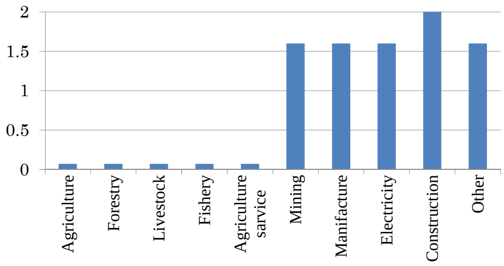

Fig.4 Primary water price of each activity (Yuan/m^3)

Table 1. Scenario definition

scenario1	Constant rate price charge for all activities $P_a^w \Rightarrow (1+\alpha)P_a^w$
scenario2	Constant additional price charge for all activities $P_a^w \Rightarrow P_a^w + P$
scenario3	Constant price for all activities $P_a^w \Rightarrow P^w$

P^w : primary water price

α : water price increase rate

P : water price increase amount

a : suffix of activity

4. RESULTS AND INTERPRETATION

4.1 Welfare Loss with Quantity of Water Saving

Please start writing here. In this section, we compare the welfare loss with quantity of water saving in each scenario. We can analyze the welfare loss when the same amount of water is saved in each scenario.

Fig.5 shows that the welfare loss with quantity of water saving in each scenario. Scenario3 is the least of welfare loss when the equal amounts of water are saved. It shows that scenario 3 is the best water price reform method. But scenario3 is also unfeasible, because water supply sector needed to be subsidies when the water prices are under 0.7 (Yuan/m^3) (dash line in fig.5), and the amount of water savings exceeds 80% of the amount of present water using when the water price is more than 0.7 (Yuan/m^3) (continuous line in fig.5). Looking at the welfare loss with quantity of water savings, scenario 2 is the best water price reform method except for scenario3.

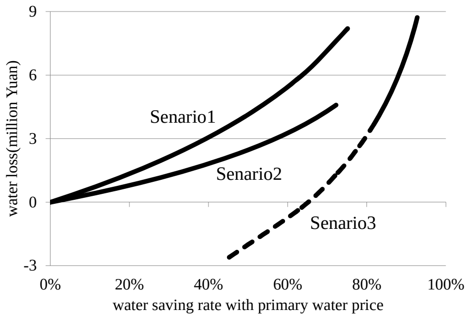

Fig.5 Welfare loss with water saving rate

4.2 Impact on Domestic Production of Water Price Reform

PFig.6 shows the change of quantity and the change rate of domestic production. Fig.6 shows that water price reform of scenario1 affects the domestic production of mostly agriculture and manufacture. On the other hand, water price reform of scenario 2 affects domestic production of mostly agriculture. Even though, impact on agriculture of scenario1 is larger than scenario 2 although the water price charge for agriculture of scenario1 are smaller than scenario 2.

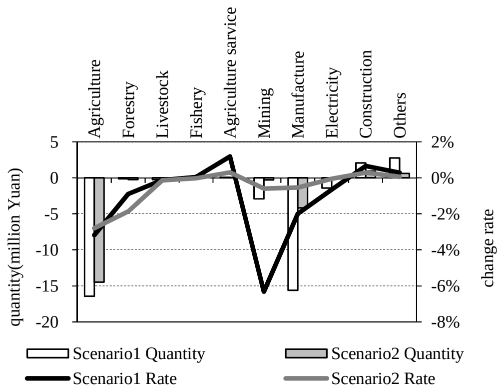

Fig.6 Change of quantity and change rate of domestic production to save the water of 1 billion m3

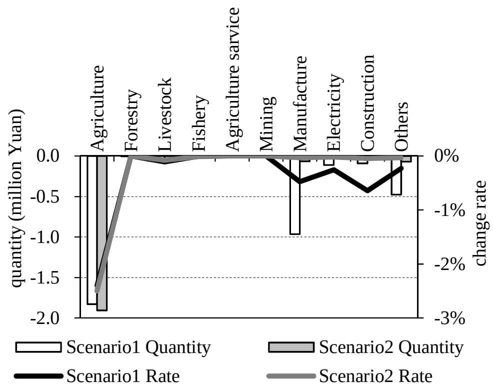

Fig.7 Change of quantity and change rate of final demand to save the water of 1 billion m^3

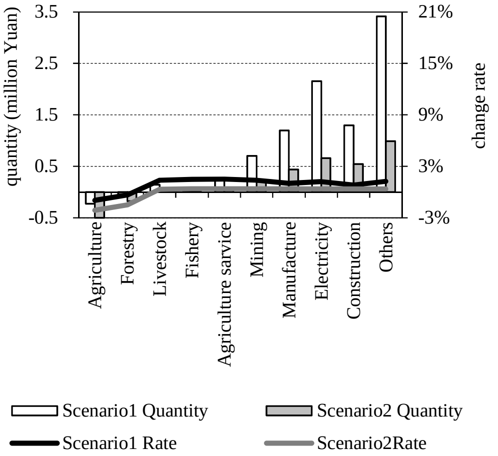

Fig.8 Change of quantity and change rate of investment demand to save the water of 1 billion m^3

Looking at fig.7 and 8, the impact on final demand of agriculture of scenario 1 is smaller than scenario 2, and the impact on final demand of agriculture of scenario 1 is also smaller than scenario2. Looking at fig.9, the impact on total intermediate dmand of agriculture of scenario1 are larger than scenario2. This means that the impact on domestic production are caused by total intermediate demand (fig.10). Because, manufacture demand has a relative large amount of intermediate from africulture , and water price reform of scenario1, therefore there is a decrease of domestic production in manufacture.

Fig.9 Change of quantity and change rate of total intermediate demand to save the water of 1 billion m^3

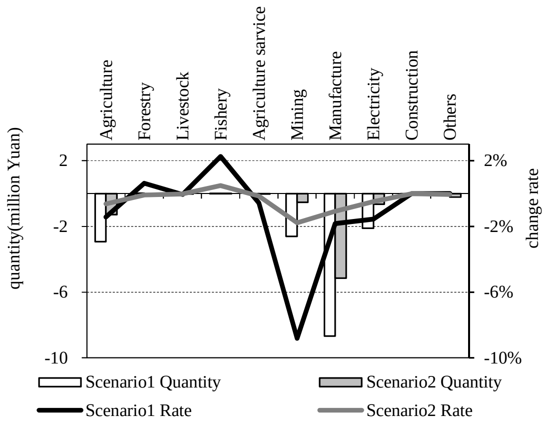

Fig.10 Input coefficient of manufacture

5. CONCLUSION

In this paper, we built a CGE model for water price reform.

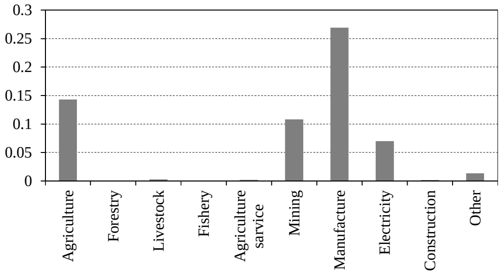

We applied the CGE model to the Zhangye economy. The proposed method provided three water price reform scenarios and these impacts on economy. Constant price for all activities of welfare loss is the least when the equal amounts of water are saved. But it is also unfeasible, because the water supply sector are needed to be subsidies when the water prices are under 0.7 (Yuan/m3). And the amount of water savings has exceed 80% beyond the amount of present water using when the water prices are more than 0.7 (Yuan/m3). Looking at the welfare loss with quantity of water savings, constant additional price charge for all activities has larger decrease of welfare loss than constant rate price charge. But, additional price charge for all activities affects mostly agriculture. On the other hand, constant rate price charge for all activities more decrease welfare loss than constant additional price charge. But constant rate price charge for all activities affects mostly agriculture and manufacture. In other words, constant rate price charge for all activities decreases more in welfare loss, and decrease of domestic production are incurred by mainly agriculture and manufacture. On the other hand, constant additional price charge for all activities decreases less in welfare loss and the decrease of domestic production are incurred mainly by agriculture.

6. ACKNOWLEDGMENTS

7. REFERENCES

[1] Alexander Smajgl, Romy Greiner, Colin Mayocchi, “Estimating the implications of water reform for irrigators in a sugar growing region”, Environmental Modeling and Software, vol. 21, 2006, pp. 1360-1367.

[2] Basanta K. Pradhan, M.R. Saluja, Shalabh K. Singh, Social Accounting Matrix for India: SAGE Publication, 2006.

[3] Bell, C. and S, Devaraian, “Intertemporally Consistent Shadow Prices in an Open Economy "Estimate for Cyprus"”, Journal of Public Economics, Vol.32, 1987, p. 263-285

[4] Bureau of Statistics of Zhangye, Zhangye Statistical Yearbook. Zhangye, China. (in Chinese), 2007

[5] Chang K. Seung, Thomas R. Harris, MacDiarmid, “Economic impacts of surface water reallocation policies: A comparison of supply-determined SAM and CGE models”, The Journal of Regional Analysis and Policy. vol. 27, 1997, p.55-76.

[6] Frederick, K.D., “Balancing water demands with supplies: the role of management in a world of increasing scarcity”, World Bank Technical Paper No. 189, 1993.

[7] (GPBWR), Gansu Provincial Bureau of Water Resources, Gansu water resource official report of 2002. Beijing : China Water Power Press. (in Chinese), 2003.

[8] Gansu Statistical Bureau (GSB), Gansu Yearbook. Beijing (1979–2005): China Statistics Press. (in Chinese), 1978–2004.

[9] Gao, Q. Z. and Li, F. X. “Case Study of Rational Development and Utilization of Water Resources in the Heihe River Basin. Lanzhou”, Gansu Science and Technology Press, 1991.

[10] Hanemann, M., Pricing as a tool for demand management: Workshop water for the sity: strategic planning, demand management and network losses control. Athens : National Technical University of Athens, University of the Aegean, Water Supply and Sewerage Company of Athens, 2001.

[11] Peter Berck, Sherman Robinson, George Goldman, “The Use of Computable General Equilibrium Models to Assess Water Policies”, California Agricultural Experiment Station Giannini Foundation of Agricultural Economics. Working Paper No. 545. 1990.

[12] Postel, S, Dividing the Waters: Food Security, Ecosystem Health and the New Politics of Water Scarcity : World Watch Institute, 1996, p.65-76.
[13] Takaaki Okuda and Takayuki Hatano, “A General equilibrium modeling on water allocation in the Yellow River Basin,China”, Proceedings Annual Meeting of Environmental Systems Research. 33, 2005, p. 65-72. (in Japanese)
[14] Water Authority of Zhangye, Water Management Practices in Zhangye. Zhangye, China. (in Chinese), 2007.
[15] Yan Chen, Dunqiang Zhang, Yangbo Sun, Xinai Liu, Nianzhong Wang, Hubert H.G. Savenije, “Water demand management: A case study of the Heihe River Basin in China”, Physics and Chemistry of the Earth 30, 2005. p. 408–419.
[16] Yong Wang, Hong-lang Xiao, Rui-fang Wang, “Water Scarcity and Water Use in Economic Systems in Zhangye City. Northwestern China” , Water Resour Manage 23, 2009, p. 2655–2668.
[17] Y. Wang, H.L. Xiao, M.F. Lu, “Analysis of water consumption use a regional input–output model: Model development and application to Zhangye City. Zhangye” , Northwestern China Journal of Arid Environments 73, 2009, p.894–900.

Appendix. Model equation

Income of Household

$$IH = P^L \cdot \overline{L}_H + P^K \cdot \overline{K}_H + TG + TR \tag{1}$$

$$TG = \gamma^G \cdot IG \tag{2}$$

IH : income of household
P^L : wage
P^K : capital rent
$\overline{L}_H$: labor endowment (exogenous variable)
$\overline{K}_H$: capital endowment (exogenous variable)
TG : income transfer to household from government
TR : income transfer to household from the rest of the world(exogenous variable)
γ^G : share parameter
IG : government revenue

Government Revenue

$$IG = \sum_a \tau_a^V \cdot P_a^V \cdot V_a + \tau^H \cdot IH + \tau^W \cdot IW \tag{3}$$

P_a^V : price of value added
V_a : quantity of value added
τ_a^V : value added tax rate
τ^H : direct income tax rate of household
τ^W : direct tax rate of water authority

Household Expenditure

$$U_c = \sum_c H_c^{\beta_c^H} \tag{4}$$

$$\sum_c \left(P_c^{DC} \cdot H_c\right) = \left(1-\tau^H\right) \cdot IH - SH \tag{5}$$

$$H_c = \frac{\beta_c^H}{P_c^{DC}} \left\{\left(1-\tau^H\right) \cdot IH - SH\right\} \tag{6}$$

$$\beta_c^H = \frac{P_{0c}^{DC} \cdot H_{0c}}{\sum_c \left(P_{0c}^{DC} \cdot H_{0c}\right)} \tag{7}$$

U_c : utility level
H_c : quantity of household domestic consumer goods
P_c^{DC} : price of domestic consumer goods
β_c^H : share parameter of household demand
SH : household saving
H_{0c} : initial quantity of household domestic consumer goods
P_{0c}^{DC} : initial price of domestic consumer goods

Water Supply Authority Expenditure

$$IW = \tau^W \cdot IW + SW \tag{8}$$

SW : saving of water authority

Government Expenditure

$$G_c = \frac{\beta_c^G}{P_c^{DC}} \left\{IG - SG - TG\right\} \tag{9}$$

$$TG = \gamma^G \cdot IG \tag{10}$$

G_c : quantity of government domestic consumer goods
β_c^G : share parameter of government demand
SG : government saving (exogenous variable)

Investment

$$I_c = \frac{\beta_c^I}{P_c^{DC}} \left\{SH + SW + SG + IR\right\} \tag{11}$$

$$SH = \gamma^H \cdot IH \tag{12}$$

$$SW = IW - \tau^W \cdot IW \tag{13}$$

I_c : quantity of investment demand for commodity
IR : investment of rest of the world
β_c^I : share parameter of investment demand
γ^H : share parameter of household saving

Domestic Production

$$DP_a = \min\left(\frac{X_{1a}}{\beta_{1a}}, \frac{X_{2a}}{\beta_{2a}}, \cdots, \frac{X_{ca}}{\beta_{ca}}, \cdots, \frac{X_{Ca}}{\beta_{Ca}}, \frac{X_a}{\beta_{0a}}\right) \tag{14}$$

$$X_{ca} = \beta_{ca} DP_a \tag{15}$$

$$V_a = \beta_{0a} DP_a \tag{16}$$

DP_a : quantity of domestic production
X_{Ca} : quantity of intermediate inputs
β_{ca} : intermediate input coefficient
β_{0a} : value added input coefficient

Composite Commodity Market

$$P_a^{DP} = \frac{\left(\sum_c P_a^{DC} X_{ca}\right) + \left(1-\tau_a^V\right)_a^{DC} P_a^V V_a}{DP_a} \tag{17}$$

$$DC_c = \left(\sum_a X_{ca}\right) + H_c + G_c + I_c \tag{18}$$

P_a^{DC} : price of domestic consumer goods
X_{ca} : quantity of Intermediate inputs
DP_a : quantity of domestic production
τ_a^V : production tax rate

Factor Market

$$\sum_a K_a = \overline{K}_H + \overline{K}_W \tag{19}$$

$$\sum_a L_a = \overline{L}_H \tag{20}$$

$\overline{K}_W$: capital endowment of enterprise (exogenous variable)

Interregional Balance

$$\left(\sum_c E_c P_c^{DC}\right) + IR + TR = \left(\sum_c M_c P_c^M\right) \tag{21}$$

M_c : quantity of import
P_c^M : import price (exogenous variable)

First International Conference on Geotechnique, Construction Materials and Environment, Mie, Japan, Nov.21-23, 2011, ISBN: 978-4-9905958-0-7 C3051

Post Earthquake Rapid Inspection Planning for Bridges in Western Kentucky

Norimitsu Koike, Department of Civil Engineering, Aichi Institute of Technology
Issam E. Harik, Department of Civil Engineering, University of Kentucky

ABSTRACT: This paper presents a methodology for the rapid assessment of bridge's safety and functionality following a major seismic event in flat rural areas. The proposed model considers a combination of the bridge ranking prior to the seismic event and a computer assist program to identify the "efficient completion time" strategy for the post earthquake bridge inspection team to inspect the critical bridge's components damage level. Application of the proposed methodology is conducted on the Purchase Parkway in Western Kentucky. By setting the required inspection time to 40 minutes per bridge, it is estimated herein that a non trained inspection team and without computer assist would conduct the inspection for all bridges 61 in a period exceeding 40 hours. On the other hand, by setting the time to 20 minutes for a well trained team with computer assist, it will need 22 hours to inspect all bridge 61, and 5 hours to inspect provisionally the high risk bridges 9.
Keywords: Bridge rank, Inspection Strategies, Post-earthquake inspection, Risk Potential

1. INTRODUCTION

Bridges have historically presented significant vulnerabilities during major seismic events. Although engineers have taken steps to restore and reinforce bridges against earthquakes, it is inevitable that unexpected damage caused by lack of maintenance, poor design, etc., will occur. Therefore, immediate dispatch for bridge inspection is very important following an earthquake.

To assist in decision making and timely response to ensure safety of the public and restore the transportation system functionality, ShakeCast has been developed and provided freely by U.S.Geological Survey (USGS) for emergency responders[1]. In addition, Caltrans (California Department of Transportation) has developed and implemented a Caltrans-specific version of ShakeCast, a post-earthquake analysis tool for rapid evaluation of potential damages structures[2].

In Japan, postearthquake response systems for road networks have already been developed. The system is composed with early earthquake alerts which warn about severe earthquake tremors a few seconds before they happen, a GIS database, ground shaking sensors, CCTV monitors and inspection tours by construction office staff[3].

Those post-earthquake response systems above mentioned may be useful in the construction of real time information facilities such as monitors, seismic sensors and communication lines. Although accurate real-time information may be helpful for an efficient inspection tour, it is difficult to extend those systems for a rural area road network. In rural areas, the cost benefit balance of real-time information systems may be lower than one in an urban area. The financial demands for the construction and maintenance of these systems are unavoidable. Consequently, for inspections that take place without real-time information systems, a rapid inspection methodology is very important.

In Japan, post earthquake inspection systems for building damage are conducted by architects and building engineers who volunteer to evaluate the building damage and risk to the public. The public sector organizes seminars to train inspectors and registers them as volunteers. The results of inspections, containing comments and remarks from resident and visiting inspectors, are displayed on placards[4]. Following an earthquake in Japan, color inspection stickers are seen at the site of a damaged building. However, this system is not used for bridge structures.

For bridge structures in Kentucky, the rapid inspection system assists in providing a uniform approach for rating the damage that has taken place[5]. The inspection teams can fill out an electronic form for all components of the bridge structure with assistance from sample pictures and key point comments. A computer assist program provides recommendation based on whether the observed damage was none, minor, moderate, or severe for each bridge component. The recommendation is made based on the level of damage in the bridge components. The inspection system interface in Kentucky Transportation Center is composed of a laptop PC that contains all the bridge data in Kentucky and a GPS unit attached to the laptop that identifies the bridge once the inspector is at the site. The inspection systemin Kentucky is inexpensive and does not require any special tools or equipment.The system in Kentucky can be used not only by professional but also by a variety of personnel since it has the tools that assist the inspector embedded in the software. This is an important issue in the limitation of manpower and resource at a disaster.

This study attempts to understand the efficacy of the inspection system with a combination of pre-earthquake investigations and rapid inspections. In addition, scenarios and discussions are presented for the inspection tour planning for safety and road link recovery. The framework of the inspection system is discussed herein thorough an application example using the Purchace Parkway which has one of the priority routes on the Western Kentucky Parkway System.

2. METHODOLOGY

2.1Outline of proposed method

The proposed time outline for the rapid inspection planning is shown in Fig.1. Firstly, pre-earthquake investigations should be carried out to ascertain the present condition of bridges. The data from the pre-earthquake investigation is used for forecasting possible damage and ranking the risk. Rapid inspection immediately following an earthquake will be carried out to make recommendations for maintaining public safety and relieving traffic congestion. If the inspection staff has the data from pre-earthquake investigations, their inspection is more effective and rapid. They can check high risk bridges, identified in the pre-earthquake investigation, as a priority.

When making recommendations for traffic relief, inspections should be finished in a short time, and the shorter the better for rescue activities. However, a few hours may be required for decision making to dispatch the inspection team(s) following the announcement of the magnitude and location of the earthquake.

The objective of this study is to produce a recommendation for a rapid inspection of bridges on priority routes. The areas of interest for this study are underlined in Fig.1.

2.2 Bridge risk ranking

The bridge risk ranking against an earthquake is needed to make priorities for rapid inspection. In general, the risk defines the product of the damage probability by the expected loss. The damage to roadways may vary from minor damage such as slight cracking of road surfaces to the bridge collapse. The expected loss depends on the demand of the road. The demand of the main roads is higher than that of the local roads because the main roads may be used as the evacuation route for residents and as designated routes of the relief teams. Therefore, damage and demand have a direct influence on the risk potential. Consideration of demand for roads which are in different regions is also important. However, a uniform demand can be on road sections that are direct routes. If road sections are awarded a uniform demand, it means that the relative risk potential may be decided only by the damage probability. Since the objective is to create a bridge risk ranking, a relative calculation of the risk potential is sufficient.

The challenge is how to calculate the damage probability. The seismic retrofitting manual for preliminary seismic evaluation can be used [6]. The manual describes the rating method for a bridge retrofitting program. Since this manual addresses multiple factors such as structural vulnerabilities, seismic and geotechnical hazards, and bridge importance, it is a suitable method to define the post-earthquake inspection ranking. The outline of the method is as follows:

Firstly, the acceleration and importance coefficient are determined. The acceleration is provided by any seismic data. Some patterns of the importance of the bridge are described in the original manual. Since all bridges on the parkways in Western Kentucky are on essential or “priority” roads, the importance coefficient of bridges targeted for application of the proposed methodology can be classified as “essential”. The seismic performance category (SPC) is determined by the acceleration and the importance confidence by a table contained in the manual. If the bridge is categorized as SPC A, this is omitted from the inventory. Secondly, the soil profile type (S) and structural vulnerability rating (V) are set. In addition, the seismic hazard rating (E) is modified by the soil profile coefficient (S). Finally, the bridge rank (R) is calculated based on a structural vulnerability rating (V) and a seismic hazard rating (E) as follows:

$$R=V*E \qquad (1)$$

In general, a bridge of high R value is more vulnerable than one with a low R value. Since V and E each range from 0 to 10, the value of R will vary from 0 to 100. The R value is easy to understand as a relative index for the vulnerability of the bridge.

2.3 Rapid Inspection system

An essential tool is the inspection assist system, which has been developed by the Kentucky Transportation Center for rapid inspection after an earthquake. Although the target region of the original system development is for the state of Kentucky, if the bridge database of the target area is compiled and installed into the system, its use in any region is possible.

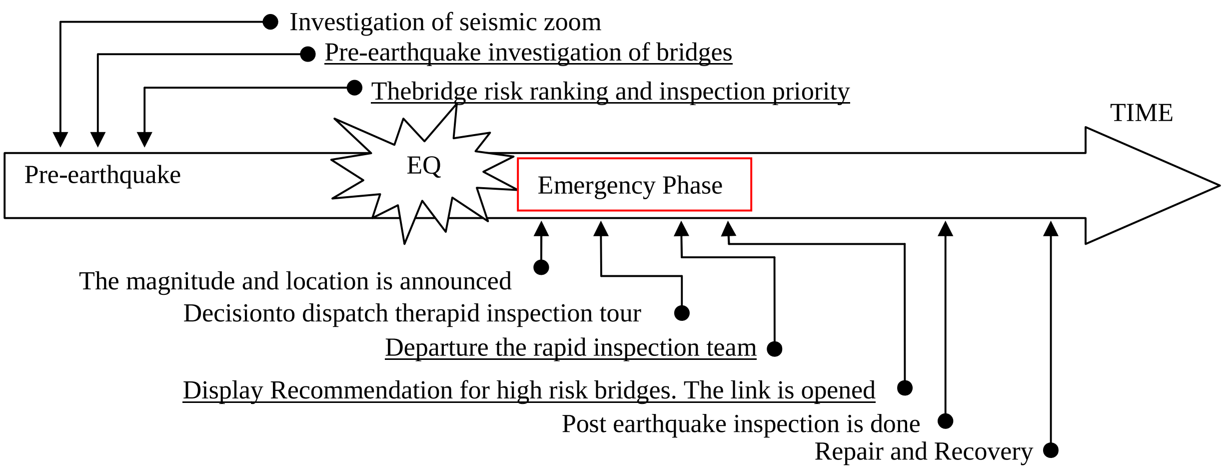

Fig.1. Time outline for rapid inspection planning

The rapid inspection procedures with the system are as follows:

Firstly, the inspector checks the bridge type. The system provides the 17 types of bridge structure. If the database has already been compiled, the inspector needs to select the bridge code number only. Secondly, the inspector makes a visual inspection. The points of view are embankment, span, deck, abutment, bearing, pier or column, and so on. An internal program will provide an associated recommendation based on whether the observed damage was none, minor, moderate or severe for each component. Thirdly, the recommendation is made through the additional points from each component damage score. If the column leans, the recommendation is just "sever". If some silly damage can see, the recommendation will be given by adding damage score. The recommendation may be one of five grades- Green, Blue, Yellow, Orange, and Red. Green means "Bridge Open", Blue means "Travel with Caution", Yellow means "Reduced Speed Limit", Orange means "Bridge closed for Traffic Except for Emergency Vehicles at Reduced Speeds" and Red means "Bridge Closed completely". The inspector prints out the recommendation sheets for public awareness. Civil engineers may also find the data useful information for follow-up inspection.

If the time required for carrying out the inspection is too long, the efficacy of the system for rapid inspection is decreased, so training and rehearsal drills for qualified personnel and rapid inspection are required.

2.4 The strategy of an inspection tour

If a long time is required to inspect all bridges, the inspection team should limit the inspection to bridges with high priorities. However the risk potential of non-inspected bridges cannot be ignored. Thus, the problem between the risk potential for inspection and the time required can be thought of as a trade-off relation. Normally, all bridges should be inspected immediately following an earthquake. The priority of inspections should be considered carefully. For the strategy of the inspection tour, a check should be made to determine whether the inspection tour can be completed within the time limit for relief activity. If inspection for all bridge is impossible, risk potential can't be decreased. This proposal's methodology defines the sum of the R values as previous risk potential in the region. After inspections and recommendations for each bridge, the risk potential will gradually decrease. When the inspection tour is finished, the sum of non-inspected bridges'R value will be shown as non-inspected bridges' risk potential. The non-inspected bridges' risk potential can be used as an important index for evaluating a post earthquake bridge inspection strategy.

The time required per bridge is an important parameter. This depends on the proficiency of the system and bridge structure. Of course the inspection can be carried out without the system; the team needs the handbook and calculation for making the recommendation level by themselves. The team may take a long time. When considering the time required for inspecting and assessing each bridge, this is ample motivation for the training of personnel.

3 CASE STUDY

3.1 Example Area

The study area is in the Western Kentucky region located in the New Madrid and the Wabash Valley Seismic zones. This is potentially one of the most destructive fault zones in the United States. The broad impact has direct implications for virtually every aspect of mutual emergency response.

Kentucky's parkway were constructed during the 1960s and '70s to augment the state's interstate highways. Unlike roads called parkways in other states, Kentucky's parkways are not closed to commercial and recreational traffic. Hence, it is essential that the parkways remain functional and operational following an earthquake, especially, in the Western Kentucky region.

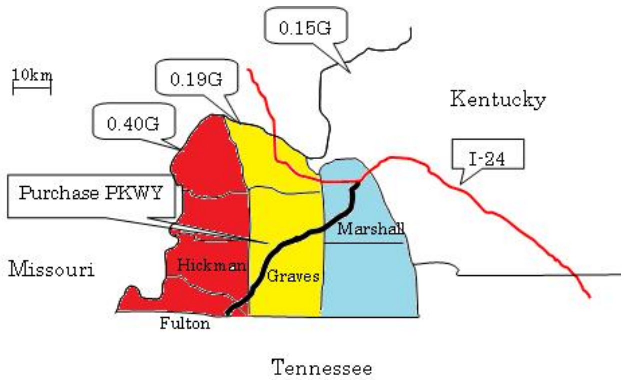

Fig.2.Purchace Parkways in Western Kentucky and PGA for a 250-year earthquake event8)

I.E. Harik et al. have evaluated bridges on and/or over the parkways in Western Kentucky for seismic events[7], [8]. Their investigation included not only bridges, but also their corresponding approaches and embankments. As a result of their research, the risk to the Julian M. Carroll Purchase Parkway (after this "Purchase PKWY") is higher than other parkways. On such purpose, I.E.Harik et.al.used the Peak Ground Acceleration map showed in Fig.2 which corresponds to a 250-year earthquake event in Western Kentucky. The 250-year earthquake event implies that there is a 90% probability for the expected earthquake not being exceeded in 250 years. PGA showed in Fig.2 were calculated from a time history response spectra. The result of the investigation, preliminary analysis and ranking, shows that 13 bridges of the Purchase PKWY are deemed critical because they were constructed in the 1960s, in which seismic design was not taken into consideration. Purchase PKWY is connected with the state of Tennessee, so it is an important route for response on multi-state issues.

3.2 Strategy and Scenario

One of the important issues of the inspection strategy is the accessibility of inspection teams. However there are no deep ravines and no elevated roads in the area. So, it is considered that the inspection team may be able to move beyond the damage bridge site. Therefore, the inspection team transportation speed may be set at about 48km/h(30miles/h).

There are two main purposes of the inspections. One is to make a rapid recommendation of bridge safety. The other is to provide road information as to whether people can travel from origin to destination smoothly. To accomplish the first purpose, the team goes to bridges which are estimated to have serious damage in advance, and displays a recommendation regarding the risk to the public. Although people are able to avoid dangerous bridges, they will be given more detailed road link information later on. If the second purpose takes precedence, the team checks all the bridges in the road section. It is recommended to sweep the road link step by step. However, it will require substantial time, as all bridges should be inspected to ensure that they have only slight damage. It will be difficult to accomplish the two objectives at the same time due to the restriction of human inspection resources. The problem is how to assign priorities and use inspection manpower efficiently.

In order to provide both information of bridge safety and road information to the public timely, the dispatch patterns of the Kentucky Transportation Cabinet personnel are defined under the following strategies:

Strategy 1

The required time of inspection per bridge is varied between 20, 30 and 40 minutes. The time relates to the skill of the inspection team. This will have a large impact on the inspection completion time. In all cases, the inspection team will start from the I-24 junction.

Strategy 2

If the time required to inspect all bridges in one road section is considered to be too long, a more efficient method may be to omit the low risk bridges. The R value can be used for screening in order to shorten the time for inspection in this road section. Since all of bridges are not inspected, it is necessary to show how many risk potential of bridges are dispelled by the inspection teams. The inspection percentage (I) is defined as follows,

$$I = \frac{S}{T} * 100(\%) \qquad (2)$$

Where S is sum of inspected bridge's risk potential, and T is the total of all bridges' risk potential

Strategy 3

If two inspection teams can be assigned, deciding how to divide the roles between them is important for the inspection strategy. This study proposes how to share the role based on theR value. One team is the express team that checks the high risk bridges. This team aims to display recommendations for dangerous bridges as soon as possible. This may permit the avoidance of traffic congestion and maintain public safety. To establish safety in this road section, the other team checks all bridges except those which have already been awarded recommendations by the express team. The aim of this method is to share the bridges that have border R value among both teams. Therefore, the R value can be varied for sharing the teams' roles and to create the optimal strategy.

3.3 Result of Bridge Risk Potential

Fig.3 shows the frequency distribution of the R value versus the Number of Bridges or "Number"of the Purchase PKWY. The original data source is provided by the Kentucky Transportation Center report [9]. Although many bridges are varied between R=0 to 45, 8 bridges are over 75. It means that some specific bridges have a high risk potential and many bridges have a lower probability of being damaged by an earthquake. In addition, two peaks can be seen between R=0 to 45. One peak can be seen in the low level range from 0-10. The second peak is in the range of 20 to 30. The "Ratio" values in Fig. 3 defines the number of bridges with an R value less than or equal to a specific value of R on the abscissa axis over the total number of bridges.

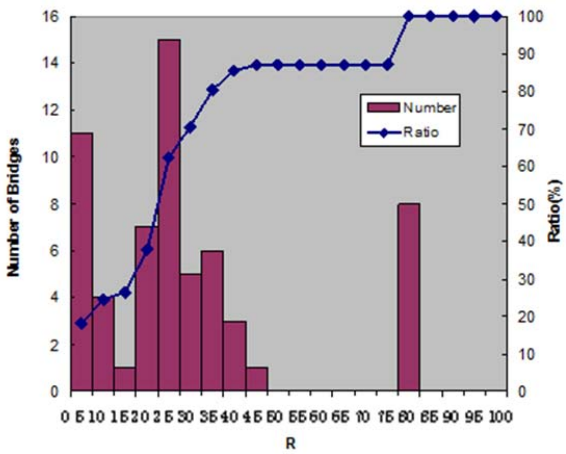

Fig.3. The frequency distribution of the bridge risk potential

4 RESULTS AND DISCUSSION

4.1 Results of Each Strategy

Strategy 1

The fastest case (or 20 minutes per bridge) implies an inspection with a computer assist system by a well trained team. The middle case (or 30 minutes per bridge) is with computer assistance, but by a non-trained team. The results are shown in Table 1.In all cases, the inspection teams start from the I-24 junction. Cases with the computer assist system may decrease the time of inspection drastically. The improvement of inspection time per bridge is effective for short inspection tours.

Strategy 2

In strategies 1, there are recommendations to check all bridges in the road section. However, there is the possibility that inspections will take considerable time the 61 bridges. Therefore, the case for checking only high risk bridges is debatable. Through examination of Fig.3, it is found that high risk bridges are limited in Purchase PKWY. For rapid recommendations, it may not be necessary to inspect all bridges here.

Table 1. Results of the four post earthquake inspection strategies

Strategy	Case	Provisional inspection duration for high risk bridges(Hours)	Inspection duration for all bridges (Hours)	Percentage of Inspected Bridges (%)
Strategy 1	Well trained team with computer assist	-	22.1	100.0
	Non trained team with computer assist	-	32.2	100.0
	Non trained tem without computer assist	-	42.4	100.0
Strategy2 (One team)	Bridges with R> 20 are inspected	9.4	-	72.8
	Bridges with R> 35 are inspected	4.7	-	45.6
Strategy3 (Two teams)	One team inspects bridges with R> 20 and another team inspects bridges with R $\leq$20	9.4	14.4	100.0
	One team inspects bridges with R> 35 and another team inspects bridges with R $\leq$ 35	4.7	19.1	100.0

As the Kentucky Transportation Center, bridges having an R >35, are listed as high risk bridges[7]. In addition, Fig. 3 shows that the mid range bridges' risk potential varies from R=20 to 30. Thus, the target bridges for inspection are selected based on their R value.

Fig.4 shows the risk potential in cases when the inspection team checks bridges based on their risk potential. In case that the team inspects bridges having R> 20, the inspection will finish within 10 hours. The inspection percentage I is approximately 72.8%. The number of bridges inspected is 23 out of 61. This number implies that 37.7 % of the bridges are inspected in this road section. In case bridges having R>35 are inspected, the inspection tour will finish in approximately 5 hours. The inspection percentage I is 45.6%, and the number of bridges that have been inspected is 9 out of 61 (or 14.8% of the bridges in this road section).

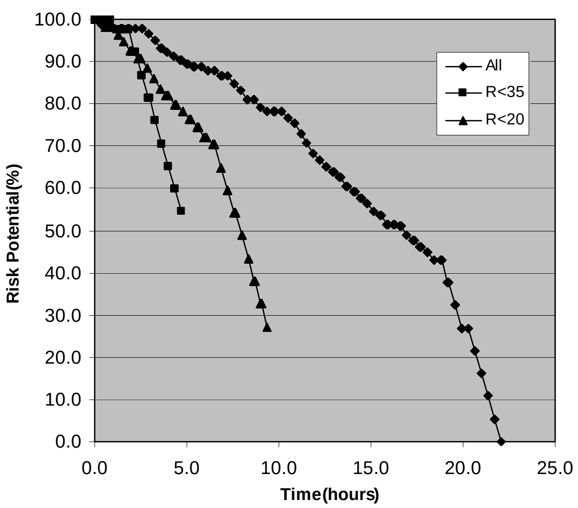

Fig.4.The decrease of the non-inspected bridges' risk potential for different R values

Strategy 3

Fig. 5 shows the result of the inspection of bridges having R< 20 and R> 20. The express team for high risk bridges (shown "HR Team") inspects 23 bridges having R> 20, and another team for low risk bridges (shown "LR Team") inspects 38 bridges having R< 20. The HR team may finish the inspection after 10 hours. At this point in time, because inspection of high risk bridges has been finished, people may be able to use the road slowly and carefully. The other team may finish about 17 hours later. Bridges can receive risk recommendations and people can travel using the road according to the recommendation displayed at each bridge.

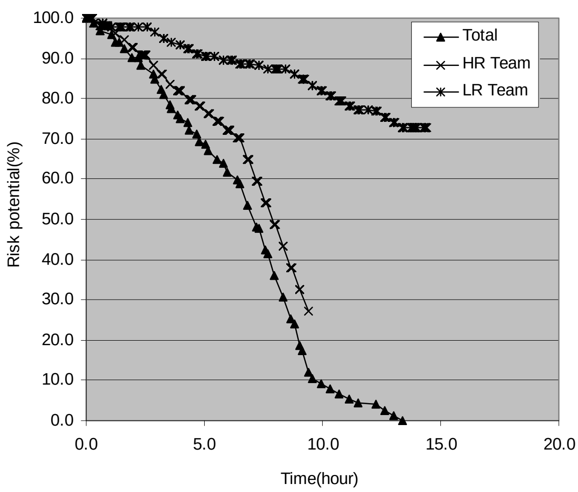

Fig.5.The decrease of the non-inspected bridges' risk potential by the express team for high risk bridges (R> 20) and the team for low risk bridges (R< 20)

Fig.6 shows the result of the inspection of bridges having R< 35 and R> 35. The HR Team (R> 35) inspects only 9 bridges, and the LR team inspects 52 bridges. The HR Team may finish the inspection after 5 hours. The LR Team may finish about 17 hours later.

Comparing the cases when the cutoff values for Rare 20 and 35, the completion time of the comprehensive bridge inspection in the case of the cutoff value is 20 may be faster than in the case when it is 35. This is because the number of bridges inspected is balanced among two teams in the case when the cutoff value is 20. However, in the case when the cutoff value is 35, the inspection of the check high risk bridges is faster.

Decision making regarding the inspection strategy is difficult without estimating the magnitude of the earthquake in the region. For example, if some bridges were to collapse, the road link cannot be opened early by rapid inspection. Rapid inspection for high risk bridges may be required for the public safety. On the other hand, if many bridges suffer damage without collapse, all bridges should be checked early to open the road link. In this scenario, when a severe earthquake occurs, the cutoff value of R = 35 is a better to choice.

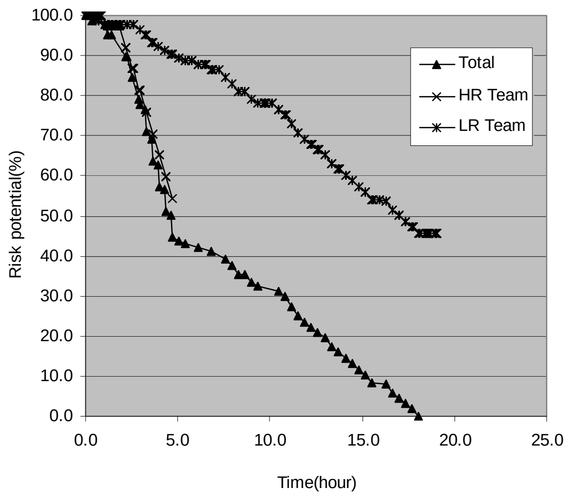

Fig.6.The decrease of the non-inspected bridges' risk potential by the express team for high risk bridges (R> 35) and the team for low risk bridges (R< 35)

4.2 Discussion and Adoptable Strategy

Table 1 presents the result of all four strategies, and the following can be deduced:

1. If an inspection team, without training, carries out the inspection for all bridges, an inspection time of over 40 hours may be required. This may prove to be too late for relief activity. By deploying a well trained team with an assist system, the inspection will be finished in about 22 hours. Training is significant in reducing the inspection time per bridge.
2. In cases that only high risk bridges are inspected by a well trained team, the inspection will be finished in about 5 hours. Although all bridges may not be able to receive recommendations, people can go through the Purchase PKWY carefully. This may be the swiftest strategy,
3. If two inspection teams are deployed, the high risk bridges can be inspected in about 5 hours, and all bridges within 15 hours.

In conclusion, a well trained inspection team dispatched to inspect high risk bridges with R> 35, travelers can expect to go through the Purchace PKWY within 4.7 hours following a major earthquake. It's the adoptable plan for this area.

5 CONCLUTION AND FUTURE DIRECTIONS

This paper presented a rapid inspection tour planning following an earthquake. The combination of the bridge ranking with pre-earthquake investigation and the computer assist system is our principal proposal in this paper. The proposed model is inexpensive, as daily system maintenance is not required. It may be a useful method for rural areas in which it is difficult to set many telemeter sensors. A sample application for the Purchase PKWY in Western Kentucky region was provided with the recommendation that inspection time will be reduced dramatically by using more than one team with good training and bridge risk ranking information.

As Western Kentucky is a flat land area, accessibility to the bridges' sites by the inspection team is not accounted for in this paper. We have fixed the speed of the inspection team and haven't done a sensitive analysis for this parameter. In cases where ravines and steep cliffs form the landscape of the priority route(s), urban areas, and other characteristics, transportation of the inspection team(s) by helicopter or other special transportation should be considered. Other strategies will need to be formulated to suit the geographical characteristics of each area.

The previous field survey was done in 2002 in Western Kentucky area. And the R value was calculated by Seismic retrofitting manual in 1995 version. However, new manual is published in 2006[10]. Equation (1) hasn't changed in new version. The attempt with 2006 version is need in future.

6 ACKNOWLEDGMENT

We wish to acknowledge Kentucky Transportation Center and University of Kentucky for their contribution.

7 REFERENCES

[1] David Wald, Kuo-Wan Lin, Keith Porter, Loren L. Turner, "ShakeCast: Automating and Improving the Use of ShakeMap for Post-Earthquake Decision Making and Response", Earthquake Spectra, Vol.24, No.2, 2008, pp.533-553.

[2] Loren L. Turner, David Wald, Kuo-Wan Lin; Shakecast Caltrans Deploys a Tool for Rapid Post-earthquake Response, TR NEWS, No.261, pp.40-41. 2009.

[3] Yasuhiro Shoji," Developing Earthquake Damage Detection and Information Sharing Tools for Road Administrators", Society for social management systems 2009, P.81.

[4] The Japan Building Disaster Prevention Association," Post-Earthquake Temporary Risk Evaluation of Damaged Buildings", http://www.kenchiku-bosai.or.jp/english/file/epanfall.PDF, 2009.

[5] A.G. Sardo, T.E. Sardo, I.E. Harik," Post Earthquake Investigation Field Manual for the State of Kentucky, Kentucky, Kentucky Transportation Center", University of Kentucky, 2006,KTC-06-30/SPR234-01-1F.

[6] Buckle, I.G., and Friedland, I.M. ,"Seismic retrofitting manual for highway bridges", Federal Highway Administration, US Department of Transportation. Publication, 1995,No.FHWA-RD-94-052.

[7] Issam E. Harik et.al," Seismic evaluation of bridges on and over the parkways in Western Kentucky Summary Report", Kentucky Transportation Center, University of Kentucky, 2008, KTC-07-02/SPR246-02-1F.

[8] R. Street, Z. Wang, I. E. Harik and D. Allen; Source zones, Recurrence rates, and time histories for earthquake affecting, Kentucky, Kentucky Transportation Center, University of Kentucky, KTC-96-4, 1996.

[9] JianXie, Issam E. Harik, Tong Zhao and Jindong Hu,"Preliminary Seismic and Ranking of Bridges On and Over the Parkways in Western Kentucky", Kentucky Transportation Center, University of Kentucky, 2008, KTC-07-04/SPR246-02-3F.

[10] Ian Buckle, Ian Friedland, John Mander, Geoffrey Martin, Richard Nuttand Maurice Power," Seismic retrofitting manual for highway bridges, Federal Highway Administration", US Department of Transportation. Publication,2006,No.FHWA-HRT-06-032.

First International Conference on Geotechnique, Construction Materials and Environment, Mie, Japan, Nov.21-23, 2011, ISBN: 978-4-9905958-0-7 C3051

Organophosphoric Acid Triesters from Landfill Sites and Sewage Plants in Japan

Haruki Shimazu, School of Science & Engineering, Kinki University

ABSTRACT: Seven organophosphoric acid triesters (OPEs) were measured in the water emissions from five active landfill sites and three closed inactive landfill sites. Many kinds of OPEs were detected and the highest concentration levels are 10,000ng/L orders of magnitude. The OPE concentration levels for the closed inactive landfill sites were almost same with those for the active landfill sites. It will be necessary for the closed inactive landfill sites to do continuous monitoring and further maintenance. The same OPEs were measured in the inlet waters and the outlet waters from two sewage plants. The OPE concentration levels in the inlet waters were almost same with those for landfill sites. The OPE concentrations in the outlet waters were lower than those in the inlet waters. Some OPEs could be removed in the treatment process of sewage plants. It is probably effective for OPE reduction to introduce the treatment process into landfill sites.

Keywords: Organophophoric acid triesters, active landfill site, closed inactive landfill site, sewage plant

1. INTRODUCTION

Organophosphoric acid triesters (OPEs) are ubiquitous environmental pollutants because OPEs have been used for plasticizer, flame retarder, antifoaming agent, surface active agent and so on. Several OPEs have carcinogenic and/or neurotoxic properties. Some reports indicate the elution from plastic products and the emissions from landfill sites. However, little is known about the occurrence and the emission characteristics of OPEs from landfill sites and sewage plants. The purposes of this paper are to measure OPEs from active landfill sites, closed inactive landfill sites, and sewage plants and to investigate the OPE emission characteristics from those sites and plants. It is determined that the water emissions from landfill sites and sewage plants have an influence on OPE pollution in aquatic environments.

2. METHODS AND MATERIALS

2.1 Landfill site description

This study focused on five active landfill sites shown in Table 1. The landfill areas were from 8,469-100,816 m^2.Many kinds of wastes were disposed in B landfill. Plastics were disposed in almost landfills.

Table 1. Active landfill sites monitored in this study

	A	B	C	D	E
Opetation time	1995～	1991～	1990～	1989～	1982～
Landfill classification	Inert landfill	Controlled landfill	Inert landfill	Inert landfill	Inert landfill
Area [m^2]	13,421	64,688	100,816	11,478	8,469
Capacity [m^3]	135,404	874,850	1,302,908	104,270	35,098
Composition of waste	Glass, Metals, Plastics, Rubber.	Ash, Glass, Incineration residue, Metals, Papers, Plastics, Rubber, Slag, Sludge, Textiles.	Glass, Metals, Plastics, Rubble.	Glass, Plastics, Rubble.	Rubble.

In 2007, the water emissions from A landfill site, B landfill site and C landfill site were taken three times on 11 November, 1 and 26 December. Furthermore, the water emissions from A landfill site were taken five times on 20 November 2007 and six times on 6 January 2008 to investigate temporal change of OPE concentrations.

In 2008, the water emissions from A landfill site and B landfill site were taken three times on 29 July, 17 October and 21 November. The water emissions from C landfill site were taken four times on 14 June, 29 July, 17 October and 21 November.

In 2009, the water emissions from A landfill site and B landfill site were taken three times on 20 July, 25 August and 25 September. The water emissions from C landfill site were taken five times on 20 June 18 July, 25 August, 25 September and 31 October. Furthermore, the water emissions from D landfill site and E landfill site were taken one time on 25 August and 31 October, respectively.

This study focused on three closed inactive landfill sites shown in Table 2. Many kinds of wastes were disposed in G landfill site.

Table 2. Closed inactive landfill sites monitored in this study

	F	G	H
Opetation time	1986～approx.1990	1986～2007	-
Landfill classification	Inert landfill	Controlled landfill	Inert landfill
Area [m^2]	12,445	20,445	-
Capacity [m^3]	65,822	309,380	-
Composition of waste	Plastics, Metals, Glass, Rubber.	Ash, Glass, Incineration residue, Metals, Papers, Plastics, Rubber, Slag, Sludge, Textiles.	-

In 2008, the leachates from F landfill site were taken twice on 17 October and 21 November.

In 2009, the leachates from F landfill were taken five times on 20 June, 18 July, 25 August, 25 September and 31 October. The leachates from G landfill site were taken twice on 18 July and 31 October. Furthermore, the leachates from H landfill site were taken four times on 18 July, 25 August, 25 September and 31 October.

For active landfill site, there were 20 samples, 9 samples, 12samples, 1 sample and 1 sample from A, B, C, D and E, respectively. For closed inactive landfill site, there were 7 samples, 2 samples and 4 sample from F, G and H, respectively.

2.2 Sewage plant description

This study focused on two sewage plants shown in Table 3.

Table 3. Sewage plants monitored in this study

	I	J
Opetation commencement	1986	1972
Service area [km^2]	28.81	72.13
Service population	163,209	651,737
Treatment capacity [m^3/d]	75,000	380,000
Treatment process	Anaerobic-anoxic-oxic process	Step aeration process

The treatment capacities for I sewage plant and J sewage plant were 75,000 m^3/d and 380,000 m^3/d, respectively. The treatment processes were anaerobic-anoxic-oxic process and step aeration process.

In 2009, the inlet water in I sewage plant was taken one time on 19 October. The outlet waters in I sewage plant were taken twice on 18 September and 19 October. Furthermore, the inlet waters in J sewage plant were taken eight times on 29 September, 2 and 3 October to investigate temporal change of OPE concentrations. The outlet water in J sewage plant was taken one time on 29 September. There were 3 samples and 9 samples for I and J, respectively.

2.3 Analytical methods and instruments

Seven OPEs shown in Table 4 were measured. Those are object chemicals because many kinds of studies have been reported that they are fluently detected in aquatic and airborne environments.

Table 4. Measured OPEs in this study

Chemicals	CAS Number	abbr.	logKow
Tributyl phosphate	000126-73-8	TBP	4.00
Tri-2-butoxyethyl phosphate	000078-51-3	TBXP	3.75
Tri-2-chloroyethyl phosphate	000115-96-8	TCEP	1.44
Tris (1,3-dichloroisopropyl) phosphate	013674-87-8	TDCPP	3.65
Triethyl phosphate	000078-40-0	TEP	0.80
Tris (2-ethylhexyl) phosphate	000078-42-2	TEHP	4.23
Triphenyl phosphate	000115-86-6	TPP	4.59

* These abbreviations are used in this study.

** logKow values are obtained from reference

In the preparation, the water sample is filtered with glass fiber prefilter (MILLIPORE AP40, nominal pore size 0.7 μ m). OPEs in the filtered water are given as the solved OPEs. OPEs in the suspended matter on the glass fiber are given as the suspended OPEs.

Each 1000 ml filtered sample is passed into the solid phase extraction column (WATERS PS-2) at the rate of 20 ml/min. The column is dried with air by means of sanction pump. The chemicals are eluted by passing 5 ml of dichloromethane through the column. The extract is concentrated to 0.1 ml under a N_2 flow. Hexane is added to the extract until 2 ml.

Each glass fiber prefilter sample is dried in a dark place overnight and put into a vial with 15ml of dichloromethane. The chemicals are extracted with ultrasonic waves. The extract is filtered and concentrated to 0.1 ml under a N_2 flow. Hexane is added to the extract until 2 ml. The chemicals in these extracts are determined with gas chromatograph with mass spectrometer (Agilent technologies, 5975B inert XL E/CI MSD).

The operation condition for GC/MS (gas chromatograph with mass spectrometer) is shown in Table 5. After qualifying by three typical SIM mass, each OPE is quantified by the largest SIM mass. The detection limits were calculated from threefold values of signal-noise ratio in the baseline of chromatogram. The recoveries and the variation coefficients for solved OPEs in this analysis ranged from 70% to 120% and from 7% to 20%, respectively.

Table 5. Operation condition for GC/MS in this study

5975B inert XL E/CI MSD (Agilent Technologies)	
Column	HP-5MS(30m×0.25mmf, 0.25μm)
Oven temperature	50℃(1.5min)→20℃/min→180℃→5℃/min→280℃(1min)
Injection temperature	250℃
Injection method	Splitless, 2μL
Carrier gas	He
Detector temperature	230℃
SIM mass	TBP : 99, 151, 211 TBXP : 125, 199, 227 TCEP : 249, 205, 251 TDCPP : 191, 209, 193 TEP : 155, 99, 127 TEHP : 99, 113, 211 TPP : 326, 325, 215

3 RESULTS AND DISCUSSION

3.1 OPEs from active landfill sites

Seven OPEs were measured in the water emissions from five active landfill sites. The solved OPEs and PAHs in the water emissions from the active landfill sites are shown Table 6.

Table 6. OPE concentrations in the water emissions from the active landfills

	Solved OPEs		Suspended OPEs	
	[ng/L]*	DR**	[ng/L]*	DR**
TBP	337(49.0-2670)	39/43	61.4(9.22-1340)	43/43
TBXP	1250(49.2-6110)	26/43	755(456-834)	5/43
TCEP	926(47.4-3850)	31/43	252(8.12-713)	18/43
TDCPP	51.9(20.6-83.1)	2/43	204(41.3-366)	2/43
TEP	1400(43.1-20900)	40/43	18.4(4.32-415)	36/43
TEHP	31.0(3.9-58.1)	2/43	8.77(1.17-29.0)	18/43
TPP	58.7(15.0-329)	13/43	49.1(18.1-204)	5/43

* Median(min-max)

** Detection rate

For active landfill sites, the solved OPEs for the high detected frequencies were TBP, TBXP, TCEP, and TEP. The suspended OPEs for the high detected frequencies were TBP and TEP. The highest concentrations of the solved OPEs and the suspended OPEs were 20900 ng/L for TEP and 1340 ng/L for TBP.

The total concentrations and the component ratios of OPEs in water emissions from active landfill sites were shown Fig.1. The concentrations and component ratios were different in each landfill site. The total of solved OPEs and suspended OPEs from B landfill site were lower than those from the other landfill sites because many kinds of wastes were disposed. However, the OPE concentrations for A and C landfill sites were high. It may be due to plastic wastes because typical OPEs containing plastic products such as TBXP, TCEP, and TEP were so high [1].

The temporal changes of OPEs in the water emissions from A landfill site on 20 November 2007 were shown in Fig.2. TBP, TBXP, TCEP, and TEP ranged from approximately 1000 ng/L to 2000 ng/L. The specific trends of OPE concentrations were not observed. The trends of OPE concentrations on 6

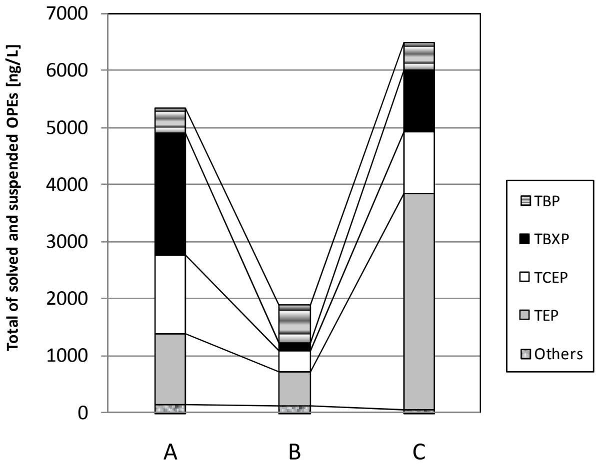

Figure 1 Total concentrations and component ratios of OPEs in the water emissions from the active landfill sites

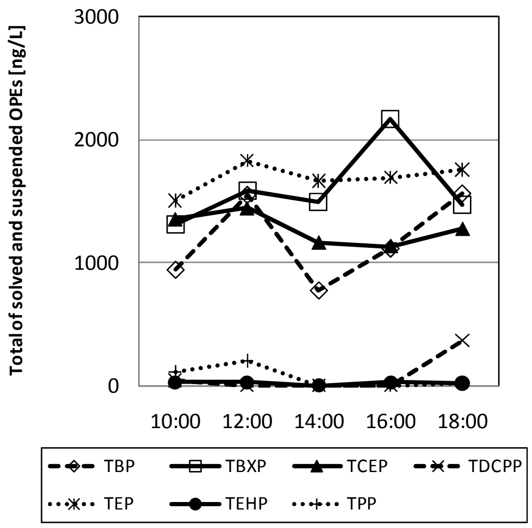

Figure 2 Temporal chenges of OPEs in the water emissions from A landfill site (Nov. 2007)

January 2008 were almost same. It probably indicates that these OPEs were gradually dissolved from plastic wastes and/or contaminated soils and emitted to the environment [2].

3.2 OPEs from closed inactive landfill sites

Seven OPEs were measured in the water emissions from three closed inactive landfill sites. The solved OPEs and PAHs in the water emissions from the closed inactive landfill sites are shown Table 7.

For closed inactive landfill sites, the solved OPEs for the high detected frequencies TBP, TBXP, TDCPP, and TEP. The suspended OPEs for the high detected frequencies were TBP, TEP, and TEHP. The highest concentrations of the solved OPEs and the suspended OPEs were 6870 ng/L for TBP and 3780 ng/L for TBP. The OPE concentration levels for the closed inactive landfill sites were almost same with those for the active landfill sites. In spite of the closed inactive landfill

Table 7. OPE concentrations in the water emissions from the closed inactive landfills

	Solved OPEs		Suspended OPEs	
	[ng/L]*	DR**	[ng/L]*	DR**
TBP	1490(321-6870)	13/13	50.4(4.05-3780)	13/13
TBXP	628(210-4230)	8/13	6.21	1/13
TCEP	89.3	1/13	29.2	1/13
TDCPP	52.5(37.0-277)	7/13	ND	0/13
TEP	1360(30.9-4290)	13/13	15.8(2.05-503)	10/13
TEHP	3.00	1/13	6.59(3.36-17.8)	10/13
TPP	ND	0/13	ND	0/13

* Median(min-max)
** Detection rate
*** ND means Not detected.

sites, the OPE concentration levels were high. It shows that the closed inactive landfill sites need continuous monitoring and further maintenance.

3.3 Effects of water temperature and rainfall on OPE emissions from landfill sites

Effects of water temperature and rainfall on OPE emissions from landfill sites were investigated. Figure 3 shows the relationship between OPE concentrations in the water emissions from the landfill sites and water temperature. The correlation coefficient for the active landfill sites is so low because wastes are continuously disposed in the active landfill sites. However, the relationship between OPE emissions and water temperature for the closed inactive landfill sites is a little significant. The disposed wastes containing OPEs were so closed for a long time that water temperature could depend on the elution characteristics for OPEs. Figure 4 shows the relationship between OPE concentrations in the water emissions from the landfill sites and rainfall. For both active landfill sites and closed inactive landfill sites, the significant relationship between OPE emissions and rainfall were not observed. The quantity of water emissions is not related with total of rainfall for seven days before sampling. It could be due to the complex mechanism of rainfall elution from landfill sites.

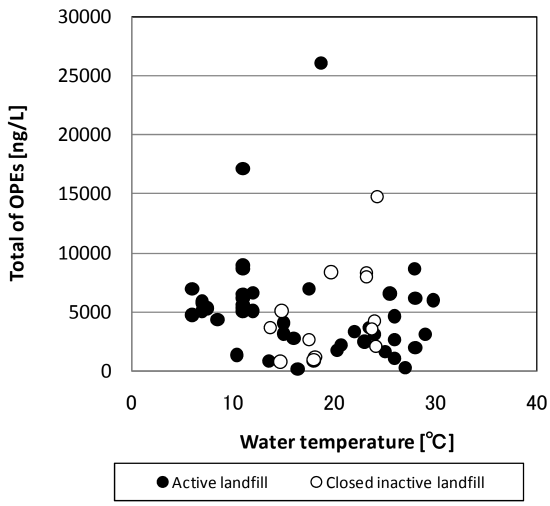

Figure 3 Relationship between OPEs in the water emissions from landfillsites and water temperature

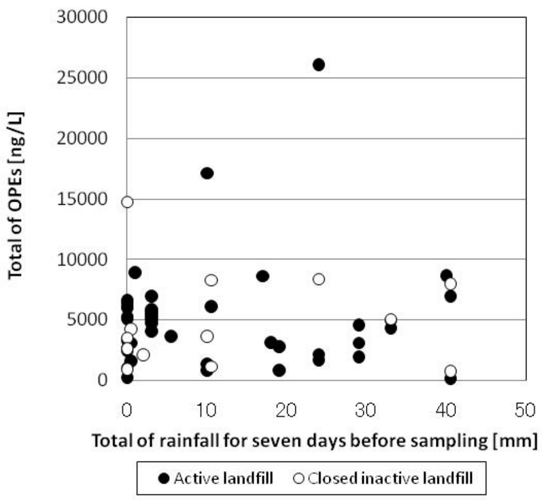

Fig.4 Relationship between OPEs in the water emssions from landfill sites and rainfall

3.4 OPE partition characteristics in water emission from active landfill sites

Suspended OPEs / solved OPEs partition coefficients (Ksw) in water emissions from active landfill sites are shown Fig. 5. The shown OPEs were detected both filtered water and suspended matter. Each dot means the median value of Ksw. Each Ksw range means from minimum value to maximum value. TEP is the most hydrophilic and TPP is the most hydrophobic, as shown in Table 4. The trend indicates that logKsw would be higher for hydrophobic OPEs.

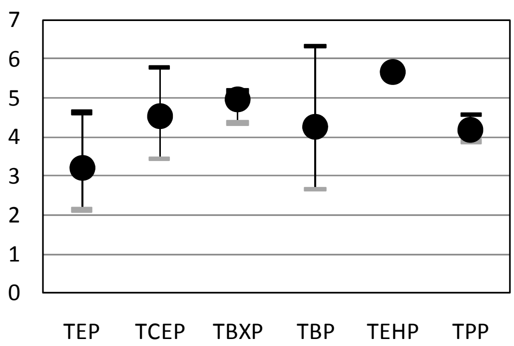

Figure 5 Median and range of Ksw for detected OPEs both filtered water and suspended matter

3.5 OPEs from sewage plants

Seven OPEs were measured in the inlet waters and outlet waters for two sewage plants. The solved OPEs and PAHs in the inlet waters and the outlet waters for the sewage plants are shown Table 8 and Table 9.

In the inlet waters, the solved OPEs for the high detected frequencies were TBP, TDCPP, TEP, TEHP, and TPP. The suspended OPEs for the high detected frequencies were TBP and TEHP. The highest concentrations of the solved OPEs and the suspended OPEs were 36200 ng/L for TBXP and 842

Table 8. OPE concentrations in the inlet waters for the sewage plants

	Solved OPEs		Suspended OPEs	
	[ng/L]*	DR**	[ng/L]*	DR**
TBP	764(441-14,700)	9/9	159(40.3-842)	9/9
TBXP	6920(1530-36200)	9/9	140	1/9
TCEP	3150(1320-4500)	4/9	ND	0/9
TDCPP	190(106-404)	7/9	ND	0/9
TEP	129(86.3-357)	9/9	36.1	1/9
TEHP	76.4(28.7-115)	9/9	266(118-508)	9/9
TPP	79.4(61.2-108)	9/9	ND	0/9

* Median(min-max)
** Detection rate
*** ND means Not detected.

Table 9. OPE concentrations in the outlet waters for the sewage plants

	Solved OPEs		Suspended OPEs	
	[ng/L]*	DR**	[ng/L]*	DR**
TBP	1050(133-2690)	3/3	25.0(5.60-71.0)	3/3
TBXP	871(564-1400)	3/3	50.7	1/3
TCEP	1810(1600-2170)	3/3	ND	0/3
TDCPP	109(106-138)	3/3	20.8	1/3
TEP	143(103-203)	3/3	5.64(2.14-9.14)	2/3
TEHP	5.30(1.89-8.72)	2/3	15.6(8.77-22.5)	2/3
TPP	16.5	1/3	ND	0/3

* Median(min-max)
** Detection rate
*** ND means Not detected.

ng/L for TBP. The temporal changes of OPEs in the inlet waters from O sewage plant were investigated. The specific trends of OPE concentrations were not observed as those for A landfill site shown in Fig.2. In the outlet waters, the highest concentrations of the solved OPEs and the suspended OPEs were 2690 ng/L for TBP and 71.0 ng/L for TBP. The concentration levels for TBXP, TEHP, and TPP in the outlet waters were lower than those in the inlet waters. Some OPEs could be removed in the treatment process of sewage plants.

4 CONCLUSION

Seven OPEs were measured in the water emissions from five active landfill sites and three closed inactive landfill sites. The same OPEs were measured in the inlet waters and the outlet waters in two sewage plants. Many kinds of OPEs were detected and the highest concentration levels are 10,000ng/L orders of magnitude. The OPE concentration levels for the closed inactive landfill sites were almost same with those for the attractive landfill sites. It will be necessary for the closed inactive landfill sites to do continuous monitoring and further maintenance. The OPE concentrations in the outlet waters were lower than those in the inlet waters for sewage plants. Some OPEs could be removed in the treatment process of sewage plants. It is probably effective for OPE reduction to introduce the treatment process into landfill sites.

5 REFERENCES

[1] Kagawa Environmental Research Center, http://www.k-erc.pref.kanagawa.jp/kisnet/

[2] Yasuhara A, "Elution of tris(2-chloroethyl) phosphate from waste plastics into water", *J.Environ. Chem.*, Vol.6, No.1, 1996, pp.43-47

First International Conference on Geotechnique, Construction Materials and Environment, Mie, Japan, Nov.21-23, 2011, ISBN: 978-4-9905958-0-7 C3051

Ground Water Pollution around the Oyachi–Heizu District of Yokkaichi City

Takemoto Y, Takahashi M, Awaya K, Ioka M and Guo P, Kayou -cho 1200, Yokkaichi, Mie, Japan 512-8512
Yokkaichi University, Faculty of Environmental and Information Sciences

ABSTRACT: Arsenic pollution in the ground water has been widely found in the Tomida district in northern Yokkaichi city as shown in previous studies. The biggest illegal disposal site of industrial waste in midland of Japan was found in this area.

In order to identify the source of this pollution, we have investigated the ground water pollution around this illegal landfill site. In this study, sampling of well and the seepage water was carried out at 13 observation sites, and the concentrations of the following materials such as pH, EC, COD, T-N, T-P, D-Fe, D-Mn, NH_4-N, NO_3-N, Cl, Mg, Ca and 1,4dioxan were analyzed. In order to identify the origin of this water pollution (D-Fe, D-Mn and Arsenic) and to examine relation to the illegal disposal place, the analysis of the ion ingredient of the ground water was also investigated. However, the ion composition of the water in the place which left remote from this landfill site was clearly different from the analysis of the ion ingredient of the water of this disposal site. The results indicated that the pollution (Arsenic, etc) found widely in the area which left far from the disposal site is not directly related with the illegal disposal site.

Keywords: Arsenic pollution, Illegal disposal site, Ion composition of ground water

1. INTRODUCTION

Arsenic pollution in the ground water has been widely found in the Tomida district in northern Yokkaichi city as shown in previous studies which were carried out in 2008[2]. The biggest illegal disposal site of industrial waste in midland of Japan was found in this area, and many toxic substances (As, Pb and 1,4Dioxan) are detected in the ground water of the landfill site[1]. In order to identify the relation of this pollution with the disposal, we have investigated the ground water pollution around this illegal landfill site[4][5].

2. FEATURES OF THE INVESTIGATION SITES

Investigation was carried out at 12 sites, and outline of the site is shown in Table 1. It was found that the higher values than the Japan environmental standard of Arsenic were detected in St3, St8, St12 in previous research[2].

The concentrations of EC,COD,CL values are very high levels around this illegal landfill disposal site.

3. SURVEY DATE AND ANALYTICAL METHODS

Survey and observation was carried out in 9 May, 2011 and parameters and analytical methods used in this survey were as the following features;

Table. 1 Features of the survey sites

Site	Features of the ground water	Distance from the boundary of dump site	Well depth
St1	Leaching water	500m	---
St2	Deep well for irrigation	800m	200m
St3	Artesian water from well	1 km	200m
St6	Leaching water	1.5km	---
St7	Deep well for irrigation	2 km	200m
St8	Deep well for irrigation	2 km	200m
St9	Deep well for irrigation	2.5km	200m
S12	Leaching water from retaining wall	500m	---
St51	Leaching water, near disposal site	100m	---
St52	Leaching water near disposal site	100m	---
St54	Leaching water near disposal site	200m	---
St55	Leaching water from disposal site	0m	---

pH: Glass-electrode,
EC: Platinum electrode,
COD: Acidic Potassium per manganese method,
TN: Ultra violet absorption method,
TP: Molybdenum Ammonite method,
NO_3-N: Simple analysis (of Pack test),
NH_4-N: Simple analysis (of Pack test),
NO_2-N: Simple analysis (of Pack test),
C l: Simple analysis (of Pack test),
F^-: Simple analysis (of Pack test),
1,4Dioxan: LC-MS,
As: Data of the previous report [2][3]

4. RESULTS AND DISCUSSIONS

Results are shown as the following Tables. In order to investigate the data, survey sites are divided in three groups, <u>one group</u> is the site of near this landfill site (within 300m from dumping site, St51, St52 , st54, St55, to be indicated as **N**-group), <u>another group</u> is the sites remote from this landfill site (over 1 km away, St3 and St6 to St9, to be indicated as

R-group), and <u>the other group</u> (St1, St2, St12, to be indicated as **O**-group) in Fig 1.

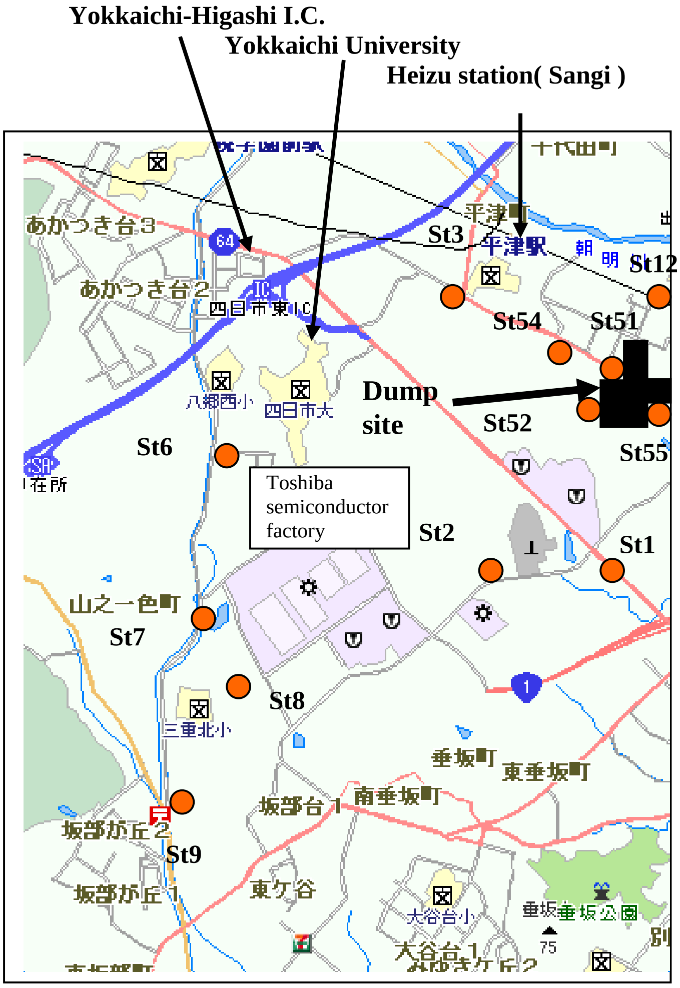

Fig.1 Investigation sites around the biggest illegal disposal site

4.1 Grouping of the Results

D-Fe, D-Mn were detected in many site independently in all groups. In <u>**N**-group</u>, where is regarded as the place of highly influenced by the disposal, high concentrations of EC, COD, CL, Mg, Ca, 1,4 dioxan were detected, these contaminants are regarded as reaching substance from dumping site. However, contrarily, in <u>**R**-group</u>, concentration of these contaminant were low. In the previous research, high concentration of Arsenic was found in St3, St12, St8, these sites belong to <u>**R**-group</u> or <u>**O**-group</u>. From these results, we considered that the As contamination found widely in these area is not directly related with the illegal waste disposal.

4.2 Results of Analysis presented by the Tables

We show our analyzed results of the ground water pollution in the following Tables.

Table. 2 Results of the analysis (No.1)

Parameter	**St 1**	**St 2**	**St 3**
pH	6.8	6.5	7.9
EC mS/cm	0.44	0.42	0.23
COD mg/L	4.6	2.5	1.7
TN mg/L	1.2	1.9	0.78
TP mg/L	0.02	0.06	0.56
F^- mg/L	1	1	0.6
As mg/L	0.005	0.002	0.012
D-Fe mg/L	8	10	<0.05
D-Mn mg/L	1	1.5	<0.25
NH_4 mg/l	0.5	---	0.5
NO_2 mg/l	<0.02	<0.02	<0.02
NO_3 mg/l	<0.5		<0.5
Cl mg/L	30	50	6
Mg mg/L	20	15	0.5
Ca mg/L	60	30	2
1,4Dioxan mg/L	0.019	0.009	<0.005

Table. 3 Results of the analysis (No.2)

Parameter	**St 6**	**St 7**	**St 8**
pH	6.3	6.6	7.4
EC mS/cm	0.18	0.22	0.19
COD mg/L	0.7	0.9	1.5
TN mg/L	0.11	0.74	1.2
TP mg/L	0.08	0.08	1.5
F^- mg/L	1.3	1	0.8
As mg/L		<0.001	0.014
D-Fe mg/L	3	10	0.8
D-Mn mg/L	<0.25	1	<0.25
NH_4 mg/l	0.2	---	0.7
NO_2 mg/l	<0.02	<0.02	<0.02
NO_3 mg/l	<0.5	<0.5	<0.5
Cl mg/L	6	4	3
Mg mg/L	5	8	3
Ca mg/L	8	10	3
1,4Dioxan mg/L	<0.005	<0.005	<0.005

Table. 4 Results of the analysis (No.3)

Parameter	St 9	St12	St51
pH	6.5	6.9	6.8
EC mS/cm	0.19	0.71	0.60
COD mg/L	0.1	16	16
TN mg/L	2.8	1.8	6.4
TP mg/L	0.01	0.18	0.63
F^- mg/L	0.7	0.8	0.8
As mg/L		0.020	<0.0005
D-Fe mg/L	0	10	1
D-Mn mg/L	<0.25	0.5	<0.25
NH_4 mg/l	---	1	0.5
NO_2 mg/l	<0.02	<0.02	<0.02
NO_3 mg/l	10	<0.5	<0.5
Cl mg/L	7	0	30
Mg mg/L	10	30	8
Ca mg/L	10	80	50
1,4Dioxan mg/L		<0.005	0.024

Table. 5 Results of the analysis (No.4)

Parameter	St52	St54	St55
pH	6.5	7.3	7.9
EC mS/cm	0.94	2.4	3.9
COD mg/L	23	14	64
TN mg/L	3.3	2.0	86
TP mg/L	0.45	0.25	0.35
F^- mg/L	1.3	0.5	7.5
As mg/L			<0.001
D-Fe mg/L	8	0.3	10
D-Mn mg/L	2	5	<0.25
NH_4 mg/l	---	0.5	50
NO_2 mg/l	<0.02	<0.02	1.5
NO_3 mg/l	<0.5	<0.5	20
Cl mg/L	50	600	1000
Mg mg/L	20	30	150
Ca mg/L	50	30	70
1,4Dioxan mg/L	---	0.097	0.23

4.3 Results of Analysis presented by the Radar Charts

Results of analysis are presented by the graph of the radar chart in the following. We select the concentrations of EC,COD,Cl ,Mg,Ca as drawing with the radar charts.

Group of high concentration of calcium ion (Ca) is St51 and St52.
The high dense calcium ion (Ca) pollution indicates that waste wood and gypsum wall board from houses and buildings seem to have been filled in the underground of these sites.

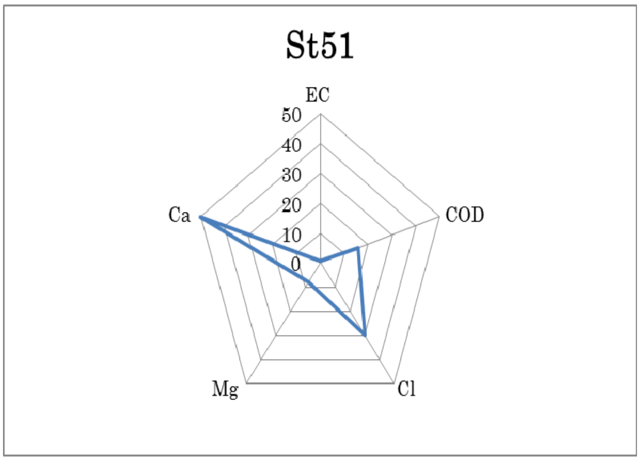

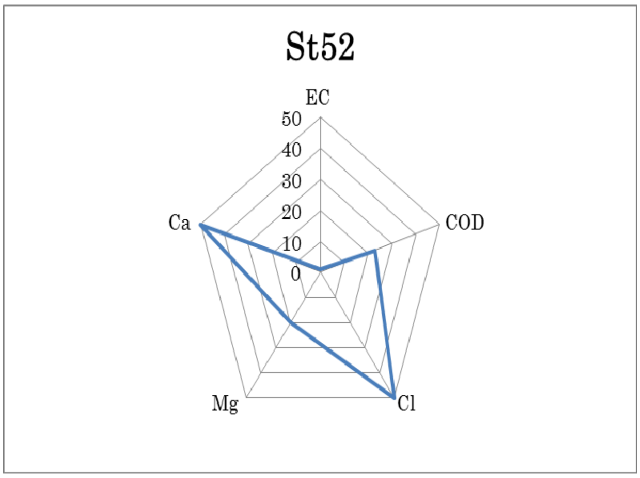

Group of high concentration of Cl ion is St54 and St55.
High values of chloride ion (Cl) indicate the influence of contamination from the waste disposal field.
The high concentration of chloride ion in the groundwater, soil water, and river water are often observed because chloride ion (Cl) is nonreactive and not sorptive and has no redox or precipitation. Near the waste disposal site groundwater with high ammonium ion (NH4) and chloride ion (Cl) usually dominates.

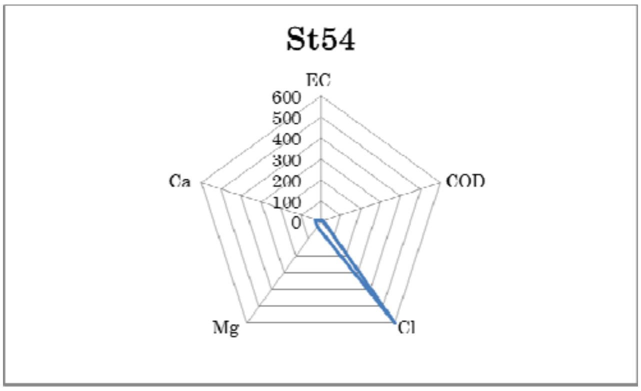

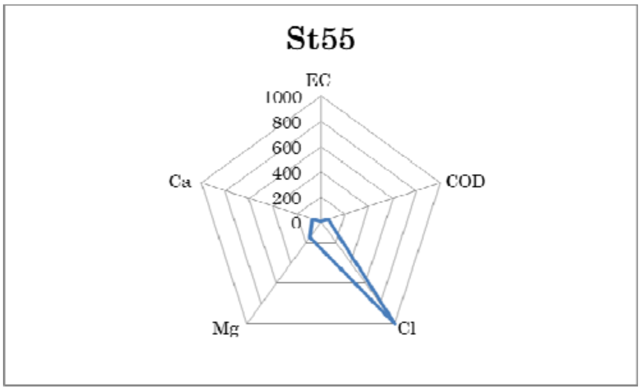

There are the places with less ground water pollution in the long range from the waste disposal field. For example, St3,St6 and St9.

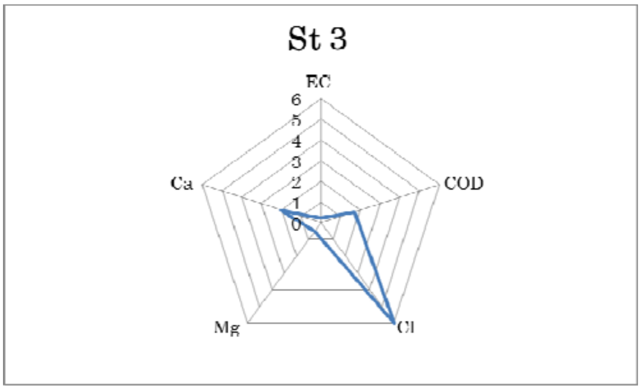

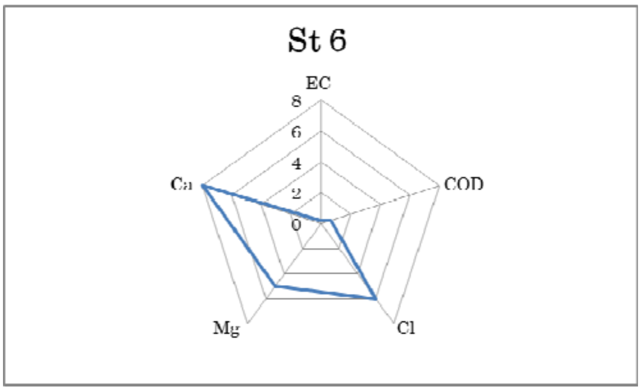

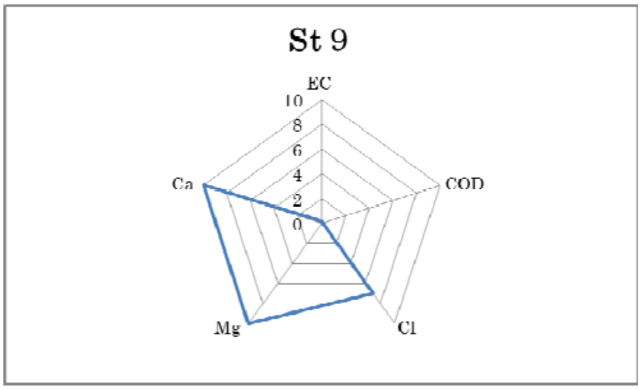

5 CONCLUSION

In order to identify the origin of the ground water pollution (D-Fe, D-Mn, As, P) in northern Yokkaichi city, investigation has carried out. Ion composition of the ground water in the place remote from landfill site was clearly different from the ion ingredient of the water of disposal site. These results indicate that the pollution in order to identify the origin of the ground water pollution (of Fe, Mn, As) found widely in the area which left from the disposal site is not directly related with the illegal disposal site. So, it is necessary that we should advance the research more and more.

6 REFERENCES

[1] Survey report on matters of the Yokkaichi-Ohyachi-Heizu disposal site, Risk Hyouka-Hyou 2nd version ,2011.

[2] Takahashi M, Awaya K, Ioka M, Takemoto Y, “Ground water and Soil pollution near Ohyachi-Heizu Waste Disposal Site”, J. of EIS, Yokkaichi University ,Vol, 11, No.2, 2008, pp. 27-31.

[3] Takahashi M, Awaya K, Ioka M, Takemoto Y, “Ground water Pollution in Yokkaichishi Tomida area”,J of EIS, Yokkaichi University, Vol, 12, No.2, 2009, pp.39-42.

[4] Awaya K,”The build up of the illegal dump of industrial waste in the Ohyachi-Heizu district, Yokkaichi city, based on the information released by Mie Prefecture”, J. of EIS, Yokkaichi University ,Vol, 11, No.2, 2008, pp. 113-136.(in Japanese)

[5] Ioka M, Takahashi M, Awaya K, Takemoto Y, ”Visualization of Elution Tests and Ground water Pollution of the Disposal Field in Ohyachi-Heize, Yokkaichi, based on the Report of Mie Prefecture”, J. of EIS, Yokkaichi University ,Vol, 13, No.1, 2009, pp. 11-23.(in Japanese)

First International Conference on Geotechnique, Construction Materials and Environment, Mie, Japan, Nov.21-23, 2011, ISBN: 978-4-9905958-0-7 C3051

Characteristics of Damage to Structures Induced by The Tsunami of The 2011 East Japan Mega Earthquake

Ö. Aydan, Tokai University, Ocean Research Institute, Shizuoka, Japan

H. Tano, Nihon University, Dept. of Civil Eng., Koriyama, Japan

T. Iwatate, Tokyo Metropolitan University, Dept. of Civil. Eng., Tokyo, Japan

ABSTRACT: The East Japan Mega Earthquake with a moment magnitude of 9.0 occurred off the shore of Tohoku Region of Japan. Although the seismologist of Japan anticipated an earthquake with a magnitude of 7.5 in the source area, the magnitude of this earthquake was much greater than their anticipation. Furthermore, the anticipated level of the tsunami induced by this earthquake also exceeded the level anticipated by the seismologists of Japan. Therefore, the damage caused by the tsunami was tremendous and killed more than 28000 people due to the insufficiency of the counter-measures. The authors first present the characteristics of the tsunami and then describe damage to buildings and various structures. In the final part of the article, lessons from this earthquake are described and some recommendations for tsunami resilient structural design are put forward.

Keywords: Tsunami, East Japan Earthquake, damage, lessons

1 INTRODUCTION

The East Japan Mega Earthquake with a moment magnitude 9.0 took place at 14:46 (JST) on March 11, 2011[1]. The earthquake was a subduction plate-boundary earthquake and the rupture area was 450 km long and 200 km wide. This earthquake caused gigantic tsunami waves, which destroyed many cities and towns along the shores of Tohoku and Kanto Regions of Japan. The casualties caused by this tsunami exceed 28,000 people. The tsunami destroyed and heavily damaged buildings of various types, transportation facilities and infrastructures. The authors visited an area from Orai to Hitachi in Kanto region and Iwanuma to Rikuzentakata in Tohoku region and made observations on the damage of various structures (Figure 1).

In this paper, the authors first present the characteristics of the tsunami and then describe damage to buildings and various structures. In the final part of the article, lessons from this earthquake together with those from the Aceh earthquake are described and some recommendations for tsunami resilient structural design are put forward.

2 CHARACTERISTICS OF THE TSUNAMI

The earthquake was an offshore plate boundary earthquake with a sense of thrust faulting. The estimated inclination and offset of the fault were between 14-16 degrees and 25-30 m, respectively. The seabed was uplifted by 5 m while the land sank-down by about 0.8 m with a horizontal movement of 4.6 m [2]. The crustal deformation caused the intrusion of the sea front into the land as illustrated in Figure 2. If the strained overriding plate slip along the plate boundary, it rebounds to its unstrained state. As a result, the upper surface (before) configuration changes to "after" configuration. This configuration change causes ground uplift near the plate front and subsidence of ground away from the plate front. As a result, the sea front moves towards the land and causing inundated areas. This caused inundation problems particularly in the settlements during the high tides and the erosion along the seashore.

Figure 1: Investigation routes and epicenter location

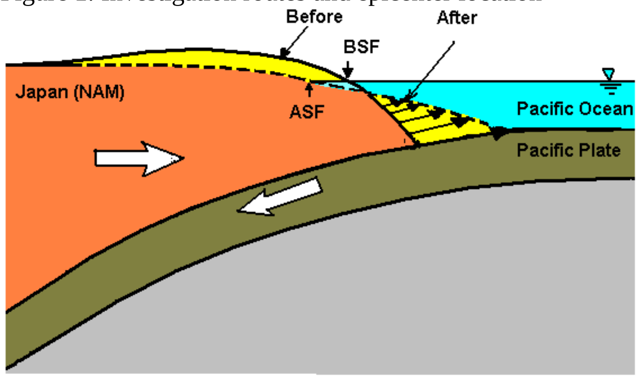

Figure 2: An illustration of mechanism for the inundation problem along the seashore.

The Port Authority Research Institute (PARI) operates DARTS along the shores of Japan [3]. Figure 3 shows locations of DARTS and their records of tsunami waves. The DARTS are approximately 20 km away from the shore and the sea depth varies between 125 m and 204 m. The maximum tsunami height by DARTS was about 7m.

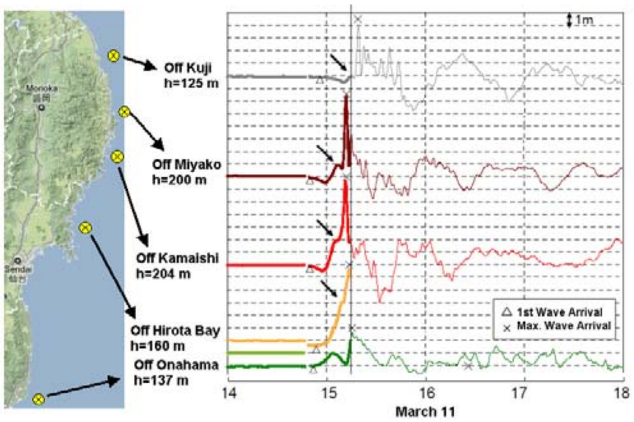

Figure 3: Locations and measured tsunami heights by DARTS along the Tohoku region (modified from PARI[2]).

There are two different definitions for characterizing the tsunami height, namely, the tsunami height at the shoreline and inundation-height or run-up height (Figure 4). As it was previously difficult to measure the tsunami height at shoreline, the inundation tsunami-height obtained from traces of tsunami front on the land is commonly quoted as the tsunami height in the past. This may have tremendous values depending upon how it is measured. For example, the newspapers reported a tsunami height of 38.9 m at Aneyoshi (Miyako) measured by Tokyo University of Marine Science and Technology, which probably includes the splash zone. The maximum tsunami height at shoreline in this earthquake was measured as 15.3 m at Onagawa town by the authors. Figure 5 shows the measured tsunami height together with estimations from some empirical relations.

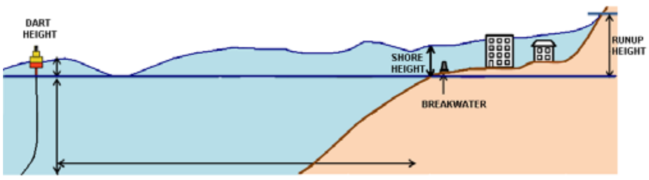

Figure 4: Illustration of different tsunami heights (modified from PARI[2])

The maximum tsunami waves arrived at major towns and cities such as Kamaishi, Rikuzentakata, Kesennuma, Minami Sanriku, Ofunato and Onagawa about 30-40 minutes after the earthquake. Figure 6 shows a computational result for the arrival time estimation for Ishinomaki City. The arrival times of the maximum tsunami waves at several locations are roughly equal to those estimated from the single source model with the use of seabed topography and epicenter location.

Japan has a warning system based on a database of previously computed results for scenario offshore earthquakes. This system performed well until this earthquake. Once the epicenter and magnitude of the earthquake are determined, the system evaluates the expected tsunami heights at shores and their arrival times. As the magnitude of this earthquake could not be accurately determined for a considerable time following the earthquake, the appropriate warnings could not be issued until 15:33 [1]. When it was issued, it was too late for the cities and towns, which were already heavily hit by the tsunami waves.

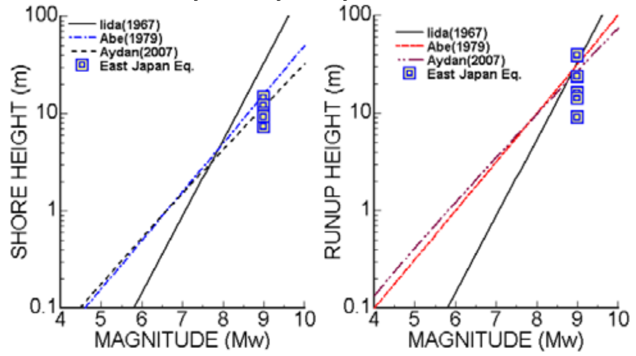

Figure 5: Comparison of observation with empirical relations for tsunami shoreline and run-up heights [4,5,6].

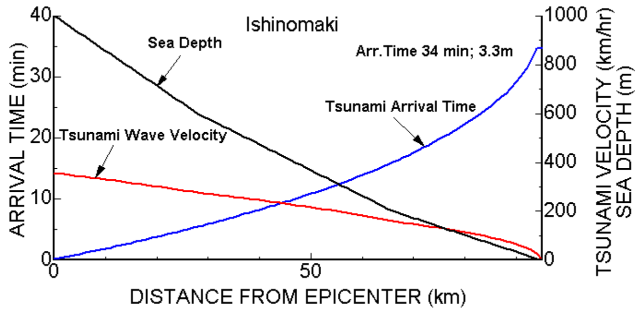

Figure 6: Estimation of the arrival time of tsunami wave at Ishinomaki.

3 COUNTER MEASURES AGAINST TSUNAMI

Counter-measures against tsunami can be broadly classified into two categories, specifically, software measures and hardware measures. Software measures involve recommending people to escape locations with higher elevations and/or earthquake and tsunami resistant high buildings and terraces. However, when higher ground is far, it may be extremely hard for elderly or sick people, pregnant women and small kids to escape higher grounds, which may be called as horizontal evacuation. At such places, the vertical evacuation in the form of escaping to higher buildings, terraces and towers becomes the most effective software counter measure [6].

Hardware countermeasures are a) Constructing high breakwaters, b) Constructing evacuation terraces; c) Tsunami gates at the estuary of rivers, and d) Planting trees. Japan with rich experiences of tsunami damage has tried very hard to implement both software and hardware counter-measures. However, tsunami shore-height was generally assumed to be up to 5-6 m in hardware countermeasures so far. The actions of tsunami waves can be impact, surge, drag, buoyant and hydrostatic forces. Tsunami-resistant structures must be capable of resisting against these forces.

4 RESPONSES OF STRUCTURES AGAINST TSUNAMI WAVES AND ASSOCIATED DAMAGE

The authors investigated an area from Orai to Hitachi in

Kanto region and Iwanuma to Rikuzentakata in Tohoku region. Figure 7 shows the images of Rikuzentakata City before and after the tsunami as an example. There were many hardware counter-measures implemented in Rikuzentakata City. These counter measures were the construction of breakwaters along the river and seashore, tsunami gates at the estuary of small rivers and planting very dense pine trees. When two images are compared with each other, it is easily noticed that none of hardware counter-measures were effective. Tsunami waves overtopped breakwaters, the pine-tree forest and tsunami gates resulting in the inundation of the almost entire city. This observation clearly indicated that if the tsunami wave height at shoreline is greater than the height of any of these hardware counter-measures, the counter-measures become ineffective. Figure 8 shows some views of counter-measures after the tsunami in Rikuzentakata. In this section, responses of structures observed in various locations against tsunami waves are described.

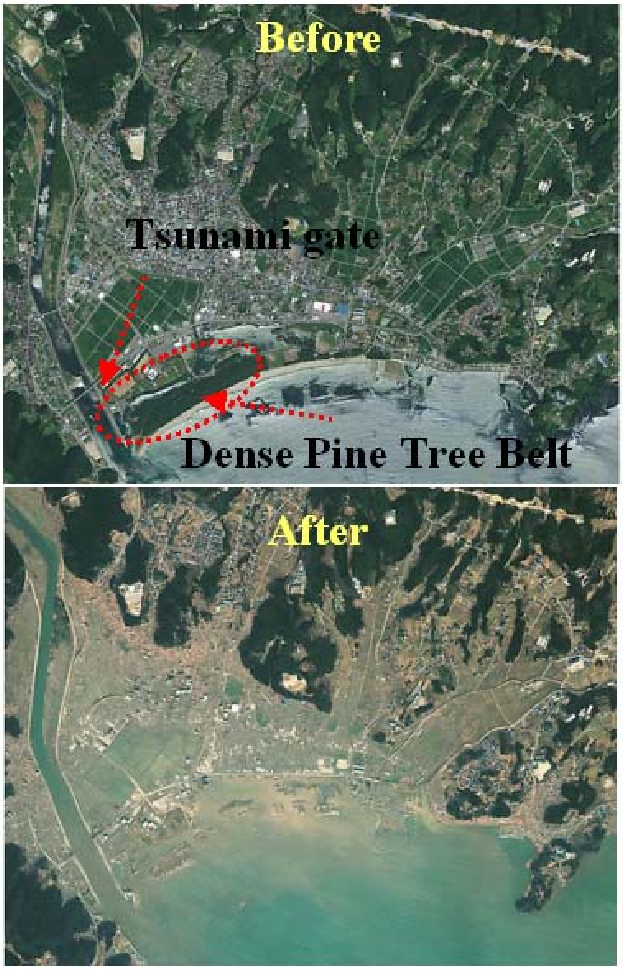

Figure 7: Images of Rikuzentakata City before and after the tsunami (images from GSI [2]).

4.1 Responses of Timber, Masonry, and RC and Steel Framed Buildings

Timber buildings are the less-resistant building type among all other types of buildings (Figure 9). As they are very light, there are easily uplifted and carried away and crushed. Therefore, such structures should not be built in tsunami-prone areas. Although stone masonry buildings are rare in the tsunami affected areas, they are much more resistant against tsunami waves (Figure 10). Steel-framed structures also performed poorly (Figure 11). The infill panels of the steel-framed structures were punctured by impact forces of tsunami and debris, and steel frames bended or buckled. Reinforced concrete (RC) structures or steel reinforced concrete (SRC) structures performed much better among all building types (Figure 12). Except damage to some of RC or SRC buildings observed in Onagawa town, almost all of these type buildings were structurally sound and they were the only remaining structures in all visited towns and cities.

Figure 8: Views of the state of counter-measures after the tsunami.

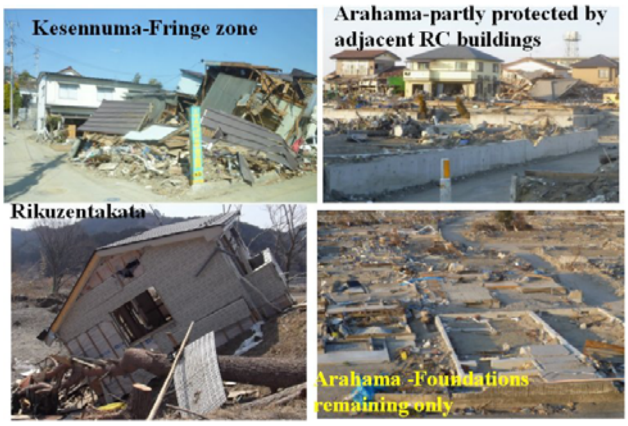

Figure 9: Views of damage to timber buildings.

In Onagawa town, RC or SRC buildings were even damaged and some of them were toppled and dragged for several ten meters (Figure 13). It was interesting to note that one building, which had piles with a diameter of 30cm and length of 4 m, was uplifted from its piled foundations and dragged for about 70 m. The back-analysis of damage to RC and SRC buildings in Onagawa should be the starting point for the tsunami-resistant building design in years to come.

Figure 10: Views of damage to masonry buildings.

Figure 11: Views of damage to steel-framed buildings.

Figure 12: Views of damage to RC buildings.

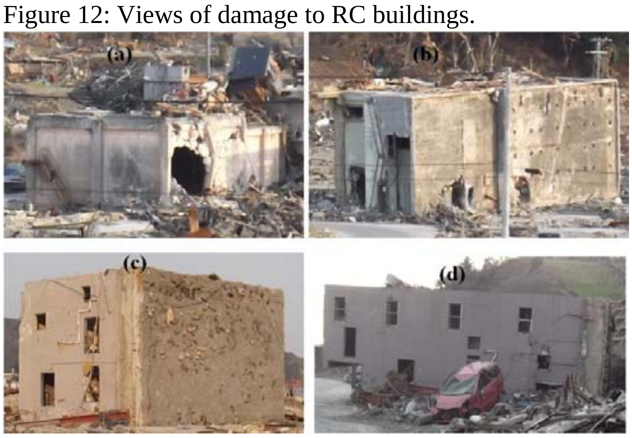

Figure 13: Views of damage to RC or SRC buildings.

4.2 Responses of Railways and Railway Bridges

Damage to railways and railway bridges occurred along railway lines running close to the seashore. The piers of railway bridges were toppled, rails were dragged and embankments were scoured (Figure 14). Furthermore, trains were uplifted and dragged for a considerable distances.

Figure 14: Damage to railways and railway bridges

4.3 Responses of Roadways and Roadway Bridges

Fundamentally damage to roadways and roadway bridges were similar to that of railways and railway bridges and it occurred when roadways were running close to the seashore. The bridge decks were uplifted and dragged and embankments were scoured (Figure 15).

Figure 15: Views of damage to roadways and roadway bridges.

4.3 Responses of Airports

The Sendai Airport, which is about 1 km away from the sea shore and at the elevation of 2m above sea, was inundated by the tsunami. Tsunami height at the airport was about 4.9-5.7 m. The runway and ground floor facilities were all damaged by the inundation, mud and debris of the tsunami (Figure 16) The airport was cleaned up and it started its function on April 13, 2011 with some domestic flights. The piers and embankments of railway and roadway bridges were also scoured and at some locations and there were deck falls (Figure 17).

Figure 16: Views of damage to Sendai Airport

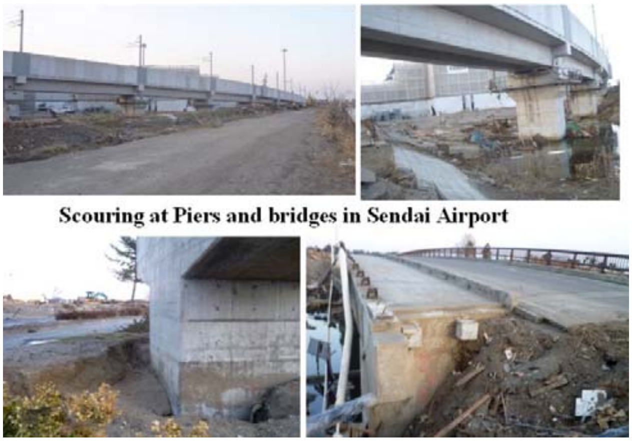

Figure 17: Views of souring at piers and embankment damage of roadways and railways in Sendai Airport

4.4 Responses of Embankments

The damage to embankments by tsunami waves is due to tsunami induced liquefaction and erosion from drag forces. Such damages were observed along river embankments, at railway and roadway embankments (Figure 18). Furthermore, the erosion of approach embankments of railway and roadway bridges was also common in the tsunami-affected areas.

Figure 18: Views of souring in embankment of roadways and railways in Sendai Airport

4.5 Responses of Rock Slopes and Tunnels

The damage to slopes by tsunami waves is due to drag and hydrostatic forces. In some places, shotcrete was peeled off (Figure 19). Tsunami waves inundated the West Makiyama Tunnel (Ishinomaki) up to 1 m. However, the damage to the tunnel itself was none (Figure 20).

Figure 19: Views of damage to slopes

Figure 20: Views of inundated Makiyama Tunnel

4.6 Responses of Gigantic Breakwaters and Causes of Their Damage

Japan constructed gigantic breakwaters at various locations. Breakwaters at Kamaishi, Ofunato, Rikuzentakata and Taro were all damaged and they could not perform as they were supposed to be. The Kamaishi gigantic breakwater was 61 m high from the sea bottom. Figure 21 shows a cross-section of the gigantic breakwater. The caissons of the breakwater were sank down and tilted after the tsunami. The video images taken during the arrival of tsunami clearly demonstrated that the tsunami surf appeared at locations where they should not be. This simply implied that the damage to caissons of the breakwater already took place before the arrival of the tsunami due to ground shaking induced by the earthquake. It is most likely the rubble mound below the caissons sank down due to ground liquefaction of seabed soil. This is actually a commonly observed phenomenon in the past earthquakes as well as in this earthquake (Figure 22).

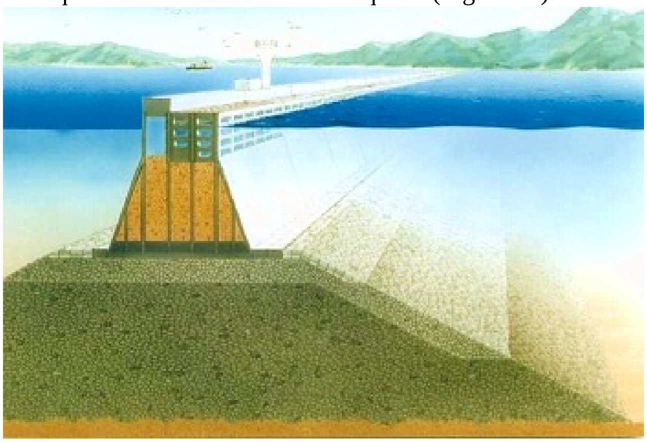

Figure 21: An illustration of cross section of Kamaishi port gigantic breakwater [3].

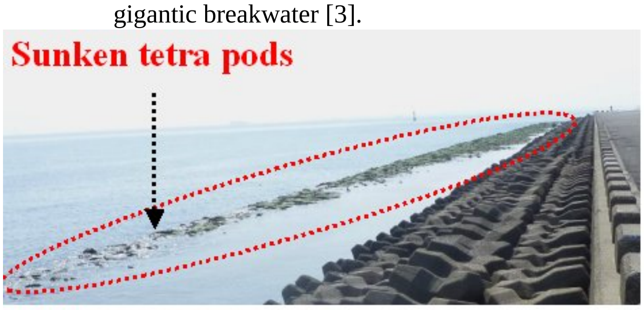

Figure 22: Settlement of tetra-pods in Shin-Urayasu caused by the 2011 East Japan Earthquake.

5 CONCLUSIONS

The following conclusions and lessons may be drawn from the observations reported in this article and previous earthquakes:

1) The shore height (inundation height at seashore) is the most important parameter for the design of structures against potential tsunamis. The shore height induced by this tsunami is in accordance with the estimations from the empirical relations by Abe (1979) and Aydan (2008).

2) Although Japan has been well prepared for tsunami and its disasterous effects, the anticipated tsunami height for implementing hardware measures was much less than that induced by this tsunami.

3) The observations on the damage induced by the tsunami of the 2011 East Japan mega-earthquake were basically similar to those of 2004 Aceh (or Off Sumatra).

4) Timber buildings can not stand against high tsunami waves. Steel framed structures are also weak against tsunami waves due to the weakness of the infill panels. Reinforced concrete buildings performance was best to resist gigantic tsunami waves provided that they are well built against ground shaking. Therefore, timber buildings must not be allowed in tsunami-vulnerable areas.

5) This earthquake also showed that the vertical evacuation in relatively flat areas was important to save lives.

6) The effectiveness of planting trees against tsunami must be re-evaluated.

7) Very strong impact, surge, buoyancy, and dragging forces of the tsunami waves were the primary factors for the damage to bridges despite they are well-designed against ground shaking.

8) The failure of breakwaters to protect the settlements may have been caused by the failure of seabed ground due to the strength loss resulting from the reduction of effective stress under high prolonged tsunami waves and/or ground liquefaction.

9) The inundation of ground along sea shores is due to rebound of strained overriding plate. It would be quite difficult to preserve the previous shorelines for a considerable period of time. The current shoreline may further retreat due to erosion by high waves.

6 REFERENCES

[1] Japan Meteorological Agency (JMA), Tokyo, Japan

[2] Geographical Information Authority of Japan (GSI): Special web site for East Japan mega earthquake.http://www.gsi.go.jp/BOUSAI/

[3] Port Authority Research Institute.(PARI): Special web site for East Japan mega earthquake.http://www.pari.go.jp/info/tohoku-eq/

[4] Abe, K., " Size of great earthquakes of 1837-1974 inferred from tsunami data", J. Geophys. Res. 84(B4), 1979, 1561-1568.

[5] Iida,K, "Magnitude,energy,and generation mechanisms of tsunamis and a catalogue of earthquakes associated with tsunamis", in Proceedings, Tsunami Meetings Associated with the Tenth Pacific Science Congress, pp.7-18,Int.Union of Geod.and Geophys.,Paris, 1963.

[6] Aydan, Ö., "Seismic and Tsunami Hazard Potentials in Indonesia with a special emphasis on Sumatra Island". Journal of The School of Marine Science and Technology, Tokai University, 2008, Vol.6, No.3, pp.19-38.

First International Conference on Geotechnique, Construction Materials and Environment, Mie, Japan, Nov.21-23, 2011, ISBN: 978-4-9905958-0-7 C3051

Characteristics of Strong Motions Induced by the 2011 East Japan Mega Earthquake with an Emphasis on Tokyo Bay Area

T. Iwatate, Tokyo Metropolitan University, Dept. of Civil. Eng., Tokyo, Japan

Ö. Aydan, Tokai University, Ocean Research Institute, Shizuoka, Japan

ABSTRACT: The 2011 East Japan Mega Earthquake with a moment magnitude 9.0 occurred on March 11, 2011. This earthquake shook almost the entire Japan. There are several strong motion networks and these networks recorded strong ground motions, which may be of great value for the earthquake engineering community, as it is very rare to have such a rich source of strong ground motions. The authors processed the acceleration records obtained by NIED (namely, K-NET and KIK-NET), Port Authority Research Institute (PARI) and Tokyo Metropolitan University in this study. In this article, the authors present the outcomes of their studies on the strong motions induced by the East Japan mega earthquake with an emphasis on those in Tokyo Bay Areas.

Keywords: 2011, East Japan, earthquake, strong motion

1 INTRODUCTION

The 2011 East Japan Mega Earthquake with a moment magnitude of 9.0 occurred off the shore of Tohoku Region of Japan [1]. The earthquake was subduction plate-boundary earthquake and the rupture area was 450 km long and 200 km wide. Although the seismologist of Japan anticipated an earthquake with a magnitude of 7.5 in the source area, the magnitude of this earthquake was much greater than their anticipation.

This earthquake shook almost the entire Japan. There are several strong motion networks operated by several organizations and institutes. These networks recorded strong ground motions, which may be of great value for the earthquake engineering community, as it is very rare to have such a rich source of strong ground motions. The authors processed the acceleration records obtained by NIED[2] (namely, KNET[3] and KIKNET[4]), Port Authority Research Institute[5] (PARI) and Tokyo Metropolitan University (TMU). This earthquake also induced heavy ground liquefaction particularly in reclaimed ground around Tokyo Bay area. As an inland earthquake with a magnitude of 7.2 is anticipated in Tokyo Bay area, the ground shaking characteristics of Tokyo Bay area are of great importance in view of seismic responses of various structures. In this article, the authors will presents the outcomes of their studies on the strong motions induced by the East Japan mega earthquake with an emphasis on those in Tokyo Bay Areas.

2 CHARACTERISTICS OF THE 2011 EARTHQUAKE

The magnitude of the 2011 East Japan Mega-earthquake was estimated to be between 8.9 and 9.1, depending upon the institutions. The Japan Meteorological Agency (JMA) had difficulties to determine the magnitude of the earthquake soon after the earthquake due to several technical reasons and the magnitude was updated to 9 after several days.

The earthquake occurred along the subduction zone between North American plate (NAM) and Pacific plate (PAC) (Figure 1) and the inclination of the rupture plane was estimated to be 14-16 degrees. The faulting was due to thrust faulting with an estimated offset of 25-30 m. The seabed was uplifted by 5 m while the land sank-down by about 0.8 m with a horizontal movement of 4.6 m [6]. The rupture initiated in the area where an earthquake with a magnitude of 7.5 was anticipated and it propagated bi-laterally. The rupture plane is about 450 km long and 200 km wide and it consisted of 4 distinct segments. There have been numerous aftershocks and some of aftershocks were greater than magnitude 7 (Figure 2). The aftershock activity occurred in and around the rupture area and some of shocks along the boundary between North American Plate and the Eurasian plate (EUR) took place in Shizuoka, Nagano and Akita prefectures. The rupture front stopped at the boundary between the Philippine Sea Plate (PHS) and Pacific Plate. As the stress distribution entirely changed after this earthquake, it is feared that it may initiate mega-earthquakes in Kanto, Tokai, Tonankai and Nankai subduction zones.

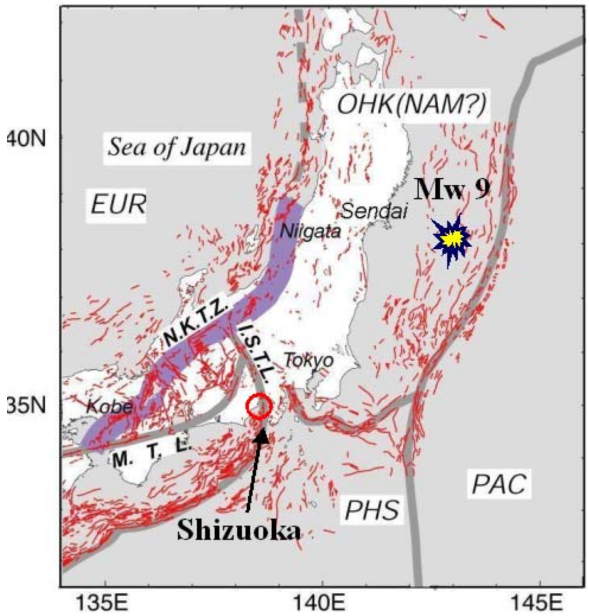

Figure 1: Location of the 2011 East Japan earthquake and tectonics of the region (modified from GSI [6]).

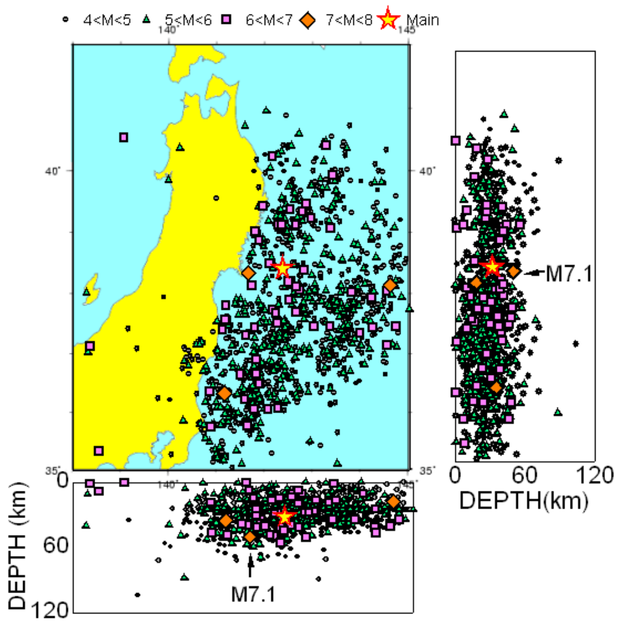

Figure 2: Aftershock distributions as of April 8, 2011.

3 STRONG-MOTION NETWORKS

There are several strong-motion networks in the earthquake-affected area, operated by several institutes and organizations. Following the 1995 Kobe earthquake (Hyogo-ken Nanbu earthquake), Japan established two strong motion networks, namely, KNET and KiKNET and they are operated by the NIED. The KNET network is for measuring strong ground motions at the the free-field ground surface while the KiKNET network is for measuring the strong-motions at the bed-rock and ground surface. The Japan Meteorological Agency also has a strong-motion network throughout Japan, which is used to estimate intensity scale and its distribution. However, the strong-motion records of this network are not always easily accessible. The Port Authority Research Institute (PARI) has a strong motion network covering the major ports in Japan and their data is accessible through the Internet. In addition, Tohoku University, Electrical Power Companies, Japan Railways, Japan Expressways (NEXCO), Building Research Institute (BRI), Tokyo University, Tokyo Metropolitan University and other institutes and organizations have their own networks. However, their records are generally not accessible through the Internet. In this article, the records obtained by the KNET, KiKNET, PARI and Tokyo Metropolitan University (TMU) are processed and the results are reported.

4 CHARACTERISTICS OF STRONG-MOTIONS

Figure 3 shows the NS, EW and UD components of acceleration records of some selected strong motions stations of KNET and KiKNET networks from Shimizu to Hachinohe. As noted from the figure, the records strongly reflect the rupture propagation. While the strong motion stations to the north of the epicenter clearly shows the rupture sequence of 4 segments, the records of the stations to the south of the epicenter are superimposed so that it is indistinguishable.

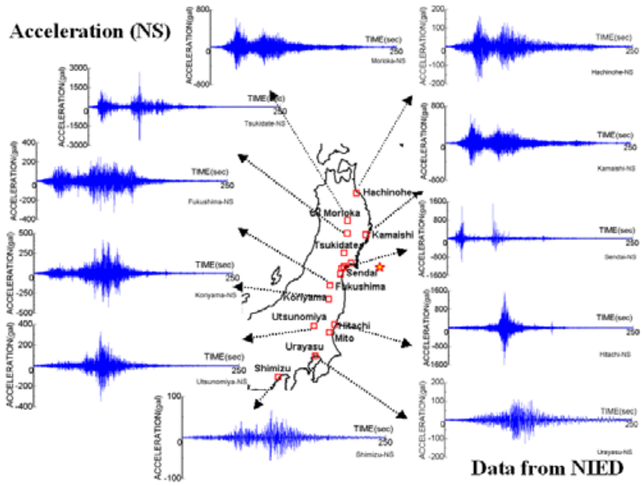

(a) NS component

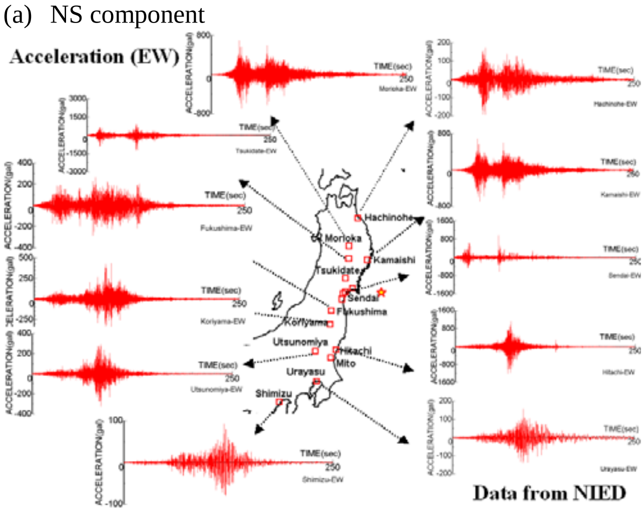

(b) EW component

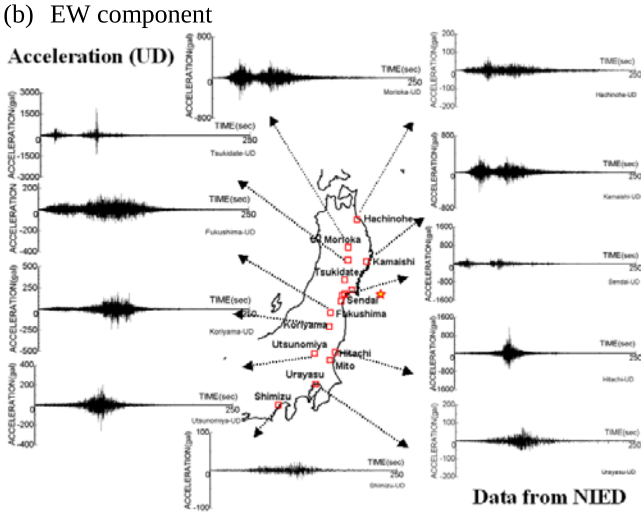

(c) UD Component

Figure 3: Acceleration records of some selected strong motion stations of KNET and KiKNET of NIED.

Figure 4 shows the maximum ground acceleration contours, which are obtained using the data of KNET and KiKNET. The highest ground acceleration reaching to the level of 3g was recorded at the Tsukidate strong motion station of KNET.

Although the ground conditions are very good at this station, it is still difficult to understand why such a high ground motions recorded at the Tsukidate station.

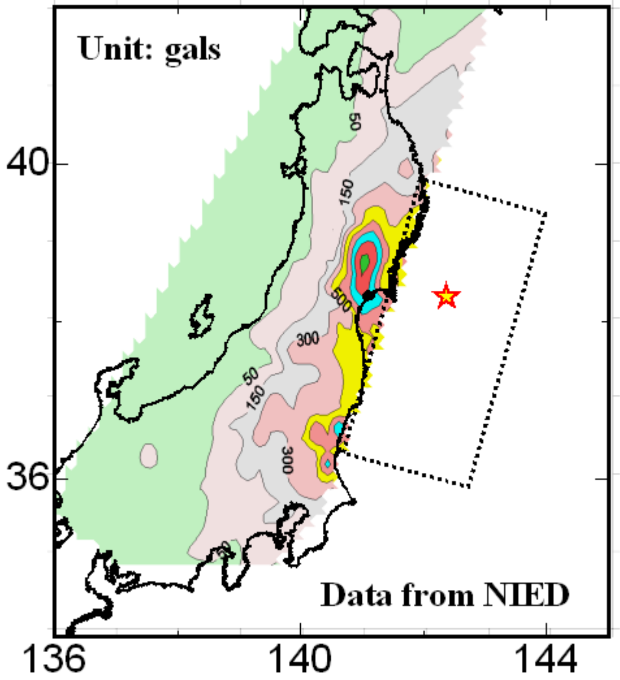

Figure 4: Maximum acceleration contours.

The attenuation of maximum ground acceleration and maximum ground velocity are shown in Figure 5 together with several empirical attenuation relations. As noted from the figures, none of attenuation relations [7,8,9,10] can estimate the attenuation of maximum of ground acceleration and velocity except the relation proposed by Aydan and Ohta [11]. In other words, so-called NGA(Next Generation Attenuation)-like relations can not estimate the strong motion attenuation recorded during the 2011 East Japan Mega-earthquake.

Aydan and Ohta [11] relation given below in which the position of observation point, inclination and length of earthquake fault and ground properties are considered:

$$\alpha_{\max} = F_1(V_s) * F_2(R,\theta,\varphi,L^*) * F_3(M) \quad (1)$$

where V_s, θ,φ,L^* and M are the shear velocity of ground and the angle of the location from the strike and dip of the fault (measured anti-clockwise with the consideration of the mobile side of the fault) and earthquake magnitude. L^* (in km) is a parameter related to the half of the fault length. The following specific forms of functions in Equation (1) are as follow

$$F_1(V_s) = Ae^{-V_s/B} \quad (2a)$$

$$F_2(R,\theta,\varphi,L^*) = e^{-R(1-D\sin\theta+E\sin^2\theta)(1+F\cos\varphi)/L^*} \quad (2b)$$

$$F_3(M) = e^{M/G} - 1 \quad (2c)$$

L^*, which is the half of the fault length, is related to the moment magnitude in the following form

$$L^* = a + be^{cM_w} \quad (3)$$

The specific values of constants of Eqs. (1)-(3) for this earthquake are given in Tables 1 and 2.

Table 1: Values of constants in Equation (2) for inter-plate earthquakes

	A	B(m/s)	D	E	F	G(Mw)
Amax	2.8	1000	0.5	1.5	0.5	1.05
Vmax	0.4	1000	0.5	1.5	0.5	1.16

Table 2: Values of constants in Equation (3) for earthquakes

Faulting Type	*a*	*b*	*c*
Normal faulting	30	0.002	1.35
Strike-slip faulting	20	0.002	1.40
Thrust faulting	20	0.002	1.27

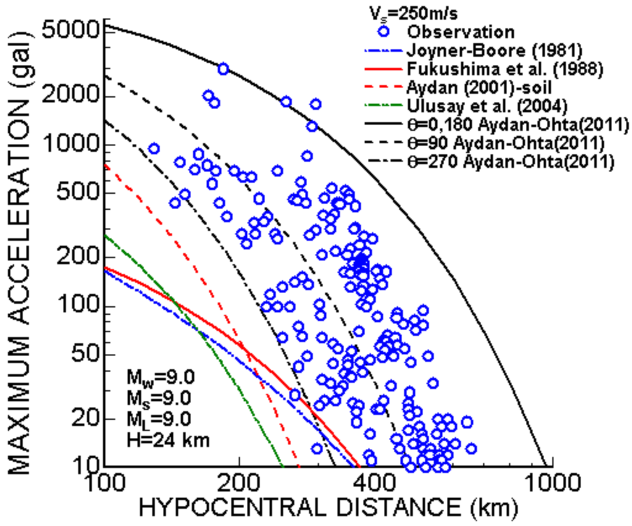

(a) Attenuation of maximum ground acceleration

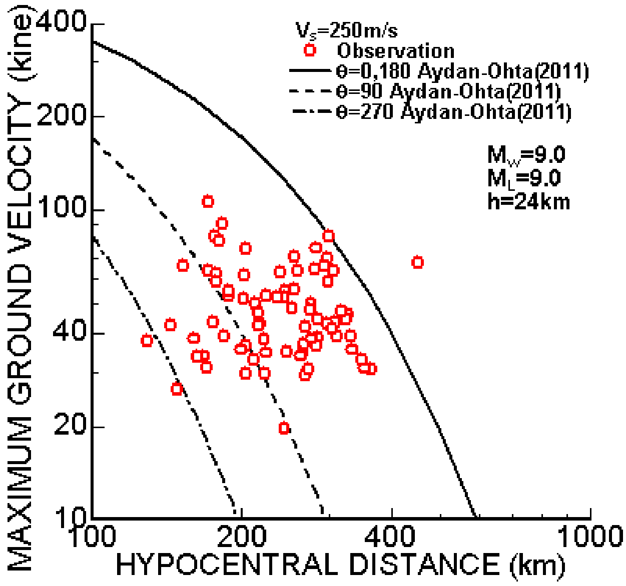

(b) Attenuation of maximum ground velocity

Figure 5: Attenuation of maximum ground acceleration and velocity.

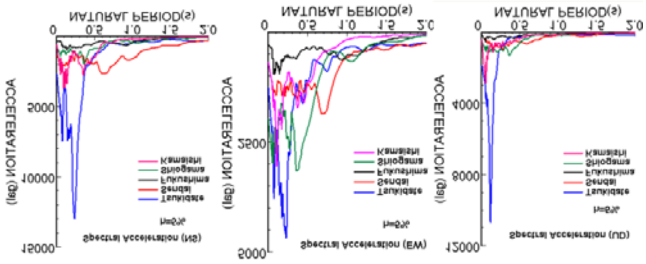

(a) Acceleration response spectra

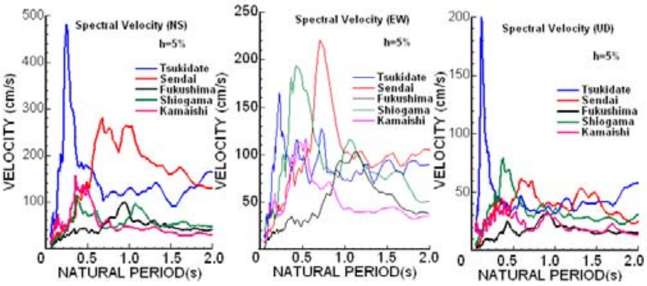

(b) Velocity response spectra

Figure 6: Response spectra of acceleration records at several selected station nearby the earthquake epicenter

The acceleration and velocity response spectra of selected strong motion stations in the close vicinity of the earthquake epicenter are computed and shown in Figure 6. It is important to notice that the response spectra of the Tsukidate strong motion station is extremely high and such high values of response spectra can not be enveloped by neither Japanese seismic design code or other countries code. The response spectra of acceleration and velocity are particularly high at a period less than 0.2s. As the damage was particularly light in the close vicinity of the Tsukidate strong motion station, this may be explained through the characteristics of the strong motion spectra of acceleration and velocity although the maximum values of strong motions were unusually high.

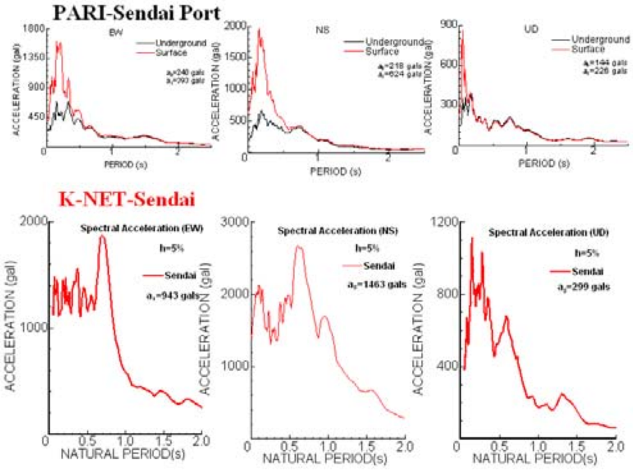

Figure 7: Response spectra of acceleration records at Sendai K-NET and PARI strong motion stations.

One of the interesting observations regarding the strong motion records recorded by several institutes was that the records were quite dissimilar, quantitatively. Figure 7 shows the acceleration response spectra of records in Sendai City. The strong motion stations of the KNET and PARI are very close to each other. While very high motions are observed in

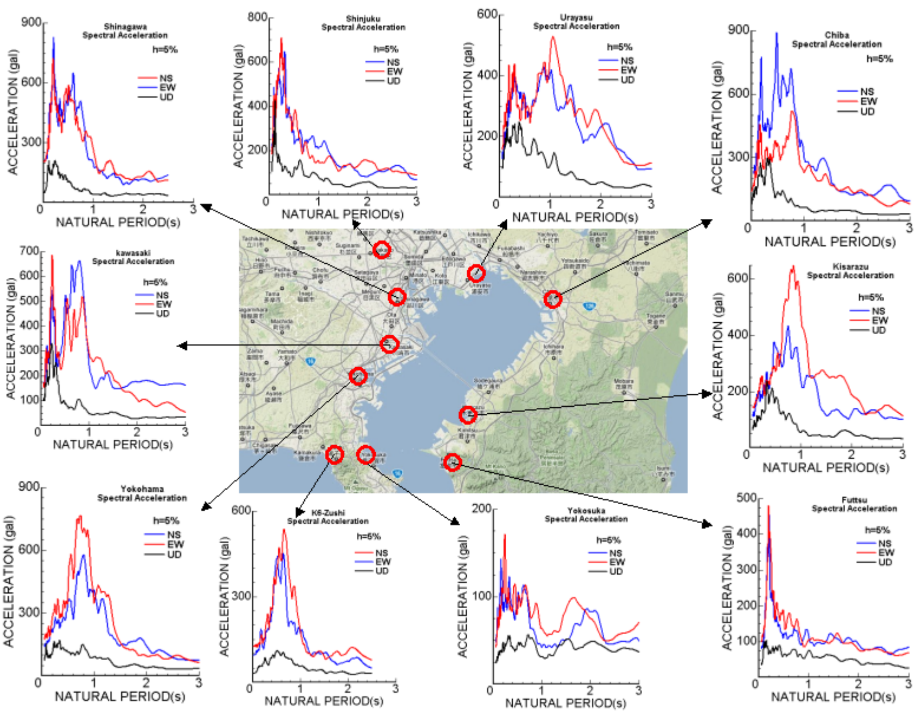

Figure 8: Spectral response accelerations of selected strong motion stations around Tokyo Bay.

the records by the KNET for a considerable period range, the high ground motions are only limited to the short period in the records by the PARI. Furthermore, the maximum ground accelerations of the PARI is almost twice or three-times smaller than those of the KNET. Similar situations were observed at other strong motion stations. This topic deserves very detailed further investigations including the characteristics of the strong motion instruments as well as local ground conditions.

5 CHARACTERISTICS OF STRONG-MOTIONS AROUND TOKYO BAY AREA

There are many strong motion records obtained by various institutes and organizations around Tokyo Bay area. In this article, the strong motion records obtained by KNET, PARI and Tokyo Metropolitan University (TMU) are only reported. Tokyo Bay area is roughly 375 km away from the earthquake epicenter, the surface ground accelerations ranged between 100 to 280 gals. Figure 8 shows the acceleration spectra of strong motion stations around the Tokyo Bay. The strong motion stations such as Yokosuka and Shinjuku are located on relatively hard ground while the rest of stations are on the soft sedimentary ground. Particularly, the spectral amplification of ground motions with long period components at Urayasu, Yokohama, Kisarazu strong motion stations are of great significance.

Next, the spectral acceleration of surface ground motion taken at Chiba by KNET, KiKNET and PARI strong motion networks are compared with each other (Figure 9). As noted from the figure, the absolute values are quite different from each other although the results seem to be similar. Without any doubt, the differences may be related to the difference of the ground conditions at each station. However, the difference in the characteristics of the strong motion devices might also have some influences on the measured strong motions. This aspect still needs some further clarification as it was pointed out in the previous section.

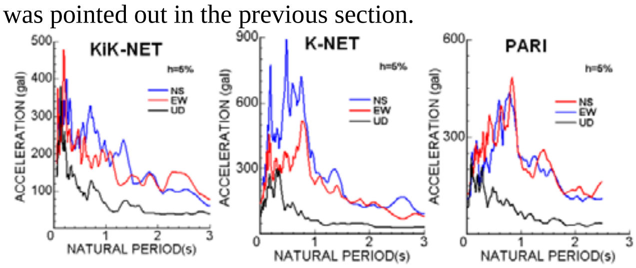

Figure 9: A comparison of acceleration response spectra at Chiba of K-NET, KiK-NET and PARI strong motion networks.

Figure 10 shows the acceleration spectra of strong motions taken at ground surface and bedrock (underground) at K6 Zushi Elementary School (TMU), Hiroba Tokyo Metropolitan University (TMU), Yokohama (KiKNET), Shinagawa (PARI) and Chiba (PARI & KiKNET). As noted from the figure, The ground motions are highly amplified for periods up to 1 second. However, the horizontal ground motions at Chiba strong motion station of KiKNET are amplified for periods more than 2 seconds.

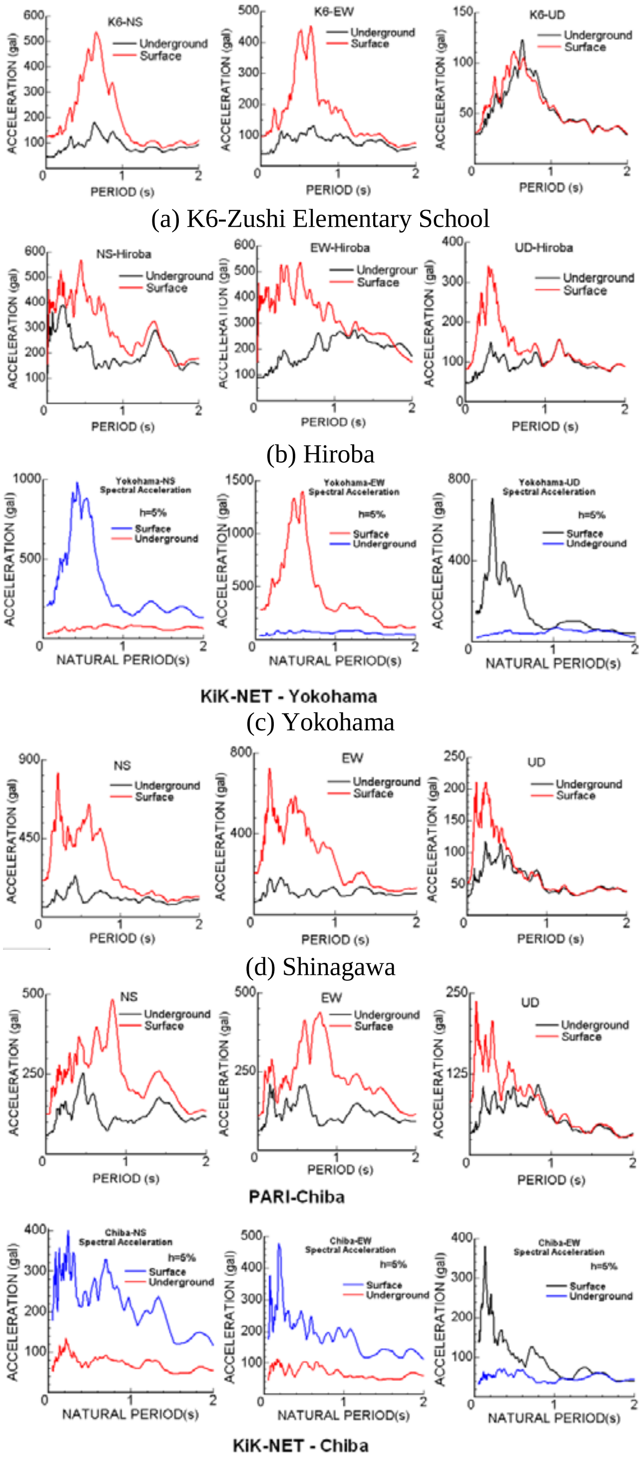

Figure 10: Acceleration response spectra of K6 Zushi Elementary School, Hiroba Tokyo Metropolitan University, Yokohama, Shinagawa and Chiba.

Except the response acceleration at Yokohama station of KiKNET, the ground amplification generally ranges between

3-5 times. However this value reaches up to 20 times at Yokohama strong motion station of KiKNET. This is an extremely high value and it deserves further detailed studies before drawing any conclusion.

6 CONCLUSION

The following conclusions can be drawn from this study as follow:

1) Numerous strong motions stations operated by several institutes and organizations recorded ground motions induced by the 2011 East Japan Mega-earthquake. It is probably the first case to obtain such an extensive source of information for a mega earthquake. Ground motions recorded by the KNET and KiKNET networks of the NIED were extremely high particularly in the vicinity of the initial rupture area.

2) The current attenuation relations for strong ground motions are mostly incapable of estimating the attenuation of maximum ground motions. However, the ground motion records differed depending upon the network even though they were very close to each other. This topic strongly deserves very detailed further investigations including the characteristics of the strong motion instruments as well as local ground conditions.

3) Although the Tokyo Bay area was roughly 375 km away from the earthquake epicenter, the surface ground accelerations ranged between 100 to 280 gals. The ground motions were amplified at locations with thick soft sedimentary deposits. Particularly, the spectral amplification of ground motions with long period components at Urayasu, Yokohama, Kisarazu strong motion stations were of great significance.

4) The ground motions around the Tokyo Bay area were highly amplified up to 1 second. However, the horizontal ground motions at Chiba strong motion station of KiK-NET were amplified more than 2 seconds.

ACKNOWLEDGEMENTS

The authors sincerely acknowledge Tokyo Metropolitan University, National Research Institute for Earth Science and Disaster Prevention (NIED) and Port Authority Research Institute (PARI) for making available the strong motion of the 2011 East Japan Mega Earthquake through the Internet.

7 REFERENCES

[1] Japan Meteorological Agency (JMA), Tokyo, Japan
[2] National Research Institute for Earth Science and Disaster Prevention (NIED). http://www.hinet.bosai.go.jp/topics/
[3] KNET: http://www.kyoshin.bosai.go.jp/kyoshin/
[4] KiKNET: http://www.kik.bosai.go.jp/kik/
[5] Port Authority Research Institute.(PARI): Special web site for East Japan mega earthquake.http://www.pari.go.jp/info/tohoku-eq/
[6] Geographical Information Authority of Japan (GSI): Special web site for East Japan mega earthquake.http://www.gsi.go.jp/BOUSAI/
[7] Joyner, W.B. and Boore, D.M. "Peak horizontal acceleration and velocity from strong motion records from the 1979 Imperial Valley California Earthquake", Bull. Seis. Soc. Am., 71(6), 2011-2038, 1981.
[8] Fukushima, Y., Tanaka, T. and Kataoka, S. " A new attenuation relationship for peak ground acceleration derived from strong motion accelerograms.," 9th WCEE, Tokyo, 343-348, 1988.
[9] Aydan, Ö. "Comparison of suitability of submerged tunnel and shield tunnel for subsea passage of Bosphorus (in Turkish)", Geological Engineering Journal, 25(1), 1-17, 2001.
[10] Ulusay, R., E. Tuncay, H. Sonmez and C. Gokceoglu " An attenuation relationship based on Turkish strong motion data and iso-acceleration map of Turkey", Engineering Geology, V. 74, 265-291, 2004.
[11] Aydan, Ö., Ohta, Y. "A new proposal for strong ground motion estimations with the consideration of characteristics of earthquake fault", Seventh National Conference on Earthquake Engineering, Istanbul, Turkey. (on CD), 2011.

First International Conference on Geotechnique, Construction Materials and Environment, Mie, Japan, Nov.21-23, 2011, ISBN: 978-4-9905958-0-7 C3051

Inquiry of the Value of Parks in the Characteristics and Use of Park through Urban Revival Planning Projects in Maebashi City

*Shinya TSUKADA, **Tetsuo MORITA and ***Akira YUZAWA

ABSTRACT: This study looks at Maebashi City in Gunma Prefecture, one example of a local city with a stock of many parks from post-war urban revival planning projects, and aims to consider future park developments by evaluating park planning and use through an understanding of (1) the features of park arrangement in urban revival planning projects, and (2) the changing use of planned parks.

First, this study will demonstrate the features of park arrangement planning in post-war urban revival planning projects. Next, this study will investigate the changing use of three parks placed through urban revival planning projects: Maebashi Park, Shikishima Park, and Hirose Riverside park road.

By evaluating the features of parks planning and subsequent park use, this study considers present issues and future focal points in park planning. This study has focused on three parks in Maebashi City's urban revival planning projects, and considered the changing use of these parks. It has found that all three parks began by opening up scenery, and by clarifying park recreational functions they have become large-scale facilities for public gatherings.

However, while park recreational functions have increased, there is also the possibility that the original intent for a connection with the scenery has been diluted.

Therefore, in future park preparation, even as partial improvements, three considerations are significant in landscape design: (1) the origin of the natural scenery and land, (2) integrating natural features and nature with design, and (3) subsequent use of the park.

Keywords: Maebashi City, change of using, Urban Park

1. INTRODUCTION

This study looks at Maebashi City in Gunma Prefecture, one example of a local city with a stock of many parks from post-war urban revival planning projects, and aims to consider future park developments by evaluating park planning and use through an understanding of (1) the features of park arrangement in urban revival planning projects, and (2) the changing use of planned parks.

First, this study will demonstrate the features of park arrangement planning in urban revival planning projects. Next, this study will investigate the changing use of three parks placed through urban revival planning projects: Maebashi Park, Shikishima Park, and Hirose Riverside Park Road. By evaluating the features of urban park planning and subsequent park use, this study considers present issues and future focal points in park planning.

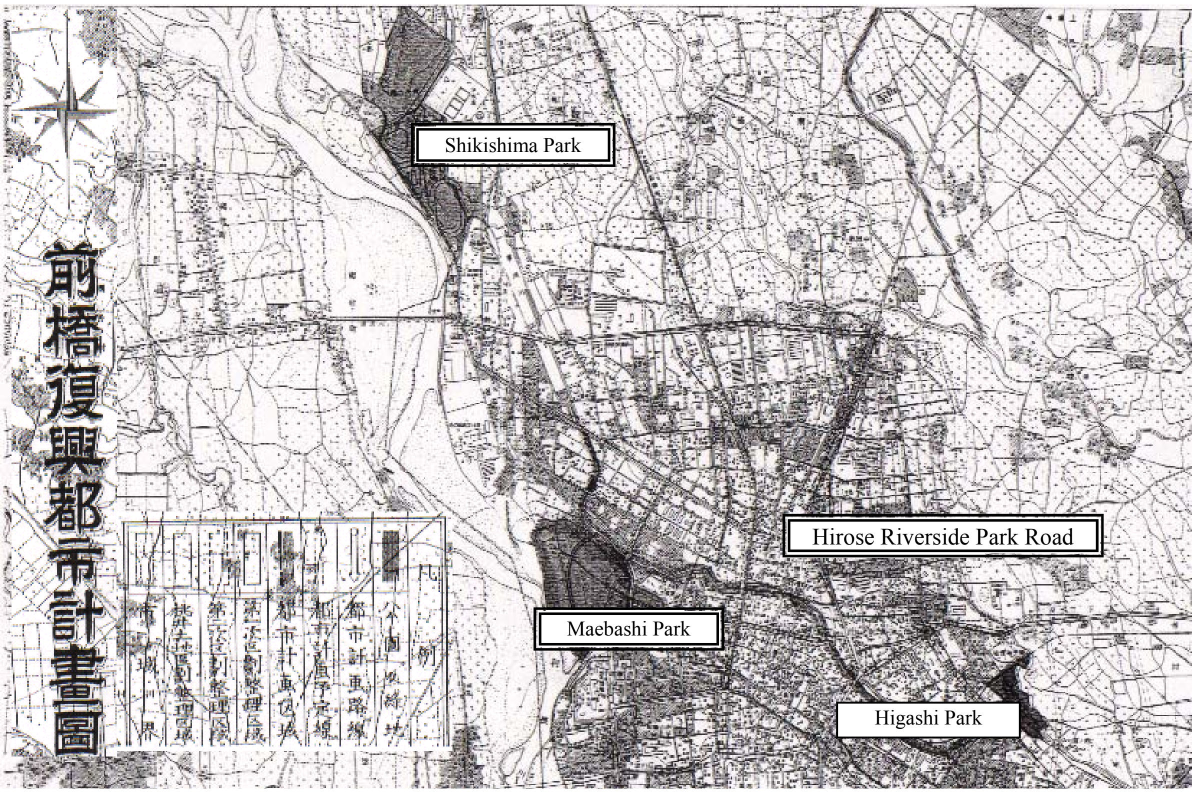

Figure.1 War-devastation urban revival planning in Maebashi City[1]

*Maebashi City Office **Gunma National College of Technology ***Maebashi Institute of Technology

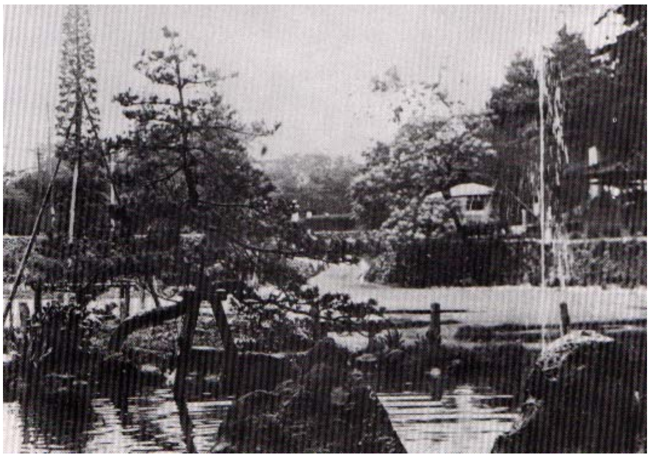

Picture.1 Maebashi Park[2]

Picture.2 Maebashi Park[3]

2. Features of Park Planning in Urban Revival Planning Projects in Maebashi City

The Japanese park system began by official notice of the Department of State in 1873. Planned preparations were made with the promulgation of regulatory reforms in Tokyo in 1889. Through the promulgation of the former City Planning Law of 1919, opportunities arose for securing planned parks even in local cities through the use of "rezoning projects."

However, genuine park preparation began with the urban disaster revival planning projects that followed the World War II, and the enactment of the City Park Law of 1956. The city planning of Maebashi City progressed with the promulgation of the city Planning Law of 1919, and in 1929 city planning zones were determined. These brought opportunities for city planning projects in Maebashi City. However, because approximately 80% of the city was destroyed in the world War II, city planning projects could not be carried out.

In 1946, Maebashi City was designated a war-devastated city, and this was used as an opportunity to examine city plans from before the war, and to move forward with road and park planning.

The area of rezoning projects for war-devastation urban revival planning projects in Maebashi City was set in 1946 at 343.2 hectares, and the cabinet approved a plan for major thoroughfares. In 1947, Gunma Prefecture officially announced route 120.

This plan included three items regarding parks in the basic policy of city revival planning. First is the planning of parks, sports grounds, and park roads. Second is the securing of over 10% of urban area as open space. Third is the designation of agricultural land, mountain and forests surrounding the urban as open space. Park arrangement was attempted under these three items.

However, citizens protested, demanding the prefecture "make it Maebashi City's original planning. Therefore, the basic policy for post-war urban revival planning was changed in 1949. The aim became quick execution of projects.

Already in Maebashi City preparations had been made for Maebashi Park along the left bank of the Tone River flowing north-south through the city center, and for Shikishima Park. However, due to the rising demand for open spaces and tree, park plans through war-devastation urban revival planning projects were proposed.

First, Maebashi Park was prepared for the west side of Maebashi City, and Higashi Park was planned for the east side of the city. Also, a park road was planned for Hirose riverside flowing east-west through the city, connecting the parks (figure 1).

3. Changing Use of Maebashi Park

The establishment of Maebashi Park was decided by resolution of the Maebashi city council in 1903 in commemoration of the Russo-Japanese War of 1905.

It is recorded that this place was used for recreational cherry-blossom viewing. Cherry-blossom viewing was a popular outdoor recreation in Japan from the Edo period. Records of park use show a design of cultivated cherry-blossom trees and garden-like views with additional trees. Monuments were erected, increasing symbolism, and the park was used as a place for holding national events.

Female factory workers and geisha used the park as a place to enjoy cherry-blossom viewing and strolls. With symbolism in its scenery from the Meiji era, and use for strolls and events, everyday use of Maebashi Park increased, and the convenience of the facility improved with the arrangement of gazebos and flower beds.

Everyday use of the park increased, and a boat dock facing the Tone River was built. Neighboring farms were bought, and the park was expanded.

Waterfalls and fountains (picture 1), and children's playing equipment were built in the expanded areas. On the other hand, management problems such as public disturbances, crime, and safety appeared in the park. Lighting was set up to prevent crime, and moral edification was conducted in response to vandalism of facilities. Records show that bicycle competitions and plays were abundantly held. During public gatherings, rice cakes called "hagi-mochi" were sold in the park.

Accompanying the park's change from scenery viewing to more daily use, park use became more integrated with daily life, and modern culture such as food and the arts ripened.

In 1946 at the start of urban revival planning projects, Maebashi Park became a normal park of approximately 18.6 hectares. In 1954, to celebrate the 60th anniversary of the founding of Maebashi City, the Maebashi Ground Fair was held.

In 1986 to celebrate the 100th anniversary of the founding of Maebashi City, a plan for improving Maebashi Park was revealed that would make the park a general park of 64.4 hectares, and even at present plans for refurbishing the park are being advanced (picture 2)[6].

4. Changing Use of Shikishima Park

Shikishima Park lines the clear waters of the Tone River, rich in scenery symbolized by stretching pine forests, and blessed with views of the Three Jōmō Mountains of Akagi, Haruna, and Myōgi.

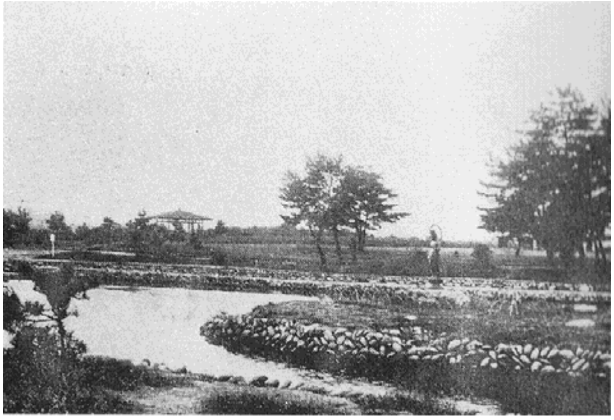

Picture.3 Shikishima-Park[4]

Picture.4 Shikishima-Park[3]

In 1921, an outdoor school was created in the summer in Maebashi City using pine forests, and it served as a place for improving the constitution of children. In 1922, the Maebashi City Council resolved to make the land a park site, and the park was made by disposing of the riverbed and national forest.

Such was the origin of Shikishima Park, which opened an area that included a riverbed blessed in natural scenery to the public as a recreational garden.

In 1925, a local youth labor service built a sports ground. The park name of "Shikishima Park" was decided by accepting submissions from Maebashi citizens. In 1924, citizens donated Yoshino Cherry-blossom, improving park scenery. In 1929, Dr. Honda Seiroku and Dr. Inoshita Kiyoshi proposed a lake with islands as seen in the Chinese Imperial Garden, a stone-made rest area imitating a French garden, and toilets (Picture 3).

In a place blessed with a natural environment favorable enough to house an outdoor school, athletic facilities were enriched.

In 1930, a baseball field was built. In 1920, U.S. and Japanese professional baseball teams met for a friendly game that including Sawamura Eiji and homerun-king Babe Ruth. In 1938, municipal rental boats were opened for people to enjoy the scenery.

In 1950, the grounds were expanded for the construction of a Gunma Prefectural General Sports Ground. In 1953, a volunteer park beautification club was organized of townspeople to clean the park, and townspeople conducted cleaning activities. In 1956, Meiji Shine conveyed 500 irises, and an iris garden was created. In 1971, with the creation of a rose garden, the institutionalization of the park as a tourist resource progressed. In 1983, a national sports festival was held at the sports grounds of Shikishima Park (Akagi Kokutai). In 1985, with the addition of a drainage channel, a water playground, and a large wooden playground in the connection point between the recreational walking zone and the sports facility zone, the park was given general functions that various generations could use (Picture 4). In 1989, Shikishima Park was chosen by the Parks & Open Space Association of Japan as one Japan's top 100 parks.[7]

5. Changing Use of Hirose Riverside Park road

The Hirose River was a part of life during the Edo period as a transportation route for boats, and in the early Meiji period powering water wheels. The city center side was mainly used as commercial land, and the new city center side was mostly used as industrial land (silk factories). On holidays, many female factory workers would cross the Hitone Bridge to enjoy the city center (figure 2).

Figure.2 Shinkeizu in Maebashi city[5](1909)

Picture 5 Hirose Riverside Park Road[2]

Picture 6　Hirose Riverside Park Road[3]

Hagiwara Sakutarō, who influenced modern poetry, announced his poem "Kyōdo Bōkyōshi" in 1925, which includes reference to Hirose River, and he is said to have liked this scenery. In 1930, preparations began for Hirose River park road, 3.6 meters wide and 283 meters long. In the early Shōwa period, Hirose riverside was prepared as a street.

Following the end of the World War II, in 1948 Maebashi Park (general park) was planned to the west of the city center, Higashi Park (normal park) was planned to the east of the city center, and "Hirose Riverside Park road" was planned as a park road connecting the two parks in light of city disaster prevention.

The land for "Hirose Riverside Park Road" was secured through rezoning projects for the purpose of urban disaster prevention in Maebashi City's central areas. Weeping willows were planted at even intervals on both banks, and a dirt promenade along the right bank was built. A concrete bench was built along the promenade, and a green tract of land was built in a concrete tree-planting box. Through this preparation, the weeping willows planted alongside both banks of the river became familiar to citizens as the scenery representing Maebashi City.

In 1970, a monument inscribed with a poem entitled "Hirose River" was built. This was followed by many other hometown poetic monuments erected in the promenade. In 1974, Maebashi City enacted the "Maebashi City Water and Green Community Development Ordinance," and for five years from 1974 to 1979 reconstructed Hirose Riverside Park road as a cultured and high-quality space, with the theme of making a symbolic road of water and tract.

Inside, a stone walking path was added, a viewing lake and monument were built, and preparations focusing on recreation and scenery-viewing progressed.

After this, cultural hues were deepened in the areas surrounding Hirose Riverside Park Road, and in 1993 the Maebashi Museum of Literature was built along the Hirose Riverside Park road, with materials from poets on display and for research including the work of Hagiwara Sakutarō. Every year since 1999, from autumn to winter both sides of the riverside promenade are lit with lights by volunteers, making an elegant scene[8].

6. CONCLUSION

This study has focused on three parks in Maebashi City's urban revival planning projects, and considered the changing use of these parks. It has found that all three parks began by opening up scenery, and by clarifying park recreational functions they have become large-scale facilities for public gatherings.

However, while park recreational functions have increased, there is also the possibility that the original intent for a connection with the scenery has been diluted.

Therefore, in future park preparation, even as partial improvements, three considerations are significant in landscape design: (1) the origin of the natural scenery and land, (2) integrating natural features and nature with design, and (3) subsequent use of the park.

7. REFERENCES

[1] Maebashi City (1964): War-Devastation Urban Revival Panning in Maebashi City.

[2] Hirata, K. (1990): Taisho Period from age of the Showa era.

[3] Maebashi convention :http://www.maebashi-cvb.com/tourism/view/i-kanko/03k-maebashi.htm

[4] Taro S. (2004): The history of Iwagami.

[5] Gunma Shinbunsya (1911): Shinkeizu of Maebashi-city.

[6] Tsukada, S., Yuzawa. A., (2004): A Study of the Evaluation Structure and Attractive Factors of Large-Scale Park caught from User's Consciousness -A case Study in Maebashi City-, City planning review, Special issue, Papers on City Planning(39), pp.193-198.

[7] Tsukada, S., Morita, T. and Yuzawa, A.(2009): A study on evaluation of Shikishima park as change of the spatial characteristic and the original design, journal of the Japanese Institute of Landscape Architecture72(5), pp.849-854.

[8] Tsukada, S., Morita, T. and Yuzawa, A.(2011): The Evaluation of the planning Designs in Hirose Riverside Promenades, journal of the Japanese Institute of Landscape Architecture 74(6), pp.18-21.

First International Conference on Geotechnique, Construction Materials and Environment, Mie, Japan, Nov.21-23, 2011, ISBN: 978-4-9905958-0-7 C3051

A Study on Evaluation of Quality of Life in Consideration of Water/Green Environment

Tetsuo Morita*, Yoshihito Kogure*, Hiroshi Sugita**,
Tsuyoshi Baba**, Shin-ya Tsukada***, and Naoki Miyazato*

*Gunma National College of Technology, **The Institute of Behavioral Sciences, ***Maebashi City Office

ABSTRACT: Recently, the interest about water/green environment rises. But, it does not become clear enough, that water/green environment influences Quality of Life. The purpose of this study is the analyzing Quality of Life quantitatively with the data of the questionnaire survey, from the viewpoint of water/green environment. The subject area was Maebashi City, Gunma Prefecture. We used "factor analysis" and "covariance structure analysis". Result of factor analysis we obtain five factor of the Quality of Life: Safety, Convenience, Environment, Housing conditions, Comfort. In addition we clarify evaluation structure of Quality of Life in consideration of water/green environment such as the river or the park by using covariance structure analysis. As the result, we made clear that Quality of Life is different depending on individual attribute and district characteristic, and that water/green environment affected Quality of Life. And we show measure effects.

Keywords: water/green environment, Quality of Life, evaluation, covariance structure analysis

1. Research Background and Purpose

In these modern times, with advancing industrialization and urbanization, the scenery of the water and green environment has been transformed. People in these present times, have a heightened desire, a craving for spaces where they can live at ease. Their interest for the Quality of Life with as much natural contact with those familiar green spaces, waterfront and the beautiful townscape has increased. In this research, based on the results of a questionnaire survey regarding the Quality of Life of the residential areas of Maebashi city, special attention is paid to the living environment of the residential areas that incorporate water/green and the like. Our purpose is a making structural model, for the evaluation of Quality of the Life, as seen from the inhabitant's point of view.

2. Research Position

In the research that pays attention to the Quality of Life, Kaji's research is enumerated [1]. They clarify structural analysis of the consciousness of the inhabitants. Moreover, they showed the relation between living environment and evaluation of inhabitants to living environment, and offer an evaluation method of their living environment and the Quality of life. After this research, various evaluation methods and models have been proposed by Morimoto [2], Yoshida [3], Doi [4], and Morita [5]. In addition, a Quality of Life research which pays attention to water environment, Taniguchi is also included [6]. They propose that in order to improve the quality of life, an improvement in the water environment and a better evaluation of this model need to be made. Not just as research, a plan which designates improvements to the charm of the water spaces in Tokyo is set out as a goal [7]. Such as this plan, many urban development plans that pay attention to the water environment are going on all over Japan.

The main focus of this research is on the Quality of Life especially to the living environments with water and green. The Quality of Life of the inhabitants is determined by city activity and living environment. City activity consists of traffic, land utilization and economic activity etc, living environment consists of the proximity to rivers, forested land, farmland and the growth plants and other living things. These two are thought to exert mutual influence on each other. In addition, it is clarified that the Quality of Life is different depending on individual attributes and district characteristics by existing researches. In this research, individual attributes and district characteristics are considered. As we a model which evaluate all the Quality of Life and which pays attention to a water/green environment has been established. This research aims to provide a useful model through which all aspects of quality of life can be measured quantitatively especially focusing on the water/green environment.

3. Questionnaire Survey of Quality of Life

3.1 Research Area

The area in which the Quality of Life questionnaire survey was conducted is designated as Maebashi city, Gunma prefecture. Maebashi city has three "class A rivers": Tone river, Hirose river and Momonoki river. In addition, the hydrophilic park which begins in the Shikishima park located in Maebashi city. And, Maebashi city advertises itself as: "The city of water, green and poetry". Maebashi city promotes businesses such as promenades along the rivers as well as other services and the reforestation an improvement of the cycling road following the plan which is called "The general plan for the Greening of the Maebashi city" [8]. Specially, we designated research area as Maebashi city of the left bank of Tone river that is affected by water environment. Research area is shown in Fig.1 on the next page.

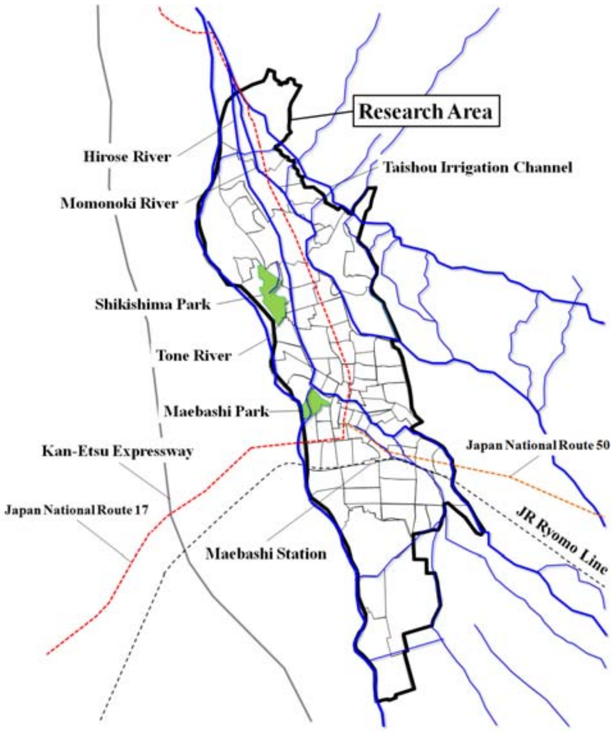

Fig.1: Research Area

3.2 Summary of Questionnaire Survey

Summary of questionnaire survey is shown in Table 1, and items of evaluation are related the Quality of Life (Subjective evaluation) is shown in Table 2. The survey was distributed to 4,000 households inside the area of our research, we received 2,118 responses. When those responses where appraised and reviewed as being valid and complete, the effective results were reduced to 1,646. Items of Subjective evaluation (Table 2) refer to appraisal items of Quality of Life research by [3] and [5], it added the item regarding water and green environment (A12, A13).

4. Factor Analysis

Factor analysis was applied to items of Subjective evaluation, the component of Quality of Life was extracted. With this analysis, because A17 and A20 is correlatively high which is shown in Table 2, it excluded the item of A20. Also A21 was excluded of analysis. Concerning items of Subjective evaluation, the typical five latent variables where sum of squares exceeds 1.0 were extracted. The Table 3 is something which rearranged the factor loading after the varimax rotation. We defined factor collected those where the respective factor load quantity is high, “Safety” and “Convenience”, “Environment” and “Housing conditions”, “Comfort” . A12 , A13 which are thought that the relation to green and water environment is high during Subjective evaluations, “Environment” in the Quality of Life which is defined, it has the respective factor loading 0.821 and 0.737. It understood that the element regarding water and green is related to the Quality of Life largely.

[redacted]

Table 1: Summary of the questionnaire survey

[redacted]

Table 2: List of Subjective evaluation

Variable	Factor1	Factor2	Factor3	Factor4	Factor5
	Safety	Convenience	Environment	Housing Conditions	Comfort
A1	0.765	0.139	0.036	0.136	0.060
A2	0.750	0.067	0.183	0.211	0.146
A3	0.602	0.185	0.156	0.081	0.132
A4	0.598	0.103	0.249	0.104	0.236
A5	0.441	0.277	0.285	0.179	0.161
A6	0.373	0.081	0.323	0.290	0.110
A7	0.109	0.731	0.090	0.042	−0.022
A8	0.049	0.723	0.029	0.063	0.155
A9	0.145	0.698	0.121	0.050	−0.011
A10	0.082	0.577	0.053	0.126	0.159
A11	0.157	0.541	0.069	−0.013	0.232
A12	0.130	0.064	0.821	0.103	0.093
A13	0.252	0.058	0.737	0.276	0.095
A14	0.209	0.250	0.504	0.139	0.174
A15	0.194	0.100	0.174	0.723	0.079
A16	0.233	0.079	0.251	0.688	0.224
A17	0.324	0.303	0.169	0.158	0.623
A18	0.291	0.169	0.270	0.299	0.504
A19	0.294	0.358	0.164	0.239	0.390
Sum of squares	2.761	2.656	2.029	1.494	1.138
Contribution ratio	14.53%	13.98%	10.68%	7.87%	5.99%
Cumulative contribution ratio	14.53%	28.51%	39.19%	47.05%	53.04%

Table 3: Result of Factor analysis

5. Presumption Evaluation Model of Quality of Life

5.1 Covariance Structure Analysis

In main research of the Covariance structural model, when Quality of Life is appraised, we use Yoshida's model [3]. This model can analyze the individual attribute, district characteristic, Subjective evaluation, and Quality of Life. Covariance structure analysis can display the complicated statistical model graphical causal relation between variables the arrow (path) with by the path figure which is displayed. It is possible because with the structural equation model to form the model which is based on the hypothesis of the analyst in comparison with former multivariate analysis, it is flexible to interpret data which is given.

Individual attribute and district characteristic were designated as Objective variable, those Latent variable (Quality of Life) exists also constructed the Covariance structural model between Subjective evaluations. Causal relation between Objective variable and Latent variable is called structural equation, this is suitable to multiple regression analysis. In addition, causal relation of Latent variable and subjective appraisal value is called measurement equation, this is suitable to factor analysis.

5.2 Presumption Covariance Structure Model

Continuously, considering five Quality of Life, it set the caus al relation of individual attribute and district characteristic, al so presumed the Covariance structural model. We obtain dat a of district characteristic on the map. Goodness of fit of the model became GFI=0.80. Sufficient goodness of fit you cann ot say, but sign condition of path coefficient, the appropriaten ess of interpretation of variable, it illuminated in purpose of t his research which pays attention to water/green environment the figure adopted the model of Fig.2 on next page. The Tabl e 4 is summary of Objective variables, and the Table 5 is pat h coefficient of the variable which is used for the model is sh own in Fig.2. Table 4 and Table 5 are on the next page.

"Safety", the flood damage, earthquake, fire, crime preventio n and traffic accident, is the Latent variable which is related t o the safety regarding hygiene. It is found that from the fact t hat path coefficient of the dummy of 65 years old or more of objective variable has shown negative value, as for the senior citizen degree of safety decreases. "Convenience" is the Lat ent variable which is related to the convenience of shopping and public traffic. From the fact that path coefficient of the a ges 65 and older dummy and the employee dummy of Object ive variable has shown negative value, the senior citizen and the employee is a tendency where convenience decreases. On the one hand, path coefficient of the student dummy has sho wn correct value, as for the student, it is found that it is the te ndency which appraises the convenience of research area hig h.

"Environment" is the Latent variable which is related to wate r/green environment which has paid attention in this research and sport recreation. As Objective variable is distance to the city park, path coefficient it reaches negative value, the city p ark becomes far, as for appraisal of "Environment". It is foun d that it decreases.

Path coefficient of the employee dummy and the apartment dummy where "Housing conditions" is the Latent variable which is related to sunshine, through wind sequence and the extent of the house and garden, is Objective variable has shown correct value. "Comfort" is the Latent variable which is related to the easiness of walking, easiness of using of the automobile. Objective variable becomes the variable whose distance to the waterfront is significant, has shown the fact that extent and the comfort where distance to the waterfront becomes far decrease. Like above, to improve the Covariance structural model is also conversely.

In Objective variable, the fact that it is related to water/green environment is distance to the city park and distance to the waterfront. Waterfront such as Tone river, Hirose river and Momonoki river, and city parks has been distributed to research area, it became the model which can explain the Quality of Life of residence area with the approach characteristic to water/green environment. In addition, also it was the model which can explain the Quality of Life with individual attribute, concerning the change of Quality of Life due to the change of future population became the model which can be appraised.

At the time of Covariance structure analysis of this research, the fact that Amos of the SPSS co. is used.

6. Evaluation Measures

By using Covariance structural model, evaluate water green environmental measure. The next two measures, "waterfront development" and "City parks development" were set. Fig.3 shows positions about new waterfront and city parks on the next page but one.

6.1 Waterfront Development

Such as Tone river, Hirose river and Momonoki river which are existence as waterfront in research area extension is 34.5km. In addition, there is a irrigation canal 29.1km inside research area, presently, it is the space which the resident can't get close, part has become the culvert. These like the Hirose river and the Momonoki river you service as the waterfront inside the city, it makes the space where the resident can become familiar in the waterfront. Because of this, rivers extension inside research area reaches approximately 2 times, it is supposed that "Comfort" improves due to the fact that distance to the waterfront becomes short from each area.

6.2 City parks Development

67 city parks are maintained inside service research area, the city park exists in inner 47 areas of 84 areas inside research area. Among 37 areas where the city park is not serviced, 6 areas of urbanization control area are excluded, the city park (the block park) to set one each in 31 areas of area designated for urbanization. Because of this, the number of city inside research area parks becomes with 98 and approximately 1.5 times from 67, "peripheral environment" improving is supposed due to the fact that distance to the city park becomes small from each area.

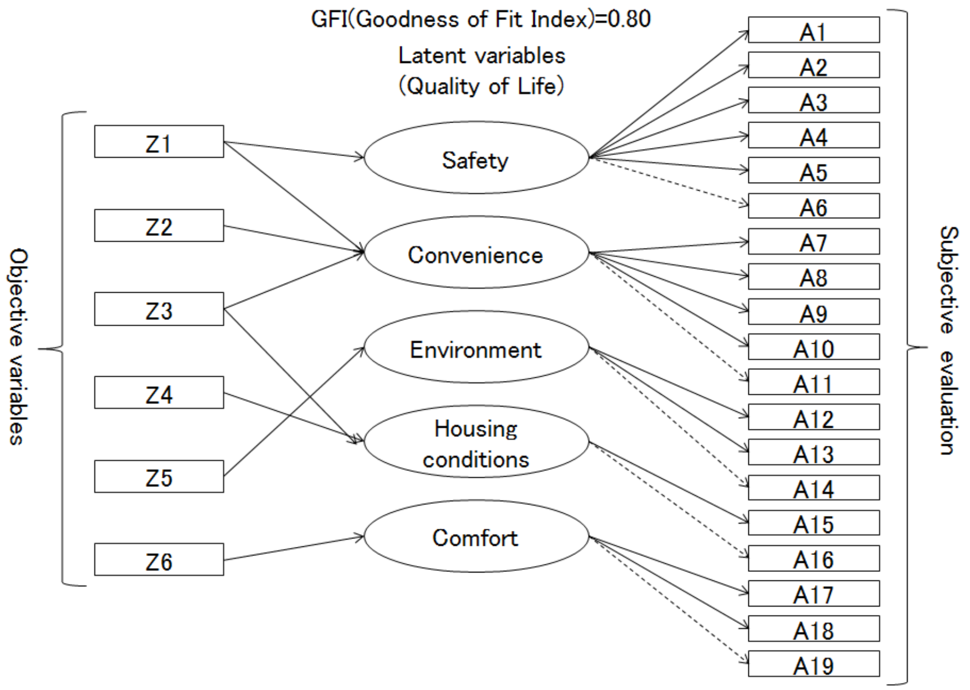

Fig.2: Estimated Covariance structure model

[redacted]

Table 4: Objective variables

Objective variables	Path coefficient	Latent variables	Path coefficient	Subjective evaluation
Z1	−0.185(6.656)	Safety	0.754(18.526)	A1
			0.802(18.927)	A2
			0.643(17.231)	A3
			0.677(17.670)	A4
			0.557(15.935)	A5
			0.492(∞)	A6
Z1	−0.070(2.536)	Convenience	0.729(19.973)	A7
Z2	0.058(2.137)		0.725(19.992)	A8
Z3	−0.057(2.089)		0.696(19.506)	A9
			0.609(18.030)	A10
			0.562(∞)	A11
Z5	−0.076(2.793)	Environment	0.863(20.881)	A12
			0.792(21.611)	A13
			0.575(∞)	A14
Z3	0.088(4.291)	Housing conditions	0.516(3.7350)	A15
Z4	0.116(5.626)		1.172(∞)	A16
Z6	−0.110(3.913)	Comfort	0.838(18.232)	A17
			0.656(19.455)	A18
			0.605(∞)	A19

The value in round brackets is “t value”.

Table 5: Path coefficient

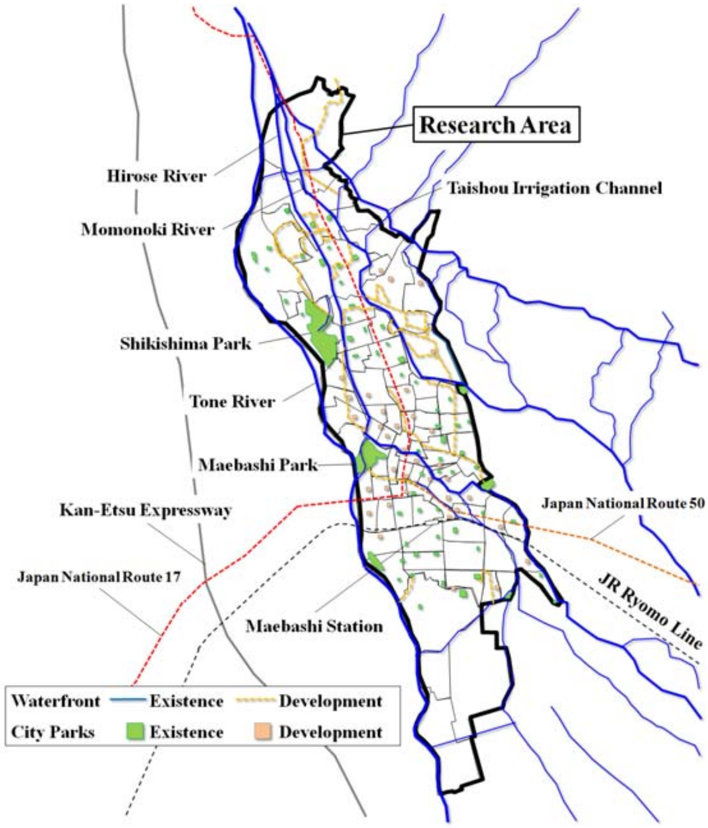

Fig.3: Waterfront and City parks Development

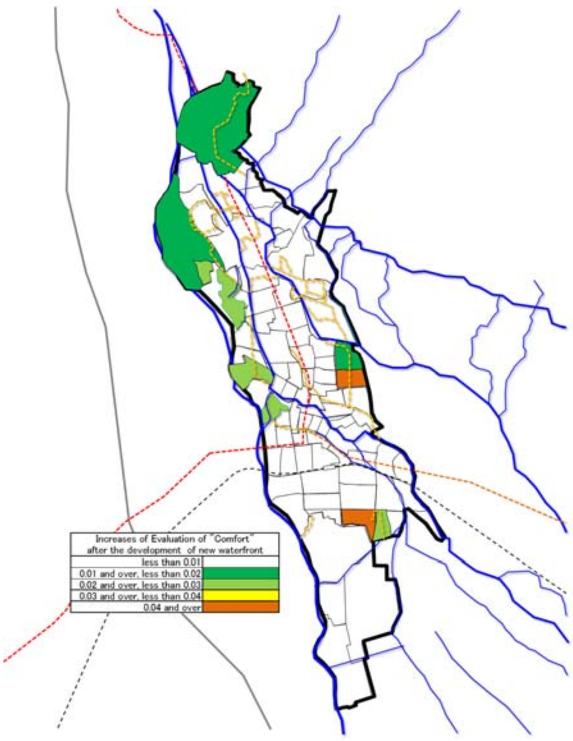

Fig.4: Result of Waterfront development

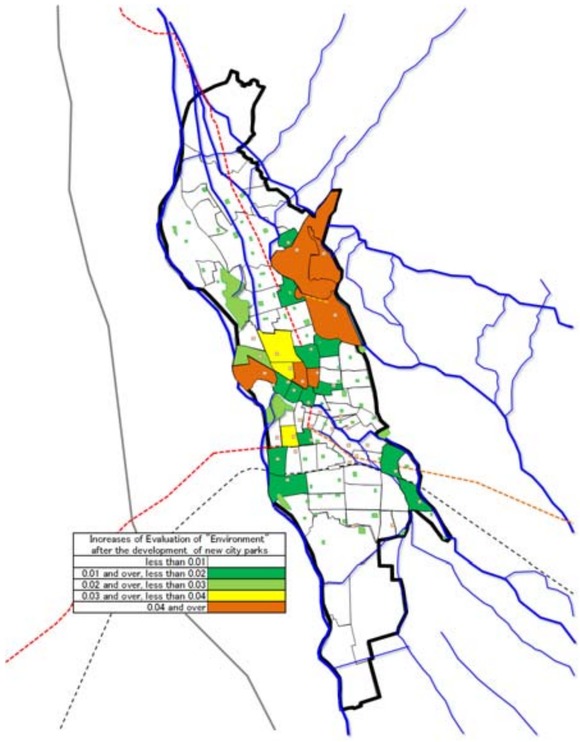

Fig.5: Result of City parks development

6.3 Evaluation of Water/green environmental Measures

The result of measuring of water/green environment, measure improves each one “Comfort” “Environment”. Increase of evaluations of “Comfort” and “Environment” after the waterfront and city parks development shows Fig.4 and Fig.5 on the previous page. In order to grasp regional the effect to the whole research area, population of classified by appraisal value ranking of Quality of Life was rearranged. The Fig.6 shows change of “Comfort” due to the service of the waterfront. The Fig.7 shows change of “Environment” due to the service of the city parks. Sooner or later the population which enjoys the improvement effect of quality of life with the measure which relates to water/green, has increased.

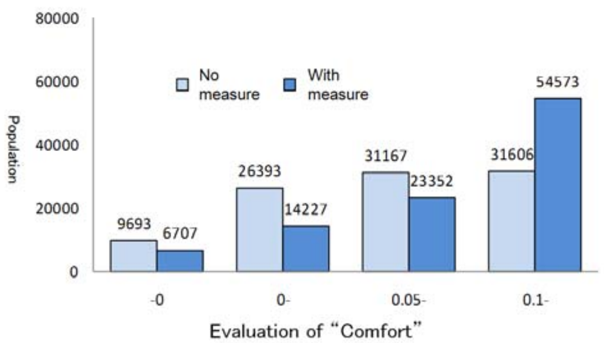

Fig.6: Change of “Comfort” due to measuring

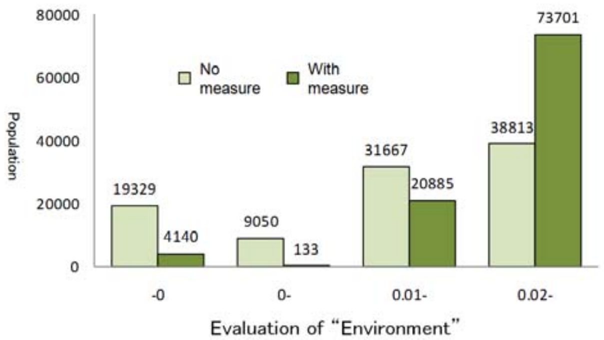

Fig.7: Change of “Environment” due to measuring

6. Research Conclusion

Summary of Objective variable of this research (individual attribute and district characteristic), Latent variable, Subjective evaluations which is due to questionnaire survey uniformly, also it was possible to construct the covariance structural model. It was constructed individual attribute and the district characteristic regarding water/green form the Quality of Life. When appraisal of waterfront and city parks service measured which relates to water green environment.
We verified that “Comfort” and “Environment” improves. As from above, the purpose in this research cleared that the appraisal structure of Quality of Life which includes water/green environment, it is thought that it was possible to do measure appraisal.

7. Future Topic

Future topic is improvement the evaluation model of Quality of Life. In this research, water quality content of the rivers and waterfront as water environment is not included. In existing research, a model involves the water cycle, matter cycle model which can estimate the change of water quality and water content. In the future, we would like to examine the appraisal Quality of Life with water quality and water content. In addition, in order for appraisal of measure other than water/green environment to become possible, we would like to keep adding various district characteristic.

8. REFERENCES

[1] Hideki, K. “Research on method of maintenance of living environments seen from resident consciousness”, Journal of the City Planning Institute of Japan, No.67, 99.19-33, 1971
[2] Akinori, M. Yoshihide, N. “Research on evaluation approach of environment in residential quarter”, Journal of Japan Society of Engineers, No.419/IV-13, pp.71-80, 1990
[3] Akira, Y. Junya, S. Ryuzo, H. “Neighborhood-relevant Measurement of Quality of Life”, City planning review. Special issue, Papers on city planning 33, pp.37-42, 1998
[4] Kenji, D. Hitomi, N. et al. “DEVELOPMENT OF A QOL-BASED MULTI-DIMENSIONAL EVALUATION SYSTEM FOR URBAN INFRASTRUCTURE PLANNING”, Journal of Japan Society of Engineers D, Vol.62, No.3, pp.288-303, 2006
[5] Tetsuo, M. Akira, Y. et al. “A STUDY ON THE MODEL SYSTEM EALUATING POLICIES OF THE URBAN ENVIRONMENT”, Journal of Japan Society of Engineers D, Vol.64, No.3, pp.457-472, 2008
[6] Mamoru, T. Hiroaki, H. et al. “EVALUATION OF NEIGHBORHOOD WATER ENVIRONMENT AND ITS MODELLING: TO REALIZE TOWN IMPROVEMENT BASED ON THE CONCEPT OF WATER RECYCLE”, Environmental system research paper collection, Vol.33, pp.125-132
[7] Tokyo Metropolitan, “Whole idea concerning charm improvement of waterside space of Tokyo”, 2006
[8] Maebashi city, “The general plan for the Greening of the Maebashi city”

First International Conference on Geotechnique, Construction Materials and Environment, Mie, Japan, Nov.21-23, 2011, ISBN: 978-4-9905958-0-7 C3051

Changes and Issues in Green Space Planning in the Tokyo Metropolitan Area: Focusing on the "Capital Region Plan"

Tetsuo Morita*, Yoshihide Nakagawa**, Akinori Morimoto***,
Masateru Maruyama*** and Yoshimi Hosokawa*

*Gunma National College of Technology, **Waseda University, ***Utsunomiya University,
****Mizuho Research Institute

ABSTRACT: Large-scale green space planning in the Tokyo Metropolitan Area was formulated in 1939 with the "Tokyo Green Space Plan," and a greenbelt was proposed, however the plan was cancelled due to the end of the war. In 1958 the "First Capital Region Plan" was formulated, and a greenbelt was again proposed, however the second and later plans became plans that approved of urbanization.

This paper focuses on the Capital Region Plan, and aims to (1) organize changes in green space planning in the Tokyo Metropolitan Area, (2) analyze the circumstances of urbanization of the area designated a greenbelt in the First Capital Region Plan, and (3) extract issues regarding green space planning in the Tokyo Metropolitan Area

Keywords: Tokyo Metropolitan Area, Capital Region Plan, National Plan, greenbelt

1. Changes in Green Space Planning in the Tokyo Metropolitan Area

1.1 Tokyo Green Space Plan

In 1939 the "Tokyo Green Space Plan" was formulated. Although this planned area had no legal basis, it included a 50 kilometer region, 962,059 hectares of production green spaces and scenic districts centered around on Tokyo. A greenbelt was planned for Tokyo's outer region, following rivers into urban areas[1].

The base section of the greenbelt was set in the city plan as a planned city green space, and preparations were made through site purchases. In 1940, with the war escalating, Tokyo industrialized six green spaces for air defense, and by 1945 had realized the plan by deciding on 22 green spaces for the city plan. The air defense designation prohibited the construction of buildings other than those affiliated with agriculture, forestry, livestock, or park sports grounds.

However, after losing the legal backing of air defense with the end of the war, these large green spaces became a target for opening agricultural space, and 62% of the 746 hectares of purchased sites were transferred to private landowners.

1.2 First Capital Region Plan

Due to the rapid concentration of population in Tokyo during the period of high economic growth, chaotic urban expansion became a problem, and the National Capital Region Improvement Act was enacted (1956). Based on this Act, the first through fifth National Capital Region Improvement Plans (abbreviation: “Capital Region Plan”) were formulated, aiming to facilitate the construction and ordered development of a metropolitan area suitable to be the center of Japanese politics, economics, and culture. The First Capital Region Plan of 1958 referenced the Greater London Plan, creating Suburban Area (Greenbelt), and aimed to "control the chaotic and swollen development of Built-up Area, and facilitate healthy development by creating an outer greenbelt." The greenbelt was planned on the outer side of Built-up Area, with a width of 10 kilometers, and satellite cities were planned outside the greenbelt (Figure 1).

However, the understanding of municipalities and land owners of the areas designated as Suburban Area was not gained, and improvement was made difficult by opposition activities of residents. Furthermore, the land use planning system regarding green spaces was left incomplete. In addition, achievement of the plan became difficult with the chaotic development of Suburban Area in the 1960s due to the intense concentration of population and the rapid expansion of urban areas, making change unavoidable..

1.3 Second Capital Region Plan

The Second Capital Region Plan was formulated in 1968 (Figure 2). The Suburban Area (Greenbelt) of the First Capital Region Plan was changed to Suburban Development Area "in order to prevent chaotic urbanization through planned maintenance of urban areas and preservation of green spaces," and the concept of a greenbelt faded. Most of the urban areas in the 50 kilometer zone designated as Suburban Area in the First Capital Region Plan became Suburban Development Area meant for commuting to Tokyo.

The greenbelt concept partially remained. Among the green space in the Suburban Development Area, areas in danger of chaotic urbanization were designated Suburban Green Space Preservation Area (18 zones, 15,693 hectares). Furthermore, 9 districts, 758 hectares of Suburban Green Space Preservation Area that were considered important districts especially in need of preservation were designated Suburban Green Space Special Preservation Area, making permission of the governor necessary before conducting certain development activities.

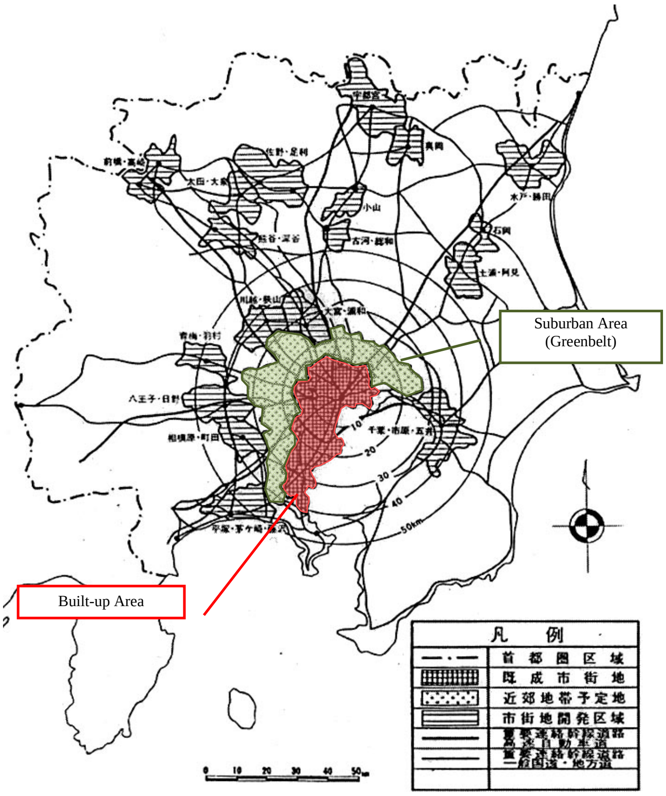

Figure 1: First Capital Region Plan[2]

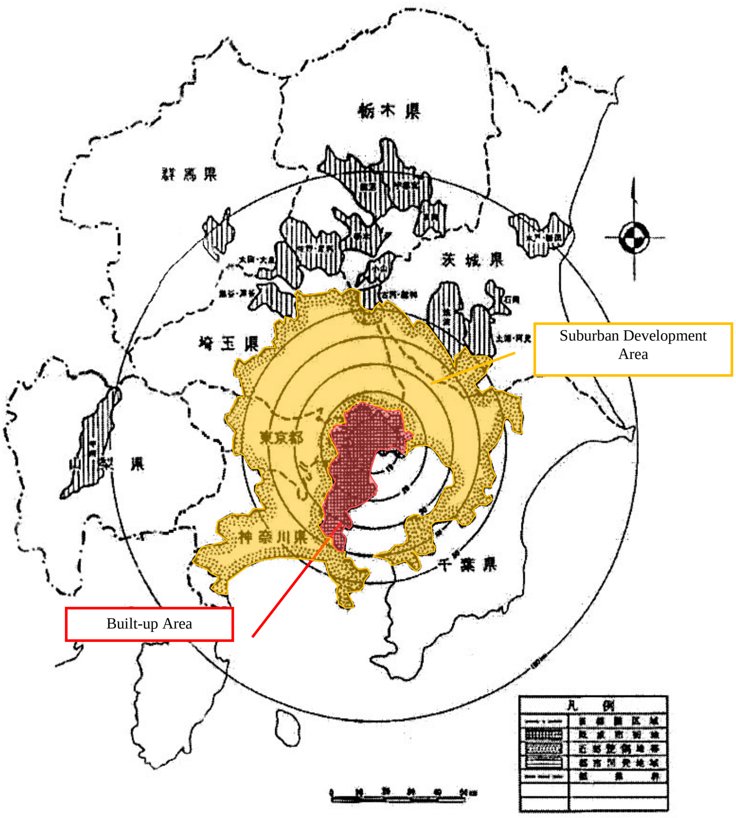

Figure 2: Second Capital Region Plan[2]

2. Changing Land Use of Suburban Area over Time

This section takes up Kawaguchi City in Saitama Prefecture, planned in the First Capital Region Plan as Suburban Area (Greenbelt), and analyzes its subsequent land use over time. Kawaguchi City contains both a designated Built-up Area and a designated Suburban Area[4] (figure 3).

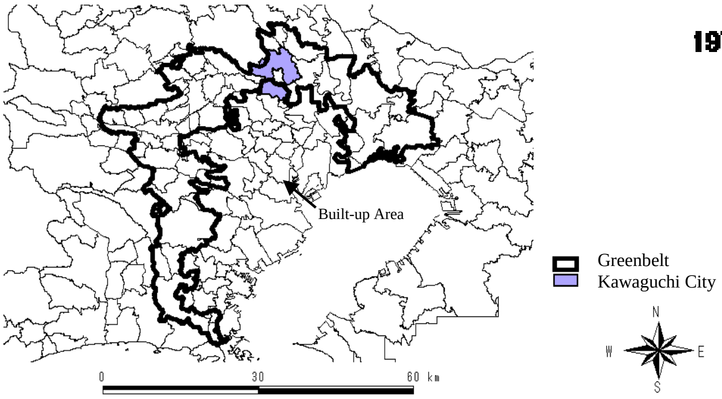

Figure 3: Kawaguchi City and Greenbelt

2.1 Changes in Land Use Planning

In 1963, five years after the formulation of the First Capital Region Plan, approximately 20% of Kawaguchi's Suburban Area was designated an urbanization area, however in 1970, with the increased demand for housing due to rapid population growth, approximately 85% had become an urbanization area. As a result, Kawaguchi City had nearly as much designated urbanization areas as existing urbanization areas (figures 4 & 5). Compared to Built-up Area, the ratio of land use of Suburban Area for residential uses had greatly increased.

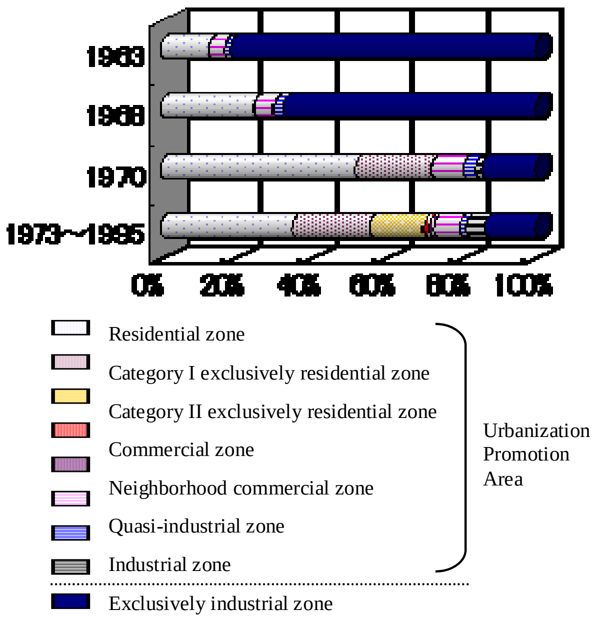

Figure 4: Percentage of Various Land Use Plan of the Suburban Area (Kawaguchi City)

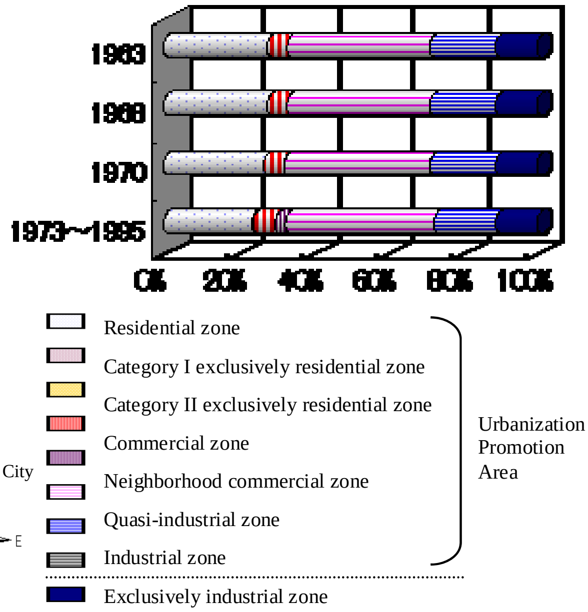

Figure 5: Percentage of Various Land Use Plan of Built-up Area (Kawaguchi City)

This indicates that Kawaguchi City, after the First Capital Region Plan (1958) was revised by the Second Capital Region Plan (1968), rapidly transitioned towards urbanization areas, and its character as a Tokyo bed town strengthened.

Viewed from a map (figure 6), in 1963, following the formulation of the First Capital Region Plan (1958), approximately 80% of the Suburban Area was designated an urbanization control area.

In 1968, when the Second Capital Region Plan was formulated, residential demand increased, and the designation of urbanization control areas for residential use can be seen. In 1970, in the period between the formulation of the Second and Third Capital Region Plans, approximately 70% of the area that had been designated as Suburban Area in the First Capital Region Plan had become designated for residential use. In 1985, when the Fourth Capital Region Plan was formulated, 85% of the Suburban Area of the first plan had been designated for use, leading to urbanization, and at the same time an intention to halt the increasing population in Suburban Area can be seen.

2.2 Changes in the Record of Land Use over Time

Looking at the change in the record of land use over time (figure 7), in Built-up Area designated in the First Capital Region Plan, there was an urban land use structure, with building sites occupying approximately 80%. Looking at the Suburban Area of the first plan, after the period of the Second Capital Region Plan in 1976, building sites increased annually, and the ratio of fields and rice paddies decreased. This can be seen as due to Kawaguchi City assuming the role of Tokyo's bed town, taking on the increase in housing in its Suburban Area. Population continued to increase in Suburban Area, and green spaces (forests, fields, rice

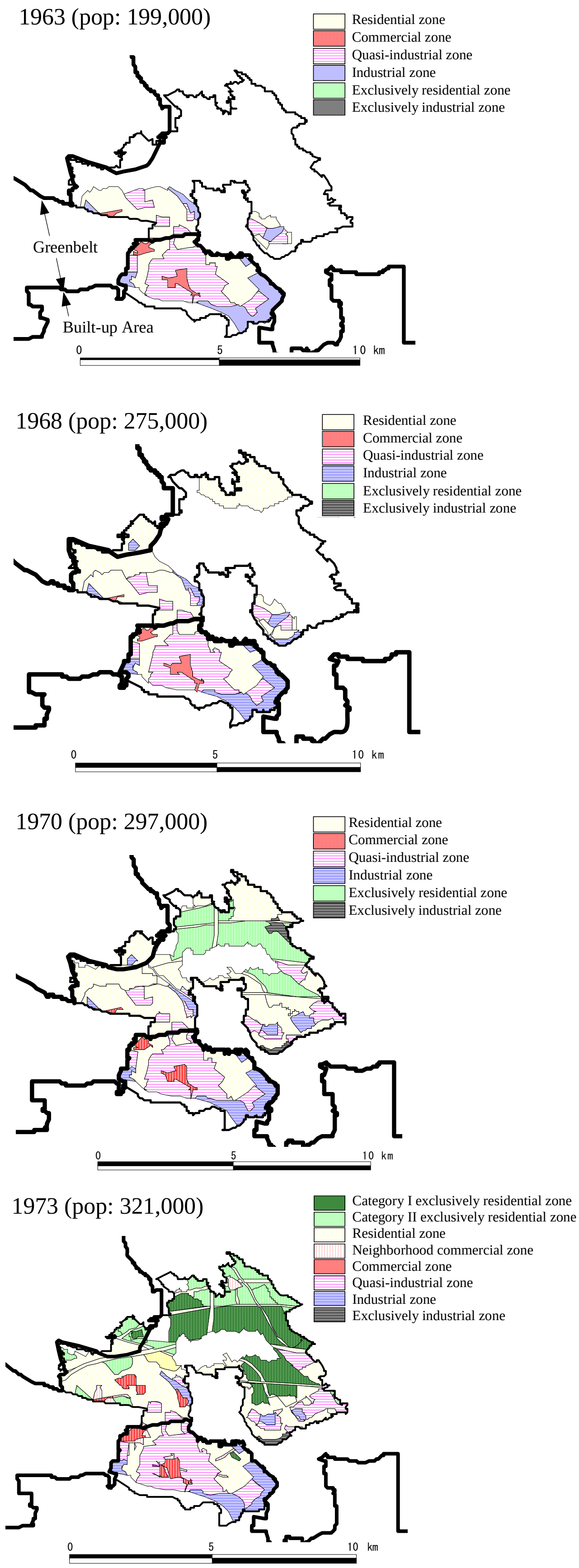

Figure 6: Changes in Land Use Planning (Kawaguchi City)

paddies) in 1996 were approximately 30% of the overall Suburban Area and decreasing annually.

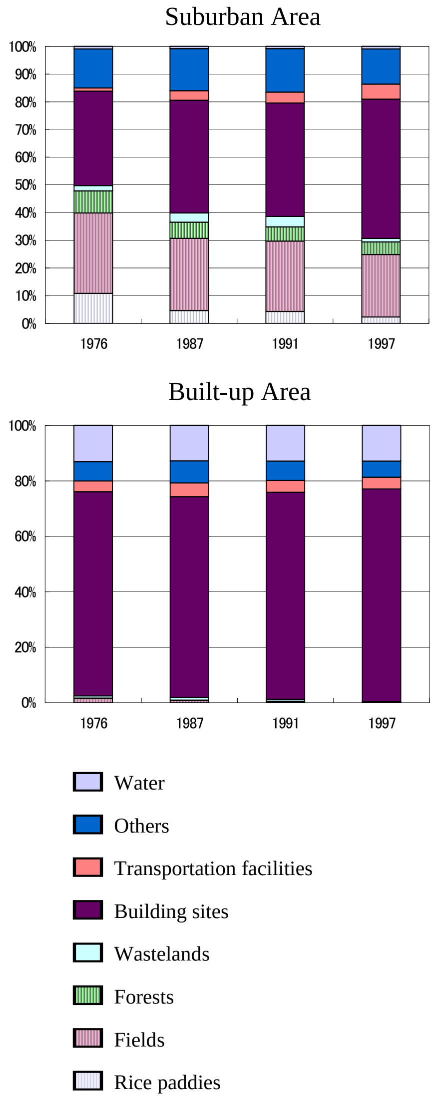

Figure 7: Changes in the Record of Land Use (Kawaguchi City)

3. Issues in Green Space Planning in the Tokyo Metropolitan Area

3.1 Verifying the Greenbelt Concept

The concept of a greenbelt in the First Capital Region Plan was an admirable plan meant to sketch an ideal city, however in reality this had little practical effect, and it remained as regional green spaces. This section will investigate the reasons why the greenbelt concept was not fully realized, covering the formative concepts of the plan, land use planning of the Suburban Area of Kawaguchi City, and changing land use.

(a) Expansion of Urban Areas Due to Population Concentration during the Greenbelt Concept Period

Following the war, the concentration of population from rural areas to Tokyo can be called rapid and extraordinary. In Kawaguchi City, designated as Suburban Area, the population was 144,000 when the First Capital Region Plan was formulated, and 343,000 in 1976 at the formation of the Third Area Plan, a 2.4 times increase. The policy of preserving green spaces can be seen to have been unable to resist the trend for expansion of urban areas due to the concentration of population in a short time. The area division system with regulatory power was introduced, however urbanization control areas were not arranged on a broad scale, and green spaces were reduced in each municipality.

(b) Political Understanding and Popular Support for the Greenbelt Concept

The period when Suburban Areas were planned coincides with Japan's high economic growth, which produced a housing shortage due to the concentration of population in large cities, and political consideration for satisfying housing demand took precedent over the greenbelt policy for controlling the expansion of urban areas. Furthermore, with the social background of prioritizing the economy, there was no understanding among municipalities and citizens, and regulation was difficult. Even among experts, arrangement and concern for green spaces was not established. Because there was no political or popular understanding, there was no agreement regarding the Suburban area, and the plan became weak with no regulatory or legal effect.

(c) Substance of the Greenbelt Plan

The Suburban Area was 10 kilometers from the city center. On the other hand, the greenbelt of the Greater London Plan was 20 kilometers from the city center. Viewed from this comparison, the Suburban Area created in the Capital Region Plan can be called too close to the city center. As a result only partial green spaces remained. This can be understood to be due to the fact that, in addition to not foreseeing the population increase, the Greater London Plan and the Town and Country Planning Law were not sufficiently studied, and the experience of England was not made use of.

3.2 Issues in Green Space Planning in the Tokyo Metropolitan Area

In 2005, the population of Japan began to decline, and further population decline is assured. The greenbelt concept of the First Capital Region Plan could not resist the pressure of population concentration during the period of high economic growth, however its significance today is worth a second look. In order to realize the creation of compact cities with a small environmental impact, city planning with appropriate arrangement of green spaces should be considered.

During the period of the First Capital Region Plan, residential policy took precedent over green space policy, however today the significance of green spaces is being reconsidered. The role of green spaces in creating scenery, food production, and disaster prevention measures is increasing. The administration, citizens, and experts share the value of green spaces, and there is a need to study the proper structure of cities and green space planning.

In addition to the Capital Region Plan, in 2009 the "Regional Plan of Metropolitan Area" was formulated, and a network connecting existing waterside space and green space has been proposed. This plan does not indicate a concrete method for preserving green space. What is needed is the creation of a green space plan in the Tokyo Metropolitan Area that is based on a study of the experiences of the greenbelt plan in the Greater London Plan, Japan's Capital Region Plan, and green space planning in various countries, as well as an understanding of present land use in Japan, and future population and economic trends.

4 REFERENCES

[1] Committee of Metropolitan Area (1959), Metropolitan Area Research, Tokyo. (in Japanese)

[2] Suzuki, S. (1993) Current of City Planning -Tokyo, London, Paris and New York-, Sankai-do, Tokyo. (in Japanese)

[3] Sato, A. (1977) History of the Development of Japanese Park Green Spaces (upper) (lower), Chikuma-syobo, Tokyo. (in Japanese)

[4] Maruyama, M. Nakagawa, Y. (2004) A study on the changes of green space policies of National Capital Region Improvement Plan, Proceedings of annual conference of the Japan Society of Civil Engineers, Vol59(4), pp334-335.

[5] Takeuchi, T., Ishikawa, M. (2009) A study on the effect of urban development projects on the open space environment in areas once designated as green districts, LRJ, 72(5), pp.705-708.

[6] Takeuchi, T., Ishikawa, M. (2009) A study on the green space policies on the planned areas for Green Belt in the National Capital Region during the period of urban expansion -a study in the North Tama Area-, Journal of the City Planning Institute of Japan, No.44-3, pp.877-882.

First International Conference on Geotechnique, Construction Materials and Environment, Mie, Japan, Nov.21-23, 2011, ISBN: 978-4-9905958-0-7 C3051

Application of Traffic Simulation in Road Policy Assessment Accompanied by Railway Elevation

Takuya MAEKAWA[1)]・Hiroshi INOUE[2)]

[1)] Graduate School of Human Science and Environment, University of Hyogo
maekawa@maruokeikaku.co.jp

[2)] Professor, School of Human Science and Environment, University Hyogo, 1-1-12, Shinzaikehoncho, Himeji,Japan
inouye@shse.u-hyogo.ac.jp

ABSTRACT: In road policy assessment, it is very important to present the influence and effect of the project simply, and to hold information in common with relatives. Thus, traffic simulation plays a part in road policy assessment. In this paper, we present how to deal with traffic simulation and introduce an example of the application, in Road Policy Assessment accompanied Railway Elevation. Lastly, we show possibility of traffic simulation in Road Policy Assessment.

Key Words: traffic simulation, road, road traffic, traffic flow, road policy, road policy assessment, railway elevation

1. INTRODUCTION

Traffic simulation is a tool to represent traffic flow on the road network by use of computer, and to estimate the influence of new road or land development on the traffic flow beforehand. The result of the simulation is represented as visual information in the series.

In recent years, public involvement is introduced to transportation policy on the view point of promoting democracy and transparency. As relatives contained local residents are likely to get mutual understanding, if information such as traffic congestion and/or the length of congestion is shown as ever changing visual scene. Whence, the meaning of traffic simulation is recognized as a tool of making mutual consent for promoting transportation policy.

In this study, we try to verity the usefulness of traffic simulation for promoting road policy in urban area.

2. OUTLINE OF TRAFFIC SIMULATOR "VISION"

2.1 Model Structure

Traffic simulator "VISION" consists of traffic flow model and route choice model.[1)] Traffic flow model determine behavior of each vehicle such as speed and vehicular gap on the condition of those at previous time.

By the repetition of the procedure, the condition of traffic flow on the road network is refreshed periodically (periodic scanning).

Thus, traffic flow is represented as continuous flow on the road network.

The input to the model is the data with respect to road network represented as the graph with nodes and links, and behavior of traffic flow on the roads. [2)] Traffic demand is also given to the model as a dynamically changing origin and destination traffic volume matrix. The output of the model is ever changing traffic flow condition shown visually. Also quantitative data on traffic volume, length of congestion travel speed and exhaust emission are provided as output of the model. These output of the simulator, visual graphics output and quantitative information, make it easy to explain and understand the effect of transportation and/or land development projects.

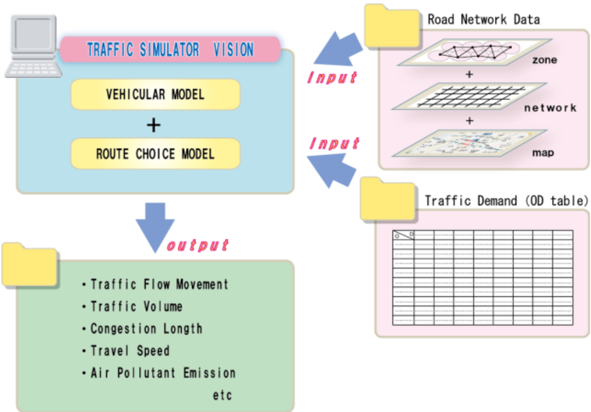

Fig.1 Input and Output of the Traffic simulation "VISION"

2.2 Traffic Flow Model of the Simulator "VISION"

In the traffic simulator "VISION", we use car-following theory as a traffic flow model. [3)] The acceleration of a vehicle is determined by a function of the gap distance with the preceding car and the difference between desired speed of the car concerned and the actual speed of the preceding car.

The function is given by

$$VS = -\alpha \cdot |s_0 - s|^{\beta} \left(1 - \frac{1}{1 + \delta \cdot \exp(-\gamma \cdot d)} \right) \qquad (1)$$

where, VS : acceleration, S^0 : desired speed, S : speed of the preceding car, d : gap distance with the preceding car, α, β, γ, δ : parameters.

The desired speed varies as regulated speed the road, radius of the curve, and longitudinal gradient.

At also varies as driver's behavior, reflecting the prove car examination data. Every car can change a lane in response to the driving situation.

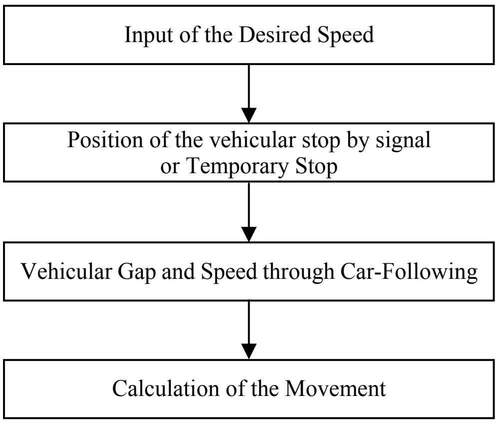

Fig.2 Calculation of the Vehicular Behavior through Traffic Flow Model

Route choice model depends ever-changing travel times on each road, these are the result of the simulation. The probability each route is selected takes large it travel time of the route gets short, applying Dial's method. Route choice is refreshed for every time intervals.

Route choice has on significant influence to the reappearance of the simulation result. The higher rank planning of the project examines the effect and influence to the surrounding road traffic by traffic assignment procedure in a wide range road network. To make sure of consistency with the higher rank planning, the route choice probability also reflects the result of traffic assignment.

3. PROCEDURE OF THE INVESTIGATION

In the traffic simulation "VISION", we integrated route choice model into the original traffic simulator with car-following traffic flow model and fixed route choice model. Traffic demand, which is expressed as origin and destination demand matrix, is made out based on traffic assignment in the higher ranking planning. Also the road network is made out of a graph with the mass of nodes and links. At first, we execute a simulation to test the reappearance of traffic simulation on the present road network. Traffic volume on each branch in the intersection, travel speed on each section, length of congestion and so on is examined comparing the simulated result and observed values. After the reappearance of the simulation is verified, we execute the simulation on each measure to improve traffic situation. The examination procedure is shown in Figure.3.

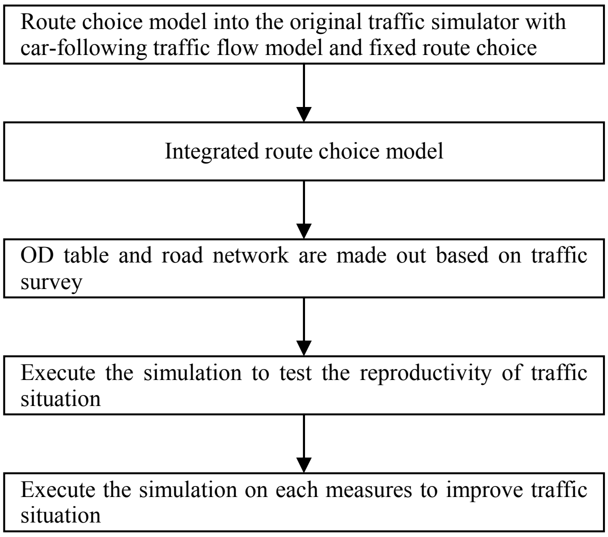

Fig.3 Examination flow of the traffic simulation

4. THE SUBJECT TO APPLY TRAFFIC SIMULATOR

We can utilize traffic simulator "VISION" in the following subjects as a tool to estimate the effect and influence of the project.

4.1 Application to the Measures to Improve Traffic Congestion

The simulator can be applied to the subject to improve traffic congestion, such as improving intersections, changing traffic management, and taking grade separation.

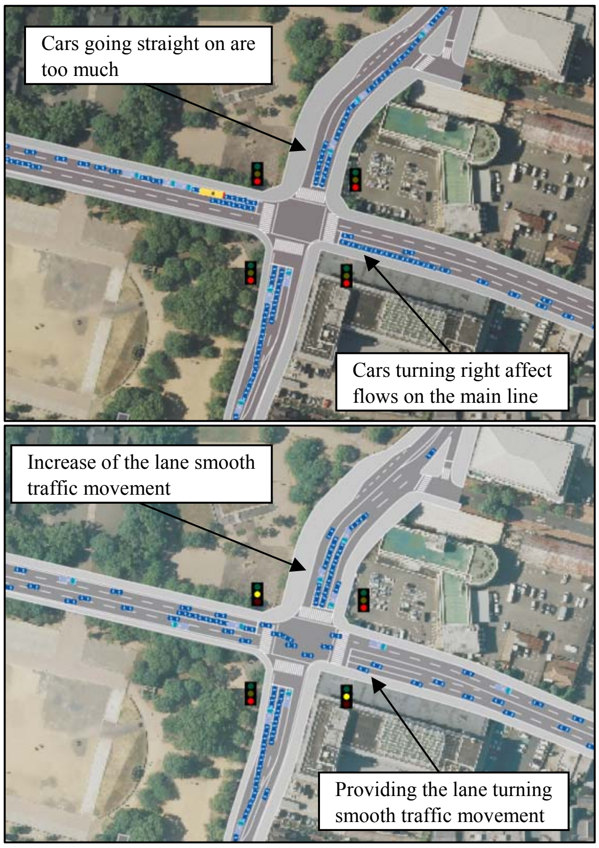

Fig.4 Example of the Application (Providing Lanes)

4.2 Application to Road Providing Plannings

The simulator can be applied to road providing planning, such as widening of existing road, providing by-pass and making ramps at intersections.

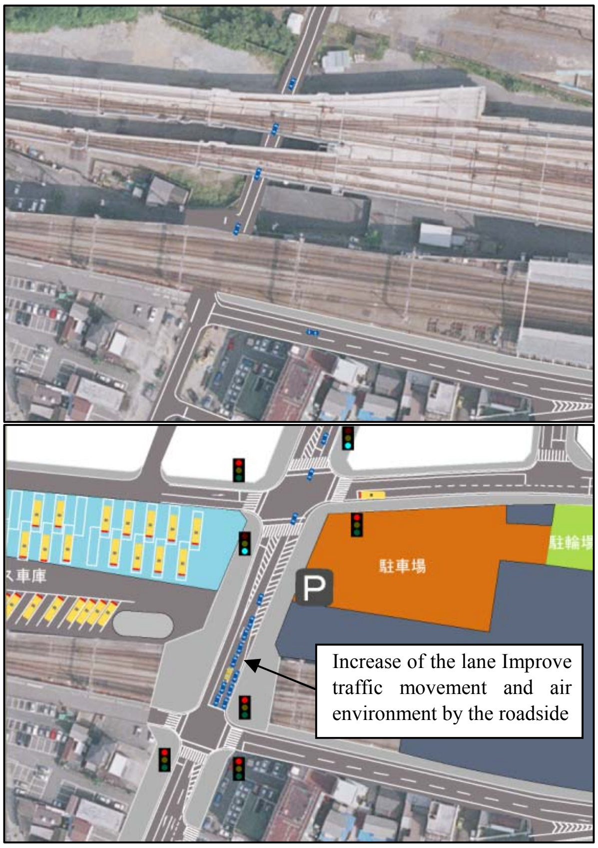

Fig.5 Example of the Application (Increase of the lane)

4.3 Application to Estimate the Influence of the Project

The simulator can be applied to estimate the influence of the project, such as changing lanes followed by construction work, in and out of working trucks, location of commercial facilities and various events.

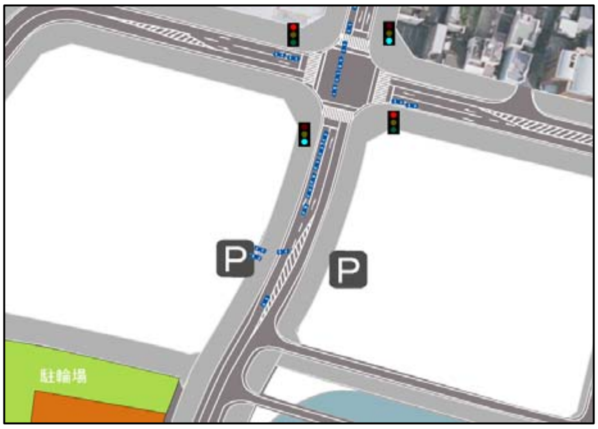

Fig.6 Example of the Application (Improve of the cars going in and out the roadside)

Fig.7 Example of the Application (Improve of the bus stops)

5. EXAMPLE OF THE TRAFFIC SIMULATOR "VISION"

5.1 Estimating the Influence of Railway Elevation

We testified the traffic management measures as the presumptions to provide station plaza accompanied by railway elevation project.

Traffic flow not only automobile traffic bat also pedestrians and bike traffic in the surrounding areas of the plaza was represented precisely.

This simulation made clear the production of new traffic congestion caused by changing traffic moving as the result of railway elevating and providing station plaza.

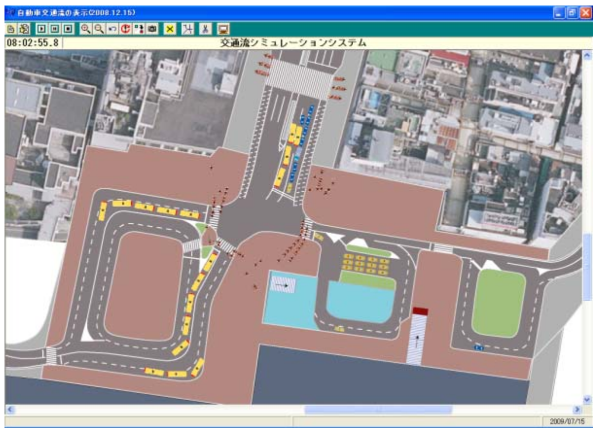

Fig.8 Traffic Movement by the provision of the Station Plaza

5.2 Estimating the Influence of Traffic Management Measures on the Arterial Roads

We testified the influence of traffic management measures to traffic flow in surrounding areas.

The change of travel speed and/or traffic congestion was represented visually.

In some places of the network, traffic congestion turns hard by introducing traffic management measures. Overall travel times and emission of carbon dioxide in the objective area can be decreased by some measures.

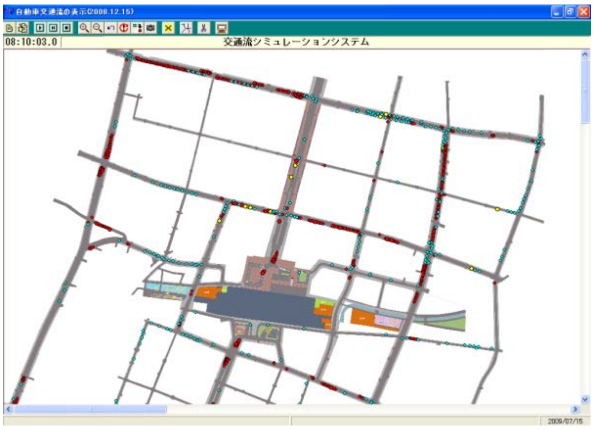

Fig.9 Traffic Movement under Traffic Regulations

6. ESTMATING INFLUENCE TO URBAN AREA THROUGH PROVIDING NEW ROAD

6.1 Outline of Providing Roads in the Surrounding Areas of Himeji Station

Now, the project of railway elevation of Japan railway lines, Sanyo line, Bantan line, and Kishin line, is proceeding. In December of 2009, railway elevation was finished. And the construction of new station building is now under way. In about 2016, new station building and new station plaza will be completed. Also, construction work of the roads to connect north and south area of the station will be finished. Traffic conditions before and after providing new roads were simulated to estimate influence to traffic in changing urban areas.

Fig.10 Road Network Surrounding Himeji Station

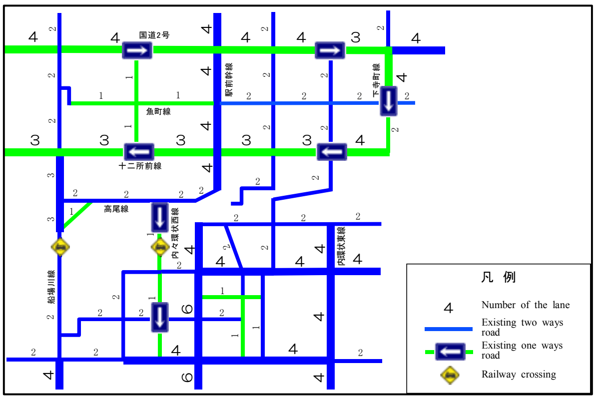

Fig.11 Condition of the Existing Road Network (year 2008)

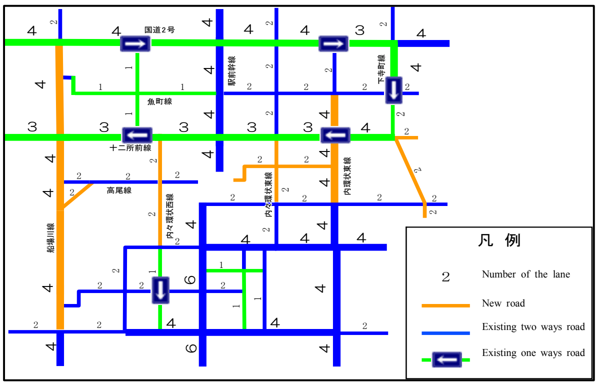

Fig.12 Condition of the Future road Network (about year 2016)

6.2 Reappearance of the Simulation

To testify the reappearance of the simulation, [4)] traffic volumes on each branches of the main intersections were compared with observed values and simulated values. The correlation coefficient is 0.97, and then we may think of good reappearance of the simulation.

Also, the length of traffic congestion and/or travel speed were compared with observed values and simulated values. Especially, blocking times and length of congestion were testified at railway crossings.

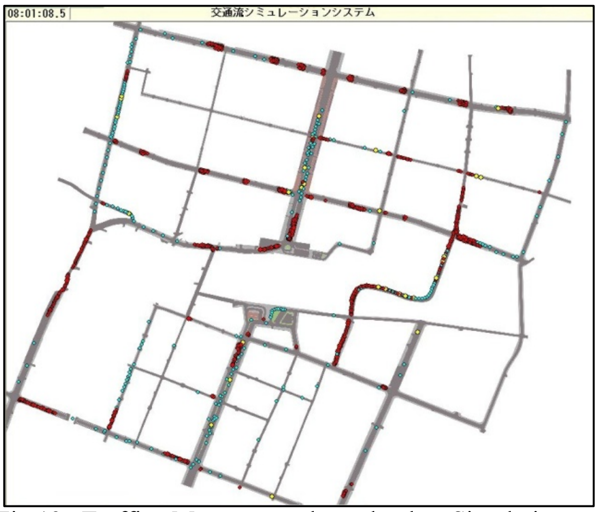

Fig.13 Traffic Movement through the Simulation on Existing Road Network

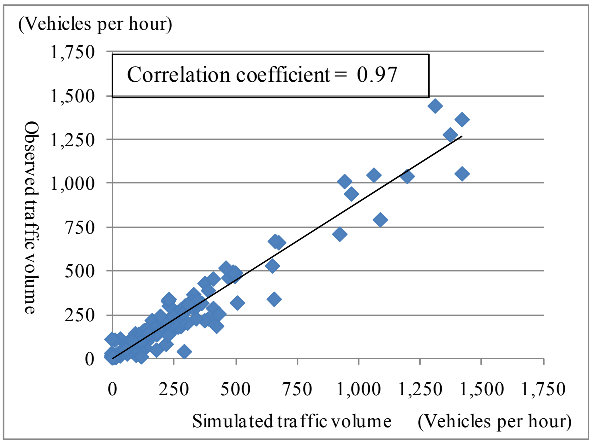

Fig.14 Correlation of the Traffic

6.3 Simulation of the Future Situation

Fig.15 illustrates the future situation of the traffic at the time when all of the project concerning railway elevation was completed. The density of roads get intimate by the project, and traffic flow on the network is made disperse and smooth. Also, congestions at railway crossing are canceled.

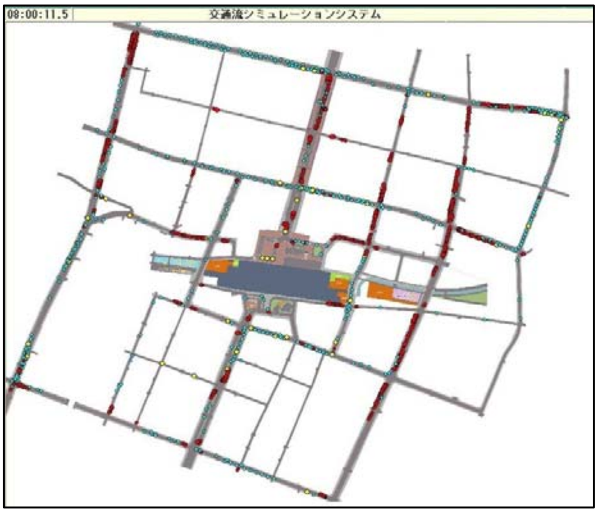

Fig.15 Traffic Movement through the Simulation on Future Road Network

6.4 Estimating Effects of the Project

(1) Outline of the Influence

Comparing the result of the simulation in present situation and in the future situation, some traffic congestions are improved considerably, and traffic flow in urban area is made smooth. Especially, the graphics output as animation pictures plays an important role in the presentation.

(2) Estimating the Effects

To show the effect of the project quantitatively, the following items were calculated in the present and future simulation.

① Shortening of Overall Travel Times

Fig.16 illustrates the shortening of overall travel times. It shows the shortening of overall travel times is about 16% of the present value in a peak hour.

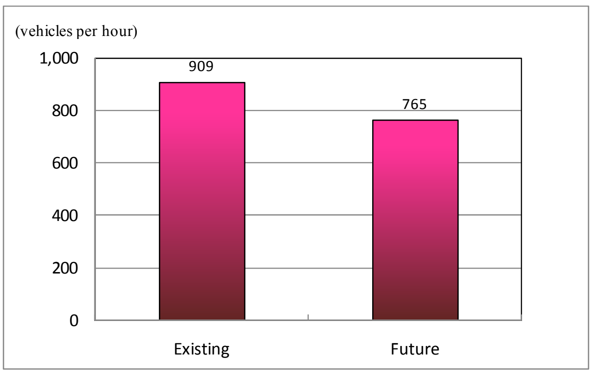

Fig.16 Comparison of Overall Travel Times

② Benefit of the shortening of Travel Times

Fig.17 illustrates the benefit of the shortening of travel times. About 25 hundred million yens are generated per year in the daytime from 7:00AM to 7:00PM.

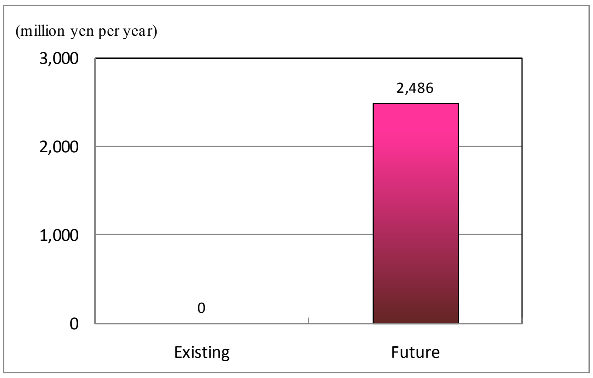

Fig.17 Comparison of the shortening of Travel times

③ Cutback of Overall Travel Distance

Fig.18 shows overall travel times in present and future situation.

Cutback of overall travel distance is about 7.2% in the peak hours compared with present situation.

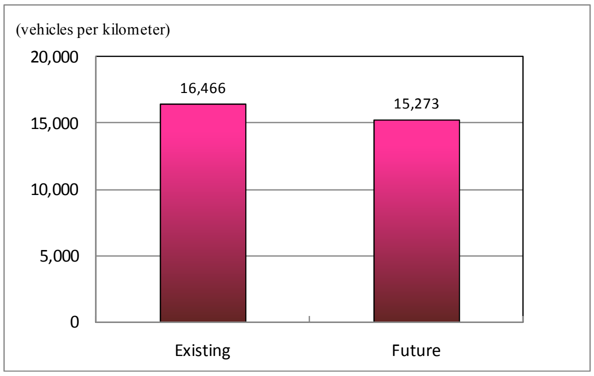

Fig.18 Comparison of Overall Travel Distance

④ Cutback of Co_2 Emission

Fig.19 Co_2 emission shows in present and future situation in the region.

Cutback of Co_2 emission is about 12.8% in the peak hours compared with present situation.

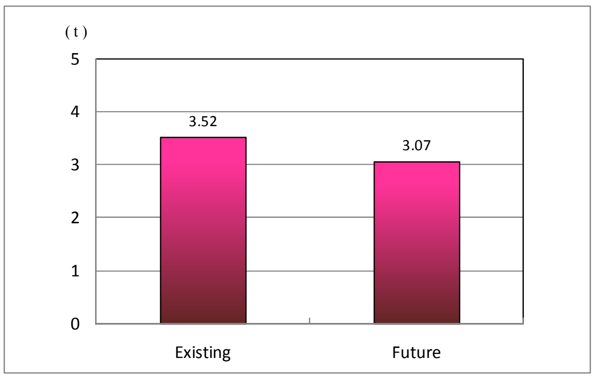

Fig.19 Comparison of the Carbon Dioxide Emission

⑤ Improvement of Average Travel Speed

Fig. 20 shows the comparison of average travel speed on the main route in the city.

Average travel speed raises 12.5% in the peak hours compared with present situation.

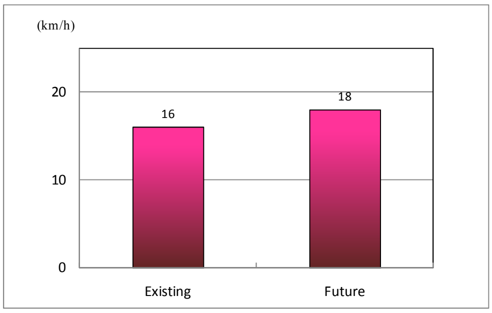

Fig.20 Comparison of Average Travel Speed on the Senbagawa Line

7. POSSIBILITY OF TRAFFIC SIMULATION IN THE FUTURE

To estimate the effect of transportation projects, macroscopic models are used in the ordinary analysis method.

Traffic demand is estimated such that traffic flow is steady. That means every vehicle is the same and travel speed does not change on a road for every times. But in actual, every vehicle is not same and travel time varies by time and by road conditions. Macroscopic and/or whence a steady model has the limit in estimating effects of the projects.

On the other hand, traffic simulation technique has individual information of the vehicles so. We can get information taking into account the characteristics of individual vehicles. Thus more precise estimation is possible to the effect of projects.

If dynamic travel demands, i.e. dynamic origin and destination demand matrix traffic simulation provides ever-changing traffic flow in the region. Then, we can analyze traffic conditions and effect of the project more precisely through the output of visual animations. In the future, three dimensional computer graphics and/or virtual reality technique will provide more real and intelligible pictures of traffic situation. Thus, we will be able to build more reliable estimating systems of transportation projects.

8. IMPROVEMENT OF TRANSPORTATION AND LAND DEVELOPPMENT

Improvement of transportation in the urban area in Himeji city, elevation of railway and traffic management measures concerned, aims to open the space in the downtown area from cars to human beings.

Elevation of railway connects front and back area of the station in a body. That promotes various kinds of human activities in downtown area of the city.

Motorization caused the expansion of urban area and development in suburban area. That came to subsidence of the position in downtown area.

Now, downtown area of the city is being revitalized through improvement of transportation in downtown area.

Traffic management measures produce smooth flow of traffic in downtown area. That concludes improvement of transportation in downtown area will reactivate commercial activities in the area.

Moreover, the open space in downtown area will produce many activities and spiritual response of human beings.

9. REFERENCES

[1] T.Akamatsu, “Prediction inducement and control of traffic flow and theory of dynamic network assignment”, Infrastructure Planning Review, Vol.18, December 1995, pp.23-39.

[2] M.Baba, I.Tanahashi, H.Kitaoka, H.Mori and E.Teramoto, “Traffic simulator NETSTREAM”, Proceeding of the Society of Information Processing, Vol.46, January 2005, pp.227.

[3] R.Horiguchi, “Developpment of arterial traffic assignment model for estimation of traffic management measures”, Proceedings of Tokyo University, September 1996, pp.18-21

[4] R.Horiguchi, “A consideration on the indexes of reappearance of dynamic traffic simulation”, Infrastructure Planning Review, June 2002, pp.1-2.

First International Conference on Geotechnique, Construction Materials and Environment, Mie, Japan, Nov.21-23, 2011, ISBN: 978-4-9905958-0-7 C3051

Impact Estimation of Land Cover Changes of Recharge Area on Spring Discharge in Marshy Environment

Masaaki KONDO and Takamitsu KAJISA, Graduate School of Bioresources, Mie University

ABSTRACT: Many valuable marshy plants, including carnivorous plants, which were designated as a national protected species in 1937, have been found in Kanasyouzu. Kanasyouzu is a spring area in Japan's Mie prefecture situated next to a cliff. The ground water level is quite high, which makes it possible to nurture wetland plants. In this study, we examined the discharge characteristics and, parameter estimation of a spring model to determine how spring water discharge is affected by change to the land cover condition. The annual average discharge was determined to be approximately three liters per second. The spring model was composed of four tank model and land cover conditions over the top tank. Model parameters were estimated by optimizer including simulated annealing, which is often used as a probabilistic procedure, and the Levenberg-Marquardt method, which is not as commonly used. The discharge was calculated under gravel and asphalt coating conditions that were both better and worse than the current coating condition. The results showed that the discharge under the worse condition decreased by approximately 20 percent and that the discharge under the better condition increased by approximately 30 percent.

Keywords: spring water, tank model, parameter estimation, impact of land cover change

1. INTRODUCTION

Attempts to restore the Kanasyouzu marsh plant community (KMPC), which is located in Mie prefecture, Japan, have revealed a recent resurgence of marshy vegetation. Kanasyouzu is an area that includes a spring situated next to a cliff. According to the local residents' association, in the past, a lot of water gushed out from Kanasyouzu - so much that it was used as irrigation water. KMPC has a high ground water level, which makes it an ideal environment for many wetland plants. However, land use has changed as the area has experienced urbanization and industrialization, and the water discharge has decreased. After an absence, spring water has recently been identified, and a study of the spring is considered important in order to restore the wetlands.

Tank model was primarily developed by Sugawara [1]. In terms of spring water analysis, non-linear two-hole tank model was developed by Oyama and Mizuno [2]. Kodama and Komura [3] used four tank model with two outlet of top tank for spring in Tokyo, Japan. As topographicly-similar study to this paper, tank model was applied in order to investigate hydrological cycle of hilly land where housing land development had progressed according to [4].

We obtained local annual data relevant to the KMPC, including rain, air temperature, discharge, and calculated evaporation in 2010. We then used a four tank model to analyze the land cover. Optimization, including simulated annealing and the Levenberg-Marquardt algorithm, was used to estimate the many parameters needed for the model. We then examined the effect that changes to the land cover condition had on the spring water discharge.

2. METHOD

2.1 Location and landscape of KMPC

Fig. 1 shows (a) the location of the Kanasyouzu marsh plant community (KMPC) and (b) a shaded 3D-contour map of the surrounding area. Most of the slopes around it are oriented northward or eastward. Kanasyouzu is situated next to a cliff, and the ground gradually slopes up toward the southwest from the KMPC site. It is located at the foot of a mild range of hill. These details helped us to determine the orientation of restoration area.

The annual amounts of spring water, precipitation and evaporation were used to determine the size of the recharge area, which is 150,000m^2 and indicated by the dotted line in Fig. 1 (b). The contour map in Fig. 1 (b) was drawn on a 10 meter resolution digital elevation model with fundamental geospatial data provided by the Geospatial Information Authority of Japan (Geographical Survey Institute, GSI).

Table 1 lists the area ratio of land-cover classification in the recharge area. There are many factories and companies related to the automotive industry around the KMPC. Office buildings, factories, and residences, account for 30% of recharge area. Gravel parking lots, bare ground, and roads account for 25%. Roads and parking lots paved with low permeability asphalt account for 13%. Sanded school ground makes up 10% of bare area. Forest, which is situated next to the KMPC, accounts for nine percent. There is a small parcel of paddy field in the recharge area. Non-agricultural land cover comprises to 80% of area of the recharge area.

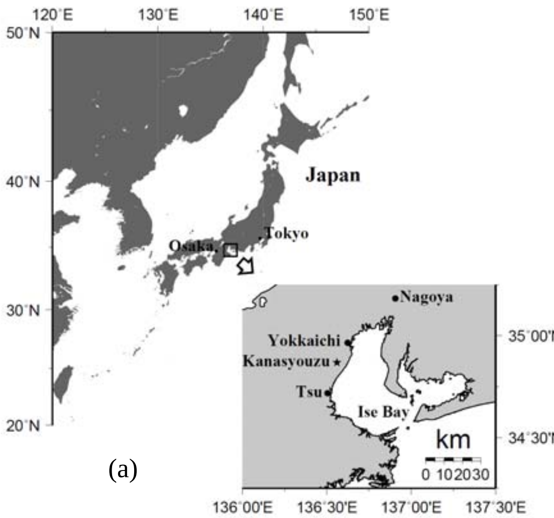

(a)

Fig.1 (a) Location of KMPC marked as star and (b) color-drawn contour map with road (DEM data provided by GSI was drawn.)

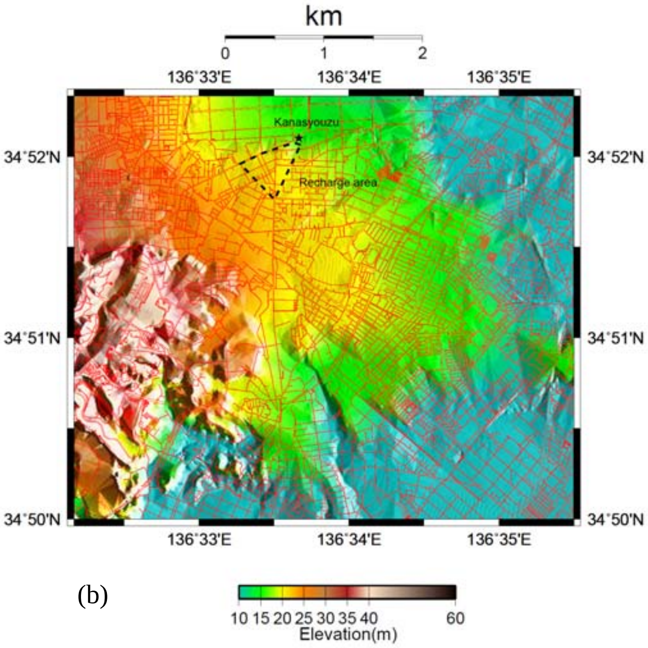

(b)

Fig.1 (continued)

Table 1 Area ratio of land-cover classification and its run-off coefficient

i	Land-cover classification	Area ratio α	Runoff coefficient f
1	Building (company19%, house11%)	30%	1.00
2	Gravel (parking22%, bare area2%, road1%	25%	0.50
3	Asphalt (road10%, parking3%)	13%	0.80
4	Farmland	13%	0.20
5	Bare area (sand)	10%	0.00
6	Forest	9%	0.30
7	Paddy field	0%	0.75

Values of f are cited from Tsutsumi et al. (2001).

2.2 Observation method

We set up 90-degree triangular v-notch weir in a channel to determine the hourly discharge of spring water from January 27th to December 31st, 2010. We used the weir because it is useful for measuring small discharges like the spring water in the KMPC. The weir was set at a location where the water discharged from a paddy field adjacent to the KMPC did not disturb the measurement of the spring during irrigation season.

A water-stage recorder was used for the measurement. An overflow depth of h was determined after the corrections to make up for the influence of water temperature, barometric pressure, and water level. We convert the formula for flow by Numachi et al. [5] as

$$Q = C \times h^{5/2}$$
$$C = 1.354 + \frac{0.004}{h} + (0.14 + \frac{0.2}{\sqrt{W}})(\frac{h}{B} - 0.09)^2 \quad (1)$$

where W is 0.1 m from channel bottom to notch bottom, and B is the 1.5-meter width of the water channel.

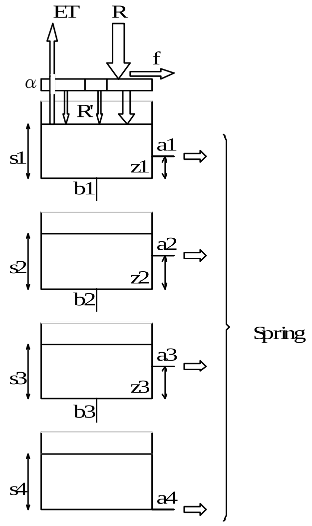

(a, runoff coefficient of side outlet;
z, height of outlet;
b, permeability coefficient;
s, height of storage)

Fig.2 Spring model

Rainfall data was observed by Suzuka Construction Department which is located 1.3 km away from the KMPC. The air temperature was determined once in every hour via an instrument screen located in the KMPC. Possible evapotranspiration, ETp, was estimated using the Thornthwaite system (2) based on monthly average temperature [6].

$$ETp_j = 0.533 D_{0j} (\frac{10T_j}{I})^a \quad (2)$$
$$I = \sum_{j=1}^{12} (\frac{T_j}{5})^{1.514}$$
$$a = 0.000000675 I^3 - 0.0000771 I^2 + 0.01792 I + 0.49239$$

where D_0 is possible hours of sunshine in a 12-hour unit depending on latitude and ETp is possible evapotranspiration per day (mm/day).

2.3 Analysis

Our spring model was composed of four tank model in series with land cover conditions over the top tank (Fig. 2). Precipitation R' (3) was added to the top tank after taking into account the permeability rate (1-f) in lieu of R. The run-off coefficient, f, was treated as constant with time. Values of f were cited from [7]. We assumed that rain flow depended on the land cover over the top tank being run off through street drains beside roads.

$$R' = R \sum_i (1 - f_i) \times \alpha_i \quad (3)$$

where the alpha is the area ratio of land cover in the recharge area.

Possible evapotranspiration, ETp, was estimated by using the Thornthwaite system [8]. Actual evapotranspiration, ET, was determined by multiplying the ETp by 0.7. ET was subtracted from the top tank in the case of a sunny day. In cases of over 5 mm of rainfall per day, actual evapotranspiration was assumed to be zero. Rainfall data was the observation value. Spring water was assumed to be the total discharge combined from all outlets beside the tanks.

Analysis of a digital aerial photograph of the recharge area around the KMPC enabled us to estimate the area ratio of land cover, alpha, shown in Table 1 [9].

Considerable skill is required to estimate the many parameters in this type of tank model. In this study, simulated annealing (SA) [10] was applied to the model parameter estimation as a global optimization. In addition to SA, the Levenberg-Marquardt (LM) algorithm [11] was used to estimate the parameters because this algorithm has not been frequently applied as global optimization according to [12], [13]. Fourteen model constants are the unknown parameters. The initial tank depths were designed for optimizing the parameters. Equation of evaluation function is as following (4). Time step is one day, and the total number of time steps is 339 days.

$$J = \sum (Q_m - Q_c)^2 \tag{4}$$

where, Qm is the measured discharge and Qc is the calculated discharge.

Model parameters were estimated to use the data between January 27th and June 30th. These parameters were then verified from July 1st to December 31st.

3. RESULTS

3.1 Properties of spring water

Fig. 3 shows the changes of the spring water discharge with time. Rainfall is also shown. From January to February, no overflow was observed because the rainfall was extremely low. Several spell of low rainfall resulted in no flooding. Starting in March, the flooding appeared in response to the increased precipitation.

The monthly average spring water is shown in Fig. 4. The average during the winter season ranged from 0.1 to 1.5 L/s, and was on the decrease due to little rain. In spring season, the average is 3 to 4.5 L/s, starting out small, and then gradually increasing. The rainfall in July and August in 2010 was lower than usual because of the record-breaking, scorching summer. However, between 1 and 4 L/s of spring water was still observed. Spring water at the channel was last observed in the KMPC in the summer of 2009. During the fall season, spring water increased due to the heavy autumnal rain.

The annual average discharge was determined to be approximately 2.7 liters per second, and the annual amount of spring water was 85,000m^3. The spring was not measured between January 1st and January 26th because the amount of spring water was considered to be too little in the consideration of low rainfall.

We compared the spring water in KMPC with that of a spring near the Kokubunji cliff line because both are springs near cliffs. A previous report [14] has shown that the average spring in the Shinmei-no-mori Mitsuike special conservation area in Setagaya Ward is 3.2 L/s when numerically integrated for a times series of spring

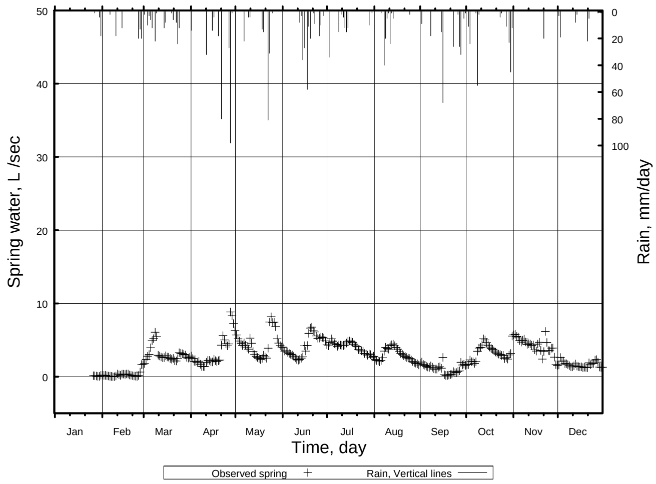

Fig.3 Change of spring water and rainfall with time in 2010

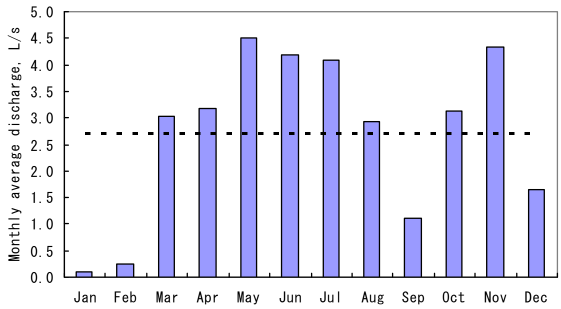

Fig.4 Monthly average spring water in 2010 (average indicated with dotted line is 2.7 L/s)

discharges. Although rainfall conditions such as the amount of spring water and rainfall pattern differ every year, the KMPC was comparable in annual discharge to the Mitsuike spring famous in Japan.

3.2 Parameter estimation results

The model parameters were estimated with optimizers including simulated annealing (SA), which is often used as a probabilistic procedure and the Levenberg-Marquardt (LM) algorithm, which is not used as much.

Fig. 5 shows the calibration results of (a) SA and (b) LM. The measured discharge, Qm, is indicated by a plus mark and the calculated discharge, Qc, is indicated by a thick solid line. While Qc is only passably in agreement with Qm during the entire term, both agree to some extent early in March. It seems that low rainfall during January and February resulted in not only a long dry spell but also the discharge difference in March. Fig. 6 shows the validation results of SA and LM. The precious evaluation equation (5), referred to in [15], showed that both methods had equal accuracy, E = 0.97. In addition, the LM algorithm was advantageous in terms of its computation time.

$$E = \left\{ 1 - \frac{\sqrt{\sum (Q_m - Q_c)^2}}{\sum Q_m} \right\} \times 100(\%) \tag{5}$$

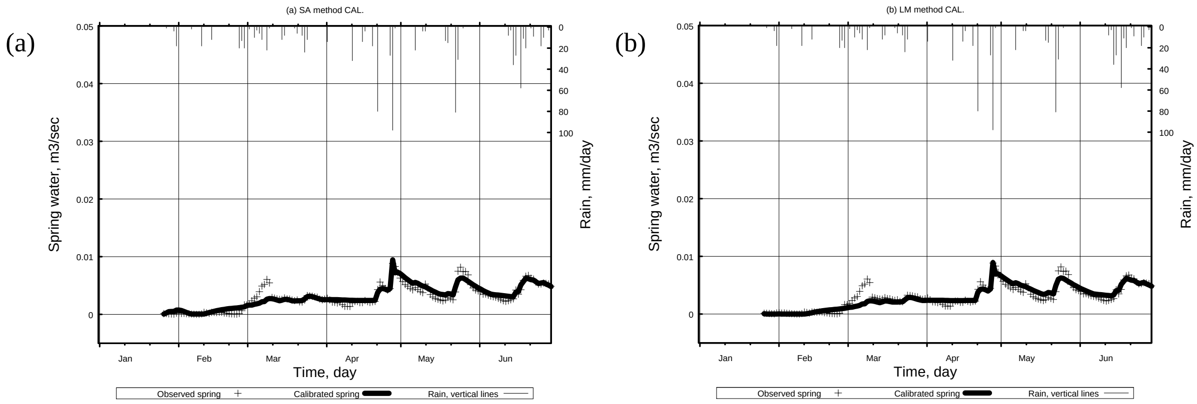

Fig.5 Parameter calibration with (a) SA method and (b) LM method

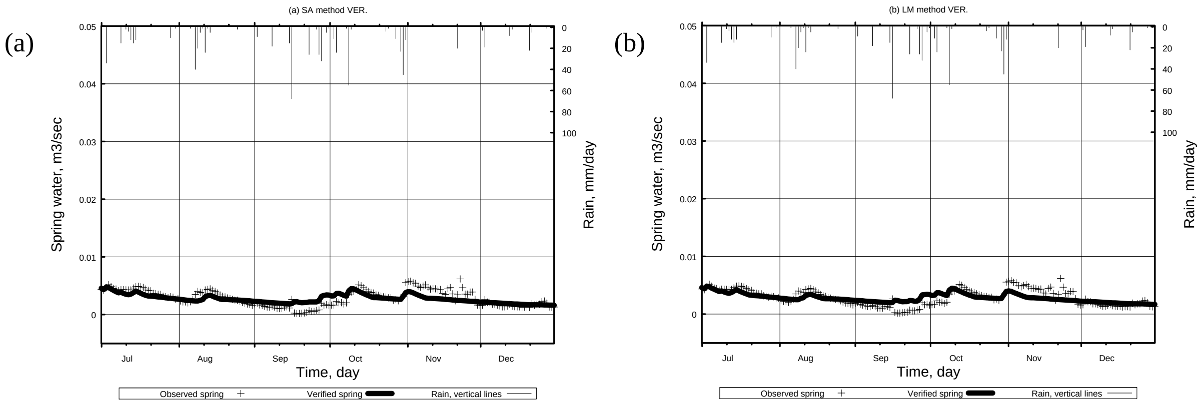

Fig.6 Parameter verification with (a) SA method and (b) LM method

Table 2 Impact of change of land-cover condition on spring water

	Low permeable asphalt pavement (f = 0.8)	(CURRENT) **Gravel** (f = 0.5)	High permeable asphalt pavement (f = 0.3)
(CURRENT) **Low permeable asphalt pavement** (f = 0.8)	80 (68,373m^3)	100 (85,722m^3)	111 (95,312m^3)
High permeable asphalt pavement (f = 0.3)	96 (82,287m^3)	115 (98,584m^3)	128 (109,522m^3)

4. DISCUSSION

We roughly classified the land cover of the recharge area into two groups (Table 1). The municipality and companies take up the roads, parking lots, and bare areas, while farmland fields and forests are privately owned. Almost all of the recharge area used for non-agricultural purposes is owned by the municipality or companies. This means that the results of this study could have an effect on future environmental strategies.

We examined how changes to the land cover affected the spring. Provided that the asphalt used in roads and parking lots changed from low (f = 0.8) to high (f = 0.3) permeability, and that parking lots, roads, and bare areas made of gravel were turned into such asphalt (f = 0.8, or f = 0.3), the annual amounts of spring water were calculated by using of the rainfall pattern of 2010 and the model parameters estimated in section 3.2.

Table 2 shows the annual amount of spring water under a combined land cover. The discharge under the current land cover was normalized to 100, and it is compared with other conditions in Table 2. The combination of high permeability asphalt increased spring water by approximately 30% compared to the current land cover. The combination of low run-off coefficients had an effect on the recharge, which resulted in the increased flow from the spring.

When the surfaces of parking lots, roads, and bare areas were covered with low permeability asphalt, the spring water was reduced by approximately 20% compared to the current condition. This means that the worse condition in low permeability will further reduce the spring water in the winter season.

5. CONCLUSION

We set up a triangular weir to determine the discharge of spring water in Kanasyouzu. Rainfall in July and August of 2010 was lower than usual because of the scorching summer. However, even in these months some spring water was observed. The annual average discharge was determined to be approximately three liters per second, which is equal to that of the famous Mitsuike spring in Japan.

We created a spring model composed of four tank model in series with land cover conditions over the top tank. The model parameters were estimated by optimizers including simulated annealing (SA), which is often used as a probabilistic procedure, and the Levenberg-Marquardt (LM) algorithm, which is not often used. The parameters calibrated with the LM algorithm were equally as precious as those with SA. In addition, the LM method was advantageous in terms of computation time.

We used the spring model with land cover conditions, and the estimated model parameters, to calculate the discharge under both better and worse coating conditions than the current gravel and asphalt have.

The results showed that the discharge under the worse condition decreased by approximately 20 percent and that the discharge under the better condition increased by approximately 30 percent.

6. ACKNOWLEDGMENT

The authors would like to extend sincere thanks to Suzuka Municipal Office for providing the digital aerial photograph.

REFERENCES

[1] Sugawara M, “Runoff analysis”, Tokyo, KYORITSU SHUPPAN, 1975.

[2] Oyama M and Mizuno A, “Numerical simulation of spring water discharge (characteristics and application of a nonlinear two-hole tank model)”, J. of Groundwater Hydrology, vol.36, 1, 1994, pp.1-11.

[3] Kodama H and Takamura H, “Water balance of cliff line spring water; For the Seijyo-santyoume Ryokuchi spring water of the Tokyo Setagaya Ward”, Chishitsu News, No.655, 2009, pp.50-58.

[4] Ando Y, Mushiake K, and Takahashi Y, "Hydrological cycle of hilly land and effects of urbanization on it", Proceedings of hydraulic engineering, JSCE, vol.25, 1981, pp.197-208.

[5] Japan Society of Civil Engineers, “Manual of Hydraulic Engineering”, Tokyo, Maruzen, 1990, p.284.

[6] Japan Society of Civil Engineers, “Solving Problems based on Manual of Hydraulic Engineering”, Tokyo, Gihodo shuppan, 1999, p.37.

[7] Tsutsumi A, Jinno K, and Oheda Y, “Study on the rainwater recharge model using the groundwater variation”, Proceedings of hydraulic engineering, JSCE, vol.45, 2001, pp.367-372.

[8] Thornthwaite C W, "An Approach toward a Rational Classification of Climate", Geographical Review, Vol. 38, No. 1. 1948, pp.55-94.

[9] Kondo M and Kajisa T, “Effect of land-cover classification in recharge area on Spring Changes at Kanasyouzu Marsh Plant Community”, Proc. of Kyoto branch of JSIDRE, vol.67, 2010, pp.611-612.

[10] Goffe, Ferrier, and Rogers, “Global Optimization of Statistical Functions with Simulated Annealing”, J. of Econometrics, vol.60, 1994, pp.65-100.

[11] Doherty J, “Model-independent parameter estimation user manual:5th edition”, WNC, 2004

[12] Kobayashi K, Takara K, and Tachikawa Y, “Parameter estimation of a distributed rainfall-runoff model by a Levenberg-marquardt optimization algorithm”, Proc. of hydraulic engineering, JSCE, vol.51, 2007, pp.409-414.

[13] Kim J H, Paik K R, Lee D R, and Kim H S (2001), "Comparison of optimization algorithms in parameter calibration of tank model", Electronic version of the XXIX IAHR CONGRESS PROCEEDINGS,<http://www.iahr.org/e-library/beijing_proceedings/Theme_A/COMPARISON%20OF%20OPTIMIZATION%20ALGORITHMS.html>, browsed on Apr. 1, 2011

[14] Tokyo's Setagaya Ward Office (2010) “Report of spring water investigation at Kokubunji cliff line in Setagaya Ward”, < http://www.city.setagaya.tokyo.jp/030/d00016969.html>, browsed on Mar. 17, 2011.

[15] Kunimatsu T and Muraoka K, “Model analysis on river pollution”, Tokyo, Gihodo shuppan, 1994, p.160.

Numerical Study on Characteristics of Levee Breach Flood Disasters in Alluvial Floodplain

Md. Serazul Islam[1] and Tetsuro Tsujimoto[2]

[1]PhD Candidate and [2]Professor, Department of Civil Engineering, Nagoya University, Japan.
(Furo-cho, Chikusa-ku, Nagoya, 464-8603, Japan)

ABSTRACT: Levee breach flood disaster is one of the common natural hazards in Bangladesh. During flooding season, large amount of water flows through Bangladeshi river and it causes earthen levee failure and huge damage occurs in the inhabitants inside the levees. Thus it is important to recognize the process of inundation and we have attempted to do through numerical simulation. As for simulation scheme, schematic model area is considered with main channel, levee and floodplain, and they are roughly composed of the same sediment characteristics because the flood plain have been formed by flooding sediment, the levees have been made by piling up the sediment dredged from the river bed. Therefore, we treat these three components simultaneously in the simulation model.
The main channel, levee, floodplain and flow parameters are selected in conformity with the study field of Sirajganj district and Jamuna River in Bangladesh. And RIC-Nays a two-dimensional numerical model for flood flow and morphology is utilized in this study upon confirmation through the experimental and other numerical study. Based on the calculated results, evolution process of levee breach and inundation of water and sediment in the floodplain are investigated. Levee breach is considered to initiate in the middle of the levee with crest opening. We change the opening size in vertical and longitudinal scales, and the inflow discharge. For the floodplain slope is also taken into account.

Keywords: Levee, floodplain, sedimentation, inflow discharge.

1. INTRODUCTION

Bangladesh is a disaster prone country where flood and river embankment failure resulting in inundation and sedimentation to the country side floodplain are common and frequent natural disasters. On the average, the area inundated every year is about 26,000 km^2, nearly 18% of the country's total area [1]. The average flood discharges of the three main (Ganges-Brahmaputra-Meghna) rivers individually are within the range 14,000 to 100,000 m^3/s [11]. The mean annual rainfall within Bangladesh varies from 1250 mm to 5700 mm [13]. During the rainy seasons (June to September), nearly a trillion cubic meter of water laden with about two billion tons of silt passes through the main rivers, it's come from upstream catchment in India, Nepal, Bhutan and China. These sediments settle over the river beds, floodplains and low lying areas during the inundation and with the recession of flood water. As a result river channels and their distributaries are silted up with sediments composed of fine sands and silts causing drainage congestion and overbank flow resulting in river embankment failure [8], [9].

Levee breached during the rainy seasons due to excess load of flooding water. Failure of levees not only increases the siltation in the river beds and floodplains but it causes huge damage in agricultural production, residents, roads and other infrastructures. Due to geographical position of Bangladesh, we do not avoid levee breach disaster and suffering to the inhabitants in the floodplain. In order to save huge amount of money, lives, agriculture and ecology, it is most important to carry out research on investigation of flood disasters over the alluvial floodplain during levee breach for the vulnerable area of Sirajganj district in Bangladesh. This kind of study is rare in the available literatures except for few numerical, field investigation and experimental studies which can be found in Tsujimoto, Mizoguchi and Maeda [14], Aureli and Mignosa [3], and Fujita and Tamura [5].

Computational simulation can make comprehensive analysis on levee breach flooding and its impacts on the entire floodplains. In this paper, we have attempted to recognize the process of inundation and sedimentation in the floodplain after levee breach in a numerical simulation scheme for different breach opening lengths, depths and discharge conditions by changing the inflow duration in the river channel.

2. DESCRIPTION OF STUDY AREA

Sirajganj district is located in the northwestern part of Bangladesh. Geographically, extension of Sirajganj District is within the area of longitude from 89°20' west to 89°50' east and in latitude it is 24°00' south to 24°20' north. Total area of the district is 2497.92 km^2 and it is relatively a plain land area. Most of the area of this district goes under water during the rainy season. Total cultivable land is 1799.64 km^2, fallow land 157.02 km^2, and forestry 0.50 km^2. The annual rainfall is 1610 mm. The mighty Jamuna River is following at the right edge of the district [10]. Fig. 1 depicts the map of study area of Sirajganj district with Jamuna River and flood protection levee.

Embankment breach is the most common phenomenon for Jamuna River especially on Jamuna right embankment (JRE). There are so many evidence of breaching of embankment during severe flood year of 1988, 1998, 2004 and 2007. In the year 2007, JRE at Khokshabari was breached of 700 m out of 52 km total length and floodwater entered into the breached embankment at Polashpur, Meghai, Dhekuria and Shubhogaccha areas in Kazipur Upazila of Sirajganj district (The Financial Express, 27 July 2007). At least 3500 homesteads and about 6.07 km^2 of croplands in 35 villages in the five Upazilla have damaged in two weeks. The five affected

Upazilla was Kazipur, Sirajganj Sadar, Belkuchi, Shahzadpur and Chauhali [7].

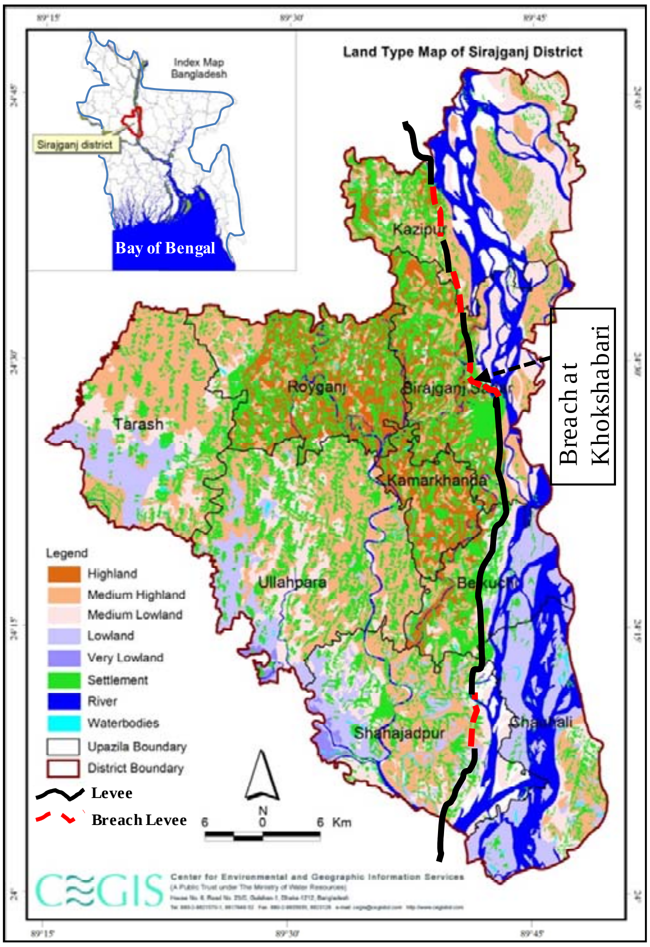

Fig. 1 Map of study area.

3. MODEL SET-UP TO DESCRIBE EVOLUTION PROCESS OF LEVEE BREACH

We analyze a process appearing in river, levee and floodplain in a same simulation scheme during flood. RIC-Nays, a two-dimensional (2D) model for flood flow and morphology is utilized in the present study upon confirmation through the experimental and other numerical study. It is developed by Hydraulic and Hydrology laboratory, Hokkaido University [12]; where shallow-water equations for 2D unsteady flow expressed in general coordinate system are solved on the boundary-fitted structured grids using the finite-difference method. Bed-load is calculated by Ashida and Michiue (1972) equation; the effect of cross-gradient and the influence of secondary flow, are taken into account [2], [4], [6]. In considering suspended sediment, an exponential profile of concentration is assumed to know planar distribution of depth-averaged concentration and the 2D advection-diffusion equations are solved. Finally the bed deformation is determined using the 2D sediment continuity equation. Equations are solved for the unknown nodal values by an iterative process. First the flow field is computed utilizing initial and boundary conditions; the sediment transport field is then computed, to evaluate sedimentation rates, and followed by bed topography changes. Fig. 2 depicts the outline of the simulation steps for computation.

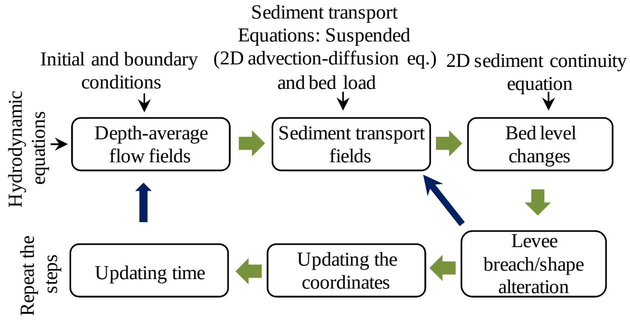

Fig. 2 Outline of model computation steps.

As for simulation scheme, the main channel, levee, floodplain and flow parameters are selected in conformity with the study field of Sirajganj district and Jamuna River in Bangladesh. Schematic model area is spatially limited in a part of actual field, which is 5500 times less in horizontal scale. For the first case of simulation, computation reach is 900 m long (L) and 500 m wide (Y) (river channel=100 m, levee=25 m and floodplain=375 m) with a bed slope of river channel is 7.5cm/km. Fig. 3 (a, b) depicts one of the model fields for simulation, which approximates the levee breach area of the JRE, Khokshabari and model layout with computational domain (square cells with Δx=5 m and Δy=5 m) of river channel, breach levee and floodplain, respectively.

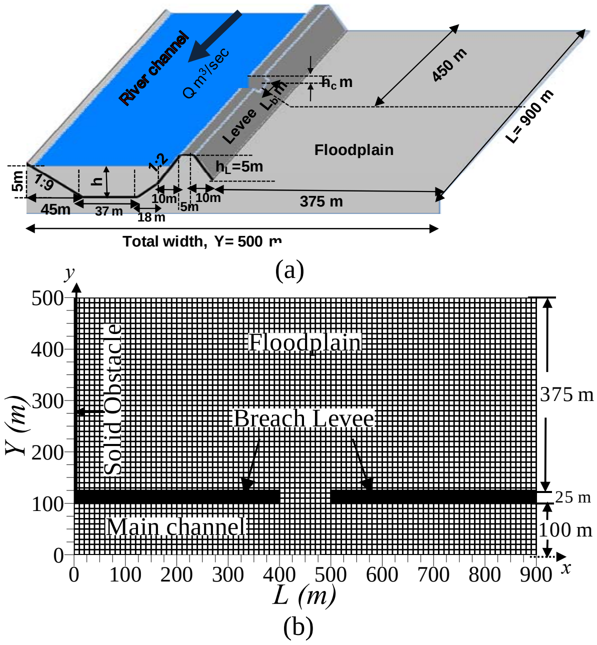

Fig. 3 (a) simulated model area; (b) Plan view of the reach with river channel, breach levee and floodplain.

The country side bank regions of main channel are provided with mild slope of 1:9. Levee slope is considered as S_l= 1:2 on both country side and river side and levee height is taken as h_L=5 m from the floodplain and 7 m from the river bed. Idealized flow and sediment parameters are considered in the computation: inflow discharge in the river channel before breach, 750 m^3/s (Q)

is considered with the peak flow of Jamuna River in flooding season, and the median size of sediment is chosen as d_m= 0.10 mm for the whole domain. Overflow starts from the hypothetical notch on top of the levee as a trigger of breach where initial breach is 100 m long (L_b) and crest height is 2 m (h_c) from the floodplain. Though the river discharge has a hydrograph in general, a uniform discharge corresponding to the peak is assumed here. Solid boundary is imposed on the left side of the floodplain.

4. MODEL VALIDATION

The present study model is verified with experimental and numerical data of Aureli and Mignosa (2001), where they investigated the flow velocity field near breach in the main channel without considering morphological change in the floodplain [3]. They were conducted the experiment in a laboratory flume which was 10 m long and 0.30 m wide and consider the breach region was 2.60 m long and 2.00 m wide. Inflow discharge and slope were maintained equal to $0.035 m^3 s^{-1}$ and 0.1%. The manning's roughness coefficient for the bottom and walls of the laboratory flume was 0.009 and breach width was considered as 0.28 m. The simulation time was 29.5 sec for computed and measured velocity profile. Longitudinal velocity measurement made at different sections with distances of y = 0.28, 0.26 and 0.16 m in the main channel are compared with the experimental and numerical values and Ric-Nays model results which are shown in Fig. 4, the present model results agree satisfactorily with the experimental and numerical data by Aureli and Mignosa as a whole but it was not perfect match due to the presence of solid wall normal to the breach opening in a laboratory flume and it induced strong curvature in the water surface with a vertical pressure distribution.

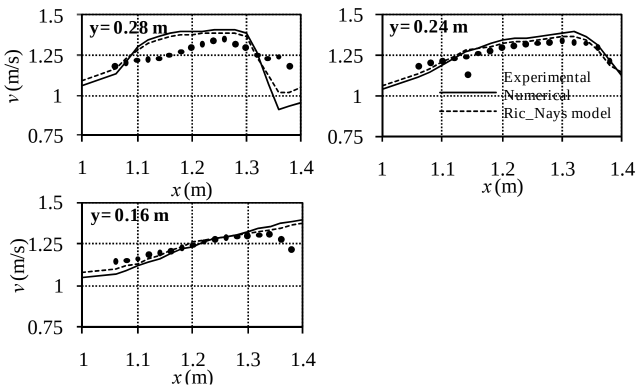

Fig. 4 Longitudinal velocity (v) profiles comparison between RIC-Nays model results with Aureli and Mignosa simulation and experimental data.

5. EFFECT OF FEATURES OF FLOW AND SEDIMENTATION PATTERNS OVER THE ALLUVIAL FLOODPLAIN

5.1 Effect of Inflow Duration

In Bangladesh, alluvial floodplain was formed by flooding and levees were constructed by dredging from river bed. Normally river bed is lower than the floodplain level. To observe the time dependent evolution process over the floodplain due to levee breach of 100 m is carried out for inflow discharges of 750 m^3/s each with duration of 3, 10 and 20 minutes, respectively for levee crest height of 2 m from floodplain and floodplain slope is not taken into consideration are shown in Fig. 5. Initially river water depth observed high and it decreased by increasing inflow duration in the main channel because of river flow diverted to the floodplain through breach with time. Floodplain inundation depth increased in certain duration. It can be concluded that after certain period of time at any specific discharges, inundation depth is not increase in the floodplain with time. The sediment deposition thickness is highest at just downstream of the levee breach and it decreased gradually towards the downstream of the floodplain with increases distance from the breach location. Fig. 6 depicts the transverse distribution of velocity and sedimentation profile in the main channel, levee and floodplain at x =450 m on breach with time. Overtopping water passes from the river to the floodplain through the breach initially at high velocity and the velocity reduces with time because of elevation difference in levee crest and floodplain. River water flows from left to right side in

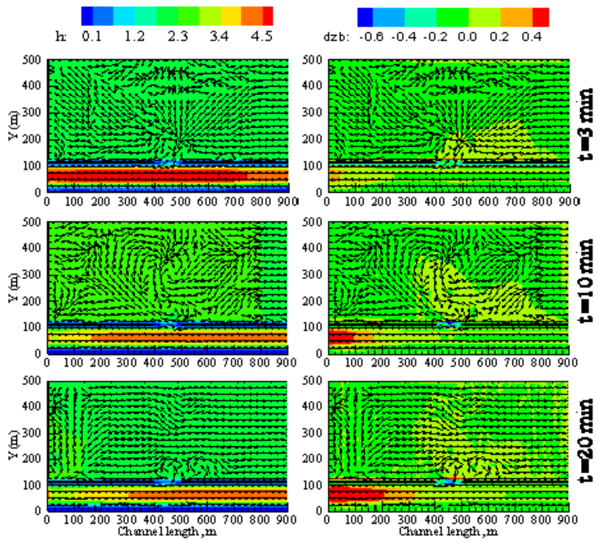

Fig. 5 Simulated flow field in the vicinity of the river, breach levee and floodplain (S= 0) where h_c = 2m from floodplain; contours indicate the water depth (h) and deviation of bed elevation (dzb) with time.

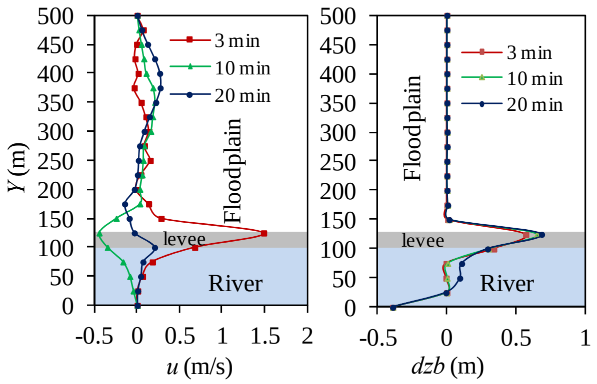

Fig. 6 Transverse distribution of velocity (u) and sedimentation (dzb) profile at x=450 m on breach with time where h_c=2m from floodplain.

the main channel and some portion of water diverted to the floodplain through breach levee. So, it is clearly seen that high velocity is observed at short duration near the breach inside the river, top of the levee and as well as floodplain adjacent to the breach. It is concluded that along the flow direction velocity is high and it decreased with time. Also, velocity distribution pattern is not same in the floodplain due to vortex form in the floodplain. Sediment deposition is occurred near the breach and it decrease along the flow direction in the floodplain. Depth of sedimentation increased with time and it is clearly observed at x =450 m.

Fig. 7 shows the comparison of flow and sedimentation pattern over floodplain where floodplains slope is taken into consideration as 10 cm/km. This slope criterion is taken from actual field condition. Due to sloping floodplain, mass transfer rate observed high from river to the floodplain through breach levee. Velocity of flow is changed rapidly in compare to without slope condition and slightly more sediment deposited in the sloping floodplain near to the breach.

Considering small crest opening as 1 m from top of levee and sloping floodplain as S = 10 cm/km, the transverse velocity and sedimentation profile in the main channel, levee and sloping floodplain at x = 450 m on breach with time are shown in Fig. 8. Inside the river, top of the levee and floodplain adjacent to the breach velocity is observed high and it decreased with time in the main channel. Also, near breach deposition is observed high as larger crest opening.

Using advection time ratio of 100, the time duration in the simulation corresponds to 33 hours in the field, which is within a possible range and the simulation covers long enough time span.

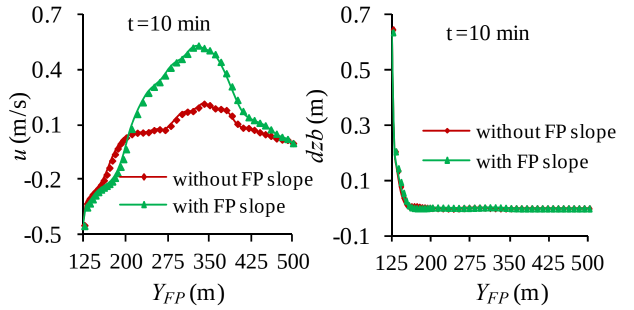

Fig. 7 Comparison of transverse distribution of velocity and sedimentation profile in the floodplain at x= 450 m on breach considering with and without floodplain slope where h_c=2m from floodplain.

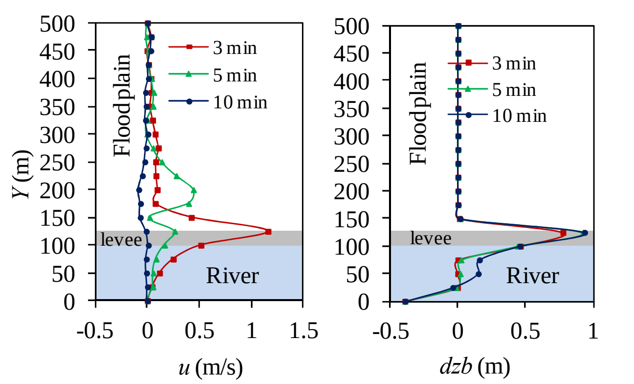

Fig. 8 Transverse distribution of velocity (u) and sedimentation (dzb) profile at x=450 m on breach with time where h_c=4m from floodplain.

5.2 Effect of Inflow Discharges

Inundation and sedimentation patterns over the floodplain at different discharges are shown in Fig. 9. To observe the discharge dependent inundation and sedimentation process over the floodplain due to levee breach of 100 m is carried out for 15 minutes each with inflow discharges of 700, 750 and 800 m^3/s, respectively. Floodplain inundation depth increased with increase of inflow discharges in the main channel. More area of floodplain sedimentation observed at high inflow discharge in the main channel. Transverse velocity and sedimentation profile in the main channel, levee and floodplain at x = 450 m on breach with discharge are shown in Fig. 10. Adjacent to the breach inside the river, top of levee and floodplain; velocity observed high at any inflow discharges and then it decreased suddenly in the floodplain due to river water passes through the levee crest at a high gradient to a low gradient in the floodplain. Sediment deposition area is increased and depth decreased by increasing inflow discharges in the main channel.

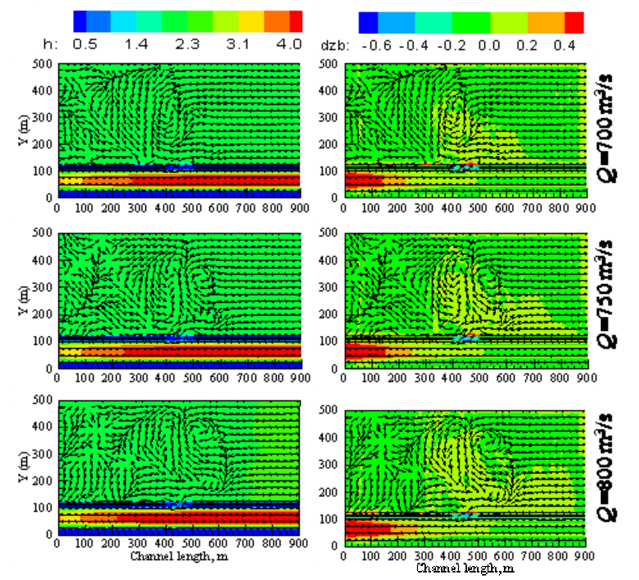

Fig. 9 Simulated flow field in the vicinity of the river, breach levee and floodplain where h_c = 2m from floodplain; contours indicate the water depth (h) and deviation of bed elevation (dzb) with inflow discharges.

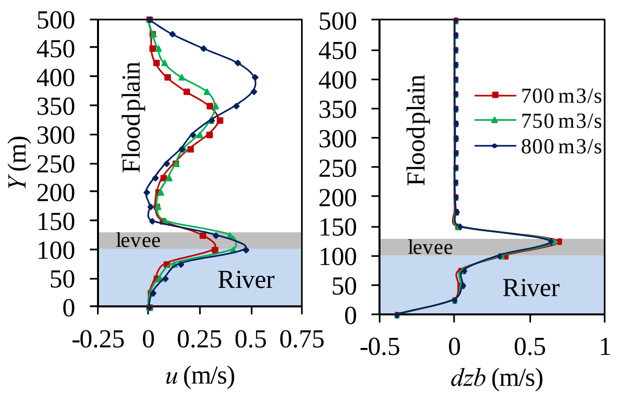

Fig. 10 Transverse distribution of velocity (u) and sedimentation (dzb) profile at x=450 m on breach with inflow discharges where h_c=2m from floodplain.

5.3 Effect of Breach Lengths on the Levee

Levee breach is considered to initiate in the middle of the levee with crest opening. To investigate inundation and sedimentation process over the floodplain with different lengths of levee breaches as 100 m, 200 m and 300 m, respectively are carried out with duration of 15 minutes and discharge of 750m^3/s which are shown in Fig. 11. Floodplain inundation depth increased with large breach opening than smaller one. Sedimentation depth and deposition area is more when overflow water passes at larger breach opening. At different breach opening length, the transverse velocity and sedimentation profile in the main channel, levee and floodplain at x =450 m on breach is shown in Fig. 12. Near breach velocity is observed high at small breach opening and the velocity is reduced by increasing breach length in the levee. Sediment depositions took place over the floodplain along the flow direction.

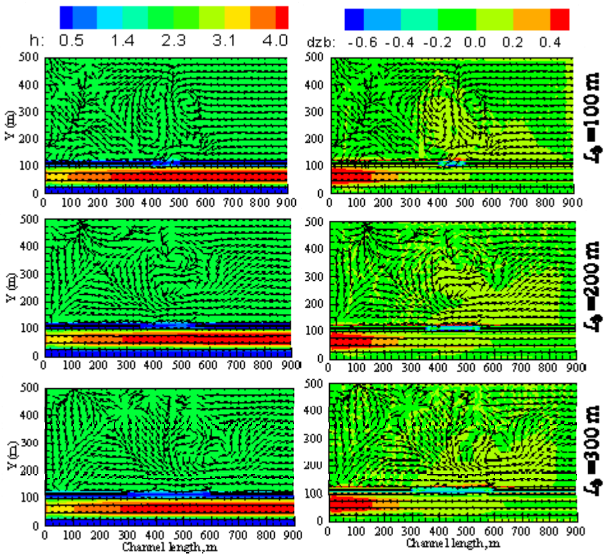

Fig. 11Simulated flow field in the vicinity of the river, breach levee and floodplain where h_c = 2m from floodplain; contours indicate the water depth (h) and deviation of bed elevation (dzb) with breaching lengths.

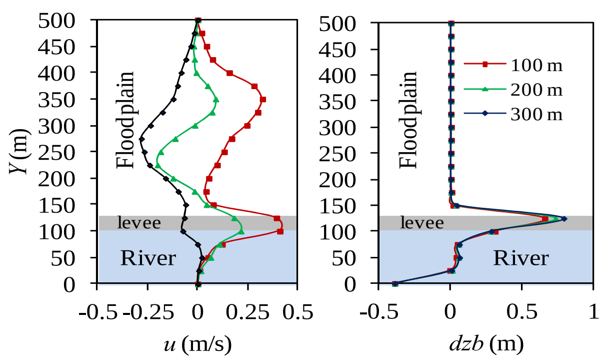

Fig. 12 Transverse distribution of velocity (u) and sedimentation (dzb) profile at x=450 m on breach by changing breach length where h_c=2m from floodplain.

6. LEVEE DEFORMATION DUE TO OVERFLOW THROUGH BREACH

Levee deformation is observed along the river flow direction at top of the levee (y=115 m). To investigate levee deformation through overflow breach of 100 m is carried out for 1 and 20 minutes, respectively and discharges, 750m^3/s and 1550 m^3/s for levee crest height of 2 m and 4 m from floodplain, respectively are shown in Fig. 13. We have seen that vertical deformation observed 0.4 m in 1 minute at h_c=4 m and no vertical erosion at h_c=2 m whereas 0.65 m and 0.45 m vertical erosion observed in 20 minutes at h_c=4 m and h_c=2 m, respectively.

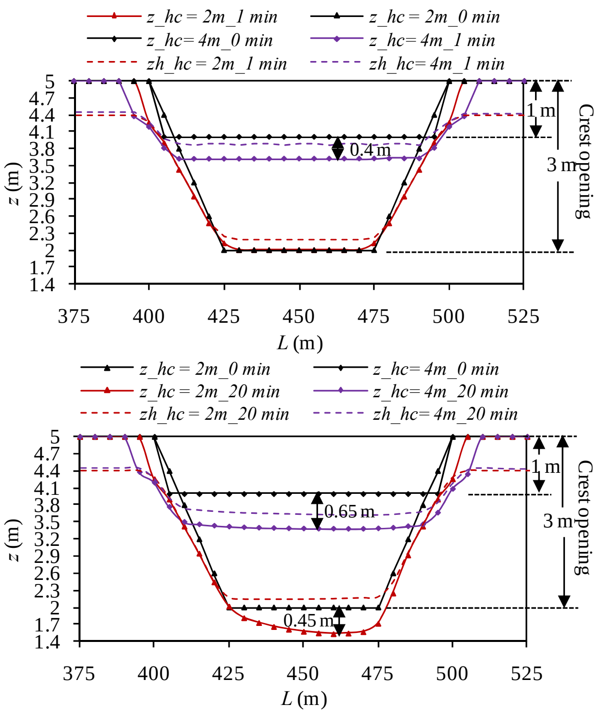

Fig. 13 Time dependent comparison of levee evolution process with crest opening at top of the levee (y= 115 m).

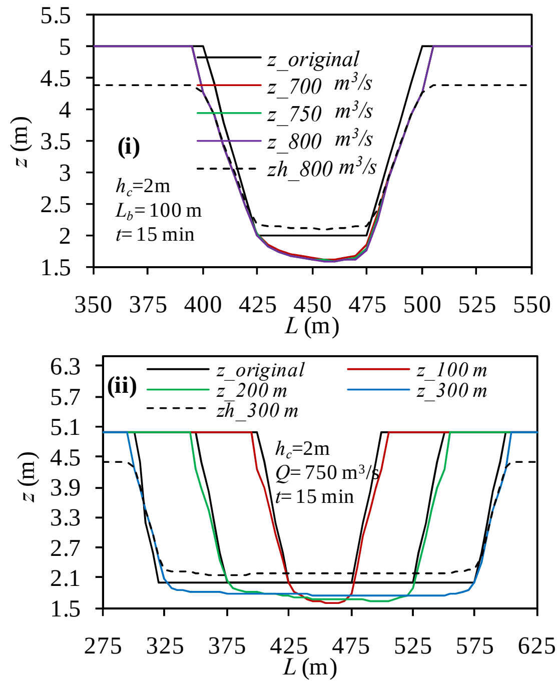

Fig. 14 Levee deformation at top of the levee (y= 115 m) with (i) inflow discharges; and (ii) different breach lengths.

Not only vertical erosion but also more horizontal erosion is observed when overtopping water passes through small crest opening in breach levee at h_c=4 m. It can be concluded that levee breach overflow causes more deformation and consequences as more sedimentation in the floodplain at small crest opening than larger one. Obviously, breaching section of higher duration is higher, and it results that the large amount of discharge causes serious inundation as well as sedimentation in the floodplain. To observe levee deformation is carried out for 15 minutes through breaches of 100 m and different discharges of 700, 750 and 800 m^3/s, respectively [Fig. 14 (i)] also different initial breach opening as 100, 200 and 300 m and discharge of 750m^3/s [Fig. 14 (ii)]. In discharge dependent conditions (i), slightly more vertical erosion is observed with inflow discharge increases in the main channel and breach length dependent conditions (ii), breach enlarged in vertical and horizontal direction for all length of breaches but vertical enlargement is observed more when water passing through small breach (100 m) opening as compared to larger (300 m) one.

7. CONCLUSIONS

The conclusions drawn are as follows:

i. Floodplain inundation depth is increased in certain duration. Inundation depth increased with increase of inflow discharge in the main channel and with large breach opening than smaller one.
ii. Near breach velocity is observed high both in the river and in the floodplain at short duration and any inflow discharges in the main channel. Velocity is reduced by increasing breach length in the levee.
iii. Sediment deposition is occurred near the breach and it decrease along the flow direction in the floodplain. Deposition depth increased with time, discharges in the main channel and breach length in the levee.
iv. Levee breach overflow causes more deformation and consequences as more sedimentation in the floodplain at small crest opening than larger one.

However, details laboratory experiments and field observation are required to get more clarification about the process of levee breach inundation and sedimentation as well as inhabitant's suffering who are lived in the alluvial floodplain. In the study area there are different land use pattern and effect of flood disasters are not same in everywhere. In order to get basic differences of flood disasters using various land type of study area we have plan for future study.

LIST OF SYMBOLS

The following symbols are used in this paper:

L	length of channel	m
Y	wide of channel	m
Y_{FP}	wide of floodplain,	m
S_L	levee side slope	-
S	floodplain slope	-
h_L	height of levee	m
t	time	min
Q	inflow discharge rate	m^3/s
d_m	mean sediment diameter	mm
b	length of levee breach	m
h_c	levee crest height	m
y	distance in y-direction	m
x	distance in x-direction	m
h	depth of flow	m
zh	water surface elevation	m
dzb	deviation of bed elevation	m
v	longitudinal velocity	m/s
u	transverse velocity	m/s
z	bed elevation	m

8. REFERENCES

[1] Ahmed SMU, Hogue MM and Hossain S, "Floods in Bangladesh: A Hydrological Analysis," Final Report R01/92, Institute of Flood Control and Drainage Research (IFCDR), Bangladesh University of Engineering and Technology(BUET), Dhaka, 1992, pp.1-5.

[2] Ashida K and Michiue M, "Studies on bed load transportation for non-uniform sediment and river bed variation," Disaster Prevention Research Institute Annuals, Kyoto University, No 14B, 1972, pp. 259-273 (in Japanese).

[3] Aureli F and Mignosa P, "Comparison between experimental and numerical results of 2D flows due to levee-breaking," XXIX IAHR Congress Proceedings, Theme C, September 16-21, 2001, Beijing, China

[4] Engelund F, "Flow and Bed Topography in Channel Bend" J. of Hydraulic Division, ASCE, Vol.100, No. 11, 1974, pp. 1631-1648.

[5] Fujita Y and Tamura T, "Enlargement of breaches in flood levee on alluvial plains," J. of Natural Disaster Science, Vol. 9, No. 1, 1987, pp. 37-60.

[6] Hasegawa K and Yamaoka S, "The Effect of plane and bed forms of channels upon the meander development," J. of Hydraulic, Coastal and Environmental Engineering, JSCE, Vol. 29, 1980, pp. 143-152 (in Japanese).

[7] Hossain MZ and Sakai T, "Severity of Flood Embankments in Bangladesh and Its Remedial Approach," Agricultural Engineering International: the CIGR E-journal, Manuscript LW 08 004, Vol. X, May 2008.

[8] Islam MZ, Okubo K and Muramoto Y, "Embankment Failure and Sedimentation over the Flood Plain in Bangladesh: Field Investigation and Basic Model Experiments," J. of Natural Disaster Science, Vol.16, No.1, 1994, pp. 27-53.

[9] Islam MZ, Okubo K, Muramoto Y, and Morikawa H, "Experimental Study on Sedimentation over the Floodplain due to River Embankment Failure," Bulletin of the Disaster Prevention Research Institute, Kyoto University, 44(2), 1994, pp. 69-92.

[10] Report on Flood Hazard Model, "Index Based Flood Insurance Products for Sirajganj District, Bangladesh,: Institute of Water Modeling (IWM), Dhaka, Bangladesh, 2010, pp 1-48.

[11] Sarker MH, Huque I, Alam M and Koudstaal R, "Rivers, chars, char dwellers of Bangladesh," Int. J. of River Basin Management, Vol. 1, 2003, pp. 61-80.

[12] Shimizu Y, "Ric-Nays model," Hydraulic and Hydrology laboratory, Hokkaido University, Japan, 2009.

[13] Tingsanchali T and Karim MF, "Flood hazard and risk analysis in the southwest region of Bangladesh," J. of Hydrological Process, Vol.19, 2005, pp. 2055-2069.

[14] Tsujimoto T, Mizoguchi A and Maeda A, "Levee breach process of a river by overflow erosion," Int. Conf. of Fluvial Hydraulics, Portugal 6-8 Sep. 2006.

First International Conference on Geotechnique, Construction Materials and Environment, Mie, Japan, Nov.21-23, 2011, ISBN: 978-4-9905958-0-7 C3051

Purification System of Ocean Sludge by Activating Microorganisms

Kyoichi OKAMOTO and Kenji HOTTA

Department of Oceanic Architecture and Engineering, CST, Nihon University

Takeshi TOYAMA

Department of Materials and Applied Chemistry, CST, Nihon University

Hideki KOHNO

Department of Applied Molecular Chemistry, College of Industrial Technology, Nihon University

ABSTRACT: Sludge exerts a very big environmental load to local sea area. Here, attention was paid to micro-bubble technology for application to the purification of sludge. The important point in this technique is to activate the bacteria existing in the area by micro-bubbles.
In this study, our objects are to develop a new powerful purification system for sedimentary sludge using a micro-bubble device and by activating microorganism. As the results of our experiments, we succeeded in reducing the time needed to purify the sludge.

Keywords: Micro-bubble, Microorganism, Purification, Sludge

1. INTRODUCTION

It is very important to reduce sedimentary sludge in the ocean. Plans to reduce the sludge are usually dreading or sand covering. Dredging is a simple way and aims to cut off the sludge. But after cutting off, treating the dredged sludge takes much more time and, of course, cost. Sand covering, in general, gives a big load to living organisms and the ecological system. Here, a more efficient way is needed to reduce the sludge while not imparting environmental load in the local sea area.
Now, we have micro-bubble technology. Micro-bubbles can change conditions into an aerobic state. If the bubbling stops, the situation changes into anaerobic state, according to recent research. So, we selected a method for decomposing the sludge by microorganisms.
Therefore, our research targets purification experiments on oceanic sedimentary sludge by micro-bubbles and microorganism activator.

2. EXPERIMENT

2.1 Experimental Devices

The experimental devices consist of two parts, shown in Fig. 1 and 2. The water circulates through two tanks. One tank generates micro-bubbles. The micro-bubbles have micro-size diameter and high solubility.
The other part is the experimental tank. The sludge is put in this tank. The two tanks are separated due to the high flow velocity created by the bubble generating pump.
We used sludge sampled from the ocean, as shown in Fig 3. Microorganism activator is used; this is liquid and mainly comprises Kelp and also includes nutrients and some enzymes.
Our used activator is reported to show effective results in purification for grease trap.

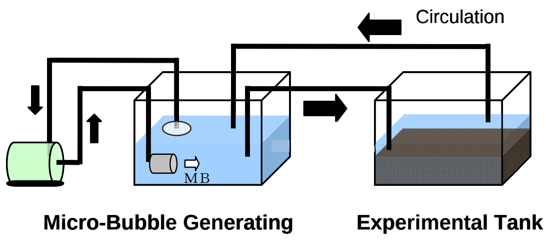

Fig. 1 Experimental Devices

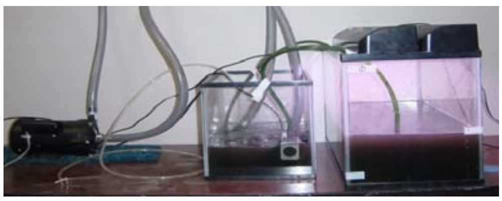

Fig. 2 Experimental Devices

Fig.3 Catching Sludge

2.2 Experimental Procedure

At first, the sludge is put in the tank and the micro-bubble device is powered on. After 6 hours, the microorganism activator is put in the tank. The measurement items are dissolved oxygen (DO), water temperature, pH, hydrogen sulfide (H2S), total nitrogen (T-N) and total phosphorus (T-P). In Case 8, only the micro bubble device was operated. Experimental condition is shown in Table 1.

Table 1 Experimental Conditions

Case	Room Temp. (degree)	Density of Activator (ppm)	Circulation Velocity (cm/s)
①	20	100	0.6
②	23	100	0.6
③	20	200	0.6
④	30	200	0.6
⑤	20	200	5
⑥	20	200	8.4
⑦	20	200	10.7
⑧	20	0	0.6

3. EXPERIMENT

3.1 DO, Water Temperature and pH as Environmental Conditions for this Experiment

Measured results of water temperature, pH and DO in all experimental cases are shown in Fig.4 to Fig.6, respectively. Water temperature up to 12 hours increased rapidly, and then became constant between 25 and 30 centigrade. It seems this was caused by the heat from friction of the micro-bubble device. pH up to 6 hours increased a little and then became constant. The constant value was 8.0 to 8.6. Dissolved oxygen up to 6 hours increased a little and then became constant. It seems oxygen dissolved and reached the saturation point. From these results, we can recognize anaerobic state changing into aerobic state.

It seems that these results are very good conditions for growth of microorganisms.

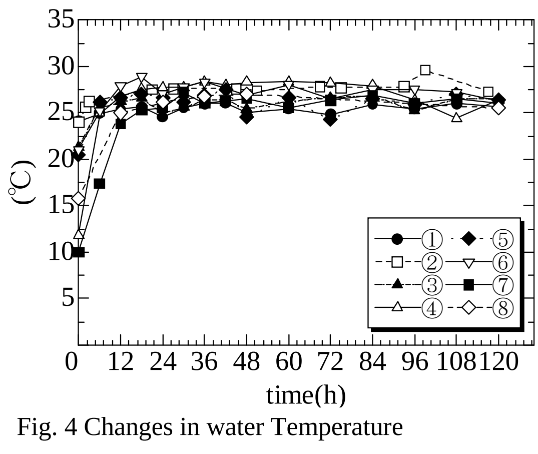

Fig. 4 Changes in water Temperature

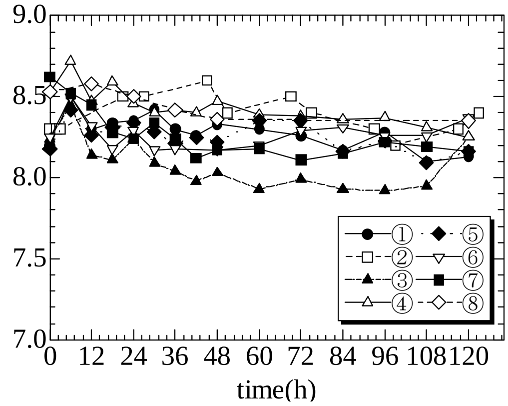

Fig. 5 Changes in pH

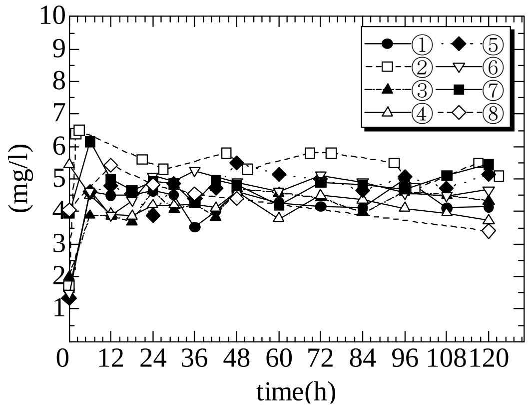

Fig. 6 Changes in DO

3.2 Effects on Activator of Microorganisms

Checking the mechanism in this experimental system, the density of sulfate was analyzed. Comparing with the effects on activator of microorganism, experimental conditions are shown in Table 2.

The density of sulfate is shown in Fig. 7. The result was obtained by the iron chromatography. The slope of the density of sulfate in Case 7 is bigger than the one in Case 3. But the slope in Case 8 is almost no change or less. It seems that sulfate increases due to the activity of sulfur bacteria. It also seems sulfate increases according to the circulation velocity. On the other hand, there is no effect in Case 8 for only bubbling.

The content of sulfur is shown in Fig. 8. This result was obtained by the elementary analysis. These are normalized expression divided by the initial value at time=0. The initial values are 3.18, 1.66 and 1.66 in the order of Case 3, 7, 8.

Especially in Case 3, the content of sulfur up to 6 hours did not change but after 6 hours it decreased rapidly since the activator of microorganisms was put in the experimental tank after 6 hours. It seems that microorganisms changed the sludge into the sulfur.

This is similar in Case 8 which is only bubbling. But we cannot see the same thing in Case 7 in which circulation velocity is fast, and also the values decrease.

Table 2 Experimental condition for checking the mechanism

Case	Room Temp. (degree)	Density of Activator (ppm)	Circulation Velocity (cm/s)
③	20	200	0.6
⑦	20	200	10.7
⑧	20	0	0.6

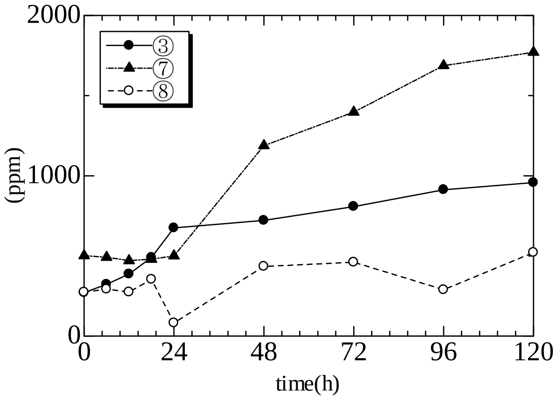

Fig. 7 Result of density of sulfate

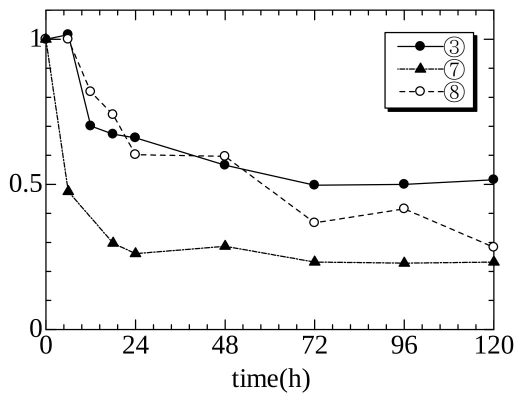

Fig. 8 Result of content of sulfur

3.3 Effects of Purification in Relation to Water Temperature

We checked the effects of purification in relation to the water temperature. Comparing with the water temperature, experimental conditions are shown in Table 3. When the density of activator is 100 (ppm), Case 1 and Case 2 are shown. When the density of activator is 200 (ppm), Case 3 and Case 4 are shown. Case 8 is only bubbling by the micro-bubble device. The H2S is shown in Fig.9, and also the reduction speed of H2S in Fig.10.

When the density of activator was 100 (ppm), comparing with Case 1 and Case 2, the reduction speeds of H_2S in Case 1 was faster than in Case 2, and then the average water temperature in Case 1 was 25.1 degrees centigrade.

When the density of activator was 200 (ppm), comparing with Case 3 and Case 4, the reduction speeds of H_2S in Case 3 were faster than in Case 4, and then the average water temperature in Case 3 was 25.7 degrees centigrade.

Therefore, the reduction speed of H_2S is more effective at water temperature of about 25 degrees centigrade, but purification at over 25 degrees centigrade takes a little longer. Moreover, H_2S except in Case 8 was reduced to the lower limit for measurement within 24 hours. H_2S in only bubbling case in Case 8 took a little longer.

Table.3 Experimental condition for purification effect in relation to water temperature

Case	Room Temp. (degree)	Density of Activator (ppm)	Circulation Velocity (cm/s)
①	20	100	0.6
②	23	100	0.6
③	20	200	0.6
④	30	200	0.6
⑧	20	0	0.6

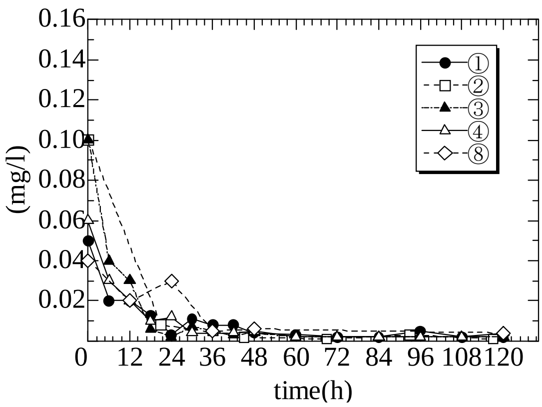

Fig. 9 Changes in H_2S

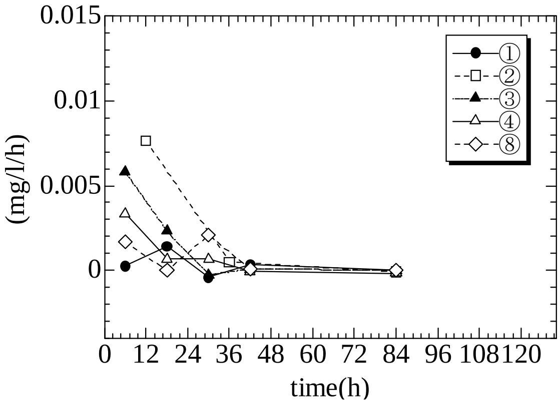

Fig. 10 Changes in speed of H_2S

Measured results of T-N and T-P are shown in Fig. 11 and 12, respectively. T-N has tendency of decreasing. Reduction ratio of T-N has no differences among all cases. T-P has also no difference among all cases. Here, water temperature does not influence the reduction ratio on T-N and T-P.

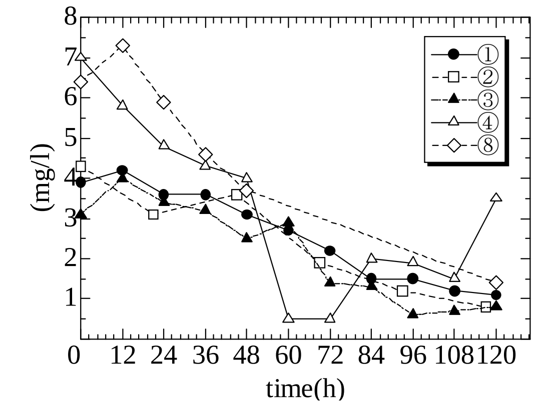

Fig. 11 Changes in T-N

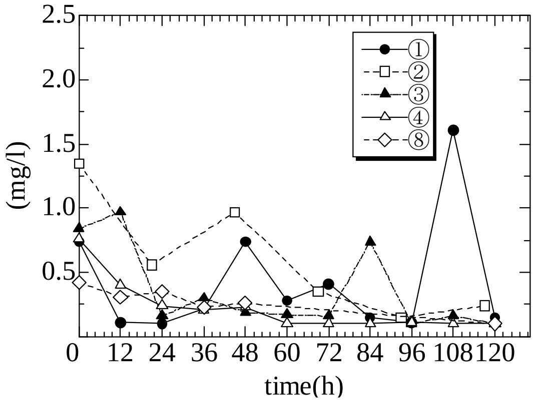

Fig. 12 Changes in T-P

3.4 Effects of Purification in Relation to Circulation Velocity

We checked the effects of purification in relation to the circulation velocity. Comparing with the circulation velocity, experimental conditions are shown in Table 4. Measured results of H_2S are shown in Fig.13 and also the reduction speed of H_2S in Fig.14. The reduction speed in Case 7 was faster than in the other cases. When the circulation speed became faster, reduction speed became faster. However, we could not clarify the maximum circulation speed for suitable purification. Moreover, reduction of H_2S in the case of only bubbling in Case 8 took a little longer.

Measured results of T-N and T-P are shown in Fig. 15 and 16, respectively. T-N in all cases decreased. Reduction speed of T-N in Case 7 was almost the same or a little faster. This was caused by the high initial value of Case 7. T-P in all cases decreased. The circulation speed does not influence the reduction of T-N and T-P. T-P in Cases 3, 5 and 6 increased from 0 to 24 hours, but it did not increase in Cases 7 and 8. It is assumed the circulation velocity in Case 7 was too fast to allow microorganisms to grow.

Table 4 Experimental condition for purification effect in relation to circulation velocity

Case	Room Temp. (degree)	Density of Activator (ppm)	Circulation Velocity (cm/s)
③	20	200	0.6
⑤	20	200	5
⑥	20	200	8.4
⑦	20	200	10.7
⑧	20	0	0.6

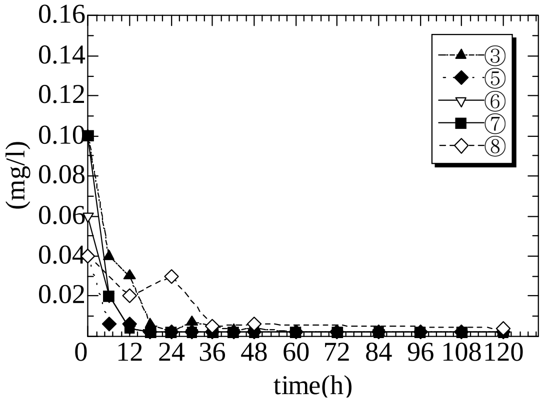

Fig.13 Changes in H_2S

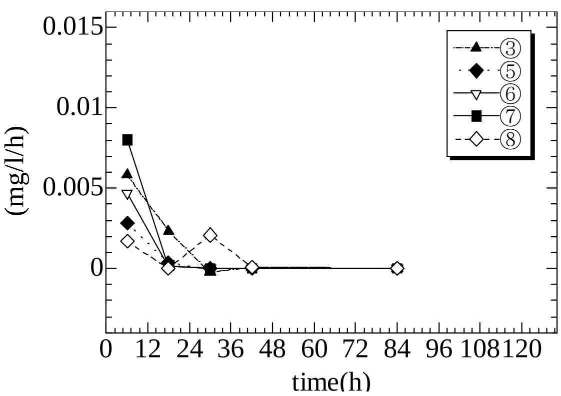

Fig.14 Changes in speed of H_2S

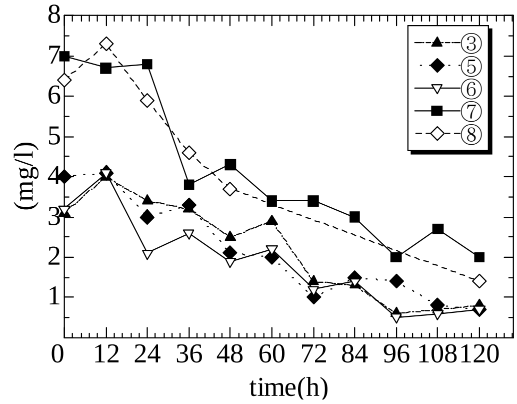

Fig.15 Changes in T-N

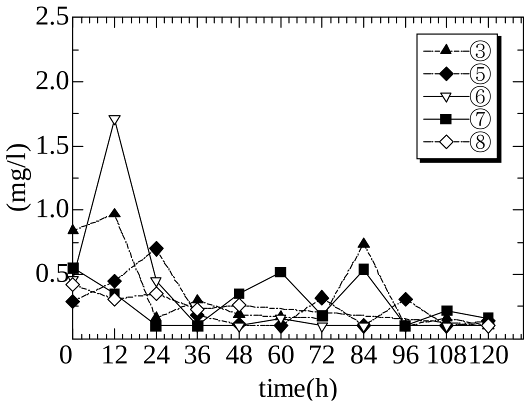

Fig.16 Changes in T-P

4. CONCLUSION

We carried out purification experiments on oceanic sedimentary sludge by micro-bubbles and microorganism activator.

As a result, our system could purify the sludge up to 120 hours by microorganism activation. Our system could reduce the hydrogen sulfide in the sludge to the lower limit for measurement within 24 hours.

As the mechanism for our experimental system, it seems that microorganisms change the sludge into the sulfur.

From the comparison with water temperature, it seems microorganisms are more active at around 25 degrees centigrade and purification takes a long time when the temperature is over 25 degrees centigrade.

From the comparison with the circulation velocity, the purification speed of hydrogen sulfide accelerates as circulation speed gets faster.

5. ACKNOWLEDGMENT

The authors would like to express sincere thanks to Mr. M. Machida, the former graduate student of Nihon University, in Japan.

6. REFERENCES

[1] Hibino, T, and Matsumoto, H (2006). “Distribution of Fluid Mud Layer in Hiroshima Bay and its Seasonal Variation”, Proc. Civil Engineering, Vol. 62, No 4, pp 348-359.

[2] Okamoto, K, and Hotta, K (2008). “An Experiment on Purification of Water Quality by Coagulants and Micro Bubble” Book of Recent Advances in Marine Science and Technology

[3] Mizoguchi, M (1996). “Observation of Water Purification Process in a Moat by Microbiological Treatment Technique”, Proceedings of Biological Resource in Mie University, No.16, pp.25-37.

[4] Matsui, R, Okamoto, K, and Hotta, K, (2006). "Water Purification Experiments by Micro Bubble", Book of Recent Advances in Marine Science and Technology, pp 119 126.

[5] Matsuo, K, Maeda, K, Ohnari, H, Tsunami, Y, and Ohnari H, (2006). “Water Purification of a Dam Lake Using Micro Bubble Technology”, Progress in Multiphase Flow Research I, pp.279-286

PROCEEDINGS OF FIRST INTERNATIONAL CONFERENCE - GEOMAT2011
GEOTECHNIQUE, CONSTRUCTION MATERIALS AND ENVIRONMENT MIE JAPAN, 21-23 NOVEMBER, 2011

Geotechnique, Construction Materials and Environment

Volume 2

Edited by

Md. Zakaria Hossain
Department of Environmental Science and Technology
Mie University

Toshinori Sakai
Department of Environmental Science and Technology
Mie University

THE GEOMATE INTERNATIONAL SOCIETY, MIE 2011

Published by:
The GEOMATE International Society
Tsu city, Mie, Japan
E-mail: geomate@gi-j.com
www.gi-j.com

ISBN Number: 978-4-9905958-0-7 C3051

Printed in Japan

First International Conference on Geotechnique, Construction Materials and Environment, Mie, Japan, Nov.21-23, 2011, ISBN: 978-4-9905958-0-7 C3051

Table of Contents

First International Conference on Geotechnique, Construction Materials and Environment, Mie, Japan, Nov.21-23, 2011, ISBN: 978-4-9905958-0-7 C3051

Preface

The First International Conference on Geotechnique, Construction Materials and Environment GEOMAT2011 is organized in Center Palace Miyako Hotel, Tsu city, Mie Japan in conjunction with Japanese Geotechnical Society (JGS), Japanese Society of Irrigation Drainage and Rural Engineering (JSIDRE), Mie University, JCK Comp. Ltd and Glorious International. It aims to provide with great opportunities to share common interests on geo-engineering, construction materials, environmental issues, water resources, and earthquake and tsunami disasters. The key objective of this conference is to promote interdisciplinary research from various regions of the globe. On Friday 11 March at 14:46 Japan Standard Time, the north east of Japan was severely damaged by the tragic earthquake and tsunami. The conference is dedicated to the tragic Tohoku-Kanto earthquake and tsunami disasters.

The conference has 3 major themes with 17 specific themes including

- Advances in Composite Materials
- Computational Mechanics
- Foundation and Retaining Walls
- Slope Stability
- Soil Dynamics
- Soil-Structure Interaction
- Pavement Technology
- Tunnels and Anchors
- Site Investigation and Rehabilitation
- Ecology and Land Development
- Water Resources Planning
- Environmental Management
- Public Health and Rehabilitation
- Earthquake and Tsunami Issues
- Safety and Reliability
- Geo-Hazard Mitigation
- Case History and Practical Experience

The proceedings contain 7 keynote papers along with 115 technical papers from 22 countries. The technical papers are selected from the vast number of contributions submitted, after review of the abstracts. The final papers included in the proceedings have been peer reviewed rigorously and revised as necessary by the authors. We are grateful to the authors of the contributed papers for their resourceful papers and their help in maintaining the high assessment of the papers and the co-operation in complying with the requirements of the editor and the reviewers. We wish to express our sincere thanks to the Organizing Committee Members, National Advisory Committee Members and International Advisory Committee Members for their valuable supports. We acknowledge the support of Japanese Geotechnical Society (JGS), Japanese Society of Irrigation Drainage and Rural Engineering (JSIDRE), Mie University, JCK Comp. Ltd and Glorious International.

Prof. Dr. Toshinori Sakai
Conference Chairman

Dr. Md. Zakaria Hossain
Conference Secretary

Organization

Scientific Committees:

Conference Chairman: Prof. Dr. Toshinori Sakai, Mie University, Japan
Conference Honorary Chairman: E/Prof. Dr. Sohji Inoue, Mie University, Japan

Conference Organizing Committee:

Prof. Dr. Takamitsu Kajisa, Mie University, Japan
Prof. Dr. Ishiguro Satoru, Mie University, Japan
Prof. Dr. Sigeko Haruyama, Mie University, Japan
A/Prof. Dr. Atsushi Ishii, Mie University, Japan
A/Prof. Dr. Maasaki Kondo, Mie University, Japan
A/Prof. Dr. Kenji Okajima, Mie University, Japan
A/Prof. Dr. Ryoei Ito, Mie University, Japan

National Advisory Committee:

Prof. Dr. Fumio Tatsuoka, Tokyo University of Science, Japan
Prof. Dr. Kazunori Uchida, Kobe University, Japan
Prof. Dr. Fusao Oka, Kyoto University, Japan
Prof. Dr. Jing-Cai Jiang, University of Tokushima, Japan
Prof. Dr. Akira Murakami, Kyoto University, Japan
E/Prof. Dr. Tadatsugu Tanaka, University of Tokyo, Japan
A/Prof. Dr. Kingshuk Roy, Nihon University, Japan
A/Prof. Dr. Md. Shahin Hossain, Nagoya Institute of Technology, Japan
A/Prof. Dr. Sayuri Kimoto, Kyoto University, Japan
Engr. Hirondo Inagali, President, JCK Com. Ltd. Japan
A/Prof. Dr. Inui Toru, Kyoto University, Japan
A/Prof. Dr. Fujisawa Kazunori, Okayama University, Japan
A/Prof. Dr. Inoue Kazuya, Kobe University, Japan

International Advisory Committee:

Prof Sai Vanapalli, University of Ottawa, Canada
Prof. Dr. Mounir Bouassida, National School of Engineering of Tunis
Prof. Dr. Lilia Robles Austriaco, Angles University Foundation, Philippines
Prof. Dr. A.S.M. Abdul Awal, University Technology Malaysia, Malaysia
Prof. Dr. Muhammad Ibn Ibrahimy, International Islamic University, Malaysia
Prof. Dr. Zahurul Islam, Bangladesh University of Engineering and Technology, Bangladesh
Prof. Dr. Bujang B.K. Huat, University Putra Malaysia, Malaysia
Prof. Dr. Nemy Banthia, University of British Columbia, Canada
Prof. Dr. Ian Jefferson, University of Birmingham, UK
Prof. Dr. John Bolander, Univesity of California, USA
Prof. Dr. Shamshul Chowdhury, Roosevelt University, USA
Prof. Dr. Isabel Pinto, University of Coimbra, Portugal
A/Prof. Mark Jaksa, University of Adelaide, Australia
A/Prof. Dr. William Sebudde Kaggwa, University of Adelaide, Australia
Dr. John N. Mukabi, President of Kenya Geotechncal Society, Kenya

Conference Secretariat:

Dr. Zakaria Hossain, Associate Professor
Division of Environmental Science and Technology
Graduate School of Bioresources
Mie University, 1577 Kurima Machiya-cho
Tsu-city, Mie 514-8507, Japan
E-mail: zakaria@bio.mie-u.ac.jp
Tel: +81-59-231-9578、Fax: +81-59-231-9591

Editorial Committee:

Md. Zakaria Hossain
Md. Bellal Hossain
Toshinori Sakai
Md. Toriqul Islam

Executive Committee:

Toshinori Sakai
Md. Zakaria Hossain
Md. Bellal Hossain
Kazuki Ito
Md. Toriqul Islam
Muhammad Ibn Ibrahimy
Ms. Emi Ueno
Ms. Mayumi Matsumoto

First International Conference on Geotechnique, Construction Materials and Environment, Mie, Japan, Nov.21-23, 2011, ISBN: 978-4-9905958-0-7 C3051

Characterization and Modeling of Various Aspects of Pre-failure Deformation of Clayey Geomaterials – Applications in Modeling

John N. MUKABI* and Zakaria HOSSAIN**

*EngineerIntel – Research & Development Department, Kensetsu Kaihatsu Consultants, Nairobi, Kenya
**Division of Environmental Science and Technology, Graduate School of Bioresources, Mie University, Japan

ABSTRACT: Having undertaken comprehensive analysis in characterizing various aspects of clayey geomaterials, the expanded applications of the fundamental theories and geo-concepts developed from that knowledge are discussed in simulating the impact of geotechnical changes through modeling. Of particular interest is the simulation of post-seismic and/or dynamic loading destructuration. Destructuration and restructuration models are then introduced through engineering application of a versatile GECPRO (Geotechnical Engineering Changes Probing) Model, developed from a mechanistic-empirical geo-mathematical perspective, designed to probe, predict and simulate changes in geo-properties of clayey ground and geomaterials. Applications of the GECPRO model in bridging the small strain parameters determined from the field as well as sophisticated laboratory tests and, the failure parameters measured in the laboratory, which are vital in geotechnical engineering design, whilst probing geo-changes, are also demonstrated.

Keywords: model, destructuration, reconsolidation, restructuration, geo-changes, GECPROM

1. INTRODUCTION

The response and behavior of ground or geotechnical structures subjected to seismic loading is, in most cases, complex and challenging to the geotechnical engineer. Such challenges can only be progressively solved through intensive Research & Development involving the application of sophisticated testing equipment, advanced analytical tools, as well as highly undisturbed samples in the case of laboratory testing. Nevertheless, this can be economically curtailing particularly for developing and least developed countries. Furthermore, the continuously changing physical environment in the face of global astronomical development and increased intensity and frequency of seismic action only serves to aggravate the situation.

Consequently, it is imperative that techniques which are versatile yet reasonably affordable and able to provide reliable solutions to such challenges be developed.

Mukabi et al. [1] introduced some recently developed geo-scientific theories, concepts and geo-mathematical functions providing the basis for some new perceptions and approaches that can be incorporated within global geotechnical engineering systems aimed at enhancing precision and confidence levels of data, parameters, as well as constitutive and numerical models that are employed in the characterization of ground and geomaterials for design, construction control as well as risk prediction and mitigation. The importance of adopting the Modified Critical State Theory (MCST) and the most versatile modes of applying the Consolidation and Stress Ratio (CSSR) functions were also briefly introduced in [1].

2. MODELING PROPERTIES ASSOCIATED WITH DESTRUCTURATION

2.1 Introduction of Generalized Models

The generalized models are proposed for the characterization of stiff to very stiff (hard) well cemented and highly structured Pleistocene clays reconsolidated tracing any designated anisotropic stress path and subjected to static and/or dynamic (monotonic and/or cyclic) loading under undrained and/or drained conditions. Conceptual models for four aspects of destructuring, namely; swelling, cyclic prestraining, SHANSEP reconsolidation and remolding (reconstitution) and two models for restructuration (ageing and controlled prestraining) [1], are proposed. The generalized models are schematically depicted in Figs. 2.1, 2.2 and 2.4.

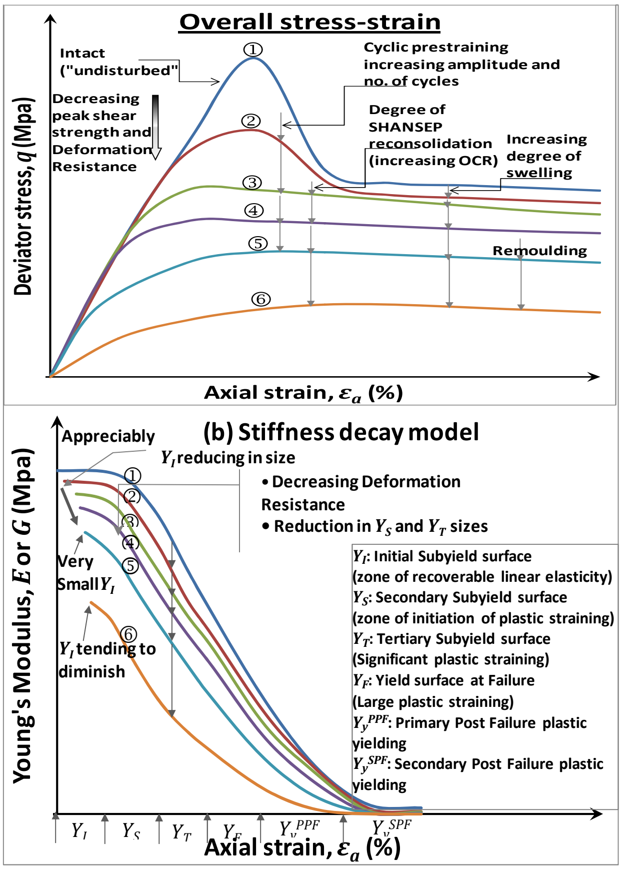

Figure 2.1 Projection Models for: (a) Overall stress ~ strain $\{(\varepsilon_a)_{FYS}(Y_F)\}$., and, (b) Stiffness decay characteristics $\{(\varepsilon_a)_{ELS}(Y_I)\} \sim \{(\varepsilon_a)_{FYS}(Y_F)\}$.

Some of the basic mathematical relations that are applicable in the respective models within Y_I and Y_S sub-yield envelopes are introduced hereafter. Modeling of the behavior within the rest of the sub-yield can be determined retrospectively, by interpolation or extrapolation based on the concepts and equations introduced in this Study.

It is important to note that, whereas the sizes of the sub-yield and yield surfaces may be determined from yield strain and 3D Transformation Mapping method proposed in this Study, derivation of the shape, directions of strain increment vectors as well as magnitude and rate of engagement, engulfment, and diminishing rate is rather complex [1] and has yet to be investigated comprehensively.

2.2 Damage Caused by Swelling

In this case, the simulation considers a model whereby mainly suction stresses and moisture equilibrium (gradients) change as a result of loading components and environmental factors and destructures (ref. to Fig. 2.2).

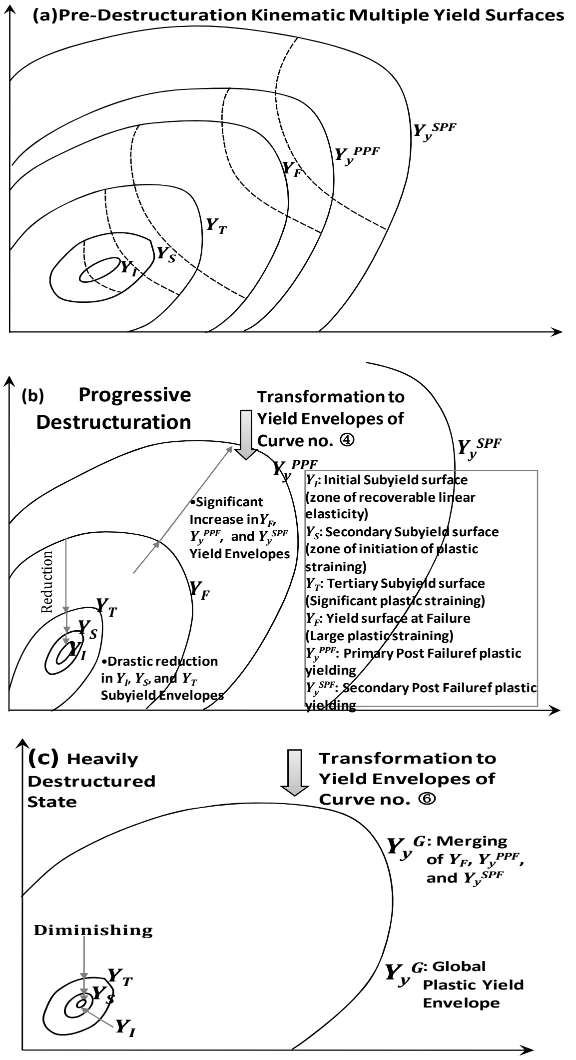

Figure 2.2 Varying states of destructuration models; (a) Pre-destructuration kinematic multiple yield surfaces depicting mode of engulfment, (b) progressive destructuration and, (c) Heavily destructured state.

2.3 Damage Caused by Prolonged Cyclic Prestraining

The damage and/or change in the geotechnical engineering properties and characteristics caused by light densification was investigated by performing Cyclic Prestraining (CP). Fig. 2.3 compares the stress-strain behavior of lightly prestrained to non-prestrained characteristic curves. The results indicate that although the CP effects are virtually insignificant in the Y_I zone, they become exceedingly pronounced in the subsequent zones up to post-failure. Furthermore, the overall stress ~ strain behavior presented in Fig. 2.3 shows that the CP specimen exhibits a considerably lower peak strength and less brittle characteristics in the region of large scale plastic straining.

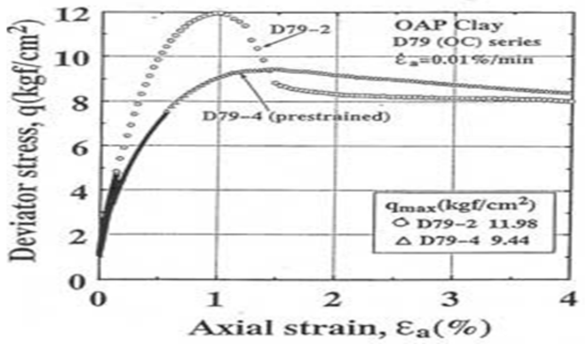

Figure 2.3 Comparison of cyclically prestrained stress ~ strain characteristics for (a) Overall stress ~ strain relations $\{(\varepsilon_a)_{ELS}(Y_I)\} \sim \{(\varepsilon_a)_{FYS}(Y_F)\}$ ($\varepsilon_a \leq 4\%$).

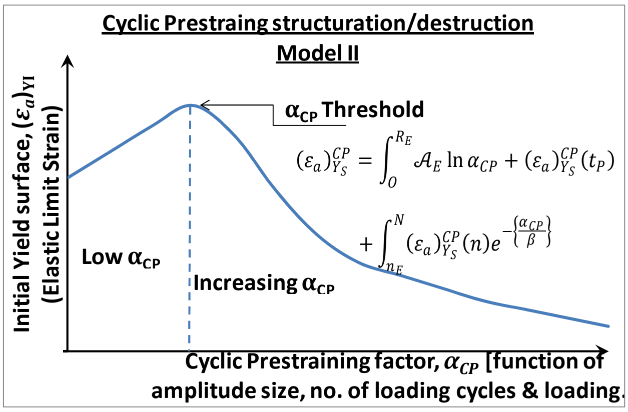

Figure 2.4 Cyclic Prestraining structuration/ destruction model [Initial Yield Surface $\{(\varepsilon_a)_{ELS}(Y_I)\}$].

The modeling functions are defined as:

$$[G_o]_{CP} = \int_O^{R_E} \mathcal{A}_E \ln \alpha_{CP} + [G_o]_{CP}(t_P) + \int_{n_E}^{N} [G_o]_{CP}(n) e^{-\left\{\frac{\alpha_{CP}}{\beta}\right\}} \qquad (1)$$

$$(\varepsilon_a)_{Y_S}^{CP} = \int_O^{R_E} \mathcal{A}_E \ln \alpha_{CP} + (\varepsilon_a)_{Y_S}^{CP}(t_P) + \int_{n_E}^{N} (\varepsilon_a)_{Y_S}^{CP}(n) e^{-\left\{\frac{\alpha_{CP}}{\beta}\right\}} \qquad (2)$$

Fundamentally, the preliminary study on this topic tends to show that, depending on the magnitude of the amplitude, number of loading cycles and frequency, CP may enhance the inherent microstructure linear elastic and recoverable properties as well as the deformation resistance and shear strength; or otherwise damage, or even completely destroy the soil structure (microstructure, fabric) of well structured and cemented Pleistocene clays [1].

2.4 Destruction Caused by Heavy Densification (SHANSEP Reconsolidation)

In this case, destruction caused by heavy densification is simulated by adopting the SHANSEP concept. As discussed in the preceding sections, densification within the natural boundary limits of a geomaterial enhances its properties. However, excessive densification beyond the yield stress leads to large scale straining (softening) and destruction of cementation, bonding and thixotropic components as well as causing change in the preferred particle orientation and inherent/induced anisotropic properties of natural clayey geomaterials. The basic definition functions of this characterization are presented in the following equations where the degree of destruction due to densification is expressed as a function of OCR.

(1) For OCR≦2.5

$$E_o^R = \frac{(E_o)_y^R}{(E_o)_{Ref.}} \times 10^4 \times \begin{bmatrix} \mathcal{A}_{OCR}OCR^4 - \mathcal{B}_{OCR}OCR^3 \\ +\mathcal{C}_{OCR}OCR^2 - \mathcal{D}_{OCR}OCR + \mathcal{E}_{OCR} \end{bmatrix} \text{(Mpa)} \qquad (3)$$

Where, $(E_o)^R$ is the resulting initial modulus, $(E_o)_{ref}$ =915Mpa is the reference initial modulus, $(E_o)_y^P$ is the pseudo-yield initial modulus determined at the stress level (pseudo-yield stress) which is higher than the yield stress $(\sigma'_a)_y$ and from which the specimen is rebound [1], expressed as;

$$(E_o)_y^P = (E_o)_{\sigma'_{ao}} \times \left[(\sigma'_a)_y^P \big/ (\sigma'_{ao})_y^{NC} \right]^{0.39} \qquad (4)$$

and, $\mathcal{A}_{OCR}$=0.225, $\mathcal{B}_{OCR}$=1.78, $\mathcal{C}_{OCR}$=5.22, $\mathcal{D}_{OCR}$=6.85 and $\mathcal{E}_{OCR}$ = 4.1 are constants for stiff to hard Pleistocene clays determined in this Study.

(2) For OCR>2.5

$$E_o^R = (E_o)_y^P \times OCR^{-0.39} \qquad (5)$$

Deterioration leading to the reduction of the initial yield strain $\{(\varepsilon_a)_{ELS}(Y_I)\}$ (Elastic Limit Strain) is defined from the equation below.

$$[\varepsilon_a]_{Y_I}^R = \mathcal{A}_{ys} \ln OCR + (\varepsilon_a)_{Y_I}^{py} \qquad (6)$$

Where, $[\varepsilon_a]_{Y_I}^R$ is the resulting size of the initial yield strain, $(\varepsilon_a)_{Y_I}^{py}$ is the initial yield strain determined at the pseudo-yield stress level and $\mathcal{A}_{ys}$ =3.1×10^{-3} is the geomaterial constant.

2.5 Destruction Caused by Remolding (Reconstitution) – Destructuration Model

As discussed in [1], reconstitution of natural clays results in total remolding and destruction of the vital structural components, fabric, diagenetic properties, inherent anisotropy and; transformation to enhanced rheological behavior of otherwise well cemented and highly structured Pleistocene clays. This model considers cases whereby clayey ground is subjected to strong vibrational and/or earthquake loading, resulting in large plastic straining. Consequently, characterization of the behavior of progressive failure and determination of the original in-situ properties [2] based on retrospective analysis for purposes of performance based design and prediction, is considered of utmost importance. A Destructuration Index, $\mathcal{D}_I$ which defines the degree of destruction as a result of seismic loading, is introduced as:

$$\mathcal{D}_I = \frac{S_f a_g}{S_r g} \qquad (7)$$

where, S_f is a soil factor depending on the seismic zone considering local amplification due to stratification of subsoil and topographic effects, a_g is the reference peak ground acceleration, g is the gravity of acceleration and S_r is the soil resistance to deformation. $\mathcal{D}_I$ is introduced into the CSSR functions [3] that quantitatively correlate the non-disturbed properties to those of the remolded ground enabling the retrospective derivation of the intact (non-disturbed) initial shear/Young's modulus and initial yield strain (Elastic Limit Strain) from the proposed equations expressed as:

$$[G_o]_I = \left[\frac{\mu_e^R \eta_c}{K_{cf}^R - \{\mu_e^R A_\phi f_{CSR}^R\}} \right] \times \mathcal{D}^{-1} \times [G_o]_R \qquad (8)$$

where, $[G_o]_I$ is the initial shear modulus of the intact ground and $[G_o]_R$ is the initial shear modulus determined from CU TC and CD TC laboratory tests performed on specimens reconstituted from the original clayey geomaterial.

The corresponding elastic yield strain is determined as:

$$[\varepsilon_a]_{Y_I}^I = \left[\frac{\mu_e^R \eta_c}{K_{cf}^R - \{\mu_e^R A_\phi f_{CSR}^R\}} \right] \times \mathcal{D}^{-1} \times [\varepsilon_a]_{Y_I}^R \qquad (9)$$

3. QUASI-RESTRUCTURATION MODELS

Due to the diagenetic, intricate nature and complexity of natural well cemented and highly structured clayey geomaterials, perfect recoverability is most definitely not envisaged. Nevertheless, it is considered that, with ageing, restructuration can be achieved to a certain degree [1]. As a consequence, the restructuration models are defined predominantly as functions of secondary consolidation time. The coupling effect of strain amplitude and loading rate controlled CP has not been exhaustively examined for its inclusion in this Study.

The post-destructuration Structural Recoverability Models (SRM) are mathematically defined in the following equations.

$$E_o^{SR} = \mathcal{A}_{SR}^E \ln t_{SC}^{SR} + E_o^{Pd}(t_{STC}) \text{ (MPa)} \qquad (10)$$

The rate of recoverability for the initial elastic modulus is computed from;

$$\frac{\partial E_o^{SR}}{\partial t_{SC}^{SR}} = \frac{\mathcal{A}_{SR}^{E}}{t_{SC}^{SR}} \tag{11}$$

The rate of recoverability for the elastic yield strain is computed as:

$$\frac{\partial [\varepsilon_a]_{Y_I}^{SR}}{\partial t} = \frac{\mathcal{A}_{SR}^{E}}{t_{SC}^{SR}} \tag{12}$$

The Secondary Consolidation Time (SCT) required to achieve the structural recoverability initial modulus is therefore computed from:

$$t_{SC}^{SR}(E_o^{SR}) = exp.\left\{\frac{E_o^{SR} - E_o^{Pd}(t_{STC})}{\mathcal{A}_{SR}^{E}}\right\} \tag{13}$$

where, E_o^{SR} is the initial modulus after quasi structural recoverability, $E_o^{Pd}(t_{STC})$ is the post-destructuration initial modulus determined after Short-Term Consolidation (STC) and $\mathcal{A}_{SR}^{E}$=19.3 is LTC related material constant. On the other hand, the elastic yield strain is computed from,

$$[\varepsilon_a]_{Y_I}^{SR} = \mathcal{A}_{SR}^{E} \ln t_{SC}^{SR} + [\varepsilon_a^{Pd}(t_{STC})]_{Y_I}^{pd} \ (\%) \tag{14}$$

Hence, the SCT required for SR is then determined as:

$$t_{SC}^{SR}(\varepsilon_a)_{Y_I}^{SR} = exp.\left\{\frac{(\varepsilon_a)_{Y_I}^{SR} - [\varepsilon_a^{Pd}(t_{STC})]_{Y_I}}{\mathcal{A}_{SR}^{\varepsilon}}\right\} \tag{15}$$

where $(\varepsilon_a)_{Y_I}^{SR}$ is the elastic yield strain after quasi-structural recoverability, while $[\varepsilon_a^{Pd}(t_{STC})]_{Y_I}$ is that determined within STC and $\mathcal{A}_{SR}^{\varepsilon}$=7×10^{-4}. Note that in all cases, t_{SC}^{SR}=Δt_{SC}^{SR}=t_{SC}^{LTC}=t_{SC}^{ST}.

The degree of recoverability can thence be confirmed from the following relations.

$$E_o^{PR} = \mathcal{A}_{SR}^{E} \ln t_{SC}^{SR} + E_o^{Pd}(t_{STC}) \ (\text{Mpa}) \tag{16}$$

$$[\varepsilon_a]_{Y_I}^{PR} = \mathcal{A}_{SR}^{E} \ln t_{SC}^{SR} + [\varepsilon_a^{Pd}(t_{STC})]_{Y_I}^{pd} \ (\%) \tag{17}$$

where, E_o^{PR} is the post-recovery elastic modulus, $[\varepsilon_a]_{Y_I}^{PR}$ is the post-recovery elastic yield strain and $\mathcal{A}_{SR}^{E}$ =5.42, $\mathcal{A}_{SR}^{\varepsilon}$=1.4×10^{-3} are geomaterial constants.

4. PROPOSED GEO-CHANGES PROBING MODEL (GECPROM)

4.1 Derivation of GECPROM Mathematical Functions Based on Experimental Testing

An appreciably versatile mechanistic-empirical geo-mathematical model (GECPROM) encompassing most of the concepts developed in this Study as well as other related studies, is proposed. GECPROM is designed to probe and estimate changes in vital seismic geo-properties for clayey geomaterials and ground. The significant advantage of this model is that various geotechnical changes and geostructural behavior can be modeled from a single sophisticated experimental test, whilst simultaneously catering for the effects of drainage conditions, loading rate, and consolidation stress-strain-time history. The complete and perfect model would, categorically, have to be multidimensional with relativistic coaxiality, relations and consequences. The GECPROM is primarily designed to be adopted at the study or investigative stage facilitating basic data and information that can then be applied for design of foundations, pavements and other geostructures and/or comprehensive experimental testing and research regimes, input for global and constitutive models, counter/cross-checking and designating the confidence levels of laboratory and field experimental testing, construction control, risk analysis and technical mitigation measures in seismic zones besides the integral role of prediction of ground response and retrospective behavior. This model is to be further developed to incorporate the CSSR modules and MCST concept [1], [3] in order to effectively complement the ESDAM (Environmental, Strength and Deformation Analysis Model [4] based on some of the concepts developed in the process based sedimentary model that merges the Simsafadim-Clastic and Discrete Element model [5]. Fig. 4.1 represents the generalized web mesh Central Processing (CP) graphical component of the GECPROM in a 2D p′~q stress plane.

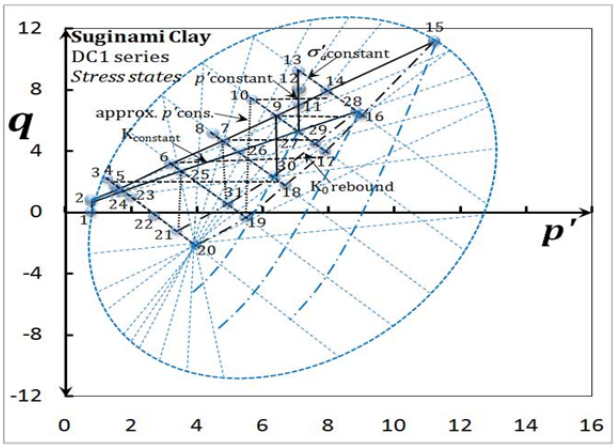

Figure 4.1 Graphic representation of the base CP GECPROM module in 2D $p' - q$, effective stress plane.

Some of the fundamental functions and mathematical equations of the GECPROM are briefly introduced herein.

(1) Probing and prediction of shear and elastic moduli

The fundamental equation for the shear modulus developed from CSSR functions is expressed as:

$$[G_o]_{p'} = \left\{\mathcal{A}_{p'_o}\left[(K_{cs})^{\alpha} \times \left(\frac{p'}{p'_o}\right)^{\beta}\right] + \mathcal{B}_{p'_o}^{K_{cs}}\right\} \times [G_o]_{p'_o} \tag{18}$$

where $[G_o]_{p'}$ is the initial shear modulus at a variable stress point p', K_{cs}=σ'_r/σ'_a is the arbitrary or designated consolidation stress ratio traced to p', $[G_o]_{p'_o}$ is the initial shear modulus determined at in-situ overburden pressure, $\mathcal{A}_{p'_o}$=0.95 and $\mathcal{B}_{p'_o}$=0.35 are geomaterial constants, the values of which are applicable for most natural stiff to hard clayey geomaterials, while β=1.16 and α=0.4 for stress states in the 1st quadrant and α=-1 for stress states in the 4th quadrant accordingly.

In developing the model functions it is important to consider the relativistic rates of change of $[G_o]_{p'}(\Delta,\delta)$ at least within the 1st quadrant of the $\{p',q\}$ stress plane for stress ratio and orientation whereby, $\psi_{p'} = p'/p'_o$ and

$\delta_k = K_{cs}$ and the total derivative is expressed in a generalized form as:

$$\frac{d[G_o]_{p'}}{d\psi_{p'}} = \frac{\partial[G_o]_{p'}}{\partial\psi_{p'}} + \left(\frac{\partial[G_o]_{p'}}{\partial\delta_k}\right) \times \frac{d\delta_k}{d\psi_{p'}} \tag{19}$$

$$\therefore \frac{d[G_o]_{p'}}{d\psi_{p'}} = \mathcal{A}_{p'_o}\left[(K_{cs})^{\alpha} \times \beta\left(\frac{p'}{p'_o}\right)^{\beta-1}\right]$$

$$+\left\{\mathcal{A}_{p'_o}\left[\alpha K_{cs}^{\alpha-1} \times \left(\frac{p'}{p'_o}\right)^{\beta}\right] + \frac{\mathcal{B}^{K_{cs}}}{K_{cs}}\right\} \times \frac{d\delta_k}{d\psi_{p'}} \tag{20}$$

The change of variables within the model is made by applying Leibnitz's theorem of the chain rule expressed as:

$$\frac{\partial[G_o]_{p'}}{\partial\xi_j} = \sum_{i=1}^{n} \frac{\partial[G_o]_{p'}}{\partial\psi_{p'}} \cdot \frac{\partial\psi'_i}{\partial\xi_j}, j = 1,2,\cdots,m, \tag{21}$$

Whereof, for higher derivatives of products, the differentiation generalizes to:

$$f^{(n)} = \sum_{r=0}^{n} \frac{n!}{r!(n-r)!} u^{(r)} v^{(n-r)} \tag{22}$$

Furthermore, infinitesimal changes in stress at cross stress points are delineated and converged by simply applying Taylor's theorem for multi-variable functions expansion with f as a substitution for $[G_o]_{p'}$;

$$f(\psi_{p'}, \delta_k) = f(\psi_{p'_o}, (\delta_k)_{p'_o}) + \frac{\partial f}{\partial\psi_{p'}}\Delta\psi_{p'}$$

$$+\frac{\partial f}{\partial\delta_k}\Delta\delta_k + \frac{1}{2!}\begin{bmatrix} \frac{\partial^2 f}{\partial\psi_{p'}^2}(\Delta\psi_{p'})^2 \\ +2\frac{\partial^2 f}{\partial\psi_{p'}\Delta\delta_k}\Delta\psi_{p'}, \Delta\delta_k \\ +\frac{\partial^2 f}{\partial\delta_k^2}(\Delta\delta_k)^2 \end{bmatrix} \cdots + \cdots \tag{23}$$

The more generalized form applied in analyzing a multivariable function for stress points sprouting in n-directions with $\mathbf{X}$ as the vector from the origin, is then expressed as;

$$f(\mathbf{X}) = \sum_{n=0}^{\infty} \frac{1}{n!}[(\Delta\mathbf{X} \cdot \nabla)^n f(\mathbf{X})]_{\mathbf{X}=\mathbf{X}_o} \tag{24}$$

Where the deviatoric stress increment magnitude, Δq is larger, exhibiting less error factors, the following equation may be employed.

$$[G_o]_q = \left\{\mathcal{A}_q \ln\begin{bmatrix} \left({}^{q}/_{p'_o}\right) \\ \times\left(\frac{\Delta p'_{\{D,U\}}}{\Delta q_{p'_m}}\right)^{10^{-1}} \end{bmatrix} + \mathcal{B}_q\right\} \times [G_o]_{p'_o} \tag{25}$$

The model function analyses for (25) are analogous to those presented in (18) – (24).

(2) *Geo-mathematical determination of Initial Yield Strain (IYS) for varying conditions*

GECPROM retrospectively reflects and mirrors the conditions applied during the testing at stress point p'_o. Unlike the initial shear and elastic moduli which can be ideally considered to be only stress state dependent, the Initial Yield Strain $\{(\varepsilon_a)_{ELS}(Y_I)\}$ representing the threshold of the initial sub-yield surface, Y_I , which is dependent on various factors such as consolidation stress-strain-time history, shear strain rate, drainage conditions and OCR [1], is rather complicated in terms of modeling it in singularity. In the generalized state therefore, the $(\varepsilon_a)_{Y_I}$ is expressed as a function of multi-variables in the form;

$$(\varepsilon_a)_{Y_I} = p'{\sim}qf(\sigma_{ss}, \mathcal{L}_{CSSH}, \delta_{SCT}, \phi_{OCR}, \alpha_{cp}, \varphi_{DC}, \dot{\varepsilon}_{SR}) \tag{26}$$

where, σ_{ss} is the current stress state, $\mathcal{L}_{CSSR}$ represents the consolidation stress-strain history, $\varphi_{SCT} = (d\varepsilon_a/dt)_{SCT}$ is the secondary consolidation time (ageing), ϕ_{OCR} is the overconsolidation ratio factor, φ_{DC} defines the drainage conditions and $\dot{\varepsilon}_{SR}$ is the strain rate effect. However, corroborative deduction made from [1] and the preceding subsections indicates that the variables can essentially be simplified as: $f[(\sigma_{ss}, \mathcal{L}_{CSSR}, \varphi_{DC}, \dot{\varepsilon}_{SR})]$ (ref. to Fig. 4.2). The generalized analytical function of the resulting $(\varepsilon_a)_{Y_I}^R$ expressed in compound terms is:

$$(\varepsilon_a)_{Y_I}^R = \oiint\oiint\oint_{\{\Delta q,\varepsilon_a\}}^{\{\Delta qY,\varepsilon_aY\}} f(\sigma_{ss}, \mathcal{L}_{CSSR}, \varphi_{DC}, \alpha_{cp}, \dot{\varepsilon}_{SR}) d\sigma_{ss}\, d\mathcal{L}_{CSSR} d\varphi_{DC} d\alpha_{cp} d\dot{\varepsilon}_{SR} \tag{27}$$

Furthermore, (27) can be transformed into a more simplified analytical function whereby the resulting $(\varepsilon_a)_{Y_I}^R$ is considered to be the zonal cumulative magnitude bounding at the $(\varepsilon_a)_{ELS}$ for each singularity effect, the summation of which is then given by;

$$\sum_{n=0}^{(\varepsilon_a)_{Y_I}^N} ((\varepsilon_a)_{ELS})_n. \tag{28}$$

The Boundary Limits (BL) for each of the effects on the initial yield strain are determined as follows; based on the stationary saddle point of inflection, Taylor's Theorem of multivariable functions (23), Taylor's Remainder Theorem and the Euler-Lagrange Equation for stationary points for Integrals, as well as Maclaurin's series [6], [7].

I. Stress States (σ_{ss}) BL

The basic generalized equation defining the impact of stress states is expressed as:

$$[\varepsilon_a]_{Y_I}^{\sigma_{ss}} = \frac{\left\{\mathcal{A}_{p'_o}^{\varepsilon}\left[(K_{cs})^l \times \left(\frac{p'}{p'_o}\right)^m\right] + \mathcal{B}_{p'_o,\varepsilon}^{K_{cs}^r}\right\}^{\alpha}}{\psi_{(\varepsilon_a)_{Y_I}}}$$

$$\times \left[(\varepsilon_a)_{Y_I}\right]_{p'_o}, \left|\psi_{(\varepsilon_a)_{Y_I}}{}_{>1,\alpha=-1}^{\leqq 1,\alpha=+1}\right. \tag{29}$$

where, constants $\mathcal{A}_{p'_o}^{\varepsilon}$=0.98, $\mathcal{B}_{p'_o,\varepsilon}$=0.32, l=0.4, for stress states in the 1st quadrant and, l=-1, in the 4th quadrant, while m=1.16.

Considering $\rho_{p'} = p'/p'_o$ and $\kappa = K_{cs}$ then the Boundary Conditions (BC) are defined as:

$$\frac{\partial^2(\varepsilon_a)_{Y_I}^{\sigma_{ss}}}{\partial\rho_{p'}^2} < 0 \; or \; \frac{\partial^2(\varepsilon_a)_{Y_I}^{\sigma_{ss}}}{\partial\kappa^2} < 0 \tag{30}$$

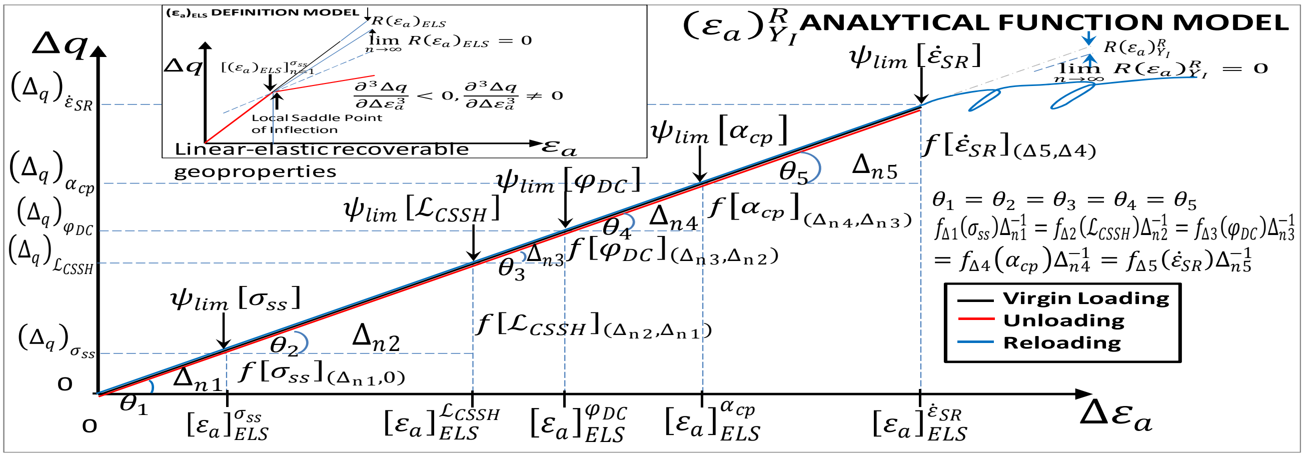

Figure 4.2 Resulting Initial Yield Strain, $(\varepsilon_a)_{Y_I}^{R}$ $\{(\varepsilon_a)_{ELS}(Y_I)\}$ simplified Analytical Function Model (AFM)

and;

$$\frac{\partial^3 (\varepsilon_a)_{Y_I}^{\sigma_{ss}}}{\partial \rho_{p'}^3} \neq 0 \; or \; \frac{\partial^3 (\varepsilon_a)_{Y_I}^{\sigma_{ss}}}{\partial \kappa^3} \neq 0 \tag{31}$$

Carrying out 2nd order partial differentiation w.r.t ρ we obtain,

$$\left(\frac{\partial^2 (\varepsilon_a)_{Y_I}^{\sigma_{ss}}}{\partial \rho_{p'}^2}\right)_{\kappa} = \mathcal{A}_{p_o'}\left[(K_{cs})^l \times m(m-1)\left(\frac{p'}{p_o'}\right)^{m-2}\right]^{-1} \times \left[(\varepsilon_a)_{Y_I}\right]_{p_o'} < 0 \tag{32}$$

Performing the same w.r.t κ we obtain,

$$\left(\frac{\partial^2 (\varepsilon_a)_{Y_I}^{\sigma_{ss}}}{\partial \rho_{p'}^2}\right)_{\rho_{p'}} = \left\{\begin{matrix} \mathcal{A}_{p_o'}\left[l(l-1)K_{cs}^{l-2} \times \left(\frac{p'}{p_o'}\right)^{m}\right] \\ + \left[\frac{K_{cs}\mathcal{B}^{K_{CS}^{(n-2)}} - mK_{CS}^{(n-1)}\mathcal{B}^{K_{CS}^{(n-1)}}}{(K_{cs}^{n})^2}\right]\end{matrix}\right\}^{-1} \times \left[(\varepsilon_a)_{Y_I}\right]_{p_o'} < 0 \tag{33}$$

$\delta R\left(\varepsilon_a^{\Delta_{n1}}\right)$, indicated in the lower BL of the second component, which defines the interface of the transition and transposition from the end of $\psi_{lim}[\sigma_{ss}]$ to the beginning of $\psi_{lim}[\mathcal{L}_{CSSH}]$ depicted in Fig. 4.2 is solved analogous to (23) along with Taylor's Remainder Theorem resulting in the function;

$$\delta R\left(\varepsilon_a^{\Delta_{n1}}\right) = \left\{\frac{\left[(\varepsilon_a)_{ELS}^{\mathcal{L}_{CSSH}}\right]_n - \left[(\varepsilon_a)_{ELS}^{\mathcal{L}_{CSSH}}\right]_{n-1}}{n!}\right\} \times f^{(n)}(\xi), |\lim_{n\to\infty} \delta R \to 0 \tag{34}$$

In the case where it is necessary to determine the nature of a stationary point and stationary values for multivariable functions, the function is expanded as a Taylor series about the stress point in reference to (24), which is the full form of the approximation;

$$\Delta f = f(\widetilde{\Delta\boldsymbol{\varepsilon}_a}) - f\left((\widetilde{\Delta\boldsymbol{\varepsilon}_a})_0\right)$$

$$\approx \frac{1}{2}\sum_i \sum_j \frac{\partial^2 f}{\Delta(\varepsilon_a)_i \Delta(\varepsilon_a)_j}\Delta(\varepsilon_a)_i \Delta(\varepsilon_a)_j \tag{35}$$

Defining a matrix M having elements given by

$$M_{ij} = \frac{\partial^2 f}{\Delta(\varepsilon_a)_i \Delta(\varepsilon_a)_j}, \tag{36}$$

Equation (35) can then be rewritten in the form;

$$\Delta f = \frac{1}{2}\boldsymbol{\Delta}|\boldsymbol{\varepsilon_a}|^T M \Delta|\varepsilon_a| \tag{37}$$

where $\boldsymbol{\Delta}|\boldsymbol{\varepsilon_a}|$ is the column vector with $\Delta(\varepsilon_a)_i$ as its components and $\boldsymbol{\Delta}|\boldsymbol{\varepsilon_a}|^T$ is its transpose. Since M is real and symmetric it has n eigenvalues λ_r and n orthogonal eigenvectors e_r, which can be normalized to the form;

$$Me_r = \lambda_r e_r, e_r T e_s = \delta_{rs}, \tag{38}$$

where the Kronecker delta symbol $\delta_{rs} = 1$ for $r = s$ and $\delta_{rs} = 0$ for $r < s$. Expanding $\boldsymbol{\Delta}|\boldsymbol{\varepsilon_a}|$ in these terms yields;

$$\boldsymbol{\Delta}|\boldsymbol{\varepsilon_a}| = \sum_r a_r e_r, \tag{39}$$

where, a_r are coefficients dependent upon $\boldsymbol{\Delta}|\boldsymbol{\varepsilon_a}|$. Substituting this into (41) yields;

$$\Delta f = \frac{1}{2}\boldsymbol{\Delta}|\boldsymbol{\varepsilon_a}|^T M \Delta|\varepsilon_a| = \frac{1}{2}\sum_r \lambda_r a_r^2 \tag{40}$$

Consequently, for the stationary point to be;

(i) minimum; $\Delta f = \frac{1}{2}\sum_r \lambda_r a_r > 0$: for all sets of values of the a_r

(ii) maximum; $\Delta f = \frac{1}{2}\sum_r \lambda_r a_r > 0$: therefore, eigenvalues of M>0

(iii) saddle; $\Delta f = \frac{1}{2}\sum_r \lambda_r a_r < 0$: therefore, eigenvalues of M>0

Considering (34), which is a two variable function, i.e. $\rho_{p'}$=p'/p_o' and $\kappa = K_{cs}$ then the matrix M is given by

$$M = \begin{pmatrix} \frac{\partial^2 (\varepsilon_a)_{Y_I}^{\sigma_{ss}}}{\partial \rho_{p'}^2} & \frac{\partial^2 (\varepsilon_a)_{Y_I}^{\sigma_{ss}}}{\partial \rho_{p'}\partial \kappa} \\ \frac{\partial^2 (\varepsilon_a)_{Y_I}^{\sigma_{ss}}}{\partial \kappa \partial \rho_{p'}} & \frac{\partial^2 (\varepsilon_a)_{Y_I}^{\sigma_{ss}}}{\partial \kappa^2} \end{pmatrix} \tag{41}$$

Hence,

$$\left[\frac{\partial^2(\varepsilon_a)_{Y_I}^{\sigma_{ss}}}{\partial\rho_{p'}^2}-\lambda\right]\left[\frac{\partial^2(\varepsilon_a)_{Y_I}^{\sigma_{ss}}}{\partial\kappa^2}-\lambda\right]-\left[\frac{\partial^2(\varepsilon_a)_{Y_I}^{\sigma_{ss}}}{\partial\rho_{p'}\partial\kappa}\right]^2 \quad (42)$$

which is solved to yield;

$$2\lambda=\left(\left[\frac{\partial^2(\varepsilon_a)_{Y_I}^{\sigma_{ss}}}{\partial\rho_{p'}^2}-\lambda\right]+\left[\frac{\partial^2(\varepsilon_a)_{Y_I}^{\sigma_{ss}}}{\partial\kappa^2}-\lambda\right]\right)$$
$$\pm\sqrt{\left(\left[\frac{\partial^2(\varepsilon_a)_{Y_I}^{\sigma_{ss}}}{\partial\rho_{p'}^2}-\lambda\right]-\left[\frac{\partial^2(\varepsilon_a)_{Y_I}^{\sigma_{ss}}}{\partial\kappa^2}-\lambda\right]\right)^2+4\times\left[\frac{\partial^2(\varepsilon_a)_{Y_I}^{\sigma_{ss}}}{\partial\rho_{p'}\partial\kappa}\right]^2} \quad (43)$$

Equation (43) is then solved to determine the minima.

An analogous procedure is applied for analyzing the functions of the other controlling factors whose generalized equations are presented as follows.

II. Consolidation Stress-strain history ($\mathcal{L}_{CSSH}$)

$$[\varepsilon_a]_{Y_I}^{\sigma_{ss}}=\mathcal{A}_{\mathcal{L}_{CSSH}}^{\varepsilon}\ln(\delta_{SCT}\times\phi_{OCR})+\left[(\varepsilon_a)_{Y_I}\right]_{NC}^{tp} \quad (44)$$

where $\mathcal{A}_{\mathcal{L}_{CSSH}}^{\varepsilon}$ =1.9×10^{-3} is a constant, δ_{SCT} is the secondary consolidation factor, ϕ_{OCR} is the overconsolidation factor and $\left[(\varepsilon_a)_{Y_I}\right]_{NC}^{tp}$ is the initial yield strain determined under normally consolidated conditions at a standard time period designated after the end of primary consolidation.

III. Drainage conditions (φ_{DC})

$$[\varepsilon_a]_{Y_I}^{\varphi_{DC}}=\left[\frac{(\Delta\sigma_a'-2\nu\Delta\sigma_r')}{(\Delta\sigma_a'-\Delta\sigma_r')}\right]^{\beta(d/u)}\times\left[\frac{\sigma_r'}{\sigma_a'}\right]_{KC}\times\left[(\varepsilon_a)_{Y_I}\right]_{\{d/u\}} \quad (45)$$

where $\Delta\sigma_a'$, $\Delta\sigma_r'$ are the effective axial and radial stresses respectively determined at the threshold of $\left[(\varepsilon_a)_{Y_I}\right]_{\{d/u\}}$, $[\sigma_r'/\sigma_a']_{KC}$ is the stress ratio during consolidation, $\beta(d)$=-1, $\beta(u)$=+1 (d: drained and u: undrained) and ν is the Poisson's ratio. For perfectly drained conditions ν≑0.2 and ν≑0.5 for perfectly undrained state. Under partially undrained conditions ν_{pd} can be determined as

$$\nu_{pd}=\left\{\frac{(E_o)_d}{(E_o)_u}(1+\nu_u)\right\}-1 \quad (46)$$

where $(E_o)_d$, $(E_o)_u$ are the initial drained and undrained elastic moduli respectively.

IV. Cyclic prestraining (α_{cp})

$$[\varepsilon_a]_{Y_I}^{\alpha_{cp}}=\mathcal{A}_{\alpha_{cp}}^{\varepsilon}\ln\alpha_{cp}+\left[(\varepsilon_a)_{Y_I}^{R}\right]_{(tp)},$$
$$\left|\frac{\partial^2(\varepsilon_a)_{tp}}{\partial\alpha_{cp}^2}=0\ and,\left[\frac{\partial^3(\varepsilon_a)_{tp}}{\partial\alpha_{cp}^3}\right]_{\delta R}<0\right. \quad (47)$$

Refer to Fig. 2.3 depicting cyclic prestraining structuration/ destructuration model and the modeling functions.

V. Strain rate $(\varepsilon_a)_{Y_I}^{\dot{\varepsilon}SR}$

$$[\varepsilon_a]_{Y_I}^{\dot{\varepsilon}_{SR}}=\left[\mathcal{A}_{\dot{\varepsilon}_{SR}}\ln\left(\frac{\dot{\varepsilon}_{ASR}}{\dot{\varepsilon}_{RSR}}\right)+\mathcal{B}_{\dot{\varepsilon}_{SR}}\right]\times(\varepsilon_a)_{Y_I}^{\dot{\varepsilon}_{SR}} \quad (48)$$

where, the subscripts SR denote Strain Rate, ASR: Applied Strain Rate during testing or arbitrarily designated and RSR: Reference Strain Rate.

4.2 Examination of Abrupt Variations in Small Stress-strain Characteristics

In cases whereby the stress-strain characteristics change abruptly as a result of, for example, excessive cyclic prestraining, swelling, excessive densification or other form of destructuration, structuration or geotechnical changes, the theories and concepts related to the calculus of variations are applied [6]. In particular, the Euler-Lagrange (EL) equation is applied provided that all functions are sufficiently smooth, differentiable and within differentiable spaces.

Consider that the characteristics in Fig. 4.2 change drastically and as a consequence, the functions defined in the preceding section can no longer satisfy any of the conditions within the Δq~$\Delta\varepsilon_a$ space. It would then be a matter of extreme importance that we are able to evaluate and determine the forms of such changes in order to retrofit the analytical functions.

Take for example that stress~strain characteristic changes occur within the range $(\varepsilon_a)_{ELS}^{\sigma_{ss}}$ and $(\varepsilon_a)_{Y_I}^{R}$ then, examining the changes on the basis of the EL approach yields;

$$I=\int_{(\varepsilon_a)_{ELS}^{\sigma_{ss}}}^{(\varepsilon_a)_{Y_I}^{R}}F(\Delta q,\Delta q',\Delta\varepsilon_a)d\Delta\varepsilon_a \quad (49)$$

where, $\Delta q'=\Delta Aq/\,d\Delta\varepsilon_a$.

Suppose that $\Delta q(\Delta\varepsilon_a)$ is the function required to make I stationary then,

$$\Delta q(\Delta\varepsilon_a)\rightarrow\Delta q(\Delta\varepsilon_a)+\alpha\eta(\Delta\varepsilon_a) \quad (50)$$

where, parameter α is small and $\eta(\Delta\varepsilon_a)$ is an arbitrary function with sufficiently amenable mathematical properties. For the value of I to be stationary w.r.t such variations,

$$\left.\frac{dI}{d\alpha}\right|_{\alpha=0}=0\ for\ all\ \eta(\Delta\varepsilon_a) \quad (51)$$

Substituting (49) into (50) and expanding as a Taylor series in α, then the following equation is obtained.

$$I(\Delta q,\alpha)=\int_{(\varepsilon_a)_{ELS}^{\sigma_{ss}}}^{(\varepsilon_a)_{Y_I}^{R}}F(\Delta q+\alpha\eta,\Delta q'+\alpha\eta',\Delta\varepsilon_a)d\Delta\varepsilon_a$$
$$=\int_{(\varepsilon_a)_{ELS}^{\sigma_{ss}}}^{(\varepsilon_a)_{Y_I}^{R}}F(\Delta q,\Delta q',\Delta\varepsilon_a)d\Delta\varepsilon_a$$
$$+\int_{(\varepsilon_a)_{ELS}^{\sigma_{ss}}}^{(\varepsilon_a)_{Y_I}^{R}}\left(\frac{\partial F}{\partial\Delta q}\alpha\eta+\frac{\partial F}{\Delta q'}\alpha\eta'\right)d\Delta\varepsilon_a+0(\alpha^2) \quad (52)$$

With this form, for $I(\Delta q,\alpha)$ the condition in (51) implies that for all values of $\eta(\Delta\varepsilon_a)$, we require;

$$\delta I = \int_{(\varepsilon_a)_{ELS}^{\sigma_{ss}}}^{(\varepsilon_a)_{Y_I}^R} \left(\frac{\partial F}{\partial \Delta q} \eta + \frac{\partial F}{\Delta q'} \eta' \right) d\Delta\varepsilon_a = 0 \tag{53}$$

where, δI denotes the first-order variation in the value of I due to the variation defined in (49) for the function $\Delta q(\Delta\varepsilon_a)$. Integrating the 2nd term by parts yields;

$$\left[\eta \frac{\partial F}{\Delta q'}\right]_{(\varepsilon_a)_{ELS}^{\sigma_{ss}}}^{(\varepsilon_a)_{Y_I}^R} = \int_{(\varepsilon_a)_{ELS}^{\sigma_{ss}}}^{(\varepsilon_a)_{Y_I}^R} \left(\frac{\partial F}{\partial \Delta q} \eta + \frac{\partial F}{\Delta q'} \eta' \right) d\Delta\varepsilon_a = 0 \tag{54}$$

Considering $[(\varepsilon_a)_{Y_I}^R\ ,\ (\varepsilon_a)_{ELS}^{\sigma_{ss}}]$ and, $\{\Delta q[(\varepsilon_a)_{Y_I}^R]\ ,\ \Delta q[(\varepsilon_a)_{ELS}^{\sigma_{ss}}]\}$ are fixed, then it becomes a prerequisite condition that; $\eta[(\varepsilon_a)_{Y_I}^R] = \eta[(\varepsilon_a)_{ELS}^{\sigma_{ss}}] = 0$, in which case;

$$\left[\eta \frac{\partial F}{\Delta q'}\right] = \left((\varepsilon_a)_{Y_I}^R, (\varepsilon_a)_{ELS}^{\sigma_{ss}}\right) = 0 \tag{55}$$

Consequently, since (53) must be satisfied for an arbitrary function; $\eta(\Delta\varepsilon_a)$, then;

$$\frac{\partial F}{\partial \Delta q} = \frac{d}{d\Delta\varepsilon_a}\left(\frac{\partial F}{\Delta q'}\right) \tag{56}$$

Other Euler's equations applied take the form:

$$\frac{d}{d\Delta\varepsilon_a}\left[F - \Delta q' \frac{\partial F}{\Delta q'}\right] - \frac{\partial F}{\partial \Delta\varepsilon_a} \tag{57}$$

and,

$$\frac{\partial F}{\partial \Delta q} - \frac{\partial^2 F}{\partial \Delta\varepsilon_a\, \partial \Delta q'} - \Delta q' \frac{\partial^2 F}{\partial \Delta q\, \partial \Delta q'} - \Delta q'' \frac{\partial^2 F}{(\partial \Delta q')^2} = 0 \tag{58}$$

where, $\partial\Delta q' = \partial\left[\frac{dq}{d\Delta\varepsilon_a}\right]$, $\Delta q'' = \frac{d^2\Delta q}{d\varepsilon_a^2}$ and $(\partial\Delta q')^2 = \partial\left[\frac{d\Delta q}{d\varepsilon_a}\right]^2$.

4.3 Application of GECPROM in Modeling of Pre-failure Deformation of Stiff Pleistocene Clays

Adopting the GECPROM, pre-failure stress path, stress-strain and stiffness characteristics are modeled. Typical comparisons of the modeled vs. experimental curves are presented in Figs. 4.3, 4.4 and 4.5, respectively.

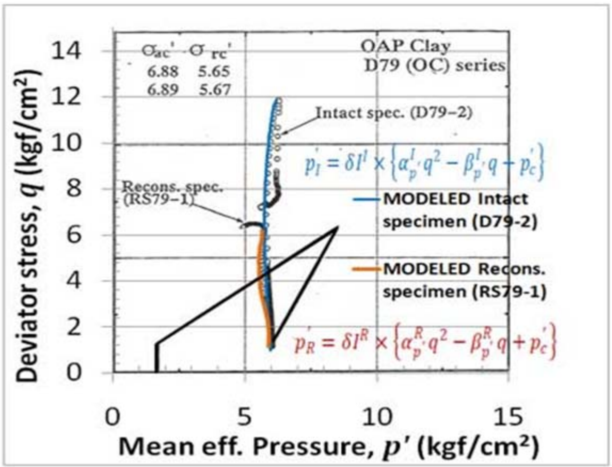

Figure 4.3 Comparison of experimental and modeled Shear Stress Paths (SSP)

The paraphrased integral model equations applied in the GECPROM, along with others not reported in this paper, for generating the simulation and prediction curves, are expressed in a generalized form as:

$$E_S = \frac{d\Delta q}{d\Delta\varepsilon_a} = \psi_{E_S} \times \begin{Bmatrix} G = {E_S}/{2(1+\nu)}\ \alpha_{E_S}(\varepsilon_a)^m \\ +\beta_{E_S}(\varepsilon_a)^n + \gamma_{E_S} \end{Bmatrix} \tag{59}$$

$\left|\begin{matrix} m=1 \\ n=0 \end{matrix}\right.$ $when\ 0 \leqq \varepsilon_a \leqq 0.1$ and, $\left|\begin{matrix} m=2 \\ n=1 \end{matrix}\right.$ $when\ \varepsilon_a > 0.1$

and,

$$E_o = \left[\alpha_{E_o}(\varepsilon_a)_{=0.001\%} + \beta_{E_o}\right] \times 10(MPa) \tag{60}$$

where, α_{E_o} and β_{E_o} are determined simultaneously at ε_a=0.001% and 0.01%, and $(\varepsilon_a)_{Y_I}$ is derived from (66).

When ε_a>0.1

(1) For Intact specimens

$$E_S^I = \psi_{E_S}^I \times \begin{Bmatrix} \alpha_{E_S}^I(\varepsilon_a)^2 \\ +\beta_{E_S}^I(\varepsilon_a)^n \\ +\gamma_{E_S}^I \end{Bmatrix} \times 10(\text{MPa}) \tag{61}$$

(2) For Reconstituted specimens

$$E_S^R = \psi_{E_S}^R \times \frac{\alpha_{E_S}^R}{(\varepsilon_a)} \times 10 \tag{62}$$

Consequently, the $\Delta q \sim \Delta\varepsilon_a$ relations are generated through the integration of (59) ~ (62), i.e.;

- *For 0≦ε_a≦0.1%*

$$\Delta q = \int \Delta q'\, d\Delta\varepsilon_a = \psi_{E_S}$$

$$\times \int_0^{\varepsilon_a=0.1\%} \begin{Bmatrix} \alpha_{E_S}(\varepsilon_a)^m \\ +\beta_{E_S}(\varepsilon_a)^n \\ +\gamma_{E_S} \end{Bmatrix} \times 10\, d\Delta\varepsilon_a \tag{63}$$

- *For ε_a>0.1%*

$$\Delta q = \psi_{E_S}^I \times \int_{0.1}^{\varepsilon_a>0.1\%} \begin{Bmatrix} \alpha_{E_S}^I(\varepsilon_a)^2 \\ +\beta_{E_S}^I(\varepsilon_a)^n \\ +\gamma_{E_S}^I \end{Bmatrix} \times 10\, d\Delta\varepsilon_a \tag{64}$$

$$\Delta q = \psi_{E_S}^R \times \int_{0.1}^{\varepsilon_a} \frac{\alpha_{E_S}^R}{(\varepsilon_a)} \times 10\, d\Delta\varepsilon_a \tag{65}$$

The sub-yield surface strain limits are mathematically defined as:

- *Initial elastic yield surface strain limit, Y_I*

$$(\varepsilon_a)_{Y_I} = \frac{\beta_{E_o} - 0.1[(E_o)_R^2/E_o]}{\alpha_{E_o}}$$

$$+f\left(\mathcal{L}_{CSSH}, \alpha_{cp}, \dot{\varepsilon}_{SR}\right)(\%) \tag{66}$$

$$\alpha_{E_o}(\varepsilon_a)_{Y_I} = \frac{\beta_{E_o} - 0.1 \times [(E_o)_{0.01}^2/E_o]}{6\alpha_{E_o}}$$

$$+f\left(\mathcal{L}_{CSSH}, \alpha_{cp}, \dot{\varepsilon}_{SR}\right)(\%) \tag{67}$$

where $(E_o)_R > E_o$ then,

$$(\varepsilon_a)_{Y_I} = (\varepsilon_a)_{Y_I}^R - (\varepsilon_a)_{Y_I}^{\alpha,\beta} \tag{68}$$

- *Secondary sub-yield surface strain limit, Y_S*

$$(\varepsilon_a)_{Y_S} = \frac{\beta_{0.01} - 0.1[(E_{0.01})_R^2/E_o]}{\alpha_{0.01}} + (\varepsilon_a)_{Y_I} \quad (69)$$

- *Tertiary sub-yield surface strain limit, Y_T*

$$(\varepsilon_a)_{Y_T} = \frac{\beta_{0.1} - 0.1[(E_{0.1})_R^2/E_{0.01}]}{\alpha_{0.1}} + (\varepsilon_a)_{Y_S}(\%) \quad (70)$$

- *Ultimate yield surface strain limit, Y_U*

$$(\varepsilon_a)_{Y_U} = \frac{\beta_1 - 0.1[(E_1)_R^2/E_{0.1}]}{\alpha_1} + (\varepsilon_a)_{Y_T}(\%) \quad (71)$$

(3) Limiting Elastic Modulus (LEM) at given SS

On the other hand, at any given Stress State (SS), the Limiting Elastic Modulus, E_{LEM} is computed as follows.

$$E_{LEM} = \{0.1E_o + \alpha_{E_o} \times (\varepsilon_a)_{Y_I}\} \times 10\ (MPa) \quad (72)$$

This represents the Limiting Elastic State [LES], beyond which the elastic and/or shear moduli cannot increase notwithstanding any further effects such as OCR, ageing, strain rate, cyclic prestraining, and drainage (which would, on the contrary, be detrimental beyond this state) provided that the soil fabric does not undergo change and is devoid of extrinsic geomaterial influence and/or contamination.

(4) Limiting Yield Stress (LYS)

The Limiting Yield Stress (LYS), $(\sigma'_a)_Y$ equation can therefore be derived from (4) ~ (6) and (72) as:

$$(\sigma'_a)_Y = \frac{\sigma'_{ao} \times OCR^{\phi_E} \times E_{ELL}}{(E_o)_{\sigma'_{ao}}} \quad (73)$$

where, $\phi_E = E_{ELL}/(E_o)_{\sigma'_{ao}} = 1$ for HOC and $(E_o)_{\sigma'_{ao}}$ is the elastic modulus determined at the in-situ overburden pressure (σ'_{ao}), while the limiting initial yield strain, $(\varepsilon_a)_{LYS}$ can be retrospectively extrapolated by adopting (74).

$$(\varepsilon_a)_{Y_I}^{LYS} = \left\{\frac{\beta_{E_o}^{\sigma'_{ao}} - 0.1(E_o)_{\sigma'_{ao}}}{6\alpha_{E_o}^{\sigma'_{ao}}}\right\}_{\sigma'_{ao}} - A_{ys}\ln(OCR) \quad (74)$$

where, A_{ys}=3.1×10^{-3} for intact specimen and 1.52×10^{-3} for reconstituted specimens are constants applicable for stiff to hard clayey geomaterials.

The LYS is vital in determining the ultimate Boundary Surface (BS) and also establishing control parameters applicable in design, risk analysis and construction control.

The results observed in Figs. 4.3 ~ 4.6 show virtually similar characteristics between the modeled and experimental curves for the very stiff, well structured and overconsolidated OAP Pleistocene clay, thereby verifying the confidence level of the GECPROM at this stage.

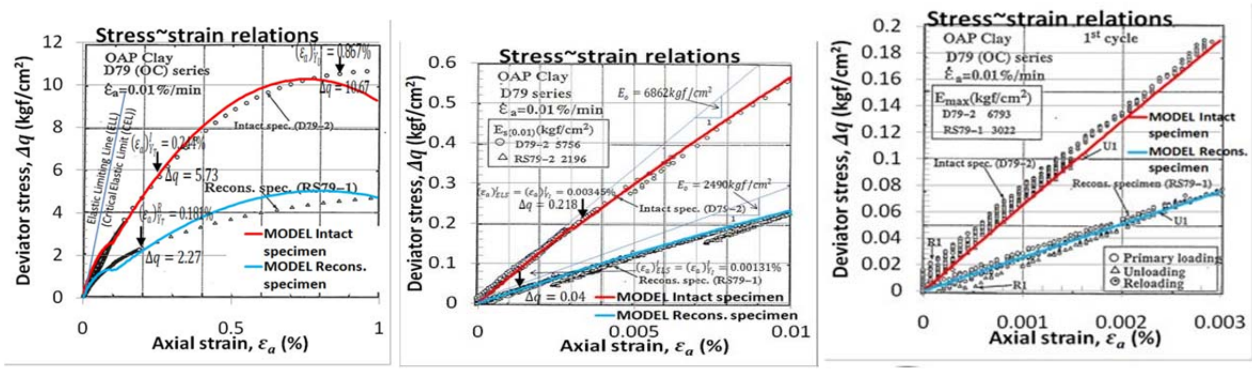

Figure 4.4 Comparison of modeled and measured stress~strain relations for Over-Consolidated (OC) OAP clay for: (a) intermediate strains $\{(\varepsilon_a)_{ELS}(Y_I)\} \sim \{(\varepsilon_a)_{TYS}(Y_T)\}$, ($\varepsilon_a \leq 1\%$); (b) small strains $\{(\varepsilon_a)_{SYS}(Y_S)\}$, ($\varepsilon_a \leq 0.01\%$) and, (c) very small strains $\{(\varepsilon_a)_{ELS}(Y_I)\}$, ($\varepsilon_a \leq 0.003\%$).

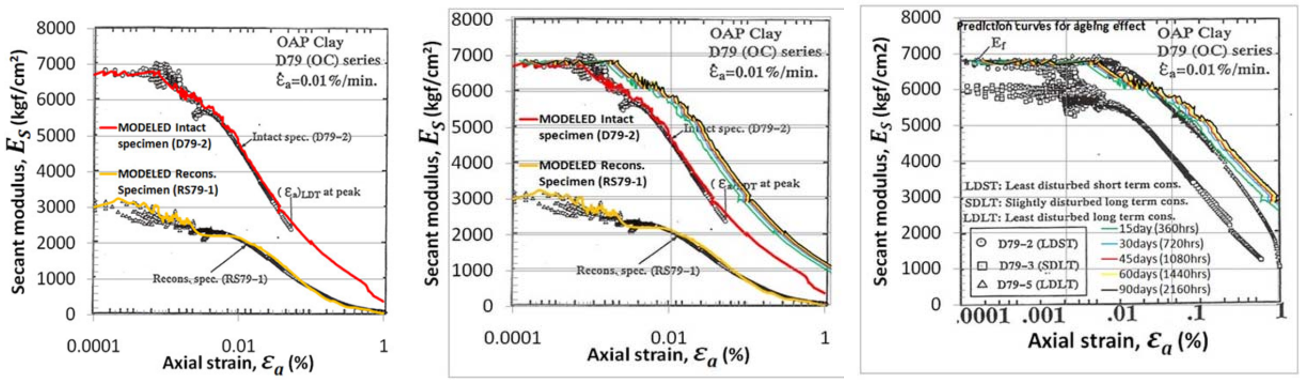

Figure 4.5 Comparison of modeled and experimentally determined strain level dependency of stiffness decay curves including predicted curves $\{(\varepsilon_a)_{ELS}(Y_I)\} \sim \{(\varepsilon_a)_{FYS}(Y_F)\}$, ($\varepsilon_a \leq 1\%$) for ageing effects for: (a) intact and reconstituted specimens, $\{(\varepsilon_a)_{ELS}(Y_I)\} \sim \{(\varepsilon_a)_{FYS}(Y_F)\}$ for $\varepsilon_a \leq 1\%$ and , with prediction for ageing for: (b) intact and reconstituted specimens and, (c) intact specimens only.

On the other hand, Fig. 4.6 is a graphical depiction of the comparison of modeled and experimentally derived multiple kinematic sub-yield surfaces; hypothetic-empirically bound around the respective computed Yield Strain Limit [{YSL $\{(\varepsilon_a)_{YLS}(Y_{LS})\}$] related congruent $p'\sim q$ stresses.

The following derivations can be made from this figure: 1) the intact specimen exhibits much larger sub-yield as well as yield surfaces compared to the reconstituted one; a manifestation of destructuration effects; 2) the orientations of reconstituted specimen surfaces are different from those of intact surfaces in all cases; a manifestation of the differences in structure; 3) by extension, it can therefore be considered that the intact and reconstituted surface sizes vary in all directions; 4) a link exists between the magnitude of stiffness and the configuration of the multiple kinematic sub-yield surfaces; 5) within the Y_u surface, the magnitude and stress path rotation increases as the size of the sub-yield surfaces becomes larger; 6) the farther the distance of the current stress point from the failure line, the closer the range of engagement of the neigboring surfaces and, 7) the modeled and experimetal curves are practically the same in all cases demonstrating the confindence and reliability levels of the GECPROM.

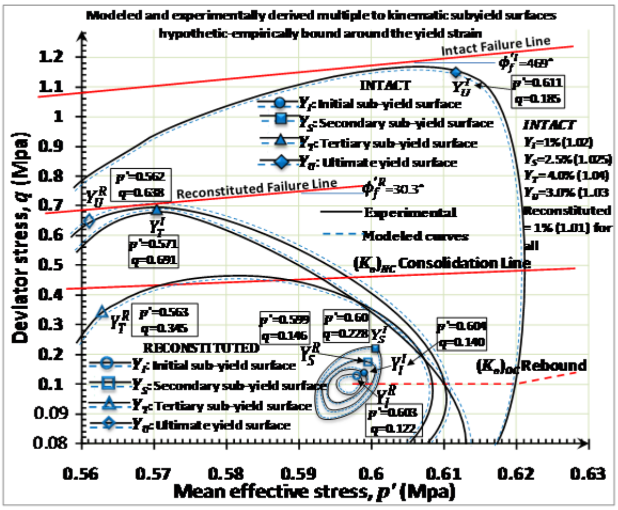

Figure 4.6 Comparison of modeled and experimentally derived multiple kinematic sub-yield surfaces; hypothetic-empirically bound around the Yield Strain Limit [{YSL $\{(\varepsilon_a)_{YLS}(Y_{LS})\}$] congruent $p'\sim q$ stresses.

As hypothetically suggested by various researchers; [8] – [12], the scientifically determined results of this Study show that the history surface, Y_T is highly susceptible to the recent stress history and that the memory of the previous history is temporarily maintained notwithstanding changes in loading direction and stress path (also ref. to [1]).

5. CONCLUSIONS

Although these results confirm some theories, hypothesis and concepts that have been adopted in most constitutive multiple kinematic hardening models such as the translation laws, magnitude of strain development and mode of changes in stiffness, they also seem to contradict some others such as the dragging of surfaces by current stress states, their geometry, size, configuration and relativistic consequences. This is certainly a subject for further research. However, it can derivatively be concluded that:

1) The methods of quantitatively determining the magnitudes of the zonal sub-yield strain and the Limiting (Critical) Elastic State proposed in this Study are useful in modeling and prediction of geo-structural behavior, risk analysis and construction control.
2) The proposed GECPROM is versatile and appreciably effective in probing, simulating, modeling and predicting geotechnical changes in ground and geomaterial properties.
3) The GECPROM mathematical functions and modules may be useful in correcting the models that have been developed based on tests performed on reconstituted clays, in order to model the behavior of natural clays.

6. ACKNOWLEDGMENT

The authors are highly indebted to Prof. Fumio Tatsuoka, formerly of the University of Tokyo. Special appreciation is extended to the Japan International Cooperation Agency (JICA), Taisei Corporation, Japan, Kajima Corporation, Japan, for sponsoring most of this research and the support of the Materials Testing and Research Department, Ministry of Roads and Public Works, Kenya.

REFERENCES

[1] Mukabi JN, "Characterization and modeling of various aspects of pre-failure deformation of clayey Geomaterials – Fundamental theories and analyses", Proc. 1st Int. Conf. on GEOMAT, Mie, 2011.

[2] Tatsuoka F, "Laboratory stress-strain tests for developments in geotechnical engineering research and practice", Bishop Lecture, to be published in Proc. Int. Symp., Seoul, 2011.

[3] Mukabi JN, Kotheki S, Mathematical derivative of the modified Critical State Theory and its application in Soil Mechanics. Procs. 2nd International Conf. on Applied Physics & Mathematics, 2010 IACSIT, Kuala Lumpur, pp. 484-492.

[4] Mukabi JN, Kotheki S, "A Geo-mathematical model for quantitative analysis and prediction of the impact of environmental changes on the characteristics of geomaterial formation", in Proceedings of 14th Int. Conf. on Mathematical Geosciences, Budapest, 2010, pp 382-406.

[5] Carmona A, Clavera-Gispert R, Gratacos O, Hardy S, "Modeling syntectonic sedimentation: Combining a Discrete Element Model of techtonic deformation and a process-based sedimentary model in 3D", J. of Mathematical Geosciences, vol. 42, No. 5, July 2010, pp. 519-534.

[6] Riley KF, Hobson MP, Bence SJ, Mathematical Methods for physics and engineering .Cambridge: Cambridge University Press, 1998.

[7] Dass HK, Advanced Engineering Mathematics. New Delhi: S. Chand & Company Ltd., 1999.

[8] Jardine RJ, "Investigations of pile-soil behavior with special reference to the foundations of offshore structures", Ph.D thesis, Imperial College, University of London, 1985.

[9] Jardine RJ. "Some observations on the kinematic nature of soil stiffness", Soils & Foundations, JSFE Vol. 32, No. 2, 1992, pp111-124.

[10] Atkison JH, Stallebrass SE, "Experimental determination of stress-strain-time characteristics in laboratory and in-situ tests" in Proc. of 10th Eur. Conf. on SMGE. Florence 3, 1991, pp. 915-956.

[11] Stallebrass SE, Taylor RN, "The development of a constitutive model for the prediction of ground movements in overconsolidated clay", Geotechnique, vol. 47, No. 2, 1997, pp. 235-253.

[12] Tatsuoka F, Jardine RJ, Presti DL, Benedetto HD, Kodaka T, "Characterizing the pre-failure deformation of geomaterials". XIV IC on SMFE, Theme Lecture, Hamburg, 1999, pp. 2129-2164

An Emergency Medical Care Information System for Fetal Monitoring

Muhammad Ibn Ibrahimy
Department of Electrical and Computer Engineering
International Islamic University Malaysia
Kuala Lumpur, Malaysia

ABSTRACT: Developing and less developing countries are identified in risk of stillbirth due to insufficient emergency medical take-care supports. The regular check-up of the fetal electrocardiography could be an earliest prevention of this occurrence. This paper presents a research work aims to implement a simple, customize and portable emergency medical care system for fetal ECG monitoring from remote location. After acquisitions of the ECG signal from the abdomen wall of a pregnant woman (patient), the local terminal then transfers this ECG signal as data to the remote terminal at the expert physician for diagnosis purpose. At the remote terminal, the fetal ECG signals are then extracted from the ECG signals. In this case, computer network establishes a bridge between the patient and a distant expert physician. The network program developed based on the client/server applications. The developed network program is capable to support both the ECG data transfer and online chat session simultaneously. A specialist physician at the remote terminal can diagnose the fetal ECG signal and provides instruction to the local terminal in case of emergency. A number of cases studied by this developed system and found approximately same result compared with a commercial one.

Keywords- Telemedicine; ECG; AFECG; FECG; FHR

1. INTRODUCTION

Nowadays, telemedicine is producing a great impact in our daily life for health take-care support, especially the patient whose are located in remote nonclinical environment or if there is no expert physician. The stillbirth rate is still higher in the developing and less developing countries compared to the developed countries due to insufficient emergency medical take-care supports. The telemedicine support for the FECG monitoring systems can be a sort of solution of this crisis. An FECG monitoring systems based on the telemedicine support consist of three major parts: (1) data acquisition system, (2) networking system, and (3) fetal hart rate (FHR) monitoring system. The AFECG data acquisition system acquires the fetal ECG signal from mother's abdominal wall and stores into a local computer terminal as a data. The network application serves the purpose to transfer the AFECG data to the remote terminal for diagnosis purpose. The AFECG signals are then processes at the remote terminal and extract the FECG from the AFECG signal by an FHR monitoring program. However, still the total systems are huge, complex and costly for individual. The AFECG signal obtains from the abdominal wall of the pregnant mother contains many vital information regarding the fetus. This signal provides significant information about the heart rate, arterial blood oxygenation, blood pressure and respiratory-rate, etc [1]. Most of the stillbirth occurs during the maternal sleep, since during this period, blood pressure of the mother becomes lowest, and also a cord compression occurs when the mother is lying down especially, in late term while there is a little space for the baby to move. An FECG monitor systems may have a potential effect to detect any dangerous fluctuation or decline in the baby's ECG and allows some scope for appropriate medical intervention. To observe such abnormalities, compact, portable, long-term ambulatory monitoring system has approved by the mainstay of fetal surveillance during pregnancy [1].

2. METHODOLOGY

This research has been divided into three parts such as (1) developing a compact portable AFECG data acquisition system, (2) developing a customized network program for communication between local terminal and remote terminal (3) improving the accuracy of the existing techniques for automatic analysis of the AFECG signals for FHR monitoring. The overall flow of the research work as shown in Fig. 1.

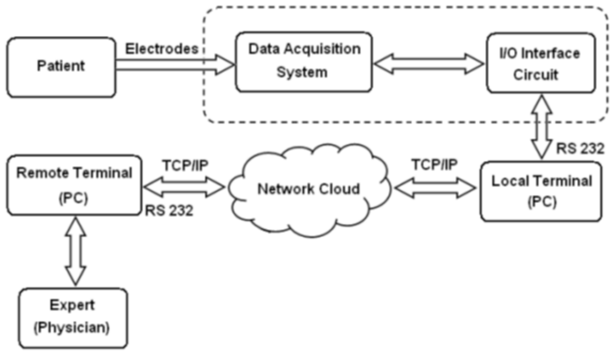

Figure 1. The basic block diagram of the overall system.

2.1 Data Acquisition System

The purpose of the data acquisition system is to collects the maternal AFECG signal and sends it to a local computer through RS232 serial port. The system developed based on a commercial ECG front-end ASIC hardware module named "CARD*IC*". A microcontroller module (18F4550) controls all the functions of the system. An optical isolator is used in between the system and computer for electrical isolation, which prevent the damage from unexpected electrical short circuit condition as shown in Fig. 2.

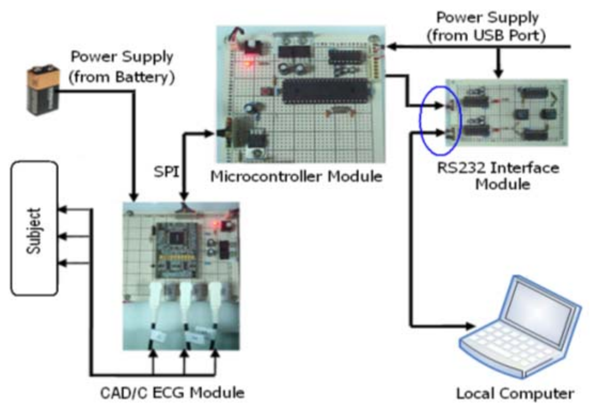

Figure 2. Pictorial view of the AFECG data acquisition systems

2.2 Networking

The networking part is developed by using Visual Basic client/server pair applications. In brief, this part of the project is included two sections (1) chat section, and (2) file transfer section. The main purpose of the chat section is to establish a connection between patient (client) and physician (server), so they can make conversation to each other on real time. On the other hand, the file transfer section establishes a network connection using TCP/IP protocol, so that client can transfer any types and any size of data file(s) to the server terminal. The computers are identified by their 32-bit IP address and a 16-bit number is used to identify the ports during the network communication.

2.3 Software Design and Development

The network program is in the form of client/server pair applications. The client application, known as Local Patient Monitoring System (LPMS), which is installed in the local terminal.

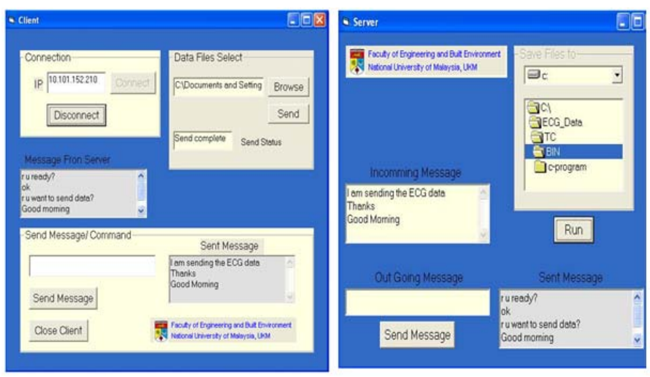

(a) (b)

Figure 3. (a) Local Patient Monitoring System (LPMS) and (b) Remote Patient Monitoring System (RPMS)

On the other hand, the server application, known as Remote Patient Monitoring System (RPMS), is deeds to be install in the remote terminal. The most fundamental feature of the network program is to setup a connection between the local and remote terminal via TCP/IP. When a network connection is successfully setup, the user can send the data from local terminal to the remort terminal. The physician at the remote location can display the fetal ECG graph with the graph plot features of the RPMS. In addition, both the users can communicate via a simple chat program. The Fig. 3(a) and Fig. 3(b) are the screenshot of LPMS and RPMS respectively.

2.4 Summary of the Network Program

Local Patient Monitoring System (LPMS) provides:

- Dial up to predefined hospital or clinic terminal and hence setup a full duplex communication with RPMS
- Setup a chat/dialog session with RPMS
- Transfers the AFECG data

Remote Patient Monitoring System (RPMS) provides:

- Setup a network connection with LPMS
- Setup a chat/dialog session with LPMS
- Receives the AFECG data and processed for graph plots

2.5 Networking Module and Algorithm

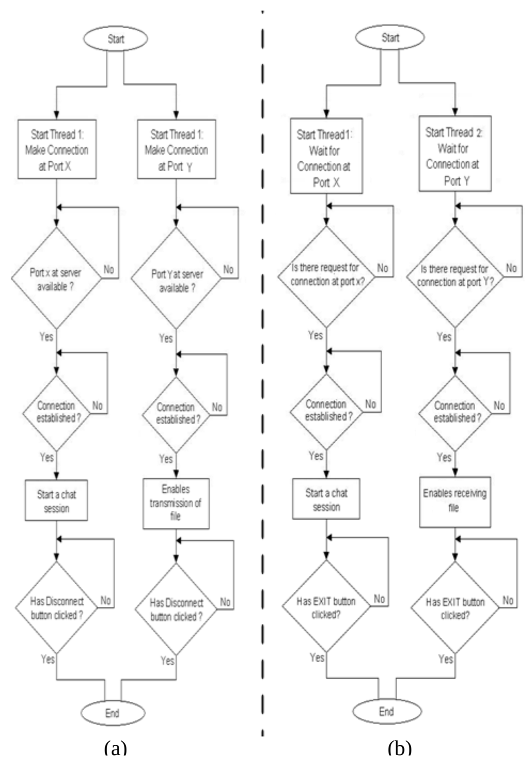

Figure 4. (a) LPMS networking module flowchart and (b) RPMS networking module flowchart.

The network module of LPMS works in synchronization with its counterpart RPMS. The function of these modules is to setup a full duplex connection between the local terminal and the remote terminal [2]. Multithread programming concepts are used for developing the network modules. Multithread programming is necessary due to the requirement of multitasking operation [3] in the networking applications. For instance, some times LPMS is required to hold a chat session, at the same time it sends the AFECG signal RPMS terminal. Figure 4a and Figure 4b are the flowcharts for the LPMS and RPMS respectively. At any instance, when the client is connected to the *X* number port of the server, then the server assigned a thread that waits for its connections at port *X*. Ones the connection is accepted, the client and the server can communicate with each other through the connection bound at the port *X*. file module (in LPMS)

Sending/Receiving Data Module Algorithm:

The send file and the receive file modules in the LPMS and the RPMS respectively are responsible for enables the transmission and reception of AFECG data via the networking module. The algorithm for sending AFECG data file and the fetal heart bit sound file are almost same except, the data types employed in each cases are slightly different.

Fig. 5(a) and Fig. 5(b) are the flowchart for send file and file receive modules respectively. Based on the Figure 5a, the first step is to open a socket for connection. A socket is one endpoint of a two-way communication link between two programs running on the network [4]. It is bound to a port number so that the TCP layer can identify which data is send to which destination. Then, an I/O stream is opened for connection. The socket I/O stream will remain open until the LPMS is exited.

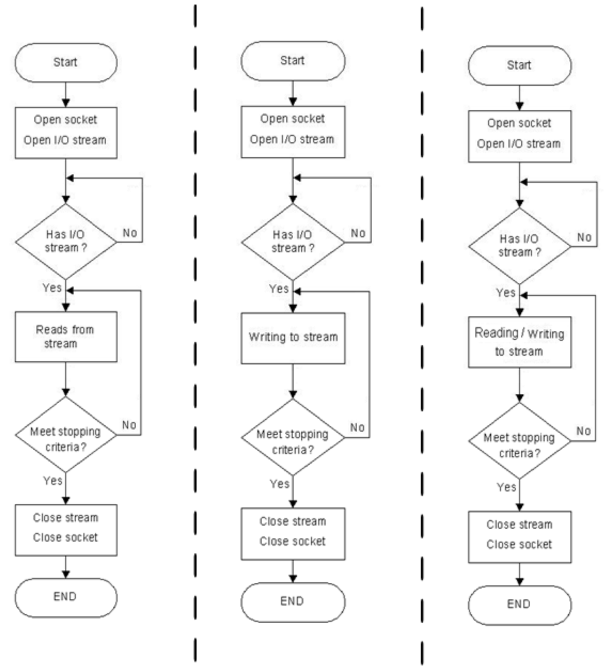

(a) (b) (c)

Figure 5. (a) Send file module flowchart (b) Receive file module flowchart and (c) Chat module flowchart.

The algorithm for receiving the file is almost similar with the file-sending algorithm except, in this case data will be read from the I/O stream. The flowchart of the file receive algorithm is shown in Figure 5b. The socket and I/O stream will remain open until the RPMS exited.

Chat Session Module Algorithm:

The chat session module is intended to provides connection for communication between the patient (or patient's attendant) at LPMS and physician at RPMS. This is necessary because the physician cannot know the patient's all health condition only through the data file, but also need to know the health condition during some discussions. Moreover in case of received data or file is corrupted, the physician can request for retransmission. Also a chat session can enable the online consultation.

Fig. 5 (c) shows the flowchart for chat session module. The logical flow of this module is almost same as the file send and file receive modules. The significant difference is that there is a write to and read from I/O stream mechanism are used in the case of chat module.

3. FECG EXTRACTION AND DETECTION

In this article, our intention is to focus on the network part of the systems then, we feel to need a brief description on the others parts of the systems like, FECG Extraction and detection from the AFECG signal. The algorithm of this portion is a crucial part of the ambulatory recorder for processing the AFECG signal. For measuring the FHR and maternal heart rate (MHR) [5] its needs to extract and detect the fetal and maternal R peaks from the AFECG signal. The algorithm has been developed for this purpose based on the digital filtering, adaptive threshold, and statistical properties of the time domain signal as shown in Figure 6. Equation 1 expresses an AFECG signal obtains from the maternal abdomen wall.

$$A(t) = R(t)M(t) + F(t) + N(t) + B(t) \qquad (1)$$

Where, R(t) is modulation functions from respiration, M(t) is MECG, F(t) is FECG, N(t) is noise and B(t) is low frequency baselines (< 10 Hz) from the muscle movement. After filtering the AFECG signal, the equation (1) can be written as equation (2). This equation consist only the maternal and fetal ECG signals with a small noise.

$$A(t) = M(t) + F(t) + N(t) \qquad (2)$$

The algorithm then detects the maternal QRS complexes by threshold the maximum value of the match filter output [6]. A maternal ECG template is formed from the successfully detected the maternal QRS complexes using the R peak as the fiducial point [7]. This routine first measures the slope of the matched filter output by the equation (3).

$$y'(n) = y(n) - y(n-1) \qquad (3)$$

A maxima in the sample (n-1) is considered when the slope changes from y'(n-1) ≥ 0 to y'(n) < 0. This duration is assumed minimum fetal QRS duration. In this search routine, the time instant of the successive three maxima such as max1, max2, and max3 are stored within an R wave search interval. When the value of max1 is greater than of the threshold, an R peak is assumed to be found and the value of max2 is considered as noise peak. If the value of max2 is validated as the R peak then the value of max3 is kept as a noise peak. In this way the threshold is continually updated the R peak and noise levels. A moving average routine is used to average the MECG template, the fetal QRS template, noise peaks and the RR intervals.

4. RESULTS AND DISCUSSION

A number of cases examined by transmission and reception of the data files. The received data after processed compared with the sent data and found almost same. Fig. 6 shows one of the result indicate the heart rate of a patient at 38 weeks of pregnancy. In this case, the AFECG signal is processed at the remote terminal by our developed program. It compared with the practical data and found the MHR and FHR recording performance is almost same. In addition, the chatting section of the network program also worked well. The developed algorithms can extract both the maternal and fetal heart rates in real-time utilizing a single-lead configuration. In this comparison, we used a simultaneous ECG signals from the same subjects. A few snap shot has been representing here in Fig. 7 and found they are almost same nature of graphs.

Figure 6. FHR and MHR traces from patient (week 38)

5. CONCLUSION

The performance of the system for determining the FHR depends upon the FECG signal, which is obtained by subtracting the average MECG from the AFECG signal. It is found that the performance of the system also depends on the amplitude of FECG signal within the AFECG signal. If the FECG is very small (less than 3 μV) accurate detection of the fetal R peaks would not be possible.

The TCP/IP provides a reliable and point-to-point communication channel for the client-server application for transfer the AFECG signal through the Internet.

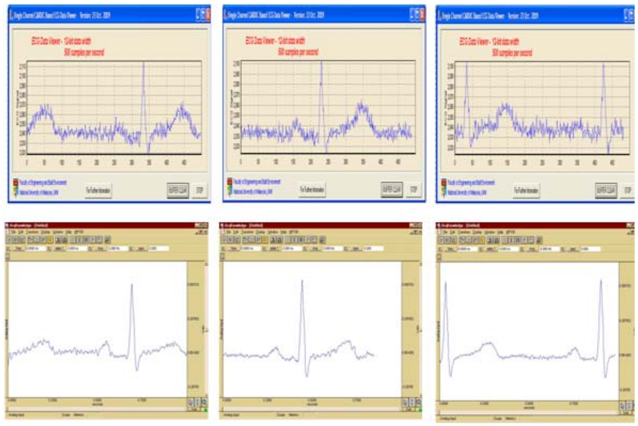

Figure 7. Samples comparison- above three figures are our CARDIC based ECG records and below three figures are the commercial BIOPAC System ECG records

6. REFERENCES

[1] M. A. Hasan, M. B. I. Reaz, M. I. Ibrahimy, M. S. Hussain, J. Uddin. Detection and Processing Techniques of FECG Signal for Fetal Monitoring", Biological Procedures Online, 2009, pages 33.

[2] R. Vaze, R. W. Heath Jr, On the Capacity and Diversity-Multiplexing Tradeoff of the Two-Way Relay Channel, computer Science, Information technology, 2008, pp. 1-36.

[3] C. J. Konig, M. Buhner, G. Murling, Working Memory, Fluid Intelligence, and Attention Are Predictors of Multitasking Performance, but Polychronicity and Extraversion Are Not, Human Performance, 2005, vol. 18 (3), pp. 243-266.

[4] G. J. Fakas, A. V. Nguyen, D. Gillet. A Collaborative and Cooperative Learning Environment for Web-based Experimentation, The electronic laboratory journal, 2005, vol. 14 (3), pp. 189-216.

[5] R. W. F. Campbell, P. Gardiner, A. Murray. Automatic Analysis of Ambulatory ECG Records, European Heart Journal, 1984, vol. 5, pp. 31-34.

[6] A. Matonia, J. Jezewski, T. Kupka, K. Horoba, J. Wrobel, A. Gacek. The Influence of Coincidence of Fetal and Maternal QRS Complexes on Fetal Heart Rate Reliability, Medical and Biological Engineering and Computing, 2006, pp. 393-403.

[7] F. Ahmed, M. I. Ibrahimy, M. A. M. Ali, E. Zahedi. A Portable Recorder for Long-Term Fetal Heart Rate Monitoring, Microprocessors and Microsystems, 2002, vol. 26(7), pp. 325-330.

First International Conference on Geotechnique, Construction Materials and Environment, Mie, Japan, Nov.21-23, 2011, ISBN: 978-4-9905958-0-7 C3051

Effects of Gypsum on the Swelling and Dispersion Behavior of Fine Grained Soils from Sudan

Abdul Karim M. Zein and Ahmed M. Elsharief,
Building and Road Research Institute (BRRI), University of Khartoum, SUDAN

ABSTRACT: This paper presents a study on the effect of gypsum addition in improving the swelling and dispersion characteristics of four compacted expansive and dispersive soil samples from Sudan. Gypsum was added to the soil samples studied in amounts varied from 2 to 9% after being prepared at specified placement conditions. Swelling tests performed on two highly expansive soils included the free swell, linear shrinkage, swell percent and swelling pressure. The double hydrometer, pinhole and chemical tests were used for the evaluation of soil dispersion behavior in two samples of the River Nile alluvial deposits. The study results showed that the swelling potential of the highly expansive clay soils could be reduced significantly upon their treatment with around 5 to 6% of gypsum admixture but adverse effects may result if this gypsum content is exceeded. The results of dispersion tests indicated that the addition of 2 to 4% of gypsum resulted in an improvement in the dispersive characteristics such that the dispersion degree in the two soils changed from dispersive or highly dispersive to intermediate or completely non-dispersive states.

Keywords: Expansive soils; dispersive soils; gypsum; soil treatment; swelling potential; dispersion phenomenon

1. INTRODUCTION

Soil types that exhibit significant volume changes in associated with changes in their moisture content are referred to as expansive or swelling soils. Such significant changes due to the swelling/shrinking nature are likely to cause heavy distress or damage to engineering structures built on them. Expansive soils are internationally widespread and of major economic significance. The annual value of damages to various types of structures built on or within these soils runs into extremely high costs worldwide. In Sudan, the expansive soil problem has been recognized since 1967 and several studies have been carried out to study their engineering properties and evaluate the performance of some foundation types placed on them [1], [2], [3]. Sudan's climate is wholly tropical and the expansive soils represent about 25% of the country area and occur within the central and eastern clay plains. The expansive soils treatment methods currently used include soil removal and replacement, remoulding and compaction, pre-wetting, and chemical stabilization. Dispersive soils may be defined as those soils that have repulsive forces between the clay particles that exceed the attractive forces when placed in water. The tendency of the clay soils to disperse or de-flocculate depends upon the mineralogy, soil chemistry, the salts dissolved in the pore water and the water causing soil dispersion. Many earth dam or highway embankments and hydraulic structures constructed partially or entirely with dispersive soils have suffered serious erosion problems or have failed as reported in published literature [4]. There are many studies carried out worldwide on the characterization of dispersive behavior of soils and evaluation of the methods and techniques which may be adopted for their treatment. The experience with dispersive soils when used for construction of civil engineering works is rather short in Sudan and there are only few reported studies and investigations [5] in this field.

Most of the failures and distresses that have occurred in engineering structures associated with expansive and dispersive problems are related to the presence of the clay mineral montmorillonite in such soils. The mechanisms of soil swelling and soil dispersion are dependent on the thickness of the diffusion double layer and the concentration and valence of absorbed ions around clay particles. Soil swelling occurs due to the unbalanced electrical charge and cation exchange capacity produced by sodium based montmorillonite. However, soil dispersion seems to be a result of the presence of sodium ions adhering to montmorillonite particles rather than the sodium present in the pore water [6]. Soil tendencies to swell or disperse can be reduced by replacing sodium ions by compounds which may produce cations of lower ion exchange capacity to form a more balanced electrical charge in soil structure. Replacement of monovalent sodium by substances with divalent calcium ions such as lime and gypsum may lead to marked reduction in diffuse double layer thickness which in turn leads to a lower swelling potential and reduced potential for dispersion. By mixing lime or gypsum with a soil, the calcium present in these substances encourages the flocculation of the soil particles thereby improving the soil structure.

Many previous investigations were performed using chemical admixtures to reduce the swelling potential of expansive soils and improve the behavior of dispersive soils. However, only a few studies can be cited in published literature on the use of gypsum stabilization for the treatment of expansive and dispersive soils.

The study presented in this paper is aiming to contribute in this research area by investigating the effects of gypsum addition on the behavior of selected highly expansive and dispersive Sudanese soils.

2. SOIL TYPES AND TESTING METHODLOGY

Four different soil types collected in disturbed conditions from three different locations in the country were considered in this study. They included two potentially expansive soils collected from central and southern Sudan (designated hereinafter as Soils A and B) and two dispersive soils sampled from northern Sudan (designated as Soils C and D). Previous studies have shown that montmorillonite is the dominant clay mineral present in all the studied soils [5], [7].

Gypsum in a chemical form of hydrated calcium sulphate ($CaSO4\text{-}2H_2O$) was added in predetermined quantities to portions of the soil samples and mixed properly and stored for curing to obtain variable gypsum percentages based on the total dry mass of the soil samples. The expansive soils samples were mixed with 3%, 6% and 9% of gypsum, whereas the dispersive soil samples were mixed with 2% and 4% of gypsum.

The basic index and engineering properties of the natural and gypsum treated soil samples were determined to classify their types in accordance to BS1377 soil testing standards. Compaction tests were performed according to the standard Proctor compaction test method to determine the optimum moisture content (OMC) and maximum dry density (MDD) for each soil.

A concise summary is given in Tables I and Table II for the basic properties and the compaction test results of the expansive and dispersive soil types respectively before and after treatment with gypsum.

Table I Index and compaction properties of expansive soils

Soil type	A				B			
Gypsum (%)	0	3	6	9	0	3	6	9
FC (%)	83	87	88	86	80	81	80	78
CC (%)	47	14	3	2	12	10	7.5	3
LL (%)	66	58	66	65	62	58	56	60
PI (%)	36	34	41	37	38	39	37	36
OMC (%)	27	28	28	28	23	24	24	25
MDD (kN/m^3)	14.7	14.7	14.4	14.5	15.6	15.4	15.1	14.9

The main aspects relating to the effects of the gypsum on the swelling characteristics and dispersive behavior of study soils are described and discussed separately in the following sections.

3. EFFECT OF GYPSUM ADDITION ON SWELLING BEHAVIOR OF EXPANSIVE SOILS

3.1 General

The behavior of expansive soils is normally evaluated in terms of two main swelling potential components; volume change and development of swelling pressure due to an increase in their moisture content. These two parameters are determined in the laboratory using an oedometer apparatus and the test results are used for the prediction of the soil heave under field conditions.

Table II Index and compaction properties of dispersive soils

Soil type	C			D		
Gypsum (%)	0	2	4	0	2	4
FC (%)	57	55	60	73	72	70
CC (%)	11	10	11	14	0	0
LL (%)	44	34	36	37	33	36
PI (%)	18	7	7	11	7	7
OMC (%)	21	21	21	21	22	22
MDD (kN/m^3)	16.1	16.7	16.8	16.2	16.5	16.4

3.2 Soil Conditions and Swelling Properties Considered

Four direct and indirect tests were performed to evaluate the swelling potential of the two compacted expansive soils in their natural and gypsum treated states namely; linear shrinkage, free swell, swell percent (one dimensional volume change) and swelling pressure tests. The former two tests are used for the identification and classification of the swelling potential of expansive soils. The swell percent and swelling pressure tests were performed on samples prepared in the laboratory at two different initial placement conditions; one at OMC (denoted as Samples A1 and B1) and the other at a dry of optimum moisture content but with the dry density approximately maintained at the MDD value of each soil (denoted here as Samples A2 and B2). The swell percent and swelling pressure tests were performed in an oedometer apparatus on soil specimens, 76mm in diameter and 20mm thick. During testing, the samples were allowed to saturate under the conditions of free vertical swelling under a nominal load (0.125kN) in the swell percent test and a full restrained condition in the constant volume swelling pressure test.

3.3 Analysis and Discussion of Swelling Test Results

To evaluate the effects of gypsum addition on the swelling characteristics of Soils A and B, the various classification and swelling test results were plotted against gypsum content as shown in Figures 1 through 4. The variations of the plasticity index (PI), linear shrinkage (LS), free swell (FS) and clay content (CC) fraction with added gypsum percents are as shown in Fig. 1(a) and 1(b) for Soils A and B respectively.

As may be noted from the graphical relationships shown in Fig. 1, the addition of up to 9% gypsum indicated small reductions in the values of the plasticity index (PI) for both soil types. However, mixing gypsum with soil samples has in general produced more significant changes in the values of the other three swelling indicative indices. The addition of 3 to 9% gypsum content resulted in reductions in the free swell (FS) by 4 to 25%, linear shrinkage (LS) by 4.3 to 50% and clay content (CC) by 16.7 to 96%. It may also be noted that the effect of gypsum addition on the swelling potential indices is more evident in the samples of Soil B than in those of Soil A.

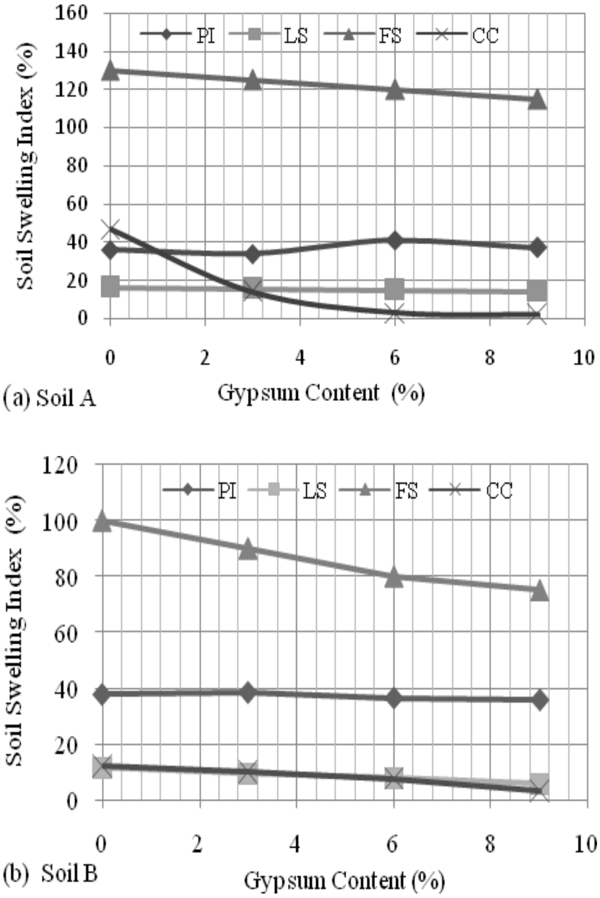

Figure1: Swelling indices versus added gypsum content for Soils A and B.

To investigate the effects of gypsum addition on soil swelling in a rational manner, six published classification schemes were used to evaluate the swelling potential on the basis of the measured properties before and after treatment. A summary of the soil swelling potential rating comparisons for the natural and treated soil samples made according to the selected methods is given in Table III.

It may be noted from Table III that similar swelling potential ratings were revealed by the three classification methods based on single indices (PI, FS and LS) in Soil A even for those samples mixed with 9% gypsum but the effects of gypsum in reducing the swelling potential of Soil B are obvious. The schemes based on soil indices combinations (e.g. PI and CC) and measured swelling parameters indicate clearly that the swelling potential in both soil types changed from a high or very high degrees to low or medium at 3% gypsum content and to mostly low swelling potential at 6% and 9% percentages. Based on these observations, it may be disclosed that the degree of swelling potential of highly expansive soils can be significantly reduced through mixing with 3 to 6% of gypsum.

Table III Swelling potential classification of Soils A and B before and after treatment with gypsum

Swelling potential rating method	Soil Index or property	Soil A + % gypsum				Soil B + % gypsum			
		0	3	6	9	0	3	6	9
Holtz and Gibbs [8]	Free Swell	H	H	H	H	H	M	M	M
Altmeyer [9]	Linear Shrinkage	H	H	H	H	H	H	M	M
Chen [10]	PI	H	H	H	H	H	H	H	H
Van derMerwe[11]	PI and CC	VH	M	L	L	M	L	L	L
Thomas et al [12]	Swell percent	H	M	M	M	H	L	L	H
Thomas et al [12]	Swelling pressure	M	M	M	L	M	M	L	L
Swelling potential ratings: VH =Very high, H = High, M = Medium/ moderate/marginal and L = Low									

Figures 2 and 3 show the variations in the swell percent and swelling pressure values respectively with added gypsum for the four samples (two from each soil) initially prepared at different placement conditions.

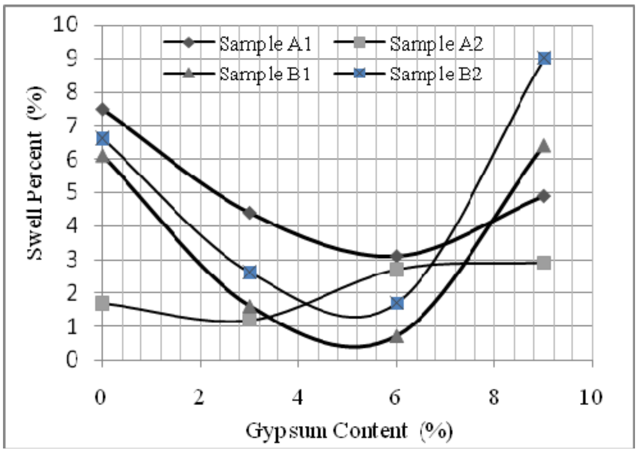

Figure 2 Swell percent versus gypsum content

The trends of the swell percent versus gypsum percent depicted in Figures 2 indicate significant reductions in swelling potential in three samples of both soil types upon treatment with 5 to 6% gypsum. In Sample A2 of Soil A, only a slight reduction in the swell percent was noted for gypsum content ranging from 0 to 3%. The observed swell percent-gypsum content trends suggest that there is optimum 5-6% gypsum content which seems to effectively reduce the swelling potential of highly compacted expansive soils placed around their OMC and MDD conditions. However, gypsum contents exceeding 6% produced an adverse effect on swelling potential particularly in the two samples compacted at OMC whereby the swell percent increases considerably with increasing gypsum content.

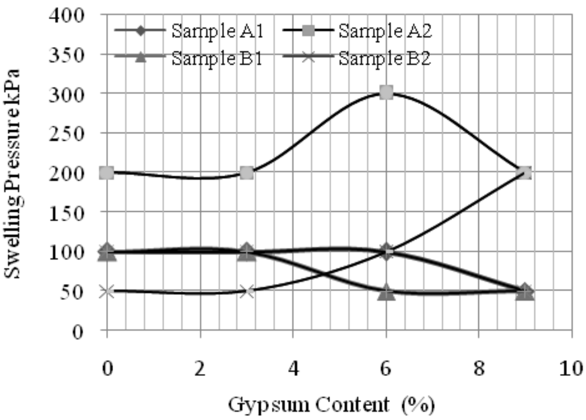

Figure 3 Swelling pressure versus gypsum content

Somewhat different swelling pressure versus gypsum content trends were noted in Figure 3 for the soil samples compacted at OMC and those compacted dry of OMC in both soil types. In the two samples compacted at OMC, the swelling pressure remained unchanged up to 3% and 6% of gypsum content in Soils A and B respectively but then it dropped to 50% of the magnitudes corresponding to untreated soil samples. Reductions in the swelling pressure values exceeding 60% have been reported in another study [13] to occur as a result of adding 6% gypsum to expansive soil samples from India compacted at various dry densities.

In the samples compacted dry of OMC, there was no change in the swelling pressure values up to 3% of gypsum content but beyond this the swelling pressure increased steadily to 6% and 9% gypsum content in Soils A and B respectively.

In other words, the effect of gypsum content on the swelling pressure is generally conforming to that noted in the case of swell percent of the two samples compacted at OMC and MDD in both soil types. Fortunately, most of the design codes and specifications applied in practice call for the placement of compacted soil fill at field placement conditions equal or closely comparable to the OMC and MDD for most engineering projects.

Based on the finding of this study, gypsum addition proved to be an effective technique in reducing the swelling potential of highly expansive soils placed at such placement conditions. However, gypsum addition does not seem to be an effective measure for treatment of expansive soil samples compacted at moisture contents below OMC values. Perhaps this may be attributed to the complex nature of soil swelling phenomenon. The behavior of expansive soils can best be evaluated by considering all the physical, chemical, and mineralogical factors. The role and importance of each of these factors in contributing to the total swelling magnitudes measured is largely dependent on the soil type and initial soil placement conditions. Further investigations are required to study the effect of placement conditions on the swelling behavior of compacted expansive soils that can be achieved by mixing with gypsum.

4. EFFECT OF GYPSUM ADDITION ON THE BEHAVIOR OF DISPERSIVE SOILS

4.1 General

Dispersive soils cannot be identified through visual inspection or by using the results of standard laboratory soil classification tests and therefore some other special tests have been developed for this purpose. These include; the double hydrometer test, the pinhole test, the crumb test and the sodium absorption ratio (SAR) based tests.

4.2 Materials and Sample Preparation

Separate portions of the two samples representing Soils C and D were mixed with 2% and 4 % of gypsum and subsequently used for performing the required dispersion tests. The dispersion behavior of Soils C and D was evaluated by three different methods namely; the double hydrometer test, pinhole test described in Clauses 6.4 and 6.2 in Part 5 of the BS1377 respectively and chemical analysis done following the methods proposed by Sherard et al. [14] shown in Fig. 4.

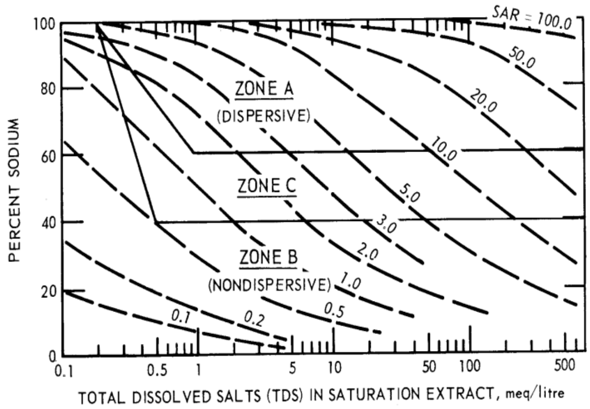

Figure 4 Relation between dispersion and soil pore water chemistry [14]

Figure 5 shows the double hydrometer test results for the samples of the CL type material (Soil C) treated with 2 and 4% gypsum tested with and without dispersant agents. Treated samples of Soil D were not tested by the double hydrometer method because of their extremely low clay fractions.

4.3 Analysis and Discussion of Results

4.3.1 Effects of Gypsum on the Soil Gradation and Index Properties

Table IV shows the effects of mixing Soils C and D with 2 and 4% gypsum on the fines content (FC), clay content (CC), liquid limit (LL) and plasticity index (PI). For Soil C samples mixed with gypsum, there was at most a slight increase in the FC whereas the CC did not change compared to the values corresponding to the untreated samples implying that the addition of gypsum did not seem to have caused any aggregation in this material. The LL and PI of samples treated with 2% gypsum were noted to be much lower than those of the untreated Soil C sample. Increasing the gypsum content from 2 to 4 % did not lead to any further changes in the Atterberg limits test results.

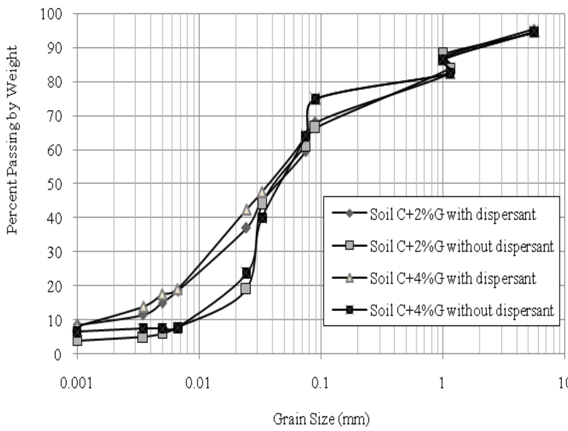

Figure 5 Double hydrometer test results for Soil C

For Soil D, the FC of treated sample indicated no change after gypsum treatment but the CC decreased significantly from 14 % to zero. Practically the same LL values were obtained for untreated and treated samples of Soil D however there was a small reduction in the PI value compared to its value in the untreated material.

4.3.2. Effect of Gypsum Treatment on Soil Dispersion

A summary of the results of dispersion evaluation for the samples of Soils C and D in their natural state and after being treated with 2 and 4% of gypsum is given in Table IV.

Table IV: Summary of soil classification and dispersion evaluation based on various test results.

Soil type	C			D		
Gypsum (%)	0	2	4	0	2	4
FC (%)	57	55	60	73	72	70
CC (%)	11	10	11	14	0	0
LL (%)	44	34	36	37	33	36
PI (%)	18	7	7	11	7	7
DH	D	ID	ID	ID	NA	NA
Pinhole	D1	ND2	ND1	D2	ND1	ND1
Chemical	D	D	ND	D	ID	ND

D1 = Highly dispersive, D2 = Dispersive ID = Intermediate dispersion, ND2 = Non-dispersive, ND1 = Completely erosion resistant
NA = Not appropriate, DH = Double hydrometter

The double hydrometer test results showed that the treated samples of Soil C has an intermediate degree of dispersion whereas the pinhole test results revealed that the treated samples were non-dispersive (ND2 dispersion category). On the other hand, the chemical analysis of the pore water salts in the material revealed that the material was still dispersive even after being treated with gypsum.

The pinhole test results showed that the treated samples of Soil D were completely erosion resistant (ND1 category) material. On the other hand, the chemical analysis of the pore water salts in the treated material revealed that the degree of dispersion improved upon treatment with gypsum from dispersive in its natural state to an intermediate degree of dispersion for 2% gypsum and almost non-dispersive for 4% gypsum. The evaluation based on chemical analysis results is relatively consistent with that based on the pinhole test results. The double hydrometer test was considered inappropriate for assessing the dispersion behavior in samples of Soil D treated with gypsum.

5. CONCLUSIONS

On the basis of the results of the study undertaken on the effects of added gypsum on the geotechnical characteristics of two highly expansive and two potentially dispersive materials from Sudan presented in this paper the following conclusions are drawn.

a) Expansive Soils

i) Gypsum addition has produced noticeable changes in the swelling potential of the two highly expansive soils (soils A and B). The swelling potential ratings made according to certain widely used published classification schemes changed from high or very high in the natural states to a low or medium after treatment with 3 to 9% of gypsum.

ii) The swell percent of the untreated samples of Soils A and B compacted at OMC and MDD decreased considerably to about 50% and 10% respectively upon mixing with 5-6% gypsum. This gypsum content appears to represent an optimum value which may be used for the stabilization of highly expansive soils. However, gypsum contents exceeding 6% caused an increase in measured swell percent values in both expansive soil types, thus producing an adverse effect on their swelling behavior.

iii) The results of gypsum addition on the swelling pressure of the two soils were consistent with those noted in the case of swell percent of the samples compacted at OMC and MDD. However, gypsum addition does not seem to be an effective in reducing the swelling pressure of expansive soil samples compacted dry of the OMC values.

b) Dispersive Soils

i) The results obtained from the various dispersion tests performed (i.e. the double hydrometer, pinhole and chemical tests) clearly indicated that Soils C and D soil samples are potentially dispersive in their natural state with a degree of dispersion evaluated to vary from dispersive to highly dispersive.

ii) Additions of 2 and 4 % of gypsum did not affect the gradation or the clay content of Soil C, suggesting that the samples did not experience aggregation formation. As for Soil D, the addition of gypsum significantly reduced the clay fraction. The addition of gypsum considerably reduced the plasticity of Soil C, but the reduction in the plasticity of Soil D was less significant.

iii) The results from the three different dispersion tests performed showed that, for both soil types studied, the addition of gypsum resulted in significant improvements in their degree of dispersion such that the treated samples became non-dispersive.

6. REFERENCES

[1] El-Jack, S. A. (1967), Physico-chemical mechanism of clay swelling and identification of swelling potential, Journal of Sudan Engineering Society No. 12

[2] Osman, M. A. and Charlie, W. A. (1984), Engineering properties of expansive soils in Sudan, Proc. 5th Int. Conf. on Expansive Soils, Adelaide, pp. 311-315.

[3] Osman, M. A. and Hamadto, M. E. (1984), Damage assessment of residential houses built on expansive soil areas in Sudan. Proc. 5th Int. Conf. on Expansive Soils, Adelaide, pp. 222-226.

[4]Paige-Green, P. (2008), Dealing with road subgrade problems in South Africa, Proc. 12th Int. IACMAG Conf. Geo, India pp 4345-4353

[5] Zein, A.K.M. and El Sharief, A.M. (2011), Effects of lime and Gypsum additives on the dispersive behavior of two River Nile deposits. Sudan Engineering Society Journal, Vol. 57, No. 1, pp 29-36.

[6] Indraranta, B. (1991), Erosion of dispersive soil in North East Thailand, Geotechnical Engineering, Vol. 22, pp 1-3.

[7] Ahmed M. M. (2008), Swelling potential of some expansive soils from Sudan, M.Sc. Thesis, Faculty of Engineering, University of Khartoum.

[8] Holtz, W.G. and Gibbs, H.J., (1956), Engineering properties of expansive clays. Transactions ASCE, 121:641-677.

[9] Altmeyer, W.T. (1955), Discussion of engineering properties of expansive clays. Proc. ASCE, 81(Separate No. 658):17-19.

[10] Chen, F.H. (1988), Foundation on Expansive Soils, Elsevier Science Publishers, N.Y.

[11]Van der Merwe, D.H., (1964), The prediction of heave from the plasticity index and the percentage clay fraction of soils. Civil Engineering, South Africa 6:103-107.

[12] Thomas, P.J., Baker, J.C. & Zelazny, L.W. (2000) An expansive soil index for
predicting shrink-swell potential. Soil Sci. Soc. Am. J. 64, 268-274.

[13] Ameta, N.K., Purohit, D.G.M. and Wayal, A.S. (2007), Characteristics, problems and remedies of expansive soils of Rajasthan, India. 2007EJGE.

[14] Sherard, J.I. Dunnigan, L.P.and Decher, R.S. (1977), Some engineering problems with dispersive soil, *ASTM STP* 623**:** 3-12.

Comparison of Bearing Capacity Equations for Vertical Central Loading

Muhammad Awais Shafique and Tanvir Iqbal Qayyum, Department of Transportation Engineering and Management, University of Engineering and Technology, Lahore, Pakistan

ABSTRACT: Bearing Capacity is the measure of the load that the soil can sustain when a structure is built over it. Building codes, field tests, laboratory tests and analytical equations are the four main sources from which the bearing capacity of soils can be taken. Researchers have come up with a number of analytical equations over the years for the determination of bearing capacity. This study addresses the bearing capacity equations for vertical central loading ranging from Rankine (1885) to Padmini (2008). The data of 13 load tests done by various researchers were used to evaluate the bearing capacity theories studied. The bearing capacity values calculated from the equations were compared with the test values. Moreover mean squared error was also determined. The evaluation shows that in most cases Meyerhof's Bearing Capacity equation provides much closer results to the actual ones, and therefore should be preferred except for square footings where the equation by Balla yields better results.

1. INTRODUCTION

Bearing capacity of soil is the capacity of soil to bear the load applied by the structures constructed over it. It is perhaps the most important aspect of soil.

Bearing capacity values are obtained by four main sources; building codes, field tests, laboratory tests and analytical methods. The use of analytical equations for computing bearing capacity is one of the widely used methods. Over the ages a lot of researchers have developed different concepts about the bearing capacity calculations and hence have added to the wide range of equations which can be used for bearing capacity calculations. The problem with so many theories is to decide which may give the best result for a particular soil, under given conditions.

The scope of work covers the bearing capacity equations dating back from Rankine's theory to the present era bearing capacity equations. The aim of the study is to evaluate various equations under vertical central loading and propose the most suitable.

2. METHODOLOGY

Various equations developed over the years for the calculation of bearing capacity under vertical central loading were studied. The data of 13 load tests carried out and documented by Muhs and Weiss [1], Melovic [2] and Muhs et al [3] was used to evaluate and compare the bearing capacity equations studied. The bearing capacities were calculated using different equations for the primary data provided by the researchers and then compared with the actual bearing capacities mentioned. The mean squared error for each approach was calculated and the most suitable theory was then figured out.

3. BEARING CAPACITY EQUATIONS

Rankine was perhaps the first researcher who proposed an equation for calculation of the bearing capacity of cohesionless soils. He derived his equation from the Rankine's earth pressure theory [4].

$$q_{ult} = \gamma D_f \left(\frac{1+sin\phi}{1-sin\phi}\right)^2 \quad (1)$$

Where

q_{ult} = Ultimate bearing capacity
γ = Density of soil
D_f = Foundation depth
ϕ = Angle of internal friction

Rankine was unable to accommodate the effect of footing size on bearing capacity. Pauker came up with a similar equation for sands as the one given by Rankine. His equation became very popular but had the same limitations as that of Rankine's [5].

$$q_{ult} = \gamma D_f tan^4\left(45 + \frac{\phi}{2}\right) \quad (2)$$

The Pauker-Rankine equation was modified by Bell to be used for cohesive-frictional soil. Again the effect of footing size was neglected [6].

$$q_{ult} = \gamma D_f {N_\phi}^2 + 2c\sqrt{N_\phi}(1 + N_\phi) \quad (3)$$

Where

$$N_\phi = tan^2\left(45 + \frac{\phi}{2}\right) \quad (4)$$

The first prominent achievement in the field of bearing capacity calculation was by Terzaghi. He studied failure zones beneath strip footings and thereby developed his famous bearing capacity theory. The equation proposed by Terzaghi incorporated the influence of footing size on bearing capacity in the form of shape factors [7].

$$q_{ult} = cN_cS_c + qN_q + {}^1\!/_2\,\gamma BN_\gamma S_\gamma \quad (5)$$

Where

c = Cohesion
q = Overburden soil pressure
B = Width of footing
N_c, N_q, N_γ = Bearing capacity factors
S_c, S_γ = Shape factors

Meyerhof modified the equation given by Terzaghi by adding depth factors and inclination factors. So the equation became equally applicable for inclined loads. Furthermore the values of bearing capacity factors were different from those given by Terzaghi [8], [9].

$$q_{ult} = cN_cS_cd_c + qN_qS_qd_q + 0.5\gamma BN_\gamma S_\gamma d_\gamma \quad (6)$$

Where

d_c, d_q, d_γ = Depth factors

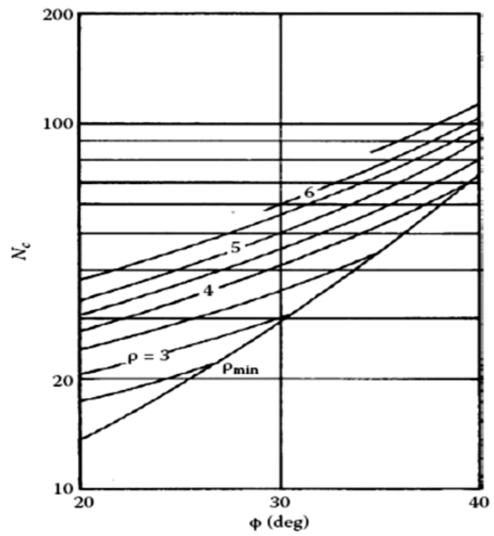

Fig. 1: Balla's bearing capacity factor N_c

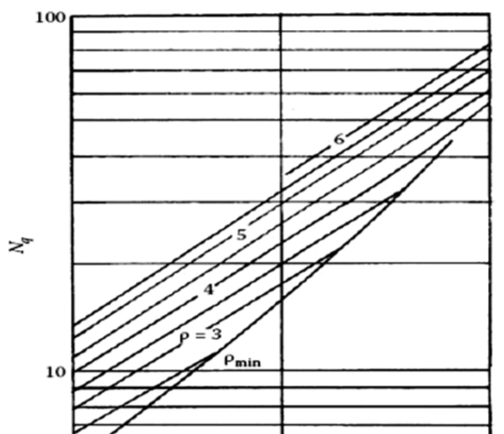

Fig. 2: Balla's bearing capacity factor N_q

Balla developed graphs (Fig. 1, 2 and 3) for calculating the bearing capacity factors to be used in Terzaghi's Equation [10].

Hu studied the base angle of the triangular wedge below a rough foundation and proposed his own graph (Fig. 4) for determination of bearing capacity factors [11].

Terzaghi's equation was simplified by Krizek, who developed an easy equation valid for ϕ = 0 to 35^o [12].

$$q_{ult} = [(228+4.3\phi)c+(40+5\phi)q+3\phi\gamma B]/(40-\phi) \quad (8)$$

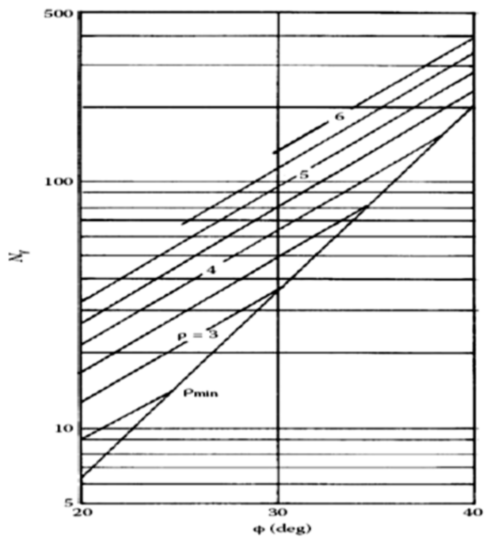

Fig. 3: Balla's bearing capacity factor N_γ

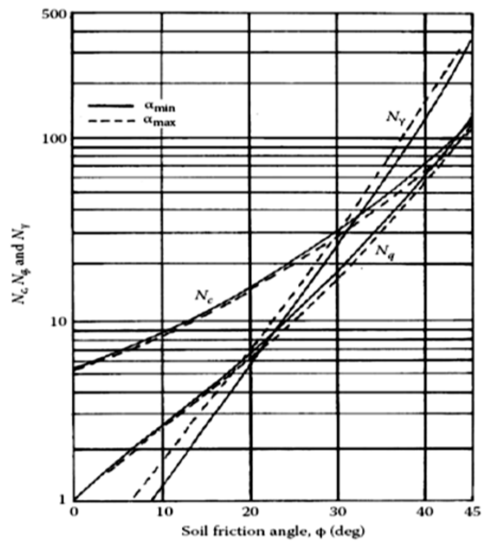

Fig. 4: Hu's bearing capacity factors

Meyerhof's equation was further extended by Hansen who included base factors and ground factors in addition to some slight changes [13].

$$q_{ult} = cN_cS_cd_ci_cb_cg_c + qN_qS_qd_qi_qb_qg_q + 0.5\gamma BN_\gamma S_\gamma d_\gamma i_\gamma b_\gamma g_\gamma \quad (9)$$

Where

b_c, b_q, b_γ = Base factors
g_c, g_q, g_γ = Ground factors

Vesic proposed a similar equation like the one suggested by Hansen. Both these equations are applicable for vertical as well as for inclined loading [14].

Table I: N_c and N_q by Bolton and Lau

ϕ	N_q		N_γ			
	Smooth or rough		*Smooth*		*Rough*	
(deg)	*Strip*	*Circle*	*Strip*	*Circle*	*Strip*	*Circle*
5	1.57	1.65	0.09	0.06	0.62	0.68
10	2.47	2.80	0.29	0.21	1.71	1.37
15	3.94	4.70	0.71	0.60	3.17	2.83
20	6.40	8.30	1.60	1.30	5.97	6.04
25	10.7	15.2	3.5	3.0	11.6	13.5
30	18.4	29.5	7.7	7.1	23.6	31.9
31	20.6	34.0	9.1	8.6	27.4	38.3
32	23.2	39.0	10.7	10.3	31.8	46.1
33	26.1	45.0	12.7	12.4	37.1	55.7
34	29.4	52.2	15.0	15.2	43.5	67.6
35	33.3	61.0	17.8	18.2	51.0	82.4
36	38	71	21	22	60	101
37	43	83	25	27	71	124
38	49	99	30	33	85	153
39	56	116	36	40	101	190
40	64	140	44	51	121	238
41	74	166	53	62	145	299
42	85	200	65	78	176	379
43	99	241	79	99	214	480
44	115	295	97	125	262	619
45	135	359	120	160	324	803
46	159	444	150	210	402	1052
47	187	550	188	272	505	1384
48	222	686	237	353	638	1847
49	265	864	302	476	815	2491
50	319	1103	389	621	1052	3403
51	386	1427	505	876	1373	4710
52	470	1854	663	1207	1812	6628

Based on soil strength parameters, Bolton and Lau established a bearing capacity calculation procedure. The values of N_q and N_γ, given in Table I, were proposed for circular and strip footings subjected to vertical loading [15]. Qayyum experimented on sand under rapid loading and proposed a general ultimate bearing capacity equation applicable for vertical as well as inclined central and eccentric loading [16].

The simplified form of the equation for vertical central loading is,

$$q_u = 0.45\gamma BN_\gamma \quad (10)$$

Salgado et al (2004) determined the bearing capacities of square, rectangular, strip and circular foundations in clay accurately based on finite element limit analysis. Using these analyses precise values of shape and depth factors were proposed [17].

$$d_c = 1 + 0.27\sqrt{\frac{D}{B}} \quad (11)$$

$$S_c = 1 + C_1\frac{B}{L} + C_2\sqrt{\frac{D}{B}} \quad (12)$$

Where

C_1 and C_2 are determined from Table II

Padmini et al developed neurofuzzy models for the prediction of ultimate bearing capacity of shallow foundations on cohesionless soils [18].

Table II: Regression constants in (12) for the shape factor

B/L	*C_1*	*C_2*
1 (circle)	0.163	0.210
1 (square)	0.125	0.219
0.50	0.156	0.173
0.33	0.159	0.137
0.25	0.172	0.110
0.20	0.190	0.090

4. DATA COLLECTION

Data from 13 different Test scenarios was collected from literature. The researchers have actually performed these load tests on different soils and determined the bearing capacities. The data sets taken from [1], [2] and [3] are given in Table III, IV and V respectively.

Table III: Data from Muhs and Weiss (1969)

Data Set	**1**	**2**	**3**	**4**
Depth, D_f(m)	0	0.5	0.5	0.5
Width, B (m)	0.5	0.5	0.5	1
Length, L (m)	2	2	2	1
Unit wt. γ (KN/m^3)	15.69	16.38	17.06	17.06
Angle of internal friction, φ	38.5	36.25	40.75	38.5
Cohesion, c (KPa)	6.37	3.92	7.8	7.8
Actual Bearing Capacity, q_u (KN/m^2)	*1059.12*	*1196.41*	*2373.21*	*3236.20*

Table IV: Data from Melovic (1965)

Data Set	**5**	**6**	**7**	**8**
Depth, D_f(m)	0.4	0.5	0	0.3
Width, B (m)	0.71	0.71	0.71	0.71
Length, L (m)	0.71	0.71	0.71	0.71
Unit wt. γ (KN/m^3)	17.65	17.65	17.06	17.06
Angle of internal friction, φ	22	25	20	20
Cohesion, c (KPa)	12.75	14.7	9.8	9.8
Actual Bearing Capacity, q_u (KN/m^2)	*402.07*	*539.37*	*215.75*	*254.97*

Table V: Data from Muhs et al (1969)

Data Set	**9**	**10**	**11**	**12**	**13**
Depth, D_f(m)	0.3	0	0.3	0	0.3
Width, B (m)	0.6	0.6	0.6	0.6	0.6
Length, L (m)	1.2	1.2	1.2	1.2	1.2
Unit wt. γ (KN/m^3)	9.85	10.2	10.2	10.85	10.85
Angle of internal friction, φ	34.9	37.7	37.7	44.8	44.8
Cohesion, c (KPa)	0	0	0	0	0
Actual Bearing Capacity, q_u (KN/m^2)	*270*	*200*	*570*	*860*	*1760*

5. EVALUATION AND COMPARISON

Using the data collected from various researchers, the bearing capacity values were calculated using the equations studied. The comparison is given in Table VI. It can be seen from the table that no individual equation gave the best results in all the cases. The safe values or under-estimated values closest to the actual ones were figured out for each case. The mean squared error was then calculated (Table VII). Although the mean squared error in case of cohesionless soil is minimum for Qayyum's equation but as it is only applicable for surface loading so it is therefore neglected.

Table VI: Comparison of Bearing Capacity Equations

	Data Set	1	2	3	4	5	6	7	8	9	10	11	12	13
Primary data	Depth, D_f(m)	0	0.5	0.5	0.5	0.4	0.5	0	0.3	0.3	0	0.3	0	0.3
	Width, B (m)	0.5	0.5	0.5	1	0.71	0.71	0.71	0.71	0.6	0.6	0.6	0.6	0.6
	Length, L (m)	2	2	2	1	0.71	0.71	0.71	0.71	1.2	1.2	1.2	1.2	1.2
	Unit wt. γ (KN/m^3)	15.69	16.38	17.06	17.06	17.65	17.65	17.06	17.06	9.85	10.2	10.2	10.85	10.85
	Angle of internal friction, ϕ	38.5	36.25	40.75	38.5	22	25	20	20	34.9	37.7	37.7	44.8	44.8
	Cohesion, c (KPa)	6.37	3.92	7.8	7.8	12.75	14.7	9.8	9.8	0	0	0	0	0
	Actual Bearing Capacity, q_u (KN/m^2)	1059.1	1196.4	2373.2	3236.2	402.1	539.4	215.7	255.0	270	200	570	860	1760
Bearing Capacity equation	Terzaghi	883.3	896.5	2189.7	1985.0	426.4	634.3	243.0	281.1	239.8	205.5	386.7	915.7	1463.1
	Meyerhof	807.1	1009.7	2597.8	**2789.2**	468.3	744.1	225.5	293.3	**266.3**	224.7	439.5	1058.9	1801.4
	Balla	**1009.8**	889.0	2157.5	1941.8	**355.2**	**533.9**	195.4	**233.5**	253.0	228.3	409.6	1017.5	**1564.9**
	Hu	904.4	859.7	1932.1	1887.6	338.8	476.2	**199.2**	230.9	298.5	336.6	465.1	992.8	1367.1
	Krizek	-	-	-	-	333.3	488.5	190.2	226.0	245.6	-	-	-	-
	Hansen	711.8	949.2	**2293.8**	2218.1	490.8	779.8	218.8	303.7	220.0	130.9	341.2	504.1	1130.6
	Vesic	795.3	**1025.5**	2462.0	2425.2	504.0	800.3	227.6	313.4	259.8	**182.1**	405.4	**682.5**	1375.8
	Bolton & Lau	777.2	782.9	1840.9	1746.1	333.5	472.9	181.6	214.3	245.7	247.2	391.7	1014.3	1440.7
	Qayyum	-	-	-	-	-	-	-	-	-	205.5	-	915.7	-
	Padmini et al	-	-	-	-	-	-	-	-	169	95	**495**	632	1986

- The underlined values are safe values closest to the actual values.

Table VII: Mean Squared Error

Bearing Capacity Equations	Mean Squared error		
	c-ϕ soil (1 - 8)	ϕ soil (9 - 13)	Overall
Terzaghi	216394	25155	142840
Meyerhof	**49564**	**11789**	**35035**
Balla	227749	17942	140153
Hu	269915	40494	181676
Krizek	-	-	-
Hansen	161589	116488	144242
Vesic	105803	41331	81006
Bolton & Lau	345756	32078	225111
Qayyum	-	1568	-
Padmini et al	-	25982	-

After Qayyum [16] the minimum value of error is for Meyerhof's equation, which suggests that Meyerhof [8], [9] gives results closest to the actual ones. But Meyerhof [8], [9] yields over estimated results in case of square footings (data sets 5 – 8). Here the equation by Balla [10] gives close and safe results.

6. CONCLUSION

From the above discussion the following conclusions can be drawn.

- No single equation gives the best results for all the cases.
- Meyerhof's bearing capacity equation gives better results than the others in most cases, but over estimate for square footings.
- The equation proposed by Balla yields good results in case of square footings.

7. ACKNOWLEDGEMENT

The authors are thankful to the efforts put in by Prof. (R) Muhammad Siddique Qureshi in reviewing this work and giving valuable feedback.

8. REFERENCES

[1] Muhs, H., and K. Weiss, "The Influence of the Load Inclination on the Bearing Capacity of Shallow Footings", *7th ICSMFE*, vol. 2, 1969, pp. 187-194.

[2] MiIovic, D. M., "Comparison between the Calculated and Experimental Values of the Ultimate Bearing Capacity", *6th ICSMFE*, vol. 2, 1965, pp. 142-144.

[3] Muhs, H, Elmiger R, Weiß K., "Sohlreibung und Grenztragfähigkeit unter lotrecht und schräg belasteten Einzelfundamenten", *Deutsche Forschungsgesellschaft für Bodenmechanik (DEGEBO)*, Berlin. HEFT 62, 1969.

[4] Rankine, W. J. M., "A manual of applied mechanics", *Charles Griffin and Co*., London, 1885.

[5] Pauker, H. E., "An explanatory report on the project of a Sea-battery" (in Russian), *Journal of the Ministry of ways and communication*, St. Petersburg, 1889.

[6] Bell, A. L., "Lateral pressure and resistance of clay and the supporting power of clay foundations", Minutes, *Proceedings of the Institution of Civil Engineers*, London, vol. 199, 1915.

[7] Terzaghi, K., "Theoretical Soil Mechanics", *John Wiley & Sons,* New York, 1943.

[8] Meyerhof, G. G., "The ultimate bearing capacity of foundations", *Geotechnique.* 1951, 2: 301.

[9] Meyerhof, G. G., "Some recent research on the bearing capacity of foundations", *Canadian Geotech.* 1963, *J.* 1(1): 16.

[10] Balla, A., "Bearing capacity of foundations", *J. Soil Mech. Found. Div.*, ASCE, 1962, 88(5): 13.

[11] Hu, G. G. Y., "Variable-factors theory of bearing capacity", *J. Soil Mech. Found. Div.*, ASCE, 1964, 90(4): 85.

[12] Krizek, R. J., "Approximation for Terzaghi's bearing capacity", *J. Soil Mech. Found. Div.*, ASCE, 1965, 91(2): 146.

[13] Hansen, J. B., "A revised and extended formula for bearing capacity",Bulletin No. 28, *Danish Geotechnical Institute*, Copenhagen, 1970.

[14] Vesic, A. S., "Analysis of ultimate loads of shallow foundations", *J. Soil Mech. Found. Div.*, ASCE, 1973, 99(1): 45.

[15] Bolton, M. D., and C. K. Lau, "Vertical Bearing Capacity Factors for Circular and Strip Footings on Mohr-Coulomb Soil", *CGJ,* vol. 30, no. 6, Dec, 1993, pp. 1024-1033.

[16] Qayyum, T. I., "Bearing capacity of reinforced and unreinforced soil under rapid loading", *Ph.D. thesis*, University of Strathclyde, Glasgow, 1995.

[17] Salgado, R., Lyamin, A. V., Sloan, S. W. & Yu, H. S., "Two- and three-dimensional bearing capacity of foundations in clay",*Geotechnique 54*, No. 5, 2004, pp. 297–306

[18] Padmini, D., Ilamparuthi K., Sudheer K.P., "Ultimate bearing capacity prediction of shallow foundations on cohesionless soils using neurofuzzy models", *Computers and Geotechnics 35*, 2008, pp. 33–46

First International Conference on Geotechnique, Construction Materials and Environment, Mie, Japan, Nov.21-23, 2011, ISBN: 978-4-9905958-0-7 C3051

Pull-out Resistance of Selected Native Plants in Hong Kong

Leung, F.T.Y., Yan, W.M., Tham, L.G., Department of Civil Engineering, The University of Hong Kong, Hong Kong, China

Hau, B.C.H., School of Biological Sciences, The University of Hong Kong, Hong Kong, China

ABSTRACT: The use of live plants to stabilize slopes is attractive to society due to its environmental friendliness and sustainability. However, stability of the plant itself is a major safety concern. In this study, field pull-out tests are performed on selected native woody species that are commonly planted on slopes in Hong Kong to investigate their pull-out characteristics. The peak pull-out resistance for individual species is correlated to plant height, basal diameter, canopy size, and above-ground dry weight. It was found that basal diameter is a good predictor of the peak resistance. Root architecture of the plants was also studied. Attempts are made to predict the pull-out characteristics of a species from its root architecture.

Keywords: Slope stability, Plants, Pull-out resistance,
Soil-root interactions

1. INTRODUCTION

Slope instability remains a major geotechnical hazards in Hong Kong due to its rugged and hilly topography and frequent rainstorms in the summer. The traditional approach of concrete-covering for slope protection cannot meet nowadays requirement for a green and sustainable environment. The use of live plants as a slope cover thus becomes an attractive and favorable solution. Firstly, the plants increase the suction level of the ground soil through water absorption and transpiration. An increase in soil suction enhances the shear strength of the soil and thus improves slope stability. Secondly, the root system reinforces the ground through the mechanical interaction between roots and soil. It also protects the soil from erosion. The aim of this study was to find out the pull-out characteristics of selected woody plant species that are commonly planted on man-made slopes in Hong Kong.

In this study, four native woody species with high ecological values, which had good survival rates in previous investigations in slope greening, were selected [1]. The pull-out characteristics of the plants is studied through a series of field pull-out tests. In addition, the height, basal diameter, canopy size and above ground dry weight of the plant were measured and attempts were made to correlate them to the peak pull-out resistance of the plant. Root architecture was studied to shed light on the pull-out characteristics.

2. SELECTED SPECIES

To offer a sustainable solution for slope greening, the plant species used must be able to promote natural regeneration in order to form a sustainable vegetation cover. Besides, plants with high ecological values are preferable as many slopes are situated in the countryside or even within Country Parks. As such, native plant species is preferred. On the other hand, many man-made slopes are quite steep (>45 degrees), large and tall trees on slopes may become a negative attribute to slope stability. Therefore, shrubs and small trees are more suitable for Hong Kong's application [2]. In this study, the 4 native species chosen are *Rhodomyrtus tomentosa*, *Melastoma sanguineum*, *Schefflera heptaphylla* and *Reevesia thyrsoidea*. The former two are shrubs and the latter two are small trees (Table 1). All of them have been commonly planted on man-made slopes in Hong Kong since the last decade.

Table 1. The ecology of the four selected plant species

Species	Growth form [1]	Typical height [3],[4]	Fruit type [3]	Seed dispersal agent [5]-[7]	Ecological status in Hong Kong [5][7][8]
Rhodomyrtus tomentosa	Shrub	1-2 m	Berry	Bird, rat, civet	Common pioneer species on Hong Kong's shrubland
Melastoma sanguineum	Shrub	1.5-3 m	Fleshy capsule	Rat, bird	
Schefflera heptaphylla	Small tree	5-10m	Berry	Bird	Common pioneer species on Hong Kong's shrubland and secondary forest
Reevesia thyrsoidea	Small tree	5 m	Capsule	Wind	

3. FIELD PULL-OUT TEST

3.1 Site and Equipment

The field pull-out tests were conducted in the natural sloping terrains in Hong Kong. A tailor-made pull-out apparatus was assembled to perform the tests. Fig. 1 shows the equipment set-up. It comprises of a reaction frame, a 10 kN load cell (TML TCLP-1B), a displacement transducer (Hoskin Scientifique DP-2000C), and a winch system. The sensors are connected to an automatic data acquisition system (TML TC-31K).

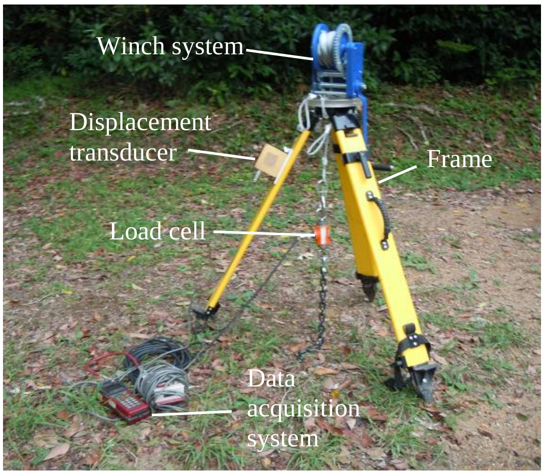

Fig. 1 Field pull-out apparatus.

3.2 Size Characteristics of a Plant

Prior to a pull-out test, some simple plant size characterizing parameters were recorded, including height, basal diameter, canopy size (which is defined as the average diameter of the plant crown), and above-ground dry weight. The former three parameters can be directly measured at the site whereas the last one can only be determined in the laboratory. The above-ground plant parts of the samples were first cut into pieces in the field. They were then brought back to the laboratory for oven drying at 105 degree Celsius overnight. The weight of the dried sample is its above-ground dry weight.

3.3 Results and Discussions

First the above-ground part of a plant was cut. The remaining stem was then tied to the cable in the winch system with a load cell and a displacement transducer connected. The stem was then pull-out steadily with the displacement and pull-out resistance recorded continuously until the whole root system was hanged freely from the ground. A total of 10 *Rhodomyrtus*, 9 *Melastoma*, 18 *Schefflera*, and 10 *Reevesia* are uprooted. Fig. 2 shows the typical pull-out response of the plants where local fluctuation of the pull-out resistance can be seen. The pull-out resistance of a plant is attributed by three major factors: root-soil interface friction, tensile strength of individual root segments, and spatial distribution of the root (i.e., root architecture). When a root breakage or a root-soil slippage occurs, a sudden drop in the pull-out resistance is expected (see Point A in Fig. 2). Sometimes it is followed by a subsequent recuperation (see Point B in Fig. 2) due to the strength mobilization of other root branches until the entire root system is uprooted.

In general, *Rhodomyrtus* shows smaller pull-out resistance with large displacement before the plant can be fully uprooted. On the other hand, *Schefflera* and *Reevesia* show larger pull-out resistance but smaller pull-out displacement (i.e., small displacement is required to uproot the plants). The behavior is highly related to the root architecture of the plant, which will be discussed more in a later section.

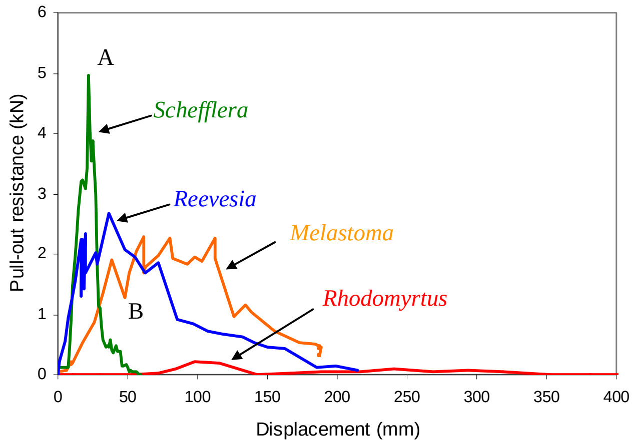

Fig. 2 Pull-out response of the plants.

Regression analyses were carried out to investigate the correlations between the peak pull-out resistance and the size characteristics of individual species. It is believed that with these simple empirical correlations the peak pull-out resistance of a plant can be quickly estimated in the field. Table 2 summarizes the peak pull-out resistance and other size-characterizing parameters for each species. It can be seen that plants between 0.5-2.5 m tall with canopy size from 0.2-1.5 m are investigated. The pull-out resistance can be as low as 0.1 kN but as large as 6 kN.

Table 2. Summary of the pull-out resistance and plant size in this study

Species	Peak pull-out resistance (kN)	Height (cm)	Basal diameter (cm)	Canopy size (cm)	Above-ground dry weight (g)
Rhodomyrtus tomentosa	0.21-2.45	58-191	0.4-1.4	18-160	5-697
Melastoma sanguineum	0.17-2.95	56-210	0.6-4.6	19-139	5-1393
Schefflera heptaphylla	0.31-6.28	55-250	0.9-7.1	25-127	9-759
Reevesia thyrsoidea	0.13-2.67	70-190	1.0-3.0	29-104	11-254

Fig. 3 shows the correlation between the peak resistance and individual size parameters. In general a better correlation can be observed between the peak pull-out resistance and the basal diameter of the plant (see Fig. 3(b)). The peak pull-out resistance of the plants increases as their basal diameter increases which are more obvious in the cases of *Schefflera* and *Reevesia*. Coefficients of determination (R^2 values) are relatively low in the correlation between the resistance and other size parameters (height: 0.17-0.86; canopy size: 0.0004-0.61; and above-ground dry weight: 0.12-0.84). This means that plant height, canopy size and above-ground dry

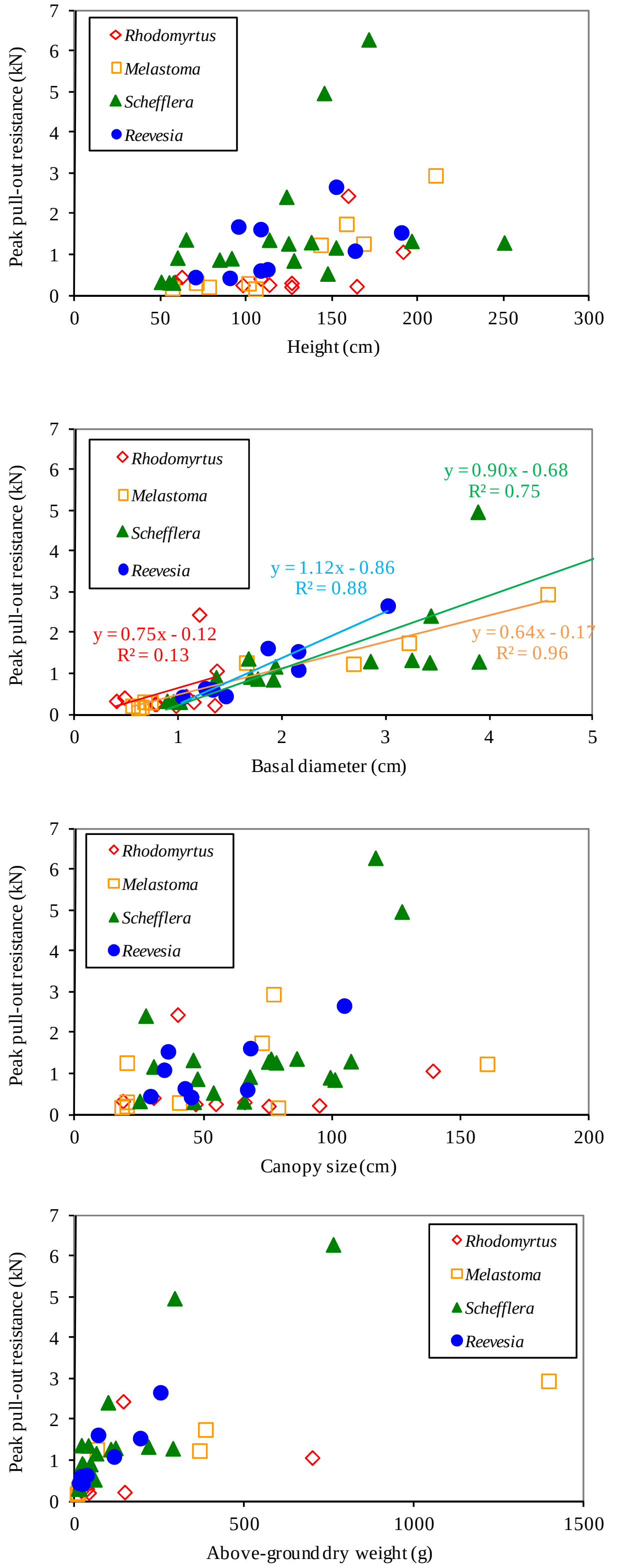

Fig. 3. Correlations between the peak pull-out resistance with plant characteristics: (a) height; (b) basal diameter; (c) canopy size; (d) above-ground dry weight.

weight may not be good predictors of the peak resistance. Generally, *Melastoma*, *Schefflera* and *Reevesia* give larger pull-out resistance than *Rhodomyrtus* (shrub). Root architecture of the plant may shed light on the magnitude of the resistance against uprooting.

4. ROOT ARCHITECTURE

Root architecture describes the spatial distribution of a root system and it has been generally classified into three types: plate, heart and tap as shown in Fig. 4 [9].

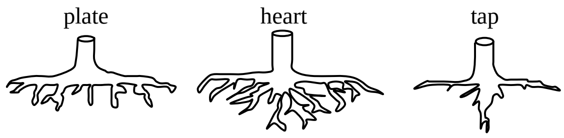

Fig. 4. Shape of a root system: plate, heart and tap (redrawn based on [9]).

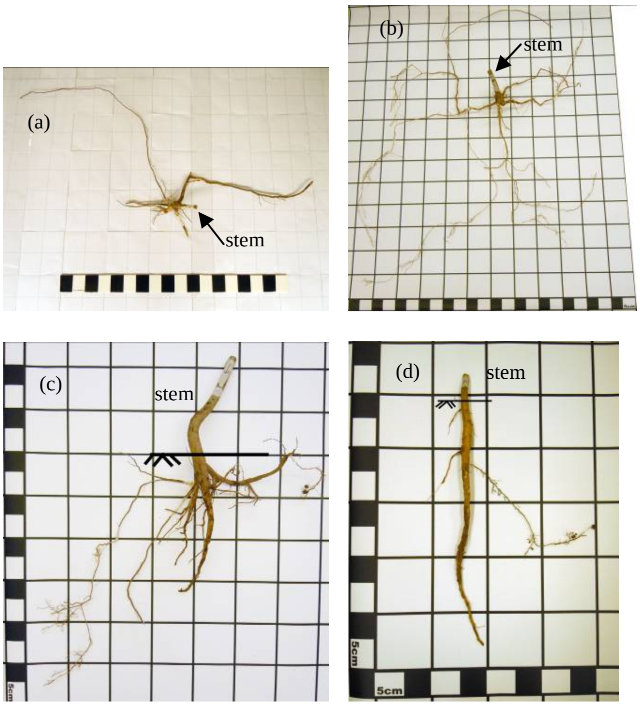

Fig. 5. Root architecture of: (a) *Rhodomyrtus* (top view); (b) *Melastoma* (top view); (c) *Schefflera* (side view); (d) *Reevesia* (side view).

In this study, the plants were carefully dug out from the ground and the root architecture was studied according to this classification system. Fig. 5 shows the typical root system of the studied plants. Fig. 5(a) and (b) show a *Rhodomyrtus* and a *Melastoma* respectively which clearly demonstrate their plate root system. Fig. 5(c) shows a *Schefflera* which is classified as a heart system with many vertical, horizontal and inclined roots. Fig. 5(d) shows the root system of a *Reevesia* in which a tap root system can be easily observed. Fig. 6 gives a summary of the root architecture of the sampled plants in this study. It shows that the tap root system dominated in these species except for *Rhodomyrtus*. In fact, all *Reevesia* specimens in this investigation show the tap root system. Previous investigations showed that plants with tap or heart root systems give generally higher resistance against uprooting [10]. This study confirms the findings - *Schefflera* and *Reevesia* give noticeably higher peak resistance against uprooting than *Melastoma* and *Rhodomyrtus*.

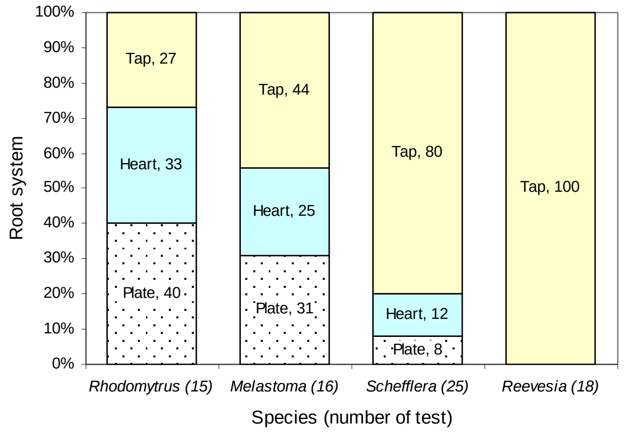

Fig. 6. A summary of the root architecture of the studied species.

5. CONCLUSIONS

Slope greening with native shrubs and small trees has received much public attention due to its sustainability potential. In this study, pull-out resistance and root architecture of four native shrub and small tree species are investigated. Pull-out characteristics of individual species is discussed with reference to its root architecture.

6. ACKNOWLEDGMENT

The authors would like to acknowledge the support by research grant HKUST9/CRF/09 provided by the Research Grants Council of the Hong Kong Special Administrative Region (HKSAR).

7. REFERENCES

[1] Hau BCH, So KKY, Choi KC and Chau RYH, "Using native tree and shrub species for ecological rehabilitation of man-made slopes in Hong Kong," in Proc. 25th Annual Seminar of the Hong Kong Institute of Engineers, 2005, pp. 273-286.

[2] GEO, "Technical Guidelines on Landscape Treatment and Bio-engineering for Man-Made Slopes and Retaining Walls," Hong Kong: Civil Engineering Department, HKSAR, 2000.

[3] Hu QM, and Wu DL, "Flora of Hong Kong," Vol. 2, Hong Kong: Agriculture, Fisheries and Conservation Department, HKSAR., 2008.

[4] ISSG, "Global Invasive Species Database," Invasive Species Specialist Group (ISSG) of the IUCN Species Survival Commission, National Biological Information Infrastructure, Manaaki Whenua-Landcare Research and the University of Auckland, 2011.

[5] Hau BCH and So KKY, "Using native tree species to restore degraded hillsides in Hong Kong, China," Bring Back the Forests: Policies and Practices for Degraded Lands and Forests, Sim HC, Appanah S and Durst PB, Ed. Bangkok, Thailand, FAO, 2003, pp. 179-190.

[6] Dudgeon D and Corlett RT, "The Ecology and Biodiversity of Hong Kong," Hong Kong: Friends of the Country Parks & Joint Publishing (HK) Company Ltd., 2004.

[7] Hau BCH and Corlett RT, "A survey of trees and shrubs on degraded hillsides in Hong Kong," Memoirs of the Hong Kong Natural History Society, vol. 25, 2002, pp. 83-94.

[8] Chau KC, "The Ecology of Fire in Hong Kong." Hong Kong: Department of Ecology and Biodiversity, The University of Hong Kong, 2004.

[9] Stokes A, Atger C, Glyn Bengough A, Fourcaud T and Sidle RC, "Desirable plant root traits for protecting natural and engineered slopes against landslides," Plant Soil, vol. 324, 2009, pp. 1-30.

[10] Norris JE, Strokes A and Mickovski SB, "Slope stability and erosion control: Ecotechnological solutions," Dordrecht: Springer, 2008.

First International Conference on Geotechnique, Construction Materials and Environment, Mie, Japan, Nov.21-23, 2011, ISBN: 978-4-9905958-0-7 C3051

Inland navigation in carrying injured and sick disaster victims in case of a massive earthquake in the Tokyo metropolitan area

Kazuya EGAMI[1)], Keiichi NOTO[2)], Wataru MIYAZAKI[2)], Kazukiyo YAMAMOTO[2)], Takeo KONDO[2)]
1) ECOH CORPORATION 2) Graduate School of Science and Technology , Nihon University

ABSTRACT: The Tokyo metropolitan government plans to organize a waterway transportation system utilizing boats and ships to enhance transportation capacity to carry injured and sick people during an earthquake disaster. However, the existing regional disaster prevention plan formulated by the Tokyo government does not stipulate specific operational procedures.

This paper investigates the prospect of the implementation of earthquake disaster countermeasures using Inland navigation. To begin with, we examined the presence of agreements on disaster response procedures concluded between the municipalities in Tokyo, who installed and administered the piers, and the organizations representing boat and ship operators, such as fishermen's unions, leisure fishing boat cooperative unions and marinas. We also surveyed 252 users of Inland navigation on their awareness of disaster prevention using Inland navigation. To conclude, we propose a concept of an institutional design which utilizes Inland navigation for emergency evacuation of vulnerable people affected by an earthquake disaster.

Keywords: Inland navigation, Disaster prevention piers, Institutional design, Regional disaster prevention plan, Operating plan

1. INTRODUCTION

The Great Hanshin-Awaji Earthquake on 17 January 1997 led to enhanced recognition of the importance of Inland navigation and triggered the construction of disaster prevention piers throughout Japan. A disaster prevention pier serves as a base in reconstructing river administration facilities and conducting relief operations following the occurrence of flood, high tide and earthquake, which include shipments of aid supplies, relief efforts for people in isolated areas, transportation of disaster victims such as people unable to get home, removal of rubbles, and transportation of relief workers. In the Great East Japan Earthquake on 11 March 2011, however, those piers did not function well and over 100,000 people in Tokyo could not get home. It is attributed to the fact that the regional disaster prevention plans do not clearly stipulate the role of Inland navigation, which enhance the disaster mitigation capacity, and the usage of disaster prevention piers. It is also caused by the lack of a plan that considers vulnerable disaster victims. This study analyzes the transportability of sick and injured people, the disaster prevention agreements among relevant parties under the regional disaster prevention plans, and people's awareness of disaster prevention. Finally, the institutional design on the utilization of Inland navigation and disaster prevention piers which focuses on the vulnerable disaster victims is proposed.

2. DISASTER PREVENTION PIERS WITHIN REGIONAL DISASTER PREVENTION PLANS

2.1 Organizations responsible for operation and administration of disaster prevention piers

In principle, river administrators maintain disaster prevention piers. They or park administrators are in charge of their operation at normal times, and so does disaster prevention departments in time of a disaster. The regional disaster prevention plan formulated by the Tokyo government stipulates that each ward is the main administrator of the disaster prevention piers under the jurisdiction of Tokyo within its region in time of a disaster, in order to realize the comprehensive operation of the piers. The disaster prevention piers under the jurisdiction of the national government are set to be operated and administered by river administrators, but the detailed are not stipulated.

2.2 Administration and operation of disaster prevention piers in regional disaster prevention plans

As shown in Table 1, the Tokyo metropolitan government defines in its regional disaster prevention plan that the operation of disaster prevention piers and boats consists mainly of (a) construction of an emergency transportation network, (b) transportation of evacuees, (c) transportation of medical staffs and sick/injured people, (d) transportation alternative for victims unable to get home, and (e) transportation of materials and equipments. The specific rules for the operation, however, are not designated in the plan. The disaster prevention plans of the wards, the lower administrative organs in Tokyo, specify only (a) construction of the emergency transportation network. Each ward defines different responses regarding the specific operation of the disaster prevention piers and it is not clearly stipulated.

Table 1: Number of current disaster prevention piers and their operations

	Number of current disaster prevention piers (by administrator)						Operation of disaster prevention piers or boats				
Administrative Body	Year	National government	Prefecture	Ward	Private	Total	Emergency transportation network	Evacuation	Medical staffs /Sick and injured people	People unable to get home	Materials and Equipments
Tokyo Metropolis	2007	10	15	33	1	58	•	•	•	•	•
Chiyoda Ward	2007	0	0	3	0	3	•			•	
Chuo Ward	2009	0	4	1	0	5	•	•	•	•	
Bunkyo Ward	2007	0	0	1	0	1	•	•		•	
Taito Ward	2008	0	1	0	1	2	•		•	•	•
Sumida Ward	2009	0	1	1	0	2	•				
Koto Ward	2008	1	2	7	0	10	•				
Shinagawa Ward	2007	0	0	1	0	1	studying the feasibility of a water way transportation system				
Ota Ward	2009	1	0	1	0	2	•				
Kita Ward	2008	1	0	3	0	4	•		•	•	
Arakawa Ward	2009	0	1	2	0	3	•	•	•		
Itabashi Ward	2009	1	0	1	0	2	•		•		•
Adachi Ward	2008	2	1	0	0	3	•	•			
Katsushika Ward	2008	2	1	1	0	4	•				
Edogawa Ward	2009	2	4	10	0	16	•				

Table 2 shows the presence or absence of concrete operational plans in Tokyo and its wards. Currently, Tokyo has no uniform operational plan and has entrusted it to the wards in compliance with the article 5 of the Disaster Countermeasure Basic Act. However each ward does not specify the development of the concrete operational plan. Eight among 12 wards cite it as a subject of future investigation, and the two plan to consolidate the system in the next fiscal year. The result of the survey also presents that the certain properties of a river and a bridge restrict the navigation of the boats and it causes the inadequate development of the plan.

Table 2: Existence of an employment plan

Tokyo Metropolis	No uniform operational plan formulated		
	Details	* Entrust each ward with the specific operational plans, in compliance with the article 5 of the Disaster Countermeasure Basic Act (obligation of municipalities). * Have no firm grasp of the navigable areas in the rivers.	
Wards in Tokyo	No concrete operational plan at present		(12/12)
	Details	* See it as a subject of future investigation	(8/12)
		* Incorporate the detailed operational plan in the regional disaster prevention plan for the next year.	(2/12)
		* Set no plan due to the difficulty in predicting the situation at a time of disaster. Intend to use disaster prevention piers according to the circumstances when the earthquake occurs.	(1/12)
		* Unable to develop the plan because the property of the river may restrict the navigation of the boats.	(1/12)
		* Consider the reception of supplies as a main operation.	(5/12)
		* Consider the transportation for the rescue effort.	(1/12)
		* Own no boat. Need to request the Tokyo Metropolitan government to dispatch the boats when the disaster strikes, or to make an agreement with a shipping company.	(5/12)

2.3 Administration and operation of disaster prevention piers by river administrators

The administration and operation of disaster prevention piers under the jurisdiction of the Minisry of Land, Infrastructure, Transport and Tourism are part of river management. At present, there is no concrete plan for the administration and operation of the piers but its formulation is under consideration. The Arakawa-Karyu Office in the Ministry of Land, Infrastructure and Transport is considering hosting a workshop to formulate the rules regarding the operation of the disaster prevention piers at normal times, but the administration and the operation of the piers and Inland navigation facilities remain as an issue. Some disaster prevention piers where municipalities bear the expenses and draw up the regulations are administered by the municipalities at normal times and by the national government in time of an earthquake. The details, however, are not defined.

2.4 Anti-disaster measures based on disaster prevention plans of disaster prevention piers

The Tokyo metropolitan government has concluded the agreement on transportation between thirteen boat and ship operators and the Fire and Disaster Management Agency, the Bureau of Construction and the Ports and Harbors Bureau, in the regional disaster prevention plan. However, the detailed operation remains unclear and is entrusted to the operators with full authority. Table 3 indicates that most municipalities have not concluded a disaster prevention agreement to evacuate the people who are unable to get home by boats. The government develops partnerships with public transport operators and has no adequate partnership with private sector entities, which exposes the weakness of the transportation infrastructure in time of an earthquake. Behind this lies the lack of radio communications networks for disasters and the insurance system which are available in the private sector, and the mechanism that clarifies the procedures of arranging boats and giving instructions and orders.

Table 3: Presence or absence of disaster prevention agreement

Municipality	Department in charge	Concluded disaster prevention agreement
Edogawa Ward	Disaster Countermeasures Division	no
Katsushika Ward	Disaster Prevention Department	no
Adachi Ward	Disaster Countermeasures Division	no
Koto Ward	Disaster Prevention Department	no
Sumida Ward	Disaster Prevention Department	no
Arakawa Ward	Disaster Prevention Department	no
Chuo Ward	Disaster Prevention Department	no
Minato Ward	Disaster Prevention Department	yes
Shinagawa Ward	Disaster Prevention Department	no
Ota Ward	Disaster Prevention Department	no

3 PUBLIC AWARENESS OF DISASTER PREVENTION AND EVACUATION BEHAVIOR

3.1 Overview of survey

We conducted an opinion survey of the users of Inland navigation on their awareness of disaster prevention, as shown in Table 4.

Table 4: Investigation outline

Item	Summary
Period	August 1, 2008 ~ September 15, 2008
Type of boat	2 electric boats of 10 passengers
Fare	Adult: 4,000 yen
Operating hours	4 hours
Method	Interview, Self-completion questionnaire
Number of respondents	252 people
Navigation route	Tour around Kanda River, Nihonbashi River and Sumida River

3.2 Need of Inland navigation in time of a disaster

Fig. 1 shows the result of the survey on the need of Inland navigation when an earthquake occurs. Seventy-nine percent of respondents regarded it as necessary and 7 % as unnecessary, which shows a great need for Inland navigation in time of a disaster. It is considered that people saw the damaged roads during the Great Hanshin-Awaji Earthquake and recognized the need of alternative traffic routes.

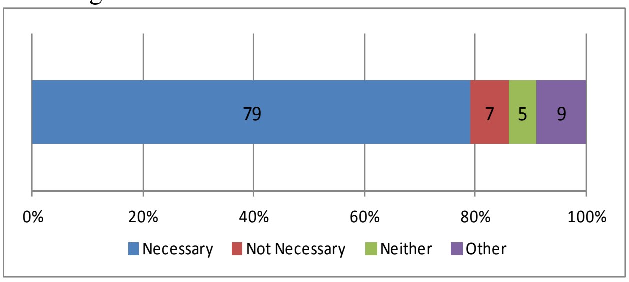

Figure 1: Recognition of the need of river boat transportation

3.3 Evacuation behavior in an earthquake disaster

The public awareness of evacuation behavior in an earthquake disaster is shown in Fig. 2. Thirty-nine percent of respondents said that they would walk home; 9 % walk to where they can take a taxi or a car; 22% take a boat and go home, if possible; 8% walk to a pier; 3% take a boat and go home; and 16% go to an evacuation center. The fact that about 40% of respondents intended to walk home during an earthquake indicates the low public awareness of the availability of Inland navigation and disaster prevention piers. In order to raise the awareness, it is necessary to disseminate information on the locations of the piers.

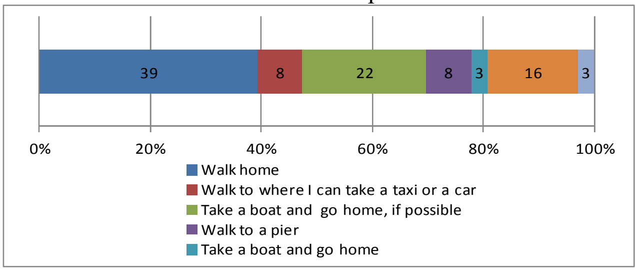

Figure 2: Evacuation behavior in times of earthquake disasters

3.4 Awareness of using Inland navigation in an earthquake disaster

Fig. 3 shows what people expect from Inland navigation during an earthquake disaster. Thirty-nine percent of respondents agreed that it could be used to transport goods; 27% to transport people. Eighteen percent recognized its function as a hospital ship; 9% as a temporal evacuation center; and 7% as an accommodation. In order to respond to their diversified demand shown in the survey and make effective use of the boats, a concrete division of roles between administrative bodies and boat operators is required.

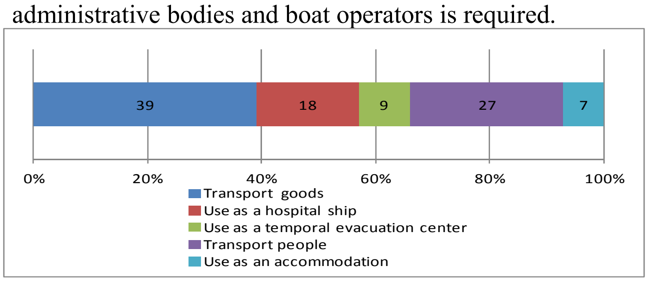

Figure 3: Awareness of using river boat transportation in times of earthquake disasters

4 POSSIBILITY OF TRANSPORTATION OF SICK AND INJURED PEOPLE

4.1 Problems of the structural design of disaster prevention piers

Previous studies clearly show that the limited use of the disaster prevention piers at normal times prevents their full utilization in time of an earthquake disaster. The structures of the piers, which building codes are not defined in the Government Ordinance for Structural Standard for River Administration Facilities, lack sufficient consideration to vulnerable disaster victims. Many of the piers are not easily accessible to wheelchair users. A gurney cannot be used to transport sick and injured people and only the transport with a stretcher or by foot is possible (see Picture 1).

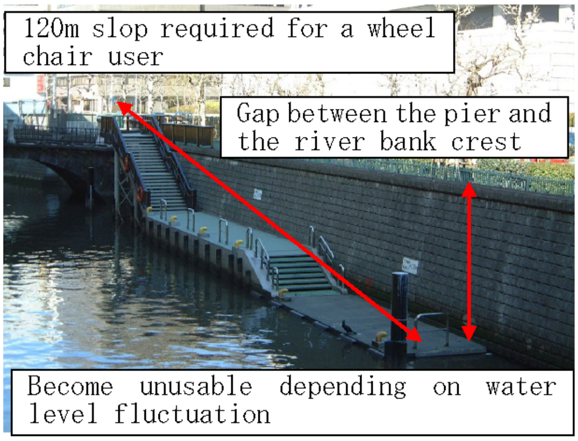

Picture 1: Constructional example

4.2 Disaster base hospitals

The Tokyo metropolitan government has designated the local disaster base hospitals which are used in time of an earthquake disaster. There are also 152 rear area medical facilities and one field hospital system which is developed by the Ground Self-Defense Forces in the property of the municipalities who own disaster prevention piers. Six piers are within about 0.5 km as the shortest path from the rear area medical facilities; 4 are within about 1.0 km. Those 10 piers are accessible and they account for 14 % of the total.

4.3 Navigability to disaster prevention piers

The boats which can sail to the disaster prevention piers are limited due to the hull form, properties of the rivers, and fluctuation of physical environment. While all the intended boats can sail to the piers in Akashicho, the Wakasu Seaside Park, and Ryogoku, only small passenger boats can navigate in the Kanda River and the rivers in Koto Ward except the sections, such as the Onagigawa River, because of the restriction (Navigable width of the river > 1.5 × entire length of the boat).

According to the Tokyo regional disaster prevention plan, the procurement of the affiliated boats starts from four days after the earthquake. If roads are blocked and no traffic is available immediately after an earthquake occurs, the water buses of the Tokyo Metropolitan Park Association are to be used as a way to transport medical staffs and severely affected people. Privately-owned boats such as houseboats are not used in that situation. Since the water buses are not able to navigate in the Kanda River and the rivers in Koto Ward depending on the tide level and the restriction of the hull form, small boats are the mainstay of the transportation in an earthquake.

Floodgates are closed as soon as an earthquake occurs, which make it impossible to use the waterway transportation to the disaster prevention piers located in the area below sea level. It also prevents boats from sailing the area enclosed by the floodgates.

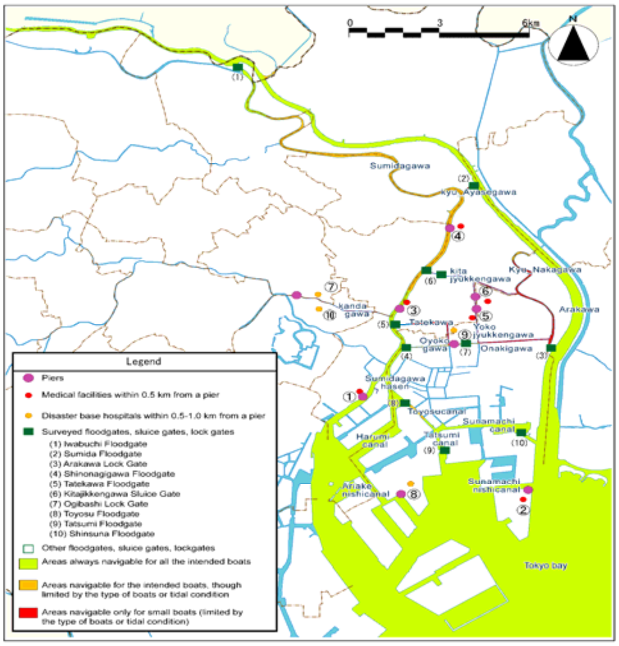

Figure 4: Navigability

4.4 Possibility of transporting sick and injured people

Table 5 shows the possibility of utilizing the piers in transporting sick and injured people in the initial stage of an earthquake disaster. The Wakasu Seaside Park and the Ariake Passenger Ship Terminal in the Tokyo Bay area are available for receiving boats from urban rivers and cooperating with wide-area disaster management bases. The piers in Akashicho, Ryogoku and Shirahigebashi-south are available as a base of the banks of the Sumida River. Those five disaster prevention piers are expected to function as a center to transport sick and injured disaster victims.

Other piers have restrictions, such as operations of floodgates, conditions preventing navigation, and danger in transportation routes. Kameido, Tenjinbashi, and Ogibashi Lock Gate block the navigation due to the closure of the gates. Although the Yokojikken River and the Kanda River cannot be used in the initial period of an earthquake because of the procurement plan of Tokyo, the transportation of many sick and injured people become possible if the small boats which can sail the narrow rivers are available. The waterway transportation is accessible in Ichibeigashi if quake resistance in inland areas is enhanced and the fire is contained.

Table 5: Possibility of transporting injured and sick people by disaster prevention piers

Pier	River	Distance (m)	Medical facility	Type of boats	Obstacle in the initial stage of disaster	Impact on water area	Potential danger on the land	Transportability
Akashi-cho	Sumida River	270-500	St. Luke's International Hospital	All types	/	Damaging road bridges	Damaged buildings, Blocked roads	Reception from water areas
Ryogoku		340-360	Doai Memorial Hospital					Transport to Ariake
Shirahigebashi-south		adjacent	Shirahigebashi Hospital					
Kameido	Yokojikken River	500	Tokyo Metropolitan Bokuto Hospital	Small boats	Floodgate operation, Securing of boats	Damaging road bridges and floodgates		
Tenjinbashi		520	Yujin Hospital					
Ichibeigashi	Kanda River	720-1200	Juntendo Hospital, Surugadai Nihon University Hospital		Securing of boats	Damaging road bridges		
Ogibashi Lock Gate	Onagi River	960	Asoka Hospital		Floodgate operation	Damaging road bridges and floodgates		
Ariake Passenger Ship Terminal	Tokyo Bay	700-820	Ariake Hospital	All types	/	/	/	Reception from urban rivers
Wakasu Seaside Park	Sunamachi-minami Canal	330	A field hopsital					

5 CONCLUSION

This study shows that there is a need to specify the rules regarding the administration and operation of disaster prevention piers in regional disaster prevention plans, to enhance public awareness of the piers, and to establish a system to transport vulnerable disaster victims efficiently. The concrete plan of administration and operation of the Inland navigation should be clearly incorporated in the disaster prevention plans of the municipalities and that of the Ministry of Land, Infrastructure, Transport and Tourism. Based on these observations, we propose the institutional design as follows.

First of all, a council consisting of administrative bodies and private-sector entities should be established. It develops a system for operation, management and cooperation of disaster prevention piers. It also consolidates the disaster prevention support system which contains conclusion of disaster prevention agreements with private sector entities, rules of the uniform management of rivers, and a security system for boat operators.

Second, we propose the development of an operational plan applicable to disaster base hospitals, disaster prevention piers, and boats suitable to its water area to construct a transportation network centering on each pier. It enables smooth and prompt transportation of sick and injured people in time of an earthquake. It is also important to organize a disaster mitigation system by developing information sharing system between hospitals and piers, and linking transmission systems, transportation operations and ship operations.

Additionally, measures to support vulnerable disaster victims in an earthquake, such as development of structural standards of the disaster prevention piers friendly to their conditions, should be incorporated in the regional disaster prevention plans. Administrational and operational plans of the piers should also give attention to this issue. Furthermore, the system which enables the safe transportation of sick and injured people should be developed by promoting the accessibility of the piers at normal times.

The development of these systems is considered to make the disaster prevention piers safer and enable more efficient use of the piers in time of an earthquake disaster.

6 REFERENCES

[1] Jinnai H, Yoshikawa K and Miura Y, Shuun Toshi: Mizube Kara No Toshi Saisei. Kajima Shuppankai, 2008.

[2] Egami K, Kondo T, Miura Y and Goto K, “A study on disaster prevention using Inland navigation,” in Proc. of the 63rd Annual Conference of the Japanese Society of Civil Engineers, 2008.

[3] Koga T, Kondo T, Yamamoto K, Egami K and Orimo R, “A study on the organization a sea-based relief network system at the time of epicentral earthquake in metropolitan Tokyo,” The 23rd Conference on Environmental Information Science, 2009, pp. 101-106.

[4] Egami K, Sakanoi K, Goto K and Ino H, “A Study on Effective Use of River Jetty,” World City Water Forum, 2009, Incheon, Korea, pp. 19-21.

[5] Egami K,Study on Appropriate System Design for Inland Water Transport and Jetty for Disaster Management. Nihon University Thesis ,2010

First International Conference on Geotechnique, Construction Materials and Environment, Mie, Japan, Nov.21-23, 2011, ISBN: 978-4-9905958-0-7 C3051

Model Calculation and Geotechnical Interpretation of the Correlation Co-efficient Between Finite and Incremental Strain Path of a Formation

J.Rajaraman[1] and K.Thiruvenkatasamy [2]

ABSTRACT: The measure of strain that compares the initial and final configuration is called the finite strain, which is independent of the details of the steps toward the final configuration. When these intermediate strain steps are determined they are called incremental strains. The incremental strain may be more crucial for unraveling the deformation history of a formation than finite strain. In this paper two different strain sequence are considered for correlation and interpretation. For both the strain sequences the finite strains reached are the same. In other words the initial and final configuration are identical. The steps or strain increments by which these final shapes were reached, are very different. It means the strain path of two examples is different, but the finite strains are the same. In one example the incremental strains reflect a strain ellipse that becomes increasingly elliptical [the ratio of the long over the short axis [X/ Y] becomes greater. In the second example the path shows that the orientation of the X and Y axis was perpendicular to those of the finite strain ellipse during part of the history. Between these two examples the correlation co-efficient [r] is calculated. Geotechnically the two paths would represent very different strain histories of the formation, yet their finite strains would be identical. If the strain path is not followed accurately, many such important piece of information is lost. Geotechnically it means that the over consolidation ratio [OCR] for each strain path is different, because the geo fatigue experienced by each strain path is different. This interpretation is amply supported by correlation co-efficient[r].

1.0 Strain Path

The measure of strain that compares the initial and final configuration is called the finite strain ,identified by subscript f,which is independent of the details of the steps towards the final configuration. When these intermediate strain steps are determined they are called incremental strains identified by subscript i. The summation of all incremental strains (i.e.,their product) therefore , is the finite strain. There are many ways to measure finite strain in a rock, but measurement of strain increments is more difficult. Yet, incremental strain may be more crucial for unraveling the deformation history of a rock or region than finite strain .The following figure 1 explains to explore the deformation history of a rock or region.(from Reference[1]as shown in figure1 the finite strains for the distortion of a square in figure 1a and 1b are the same, because the initial and final configuration are identical.The steps or strain increments by which these final shapes were reached , however, are very different. We say that the strain path of two examples is different , but the finite strains are the same. The path presented in figure 1a has incremental strains that reflect a strain ellipse that becomes increasingly elliptical . In other words , the ratio of the long over the short axis (X/Y)becomes greater . The path in figure 1b, on the other hand, shows that the orientation of the X_i and Y_i axes was perpendicular to those of the finite strain ellipse during part of the history. Consider this in a geologic context; the two paths would represent very different strain histories of a region, yet their finite strains would be identical. Therefore obviously, an important piece of information is lost without the knowledge of the strain path. It is therefore critical for structural analysis to distinguish finite strain from incremental strain.

1.1 Coaxial and Non- Coaxial Strain Accumulation

The principal incremental strain axis rotate relative to the finite strain axis, is called non-coaxial strain accumulation.The case in which the same material lines remain the principal strain axis at each increment is called coaxial strain accumulation as shown in figure 2a and 2b .

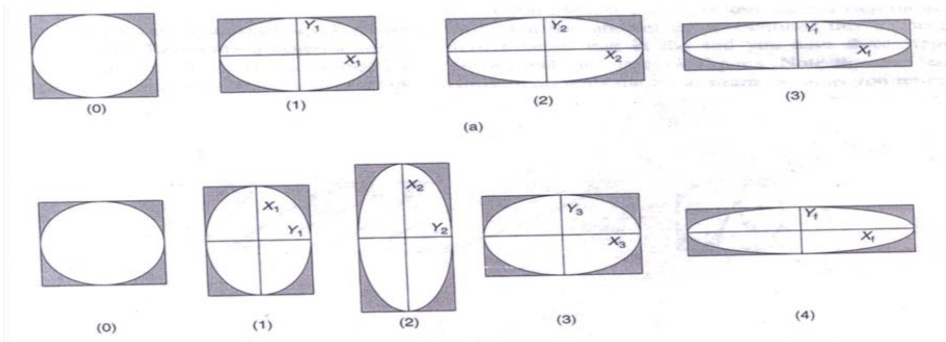

Figure 1The finite strains,X_f and Y_f in (a) and (b) are the same,but the strain path by which each was reached is different,This illustrates The importance of understanding the incremental strain history(X_i and Y_i) of rocks and regions and inherent limitations of finite strain analysis.

1,2 Professor, Department of Harbour Engineering and Off Shore Technology , AMET University, 135 East Coast road, Kanathur -603 112 , CHENNAI, INDIA . E-Mail swamy2667@yahoo.co.in[1] rajaraman.usha44@gmail.com[2]

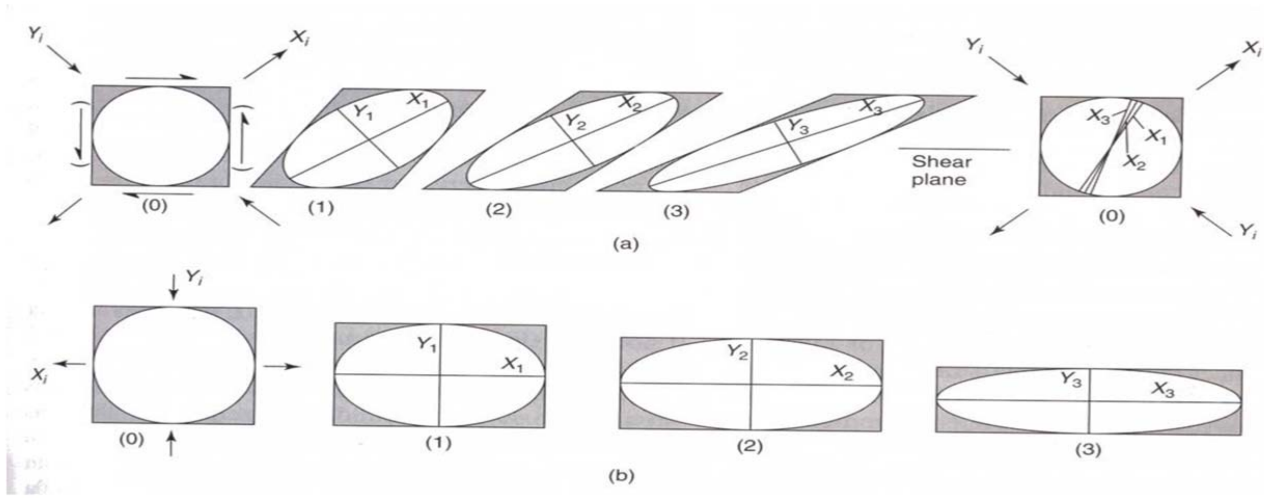

Figure 2 Non-coaxial [a] and coaxial [b] strain. The incremental strain axes are different material lines during non-coaxial strain. In coaxial strain the incremental strain axes are parallel to the same material lines. Note that the magnitude of the strain axes changes with each step. From [1].

2. CORRELATION

The word "correlation" is used to denote the degree of association between variables. If two variables *x* and *y* are so related that variations in the magnitude of one variable tend to be accompanied by variations in the magnitude of the other variable, they are said to be correlated. If y tends to increase as x increases , the variables are said to be positively correlated. If y decreases as x increases , the variables are negatively correlated If the values of y are not affected by changes in the values of x , the variables are said to be uncorrelated. Correlation may also be linear or non-linear. If the amount of change in one variable tends to bear a constant ratio to the amount of change in the other variable , then correlation is said to be "linear";because the scatter diagram would show a linear path. Here we shall be concerned with linear correlation or simple correlation only. This is measured by "Correlation Coefficient"

2.1 COVARIANCE

Given a set of n pairs of observations (x_1, y_1), (x_2,y_2),…..(x_n,y_n) relating to two variables x and y , the covariance of x and y , usually represented by cov (x, y) , is defined as

$$\mathbf{cov\,(x,y)} = \frac{1}{n}\sum(x-\bar{x}\,(y-\bar{y})$$

expanding the equation on the right, it can be shown that

$$\mathbf{cov\,(x,y)} = \frac{\sum xy}{n} - \left[\frac{\sum x}{n}\right]\left[\frac{\sum y}{n}\right]$$

this is generally used for calculation as in [2].

2.2 CORRELATION COEFFICIENT (r)

Let (x_1, y_1) , (x_2, y_2) … (x_n, y_n) be a given set of n pairs of observation on two variables x and y. The correlation coefficient or coefficient of correlation , between x and y (denoted by the symbol r) is then defined as

$r = \frac{cov(x,y)}{\sigma_x\ \sigma_y}$ where σ_x and σ_y are the standard derivation of x and

y respectively cov (x,y) denotes the covariance of x and y (section 9.6). This expression is known as Pearson's product – moment formula , and is used as a measure of linear correlation between x and y.The formula for r may be written in various other forms. Putting the explicit expression for cov(x,y) , σ_x and σ_y in (9.7.1), and multiplying both the numerator and the denominator by n , we have

$$\mathbf{r} = \frac{\sum(x-\bar{x})\,(y-\bar{y})}{\sqrt{[\sum(x-\bar{x})^2\,.2(y-\bar{y})^2\,]}}$$

now expanding the expressions

$$r = \frac{\sum xy - n\overline{xy}}{\sqrt{[\sum(\,x^2 - n\,\overline{x^2})\,.\,(\sum y^2 - n\overline{y^2})]}}$$

Multiplying the numerator and the denominator by n again and since $n\bar{x} = \sum x$ and $n\bar{y} = \sum y$, we may write r

$$r = \frac{n\sum xy - (\sum x)\,(\sum y)}{\sqrt{[[n\sum x^2 - (\sum x)^2]\,.(n\sum y^2 - (\sum y)^2)]}}$$

Note : In all the forms shown above , the denominators contains two factors under the square root. They may be obtain On replacing y by x , and x by y in the numerator. as in [2].

TABLE I Correlation Coefficient from strain ratios (x/y) from figure 1.

x	y	$x-\bar{x}$	$y-\bar{y}$	x^2	y^2	xy
2.0	2.0	- 1.1	-0.36	4.0	4.0	4.0
2.6	1.8	-0.5	-0.56	6.76	3.24	4.68
3.3	1.6	0.2	-0.76	10.89	2.56	5.28
3.8	2.6	0.7	0.24	14.44	6.76	9.88
3.8	3.8	0.7	1.44	14.44	14.44	14.44
15.5	11.8	0.0	0.0	50.534	31.0	38.28

2.3 Properties of Correlation Coefficient:

(i) The correlation coefficient r is independent of the choice of both origin and scale of observations. This means that if
$U = \frac{x-c}{d}$ and $v = \frac{y-ć}{d'}$
Where c,ć ,d ,d' are arbitrary constants (d and d' positive), then
$r_{xy} = r_{uv}$ i.e. correlation coefficient between x and y
= correlation coefficient between u and v
In general , if $X = a + bx$, $Y = á + b`$ y, then
$r_{xy} = \pm\ r_{xy}$
according as b and b` have the same sign or opposite signs.
(ii) The correlation coefficient r is a pure number and is independent of the units of measurement. This means that if, for example x represents height in inches and y weight in lbs., then the correlation coefficient between x and y will neither be in inches nor in lbs. or any other unit , but only in number.
(iii) The correlation coefficient r lies between -1 and +1 ; i.e. r cannot exceed 1 numerically.
$-1 \leq r \leq +1$

$$\sigma_x^2 = \frac{\sum x^2}{n} - \left(\frac{\sum x}{n}\right)^2$$

$$\sigma_x^2 = \left(\frac{50.534}{5}\right) - \left(\frac{15.5}{5}\right)^2$$

$$= \frac{50.534}{5} - (3.1)^2$$

$$=(10.1068) - 9.61 = 0.4968$$

$$\sigma_y^2 = \frac{\sum y^2}{n} - \left(\frac{\sum y}{n}\right)^2$$

$$\sigma_y^2 = \left(\frac{31.0}{5}\right) - \left(\frac{11.8}{5}\right)^2$$

$$= 6.2 - (2.36)^2$$

$$= 6.2 - 5.569 = 0.631$$

Covariance (x, y) $= \left(\frac{38.28}{5}\right) - \left(\frac{15.5}{5}\right)\left(\frac{11.8}{5}\right)$

$$= (7.656) - (3.1)(2.36)$$

$$= 7.656 - 7.316$$
$$= 0.34$$

$$r = \frac{cov(x,y)}{\sigma_x \sigma_y} = \frac{0.34}{\sqrt{0.4968}\ \sqrt{0.631}} = \frac{0.34}{(0.704)(0.794)}$$

$$= \frac{0.34}{0.5589} = 0.6083$$

2.4 Strain History And Correlation Coefficient (r)
(flexibility of r as a method).
The strain ratios need not necessarily be small values .The strain ratio can be larger in size. The statistical methods can handle different types of strain ratios. This is illustrated by a statistical method which is also applicable to strain ratios (coaxial stains) The general data assumed to find the coefficient of correlation is given below :

TABLE II Illustrative example for x,y.

X	65	63	67	64	68	62	70	66
Y	68	66	68	65	69	66	68	65

Solution : Since the correlation coefficient is unaffected by change of origin (and also scale), let us change the origins of X and Y to 65 and 67 respectively so we can write x = X – 65 , y = Y – 67 .The new table for calculations for correlation coefficient is as follows :

TABLE III Correlation Coefficient (r) data

X	Y	x=X-65	y=Y-67	x^2	Y^2	xy
(1)	(2)	(3)	(4)	(5)	(6)	7
65	68	0	1	0	1	0
63	66	-2	-1	4	1	2
67	68	+2	1	4	1	2
64	65	-1	-2	1	4	2
68	69	+3	2	9	4	6
62	66	-3	-1	9	1	3
70	68	+5	1	25	1	5
66	65	+1	-2	1	4	-2
525	535	5	-1	53	17	18

$\sigma_x^2 = \frac{53}{8} - \left(\frac{5}{8}\right)^2 = \frac{399}{64}$

$\sigma_Y^2 = \frac{17}{8} - \left(\frac{-1}{8}\right)^2 = \frac{135}{64}$

Cov (x.y) $= \frac{18}{8} - \left(\frac{5}{8}\right)\left(\frac{-1}{8}\right) = \frac{149}{64}$

$$r_{xy} = \frac{cov(x,y)}{\sigma_x \sigma_Y} = \frac{\frac{149}{64}}{\sqrt{\frac{399}{64}}} \frac{1}{\sqrt{\frac{135}{64}}} = \frac{149}{\sqrt{(399)(135)}} = .65$$

Therefore, the required correlation coefficient is .64

The origin is changed to values near the means. The means of X and Y are 525/8 = 65.625 and 535/8 = 66.875 respectively.

Conclusions :

1. In a geologic context two different strain paths maybe very different in strain histories of a region yet their finite strains would be identical .without this if the finite strain analysis is carried out the correlation coefficient are will be unity or one.
2. In reality the correlation coefficient is only 0.6083
3. If an important strain history is lost and yet we get correlation coefficient as 1 is erroneous .
4. The correlation coefficient r is flexible and the properties of r is capable of managing large data by shifting the origin as stated in illustration 2.
5. The deviation of correlation coefficient from 1 indicates different Geo – fatigue due to incremental strain during stress history of the region.
6. By preparing correlation coefficient data for many Geo-profiles the stress history through strains could be prepared.
7. Rapid change in strain data / correlation coefficient will indicate the complex Geology especially in Japan.

References

1. Van der pluijm, ben a, *Earth Structure*-2003 W.W.Norton & company inc, New York 10110. pp65-68
2. Das N.G.Statistical Methods combined edition vol.1&2 2009 Tata McGraw-Hill co New Delhi pp275 -280
3. Jensen Jerry,1997,Statistics for petroleum engineers and geoscientists, Prentice Hall, Cuevas 1993 p32 -36

First International Conference on Geotechnique, Construction Materials and Environment, Mie, Japan, Nov.21-23, 2011, ISBN: 978-4-9905958-0-7 C3051

Geocell Reinforced Bed Subjected to Simulated Traffic Loads

P. Sharifi, S.N. Moghaddas Tafreshi., Department of Civil Engineering, K.N. Toosi University of Technology, Tehran, Iran. E-mail: Sharifipayam.civil@gmail.com

ABSTRACT: This paper describes a series of laboratory, pilot scale tests were performed on geocell reinforced sand beds with different number of geocell layers and with different heights of geocell in terms of H/D (H: the thickness of geocell and D: the loading surface diameter) under repeated loads to simulate the vehicle traffic loads. The influences of the thickness of geocell layers and arrangements of geocell layers embedded in bed were studied. Assessment of performance was investigated for different number of layers while the used mass of geocell material, was kept constant. For example, the experiment reinforced by two layers of geocell with H/D=0.5 has exactly the same mass of geocell compared with the experiment reinforced by one thicker layer of geocell reinforcement with H/D=1.0. The results show that the reinforced bed with more layers of geocell has more efficiency than one layer of geocell in reducing the surface settlement under repeated loading while the mass of geocell used in the foundation bed is kept constant.

Keywords: geocell-reinforced sand; soil surface settlement, repeated load, geocell layers

1. INTRODUCTION

In recent decades, due to its economy, ease of construction and ability to improve the visual appearance, reinforced soil has been widely exploited in geotechnical engineering applications such as the construction of roads, railway, stabilization of slopes, improvement of soft ground, embankments and footings {(Das and Shin, 1994); (Raymond, 2002); (Shin et al., 2002); (Hufenus et al., 2006); (Dash et al., 2004); (Sitharam et al., 2007); (Al-Qadi et al., 2007); (Moghaddas Tafreshi and Khalaj, 2008); (Sireesh et al., 2009); (Moghaddas Tafreshi and Dawson, 2010a); (Moghaddas Tafreshi and Dawson, 2010b)}. Generally, when a reinforced soil is subjected to loading, it shows a higher load carrying capacity and a lower settlement compared with a soil mass without reinforcement {e.g., (Dash et al., 2003); (Yoon et al., 2004); (Patra et al., 2005)}. Among of the different types of geosynthetics-reinforcement, in the case of geocell-reinforcement, in addition to the tensile strength of the reinforcement and friction at the soil-geosynthetic interface, a confining stress will be developed on the infilling soil due to passive resistance provided by the cell structure {(Bathurst and Karpurapu, 1993); (Madhavi et al., 2006)} Thus, the lateral resistance in the geosynthetic restrains the lateral movement of the soil and, consequently, reduces the vertical deformation. In this paper, an experimental study was conducted to understand the role of geocell-reinforcement to mitigate the hazardous effect of repeated loading. A series of tests on the single and double layers of geocell were performed to evaluate the role of different factors on the soil-geocell behavior such as number of geocell layers.

2. TESTING EQUIPMENTS

The testing apparatus is comprised of three main parts include the loading system, the testing tank and the data acquisition system. The general arrangement of the laboratory test is shown in Fig.1.

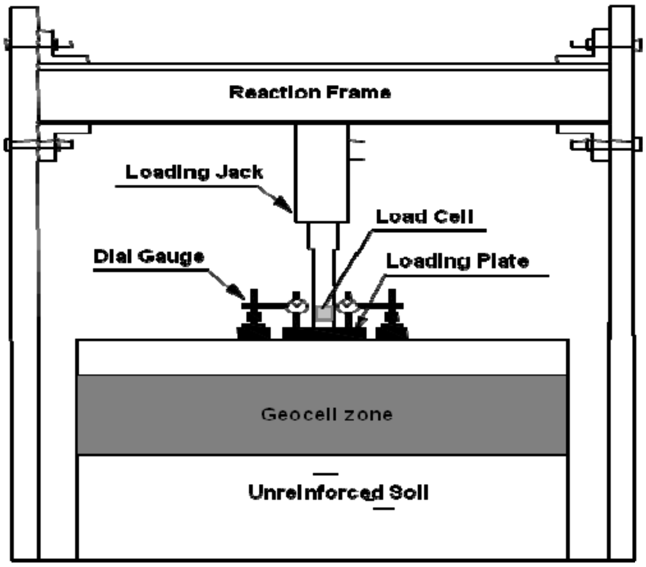

Fig. 1. General arrangements of tests.

The loading system is composed of a loading frame, a hydraulic actuator and a controlling unit. The loading frame includes two stiff and heavy steel columns of 1600 mm height and a horizontal beam of 1270 mm length, which supports the hydraulic cylinder. The controlling unit is comprised of an electro-mechanical valve, which can regulate the intensity of the compressed oil required to produce a cyclic load with the desired amplitude and frequency. The soil beds were prepared in a test tank (rigid steel box) with inside dimensions of 700mm in length, 700mm in width, and 600mm in height. According to the preliminary tests, the measured deflection of the side faces of the tank proved to be negligible and in the ranges to satisfy the rigidity of the system. The geometry of the test configurations for the geocell-reinforced bed is shown in Fig.2. In order to provide experimental control and repeatability of the tests, the compaction energy produces by means of hydraulic cylinder which applies constant pressure on a wooden stiff plate (680 mm * 680 mm). The wooden plate is fitted to the soil surface so all the energy will transfer to soil uniformly. A special data acquisition system was developed by which stress and settlement could be read and recorded automatically. The system was able to read the data from channels simultaneously. An S-shape load cell was also used and placed in the loading shaft to measure the pattern of the applied loads on the trench surface accurately. Two LVDTs were placed on the loading surface to measure the settlement of soil surface during the repeated loads. The loading surface was simulated by a rigid steel plate and measured 110mm diameter (D) and 30mm thickness.

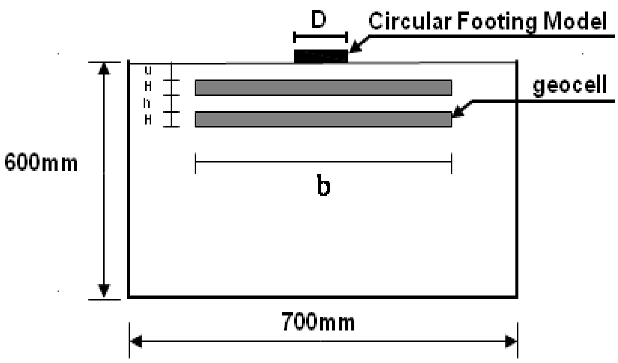

Fig. 2. Geometry of geocell-reinforced foundation bed.

3. TESTING MATERIALS

According to Fig. 2, the soil used in the tests was natural soil with grains size between 0.002 and 15 mm, D_{50}=1.4 mm, C_c=1.2, C_u=13.86 and G_s=2.645. This soil is classified as SW in unified soil classification system. The maximum and minimum porosities of this soil (e_{max} and e_{min}) were obtained 0.66 and 0.36, respectively. The relative density of soil was selected 70% in all of the tests. Geocells used as reinforcement was made of a type of non-woven Geotextile – an innovative approach for use in ground stabilization. When cells fill with soil, the combination of geocell and soil provides an ideal surface for construction projects such as pavement, road, foundations, slopes, driveways and so on. The pocket size of the geocell kept constant of 50 mm). It was used at heights (H) of 25, 50, and 100 mm in the testing program. Fig. 3 shows an isometric view of the geocell used in the investigations. The engineering properties of this geotextile, as listed by the manufacture, are presented in Table 1.

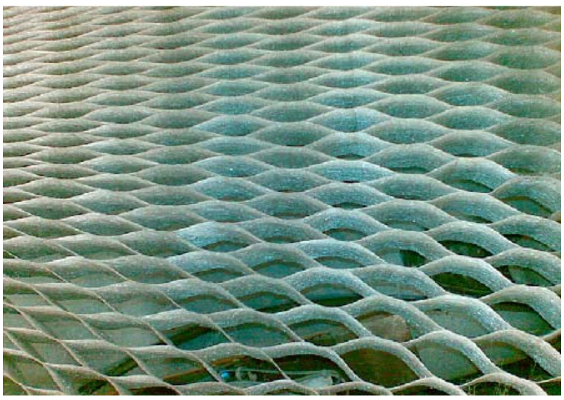

Fig. 3. Isometric view of the geocell

Table 1. The engineering properties of the Geotextile used in the tests.

Description	Value
Type of geotextile	Non-woven polymer
Type of polymer	100% polypropylene
Area weight (g/m^2)	190
Thickness under 2 kN/m^2 (mm)	0.57
Thickness under 200 kN/m^2 (mm)	0.47
Tensile strength (kN/m)	13.1
Strength at 5% (kN/m)	5.7

4. PREPARATION OF MODEL TEST

At first the piston force and number of impact to achieve the desired density was determined by a series of trials with different piston force and number of impact. Sand was then compacted in layers of specific thickness depend on height of the geocell used to consistently maintain a relative density of 70% in all the tests. According to the test type, each of the geocell-reinforced layer was placed carefully and prior to start compaction a surcharge approximately 10mm was applied above geocell-reinforced matters. Soil mixture placed either between the two geocell layers or inside the pocket of geocell. The surface of the soil was then leveled and the steel plate as a model of loading surface was centered in the testing tank. A load cell was placed in the loading shaft to record the applied loads and two LVDTs were placed on the steel plate accurately to measure the settlement of soil surface during the repeated loads. Reference {(Moghaddas Tafreshi and Dawson, 2010b)} reported that the optimum distance between of the topmost layer of the geocell and soil surface under repeated load should be approximately 0.1 times of the loading surface width. Hence, in this investigate in all tests the first layer of reinforcement was placed at u/D=0.1.

5. PATTERN OF APPLIED LOAD

Trapezoidal load was used by many researchers for modeling traffic load and the loading arrangements were those representatives of typical trucks on LVRs in the United Kingdom. Although lorries may run with tyre pressures as low as 240kPa and as high as 900kPa, pressures of 400kPa and 800kPa were deemed to be closer to the operational values {(Brito et al., 2009)}.

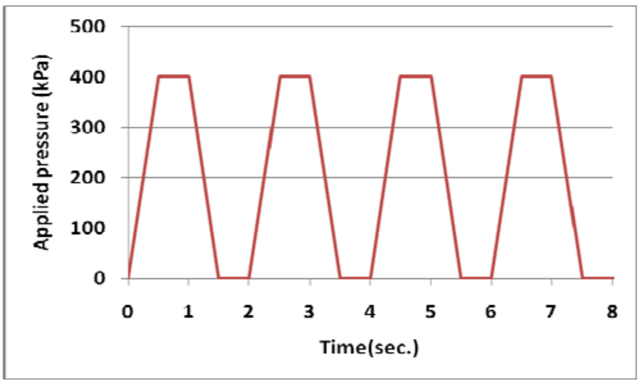

Fig. 4 Typical time history of initial static and repeated load on footing.

Fig. 4 shows the typical time history of applied load on the soil surface used in present experiments. As can be seen, the soil surface is subjected to a trapezoidal load having the minimum amplitude of 0 kPa and the maximum amplitude of 400 kPa. A trapezoidal load cycles with a frequency of 0.5 Hz would be continued until the rate of change of total settlement drops to an insignificant amount or, alternatively, excessive settlement and unstable behavior is observed. In the case of stable tests, settlement due to up to 20,000 subsequent load repetitions was recorded.

6. TEST PARAMETERS AND TESTING PROGRAM

14 tests in different series were planned and carried out in this research. According to table 2, the tests were scheduled to find out the effect of the distance between of the first geocell layer and second geocell layer (h), the number of geocell layers (N) and performance of a composite material (geocell-reinforced soil) on the behavior of foundation bed under cyclic load. All these variable parameters used to describe the tests are expressed in non-dimensional form with respect to loading surface width (D) as H/D and h/D. The value of b/D was kept constant 3.2 in all reinforced tests {(Moghaddas Tafreshi and Dawson, 2010a); (Moghaddas Tafreshi and Dawson, 2010b)}. It should be noted that some of the tests were repeated carefully at least twice to examine the performance of the apparatus, the accuracy of the measurements, the repeatability of the system, reliability of the results and finally to verify the consistency of the test data. The results obtained depicted a close match between results of the two or three trial tests with maximum differences in results of around 10%. This difference was considered to be small and is subsequently neglected. It demonstrates that the procedure and technique adopted can produce repeatable tests within the bounds that may be expected from geotechnical testing apparatuses.

Table2. Tests schedule

Type of reinforcement	Number of geocell layers, N	H/D	h/D	No. of Tests
unreinforcement	--	--	--	1+1*
geocell reinforcement	1, 2	0.45	--	2+2*
	2	0.25	0.1, 0.2	2+2*
	1	0.9	--	1+1*

7. RESULTS AND DISCUSSION

In this section, the tests results of the laboratory model are presented with a discussion highlighting the effects of investigated parameters.

7.1. THE EFFECT OF THE THICKNESS OF SAND BETWEEN TWO SUBSEQUENT GEOCELL LAYERS (h/D)

In order to show the influence of the thickness of sand between two layers (i.e., the distance between two subsequent geocell layers: ratio h/D), two test series was done. Fig. 5 summarizes the variation of the footing settlement (non-dimensional parameter as S/D) with time for the two geocell-reinforced beds (N=2) with a constant thickness of geocell (H/D= 0.45) and two different h/B values of 0.1 and 0.2 (h/D = 0.1, 0.2) and also for unreinforced soil bed. The results illustrated in Fig. 5 show that in the case of geoecell reinforced beds, the rate of change of both the total settlement and accumulated plastic settlement reduces as the number of cycles (or time) increases.

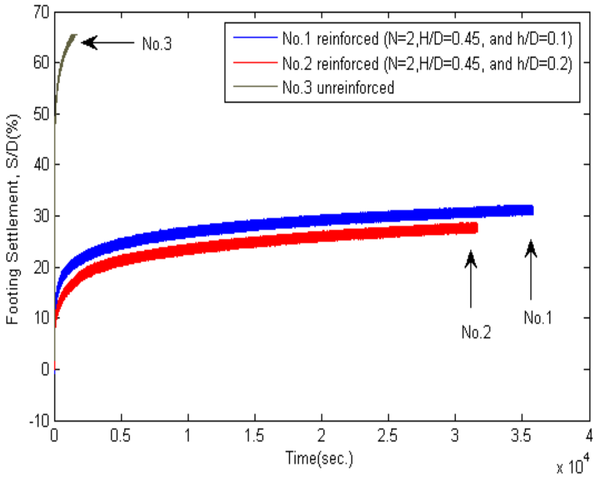

Fig. 5. Variation of settlement with time for unreinforced and reinforced beds (N=2, H/D=0.45 and h/D=0.1 and 0.2).

The variation of settlement becomes stable after about 18000 number of load cycles. Besides, Fig. 5 indicates that in the case of unreinforced bed, after the initial load cycles (about 10 in this case), settlement of the footing increases significantly and then excessive settlement and, consequently, unstable behaviour is observed.
The results depict for the reinforced beds the total footing settlement is considerably decreased relative to the unreinforced settlement. It is also clear that the rate of reduction in the total footing settlement reduces with increase in the value of h/D as no marked further decrease in footing settlement may be expected when the distance between two geocell layers, h/D increases to h/D>0.2.

7.2. COMPARISON OF SINGLE AND TWIN LAYERS OF GEOCELL REINFORCEMENT AT THE SAME MASS OF GEOTEXTILE MATERIAL USED

The performance of single layer and twin layers of geocell-reinforcement, for the same mass of geotextile material used, in decreasing the settlement of a sand bedis the subject of Fig. 6 and Fig. 7. The variation of the footing settlement (in terms of S/D) with time (or number of load cycles) as a function of the number of layers of geocell (N) and thickness of geocell (H/D) as compared with unreinforced soil bed is shown in Fig. 6 and Fig. 7.

Overall, these figures indicate that for the same mass of geotextile material used, the value of maximum footing settlement decreases considerably due to more layers of geocell (N). On the other hand, the geocell-reinforced bed system with 2 layers clearly has a superior ability to reduce the maximum settlement of the footing as compared with the geocell-reinforced bed system with 1 layer system.
For example, the maximum footing settlements for the 2 layers of geocell-reinforced soil bed with H/D=0.225 (h/D= 0.2) and for one layer of geocell-reinforced soil bed with H/D=0.45 at the end of loading are36% and 28% of the loading plate diameter, respectively (as per Fig. 6).

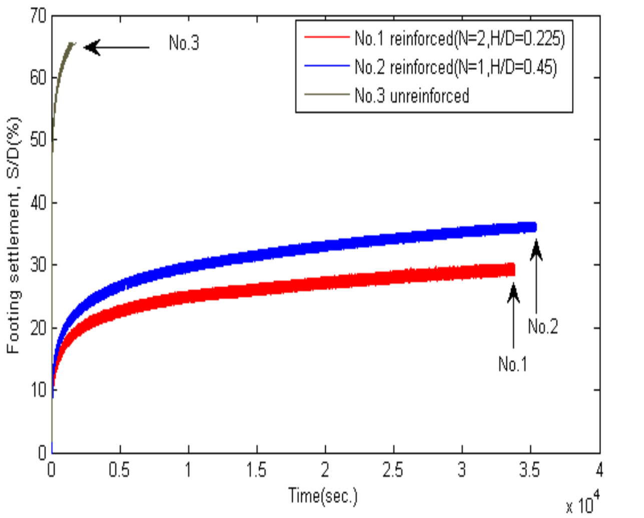

Fig. 6. Variation of settlement with time for unreinforced and reinforced beds (N=2,H/D=0.225 with h/D=0.1 and N=1, H/D=0.45)

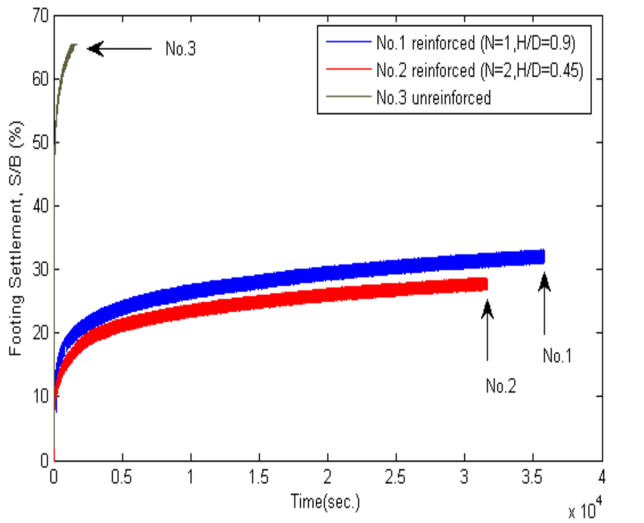

Fig. 7, Variation of settlement with time for unreinforced and reinforced beds. (N=2, H/D=0.45 with h/D=0.2 and N=1, H/D=0.9)

The increase in performance improvement of two layers as compared with one layer could be attributed to two following reasons (1) the thicker geocell may be made a major obstacle to achieve a suitable density inside of geocell's cells, consequently using more geocell layers with lower thickness (while the mass of geocell is kept constant) would be more beneficial, (2) if the reinforced zone is considered analogous to a beam, the competent thickness of soil layer between two layers increases the moment of inertia, and hence shear and bending rigidity of the geocell zone significantly increases Therefore, it would be expected the multiple geocell-sand mattress has more effective than one layer with the same mass.
The hysteresis loop of loading plate settlement for the unreinforced bed, the 2 layers of geocell-reinforced soil bed with H/D=0.225 (h/D= 0.2) and one layer of geocell-reinforced soil bed with H/D=0.45, shown in Fig.8. The hysteresis curve shows that there is an increase in the slope of the repeated pressure-settlement curve with an increase in the number of load–unload cycles. This corresponds to a reduction in the rate of change of peak settlement with number of load applications which, together, are indicative of a hardening of the reinforced system. The general behavioural patterns observed in these tests is in-line with those observed in the repeated load testing of unreinforced and reinforced bed as observed by several authors {(Moghaddas Tafreshi and Dawson, 2010b); (Werkmeister, 2005)}.

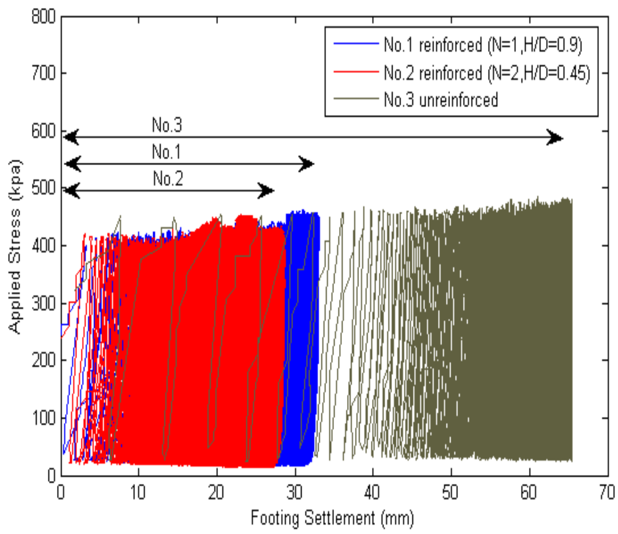

Fig. 8. Hysteresis curve for unreinforced and reinforced beds (N=2, H/D=0.45 with h/D=0.2 and N=1, H/D=0.9).

8. SUMMERY AND CONCLUSIONS

A series of laboratory tests have been carried out on the unreinforced and geocell-reinforced bed which is a representative of traffic load on the surface road. Benefits were assessed in terms of the decreased settlement of a soil surface subjected to the repeated loads. The various parameters studied in this testing program include: number of the geocell-sand mattress and thickness of sand between layers. The repeated load test results show that the rate of change in peak settlement and residual settlement reduced with the cycle numbers increasing. Also as the number of geocell layers increase, the settlement of the foundation bed decreased. Furthermore, the performance of the geo-composite material increases when the number of reinforced layer increases, while the mass of geocell is kept constant. For example, the settlement for N=1 (H/D=0.45) is approximately 28% more than the settlement with N=2 (H/D=0.225 and h/D=0.2) at the same mass of geocell.

9. REFERENCES

[1] Al-Qadi, I.L., et al., 2007. Accelerated full-scale testing of geogrid-reinforced flexible pavements. TRB 2007 Annual Meeting (CD-ROM). Washington, DC: Transportation Research Board, National Research Council.

[2] Bathurst, R.J., Karpurapu, R., 1993. Large-scale triaxial compression testing of geocell- reinforced granular soils. Geotechnical Testing Journal, ASTM 16, 296–303.

[3] Brito, L.A.T., Dawson, A.R., Kolisoja, P.J. 2009. Analytical Evaluation of Unbound Granular Layers in Regard to Permanent Deformation. In: Proceedings of the 8th International on the Bearing Capacity of Roads, Railways, and Airfields (BCR2A'09), Champaign IL, USA, pp 187-196.

[4] Das, B.M., Shin, E.C., 1994. Strip foundation on geogrid-reinforced clay: behavior under cyclic loading. Geotextiles and Geomembranes 13 (10), 657–667.

[5] Dash, S.K., Rajagopal, K., Krishnaswamy, N.R., 2004. Performance of different geosynthetic reinforcement materials in sand foundations. Geosynthetics International 11 (1), 35–42.

[6] Dash, S. K., Sireesh, S. and Sitharam, T. G. (2003). Behaviour of geocell reinforced sand beds under circular footing. Ground Improvement, 7, No. 3,111–115.

[7] Hufenus, R., Rueegger, R., Banjac, R., Mayor, P., Springman, S.M., Bronnimann, R., 2006. Full-scale field tests on geosynthetic reinforced unpaved on soft subgrade. Geotextiles and Geomembranes 24 (6), 21–37.

[8] Madhavi Latha G., Rajagopal K. and Krishnaswamy N.R. 2006. Experimental and theoretical investigations on geocell supported embankments. Int. J. of Geomechanics, ASCE, 6(1),

[9] Moghaddas Tafreshi, S. N. and Dawson, A.R. 2010a. Behavior of footings on reinforced sand subjected to repeated loading – Comparing use of 3D and planar geotextile. Geotextiles and Geomembranes, Elsevier, 28, 434–447.

[10] Moghaddas Tafreshi, S. N. and Dawson, A.R. 2010b. Comparison of bearing capacity of a strip footing on sand with geocell and with planar forms of geotextile reinforcement. Geotextiles and Geomembranes, Elsevier, 28, 72–84.

[11] Moghaddas Tafreshi, S.N., Khalaj, O., 2008. Laboratory tests of small-diameter HDPE pipes buried in reinforced sand under repeated load. Geotextiles and Geomembranes 26 (2), 145–163.

[12] Patra, C.R., Das, B.M., Atalar, C., 2005. Bearing capacity of embedded strip foundation on geogrid reinforced sand. Geotextile and Geomembranes 23 (5), 454–462.

[13] Raymond, G.P., 2002. Reinforced ballast behaviour subjected to repeated load Geotextiles and Geomembranes 20 (1), 39–61.

[14] Shin, E.C., Kim, D.H., Das, B.M., 2002. Geogrid-reinforced railroad bed settlement due to cyclic load. Geotechnical and Geological Engineering 20 (3), 261–271.

[15] Sireesh, S., Sitharam, T.G., Dash, S.K, 2009. Bearing capacity of circular footing on geocell–sand mattress overlying clay bed with void. Geotextiles and Geomembranes, Elsevier.

[16] Sitharam G., Sireesh, S. T. and Dash, S. K. 2007. Performance of surface footing on geocell-reinforced soft clay beds. Geotech Geol Eng, 25:509–524.

[17] Werkmeister, S, Dawson, A R & Wellner, F., 2005. Permanent deformation behavior of granular materials: the shakedown theory. Transportation Research Board. 6 (1), 31-57.

[18] Yoon, Y.W., Cheon, S.H., Kang, D.S., 2004. Bearing capacity and settlement of tire-reinforced sands. Geotextile and Geomembranes 22 (4), 439–453.

[19] beds. Geotech Geol Eng, 25:509–524.

Effects of Gradation of Various Sand Deposits of Pakistan on Strength of Hardened Concrete

Gauhar Sabih [1] and S. Muhammad Jamil[2]

[1]*Graduate Student, School of Civil and Environmental Engineering, National University of Science and Technology, Islamabad, Pakistan, gauhar73@yahoo.com*
[2]*HOD, Department of Geotechnical Engineering, National University of Science and Technology, Islamabad, Pakistan, smuhammadjamil@ymail.com*

ABSTRACT: Various sand deposits of varying gradation are available in different regions of Pakistan. The gradation of different sands was compared with the ASTM specifications. It was revealed that only two sands satisfy the ASTM gradation limits. The same was also confirmed by the results of workability and compressive strength. For betterment of the construction industry, optimization of sand was carried out. The grading curves of optimized sands became compatible with the ASTM specifications and the concrete made with improved sands showed up to 39% increase in compressive strength. The optimized sands were cost effective also.

Key words: sand, concrete, Pakistan, Lawrencepur, stone dust, compressive strength

1. INTRODUCTION

Since up to 30 percent of the total volume of concrete consists of sand/fine aggregate consequently fine aggregate characteristics significantly affect the performance of fresh and hardened concrete and have an impact on the cost effectiveness of concrete [1]. Gradation or particle size distribution of sand affects the properties of concrete like packing density, voids content, workability and strength [2]. Uniformly distributed mixtures generally lead to higher packing resulting in concrete with higher density and less permeability, and improved abrasion resistance. Consequently, uniformly distributed mixtures require less paste, thus decreasing bleeding, creep, and shrinkage [3]-[4]. The fine aggregate should be uniformly graded. If fine aggregate is too coarse it will produce bleeding, segregation and harshness, but if it is too fine, the demand for water will be increased [5].

Various sand deposits of varying gradation are available in different regions of Pakistan. The existence of large water reservoirs usually transports finer sands towards downstream; consequently the sand in the Northern region is coarser as compared to the sand from Central and Southern regions. There is a general trend in the country to use coarser sand from Lawrencepur, a site located in the Northern region. Transportation cost of sand from this place to far flung areas in Centre and South makes any project cost intensive. This study was aimed at evaluating the grain size distribution and absorption of various types of sands in the light of ASTM standards and to contrast the effects of gradation on the strength and workability of concrete. Finally devising a technique for optimizing the gradation of fine sands by sieving the stone dust and mixing different fractions of stone dust with the natural sand to get optimized sand gradation and evaluating its effects on strength of hardened concrete.

2. IDENTIFICATION OF SAND DEPOSITS

Various well known material suppliers and construction firms were approached for identification of major sand deposits of the country. The locations of identified sand deposits are shown in Fig 1.

3. EXPERIMENTAL PROGRAM

3.1 Sieve Analysis and Classification

All the sand samples were classified by sieve analysis, carried out according to ASTM C-136-96 [6] and the classification of sand was done according to ASTM D-2487-93 [7]. ASTM C-33-03 specifies the gradation limits for sands to be used as fine aggregate in concreting [8]. The gradation curves of all the sands were compared with the ASTM gradation limits to contrast the variations.

3.2 Absorption Percentage

All the sand samples were tested for their absorption percentage in saturated surface dry (SSD) condition according to ASTM C-128.

3.3 Organic Impurities in Sands

This test was conducted for all the sands according to ASTM C-40 [9]. The test procedure consisted of making a reference standard colour solution by dissolving reagent grade potassium dichromate in concentrated sulfuric acid at the rate of 0.25 gram per 100 ml of acid. The sand sample was filled in a glass bottle up to 130 ml mark and sodium hydro oxide solution (3% by mass in 97% water) was added up to 200 ml mark. The bottle was shaken vigorously and allowed to stand for 24 hours. After 24 hours the colour of the sand solution was compared with freshly made reference colour solution. The darker colour

Fig 1. Locations of Identified Sand Deposits

than reference colour indicates the possibility of sand containing injurious organic impurities and requires further testing for sand before use in concreting. The lighter or equal colour means that the sand does not contain injurious organic impurities and no further testing is required.

3.4 Evaluation of Sands in Concreting

3.4.1 Concrete Mix

The concrete mixes were prepared using sand / fine aggregate from eight different sources and remaining variables as constant with the cement: sand: coarse aggregate ratio of 1: 2: 4 (by weight) respectively, cement content (201.7 kg/cum) and water cement ratio of 0.5 with constant slump value. The course and fine aggregates were used in SSD condition. The course aggregate used was taken from Margallah quarry located in the Northern region. The cement used was Fauji cement (type 1, portland cement). The water used was normal tap water without any undesired colour.

3.4.2 Workability of Fresh Concrete

The workability was evaluated by measuring the slump of fresh concrete according to ASTM C-143. The concrete was filled in the slump cone in 3 equal layers with 25 blows of tamping rod each. After leveling the top layer, the cone was lifted and slump was measured as reduction in original height.

3.4.3 Compressive Strength of Hardened Concrete

The test was conducted on 4x4 inches cubes (as per BS-1881) and 4x8 inches cylinders (as per ASTM C-39). The compressive strength was determined at the age of 3, 7, 14 and 28 days [10]-[11].

4. TEST RESULTS AND DISCUSSIONS

4.1 Sieve Analysis and Classification

All the sand types are poorly graded sands classified as SP, except the Wadd sand which contains silt as well and classified as SP-SM. The Percentage of micro fines (material passing No. 200 sieve) is below 5% in all sands except Wadd sand which contains 9% micro fines. According to ASTM C-33, the allowable limit of micro fines in sand for concreting is up to 5% so all the sands satisfy the ASTM criteria except the Wadd sand.

4.2 Comparison of Gradation with ASTM Gradation Limits

The comparative results of all the sands with the ASTM gradation limits are shown graphically in Fig 2. All the sands are finer than ASTM gradation limits except the Qiblabandi and Bollari sand. The Qiblabandi sand is the best match to ASTM gradation limits while Bollari sand is little finer than Qiblabandi sand.

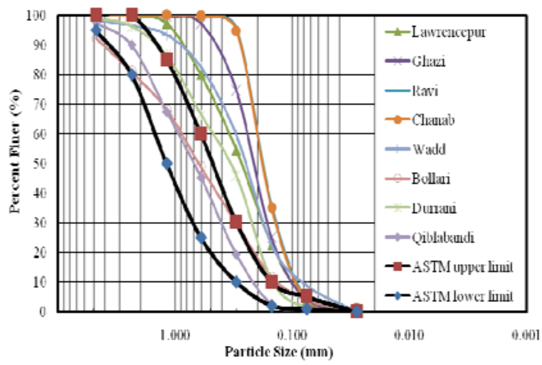

Fig 2. Sand Gradation versus ASTM Gradation Limits

4.3 Absorption Percentage

All the sands have absorption less than 3 % so they are within range of the limiting range as per BS-8007. The Qiblabandi sand has the lowest absorption percentage i.e. 1.75% being the coarsest sand of all types while the Bollari sand has the highest absorption percentage of 2.11% but it is also within range of the acceptable limit.

4.4 Organic Impurities in Sands

All the sand sample solutions have the colour lighter than the reference standard colour solution so all the sands do not contain injurious organic impurities and no further testing is required for the organic impurities (according to ASTM C-40). Consequently all the sands are suitable for concreting as per the results of this test.

4.5 Workability of Fresh Concrete

The slump values of the concrete made with different types of sands are ranging between 1.1 to 1.2 inches with same water cement ratio. This slump value was taken as constant for further compressive strength testing of hardened concrete. According to specifications, hand tamping was resorted in the preparation of cubes while vibrator insertions were used in preparation of cylinders [12]-[13].

4.6 Compressive Strength of Concrete Cylinders and Cubes

The compressive strengths of both of concrete cubes and cylinders follow the same trend line thus confirming the results. The comparative results of compressive strength of concrete cylinders are graphically shown in Fig 3. The Qiblabandi sand proved to be the best fine aggregate giving highest compressive strength of 3463 psi. Gradation meeting the ASTM specifications, lowest percentage of micro fines and within range fineness modulus of Qiblabandi sand are the supporting factors for the highest compressive strength. The trend of gradation of different sands as compared with the ASTM gradation limits is also confirmed by the results of the compressive strength. The Ghazi, Ravi and Chanab sands are below 3000 psi which is not desirable for concreting works.

5. OPTIMIZATION OF SAND GRADATION

Having observed the gradation of various sands, an endeavor was made to bring them within the specified limits of ASTM by adding a fraction of coarse material. The stone dust from Margallah quarry site was taken and various fractions of stone dust were produced by sieving the stone dust on Number 4, 8, 16, 30 and 50 sieves (These fractions are denoted as R4, R8, R16, R30 and R50 in this study). Different percentages of various fractions of stone dust were added to the sand samples and optimized samples were produced. The optimized samples were than tested for their gradation to check the compatibility with ASTM limits. The optimized samples were then used for making concrete cubes and cylinders thus determining the improvement in the compressive strength of concrete specimens.

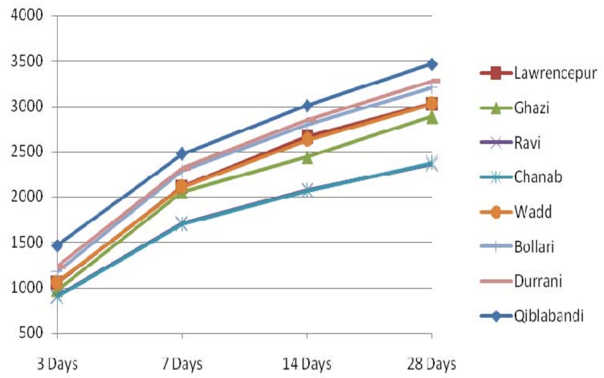

Fig 3. Comparison of Compressive Strength of Concrete Cylinders (psi)

This resulted in significant improvement of sand gradation as well as the compressive strength of concrete. Six sands which were out of range of ASTM standards were optimized. Various different combinations were tried for making the improved sand samples to attain the best mix.

5.1 Gradation of Optimized Sands

The gradation curves of optimized sands were compared with the gradation curves of original sands in the light of ASTM gradation limits to determine the effects on the gradation curves. The comparison clearly shows that the gradation curves of optimized sands are satisfying the ASTM gradation limits where as the original ones were out of the limits. The comparison of original and optimized gradation curves is shown in Fig 4.

5.2 Compressive Strength of Concrete

The optimized sand samples were tested by making concrete cubes and cylinders with the cement: sand: coarse aggregate mix of 1: 2: 4 (by weight) and the variables like cement (201 kg/cum), water-cement ratio (0.5), curing conditions and course aggregate (Margallah) as constant. The concrete specimens were than tested for compressive strength at the age of 3, 7, 14 and 28 days to get the improved compressive strengths. These improved strengths were than compared with the original compressive strength values to get the percentage improvement.

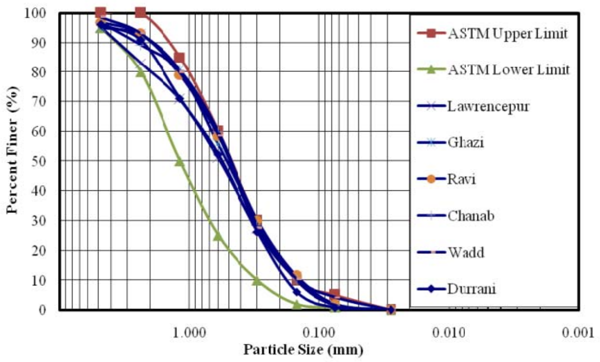

Fig 4. Comparison of Optimized Gradation Curves with ASTM Limits

5.3 Results of Compressive Strength of Optimized Sands

The compressive strengths of both cubes and cylinders follow the same trend line thus confirming the results. The comparative results of compressive strength of concrete cylinders are graphically shown in Fig 5. The results show that there is significant improvement in the compressive strengths and all the improved sands are above 3000 psi which is the foremost requirement for a sand to be used in concreting works. The improved Lawrencepur sand and Durrani sand (with fineness modulus of 2.62 and 2.58) respectively are giving the highest strength of 3441 psi and 3547 psi respectively.

6. COMPARISON OF ORIGINAL AND OPTIMIZED SAND PROPERTIES BASED ON COMPRESSIVE STRENGTH OF CONCRETE

The cylindrical compressive strengths of optimized sands at the age of 28 days were than compared with the cylindrical compressive strength values of original sands to get the percentage improvement.

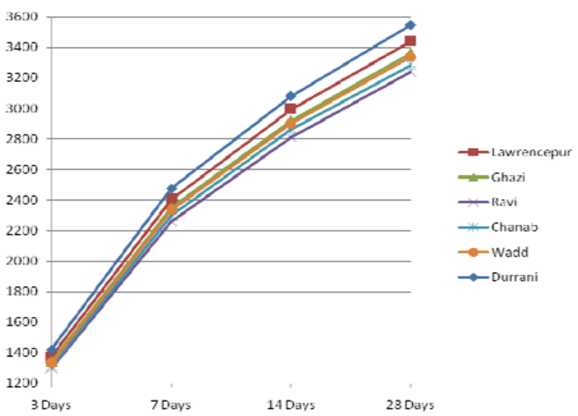

Fig 5. Comparison of Improved Compressive strength of Cylinders (psi)

6.1 Comparative Results of Cylinder Strength

The comparative summary is shown graphically in Fig 6. The comparison of percentage improvement of optimized sands in comparison to original sands is shown in Fig 7. The results show that all the optimized sands gave increased compressive strength. The optimized Ravi and Chanab sands show the most significant increase of 37% to 39% in the compressive strength when compared with original sands.

7. CONCLUDING REMARKS

Based on laboratory investigations and data analyses, following conclusions are drawn:

- Local sands can be utilized in the construction projects by optimizing the gradation using stone dust to avoid high costs of transportation.
- Even the best considered sand deposit requires fractions of stone dust to maximize its potential in concreting.
- The optimized Ravi and Chanab sands show the most significant improvement of 37% to 39% in the compressive strength while the optimized Lawrencepur, Ghazi, Wadd and Durrani sands also show greater strength than original sands with percentage improvement of 8% to 16%.
- The optimized Ghazi, Ravi and Chanab sands can be utilized in concreting works where as they were not suitable for concreting in their original form.
- All the optimized sands show higher compressive strength than the original sands in concrete cubes and cylinders both and are above 3000 psi which is the minimum criteria for any sand to be used as fine aggregate in concreting works.

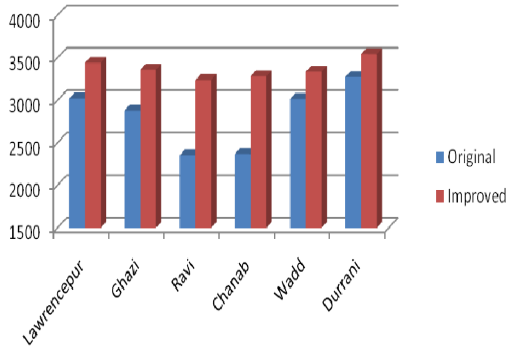

Fig 6. Comparison of Original versus Improved Cylinder Strength

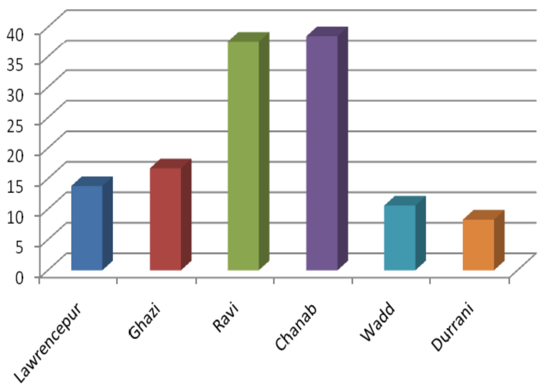

Fig 7. Comparison of Percentage Improvement of Optimized Sands

ACKNOWLEDGEMENTS

The authors thank Dr. S. Ali Rizwan for his critical review which greatly helped in improving the manuscript. The study was funded by the National University of Sciences and Technology.

REFERENCES

[1] Hudson, B.P, “Concrete Workability with High Fines Content Sands”, 1999.

[2] Golterman, P., Johansen, V., Palbfl, L., “Packing of Aggregates: An Alternative Tool to Determine the Optimal Aggregate Mix,” ACI Materials Journal, Vol. 94, No. 5, 1997.

[3] Shilstone, J. M., “The Aggregate: The Most Important Value-Adding Component in Concrete,” Proceedings, Seventh Annual International Center for Aggregates Research Symposium, Austin, Texas, 1999.

[4] Washa, G.W., Workability, Chapter 5, Concrete Construction Handbook, 1998, 4th edition, New York.

[5] Galloway, J. E. Jr., “Grading, Shape, and Surface Properties,” ASTM Special Technical Publication No. 169C, Philadelphia, 1994.

[6] ASTM C-136, Standard Test Method for Sieve Analysis of Fine and Coarse Aggregates, Philadelphia, PA: American Society for Testing and Materials, 2001.

[7] ASTM D-2487, Standard classification of soils for engineering purposes (Unified soil classification system), Philadelphia, PA: American Society for Testing and Materials, 1993.

[8] ASTM C-33, Standard Specification for Concrete Aggregates, Philadelphia, PA: American Society for Testing and Materials, 2003.

[9] ASTM C-40, Standard test method for organic impurities in sand for concrete, Philadelphia, PA: American Society for Testing and Materials, 1992.

[10] ASTM C-192, Standard Practice for Making and Curing Concrete Tests Specimens in the Laboratory, Philadelphia, PA: American Society for Testing and Materials, 2000.

[11] British Standards Institution, "Methods for making of concrete cubes in laboratory," BS-1881-116: Part 110, 1990.

[12] British Standards Institution, "Methods for Determination of compressive strength of concrete cubes," BS 1881-108: Part 110, 1990.

[13] ASTM C-39, Standard Specification for Compressive Strength of Cylindrical Concrete Specimens, Philadelphia, PA: American Society for Testing and Materials, 2003.

First International Conference on Geotechnique, Construction Materials and Environment, Mie, Japan, Nov.21-23, 2011, ISBN: 978-4-9905958-0-7 C3051

Strengthening of Landslide Retaining Pile Wall after Geodetic Monitoring

Frangov G., Zayakova H., Hamova M.,

Higher School of Civil Engineering "L. Karavelov", Sofia, Bulgaria

ABSTRACT: The investigated landslide occurred in the spring of 2004 on the road through the Balkan Mountains, Bulgaria. It was part of a larger ancient landslide that continues down the slope. To restore the traffic it was decided not to strengthen the whole landslide, but only the upper part near the road. It was designed and implemented strength support structure consisting of two rows of steel concrete piles incorporated by a beam. To prevent the influence of groundwater a horizontal drainage above the landslide was carried out. Geodetic monitoring network was built and periodic measurements were held in the period 2005 - 2010 to monitor the behaviour of the structure. During this period the largest horizontal displacements were found in the area between first and second section of the pile construction. Geodetic monitoring was used to determine the most vulnerable area of the structure. It was reinforced with additional steel concrete piles combined with a beam.

Keywords: landslide reinforcement, geodetic monitoring

1. INTRODUCTION

Roads often pass through hilly and mountainous areas and there a greater risk of old landslides activation exists. Some of the main causes of landslide appearance on mountainous roads are: steep gradient of slope, river erosion, weak soil cover above rock basement, usage of an unsuitable soil for construction of embankments, not enough geological survey, technological errors during execution of earth work as poor drainage and compaction of embankments, increasing the load due to more traffic and increase the weight of vehicles. The most common reasons are complex and lead to landslides, which reduce the width of the road or completely interrupt traffic through this section. The road Trojan-Karnare which crosses the Balkan Mountains is a typical example [1]. The aim of this study is to evaluate the trends of the observed deformations of the pile construction and to strength it.

2. LANDSLIDE ACTIVITY AND CONTROL MEASURES

2.1 Geology and geomorphology

The region refers to highest part of the Balkan mountain. The southern slope of the mountain is consequent, deeply incised by many river valleys. The northern slope is steep only in its upper part, dismembered by river valleys in long transverse elevations. The territory in a close perimeter from the site is built of differing in genesis and composition rock complexes: Cherni Ossam Formation (coJ3t – K1bs) is characterized by thin fore-component rhythmic: sandstones, aleurites, marls and clayey limestones.

Zlataritsa–Cherni Ossam Formation (z-coJ3k – K1bs) consists of alternation of thick benches with coarse two-component (flyschoid) rhythmic with benches, characterized by thin three-component rhythmic.

Alluvial formations (aQh) are observed along the Beli and Cherni Ossam Rivers. Alluvium is represented by unsorted gravels and differing in grainsize sands and sandy clays.

Deluvial (dQh) and eluvial (eQh) formations are built of sandy clays and differing in size gravels. They are observed at the foot of the slope sections. At some places the deluvial clays have significant thickness. The eluvial deposits are not thick and often they are entirely absent.

A specific feature of the structures is their Early Cretaceous origin. They are distinguished by their linearity and moreover – by their complexity due to the numerous faults, most often normal faults, which is typical for the fold-block structure of the area.

The region is characterized by low water abundance. The springs are very rare and have insignificant flow rate. They depend either on tectonic fissures or are formed in the base of Quaternary deposits. The groundwater is of the fissure type and is drained in the rivers.

2.2 Landslide features

The great distribution of clayey and flysch sediments, the strongly rugged terrain, the tectonic structure and the hydrogeological specific features create the conditions for the development of landslides along the valley slopes [2]. Their activation is associated with incorrect cutting of slopes and excessive loading from big embankments. The landslide activity has been repeatedly displayed, the last activation being in March, 2004. The developed landslide is a part of a bigger older landslide, which continues downwards along the slope. In the upper part its width is 36 m and the depth varies between 4,5 m and 6,3 m. The landslide body is formed by intensively mixed clays [3].

2.3 Landslide control

A radical solution to this landslide would be the construction of buttresses at the base of the slope foot, with the adequate drainage of the terrain. Due to different reason like private forests, the increasing range of the area and depth of the landslide under the road etc., it has been decided to develop stabilizing facilities in the close proximity of the roadbed for ensuring the road stability. The depth of the slide surface, the passing through a thick layer of asphalt concrete and an embankment of heterogeneous soil, as well as the requirement to carry out the construction works without stopping the traffic, made it necessary to perform the stabilization with a structure of two rows of piles, cantilever anchored in the strong marl layer, united by a beam (Fig.1). The piles were borehole-cast with a diameter of 0.4 m and a length of 10 m. The whole structure is 42.0 m long and [2] it is divided in three sections with a length of 14.0 m each. The grid is situated under the road bench and there are drainage openings in it with diameter 75 mm at a distance of 1.5 m from one another.
To reduce the negative effects of ground water on landslide stability horizontal drainage above the road is built. Its purpose is to intercept water from the slope and take it away from landslide.

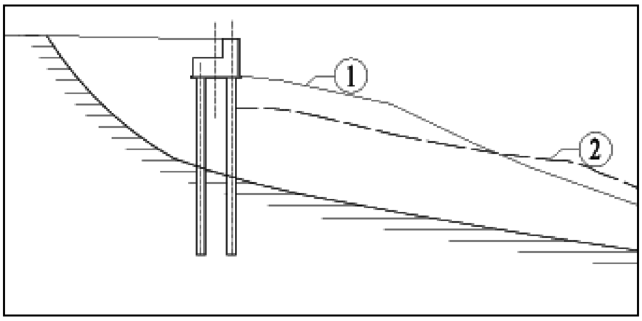

Fig.1. Longitudinal cross section trough the pile wall
1 – initial terrain, 2 – terrain after new landslide activation

After implementation of the retaining structure landslide continued to move down the slope. For this reason the terrain sank and the top of the piles under the unifying beam partially had shown.

3. GEODETIC MONITORING

3.1 Geodetic grid

Measuring and control system was built on the site for conducting geodetic surveying regime measurement. It consists of 2 pcs. basic benchmarks located outside the scope of the landslide and 6 pcs. observed benchmarks on the crown of unifying beam (fig. 2). Nine measurements have been carried out with a total station TOPCON GTS - 105 N during the period 2005 - 2010. Direct measurement accuracy for angles is 5" and for length 2 mm. Leveling of observed benchmarks is done by trigonometric leveling. Coordinate system is relative, as a starting benchmark was used BB 1 and conditionally accepted elevation 100.000 m.

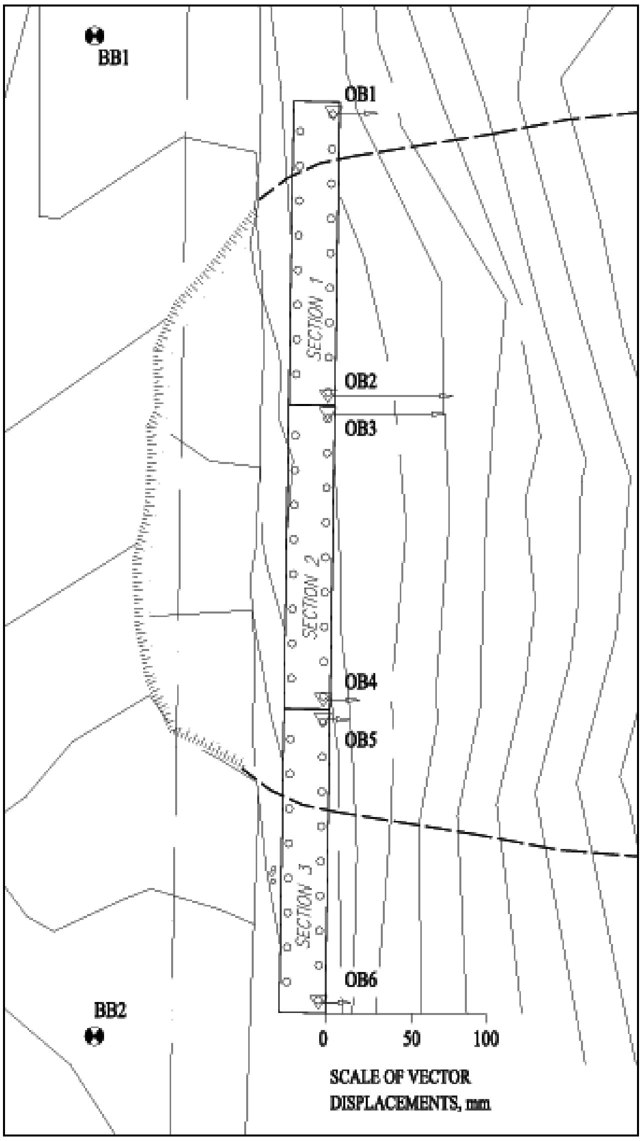

Fig.2. Location map of the geodetic measurement grid
BB – basic benchmark, OB – observed benchmark

3.2 Discussion

The retaining pile structure is subjected to the action of landslide pressure and dynamic loads from vehicles after its construction. Because of these actions, it is strained and deformed. For this reason, relocations have been reported at the starting moment in all observed benchmarks (fig. 3). The landslide has a different depth in the area of pile construction and this affects the landslide pressure. It is the largest in the area between first and second section where the observed benchmarks 2 and 3 are located. There the largest displacements are measured.
The speeds of surveying displacements are not constant. For five years the vector displacement of observed benchmark 2 is 74.46 mm, while for the benchmark 3 is 69.35 mm. The main part of these movements, respectively 40.01 mm and

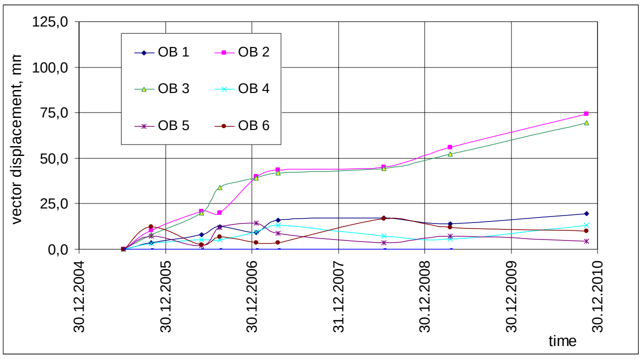

Fig.3. Diagrams of vector displacement of the observed benchmarks

39.20 mm, were appeared during the first year of measurement. The trend is the gradual decay of the deformation. The most vulnerable area of the structure is in the area between first and second section.

The landslide was activated several times in the past. Then a new layer asphalt is performed to restore the level of road. So at this zone the thickness of asphalt in the sunken part of the road reached up to 3.10 m. This asphalt creates a barrier to groundwater and prevent their drainage, regardless of the constructed drainage. The water pressure on asphalt body increases additionally landslide pressure on the retaining structure.

4. STRENGTHENING OF EXISTING CONSTRUCTION

Horizontal displacement of a single pile is obtained according to following equation [4]:

$$\delta_1 = \frac{l_0}{3EI} + \delta_{nn} \quad (1)$$

where:

δ_1 - horizontal displacement of a single pile with a free top on the level of the pile cap under the horizontal force H = 1, applied at this level.

$$\delta_{nn} = \frac{1}{\alpha_c^3 EI} A_0 \quad (2)$$

$$\alpha_c = \sqrt[5]{\frac{K\bar{b}}{EI}} \quad (3)$$

where:

A_0 - coefficient depending on the effective depth of the pile $\bar{h}$;

EI - stiffness of the pile;

α_c - elastic characteristics of the pile;

$$\bar{h} = \alpha_c h \quad (4)$$

K- modification of the subgrade reaction;

$\bar{b}$ - effective width of the pile. For boring piles it has to be obtained trough:

$$\bar{b} = kk_f(d+1) \quad (5)$$

where:

k_f - coefficient depending on the form of the section of the pile. For a circular section k_f =0.9;

$$k = k_1 + \frac{(1+k_1)L_p}{2(d+1)} \quad (6)$$

where:

k_1 - coefficient depending on the number of drilling piles in a row parallel to the plane of action of the load, for n>4, k_1 =0.45;

L_p - average distance between the piles;

The resulting displacements have not reached critical values, the structure is not threatened by the destruction and the trend of deformation is towards extinction, but to reduce the risk of new landslides activation and the interruption of the road it was decided to strengthen the construction in the area between first and second sections (fig. 4).

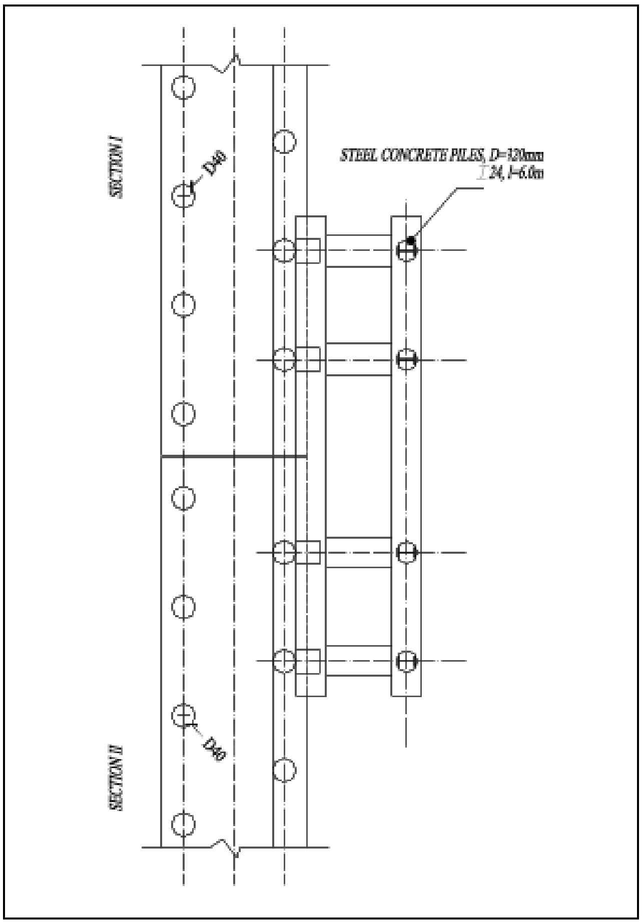

Fig. 4. Plan of the most vulnerable zone of existing pile wall and additional strengthening with steel concrete support pile structure

This reinforcement consists of four additional piles with diameter 320 mm and length 6.0 m, full of concrete B25 and reinforced with double T № 24, unified with reinforced steel concrete beam Among the earlier support structure of the landslide and new one cross beams and short columns are applied (fig. 5).

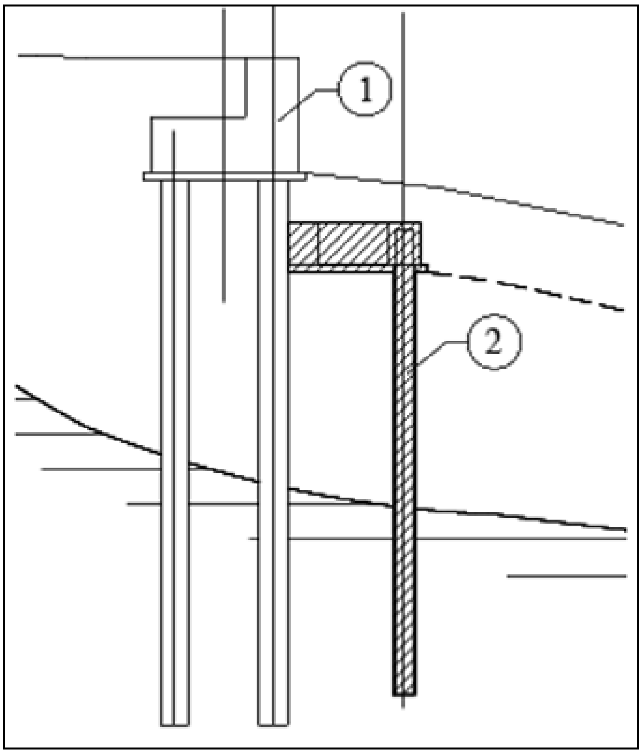

Fig.5. Cross section trough previously built pile wall (1) and new support structure (2)

Additional support structure has been completed and it is expected that the displacements will be reduced completely. The monitoring of the construction should continue and the adequate measures should be taken, if necessary.

5. CONCLUSION

Landslides stabilization is a complex problem that requires a good understanding of geological, geomorphological and hydrogeological conditions of the particular landslide and the influence of various factors on its stability.

The selection of earth retaining structures are often determined not only by geotechnical arguments but also by financial, economic and social considerations.

Strengthening only a facility, such as this road, without taking into account the slope stability as a whole, can cause rupture of the landslide body, partially crossing the landslide masses between piles and stripping of the upper part of retaining structure. Ultimately, static scheme of strengthening changes and this can lead to deformation of the structure. The retaining structure begins to strain after construction under the action of landslide pressure. The greatest load on it is in the section with the deepest slip surface and most intensive landslide movements. This causes a correspondingly larger displacements in this zone. Subsequently, the load is redistributed on the rest of the structure, hence deformations in this area delay and the landslide pressure is intaken more evenly.

In such cases, very useful is to conduct geodetic monitoring. The data obtained make it possible to check the status of construction, the values of the displacements, the trends in their development. The most vulnerable area of the structure can be established and additional support to be implemented. In the case such action is timely taken the construction can be prevented from destruction.

6. ACKNOWLEDGMENT

This study was possible thanks to the courtesy Road Infrastructure Agency of Bulgaria and Regional Traffic Management Lovech. The authors owe their gratitude for the opportunity to participate in solving the landslide problem of road Trojan-Karnare.

7. REFERENCES

[1] Hamova, M., G. Frangov, H. Zayakova. Stabilization of a Landslide Section Along a Road Passing Through the Stara Planina mt., Bulgaria. Proc. 13th Danube-European Conference on Geotechnical Engineering, Ljubljana, Slovenia, 29-31 May 2006, (on CD).

[2] Kolev Ch, Rehabilitation of sliding motorway slopes on deep failure in Bulgaria. Proc. of the 6th International Conference on Case Histories in Geotechnical Engineering , Arlington, VA, August 11-16, 2008, paper No. 2.35.

[3] Ivanov, P., N. Dobrev. 2006. Results from laboratory tests of samples from Fore-Balkan landslides. Proc. National Scient. Tech. Conf. on Landslides and Erosional Processes in Bulgaria, Prof. M. Drinov, 2006, 155-160.

[4] Dingozov G, Bozhinov B, Pile foundation. Sofia: Technica, 1979, ch.5.

First International Conference on Geotechnique, Construction Materials and Environment, Mie, Japan, Nov.21-23, 2011, ISBN: 978-4-9905958-0-7 C3051

Response of Tapered Piles under Lateral Harmonic Vibrations

Ahmad Dehghanpoor, Yazd University, Yazd, Iran
Mahmoud Ghazavi, Professor of Civil Engineering, K.N. Toosi University of Technology, Tehran, Iran

ABSTRACT: This paper presents a new method for analysis tapered piles under lateral harmonic vibration. The behavior of tapered piles is assumed to be as elastic and linear. The soil consists of some elastic horizontal layers that they are homogeneous, isotropic, and linearly visco–elastic. The pile is divided to some segments and the differential equation for a given desirable segment is obtained and solved. Then the dynamic complex stiffness parameters are derived for the pile head. Parametric studies have been performed to investigate the influence of pile geometry, soil properties, and loading details on pile-soil system amplitudes. It has been found that under lateral harmonic vibrations, with increasing the pile taper angle, the resonant amplitude decreases. In addition, it has been concluded that under lateral harmonic vibrations, a tapered pile experiences lower amplitude than a cylindrical pile of the same length and material volume.

Keywords: Tapered Piles, Lateral Harmonic Vibration, Stiffness, Damping

1. INTRODUCTION

There are various methods for studying behavior of dynamically loaded uniform piles. These are continuum approach (Novak, [1]; Novak and Aboul – Ella, [2]; and Nogami, [3]), boundary element method (Kaynia and Kausel, [4]; Sen, Kausel and Banerjee, [5]), lumped–mass method (Penzien, [6]); and finite element solutions (Blaney, Kausel and Rosset, [7]; Wolf and Von Arx, [8]; chow, [9]). Novak presented an approximate continuum approach to account for soil-pile interaction: it is assumed that the soil is composed of a set of independent horizontal layers of infinitesimal thickness, which extend to infinity. As each plane is considered independent, this model may be viewed as a generalized Winkler model. The planes are homogeneous, isotropic, and linearly elastic, and they consider being in a plane strain state. Using Baranov's [10] solution for the horizontal soil reaction to a rigid circular disc with harmonic horizontal displacement (representing a pile cross section), Novak formulated the differential equation of the damped pile in horizontal vibration. He found the steady state (particular) solution for harmonic motion induced through pile ends, and used this solution to find the dynamic stiffness of the pile head for different boundary conditions.

The existent methods are few for analyzing tapered piles under dynamic loads, so recently it has been attracted many investigators. The most studies in this piles, related to vertical harmonic vibrations such as finite difference method (Saha and Ghosh, [11]) and mathematical method (Xie and Vaziri, [12]).

Investigations have been done on tapered piles includes: Full finite element, analytical solution and laboratory tests (Kurian and Moola, [13]), and centrifuge model tests (El Naggar and sakr, [14]). Field load tests were also conducted on tapered piles to investigate their load-carrying capacity (Rybnikov,) and indicate that bored cast-in-place tapered piles can have bearing capacity 20-30% higher than that for cylindrical piles with the same volume and same mean radius. The Ghazavi has also recently performed full-scale tests on a tapered pile driven into a cohesive soil profile in the field. These tests showed that, in long term, the tapered pile had 80% more capacity than a uniform pile of the same volume and length. Zil'berberg and Sherstnev [15] have re-ported from their field tests that driven tapered piles in sandy soils can give a stiffer and stronger axial response resulting in a 200-250% increase in bearing capacity when compared to the capacity of cylindrical piles with the same volume and mean radius. The response of these piles under lateral static loads was also investigated El Naggar and Wei, [16]. El Naggar and Wei [17] also conducted tests in a pressure chamber on tapered model piles subjected to uplift loads.

Ghazavi et al. [18] described the performance of tapered Pile during Pile driving and Ghazavi and Tavassoli [19] Study of Pile geometry on Pile driving. Also has proceeded analysis of kinematic seismic response of tapered piles (Ghazavi, [20]) and Response of tapered piles to axial harmonic loads and effect of angles on tapered piles has been discussed then obtained has been verified whit finite element methods and they were satisfactory (Ghazavi, [21]).

SSM (Segment by Segment Method) is based on continuum method of Novak elasto- dynamic approach for analysis of piles. The SSM has been applied to uniform piles under axial compressive loads (Ghazavi et al. [22]), uplift static loads (Ghazavi et al. [23]), and axial and lateral harmonic vibrations (Ghazavi, [24], Ghazavi and Dehghanpour [25]) in this paper SSM was applied to analyze dynamic behavior of tapered piles under lateral harmonic loads.

2. ANALYTICAL MODEL

The characteristic effects of surrounding soil on the pile response are determined with stiffness and damping parameters of soil – pile system. These effects can be taken in to account if a proper soil reaction is employed.

For analyzing tapered pile, it was idealized to some cylindrical segments with different diameter that connected together by rigidly at nodes. This idealization was used in tapered piles under harmonic axial vibration [11-12] and [21].

Surrounding soil reaction to the loaded tapered pile segments had been presented by $V_s(z, t)$ and $V_r(z, t)$, that shear resistance per unit length of the pile shaft and horizontal reaction at the horizontal annular projections of the pile shaft, respectively. Parameters z and t represent depth and time in order as shown in Fig l.

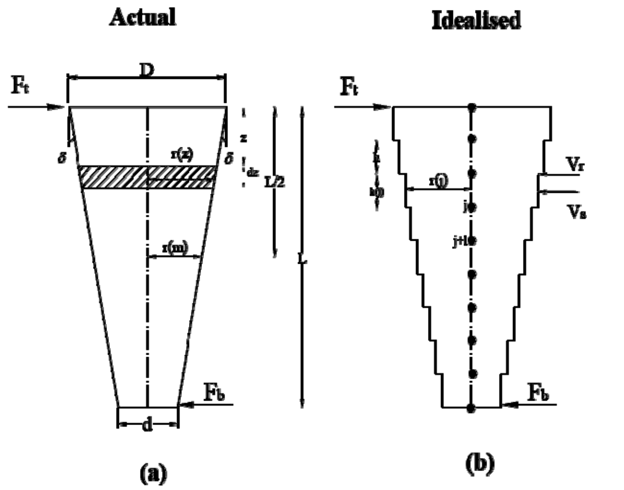

Fig.1 Idealization of tapered pile for dynamic analysis in laterally inhomogeneous media using segment by segment, (a) Actual pile; (b) Idealized pile

The soil response with time to motion of the pile toe, $F_b(t)$, is taken as that of a viscoelastic half – space to rigid, mass less, circular disc of radius r_b undergoing harmonic vibration. This can be expressed as:

$$F_b(t) = G_b r_b [C_{u_1}(a_{\circ b}, v, D) + iC_{u2}(a_{\circ b}, v, D)] u_b(t) \quad (1)$$

Where G_b is the soil shear modulus at the pile toe, C_{ul} , C_{u2} are dimensionless complex parameters given in the form of polynomial expressions (Veletsos and Vbric, [26]), $u_b(t)$ is the toe horizontal displacement, r_b is pile radius at the pile tip, $a_{\circ b} = \frac{r_b \omega}{V_b}$, where V_b is shear wave Velocity of soil below the tip, ω is circular frequency, v is Poisson's ratio, D is material damping.

The soil reaction on the pile is represented by springs and dashpots, which are modeled on elasto – dynamic theory. The interaction of the soil and the pile is then determined for each segment according to the characteristics of soil. This interaction can be demonstrated by a complex displacement, shear force, rotation and bending moment at the end of the adjacent segment. This procedure is performed from the lowest pile segment and extends to the next upper segment. This manner is continued to reach the topmost segment. That is why this procedure is called the SSM (Ghazavi [18-25]).

In the analysis, it is assumed that the soil reaction associated with a given soil layer is identical to that of an infinite rigid pile undergoing a uniform displacement of the same properties as the soil of that layer. This assumption is essential to the solution and will be examined subsequently using other, existing solutions. This assumption has also been used by other researcher [2]. In one dimensional finite element analysis of cylindrical piles under torsional vibrations, Novak and Howell also used the same assumption. A somewhat similar assumption was also made and by Mylonakis and Gazetas [30] for axially loaded cylindrical piles in a layered soil profile. It is note that Novak and Aboul – Ella used finite element method (FE) for analysis of piles embedded in inhomogeneous soil and subject to lateral harmonic vibrations. By considering the typical embedded segment j at depths, shown in Fig 1 and on the basis of the above assumption, the following governing dynamic differential equation of a soil – pile system subjected to harmonic lateral load can be obtained [1]:

$$m_{pj} \frac{\partial^2 u_j(z,t)}{\partial t^2} + C_{pj} \frac{\partial^2 u_j(z,t)}{\partial t} + E_{pj} I_{pj} \frac{\partial^4 u_j(z,t)}{\partial z^4} + G_{sj} S_{uj} u_j(z,t) = 0 \quad (2)$$

Where m_{pj} the pile mass per unit length, C_{pj} is the damping coefficient of the pile material, $E_{pj}I_{pj}$ is the bending stiffness of the pile segment j, G_{sj} is the shear modulus of the soil layer surrounding the pile segment j , u_j (z, t) is the local time – dependent complex amplitude at depth z from the top of segment j and S_{uj} is Complex dimensionless soil resistance parameter defined elsewhere [1] as a function of Poisson's ratio and dimensionless frequency, $a_{\circ j} = {r_{oj}\omega}/{V_{sj}}$

Here r_{oj} is the pile segment radius, ω is the circular frequency, and V_{sj} the shear Wave velocity of the soil surrounding the pile segment j.

The four terms in (2) represent the inertia force due to lumped mass of the pile, the damping force of pile material, the lateral interaction between pile segments, and the soil resistance, respectively. For harmonic vibration, the local displacement u_j (z, t) is given by:

$$u_j(z,t) = u_j(z)_e{}^{i\omega t} \quad (3)$$

Where $u_j(z)$ is the complex amplitude at depth z from the top of segment j and ω is the excitation frequency:

$$u_j(z) = u_{1j}(z) + iu_{2j}(z) \quad (4)$$

Combining (2) and (3) gives

$$E_{pj} I_{pj} \frac{\partial^4 u_j(z)}{\partial z^4} + u_j(z)[G_{sj} S_{u1} - m_{pj}\omega^2 + i(C_{pj}\omega + G_{sj} S_{u2})] = 0 \quad (5)$$

The above equation can be solved explicitly. The solution for the displacement at a point at vertical distance z below the upper node of segment j is given by:

$$u_j(z) = A_j Cosh(\zeta_j \frac{z}{h_j}) + B_j \sinh(\zeta_j \frac{z}{h_j}) + C_j \cos(\zeta_j \frac{z}{h_j}) + D_j \sin(\zeta_j \frac{z}{h_j}) \quad (6)$$

Where

$$\zeta_j = h_j \sqrt[4]{\frac{1}{E_{pj} I_{Pj}} [m_{pj}\omega^2 - G_{si} S_{uq} - i(C_{pj}\omega + G_{sj} S_{u2})]}$$

(7)

Where A_j, B_j, C_j and D_j are integration constants determined using appropriate boundary conditions.

If the displacement, rotation, shear force and bending moment transmitted by the pile at node 2 of segment j are know, the integration constants A_j, B_j, C_j and D_j can be calculated. Thus, the displacement, rotation, bending moment and shear force at node 1 of segment j are respectively given by (8a-8d).

3. PARAMETRIC STUDIES FOR PILE GEOMETRY EFFECT

In this section, four type of piles whit difference geometry under lateral harmonic load and have same length and volume had been studied and the results are compared. Properties of tapered piles and soil have presented in Table 1. All piles are 10m of length and there volumes are 1.36 m^3. Pile C is cylindrical. Pile T-C consists of a top tapered segment with 5m length and a lower cylindrical segment with 5m length. Pile C-T has top cylindrical part with 5m followed by a tapered part with 5m length. Pile T is tapered. Taper angles of piles are 0.5° and 1.5° that has been shown in Fig 2 and Table 2.

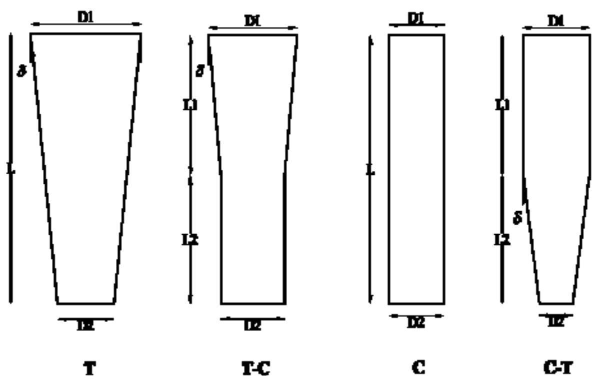

Fig. 2 Pile configurations

$$u_{j1} = \frac{V_{j2}h_j^3(\sinh\xi_j - \sin\xi_j) + \xi_j^2 E_{p_j} I_{p_j} \theta_{j2} h_j(\sinh\xi_j + \sin\xi_j) + \xi_j^3 E_{p_j} I_{p_j} u_{j2}(\cosh\xi_j + \cos\xi_j) + M_{j2}h_j^2\xi_j(\cos\xi_j - \cosh\xi_j)}{2E_{p_j} I_{p_j} \xi_j^3}$$

$$\theta_{j1} = \frac{V_{j2}h_j^3(\cos\xi_j - \cosh\xi_j) - \xi_j^2 E_{p_j} I_{p_j} \theta_{j2} h_j(\cosh\xi_j + \cos\xi_j) + \xi_j^3 E_{p_j} I_{p_j} u_{j2}(\sin\xi_j - \sinh\xi_j) + M_{j2}h_j^2\xi_j(\sinh\xi_j + \sin\xi_j)}{2E_{p_j} I_p \xi_j^2 h_j}$$

$$M_{j1} = \frac{V_{j2}h_j^3(\sinh\xi_j + \sin\xi_j) + \xi_j^2 E_{p_j} I_{p_j} \theta_{j2} h_j(\sinh\xi_j - \sin\xi_j) + \xi_j^3 E_{p_j} I_{p_j} u_{j2}(\cosh\xi_j - \cos\xi_j) - M_{j2}h_j^2\xi_j(\cosh\xi_j + \cos\xi_j)}{-2\xi_j h_j^2}$$

$$V_{j1} = \frac{-V_{j2}h_j^3(\cosh\xi_j + \cos\xi_j) - \xi_j^2 E_{p_j} I_{p_j} \theta_{j2} h_j(\cosh\xi_j - \cos\xi_j) - \xi_j^3 E_p I_p u_{j2}(\sinh\xi_j + \sin\xi_j) + M_{j2}h_j^2\xi_j(\sinh\xi_j - \sin\xi_j)}{-2h_j^3}$$

(8a)- (8d)

Table1. Properties of tapered piles and soil

Radius of equivalent circular pile, r_{eq} *	0.208 m
Shear wave velocity in soil, V_s	84m/s
Soil Poisson's ratio, ν_s	0.45
Soil unit weight, γ_s	17.5 kN/m^3
Pile modulus of elasticity, E_p	1.962×10^7 kN/m^2
Soil modulus of elasticity, E_s	3.58×10^4 kN/m^2
Pile unit weight, γ_p	25 kN/m^3

(* r_{eq} is radius of cylindrical pile of the same volume and length as tapered pile)

Table2. Dimension of tapered piles for Fig 3.

Piles	Taper Angle	$\delta = 0.5^\circ$				$\delta = 1.5^\circ$			
T		L=10m		D_1=0.5m	D_2=0.326m	L=10m		D_1=0.65m	D_2=0.126m
C		L=10m		D_1=0.416m	D_2=0.416m	L=10m		D_1=0.416 m	D_2=0.416m
TC		L_1=5 m	L_2=5 m	D_1=0.48m	D_2=0.393m	L_1=5 m	L_2=5 m	D_1=0.603m	D_2=0.342m
CT		L_1=5 m	L_2=5 m	D_1=0.4369 m	D_2=0.3497 m	L_1=5 m	L_2=5 m	D_1=0.4729 m	D_2=0.2111 m

SSM was applied with assumption pinned–ended for all of above piles and Fig. 2 illustrate the dimensionless amplitude lateral versus the excitation frequency for piles with taper angles $\delta = 0.5^\circ$ that results have been shown in Fig. 3 the T pile have the least lateral and rotary response amplitude and after T Pile. There are T –C, C-T and C respectively**.**

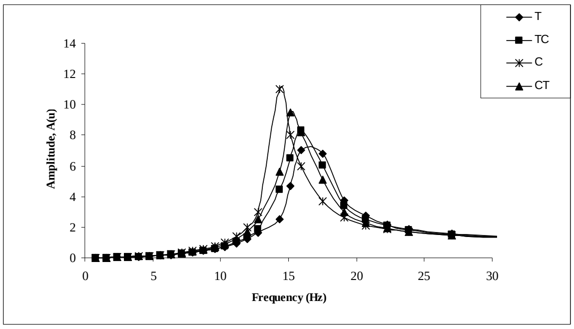

Fig. 3 Variation of lateral dimensionless amplitude versus frequency for T pile ($\delta = 0.5^\circ$)

It is noted that in the C piles, the resulted values of are exactly the same as those reported by Novak [1].
In Fig. 4, the dimensionless amplitude lateral versus the excitation frequency had been compared based on taper angle in T pile and observed with increasing taper pile, dimensionless response amplitudes will decrease.

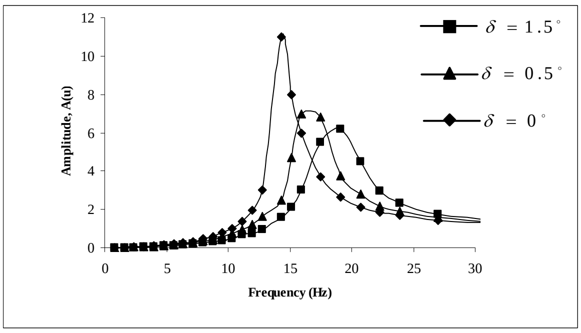

Fig. 4. Comparison variation of lateral dimensionless amplitude versus frequency for T pile according to taper angle

5. CONCLUSION

A simple approach, called SSM, has been presented in this paper for determination of stiffness and damping parameters of laterally loaded tapered piles subjected to harmonic vibrations. The soil-pile interaction in this method is modeled within each segment and applied via the segment nodes to the analysis of the adjacent segment. Therefore, the stiffness and damping parameters for the whole pile-soil system are determined. According to results SSM, T, TC, CT and C piles respectively have the least lateral and rotary response amplitude and observed that for tapered piles of the same volume and length under lateral harmonic vibrations, with increasing the taper angle, the resonant frequency increases slightly. However, the reduction of the amplitude is more pronounced.
The SSM is an efficient and simple method for analysis of tapered piles under harmonic vibration. In particular, the effects of the soil in homogeneity in the vertical direction even with complicated stratifications can be easily captured. This method involves less computational work than available numerical method based on the FE.

6. REFERENCES

[1] Novak, M. (1974): Dynamic stiffness and damping of piles, Canadian Geotechnical Journal, Vol. 11, No. 4, 574-598.

[2] Novak, M. and Aboul-Ella, F. (1978): Impedance functions of piles in layered media, Journal of Geotechnical Engineering Division ASCE, Vol. 104, No. 6, 643-661.

[3] Novak, M. and Nogami, T. (1980): Coefficients of soil reaction to pile vibration, Journal of Geotechnical Engineering Division ASCE, Vol. 106, No. 5, 565-570.

[4] Kaynia, A.M. and Kausel, E. (1982): Dynamic behaviour of pile groups, Proceedings 2nd International Conference on Numerical Methods in Offshore Piling, Austin, Texas, 509-532.

[5] Sen, R., Kausel, E., and Banerjee, P.K. (1985): Dynamic analysis of pile groups embedded in non-homogeneous soils, International Journal for Numerical and Analytical Methods in Geomechanics, Vol. 9, No. 6, 507-524.

[6] Penzien, J. (1975): Soil-pile interaction. Earthquake Engineering, R.L. Wiegel, ed., Prentice Hall Inc., Englewood Cliffs, N.J. 349-381.

[7] Blaney, G.W., Kausel, E., and Roesset, J.M. (1976): Dynamic stiffness of piles, *Proceedings 2nd International Conference on Numerical Methods in Geomechanics,* Blacksburg, Virginia, 1001-1012

[8] Wolf, J.P. and von Arx, G.A. (1982): Horizontally travelling waves in a group of piles taking pile-soil-pile interaction into account, International Journal of Earthquake Engineering and Structural Dynamics, Vol. 10, 225-237.

[9] Chow,Y.K. (1985): Dynamic response of axially loaded piled foundations, Proceedings 5th International Conference on Numerical Methods in Geomechanics, Nagoya, Japan, 1485-1492.

[10] Baranov, V.A., (1967): On the calculation of an embedded foundation, (in Russian), Voprosy Dinamiki Prochnosti, Polytechnical Institute of Riga, No. 14, 195-209

[11] Saha, S. and Ghosh, D.P. (1986): Vertical vibration of tapered piles, Journal of Geotechnical Engineering, ASCE, vol. 112, No. 3, 290-301.

[12] Xie, J., and Vaziri, H.H. (1991): Vertical vibration of nonuniform piles, Journal of Geotechnical Engineering ASCE, Vol. 117, No. 5, 1105-1118.

[13] Kurian, N.P. and Srivinas, M.S. (1995): Studies on the behavior of axially loaded tapered piles by the finite element method, International Journal of Numerical and Analytical Methods in Geomechanics, Vol. 19, 869-888.

[14] El Naggar, H. and Sakr, M. (2000): Evaluation of axial performance of tapered piles from centrifuge tests, Canadian Geotechnical Journal, Vol, 37, 1295-1308.

[15] Zil'berberg, S. D., and Sherstnev, A. D. (1990):Construction of compaction tapered pile foundations (from the experience of the "Valdespetsstroi" Trust), Soil Mechanic and Foundation Engineering, 27(3), 96-101.

[16] El Naggar, H. and Wei, J.Q. (1999): Response of tapered piles subjected to lateral loading, Canadian Geotechnical Journal, Vol, 36, 52-71.

[17] El Naggar, H. and Wei, J.Q. (1998): Experimental study of axial behaviour of tapered piles, Canadian Geotechnical Journal, Vol, 35, 641-654.

[18] Ghazavi, M., Williams, D. J., and Wong, K.Y. (1996): Analysis of a tapered pile during pile driving, Proceedings 2nd International Conference on Multi - Purpose High-Rise Towers and Tall Buildings, Singapore, 87-94.

[19] Ghazavi, M. and Tavassoli, O., (2008): Numerical Analysis for Pile Geometry Effect on Drivability. Proceedings of the 8th International Conference on the Application of Stress Wave Theory to Piles, Lisbon, Portugal, pp. 271- 276.

[20] Ghazavi, M., (2007): Analysis of Kinematic Seismic Response of Tapered Piles. Geotechnical and Geological Engineering, an International Journal, vol. 25, No. 1, 37-44**.**

[21] Ghazavi, M., Response of Tapered Piles to Axial Harmonic Loading. Canadian Geotechnical Journal, in press

[22] Ghazavi, M., Williams, D. J., and Morris, P.H. (1997a): Analysis of axially loaded piles embedded in layered deposits, Proceedings 2nd International Conference on the Application of Numerical Methods in Engineering, Universiti Pertanian Malaysia, Selangor, Malaysia, 335-344.

[23] Ghazavi, M., Wiiliams, D.J., and Morris, P.H. (1997b): Analysis of piles subjected to uplift loads, Proceedings 2nd International Symposium on Structures and Foundations in Civil Engineering, Hong Kong, 177-183.

[24] Ghazavi, M. (2002): Vertical vibration of deep foundations in layered deposits, Proceedings of Iranian Third International Seminar on Soil Mechanics and Geotechnical Engineering (ISSMGE), Tehran, Iran, Vol. I, 223-228.

[25] Ghazavi ,M., Dehghanpour, A., “Dynamic Analysis of Piles under Lateral Harmonic Vibration”. Fifth International Conference on Recent Advances in Geotechnical Earthquake Engineering and Soil Dynamics, May 24-29, 2010; San Diego, California, USA.

[26] Veletsos, A.S., and Verbic, B., (1973): Vibration of Viscoelastic Foundations. Earthquake Engineering and Structural Dynamics, Vol 2, No. 1, 87-102

First International Conference on Geotechnique, Construction Materials and Environment, Mie, Japan, Nov.21-23, 2011, ISBN: 978-4-9905958-0-7 C3051

Investigation of Ground Movement in Soil-nailed Walls Using 1g Models and PIV Method

H. Mahdavi and M. Hajialilue-Bonab, Civil Engineering Department, University of Tabriz

ABSTRACT: Soil nailing due to its unique advantages has gained great popularity in recent years. In urban areas, the impact of the created excavation on the surrounding structures and utilities is of great consequence. This paper is mainly focused on the investigation of the ground movements in soil-nailed walls. 1g models were constructed to study the impact of nail inclination on the movements induced by the excavation. Despite the limited use of 1g models owing to some similarity problems, they can provide valuable results with low costs. An intermediate method was used to simulate the excavation process and images were captured during this process. Then the captured images were analyzed using particle image velocimetry (PIV) method. The results provide a better understanding of the deformations in the soil-nailed walls.

Keywords: nail inclination, physical modeling, PIV, soil nailing

1. INTRODUCTION

In recent years, due to an increase in urban construction there seems a necessity to create deep excavations to build new structures. Experience shows when the importance of the impact of the ground movements resulted from the created excavation on the adjacent structures is underestimated, great costs have been inflicted upon engineers. Soil nailing, due to its rapid construction and competitive costs, has gained great popularity in recent years. Ground movements induced by soil nailed excavations are relatively large compared to other retaining structures; however, this could be somewhat controlled using the optimum layout of the nails. This research was done to find the optimum layout for the nails. As discussed in Clouterre (1993) [1], the nails are more efficient at controlling lateral displacements of the structure when there is no inclination. A numerical study on the optimum layout of soil-nailed slopes was conducted by Fan and Luo (2008) [2]. Effect of nail orientation and geometric layout on the overall stability of soil–nailed slopes with various geometric conditions was investigated using a non-linear finite element approach. Stability of soil–nailed slopes was evaluated in terms of factor of safety. They found the horizontal placement of the nails to be the optimal nail orientation for slope angle of 90˚. The effect of the nail skew angle of soil nailing wall was investigated by Bang and Chung (1999) [3]. They developed a finite element method of analysis utilizing the generalized plane strain approach to analyze three dimensional stress, strains, and displacements. Shafiee (1986) [4] used finite element method to investigate the impact of the nail inclination on soil-nailed wall deformation. He concluded that the horizontal placement of the nail leads to a smaller deformation than the inclined nails. Experimental studies conducted by Marchal (1984) [5] showed that the direction of the nails with respect to the potential failure surface plays a role in the mobilization of tension and shear. Jewell (1980) [6], [1] experimentally verified that the optimum direction for the mobilization of tension in the flexible nails is approximately 30˚ in relation to the normal at the shear surface. The above mentioned list of the studies just gives a brief account of the conducted research and is not complete for the sake of succinctness. This paper is focused on the investigation of the effect of the nail inclination on the movements of the soil behind the soil-nailed wall. 1g models were constructed to study this issue and particle image velocimetry (PIV) method was employed to further investigate its behavior. PIV is an image analysis technique developed by D. J. White and W.A. Take in Cambridge [7]

2. MODEL PREPARATION

The dimensions of the box used for the tests were 100×60×30cm. It was made of steel plates with the thickness of 3mm and stiffeners were used to minimize its deformation under the applied stresses. The box had a side made of plexiglass with a thickness of 3cm so that the model deformation could be monitored during the tests. Another plate of plexiglass was glued onto the opposite side of the plexiglass side in order to create symmetrical models and to reduce the sidewall friction. Dry sand was used to construct the models. The properties of sand are presented in Table I. The dry sand was pluviated using a special perforated container to construct uniform and repeatable models. Nails were made of rods with the diameter of 3mm.The end part of these rods were threaded using a threading die in order to use nuts to fix the nails on the facing. A uniform layer of sand was glued onto the nails to create rough nails which increased the diameter to 4mm. Hard facing was used in this research. It was made of an aluminum plate with the thickness of 1.5mm, and width and height of 30cm each. Since there is a good connection between the shotcrete and the facing in prototype walls, another uniform layer of sand was glued onto the inner surface of this plate and a rough surface was created. The thickness of the facing increased to 2mm after the sand was glued. The layout of nails is shown in Fig.1. Thirteen nails were used in the models.

Table I. Properties of the used sand

Φ	G_S	C_C	C_U	γ_{dmin}	γ_{dmax}
28˚	2.637	0.87	1.36	14.20 KN/m^3	16.76 KN/m^3

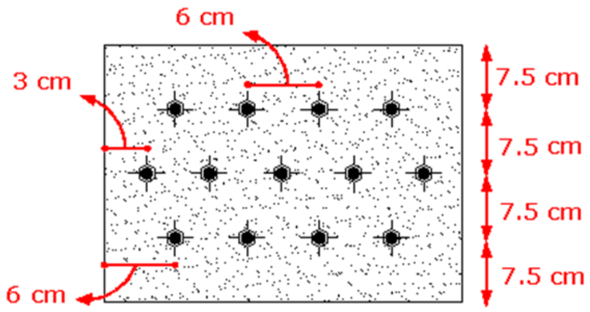

Fig. 1. The layout of the nails and the dimensions of the facing

3. TESTING PROCEDURE

The first stage of the model construction involved pluviating the dry sand from a special perforated container, which was held approximately 50cm above the test box to gain uniformity. When an appropriate height was achieved, the facing was placed in the box. Then the pluviating process continued in both sides of the facing until the first row of the nails was reached. Then the nails were placed with the intended inclinations. In the next step, sand pouring was resumed on both sides of the facing and the model construction was completed. In order to model the construction process of soil-nailed wall, the fill on the front side of the facing was excavated to model the top down construction phases of the wall. The excavation was conducted in 8 stages using vacuum in the vicinity of the wall to prevent any disturbance. Images were captured using a Canon PowerShot G10 camera with the resolution of 14.1 megapixels and a CCD sensor. Remote Capture software and a PC were used to capture the images in order not to disturb the camera during the test. Two 1000W lamps were used to illuminate the models during the production of images. Figs. 2 and 3 show how the excavation process is modeled.

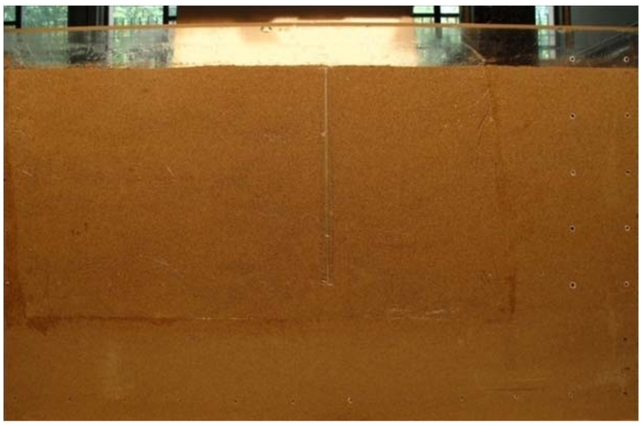

Fig. 2. A completed model

Fig. 3. Excavation of soil in front of the soil-nailed wall

4. RESULTS OF THE 1G TESTS

The details for the conducted tests and the schematic diagrams for them are presented in Table II. Five models were constructed using different nail inclinations and all the other variables (such as S_v, S_h, nail length, back slope…) were considered to be control variables.

Table II. Details of the tests

Test No.	Nail Inclination	Nail Length	Test Configuration
1	0°	30 cm	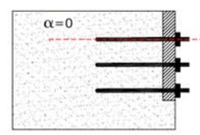
2	10°	30 cm	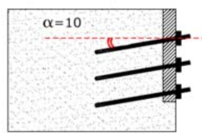
3	20°	30 cm	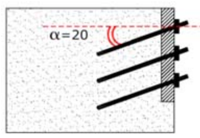
4	30°	30 cm	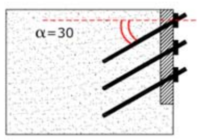
5	40°	30 cm	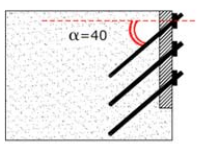

GeoPIV [8], [9] and Matlab software programs were used to analyze the captured images and to calculate the displacement vectors and shear strains in the soil behind the soil-nailed wall. In Figs. 4-7, both x and y axes are normalized to the wall height (H), and the origin is assumed to be the wall toe ($\frac{X}{H}$=0, $\frac{Y}{H}$=0). As shown in Figs. 4-7, the displacement vectors increase with increasing nail inclination. The reason for this could be explained in terms of tensile force in the nails. As the inclination of the nails increases, the tensile force in the nails decreases; therefore, the overall shear strength of the slope decreases [6]. The displacement observed in the test with the nail inclination of 40˚ was large and caused wild vectors in the results. The comparison of displacements for different cases is presented in Fig. 8. The displacement of wall top is chosen for this comparison.

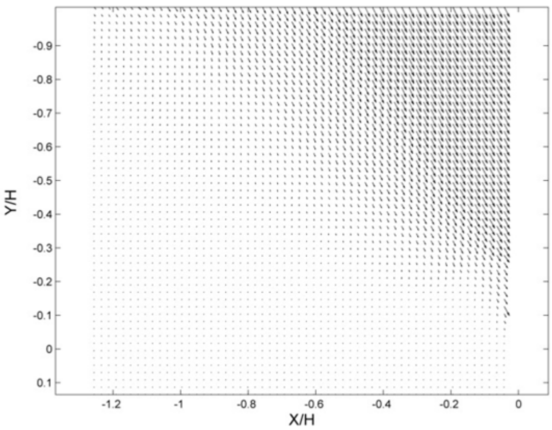

Fig. 4. Displacement vectors for nail inclination of 0˚

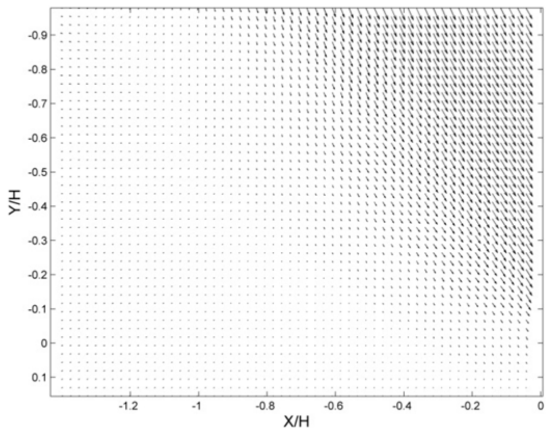

Fig. 5. Displacement vectors for nail inclination of 10˚

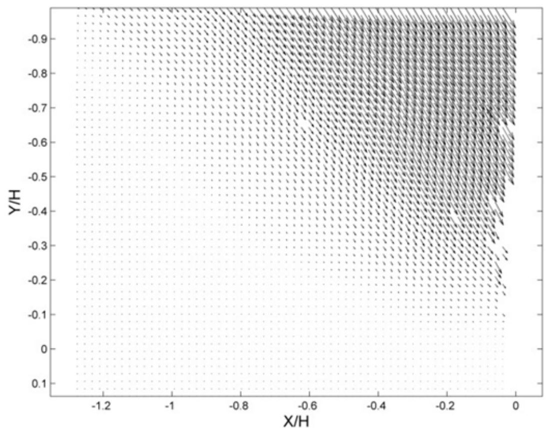

Fig. 6. Displacement vectors for nail inclination of 20˚

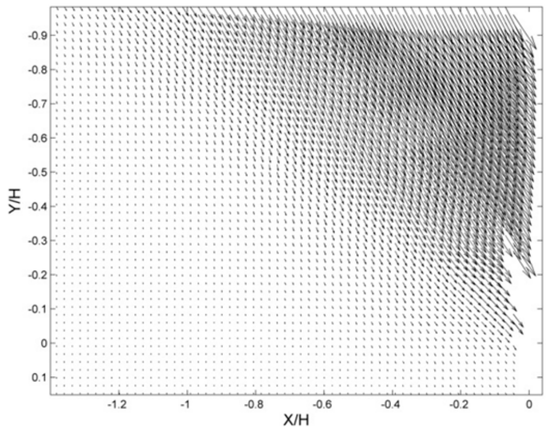

Fig. 7. Displacement vectors for nail inclination of 30˚

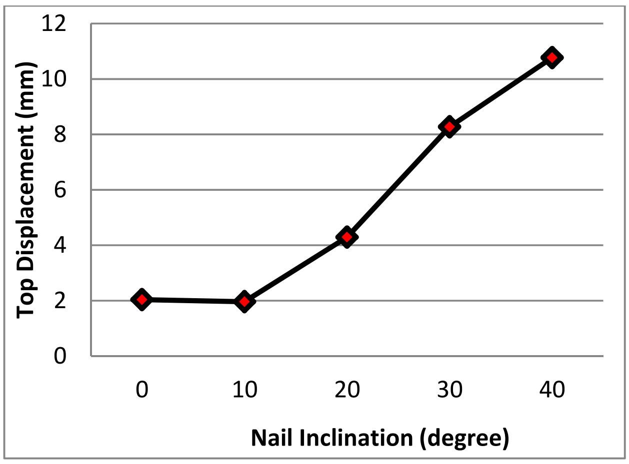

Fig. 8. Wall top displacements for different nail inclinations

In Figs. 9-12, the maps for shear strains are presented. Strain maps give a better view of the shear bands formed in the soil mass. The red color denotes large deformations and the blue color is assigned to zero strains. Same strain ranges (0-0.5) were chosen for all the diagrams in order to make a comparison between different tests. It can be clearly seen that with the inclination of the nails increasing, the movement of the soil increases i.e. the red colored area gets bigger.

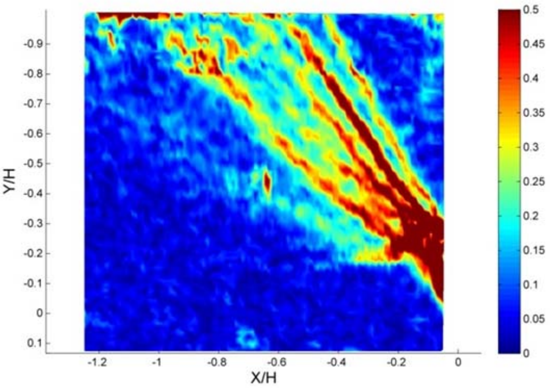

Fig. 9. Shear strains for nail inclination of 0˚

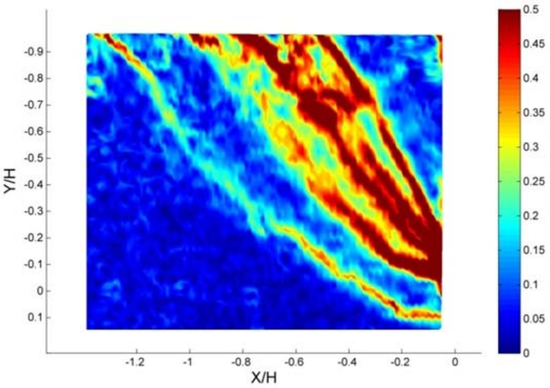

Fig. 10. Shear strains for nail inclination of 10˚

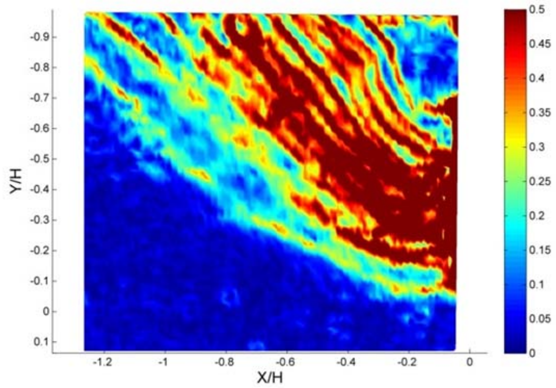

Fig. 11. Shear strains for nail inclination of 20˚

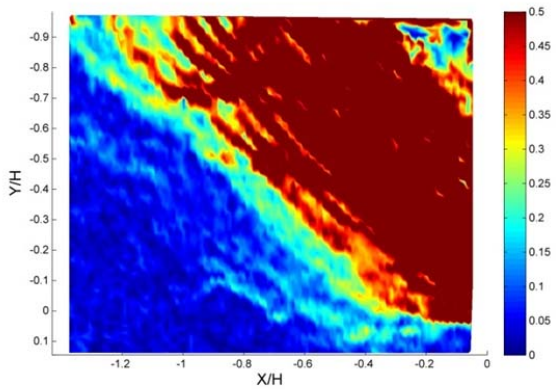

Fig. 12. Shear strains for nail inclination of 30˚

The other important issue is the interesting pattern of multiple shear bands formed in the nailed mass. Using Matlab Image Processing Toolbox and Curve Fitting Toolbox the shape of these shear bands were determined as parabolic. In Figs. 13-16, the parabolic shear band and its formula are presented. It is worth mentioning that the axes and the presented formula are in pixels.

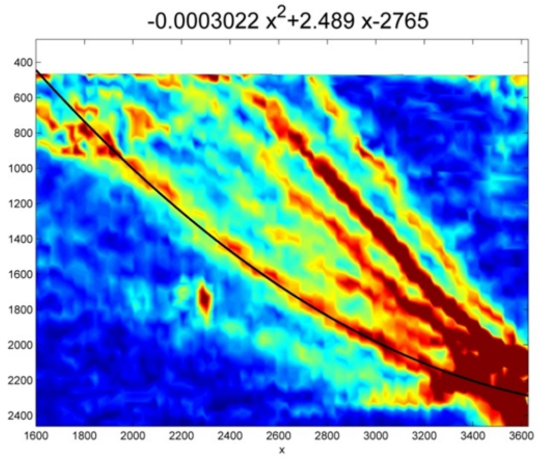

Fig. 13. Parabolic shape of the shear band, nail inclination=0˚

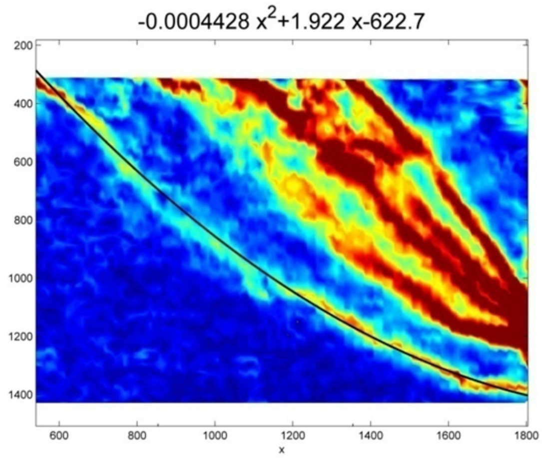

Fig. 14. Parabolic shape of the shear band, nail inclination=10˚

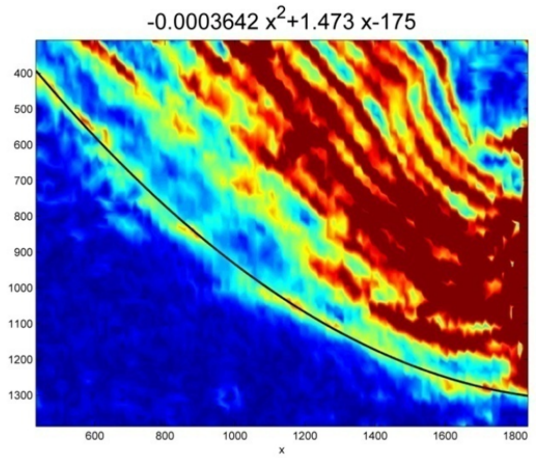

Fig. 15. Parabolic shape of the shear band, nail inclination=20˚

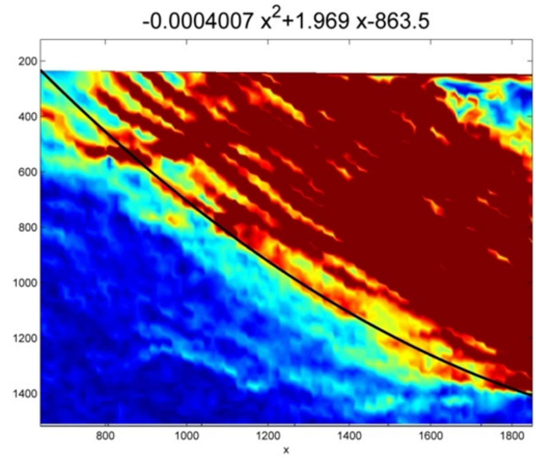

Fig. 16. Parabolic shape of the shear band, nail inclination=30˚

5. CONCLUSIONS

A number of conclusions can be drawn from the 1g tests conducted in this research. The results are summarized as follows,

- Displacement vectors increase with increasing nail inclination

- Shear strains in the retained soil behind the wall increase with increasing nail inclination

- The shear bands formed behind the nailed-wall with parabolic shape

6. REFERENCES

[1] CLOUTERRE, "Recommandations CLOUTERRE 1991 - Soil Nailing Recommendations 1991," English Translation, 1993.

[2] C-C Fan and J-H. Luo, "Numerical study on the optimum layout of soil-nailed slopes," Computers and Geotechnics 35, 2008, pp. 585-599.

[3] S.C. Bang and Y.I. Chung, "The effect of the Nail Skew Angle of Soil Nailing Wall," KSCE Journal of Civil Engineering, Vol. 3, No. 1, 1999, pp. 73-79.

[4] Shafiee S., "Simulation nume´rique du comportement des sols cloue´s. Interaction sol reinforcement et comportementde l'ouvrage," The`se de Doctorat de l'Ecole Nationale des Ponts et Chausse´es, Paris, France; 1986.[In French]

[5] Marchal J., "Reinforcement des sols par clouage. E´ tude expe´rimentale en laboratoire," In Proceedings of International Conference In Situ Soil and Rock Reinforcement, Paris; 1984, pp. 275–8. [In French]

[6] Jewell RA., "Some effects of reinforcement on the mechanical behavior of soils," Doctor of Philosophy Thesis, Cambridge University, 1980.

[7] White, D. J., Take, W. A., and Bolton, M. D., "Soil deformation measurement using particle image velocimetry (PIV) and photogrammetry," *Geotechnique* 53, No. 7, 2003, pp. 619–631.

[8] White, D. J., Randolph, M., and Thompson, B., "An image-based deformation measurement system for the geotechnical centrifuge," *Int. J. Phys. Modell. Geotech.* 3, 2005, pp. 1–12.

[9] White, D. J., and Take, W. A.. "GeoPIV: Particle Image Velocimetry (PIV) software for use in geotechnical testing," *Rep. No. D-SOILS-TR322*, Cambridge Univ, 2002.

ISBN978-4-9905-9580-7
C3051 ¥21000E

9784990595807

定価（本体21000＋税）

1923051210008

- The “International Journal of GEOMATE” is a Scientific Journal the GEOMATE International Society that encompasses a broad area in Geotechnique, Construction Materials and Environment.
- The key objective of this journal is to promote interdisciplinary research from various regions of the globe.
- The editorial board of the journal is comprised of extensively qualified researchers, academicians, scientists from Japan and other countries of the world.
- It is peer-reviewed journal that is published quarterly. All articles published in this journal are available on line.
- For more details, please visit: http://www.gi-j.com/